IntechOpen

Effective and Sustainable Hydraulic Fracturing

Edited by Andrew P. Bunger, John McLennan and Rob Jeffrey

EFFECTIVE AND SUSTAINABLE HYDRAULIC FRACTURING

Edited by **Andrew P. Bunger, John McLennan** and **Rob Jeffrey**

Effective and Sustainable Hydraulic Fracturing
http://dx.doi.org/10.5772/45724
Edited by Andrew P. Bunger, John McLennan and Rob Jeffrey

Contributors

Mike Vincent, Xi Zhang, Rob Jeffrey, Safdar Abbas, Brice Lecampion, Xiaoxi Men, Chun'An Tang, Shanyong Wang, Y.P. Li, Tao Yang, Tianhui Ma, Norman Warpinski, Dimitry Chuprakov, Olga Yurievna Melchaeva, Romain Prioul, Alexander Linkov, Gennady Mishuris, Nikolai Weber, Bisheng Wu, Neda Zangeneh, Nima Gholizadeh Doonechaly, Sheik Rahman, Andrei Kotousov, Michael Molenda, Sebastian Brenne, Ferdinand Stoeckhert, Michael Alber, Sergey Turuntaev, Evgeny Zenchenko, Branko Damjanac, James Kear, Justine White, Andrew Bunger, Mir-Akbar Hessami, Mao Bai, Arturo Diaz, John Mclennan, Juan Reyna, Tsuey Cham, Peter Stone, Lucas W Bazan, Bruce R Meyer, Olga Kresse, Xiaowei Weng, Charles Cohen, Charles Fairhurst, Azadeh Riahi, Anthony Peirce, Emmanuel Detournay, Zuorong Chen, Christine Detournay, Dmitry Garagash, Sau-Wai Wong, Mikhail Geilikman, Guanshui Xu, Arcady Dyskin, Hyunil Jo, Robert Hurt, Yevhen Kovalyshen, Ian Walton, Jacob Bradford, Walter Glauser, Erfan Sarvaramini, Marte Gutierrez, Feng Gui, Neal Nagel, Fengshou Zhang, Marisela Sanchez-Nagel, Byungtark Lee, Xavier Garcia, Reinhard Jung, S. Sengupta, Arshad Islam, Antonin Settari, Reza Keshavarzi, Clem Rowe, Joel Adams, Arash Dahi Taleghani, Jon Olson, Mirko Van Der Baan, Peter K. Kaiser, Benoit Valley, Damien Duff, Maurice B. Dusseault, Varahanaresh Sesetty, Ahmad Ghassemi, Milind Deo, Farrokh Sheibani, Carl T. Montgomery, Barry Goldstein, G. Steyl

Notice

First published in Croatia, 2013 by INTECH d.o.o.
eBook (PDF) Published by IN TECH d.o.o.
Place and year of publication of eBook (PDF): Rijeka, 2019.
IntechOpen is the global imprint of IN TECH d.o.o.
Printed in Croatia

Legal deposit, Croatia: National and University Library in Zagreb

Additional hard and PDF copies can be obtained from orders@intechopen.com

Effective and Sustainable Hydraulic Fracturing
Edited by Andrew P. Bunger, John McLennan and Rob Jeffrey

p. cm.

ISBN 978-953-51-1137-5

eBook (PDF) ISBN 978-953-51-6341-1

Meet the editors

Andrew Bunger is an Assistant Professor in the University of Pittsburgh's Department of Civil and Environmental Engineering. He recently joined the University of Pittsburgh after spending 10 years in Melbourne, Australia working in the Geomechanics Group within the Commonwealth Scientific and Industrial Research Organisation (CSIRO). His research interests include the mechanics of hydraulic fractures, coupled fluid-shale interaction, and the emplacement dynamics of magma-driven dykes and sills. He holds a PhD in Geological Engineering from the University of Minnesota.

Since October 2009, John McLennan has been a USTAR Associate Professor in the Department of Chemical Engineering at the University of Utah. He has been a Senior Research Scientist at the Energy & Geoscience Institute and a Research Professor in the Department of Civil Engineering at the University of Utah, since January 2008. He has a Ph.D. in Civil Engineering from the University of Toronto, in 1980. He has thirty years of experience with petroleum service and technology companies. He worked nine years for Dowell and Dowell Schlumberger in their Denver, Tulsa and Houston facilities. Later, John was with TerraTek in Salt Lake City, Advantek International, in Houston, and ASRC Energy Services in Anchorage. He has worked on projects concerned with subsurface energy recovery in a variety of reservoir environments, in domestic and international settings.

Prior to joining CSIRO in 1989, Rob Jeffrey worked for Dowell Schlumberger, working on hydraulic fracturing and specifically fracturing of coalbed methane wells. He continued with this research interest at CSIRO and has run a range of projects investigating hydraulic fracture mechanics in coal and in naturally fractured orebodies. Rob was instrumental in introducing hydraulic fracturing to the mining industry for cave inducement and preconditioning of rock masses and this technology is now being used at mines in Australia and Chile. He is an expert on hydraulic fracture growth in naturally fractured rock as applied to oil and gas stimulations, preconditioning of mining orebodies and hot fractured rock reservoirs.

Contents

Preface XVII

Section 1 Keynote Lectures 1

Chapter 1 **Fracturing Fluids 3**
Carl Montgomery

Chapter 2 **Fracturing Fluid Components 25**
Carl Montgomery

Chapter 3 **Fractures and Fracturing: Hydraulic Fracturing in Jointed Rock 47**
Charles Fairhurst

Chapter 4 **Five Things You Didn't Want to Know about Hydraulic Fractures 81**
Vincent M. C.

Chapter 5 **EGS — Goodbye or Back to the Future 95**
Reinhard Jung

Chapter 6 **Understanding Hydraulic Fracture Growth, Effectiveness, and Safety Through Microseismic Monitoring 123**
Norm R. Warpinski

Section 2 Naturally Fractured Reservoirs 1 137

Chapter 7 **Development of Fracture Networks Through Hydraulic Fracture Growth in Naturally Fractured Reservoirs 139**
Xi Zhang and Rob Jeffrey

Chapter 8 **Hydraulic Fracture Propagation Across a Weak Discontinuity Controlled by Fluid Injection 157**
Dimitry Chuprakov, Olga Melchaeva and Romain Prioul

Chapter 9 **Effect of Flow Rate and Viscosity on Complex Fracture Development in UFM Model 183**
Olga Kresse, Xiaowei Weng, Dimitry Chuprakov, Romain Prioul and Charles Cohen

Section 3 Regulations, Risks, and Communities 211

Chapter 10 **Hydrochemical and Hydrogeological Impact of Hydraulic Fracturing in the Karoo, South Africa 213**
G. Steyl and G. J. van Tonder

Chapter 11 **Regulatory Nirvana for Hydraulic Fracture Stimulation 239**
Barry Goldstein, Michael Malavazos, Alexandra Wickham, Michael Jarosz, Dominic Pepicelli, Mieka Webb and Dale Wenham

Chapter 12 **How Can Understanding Community Concerns About Hydraulic Fracturing Help to Address Them? 257**
S.T. Cham and P. Stone

Section 4 Naturally Fractured Reservoirs 2 269

Chapter 13 **Numerical Study of Interaction Between Hydraulic Fracture and Discrete Fracture Network 271**
Azadeh Riahi and Branko Damjanac

Chapter 14 **Hydraulic Fracturing in Formations with Permeable Natural Fractures 287**
Olga Kresse and Xiaowei Weng

Chapter 15 **Injection Modeling and Shear Failure Predictions in Tight Gas Sands — A Coupled Geomechanical Simulation Approach 311**
Arshad Islam and Antonin Settari

Chapter 16 **The Role of Natural Fractures in Shale Gas Production 327**
Ian Walton and John McLennan

Section 5 Well Completions and Fracture Initiation 1 357

Chapter 17 **Do Perforated Completions Have Value for Engineered Geothermal Systems 359**
Walter Glauser, John McLennan and Ian Walton

Chapter 18 **Differentiating Applications of Hydraulic Fracturing 391**
Joel Adams and Clem Rowe

Chapter 19 **Initiation and Breakdown of an Axisymmetric Hydraulic Fracture Transverse to a Horizontal Wellbore 401**
Safdar Abbas and Brice Lecampion

Chapter 20 **Hydraulic and Sleeve Fracturing Laboratory Experiments on 6 Rock Types 425**
Sebastian Brenne, Michael Molenda, Ferdinand Stöckhert and Michael Alber

Section 6 Induced Seismicity and Slip 437

Chapter 21 **Microseismic Monitoring Developments in Hydraulic Fracture Stimulation 439**
Mirko van der Baan, David Eaton and Maurice Dusseault

Chapter 22 **Blue Shift in the Spectrum of Arrival Times of Acoustic Signals Emitted during Laboratory Hydraulic Fracturing 467**
Arcady V. Dyskin, Elena Pasternak, Andrew P. Bunger and James Kear

Chapter 23 **A Numerical Investigation of Fault Slip Triggered by Hydraulic Fracturing 477**
Neda Zangeneh, Erik Eberhardt, R. Marc Bustin and Amanda Bustin

Section 7 Well Completions and Fracture Initiation 2 489

Chapter 24 **Numerical Simulation of Hydraulic Fracturing in Heterogeneous Rock: The Effect of Perforation Angles and Bedding Plane on Hydraulic Fractures Evolutions 491**
Xiaoxi Men, Chun'an Tang, Shanyong Wang, Yongping Li, Tao Yang and Tianhui Ma

Chapter 25 **Quantitative Evaluation of Completion Techniques on Influencing Shale Fracture 'Complexity' 513**
N. Nagel, F. Zhang, M. Sanchez-Nagel and B. Lee

Section 8 Flow Paths and Flow Networks 547

Chapter 26 **Modeling of Proppant Permeability and Inertial Factor for Fluid Flow Through Packed Columns 549**
Bruce R. Meyer, Lucas W. Bazan and Doug Walls

Chapter 27 **A New Approach to Hydraulic Stimulation of Geothermal Reservoirs by Roughness Induced Fracture Opening 571**
Nima Gholizadeh Doonechaly, Sheik S. Rahman and Andrei Kotousov

Chapter 28 **Fracture Network Connectivity — A Key To Hydraulic Fracturing Effectiveness and Microseismicity Generation 591**
F. Zhang, N. Nagel, B. Lee and M. Sanchez-Nagel

Section 9 Multiscale Modeling 605

Chapter 29 **Fluid-Driven Fracture in a Poroelastic Rock 607**
Yevhen Kovalyshen and Emmanuel Detournay

Chapter 30 **Pressurization of a PKN Fracture in a Permeable Rock During Injection of a Low Viscosity Fluid 629**
Erfan Sarvaramini and Dmitry I. Garagash

Chapter 31 **Modified Formulation, ε-Regularization and the Efficient Solution of Hydraulic Fracture Problems 641**
Alexander M. Linkov and Gennady Mishuris

Section 10 Mulitiple Hydraulic Fracture Growth 659

Chapter 32 **The Geomechanical Interaction of Multiple Hydraulic Fractures in Horizontal Wells 661**
Sau-Wai Wong, Mikhail Geilikman and Guanshui Xu

Chapter 33 **Numerical Simulation of Sequential and Simultaneous Hydraulic Fracturing 679**
Varahanaresh Sesetty and Ahmad Ghassemi

Chapter 34 **Three Dimensional Forms of Closely-Spaced Hydraulic Fractures 693**
James Kear, Justine White, Andrew P. Bunger, Rob Jeffrey and Mir-Akbar Hessami

Section 11 Numerical Modeling 1 709

Chapter 35 **The XFEM With An Explicit-Implicit Crack Description For Hydraulic Fracture Problems 711**
N. Weber, P. Siebert, K. Willbrand, M. Feinendegen, C. Clauser and T. P. Fries

Chapter 36 **An ABAQUS Implementation of the XFEM for Hydraulic Fracture Problems 725**
Zuorong Chen

Chapter 37 **Stress Intensity Factor Determination for Three-Dimensional Crack Using the Displacement Discontinuity Method with Applications to Hydraulic Fracture Height Growth and Non-Planar Propagation Paths 741**
Farrokh Sheibani and Jon Olson

Section 12 Injection and Efficiency 771

Chapter 38 **Secondary Fractures and Their Potential Impacts on Hydraulic Fractures Efficiency 773**
Arash Dahi Taleghani, Milad Ahmadi and J.E. Olson

Chapter 39 **Importance of Fracture Closure to Cuttings Injection Efficiency 793**
Mao Bai, Arturo Diaz, John McLennan and Juan Reyna

Chapter 40 **The Fate of Injected Water in Shale Formations 807**
Hongtao Jia, John McLennan and Milind Deo

Section 13 Numerical Modeling 2 817

Chapter 41 **Three-Dimensional Numerical Model of Hydraulic Fracturing in Fractured Rock Masses 819**
B. Damjanac, C. Detournay, P.A. Cundall and Varun

Chapter 42 **Testing and Review of Various Displacement Discontinuity Elements for LEFM Crack Problems 831**
Hyunil Jo and Robert Hurt

Chapter 43 **The Impact of the Near-Tip Logic on the Accuracy and Convergence Rate of Hydraulic Fracture Simulators Compared to Reference Solutions 855**
Brice Lecampion, Anthony Peirce, Emmanuel Detournay, Xi Zhang, Zuorong Chen, Andrew Bunger, Christine Detournay, John Napier, Safdar Abbas, Dmitry Garagash and Peter Cundall

Section 14 Mining and Measurement 875

Chapter 44 **Hydraulic Fracturing Mine Back Trials — Design Rationale and Project Status 877**
Peter K. Kaiser, Benoît Valley, Maurice B. Dusseault and Damien Duff

Chapter 45 **Monitoring and Measuring Hydraulic Fracturing Growth During Preconditioning of a Roof Rock over a Coal Longwall Panel 893**
R. G. Jeffrey, Z. Chen, K. W. Mills and S. Pegg

Chapter 46 **Estimation of the Impact of Mining on Stresses by Actual Measurements in Pre and Post Mining Stages by Hydrofracture Method–A Case Study in a Copper Mine 915**
Smarajit Sengupta, Dhubburi S. Subrahmanyam, Rabindra Kumar Sinha and Govinda Shyam

Section 15 Thermo-Hydro-Mechanical Systems 927

Chapter 47 **An Efficient and Accurate Approach for Studying the Heat Extraction from Multiple Recharge and Discharge Wells 929**
Bisheng Wu, Xi Zhang, Andrew Bunger and Rob Jeffrey

Chapter 48 **Thermal Effects on Shear Fracturing and Injectivity During CO2 Storage 945**
Somayeh Goodarzi, Antonin Settari, Mark Zoback and David W. Keith

Chapter 49 **Scale Model Simulation of Hydraulic Fracturing for EGS Reservoir Creation Using a Heated True-Triaxial Apparatus 959**
Luke Frash, Marte Gutierrez and Jesse Hampton

Section 16 Experimental Geomechanics 979

Chapter 50 **Comparison of Hydraulic and Conventional Tensile Strength Tests 981**
Michael Molenda, Ferdinand Stöckhert, Sebastian Brenne and Michael Alber

Chapter 51 **Formation Fracturing by Pore Pressure Drop (Laboratory Study) 993**
Sergey Turuntaev, Olga Melchaeva and Evgeny Zenchenko

Section 17 Optimizing Stimulation of Fractured Reservoirs 1013

Chapter 52 **Optimizing Hydraulic Fracturing Treatment Integrating Geomechanical Analysis and Reservoir Simulation for a Fractured Tight Gas Reservoir, Tarim Basin, China 1015**
Feng Gui, Khalil Rahman, Daniel Moos, George Vassilellis, Chao Li, Qing Liu, Fuxiang Zhang, Jianxin Peng, Xuefang Yuan and Guoqing Zou

Chapter 53 **Investigation of Hydraulic and Natural Fracture Interaction: Numerical Modeling or Artificial Intelligence? 1039**
Reza Keshavarzi and Reza Jahanbakhshi

Preface

This book comprises the proceedings for the International Conference for Effective and Sustainable Hydraulic Fracturing (HF2013) which was held 20-22 May 2013 in Brisbane, Australia.

The goal of HF2013 was to advance hydraulic fracturing technology that is effective in its purpose and sustainable in its impacts on communities and environments by bringing together hydraulic fracturing experts not only from the oil and gas industry, but also from other application areas of hydraulic fracturing such as mining and geothermal energy production.

HF2013 consisted of 6 keynote lectures, 10 industry and research exhibits, and 47 technical presentations that correspond to full length papers in these open access electronic proceedings. Topics include hydraulic fracturing of naturally fractured formations, well completions and fracture initiation, induced seismicity, experimental investigations, and coupled modelling. Beyond this mix of traditional and currently hot topics in hydraulic fracturing research, there are papers on applications in mining and also on regulations, risk, and communities.

We believe the conference program provided a unique mix of mainstream topics with emerging topics, complimentary areas, and input from sources that are often not tapped by oil and gas industry targeted conferences. These proceedings reflect this dynamic collection of contributors from a wide range of backgrounds, making this volume unlike any other previously compiled collection of papers on hydraulic fracturing.

HF2013 was a Specialized Conference supported by the International Society for Rock Mechanics (ISRM) via the Australian Geomechanics Society and hosted by Australia's Commonwealth Scientific and Industrial Research Organisation (CSIRO). Organisational support was also provided by the University of Utah's Energy and Geoscience Institute (EGI) and the American Rock Mechanics Association (ARMA). Itasca is the conference Gold Sponsor. The support of these organisation as well as the lunch, session, and tea break sponsors is gratefully acknowledged.

The Organising Committee
May 2013
Brisbane, Australia

Section 1

Keynote Lectures

Chapter 1

Fracturing Fluids

Carl Montgomery

Additional information is available at the end of the chapter

http://dx.doi.org/10.5772/56192

Abstract

When fracturing, viscosity play a major role in providing sufficient fracture width to insure proppant entrance into the fracture, carrying the proppant from the wellbore to the fracture tip, generating a desired net pressure to control height growth and providing fluid loss control. The fluid used to generate the desired viscosity must be safe to handle, environmentally friendly, non-damaging to the fracture conductivity and to the reservoir permeability, easy to mix, inexpensive and able to control fluid loss. This is a very demanding list of requirements that has been recognized since the beginning of Hydraulic fracturing. This paper describes the history of fracturing fluids, the types of fracturing fluids used, the engineering requirement of a good fracturing fluid, how viscosity is measured and what the limitations of the engineering design parameters are.

1. Introduction

The selection of a proper fracturing fluid is all about choices. It begins with choosing the pad volume where one must consider what and how much pad is required to create the desired fracture geometry. This is followed by choosing how much viscosity the fluid needs to have to:

- Provide sufficient fracture width to insure proppant entrance into the fracture.
- Provide a desired net pressure to either treat some desired height growth or prevent breaking out into some undesirable zone for example water.
- Provide carrying capability to transport proppant from the wellbore to the fracture tip.

- Control fluid loss. In cases where a gel filter cake cannot form the fracturing fluid viscosity (i.e. C_l) may be the main mechanism for fluid loss control.

This choice system continues when it comes to selecting the appropriate fluid system for a propped or acid frac treatment. The considerations include:

- Safe – The fluid should expose the on-site personnel to a minimal danger.
- Environmentally Friendly – The composition of the fluid should be as "green" as possible.
- Breaker – The fluid must "break" to a low viscosity so that it can flow back and allow clean-up of the fracture.
- Cost Effective – The fluid must be economical and not drive the treatment cost to an unacceptable level.
- Compatibility – The fluid must not interact and caused damage with the formation mineralogy and/or formation fluids.
- Clean-up – The fluid should not damage the fracture conductive of the fracture or, to prevent water blocks, change the relative permeability of the formation. This becomes very important in low pressure wells or wells that produce very dry gas.
- Easy to Mix – The fluid system must be easy to mix even under very adverse conditions.
- Fluid Loss – The fluid need to help control fluid loss. An ideal fluid should have fluid loss flexibility.

In summary an ideal fracturing fluid would be one that would have an easily measured controllable viscosity, controllable fluid loss characteristics, would not damage the fracture or interact with the formation fluid, would be completely harmless and inert and cost less the $4.00 US/ gallon. Unfortunately this is currently not possible so compromises have to be made. Typically cost is the driving force and chooses are made which can be disastrous to the PI of the well.

Of these factors the fluid viscosity is the major fluid related parameter for fracture design. However, **how much viscosity needed is often overrestimated**. Excessive viscosity increases costs, raises treating pressure which may cause undesired height growth, and can reduce fracture conductivity since many of the chemicals used to increase viscosity leave residue which damages the proppant permeability.

The need for a precise value of viscosity is also over engineered. This can be seen from the basic equations where treating pressure, and thus fracture width, is proportional to viscosity raised to the ¼ power (for a Newtonian fluid).

$$p_{net} \propto \frac{E'^{3/4}}{H}[\mu QL\ ]^{1/4} + P_{Tip}$$

Thus a 100% error in viscosity results in an error of about 19% in calculating fracture width. This error would, of course, lead to an error in the fluid volume requirements for a particular job. However, further assuming that 1/2 of the fracturing fluid leaks off to the formation

http://dx.doi.org/10.5772/56192

reduces the 19% error in width to only a 9.5% error in fluid volume requirements. While such an error is not desirable it does illustrate that precise viscosity data is not a requirement for treatment design which is fortunate since the measurement of the viscosity of fracturing fluids is such a difficult task. This complexity combined with multiple methods for testing and reporting viscosity data makes the selection of precise values virtually impossible.

There are several types of fracturing fluids and a wide and confusing range of fluid additives. The types of fluids include:

- Water based fluids
- Oil based fluids
- Energized fluids
- Multi-phase emulsions
- Acid Fluids

The additives include:

- Gelling agents
- Crosslinkers
- Breakers
- Fluid loss additives
- Bactericides
- Surfactants and Non-emulsifing agents
- Clay control Additives.

2. History

The fracturing fluids that were used in the first experimental treatments were composed of gasoline gelled with Palm Oil and crosslinked with Naphthenic Acid. This technology was developed during the Second World War and is commonly referred to as Nalpalm. Because of the hazards associated with this fluid and its relatively high cost work was done to develop safer fluids where the base fluid was water. The vast majority of fracturing fluids used today use water as the base fluid. Generally, the components that make up crosslinked fracturing fluids include a polymer, buffer, gel stabilizer or breaker and a crosslinker. Each of these components is critical to the development of the desired fracturing fluid properties. The role of polymers in fracturing fluids is to provide fracture width, to suspend proppants, to help provide fracture width, to help control fluid loss to the formation, and to reduce friction pressure in the tubular goods. Guar gum and cellulosic derivatives are the most common types of polymers used in fracturing fluids. The first patent (US Patent 3058909) on guar crosslinked

by borate was issued to Loyd Kern with Sinclair (later ARCO) on October 16, 1962. Metal-based crosslinking agents developed by DuPont for plastic explosive applications were found to be useful for manufacturing fracturing fluids for high temperature applications[2]. Cellulosic derivatives are residue-free and thus help minimize fracturing fluid damage to the formation and are widely used in Frac and Pack applications. The cellulosic derivatives are difficult to disperse because of their rapid rate of hydration. Guar gum and its derivatives are easily dispersed but produce some residue when broken. Strong oxidizing agents such as Sodium or Ammonium persulfate are added to the fracturing fluids to break the polymer as it reaches temperature. The first patent (US Patent 3163219) on borate gel breakers was issued to Tom Perkins, also with Sinclair, on December 29, 1964.

Buffers are used in conjunction with polymers so that the optimal pH for polymer hydration can be attained. When the optimal pH is reached, the maximal viscosity yield from the polymer is obtained. The most common example of fracturing fluid buffers is a weak-acid/weak-base blend, whose ratios can be adjusted so that the desired ph is reached. Some of these buffers dissolve slowly allowing the crosslinking reaction to be delayed.

Gel stabilizers are added to polymer solutions to inhibit chemical degradation. Examples of gel stabilizers used in fracturing fluids include methanol, TriEthanol Amine (TEA) and various inorganic sulfur compounds. Other stabilizers are useful in inhibiting the chemical degradation process, but many interfere with the mechanism of crosslinking. The TEA and sulfur containing stabilizers possess an advantage over methanol, which is flammable, toxic, expensive and can cause poisoning of reactor tower catalists.

There has been a huge volume of work done on fracturing fluids and their components. If a search is done on One Petro (http://www.onepetro.org) using "Fracturing Fluids" as the search item over 15,000 hits will result. Just using one of the main gelling agents used to manufacture water based fracturing fluid "Guar" results in over 400 hits. There are several good references [3,4,5,6] that discuss the current state of the art for fracturing fluids if the reader is interested in a more in depth study of fracturing fluids.

Another issue that has recently come to the forefront of fracturing fluids is their threat to the environment through the contamination of the groundwater. George King put it very elegantly in his JPT article[7] where he says "The use of horizontal wells and hydraulic fracturing is so effective that it has been called "disruptive". That is, it threatens the profitability and continued development of other energy sources, such as wind and solar, because it is much less expensive and far more reliable." The internal Apache article[8] that George wrote has 204 references on the subject. Table 1,2,3 provides a summary of all the various chemicals used to make Hydraulic Fracturing fluids along with a degree of hazard rating from both the US Department of Transportation and the European Union Poison Class rating. There certainly are several of these chemicals that one must take care with when handling at their full concentrations but when used to manufacture fracturing fluids the concentrations are very dilute and pose very low hazards.

http://dx.doi.org/10.5772/56192

Chemical Name	**CAS Number**	**Chemical Purpose**	**Product Function**	Hazard Rating[1]
Hydrochloric Acid HCl	007647-01-0	Removes acid soluble minerals and weakens the rock to allow lower fracture iniciation pressures.	Acid	4*,8**
Glutaraldehyde $C_5H_8O_2$	000111-30-8	Eliminates bacteria in the water to prevent frac polymer premature breakdown and well souring	Biocide	3*,6**
Quaternary Ammonium Chloride Compounds	63393-96-4	Clay Control Agents	Biocides and Clay Stabilizers	3**
Tetrakis Hydroxymethyl-Phosphonium Sulfate $C_8H_{24}O_8P_2.SO_4$	055566-30-8	Eliminates bacteria in the water to prevent frac polymer premature breakdown and well souring	Biocide	NR
Ammonium Persulfate $(NH_4)_2S_2O_8$	007727-54-0	Breaks the polymer that is used to create the fracturing fluid	Breaker	4*,5**
Sodium Chloride NaCl	007647-14-5	Product Stabilizer	Breaker	NR
Magnesium Peroxide MgO_2	1335-26-8	Delays the breakdown of the fracturing fluid gelling agent	Breaker	5**
Magnesium Oxide MgO	1309-48-4	Delays the cross linking of the fracturing fluid gelling agent	Buffer	4*
Calcium Chloride $CaCl_2$	10043-52-4	Product Stabilizer and Freeze Protection	Buffer	NR
Ammonium Chloride NH_4Cl	012125-02-9	Clay Stabilizer – Compatible with Mud Acid	Clay Stabilizer	4*,9**
Choline Chloride $[HOCH_2CH_2N^+(CH_3)_3]C$	67-48-1	Prevents clays from swelling or migrating	Clay Stabilizer	5*
Potassium chloride KCl	007447-40-7	Prevents clays from swelling or migrating	Clay Stabilizer	5*,5**
Tetramethyl ammonium chloride $(CH_3)_4NCl$	000075-57-0	Prevents clays from swelling or migrating	Clay Stabilizer	3*,6**
Sodium Chloride NaCl	007647-14-5			NR
Isopropanol $CH_3CH(OH)CH_3$	000067-63-0	Winterizing agent	Winterizing agent and Surface Tension Reduction	3**
Methanol CH_3OH	000067-56-1	Winterizing agent	Winterizing agent	3*, 3**
Formic Acid HCOOH	000064-18-6	pH adjustment	pH adjustment	4*.8**
Acetaldehyde CH_3CHO	000075-07-0	Prevents the corrosion of the pipe	Corrosion Inhibitor	4*,3**

Chemical Name	**CAS Number**	**Chemical Purpose**	**Product Function**	Hazard Rating[1]
Hydrotreated Light Petroleum Distillate	064742-47-8	Carrier fluid for gelling agents, friction reducers and crosslinkers	Carrier fluid and fluid loss control	3**
Potassium Metaborate KBO_2	013709-94-9	Crosslinker for borate crosslinked fluids	Crosslinker	3*
Triethanolamine (TEA) $N(CH_2CH_2OH)_3$	102-71-6	Maintains fluid viscosity as temperature increases	Fluid Stabilizer	5*,3**
Sodium Tetraborate $Na_2B_4O_7$	001330-43-4	Crosslinker for borate crosslinked fluids	Crosslinker	4*
Boric Acid H_3BO_3	13343-35-3	Crosslinker for borate crosslinked fluids	Crosslinker	4*
Chelated Zirconium		Crosslinker for High Temperature or low pH Fluids	Crosslinker	
Zirconium oxychloride $ZrCl_2O$	7699-43-6	Inorganic Clay Stabilizer	Clay Stabilizer	4*
Ethylene Glycol OCH_2CH_2OH	000107-21-1	Product stabilizer and / or winterizing agent.	Winterizing Agent	4*
Methanol CH_3OH	000067-56-1	Surface Tension Reduction and / or winterizing agent.	Fluid Recovery and Winterizing Agent	3*,3**
Ethanol C_2H_5OH	000064-17-5	Product stabilizer and / or winterizing agent.	Fluid Recovery and Winterizing Agent	3**
Polyacrylamide $(C_3H_5NO)_n$	009003-05-8	"Slicks" the water to minimize friction	Friction Reducer	5*
Guar Gum and its derivatives HPG, CMHPG	009000-30-0	Thickens the water in order to suspend the proppant and reduce friction	Gelling Agents	NR
Derivatives of cellulose - HEC, CMHEC $R(n)OCH_2COONa$	9004-34-6 9004-32-4	Thickens the water in order to suspend the proppant and reduce friction	Gelling Agents	NR
Xanthan gum	11138-66-2	Thickens Acid in order to control fluid loss	Gelling Agent	NR
Citric Acid $(HOOCCH_2)_2C(OH)COOH$	000077-92-9	Prevents precipitation of metal oxides	Iron Control	5*,8**
Acetic Acid CH_3COOH	000064-19-7	Prevents precipitation of metal oxides and pH control	Iron Control and pH Adjustment	4*,8**
Thioglycolic Acid $HSCH_2COOH$	000068-11-1	Prevents precipitation of metal oxides	Iron Control	3*,8**
Sodium Erythorbate $C_6H_7O_6$. Na	006381-77-7	Prevents precipitation of metal oxides	Iron Control	NR

http://dx.doi.org/10.5772/56192

Chemical Name	**CAS Number**	**Chemical Purpose**	**Product Function**	Hazard Rating[1]
Lauryl Sulfate and its Derivatives $C_{12}H_{25}OSO_2ONa$	000151-21-3	Used to prevent the formation of emulsions in the reservoir and to improve fluid recovery	Non-Emulsifier and Surfactants	4*
Sodium Hydroxide NaOH	001310-73-2	Adjusts the pH of fluid to initiate the effectiveness of other components, such as crosslinkers	pH Adjusting Agent	4*,8**
Potassium Hydroxide KOH	001310-58-3	Adjusts the pH of fluid to initiate the effectiveness of other components, such as crosslinkers	pH Adjusting Agent	2*,8**
Sodium Carbonate Na_2CO_3	000497-19-8	Adjusts the pH of fluid to maintains the effectiveness of other components, such as crosslinkers	pH Adjusting Agent	5*,5**
Potassium Carbonate K_2CO_3	000584-08-7	Adjusts the pH of fluid to maintains the effectiveness of other components, such as crosslinkers	pH Adjusting Agent	4*
Sodium Acrylate and Copolymers of Acrylamide $C_3H_3O_2$. Na	007446-81-3	Prevents scale deposits in the pipe or in the fracture	Scale Inhibitor	NR
Sodium Polycarboxylate	N/A	Prevents scale deposits in the pipe	Scale Inhibitor	
Phosphonic Acid Salt	N/A	Prevents scale deposits in the pipe	Scale Inhibitor	
Naphthalene $C_{10}H_8$	000091-20-3	Carrier fluid for the active surfactant ingredients	Surfactant	3*,4**
Ethylene glycol monobutyl ether - EGMBE $C_4H_9OCH_2CH_2OH$	000111-76-2	Surface Tension Reduction for Fluid Recovery	Surfactant	4*, 6**

1 – Hazard Rating – An attempt was made to rate the hazard associated with each of the chemicals listed. The first number with the single * is the Poison Hazard as defined by the EU/Swiss Poison Class while the second number with the double ** is the transportation Hazard as defined by the US Department of Transportation (DOT). If a NR is present in the box no rating was found and the substance was normally non-hazardous.

* EU/Swiss Poison Class

Table 1. A summary of the various chemicals used to make Hydraulic Fracturing fluids along with a degree of hazard rating. Modified from " www. http://fracfocus.org/chemical-use/what-chemicals-are-used"

Class	***Lethal Dose (mg/kg)***
1	0 to 5
1S	0 to 5, also teratogenic or carcinogenis
2	5 to 50

Class	*Lethal Dose (mg/kg)*
3	50 to 500
4	500 to 2000
5	2000 to 5000
5S	2000 to 5000, an unrestricted self-service product

** DOT Transportation Hazard Classes

Table 2. A summary of the various chemicals used to make Hydraulic Fracturing fluids along with a degree of hazard rating. Modified from " www. http://fracfocus.org/chemical-use/what-chemicals-are-used"

Class	
1	Explosives
2	Compressed Gases
3	Flammable and Combustible Liquids
4	Flammable Solids
5	Oxidizers and Organic Peroxides
6	Poisonous/Toxic Materials
7	Radioactive Materials
8	Corrosive Materials
9	Miscellaneous Hazardous Materials

Table 3. A summary of the various chemicals used to make Hydraulic Fracturing fluids along with a degree of hazard rating. Modified from " www. http://fracfocus.org/chemical-use/what-chemicals-are-used"

Additional hazard identification resources

http://fracfocus.org/welcome - The Ground Water Protection Council and the Interstate Oil and Gas Compact Commission developed this web site to provide public access to chemicals used in the hydraulic fracturing process and provides a record of the chemicals used in wells in a number of different stated in the United States. At the time of this writing the site had records on over 34,000 wells.

http://www.osha.gov/chemicaldata/ - This United States Department of Labor website proves a OSHA (Occupational Safety and Health Administration) Occupational Chemical Database

http://dx.doi.org/10.5772/56192

for most of the chemicals used by industry. The database can be searched by either Chemical Name or CAS Number.

http://ull.chemistry.uakron.edu/erd/ - The Department of Chemistry at the University of Akron developed this website to provide a database composed of over 30,000 hazardous chemicals made up of information provided by a number of different published references.

http://www.epa.gov/chemfact/ - This United States Environmental Protection Agency website provides OPPT Chemical Fact Sheets on selected chemicals that may be present in the environment in an ASCII text or Adobe PDF format along with access to other EPA databases.

3. Types of fracturing fluids

Table 4 provides a qualitative listing of the desirable and undesirable aspects of most fluid systems available today. As one studies the table it is interesting to note that there is "no magic bullet". The qualitative score is close to the same for each fluid and each fluid has its advantages and disadvantages. This means that the final decision is up to the design engineer as to what is best for his reservoir. The different types of fluid systems are outlined below. A description of all the different components used to manufacture the fluids is provided in Side Bar 1.

Fluid System	Prop Pack KfW	Low Pump Pressure	VISCOSITY			Breaking	Compatibility		Fluid Loss	Ease of Mixing	Cost	Safety and Environmentally Friendly	Total
			Prop-Transport	Stable	Life		Formation Fluid	Fluid Recovery					
Water Frac[1]	5	5	1	3	3	5	3	4	1	5	5	4	44
Linear Gel[2]	3	5	3	3	3	4	3	4	2	5	4	5	44
Linear Gel[3]	5	5	3	3	3	4	3	4	2	5	4	5	46
Borate X-Link[2]	3	3	5	5	5	3	4	3	5	4	3	5	48
Delayed Borate X-Link[2]	3	3	5	5	5	3	4	3	5	3	3	5	47
Delayed Metalic X-Link[4]	3	3	5	2	2	3	4	3	5	3	3	4	40
Delayed Metalic X-Link[5]	3	3	5	2	2	3	4	3	5	3	3	4	40
VES[6]	5	3	5	4	4	2	1	3	2	2	1	5	37
Nitrogen Foam	5	2	5	3	3	5	4	4	5	2	1	3	42
CO_2 Foams	5	2	5	3	3	5	4	5	5	2	1	2	42
Gelled Propane	5	3	4	4	3	4	5	4	4	2	1	1	40
Poly Emulsions (K1)	4	1	5	5	5	4	4	3	5	2	3	2	43
Lease Crude	2	3	2	5	5	5	5	3	2	5	5	1	43
Gelled Oil[7]	2	3	4	4	4	4	3	3	3	4	3	1	38

Qualitative Rate 1 to 5 where 1 is poor, 3 is moderate and 5 is excellent

1 - Uses Polyacrylamide (PAA) as a Friction Reducer
2 - Uses Guar, HydroxyPropyl Guar (HPG) or CarboxyMethylHydroxyPropyl Guar (CMHPG) as gelling agent
3 - Uses HydroxyEthyl Cellulose (HEC) or CarboxyMethyHydroxyEthyl Cellulose (CMHEC) as gelling agent
4 - Uses Titinium or Zirconium Crosslinkers for Guar, HPG, and CMHPG gelling agents
5 - Uses Titinium or Zirconium Crosslinkers for CMHEC gelling agents
6 - Uses a ViscoElastic Surfactant system as the gelling agent
7 - Uses a Phosphate Ester crosslinked with an Aluminum Salt and acitivated with a Base

Table 4. Qualitative Fluid Selection Chart

Water Frac is composed of water, a clay control agent and a friction reducer. Sometimes a water recovery agent (WRA) is added to try and reduce any relative permeability or water block effects. The main advantage of using a "Water Frac" is the low cost, ease of mixing and ability to recover and reuse the water. The main disadvantage is the low viscosity which results in a narrow fracture width. Because the viscosity is low the main proppant transport mechanism is velocity so water fracs are typically pumped at very high rates (60 to 120 bpm). Fluid loss is controlled by the viscosity of the filtrate which is close to that of water i.e. 1.

Linear Gel is composed of water, a clay control agent and a gelling agent such as Guar, HPG or HEC. Because these gelling agents are susceptible to bacteria growth a bactericide or biostat is also added. Chemical breakers are also added to reduce damage to the proppant pack. WRA's are also sometimes used. The main advantage of a liner gel is its low cost and improved viscosity characteristics. Fluid loss is controlled by a filter cake which builds on the fracture face as the fluid loses fluid to the formation. The main disadvantage is, as with waterfracs, the low viscosity which results in a narrow fracture width. The main disadvantage when compared to a waterfrac is that because the returned water has residual breaker the water is not reusable.

Crosslinked Gels are composed of the same materials as a linear gel with the addition of a crosslinker which increases the viscosity of the linear gel from less than 50 cps into the 100's or 1000's of cps range. The higher viscosity increases the fracture width so it can accept higher concentrations of proppant, reduces the fluid loss to improve fluid efficiency, improves proppant transport and reduces the friction pressure. This crosslinking also increases the elasticity and proppant transport capability of the fluid. Fluid loss is controlled by a filter cake which builds on the fracture face as the fluid loses fluid to the formation. A full description of the types of crosslinkers used, the chemistry and the mechanism of crosslinking is provided in the companion paper on fracturing fluid components.

Oil Based Fluids are used on water-sensitive formations that may experience significant damage from contact with water based fluids. The first frac fluid used to fracture a well used gasoline at the base fluid, Palm Oil as the gelling agent and Naphthenic Acid as the crosslinker i.e. Napalm. Although some crude oils have particulate which could build a filter cake, fluid loss is generally considered to be "Viscosity- Controlled – i.e. C-II". There are some disadvantages in using gelled oils. Gelling problems can occur when using high viscosity crude oils or crude oils which contain a lot of naturally occurring surfactants. When using refined oils such as diesel the cost is very high and the oil must be collected at the refinery before any additives such as pour point depressants, engine cleaning surfactants etc. are added. Also there are greater concerns regarding personnel safety and environmental impact, as compared to most water-fluids.

Foam/PolyEmulsions are fluids that are composed of a material that is not miscible with water. This could be Nitrogen, Carbon dioxide or a hydrocarbon such as Propane, diesel or condensate. These fluids are very clean, have very good fluid loss control, provide excellent proppant transport and break easily simply via gravity separation. PolyEmulsions are formed by emulsifying a hydrocarbon such as Condensate or Diesel with water such that the hydrocarbon is the external phase. The viscosity is controlled by varying the hydrocarbon/water ratio.

http://dx.doi.org/10.5772/56192

Foams made with Nitrogen or Carbon dioxide is generally 65 to 80% (termed 65 to 80 quality) gas in a water carrying media which contains a surfactant based foaming agent. Sometimes N_2 or CO_2 are added at a lower concentration (20 to 30 quality) to form "Energized Fluids". This is done to reduce the amount of water placed on the formation and to provide additional energy to aid in load recover during the post-frac flow back period. Nitrogen can dissipate into the reservoir quite quickly so fluids energized with N_2 should be flowed back as soon as the fracture is closed. CO_2, under most conditions, is in a dense phase at static down hole conditions (prior to the well being placed on production), so is less susceptible to dissipation. CO_2 does dissolve in crude oil so will act to reduce the crude viscosity which, again, improves cleanup and rapid recovery. When N_2/CO_2 are added is qualities greater than 80 the resulting mixture is termed a mist with a "0" viscosity. This quality is normally not used in fracturing. The main disadvantage of these fluids is safety i.e. pumping a gas at high pressure or in the case of polyemulsions and gelled Propane, pumping a flammable fluid. CO_2 has an additional hazard in that it can cause dry ice plugs as pressure is reduced. These fluids are generally also more expensive and the gases may not be available in remote areas.

4. Chacterization of fracturing fluids

Fluid viscosity for treatment design is determined from laboratory tests and is reported in service company literature. The ideal experiment for describing fluid flow in a fracture would be to shear a fluid between two plates which are moving parallel and relative to one another. The shear stress on the fluid equals the drag force on the plates divided by the area of the plates, and has units of stress or pressure (e.g., psi). The shear rate (or velocity gradient) is the relative velocity of the two plates divided by the separation distance between the plates. Shear rate has the units of 1/time (e.g., sec^{-1}). A vertical 7 ft high by 10 1/3 ft long high pressure parallel-plate flow cell, shown in Figure 1, capable of operating to temperatures of 250°F and pressures of 1200 psi is available at the University of Oklahoma[11]. Termed the "Fracturing Fluid Characterization Facility (FFCF)" the laboratory simulator is a very sophisticated; one of a kind unit that utilizes 12 servo-controlled 28" by 28" platens that can dynamically adjust the width of the slot from 0 to 1.25 inches.

Such an ideal test is not feasible for day to day applications so a rotating "cup and bob" viscometer know as a "Couette" viscometer is used. API standard RP39[12] and ISO 13503-1[13] fully describe the current testing procedures used by the industry. The viscometer uses a rotating cup and a stationary bob with a gap between the two that simulates the fracture. As shown in Figure 2 the rotational speed of the cup imparts a shear rate and the bob measures the shear stress or drag force exerted on the walls of the cup and bob. This is sensed by measuring the torque on the bob. The shear rate is the relative velocity between the stationary bob and the rotating cup divided by the separation gap. Figure 3 shows several commercial rheometers and how they are set up in the field. For a Fann 35 (See Figure 3) equipped with a R1 rotor and a B1 bob and the appropriate spring a rotational speed of 100 RPM represents a shear rate of 170 sec^{-1} and a speed of 300 RPM gives a shear rate of 511 sec^{-1}. The Fann 35, which is manufactured by the Fann Instrument Company http://www.fann.com/, the Model 3530,

Figure 1. University of Oklahoma Parallel Plate Fracturing Fluid Characterization Facility (Courtesy of the University of Oklahoma).

which is manufactured by Chandler Engineering http://www.chandlerengineering.com/ and the Model 800 8 speed viscometer manufactured by OFI Testing Equipment, Inc. http://www.ofite.com/ are atmospheric rheometers which limits their use to the boiling point of water. The Fann 50, Chandler 5550 and OFI 130-77 viscometer's are equipped with a pressurized cup and bob which can be placed into an oil bath for higher temperature measurements. Fluids, including foam, can be dynamically flowed into the cells so that the fluid can be measured under the shear conditions that it would experience in the well. These rheometers are very rugged reliable instruments but suffer from a phenomenon called the Weissenberg effect when trying to measure crosslinked viscoelastic fluids. It occurs when a spinning rod, like the rotor, is placed into a solution of polymer. Instead of being thrown outward the polymer chains entangle on the rod supporting the bob causing the polymer solution to be drawn up the rod. Figure 4 shows what the Weissenberg effect looks like. As temperature increases and the gel thins the issue goes away to a certain extent and modern rheometers try to control the effect. Overall the effect can result in some very misleading data and care must be taken when very odd looking, unusual data is presented. The testing problem is compounded in that, as illustrated in Figure 5, many fracturing fluids (particularly crosslinked gels) are not truly fluids. Trying to characterize these materials with a "viscosity" can be very difficult. Fortunately, even for these fluids, temperatures above about 120°F make the behavior more predictable.

http://dx.doi.org/10.5772/56192

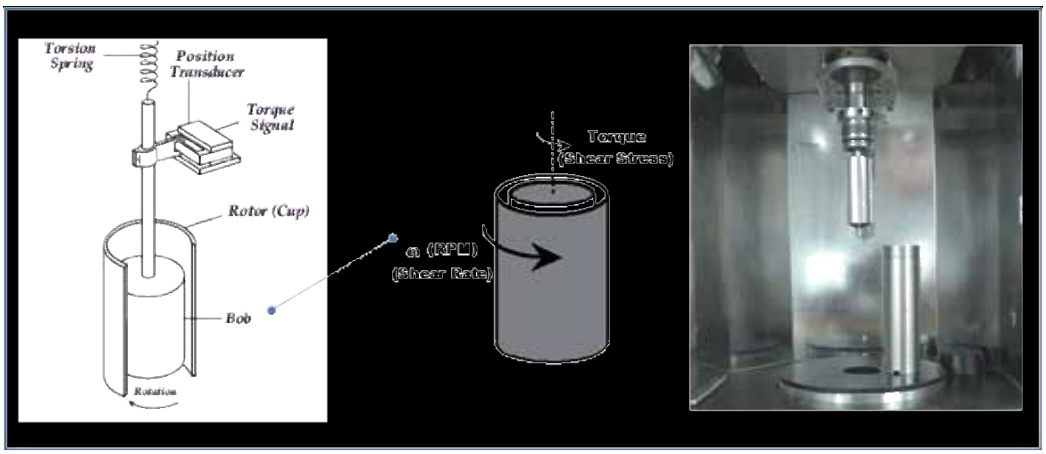

Figure 2. The geometry of a curette "Cup & Bob" Viscometer

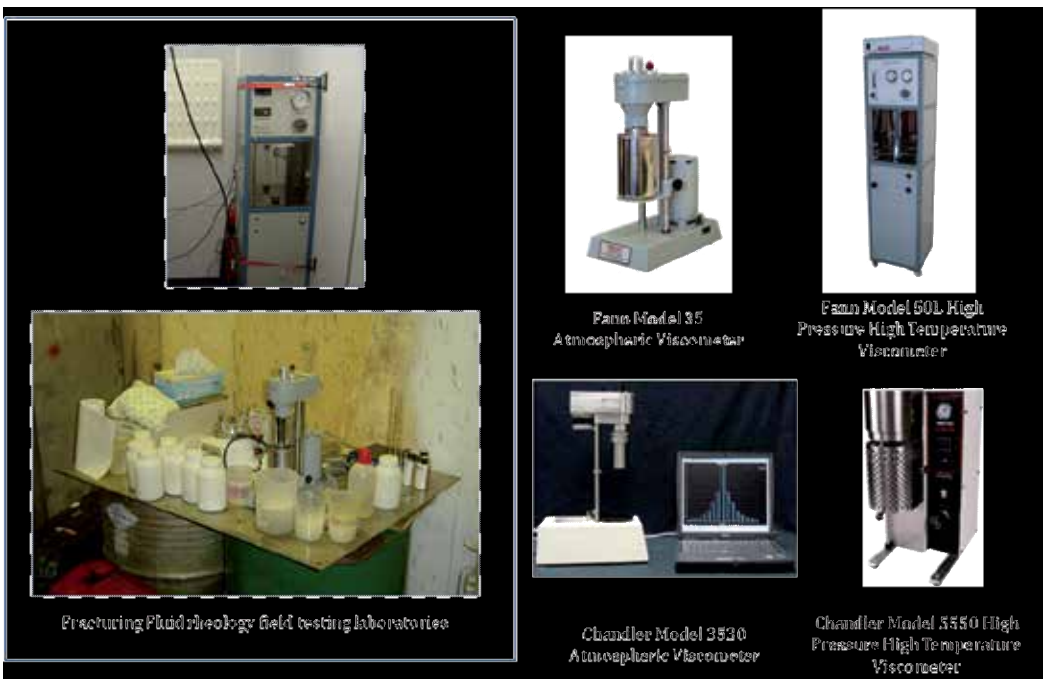

Figure 3. Rheometer's for testing fracturing fluids.

Figure 4. The Weissenberg Effect

Figure 5. Example of a Complex Dehydrated Cross-linked gel

5. Rheological models

The tests described above measure the shear stress generated by specific increasing shear rates (called a ramp), and this data is converted to a "viscosity" value by using a rheological model to describe fluid behavior. Figure 6 shows the three models that are in common use by the oil industry and these are:

http://dx.doi.org/10.5772/56192

1. Newtonian Fluid - A Newtonian fluid has a linear relation between shear rate and shear stress and fluid viscosity is the slope of the shear rate versus shear rate data.

2. Bingham Plastic - A Bingham Plastic differs from a Newtonian fluid in that a non-zero shear stress called the Plastic Yield Value is required to initiate fluid flow. The slope of the shear rate/shear stress data is labeled Plastic Viscosity and this model is routinely used for cements and many drilling muds.

3. Power Law Fluid - This is the most common fluid model used for current fracturing fluids and for this rheological model the shear stress/shear rate data give a linear relation on log-log scales. The slope of this log-log line is denoted by n', and this is labeled the Flow Behavior Index. n'=1 implies a Newtonian fluid; n'>1 is called a shear stiffening fluid; and n'<1 is a shear softening fluid. n' is generally less than 1 for fracturing fluids. The shear stress at a shear rate of "1" is labeled the Consistency Index and is denoted by K'. For real fluids K' and n' change with temperature and time with K' generally decreasing and n' tending toward unity.

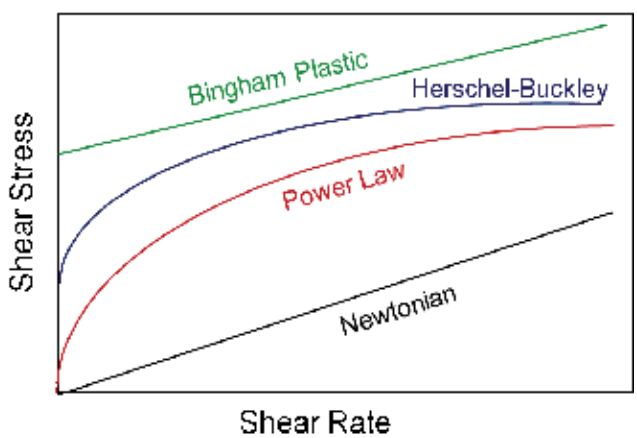

Figure 6. Rheological Models

For non-Newtonian fluids (a Power Law fluid being one example) the "apparent viscosity - (μ_a) " is used as a shorthand way of characterizing the fluid. Apparent viscosity (μ_a) is illustrated in Fig. 7 and is the ratio of shear stress to shear rate - at a particular value of shear

rate. Thus a fluids apparent viscosity depends on the shear rate at which the viscosity is measured (or calculated). For a Power Law Fluid with n'<1, the apparent viscosity will decrease with increasing shear rate.

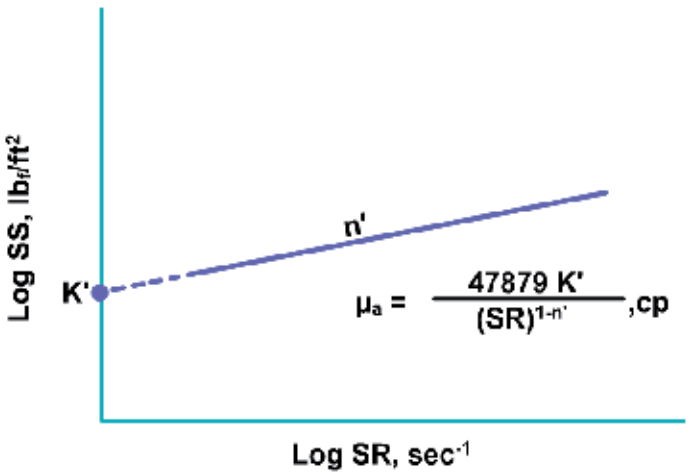

Figure 7. Apparent viscosity using a Power Law Equation

To determine n′ and K′ a fluid is placed in a rheometer and sheared at a constant rate while the temperature is brought to equilibrium. Periodically the fluid n′ and K′ is measured by bringing the shear rate up, holding the rate for a few seconds then increasing the rate again typically over a range of at least 4 shear rates. This is termed a ramp and is typically done every 30 minutes during the fluid test. Figure 8 shows an example of a shear stress vs shear rate set of ramps that was provided by C&A Inc. - http://www.candalab.com/. Note that for each ramp four shear rates where used. The slope of the line is the n′ and the intercept at a 0 shear rate is the K′. Using this information an apparent viscosity for any shear rate can be calculated with the following equation.

$$\mu_a = \frac{448000\ K'}{(SR)^{1-n'}}$$

Where μa = Apparent viscosity in cps

K′ = the Consistency Index in (lbf/ft^2/sec)

n′ = flow behavior index

SR = Shear Rate in Sec $^{-1}$

Service company literature reports viscosity at different shear rates (usually 170 or 511 sec^{-1}) and the shear rate in a fracture can be as low as 30 to 40 sec^{-1}. The example shows that the identical fluid might be reported by one company to have a viscosity of 300 cp (170 sec^{-1}), by another to have 200 cp (511 sec^{-1}), and the fluid may actually have in excess of 600 cp in the fracture (at 40 sec^{-1}). In selecting a fluid it is important to know at what shear rate the viscosity

http://dx.doi.org/10.5772/56192

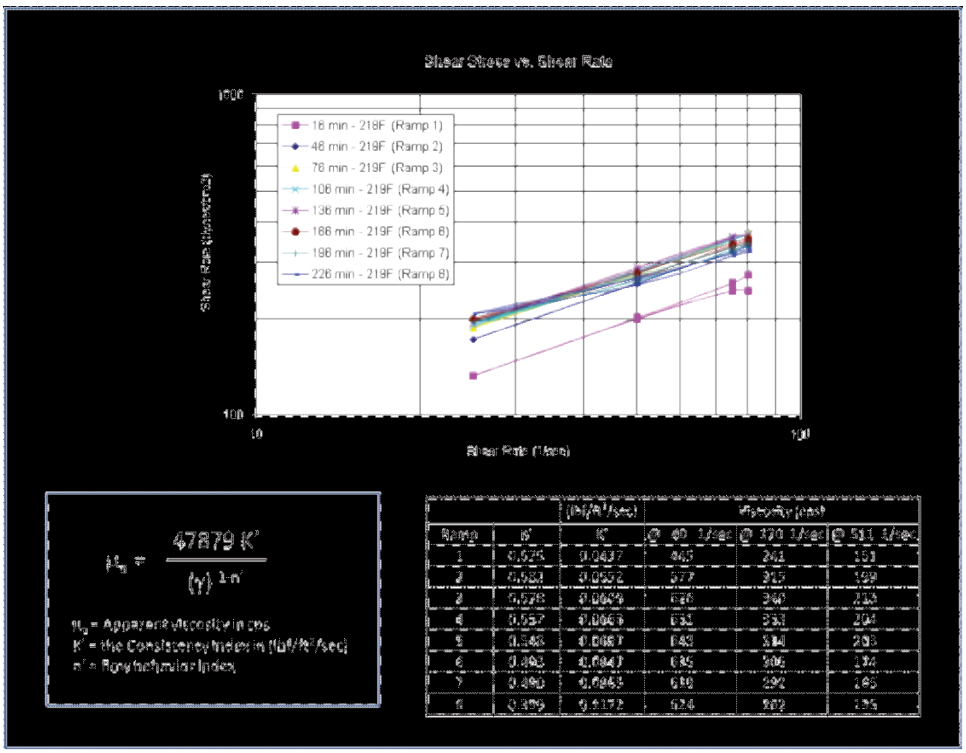

Figure 8. A set of shear stress vs shear rate set of ramps along with the calculation of apparent viscosity at three shear rates.

data was measured. In addition, **during the testing the fluid should be sheared at a shear rate somewhat representative of the behavior expected in the fracture**. This is typically on the order of 50 sec^{-1}, but for some soft rock treatments the shear rate may be much lower than this, and in some hard rock treatments, the shear rate may be much greater.

6. Shear history simulation

As the fluid is pumped through the surface equipment, well tubular, perforations and fracture it is subjected to a range of shear rates that may have a detrimental effect on the fluid rheology. For example Figure 9 shows the apparent viscosity for a borate crosslinked HPG that was used to fracture a well in China. A series of premature screenouts had occurred and an evaluation was conducted to determine why. The well was completed with an open annulus and a tubing string and the treatments were being pumped down the annulus. The shear rate was calculated to be 2200 s^{-1} and the time in the tubing/casing annulus was 5 minutes. As the figure shows the apparent viscosity without the 5 minutes of high shear was 800 cps but if subjected to shear was about 20 cps. The fluid did recover its viscosity but it took 80 minutes. The higher proppant

concentrations were settling out near the wellbore and causing the screenouts. The buffer package was adjusted by the service provider and that cured the problem.

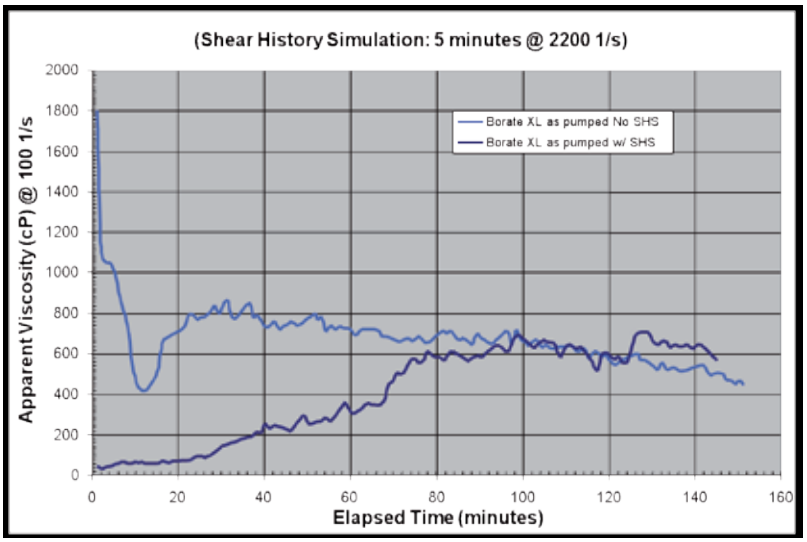

Figure 9. Viscosity Profile for a Borate Crosslinked HPG with and without shear history simulation.

Reference 13 provides a detailed procedure on how to do shear history simulation. The equipment needed is shown in Figure 10. Because the flow in the tubulars is in pipe flow rather than slot flow using a curette "Cup & Bob" viscometer at high shear rate can be misleading. The shear rate in the tubular is a function of pump rate and tubing size. The equations for determining shear rate are included in reference 13.

7. Slurry viscosity

Another factor affecting viscosity is the addition of proppant to the fracturing fluid to from slurry. For a Newtonian fluid the increase in viscosity due to proppant can be calculated from a equation originally developed by Albert Einstien[14]. The chart shown in Figure 11 demonstrates this effect. The figure shows that an 8 ppg slurry has an effective viscosity about 3 times that for the fracturing fluid alone. This increased viscosity will increase net treating pressure and may significantly impact treatment design. This increase in slurry viscosity also retards proppant fall as discussed below.

http://dx.doi.org/10.5772/56192

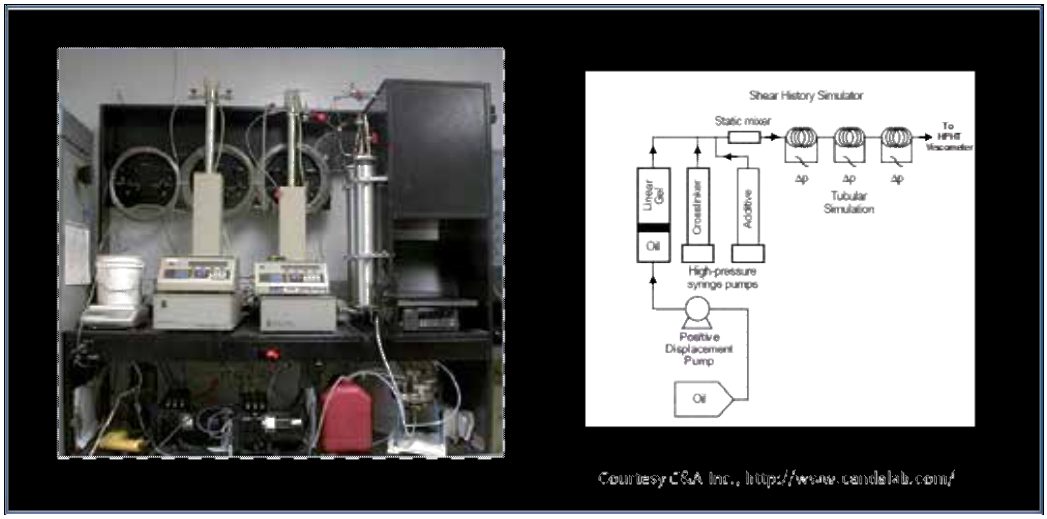

Figure 10. Shear History Simulation Laboratory Equipment

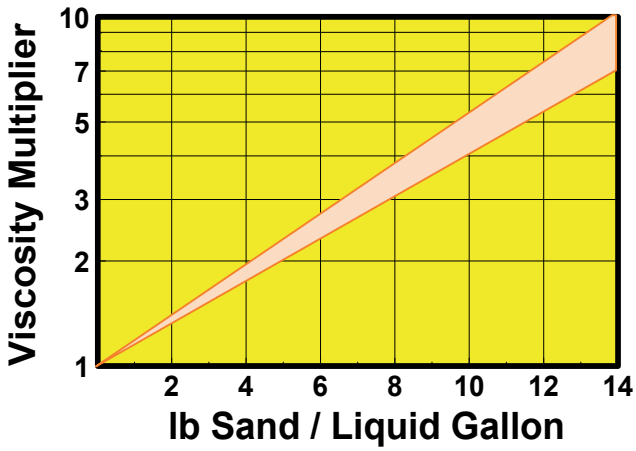

Figure 11. Slurry Viscosity Multiplier as a function of proppant concentration.[14]

8. Proppant fall rates

The rate of fall for proppant is normally calculated using Stoke's Law which can be written as:

Fall Rate = V (ft/sec) = $1.66 \times 10^5 D^2 / \mu_f [SG_{prop} - SG_{fluid}]$

Where:

D = the average proppant diameter in feet

μ_f = the apparent viscosity of the fluid in Cps

SG_{prop} = the specific gravity of the proppant (i.e. 2.65 for sand)

SG_{fluid} = the specific gravity of the fluid (i.e. 1 for water)

Stokes's Law is generally not valid for Reynolds numbers much in excess of unity[15] or for hindered settling due to proppant clustering in static fluids[16]. For crosslinked fluid the actual fall rate may be much less than Stokes Law. Hannah and Harrington[17] present lab data that shows that proppant in crosslinked fluids falls at a rate which is reduced by about 80% when compared to non-crosslinked linear gels with the same apparent viscosity. The rate of proppant fall in foams and emulsions is also much less than would be indicated by using the apparent viscosity in Stoke's Law[18]. Another factor affecting proppant fall is the particle concentration which increases slurry viscosity (Figure 11). This retards or hinders the proppant fall because of clustered settling[16] in static fluids. Finally the slurry flowing down a fracture is generally much lower that the shear rate of 170 or 511 sec^{-1} used to report the fluid apparent viscosity.

When all of these factors are put together they can significantly affect the viscosity. To provide an example consider a crosslinked gel which has a reference apparent viscosity at 170 sec^{-1} of 50 cps after four hours at reservoir temperature.

1. Shear Rate Correction – If the fluid has an n' of 0.6 and the shear rate in the fracture is 50 sec^{-1}, the effective apparent viscosity in the fracture would be $(170/50)^{1-n'}$ times the measured viscosity or (1.63*50 = 81 cps).
2. Slurry Correction – If the slurry enters the fracture at a concentration of 1 PPG (pounds of sand per liquid gallon) and concentrates to 10 PPG after four because of fluid loss, the average concentration of 5 PPG gives a viscosity multiple of 2 from Figure 11. This would give an effective average apparent viscosity of (2*81 = 162 cps).
3. Fall Rate Correction – Harrington and Hannah[17] state that for a crosslinked fluid the rate of fall is reduced by up to 80%. For this example assume that the fall rate is reduced by 50%. This effectively doubles the viscosity to (2*162 = 324 cps).
4. Temperature Correction – The fluid enters the fracture at a relatively low temperature and thus a higher viscosity. If the fluid viscosity reduces by a factor 10 over the 4 hour exposure time (down to the originally referenced 50 cps) with a log viscosity versus time relationship (typical for most crosslinked fluids) the average fluid viscosity over the four hour period would be a factor of 4.3 times the final viscosity. This gives an effective average apparent viscosity of (4.3*324 = 1393 cps).

Using a value of 1393 cps of apparent viscosity in Stoke's Law gives a total proppant fall of 15 feet during the four hour period. Almost perfect transport is achieved by a fluid system having a final reference apparent viscosity of only 50 cps.

This example may appear to be extreme but it is actually conservative. The Fall Rate Correction was reduced from 80% to 50% and the time it takes to heat up to reservoir temperature was ignored. The main point to be taken from this is that the viscosity requirements for a frac fluid can be overestimated by an order of magnitude and sufficient proppant transport can be achieved with a fluid having a reference apparent viscosity of 50 to 100 cps.

9. Viscosity and fracture treating pressure

Treating pressure is fairly insensitive to viscosity as the pressure is proportional to viscosity raised to the ¼ power. However as discussed above the viscosity estimate can easily be off by an order of magnitude which can have a drastic impact on treatment behavior. An order of magnitude would be ($10^{0.25} = 1.8$) so the treating pressure would be 80% greater than anticipated. This could cause undesired height growth and result in treatment failure. For jobs where the control of net pressure to prevent height growth is important, fluid viscosity is a critical parameter.

Author details

Carl Montgomery

NSI Technologies, Tulsa, Oklahoma , USA

References

[1] Api, R. P. M, Recommended Practice for Measurement of Viscous Properties of Completion Fluids, Jul-(2004). , 01.

[2] Api, R. P. Recommended Practice for Presenting Performance Data on Cementing and Hydraulic Fracturing Equipment, Feb-(1995). , 01.

[3] GidleyJohn L., et.al., Recent Advances in Hydraulic Fracturing SPE Henry L. Doherty Series Monograph Chapter 7, 155563020(1989). , 12

[4] ElyJohn W., Stimulation Engineering Handbook, PennWell Publishing Company, 087814417(1994).

[5] Economides, M. J, & Nolte, K. G. Reservoir Stimulation- Third Edition", John Wiley and Sons, LTD, 0-47149-192-6(2000).

[6] Economides, M. J, & Martin, T. Modern Fracturing- Enhancing Natural Gas Production", ET Publishing, 978-1-60461-688-0BJ Services Company (2007).

[7] KingGeorge E., "Hydraulic Fracturing 101: What every Representative, Environmentalist, Regulator, Reporter, Investor, University Researcher, Neighbor and Engineer Should Know About Estimating Frac Risk and Improving Frac Performance in Unconventional Gas and Oil Wells" SPE 152596 presented ath the 2012 Hydraulic Fracturing Technology Conference, February (2012). , 6-8.

[8] KingGeorge E., "Estimating Frac Risk and Improving Frac Performance in Unconventional Gas and Oil Wells", internal Apache Corporation document, 88 Jan (2012). , 23.

[9] BeckwithRobin; "Depending on Guar- For Shale Oil and Gas Development", Journal of Petroleum Technology, December (2012). , 44-55.

[10] ConwayMichael W., Almond, Stephen W., Briscoe, James Earl, Harris, Lawrence E., Halliburton Services, "Chemical Model for the Rheological Behavior of Crosslinked Fluid Systems", Journal of Petroleum Technology, Feburary (1983). , 35(2), 315-320.

[11] ShahSubhash and Fagan, John; ' Fracturing Fluid Characterization Facility (FFCF): Recent Advances" DOE/MC/C0490 presented at the (1995). Natural Gas RD&D Contractor's Review Meeting, April 4-6, Baton Rouge, Louisiana., 29077-95.

[12] Api, R. P. Recommended Practice on Measuring the Viscous Properties of a Crosslinked Water-based Fracturing Fluid", third edition, May (1998).

[13] ISO 13503-1:2003(E) International Standard "Part 1Measurement of viscous properties of completion fluids". (2003). www.iso.org,.

[14] Einstein, A. Ann. Phys. 19, 289 (1906); 34, 591 (1911), b) The second order calculation is developed by G.K. Batchelor and J.T. Green, J. Fluid Mech. 56, 401 ((1972).

[15] Blot, M. A, & Medlin, W. L. Theory of Sand Transport in Thin Fluids", SPE 14468 presented at the (1985). SPE ATC, Las Vegas, Nevada, September., 22-26.

[16] Mcmechan, D. E, & Shah, S. N. Static Proppant-Settling Characteristics of Non-Newtonian Fracturing Fluids in a Large-Scale Test Model", SPE 19735, SPE Production Engineering Journal, August (1991). , 6(3)

[17] HarringtonLarry, Hannah, Robert and Williams, Dennis, "Dynamic Experiments' on Proppant Settling in Crosslinked Fracturing Fluids", SPE 8342 presented at the (1979). SPE ATC Las Vegas, Nevada, September., 23-26.

[18] Harris, P. C. et.al., "Measurement of Proppant Transport of Frac Fluids", SPE 95287 presented at the (2005). SPE ATC Dallas, Texas, October., 9-12.

Chapter 2

Fracturing Fluid Components

Carl Montgomery

Additional information is available at the end of the chapter

http://dx.doi.org/10.5772/56422

Abstract

The materials and chemistry used to manufacture hydraulic fracture fluids are often confusing and difficult for the practicing hydraulic fracturing engineer to understand and optimize. Many times the failure of a particular fracturing treatment is blamed on the fluid because that is a major unknown from the design engineer's viewpoint. Many of the components and processes used to manufacture the fluid are held proprietary by the service company which adds to the confusion and misunderstanding. This paper makes an attempt to describe the components used in fracturing fluids at a level that the practicing frac engineer can understand and use. The paper is intended as a companion paper to the Fracturing Fluids design paper which describes how to use the fluids and viscosity generated by the fluids to design a fracturing treatment.

1. Introduction

1.1. Water

The water used for hydraulic fracturing is a critical component of the fluid. It must be carefully quality controlled as describe in the Quality Control Chapter. Typically the water is filtered to 50μ (microns) for propped fracturing treatments and to 2μ for frac and pack treatments. Fresh water is normally used but there are gelling agents available for seawater. The main disadvantage of seawater is the presence of Sulfate which can interact with connate reservoir water causing sulphate scales to form and provides a sulfur source for Sulfate reducing bacteria. The use of post frac flowback water is becoming

common especially for slickwater fracs. When flowback water is used to manufacture crosslinked gels care must be taken because the water may contain residual breaker.

2. Clay control agents

KCl or an organic clay stabilizer is added to the base fluid to prevent the water from interacting with the reservoir mineralogy. KCl is typically added at a concentration of 2% but can be added at concentrations as high as 8% depending on laboratory testing results. Most testing on the commercially available organic clay stabilizers, which are typically some form of Quaternary Amine compound, has found them to be ineffective at the normal concentrations recommended. KCl is unique in its ability to stabilize clays and is much more effective than other inorganic salts such as NaCl, $CaCl_2$ etc.

3. Friction Reducers (FR)

These materials are added to water to manufacture what is called "slickwater". They are added to reduce the friction generated as the fluid is pumped down the well tubulars. FR's are typically added to the frac fluid at a concentration of 0.25 to 2 gal/1000 gal. Figure 1 shows a comparison of the friction when pumping water, FR "Slickwater" and Guar "Waterfrac". There are several forms of FR which are also shown in Figure 1. They are:

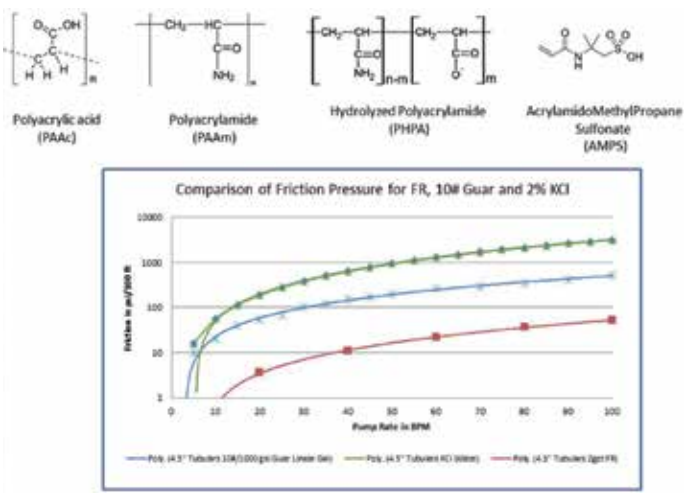

Figure 1. Chemical Structure of various Friction Reduction (FR) agents and a comparison of friction pressure for water containing only 2% KCl vs. water containing 2% KCl and 2 gallons per 1000 gallons (FR) and 10# Guar pumped down 4 ½" 11.5# 4" ID casing.

http://dx.doi.org/10.5772/56422

3.1. Polyacrylic Acid (PAAc)

PAAc which is a non-toxic synthetic high molecular weight polymer of acrylic acid. The material is sold as either a white solid or as a 50% active dispersion of the solid in mineral oil which makes it easy to disperse and solublize in water. The molecule is very sensitive to divalent cationic ions (cations) such as Ca, Mg, Fe etc. and will quickly precipitate if used in hard water. Other uses for PAAc include adsorbents for disposable diapers, ion exchange resins, adhesives and as thickeners' for pharmaceuticals, cosmetics and paints.

3.2. Polyacrylamide (PAAm)

PAAm is formed from acrylamide subunits. It is non-toxic however unpolymerized acrylamide is a neurotoxin and if the PAAm is not properly manufactured it can contain some unpolymerized acrylamide. As a solid PAAM is slower to hydrate than PAAc but is less sensitive to divalent cations. It is typically delivered to the field as a 50% active suspension of PAAM emulsified in mineral oil. The PAAm polymer is quite difficult to break and is used to gel 15% HCl so is damaging to the reservoir rock and proppant pack when used. When used in Slickwater fracturing Carman and Cawiezel [19] have reported successful breaker optimization for the material. Other uses for PAAm include flocculants for wastewater treatment and papermaking, as a soil conditioner and for making soft contact lens.

3.3. Partially Hydrolyzed Polyacylamide (PHPA)

PHPAis the most common friction reducer available. It is made by reacting sodium acrylate with acrylamide so that approximately 30 % of the acrylamide groups are in the hydrolyzed form. This improves the solubility in water, makes the polymer more compatible with cationic minerals and and is commonly marketed as a 50% active dispersion in mineral oil. Because it is widely used in industry as a flocculant for water and paper manufacture it is the least expensive FR and therefore the most widely used.

3.4. AcrylamidoMethylPropane Sulfonate (AMPS)

AMPS is chemically structured so that the molecule is less susceptible to precipitation by cationic mineral salts which may be present in hard water or to high temperatures. It is also stable at a wide range of pH so that it is functional in energized fluids that contain CO_2. The Sulfonate character of the polymer also makes it active as a scale inhibitor. It is typically marketed as a 50% active emulsion. Other uses for AMPS include electrocardiogram gels, plasticizers for concrete and as coagulants in water treatment processes.

4. Gelling agents

These materials are added to the fracturing fluid to increase the viscosity. This increases the fracture width so it can accept higher concentrations of proppant, reduces the fluid loss to improve fluid efficiency, improves proppant transport and reduces the friction pressure. The

chemical structure of some gelling agents also allow for crosslinking. The viscosity of a gelling agent in solution is a function of its molecular weight. The viscosity increases with increasing chain length and concentration. Figure 2 shows how this occurs. For slick water the polymer concentration should be below the Critical Overlap Concentration C*, for crosslinked gels the ideal range is between the C* and the Critical Entanglement Concentration C**. When the concentration exceeds the C** a process call sineresis occurs in which the gel is over-crosslinked and water is "squeezed" out of the gel matrix. As water is removed from the polymer mixture as fluid loss occurs in the fracture the concentration of polymer increases dramatically causing damage to the proppant conductivity.

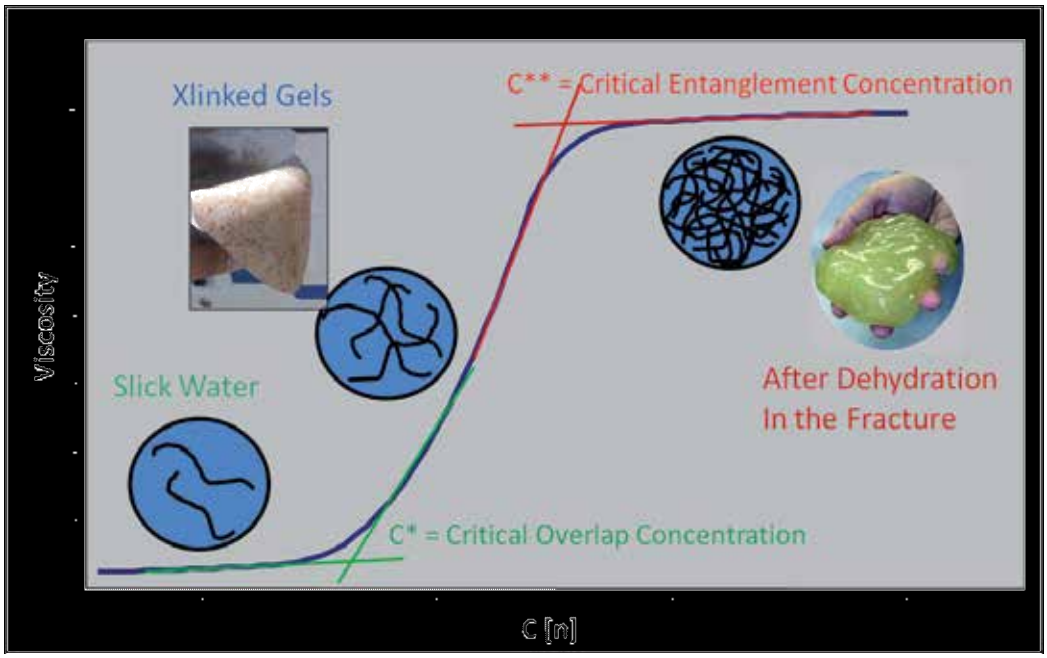

Figure 2. Intrinsic Viscosity of a Solution as a Function of the Polymer Concentration

4.1. Guar

Guar and its derivatives HydroxyPropyl Guar (HPG), CarboxyMethyl Guar (CMG) and CarboxyMethylHydroxyPropyl Guar (CMHPG) are the most common gelling agents used for fracturing. As shown in Figure 3 Guar [Cyamopsis tetragonoloba] is a natural glactomannan gum of the Legume family which is mostly grown in India. Beckwith[1] provides a very nice summary of guar and reports that in 2012 the industry used about 25,000 tons of guar a month at a wholesale cost of $1,723 US/100 kg ($7.83/lb).

After harvesting the seed coat and germ are removed to form what is called a Guar Split. This Guar Split is ground to form guar powder. This process is shown diagrammatically in Figure 4. The chemical structure of guar (See Figure 5) is unique in that it can be readily crosslinked

http://dx.doi.org/10.5772/56422

Figure 3. Guar

through the cis-hydroxyl functionality shown in Red and easily broken through the acetyl linkages shown in Blue. When Guar is broken it leave a 6 to 10% insoluble residue. To reduce this insoluble residue, improve the high temperature stability and improve the crosslinking performance in low pH fluids such as CO_2 the molecular structure of guar is chemically modified with Propylene Oxide to form HPG and with Monochloric Acetic Acid to form CMG or CMHPG. The chemical process is shown in Figure 6.

When using Guar or its derivatives the fluid loss control mechanism is "wall-building – i.e. C-III" in that when the base fluid leaks off the polymer is deposited on the rock face forming a filter cake. The initial leakoff is quite rapid and is called "Spurt". Once a filter cake forms the leak-off becomes a function of the square root of time as described in the companion paper on Fracturing Fluids.

When mixing dry powered Guar, care must be taken to avoid "fisheyes by adjusting the pH of the base water to above 7 and using a high energy mixer to allow proper dispersion. Once the polymer is dispersed the pH is adjusted to just below 6 to allow hydration. Most modern commercially packaged powered Guar systems contain a buffer package that automatically adjusts the pH of the water as the powder is added to prevent fisheyes. When packaged systems are hydrated the pH of the base water needs to be near neutral and a high energy mixer used. Care must also be taken when using very cold water (<60°F) because the rate of solution for the buffer packages can be affected. Guar emulsified in mineral oil as a 50% active material is also commonly used.

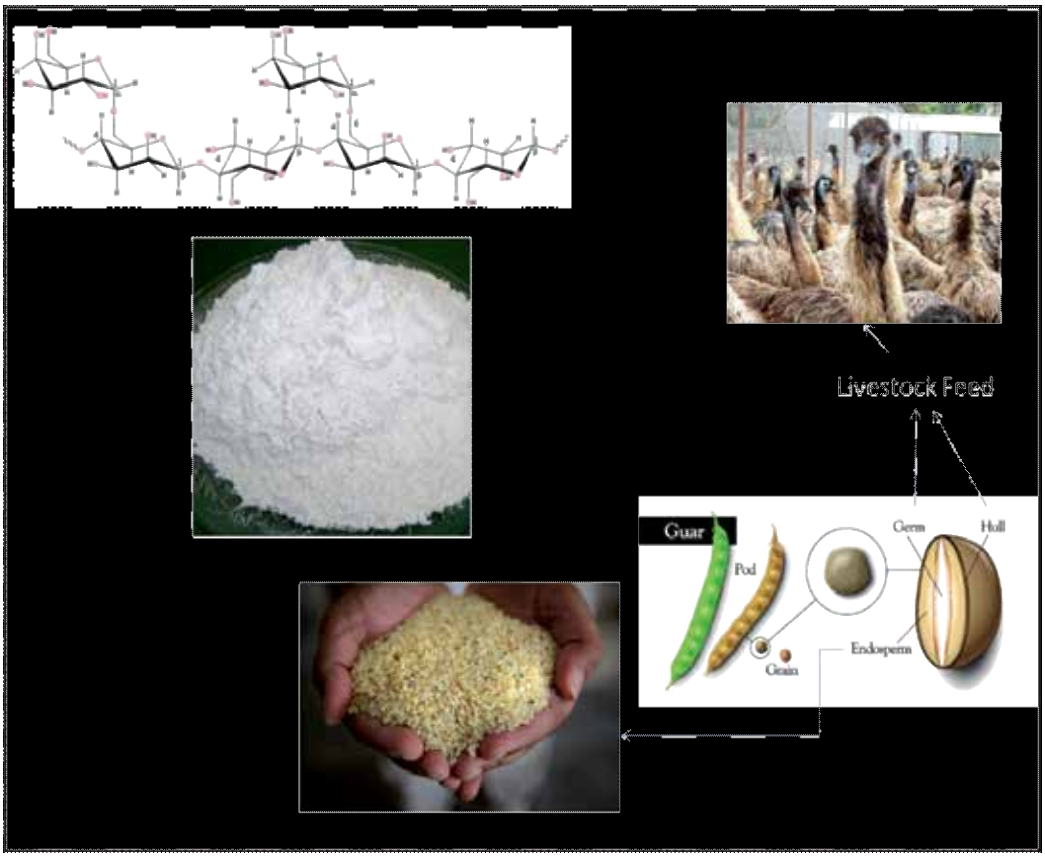

Figure 4. The process of manufacturing Guar Powder

4.2. HydroxyEthyl Cellulose (HEC)

HEC and CarboxyMethylHydroxyEthyl Cellulose (CMHEC) are derivatives of cellulose which is the most common organic compound on Earth. About 33% of all plant matter is a cellusosan organic compound with the formula $(C_6H_{10}O_5)n$, a polysaccharide consisting of a linear chain of several hundred to over ten thousand linked glucose units. As with Guar, Cellulose can be reacted with Propylene Oxide and/or Monochloric Acetic Acid to produce HEC or CMHEC. The chemical makeup of HEC and CMHEC is shown in Figure 9. The base cellulose used to make HEC and CMHEC comes mainly from cotton which is 90% cellulose. HEC and CMHEC are non-toxic and hypoallergenic and are widely used as a viscosifer and emulsion stabilizer in ice cream, K-Y Jelly, toothpaste, cosmetics, laxatives, diet pills, water-based paints, textile sizing and paper.

Because HEC and CMHEC is 100% soluble in water and contain very little insoluble residue they are used where conductivity is the main driver for design. This is in applications such as gravel packing and Frac/Packing. The fluid loss mechanism is "Viscosity- Controlled – i.e. C-II". To control fluid loss the polymers are used to produce very viscous linear gels. However

http://dx.doi.org/10.5772/56422

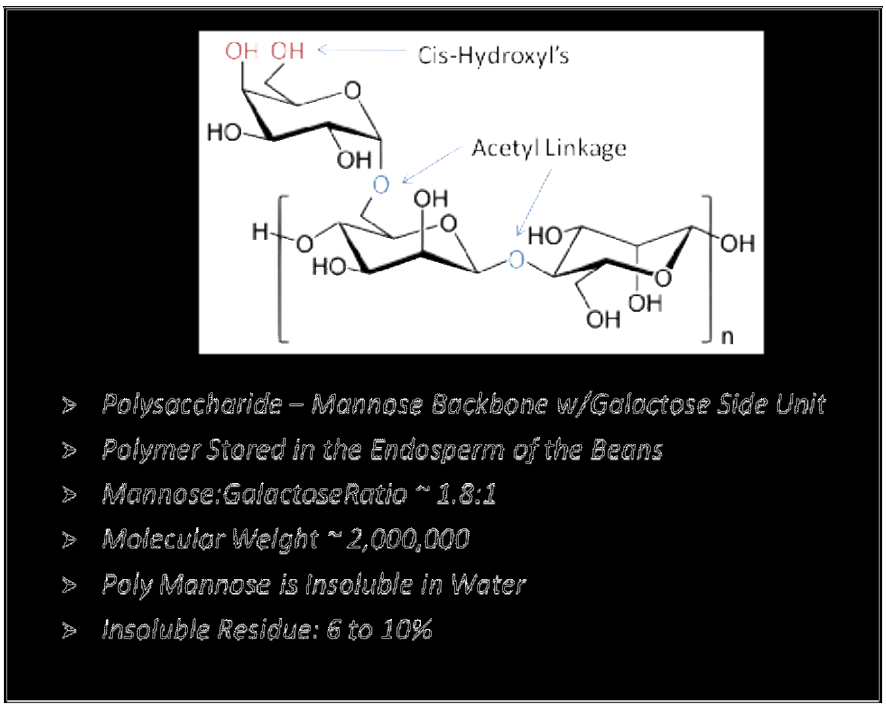

Figure 5. The chemical structure of Guar

above 60 to 80 lb of polymer/1000 gallons of water it becomes difficult to mix. Because the hydroxyls in HEC are in the trans- position (See Figure 9) it cannot be crosslinked and can only be used as a linear gel. The addition of the Carboxy Methyl group in CMHEC provides a crosslinking site so it can be crosslinked using the same mechanisms described for Guar.

4.3. ViscoElastic Surfactant (VES)

VES are polymer free aqueous based fracturing fluids that generate their viscosity through the association of surfactant molecules (Figure 10). As the concentration of surfactant is increased the molecules reach a point where they form aggregates called micelles where the hydrophobic tails form the core of the aggregate and the hydrophilic heads are in contact with the surrounding aqueous liquid. This occurs at a point called the Critical Micelle Concentration (CMC). As the concentration of micelles increase they become entangled with one another at C* as shown in Figure 10. Typically this point is at about 4 to 6% by weight of surfactant. Anionic, cationic and zwitterionic surfactants are used to formulate VES fluids. The main advantage of these fluids is that they are non-damaging to the fracture conductivity. Fluid loss is "Viscosity- Controlled – i.e. C-II" which make the fluids particularly appropriate for Frac and Pack applications. Breaking is accomplished by overflushing with a Mutual Solvent, using an encapsulated electrolyte or by dilution. The main disadvantage these fluids have is their strong surfactant base which makes them incompatible with many reservoir fluids. The

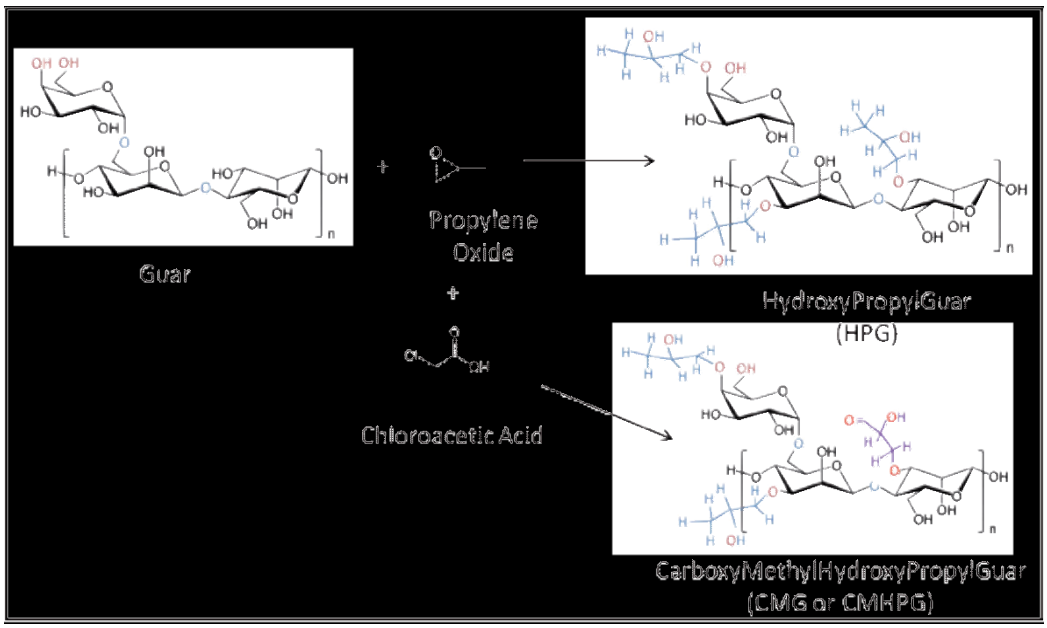

Figure 6. The formulation of HPG, CMG and CMHPG from Guar

surfactants are so strong they have been known to upset even very high API condensate type hydrocarbons.

4.4. Foam/PolyEmulsions

Foam/polyemulsions are fluids that are composed of a material that is not miscible with water. This could be Nitrogen, Carbon dioxide or a hydrocarbon such as Propane, diesel or condensate. These fluids are very clean, have very good fluid loss control, provide excellent proppant transport and break easily simply via gravity separation. PolyEmulsions are formed by emulsifying a hydrocarbon such as Condensate or Diesel with water such that the hydrocarbon is the external phase. The viscosity is controlled by varying the hydrocarbon/water ratio. Foams made with Nitrogen or Carbon dioxide is generally 65 to 80% (termed 65 to 80 quality) gas in a water carrying media which contains a surfactant based foaming agent. Sometimes N_2 or CO_2 are added at a lower concentration (20 to 30 quality) to form "Energized Fluids". This is done to reduce the amount of water placed on the formation and to provide additional energy to aid in load recover during the post-frac flow back period. Nitrogen can dissipate into the reservoir quite quickly so fluids energized with N_2 should be flowed back as soon as the fracture is closed. CO_2, under most conditions, is in a dense phase at static down hole conditions (prior to the well being placed on production), so is less susceptible to dissipation. CO_2 does dissolve in crude oil so will act to reduce the crude viscosity which, again, improves cleanup and rapid recovery. When N_2/CO_2 are added is qualities greater than 90% the resulting mixture is termed a mist with a "0" viscosity. This quality is normally not used in fracturing. The main disadvantage of these fluids is safety i.e. pumping a gas at high pressure or in the

http://dx.doi.org/10.5772/56422

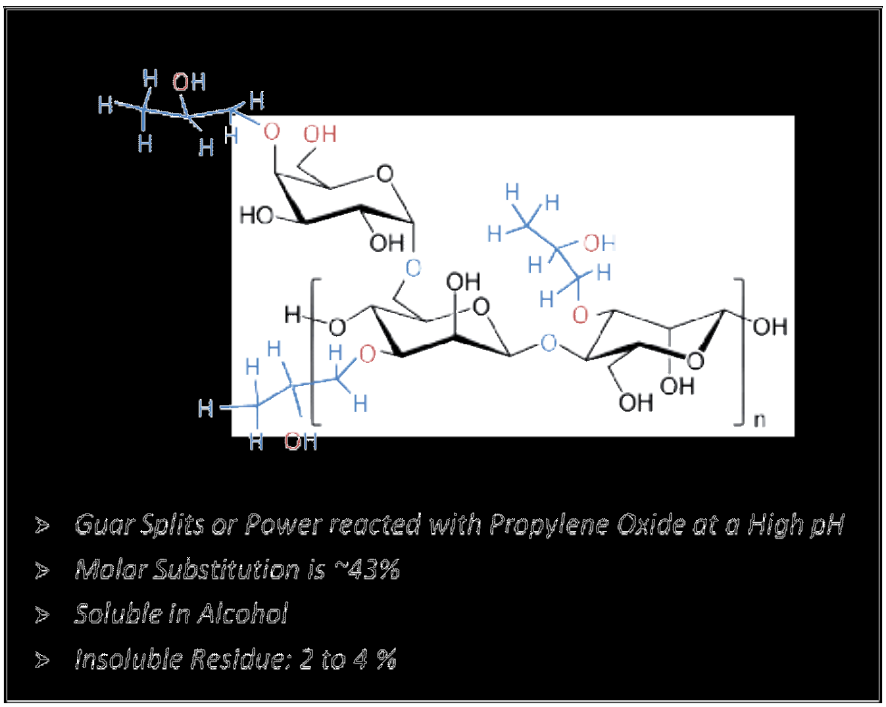

Figure 7. Chemical Structure of HydroxyPropyl Guar (HPG)

case of polyemulsions and gelled Propane, pumping a flammable fluid. CO_2 has an additional hazard in that it can cause dry ice plugs as pressure is reduced. These fluids are generally also more expensive and the gases may not be available in remote areas.

4.5. Oil based fluids

Oil based fluids are used on water-sensitive formations that may experience significant damage from contact with water based fluids. The first frac fluid used to fracture a well used Palm Oil as the gelling agent, Naphthenic Acid as the crosslinker and gasoline at the base fluid. Today most crosslinked oil based fracturing fluids use an aluminum phosphate-ester chemistry[5] that was originally developed to gel hydraulic oils. The aluminum phosphate-esters form a three dimensional structure similar to that described in the VES section. Because the aluminum will attract any polar species the presence of water in the base oil/crude will cause excess viscosity and will adversely affect the thermal stability of the fluid. Breaking of the fluid is accomplished by buffering the pH which causes the association between the base oil and the ester to break down. Although some crude oils have particulate which could build a filter cake, fluid loss is generally considered to be "Viscosity- Controlled – i.e. C-II". There are some disadvantages in using gelled oils. Gelling problems can occur when using high viscosity crude oils or crude oils which contain a lot of naturally occurring surfactants. When using refined oils such as diesel the cost is very high and the oil must be collected at the refinery before any additives such as pour point depressants, engine cleaning surfactants etc. are added. Also there

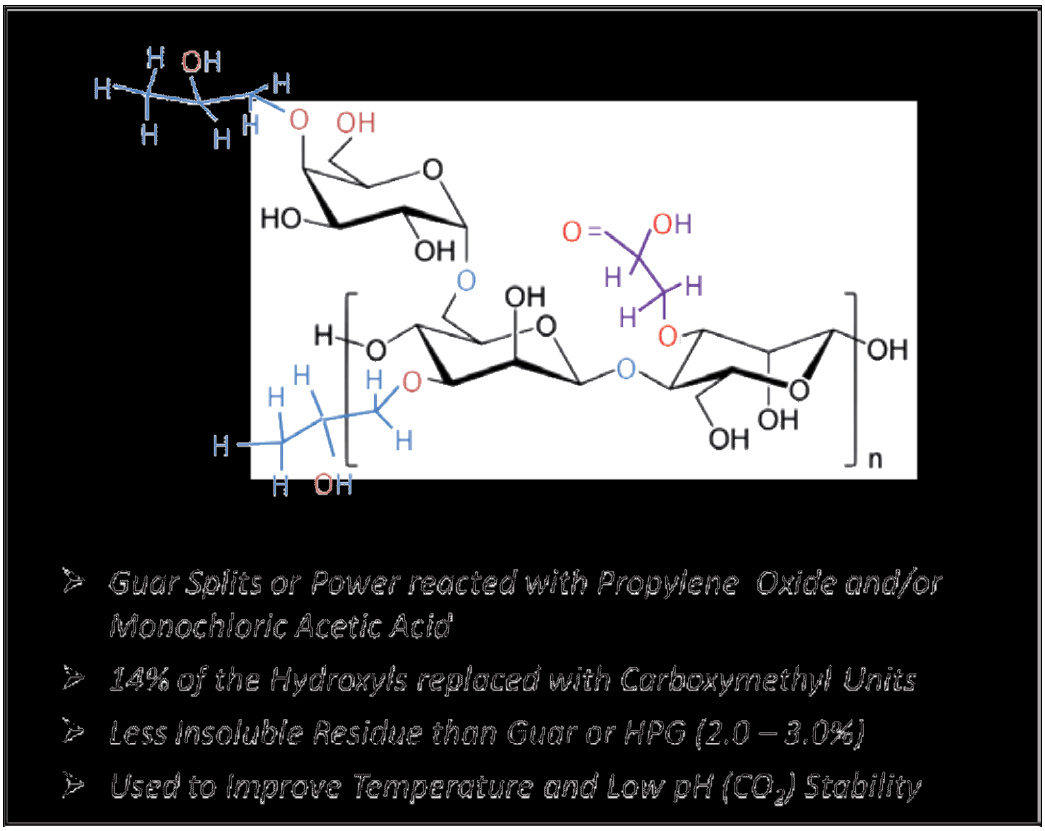

Figure 8. Chemical Structure of CarboxyMethyl Guar (CMG) and CarboxyMethylHydroxy Propyl Guar (CMHPG)

are greater concerns regarding personnel safety and environmental impact, as compared to most water-fluids.

5. Crosslinkers

Crosslinkers are used to increase the molecular weight of the polymer by crosslinking the polymer backbone into a 3D structure as shown in Figure 11. This increases the base viscosity of the linear gel from less than 50 cps into the 100's or 1000's of cps range. This crosslinking also increases the elasticity and proppant transport capability of the fluid.

For guar and CMHEC based gels, Boron and several metals including Titanium and Zirconium are used as crosslinkers. In addition to these materials Iron, Chromium and Aluminum will crosslink guar but are not commonly used. Iron is a major contaminant for fracturing fluids and is one of the metals that must be carefully controlled during the QC process to prevent premature crosslinking. Each crosslinker has a unique reaction requirement and behavior.

http://dx.doi.org/10.5772/56422

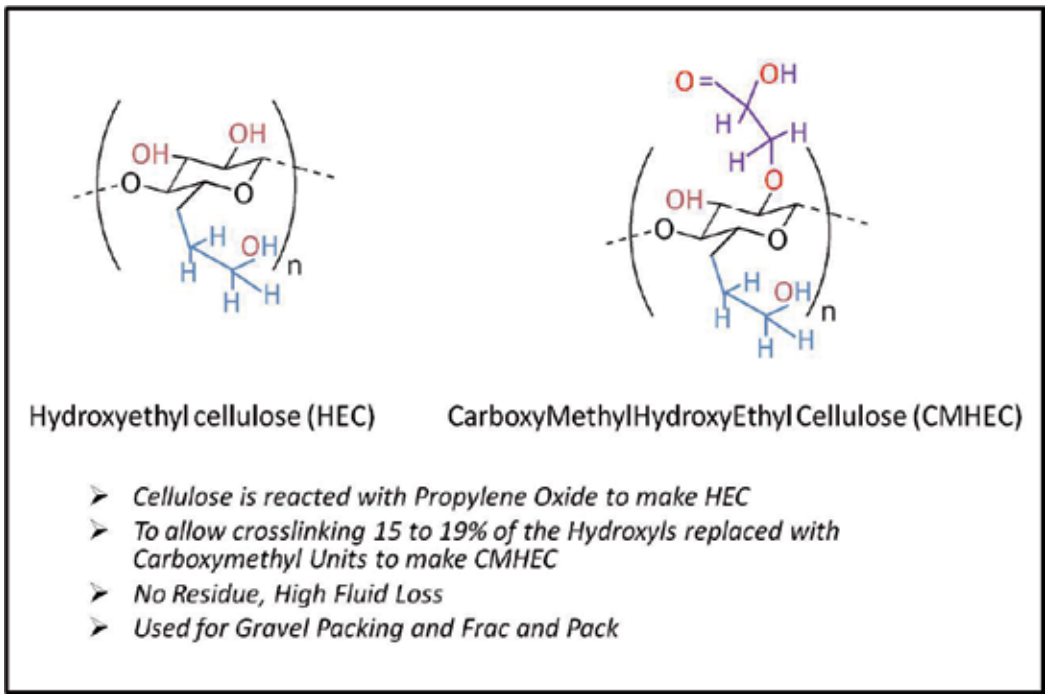

Figure 9. Chemical Structure of Hydroxyethyl Cellulose (HEC) and Carboxy Methyl Hydroxy Ethyl Cellulose (CMHEC)

5.1. Borate

Borate in the form of Boric Acid, slowly soluble salts of Ca and Mg and Organic Borate complexes is, by far, the most common crosslinker in use today. Borate crosslinked fracturing fluids can be applied across a wide range of treating conditions and are resistant to shear degradation. Figure 11 shows diagrammatically how the borate complexes with Guar. As the figure shows the Borate source forms a tetrahedral form of the borate ion when the pH of the base fluid is above about 8.2. These borate ions complexes with the hydroxyl functionality on the polymer causing a 3 dimensional network to be formed which tremendously increases the molecular weight and viscosity. Once this mechanism is understood several things become apparent.

1. The crosslinking is a function of pH which means it can be formed or reversed simply by adjusting the pH. Borate crosslinked fluids are manufactured in the field by mixing the base polymer in water at a pH above 7, adjusting the pH to below 6 and adding in the borate crosslinker and any other additives. During pumping a buffer, usually caustic, is added at the blender which brings the pH above 8 and the crosslink is formed. This also means the process can be reversed simply by dropping the pH below 8 with acid. Cement is a particularly troublesome contaminant when proppant transports are used to also transport cement because the cement raises the pH to 14 which causes premature crosslinking.

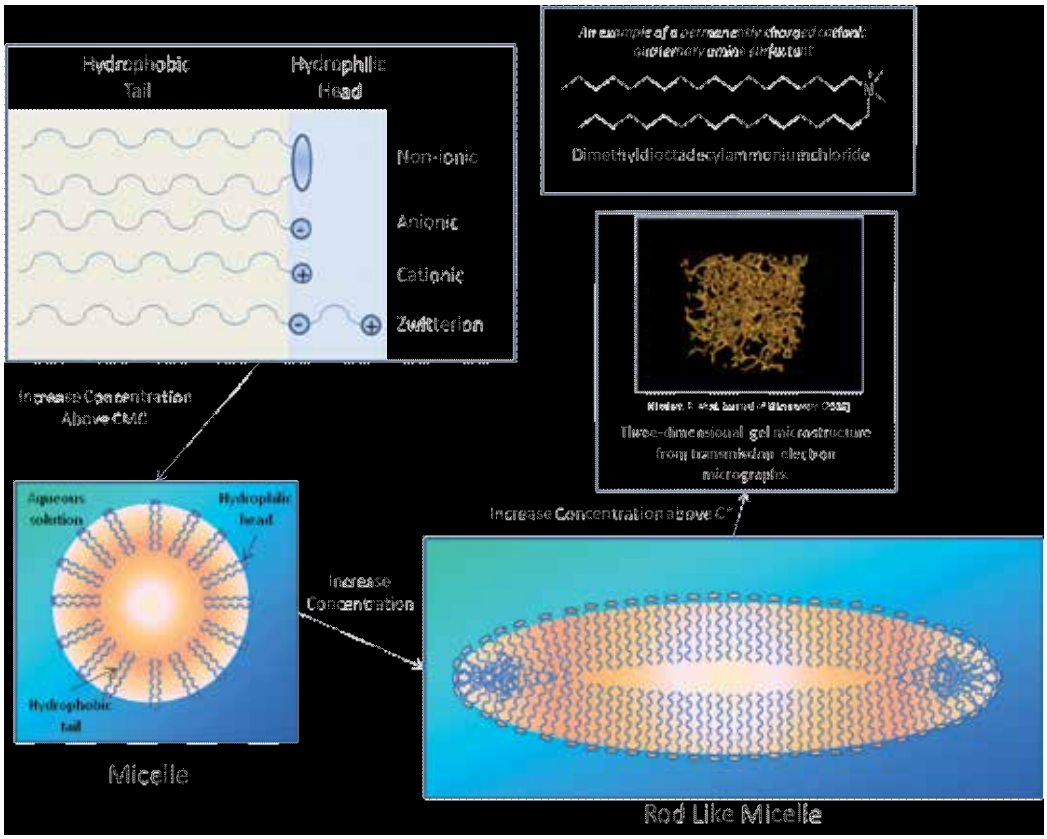

Figure 10. Structure of a Viscoelastic Surfactant Thickener

2. The optimum borate crosslinker efficiency is at a pH of about 10.5.
3. Because the crosslink is in equilibrium it can be broken by shear in the tubing and will quickly build the crosslink again once the shear is dropped.
4. Any polymer which has hydroxyls in the cis position can be crosslinked with Borate. These include Guar and all of its derivatives and CMHECellulose.

5.2. Titanium and zirconium

Titanium and zirconium crosslinkers were originally developed for manufacturing explosive gels[14]. Because Borate crosslinked systems were limited to temperatures below 250°F and pH's above 8 metallic crosslinked fluids were developed to broaden that range. The crosslinkers are manufactured in the form of a metal ligand or chelant using various complexing agents including TEA (Triethanol Amine), LA (Lactic Acid) and AA (Acetylacetone) [15]. When the chelant complex is exposed to water the metal becomes active and crosslinking can occur. Once exposed to water the ionic metal starts to oxidize and if left will become inactive. Both Zirconium and Titanium have coordination num-

http://dx.doi.org/10.5772/56422

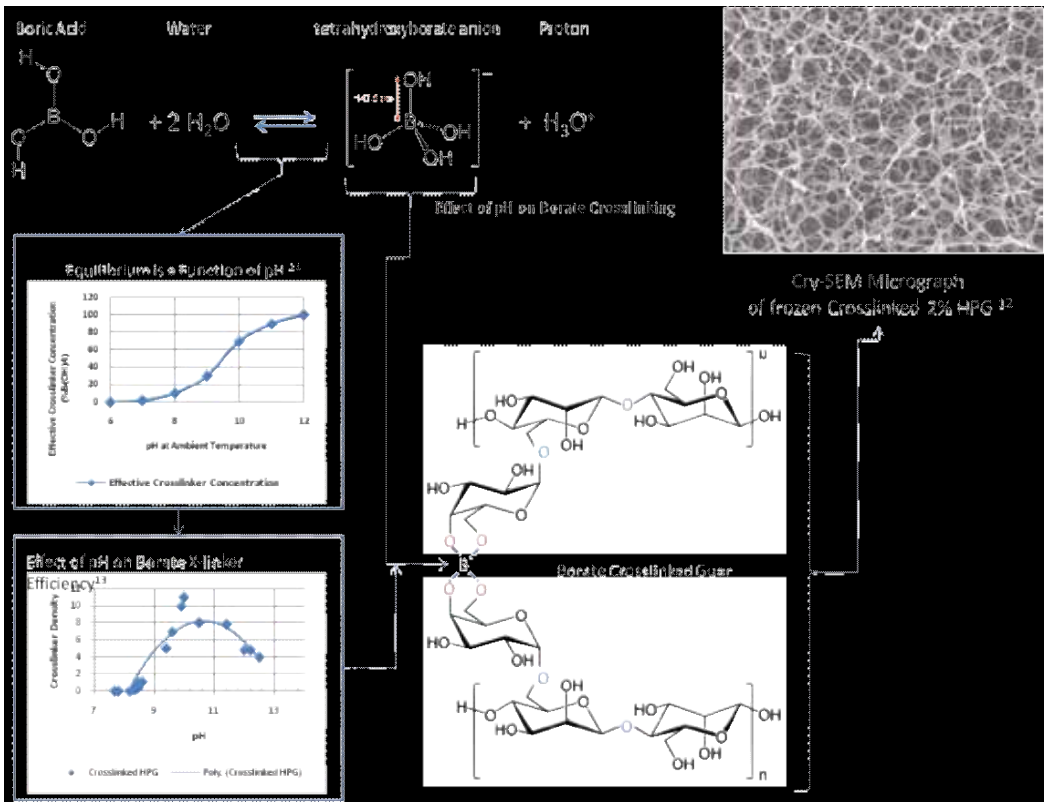

Figure 11. Crosslinking Mechanism of Borate onto Guar

bers of +4 so they form a strong covalent rigid bond with the polymers cis hydroxyls as shown in Figure 12. The various complexing agents allow the crosslinker to become active under a range of time, temperature and pH conditions. Titanium and Zirconium crosslinked fluids can be manufactured that are stable at pH levels from 3.5 to 10.5 and up to temperatures of 350°F. When compared to Borate crosslinked fluids metallic crosslinked fluids have several advantages/disadvantages.

1. The metallic crosslink is a strong covalent bond which makes the crosslink susceptible to high shear rates. Once the bond is broken it will not heal as a Borate crosslink will. To prevent shear degradation the crosslink time should always be delayed to about 2/3 of the pipe time.

2. Because it takes time for the metal to interact with the polymer the crosslink time can be delayed. The type of ligand used to complex the metal controls the delay time. Sometimes it is quite difficult to achieve any delay particularly at a pH < 5.

3. Metallic crosslinked polymer systems can be built that cover a broad range of pH conditions so they can be used in CO_2 based fracturing fluids. They are also much more stable at high temperatures.

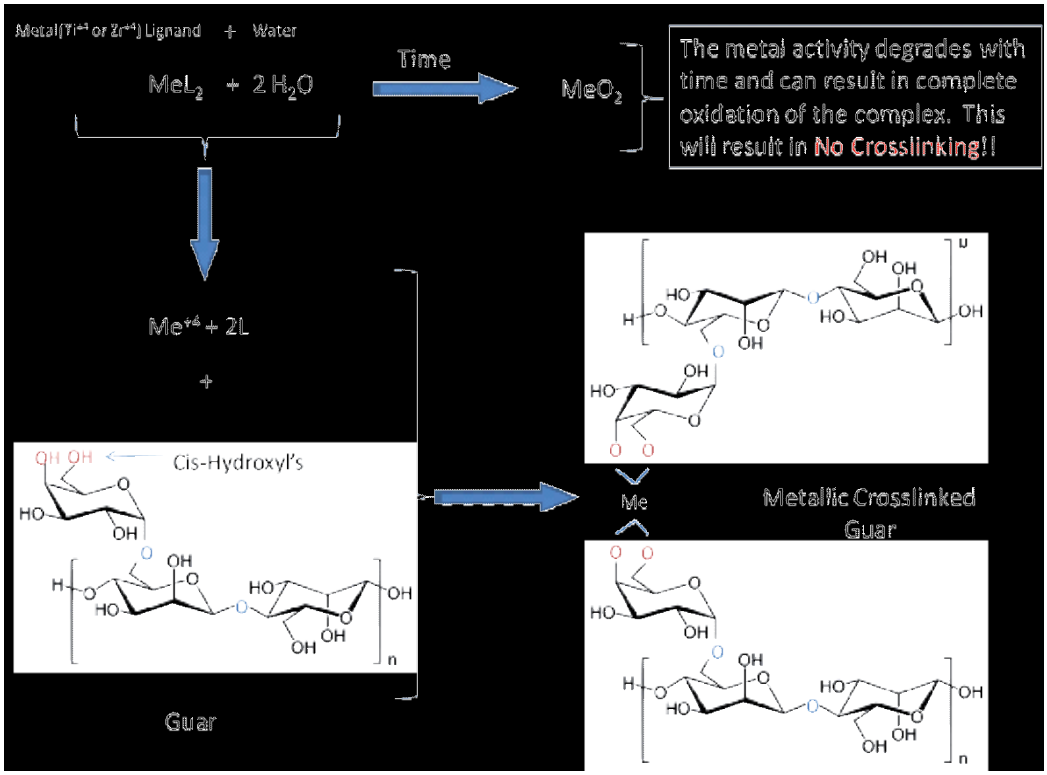

Figure 12. Crosslinking Mechanism for Metallic (Ti^{+4} and^{+4} Zr) Crosslinkers onto Guar

4. Because of the permanent nature of the metallic crosslink, the molecular weight of the broken gel residue is much greater than that formed from linear or borate crosslinked gels. This causes a greater degree of proppant pack damage and conductivity loss.

5. Any polymer which has hydroxyls in the cis position can be crosslinked with Metallic crosslinkers. These include Guar and all of its derivatives and CMHECellulose.

6. Breakers

Breakers are added to the fracturing fluid to reduce the molecular weight of the various polymers used. This reduces the viscosity and facilitates the blowback of residual polymer which allows for cleanup of the proppant pack. The inappropriate use or ineffective breakers can cause significant damage in the proppant pack and a reduced PI. Ideally these materials would be totally inactive during the treatment and then instantly "spring to action" when pumping stops, rapidly breaking the fluid back to a low viscosity preparing the fracture and formation for flow. This is very difficult to achieve as the breaker activity is very dependent

http://dx.doi.org/10.5772/56422

on fluid temperature which varies with time. The three general types of breakers are Oxidizers, Acid and Enzymes.

6.1. Oxidizer

Oxidizer breakers include Ammonium persulfate, Sodium persulfate, and Calcium and Magnesium peroxides. They work by cleaving the acetyl linkages in the polymer backbone as shown in Figure 13[6]. Ammonium persufate [$(NH_4)_2S_2O_8$] and Sodium persulfate ($Na_2S_2O_8$) are very strong oxidizers which forms a free Oxygen radical when the temperature exceeds 125°F. These free radicals attach the backbone of the polymer strand and break it down into its constitutive sugars. If left in the fracture these residual sugars will cook and form insoluble precipitates resulting in conductivity damage[7]. This is the reason flow back of the fractured well is suggested as soon as the fracture is known to be closed. Both Calcium and Magnesium peroxide (CaO_2 and MgO_2) release Oxygen when they come in contact with water. The breaking action is controlled by the solution rate of the peroxide into the water. They are not affected by temperature as much at the persulfates and are used for low temperature applications. The free radical oxidation is not specific to the polymer backbones and the materials will spend on any available free radical acceptor such as a gel stabilizer. All of these materials are strong oxidizing agents and will produce a very active fire when exposed to organic material. They are used in industry for applications such as a water disinfectant, bleach and pickling agents for metals.

The main disadvantage of oxidizing breakers is both how well they work and how fast they work is a function of the amount of chemical added. Figure 14 shows that a concentration of 0.5 lb/1000 gal of persulfate breaker will break the polymer viscosity back to the viscosity of water but will damage the proppant pack so that only 20% of the original conductivity remains. If we want to get the maximum retained permeability we need to go to concentrations of 10 to 12 lb/1000 gallons which will break the fluid viscosity instantly. To counteract this and retard the release of the persulfate encapsulated breakers were developed. There are two types of encapsulated breakers available. The release rate of the breaker in the first type is controlled by hydrostatic pressure, elevated temperatures and the pH of the fracturing fluid[10]. The second method of release is by crushing the capsule coating as the fracture closes. Because these encapsulated breakers require conditions similar to those in the fracture i.e. closure or hydrostatic pressure they are difficult to test for QC purposes in the field and to date no field test has been developed to quantify their activity in the field.

6.2. Acids

Acids such as HCl or Acetic acid will attach the polymer back bone and break the gel similar to oxidizing breakers but they are much less selective and can cause considerable amount of insoluble material to be formed. They are generally used to try and clean fractures that are believed to be damaged by a job where sufficient breaker was not used or the gel is believed to not be broken. They also work by reversing the crosslink in Borate crosslinked systems. They are typically used after a job has been completed and placement becomes the main issue.

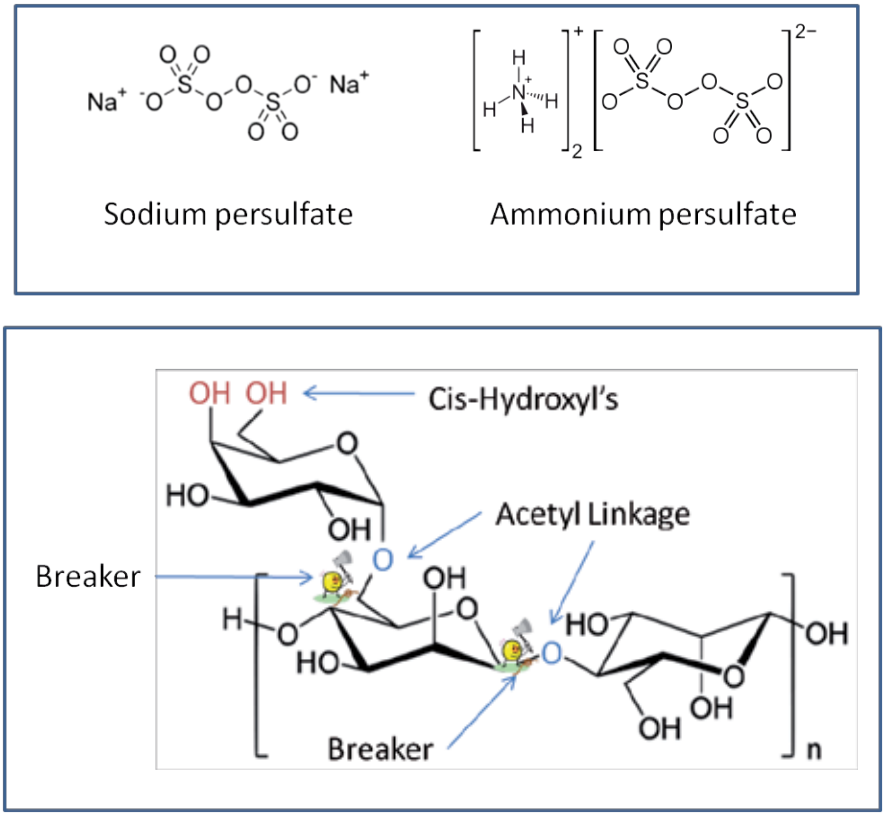

Figure 13. Oxidative Breakers and their action on Guar

6.3. Enzymes

Enzymes are protein molecules that act as organic catalysts that attach and digest the polymer at specific sites along the polymer backbone. Because they are catalysts they are not "used up" during the breaking process and persist until there is no polymer present to digest. Typical enzymes that are used include hemicellulase, cellulose, amylase and pectinase. These enzymes are susceptible to thermal degradation and denaturing when exposed to very high or very low pH so are limited to mild temperatures below 150°F (66°C) and fluid pH's between 4 and 9. Recent work by Brannon and Tjon-Joe-pin have developed proprietary GLSE (Guar Linkage Specific Enzymes) that are reported to work at temperatures more than 300°F[8]. Figure 15 shows diagrammatically how enzymes work and the degradation of the molecular weight of HPG with time as it is digested by Hemicellulase.

http://dx.doi.org/10.5772/56422

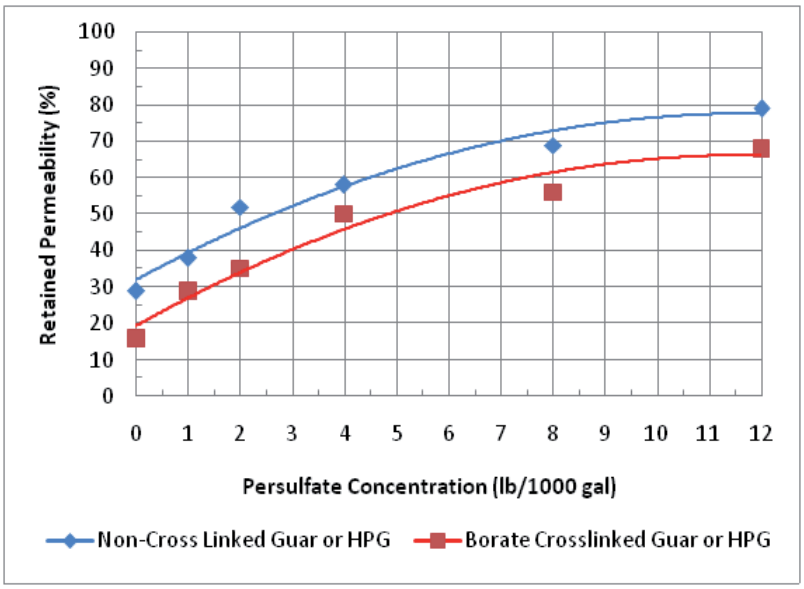

Figure 14. Gel Cleanup vs Breaker Loading (after [9])

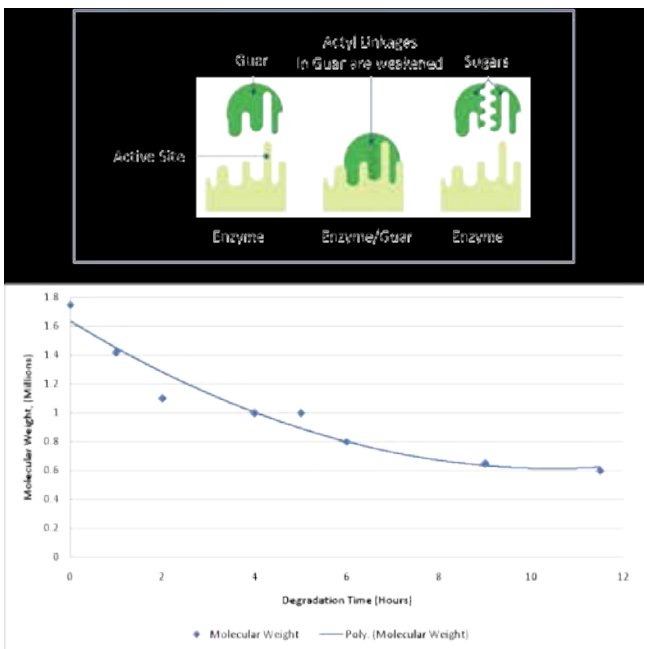

Figure 15. Degradation of Guar by Hemicellulase Enzymes

6.4. Viscosity stabilizers

Viscosity stabilizers are added to the fracturing fluids to reduce the loss of viscosity at high reservoir temperatures. The two most common stabilizers are methanol (used at 5 to 10% of the fluid volume) and Sodium thiosulfate[16]. These materials will extend the temperature range of guar based fluids to over 350°F. Thiosulfate is the more effective of the two and is less hazardous to handle. These materials act as free radical scavengers that are present in the base water. An example would be free oxygen. Without the stabilizers these free radicals can naturally oxidize the polymer as described in the breakers section. Because breakers are free radical generators and these materials are free radical scavengers they should not be run at the same time.

7. Buffers

Buffers adjust the pH of the base fluid so that dispersion, hydration and crosslinking of the fracturing fluid polymers can be engineered. Because some buffers dissolve slowly they can be used to delay crosslinking for a set period of time to reduce friction in the tubing. Typically this delay time is adjusted so that crosslinking occurs at about 2/3 of the pipe time i.e. when the fluid is about 2/3 of the way to the top perforation. The use of the proper buffer package also improves the high temperature capability of Borate crosslinked fluids and reduces the amount of polymer need to get good viscosity[17]. Table 1 shows some commonly used buffer components.

Sodium Bicarbonate	Formic Acid
Sodium Carbonate	Fumaric Acid
Sodium Hydroxide	Hydrochloric Acid
Monosodium Phosphate	Magnesium Oxide

Table 1. Commonly Used Fracturing Fluid pH buffering chemicals.

8. Surfactants/Mutual solvents

Surfactants/Mutual solvents are added to the fracturing fluids to reduce the surface tension of the fracturing fluid to improve fluid recovery and compatibility between the fracturing fluid and the formation matrix or formation fluids. Lab tests are used to determine the type and loading level of surfactant to be used. The primary goals of a surfactant are to leave the rock surface water wet, act as an emulsion preventer or as a defoamer and reduce the surface tension. In very dry gas wells the water in the frac fluid can shift the relative permeability to the water side and form a “water block” that reduces gas flow. An example of how a proper formulation can reduce this effect is shown in Figure 16. Typically if a well is producing any

http://dx.doi.org/10.5772/56422

water this "water block" effect is minimal. EGMBE (ethylene glycol monobutyl ether) used at 10 gal/1000 and BGMBE (butylene glycol monobutyl ether) used at 5 gal/1000 are common mutual solvents.

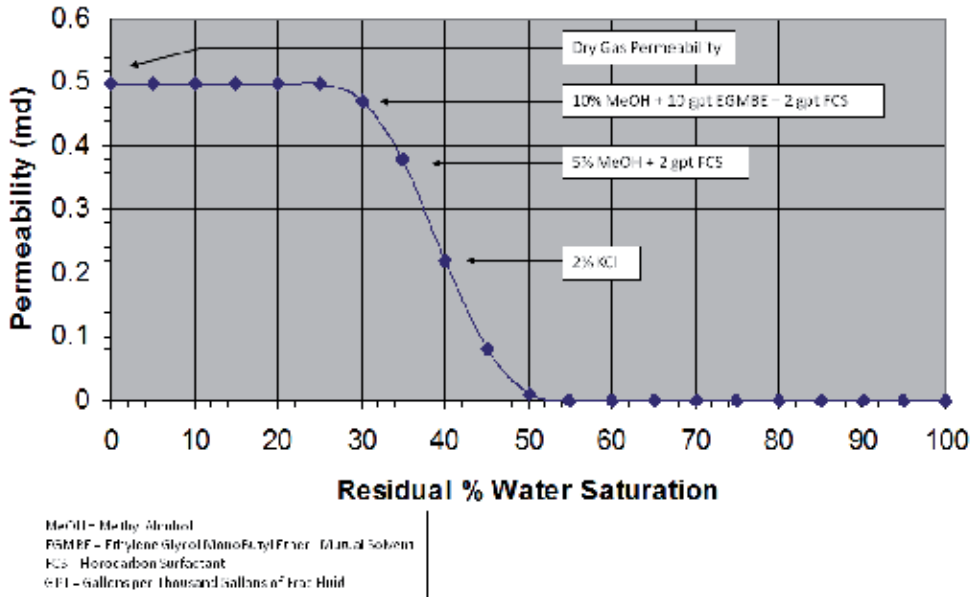

Figure 16. Residual Permeability to Dry Gas of a 0.5 md Berea Sandstone Core

9. Biocides/Bactericides

Biocides/Bactericides are added to minimize the enzymatic attack of the polymers used to gel the fracturing fluid by aerobic bacteria present in the base water. If not controlled the growth of micro-organisms will quickly degrade the polymer to a non-functional level. In addition biocides and bactericides are added to fracturing fluids to prevent the introduction of anaerobic sulfate reducing bacteria (SRB) into the reservoir. These bacteria can "sour" a well and produce corrosive hydrogen sulfide gas. They can also produce a black, slimy "biofilm" in wells that produce water which will block production. Quaternary amines, amides, aldehydes and Chlorine dioxide are effective biocides used in the industry[12]. The use of ultraviolet (UV) light as a disinfectant for fracturing water is also used[18]. A good functional bactericide not only kills the bacteria but also inactivates the enzymes that the bacteria release. Bacteria also mutate so can become resistant to a particular bactericide if used continuously i.e. use a variety of bactericides to provide protection.

Author details

Carl Montgomery*

NSI Technologies, Tulsa, Oklahoma , USA

References

[1] Beckwith Robin; "Depending on Guar- For Shale Oil and Gas Development", Journal of Petroleum Technology, December (2012). , 44-55.

[2] Conway Michael W., Almond, Stephen W., Briscoe, James Earl, Harris, Lawrence E., Halliburton Services, "Chemical Model for the Rheological Behavior of Crosslinked Fluid Systems", Journal of Petroleum Technology, Feburary (1983). , 35(2), 315-320.

[3] Whalen, R. T, & Patent, U. S. Viscoelastic Surfactant Fracturing Fluids and a Method for Fracturing Subterranean Formations", Issued March 14, (2000). , 6035936.

[4] Sullivan, P. F. et.al., "Optimization of a Visco-Elastic Surfactant (VES) Fracturing Fluid for Applications in High-Permeability Formations", SPE 98338 presented at the International Symposium and Exhibition of Formation Damage Control, February, (2006). , 15-17.

[5] Maberry, L. J. et.al. "New Complexation Chemistry Provides Improved Continuous-Mix Gelled Oil" Presented at the (1997). SPE International Symposium on Oilfield Chemistry, Houston, Texas February, 18-21.

[6] Sarwar, M. U. et.al. "Gel Degradation Studies of Oxidative and Enzyme Breakers to Optimize Breaker Type and Concentration for Effective Break Profiles at Low and Medium Temperature Ranges", SPE 140520 Presented at the (2011). SPE Hydraulic Fracturing Technology Conference, January, The Woodlands, Texas., 24-26.

[7] Bilden, D. M, & Montgomery, C. T. et.al.; "The Effect of Long-term Shut-in Periods on Fracture Conductivity" SPE 30493 presented at the (1995). SPE Annual Technical Conference, October., 22-25.

[8] BrannonHarold et.al., "Enzyme Breaker Technologies: A Decade of Improved Well Stimulation", SPE 84213 presented at the (2003). SPE Annual Technical Conference, Denver, Colorado October., 5-8.

[9] Brannon, H. D, & Pulsinelli, R. J. Breaker Concentrations Required to Improve the Permeability of Proppant-Packs Damaged By Concentrated Linear and Borate-Cross-linked Fracturing Fluids" PSC Presented at the (1990). Petroleum Society of Canada's Annual Technical Meeting, Jun 10-13, Calgary, Alberta, Canada., 90-90.

[10] Sho-Wei Lo and Matthew J Miller Encapsulated Breaker Release Rate at Hydrostatic Pressure and Elevated Temperatures", SPE 77744 presented at the (2002). Annual Meeting and Exhibition 29 Sept- 2 Oct, San Antonio, Texas.

[11] Economides, M. J, & Nolte, K. G. Section 7, "Reservoir Stimulation- Third Edition" SchlumbergerDowell, John Wiley and Sons, LTD. 0-47149-192-6

[12] Aqualon Technical Brochure 250-6109-07 "Guar and Guar Derivatives Oil and Gas Field Applications" 2007.

[13] Harris, P. C. Chemistry and Rheology of Borate-Crosslinked Fluids at Temperatures to 300°F", SPE 24339, Journal of Petroleum Technology, March (1993). , 45(3)

[14] Morgan, M. E, & Patent, U. S. 4677201 " Titanium-glycol Useful as Crosslinking Agents for Polygalactomannans", June 30, (1987).

[15] Dorf Ketal Tyzor Specification Sheet "Tyzor® Frac Fluid Crosslinkers for Oil and Gas Production. (2011). http://www.dorfketal.com/Tyzor_Prod_Sel_oilgas_frac.html,.

[16] Thomas, T. L, & Elbel, J. L. The Use of Viscosity Stabilizers in High-Temperature Fracturing" SPE 8344 presented at the (1979). SPE Annual Technical Conference and Exhibition, Las Vegas, Nevada, Sept , 23-26.

[17] Nimerick, K. H. et.al. "New pH-Buffered Low Polymer Borate Crosslinked Fluids" SPE Journal of Technology, June (1997). , 2(2)

[18] Halliburton Sales Brochure H07137 10/10 "CleanStream® Service- Ultraviolet Light Bacteria Control Process for Fracturing Fluid" 2010.

[19] Carman, P. S, & Cawiezel, K. E. Successful Breaker Optimization for Polyacrylamide Friction Reducers Used in Slickwater Fracturing" SPE 106162 presented at the (2007). Hydraulic Fracturing Conference, College Station, Texas, January., 29-31.

Chapter 3

Fractures and Fracturing: Hydraulic Fracturing in Jointed Rock

Charles Fairhurst

Additional information is available at the end of the chapter

http://dx.doi.org/10.5772/56366

Abstract

Rock in situ is arguably the most complex material encountered in any engineering discipline. Deformed and fractured over many millions of years and different tectonic stress regimes, it contains fractures on a wide variety of length scales from microscopic to tectonic plate boundaries.

Hydraulic fractures, sometimes on the scale of hundreds of meters, may encounter such discontinuities on several scales. Developed initially as a technology to enhance recovery from petroleum reservoirs, hydraulic fracturing is now applied in a variety of subsurface engineering applications. Often carried out at depths of kilometers, the fracturing process cannot be observed directly.

Early analyses of the hydraulic fracturing process assumed that a single fracture developed symmetrically from the packed off-pressurized interval of a borehole in a stressed elastic continuum. It is now recognized that this is often not the case. Pre-existing fractures can and do have a significant influence on fracture development, and on the associated distributions of increased fluid pressure and stresses in the rock.

Given the usual lack of information and/or uncertainties concerning important variables such as the disposition and mechanical properties of pre-existing fracture systems and properties, rock mass permeabilities, in-situ stress state at the depths of interest, fundamental questions as to how a propagating fracture is affected by encounters with pre-existing faults, etc., it is clear that design of hydraulic fracturing treatments is not an exact science.

Fractures in fabricated materials tend to occur on a length of scale that is small; of the order of the 'grain size' of the material. Increase in the size of the structure does not introduce new fracture sets.

Numerical modeling of fracture systems has made significant advances and is being applied to attempt to assess the extent of these uncertainties and how they may affect the outcome of practical fracturing programs. Geophysical observations including both micro-seismic activity and P- and S-wave velocity changes during and after stimulation are valuable tools to assist in verifying model predictions and development of a better overall understanding of the process of hydraulic fracturing on the field scale. Fundamental studies supported by laboratory investigations can also contribute significantly to improved understanding.

Given the widening application of hydraulic fracturing to situations where there is little prior experience (e.g., Enhanced Geothermal Systems (EGS), gas extraction from 'tight shales' by fracturing in essentially horizontal wellbores, etc.) development of a greater understanding of the mechanics of hydraulic fracturing in naturally fractured rock masses should be an industry-wide imperative. HF 2013 International Conference for Effective and Sustainable Hydraulic Fracturing is very timely!

This lecture will describe examples of some current attempts to address these uncertainties and gaps in understanding. And, it is hoped, it will stimulate discussion of how to achieve more effective practical design of hydraulic fracturing treatments.

1. Introduction

The term 'rock' covers a wide variety of materials and widely different rheological properties often proximate to each other in the subsurface. Tectonic and gravitational forces, sustained over millions of years, have deformed and fractured the rock on many scales. These forces are transmitted in part through the solid skeleton of the rock, and in part through the fluids under pressure in the pore spaces. Long-term circulation through rock at high temperatures at depth involves dissolution and precipitation along the fluid pathways, producing changes in the chemical composition of the fluids and modifying the overall fluid circulation.

Rock in situ is 'pre-loaded' and in a state of changing equilibrium. Any engineering activity changes this equilibrium (see Appendix 1). Often the changes can be accommodated in stable fashion, but serious instabilities can develop.

The rock mass is opaque. Although geophysics is making impressive advances in defining large structures such as faults and bedding planes, most of the features that influence the rock response to engineering activities remain hidden. Mining and civil engineering activities allow three-dimensional access to the underground and direct observation of smaller features such as fracture networks, but most of the newer engineering applications involve essentially one-dimensional access by borehole. Rock engineering problems fall into the 'data –limited' category, as defined by Starfield and Cundall (1988), and strategies to address them must follow a different strategy than engineering problems where detailed and precise design information is available.

http://dx.doi.org/10.5772/56366

Faced with such complexity and lack of structural details, traditional subsurface engineering design has been guided by empirical procedures developed and refined through long experience.

Projects are now venturing well beyond current experience, and for many, 'novel' applications now considered (e.g., Enhanced Geothermal Systems, Carbon Sequestration, see Appendix 1). There is little experience, few guiding rules and very little data to guide the engineering approach.

Such obstacles notwithstanding, subsurface processes, both long–term geological and short term responses, to engineering activities do obey the laws of Newtonian Mechanics.

Classical continuum mechanics has long been used to guide some aspects of design, but considerable care is required in practical application, due to the need to simplify the representation of the real conditions in order to obtain analytical solutions.

The remarkable developments in high-speed computation and associated modeling techniques over the past one to two decades provide an important new tool, which complemented by the appropriate field instrumentation, can augment the classical continuum analyses and help overcome the lack of prior experience. Some empiricism and general practical guidelines may still be useful for the design engineer, but these can and should be mechanics-informed.

This lecture attempts to illustrate the 'mechanics-informed' approach with respect to the practical application of hydraulic fracturing and related engineering procedures to rock engineering.

2. Hydraulic fracturing

Hydraulic fracturing first was used successfully in the late 1940's to increase production from petroleum reservoirs (Howard and Fast, 1970). The technology has evolved since and is now a major, essential technique in oil and gas production. This and other impressive oil industry developments, such as directional drilling, have attracted interest in application of these technologies to a variety of other subsurface engineering operations. Enhanced Geothermal Energy (EGS) is a notable example. Geothermal Energy is a huge resource. Commenting on the EGS resource in the USA, Tester et al. (2005), state:

"….we have estimated the total EGS resource base to be more than 13 million exajoules (EJ)[1]. Using reasonable assumptions regarding how heat would be mined from stimulated EGS reservoirs, we also estimated the extractable portion to exceed 200,000 EJ or about 2,000 times the annual consumption of primary energy in the United States in 2005. With technology improvements, the economically extractable amount of useful energy could increase by a factor of 10 or more, thus making EGS sustainable for centuries." [2]

1 1 exajoule =1018 joules = 1018 watt.seconds.

2 Future of Geothermal Energy (2005) Synopsis and Executive Summaryp.1-4 (2).

"At this point, the main constraint is creating sufficient connectivity within the injection and production well system in the stimulated region of the EGS reservoir to allow for high per-well production rates without reducing reservoir life by rapid cooling." [3]

Field experiments to extract geothermal energy from rock at depth by hydraulic fracturing were started in 1970 by scientists of the Los Alamos National Laboratory, USA. Two boreholes were drilled into crystalline rock (one 2.8 km deep, rock temperature 195°C; the other 3.5 km rock, 235°C) at Fenton Hill, New Mexico. Hydraulic fracturing was used to develop fractures from the boreholes in order to create a fractured region through which water could be circulated to extract heat from the rock. The experiment was terminated in 1992. Commenting on what was learned from the Fenton Hill study, Duchane and Brown (2002) note:

"The idea that hydraulic pressure causes competent rock to rupture and create a disc-shaped fracture was refuted by the seismic evidence. Instead, it came to be understood that hydraulic stimulation leads to the opening of existing natural joints that have been sealed by secondary mineralization. Over the years additional evidence has been generated to show that the joints oriented roughly orthogonal to the direction of the least principal stress open first, but that as the hydraulic pressure is increased, additional joints open."

This is an early indication that pre-existing fractures mass significantly affect how hydraulic fractures propagate in a rock mass.

3. Influence of fractures and discontinuities on the strength of brittle materials

Hydraulic fracturing can be considered as a technique to overcome the strength of a rock mass in situ, initiation and propagation of a crack through a system of pre-existing fractures, essentially planar discontinuities (e.g., bedding planes), and intact rock.

In examining the fracture propagation process, the pioneering work of Griffith (1921, 1924) is a logical point of departure. Griffith had identified planar discontinuities, or flaws, in fabricated materials as the reason why the observed technical strength of brittle materials was about three orders of magnitude lower than the theoretical inter-atomic cohesive (tensile) strength. [4] Using an analytical solution by Inglis (1913) for the elastic stresses generated around an elliptical crack in a plate, Griffith observed that the maximum tensile stress at the tip of the crack $\sigma_t = \sigma_0$ (1+ 2a/b), where a and b are the major and minor semi-axes of the ellipse, and as the ellipse degenerated to a sharp crack or flaw (i.e., as the ratio a/b became very high)[5], the stress σ_t could rise to a value high enough to reach the inter-atomic cohesive strength sufficient to cause the original crack to start to extend.

3 Future of Geothermal Energy (2005)Synopsis and Executive Summaryp.1-5 (5).

4 A fractured rock mass is typically about two orders of magnitude lower in strength than the strength of a laboratory specimen taken from the rock mass [Cundall (2008); Cundall et al, (2008)].

http://dx.doi.org/10.5772/56366

But would the crack continue to extend and lead to macroscopic failure? To address this question, Griffith invoked the *Theorem of Minimum Potential Energy,* which may be stated as "The stable equilibrium state of a system is that for which the potential energy of the system is a minimum." For the particular application of this theorem to brittle rupture, Griffith added the statement, "The equilibrium position, if equilibrium is possible, must be one in which rupture of the solid has occurred, if the system can pass from the unbroken to the broken condition by a process involving a continuous decrease of potential energy."[6]

Griffith's classical work has provided the foundation for the field of "Fracture Mechanics" [Knott (1973); Anderson (2005)] responsible for major continuing advances in the development of high-performance fabricated materials.

Since we will make reference later to this specific definition by Griffith, it is useful to re-state it here.

4. Theorem of minimum potential energy

"The stable equilibrium state of a system is that for which the potential energy of the system is a minimum. The equilibrium position, if equilibrium is possible, must be one in which rupture of the solid has occurred, if the system can pass from the unbroken to the broken condition by a process involving a continuous decrease of potential energy."

Although much of classical Fracture Mechanics has emphasized applications to problems of Linearly Elastic Fracture Mechanics (LEFM) it is important to recognize that the theorem of minimum potential applies equally to inelastic problems.

5. Mechanics of hydraulic fracturing

As used classically in petroleum engineering, hydraulic fracturing involves sealing off an interval of a borehole at depth in an oil or gas bearing horizon, subjecting the interval to increasing fluid pressure until a fracture is generated, injecting some form of granular proppant into the fracture as it extends a considerable distance from the borehole into the

5 Hydraulic fractures generated in classical petroleum applications typically extend (2b) of the order of 25m ~ 50m from a wellbore. The fracture aperture (2a) at the wellbore then will be typically of the order of 0.01 m. Thus, the tensile stress concentration at the tip is very high of the order of 103.

6 In his second paper, Griffith (1924), demonstrated that tensile stresses also developed around similar cracks loaded in compression, provided the cracks were inclined to the direction of the major principal (compressive) stress.(He also assumed that the cracks did not close under the compression.) For the optimum crack inclination, an applied compressive stress of eight times the magnitude of the tensile strength was required to develop a tensile stress on the crack boundary (close to, but not at the apex of the crack) equal to the limiting value in the tensile test. He concluded that the uniaxial compressive strength of a brittle material should be eight times greater than the tensile strength. Interestingly, he did not invoke his second (minimum potential energy) criterion. It was later determined that although a tensile crack could initiate in a compressive stress regime as predicted by Griffith (1924), the crack was stable (i.e., did not satisfy the minimum potential energy criterion). The compressive/tensile strength ratio is greater than 8 (see Hoek and Bieniawski, 1966).

petroleum bearing formation, and then releasing the pressure. This causes the sides of the fracture to compress onto the proppant, creating a high-permeability pathway to allow oil and/or natural gas to flow back to the well and to the surface.

Figure 1 shows a simple two-dimensional cross-section through an idealized hydraulic fracture. The borehole injection point is at the center of the fracture, which is assumed to be a narrow ellipse that has extended in a plane normal to the direction of the maximum[7] (least compressive) in-situ stress.

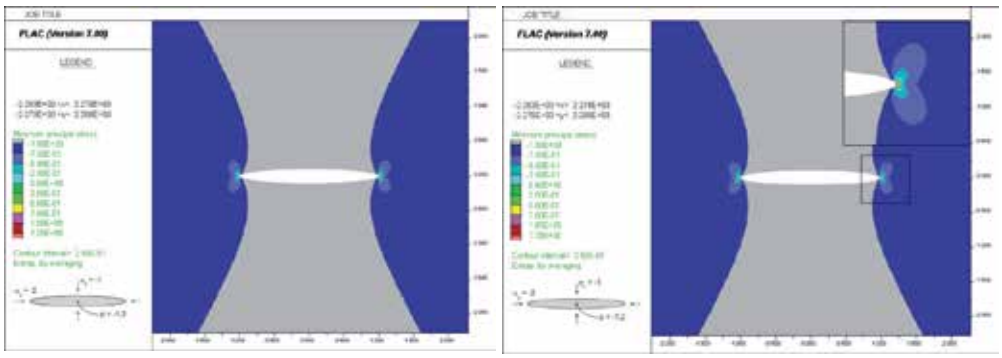

Figure 1. Left) Major and (right) minor principal stresses in the vicinity of an internally pressurized elliptical crack in an impermeable rock.

In the case shown, the crack major/minor axis ratio a/b is 10:1. The internal fluid pressure p = 1.2, while the least compressive principal stress σx = 1.0. This results in a tensile stress concentration at the crack tip. The magnitude of the elastic stress concentration at the crack tip increases directly with 2a/b, (Inglis, 1913). Hence for the case of a>>b, i.e., a 'sharp' crack[8], the concentration is very high, and the crack will extend essentially as soon as the fluid pressure exceeds the magnitude of the least compressive principal stress (σx in Figure 3) it begins to extend, and there will be a pressure gradient from the injection point towards the crack tip as the fluid flows towards the tips. This gradient will depend on the fluid viscosity. Also, since the rock will exhibit some level of permeability, fluid will also flow (or 'leak–off') into the formation as it flows under pressure along the fracture; the rock has a finite strength, or 'toughness' so that energy will be required to extend the crack.

An analytical solution for the stresses in the elastic medium and the crack-opening displacement along the crack was first published by Inglis (1913) and served as the basis for early applications to hydraulic fracturing and fracture treatment design. The Perkins, Kern (1961) and Nordgren (1972) (PKN) and Geertsma and de Klerk (1969) (GDK) models are still used, although numerical models and combinations are now popular. Details of the PKN and GDK models can be found on the SPE website: http://petrowiki.spe.org/Fracture_propaga-

7 Tension is assumed to be positive in Figure 3.

8 A typical hydraulic fracture may have a length (2a) of the order of 50m and a maximum aperture (2b) of 5mm, so that the stress concentration will be of the order of 2000:1.

http://dx.doi.org/10.5772/56366

tion_models. Several differences between the stationary crack assumed by Inglis (1913) and a hydraulic fracture introduce significant difficulties in developing an accurate model of the fracturing process. Thus, the fracture is generated by application of an increasing fluid pressure until the fracture is initiated and extends away from the injection point. Flow of fluid in the fracture is governed by classical fluid flow equations of Poiseuille and Reynolds (lubrication); the pressure drop along the fracture depends on the viscosity of the fluid, and the permeability of the rock (leading to fluid 'leak-off'); the fracture aperture depends on the stiffness of the rock mass and the fluid pressure distribution along the crack; and fracture extension depends on the mechanical energy supplied to the region around the crack tip. The tip may propagate ahead of the fluid, leading to a 'lag,'a dry region between the crack tip and fluid front.

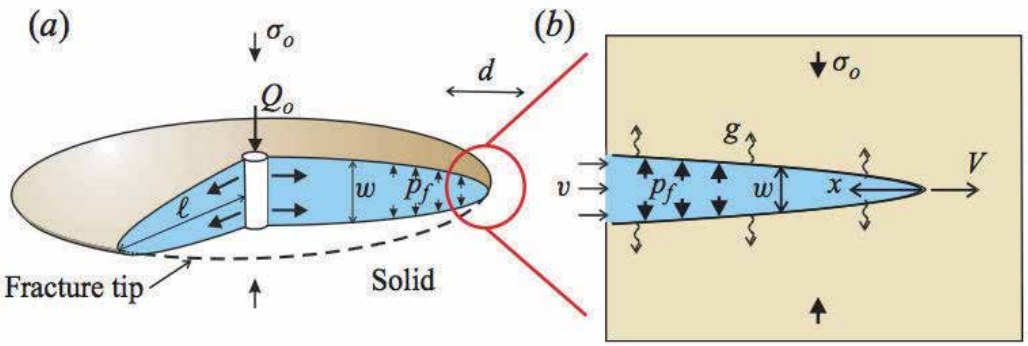

Figure 2. Radial Model of Axi-symmetric Flow and Deformation associated with Hydraulic Fracturing.

Figure 2 illustrates these features for the classical Radial Model in which it is assumed that the fracture propagates symmetrically away from the borehole in a plane normal to the minimum (least compressive) principal in-situ stress, σ0.

Development of efficient and robust Hydraulic Fracturing (HF) simulators is central to successful practical HF treatment of petroleum reservoirs. As noted earlier, competing physical processes are operative during the fracturing operation. This has led to a sustained effort over many years to understand and map the multi-scale nature of the tip asymptotics that arise as a result of these competing physical processes in fluid-driven fracture. These asymptotics solutions are critical to the construction of efficient and robust HF simulators. For example, in an impermeable medium, the viscous energy dissipation associated with driving fluid through the fracture competes with the energy required to break the solid material. Breaking of the bonds corresponds to the familiar asymptotic form of linear elastic fracture mechanics (LEFM), i.e., the opening in the tip region is of the form, e.g., (Rice, 1968), with denoting the distance from the tip. However, under conditions where viscous dissipation dominates, the coupling between the fluid flow and solid deformation leads to (Spence and Sharp, 1985; Lister, 1990; Desroches et al., 1994), on a scale that is considerably larger than the size of the LEFM-dominated region, but still small relative to the overall fracture size. In other words, in the viscosity-dominated regime, the zone governed by the LEFM asymptote is negligibly small

compared to the crack length. Thus, in the viscosity-dominated regime, the HF simulator should embed a 2/3 power law asymptote rather than the classic 1/2 asymptote of LEFM. Garagash et al.(2011) discuss the generalized asymptotics near the tip an advancing hydraulic fracture, an extension of two particular asymptotics obtained at Schlumberger Cambridge Research Laboratory in the early 1990's (Desroches et al., 1994; Lenoach, 1995).

Three classes of numerical algorithms for HF simulators have now been built: (i) a moving grid for KGD, radial, PKN and P3D fracture simulators; (ii) a fixed grid for plane strain and axisymmetric HF with allowance for a lag between the fluid front and the crack tip, and fracture curving (a versatile code has been developed at CSIRO[9] Melbourne to simulate the interaction of a hydraulic fracture with other discontinuities); and (iii) fixed grid for simulating a arbitrary shape planar fracture in a homogenous elastic rock. These codes rely on the displacement discontinuity method (Crouch and Starfield, 1983) for solving the elastic component of the problem, i.e., the relationship between the fracture aperture and the fluid pressure.

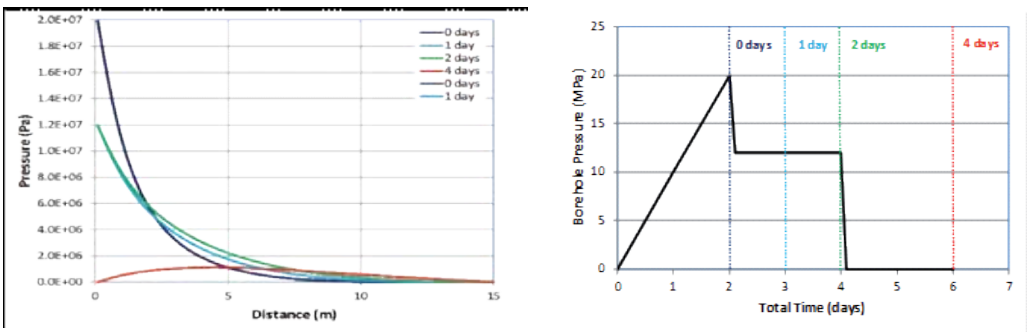

Figure 3. Fluid Pressure Distribution along the Central Axis (Ox) of Figure 1 for a permeable rock due to pressurization and de-pressurization of the borehole.

Figure 3 is presented to illustrate that the fluid pressure in a permeable rock can continue to flow away from the point of injection even after the borehole pressure is reduced to zero. The example shows the distribution of fluid pressure in the rock mass (permeability 5 mD) after (i) 2 days of pressurization up to the peak pressure of 20 MPa in the fracture; (ii) stop pumping and reduce fluid pressure quickly to 12MPa at the point of injection; (iii) hold the pressure constant for 2 days; and (iv) drop the pressure to zero.

It is seen that the pressure in the rock (red curve) has a maximum at some distance from the borehole such that fluid continues to flow into the rock for some time after the pressure in the borehole is reduced to zero. Different combinations of rock permeability, pumping rates and durations can lead to higher peak pressure values in the rock, and longer periods during which fluid can continue to flow away from the well. Such flow may contribute to slip on pre-existing fractures after the pressure in the borehole is reduced to zero.

9 Commonwealth Scientific and Industrial Research Organization.

http://dx.doi.org/10.5772/56366

6. Hydroshear

Hydraulic fracturing is considered to be initiated from a packed–off interval borehole when the net state of stress around the well bore reaches the tensile strength of the rock. It is important to recognize that fluid pressurization of a well in permeable rock will result in flow of the fluid into the rock as soon as the fluid pressure stimulation process is started. This changes the effective stress state in the rock mass and can lead to slip on pre-existing fractures at fluid pressures below the pressure required to crate and extend a hydraulic fracture. This process of inducing slip on pre-existing fractures is termed 'Hydro-shear'. Flow of pressurized fluid into the rock reduces the effective normal stress ($\sigma n - p$) everywhere in the rock { σn = normal stress at any point; p = fluid pressure.] If c and μ respectively represent the cohesion and coefficient of friction acting across the surfaces of a fracture in the rock, then the effective resistance of the fracture to (shear) sliding, τr, will be:

$$\tau r = c + \mu \left(\sigma n - p\right) \tag{1}$$

Thus, if the pressure p is raised progressively then τr will be reduced correspondingly until it reaches the limit at which sliding will occur. The situation is illustrated graphically in Figure 3. The rock is subjected to a three-dimensional state of stress represented by the principal stresses $\sigma 1$, $\sigma 2$, $\sigma 3$ and the fluid pressure p. The series of points 'X' indicate the effective state of stress on an array of pre-existing fractures in the rock. As illustrated in Figure 5, the effect of increasing the fluid pressure in the medium is to move the stress state on these cracks close to the limiting shear resistance, i.e., to the limiting value represented by the Mohr-Coulomb limit. As the stress state reaches this limit, the cracks will slip. In order to initiate a hydraulic fracture, the fluid pressure would need to be increased further, until the limiting Mohr circle reaches the tensile strength limit of the failure envelope. Since crack surfaces are often not smooth, shear slip will tend to result in crack dilation, and an associated increase in fluid conductivity. It is suggested that hydro-shearing could be more effective than hydraulic fracturing as a stimulation technique in certain applications, e.g., in stimulation of high-temperature geothermal reservoirs. Cladouhos et al. (2011) discuss the application of hydro-shearing as a geothermal stimulation technique. The possibility that silica proppant may dissolve in the aggressive high-temperature fluid environment of some geothermal reservoirs whereas slip on rough fractures develops aperture increase without the need for proppant is also presented as an argument in favor of hydroshearing.

7. Deformation and failure of rock in situ

As with fabricated materials, the deformation and failure of brittle rock is also dependent strongly on fractures and discontinuities. In a rock mass, however, the fractures occur over a very wide range of scales from sub-microscopic to the size of tectonic plates. A large specimen of rock will probably include some large fractures, and as the scale of the rock mass increases, fractures from different tectonic epochs.

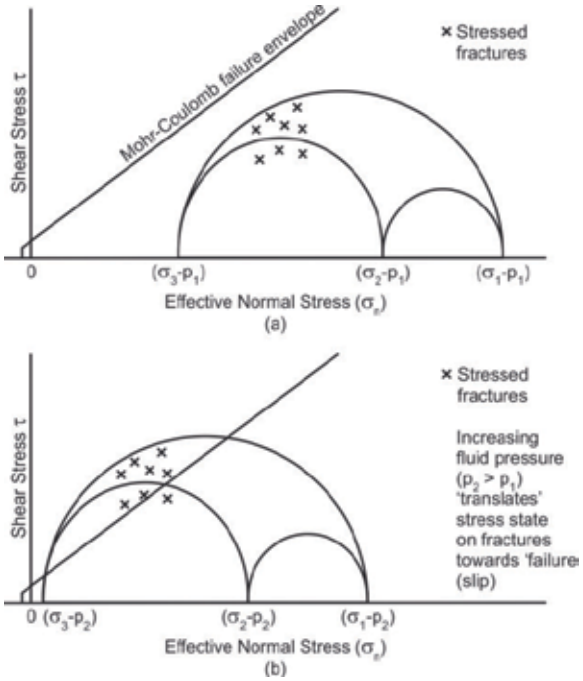

Figure 4. Hydro-shearing — a procedure to generate slip on pre-existing fractures by increasing the fluid pressure to a level below that required to generate a hydraulic fracture.

Study of fracture systems underground in mines and in civil engineering projects allow systems of fractures to be identified and classified statistically into discrete fracture networks (DFN's). The network will include intersecting sets of planar fractures, but individual fractures will tend to be of different lengths, and though organized in two or three spatial orientations, of variable, finite length and not collinear.

Figure 7 presents a two-dimensional illustration of the application of DFN's to the numerical modeling of a fractured rock mass. The in-situ rock mass is considered as a large specimen of intact rock that has been transected by the DFN determined from field observations and fracture mapping underground or at surface outcrops. The properties of the intact rock are built into a Bonded Particle Model of the rock (using the Particle Flow Code (*PFC*) code) based on results of laboratory tests of the intact rock deformability and strength. The intact rock representation is shown on the left of Figure 6. The DFN (shown on the upper right in Figure 6) then is superimposed onto the intact rock.

Cohesion and friction values are assigned to the joint planes.[10] The 'unconfined' strength of a typical large SRM is of the order of a few percent of an intact rock specimen of the same rock (Cundall, 2008). Much of the in-situ strength is derived, of course, from the in-situ stresses imposed on the SRM in situ. One of the consequences of the finite length and lack of collinearity

10 Typically, computer tests indicate the unconfined strength of a Synthetic Rock Mass of the order of 50-m to 100-m side length, to be a few percent of the unconfined strength of the laboratory specimen.

http://dx.doi.org/10.5772/56366

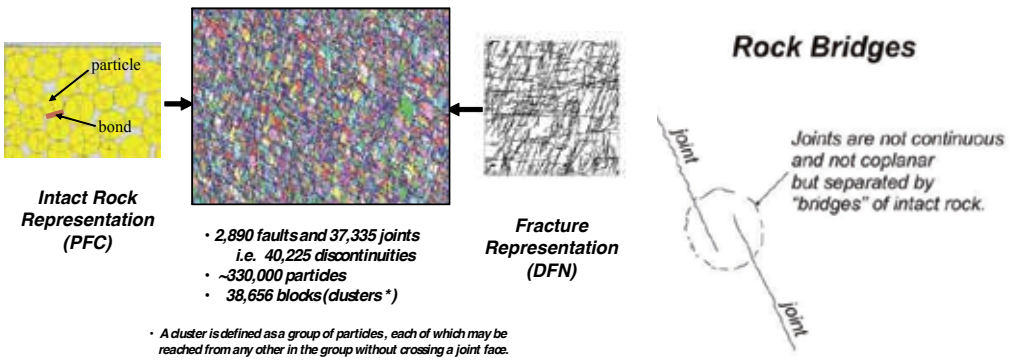

Figure 5. The Synthetic Rock Mass (SRM) representation of a fractured rock mass (in two dimensions). Damjanac et al. (2013) present a discussion of the 'construction' of an SRM in three dimensions. Pierce (2011) presents a comprehensive discussion of practical guidelines and factors involved in the construction of DFN's.

of joint sets in DFN's is the formation of bridges of intact rock Figure 4 within the SRM. These bridges provide regions of intact rock, and of stress concentration, in the SRM and account for a significant part of the overall strength of the rock mass. Earlier models of a rock mass, considered to consist of several sets of through-going fractures, exhibited much lower rock mass strength (Hoek and Brown, 1980).

Figure 5 presents selected extracts from a two–dimensional *PFC* simulation of the development of a hydraulic fracture in a jointed Synthetic Rock Mass. The SRM model was developed following the procedure outlined in Figure 5. The joint distribution was based on a DFN obtained at the Northparkes Mine in Australia.[11] Figure 5(a) shows the location of a vertical borehole that was pressurized by fluid until a hydraulic fracture was initiated. The rock mass is assumed to be impermeable. (The path of the fracture has been traced in blue for clarity.) Displacements in the rock mass produced by the hydraulic fracture are shown as vectors on each side of the fracture. It is seen that the fracture started more or less symmetrically on each side of the borehole, but propagation of the right wing was arrested when the hydraulic fracture encountered an adversely oriented pre-existing joint (Figure 5(b)). With increasing pressure, in the borehole, the hydraulic fracture continued to extend asymmetrically towards the left (Figures 5(c) and 5(d) Figure 5(d) is simply an enlarged view of Figure 5(c)). It is seen that the propagating fracture extended partially by opening existing fractures and partially by developing new fractures through intact rock. Although local deviations occur, the overall path of fracture growth is approximately perpendicular to the direction of the minimum compression stress. The existing fractures introduce an asymmetry to the rock mass. In terms of the idealized symmetric crack of Figure 2, the system in Figure 3 can be considered as two cracks, one extending to the right and one to the left of the borehole with a higher 'fracture toughness' on the right compared to the left, etc.

11 A number of important subsurface engineering problems involve borehole access only. This often means difficulty in establishing reliable, realistic DFN's. In such cases there is no recourse, at least at the start of the project, other than to try to infer fracture networks from borehole observations, perhaps supplemented by local observations of structural geological features . The DFN for Northparkes was available and convenient to use in the example shown in Figure 5.

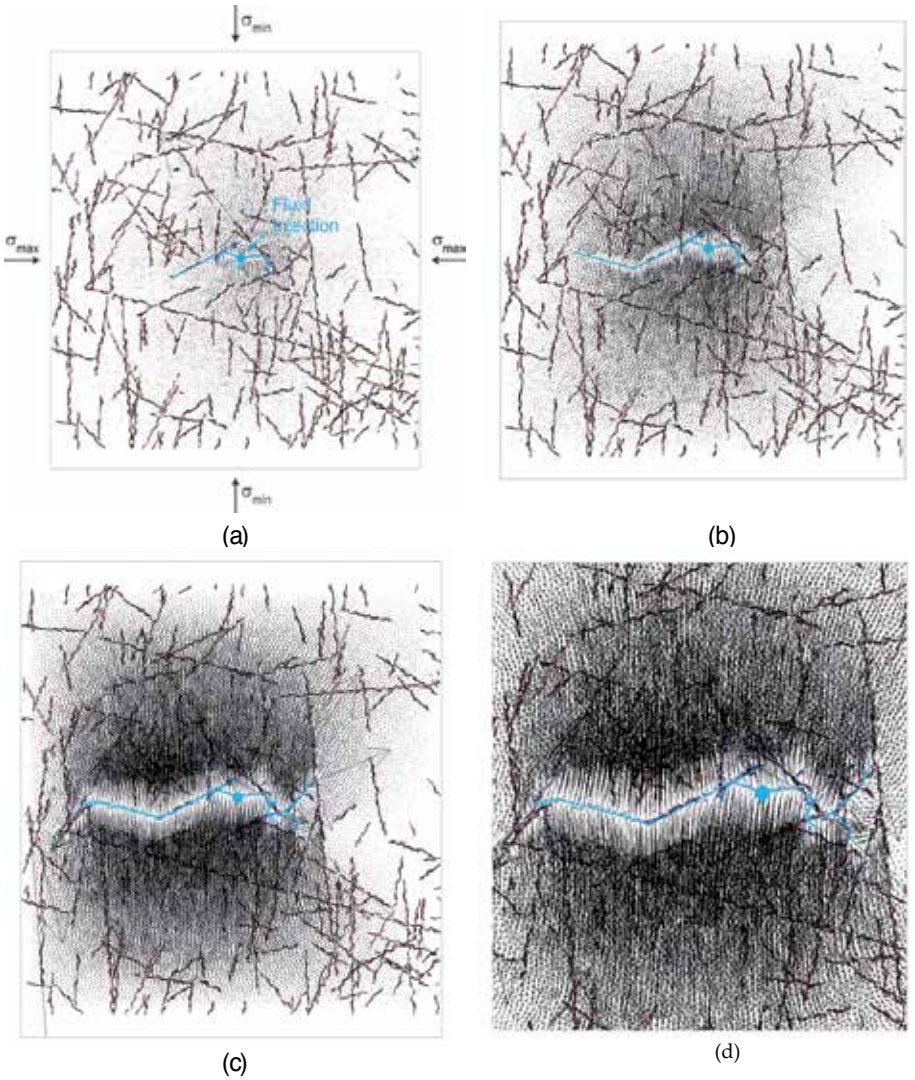

Figure 6. Extracts from simulation of the propagation of a hydraulic fracture in a two-dimensional impermeable SRM (Synthetic Rock Mass). (The horizontal stress σ_{max} is 29 MPa and the vertical stress σ_{min} is 12 MPa – Figure 5(a)). Note that the intact rock between the fractures has a finite strength and can break by rupture of the cemented bonded particles shown in Figure 5. The pressure required to propagate the fracture after breakdown was approximately 10 MPa above the minimum (i.e., least compressive) principal.

Jeffrey et al. (2009) conducted an underground test in the Northparkes Mine, Australia to observe the propagation of a hydraulic fracture in naturally fractured tock. Figure 7 shows part of the path of the fracture, as seen in a tunnel excavated into the fractured rock. The fracture path shows similar characteristics to those shown in the *PFC* simulation in Figure 6.

http://dx.doi.org/10.5772/56366

Figure 7. Hydraulic fracture (green plastic) crossing a shear zone on the face of a tunnel excavated through the fracture. "The arrows indicate the trace of the fracture with green plastic contained in it. There is no clear fracture between points 1 and 2 but the fracture may have crossed this zone either deeper into the rock or in the rock that has been excavated. Approximately 2 m of fracture extent is visible" (Jeffrey et al., 2009).

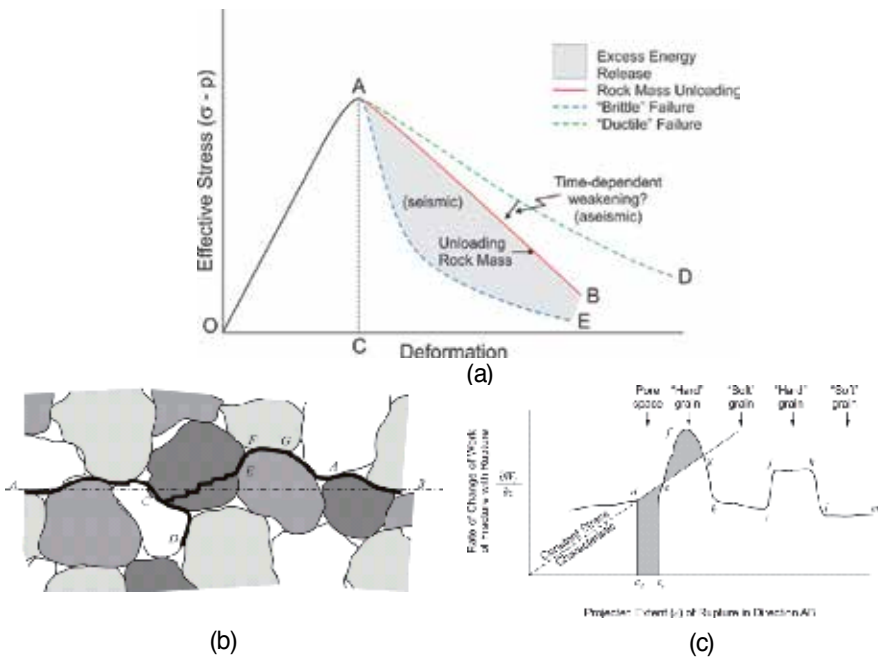

Figure 8. Energy changes during propagation of a fracture through heterogeneous rock.

The energy required to initiate crack propagation is represented by the area OAC in Figure 7(a). Whether or not the crack will extend depends on the energy that becomes available from the intact rock around the crack. If the energy released from the rock mass, represented by the area under the red curve AB, is greater than the energy required to extend the crack, represented by the area under curve AE, then the crack will extend; the excess energy represented by the shaded area serves to accelerate the crack and release seismic energy. If the energy required to extend the crack is represented by the area under the green curve AD, it is greater than the energy that would be released from the rock mass, and hence the crack would not extend. It is possible that the crack could exhibit some form of time-dependent weakening (e.g., due to fluid flow to the crack, viscous behavior, etc.) such that the energy required to extend the crack would be reduced. This could lead to crack extension, i.e., as the slope AD increased to overlap AB, but with no excess energy to produce seismicity. Figures 7(b) and 7(c)[12] illustrate another feature of crack extension on the granular scale. The energy required to extend a crack through or around a grain will be variable; the fracture may encounter pore spaces where no crack energy is required. Application of a constant load to such a heterogeneous system will result in local acceleration and deceleration of the crack-producing bursts of microseismicity. Similar effects can arise in rock fracture propagation at all scales.

It is worth noting that all of these processes of fracture propagation, albeit complex, develop in accordance with the principle of seeking the minimum potential energy of the system.

Much of the preceding discussion has focused on two-dimensional analysis or models. In reality, we are dealing with three- dimensional space (as noted in Figure 6), plus the influence of time (e.g., with respect to fluid flow, or time-dependent rock properties). Figure 8 provides an example from an actual record of hydraulic fracture propagation.

Figure 8 shows the sequence of microseismic events observed during hydraulic fracture stimulation ('treatment' in Figure 8(a)) of a borehole. Early time events are shown as green dots; later events are in red. The microseismic pattern indicates that fracturing started on both sides of the borehole at the injection horizon, but then moved up some 100 m to a higher horizon. As pumping continued, fracturing continued (red locations) on both horizons. It was concluded that the initial fracture in the lower horizon had intercepted a high-angle fault, allowing injection fluid to move to the higher level where it opened up and extended another fracture. Continued pumping led to fracture extension on both horizons. Numerical analysis Figure 8(b) indicated that initial fracture propagation at the lower level resulted in induced tension on the fault above the horizon, but compression on the fault below the lower injection horizon. This explains why injection fluid did not penetrate along the fault below the horizon, and provides a good illustration of the benefit of combining numerical analysis with field observation in understanding fracturing processes.

8. Microseismicity as an indicator of slip on fractures

Microseismicity stimulated during hydraulic fracturing and associated stimulation techniques (e.g., hydroshear) is often used to indicate slip and deformation on fractures in the rock. In

12 Adapted from Fairhurst (1971).

http://dx.doi.org/10.5772/56366

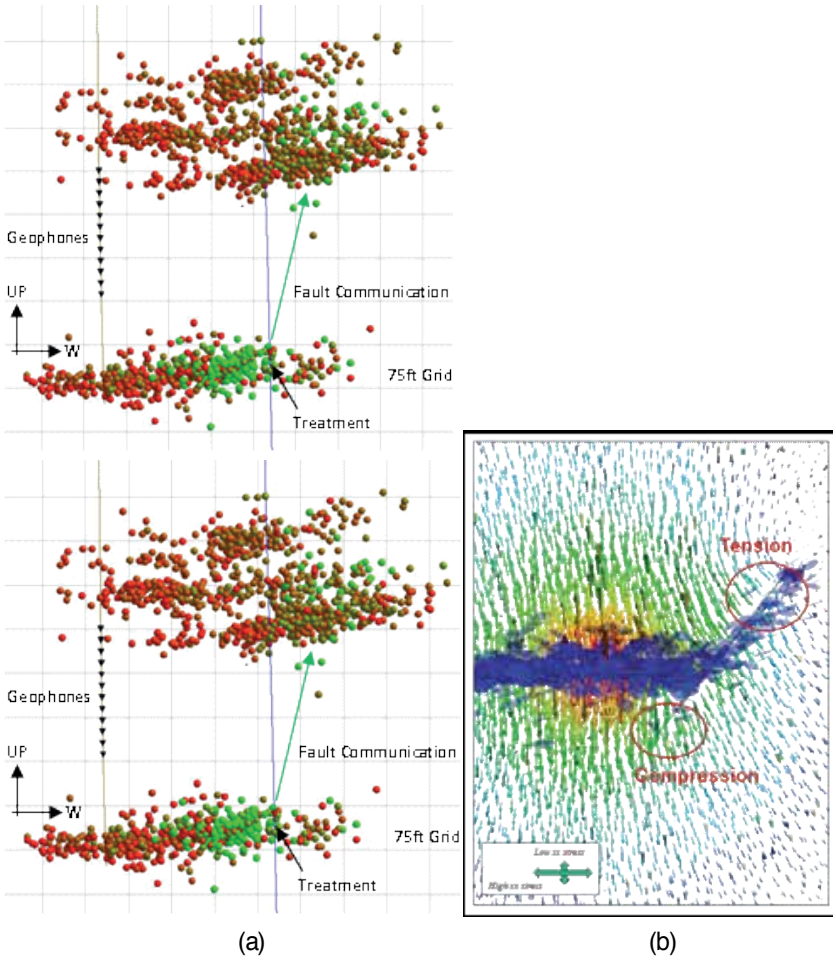

Figure 9. a) Microseismicity observed during hydraulic fracturing in a deep borehole; (b) numerical 'explanation' of the behavior observed in (a).

some cases, it is tacitly assumed that absence of microseismicity indicates absence of slip or deformation. In fact, there is growing evidence that microseismicity does not present a complete picture of deformations induced by stimulation or other effects leading to stress change. Figure 9, reproduced from Cornet (2012) (with permission from the author), shows P-wave velocity changes observed by 4D (time-dependent) tomography during the stimulation of the borehole GPK2 in the year 2000. A detailed discussion of the procedure used to observe and determine the P-wave changes is presented by Calo et al. (2012).

It is seen that the region of detected microseismicity (the cloud of black dots is small compared to the region where the P-wave velocity is reduced by as much as 20% in some regions). Some of the changes in velocity were temporary, suggesting that they may be related to temporal

changes in fluid pressure; other changes appeared to be more permanent deformation that occurred aseismically.

These observations indicate that microseismicity, although a valuable indicator of the response of a rock mass to stimulation by fluid injection, does not identify the complete region influenced by a stimulation.

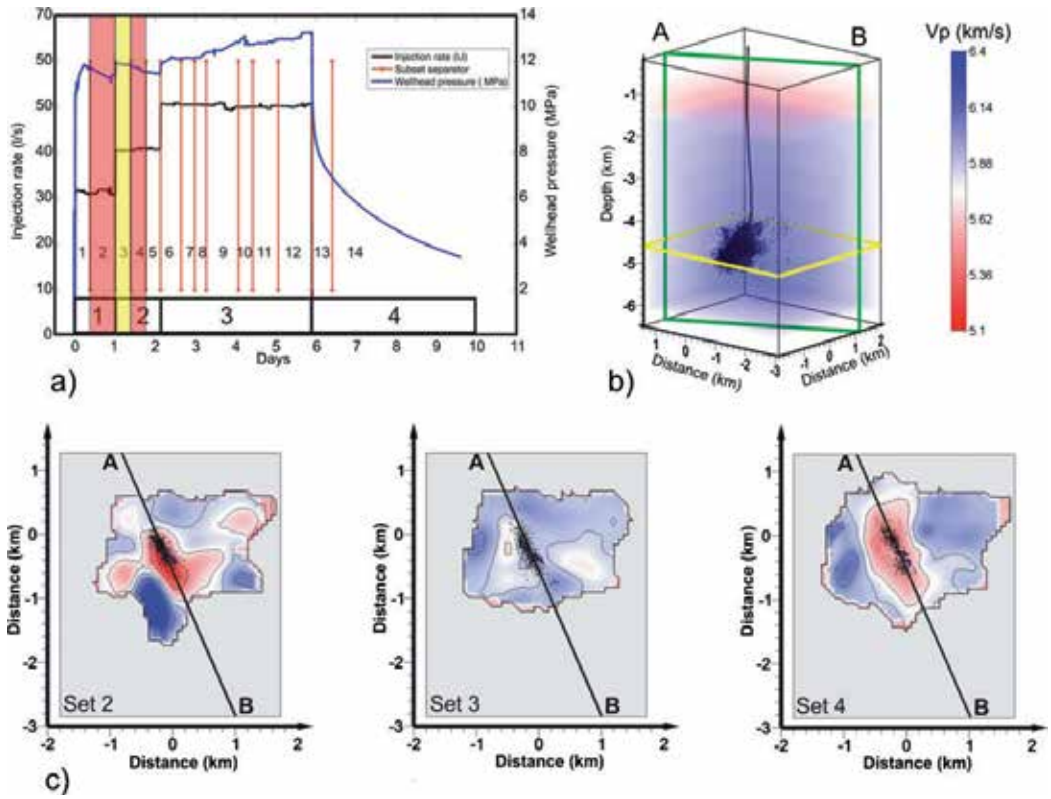

Figure 10. Aseismic slip induced by forced fluid flow as detected by P-wave tomography. (Soultz- sous- Fôrets, France. (a) The injection program (black curve is flow rate, blue curve is well head pressure, horizontal axis is time in days); (b) 3D view of the seismic cloud with respect to the GPK2 borehole. Vertical axis is depth and horizontal axes are distances respectively toward the north and toward the east; and (c) horizontal projections corresponding to the yellow horizontal plane. The vertical green plane is shown as line AB in the plots of part c. P-wave velocity tomography for sets 2, 3 and 4 are indicated respectively by orange, yellow and green colors in the injection program. The vertical axis corresponds to North.

9. In-situ stress

As already noted, hydraulic fractures tend to develop in a more or less planar fashion, extending normal to the minimum regional principal stress. Determining the direction, and perhaps the magnitude, of the regional minimum stress is an important element of hydraulic

http://dx.doi.org/10.5772/56366

fracturing strategy, especially with the development of directional drilling, which allows borehole to be drilled in the direction considered most favorable for fracturing with respect to stress direction. (see e.g., Figure 15 and related discussion).

Determination of the in-situ stress state also can be a significant challenge.

Stress in rock is distributed throughout the mass, and is influenced by the complicated structure of the mass[13]. Most techniques of stress determination rely on what are essentially 'point' determinations. One difficulty of determining the regional stress is illustrated by the simple, albeit somewhat artificial, example of Figure 11. This shows a two-dimensional numerical model of the stress distribution in an elastic plate containing several finite frictional fractures.

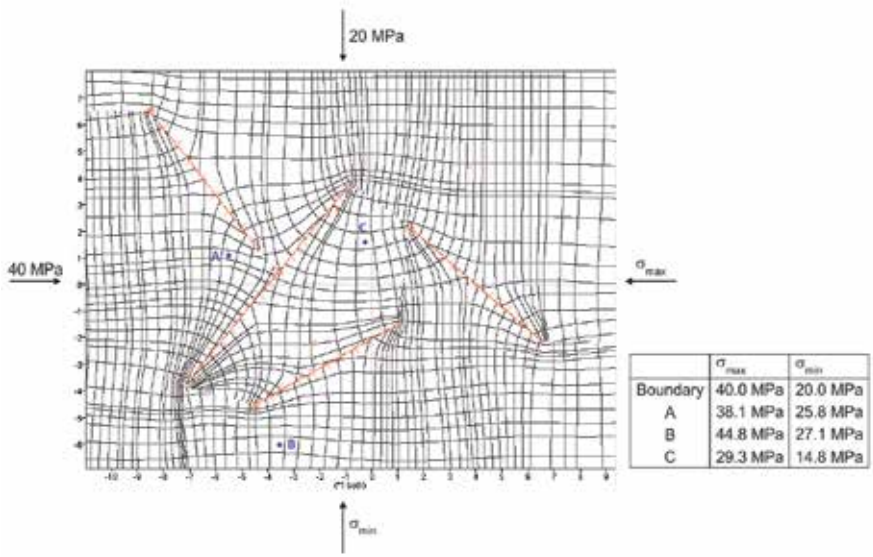

	σ_{max}	σ_{min}
Boundary	40.0 MPa	20.0 MPa
A	38.1 MPa	25.8 MPa
B	44.8 MPa	27.1 MPa
C	29.3 MPa	14.8 MPa

Figure 11. Influence of frictional cracks on the distribution and orientation of principal stresses, illustrative example.

The exercise serves to illustrate the difficulty of making stress determinations from local point measurements, be they in a borehole or on the surface. Stresses can change in orientation and magnitude locally due to geological inhomogeneities, fractures, faults, etc., many of which may be hidden or cannot be observed from the measurement location. Although determinations made at points A and B are reasonably close to the boundary values, point C is considerably different, and the directions of principal stress, as indicated by the principal stress trajectories, can be very different from the (regional) orientations, i.e., at the model boundary.

Figure 12 provides an actual example of the variability of stress over relatively short distances. (The vertical and horizontal scales are equal in Figure 12). In this case, the main interest was to assess how normal stresses were affected by the thickness of gouge in the plane of the thrust fault.

13 See also footnote 17 –Appendix 1.

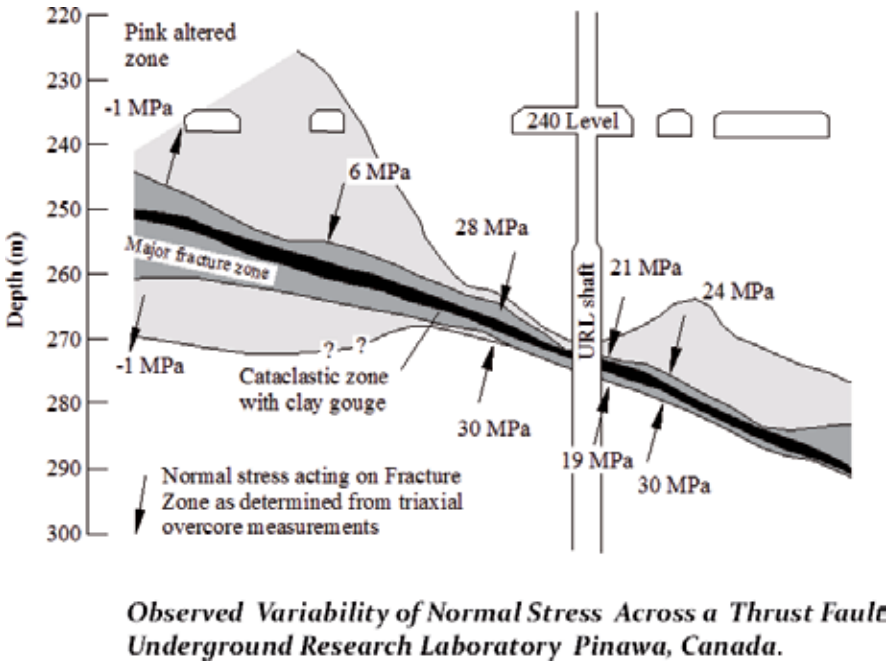

Figure 12. Normal stress variation across a thrust fault, Underground Research Laboratory, Canada.

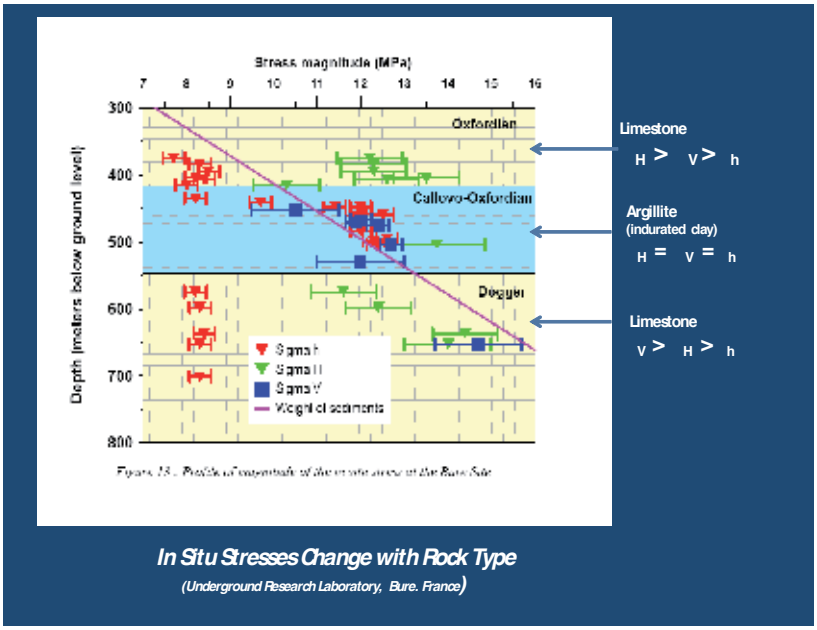

Figure 13. Observed stress distributions in argillite and limestones at the Underground Research Laboratory, Bure, France.

http://dx.doi.org/10.5772/56366

Figure 13 illustrates another important geological influence on stress distribution, changing lithology. This example is from the French Underground Research Laboratory (URL) [14]at Bure in NE France. Laboratory tests on specimens of the Callovo-Oxfordien Argillite indicate a long-term viscosity of this rock suggesting that any imposed deviatoric stresses would tend towards an isotropic stress state over the order of 10 million years.

Test specimens from the limestones above and below the argillite do not appear to exhibit such viscosity. The stress distributions determined from field measurements support such differences in rheological characteristics of the rock formations.

Commenting on the in-situ stresses observations at Bure (i.e., as shown in Figure 13) Cornet (2012) notes as follows:

"Further, the complete absence of microseismicity in the Paris Basin (Grünthal and Wahlström, 2003, Fig. 4) and the absence of large scale horizontal motion as detected by GPS monitoring (Nocquet and Calais, 2004) indicate that no significant horizontal large-scale active deformation process exists today in this area.

"The important conclusion here is that the natural stress field measured on a 100 km^2 area at depth ranging between 300 m and 700 m does not vary linearly with depth and is not controlled by friction on preexisting well- oriented faults. Rather, the stress magnitudes seem to be controlled by the creeping characteristics of the various layers rather than by their elastic characteristics, with a loading mechanism that remains to be identified but which is neither related directly to gravity nor apparently to present tectonics.

"It is concluded here that the smoothing out of stress variations with depth into linear trends may be convenient for gross extrapolation to greater depth. But it should not be taken as a demonstration that vertical stress profiles in sedimentary rocks are governed by friction along optimally oriented faults, given the absence of both microseismicity and actively creeping fault. It should not be used for integrating together stress tensor components obtained within layers with different rheological characteristics."

Other examples could be cited, but the message is clear. Determination of in-situ stress in rock is an extremely challenging task, with results subject to considerable variability and uncertainty.

Stress orientations can be estimated from consideration of regional tectonics, faulting and interpretation of evidence from local structural geology supported in some cases by evidence based on borehole logs (e.g., tensile fractures induced along the well bore). Stress magnitudes are, in general, more difficult to determine and usually less significant, except as indicators of how stresses may be distributed across a site where the geology and engineering design are complex. In such cases, interpretation of stress distribution is best done in conjunction with a

---

14 The URL at Bure was developed in order to determine the suitability of the Calllovo-Oxfordien Argillite formation for permanent storage of high–level nuclear waste.

numerical model of the site, preferably one that includes the influence of important uncertainties and discussion with structural geologists familiar with the area under study.

10. 'Critical stress state' in the Earth's crust

It is sometimes asserted that the Earth's crust is everywhere close to a 'critical state of stress,' i.e., that a small change in the devatoric stress in the rock is likely to produce slip on one or more faults with associated seismic activity. The current global interest in development of major resources of natural gas, the central role of hydraulic fracturing in this development, and the public apprehension that hydraulic fracturing will 'trigger earthquakes' has led to strong opposition to fracturing, and even legislation to ban the use of hydraulic fracturing in some countries and some States in the USA.

As illustrated by Figure 14, the seismic hazard, (i.e., probability of a damaging earthquake) varies very considerably from place to place. Thus, an earthquake of a given magnitude is 1000 times more likely to occur in Southern California than it is in the Eastern United States. The hazard is even lower in regions such as Texas, North Dakota and in the stable Canadian Shield region of the North American tectonic plate. While many earthquakes are initiated at depths considerably greater than depths where hydraulic fracturing is applied, it seems plausible to suggest that there may be less potential for fracturing to induce seismic activity in regions that have low seismic hazard. Also, as indicated by the comments of Cornet in the previous section of this paper, there is evidence that the critical stress hypothesis warrants detailed scrutiny, at least. This could have major implications for development of the world's major natural gas and EGS (enhanced geothermal systems) resources. Two recent studies, National Research Council (2012) and Royal Society – Royal Academy of Engineering (2012), have each concluded that the risk that hydraulic fracturing as used in development of energy resources would trigger significant seismic activity is small, but it would be valuable to examine the critical stress hypothesis more rigorously than has been done to date.

11. Hydraulic fracturing in tight shales

The development of inclined and horizontal drilling (see Appendix 1 - Figure A1-2) has helped stimulate intense activity to develop natural gas production from so-called tight shale, i.e., rock in which natural gas is held tightly within the very fine pore structure of the rock. Figure 15 illustrates the procedure used to stimulate these shales. The well is drilled horizontally in the gas-bearing formation, more or less in the direction of the minimum principal stress. Hydraulic fractures are generated (and propped) at intervals along the well to generate a network of connected flow paths that will allow the gas to flow to the well. Depth (i.e., extent) and spacing of the fractures should be optimized to produce the formations effectively. Bunger et al. (2012) discuss the factors in the design of an effective fracture strategy.

http://dx.doi.org/10.5772/56366

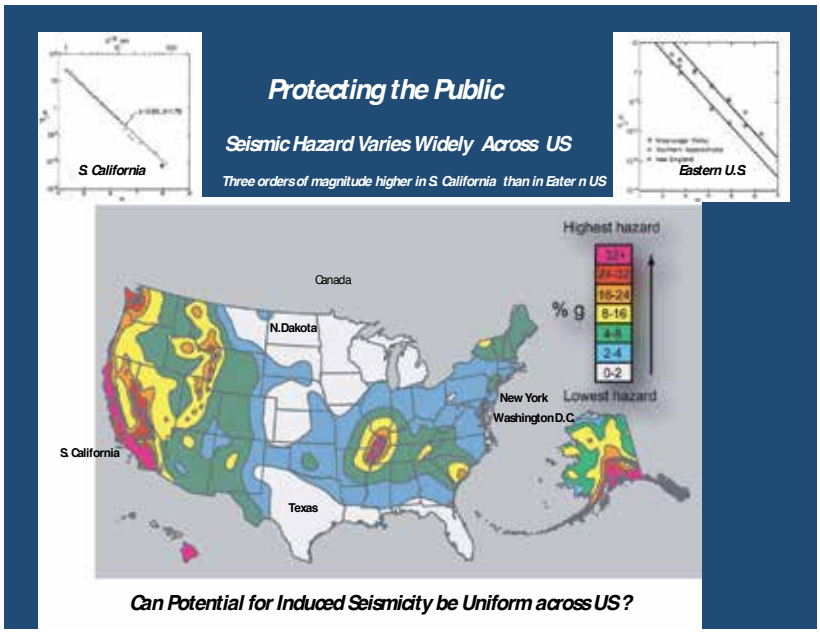

Figure 14. Seismic hazard map of the United States — US Geological Survey.

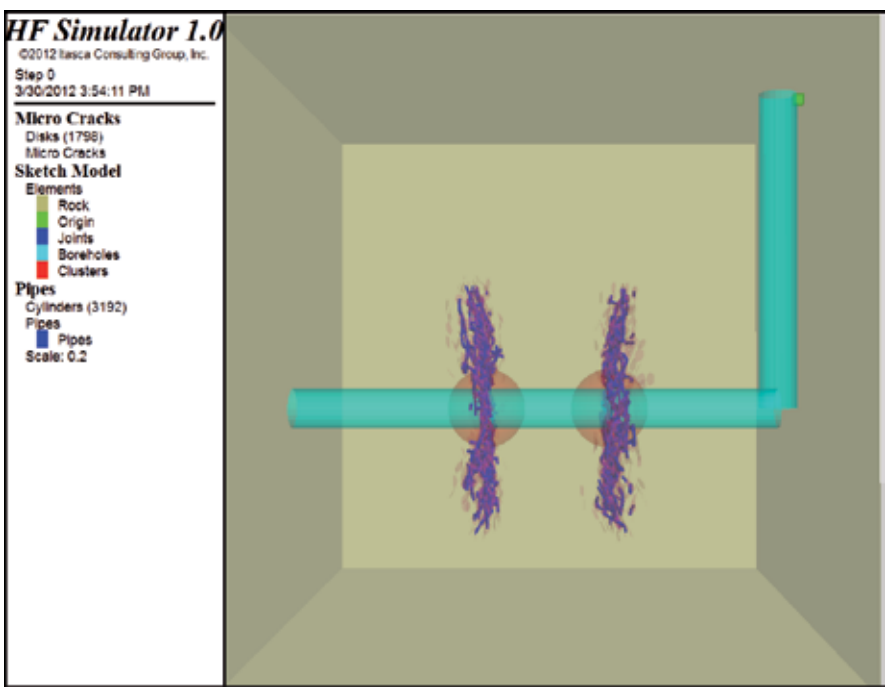

Figure 15. Staged hydraulic fracturing in a horizontal well. There may be many such wells along the horizontal well.

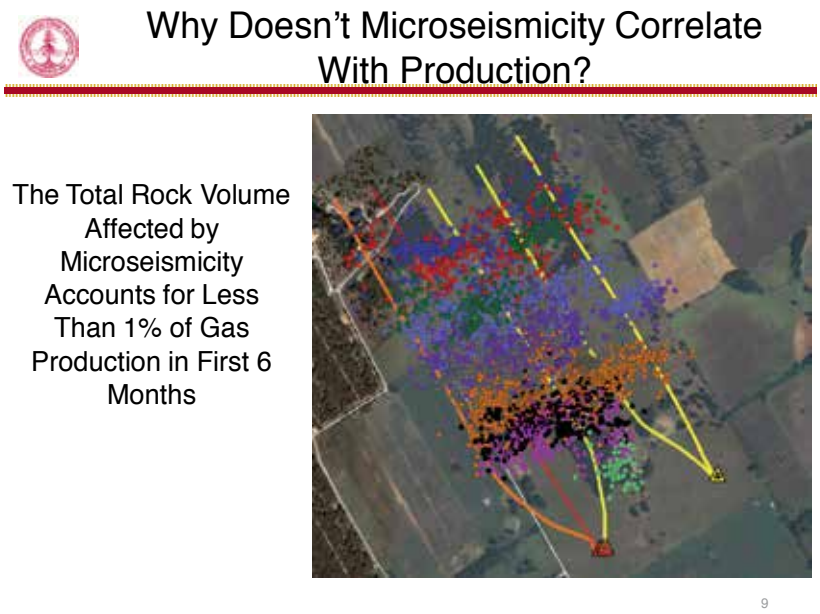

Figure 16. The volume of rock defined by microseismicity is a very small fraction of the volume producing gas.

Figure 16 shows a slide from a recent presentation by Prof. Mark Zoback, who kindly agreed to allow the author to include it here. Although on a somewhat smaller scale, the fact that considerable deformation and fracturing must be taking place that is not associated with detected microseismicity is similar to the phenomena discussed in connection with Figure 10. Prof. Zoback refers to such aseismic deformation as slow slip, and is conducting research to understand the underlying mechanisms, including the possible influence of the clay content of the shale. As can be seen in Figure 17 (courtesy of Prof. Zoback), the clay content can be large.

Figure 18 illustrates the very fine, micron scale, pore structure of a typical tight shale. Although the mechanism(s) by which flow pathways are established in such a fine structure is not clear, the level of microseismic energy release associated with brittle breakage of one or a few bonds will be very small and of high frequency (such that the radiated energy would be rapidly attenuated), and hence, not detectable by any geophone. Thus, absence of microseismicity may not indicate an absence of breakage of brittle bonds. Some mechanism must be operative that generates flow pathways. Intuitively, it might be expected that the clay content of the shale might lead to ductile and viscous deformation that could tend to close the pathways.

http://dx.doi.org/10.5772/56366

Average Shale Properties

	BARNETT	MARCELLUS	EAGLE FORD	FLOYD
Depth (ft)	3 - 9,000	2 - 9,500	4 - 13,500	6 - 13,000
TOC (%)	1 - 10	1 - 15	2 - 7	1 - 7
RO (%)	0.7 - 2.3	0.5 - 4+	0.5 - 1.7	0.7 - 2+
Porosity (%)	2 - 14	2 - 15	6 - 14	1 - 12
Qtz + Calcite (%)	40 - 50	40 - 60	50 - 80	20 - 30
Clay (%)	20 - 40	30 - 50	15 - 35	45 - 65
Areal Extent (mi²)	22,000	60,000	15,000	6,000
Resource Size (Tcf)	25 - 250	50 - 500	10 - 100	<<1

How many Floyd Shales are There?

Figure 17. Clay content of some typical 'tight' gas shales.

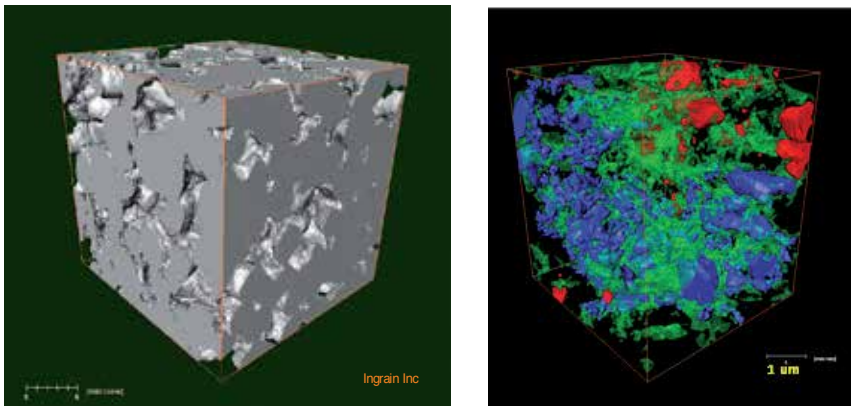

Figure 18. a) Outer surface of a FIB-SEM (Focused Ion Beam- Scanning Electron Microscope) volume of Eagle Ford Shale; (b) Transparency view of the distribution of connected pores (blue), isolated pores (red) and organic matter (green). (Courtesy of Prof. Amos Nur and J. Wallis (see Wallis et al., (2012) for details of technology.)

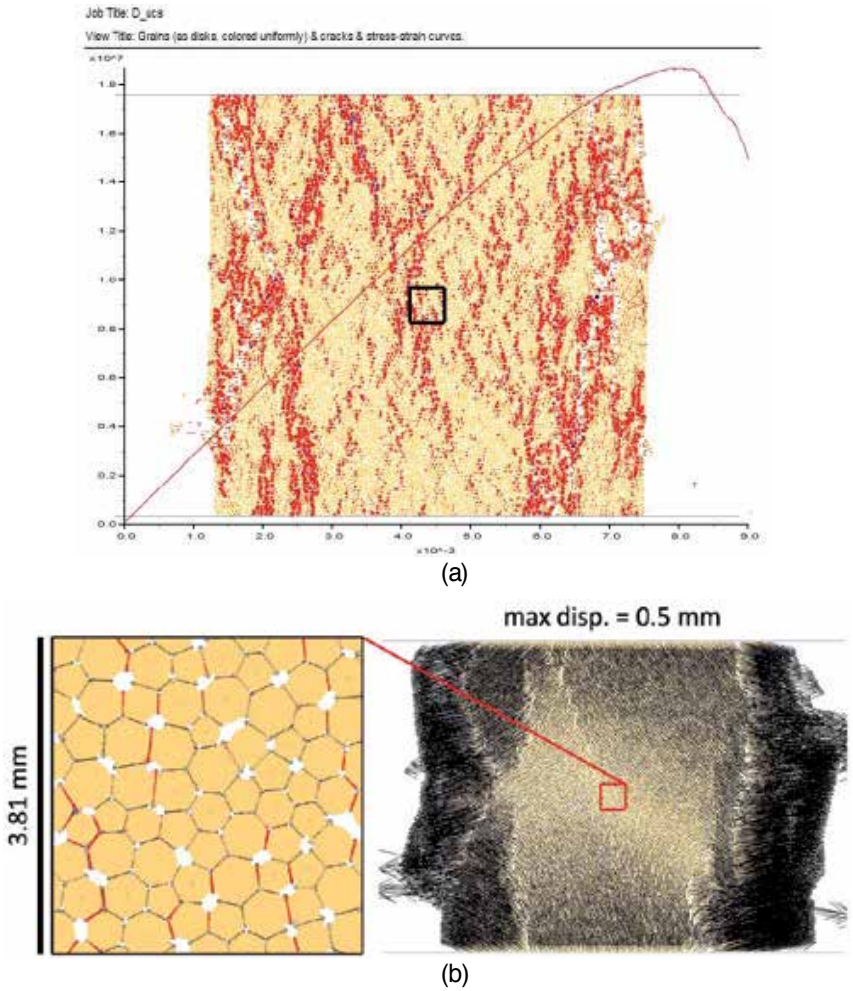

Figure 19. Micro-rupture of bonds within a *PFC* model of a rock loaded to failure, and beyond, in uniaxial compression. The darker red regions in (a) indicate coalescence of smaller groups of bonds that have ruptured. Eventually these larger regions develop to provide a mechanism that leads to collapse of the specimen. It is seen that bond breakage occurs throughout the specimen as the load is increased. The larger dark red regions will release larger amplitude, lower frequency waves that can be detected, whereas the smaller 'pathways' cannot be detected seismically. The load-deformation curve is shown as an 'overlay' on the specimen.

12. Fracture network engineering

This paper has emphasized the central role of fractures in rock, primarily natural fractures developed on a wide spectrum of scales over many tectonic epochs and many millions of years. These fractures and fracture systems are of special significance with respect to hydraulic fracturing and related techniques of fluid injection into rock since the fluid will tend to seek

http://dx.doi.org/10.5772/56366

out those fractures that can be more readily opened against the local in-situ stress field as the fluid is injected. Given the complexity and lack of information on the fracture system, stress environment, etc., how can the engineering of hydraulic fracturing and related fluid injection programs advance most effectively?

Confronted with the same complexity of rock in situ, civil engineers and mining engineers have tended to adopt the 'Observational Approach' (Peck, 1969). In essence, this approach involves developing an initial engineering design for the problem, based on a first assessment/ estimate of the rock (or soil) properties. Observe the actual performance and modify the initial design as needed to arrive at the desired performance. An example of the Observational Approach (as used in the New Austrian Tunnelling Method) is discussed in Fairhurst and Carranza-Torres (2002), see pp. 24-30.

Application of the Observational Approach to Hydraulic Fracturing and related fluid injection techniques faces some disadvantages and some advantages. We do not have 3D access to the engineering site. We do have powerful numerical modeling tools to help make a more informed initial estimate of how the system will perform; and we have sensing systems, both downhole and remote. Figure 20 illustrates a procedure that tries to apply the Observational Approach to hydraulic fracturing and related systems. The illustration describes an application to the extraction of Geothermal Energy.

Stones have begun to speak, because an ear is there to hear them. ….
Cloos, Conversations with the Earth (1954), 4

Microseismicity –predicted and observed.

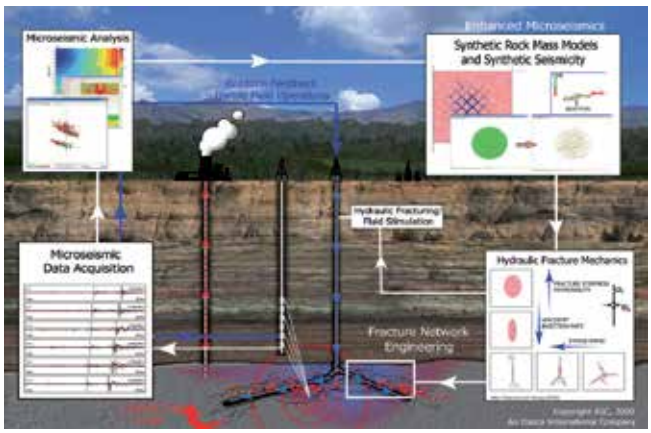

Fracture Network Engineering. *Synthetic Rock Mass and Synthetic Seismicity Models are compared with observed microseismic signals for* ***real time control of fracture network development.*** *(Enhanced Geothermal Systems.)*

Figure 20. Fracture network engineering system.

In this application, an initial design approach is developed based on a numerical modeling study incorporating any available data, insight, etc., on the site. This model provides an initial

prediction of the performance. Instrumentation, both downhole and on-surface observes the initial response of the system and compares it with the prediction. This triggers a feedback signal to modify the design input to move the performance closer to the one desired. This iteration continues, changing progressively towards the performance desired.

Although the writer knows of no such Fracture Network Engineering system currently in operation, many of the components are available and it is time to start.

13. Conclusions

Expectations for higher living standards of a rising world population, and the associated demand for Earth's resources of energy, minerals and water, lead inevitably to greater focus on resources of the subsurface.

This focus includes the need to develop improved technology to develop these resources, and a better understanding of the nature of the subsurface environment as an engineering material.

Earthquakes and dynamic releases of energy are a daily reminder that on the global scale, Earth is critically stressed, and constantly trying to adjust seeking to achieve a condition of minimum potential energy for the entire system.

On going for many, many millions of years, such adjustments have resulted in the heterogeneous assembly of blocks of rock bounded by essentially planar surfaces; fault, fractures and similar 'discontinuities' varying in scale from tectonic plates and continents down to micron and even nanometers.

Some of these volumes are critically stressed; others are far from a critical condition. National maps of seismic hazards provide evidence of this heterogeneity on a larger scale.

Although Earth Resource Engineering activities may be kilometers in extent, they are small-scale within the larger Earth context. Subsurface engineering in a critically stressed region can be a much different challenge than in a stable region. It is important to assess the initial conditions carefully for each case, and especially where fluid injection is a main component of a project.

The sub-surface is opaque in several ways. Details of the key features that can control the response to an engineering activity in the sub-surface are often unknown. Problems are data-limited. This is particularly the case when the engineering is based on deep borehole systems, as in hydraulic fracturing and related fluid injection technologies.

Although operating in ways that may appear complex, the response of the subsurface to stimulation does obey the laws of Newtonian mechanics, and it is clear that pre-existing natural discontinuities have a major influence on how the subsurface responds to engineered changes.

The advent of powerful computers and developments in numerical modeling provide a potentially major tool to help develop better-informed strategies of subsurface engineering. Used interactively in close conjunction with instrumentation, both downhole and surface

http://dx.doi.org/10.5772/56366

based, it should be possible to progressively develop a mechanics-informed understanding and path forward for more effective subsurface engineering.

Much as the field of Fracture Mechanics has led, and continues to lead, to major technological improvements for fabricated materials, so can development of the field of Rock Fracture Mechanics be of transformative value to subsurface engineering, and to society in general.

Hydraulic fracturing and related injection-stimulation systems will certainly be a central element in the future of Earth Resource Engineering. The organizers of HF 2013 are to be commended for focusing attention on this critically important topic.

Appendix 1

Earth resources engineering

In 2006, the US Academy of Engineering introduced the term 'Earth Resources Engineering' to replace 'Petroleum, Mining and Geological Engineering' in recognition of the broader range of engineering activities and concerns associated with use of the subsurface. The new title, it is hoped, will also stimulate important synergies between the various disciplines involved. Mining and civil engineers, for example, have direct three-dimensional access to the subsurface not available to colleagues in other subsurface activities. This access provides a major opportunity to conduct research and gain understanding of the mechanics of subsurface processes under actual in-situ conditions, as exemplified by Jeffrey et al. (2009), see Figure A1-1.

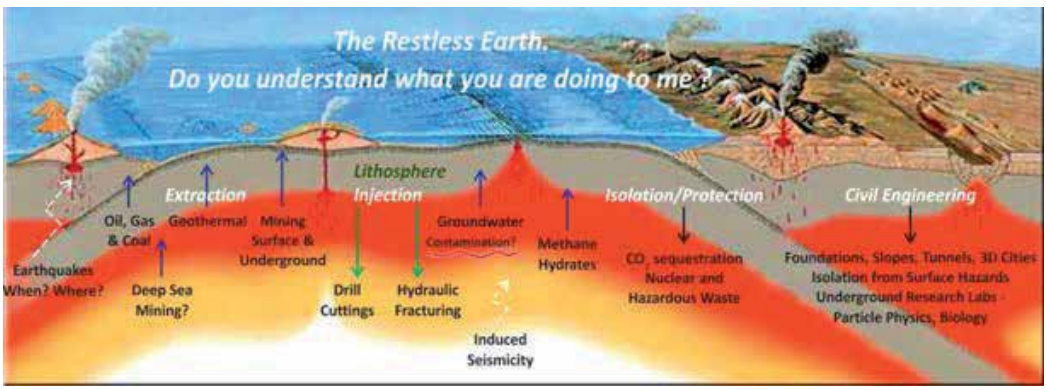

Figure A1-1. The restless Earth. Earth Resource Engineering activities are all confined to a very shallow part of the 40 km -700 km thick Earth's solid crust (lithosphere). Deepest borehole ~ 12 km; mine ~ 4km. Rock stress increases vertically σv ~ 27MPa/km; laterally σh~ (0.5- 3.0).σv: Pore water pressure p = 10 MPa /km; temperature increase ~25°C /km depth.

Study of slip on active faults is a good example.

"The physics of earthquake processes has remained enigmatic due partly to a lack of direct and near-field observations that are essential for the validation of models and concepts.

DAFSAM[15] proposes to reduce significantly this limitation by conducting research in deep mines that are unique laboratories for full-scale analysis of seismogenic processes. The mines provide a 'missing link' that bridges between the failure of simple and small samples in laboratory experiments, and earthquakes along complex and large faults in the crust. There is no practical way to conduct such analyses in other environment. To unravel the complexity of earthquake processes, this project is designed as integrated multidisciplinary studies of specialists from seismology, structural geology, mining and rock engineering, geophysics, rock mechanics, geochemistry and geobiology. The scientific objectives of the project are the characterization of near-field behavior of active faults before, during and after earthquakes". [16]See also http://www.iris.edu/hq/instrumentation_meeting/files/pdfs/IRIS_Johnston.pdf

Petroleum engineers can now reach depths in excess of 6 km and have developed advanced drilling control technologies that allow precise access to locations extending horizontally to more than 10-15 km from a single vertical hole (see Figure 2).

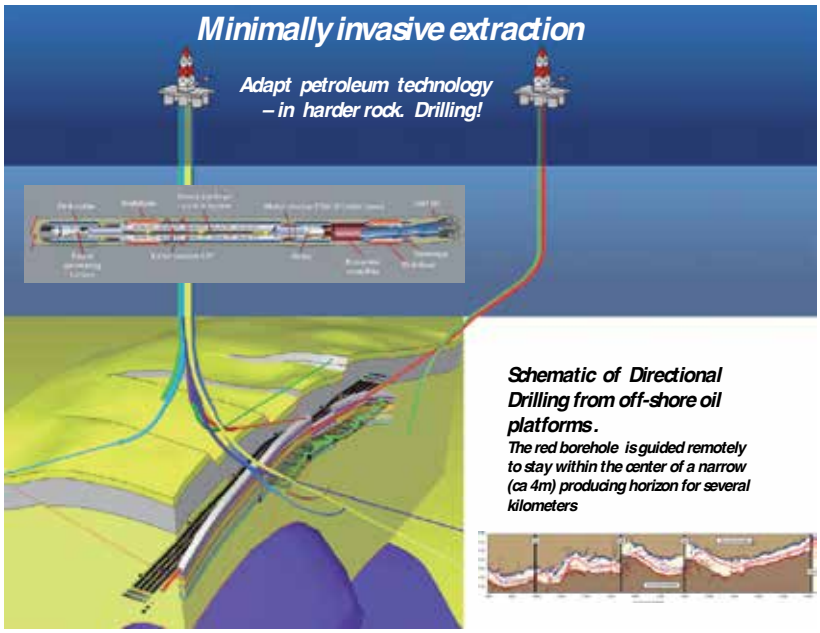

Figure A1-2. Schematic illustration of directional drilling for petroleum production.

These and related developments are stimulating interest in application of borehole technologies to other areas of subsurface engineering, including the development of less-invasive mining technologies, i.e., borehole extraction of minerals. Some applications, e.g., where crystalline rocks are involved, are contingent on the development of significantly lower-cost drilling technologies. The critical dependence of society on reliable and economic subsurface

15 DAFSAM -Drilling Active Faults in South African Mines.

16 http://www.icdp-online.org/front_content.php?idcat=460

http://dx.doi.org/10.5772/56366

engineering is illustrated by the fact that currently more than 60% of the world's energy is delivered via a borehole. The Deepwater Horizon accident in the Gulf of Mexico in April 2010 provides a sober example of the consequences of error. In summary, hydraulic fracturing and related stimulation technologies are likely to see application to an increasing range of subsurface engineering challenges. HF2013, the first International Conference for Effective and Sustainable Hydraulic Fracturing, is very timely.

Appendix 2

Effect of coring in pre-stressed rock

The consequences of disturbing a pre-stressed rock medium are illustrated by examining the rock coring operation. Figure A2-1 shows the stress concentrations in a rock core in a brittle

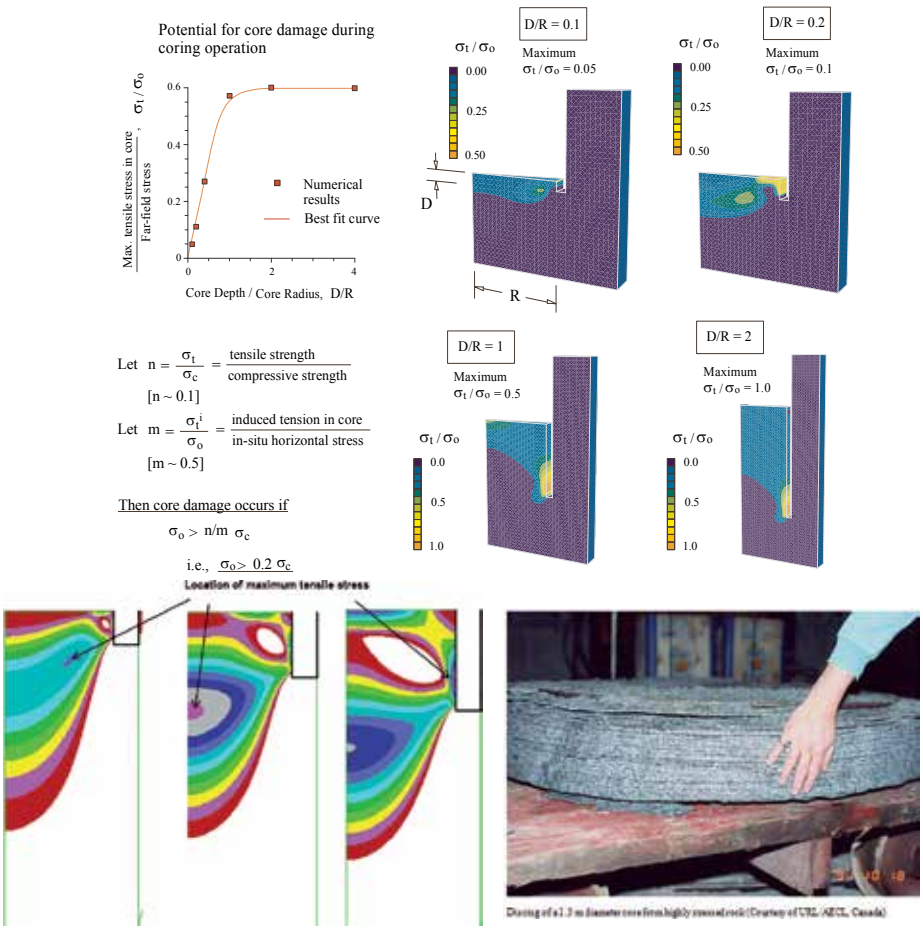

Figure A-2.1. Tensile stress concentrations induced in a brittle rock during coring.

rock. If the in-situ stress normal to the axis of drilling is sufficiently high tensile cracks can develop in the core. Where lateral stresses are very high, then tensile 'spalling' may result, as shown in the photograph of the bottom right of Figure A2-1. Where the rock is more 'ductile' the core may undergo permanent deformation without fracturing. In both cases, the mechanical properties of these cores may differ significantly from those of the rock in situ from which the core was obtained.

Acknowledgements

Much of the material and concepts discussed in this paper is the result of work and discussions over many years with colleagues at Itasca Consulting Group, Inc. in Minneapolis and faculty in GeoEngineering at the University of Minnesota, especially in this instance, Professor Emmanuel Detournay. Particular help was received from Itasca colleagues Varun, Branko Damjanac, David Potyondy and Mark Lorig, The influence of numerous stimulating discussions with Professor François Cornet of the Institut de Physique du Globe, Strasbourg, France are clearly evident in the paper. Professors Amos Nur and Mark Zoback, of Stanford University, USA and of Ingrain, Inc., Houston, USA assisted with valuable material, as acknowledged in the text. Dr. Rob Jeffrey and Andrew Bunger of CSIRO, Melbourne, the leaders in arranging HF2013, have provided valuable comments, assistance and understanding throughout. To all, I am very grateful. Such invaluable assistance notwithstanding, I accept full responsibility for the interpretations and views expressed in the paper.

Author details

Charles Fairhurst[1,2*]

1 Senior Consultant, Itasca Consulting Group, Inc, Minneapolis Minnesota, USA

2 Professor Emeritus, University of Minnesota, Minneapolis, Minnesota, USA

References

[1] Anderson, T. L. (2005). Fracture Mechanics: Fundamentals and Applications. 3rd edition, CRC Press (0-84931-656-1

[2] Artyushkov, E. V. (1973). Stresses in the Lithosphere Caused by Crustal Thickness

[3] Inhomogeneities, J. Geophy.Res. November 10, (1973). , 78(32)

[4] Bunger, A. P, Zhang, X, & Jeffrey, R. G. (2012). Parameters Affecting the Interaction Among Closely Spaced Hydraulic Fractures" SPE Journal March 2012, , 292-306.

[5] Calo, M, Dorbath, C, Cornet, F. H, & Cuenot, N. (2011). Large scale aseismic motion identified through 4D P-wave tomography; Geophys. J. Int. , 186, 1295-1314.

[6] Cundall, P. A. (2008). An Approach to Rock Mass Modelling," in From Rock Mass to Rock Model-CD Workshop Presentations (15 September, 2008)- SHIRMS 2008 (Proc. 1st Southern Hemisphere International Rock Symposium, Perth, Western Australia, September 2008) Y. Potvin et al., Eds. Nedlands, Western Australia: Australian Centre for Geomechanics.

[7] Cladouhos, T. T, Clyne, M, Nichols, M, Petty, S, Osborn, W. L, & Nofziger, L. (2011). Newberry Volcano EGS Demonstration Stimulation Modeling" GRC Transactions, , 35, 317-322.

[8] Cornet, F. H. (2012). The relationship between seismic and aseismic motions induced by forced fluid injections." Hydrogeology Journal (2012) 20: 1463-1466

[9] Cornet, F. H, & Röckel, T. (2012). Vertical stress profiles and the significance of "stress decoupling". Tectonophysics , 581(2012), 193-205.

[10] Cundall, P. A, & Pierce, M. E. and D. Mas Ivars. ((2008). Quantifying the Size Effect of Rock Mass Strength" in SHIRMS 2008 (op.cit.) , 2, 3-15.

[11] Damjanac, B, & Fairhurst, C. (2010). Evidence for a Long-Term Strength Threshold in Crystalline Rock,‖ Rock Mech. Rock Eng., 43, 513-531 (2010).

[12] Damjanac, B, Detournay, C, & Cundall, P. A. and Varun, ((2013). Three-Dimensional Numerical Model of Hydraulic Fracturing in Fractured Rock Masses" Proc. HF The International Conference for Effective and Sustainable Hydraulic Fracturing, Brisbane, May 20-22, 2013, 2013.

[13] Damjanac, B, & Fairhurst, C. Evidence for a Long-Term Strength Threshold in Crystalline Rock,‖ Rock Mech. Rock Eng., 43, 513-531 ((2010). Duchane, D and D. Brown, (2002) "Hot Dry Rock (HDR) Geothermal Energy Research and Development at Fenton Hill, New Mexico" GHC (Geo-Heat Center) Bulletin, December. 2002 , 13-19.

[14] Fairhurst, C, & Carranza-torres, C. (2002). Closing the Circle- Some Comments on Design Procedures for Tunnel Supports in Rock," in Proceedings of the University of Minnesota 50th Annual Geotechnical Conference (February 2002), J. F. Labuz and J. G. Bentler, Eds. Minneapolis: University of Minnesota, 2002. [available at www.itascacg.comgo to 'About'and Fairhurst Files], 21-84.

[15] Fairhurst, C. (1971). Fundamental Considerations Relating to the Strength of Rock. Colloquium on Rock Fracture, Ruhr University, Bochum, Germany, April 1971. (see http://www.itascacg.com/about/ff.php)Revised and published in Report of the Workshop on Extreme Ground Motions at Yucca Mountain, August 23-25, 2004, U.S. Geological Survey, USGS Open-File Report T. C. Hanks et al., Eds. Reston, Virginia: USGS, 2006., 2006-1277.

[16] Geertsma, J, & De Klerk, F. (1969). A Rapid Method of Predicting Width and Extent of Hydraulic Induced Fractures. J Pet Technol SPE-2458-PA. http://dx.doi.org/10.2118/2458-PA, 21(12), 1571-1581.

[17] Geyer, J. F, & Nemat-nasser, S. (1982). Experimental Investigation of Thermally induced Interacting Cracks in Brittle Solids Int. J. Solids and Structures , 18(4), 349-356.

[18] Griffith, A. A. (1921). The Phenomena of Rupture and Flow in Solids Phil. Trans. R. Soc. Lond. A 1921,, 221, 163-198 doi:rsta.1921.0006

[19] Griffith, A. A. (1924). Theory of Rupture. Proc. First Int. Cong. Applied Mech (eds Bienzo and Burgers). Delft: Technische Boekhandel and Drukkerij. 1924, 55-63.

[20] Grünthal, G, & Wahlström, R. (2003). An Mw-Based Earthquake Catalogue for Central, Northern and Northwestern Europe using a Hierarchy of Magnitude Conversions. J. Seismol. 7, 507-531 (Available at http://seismohazard.gfzpotsdam.de/projects/en/eq_cat/menue_e"q_cat_e.html)

[21] Hoek, E, & Bieniawski, Z. T. (1966). Fracture Propagation Mechanism in Hard Rock," in Proceedings of the First Congress of the International Society of Rock Mechanics. Lisbon, September-October, J. G. Zeitlen, Ed. Lisbon: LNEC., 1, 243-249.

[22] Hoek, E, & Brown, E. T. (1980). Underground Excavations in Rock." Inst'n of Mining and Metallurgy (London) Revised 1982, , 164.

[23] Howard, G. C, & Fast, C. R. (1970). Hydraulic Fracturing" SPE Monograph 2. Henry L.Doherty Series 203 pp. SPE 30402

[24] Inglis, C. E. (1913). Stresses in a Plate Due to the Presence of Cracks and Sharp Corners," Trans. Inst. Naval Arch., London, 55(1), , 219-141.

[25] Jeffrey, R. G, et al. (2009). Measuring Hydraulic Fracture Growth in Naturally Fractured Rock. SPE 124919; SPE Annual Technical Conference and Exhibition, New Orleans, Louisiana, USA, October 2009, 4-7.

[26] Knott, J. F. (1973). Fundamentals of fracture mechanics, Wiley (0-47049-565-0

[27] National Research Council(2012). Induced Seismicity Potential in Energy Technologies." Washington, DC: The National Academies Press, 2012. (300p.) View online at http://www.nap.edu/catalog.php?record_id=13355

[28] Nocquet, J. M, & Calais, E. (2004). Geodetic Measurements of Crustal Deformation in the Western Mediterranean and Europe " Pure Appl. Geophy., 161; , 661-668.

[29] Nordgren, R. P. (1972). Propagation of a Vertical Hydraulic Fracture. SPE J. SPE-3009-PA. http://dx.doi.org/10.2118/3009-PA., 12(4), 306-314.

[30] Peck, R. B. (1969). Advantages and limitations of the observational method in applied soil mechanics. Geotechnique, , 19(2), 171-187.

[31] Perkins, T. K, & Kern, L. R. (1961). Widths of Hydraulic Fractures. J Pet Technol SPE-89-PA. http://dx.doi.org/10.2118/89-PA., 13(9), 937-949.

[32] Pettitt, W. S, Hazzard, J. F, Damjanac, B, Han, Y, Pierce, M, Katsaga, T, & Cundall, P. A. Microseismic Imaging and Hydrofracture Numerical Simulations," in Proceedings, 21st Canadian Rock Mechanics Symposium (Alberta, Canada, May 5-9, (2012).

[33] Pierce, M. (2011). Discrete Fracture Network Simulation" DFN training session LOP (Large Open Pit). [ppt slides available on request. Itasca Consulting Group: www.itascacg.com]

[34] Riahi, A, & Damjanac, B. (2013). Numerical Study of Interaction between Hydraulic Fractures and Discrete Fracture Networks" Proc. HF The International Conference for Effective and Sustainable Hydraulic Fracturing, Brisbane, May 20-22, 2013, 2013.

[35] Royal Society and Royal Academy of Engineering ((2012). Junep. "Shale Gas Extraction in the UK: a review of hydraulic fracturing" Issued: June 2012, DES2597] View report online at: royalsociety.org/policy/projects/shale-gas-extraction and raeng.org.uk/shale

[36] Scotti, O, & Cornet, F. H. (1994). In-Situ Evidence for Fluid-Induced Asesismic Slip Events along Fault Zones. Int. J. Rock Mech Min.Sci. &Geomech. Abstr. Control in Mines (1965). South African Institute of Mining and Metallurgy, Johannesburg, 606p, 31(4), 347-258.

[37] Starfield, A. M, & Cundall, P. A. (1988). Towards a Methodology for Rock Mechanics Modelling" Int. J. Rock Mech. Min. Sci.& Geomech. Abstr. 25 (3) , 99-106.

[38] Tester, J. F, et al. (2006). The Future of Geothermal Energy"-Impact of Enhanced Geothermal

[39] Systems (EGS) on the United States in the 21st CenturyMIT Press.

[40] Wallis, J. D, Devito, J, & Diaz, E. (2012). Digital Rock Physics- A New Approach to Shale Reservoir Evaluation" Oilfield Technology, March 2012 [http://www.ingrain-rocks.com/articles/a-new-approach-to-shale-reservoir-evaluation/]

[41] Zhang, X, & Jeffrey, R. G. (2008). Re-initiation or termination of fluid-driven fractures at frictional bedding interfaces" JGR, BO 8416, doi:10.1029/2007JB005327,, 113

Chapter 4

Five Things You Didn't Want to Know about Hydraulic Fractures

Vincent M. C.

Additional information is available at the end of the chapter

http://dx.doi.org/10.5772/56066

Abstract

It is common to envision and design hydraulic fractures as if they were simple, planar features that are relatively consistent in width and durable in their flow capacity. Production forecasting is frequently based on a simplified description of the reservoir as a homogeneous single productive layer. In rare instances the pay intervals may be simulated with as many as a dozen layered strata, but even the most meticulous reservoir engineer may mistakenly assign each layer a highly conductive, durable connection with the wellbore. When analyzing the resulting production data, similar assumptions are made, which can erroneously reinforce these misconceptions.

Although our industry has been confronted with photographic evidence from minebacks and core-throughs of actual fractures, we have typically failed to incorporate those complexities and challenges into our design, interpretation, and optimization processes. Similarly, we frequently fail to recognize the challenges of highly laminated and highly compartmentalized reservoirs. In many resource plays, hydraulically stimulated horizontal wells appear to be the only completion technique that can achieve economic production rates from these low permeability reservoirs. However the productivity and ultimate recovery from these horizontal wells will be increasingly reliant on durable hydraulic fractures to contact and drain the hydrocarbons through highly laminated formations for the decades necessary to deplete low permeability reservoirs. Oversimplified models typically result in poorly designed completions and missed opportunities. Frequently, the underperformance of a well will be blamed on "poor reservoir quality" instead of correctly recognizing the inadequacy of our created fractures.

This paper will examine five limitations of hydraulic fractures and interpretation techniques, and describe the increases in well productivity that can be achieved when efforts are made to address and compensate for these deficiencies.

Keywords Frac optimization, resolving non-unique solutions, proppant degradation, realistic conductivity, laminated reservoirs, complexity, restimulation

1. Introduction

Early frac engineers certainly recognized that hydraulic fractures were complex features. Geologists, mining engineers, and prison chain gangs all assured us that rocks break in complex manners. But the math is hard, and we aren't capable of predicting nature's complexity. We cannot accurately calculate the pressure losses through a proppant pack with complex geometry, irregular aperture, and with several fluid phases flowing at high velocity. So our predecessors were forced to simplify the description. As a first-order approximation, they assumed that fracs were simple, vertical planes, with uniform width and predictable hydraulic continuity.

Two subsequent generations of petroleum engineers have been introduced to simplified planar hydraulic fractures that have been distorted to fit on a textbook page, such as in Figure 1. Unfortunately, many engineers mistakenly envision fracs as wide, highly conductive channels instead of thin, narrow ribbons of proppant that extend deeply into the reservoir but are vulnerable in their hydraulic continuity. Fractures are commonly modeled to be symmetrical, bi-wing planes that reliably contact the targeted hydrocarbons.

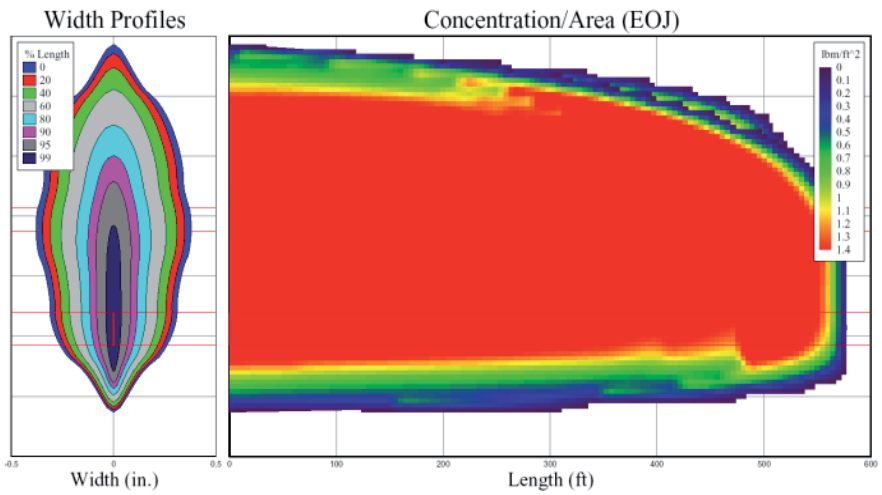

Figure 1. The proportions of fractures are often distorted and misrepresented in simplified models. This figure implicitly assumes the fracture grows symmetrically on either side of the wellbore.

http://dx.doi.org/10.5772/56066

Although chemical engineers clearly recognized that Darcy's flow would not describe pressure losses in porous media, early frac engineers disregarded non-Darcy and multiphase flow effects, and further assumed a single homogeneous reservoir layer was contacted by a highly conductive fracture that permanently connected the wellbore to the hydrocarbons. These assumptions allowed the "optimization" of frac treatments to become a mathematically simple routine. Two subsequent generations of petroleum engineers have filled our literature and conventional wisdom with simulations and "rules of thumb" that would allow us to optimize these mythical ideal fractures. Unfortunately, many of the assumptions are wrong, and our fracs are not optimized.

2. Complex flow regimes

Even if fractures were simple, wide features, with perfectly uniform proppant arrangements throughout the entirety of the fracture length and height, our industry would still overestimate the flow capacity of fractures by several orders of magnitude. Figure 2 shows the apparent flow capacity of proppant packs, measured in the laboratory.

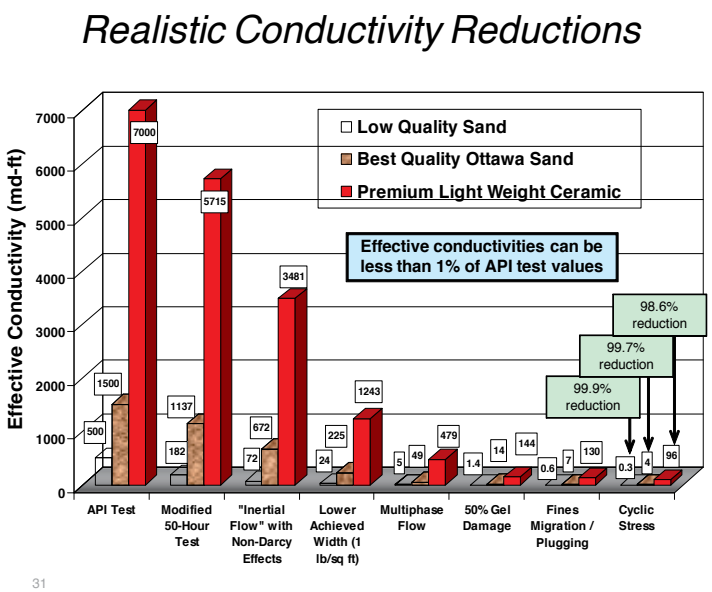

Figure 2. Even in simple, planar proppant packs with uniform proppant distribution, the effective conductivity is frequently 50 to 1000 times lower than published values [1]

Conductivity data provided by most proppant vendors, and utilized in most production simulators are collected with test procedures similar to the left two categories of bar columns in Figure 2. When testing is more sophisticated, with realistic velocities of multiphase fluids through proppant packs subjected to gel damage and cyclic stress oscillations, the pres-

sure losses are often found to be orders of magnitude higher than indicated by reference data [1,2,3].

3. Conductivity degrades

Even the meager amount of effective conductivity shown in Figure 2 appears to be unsustainable. Five different researchers have published the performance of proppants when tested in the laboratory for weeks instead of hours Montgomery [4], McDaniel [5], Cobb [6], Hahn [7], Handren [8]. All five have shown that proppants lose conductivity over time, with one representative test shown in Figure 3. Some proppants are more durable than others, and some laboratory conditions will more rapidly degrade proppant, but not a single proppant pack in the lab has sustained flow capacity without continued particle breakage and compaction during extended testing. The degradation mechanism in these tests has nothing to do with chemical damage, scale deposition, or diagenesis – these conductivity losses are related to the strength of the particles, and show similar trends when tested in dry nitrogen gas, in oil, or in brine, when confined between sandstone, stainless steel, or Teflon. [5, 9, 10]. It is surprising that none of our models incorporate frac degradation over time, despite unanimous evidence that conductivity declines.

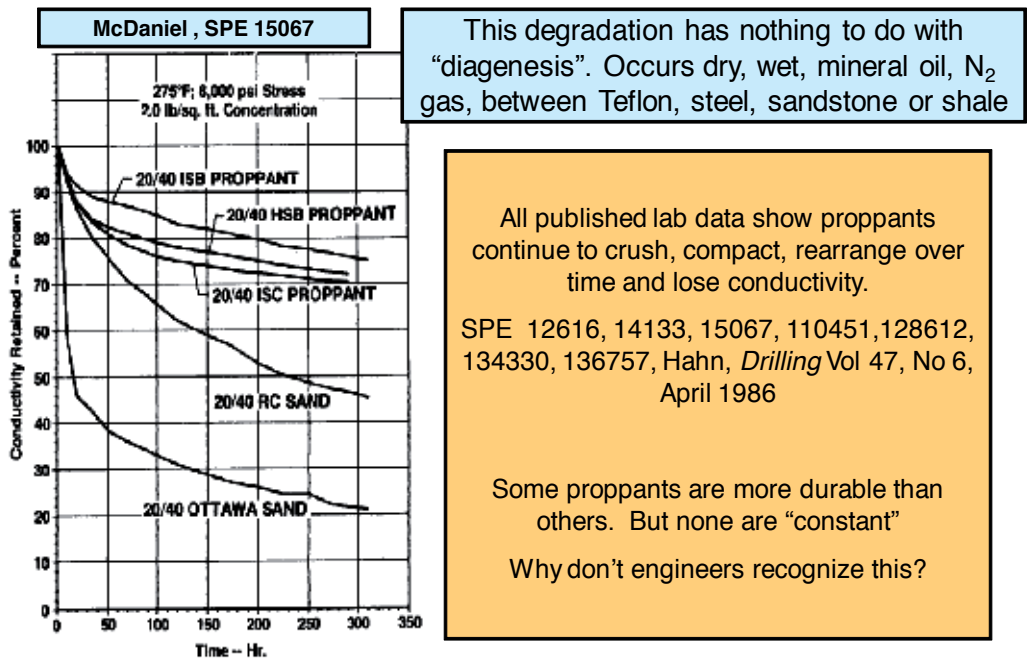

Figure 3. Extended duration tests routinely show continued mechanical crush and loss of flow capacity of proppant packs [5]

http://dx.doi.org/10.5772/56066

4. Heterogeneous reservoirs

Production forecasting is greatly simplified if the reservoir can be described as a uniform layer with predictable, consistent permeability in the vertical and horizontal directions. However, sedimentary rocks were formed from hundreds or thousands of sequential layers of sediment as shown in Figure 4. Productive lenses can have varying lateral extent.

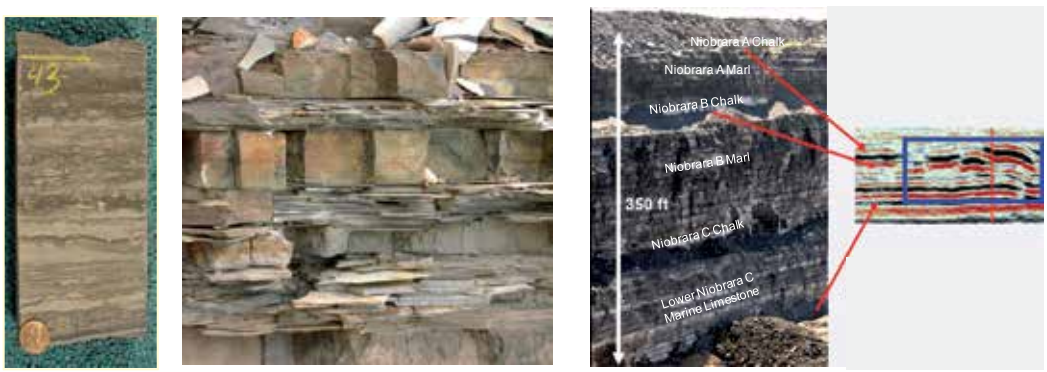

Figure 4. On every scale, formations may have laminations that hinder vertical permeability and fracture penetration. Shown are thin laminations in the Middle Bakken [11], layering in the Woodford [outcrop photo courtesy of Halliburton], and large scale laminations in the Niobrara [adapted from 12] [13]

The consequences of these laminations are two-fold:

1. Vertical perm is terrible. Often the vertical perm is only a tiny fraction of the horizontal perm; k_v/k_h <0.001. Oil and gas do not move easily in the vertical direction through rock. If you want to drain it, you have to frac it. Especially with horizontal wells drilled into a single layer, the frac engineer must create a durable, conductive pathway breaching the laminations within the hydrocarbon-bearing intervals if we have a prayer of draining the reserves from these tight, laminated resource plays, unless pre-existing natural fractures provide a vertical flow path.

2. Laminations hinder frac penetration [13]. Fracs don't like to grow through a series of bonded and unbonded layers (Fig 5).

5. Complex frac geometry

Figure 5 depicts conceptualized fracture branching as it grows through a laminated formation. Figure 6 shows minebacks of actual fracturing treatments performed at the Nevada test site and Figure 7 shows a core-through of a treatment in the Piceance Basin of western Colorado.

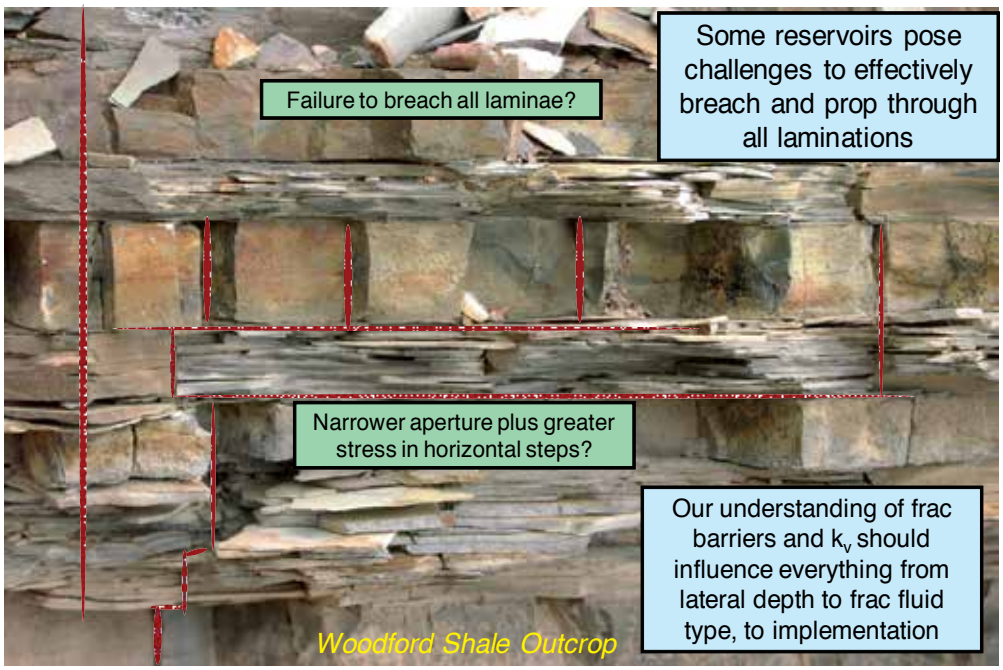

Figure 5. Instead of perfectly vertical fractures (left) it may be appropriate to anticipate difficulty creating and sustaining a conductive fracture throughout the entire pay interval [outcrop photo courtesy of Halliburton [13].

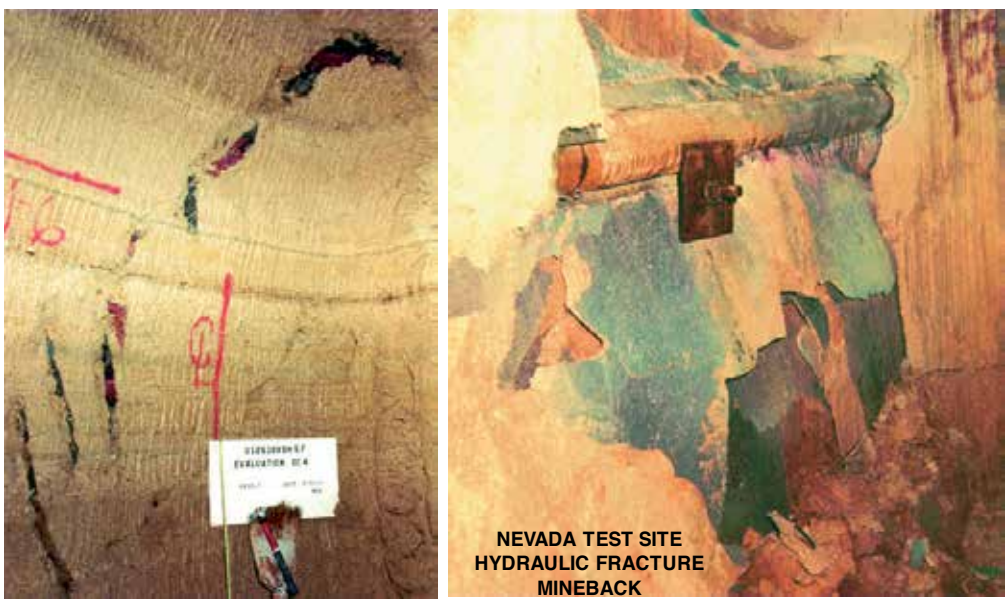

Figure 6. Photographs of mine backs at the Nevada test site demonstrate complexity [1, 14,15]

http://dx.doi.org/10.5772/56066

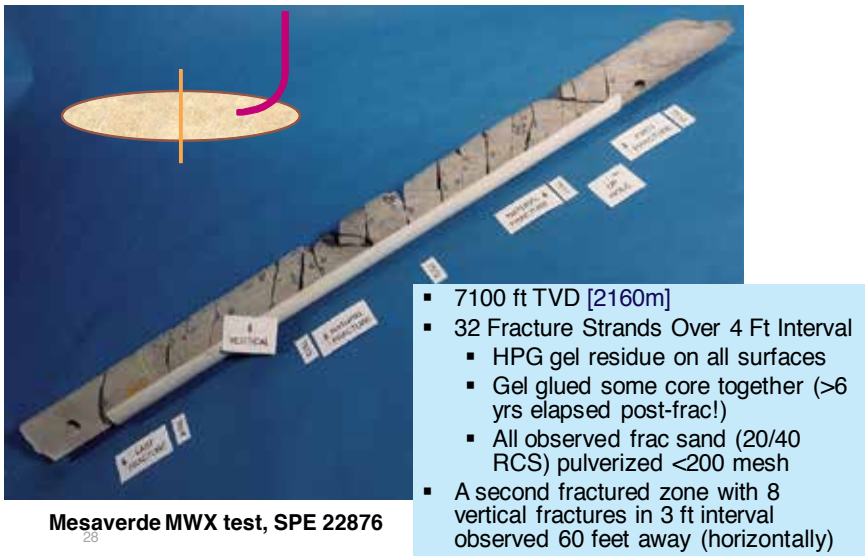

Figure 7. In the Piceance Basin, cores through a created fracture document 40 fracture strands, with only pulverized resin coated sand recovered [1, 16]

Clearly, there is evidence that fractures can grow in much more complicated manners compared to the simple, planar features that are typically presumed in our designs and "optimization" attempts. What are the implications of complexity shown in Figure 8?

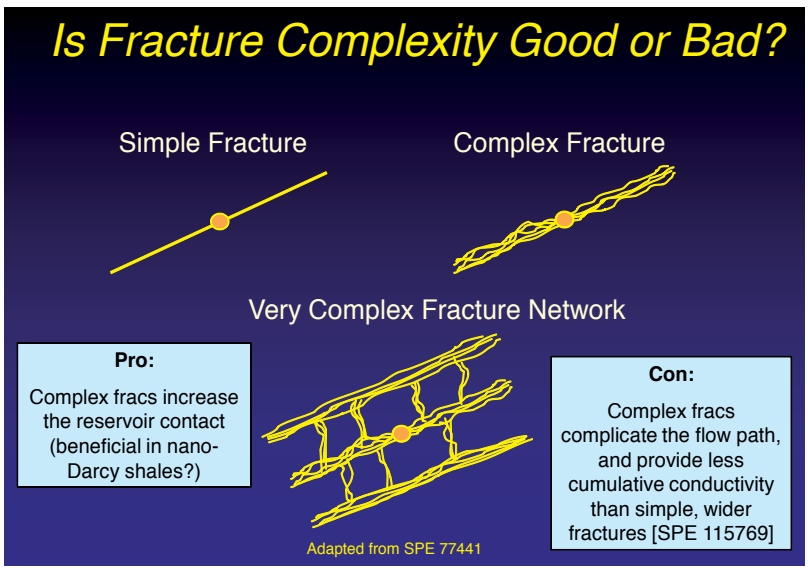

Figure 8. Fracture complexity increases reservoir contact, but challenges our ability to create a durable proppant pack with sufficient hydraulic continuity [adapted from 17]

Hydraulic fractures must achieve two primary objectives. They must:

1. Touch rock (contact hydrocarbons)
2. Provide a durable conduit for hydrocarbons to flow to the well with acceptable pressure losses (sufficient conductivity)

Complex, branching fractures do an excellent job of touching rock. However, they challenge our ability to place a commensurate degree of conductivity. Branching, complex features are often ineffectively propped, with risk of insufficient conductivity and continuity.

6. Non-unique interpretations

The fifth thing we don't want to know about fractures is that it is nearly impossible to identify the deficiencies when analyzing production data from a single well. Figure 9 shows the production history (decline curve and cumulative production) from a single fractured interval, along with three plausible production matches.

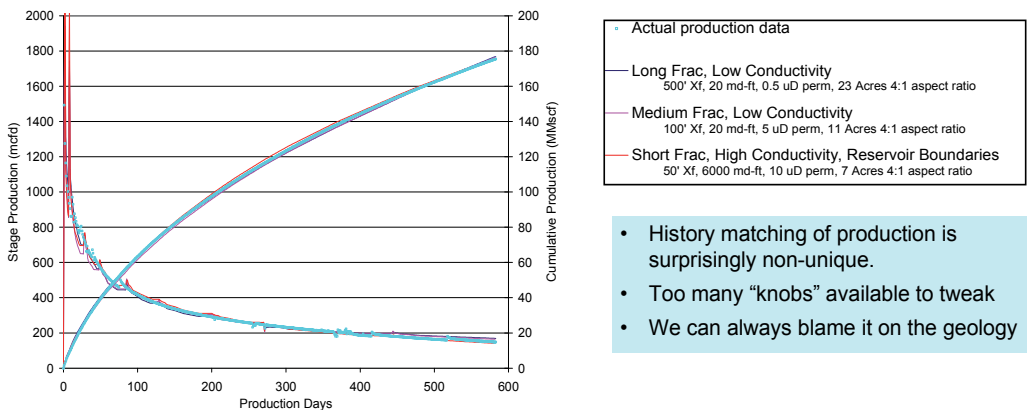

Figure 9. With a single well, the production history can be matched with a nearly infinite combination of plausible fracture and reservoir descriptions [18, 19]

From a single decline curve, we cannot uniquely determine whether the fracture is short and "infinitely conductive," or long with more significant pressure losses. We cannot prove from a decline curve whether the fracture was simple or complex in geometry. We cannot prove whether the fracture conductivity was constant or degrading. Most engineers attempt to match the data with an analytic solution or a numerical simulator that presumes the frac is fully packed with proppant throughout, providing uniform and durable flow capacity without collapse of poorly propped sections. Note that with this approach an engineer can continue to reinforce any existing misconceptions. Fracs can be interpreted to be long or short. Disap-

http://dx.doi.org/10.5772/56066

pointing well productivity can always be blamed on the geology – with no irrefutable proof that the fracture was insufficient.

7. Discussion of five deficiencies

There are certainly more than five deficiencies in our stimulation designs and our techniques to analyze well production. However, the five issues described in this paper include:

1. Hydrocarbons move in a complex manner within propped fractures, increasing the pressure losses by 50 to 1000-fold over common expectations, even if the fractures are planar and fully propped.
2. Fracture conductivity is not constant. Lab data suggest that all conventional proppant types suffer continued crush and compaction over time.
3. Reservoirs are laminated and compartmentalized. Especially with horizontal drilling, ultimate recovery is far more dependent on fracture continuity through laminations than in vertical wells in which each prospective layer can be perforated and individually stimulated. With low perm reservoirs, significantly longer well life (and proppant durability) will be required to drain the available reserves.
4. Fractures develop varying degrees of complexity. This is both good and bad. Reservoir contact is increased as fractures branch, twist, and energize pre-existing planes of weakness. However, this complexity challenges our ability to place a durable, hydraulically continuous proppant pack with conductivity commensurate to carry hydrocarbons with an acceptably small pressure loss.
5. History-matching of production data is surprisingly non-unique. An engineer can reinforce misconceptions throughout an entire career without encountering any results that cannot be matched with a simple, planar frac of durable, high conductivity in a homogenous reservoir. Underperformance can always be attributed to other factors.

While this is a fairly depressing view of the problem, there are techniques to remove some of the uncertainty and ambiguity allowing significant improvement in the performance of stimulation treatments.

8. Removing the uncertainty

Several datasets and techniques can be used to more uniquely describe the performance of propped fractures [19]:

- Wells that are restimulated. When we refrac a well, we have an opportunity to history-match the production from the initial and subsequent stimulation treatments using only a single reservoir description. Difference in well production must be uniquely attributed to the frac

design. There have been more than 140 published examples, and history-matching attempts have frequently indicated that fractures are not as effective or durable as previously anticipated [10, 20].

- Fields in which a carefully conducted field trial examines the role of a single variable in fracture design. For instance, when 150 wells are treated at 4 ppg and 150 offset wells are systematically selected to receive 6 ppg slurry, it is possible to achieve comparisons with compelling statistical significance. The difference in productivity is known to relate to the frac performance, and cannot be attributed to reservoir parameters. The evaluation of 200 published field examples [1] provides very credible evidence that fracs do not perform as most people anticipate, and that increased focus on fracture conductivity is merited.
- Wells that are connected by a propped fracture. As described previously, fractures can reach impressive lateral dimensions. It is not uncommon for fractures to intersect adjacent wellbores completed at the exact same depth or in the same formation subinterval. When this occurs, it provides a significant opportunity to investigate the initial and sustained continuity over time. In most cases, adjacent wells appear to lose hydraulic continuity over time, suggesting that the connecting fracture "collapses" or "heals".
- Infill drilling. In many tight reservoirs, we have successfully drilled wells within 200 feet of existing wells and encountered near-virgin reservoir pressures. In many shale reservoirs, infill wells are anticipated to recover nearly 80% of the reserves of adjacent parent wells drilled many years earlier, demonstrating that initial wells have not captured the available reserves.
- More sophisticated modeling and data analyses. While simple production data analyses yield non-unique solutions, several degrees of freedom can be removed with careful analyses of pressure-transient or rate-transient data. There have also been advances in interpretation of flow regimes from wells with complicated fracture networks. Even in the 400-nanoDarcy Barnett shale, production data do not indicate that the entire created network remains highly effective.

These efforts strongly indicate that additional focus on the conductivity, durability and *effectiveness* of the fracture is needed – not just a focus on created dimensions.

9. Opportunities to improve fracture performance

It is important to recognize that our intuition, our models, and our traditional interpretations of fracture performance are flawed, and can prevent us from recognizing opportunities to improve well productivity. While our industry has collected data demonstrating complexities (in reservoir description, in fluid flow regimes, in fracture geometry, in durability of proppant packs), the industry has been very slow to adapt designs to accommodate or capitalize on these realities.

More than a dozen specific recommendations have previously been discussed [19] to improve the productivity and profitability of fracturing treatments. However, a general theme is to

http://dx.doi.org/10.5772/56066

continue experimenting and studying production from wells, with a healthy skepticism of model predictions and of historic rules of thumb regarding fracture design. Another common finding is that emphasis on improving the effectiveness and durability of treatments appears to be adding more value than blindly focusing on fracture length or treatment volume. There are a great number of field examples in which modest changes to fracturing designs resulted in very large changes to well productivity, convincingly demonstrating that our initial frac designs were insufficient to capture the full well potential. Figure 10 shows surprising increases in productivity were achieved by restimulating a modest perm oil reservoir and a tight gas reservoir with improved fracture designs more focused on the durability and conductivity of the fracturing treatments.

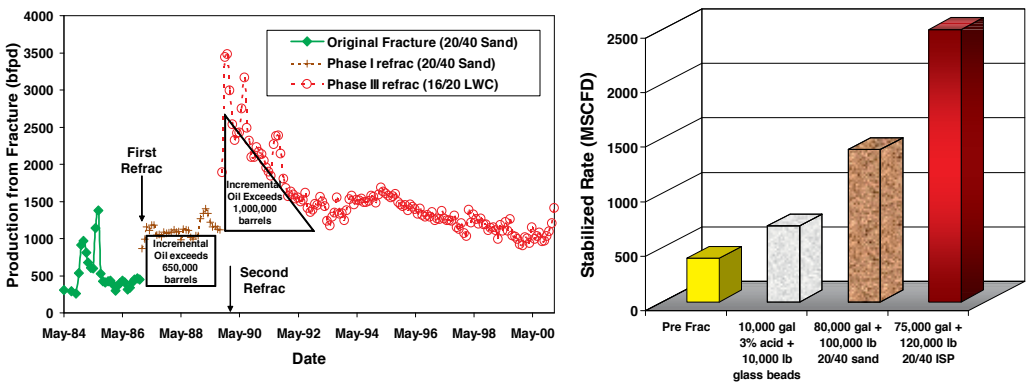

Figure 10. Experimentation with frac design often demonstrates the well potential is constrained by insufficient fracture designs [1, 20]

Similar production increases have been documented in hundreds of field studies in shales, carbonates, coals, and sandstones [1]. On one hand, it is frustrating to admit that after decades we have failed to optimize our fracturing treatments. On the other hand, it is great news that our fracs are not optimized. Reservoirs are often capable of tremendous increases in productivity with improved fracture designs that accommodate and capitalize on our understanding of complexity.

Author details

Vincent M. C.*

Address all correspondence to: mike@fracwell.com

Fracwell Llc, Golden, Colorado, USA

References

[1] Vincent, M. C. (2009). Examining our Assumptions- Have Oversimplifications Jeopardized Our Ability to Design Optimal Fracture Treatments? Paper SPE 119143 presented at the 2009 Hydraulic Fracturing Technology Conference, The Woodlands, Jan , 19-21.

[2] Barree, R. D, Cox, S. A, Barree, V. L, & Conway, M. W. (2003). Realistic Assessment of Proppant Pack Conductivity for Material Selection. SPE paper 84306 presented at the Annual Technical Conference, October , 5-8.

[3] Palisch, T, Duenckel, R, Bazan, L, Heidt, H. J, & Turk, G. (2007). Determining Realistic Fracture Conductivity and Understanding its Impact on Well Performance- Theory and Field Examples. SPE paper 106301 presented at the 2007 Hydraulic Fracturing Technology Conference, College Station, TX, Jan , 29-31.

[4] Montgomery, C. T, & Steanson, R. E. (1984). Proppant Selection- The Key to Successful Fracture Stimulation. SPE paper 12616 presented at the Deep Drilling and Production Symposium, Amarillo, TX April , 1-3.

[5] Mcdaniel, B. W. (1986). Conductivity Testing of Proppants at High Temperature and Stress. SPE Paper 15067 presented at the 56th California Regional Meeting, Oakland, April , 2-4.

[6] Cobb, S. L, & Farrell, J. J. (1986). Evaluation of Long-Term Proppant Stability. SPE paper 14133 presented at the International Meeting on Petroleum Engineering, Beijing, Mar , 17-20.

[7] Hahn, G. (1986). How Long will it Prop? Drilling, the Wellsite Publication. Issue 596, April 1986., 47(6)

[8] Handren, P, & Palisch, T. (2007). Successful Hybrid Slickwater Fracture Design Evolution. Paper 110451 presented at the 2007 Annual Technical Conference, Anaheim, Nov , 11-14.

[9] Duenckel, R, Conway, M. W, Eldred, B, & Vincent, M. C. (2011). Proppant Diagenesis-Integrated Analyses Provide New Insights into Origin, Occurrence, and Implications for Proppant Performance. SPE paper 139875 presented at the SPE Hydraulic Fracturing Technology Conference, The Woodlands, TX Jan , 24-26.

[10] Vincent, M. C. Do They Work, and Why Do They Fail in 100 Published Field Studies?, SPE 134330 presented at the 2010 Annual Technical Conference, Florence, Italy, Sept , 19-22.

[11] LeFeverJ. (2005). Overview of Bakken Stratigraphy and "Mini" Core Workshop. AAPG Rocky Mountain Meeting Short Course #1, Jackson, WY, Sept 24.

[12] Noble Energy Analyst Conference(2010). June 3.

[13] Vincent, M. C. (2011). Optimizing Transverse Fractures in Liquid-Rich Formations, SPE 146376 presented at the Annual Technical Conference, Denver, CO Oct Nov 2., 30.

[14] Warpinski, N. R. (1983). Investigation of the Accuracy and Reliability of In Situ Stress Measurements Using Hydraulic Fracturing in Perforated, Cased Holes. Proceedings, 24th U.S. Symposium on Rock Mechanics, Texas A&M University, College Station, TX, June 20-22, 1983., 773-786.

[15] Warpinski, N. R, Tyler, L. D, Vollendorf, W. C, & Northrop, D. A. Direct Observation of a Sand-Propped Hydraulic Fracture," Sandia National Laboratories Report, SANDMay (1981). , 81-0225.

[16] Warpinski, N. R, et al. (1993). Examination of a Cored Hydraulic Fracture in a Deep Gas Well. SPE 22876, SPEPF Aug , 1993, 150-158.

[17] Fisher, M. K, et al. (2002). Integrating Fracture Mapping Technologies to Optimize Stimulations. Paper SPE 77441 presented at the SPE Annual Technical Conference, San Antonio, Sep. Oct. 2., 29.

[18] Vincent, M. C, et al. (2007). Field Trial Design and Analyses of Production Data from a Tight Gas Reservoir: Detailed Production Comparisons form the Pinedale Anticline. SPE paper 106151 presented at the 2007 Hydraulic Fracturing Technology Conference, College Station, TX Jan , 29-31.

[19] Vincent, M. C. (2012). The Next Opportunity to Improve Hydraulic-Fracture Stimulation. JPT Distinguished Author Series, March SPE 144702., 2012-118.

[20] Vincent, M. C. (2010). Restimulation of Unconventional Reservoirs: When are Refracs Beneficial?. JCPT June 2011, SPE 136757 presented at the Canadian Unconventional Resources & International Petroleum Conference, Calgary, Oct. , 19-21.

Chapter 5

EGS — Goodbye or Back to the Future

Reinhard Jung

Additional information is available at the end of the chapter

http://dx.doi.org/10.5772/56458

Abstract

The heat content of the crystalline basement is by far the biggest energy resource of the earth crust. First attempts to access this resource date back to the early 1970´th and more than a dozen research and industrial projects have been performed since than in various countries. But still the technique, known as HDR (Hot-Dry-Rock) or EGS (Enhanced-Geothermal-Systems) is not mature and the thermal power achieved so far does not meet economical standards. In addition further development is now hindered by the risk of induced earthquakes.

A critical review of results and observations shows that the main reason for the poor progress is the exploitation concept being applied in all major projects since the early 1980´th. Until than the basement had been regarded as a competent rock mass and the leading exploitation scheme was to connect two inclined boreholes by a number of parallel fractures created by hydraulic fracturing in short insulated borehole sections. Realizing that the basement contains open natural fractures even at great depth this multi-fracture-concept was abandoned and replaced by the EGS-concept. The intent of this concept was to enhance the permeability of the natural joint network by massive water injection in very long uncased borehole sections. The results of all major EGS-projects however shows that this is not happening but that generally one large wing-crack is created by the stimulation process regardless of the length of the test-interval. These wing-cracks require significantly bigger fluid volumes for the envisaged fracture-area, have a highly heterogeneous and anisotropic transmissibility and are a plausible explanation for the intense and strong induced seismicity as well as for the strong after-shocks observed at various EGS-locations. These findings suggest a return to the original multi-fracture concept with the only difference that the tensile fractures are to be replaced by the same number of wing-cracks. Directional drilling and packer technology improved significantly during the last three decades and multi-fracture concepts are applied with great success in unconventional gas reservoirs. Though the conditions and requirements in geothermal applications are more

demanding in various aspects it seems almost certain that geothermal multi-fracture-systems of this kind can be realized in the near future.

1. Introduction

Hydrothermal resources at relatively shallow depth used today for geothermal power production are just pinpoints on a map of global scale. By far the biggest resource of geothermal energy is the crystalline basement in regions with normal to slightly above normal temperature gradients. Although the crystalline basement is not completely impermeable due to the presence of open fissures, fractures, or faults its overall permeability is generally far too low to achieve and maintain production flow rates sufficient for geothermal power production. The majority of the crystalline basement may therefore be included among the "petrothermal resources". The basic concept of HDR- (Hot-Dry-Rock) or EGS-technology (Enhanced Geothermal Systems) thus consists of creating or enhancing large fracture surfaces in the crystalline basement in order to hydraulically connect two or several boreholes. During operation cold water injected in one of the boreholes heats up to rock temperature while circulating through the fracture system and is produced in the second well. To prevent boiling an overpressure is maintained in the geothermal loop. Steam for power generation is produced in a secondary loop.

Depending on drilling depth (usually > 3 km) and temperature (usually > 150 °C) a doublet system of commercial size will operate at flow rates between 50 and 100 L/s and produce an electric power of 3 - 10 MW_e. To ensure a service life of at least 25 years a separation distance of at least 0.5 to 2 km between the boreholes at depth and a total fracture surface area of 5 to 10 km^2 is required. The volume of rock to be accessed by the fracture system has to be in the order of 0.1 – 0.3 km^3. Due to the high flow velocities in the fractures especially near the injection and the production borehole the flow impedance of the fracture system (difference between inlet and outlet pressure devided by the outlet flow rate) is critical for the performance of the system. For energetic and economic reasons should not exceed 0.1 MPa s/L.

Basically two concepts had been designed and tested during the 40 years of HDR-research. In the beginning the crystalline basement at great depth had been regarded as an intact almost impermeable rock mass. It seemed therefore necessary to create artificial flow paths by means of hydraulic fracturing. The original concept (HDR-concept) [1-4] proposed by a group of the Los Alamos National Laboratory in the early 1970th consists of a doublet of deviated boreholes. The boreholes are drilled parallel to the azimuth of the least compressive principal stress and are connected by a set of large parallel fractures created during hydraulic fracturing tests in insolated borehole sections. These tensile fractures are oriented perpendicular to the least compressive principal stress.

The second concept (EGS-concept) promoted mainly by the Camborne School of Mines [5] and the University of Paris [6] is based on the observation of numerous natural fractures (joints and faults) even at great depth. The crystalline basement was therefore regarded as a broken material (discontinuum) and the idea was to shear and widen the natural fracture network by massive water injection in long uncased borehole sections. This process was named hydraulic

http://dx.doi.org/10.5772/56458

stimulation. The second borehole is then directionally drilled into the region of enhanced permeability. Since the stimulated region is elongated in the direction of the maximum horizontal stress, the boreholes are aligned in this direction which is 90 ° off the direction of the HDR-concept.

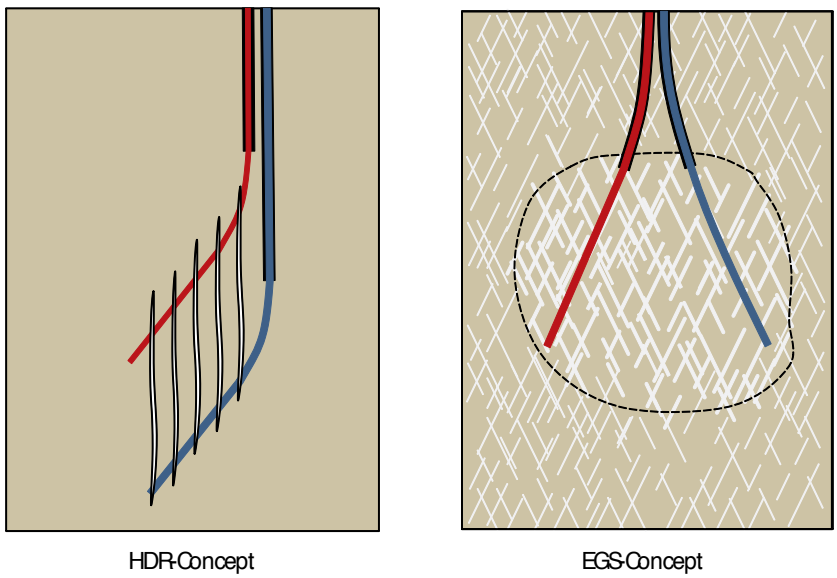

Figure 1. Basic concepts

Due to the enormous size of the created or enhanced fracture systems mainly water or brine without proppants were considered as frac-fluids since it seemed too costly or technically impossible to place proppant material over such large areas. All tests in the crystalline basement were accompanied by intense induced seismicity. Localizing and mapping the sources of induced seismicity thus became the most important tool for investigating the evolution of the fracture systems during water injection and most of the projects used this method to define the target for the second or third well. On the other hand induced seismicity has become a major obstacle for further development of the HDR- or EGS-technology since on some locations the population was shocked by events with magnitudes bigger than 3 [7].

The HDR-concept was followed only during the first years of development. Warned by the inability to create vertical fractures in the pioneering Los Alamos project and convinced by the arguments of the EGS-proponents that shearing of natural fractures is the predominant failure mechanism this concept was abandoned [8] and all projects after the 1980th followed the new EGS-concept. The rapid adoption of this concept was to a big part due to its technical simplicity. In particular, it required no high-temperature open hole packers, which created enormous technical problems in the Los-Alamos-Project. The change in the leading concept had severe consequences:

- Boreholes were no longer directional drilled parallel to the azimuth of the minimum horizontal stress but more or less parallel to the azimuth of the maximum horizontal stress.
- Very long almost vertical borehole sections containing hundreds of natural fractures were stimulated by injecting very large quantities of water.
- The development of high temperature packers was no longer important and was disregarded.
- Heat exchanging area as a measure for the service life of a HDR-system was replaced by accessible rock volume.
- Geometrical simple fracture mechanical models were replaced by geometrical complex fracture network models lacking fracture mechanical mechanisms.

It will be shown that mainly this change of concept is responsible for the poor progress of HDR-technology during the last 3 decades. The following chapters will critically review the results and observations of the major EGS-projects and proof that the basic mechanism controlling the stimulation process is not the shearing of the joint network but the formation of single large wing-cracks.

2. Characteristics of key projects

Nine research projects and 3 commercial HDR-projects have been performed since the beginning of Hot Dry Rock research at around 1970 [9]. The major projects are described briefly in the following paragraphs.

2.1. Los Alamos

This first HDR-project was located at Fenton Hill at the rim of a large caldera. HDR-Systems were established at two levels in a biotite-granodiorite body at around 2800 m depth (Fenton Hill I) and in a heterogeneous metamorphic complex below 3500 m (Fenton Hill II) [10]. Rock temperature was 190 °C at the upper level and above 230 °C at the lower level.

The main elements of the shallow system are two vertical fractures created by water-frac tests. The design of the deeper system was according to the HDR-concept as shown in Fig. 1. Since the Los Alamos team felt certain about the stress directions both boreholes were drilled and completed before stimulation. In the target zone the wells were directionally drilled with a dip of 60° and parallel to the azimuth of the minimum horizontal stress. The length of the uncased sections was 1000 m, their vertical distance 300 m. The deeper borehole reached a depth of 4400 m [3]. About a dozen hydraulic fracturing operations were conducted in various intervals of the deviated section of the deeper well (EE2). High temperature open hole packers, casing packers, and PBR (Polished Bore Receptacles) in combination with sanding-off the bottom part of the hole were used to insolate borehole sections of 20 to 150 m length within the 1000 m long open hole section [11,12]. Most of the tests showed a high frac-pressure of about 40 MPa (wellhead pressure) indicating a high value of the normal stress acting on the fracture (around

http://dx.doi.org/10.5772/56458

0.8 of the vertical stress). The most extensive hydraulic fracturing operation was conducted in the uppermost 20 m of the open hole at 3500 m depth by injecting 21,500 m³ of water at flow rates up to 130 L/s. From the spatial distribution of induced seismicity as shown in Fig. 2 it was concluded, that a volumetric structure of roughly 800 x 800 m with a thickness of 200 m was stimulated. The strike of this structure was perpendicular to the direction of the borehole azimuth as expected, but instead of being vertical it was dipping toward the East parallel to the borehole axis. A satisfactory connection between the boreholes could be achieved after sidetracking the upper well into the region of induced seismicity and after stimulating this new well section. A circulation test revealed a thermal power output of 10 MW at a production flow rate of 12 – 14 L/s. Fluid losses and flow impedance were 20–30 % and 2.1 MPa s/l respectively. The Fenton Hill test site was abandoned due to declining financial support.

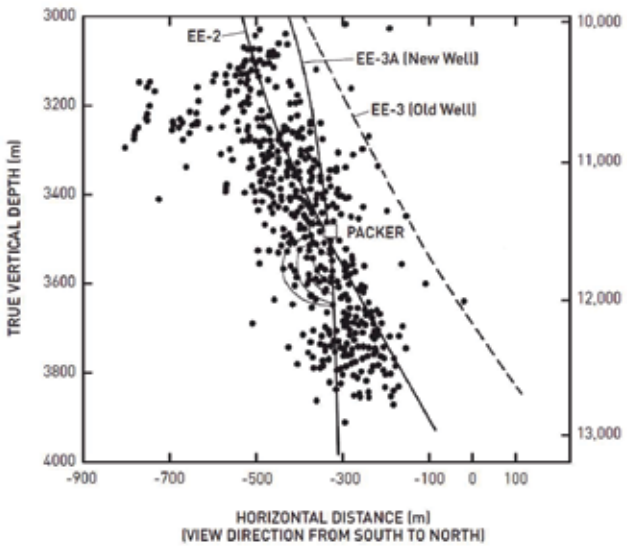

Figure 2. Hypocenters of seismic signals induced during the massive water frac-test in borehole EE1 at Fenton Hill (view is along the strike direction of the stimulated structure). EE-3A is the sidetrack of borehole EE-3, that was lend through the stimulated region. Note that the side track is not in the same plane as EE-2 but about 150 m in front of it. Re-production from [9].

2.2. Camborne

This first major project following the EGS-concept started in 1977 [5] and was operated by the Camborne School of Mines. The test site (Rosemanowes Quarry) is located near the centre of the Permian Carnmenellis granite pluton which is outcropping at the surface. Two orthogonal vertical joint sets were encountered at depth striking NNW-SSE and WSW-ENE. The stress conditions were strike slip with the maximum horizontal stress oriented NW-SE [13]. Two wells were drilled to 2000 m depth. Their arrangement is similar to the deep system in Fenton Hill but they deviate parallel to the direction of the maximum horizontal stress. Their vertical distance is about 300 m in the deviated part. Both boreholes had long open hole sections of 700

m and 360 m respectively. They were both drilled prior to stimulation. A hydraulic connection was achieved after a massive water injection in the lower well (26,000 m^3) and a less massive stimulation in the upper well. The hydraulic connection however was poor and the fracture system extended during a long term circulation test with injection flow rates obviously too high for the system. A better connection was achieved after drilling a third well perpendicular to the strike of the fracture system and intersecting it some 300 m below the other two wells. Seismic activity recorded during the frac-tests (figure 3) showed that the activated fracture system had grown predominantly downward and was elongated in the direction parallel to the maximum horizontal stress [14]. The width of the seismic cloud (spatial distribution of the seismic sources) was less than 200 m. It showed an internal clustering of events along long vertical channels. A substantial thermal drawdown was observed during the first year of a circulation test indicating that the structure was much less "volumetric" than expected.

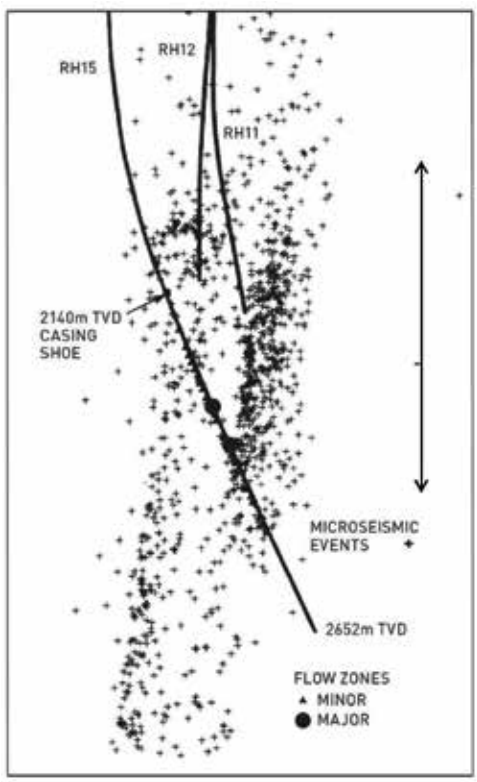

Figure 3. Front view of the seismic cloud of the EGS-system at Rosemanowes. Note the channel-like structures inside the seismic cloud. Re-production from [9]

2.3. Soultz-sous-Forêts

This project started in 1988 [15]. The site of Soultz is located in the central part of the Upper Rhine Valley 6 km east of the Western main fault. The top of the Granite is at 1400 m and holds

http://dx.doi.org/10.5772/56458

through down to the maximum depth of the boreholes (5 km). Typical for a rift setting is the high density of almost rift-parallel faults. Temperature anomalies at the site and in the region around Soultz are indications that some of the faults are permeable, transporting water from great depth into the Permian and Triassic cap rock. The joint systems are clustered with a high density of joints in fracture zones and a much lower density in competent rock [16]. Fracture zones and joints are mainly sub-vertical and striking 160°. The stress field is characterized by a low minimum horizontal stress ($\sigma_h \cong 0.54\ \sigma_V$) and a maximum horizontal stress almost equal to the vertical stress [17, 18]. It was supposed that there was a transition from normal faulting conditions in the top part to strike slip conditions below 3000 m. The direction of the maximum horizontal stress as determined from the orientation of drilling induced fractures and borehole break-outs is 170 °. Temperature reached 201 °C at 5000 m depth. Large scale in-situ permeability of the granite was determined to less than 35 μD. But some of the faults intersected by the boreholes had transmissibilities between 0.1 and 50 d m (darcy meter; 1 d m = 10-12 m^3) demonstrating that much more than 90 % of the water in the granite is carried by a few highly permeable faults and not by the joint network [19, 20].

Two HDR-Systems were established in the depths levels 2800 – 3600 m [20] and 4400 m – 5000 m [21] respectively (figure 4). The design of both systems was according to the EGS-concept, but instead of drilling production and injection wells first and connecting them afterwards the first borehole was massively stimulated after completion and the next borehole directionally drilled into the target zone defined by the spatial distribution of induced seismicity. In this way a doublet system was established at the upper and a triplet system at the lower level. All boreholes drilled at Soultz had open hole sections of 500 – 750 m in the bottom part. These sections were stimulated by injecting large volumes of water (between 10,000 and 35,000 m^3). Flow rates were comparatively low (35 – 55 L/s) and in some cases the tests were started at flow rates as low as 1 L/s in order to allow the pressure to spread out in the joint network thus stimulating as many joints as possible. Both in the upper and the lower system it was necessary to stimulate the second and (in case of the triplet) also the third well before a satisfactory connection was achieved. Borehole separation was 450 m in the doublet system and 600 m between the central injection hole and the two production holes in the triplet system.

Self propping of fractures was quite efficient and sustainable. Transmissibility of single fractures exceeded 1 d·m and was only slightly pressure dependent. Both fracture systems (upper and lower system) had open boundaries. Active pumping in the production wells was therefore introduced for the first time in an EGS-project in order to avoid fluid losses. Production flow rates reached 25 L/s in the production well of the upper system and more than 30 L/s for the two production boreholes (cumulated) of the lower system. Reinjection of the production flow in the central injection well of the lower system became a problem since induced seismicity started at an injection flow rate of about 20 L/s. In many aspects: depth, size, borehole distance, flow-impedance, circulation flow rates and fluid losses the two systems at Soultz mark the frontier of present HDR-technology. Part of this success however may be due to the favorable tectonic conditions in a rift setting and the results obtained so far are still insufficient for a commercial system.

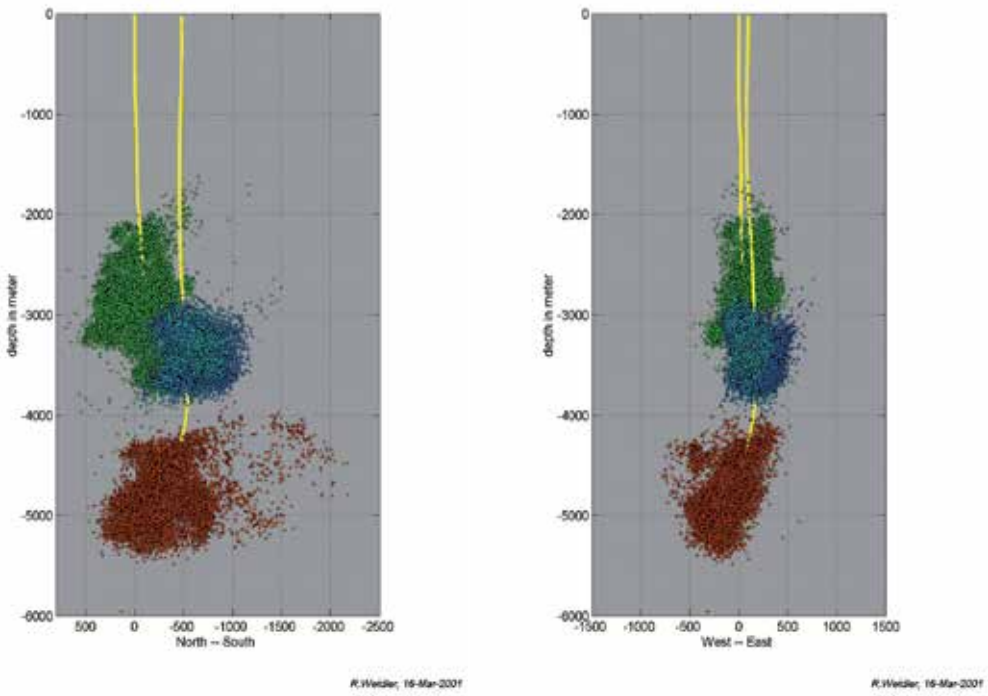

Figure 4. Seismic clouds of all stimulation tests of the upper EGS-system (Soultz I) and of the first stimulation test of the lower EGS-system (Soultz II) at Soultz [22]. General strike direction of the seismic clouds is NNW-SSE in both cases. The deeper well is GPK2, the other GPK1. The deep system was later intersected by two additional boreholes (GPK3 and GPK4) and enlarged during stimulation tests in these wells. Note the low seismic source density in the southern wing of the seismic cloud.

3. Observations and results of stimulation and circulation tests

Though the number of stimulation tests in EGS-projects is quite limited as compared to the millions of frac-tests in oil and gas reservoirs an attempt was made to find some general relationships between test-parameters and test-results. This was done with little hope since reliable data was sparse and test conditions very variable. The only constants for almost all tests were rock type (granite and granodiorite) and frac-fluid (water or brine with one exception) and the fact that all tests were done in uncased borehole sections. All other test parameters and conditions were quite variable (Tab. 1): Stress condition ranged from normal- to reverse faulting, length of frac-interval from 3 to 750 m, injected volume from 20 m^3 to 35.000 m^3, flow rates from 6 L/s to 200 L/s. Furthermore some tests were performed with constant flow rate, others with stepwise increased flow rates. Well trajectories were predominantly vertical to sub-vertical but some tests (Fenton Hill II and Camborne II) were performed in inclined borehole sections.

http://dx.doi.org/10.5772/56458

Project	Stress st.	Well	Frac-int.	Well Traj.	V_{IN}	Q_{IN}	P_{wc}	A	Cloud-Dip	Ref.
			[km]		[m^3]	[L/s]	[MPa]	[km^2]		
Falkenberg	normal	HB4a	0.25	vertical	25	3.5	2.2	0.014	60	[23]
Fenton H. I	normal		2.8	sub-vert.	587			0.15		[24]
Fenton H. I	normal		2.8	sub-vert.	761			0.16		[24]
Fenton H. I	normal		2.8	sub-vert.	5018			0.53		[24]
Fenton H. II	normal		3.7	55° II S_h	150			0.027		[24]
Fenton H. II	normal		3.7	55° II S_h	890			0.085		[24]
Fenton H. II	normal		3.7	55° II S_h	3183			0.27		[24]
Fenton H. II	normal		3.7	55° II S_h	3183			1		[24]
Fenton H. II	normal		3.7	55° II S_h	4702			1.1		[24]
Fenton H. II	normal	EE2	3.45-3.47	55° II S_h	22000	108	38	0.7	65	[8,12]
Camb. II	strike s.	RH12	1.74-2.12	60° II S_H	18500	20-90	14	0.6	sub-vert.	[25]
Camb. II	strike s.	RH15	2.1-2.25	60° II S_H	5700*	200	15	0.04	sub-vert.	[13]
Hijiori	normal	SKG-2	1.79-1.80	vertical	2000	17-100	15	0.15	60	[2,26,27]
Hijiori	normal	HDR-1	2.03-2.21	vertical	2100	17-67	26	0.25	60	[2,26]
Ogachi	(rever.)	OGC-1	1.00-1.01	vertical	10140	11	19	0.5	30	[2,28]
Ogachi	(rever.)	OGC-1	0.71-0.72	vertical	5440	8	22	0.3	sub-hor.	[2,28]
Soultz I	strike s.	GPK1	2.85-3.40	vertical	25300	0.2-36	9	1	sub-vert.	[20,29]
Soultz I	strike s.	GPK2	3.21-3.88	sub-vert.	28000	12-50	12	0.8	sub-vert.	[20]
Soultz II	strike s.	GPK2	4.40-5.00	sub-vert.	23400	30-50	14.5	3	sub-vert.	[22]
Cooper B.	reverse	Hab. 1	4.14-4.42	vertical	20000	14-26	60	3	sub-hor.	[9]
Basel	strike-s.	Basel 1	4.63-5.00	vertical	11650	0.2-55	30	0.9	sub-vert.	[30]

Table 1. Stimulation parameters and of major stimulation tests in HDR-projects, V_{IN}: injected volume, Q_{IN}: injection flow rate, p_{wc}: maximum well head pressure, A: area of the "seismic cloud"

3.1. General observations

General observations can be summarized as follows: All tests except a gel-test in the Camborne II system were accompanied by intense seismic activity. In all cases the seismic clouds were approximately 2-dimensional with a thickness in the range of the spatial resolution of the localization method. Some seismic clouds were twisted or bended or showed long tubular internal structures and straight boundaries. Width to length ratio measured along their main axis ranged generally from 0.3 to 3. The sparse seismic sources of the gel-frac were arranged tubularly. Some seismic clouds (Soultz II GPK2., Basel 1, and Fenton Hill II EE1) showed an alignment with well trajectories. Seismic clouds in strike-slip regions were vertical or sub-vertical with a general trend slightly off the direction of the maximum horizontal stress. For normal stress conditions (Hijiori, HDR-1 and Fenton Hill, EE2) the seismic clouds dipped 60° or 65° respectively toward the direction of the minimum horizontal stress. For reverse stress conditions (Cooper Basin and most likely Ogachi) the seismic clouds were horizontal or sub-horizontal. Seismic activity started generally far below the jacking pressure (pressure equal to the normal stress on the fracture) but the pressure always approached the at the end of the tests. In relation to depth the maximum injection pressure p_{wc} (measured at the well head) was comparatively low for vertical or sub-vertical fractures, higher for steeply dipping fractures and much higher for sub-horizontal fractures.

3.2. Size of the stimulated region

In contrary to the common praxis in EGS-literature of the last 2 decades but in accordance with an earlier study [24] not the volume but the area of the seismic cloud was taken as the measure for the size of the stimulated region. This was done because of the 2-dimensional nature of the seismic clouds and the strong influence of the location error on their thickness. This area, called seismic area in the following, was grossly determined by drawing an envelope around the projection of the seismic clouds on a plane parallel to its main orientation. Despite of the big variation in test and test-site conditions a clear correlation was found between seismic area and injected volume (figure 5a). 75% of the data points can well be fitted by a power law with exponent n = 0.6. Accordingly the ratio of injected volume and seismic area is fitted by a power law with exponent (1 – n) = 0.4 (figure 5b). Seismic area and the ratio of injected volume and seismic area did not correlate with flow rate or length of the frac-interval. These findings and the high coefficient of correlation of both parameters with injected volume allow establishing the following working hypotheses:

1. The stimulation process is mainly volume-controlled. This means, the majority of the injected volume is creating new fracture volume. Hydraulic diffusion (including fluid losses into the rock matrix) is not essential. Fluid efficiency η (ratio of created fracture volume and injected volume) is high (at least higher than 0.5).
2. The number of fractures created or stimulated in the frac-interval is close to "1" regardless of the length of the frac-interval.
3. Static fracture models should apply; friction pressure losses in the fractures are negligible.

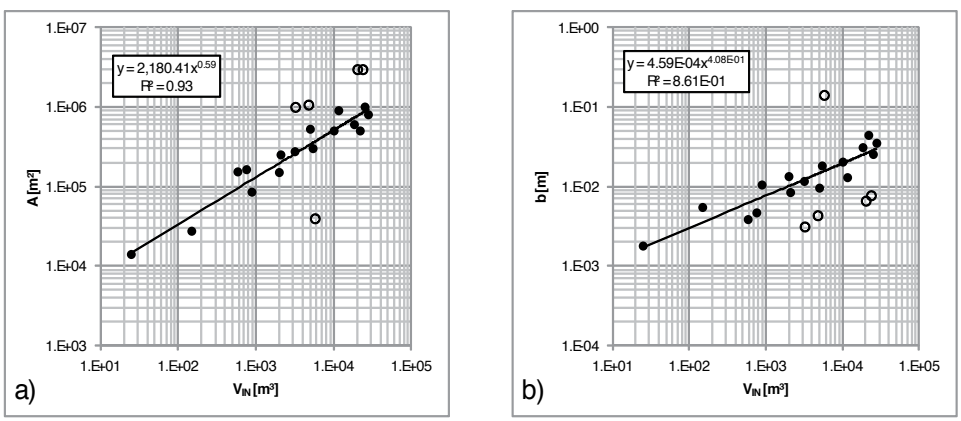

Figure 5. Results of the stimulation tests: a) Area of the seismic clouds vs. injected volume, b) ratio of seismic area and injected volume vs. injected volume. Fitting lines and coefficients of determination are for the solid data points.

3.3. Characteristics and internal structure of the stimulated region

Some of the seismic clouds showed long channel-like internal features. In the Soultz I system a first channel started to grow from the main outlet in the top part of the open hole section of

http://dx.doi.org/10.5772/56458

the first well (GPK1) and propagated sub-vertically downward (figure 6). At the end of stimulation it reached a length of about 700 m. Seismicity was spreading predominantly to one side of this channel during migration. In the final test period several other channels developed starting from almost the same region as the first but with different dip (figure 6). Views along some of these channels indicate that the main structure created by the stimulation process was a large wing crack with a central shear zone and the typical bended wings (figure 7).

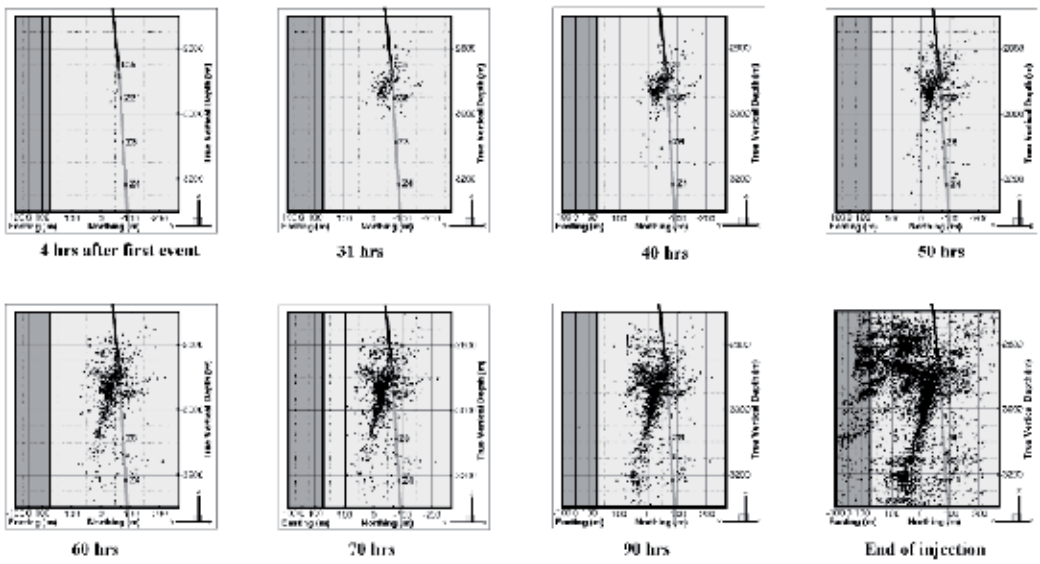

Figure 6. Evolution of the seismic cloud during the first stimulation test in the Soultz I system (front view) [31].

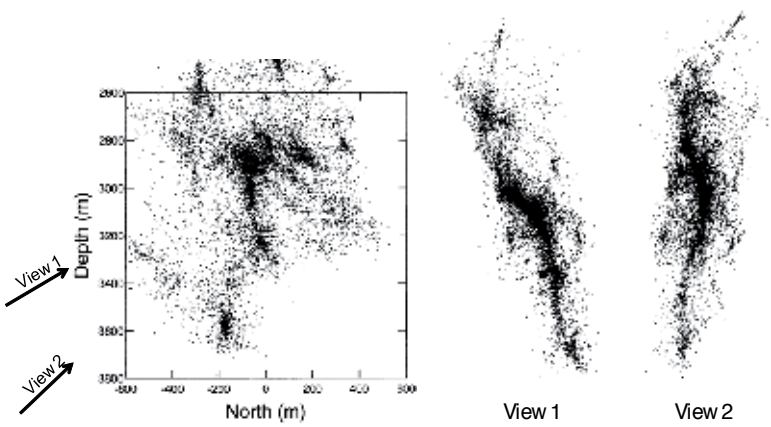

Figure 7. Seismic cloud of all located events of the first stimulation test in the Soultz I system (well GPK1). Left: front view, middle and right: views along indicated directions [32].

3.4. Number of stimulated fractures

Direct information on the number of conductive fractures was obtained by flow and temperature logging during stimulation and post-stimulation injection or production tests. In no case was the number of hydraulically significant fractures bigger than 4 and often they were in close vicinity to each other. An example from a well in the Soultz I system as shown in figure 8 demonstrates that even these small numbers should only be regarded as an upper limit [32]. The 750 m long uncased section of this well contained one significant fault with a transmissibility of 0.1 d m at 3500 m depth prior to stimulation. This fault consumed more than 90% of the injected fluid during pre-stimulation hydraulic tests. The contribution of the several hundreds of joints, a number of fracture zones and additional faults, as well as the numerous drilling induced fractures encountered by ultrasonic borehole-televiewer measurements was insignificant. During stimulation a group of drilling induced en-echelon fractures in the uppermost open hole section opened in the early test-phase and remained the dominant hydraulic feature throughout the test absorbing about 2/3 of the injected flow rate. The remaining third was absorbed by the fault at 3500 m and by 3 other fractures. A redistribution of the flow fraction of these three fractures between stimulation and production proofed that they were merely low impedance connections to the main fracture originating in the uppermost part of the open hole section (figure 8).

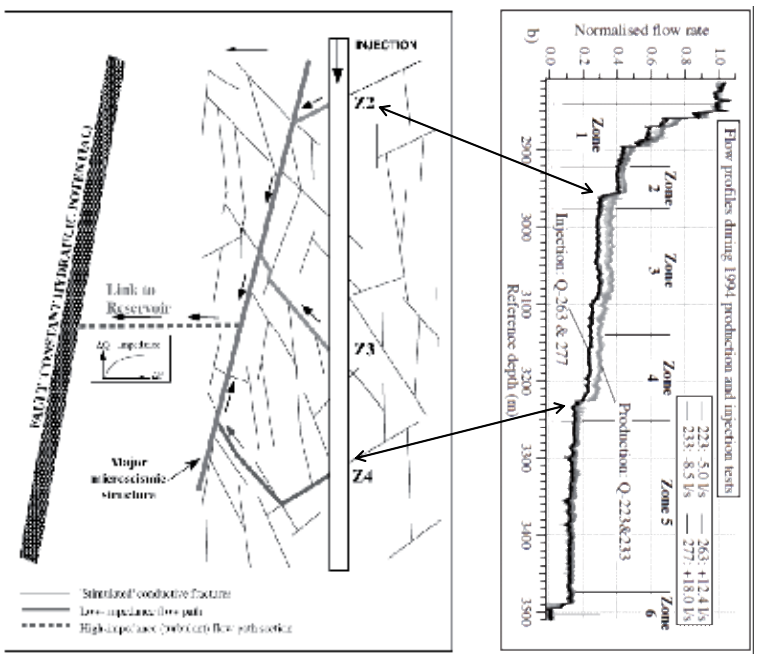

Figure 8. Right: Spinner flow logs recorded during the main stimulation test and during a post-stimulation production test in well GPK1 (Soultz I system). Left: model illustrating that fractures Z1, Z2, and Z3 are low impedance flow paths connection the well to the main fracture Z1 [31].

http://dx.doi.org/10.5772/56458

3.5. Aperture of stimulated fractures

Information on the aperture of the stimulated fractures can be obtained from tracer tests performed during circulation. The tracer response curves of EGS-systems found in reports and publications were of surprisingly uniform shape (figure 9). All had a steeply rising tracer concentration after tracer break-through, a single maximum and a monotonously declining tracer concentration afterwards. Some showed minor inflections in the tail that were interpreted by some authors as tracer arrivals from multiple flow paths but as an effect of tracer re-injection by others. None of the curves showed clear indications of multiple fracture flow.

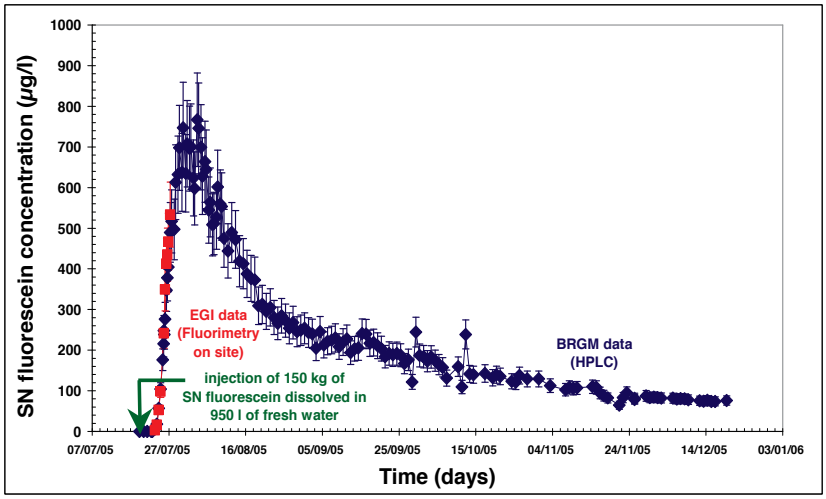

Figure 9. Tracer response curve recorded during a long-term circulation test in the Soultz II system. Source: [33].

For these reasons and in order get comparable results it seemed reasonable to use the same simple proxy model, namely that of a doublet in an infinite fracture of uniform aperture for evaluation. The tracer break-through volume for this model is given by:

$$V_b = \frac{\pi b_T \cdot a_G^2}{3} \tag{1}$$

With b_T: aperture of the fracture and a_G: geometrical inlet to outlet distance. The values of b_T determined with this equation are listed in Table 2 and plotted in figure 10. For comparison the values of b given by the ratio of seismic area and injected volume and the corresponding fit-line are included. In 3 cases (Fenton Hill I & II and Camborne II) is the aperture determined from the tracer break-through volume by a factor of 5 to 10 smaller than the aperture given by the ratio of injected volume and seismic area. In other 3 cases (Soultz I, Hijiori and Ogachi) both aperture values agree quite well. For Soultz II the aperture from the tracer break-through volume is consistent with the data from Soultz I, Hijiori and Ogachi though the ratio of injected volume and seismic area is comparatively low. The majority of the aperture values are in the

range of centimeters. For comparison: (hypothetical) tensile fractures with a fracture area of 1 km² would have an average aperture of about 1 mm.

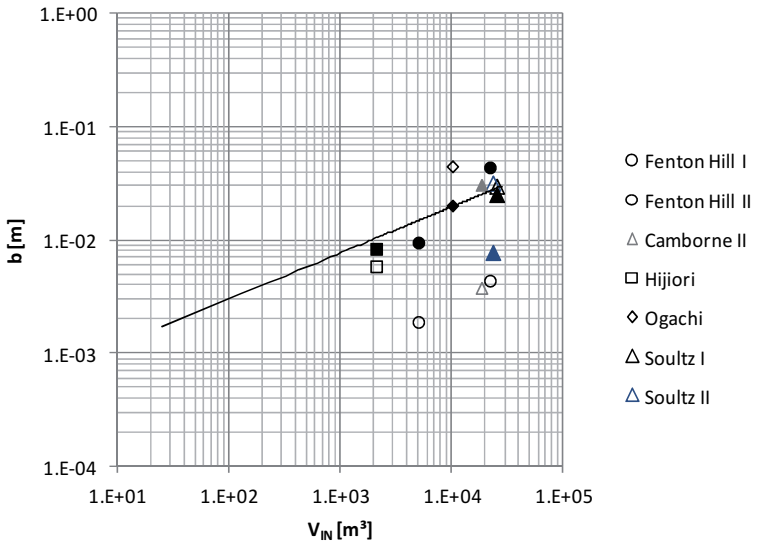

Figure 10. Fracture apertures determined from tracer break-through volumes (open symbols) and given by the ratio of injected volume and seismic area of the stimulation tests (filled symbols). Fitting line is identical with the fitting line of figure 5b.

3.6. Heat exchanging area

The observation of the thermal draw down is probably the most sensitive method to distinguish single fracture flow from multi-fracture or volumetric flow. Already two (thermally independent) fractures instead of one extent the time scale for the thermal draw-down by the square-root of two. Volumetric flow is indicated when the production flow is constant over a prolonged time period. Unfortunately data for only two cases, Camborne II and Hijiori was available. Both thermal draw down curves could well be fitted by using an analytical model and reasonable thermo-physical values for the fluid and rock. The model calculates the evolution of the production temperature for a doublet in an infinite fracture of uniform transmissibility with transient conductive heat flow from the rock matrix toward the fracture (figure 11). The inlet-outlet distance of 260 m determined by using this model agrees quite well with the geometrical inlet-outlet distance of the Camborne II system (Table 2). For two fractures this distance would reduce to 190 m, which is hardly compatible with the geometrical configuration. For Hijiori the inlet-outlet distance obtained by the model is already for one fracture smaller than the geometrical distance. Two fractures would make this discrepancy even bigger. The thermal draw down curve of a porous layer with a thickness of 10 m instead of a discrete fracture would have a thermal break through-time (end time of constant production temperature) of about 1 year for Camborne (figure 11). The observed thermal break-

http://dx.doi.org/10.5772/56458

through time is by at least a factor of 10 lower. This means a layer compatible with the thermal draw-down of Camborne II could have a maximum thickness of 1 m. The long term thermal response of such a layer is indistinguishable from that of a discrete fracture. Summarizing one can conclude that the observed thermal draw down curves give no reason to introduce more than one fracture or a porous layer (volumetric fracture system) instead of a discrete fracture as the main flow path between injection and production well.

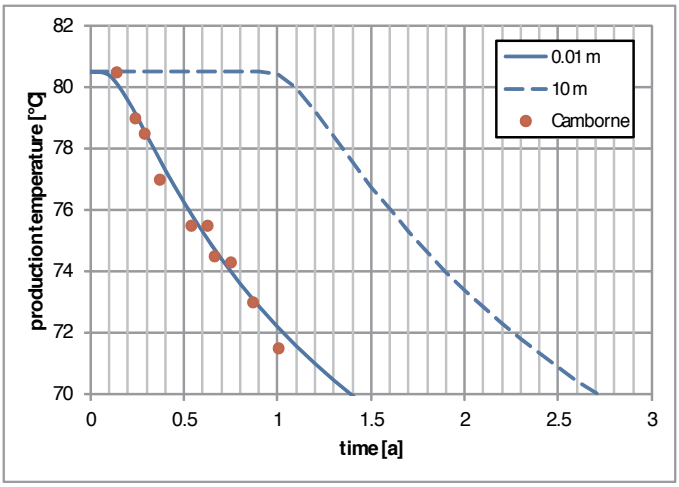

Figure 11. Evolution of the temperature draw-down in the production well of the Camborne II system (red dots from [34]) and fit-curve calculated for a doublet in an infinite fracture (solid blue line) and for a doublet in a porous layer with thickness 10 m (dashed line) for well distance: a_H = 263 m, flow rate: Q = 15 L/s, injection temperature: T_{in} = 20 °C, T_0 = 80.5 °C.

3.7. Hydraulic properties

The inter-well transmissibility of the fractures was determined from the flow impedance "I" by using the model of a doublet in an infinite fracture of homogeneous and isotropic transmissibility imbedded in an impermeable matrix. For this model the transmissibility is approximately given by the following formula:

$$T_f = \frac{2\mu}{I} \left[m^3\right] \tag{2}$$

The values calculated with Eq. 2 are listed in Tab. 2. The transmissibility of the fractures of the Camborne II and the Soultz I & II systems exceeds 1 d·m, a value which is rarely achieved with conventional propped fractures. The fractures of the other systems are in the range of 0.1 d·m or lower. The "hydraulic aperture" b_H corresponding to these transmissibility values can be calculated by:

$$b_H = \sqrt[3]{12 T_f} \tag{3}$$

This formula is for smooth fracture surfaces and was experimentally confirmed for fractures in rock but with coefficients slightly higher than 12. The hydraulic apertures calculated with this formula are by about a factor of 10 to 100 lower than the apertures derived from the tracer break-through volume (Tab. 2). This in turn means that one should expect fracture transmissibilities between 500 d·m and 7 Mio. d·m from the apertures of the tracer tests. This stupendous discrepancy can not be explained by turbulence or viscosity effects. It is also unlikely that asperities or particles are plugging the fractures to such a degree that only a small fraction of the fractures is open for the flow. In this case the tracer break-through volume would also be reduced to a high degree. The most plausible explanation is that the fractures consist of a series of wide open and very narrow fracture elements. In this case the average aperture is mainly determined by the wide fracture elements whereas the transmissibility is mainly determined by the narrow fracture elements. This kind of arrangement can neither be explained by tensile fracture propagation nor by the shearing of existing fractures or faults.

Project	a_G	T_0	Q_{EX}	I	μ	T	b_f	V_b	b_T	a_H	References
	[m]	[°C]	[L/s]	[MPa·s/L]	[Pa·s]	[d·m]	[m]	[m^3]	[m]	[m]	
Fenton Hill I	230	190	6	1.6	1.5E-04	.19	1.3E-04	100	1.8E-03	-	[9]
Fenton Hill II	150	230	6	2.1	1.3E-04	0.12	1.2E-04	100	4.2E-03	-	[8] [3]
Camborne II	250	80	15	0.6	3.6E-04	1.20	2.5E-04	240	3.6E-03	263	[13]
Hijiori	90	250	4	0.6	1.2E-05	0.04	7.9E-05	90	1.1E-02	65	[35-38]
Ogachi	80	240	1.7	8	1.2E-04	0.03	7.2E-05	289	4.3E-02	-	[39]
Soultz I	450	170	25	0.23	1.6E-04	1.39	2.6E-04	6000	2.9E-02	-	[20]
Soultz II	600	200	12	0.25	1.4E-04	1.1	2.4E-04	11500	3.1E-02	-	[34]

Table 2. Operation parameters and results of circulation tests in major HDR-systems, a_G: geometrical distance between inlet and outlet, T_0: rock temperature, Q_{EX}: production flow rate, I: impedance (ratio of pressure difference between inlet and outlet and production flow rate), μ: viscosity of produced water; T: transmissibility, b_H: hydraulic aperture, V_b: tracer break-through volume, b_T: aperture calculated from tracer break-through volume, a_H: inlet to outlet distance calculated from observed thermal draw-down.

Well test analysis of post-stimulation injection or production tests point into the same direction. All post-stimulation hydraulic tests in Soultz and in Basel showed very long fracture linear or bilinear flow periods often persisting over 10 hours or more. Such long periods need a very long start line for the flow. In cases where several hundred Meter long axial fractures are present (Soultz II well GPK4 and probably Basel) these long starting lines may be identical with the trace of these fractures along the borehole wall. In other cases they are most likely identical with the long channel-like features of the seismic clouds. Theses channels play most likely a dominant role for the flow distribution in the stimulated fractures. Channels may also exist on the scale of joints and may result in a highly anisotropic transmissibility of the large scale fracture.

http://dx.doi.org/10.5772/56458

4. Interpretation and discussion

It is obvious that the actual EGS-concept is inconsistent with almost all observations and results described in the last chapter. The main reason for this inconsistency is most likely the wrong model for the granite underlying this concept. It´s basic assumption is that the granite due to the presence of joints has to be considered as a discontinuum (figure 12) and can therefore be regarded a as coulomb-material. Accordingly the coulomb friction failure criterion is the obvious choice for the stimulation process. A more realistic model (figure 12) however considers the granite as a continuum on the scale of joints and as a discontinuum on the scale of faults or fracture zones [41, 42].

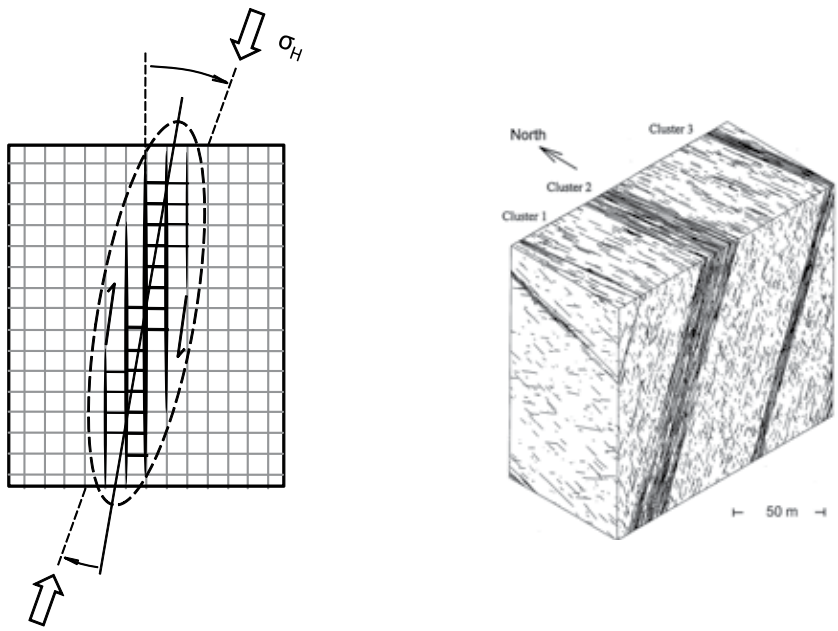

Figure 12. Conceptual models for the granite. Left: granite as a discontinuum on the scale of joints [13], right: granite as a discontinuum on the scale of faults or fracture zones and as a continuum on the scale of joints [40, 41].

The Coulomb failure criterion is therefore applicable only on the scale of faults or fracture zones whereas on the scale of joints hydraulic stimulation needs a failure mechanism that includes the formation of new fracture surface like the classical hydraulic fracturing models. Tensile fracture models are however unable to explain the onset of the failure process at a pressure far below the minimum principal stress. Furthermore they are hardly consistent with the intense seismicity and the source mechanism of the seismic events. For these reasons a new model is required that combines tensile fracture propagation with the shearing of natural discontinuities. The most obvious choice is the wing-crack model (figure 13).

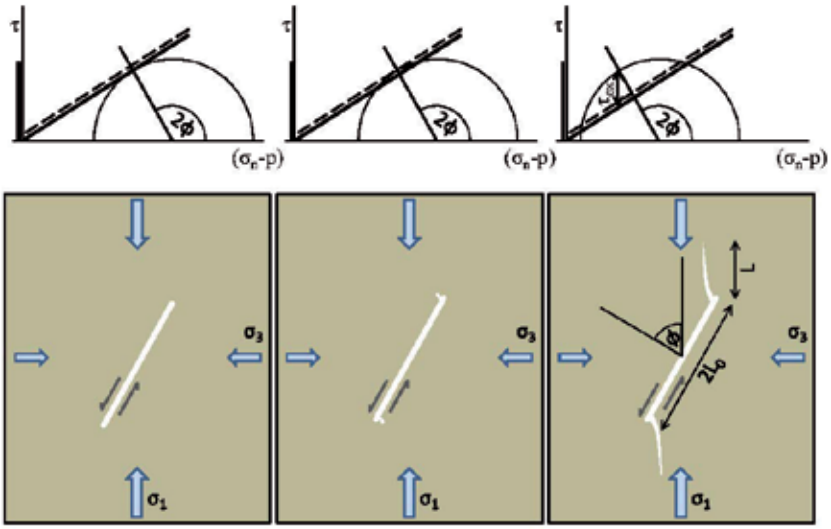

Figure 13. Wing-crack model, left: onset of shearing, middle: wing initiation, right: wing propagation.

The formation of wing-cracks is one of the micro-mechanisms discussed in material science to explain the inelastic behavior and failure of brittle material under compression. The basic observation is that fractures of finite length failing in shear will not propagate along their own plane but will form tensile wing-fractures (figure 13). Referring to results of [42] Lehner & Kachanow [43] stated that the wings start to grow at an angle of 70° to the plane of the initial shear fracture and gradually turn into the direction of the maximum principal stress. Introducing the parameter τ_{ex} which is the part of the shear stress exceeding the Coulomb friction failure line (figure 13) the criterion for the initiation of the wings can be written as [42]:

$$\tau_{ex} = \frac{\sqrt{3} K_{IC}}{2\sqrt{\pi L_0}} \tag{4}$$

With $\tau_{ex} = \tau - \mu(\sigma_n - p)$, τ: shear stress on the fracture, σ_n: normal stress on the wings, p: fluid pressure in the wings, K_{IC}: fracture toughness of the rock, L_0: half length of the initial fracture (figure 13). Inserting typical values for the fracture toughness of granite $K_{IC} = 1.5$ MPa $m^{1/2}$ and for the joint half length $L_0 = 5$ m one gets $\tau_{ex} = 0.33$ MPa. This low value indicates that joints being sheared will inevitably develop wings.

In the simplest approximation of long straight wings parallel to the axis of the maximum principal stress propagation of the wings of a stress driven fracture is governed by the following equation [24]:

$$\sqrt{\frac{L}{L_0}} = \frac{K_{IC}}{2(\sigma_3 - p)\sqrt{\pi L_0}} + \sqrt{\left(\frac{K_{IC}}{2(\sigma_3 - p)\sqrt{\pi L_0}}\right)^2 + \frac{2\tau_{ex}\cos\phi}{\pi(\sigma_3 - p)}} \tag{5}$$

http://dx.doi.org/10.5772/56458

With L: length of the wings, σ_1, σ_3: maximum and minimum principal stress respectively, p: fluid pressure in the wing-crack, Φ: angle between the normal of the joint and the maximum principal stress. For wing-cracks of the scale of joints or bigger the terms containing fracture toughness K_{IC} can be neglected and the equation reduces to:

$$\frac{L}{L_0} = \frac{2\tau_{ex}\cos\phi}{\pi(\sigma_3 - p)} \tag{6}$$

This formula shows that wing propagation is stable as long as the fluid pressure is smaller than the minimum principal stress and that the wing length can become long in comparison to L_0 only when the fluid pressure approaches σ_3. This means, in competent granite (with a low density of joints) large scale wings (in relation to the size of the joints) can only develop at a pressure close to the frac-extension pressure of conventional tensile fractures. In fracture zones where the joint density is high the situation is different (figure 14). Here the wings of the joint being sheared first may connect to the next pair of joints soon after their initiation. The fluid-pressure required for this is presumably not much higher than the pressure for wing initiation. When this pressure is maintained a through-going series of joints and wing-cracks can develop. This series is acting as one large scale shear fracture. Correspondingly much larger wings can emerge from the end of this series than from the ends of a single joint when exposed to the same pressure.

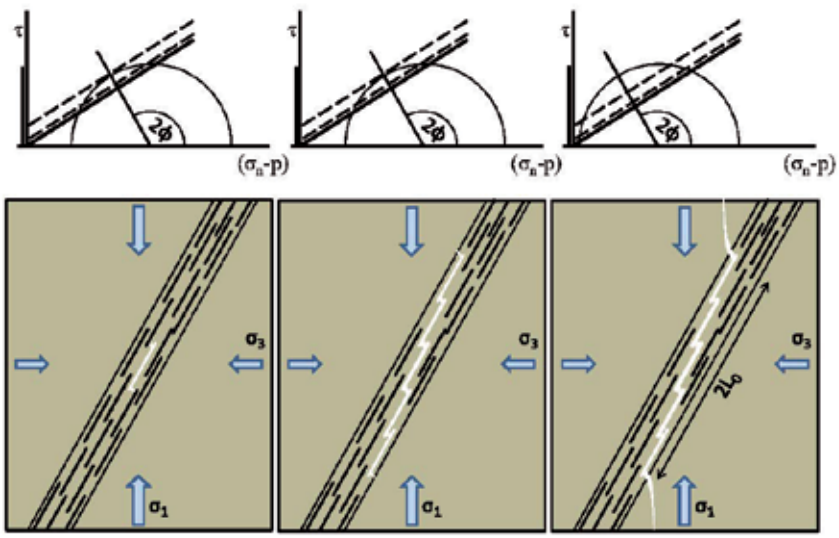

Figure 14. Wing-crack mechanism in a fracture zone, left: wings of the first sheared joint connect to the next pair of joints, middle: chain of wing-cracks reach the boundaries of the fracture zone, right: large scale wings emerge from the boundary of the fracture zone.

Before the wings become very long they will probably grow in height, i.e. in the direction perpendicular to the 2-D wing-crack model of figure 14. This can happen at any fluid-pressure higher than the pressure given by equation 4. This is a plausible explanation for the evolution of the channel-like features in the seismic clouds preceding their lateral propagation. It seems that stimulating at low flow rates as in Ogachi and in the starting periods of Basel and Soultz accentuate the formation of these channels but channeling was indicated also on other sites. For normal and reverse stress conditions these channels were predominantly horizontal or sub-horizontal (Fenton Hill, Hijiori, Ogachi, and Cooper Basin). For strike slip conditions they were pre-dominantly vertical or sub-vertical (Soultz, Basel, Camborne). In the Camborne system extremely long vertical channels developed during a long term circulation test. This demonstrates that the wing-crack mechanism may lead to uncontrolled large scale fracture growth during the operation of the EGS-Systems at a fluid pressure significantly lower than the minimum principal stress.

Neglecting fracture toughness the normalized shear displacement at the root of the wings is approximately given by:

$$\frac{U}{L_0} = \frac{4 \cdot \tau_{ex}}{E'} \tag{7}$$

With E': Young´s modulus for plane strain conditions. This equation is a good approximation of a formula given in [43] for the straight wing model. The normalized aperture of the wings at their root is given by:

$$\frac{b}{L_0} = \frac{4\tau_{ex} cos\phi}{E'} \tag{8}$$

These formulas were applied to the stimulated fracture in Basel, whose seismic cloud showed a remarkably clear wing-crack shape (figure 15) after processing source location data with the so called “collapsing method” [44].

The results of the wing-crack model agree quite well with the observations when an angle of $\Phi = 80°$ is assumed. This direction is within the uncertainty-limits of the stress data [30]. The calculated ratio of $L/L_0 \approx 2$ agrees quite well with the observed data (figures 15, 16). Similarly yields the wing-crack model the same large aperture values as derived from the tracer tests and from the ratio of injected volume and seismic area. For comparison: Static tensile fracture models like the 2-D Griffith fracture would yield average apertures of about 1 mm. One of the most striking results is the very high displacement of 100 mm at the root of the wings (for $\Phi = 80°$). This easily explains the high number of seismic events and the occurrence of high magnitudes in the central part of the seismic cloud of Basel. Interestingly the wings showed up only during the shut-in and flow-back period though they had presumably been formed much earlier. This and the fault plane solutions of the post-fracturing events [30] indicate that the seismic signals of the wings were induced not by forward-sliding but by back-sliding. This behavior can hardly be explained by shearing of a natural fault but is easily explained with the wing-crack model. The low density of seismic sources of the wings as observed in Basel is

http://dx.doi.org/10.5772/56458

not surprising. Since they are tensile fractures they may only show up where they intersect prominent natural discontinuities and cause them to shear.

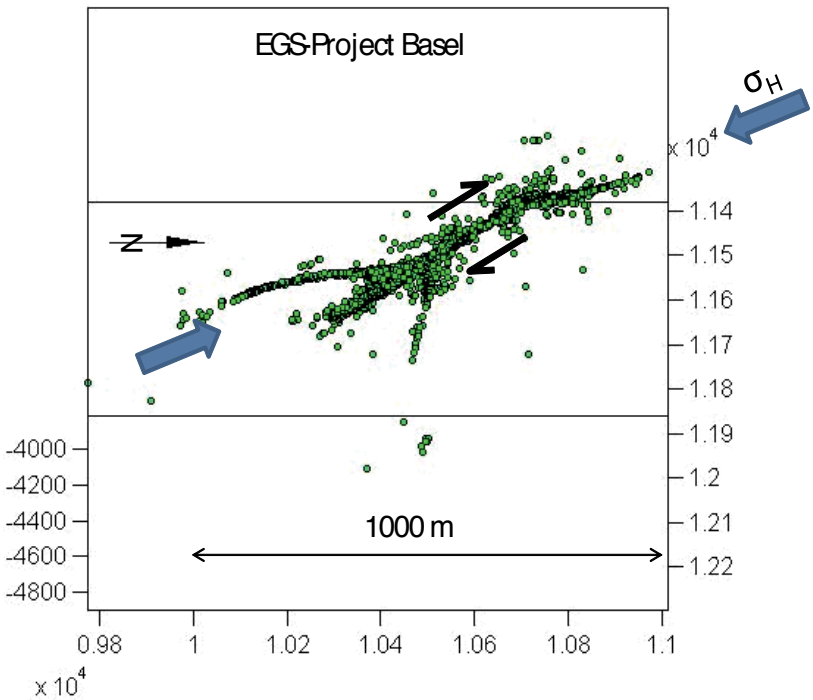

Figure 15. Processed (collapsed) seismic cloud of the stimulation test in Basel, view about 10° from vertical toward W, blue arrows: direction of the maximum horizontal stress, collapsing performed by Q-Con GmbH [44], stress direction [30].

Generally the large scale wing-crack model delivers a plausible explanations for almost all observations described in the previous chapters in particular for: the onset of fracture propagation at a fluid pressure much lower than the minimum principal stress, the high intensity and mechanism of induced seismicity, the occurrence of channel-like features in the seismic clouds, the long lasting fracture linear or bilinear flow periods during post-stimulation well tests, the occurrence of high magnitude after-shocks, the large fracture apertures derived from tracer break-through volumes and from the ratio of fracture area and injected volume. It also explains the striking discrepancy between the only moderate fracture transmissibility and the large apertures. It is clear that a more rigorous study requires 3-D-wing-crack models since the 2-D-model neglects the vertical stress gradients and it may be due to these stress gradients that some of the seismic clouds showed twisted wings.

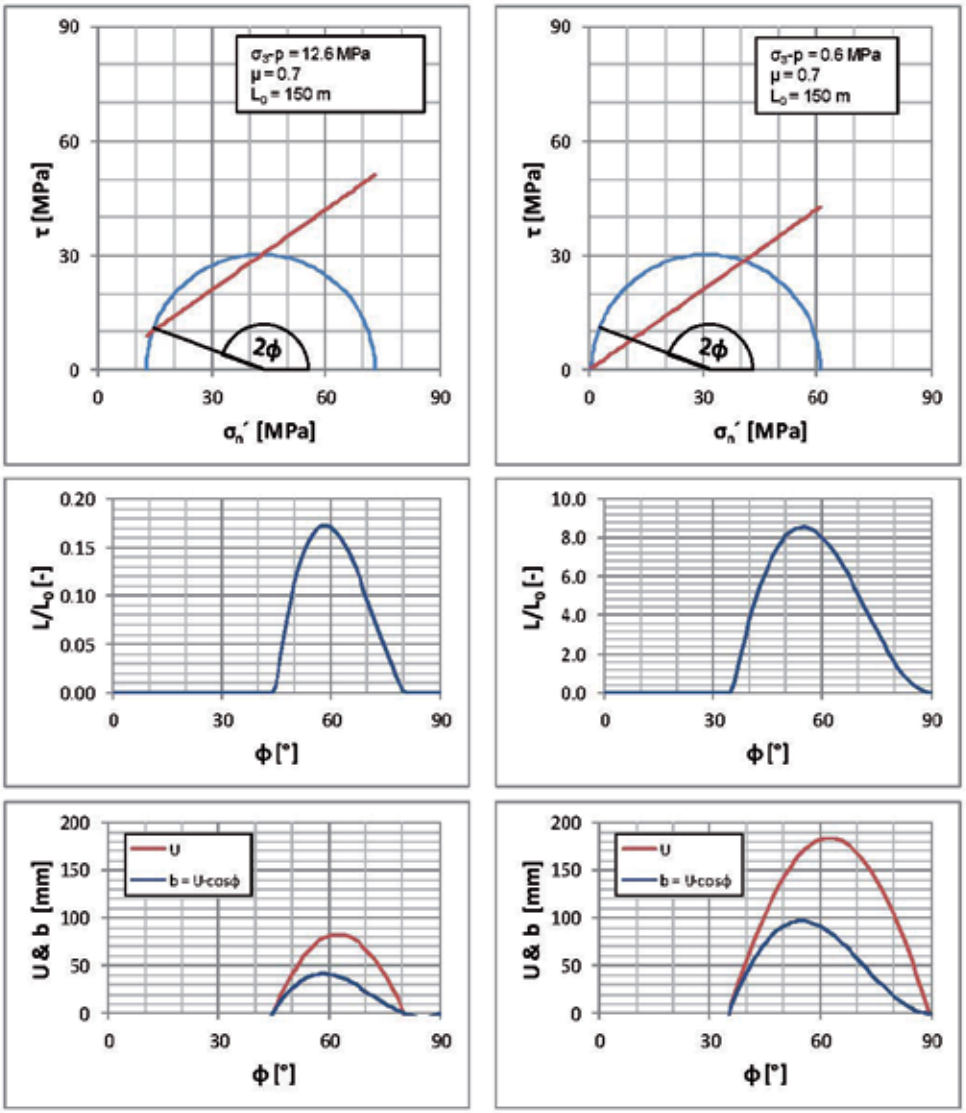

Figure 16. Calculated diagrams for the start of wing-crack propagation (left) and for the end of stimulation (right) in Basel, top: Mohr-diagram (σ_1 = 130 MPa, σ_3 = 69.6 MPa at 4600 m depth), middle: normalized wing length L/L_0, bottom: shear displacement U and aperture b at the root of the wings, calculations with equations (6-8), stress data with minor modifications from [30], Φ = 80°.

5. Summary and way forward

Observations and results of all major EGS-projects leave no doubt, that hydraulic stimulation can not be regarded as merely a pressure diffusion process accompanied by shearing and

http://dx.doi.org/10.5772/56458

widening of the joint network. The data rather suggest that generally only one large fracture is formed during massive stimulation tests regardless of the length of the test interval. The formation of these single fractures can well be explained by the wing-crack model. Wing-cracks have a significantly smaller area to volume ratio than tensile fractures of equal size and need therefore larger fluid volumes for an envisaged fracture area. The large shear displacement at the wing roots enables high magnitude seismic events during the propagation period and strong seismic after-shocks by back-sliding. The magnitudes seem to increase with the seismic area and may finally set a limit for the dimensioning of the individual wing-cracks. The post-stimulation transmissibility of wing cracks is presumably very heterogeneous and highly anisotropic. Wide open channels may persist at the roots of the main wings and at the roots of smaller wings within the central shear fracture. These channels are presumably oriented perpendicular to the slip direction and are of uttermost importance for the positioning of the second well to avoid thermal short-circuiting. The transmissibility of the fracture areas in between theses channels and of the large wings is much lower but is most likely in the range of 0.1 - 1 d·m thus enabling flow rates in the order of 1 to more than 10 L/s per wing-crack.

Theses findings suggest that the present EGS-concept will never lead to EGS-systems of industrial size and performance. It has to be abandoned and be replaced by a multi-fracture scheme as foreseen in the original Hot-Dry-Rock concept with the main difference that the tensile fractures of this concept have to be replaced by wing-cracks. This requires a more sophisticated design and planning in particular for the positioning, completion and treatment of the second well. Industrial systems of this type require wells being drilled parallel to the axis of the minimum principal stress, i.e. horizontal wells for normal and strike slip stress conditions and vertical wells for reverse faulting stress conditions. An industrial system may consist of about 30 to 40 equidistant fractures connecting two 1km long parallel well sections with a well separation of about 500 m. Systems of these dimensions should operate for at least 25 years at flow rates of 100 L/s, an electric power output between 5 and 10 MW and a pumping power of less than 1 MW. Directional drilling and packer technology have improved significantly during the last three decades and multi-fracture concepts are applied with great success in unconventional gas reservoirs. Though the conditions and requirements in geothermal applications are more demanding in various aspects it seems almost certain that geothermal multi-fracture-systems of this type can be realized in the near future.

Author details

Reinhard Jung*

Address all correspondence to: jung.geotherm@googlemail.com

Jung-Geotherm, Isernhagen, Germany

References

[1] Smith, M. C, Aamodt, R. L, Potter, R. M, & Brown, D. W. Manmade geothermal reservoirs: Proc. 2nd US Symposium on Geothermal Energy, (1975). San Francisco California, , 1781-1787.

[2] Tester, J. W, Brown, D. W, & Potter, R. M. Hot Dry Rock Geothermal Energy- A new Energy Agenda for the 21st Century. Los Alamos National Lab. Report MS (1989). (LA-11514), 11514.

[3] Duchane, D, & Brown, D. Hot Dry Rock (HDR) geothermal energy research and development at Fenton Hill, New Mexico. GHC Bulletin (2002). , 12-19.

[4] Duchane, D. Hot Dry Rock: A realistic energy option. Geothermal Resources Council Bulletin, March (1990).

[5] Batchelor, A. S. The creation of Hot Dry Rock systems by combined explosive and hydraulic fracturing. In: proceedings of the International Conference on Geothermal Energy, May 1982. Florence, Italy. BHRA Fluid Eng. Bedford; (1982). , 321-342.

[6] Cornet, F. H. Experimental investigations of forced fluid flow through a granite rock mass. In: Proceedings of 4th Int. Seminar on the results of EC Geothermal Energy Demonstration, Florence, Italy, April 27-30, (1989). , 189-204.

[7] Evans, K. F, Zappone, A, Kraft, T, Deichmann, N, & Moia, F. A survey of the induced seismic responses to fluid injection in geothermal and CO2 reservoirs in Europe, doi:j.geothermics.(2011). in Press.

[8] Murphy, H. Hot Dry Rock phase II reservoir engineering. Los Alamos Nat. Lab. Rep. LA-UR-85-3334, (1985).

[9] MIT The Future of Geothermal Energy- Impact of Enhanced Geothermal systems (EGS) on the United States in the 21st CenturyIdaho Nat. Lab., Idaho US, http://geothermal.inel.gov.(2006).

[10] Laney, R, Laughlin, A. W, & Aldrich, M. J. Geology and geochemistry of samples from the Los Alamos National Laboratory HDR Well EE-2, Fenton Hill, New Mexico. Los Alamos Scientific Lab., Los Alamos NM, USA; (1981).

[11] Rowley, J. C, Pettitt, R. A, Matsunaga, I, Dreesen, D. S, Nicholson, R. W, & Sinclair, A. R. Hot-Dry-Rock Geothermal reservoir fracturing initial field operations- (1982). Proceedings Geothermal Resources Council 1983 Annual Meeting, Oct. Portland, Oregon US; 1983., 24-27.

[12] Dreesen, D. S, & Nicholson, R. W. Well completion and operations for the MHF of Fenton Hill HDR Well EE-2. Proceedings Geothermal Resources Council, Kailua-Kona, Hawaii, Aug. (1985). , 26-30.

http://dx.doi.org/10.5772/56458

[13] Parker, R. H. Overview. In: Parker R.H. ed., Hot Dry Rock geothermal energy, Phase 2B final report of the Camborne School of Mines Project, (1989). , 1, 3-38.

[14] Baria, R, Green, A. S. P, & Hearn, K. C. Microseismic results. In: Parker R.H. ed., Hot Dry Rock geothermal energy, Phase 2B final report of the Camborne School of Mines Project., (1989). , 2, 682-740.

[15] Kappelmeyer, O, Gerard, A, Schloemer, W, Ferrandes, R, Rummel, F, & Benderitter, Y. European HDR Project at Soultz-sous-Forêts: General presentation. In: Geothermal Energy in Europe, J.C. Bresee ed., Gordon and Breach Science Publ., (1992).

[16] Sausse, J, & Genter, A. Types of permeable fractures in granite.- Geological Soc., London, Special Publications (2005). doi:10.1144/GLS.SP.2005.240.01.01., 240, 1-14.

[17] Cornet, F. H, Bérard, F. H, & Bourouis, S. How close to failure is a granite rock mass at 5 km depth?. International Journal Rock Mechanics Mining Sciences (2007). , 47-66.

[18] Klee, G, & Rummel, F. Hydrofrac stress data for the European HDR research project test site Soultz-sous-Forêts. International Journal of Rock Mechanics, Mining Science and Geomechanics Abstracts (1993). , 973-976.

[19] Jung, R. Hydraulic fracturing and hydraulic testing in the granitic section of borehole GPK1, Soultz Sous Forêts. Geotherm. Sci. & Tech. (1991). , 3, 149-198.

[20] Jung, R. HDR-Projekt Soultz- Erschließung permeabler Risszonen für die Gewinnung geothermischer Energie aus heißen Tiefengesteinen. Schlussbericht zum Forschungsvorhaben 0326690A, Archiv Nr. 118977, Bundesanstalt für Geowissenschaften und Rohstoffe, Hannover, (1999).

[21] Baria, R, Jung, R, Tischner, T, Teza, D, Baumgärtner, J, Dyer, B, Hettkamp, T, Nicholls, J, Michelet, S, Sanjuan, B, Soma, N, Asanuma, H, & Garnish, J. Creation of a HDR/EGS reservoir at 5000 m depth at the European HDR project.- Proc. 31st Stanford Geothermal Workshop (2006). Stanford, Cal., US.

[22] Weidler, R. Personal Communication, Geothermeon, Landau, Germany, (2001).

[23] Jung, R. Hydraulic in situ investigations of an artificial fracture in the Falkenberg Granite. Int. J. Rock Mech. Sci. & Geomech. Abstr.; (1989). , 26(3), 301-308.

[24] Murphy, H, Keppler, H, & Dash, Z. Does hydraulic fracturing theory work in jointed rock masses?- Geothermal Resources Council, Transactions Oct. (1983). , 7, 461-466.

[25] Camborne School of MinesGeothermal Energy Project. Internal report (1985). , 2-42.

[26] Nedo, F. Y. Summary of Hot Dry Rock Geothermal Power Project. Geothermal Energy Technology Dep., New Energy and Ind. Tech. Dev. Org., Tsukuba, Japan; (1997).

[27] Tezuka, K, & Niitsuma, H. Stress estimated using microseismic clusters and its relationship to the fracture system of the Hijiori hot dry rock reservoir, Eng. Geol. 56; (2000). , 47-62.

[28] Kaieda, H, Hisatoshi, I, Kenzo, K, Koichi, S, Hiroshi, S, & Koichi, S. Review of Ogachi HDR Project in Japan. Proc. IGA World Geotherm. Congress 2005, Antalya Turkey, April 2005; (2005). , 24-29.

[29] Jones, R, Beauce, A, Fabriol, H, & Dyers, B. Imaging induced microseismicity during the 1993 injection test at Soultz-sous-Forêts France, Proc. IGA World Geothermal Congress, Florence, Italy; (1995).

[30] Häring, M. O, Schanz, U, Ladner, F, & Dyer, B. C. Characterization of the Basel1 Enhanced Geothermal System. Geothermics; (2008). doi:10.1016/j.geothermics. 2008.06.002.

[31] Evans, K. F, Moriya, H, Niitsuma, H, Jones, R. H, Phillips, W. S, Genter, A, Sausse, J, Jung, R, & Baria, R. Microseismicity and permeability enhancement of hydro-geologic structures during massive fluid injections into granite at 3 km depth at the Soultz HDR site. Geophys. J. Int., (2005). , 2005(160), 388-412.

[32] Niitsuma, H, Asanuma, H & Jones, R. Induced seismicity, AP 3000 report. In: Baisch, S. (ed.) Deep Heat Mining Basel – Seismic Risk Analysis. Basel, Amt für Umwelt und Energie; (2009). AP 3000 p1-62.

[33] Tischner, T, Pfender, M, & Teza, D. Hot Dry Rock Projekt Soultz: Erste Phase der Erstellung einer wissenschaftlichen Pilotanlage. Abschlussbericht zum Vorhaben 0327097, Bundesministerium für Umwelt, Naturschutz und Reaktorsicherheit, 1.4.Berlin, Germany; (2006). , 2001-31.

[34] Ledingham, P. Circulation results 1983-1986, 7:2 Thermal Model. In: Parker R.H. ed., Hot Dry Rock geothermal energy, Phase 2B final report of the Camborne School of Mines Project., (1989). , 1, 390-408.

[35] Matsunaga, I, Yanagisawa, N, Sugita, H, & Tao, H. Reservoir monitoring by tracer testing during a long term circulation test at the Hijiori HDR Site. Proc. 27th Workshop on Geothermal Reservoir Eng., Stanford Univ. Stanford, Jan. (2002). , 28-30.

[36] Tenma, N, Yamaguchi, T, Tezuka, K, Oikawa, Y, & Zyvolovski, G. Comparision of heat extraction from production wells in the shallow and deep reservoirs at the Hijiori test site using FEHM code. Proc. 26. Workshop on Geothermal Reservoir Engineering, Stanford Uni., January February 1, 2001, SGP-TR-162; (2001). , 29.

[37] Matsunaga, I, Sugita, H, & Tao, H. Tracer monitoring by a fibre optic fluorometer during a long-term circulation test at the Hijiori HDR Site. Proc. 26. Workshop on Geothermal Reservoir Eng., Stanford Univ. Stanford, Jan. (2001). , 29-31.

[38] Oikawa, Y, Tenma, N, Yamaguchi, T, Karasawa, H, Egawa, Y, & Yamauchi, T. Heat extraction experiment at Hijiori Test Site. Proc. 26. Workshop on Geothermal Reservoir Eng., Stanford Univ. Stanford, Jan. (2001). , 29-31.

http://dx.doi.org/10.5772/56458

[39] Kenzo, K. Technology of reservoir estimation for Hot Dry Rock geothermal power. Volumetric Estimation of the Ogachi Reservoir by Tracer Test. Denryoku Chuo Kenkyujo Abiko Kenkyujo Hokoku, (2000). p.(U99018)

[40] Genter, A, Dezayes, C, & Gentier, S. Lede´sert B., Sausse´ J. Conceptual fracture model at Soultz based on geological data. In: Bundesanstalt für Geowissenschaften und Rohstoffe und den staatlichen Geologischen Diensten in der Bundesrepublik Deutschland (eds.) International Conference 4th HDR Forum, 29-30 Sep. 1998, Strasbourg, France. Geologisches Jahrbuch, Sonderhefte, Heft SE1, Reihe E, Geophysik, (2002). , 93-102.

[41] Valley, B. C. The relation between natural fracturing and stress heterogeneities in deep-seated crystalline rocks at Soultz-sous-Forêts (France), PhD thesis. ETH Zürich, (2007). (17385)

[42] Cotterell, B, & Rice, J. R. International Journal of Fracture 16; (1980). , 155-169.

[43] Lehner, F, & Kachanov, M. On modelling of "winged" cracks forming under compression. International Journal of Fracture 77; (1996). RR75., 69.

[44] Baisch, S, & Vörös, R. Personal Communication. Q-Con, Bad Bergzabern, Germany; (2007).

Chapter 6

Understanding Hydraulic Fracture Growth, Effectiveness, and Safety Through Microseismic Monitoring

Norm R. Warpinski

Additional information is available at the end of the chapter

http://dx.doi.org/10.5772/55974

1. Introduction

Microseismic monitoring has become a valuable tool for optimizing stimulations, completions, and overall field development, particularly in unconventional reservoirs. This technology was initially rooted in geothermal energy [1,2], but subsequently was used for many years in research projects to understand fracturing in unconventional reservoirs, such as in the Multiwell Experiment [3,4], the M-Site fracture diagnostics laboratory [5-8], the Carthage Cotton Valley fracturing test [9,10], and for other processes, such as drill cuttings injection [11]. It finally reached a level of sophistication and reliability to function as a service technology in the early 21st century [12,13], and many thousands of hydraulic fractures have been monitored since that time. In addition to providing a "window" into the subsurface for fracture optimization and control, the large amount of microseismic data that has been gathered provides a significant database that can be used for environmental surety.

Microseismicity occurs because of geomechanical changes to the reservoir as a result of the fracturing process [14,15], and detection and location of these "events" provides a methodology to monitor fracture growth patterns and overall dimensions. One of the curious features of microseismic technology is that no one has ever seen the slippage plane of a microseism that was induced by a hydraulic fracture. As a result, the understanding of microseismicity has been through a down-scaling of earthquake seismology [16], examination of fracture behaviour in minebacks [17,18], comparisons with rock bursts and laboratory acoustic emissions [19,20], and geomechanics considerations of the way in which hydraulic fractures perturb a reservoir [21].

Nevertheless, there have been several validation experiments where other measurement technologies have been used to verify the accuracy and interpretation of microseismicity, and these have been very helpful in promoting an understanding of the process of microseismic activation during a fracturing treatment. The most comprehensive of these tests was the M-Site test funded by GRI and DOE; it was developed as a fracture diagnostics laboratory in the Piceance basin of Colorado [5-8]. Intersection wells, downhole tiltmeters, tracers, pressure interference, and other technologies were used to show the accuracy of determining the fracture azimuth, length, and height by these methods in typical sandstone reservoir rocks. In these tests, it became clear that microseismicity does not necessarily occur on the hydraulic fracture, but can develop along planes of weakness at an offset distance that depends on both the formation and the treatment.

While there have been no published tests about fracturing in shale reservoirs that provide the full detail available from M-Site, the project described by Fisher et al. [12] in the Barnett shale has many of the same elements as M-Site. Both downhole and surface tiltmeters were used to supplement the microseismic data, and numerous offset producing wells were used to monitor the movement of fracturing fluid during the treatment. Wells that were "bashed" (i.e., loaded up with fracturing fluids) provided direct evidence of actual fluid presence at that location that could be compared to the microseismicity. This comprehensive test verified the actual formation of a "network" in this reservoir.

With a reasonable level of accuracy and interpretability established by validation tests, such as those described, microseismicity can be used for field development, completion design, stimulation optimization, and addressing environmental concerns. The last aspect, with respect to aquifers and seismicity, is very important for current unconventional reservoir development throughout the world.

2. Microseismic applications

There are many case studies in the literature that illustrate how microseismicity can be used to aid in the exploitation of unconventional reservoirs. One very evident one was provided by Mayerhofer et al. [22] for a two-well, multi-stage, multi-perforation-clusters completion in the Marcellus. Figure 1 shows a plan view and side view of the microseismic data color coded by the well being stimulated. In these views, there is enough information to decide if the well trajectory is correct (assuming transverse fractures are desired), if the number of stages is sufficient to access all of the reservoir, if the number and spacing of perf clusters is giving the desired behaviour, if the treatment fluids, rates, and volumes are generating appropriate lengths without causing excessive height growth, and many other more subtle aspects of completion. This example shows the type of information that one should expect to obtain in such a monitoring project.

http://dx.doi.org/10.5772/55974

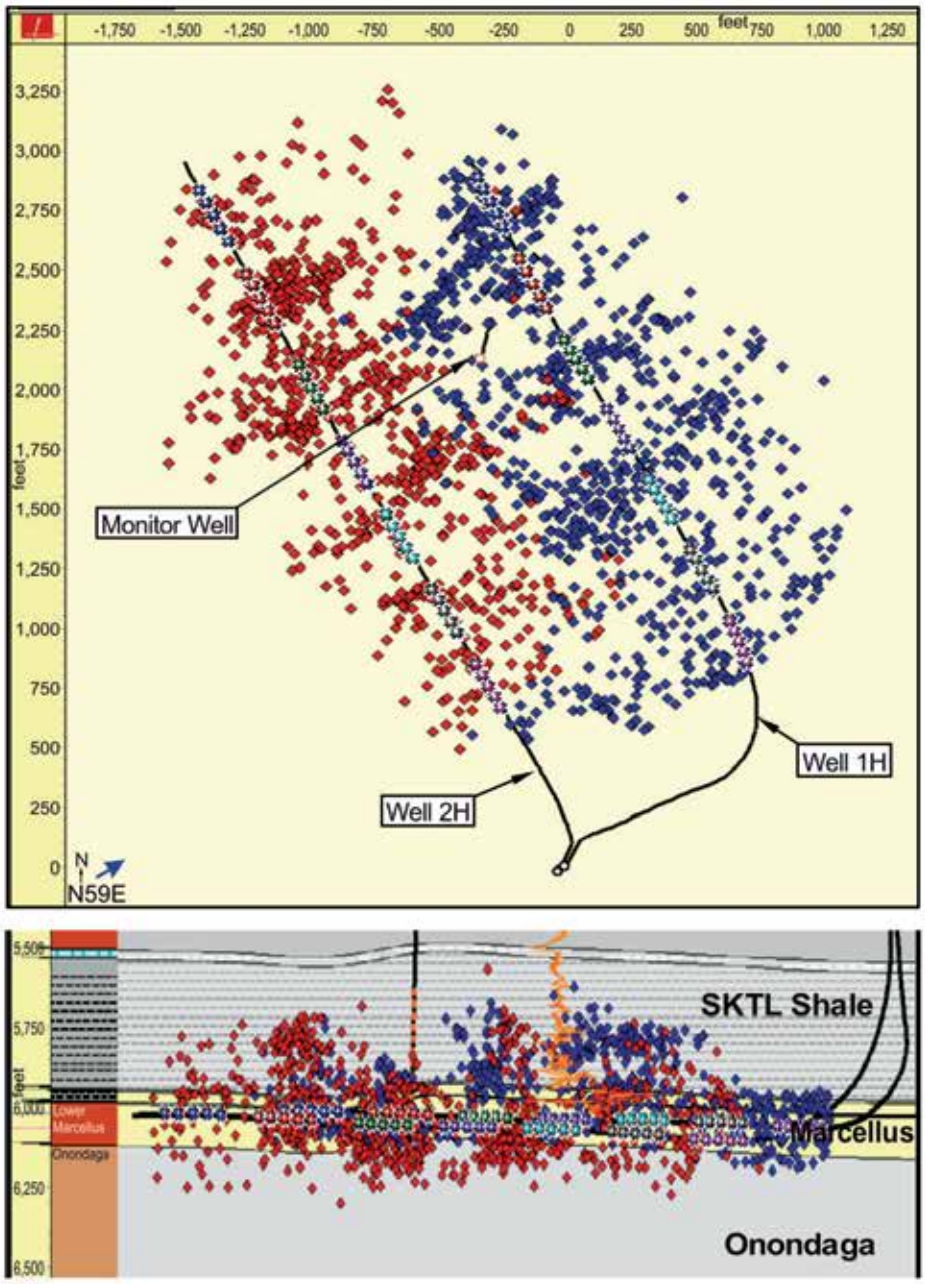

Figure 1. Example Marcellus microseismic maps for two adjacent wells.

While most interest about microseismicity tends to be focused within final dimensions of the fracture, the growth patterns often provide valuable information for designing fracture treatments. Many treatments show extremely rapid initial growth in either height or length,

followed by a highly reduced late-time development. Figure 2 shows an example of length development as a function of time, with each side of the y axis representing one wing of a planar fracture. The bounding dashed line is square-root-of-time behaviour, which is very common and would suggest high leakoff conditions, such as into natural fractures (e.g., [23]). The color coding represents tip-related events (green) and interior events (red). Generally, half or more of the microseismic events occur after the tip has passed the event location, again suggesting natural fracture interactions [15,21] as the source of much of the microseismicity.

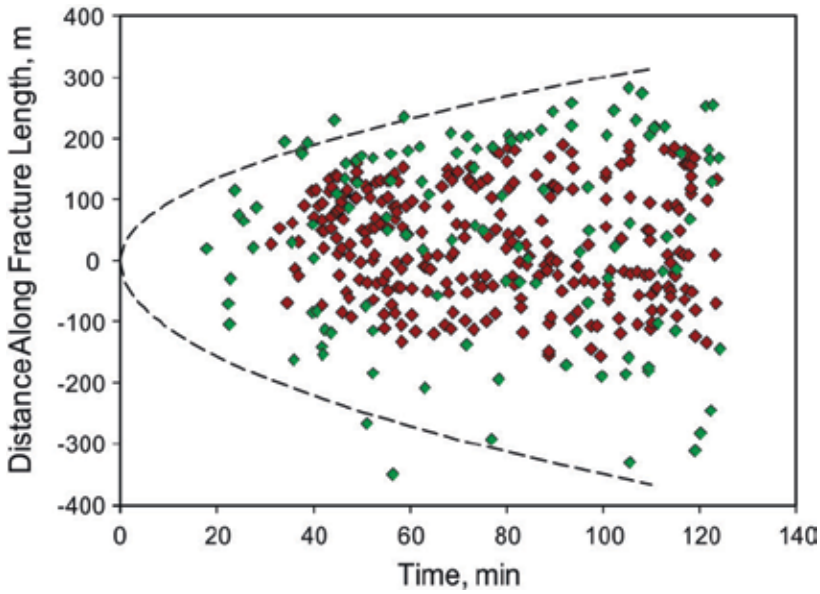

Figure 2. Fracture length development versus time and conditions.

3. Beyond dots, or beyond verification

It is well-understood that microseismicity is a scaled-down version of conventional seismicity and tools from earthquake seismology should be applicable in some sense for evaluating microseismic behaviour [16]. Certainly, the fault plane solutions that can be derived from a moment tensor inversion provide some information about the planes that are activated during fracturing. Unfortunately, there is no validation that such information can be taken much beyond a resolution of the fault planes, nor is it necessarily clear how the fault planes are being activated (stress effects, leakoff, actual tip extension processes, etc.).

To suggest that any change in behaviour of the source mechanism, such as a difference between pure shear and a large volumetric component, is somehow diagnostic of fracture behaviour is pure hypothesization without any supporting field, lab, or theoretical results. This type of theorizing is useless, and possibly deleterious, without validation because it could lead to

http://dx.doi.org/10.5772/55974

actions that jeopardize the treatment. The remote likelihood that source mechanisms can be used to evaluate the hydraulic fracture behaviour (other than dimensions from the event locations) can be easily understood in terms of both energy and volumetric considerations. The total microseismic energy released (or at least what can be detected with current instrumentation) is typically on the order of one millionth or less of both the energy input into the treatment and the strain energy that would be calculated for the fracture based on microseismic dimensions and measured pressures [21]. Similarly, the volumes associated with the sum total of the microseismic displacements are generally on the order of a few liters or less compared to hundreds or thousands of cubic meters of fluid injected. This small volume cannot be representative of SRV or other fracture parameters.

Figure 3 shows a plot of the total seismic energy associated with microseismicity in a fracture as a function of the largest event and the "b" value. The b value is the negative slope of the Gutenberg-Richter frequency distribution for earthquakes in a region over some time period. For earthquakes, it is usually near 1.0. For microseisms associated with hydraulic fracturing, it is quite variable and often between 1.0 and 2.0. Given a b value, maximum magnitude event, and low end cutoff (in this case magnitude -4), the energy released can be found by integrating the energy as a function of magnitude over the distribution. For the overwhelming majority of treatments, the maximum magnitude is less than 0 (and often much less than 0), so the typical energy released is on the order of hundreds of kilojoules or less. Fracture injections in shale stimulations usually imparts hundreds of millions kilojoules of energy.

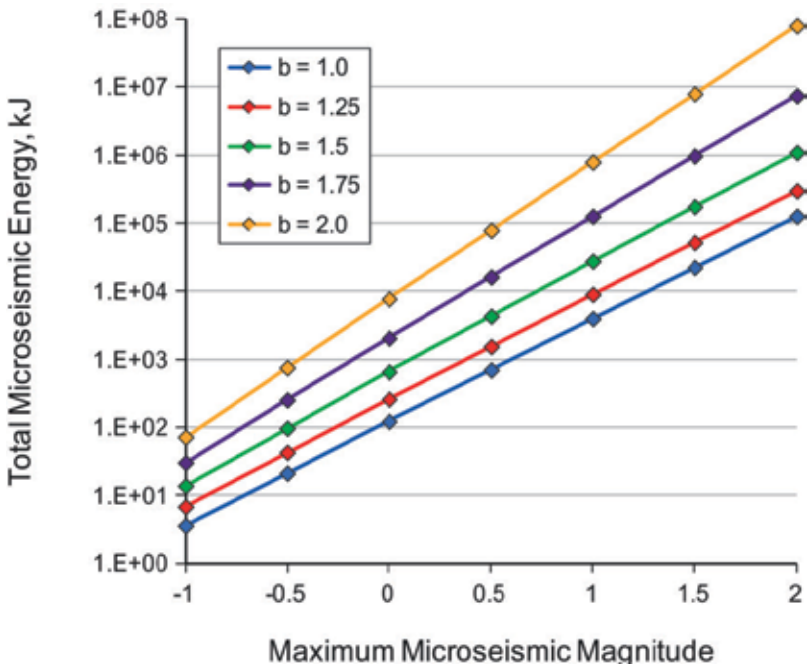

Figure 3. Seismic energy released as a function of magnitude and b value.

The actual source mechanism is a result of the geomechanical processes that occur during fracturing. There is a large perturbation in the stresses around a fracture and a bigger perturbation in pore pressure as the high pressure fracturing fluid leaks off into the reservoir through the pore space or into natural fractures. These changes alter the existing in situ conditions and impact the behaviour of any slippage or opening that might occur around the fracture. Geomechanical calculations can be useful to understanding these perturbations, and they can also provide improved understanding of the microseismic distribution by assessing the stress and failure conditions around the fracture [21, 25].

The linkage of geomechanics and source mechanisms should be helpful to understanding the reservoir and how it is impacted by the stimulation. The slippage planes that are activated should have higher permeability and could provide clues about the reservoir itself (e.g., natural fractures) and optimum methods to enhance permeability in the reservoir.

4. Environmental aspects

Proving the safety of hydraulic fracturing is a welcome side benefit of microseismic surveys. One of the issues fostered by fracturing opponents is that large shale treatments could contaminate aquifers by fracturing into near-surface water supplies. There is, first of all, a very large base of literature that demonstrates that fracture height growth is severely limited by geologic conditions; [26] provides a brief review of some of the pertinent literature. Factors such as stress changes and material property variations across layers, interface characteristics associated with the horizontal bedding, and higher-permeability layers that allow high levels of fluid leakoff are all commonly present in sedimentary basins where oil and gas are being exploited. These features cause fractures to propagate much farther laterally than vertically. There are also theoretical considerations that clearly demonstrate that fracturing volumes are smaller by an order of magnitude or more than the volumes that would be required to propagate fractures the multi-kilometer distances to approach the surface.

With the microseismic monitoring database that has been obtained throughout the last decade, there is now a large amount of information available that shows clearly that fracturing does not propagate the enormous distances required to cause contamination. Figure 4 provides an example of fracture height data from all monitored fractures in six major North American shale basins sorted by depth [26]. This plot shows thousands of fracture stages ordered by depth of the perforations. The fracture tops, as indicated by the shallowest microseism detected on each tests, are shown in red, while the fracture bottoms are green. While fractures occasionally exhibit significant vertical growth (both upward and downward), the distances are small compared to the distance required to approach typical water wells. The formations included in this data set are the Barnett, Marcellus, Woodford, EagleFord, Haynesville, and Muskwa/Evie.

It is also important to note that many of the "spikes" in the data of Figure 4 are attributed to fault interactions. There are many faults, some well below seismic detection, that can influence the behaviour of the fracture. As can be seen, many of these faults result in downward growth,

http://dx.doi.org/10.5772/55974

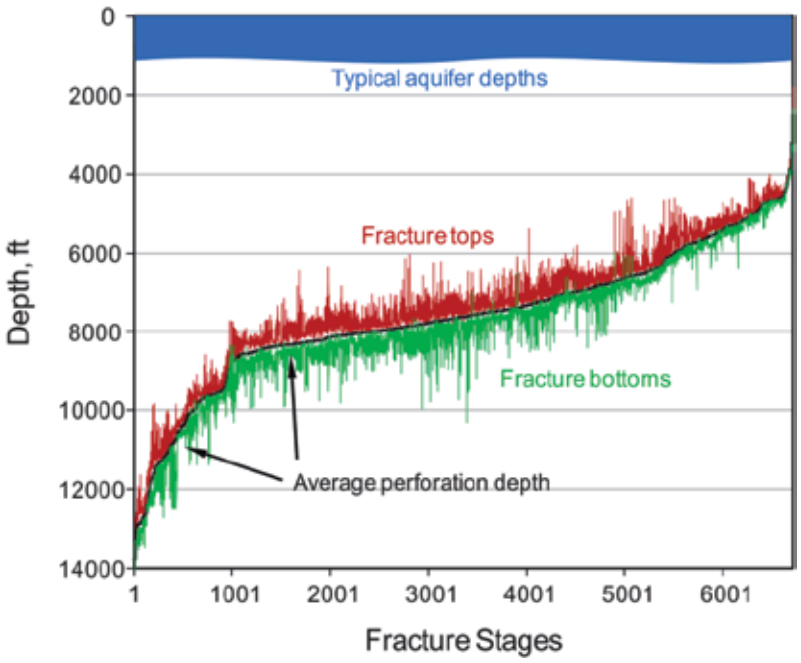

Figure 4. Hydraulic fracture height growth in shale basins of North America.

others result in upward growth, while others can veer in a different horizontal direction. These faults are easily detectable in the microseismic data because the magnitudes of the events are much larger than the magnitudes of normal reservoir events. Figure 4 shows that faults have only a limited effect on height growth. The behaviour of a hydraulic fracture when it intersects a fault is not an unanswered question. There could be some additional height growth, though all measurements show that it is limited.

Microseismic data, which is essentially the monitoring of micro-earthquakes, also provides information to show the extremely small likelihood of damaging seismic activity [27]. Figure 5 shows the maximum microseismic magnitude for all fracture treatments in major North American basins up to mid-year 2011, where each point is the maximum magnitude microseism obtained in a fracture stage. The largest monitored microseism found in several thousand stages has not exceeded +1.0, which is about 1,000 times less energy than the threshold that can just be felt at the surface.

The question of fault interaction comes into play with induced seismicity as well as height growth. Again, the data show what happens when faults are intersected. Most seismicity induced by shale stimulations, although somewhat variable across formations, is in the magnitude range of -4 to -1. Larger events are the direct result of interaction with faults, some of which are seismic and were known to exist, and others were subseismic prior to being marked by microseismicity. The general increase in magnitude that occurs as a result of fault interaction is usually one to two. The Bowland shale and Horn River basin experience suggest

that greater increases are possible, but they must be exceedingly rare given the common experience, as shown in Figure 5.

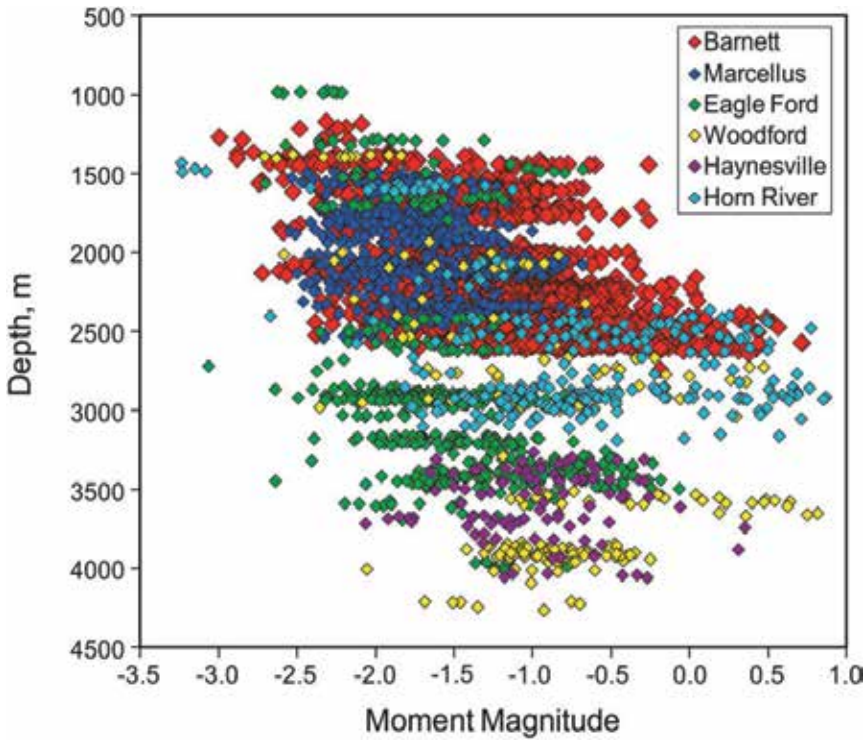

Figure 5. Microseismic magnitudes associated with fracturing in North American shale basins.

Although these results show that induced seismicity is not likely to be a problem in hydraulic fracturing, there likely will be rare cases (e.g., Bowland shale, Horn River basin) where the fracturing interacts with a major fault system that is critically stressed. In such a case, it could be possible to experience seismicity that is significant enough to be felt at the surface.

It is always useful to investigate how the seismicity might be mitigated so that development work can continue. Figure 6 addresses the issue of whether rate and volume adjustments might reduce the strength of the seismicity. These results show that the magnitudes generated by hydraulic fracturing, whether fault induced or not, is not generally a function of either rate or volume, for the range considered by this data. Data from three US basins are plotted and it can be seen that there is no definitive trend, except at very low rates and volumes. When considering the volumes necessary for effective fracturing of shale resources, the ability to influence the seismicity is very limited.

It should be noted that the maximum that occurs in each plot is most likely because most of the treatments are conducted at those particular rates and volumes. The likelihood of experiencing larger-than-normal events is predicated on the likelihood of intersecting a fault. Because

http://dx.doi.org/10.5772/55974

most treatments are conducted within a fairly limited range, it stands to reason that the largest events will generally be found when treating under those conditions.

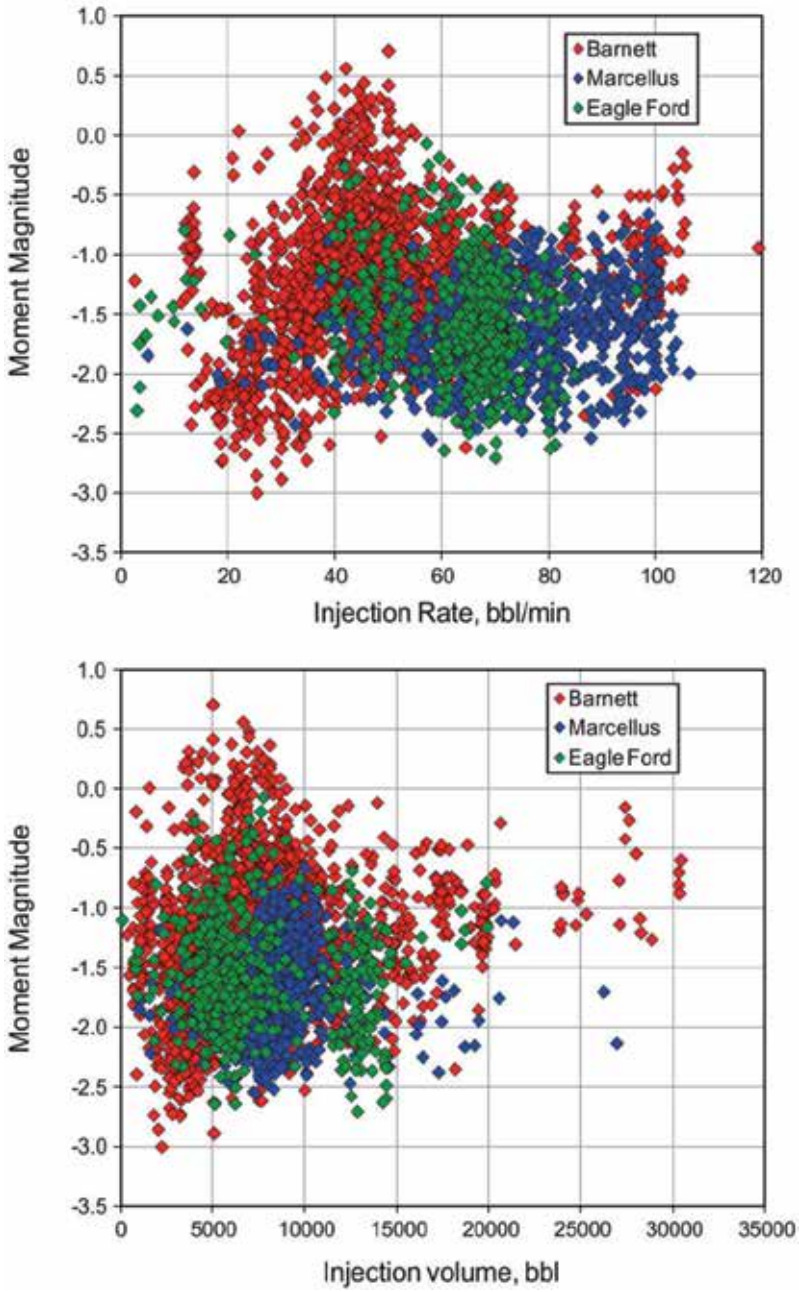

Figure 6. Effect of rate and volume on induced seismicity in three shale basins.

5. Summary

Microseismic monitoring is a very useful tool for optimizing fracture treatments, evaluating completion schemes, and assessing well layouts and spacing in unconventional reservoirs. The microseismicity is induced by the reservoir changes resulting from the hydraulic fracturing process. The dimensions and orientation of the fracture can usually be deduced from the microseismic distribution, and it is often possible to determine other features of the fracturing process, such as complexity, asymmetry, and interaction with geohazards.

It is important to understand the geomechanical process that occurs during fracturing to best interpret the microseismic distribution and to fully understand the value of any source analyses, such as moment tensor inversion. The perturbations imparted to the reservoir during fracturing are usually very large and can result in unexpected behaviour, if ignored.

Microseismicity monitoring has provided a very large data base from which environmental impacts of fracturing can be assessed. With thousands of fractures monitored, there is clear evidence that fractures do not extend the thousands of feet vertically to the shallow depths of typical aquifers. Fractures are generally much longer than they are tall as a result of the rock mechanic barriers that result from sedimentary structures.

Microseismicity monitoring has also provided evidence that hydraulic fractures are not likely to generate felt earthquakes in anything other than the rarest circumstances. Most of the seismic activity induced by a hydraulic fracture has energy levels that are 1,000 to 1,000,000 times smaller than events that would be felt at the surface, and even much farther below those that might cause damage.

Acknowledgements

The author thanks Halliburton for permission to publish this paper.

Author details

Norm R. Warpinski

Pinnacle—A Halliburton Service, Houston, Texas, USA

References

[1] Albright, J. N, & Pearson, C. F. Acoustic Emissions as a Tool for Hydraulic Fracture Location: Experience at the Fenton Hill Hot Dry Rock Site. Society of Petroleum Engineers Journal. (1982). , 22(4), 523-530.

[2] Batchelor, A. S, Baria, R, & Hearn, K. Monitoring the Effects of Hydraulic Stimulation by Microseismic Event Location: A Case Study. SPE 12109 In: SPE Annual Technical Conference and Exhibition, October, (1983). San Francisco, California., 5-8.

[3] Hart, C. M, Engi, D, Fleming, R. P, & Morris, H. E. Fracture Diagnostic Results for the First Multiwell Experiment's Paludal Zone Stimulation. SPE Formation Evaluation. (1987). , 2(3), 320-326.

[4] Warpinski, N. R, Branagan, P. T, Sattler, A. R, Cipolla, C. L, Lorenz, J. C, & Thorne, B. J. Case Study of a Stimulation Experiment in a Fluvial Tight Sandstone Gas Reservoir. SPE Production Engineering. (1990). , 5(4), 403-410.

[5] Branagan, P. T, Peterson, R, Warpinski, N. R, & Wright, T. B. The Characterization of Remotely Intersected Set of Hydraulic Fractures: Results of Intersection Well GRI/DOE Multi-Site Project. SPE 36452 In: SPE Annual Technical Conference and Exhibition, October, (1996). Denver, Colorado.(1), 6-9.

[6] Warpinski, N. R, Branagan, P. T, Peterson, R. E, Fix, J. E, Uhl, J. E, Engler, B. P, & Wilmer, R. Microseismic and Deformation Imaging of Hydraulic Fracture Growth and Geometry in the C Sand Interval, GRI/DOE M-Site Project. SPE 38573 In: SPE Annual Technical Conference and Exhibition, October, (1997). San Antonio, Texas., 5-8.

[7] Branagan, P. T, Warpinski, N. R, Peterson, R. E, Hill, R. E, & Wolhart, S. L. Propagation of a Hydraulic Fracture into a Remote Observation Wellbore: Results of C-Sand Experimentation at the GRI/DOE M-Site Project. SPE 38574 In: SPE Annual Technical Conference and Exhibition, October, (1997). San Antonio, Texas., 5-8.

[8] Warpinski, N. R, Branagan, P. T, Peterson, R. E, & Wolhart, S. L. An Interpretation of M-Site Hydraulic Fracture Diagnostic Results. SPE 39950 In: SPE Rocky Mountain Regional/Low Permeability Reservoirs Symposium, April, (1998). Denver, Colorado., 5-8.

[9] Walker, R. N, Zinno, R. J, Gibson, J. B, Urbancic, T, & Rutldge, J. Carthage Cotton Valley Fracture Imaging Project-Imaging Methodology and Implications. SPE 49194 In: SPE Annual Technical Conference and Exhibition, September, (1998). New Orleans, Louisiana., 27-30.

[10] Rutledge, J. T, Phillips, W. S, & Mayerhofer, M. J. Faulting Induced by Forced Fluid Injection and Fluid Flow Forced by Faulting: An Interpretation of Hydraulic-Fracture Microseismicity, Carthage Cotton Valley Gas Field, Texas. Bulletin of the Seismological Society of America (2004). , 94(5), 1817-1830.

[11] Peterson, R. E, Warpinski, N. R, Lorenz, J. C, Garber, M, Wolhart, S. L, & Steiger, R. P. Assessment of the Mounds Drill Cuttings Injection Disposal Domain. SPE71378 In: SPE Annual Technical Conference and Exhibition, 30 September-3 October, (2001). New Orleans, Louisiana.

[12] Fisher, M. K, Wright, C. A, Davidson, B. M, Goodwin, A. K, Fielder, E. O, Buckler, W. S, & Steinsberger, N. P. Integrating Fracture Mapping Technologies to Optimize Stimulations in the Barnett Shale. SPE Production & Facilities. (2005). , 20(2), 85-93.

[13] Maxwell, S. C, Urbancik, T. I, Steinsberger, N. P, & Zinno, R. Microseismic Imaging of Hydraulic Fracture Complexity in the Barnett Shale. SPE77440 In: SPE Annual Technical Conference and Exhibition, 29 September-2 October, (2002). San Antonio, Texas.

[14] Pearson, C. The Relationship between Microseismicity and High Pore Pressure During Hydraulic Stimulation Experiments in Low Permeability Granitic Rocks. Journal of Geophysical Research. (1981). B9) 7855-7864.

[15] Warpinski, N. R, Wolhart, S. L, & Wright, C. A. Analysis and Prediction of Microseismicity Induced by Hydraulic Fracturing. SPE Journal (2004). , 9(1), 24-33.

[16] Aki, K, & Richards, P. G. Quantitative Seismology, 2nd Edition. University Science Books. Sausalito, California. (2009).

[17] Warpinski, N. R, & Teufel, L. W. Influence of Geologic Discontinuities on Hydraulic Fracture Propagation. Journal of Petroleum Technology (1987).

[18] Jeffrey, R. G, Settari, A, & Smith, N. P. A Comparison of Hydraulic Fracture Field Experiments, Including Mineback Geometry Data, with Numerical Fracture Model Simulations. SPE30508 In: SPE Annual Technical Conference & Exhibition, October, (1995). Dallas Texas., 22-25.

[19] Nasseri MHBThompson B., Schubnel A., and Young RP. Acoustic Emission Monitoring of Mode I Fracture Toughness (CCNBD) Test in Lac du Bonnet Granite. ARMA/USRMS In: 40th US Symposium on Rock Mechanics. 25-29 June, (2005). Anchorage, Alaska., 05-741.

[20] Chitrala, Y, Sondergeld, C. H, & Rai, C. R. Acoustic Emission Studies of Hydraulic Fracture Evolution Using Different Fluid Viscosities. ARMA In: 46th US Rock Mechanics/Geomechanics Symposium., 24-27 June, (2012). Chicago, Illinois., 12-597.

[21] Warpinski, N. R, Mayerhofer, M. J, Agarwal, K, & Du, J. Hydraulic Fracture Geomechanics and Microseismic Source Mechanisms. SPE158935 In: SPE Annual Technical Conference & Exhibition, October, (2012). San Antonio, Texas., 8-10.

[22] Mayerhofer, M. J, Stegent, N. A, Barth, J. O, & Ryan, K. M. Integrating Fracture Diagnostics and Engineering Data in the Marcellus Shale. SPE 145463 In: SPE Annual Technical Conference and Exhibition, 30 October-2 November, (2011). Denver, Colorado.

[23] Nordgren, R. P. Propagation of a Vertical Hydraulic Fracture. Society of Petroleum Engineers Journal (1972).

[24] Cipolla, C, Warpinski, N. R, Mayerhofer, M. J, Lolon, E. P, & Vincent, M. C. The Relationship Between Fracture Complexity, Reservoir Properties, and Fracture Treatment

Design. SPE115769 In: SPE Annual Technical Conference and Exhibition, September, (2008). Denver, Colorado., 21-24.

[25] Agarwal, K, Mayerhofer, M. J, & Warpinski, N. R. Impact of Geomechanics on Microseismicity. SPE152835 In: SPE/EAGE European Unconventional Resources Conference and Exhibition, March, (2012). Vienna, Austria., 20-22.

[26] Fisher, M. K, & Warpinski, N. R. Hydraulic Fracture Height Growth: Real Data. SPE Prodution & Operations (2012). , 27(1), 8-19.

[27] Warpinski, N. R, Du, J, & Zimmer, U. Measurements of Hydraulic-Fracture-Induced Seismicity in Gas Shales. SPE Production & Operations (2012). , 27(3), 240-252.

Section 2

Naturally Fractured Reservoirs 1

Chapter 7

Development of Fracture Networks Through Hydraulic Fracture Growth in Naturally Fractured Reservoirs

Xi Zhang and Rob Jeffrey

Additional information is available at the end of the chapter

http://dx.doi.org/10.5772/56405

Abstract

A 2-D numerical study was carried out, using a fully coupled rock deformation and fluid flow hydraulic fracturing model, on fracture network formation by advancing, widening and interconnecting discrete natural fractures in a low-permeability rock, some of which are small enough to be considered as a flaw that acts as a fracture seed. The model also includes fractures connecting into one another to form a single hydraulic fracture. In contrast to previous fracture network models, fracture extension and fluid flow behavior, frictional slip, and fracture interaction are all explicitly addressed in this model. Incompressible Newtonian fluid is injected at a constant total rate into fractures to study viscous fluid effects on the network formation. The algorithm for flow division and coalescence is validated through some examples.

Numerical results show that the incremental crack propagation that connects isolated natural fracture sets depends on the current stress state and the fracture arrangement. The newly created connecting fracture segments increase local conductivity since they are oriented along a path that is easier to open when pressurized by fluid and provide a new path for fluid flow. However the hydraulic fracture growth process is retarded by some of the resulting geometric changes such as intersections and offsets, and the growth-induced sliding that can impose a barrier to further fracture growth and fluid flow into parts of the network. Such barriers may eventually result in a fracture branch initiating and growing that results in a relatively shorter and more conductive path through a fracture network zone.

We consider a specific fracture arrangement consisting of around 20 conductive pre-existing fractures to study the effective behavior of the hydraulic fracture growth through a natural fracture network. Mechanical responses have been studied for two different fracture and flow scenarios depending on the fluid entry details: one fracture system assumes each of four entry

fractures has one quarter of the total injection rate and the other system is defined to maintain the influx rates into each inlet fracture so that the pressure across all four inlet fractures is equal (but not necessarily constant in time). For the latter case, a preferential flow pathway is developed as a result of hydraulic fracture growth and the overall permeability of the fracture system increases rapidly after this hydraulic fracture path develops. The former injection condition results in development of more evenly distributed advancing fractures that provide a more homogeneous flow pattern.

1. Introduction

The understanding of fluid movement through fractured rock masses is essential to improving the success of reservoir stimulations for energy resources such as shale gas and geothermal energy and for stimulation by hydraulic fracturing of any naturally fractured rock mass. As we know, fractures play an important role in the flow of fluid through rock masses by building connected networks that channel flow. These networks develop either through enhanced conductivity of existing fractures or by new fracture growth that connects existing fractures. There are many studies in the literature devoted to characterising the fracture system connectivity in relation to fracture orientation, size and conductivity (see the comprehensive review [1]). Besides these static factors, the time dependent evolution of fluid pressure and stress states can generate different fracture patterns that act to assist or inhibit further fluid flow, in particular forming a preferential fluid pathway in the presence of viscous fluid flow [2, 3]. Under some circumstances, the fracture growth driven by pressurized fluids can propogate a hydraulic fracture to connect two isolated fracture clusters. Cross-cutting fractures in the connected region are filled with fluid and pressurized but may open or not. Therefore fluid movement in a fractured rock mass will involve both new fracture growth and permeability enhancement of existing fractures. Clearly, using an equivalent porous continuum model to represent fluid flow and fracture growth would be inaccurate, especially when the flow is dominated by hydraulic fracture processes. The approach here is to study the full coupled process in order to determine the parameters that control fracture development. Simplifications and averaging methods can eventually be realistically employed without degrading the ability to predict fracture growth.

Discrete fracture models, so named because these models treat fractures as discrete entities, are applicable whenever the process involves fractures growth and flow where details such as opening, shearing or growth of the fractures are being studied. If many fractures are considered, these discrete models become computationally demanding. Such a system is very heterogeneous and localized in both fracture growth and fluid flow. Early numerical models treated the hydraulic fractures as single planar fractures and did not consider fracture interaction [4-6]. The emergent behaviours associated with fracture propagation under a tensile displacement boundary condition have been described as straight paths using a subcritical failure criterion and a propagation speed exponent. Recently, the effect of curving fractures on fluid flow in both the fractures and the matrix under a tensile displacement boundary condition has been considered [7,8]. However, the pressure distributions used inside

http://dx.doi.org/10.5772/56405

the fractures are either uniform [7] or based on the steady-state solution for flow in a porous medium [8]. The effect of fluid viscosity on pressure distribution has therefore not been considered in these fracture network models. Moreover, some simplifications in the fracture geometry changes, such as the details of interactions at intersections and in regions where fractures close, are used in these models and these simplications affect fluid flux distribution. Uncoupling of deformation and fluid flow, as used in some models, limits the application of the results obtained.

Fracture models that do not consider flow in the matrix, are applicable to low-permeability rocks [9]. In general, the fracture aperture is very narrow and would be different in each fracture branch intersecting at the same point, and these differences are expected to be significant in their effect on fluid movement through the intersections. In contrast to the stress-driven uniform fracture nucleation in porous rocks subject to a tensile loading environment, the propagation of a hydraulic fracture through a network of pre-exsiting fractures is dependent on local stress states around fracture tips, which in turn depends on the fluid flow and pressure along the non-planar hydraulic fracture path. Under most circumstances, one dominant hydraulic fracture is generated and the entire injected fluid rate is carried to the outlet through this preferential flow path, while most shorter natural fractures that are intersected by this main fracture remain closed or act as dead end branches [9]. Models that include the coupling of rock deformation and viscous fluid flow provide a means of studying the fracture development and the evolution of distinct preferential flow paths and development of a dominant fracture.

At intersections of two or more fractures, the kinematic deformation transfer between slip and opening of the fractures can induce additional fracture aperture changes. In addition, the viscous effect becomes stronger for narrow channel widths, which are commonly associated with intersections and offsets. The importance of tracking the details of fracture geometry lies in the fact that although the pressure losses may diminish after a long time, initial fracture geometry details may strongly affect the final fracture patterns. Studies that neglect viscous fluid effects, by using uniform pressure or steady-state transport and deformation models, will, in many cases miscalculate the stresses and flow rates, thus producing incorrect fracture and flow patterns as time-dependent pressure responses are not determined accurately.

Mechanical interaction among fractures has not received sufficient attention in the literature involving discrete fracture models especially for cases involving pressurized viscous fluids sufficient to result in hydraulic fracture growth. Any inaccuracy in the calculated fracture pathway may cause incorrect flux redistribution at intersections, as fluid flow behaviour is strongly dependent on local width. Due to intrinsic complexity of the problem, numerical methods appear to be the only approach able to explicitly solve the nonlinear and nonlocal fracture-fluid and fracture-fracture interaction in such fracture network. The Distinct Element Method (DEM) and the Finite Element Method (FEM) have been used for this purpose [10,11]. However, the fracture pathways are confined along the element edges in classical FEM models and the out-of-plane fracture propagation is difficult to accurately simulated because it requires remeshing. We have developed a Boundary Element Method (BEM) based program for treating this coupled problem [12,13]. The validation of the code has been carried out for various simple

cases involving both viscous fluid and uniform pressure. Additionally, the program treats rock deformation and fluid flow as a whole in that the field variables are obtained in a single framework, instead of the one-way coupling scheme as used in Reference [11].

The purpose of this paper is to provide some initial results for hydraulic fracture growth through a natural fracture network. Fracture growth is allowed and is based on a local failure criterion[14] and fracture coalescence can take place to form a path through an existing network of natural fractures. The numerical treatment of fracture coalescence has been detailed in [12, 13]. The rock mass is assumed to be impermeable and the fluid flow is confined to occur along the pre-existing or newly created fractures. The fracture nucleation sites are embedded as the pre-existing secondary fractures with small sizes to reflect the tensile strength heterogeneities existing along the fracture surface [15]. For this plane-strain model, the strain in the out-of-plane direction is assumed to be zero and the fracture should be visualised as extending uniformly a significant distance in this direction.

2. The model

The basic governing equations and the boundary conditions are provided in our previous work (see References [12,13,16]), dealing with the hydraulic fracture model that fully couples mechanisms of rock deformation and viscous fluid flow. The basis of the model is briefly described here for the sake of completeness.

We allow for the fracture surfaces to be rough and tortuous, which imparts a hydraulic aperture for the closed fracture allowing fluid flow, but causing no stress and deformation changes. Fluid volumetric flux q in a closed fracture segment is described by:

$$q = -\frac{\varpi^3}{\mu'}\frac{\partial p_f}{\partial s} \tag{1}$$

and in an opened fracture portion it is

$$q = -\frac{(w+\varpi)^3}{\mu'}\frac{\partial p_f}{\partial s} \tag{2}$$

where $\mu' = 12\mu$ with μ being fluid dynamic viscocity. w and ϖ are mechanical opening and hydraulic aperture along the fracture surface and are functions of time and location. The former is determined by the stress condition given below, but the latter obeys an evolution equation linearly proportional to fluid pressure change [13]. It is noted that the initial value of hydraulic aperture is denoted as ϖ_0, which is a reflection of the fracture surface roughness and tortuosity.

Fluid flow in the opened fracture portion is based on the lubrication equation:

http://dx.doi.org/10.5772/56405

$$\frac{\partial(w+\varpi)}{\partial t}=\frac{\partial}{\partial s}\left(\frac{(w+\varpi)^3}{12\mu}\frac{\partial p_f}{\partial s}\right) \tag{3}$$

but fluid flow in the closed fracture segment is based on the pressure diffusion equation

$$\frac{\partial p_f}{\partial t}-\frac{1}{\chi_1\mu'}\frac{\partial}{\partial s}(\varpi^2\frac{\partial p_f}{\partial s})=0 \tag{4}$$

where χ_1 is the compressibility of the fracture with units of Pa^{-1} and it is set as $10^{-8}Pa^{-1}$ in this paper. When fracture surfaces are separated, the change of the hydraulic aperture ceases, but its contribution to fluid flow is retained as provided in Eq. (3).

The nonlocal elastic equilibrium equations for a system of N fractures are given as:

$$\begin{aligned}\sigma_n(\boldsymbol{x},t)-\sigma_1(\boldsymbol{x})&=\sum_{r=1}^{N}\int_0^{l_r}[G_{11}(\boldsymbol{x},s)w(s,t)+G_{12}(\boldsymbol{x},s)v(s,t)]ds\\ \tau_s(\boldsymbol{x},t)-\tau_1(\boldsymbol{x})&=\sum_{r=1}^{N}\int_0^{l_r}[G_{21}(\boldsymbol{x},s)w(s,t)+G_{22}(\boldsymbol{x},s)v(s,t)]ds\end{aligned} \tag{5}$$

where the coordinates of a location of a material point are denoted as $x=(x, y)$ in a two-dimensional Cartesian reference framework, t is time and v is the shear displacement discontinuity, ℓ_r is the length of fracture r. σ_n is the normal stress and τ_s is the shear stress carried by the fracture because of its frictional strength, obeying Coulomb's frictional law characterized by the coefficient of friction λ, which limits the shear stress $|\tau_s| \le \lambda\sigma_n$, that can act in parts of fractures that are in contact, but vanishes along the separated parts. Along the opened fracture portions, we have $\sigma_n = p_f$.

In addition, σ_1 and τ_1 are the normal and shear stresses, respectively, along the fracture direction at location x caused by the far-field stress, whose normal and shear components are denoted as σ_{xx}^{∞}, σ_{yy}^{∞} and σ_{xy}^{∞}. G_{ij} are the hypersingular Green's functions, which are proportional to the plane strain Young's modulus, E', where $E'=\frac{E}{(1-\nu^2)}$.

The global mass balance requires

$$\sum\int_0^{l_f}(w+\varpi)ds=Q_0t \tag{6}$$

And the fluid front in the hydraulic fracture will be, in general, not coincident with the fracture tip. The fluid front location is found by using Eqs. (1) and (2) with the following equation

$$\dot{l}_f = q(l_f, t) / w(l_f, t) \tag{7}$$

The fracture growth is based on using the maximum hoop stress criterion, with the maximum mixed-mode stress intensity factor reaching a critical value [14]

$$\cos\frac{\Theta}{2}(K_I \cos^2\frac{\Theta}{2} - \frac{3}{2}K_{II}\sin\Theta) = K_{Ic} \tag{8}$$

where K_I and K_{II} are calculated stress intensity factors, $K_{Ic}$is tensile mode fracture toughness and Θ is the fracture propagation direction relative to the current fracture orientation. The predicted orientation follows the maximum tensile stress direction, and the near-tip stresses are approximated by the analytical LEFM solutions [14].

The problem must be completed by specifying the imposed boundary conditions at the wellbore, that is, the sum of injection rates of hydraulic fractures connected into the wellbore or to the entry zone, should be equal to the given injection rate Q_0. At the fracture tip the displacement discontinuities are zero, $w(\ell_r, t)=0$ and $v(\ell_r, t)=0$. In addition, the entire system is assumed to initially be stationary and unsaturated.

The numerical scheme for the above nonlinear and nonlocal coupled problem has been detailed in our previous paper [16] based on the Displacement Discontinuity Boundary Element Method. The hydraulic fractures and other geological discontinuities like joints and faults, and natural fractures are discretised with constant displacement elements. The model solves the hydraulic fracture problem simultaneously including the effects of viscous fluid flow and coupled rock deformation. The solutions are consistent with existing results. Also, a fracture can intersect another one in its path and a new fracture can be nucleated from a position on the natural fracture. In particular, the new fracture seeds are pre-defined in this paper along some natural fractures. The interested reader is referred to our previous papers for the details on implementation of fracture growth and coalescence [12,16]. One important check here is the satisfication of fluid mass conservation after fluid branch coalescence, due to redirection of newly-created fractures.

Property	Value
Young's modulus E	50 GPa
Poisson's ratio	0.22
Mode I Toughness	1.0 MPa · $m^{0.5}$
Fluid dynamic viscosity	0.01 Pa · s
Injection rate	0.00002 m^2/s
Coefficient of friction along fractures	0.8

Table 1. Material properties

http://dx.doi.org/10.5772/56405

3. A simple test problem

To validate the model on coalescence of fluid flow branches, we present results for one specific case, as shown in Figure 1, where two hydraulic fractures with a spacing 0.8 m driven by the same fluid source (located at the plane with x=-1.0 m on the left of the natural fracture) intersect the natural fracture orthogonally. And the sum of their inflow rates is a constant. A new fracture site is located on the natural fracture that is 2.4 m in length, and it is assumed to be a pre-existing flaw at 0.12 m long. It is anticipated that after intersection, the fluid will invade the natural fracture until it reaches the new fracture in Figure 1(a), which is subject to a less compressive stress. As the new fracture becomes the weakest point to continue crack growth, it will propagate when the fluid pressure reaches a sufficient value, as shown in Figure 1(c). It should be noted that when the middle section of the natural fracture between two hydraulic fractures is filled with fluid, a sudden increase in the pressure occurs as indicated in Figure 1(a) and (b) for two close time steps, in the same way as injection into a closed container. At the time shown in Figure 1(c) the natural fracture appears to be full of fluid, the whole fracture system experiences a similar pressure level, high enough to cause the new fracture to propagate. The material constants used for this problem are listed in Table. 1 if not otherwise specified.

The variations of flow rates into each branch with time are provided in Figure 1(d). The two hydraulic fractures reach the natural fracture at time t=6.98 s and the fluid front reaches the new fracture site at t=10.85 s. In Figure 1(a), the inflow into the new fracture is only from the top hydraulic fractures up to the onset of coalescence of two fluid branches with the natural fracture at t=12.6 s. There is a short-time period where Q_5 occurs before fluid branch coalescence and this flux is represented by Q_4 later on. Subsequently, the value of Q_6 increases rapidly to a higher level (Q_6 / Q_0=0.8). This implies that most of injected fluid is entering the new fracture and this promotes its growth. The fluid rates at the injection fractures all meet the continuity requirement. The larger value of Q_3 compared to Q_4 indicates that the hydraulic fracture closer to the fracture nucleation site is contributing more in fluid flux to sustain the new fracture growth. As for the loss of geometric symmetry, it is interesting to note that the outflux from the top hydraulic fracture is also larger than its counterpart since $Q_1 > Q_2$ clearly shown in Figure 1(d).

4. Random fracture geometry

In this section, we present more complex cases where several high-angle joints are defined in a random distribution ahead of hydraulic fractures that grow from a left entry zone (along the plane x=-1 m) toward the right (through the plane x=2 m). The remote stress conditions and some geometric parameters are provided in the caption of Figure 2. The fracture injection occurs into four individual fractures located on the far left, as shown in Figure 2. The fracture segments coloured green denote the initial existing fracture configuration. Each existing fracture consists of a single fracture or of several connected fractures of different sizes and

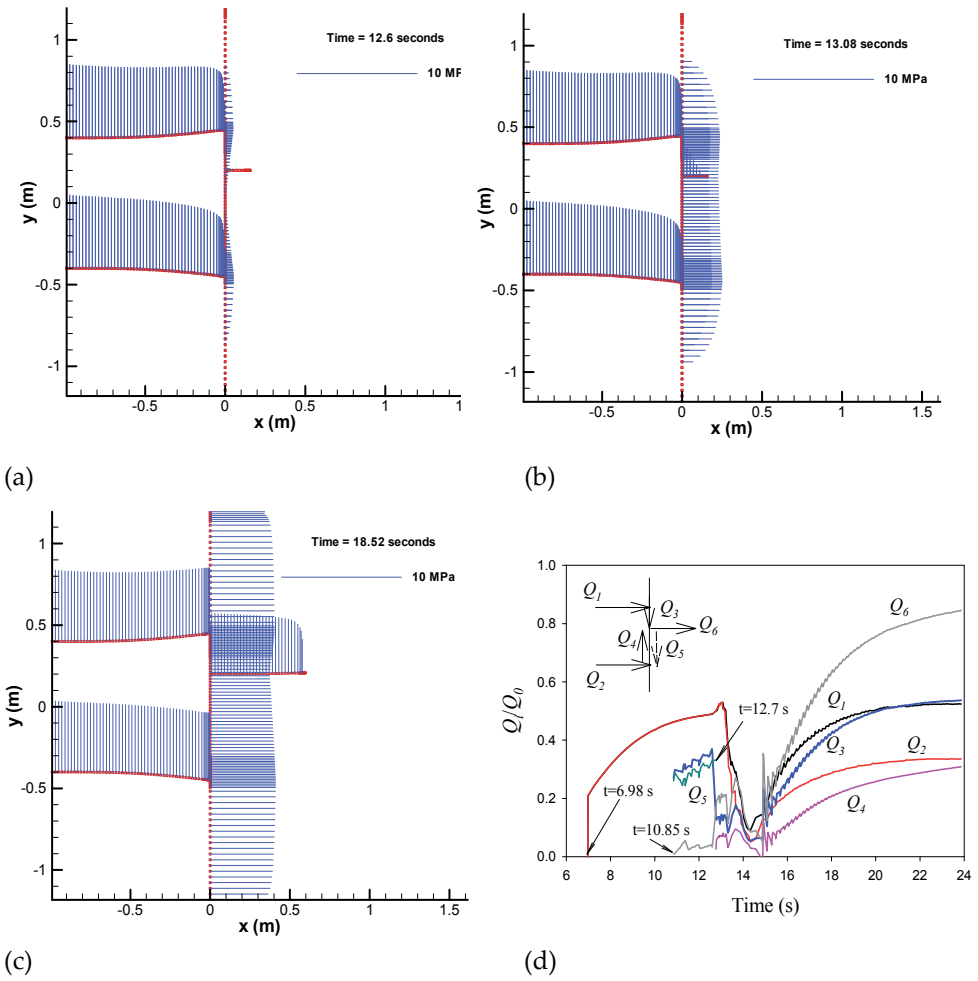

Figure 1. The pressure profiles at three specific time instants: (a) t=12.6 s, (b) t=13.08s and (c) t=18.5 s and (d) the evolution of influxes around the intersection points and the fracture nucleation site for the case of one natural fracture and two hydraulic fractures that approach the natural fracture at a right angle. The fracture nucleation site on the natural fracture is located at 0.2 m above the mid plane of the two hydraulic fractures. The applied stress components are σ_{xx}^{∞} =5 MPa, σ_{yy}^{∞} =4 MPa and σ_{xy}^{∞} =0. The initial hydraulic aperture $_0$ for the natural fracture is 0.03 mm.

orientations. The hydraulic fractures driven by pressure act to connect these separate fractures to form a conductive path from left to right and the newly created fractures are coloured in red in Figure 2. Two different injection boundary conditions are used in the computations. One is associated with even distribution of the injection rate into the four entry fractures on the left, and the second condition specifies that the pressure at each of these four initial fractures is equal. The latter condition is physically reasonable if we assume a wellbore lies along the y-axis of Figure 2, while the former condition would require isolation and injection into each fracture at the same rate.

http://dx.doi.org/10.5772/56405

Of course, some numerical difficulties exist in the simulation of the process of connecting two intersecting fractures [16]. A mesh sensitivity analysis has been carried out so that the change in fracture orientation does not affect the numerical accuracy as the fracture direction has to be such that the intersecton occurs at the the end of an element on the fracture. A fracture connection event that results in a strong deflection from the calculated direction can influence the subsequent fluid flow. In these cases, the natural fractures must be re-meshed and the job must be run again. In the numerical simulation, the individual element size in the vicinity of intersection point is chosen with care, so that the fracture connection can be completed as a smooth path.

For the sake of convenience in discussion, the above two injection types are respectively named as type I and type II injection. Figure 2 shows the results at the time of breakthrough when the hydraulic fracture emerges on the right side (x=2 m) of the network of natural fractures, for these two injection types. After fracture reorientation to the direction normal to the minimum principal stess, the fracture development through the network zone is complete. As expected, the type I injection condition results in more fracture growth paths and intersections across the network, while the type II condition results in a localized path, with only one hydraulic fracture continuing to grow past the network on the right side. In Figure 2(b) there are two separate unconnected sets of fractures from top to bottom, both of which connect to two of the initial fractures on the left which are connected to (in this case) the equal pressure fluid source. The influxes into the bottom fracture set decrease in time and more of the total volume injected enters the upper fracture set. The upper fracture set is more conductive. We define the plane x>2 m as the exit zone. There is one outlet fracture in this case. However, there are two fluid outlets or extraction sites in Figure 2(a) for type I injection. On the other hand, for the type II injection, the new fracture segments are mainly created along the upper fracture path.

Figure 3 shows the outlet flux variations in time for the two cases used in Figure 2. For type I injection, only around 43 percent of injected fluid has passed through the fracture system to the outlet at the end of simulation period and the other 57 percent is contained in fracture branch inflation or growth in the network. It is also found in Figure 3 that in this case the outlet flux (sum of outlet 1 and outlet 2 for case (a)) increases at a very slow rate at the large time. More fractures under type I injection are connected with each other as a result of crack growth near the fluid source and some fractures continue to grow after the main conductive channels are developed. Fracture segments not opened also store some fluid because of their initial conductivity. The rate that fluid is stored in the fracture network differs between the type I and type II injection conditions. For type II injection, more than 55 percent of injected fluid exits the outlet fracture at the end of the simulation and this outlet flux is increasing at a very large rate as shown in Figure 3 so that the rate of fluid volume stored in the system will become extremely small soon in light of this trend.

In addition, the breakthrough time for these two injection types is provided in this figure. The type II injection has a much earlier breakthrough time so that the fracture growth through the fracture network is more rapid.

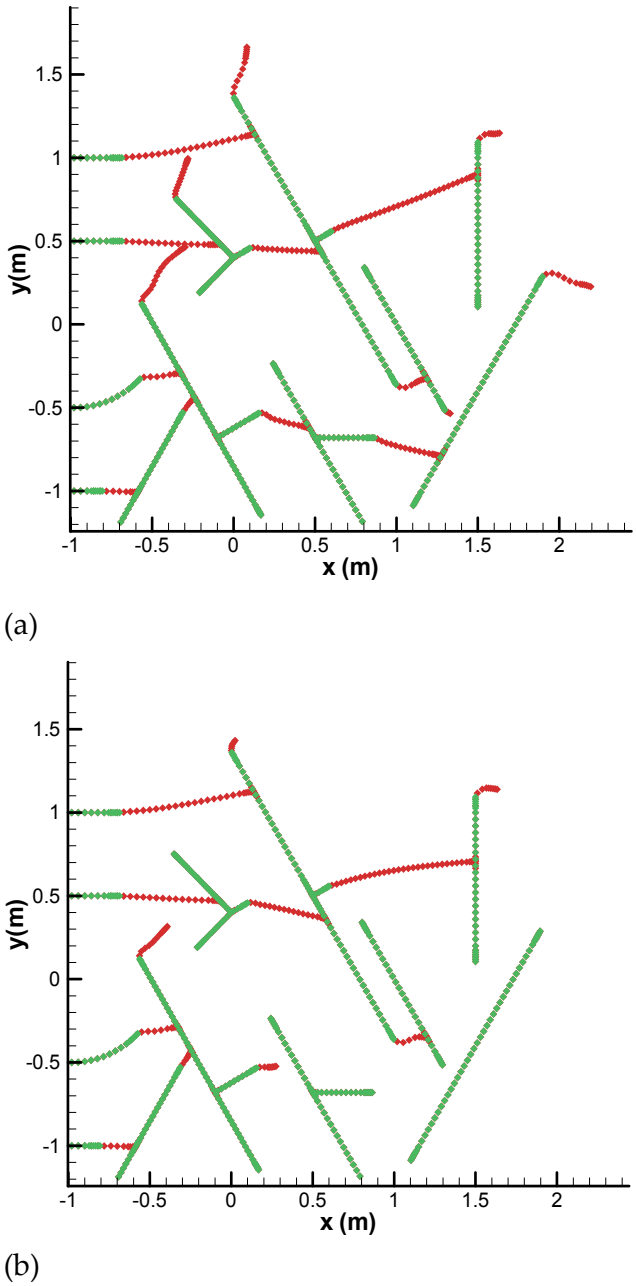

Figure 2. Fracture pathways at the time of breakthrough for two different injection conditions: (a) Type I and (b) Type II. The fracture system is subject to the applied stresses σ_{xx}^{∞}=6 MPa, σ_{yy}^{∞}=4 MPa and σ_{xy}^{∞}=0. The initial hydraulic aperture $_0$ for all natural fractures is 0.01 mm. The fluid comes into the area from four entry fractures at the left (x=-1 m) and its pressure drives some fractures to propagate and connect the separated fractures as the hydraulic fractures grow toward the right outlet zone (x=2 m). The initial fracture configuration is shown in green and the generated fracture segments are in red.

http://dx.doi.org/10.5772/56405

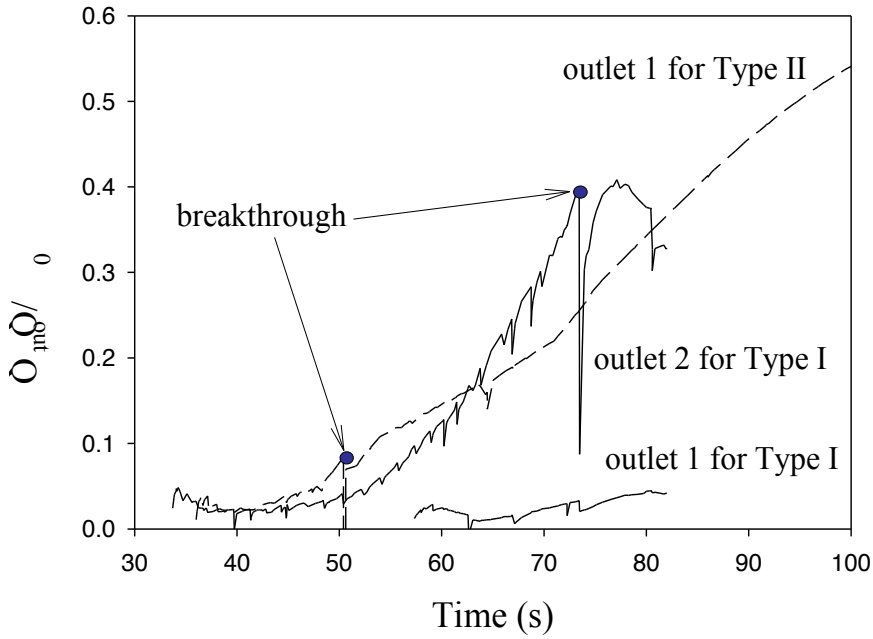

Figure 3. Evolution of normalised outlet flux that is defined by the entrance flow rate of the outlet fractures by the injection rates for two cases provided in Figure 2. There are two outlets for case (a) and they are numbered from the top to the bottom. For case (b) there is only one outlet at the top.

The rapidly increasing trend in outlet flux is also reflected in the opening profiles as shown in Figure 4(a) with the wider open fracture path corresponding to the path that carries the most fluid. The wider fracture channels are localised along the preferential pathway along the upper fracture set to the right-top fracture outlet under type II injection. It is found that at the given time instant, up to 85 percent of the injected fluid is pumped into this preferential path and the fractures not included in this path are all static at late times in the simulation. At the larger times simulated, most fluid just passes through this highly conductive channel to reach the exit zone. Thus, the localised flow channel provides the lowest resistance pathway for fluid flow. Here, we note the contribution of residual hydraulic aperture on the fluid movement and storage. As stated above, each natural fracture has a pre-existing aperture of 0.01 mm in the computations. Thus, some fluid enters and is stored in this pre-existing aperture.

It is found that fractures with wider opening have had their opening enhanced by the large slip along the longest oblique natural fracture, which is oriented at 45 degrees to the x-axis, as shown in Figure 4(b). The kinematic transfer between slip and opening assists the fracture opening.

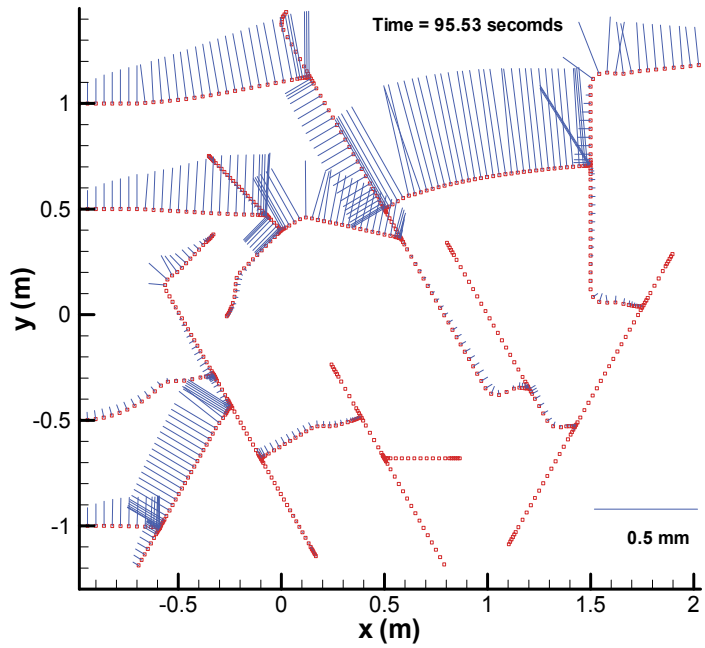

(a)

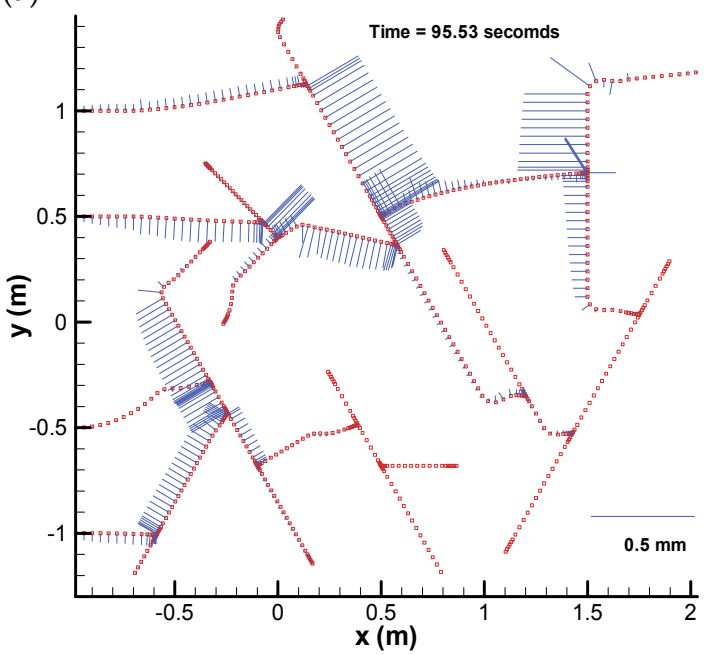

(b)

Figure 4. Fracture trajectories and opening (a) and slip (b) profiles, which are represented by the blue bars perpendicular to the fractures, under type II injection at a specific time.

http://dx.doi.org/10.5772/56405

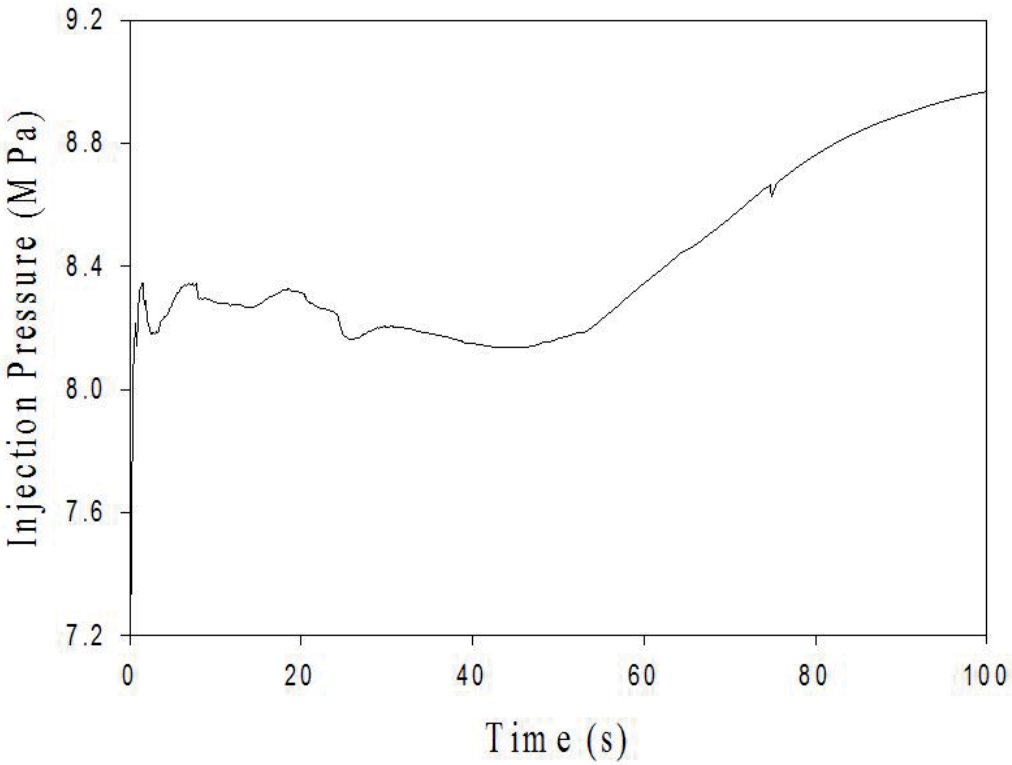

Figure 5. Evolution of injection pressure at the left entry zone for the type II injection method.

Also, it is found that some fracture connections are made even after the preferential fluid pathway is established, since fracture growth can still be generated in the higher pressure region near the entry. After the breakthrough, the injection pressure has to be retained at a higher level, to force fluid through width restrictions that occur at intersections and offsets, as shown in Figure 5. The continuing fracture growth in the network can alter the earlier opening distributions. Comparing Figure 4 and Figure 2(b), it is clear that fracture growth and fracture interconnection can occur inside the network region after the flow breakthrough. Of course, one reason for pressure increasing after breakthrough is attributed to the strong resistance to fluid flow at the last vertical natural fracture on the connected flow path for this specific geometry. This vertical fracture provides the strongest barrier to fluid flow as its opening is highly constrained by the geometry, with the approaching hydraulic fracture making a right angle to the natural fracture. A new fracture would possibly be nucleated at some location along this vertical natural fracture which would reduce this restriction. Although Figure 5 shows the increasing trend of the injection pressure, the pressure will eventually level off or even decrease as the outflux from the network increases to 100 percent of the input rate, as indicated in Figure 3.

5. Discussion

5.1. Fluid-driven fracture nucleation, growth and connection

In the model, we only consider hydraulic fracture growth through a finite set of fractures, some of which are initially very small, but potentially provide a conduit with the help of high fluid pressure. The fracture seeds are pre-assumed in this paper and are represented by these small fractures. Therefore, fracture nucleation in a highly stressed area is not dealt with in this paper. This treatment of fracture nucleation can underestimate the fracture number and the fracture connectivity. For the case shown in Figure 4, the lower fluid flow path cannot move to the right outlet and a higher stress level might create new fractures near the entry zone. It would be interesting to study the impact of crack nucleation based on stress conditions rather than just from these pre-existing fractures.

Without considering fluid loss into the rock matrix, hydraulic fracture growth as the main driving force in connecting fractures can create more new segments at the upstream end of the fracture system than at the downstream. In terms of fracture length, both pre-existing and newly created, we can define fracture density as the fracture number per unit area. Although fracture density is a significant measure for fracture connectivity, the longer fractures including the newly created parts would be more important contributors because they are more compliant and will open wider under the same internal fluid pressure [9]. Predicting the early growth of these hydraulic fractures through a pre-exising network, as modeled in this paper, must account for the effect of viscous fluid or incorrect fracture behaviour is predicted.

In this model, fracture growth occurs when the failure criterion is satisfied at any fracture tip, with the failure condition defined within the framework of linear elastic fracture mechanics. Fracture curving is the natural result of the local stress field around the tip if the growth follows the maximum tensile stress criterion. Normally, fractures will reorient themselves to the maximum compressive stress direction to increase fracture opening, resulting in local conductivity enhancement as indicated in above results. However, the fracture curving can sometimes lead to intersection of two fractures at a small acute angle, which will make it difficult for the subsequent flow to enter some segments. Sometimes, the subsequently developed sliding on one fracture can seal the fracture channels near the junctions. The development of geometric networks, produced by growing hydraulic fractures, are illustrated by the results obtained above. The results imply that not all connected fractures can contribute to overall conductivity of the system which is contrary to conventional percolation model predictions. These geometric factors affecting fracture growth and fluid flow have been mentioned in early studies [7]. Some fracture growth can occur in the wake of the fracture and flow fronts near the higher pressure entry zone. Local reversed flow has also been observed in the results due to the pressure changes.

Actually, in addition to injection conditions, many other factors such as injection rate and in situ stress can affect the crack growth and coalescence. At the elevated pressure and based on the assumed fracture geometries, one can find that, even through a network of natural fractures, the hydraulic fracture average direction tends to align as much as possible with the

http://dx.doi.org/10.5772/56405

direction of the maximum stress. This orientation reduces the viscous dissipation and injection pressure. However, an increase in fluid pressure because of increased rate or viscosity can produce higher pressures upstream of a local offset or restriction which can then lead to opening of cross-cutting natural fractures and branching.

In addition, this paper only considers a limited number of specific initial fracture geometries, the results may be different if the starting geometries are changed and more cases are being considered as a way of making our conclusions stronger and more general. Although a method to deal with network development is presented here, there is a need to work on different geometries to extract some useful general responses for rational simplifications of the expected response for hydraulic fracture network growth.

5.2. Implications for fracture-controlled flow system

Our numerical results quantify the overall path of discrete hydraulic fractures growing through a network of pre-existing natural fractures, as shown in Figs. 3 and 4. These results give insight to the behaviour of fracture-controlled flow systems, where the fluid flow and the rock deformation and fracturing are strongly coupled. It is clear that the conductivity depends on the stress-dependent fracture aperture through a strong coupling to fluid flow, as opposed to fixed aperture fractures in conventional percolation models. Local areas can exhibit higher effective permeabilities or strong growth barriers. Such enhanced or restricted opening occur at intersections and offsets, and their existence can affect the total system conductivity, producing a higher pressure level as shown in Figure 5. Early time rapid hydraulic fracture propagation and intersection of small natural fractures establishes a path for the fracture through the natural fracture network, and a single fracture connection event can cause a strong change in the hydraulic fracture channel system that develops.

The model has particular application for understanding the hydraulic fracture connection process through a network. By varying parameters, one finds the transition of fracture-controlled flow pattern from more uniform to more localized and from multi-directional to unidirectional. The hydraulic fractures tend to develop wider and more connective localized fracture channels in establishing a preferred path through the network of natural fractures. In contrast, low rate injection processes that do not involve significant fluid viscous dissipation effects, tend to result in flow occurring along all already connected conductive paths. How to better characterise this difference is still open and to find meaningful parameters in connecting the intricate topological fracture network with diffusion flow patterns requires prediction of propped and unpropped fracture permeability that remains after the hydraulic fracture treatment. The model used here may provide a tool for such parametric studies.

Acknowledgements

The authors thank CSIRO for supporting this work and granting permission to publish.

Author details

Xi Zhang[1*] and Rob Jeffrey[2*]

*Address all correspondence to: xi.zhang@csiro.au

*Address all correspondence to: rob.jeffrey@csiro.au

1 CSIRO Earth Science and Resource Engineering, Melbourne, Australia

2 CSIRO Earth Science and Resource Engineering, Melbourne, Australia

References

[1] Berkowitz B., Characterizing flow and transport in fractured geological media: A review. Advances in Water Resources, 2012; 25(8-12), 861–884.

[2] Glass R. J., Nicholl M., J., Rajaram H., Andre B., Development of slender transport pathways in unsaturated fractured rock: Simulation with modified invasion percolation. Geophysical Research Letters, 2004; 31(6), 31–34.

[3] Barnhoorn A., Cox S. F., Robinson D. J., Senden T., Stress- and fluid-driven failure during fracture array growth: Implications for coupled deformation and fluid flow in the crust. Geology, 2010; 38(9), 779–782.

[4] Dershowitz W. S. Einstein H.H., Characterizing Rock Joint Geometry with Joint System Models. Rock Mechanics and Rock Engineering, 1988; 1, 21-51.

[5] Olson J. E., Joint Pattern Development: Effects of Subcritical Crack Growth and Mechanical Crack Interaction, Journal of Geophysical Research, 1993; 98(B7), 251-265.

[6] Renshaw C.E., Pollard D.D., Numerical simulation of fracture set formation: A fracture mechanics model consistent with experimental observations, Journal of Geophysical Research-Solid Earth, 1994; 99(B5):9359-9372.

[7] Philip Z. G. Jr, Olson J. E., Laubach S. E., Holder J., Modeling Coupled Fracture-Matrix Fluid Flow in Geomechanically Simulated Fracture Networks. SPE Reservior Evaluation and Engineering, 2005; April , 300–309.

[8] Paluszny A., Matthai S. K., Impact of fracture development on the effective permeability of porous rocks as determined by 2-D discrete fracture growth modeling. Journal of Geophysical Research, 2010; 115(B2), 1–18.

[9] Long J. C. S. and Witherspoon P. A., The relation of the degree of interconnection to permeability in fracture networks, Journal of Geophysical Research, 1985; 90(B4), 3087-3098.

http://dx.doi.org/10.5772/56405

[10] Zhang X., Sanderson D.J., Harkness R.M. and Last N.C., Evaluation of the 2-D permeability tensor for fractured rock masses, International Journal of Rock Mechanics and Mining Science & Geomechanics Abstracts, 1996; 33(1), 17-37.

[11] Fu P., Johnson S. M., Carrigan C. R., Simulating Complex Fracture Systems in Geothermal Reservoirs Using an Explicitly Coupled Hydro-Geomechanical Model. 45 th US Rock Mechanics/Geomechanics Symposium, June 26-29, 2011, San Francisco, California.

[12] Zhang X., Jeffrey R. G., Thiercelin, M., Deflection and propagation of fluid-driven fractures at frictional bedding interfaces: A numerical investigation. Journal of Structural Geology, 2007; 29(3), 396–410.

[13] Zhang X., Jeffrey R. G., Thiercelin, M., Mechanics of fluid-driven fracture growth in naturally fractured reservoirs with simple network geometries. Journal of Geophysical Research, 2009; 114(B12), 1–16.

[14] Erdogan F., Sih G., On the crack extension in plates under plane loading and transverse shear, J. Basic Engineering, 1963; 85, 519-525.

[15] Pollard D.D., Aydin A.A., Progress in understanding jointing over the past century, Geological Society of America Bulletin, 1988; 100, 1181-1204.

[16] Zhang X., Jeffrey R. G., Fluid-driven multiple fracture growth from a permeable bedding plane intersected by an ascending hydraulic fracture, Journal of Geophysical Research, 2012; 117, B12402.

Chapter 8

Hydraulic Fracture Propagation Across a Weak Discontinuity Controlled by Fluid Injection

Dimitry Chuprakov, Olga Melchaeva and Romain Prioul

Additional information is available at the end of the chapter

http://dx.doi.org/10.5772/55941

Abstract

We investigated the problem of a hydraulic fracture propagation through a weakly cohesive frictional discontinuity for different conditions of fracture toughness, in situ stresses, fracture intersection angle, injection parameters and permeability of the pre-existing fracture. The parametric sensitivity of the fracture interaction process, in terms of crossing versus arresting of the hydraulic fracture at the discontinuity, was performed using numerical simulations through an extensive parameter space representative of hydraulic fracturing field conditions. The effect of the pre-existing fracture permeability on the crossing behavior was analyzed using a simple analytical model. We showed that the injection rate and viscosity of fracturing fluid are the key parameters controlling the crossing/non-crossing interaction behavior, in addition to already known fracture interaction angle and in-situ stress parameters. We have also found that the pre-existing fracture hydraulic aperture, when as large as that of the hydraulic fracture aperture, has significant influence on the interaction and may more likely cause the hydraulic fracture to arrest.

1. Introduction

The main function of a hydraulic fracture (HF) treatment is to effectively increase reservoir permeability and drainage by creating one or more conductive fractures that connect to the wellbore [1-2]. The stimulation treatments are especially necessary in low-permeability unconventional source rocks such as shales, which are not economical without fracturing [3] and sometimes even subsequent refracturing [4]. The modeling of HF propagation is important

to the design of the treatment and the ability to evaluate post-treatment production. Most fracture propagation models assume an oversimplified single planar geometry of fracture propagation [1, 5]. However, in highly heterogeneous and naturally fractured formations, the geometry of HFs can be complex because of their interaction with preexisting discontinuities in the rock, such as natural fractures, faults, and bedding interfaces [3, 6-7], which will be referred as NFs. For example, it is well known that an HF can be arrested by an NF or can reinitiate after the contact [8-16]. The result of the interaction depends on the in-situ stresses [10, 15, 17-18]; friction [12], cohesion [19], and permeable properties of the NF [20]; the rheological properties of the injecting fluid; and injection flow rate [21-22].

To predict the ultimate geometry of HFs, one needs to predict the result of every HF-NF interaction [23]. Several theoretical, numerical, and experimental studies have focused on this task [8, 10, 24-26]. One of the simplest analytical criterion for predicting the outcome of the HF-NF orthogonal interaction was developed by Renshaw and Pollard [18] and extended to arbitrary angle of interaction by Gu et al. [15]. This criterion predicts initiation of the secondary fracture (SF) on the opposite side of the interface influenced only by the friction, cohesion, and in-situ stresses. However, the HF activation and stress field near the intersection point are strongly dependent on the opening of the HF at contact and hence on pumping rate and fluid viscosity — a key point that has been ignored up to now [27]. Recent theoretical developments and laboratory experiments [21-22] have shown it is possible to derive an analytical crossing model taking into account the effect of flow rate and fluid viscosity on the HF-NF crossing behavior [27]. The results of this new HF-NF crossing model in a fracturing simulator environment are presented in a companion paper [28].

This paper offers dimensionless formulation and interpretation of the problem of fracture interaction. The numerical investigations are made by means of the code MineHF2D developed by Zhang et al. [20, 29]. This work focuses primarily on the parametric sensitivity analysis of the problem in terms of HF reinitiation at the NF and takes into account a more rigorous initiation criterion based on stress and energy premises.

The content of the paper is organized as follows. First, we define the problem of the HF-NF interaction mathematically and select all independent dimensionless parameters that influence the result. Next, we discuss the results of the parametrical study in terms of crossing or arresting behavior in the selected parametric diagrams. Finally, we concentrate on the particular effect of the hydraulic permeability of the NF by means of analytical and numerical models.

2. Problem statement

Consider the interaction between an HF and a preexisting discontinuity that represents a mechanically closed fracture with finite permeability, which is higher than that of the surrounding rock. In what follows the discontinuity will be referred to as an NF.

In nature, both the HF and the NF have certain 3D extents in the vertical and horizontal directions and their interaction should be described in 3D. If the vertical heights of the

http://dx.doi.org/10.5772/55941

fractures (perpendicular to the plane of Fig. 1) are far more comparable to or significantly exceed the horizontal size of the fractures affected by the interaction (in a plane of Fig. 1), the consideration of fractures can be reduced to plain-strain geometry. In this work we use a plain-strain model for the interacting fractures in the cross-sectional plane defined by the 1D flow direction (Fig. 1).

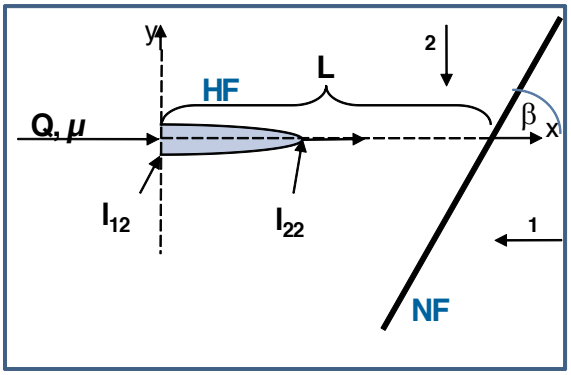

Figure 1. Schematic representation of the problem statement where a plain-strain (Khristianovich-Zheltov-DeClerk) model is considered with a one-wing HF is propagating toward a discontinuity (NF)

Suppose that the HF propagates from the injection point (point l_{11}= (0;0) in Fig. 1) toward the NF perpendicular to the minimum horizontal far-field stress σ_2, coinciding with axis *Oy*. When the HF reaches the NF (point l_{12}=(*L*;0) in Fig. 1) it forms a T-shape contact with an angle β. Maximum and minimum far-field stresses, σ_1 and σ_2, acting parallel to x- and y-axes respectively, are constant and uniformly distributed. The rock is assumed impermeable, isotropic, and elastic.

Following Zhang and Jeffrey [12], the elasticity equations for the system of interacting fractures can be written as the following sum of the contributions from each fracture with coordinates of their tips l_{i1}, l_{i2}, where i = 1,2, (1 refers to the HF, 2 refers to the NF):

$$\begin{cases} \sigma_n(x, y) - \sigma_n^{\infty}(x, y) = \sum_{i=1}^{N} \frac{E}{2\pi(1 - \nu^2)} \int_{l_{i1}}^{l_{i2}} [G_{11}(x, y, \xi)w(\xi) + G_{12}(x, y, \xi)v(\xi)]d\xi \\ \tau(x, y) - \tau^{\infty}(x, y) = \sum_{i=1}^{N} \frac{E}{2\pi(1 - \nu^2)} \int_{l_{i1}}^{l_{i2}} [G_{21}(x, y, \xi)w(\xi) + G_{22}(x, y, \xi)v(\xi)]d\xi \end{cases} \quad (1)$$

where integration is performed along the fracture path, *N* is the number of fractures (initially *N* = 2), G_{ij} is the hypersingular Green's functions for this problem [30-32], *E* is Young's modulus, ν is Poisson's ratio. The equations describe the integral relationship between the net normal and shear stress applied at the fracture, σ_n and τ respectively, and fracture opening and sliding, w and v respectively. Frictional slippage at the NF obeys the following Mohr-Coulomb friction criterion with cohesion *C* and friction coefficient λ:

$$|\tau| = \lambda(\sigma_n - p_f) + C \tag{2}$$

where p_f is the fluid pressure in the NF. The mechanically closed NF can possess a finite hydraulic permeability, which is significantly higher than that of the surrounding rock. To describe the NF permeability the concept of hydraulic aperture w_h is introduced. Hydraulic aperture is an imaginary opening of the closed crack simulating the residual conductivity of the NF and does not contribute to stress change. The permeability of the NF, k, and the hydraulic opening, w_h, are related by

$$k = \frac{w_h^2}{12} \tag{3}$$

If the fluid penetrates the closed NF, the hydraulic aperture w_h can be changed depending on the infiltrated fluid pressure in the NF. When the fluid pressure exceeds the normal stress applied to the NF, the NF will open mechanically, leading to the associated increase of its hydraulic aperture, which is the sum of mechanical and hydraulic opening, and

$$k = \frac{\left(w + w_h\right)^2}{12} \tag{4}$$

To describe the dependency of the hydraulic aperture w_h on the fluid pressure p_f, a nonlinear spring model is used [20]:

$$\frac{dw_h}{dp_f} = \chi w_h \tag{5}$$

where χ is the empirical constant of order of 10^{-8}Pa^{-1} - 10^{-6}Pa^{-1} that characterizes the compliance of a NF with respect to the increase of net pressure inside the fracture.

Restricting our study to incompressible and Newtonian fluids, the fluid flow in the growing HF is described by the following continuity equation and Poiseulle's law:

$$\frac{dw}{dt} + \frac{dq}{dx} = 0 \tag{6}$$

$$q = -\frac{w^3}{12\mu}\frac{dp_f}{dx} \tag{7}$$

http://dx.doi.org/10.5772/55941

where q is the 1D flow rate inside the fracture, and μ is the dynamic fluid viscosity. For fluid flow inside the NF, the same equations can be written with slight modification of the total hydraulic opening, so that

$$\frac{d(w+w_h)}{dt}+\frac{dq}{dx}=0 \tag{8}$$

$$q=-\frac{(w+w_h)^3}{12\mu}\frac{dp_f}{dx} \tag{9}$$

At the inlet of the HF the fluid flow is prescribed as constant:

$$q(x=0,t)=Q_0 \tag{10}$$

When the HF and the NF are in contact at the junction point, the fluid flux is required to satisfy the local continuity equations, meaning that the income flux from the HF is equal to the flux outgoing to the NF. Additionally, the fluid pressure profile along the HF and the NF must have a common value at the junction point. The coupling condition at the junction is

$$\begin{aligned} p_f^{(\mathrm{HF})}(x=L)&=p_f^{(\mathrm{NF})}(x'=0)\\ q(x=L)&=q(x'=+0)+q(x'=-0) \end{aligned} \tag{11}$$

The imposed boundary conditions at the inlet and junction point are sketched in Fig. 2.

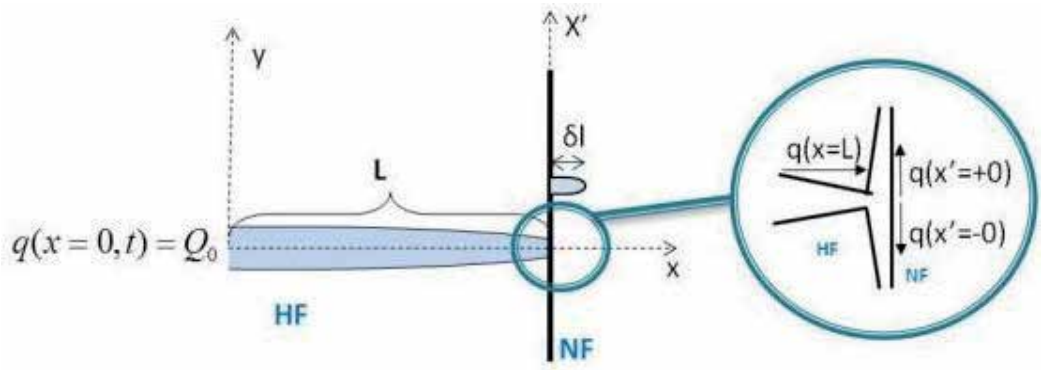

Figure 2. Boundary conditions of the problem

The condition for the HF tip propagation implies the quasi-static growth of the Mode I fracture such that Mode I stress intensity factor at the tip of the HF, K_I , equals the fracture toughness of rock K_{IC}:

$$K_I = \frac{w(x)E}{4(1-\nu^2)}\sqrt{\frac{\pi}{2}}\frac{1}{\sqrt{l_{(op)}-x}}\Bigg|_{l_{(op)}-x \ll l_{(op)}} = K_{IC} \tag{12}$$

where $l_{(op)}$ is the half-length of the open fracture zone. A condition similar to zero toughness can be written for the tip of the open zone created at the NF when the sliding zone propagates farther than the open zone. At the tip of the NF sliding zone we have then

$$K_{II}^{(NF)} = \frac{v(x)E}{4(1-\nu^2)}\sqrt{\frac{\pi}{2}}\frac{1}{\sqrt{l_{(sl)}-x}}\Bigg|_{l_{(sl)}-x \ll l_{(sl)}} \le K_{IIC}^{(NF)} \tag{13}$$

where $l_{(sl)}$ is the half-length of the sliding fracture zone. If the sliding zone and open zone coincide at cohesive NF, the following mixed mode criterion is used instead of (13):

$$\begin{cases} K_I^{(NF)} = K_{IC}^{(NF)} \\ K_{II}^{(NF)} = K_{IIC}^{(NF)} \end{cases} \tag{14}$$

Modeling of the new fracture initiation has been traditionally based on stress criterion only [26]. Following Leguillon [33], this work presents an extension in which the initiation of a new fracture must meet the joint stress and energy criteria, which is dependent on the initial length of the fracture initiated, δl. To create a new tensile crack, the stress acting normally to the crack must exceed tensile strength of the rock, T_0. Energy criterion for crack creation is simplified here to the requirement that the stress intensity factor at the initiated crack tip, K_I, exceeds fracture toughness of the rock, K_{IC}. Using the sign convention for the tensile stress to be negative, the joint initiation criterion used reads

$$\begin{cases} \sigma_{\tau\tau}(\delta l) \le -T_0 \\ K_I(\delta l) > K_{IC} \end{cases} \tag{15}$$

where $\sigma_{\tau\tau}$ is the tangential normal stress parallel to the NF and evaluated along the initiated crack path. Once the new crack is initiated, its further growth is determined by the following criterion of mixed-mode fracture propagation [34]

$$\left[K_I \cos^2\frac{\theta}{2} - \frac{3}{2}K_{II}\sin\theta\right]\cos\frac{\theta}{2} = K_{IC} \tag{16}$$

http://dx.doi.org/10.5772/55941

where θ is the deflection angle from the original fracture tip growth orientation.

In what follows we are interested in the ultimate result of the HF-NF interaction. After the contact with the NF, the HF can either stay arrested by the NF or reinitiate at the NF and continue propagation to the remainder of the rock behind the NF. Possible outcomes of HF-NF interaction are schematically drawn in Fig. 3.

In the case of arresting, the NF is extensively activated in opening and sliding such that the tensile stresses near the HF tip become insufficient for continuous fracture propagation or initiation of a new crack behind the NF. After the contact, the fracturing fluid is injected into the NF and the dilated NF becomes a part of a complex hydraulic fracture network. In contrast, if the NF appears to be frictionally or cohesively strong, the HF will reinitiate at the NF and continue its propagation into the remainder of the rock. The fracture often reinitiates at the offset positions, forming a more complex kinked fracture path after the interaction with the NF.

In this work, the problem of the HF-NF interaction is solved by means of the computational code developed by Australia's Commonwealth Scientific and Industrial Research Organization, CSIRO. The details of numerical scheme implemented in this code can be found in [12-13, 20, 24, 29].

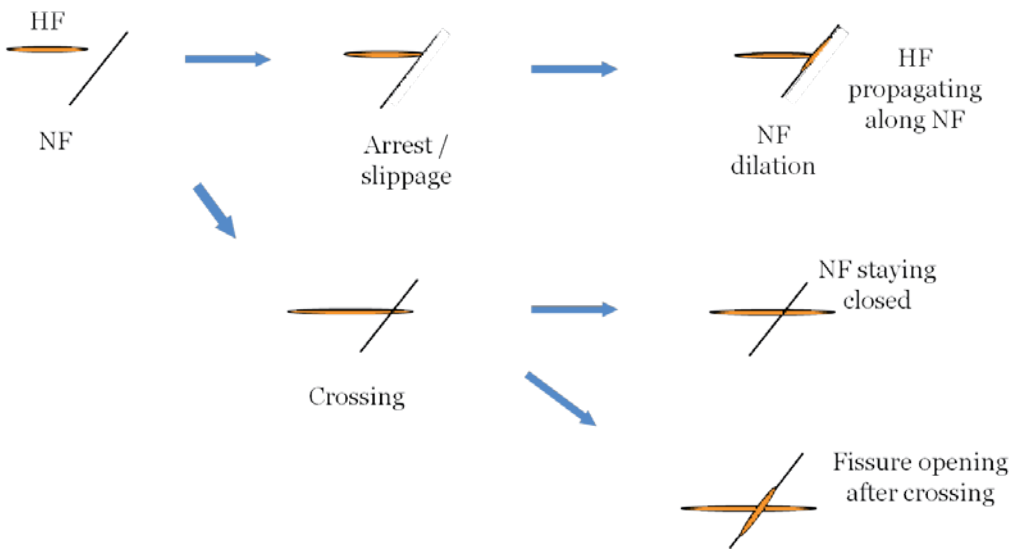

Figure 3. Schematic diagram of possible HF-NF interaction scenarios

3. Parameterization of HF-NF problem

The complete system of coupled equations (1, 5-7) subject to the boundary and initial conditions (2, 10-14) and criteria for crack initiation and propagation (15-16) is a complex multiparameterized problem. The aim of the work is to study parametric sensitivity of the result of HF-NF interaction, and the challenge of this undertaking substantially grows with the number of the independent parameters in the study. Our first initiative is to come up with proper parameterization of the problem that will be used in the numerical computations.

There are 14 dimensional parameters that impact the solution: injection rate into fracture, Q_0; fracturing fluid viscosity, μ; plain-strain Young's modulus, $E' = E/(1 - \nu^2)$; Mode I fracture toughness of the rock, K_{IC} ; tensile strength of the rock, T_0; maximum in-situ stress, σ_1; minimum in-situ stress, σ_2; length of the HF at contact with the NF, L; angle between the fractures, β; friction coefficient, λ; Mode I NF toughness, $K_{IC}^{(\mathrm{NF})}$ Mode II NF toughness, $K_{IIC}^{(\mathrm{NF})}$; hydraulic permeability of the NF, k, which is coupled to the residual NF opening as $k = w_h^2/12$; and NF compliance, χ. For the sake of concise expressions, we introduce the following notations for viscosity $\mu' = 12\mu$, for the fracture toughness in rock $K_{IC}^{'} = \sqrt{32/\pi}K_{IC}$, and at the NF $K_{IC}^{(\mathrm{NF})'} = \sqrt{32/\pi}K_{IC}^{(\mathrm{NF})}$, $K_{IIC}^{(\mathrm{NF})'} = \sqrt{32/\pi}K_{IIC}^{(\mathrm{NF})}$.

Table 1 summarizes the expected range of dimensional parameters for the majority of HF jobs in unconventional reservoirs from various sources [35-36]. The data were obtained from laboratory experiments and field measurements.

	Parameter	***Range***
Q	*Volumetric injection rate*	*0.01–0.25 m^3/s mmoposdvrgenmk m^3/sec*
L	*Distance between HF and NF*	*1–10 m*
μ	*Fluid viscosity*	*1–1000 cP*
E	*Young's modulus*	*9–110 GPa*
ν	*Poisson's coefficient*	*0.11 –0.252*
K_{IC}	*Mode I fracture toughness*	*0.1–2.7 MPa($m^{1/2}$)*
$K_{IC}^{(NF)}/K_{IC}^{(HF)}$	*Toughness ratio for NF vs. rock matrix*	*0–0.5*
$K_{IIC}^{(NF)}/K_{IC}^{(NF)}$	*Toughness ratio for NF*	*~1*
σ_1	*Maximum in-situ stress*	*13–105 MPa*
σ_2	*Minimum in-situ stress*	*11–100 MPa*
λ	*Friction coefficient at the NF*	*0.2–1*
k_h	*Permeability of NF*	*1 md–1 darcy*
β	*Fracture interaction angles*	*30°–90°*

Table 1. Range of the problem's dimensional parameters specific to gas shale fracturing jobs

http://dx.doi.org/10.5772/55941

Let us normalize the equations by the convenient choice of the scaling. First we introduce the displacement scale W for the opening, shear displacement of the fractures, and the residual aperture of the NF as

$$w = \Omega W, \quad v = \Psi W, \quad w_h = \Omega_h W \tag{17}$$

where Ω, Ψ and Ω_h are the dimensionless opening, sliding, and residual NF opening, respectively. The fluid flow rate is scaled by the injection rate at the inlet $Q = Q_0$ as

$$q = \tilde{q} Q_0 \tag{18}$$

where $\tilde{q}$ is the dimensionless flow rate. Similarly, we introduce the dimensionless fluid pressure, Π, and stress components, Σ_i, with the stress and pressure scale P

$$p_f = \Pi P, \quad \sigma_n = \Sigma_n P, \quad \tau = \Sigma_\tau P, \quad \sigma_i = \Sigma_i P \tag{19}$$

The coordinates, including coordinates of fracture tips, are scaled by the length of the contacted fracture L as

$$(x, y) = (\bar{x}, \bar{y}) L, \quad l_{ij} = \gamma_{ij} L \tag{20}$$

and the time is scaled by a certain time scale T as

$$t = \bar{t} T \tag{21}$$

After substitution of (17-21) into equations (1-13) we obtain these seven dimensionless groups

$$\begin{aligned} &\alpha_1 = \frac{TQ}{WL}, \quad \alpha_2 = \frac{W^3 P}{Q\mu' L}, \quad \alpha_3 = \frac{E' W}{PL}, \quad \alpha_4 = \frac{Q_0}{Q} = 1, \\ &\kappa_{IC} = \frac{K_{IC}' \sqrt{L}}{WE'}, \quad \kappa_{IC}^{(NF)} = \frac{K_{IC}^{(NF)'} \sqrt{L}}{WE'}, \quad \kappa_{IIC}^{(NF)} = \frac{K_{IIC}^{(NF)'} \sqrt{L}}{WE'} \end{aligned} \tag{22}$$

Choosing the viscosity scaling by setting $\alpha_i = 1$ in (22), we define the following expressions for the chosen scales:

$$W = \sqrt[4]{\frac{L^2 Q\mu'}{E'}}, \quad P = \sqrt[4]{\frac{E'^3 Q\mu'}{L^2}}, \quad T = \sqrt[4]{\frac{L^6 \mu'}{E' Q^3}} \tag{23}$$

After the scaling we obtain nine dimensionless parameters $\left(\kappa_{IC},\ \kappa_{IC}^{(\mathrm{NF})},\ \kappa_{IIC}^{(\mathrm{NF})},\ \Sigma_1,\ \Sigma_2,\ \Omega_h,\ \beta,\ \lambda,\ \chi\right)$ that characterize our dimensionless problem. We also note the parameters have nonequal sensitivity to the result of fracture interaction. For example, all previous theoretical and experimental studies have shown that the significant effect of the relative difference of the applied stresses can be written as $\Delta\Sigma=(\Sigma_1-\Sigma_2)/\Sigma_2$, rather than as the mean stress. The effect of NF compliance and the difference between Mode I and Mode II NF toughness can be neglected in the first attempt of parametric study, so we assume here $\kappa_{IC}^{(NF)}=\kappa_{IIC}^{(NF)}$. Consequently, we restrict our parametric analysis with the following six parameters $\left\{\kappa_{IC},\ \Delta\Sigma,\ \beta,\ \lambda,\ \kappa_{IC}^{(NF)},\ \Omega_h\right\}$.

This study is mainly intended for the oil and gas industry, so the comprehensive numerical study in infinite limits of these parameters in the present study is not necessary. In what follows we limit the range of the dimensionless parameter values to the practical range by use of the compilation of dimensional parameters of the problem shown in Table 1. Using the scaling introduced previously it is possible to calculate the corresponding range of the dimensionless parameters (Table 2).

Parameter	Minimum Value	Maximum Value
κ_{IC}	0.002	11
$\kappa_{IC}^{(NF)}/\kappa_{IC}^{(HF)}$	0	0.5
$\Delta\Sigma$	0	2
Ω_h	0.0001	0.37
β	30°	90°
λ	0.2	1

Table 2. Range of dimensionless parameters calculated from Table 1 using introduced scaling

The following parametric study is restricted to the range of values of dimensionless parameters shown in Table 2, as practically required.

4. Results of parametric study

We performed numerical simulations of the HF propagation and interaction with the preexisting NF by use of the modified CSIRO code (with stress-and-energy initiation criterion) [12, 20]. Dimensionless parameters of the simulations have been selected within the range specified in Table 2. Systematic analysis of the obtained results of HF-NF interaction allowed us to project them onto the specific parametric diagrams containing dimensionless toughness of the rock, fracture intersection angle, stress contrast, frictional coefficient. and relative toughness of the NF. For better representation they are divided into several cross sections of one global multiparametrical cube.

http://dx.doi.org/10.5772/55941

4.1. Dimensionless toughness κ_{IC} vs. angle β diagram

Fig. 4 shows the results of a large number of numerical computations performed with various independent parameters of the problem. They are projected on the diagram of dimensionless toughness versus interaction angle. These results represent the final outcome of the HF-NF interaction in terms of either fracture crossing or arresting at the NF. We observe that the HF crosses the NF predominantly at large angles of intersection (i.e., close to 90°) and smaller values of dimensionless toughness as expected. Note that the dimensionless toughness κ_{IC} we used for plotting depends not only on the Mode I toughness but also on the injection rate and fluid viscosity, as seen from Eqs. (22-23). If the fluid viscosity μ or the flow rate at the fracture inlet Q increases, the value of the dimensionless toughness decreases and the crossing behavior becomes more favorable.

The computations have been performed for several values of in-situ rock stress difference $\Delta\Sigma$. To denote this important parameter in the plotted results, we have used different colors for different values of $\Delta\Sigma$. To separate the crossing or arrest tendency at small stress contrast from the similar tendency at large stress contrast, we have presented the results (Fig. 4) in two diagrams for the small and large values of $\Delta\Sigma$ respectively. After using such a representation of the results, one can still observe that some points remained nonseparated and overlapped. For example, in the bottom diagram, the results from the computations with different stress contrast coincide at the same point in the angle-toughness diagram. They can have opposite outcome as shown by arrows at the bottom of Fig. 4.

4.2. κ_{IC} vs.$\Delta\Sigma$ diagram

The next series of parametric diagrams represent the results of numerical experiments in the dimensional toughness vs. stress contrast cross section. This representation better emphasizes the role of the dimensionless relative stress and with the flow rate and viscosity that are inversely proportional to the dimensionless toughness. Plots in Fig. 5 clearly show that the higher relative stress difference $\Delta\Sigma$, the larger the region of the dimensionless toughness values where fracture crossing occurs. The highest threshold value of the dimensionless toughness for crossing behavior increases with the stress contrast; i.e., in the formations with high stress contrast the crossing behavior will most probably happen even with low viscosity and/or low pumping rate during fracturing jobs. At the same time, it is unlikely that the rock with relatively small stress difference $\Delta\Sigma<1$ will support fracture crossing unless the dimensionless toughness value is sufficiently decreased by stronger injection power (larger pumping rates or higher fluid viscosity). This is especially the case if the preferential inclination of the NFs with respect to the orientation of the HF is far from 90°.

4.3. λ vs. $\kappa_{IC(NF)}$ / κ_{IC} diagram

Next we analyzed the influence of the friction coefficient λ and the relative NF Mode I toughness $\kappa_{IC(NF)}/\kappa_{IC}$ on the result of HF-NF interaction (Fig. 6). In this series of numerical tests we observe a sharp boundary for the friction coefficient values where the crossing behavior

ceases. We also observed that there is no influence of the relative NF toughness, compared to that of the friction, although this parameter deserves more attention in the future.

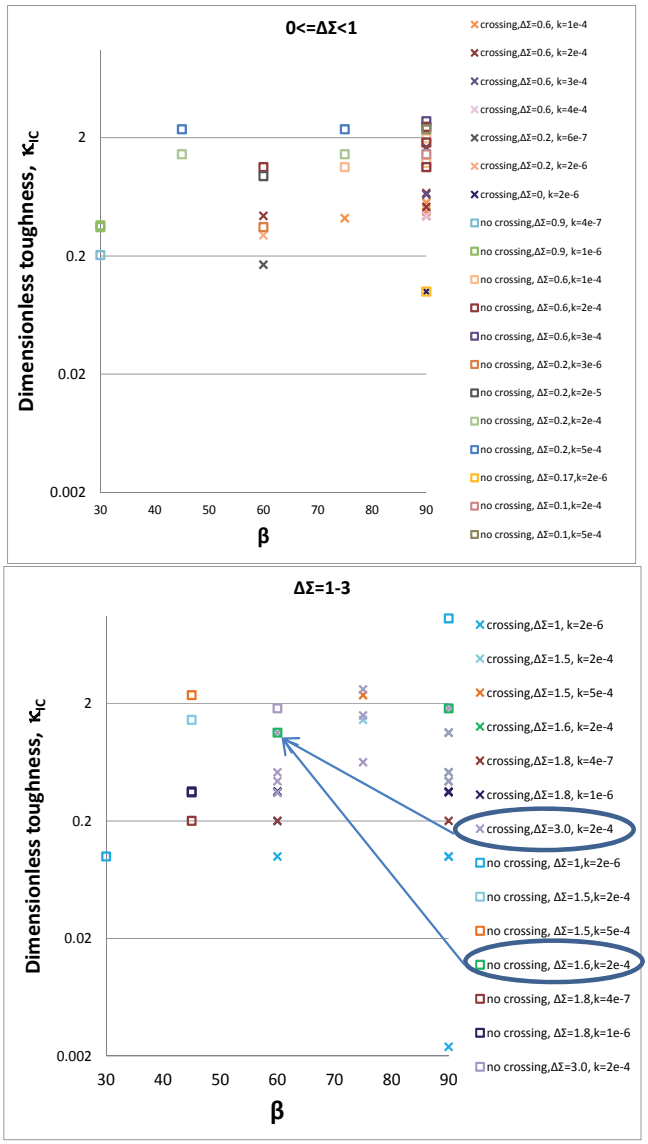

Figure 4. Crossing vs. arresting diagram in (κ_{IC}, β) for different range of relative stress contrast. $\kappa_{IC}^{(NF)} = 0$.

http://dx.doi.org/10.5772/55941

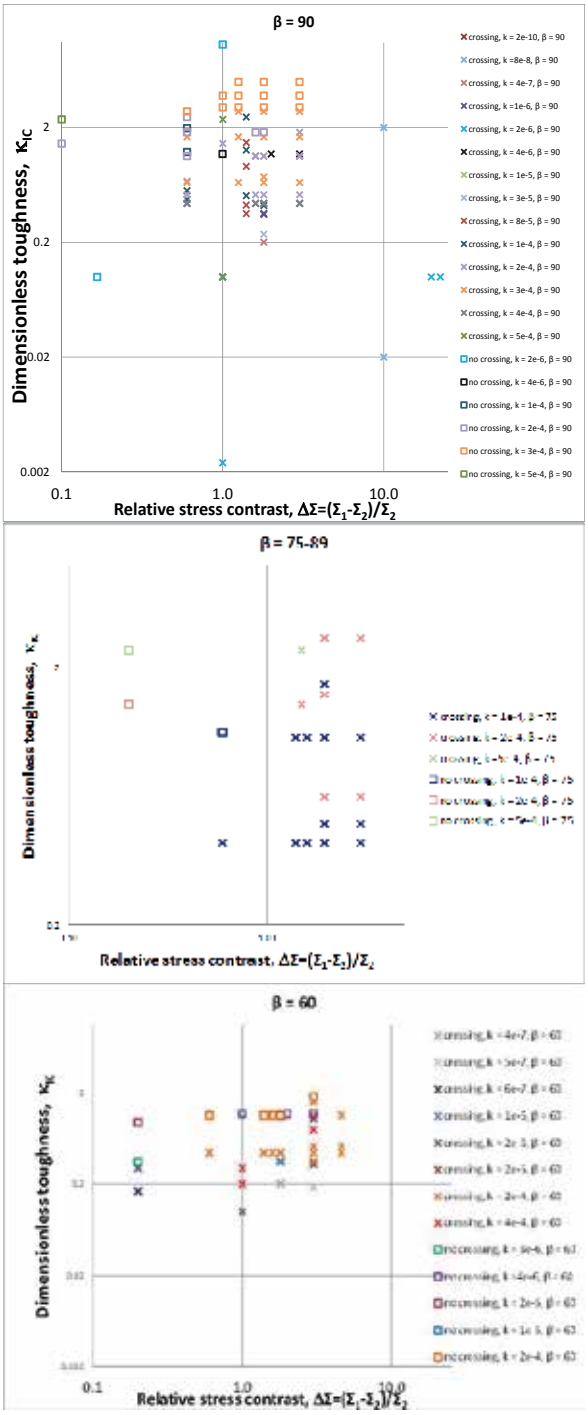

Figure 5. Crossing vs. arresting diagram in (κ_{IC}, $\Delta\Sigma$) for different angles of fracture interaction. $\kappa_{IC}^{(NF)} = 0$.

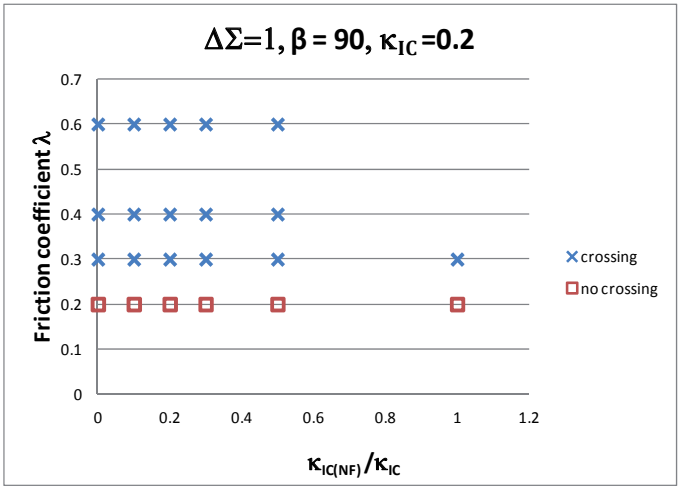

Figure 6. Crossing vs. arresting diagram in (λ, $\kappa_{IC(NF)}/\kappa_{IC}$).

5. Effect of NF permeability

5.1. Analytical model

The numerical investigation of the HF-NF interaction with the help of MineHF2D code did not allow us to extract the dependency of the fracture interaction outcome on the permeability of the NF. To accomplish the goal of the parametric study, we built an analytical model of the T-shape contact between the HF and the permeable NF with the following assumptions (Fig. 7).

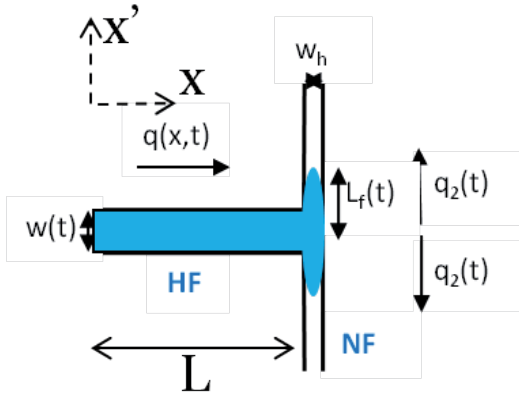

Figure 7. Illustration of the HF-NF interaction scheme in analytical model

http://dx.doi.org/10.5772/55941

Consider the HF in a T-shape contact with a permeable NF as schematically shown in Fig. 7. Both fractures have uniformly distributed but different hydraulic openings. After the contact, the fracturing fluid penetrates the NF from the tip of the HF. Representation of the HF with blunted tip of width w is realistic when the HF contacts a frictionally weak NF [25]. The NF remains mechanically closed with finite hydraulic conductivity described by the residual hydraulic opening w_h. It is assumed that w_h does change with time and the NF remains mechanically closed all the time. We also neglect fluid lag in the HF and solve the problem assuming that the injected fluid entirely fills the HF right after contact. The fracturing fluid penetrates the NF from the junction point symmetrically on both sides along the NF (Fig. 7).

First, we prescribe the uniform distribution of the fluid pressure along the HF from the inlet point to the contact point:

$$p_f(x,t) = p_0(t) \tag{24}$$

where p_0 is the fluid pressure at the inlet. The approximate solution of the elasticity equation for the opening of the HF w can be written as

$$w(t) = \frac{4L}{E'}[p_0(t) - \sigma_2] \tag{25}$$

where σ_2 is the minimum far-field stress.

Poiseuille's law and continuity equation for the fluid flow $q(x,t)$ along the HF are described by Eqns. (6–7). The fluid flow rate at the junction point is denoted as

$$q(x = L) = q^* \tag{26}$$

As long as $w = w_h = \text{const}$ along the NF, the Poiseuille's law and continuity equation can be written for the fluid flow along the NF as

$$\begin{cases} q_2 = -\dfrac{w_h^3}{12\mu}\dfrac{dp_{f^2}}{dx'} \\ \dfrac{dq_2}{dx'} \end{cases} \tag{27}$$

where q_2 is the fluid flow rate along the NF on one side of the junction point (see Fig. 7), and $p_{f2}(x',t)$ is the distribution of fluid pressure in the NF. As the fluid penetrates the NF symmetrically from the junction point, using (26) we can write

$$q_2(t) = \frac{1}{2} q^*(t) \tag{28}$$

For steady flow the fluid pressure at the fracture junction point must be the same at the HF and NF sides, so using assumption (24) we write

$$p_{f2}(x' = 0) = p_f(x = L) \approx p_0(t) \tag{29}$$

The total fluid mass balance in the system of the HF and the NF can be written by making use of continuity equations (6) and (27), inlet condition (10), and elasticity equation (25) as follows:

$$Q = \frac{d}{dt}\left(\int_0^L w dx + 2\int_0^{L_f} w_h dx'\right) = \frac{4L^2}{E'}\frac{dp_0}{dt} + 2w_h \dot{L}_f \tag{30}$$

where L_f is the length of fluid penetration into the NF, and the upper point denotes the differentiation with respect to time. Using now the fluid flow equations (27) and the pressure relationship at the junction point (29), we can write

$$q_2 = w_h \dot{L}_f = \frac{{w_h}^3}{12\mu}\frac{p_0}{L_f} \tag{31}$$

Thus, from (30) and (31) we obtain the following system of ordinary differential equations for the fluid penetration length L_f and fluid pressure at the inlet p_0

$$\begin{cases} \dot{L}_f = \dfrac{w_h^2}{12\mu}\dfrac{p_0}{L_f} \\ Q - 2w_h \dot{L}_f = \dfrac{4L^2}{E'}\dot{p}_0 \end{cases} \tag{32}$$

The solution of these equations can be found after setting up the initial condition at the time of fracture contact, $t = 0$. We presume the fluid pressure at the HF tip is prescribed and there is not yet fracturing fluid penetration into the NF. The initial conditions are thus written as

$$\begin{cases} p_0(0) = p_{00} \\ L_f(0) = 0 \end{cases} \tag{33}$$

http://dx.doi.org/10.5772/55941

Rewriting the equations (32) and initial conditions (33) in terms of dimensionless parameters already introduced, and using substitutions $L_f = L\,\gamma_f$, $w_h = W\Psi_h$, $p_0 = P\Pi_0$, $t = T\tau$, we get

$$\begin{cases} \dot{\gamma}_f = \Psi_h^2 \dfrac{\Pi_0}{\gamma_f} \\ 1 - 2\Psi_h \dot{\gamma}_f = 4\dot{\Pi}_0 \\ \gamma_f(0) = 0 \\ \Pi_0(0) = \Pi_{00} \end{cases} \tag{34}$$

Numerical solution of the problem (34) is plotted in Fig. 8. Fluid penetration length (Fig. 8, left) grows fast at the very beginning ($\tau << 1$) and turns to nearly linear dependence on time when $\tau > 1$. The pressure at the junction point drops right after the HF-NF contact (Fig. 8, right). The velocity of pressure drop rapidly slows, and after the certain inflection point it starts to grow linearly. As it will be shown later, the inflection point depends on the NF permeability and initial fluid pressure at fracture contact.

The numerical solution helps in the general solution of the problem (34) but hides the parametrical dependency of the fluid penetration and pressure behavior shown in Fig. 8. To evaluate the pressure inflection point τ^* and reveal the parametric sensitivity of the velocity of fluid penetration into the NF and the HF pressure dynamics during the contact, we further investigate the asymptotical behavior of the fluid length γ_f and the fluid pressure Π_0 at the very beginning of fracture contact and at large time after contact.

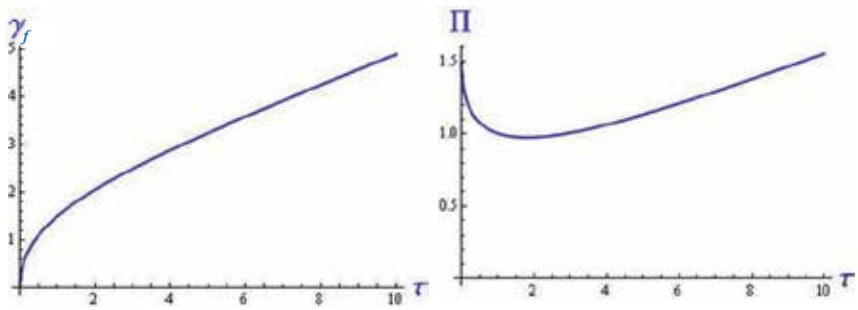

Figure 8. Analytical solution of the dimensionless problem for fluid penetration into NF (34) for dimensionless permeability $\Psi_h = 1$, and initial pressure $\Pi_{00} = 1.5$. Left plot is the dimensionless fluid front propagation along the NF in time. Right plot is the change of dimensionless pressure at the HF-NF intersection point.

Early-time (left) asymptote: $0 < \tau << \tau^*$.

Let us assume the following law for the fluid pressure and penetration length at the beginning of fracture contact,

$$\begin{aligned} \Pi_0 &= \Pi_{00} - \Pi_1\sqrt{\tau} \\ \gamma_f &= v_f\sqrt{\tau} \end{aligned} \tag{35}$$

where Π_1 and v_f are unknown positive constants that must be determined. After substitution of (35) in (34), in the limit $\tau \ll 1$ we arrive at the following relations for Π_1 and v_f:

$$\begin{cases} v_f^2 = 2\Psi_h^2\Pi_{00} \\ 2\Pi_1 = \Psi_h v_f \end{cases} \tag{36}$$

The unknown constants Π_1 and v_f are thus found as

$$\begin{cases} \Pi_1 = \Psi_h^2\sqrt{\Pi_{00}/2} \\ \nu_f = \Psi_h\sqrt{2\Pi_{00}} \end{cases} \tag{37}$$

From this analysis it is obvious that the rate of fluid pressure drop at the beginning of fracture contact as well as the velocity of fluid penetration into the NF are affected more strongly by the permeability of the NF Ψ_h than by the initial fluid pressure in the HF Π_{00}.

The asymptotes (35) can be plotted with the accurate numerical solution of the equations (34). Fig. 9 shows the comparison of the numerical solution of the problem and asymptotes (35) with coefficients (37).

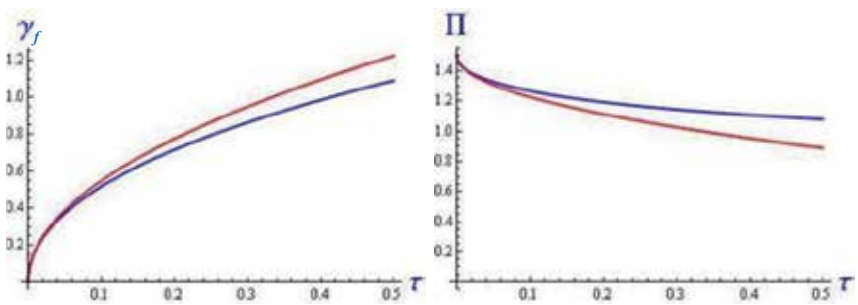

Figure 9. Asymptotic (red) and numerical (blue) solutions for the dimensionless fluid penetration length (left) and fluid pressure in junction point (right) at the early time of fracture contact

Large-time (right) asymptote: $\tau >> \tau^*$

Now consider the large-time behavior of the system of contacted fractures. In that limit let us employ the linear asymptotes for the pressure and fluid penetration length

http://dx.doi.org/10.5772/55941

$$\begin{aligned} \Pi_0 &= \Pi_1 \tau \\ \gamma_f &= v_f \tau \end{aligned} \tag{38}$$

where Π_1 and v_f are new unknown positive constants. From (34) we then obtain

$$\begin{cases} v_f^2 = \Psi_h^2 \, \Pi_1 \\ 1 - 2\Psi_h v_f = 4\Pi_1 \end{cases} \tag{39}$$

Solution of (39) for the unknown Π_1 and v_f gives the expressions

$$\begin{cases} \Pi_1 = \dfrac{1}{4} - \dfrac{\Psi_h^2}{8}\left[\sqrt{\Psi_h^4 + 4} - \Psi_h^2\right] \\ \nu_f = \dfrac{\Psi_h}{4}\left[\sqrt{\Psi_h^4 + 4} - \Psi_h^2\right] \end{cases} \tag{40}$$

Comparison of the asymptotes (38) with numerical solution of the equations (34) gives excellent agreement. Fig. 10 demonstrates this comparison.

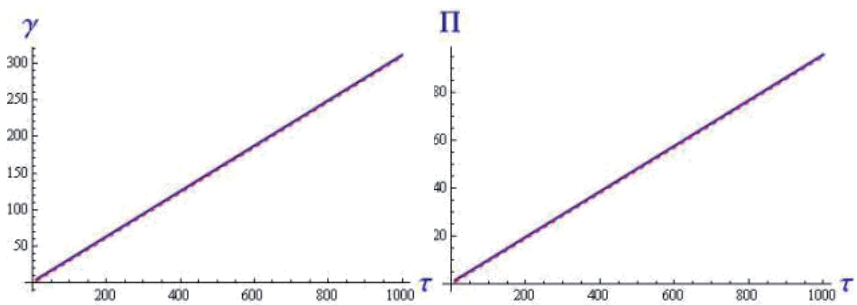

Figure 10. Asymptotic (red) and numerical (blue) solutions for the dimensionless fluid penetration length (left) and fluid pressure at junction point at large time of fracture contact

The inflection point: $\tau = \tau^*$, $\dot{\Pi}_0 = 0$

To find the parametric expression for the inflection point in time scale, where the fluid pressure starts to increase, we substitute $\dot{\Pi}_0 = 0$ into the second equation of (34) and have

$$\dot{\gamma}_f = \frac{1}{2\Psi_h} \tag{41}$$

If τ^* is close to zero, the velocity of fluid penetration can be taken from the early-time solution (35) with (37):

$$\dot{\gamma}_f = \Psi_h \sqrt{\frac{\Pi_{00}}{2\tau^*}} \tag{42}$$

Comparing now (41) with (42), one obtains the following estimation for the time of pressure drop-growth inflection:

$$\tau^* = 2\Pi_{00}\Psi_h^4 \tag{43}$$

This simple expression tells again that practically it is the magnitude of NF permeability that plays a key role in the transient pressure behavior and intensity of NF infiltration by the fracturing fluid.

5.2. Numerical simulations

To validate the analytical model predictions we performed several numerical simulations by MineHF2D code with $\kappa_{IC}=0.32$, $\Sigma_2=0.8$, $\Delta\Sigma=1$, $\beta=90$, $\lambda=0.2$ and various permeabilities of the NF. The residual hydraulic opening of the NF Ω_h in these numerical runs was intentionally chosen to be a magnitude close to the average opening of the HF at the point of intersection.

Fig. 11 shows the results of simulations for three different values of the residual hydraulic opening prescribed at the NF Ω_h : 1 mm, 0.1 mm, and 0.01 mm. In all these test cases the average opening of the HF close to the fracture intersection was 3 mm. Pressure records at the injection point and the length of fluid penetration into the NF after the fracture contact are compared with predictions of the analytical model and shown in Fig. 11 (left top and left bottom).

For two cases with lower NF permeability (green-, red-dashed line in Fig. 11) the pressure starts to grow immediately after the fracture intersection. As the fluid weakly propagates into the NF in these cases, the net pressure and HF opening almost equally quickly grow with time. In the second example, for Ω_h = 0.1 mm at t = 0.55 s, the NF opens mechanically as a result of increased net pressure of the penetrated fluid and the penetration rate increases (red line, Fig. 11); the pressure and opening of the HF decrease because of the enhanced leakoff along the NF.

In the third case, when the residual hydraulic opening at the NF is of the same order of magnitude as the average opening of the HF (3 times less), we observe comparably fast fluid leakoff into the NF after the contact (blue line, Fig. 11), which given the fixed injection rate into the HF does not allow the net pressure in the HF to grow. Very soon after the fluid reaches the tips of the NF prescribed in the numerical model (1.5 m in this example), the NF rapidly opens mechanically and the HF opening starts to grow.

http://dx.doi.org/10.5772/55941

Careful investigation of the complex dynamics of fluid-coupled fracture interaction deserves a separate work.

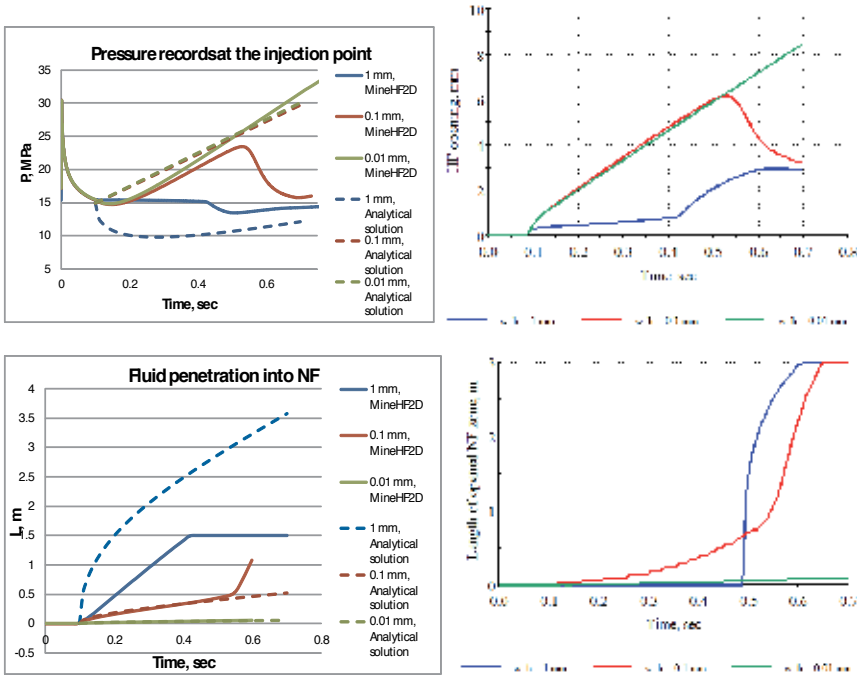

Figure 11. Results of numerical experiments with $\kappa_{IC}=0.32$, $\Sigma_2=0.8$, $\Delta\Sigma=1$, $\beta=90$, $\lambda=0.2$ and three values of residual hydraulic opening at the NF permeability (blue: 1 mm; red: 0.1 mm; green: 0.01 mm). Top left: fluid pressure changes at the inlet. Top right: opening of the HF at junction. Bottom left: fluid penetration length along the NF. Bottom right: total length of the mechanically open zone at the NF in meters.

6. Conclusions

In conclusion, we conducted an extensive parametric study of the problem of HF-NF interaction by means of numerical simulator MineHF2D developed by CSIRO. This research was mainly focused on the result of fracture interaction in terms of crossing or arresting of the HF at the NF as a function of the most sensitive parameters, such as fracture approach angle β, friction coefficient λ, dimensionless toughness κ_{IC}, inversely proportional to the injection rate and fluid viscosity, relative stress contrast$\Delta\Sigma$, and the NF permeability k.

In a system of interacting hydraulic and NFs, the number of physical parameters that can affect the result of interaction is large. The proper scaling of the problem allowed us to decrease the number of independent parameters from 14 dimensional parameters to 9 dimensionless parameters, and effectively perform the parametric study in the space of 6 of the most critical dimensionless parameters. We summarized the results of the large number of numerical

simulations performed in the range of parameters values relevant to fracturing field operations. The resultant solid picture of parametric sensitivity to the arresting versus crossing behavior helps provide a better understanding of the relative role of each parameter. In particular, aside from the well-known effect of the fracture approach angle and stress contrast, we revealed the influence of the injection rate and fluid viscosity on reducing the angle and stress threshold for HF-NF crossing.

The presented analytical model of the infiltration of the permeable NF by the contact with the HF allowed us to understand a parametric dependency of the HF pressure response and fracturing fluid penetration at early and large time after the HF-NF contact. We have seen a predominant role of the hydraulic permeability of the NF in the evaluation of the pressure decay curve after the fracture contact. It appears that at T-shape fracture contact, initially the pressure quickly drops and after some saturation it rebounds to grow. The rebound time of pressure response τ^* separating the early and large time regimes is strongly dependent on the permeability of the NF (as its forth power) and to a much lesser extent by fluid pressure at the HF-NF junction (linearly). Such fast pressure decay means that during $\tau < \tau^*$ the fluid penetration supports temporal arrest of the HF by the NF. Independent numerical computations with large residual aperture of the NF led us to the conclusion that the result of HF-NF interaction is affected by permeable properties of the NF only when the residual opening of the NF is comparable in magnitude with the opening of the HF at the contact.

Acknowledgements

The authors are grateful to Schlumberger for permission to publish this paper. Special thanks go to Xi Zhang (CSIRO) for his constant attention and enormous help with improvement of the numerical code MineHF2D during the study, and to Xiaowei Weng (Schlumberger) for constructive discussions of the obtained results and valuable recommendations.

Author details

Dimitry Chuprakov[1*], Olga Melchaeva[2,3] and Romain Prioul[1]

*Address all correspondence to: dchuprakov@slb.com

1 Schlumberger-Doll Research, Cambridge, MA, USA

2 Schlumberger-Doll Research, Cambridge, MA, USA

3 JSC Gazprom neft, Saint Petersburg, Russian Federation

http://dx.doi.org/10.5772/55941

References

[1] Valko P, Economides MJ. Hydraulic Fracture Mechanics: John Wiley & Sons; 1995.

[2] Fjær E, Holt RM, Horsrud P, Raaen AM, Risnes R. Petroleum related rock mechanics, Chapter 11 Mechanics of hydraulic fracturing. In: Fjaer E, Raaen AM, Risnes R, Holt RM, Horsrud P, editors. 2008. p. 369-390.

[3] Warpinski NR, Mayerhofer MJ, Vincent MC, Cipolla CL, Lolon EP. Stimulating Unconventional Reservoirs: Maximizing Network Growth While Optimizing Fracture Conductivity, SPE-114173-PA, 2009.

[4] Vincent M. Restimulation of Unconventional Reservoirs: When Are Refracs Beneficial? SPE-136757-PA, 2011.

[5] Vincent MC. Examining Our Assumptions—Have Oversimplifications Jeopardized Our Ability to Design Optimal Fracture Treatments? SPE Hydraulic Fracturing Technology Conference; The Woodlands, Texas, 2009.

[6] Thiercelin M. Hydraulic fracture propagation in discontinuous media. Presented at the International Conference on Rock Joints and Jointed Rock Masses, Tucson, Arizona, USA, 7-8 January. 2009.

[7] Cipolla CL, Warpinski NR, Mayerhofer MJ. Hydraulic Fracture Complexity: Diagnosis, Remediation, and Exploitation. SPE Asia Pacific Oil and Gas Conference and Exhibition; 01/01/2008; Perth, Australia: Society of Petroleum Engineers; 2008.

[8] Daneshy AA. Hydraulic Fracture Propagation in the Presence of Planes of Weakness. SPE European Spring Meeting; Amsterdam, Netherlands, 1974.

[9] Keer LM, Chen SH. Intersection of a Pressurized Crack with a Joint. Journal of Geophysical Research. 1981;86(B2):1032-8.

[10] Blanton TL. An Experimental Study of Interaction Between Hydraulically Induced and Pre-Existing Fractures. SPE Unconventional Gas Recovery Symposium; Pittsburgh, Pennsylvania, 1982.

[11] Cooke ML, Underwood CA. Fracture termination and step-over at bedding interfaces due to frictional slip and interface opening. J Struct Geol. 2001 Feb-Mar;23(2-3): 223-38.

[12] Zhang X, Jeffrey RG. The role of friction and secondary flaws on deflection and reinitiation of HFs at orthogonal pre-existing fractures. Geophys J Int. 2006 Sep;166(3): 1454-65.

[13] Zhang X, Jeffrey RG. Reinitiation or termination of fluid-driven fractures at frictional bedding interfaces. J Geophys Res-Sol Ea. 2008 Aug 28;113(B8)

[14] Zhang ZX, Kou SQ, Lindqvist PA, Yu Y. Relationship between fracture toughness and tensile strength of rock. Strength Theories: Applications, Development and Prospects for 21st Century. 1998:215-9.

[15] Gu H, Weng X, Lund JB, Mack MG, Ganguly U, Suarez-Rivera R. Hydraulic Fracture Crossing Natural Fracture at Non-Orthogonal Angles, A Criterion, Its Validation and Applications. SPE Hydraulic Fracturing Technology Conference; The Woodlands, Texas, 2011.

[16] Taleghani AD. Fracture Re-Initiation As a Possible Branching Mechanism During Hydraulic Fracturing. 44th US Rock Mechanics Symposium and 5th US-Canada Rock Mechanics Symposium; Salt Lake City, Utah: American Rock Mechanics Association; 2010.

[17] Blanton TL. Propagation of Hydraulically and Dynamically Induced Fractures in Naturally Fractured Reservoirs. SPE Unconventional Gas Technology Symposium; Louisville, Kentucky, 1986.

[18] Renshaw CE, Pollard DD. An Experimentally Verified Criterion for Propagation across Unbounded Frictional Interfaces in Brittle, Linear Elastic-Materials. International Journal of Rock Mechanics and Mining Sciences & Geomechanics Abstracts. 1995 Apr; 32(3):237-49.

[19] H.Gu, X.Weng. Criterion For Fractures Crossing Frictional Interfaces At Non-orthogonal Angles. 44th US Rock Mechanics Symposium and 5th US-Canada Rock Mechanics Symposium; Salt Lake City, Utah: American Rock Mechanics Association; 2010.

[20] Zhang X, Jeffrey RG, Thiercelin M. Mechanics of fluid-driven fracture growth in naturally fractured reservoirs with simple network geometries. Journal of Geophysical Research. 2009;114.

[21] Beugelsdijk LJL, Pater CJd, Sato K. Experimental Hydraulic Fracture Propagation in a Multi-Fractured Medium. SPE Asia Pacific Conference on Integrated Modelling for Asset Management; Yokohama, Japan, 2000.

[22] Pater CJd, Beugelsdijk LJL. Experiments and numerical simulation of hydraulic fracturing in naturally fractured rock. 25-29 June 2005: American Rock Mechanics Association; 2005.

[23] Wu R, Kresse O, Weng X, Cohen C-e, Gu H. Modeling of Interaction of Hydraulic Fractures in Complex Fracture Networks. SPE Hydraulic Fracturing Technology Conference; The Woodlands, Texas: Society of Petroleum Engineers; 2012.

[24] Zhang X, Thiercelin MJ, Jeffrey RG. Effects of Frictional Geological Discontinuities on Hydraulic Fracture Propagation. SPE Hydraulic Fracturing Technology Conference; College Station, Texas USA: Society of Petroleum Engineers; 2007.

[25] Warpinski NR, Teufel LW. Influence of Geologic Discontinuities on Hydraulic Fracture Propagation. SPE Journal of Petroleum Technology. 1987; 39(2).

[26] Chuprakov DA, Akulich AV, Siebrits E, Thiercelin M. Hydraulic-Fracture Propagation in a Naturally Fractured Reservoir. SPE Production & Operations. 2011; 26(1).

[27] Chuprakov D, Melchaeva O, Prioul R. Injection-sensitive mechanics of HF interaction with discontinuities. The 47th US Rock Mechanics Symposium (USRMS); San Francisco, CA, 2013.

[28] Kresse O, Weng X, Chuprakov D, Prioul R. Effect of Flow Rate and Viscosity on Complex Fracture Development in UFM model. The International Conference for Effective and Sustainable Hydraulic Fracturing; 20-22 May 2013; Brisbane, Australia, 2013.

[29] Zhang X, Jeffrey RG, Thiercelin M. Deflection and propagation of fluid-driven fractures at frictional bedding interfaces: A numerical investigation. J Struct Geol. 2007; 29(3):396-410.

[30] Crouch SL, Starfield AM. Boundary Element Methods In Solid Mechanics: George Allen & Unwin; 1983.

[31] Cheng AHD, Detournay E. On singular integral equations and fundamental solutions of poroelasticity. Int J Solids Struct. 1998 Dec;35(34-35):4521-55.

[32] Hills DA, Kelly PA, Dai DN, Korsunsky AM. Solution of crack problems. The distributed dislocation technique. Solid Mechanics and its Applications. 1996;44.

[33] Leguillon D. Strength or toughness? A criterion for crack onset at a notch. Eur J Mech a-Solid. 2002 Jan-Feb;21(1):61-72.

[34] Erdogan F, Sih GC. On the crack extension in plates under plane loading and transverse shear. Journal of Basic Engineering. 1963;85:519-27.

[35] Prioul R, Karpfinger F, Deenadayalu C, Suarez-Rivera R. Improving Fracture Initiation Predictions on Arbitrarily Oriented Wells in Anisotropic Shales. Canadian Unconventional Resources Conference; 15-17 November 2011; Alberta, Canada: Society of Petroleum Engineers; 2011.

[36] King GE. Thirty Years of Gas Shale Fracturing: What Have We Learned? SPE Annual Technical Conference and Exhibition; Florence, Italy: Society of Petroleum Engineers; 2010.

Chapter 9

Effect of Flow Rate and Viscosity on Complex Fracture Development in UFM Model

Olga Kresse, Xiaowei Weng, Dimitry Chuprakov,
Romain Prioul and Charles Cohen

Additional information is available at the end of the chapter

http://dx.doi.org/10.5772/56406

Abstract

A recently developed unconventional fracture model (UFM®) is able to simulate complex fracture networks propagation in a formation with pre-existing natural fractures. Multiple fracture branches can propagate at the same time and crisscross each other. The behaviour of a hydraulic fracture when it intersects a natural fracture, whether being arrested, crossing, creating an offset, or dilating the natural fracture, plays a key role in predicting the resulting fracture footprint, microseismicity, and improving production evaluation. It is therefore critical to properly model the fracture interaction in a complex fracture model such as UFM.

A new crossing model, called OpenT, taking into account the effect of flow rate and fluid viscosity on the hydraulic/natural fracture crossing behaviour is integrated in UFM simulator. The previous fracture crossing model is primarily based on the stress field at the approaching hydraulic fracture tip and its interaction with the natural fracture. A new elasticity solution for the fracture contact has been developed. The new OpenT semi-analytical crossing model quantifies the localized stress field induced in the natural fracture and in the rock and evaluates the size and length of open and shear slippage zones along the natural fracture. The natural fracture activation and stress field near the intersection point are strongly dependent on the contacting hydraulic fracture opening and thus on fluid flow rate and viscosity. This new model is validated against laboratory experimental results and an advanced numerical model.

In this paper we present the results of several test cases showing the influence of injection rate and fluid viscosity on the generated hydraulic fracture footprint in formations with pre-

existing natural fractures. The influence of the stress field anisotropy, intersection angle, as well as natural fractures properties are also important and are discussed. The results are then compared with the simulations using the previous crossing model which does not account for the influence of fluid properties.

1. Introduction

It is believed that complexity of the fracture network created during hydraulic fracturing treatments in formations with pre-existing natural fractures is caused mostly by the interaction between hydraulic and natural fractures. The understanding and proper modelling of the mechanism of hydraulic-natural fractures interactions are keys to explain fracture complexity and the microseismic events observed during hydraulic fracturing treatments, and therefore to properly predict production.

When a hydraulic fracture (HF) intercepts a natural fracture (NF) it can cross the NF, open (dilate) the NF, or be arrested at NF. If the hydraulic fracture crosses the natural fracture, it remains planar, with the possibility to open the intersected NF if the fluid pressure at the intersection exceeds the effective stress acting on the NF. If the HF does not cross the NF, it can dilate and eventually propagate into the NF, which leads to more complex fracture network. So the crossing criterion in general controls the complexity of the resulting fracture network.

The interaction between HF and NF depends on the in-situ rock stresses, mechanical properties of the rock, properties of natural fractures, and the hydraulic fracture treatment parameters including fracturing fluid properties and injection rate. During the last decades, extensive theoretical, numerical, and experimental work has been done to investigate, explain, and develop the rules controlling HF/NF interaction. Among the main contributions to this topic are the work listed in references [1-15].

Most of the existing crossing models do not take into account fluid properties due to the complexity of modelling fluid-solid interaction in the vicinity of the intersection, so crossing behaviour is explained purely from elasticity point of view. Field and laboratory observations, however, show that fluid properties are important and should be accounted for [9, 16].

It is well known that the microseismic events cloud is related to the hydraulic fracture propagation pattern which in turn strongly depends on the HF/NF interaction rules [17].

Figure 1 shows the microseismic events observed in the same well first treated with a cross-linked gel, and then re-fractured with slick water [16]. Cross-linked gel was pumped at 70 bpm for about 3 hours with sand concentration ramped up to 3 ppg. Most of the microseismic activity suggests longitudinal fracturing with only modest activation of natural fractures, resulting in a narrow stimulated network (less than 500 feet from the wellbore in many sections of the lateral), as seen in Figure 1a with resulting Stimulated Reservoir Volume (SRV) equal to 430 million ft^3. During the full re-frac conducted the following day 60,000 bbl of slick water and 285,000 lb of sand was pumped at 125-130 bpm for most of the treatment lasting 6.5 hours.

http://dx.doi.org/10.5772/56406

The stimulated network was approximately 1500ft wide and 3,000 ft long (Figure 1b) with considerable height growth and SRV of 1450 million ft^3. Clearly, the re-fracturing treatment stimulated a much larger volume of rock than the initial gel treatment (1450 million ft^3 vs 430 million ft^3), and showed the patterns of development that suggested the opening of both northeast and northwest trending fractures [16].

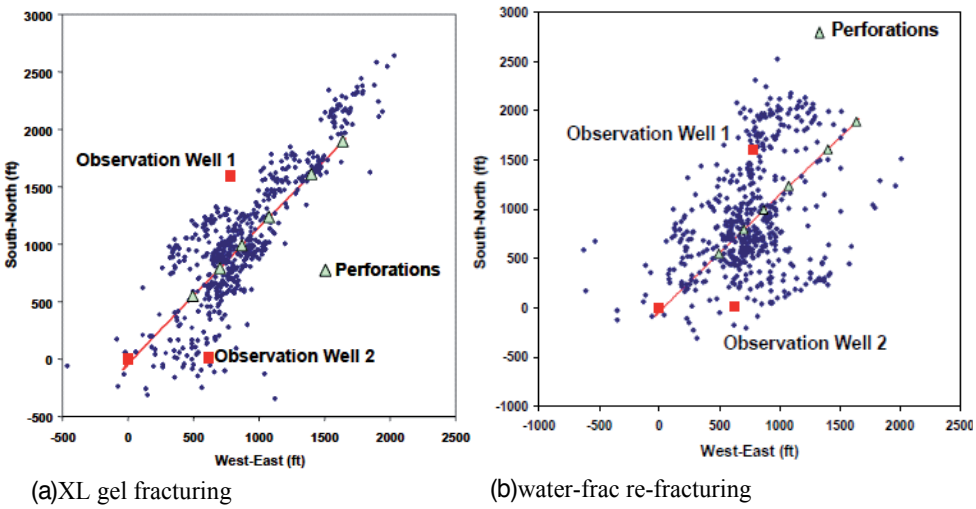

(a)XL gel fracturing (b)water-frac re-fracturing

Figure 1. Single-well microseismic event locations for XL gel stimulation and water-frac re-fracturing treatment, horizontal Barnett Shale well [16]

This field example indicates the importance of proper consideration of fluid properties when modelling the interaction of hydraulic fractures with pre-existing natural fractures. In general it is observed that for the same field conditions more viscous fluid tends to cross the natural fractures more easily, while slick water tends to penetrate into the natural fractures more easily and open them without crossing. Pumping rate as well as rock properties should also be taken into account.

The importance of fluid properties on the created hydraulic fracture network has been mentioned in some experimental and numerical studies [9, 18, 19]. The experimental study of the influence of flow rate and fracturing fluid viscosity on the hydraulic fracture geometry have been performed in [9] based on analysis of different $Q\mu$ value (product of the injection rate and fracturing fluid viscosity). The experiments show that with low $Q\mu$ value fluid tends to leak into the pre-existing discontinuities despite the influence of fluid pressure and once the discontinuity accepts fluid, the pressure can rise far above the confining stress without inducing new fractures. With large $Q\mu$ value the hydraulic fracture tends to cross natural fracture due to increase of the pressurization rate.

The influence of fluid injection rate and viscosity on the amount of the tensile failure in the rock with natural fractures has been investigated based on 3DEC DEM model in [18, 19]. For low viscosity fluid the amount of area failing in shear is dramatically higher than in the case

with high viscosity. Their results show that an increase in injection rate greatly increases the amount of tensile failure within the model leading potentially to creating more fractures, while a lower injection rate favours the creation of shear failure resulting mostly in activating (opening) pre-existing natural fractures.

A new analytical model, called OpenT, for hydraulic fracture interaction with a pre-existing discontinuity has been developed to predict the fracture crossing or deflection at the encountered interface [20, 21]. The new physically rigorous criterion of fracture re-initiation at the discontinuity has been implemented, which combines both stress criterion and energy release rate. It has been shown that the OpenT model adequately predicts the fracture crossing of non-cohesive frictional interfaces observed in various laboratory experiments with different interface orientations with respect to hydraulic fractures [21].

The new crossing model predicts the dimensions of open and sliding zones created at cohesive and non-cohesive interfaces after the intersection with a fluid-driven fracture. Such information can be valuable, for example, in passive microseismic monitoring of fracture treatments in naturally fractured formations. By thoroughly examining the stress field generated by the hydraulic fracture and activated open and sliding zones at the discontinuity, it was shown that the new fracture initiation point is shifted along the inclined interface. The model predicts the offset of a secondary fracture as a function of the geometrical, loading, and mechanical parameters of the system, such as the fracture-interaction angle, in-situ stress components and fracture toughness in rock.

New OpenT crossing model incorporates the influence of rock properties (local horizontal stresses, rock tensile strength, toughness, pore pressure, Young's modulus, Poisson ratio), natural fracture properties (friction coefficient, toughness, cohesion, permeability), intersection angle between hydraulic and natural fractures, fracturing fluid properties (viscosity, tip pressure), and injection rate to define crossing rules.

This new OpenT model has been validated against laboratory experiments and against rigorous numerical models [3,20,21]. It was incorporated into the UFM model that simulates complex fracture network propagation in a formation with pre-existing natural fractures [22-24]. We present several UFM test cases showing the influence of injection rate and fluid viscosity on the generated hydraulic fracture footprint and production impact by comparing of two crossing criteria, the extended Renshaw & Pollard (hereafter referred as eRP) [14, 15] and the OpenT.

2. UFM model specifics

A complex fracture network model, referred to as Unconventional Fracture Model (UFM), had recently been developed [22,23,24]. The model simulates the fracture propagation, rock deformation, and fluid flow in the complex fracture network created during a fracture treatment. The model solves the fully coupled problem of fluid flow in the fracture network and the elastic deformation of the fractures, which has similar assumptions and governing

http://dx.doi.org/10.5772/56406

equations as conventional pseudo-3D fracture models. Transport equations are solved for each component of the fluids and proppants pumped. A key difference between UFM and the conventional planar fracture model is being able to simulate the interaction of hydraulic fractures with pre-existing natural fractures, i.e., determine whether a hydraulic fracture propagates through or is arrested by a natural fracture when they intersect and subsequently propagates along the natural fracture.

To properly simulate the propagation of multiple or complex fractures, the fracture model takes into account the interaction among adjacent hydraulic fracture branches, often referred to as "stress shadow" effect. It is well known that when a single planar hydraulic fracture is opened under a finite fluid net pressure, it exerts a stress field on the surrounding rock that is proportional to the net pressure. The details of stress shadow effect implemented in UFM are presented in [24].

The branching of the hydraulic fracture at the intersection with the natural fracture gives rise to the development of a complex fracture network. A crossing model that is extended from the Renshaw-Pollard [10] interface crossing criterion, applicable to any intersection angle, has been developed [14], validated against the experimental data [15], and was integrated in the UFM. The previous crossing model, showing good comparison with existing experimental data, does not account for the fluid impact on the crossing pattern.

The new crossing model (OpenT) which accounts for the fluid properties is presented in short below and is implemented in a new version of UFM.

3. New crossing model in UFM

There are a few analytical criteria describing the mechanical HF-NF interaction developed in the past [10, 11, 13, 14]. With their relative simplicity they do not take into account the influence of the fluid injection into the hydraulic fracture and the fluid infiltration into the natural fracture after contact. These criteria were designed to capture the effect of the fracture approach angle, the NF friction coefficient and the anisotropy of the in-situ stresses. To improve the description of HF-NF interaction a new analytical model that takes the mechanical influence of the HF opening and the hydraulic permeability of the NF into account has been developed.

The analytical model of the HF-NF interaction (OpenT) solves the problem of the elastic perturbation of the NF at the contact with the blunted HF tip, which is represented by a uniformly open slot (i.e. giving its name OpenT) [21]. The opening of the HF at the junction point w_T (blunted tip) develops soon after contact, and approaches the value of the average opening of the hydraulic fracture $\overline{w}$, defined by the injection rate Q and the fluid viscosity μ. In a viscosity-dominated regime, the average opening of the KGD fracture with half-length L and height H can be estimated as [25]

$$\bar{w} = 2.53\left[\frac{Q\mu L^2}{E'H}\right]^{1/4} \tag{1}$$

where $E' = E/(1-\nu^2)$, E is the Young modulus, ν is the Poisson coefficient. The OpenT model looks for the solution of the elastic problem for the NF perturbed by the HF, and outputs the profiles and boundaries of the opening and sliding zones as a result of the contact (b_o and b_s respectively shown in Figure 2, left).

The solution shows that the spatial extent of the open and sliding zones strongly depends on the fluid pressure inside the activated part of the NF. The larger the inner fluid pressure, the larger the open and sliding zones at the NF are. Consequently, it is expected that after the HF-NF contact, the injected fracturing fluid will gradually penetrate the NF with finite hydraulic permeability κ and thus enhance the inner fluid pressure within the NF, p_{NF}.

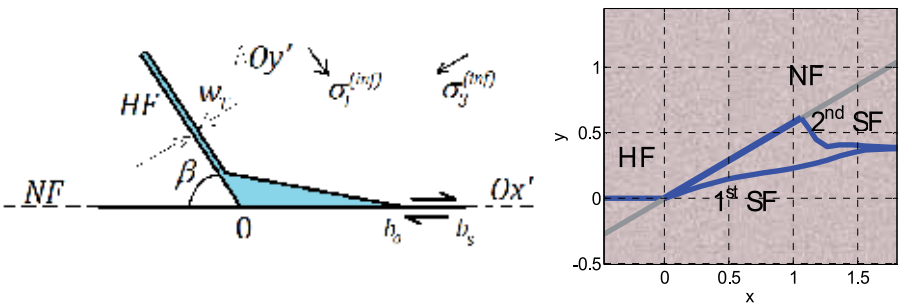

Figure 2. Left –Schematic diagram of the HF-NF interaction. Right – result of the computed HF/NF interaction with the initiation of two secondary fractures and their subsequent propagation

The average pressure of the fracturing fluid penetrated the NF can be as approximated by the following function of the contact time t

$$p_{NF}(t) = p_f \tanh\left(\sqrt{\frac{2\kappa p_f}{\mu b_s^2}t}\right) \tag{2}$$

where p_f is the fluid pressure at the contacting HF tip. As a result of the NF activation due to the fracturing, the fluid penetration becomes very active in highly permeable NFs or with low viscosity fracturing fluids. This could potentially prevent the HF from propagation across the weak interfaces.

The elasticity model of the fracture interaction enables the computation of the stress field in the vicinity of the activated NF. The analysis of the generated stress field gives the positions of sufficient tensile stress concentration where the new fractures can be nucleated. These

http://dx.doi.org/10.5772/56406

positions in most situations correspond to the two opposite tips of the NF open zone (see Figure 2, right). In order to decide on the possibility of a secondary fracture (SF) re-initiation at these points, a criterion of fracture initiation which combines both stress criterion and energy release rate has been employed. The stress criterion requires that the maximum tensile hoop stress $\sigma_{\theta\theta}$ in the vicinity of the stress concentration point x_j having direction θ_j with respect to the orientation of the NF must exceed the tensile strength of the rock T_0 along the distance δ_T

$$\sigma_{\theta\theta}(x_j, r, \theta_j)_{r<\delta_T} \leq -T_0 \tag{3}$$

In addition, the energy criterion states that the elastic energy release rate due to the incremental initiation of a fracture of length δl must overcome the critical energy release rate for the given rock

$$\Im_{inc}(\delta l) > \Im_{1C}, \quad \delta l < \delta_T \tag{4}$$

The length of the fracture must not exceed the critical stress zone, δ_T. The mixed stress-energy criterion has been verified experimentally [26].

The model of HF-NF re-initiation has been validated against the results of various laboratory block tests [11, 12, 15]. The predictions of the analytical model for crossing and arresting behaviour agree with the experimental results for various fracture intersection angles, stress contrasts and fluid injection conditions used in different experimental groups. Figure 3 shows the comparison between different analytical models [13, 14, 21], and the experimental results from [15].

The experiments clearly show that the new model agrees with the experiments as well as other analytical models as it captures the first order crossing-arresting behavior. We note that the discrimination between the different models would require additional data points in the transition zone, unfortunately not available here.

Additionally, it should be noted that the injection rate and viscosity were not changed in this series of experiments, and so it was not possible to assess their effect on the fracture interaction outcome. In order to compensate for this lack of lab experiments, numerical experiments were conducted using MineHF2D code [4, 5, 8] to assess the sensitivity of the injection rate on fracture crossing. The results are demonstrated on Figure 4 and show that the OpenT model [20,21] agrees well with numerical computation results in the sense that it captures the crossing-arresting transition.

It should be mentioned that the OpenT incorporates the influence of rock properties (local horizontal stresses, rock tensile strength, toughness, pore pressure, Young's modulus, Poisson ratio), natural fracture properties (friction coefficient, toughness, cohesion, permeability), intersection angle between hydraulic and natural fractures, fracturing fluid properties (viscosity, tip pressure), and injection rate to define crossing rules [21]. The eRP criterion

[14,15] accounts for the local stress field, pore pressure, crossing angle, rock tensile strength and frictional properties of the natural fractures.

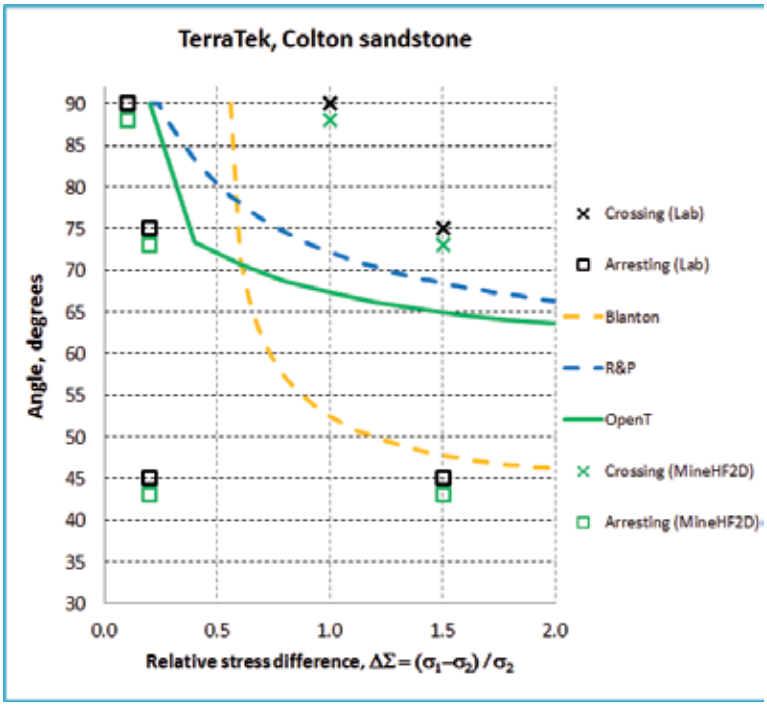

Figure 3. Comparison between analytical models given in [13,14,15], OpenT [21], and the experimental results [15]

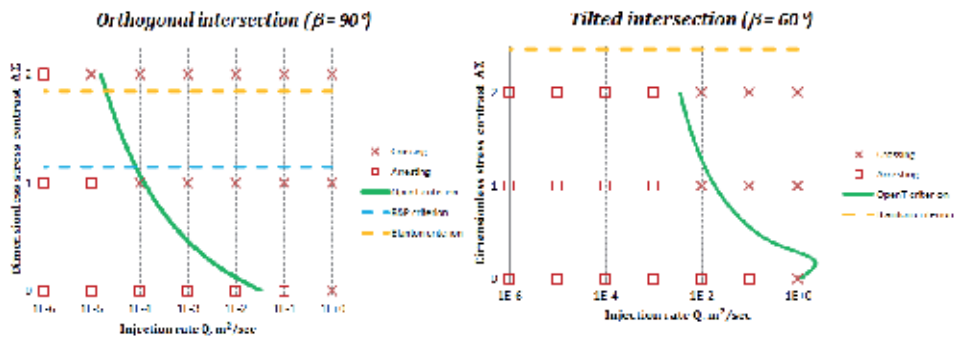

Figure 4. Comparison between numerical crossing-arresting HF-NF behavior using MineHF2D code [4,5,8]. The red crosses and squares respectively indicate crossing and arresting behavior from MineHF2D code, solid green curves correspond to analytical predictions using OpenT [21], dash yellow curve corresponds to Blanton criterion [13], and eRP criterion [14,15] is given by dash blue lines. The interaction is studied for various injection rate and relative stress difference for two different HF-NF contact angles, β=90º (left) and β=60º (right).

http://dx.doi.org/10.5772/56406

This new model has been implemented in UFM. Below we present comparison of UFM results with new and old crossing models and provide some analysis about the influence of fluid properties on the geometry of stimulated fracture network, and as a result on the production predictions.

4. Comparison of hydraulic fracturing simulations with OpenT versus eRP

4.1. Influence of viscosity

The comparison of results generated using two crossing criteria - eRP criterion [14,15] and new OpenT criterion [20, 21] - is presented in Figure 5 and Figure 6 for a simple example given in Table 1 (values shown in italic are used only in OpenT crossing criterion). The cohesion and toughness of natural fracture are considered to be negligible.

Injection rate	0.13 m^3/s
Stress anisotropy	0.9 MPa
Young's modulus	2.8×10^{10} Pa
Poisson's ratio	0.2
Fluid viscosity	0.001-0.01 Pa-s
Fluid Specific Gravity	1.0
Fracture toughness	1.3 MPa-$m^{0.5}$
Tensile strength	3.5 MPa
NF friction Coefficient	0.5
NF permeability	1 Darcy

Table 1. Input data Example 1

For the case of lower fluid viscosity (Figure 5a and Figure 6a) both criteria show similar hydraulic fracture patterns with no crossing of the natural fractures. For higher viscosity fluid OpenT crossing criterion shows that hydraulic fractures cross the NF#1 and NF#3 (Figure 6b), while with eRP the hydraulic fracture network (HFN) pattern does not change. The intersection angle between HF and NF#1 was 62.5 deg, between HF and NF#2 was 15 deg, and the interaction angle between HF and NF#3 was 75 deg.

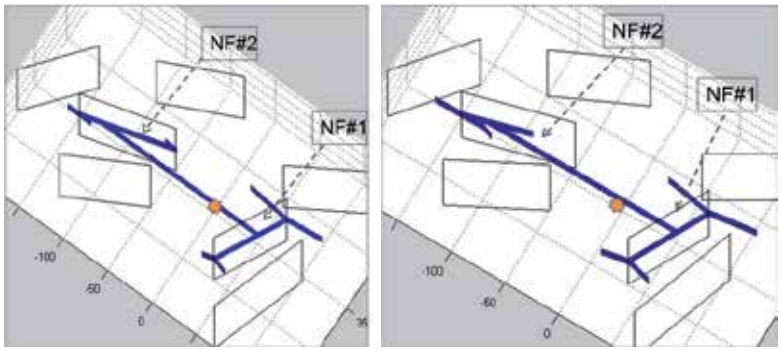

a) Low viscosity, no crossing b) higher viscosity, no crossing

Figure 5. Hydraulic fracture networks generated for Example 1 with eRP crossing criterion [14] with fluid viscosity K'=0.001Pa-s (left), and K'=0.01Pa-s (right)

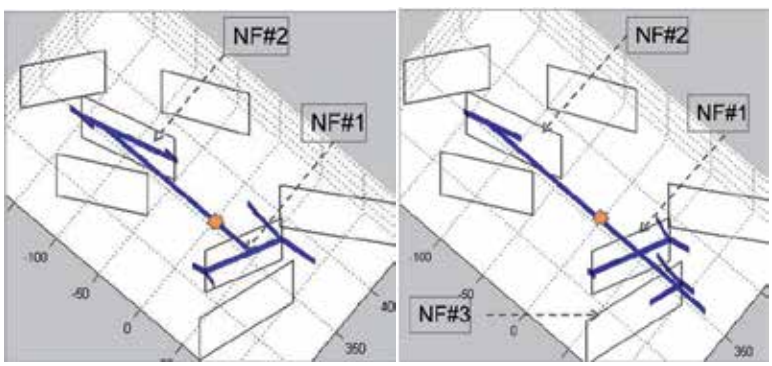

a) Low viscosity, no crossing b) Higher viscosity, crossing NF#1and NF#3

Figure 6. Hydraulic fracture networks generated for Example 1 with OpenT crossing criterion [21] with fluid viscosity K'=0.001pa-s (left) and K'=0.01Pa-s (right)

So, while eRP criterion gives for this case the same prediction (no crossing) for both low and high viscosity fluids, OpenT criterion predicts crossing the NF with higher crossing angle for the more viscous fluid.

Differences in the predicted hydraulic fracture network result in different proppant placement (Figure 7), and will result in differences in production evaluation and prediction.

Example 2 with more dramatic output differences is presented in Figure 8 for the same pumping schedule, zone properties, fluid and natural fractures properties. In Table 2 the main input data is shown (values shown in italic are used only in OpenT crossing criterion), the toughness and cohesion of natural fractures are considered to be negligible. Natural fractures are oriented mostly perpendicular (~ 90deg) to the maximum horizontal stress direction, i.e. to the preferred direction of hydraulic fracture propagation.

http://dx.doi.org/10.5772/56406

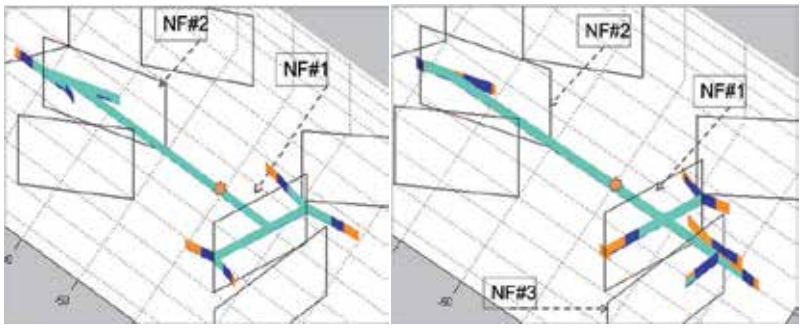

Figure 7. Proppant placement prediction for Example 1 from eRP (left) and OpenT (right) criteria with fluid K'=0.01Pa-s after 100 min of shut-in. Slurry is shown in light blue, bank is in dark blue, and clean fluid is in orange.

Injection rate	0.13 m^3/s
Stress anisotropy	2 MPa
Young's modulus	3.5×10^{10} Pa
Poisson's ratio	0.25
Fluid viscosity	0.0004-0.04 Pa-s
Fluid Specific Gravity	1.0
Min horizontal stress	42.7 MPa
Max horizontal stress	44.6 MPa
Fracture toughness	1 MPa-$m^{0.5}$
Tensile strength	3.4 MPa
NF friction Coefficient	0.4
NF permeability	1 Darcy

Table 2. Input data for Example 2

For the case of low viscosity fluid (Figure 8 left) both criteria show similar hydraulic fracture patterns with mostly no crossing of the natural fractures. When fracturing fluid viscosity was increased, considerable differences in patterns have been observed (Figure 8 right). The results for eRP approach stay mostly the same, showing that fluid eventually penetrated into the NF and opens it. But the simulation based on OpenT criteria shows that for higher viscosity fluid hydraulic fracture intersects most of the natural fractures, resulting in a bi-wing like HFN pattern, which will produce a narrow microseismic events cloud.

The example presented on Figure 8b is consistent with the general observations that hydraulic fracturing treatments with higher fluid viscosity HFN tend to cross natural fractures and

generate a narrower fracture network, while for low viscosity fluids it is easier to penetrate into the natural fracture and open it [9] and generate a wider fracture network.

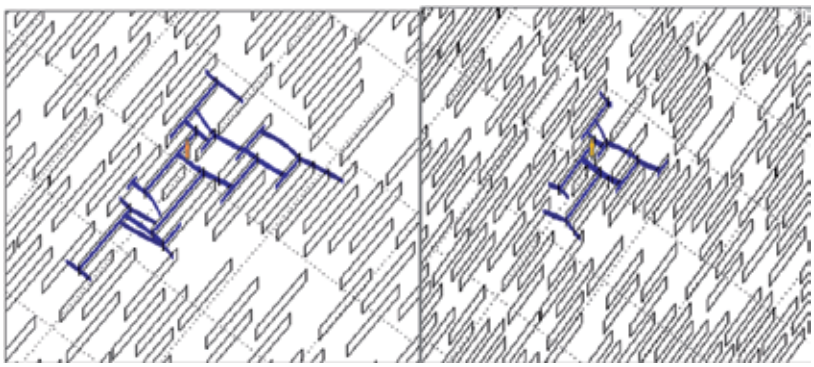

a) HFN predicted for Example 2 with eRP criterion for low viscosity fluid on the left (K'=0.0004Pa-s), and higher viscosity fluid on the right (K'=0.04Pa-s)

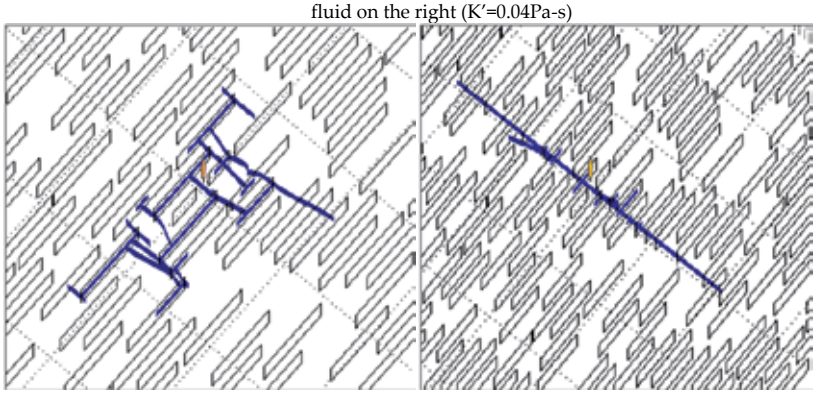

b) HFN predicted for Example 2 with OpenT criterion for low viscosity fluid on the left (K'=0.0004Pa-s), and higher viscosity fluid on the right (K'=0.04Pa-s)

Figure 8. Hydraulic fracture networks generated for Example 2 with eRP crossing criterion (a) and OpenT crossing criterion (b) for low and high fluid viscosity cases. The pre-existing DFN is also shown

It should be mentioned that rock properties, crossing angle between natural fracture and hydraulic fracture, and natural fractures properties all work together with fluid properties to define the crossing pattern and the resulting fracture footprint. This paper intends to emphasize the importance of fluid properties to be included into the general consideration for HF/NF interaction prediction.

4.2. Influence of pumping rates

As it was mentioned before, injection rate works together with fluid viscosity when HF interacts with NF [9, 18, 19]. In the OpenT crossing model the injection rate is also taken into account to predict (evaluate) HF/NF crossing or opening (Equation 1).

http://dx.doi.org/10.5772/56406

Notice that while using eRP criterion, the change in pumping rate can change fracture footprint due to change in fluid pressure, width, and therefore local stresses and crossing angle, while OpenT model introduces additional change due to the rate effect on the crossing behaviour.

The cases presented in Examples 1-2 above, demonstrated the impact of fluid viscosity. Now these examples will be considered again to demonstrate the impact of pumping rate, which is also accounted for in the new crossing model. The base case of pumping rate Q=0.132 m^3/s is considered and compared with additional cases when rate is changed (Table 3). The total pumping time in schedule was changed accordingly for different pumping rates to maintain the same total fluid volume.

Fluid viscosity	0.0004-0.04 Pa-s
Injection rate : Q	0.132 m^3/s
Injection rate: Q/2	0.066 m^3/s
Injection rate: 5Q	0.66 m^3/s

Table 3. Input data to test impact of pumping rate

First, on Figures 9a-10a the results of using the eRP crossing model with different rates as given in Table 3, and two types of fluid viscosity are presented for Example 1 and compared with the same simulations using OpenT crossing model (Figures 9b-10b). Due to relatively high leakoff coefficient used in the presented case the fracture network for higher rate is larger due to greater fluid efficiency.

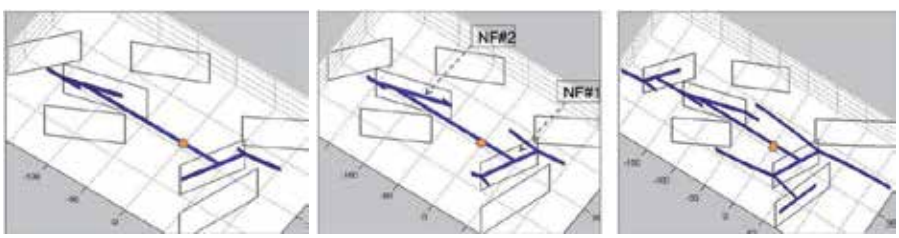

a) Hydraulic fracture networks generated with eRP crossing criterion for low viscosity fluid (K′=0.001Pa-s) with various injection rates (0.066 m^3/s, 0.132 m^3/s, and 0.66 m^3/s)

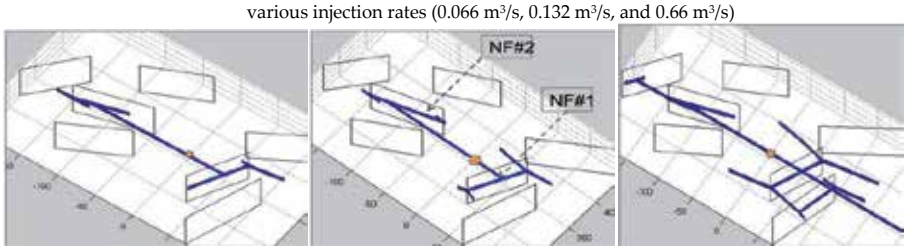

b) Hydraulic fracture networks generated with OpenT crossing criterion for low viscosity fluid (K′=0.001Pa-s) with various injection rates (0.066 m^3/s, 0.132 m^3/s, and 0.66 m^3/s)

Figure 9. Influence of Pumping Rate: Hydraulic fracture networks generated for Example 1 with low viscosity fluid and with eRP (a) and OpenT(b) crossing models at injection rates from Table 3

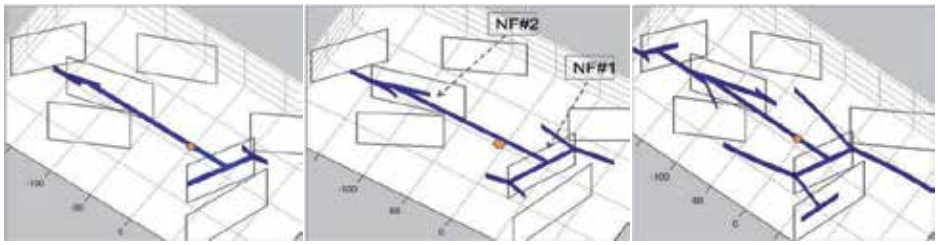

a) Hydraulic fracture networks generated with eRP crossing criterion for higher viscosity fluid (K'=0.01Pa-s) with various injection rates (0.066 m^3/s, 0.132 m^3/s, and 0.66 m^3/s)

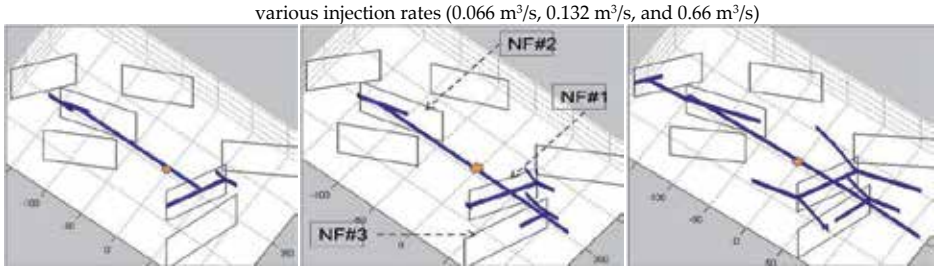

b) Hydraulic fracture networks generated with OpenT crossing criterion for higher viscosity fluid (K'=0.01Pa-s) with various injection rates (0.066 m^3/s, 0.132 m^3/s, and 0.66 m^3/s)

Figure 10. Influence of Pumping Rate: Hydraulic fracture networks generated with higher viscosity fluid for Example 1 with eRP (a) and OpenT(b) crossing models at injection rates from Table 3

The first observation is that for low injection rate and for both high and low fluid viscosities fracture network is similar with both crossing models for this simple Example 1, and no crossing is observed. When injection rate is increased, HFN becomes more complex: OpenT shows crossing at the first natural fracture at the angle of 62.5 deg with both low and high viscosity fluids. The eRP criterion does not show crossing, and network complexity is due to the smaller time required to open NF and higher injection rates, so HFN can propagate faster. Again, the resulting HFN with eRP model does not depend on the fluid viscosity (Figure 9a and Figure10a). Results for the test case of Example 2 are given in Figures 11-12.

As we can see from Figures 11a and 12a, eRP criterion exhibits similar HFN footprints for both low and high viscosity fluids and for different injection rates. The reason for the relative insensitivity to the injection rate as compared to Example 1 is due to the higher stress anisotropy for Example 2.

With OpenT crossing criterion, for lower fluid viscosity the chance of crossing perpendicular NF increases with increasing injection rate. At the same time for a higher viscosity fluid, while it can cross the natural fracture more easily, it is more difficult to open the crossed natural fracture. The observed behaviour with new crossing model is consistent with experimental observations [9].

So we can conclude from the observations in these cases that the fluid viscosity together with pumping rate could play a major role on the crossing. At the same time the influence of pumping rate is not as strong as viscosity, and mostly affects the opening of the intersected natural fractures.

http://dx.doi.org/10.5772/56406

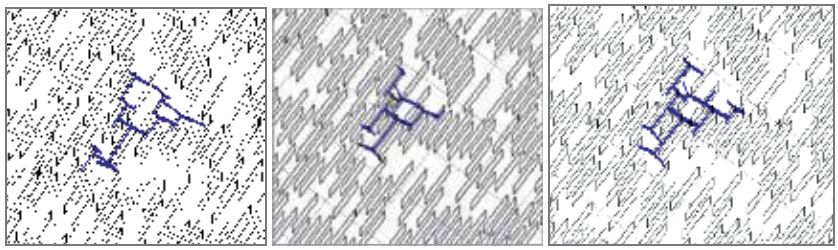

a) Hydraulic fracture networks generated with eRP crossing criterion for low viscosity fluid (K'=0.0004Pa-s) with various injection rates (0.066 m^3/s, 0.132 m^3/s, and 0.66 m^3/s)

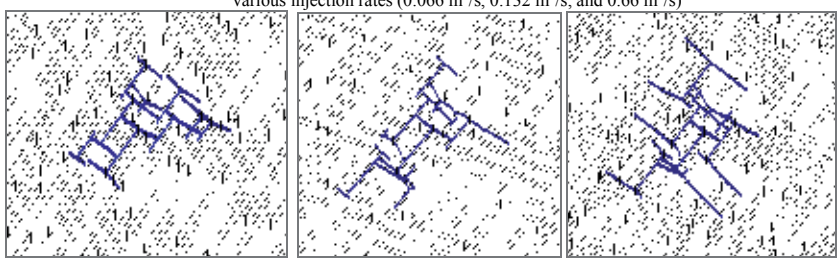

b) Hydraulic fracture networks generated with OpenT crossing model for low viscosity fluid (K'=0.0004Pa-s) with various injection rates (0.066 m^3/s, 0.132 m^3/s, and 0.66 m^3/s)

Figure 11. Influence of Pumping Rate: Hydraulic fracture networks generated with low viscosity fluid for Example 2 with eRP (a) and OpenT(b) crossing models at injection rates from Table 3

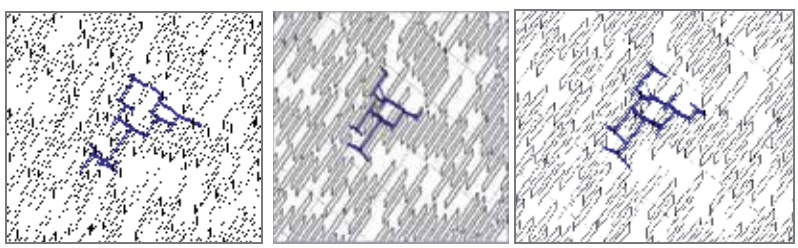

a) Hydraulic fracture networks generated with eRP crossing model for higher viscosity fluid (K'=0.04Pa-s) with various injection rates (0.066 m^3/s, 0.132 m^3/s, and 0.66 m^3/s)

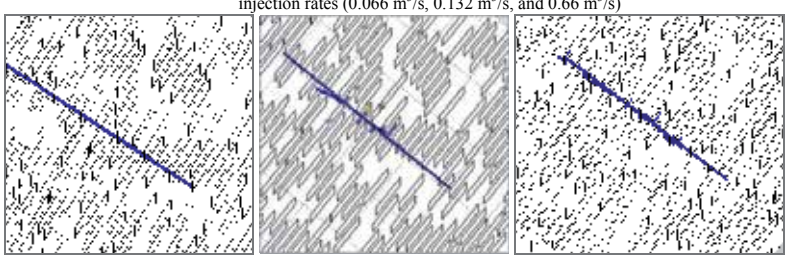

b) Hydraulic fracture networks generated with OpenT crossing model for higher viscosity fluid (K'=0.04Pa-s) with various injection rates (0.066 m^3/s, 0.132 m^3/s, and 0.66 m^3/s)

Figure 12. Influence of Pumping Rate: Hydraulic fracture networks generated for Example 2 with old and new crossing models for high viscosity fluid at injection rates from Table 3

4.3. Barnett example

To further validate the model in a realistic field condition, we examine a synthetic case that mimics the field example in Barnett Shale presented by Warpinski et al. [16] as shown in Figure 1. Though the details of the well and formation data and pumping schedule are not exactly replicated, the synthetic case is created using the data that is available in [16], so the well and formation configurations are very close to the real case.

Some of the critical information for fracture simulation, including Young's modulus and description of the natural fractures, is prescribed based on the work by Gale et al. [27]. According to [27], the Young's modulus for Barnett Shale is 33 GPa (4.8×10^6 psi). The natural fractures contain a dominant set trending West-Northwest direction (approximately North 70° West). There is also another set trending North-South direction. The hydraulic fractures in Barnett trend in the Northeast-Southwest direction. The natural fractures are mostly sealed and filled with calcite. Only largest fractures may be open and largest fracture clusters are expected to space couple hundred feet apart. To construct the natural fractures for UFM simulation, we assume that only the largest natural fractures contribute to the complex fracture network development. The exact values of fracture spacing and fracture length are difficult to determine. We make the assumption that the average fracture spacing is 100 ft and average fracture length is 200 ft. Only the dominant set of fractures is assumed. Figure 13 shows the top view of the well configuration, perforation clusters and the 2D traces of the generated natural fractures. The well geometry closely mimics the field case as shown in Figure 1.

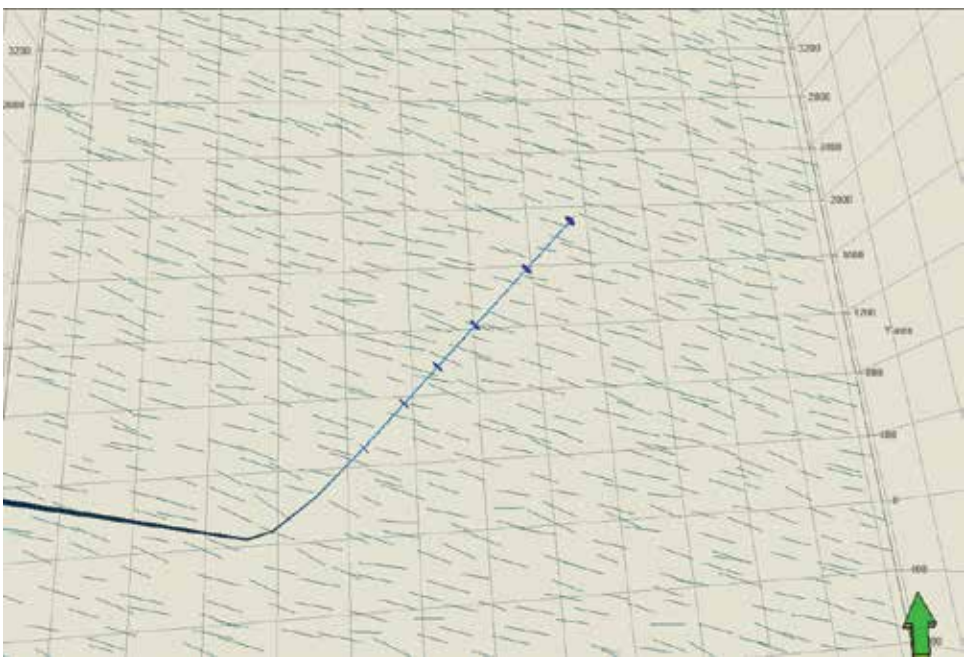

Figure 13. Top view of the wellbore, perforations and the natural fractures used for the Barnett simulations

http://dx.doi.org/10.5772/56406

For the complex fracture simulation, detailed vertical stress profile is not available from [16]. Instead a fixed height model is used based on the microseismic measurements presented in [16]. It is assumed that the fracture height is 310 ft covering Lower Barnett for the case of cross-linked gel treatment, and 360 ft for the slick water treatment. For the simulation of slick water refrac, any potential effect of previous cross-linked treatment and the small slick water treatment prior to the main treatment is not considered. Furthermore, a difference between maximum and minimum horizontal stress is assumed to be 200 psi. Table 4 shows the main parameters used for the fracture simulations.

Parameters	Xlink Gel treatment	Slick Water treatment
Young's modulus	4.8 x 10^6 psi	
Natural fracture direction	Average N70˚W, standard deviation 5˚	
Natural fracture length	Average 200 ft, standard deviation 40 ft	
Natural fracture spacing	Average 100 ft, standard deviation 20 ft	
Coefficient of friction	Average 0.6, standard deviation 0.1	
Hydraulic fracture direction	N40˚E	
Minimum horizontal stress	5324 psi	
Maximum horizontal stress	5524 psi	
Fracture height	310 ft	360 ft
Fluid rheology	n' = 0.42, k' = 0.002 lb-s/ft^2	1 cp
Injection rate : Q	70 bpm	125 bpm
Pump time	174 min	386 min
Proppant volume	715,000 lbs	600,000 lbs

Table 4. Input data for Barnett Shale case

Figure 14 shows the UFM simulated fracture geometry and width for both gel and slick water fracs at the end of the treatments.

Planar hydraulic fractures first initiate from the perforations. These fractures propagate as longitudinal fractures since the wellbore direction is closely aligned with the fracture orientation. For the cross-linked gel treatment, as these initial longitudinal fractures intersect the natural fractures that are approximately orthogonal to the fracture direction, the OpenT crossing model mostly predicts crossing through the natural fractures. Only when the fluid pressure is sufficiently high to exceed the normal stress acting on the natural fractures, do the natural fractures be opened up and accept fracturing fluid. The overall geometry predicted by UFM model shows a strong planar trend along the well with very narrow network width, consistent with the microseismic observation shown in Figure 1a.

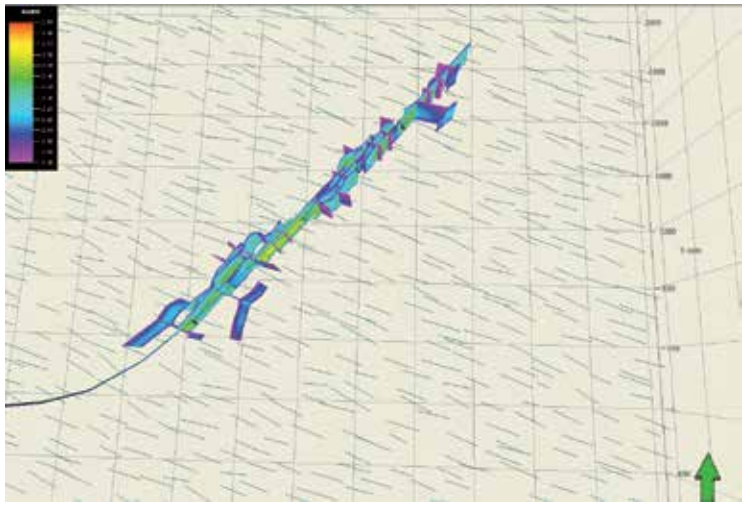

(a)Cross-linked gel treatment

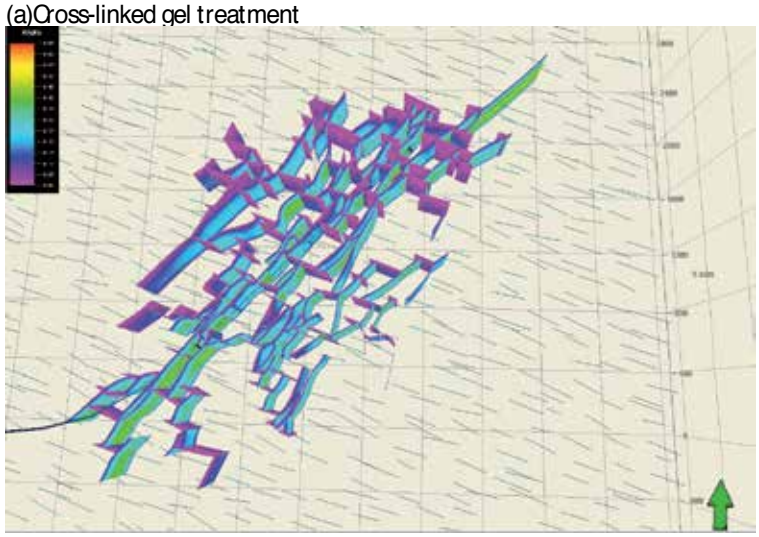

(b)Slick water treatment

Figure 14. UFM simulation results for the Barnett case

For the slick water treatment, the OpenT crossing model mostly predicts non-crossing condition when a hydraulic fracture intercepts a natural fracture. This results in a much wider fracture network width as the fractures branch out as shown in Figure 14b. The width of the network is approximately 1700 ft wide, approximately the same as indicated by the micro-seismic data as shown in Figure 1b.

Example presented on Figure 14 showing the difference in HFN from two treatments with different types of fluid, matches microseismic cloud trend observed in [16] and definitely shows ability of UFM simulator with new implemented crossing model correctly predict hydraulic fracture complexity in naturally fractured formation.

http://dx.doi.org/10.5772/56406

5. Possible impact on production forecast

Unconventional Fracture Model (UFM) presents a powerful tool to evaluate hydraulic fracture network propagation under the specified field pumping conditions and can be used to predict developed hydraulic fracture network and match it with observed microseismic event cloud. The proper understanding of the fracture footprint as well as propped fracture surface estimation is an important input for the production evaluation. Because the OpenT crossing model predicts some changes in crossing patterns with different fluids used, it is important to understand the impact it could have on the production evaluation.

This section illustrates how the crossing criterion can influence the production. It presents simulation results of a fracturing-to-production simulation. The production part is done with the UPM model [28]. The base case for this Example 3 is from the paper [29] (Table 5).

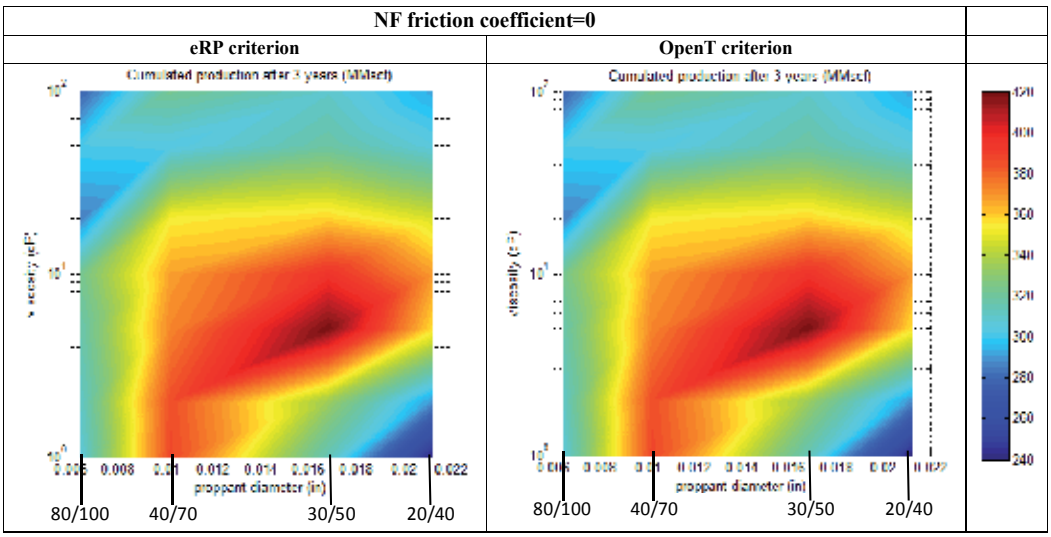

Figure 15. Cumulated production after 3 years for the two crossing criterion and a friction coefficient at NF = 0, as a function of the fracturing fluid viscosity and the proppant size

Figure15 shows the cumulated production after 3 years as a function of the proppant size and the fracturing fluid viscosity for the case when zero friction coefficient at NF is used and the two crossing models are applied. From Figure 15 we see that if there is no friction at the natural fractures, there is no difference between results from the two crossing criteria for this case. The reason is that if friction coefficient for the natural fracture is zero, both crossing criteria show that HF will not cross NF. The HFN footprint and fracture conductivity (identical when using both crossing criteria with zero friction coefficient) are shown at Figure 16 a,b for cases of slick water and more viscous fluid pumped.

Injection rate	0.21 m^3/s
Number of Perforated Intervals	4
Stress anisotropy	0.3 MPa
Young's modulus	1.3×10^{10} Pa
Poisson's ratio	0.23
Fluid viscosity	0.001-0.1 Pa-s
Min horizontal stress	28.47 MPa
Max horizontal stress	28.76 MPa
Fracture toughness	1.5 MPa-$m^{0.5}$
Tensile strength	3.4MPa
NF friction Coefficient	0 -0.75
NF permeability	1 Darcy

Table 5. Input data for Example 3

If HF cannot cross NF, it is easier for slick water to penetrate and open NFs than for more viscous fluid, so HFN is generally more extended (Figure 16a left). While for the case of more viscous fluid it takes more time to open NF, HFN pattern is smaller (Figure 16)

When friction coefficient at NF is increased from 0 to 0.75, the output changes depending on the type of fluid pumped. The cumulated production forecast looks different for two crossing criteria used (Figure17).

For slick water treatments (Figure 18), eRP criterion shows some crossing of NFs (Figure18 left), while OpenT claims that no crossing should occur for slick water treatments (Figure 18 right). This difference in crossing models, produces considerable differences in production prediction after 3 years for low viscosity fluid treatments (Figure 17). It is important to mention, that it is a common observation that low viscosity fluids usually do not cross NFs, mainly because it is easier for them to penetrate to NF and open it [9]. The eRP criterion cannot capture this effect, while OpenT model correctly predicts HF/NF interaction for slick water case with friction coefficient at NF of 0.75.

When more viscous fluid pumped, results also show some differences (Figure19). With both criteria some crossing is observed, but OpenT in this case predicts more crossing than eRP criterion. Mention, that differences in results from eRP criterion for slick water and 100cP fluid are due to some differences in interaction angles between HF and NFs due to change in fluid properties, fluid pressure and due to stress shadow effect.

Due to small stress field anisotropy, the differences in production prediction for more viscous fluid are not significant (Figure 17), but still visible.

http://dx.doi.org/10.5772/56406

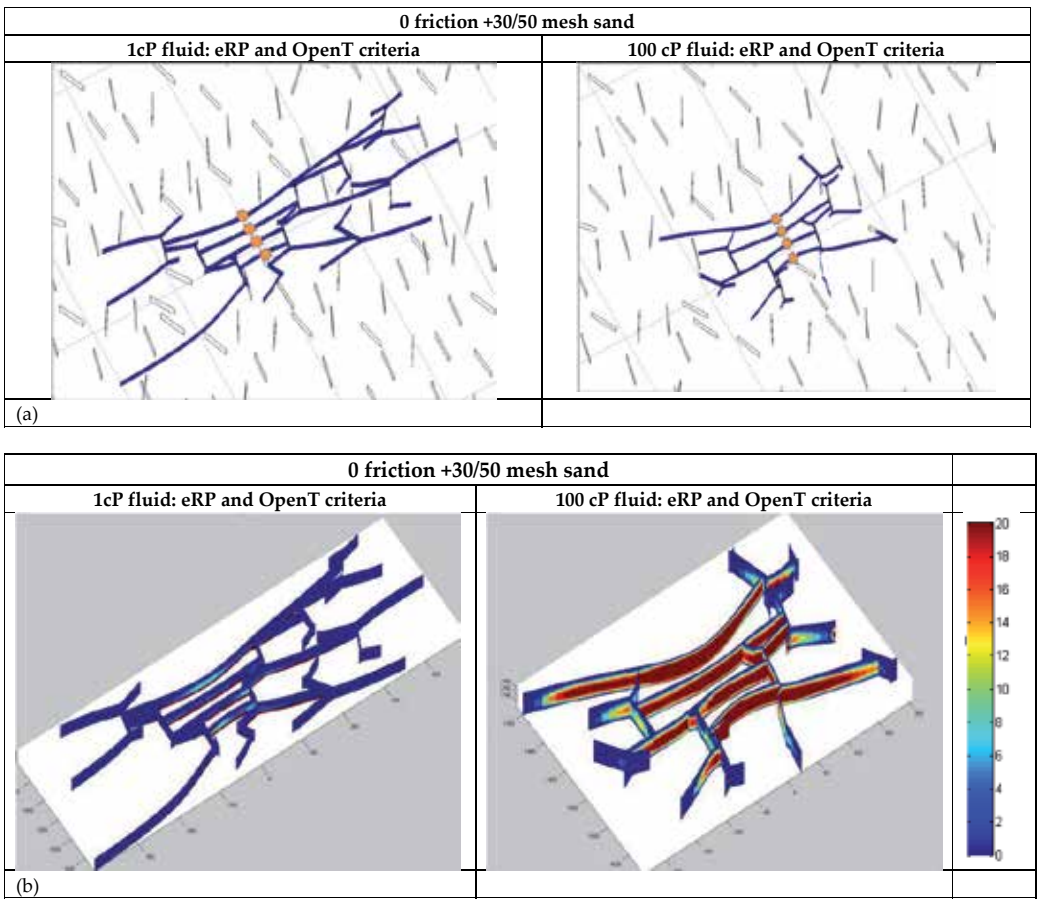

Figure 16. (a). HFN footprint for two types of fluid (with 30/50 mesh sand) for zero friction coefficient at NF. Both criteria show the same HFN footprint. (b). Fracture conductivity for two types of fluid (with 30/50 mesh sand) for zero friction coefficient at NF. Both criteria show the same HFN footprint

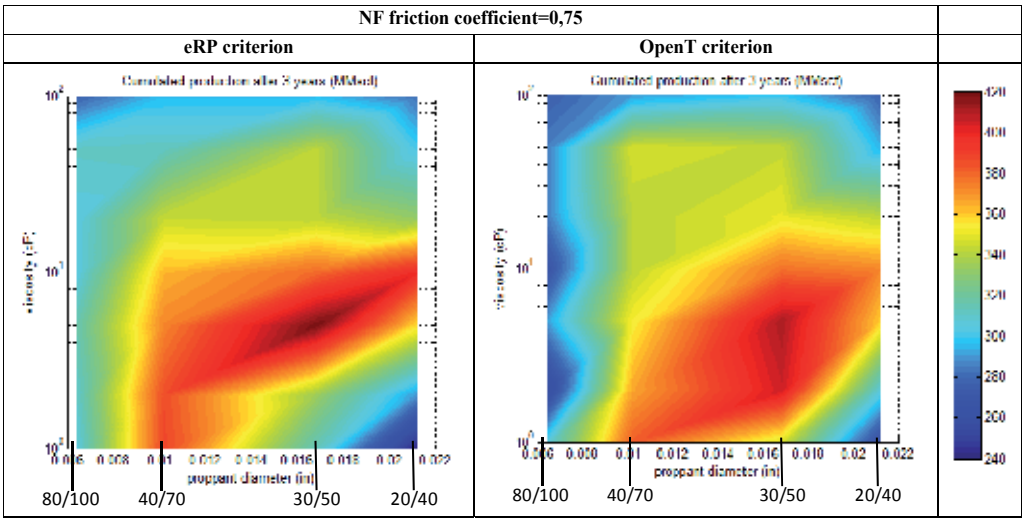

Figure 17. Cumulated production after 3 years for the two crossing criteria and a friction coefficient at NF of 0.75, as a function of the fracturing fluid viscosity and the proppant size

The main conclusion related to presented production examples, is that the difference between the two crossing criteria seems to be maximum for low viscosity fluid (slick water) and large proppant (30/50). This observation is expected because the lower the viscosity, the longer the fracture length and the stronger interaction with NF are. Also, eRP criterion shows some crossing of NFs for slick water case, while OpenT shows no crossing, and larger proppants are more sensitive to fracture intersections. The fracture width is larger if the HF does not cross NF and slurry propagated inside the NF with a larger normal stress (in case of stress anisotropy) and smaller width, thus increasing the likelihood of bridging. Also, the less crossing occurs, the more time HF needs to spend stopped at NF before building enough pressure to overcome the stress anisotropy and resume propagating inside the NF for high viscosity fluids. In this case, more proppant will settle close to the perforations, reducing the propped length and thus the production.

http://dx.doi.org/10.5772/56406

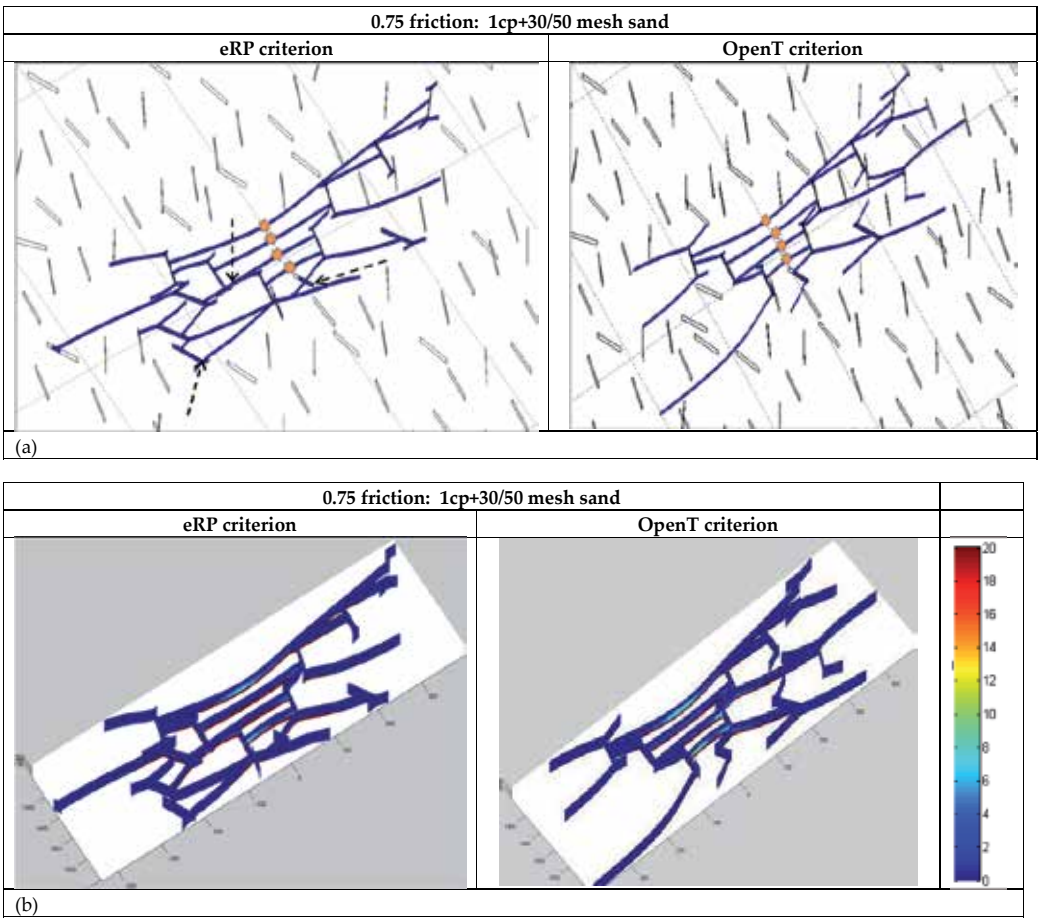

Figure 18. (a). HFN footprint for slick water (with 30/50 mesh sand) for friction coefficient at NF=0.75. Both criteria show similar HFN footprint. eRP shows some crossing (shown by dashed arrows), while OpenT shows no crossing for slick water case (b). Fracture conductivity for slick water (with 30/50 mesh sand) for friction coefficient at NF=0.75

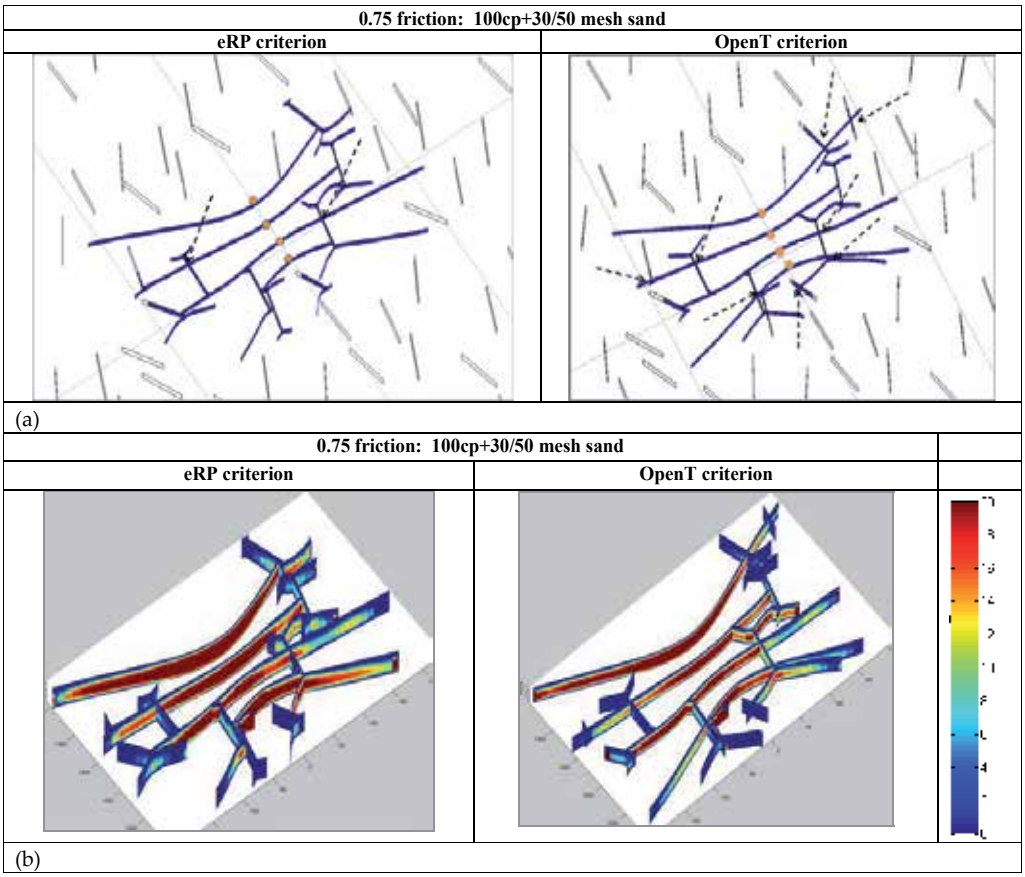

Figure 19. (a). HFN footprint for 100cP viscosity fluid (with 30/50 mesh sand) for friction coefficient at NF=0.75. Arrows point at crossing (b). Fracture conductivity for 100cP viscosity fluid (with 30/50 mesh sand) for friction coefficient ant NF=0.75

6. Conclusions

A new crossing model (OpenT) which takes into account fluid properties, properties of the rock mass and natural fractures, have been developed, validated [20, 21], and implemented in UFM. The similarities and differences in fracture footprint predicted based on the OpenT model and eRP criterion have been demonstrated and discussed. OpenT crossing model shows more realistic results for some cases (as for the field and laboratory observations) than existing purely rock property based models.

While eRP model properly accounts for interaction angle, stress anisotropy, rock tensile strength and NF friction coefficient, the OpenT model accounts also for NF and fluid properties. The crossing prediction from OpenT criterion, and therefore corresponding HFN foot-

http://dx.doi.org/10.5772/56406

print, could be different for low viscosity fluids and high viscosity fluids, while eRP model shows similar crossing patterns for low and high viscosity fluids. In the mean time both criteria show similar results for some cases.

It is important to mention that whether HF will cross (dilate, or open) NF depends on the combined impact of rock properties (local stress field, tensile strength, toughness, etc), NF properties (permeability, toughness, friction coefficient, cohesion, etc), HF/NF interaction angle, fluid properties, injection rate and other properties.

In general, the Unconventional Fracture Model (UFM) with new OpenT crossing model provides more reliable results to predict and evaluate hydraulic fracture network geometry and improve production forecast. The Barnett Shale example presented in Figure 14 shows the differences in HFN from two treatments with two different types of fluids. The predicted results closely match the microseismic cloud observed in [16] and show the ability of UFM simulator with the new crossing model (OpenT) to correctly predict hydraulic fracture complexity in naturally fractured formation.

Acknowledgements

The authors would like to thank Schlumberger for permission to present and publish this paper

Author details

Olga Kresse[1*], Xiaowei Weng[1], Dimitry Chuprakov[2], Romain Prioul[2] and Charles Cohen[1]

*Address all correspondence to: okresse@slb.com

1 Schlumberger, Sugar Land, USA

2 Schlumberger Doll Research, Boston, USA

References

[1] Chuprakov DS, Akulich AV, Siebrits E, Thiercelin M. Hydraulic Fracture Propagation in a Naturally Fractured reservoir. SPE 128715, Presented at the SPE Oil and Gas India Conference and Exhibition held in Mumbai, India, 20-22, January, 2010.

[2] Zhao J, Chen M, Jin Y, Zhang G. Analysis of fracture propagation behavior and fracture geometry using tri-axial fracturing system in naturally fractured reservoirs. Int. J. Rock Mech. & Min. Sci 2008; 45: 1143-1152.

[3] Thiercelin M, Makkhyu E. Stress field in the vicinity of a natural fault activated by the propagation of an induced hydraulic fracture. In: Proceedings of the 1st Canada-US Rock Mechanics Symposium 2007; 2:1617-1624.

[4] Zhang X, Jeffrey RG. The role of friction and secondary flaws on deflection and re-initiation of hydraulic fractures at orthogonal pre-existing fractures. Geophys J Int. 2006;166(3): 1454-1465.

[5] Zhang X, Jeffrey RG. Reinitiation or termination of fluid-driven fractures at frictional bedding interfaces. J Geophys Res-Sol Ea. 2008; 113(B8), B08416.

[6] Zhang X, Jeffrey RG, Thiercelin M. Effects of Frictional Geological Discontinuities on hydraulic fracture propagation. SPE 106111, Presented at the SPE Hydraulic Fracturing Technology Conference, College Station, Texas, January29-31, 2007.

[7] Zhang X, Jeffrey RG., Thiercelin M. Deflection and propagation of fluid-driven fractures as frictional bedding interfaces: a numerical investigation. Journal of Structural Geology 2007; 29: 390-410.

[8] Zhang X, Jeffrey RG, Thiercelin M. Mechanics of fluid-driven fracture growth in naturally fractured reservoirs with simple network geometries. Journal of Geophysical Research 2009;114, B12406.

[9] Beugelsdijk LJL, de Pater CJ, Sato K. Experimental hydraulic fracture propagation in a multi-fractured medium. SPE 59419, Presented at the SPE Asia Pacific Conference in Integrated Modeling for Asset Management, Yokohama, Japan, April 25-26, 2000.

[10] Renshaw CE, Pollard DD. An Experimentally Verified Criterion for Propagation across Unbounded Frictional Interfaces in Brittle, Linear Elastic-Materials. International Journal of Rock Mechanics and Mining Sciences & Geomechanics Abstracts. 1995 Apr, 32(3): 237-49.

[11] Warpinski NR., Teufel LW. Influence of Geologic Discontinuities on Hydraulic Fracture Propagation (includes associated papers 17011 and 17074). SPE Journal of Petroleum Technology 1987;39(2): 209-220

[12] Blanton TL. An Experimental Study of Interaction Between Hydraulically Induced and Pre-existing Fractures. SPE 10847, Presented at the SPE/DOE Unconventional Gas Recovery Symposium, Pittsburgh, PA, May 16-18, 1982.

[13] Blanton TL. Propagation of Hydraulically and Dynamically Induced Fractures in Naturally Fractured Reservoirs. SPE Unconventional Gas Technology Symposium; 01/01/1986; Louisville, Kentucky,1986.

[14] Gu H, Weng X. Criterion For Fractures Crossing Frictional Interfaces At Non-orthogonal Angles. 44th US Rock Mechanics Symposium and 5th US-Canada Rock Mechanics Symposium; 01/01/2010; Salt Lake City, Utah: American Rock Mechanics Association; 2010.

[15] Gu H, Weng X, Lund JB, Mack M, Ganguly U, Suarez-Rivera R. Hydraulic fracture crossing natural fracture at non-orthogonal angles, a criterion, its validation and applications. Paper SPE 139984 presented at the SPE Hydraulic Fracturing Conference and Exhibition, Woodlands, Texas, 24-26 January, 2011.

[16] Warpinski NR, Kramm RC, Heinze JR, Waltman CK. Comparison of Single- and Dual-Array Microseismic mapping Techniques in the Barnett Shale. SPE 95568. Presented at the 2005 SPE Annual Technical Conference and Exhibition, Dallas, Texas, October 9012, 2005.

[17] Cipolla C, Weng X, Mack M, Ganguly U, Gu H, Kresse O, Cohen C. Integrating Microseismic Mapping and Complex Fracture Modeling to Characterize Fracture Complexity. SPE 140185 Presented at the SPE Hydraulic Fracturing Technology Conference and Exhibition in The Woodlands, Texas, USA, January 24-26 2011.

[18] Gil I, Nagel N, Sanchez-Nagel M. The Effect of Operational Parameters on Hydraulic Fracture Propagation in Naturally Fractured Reservoirs – Getting Control of the Fracture Optimization Process. Presented at 45th US Rock Mechanics/ Geomechanics Symposium, San Francisco, CA, 26-29 June, 2011.

[19] Nagel N, Gil I, Sanchez-Nagel M, Damjanac B. Simulating Hydraulic Fracturing in Real Fractured Rock – Overcoming the Limits of Pseudo 3D Models. SPE 140480, presented at the SPE HFTC in Woodlands, Texas, USA, 24-26 January, 2011.

[20] Chuprakov D, Melchaeva O, Prioul R. Hydraulic Fracture Propagation Across a Weak Discontinuity Controlled by Fluid Injection. InTech; 2013.

[21] Chuprakov D, Melchaeva O, Prioul R. Injection-sensitive mechanics of hydraulic fracture interaction with discontinuities. Submitted for ARMA Symposium 2013.

[22] Kresse O, Cohen C, Weng X, Wu R, Gu H. Numerical modeling of hydraulic fracturing in naturally fractured formations. 45th US Rock Mechanics/ Geomechanics Symposium, San Francisco, CA, 26-29 June, 2011.

[23] Weng X., Kresse O., Cohen C., Wu R., Gu H. Modeling of Hydraulic Fracture Network Propagation in a Naturally Fractured Formation. Paper SPE 140253 presented at the SPE Hydraulic Fracturing Conference and Exhibition, Woodlands, Texas, USA, 24–26 January, 2011.

[24] Kresse O, Weng X, Wu R, Gu H. Numerical modeling of Hydraulic fractures interaction in complex Naturally fractured formations. ARMA-292, Presented at 46th US Rock Mechanics /Geomechanics Symposium, Chicago, Il, USA, 24-27 June 2012.

[25] Valko P, Economides MJ. Hydraulic Fracture Mechanics: John Wiley & Sons; 1995.

[26] Leguillon D. Strength or toughness? A criterion for crack onset at a notch. Eur J Mech a-Solid. 2002 Jan-Feb;21(1):61-72.

[27] Gale JFW, Reed RM, Holder J. Natural fractures in the Barnett Shale and their importance for hydraulic fracture treatment. AAPG Bulletin, v91, No. 4: 603-622, April 2007.

[28] Cohen CE, Xu W, Weng X, Tardy P. Production Forecast After Hydraulic Fracturing in Naturally Fractured Reservoir: Coupling a Complex Fracturing Simulator and a Semi-Analytical Production Model. SPE paper 152541 presented at the SPE Hydraulic Fracturing Technology Conference and Exhibition held in The Woodlands, Texas, USA, 6-8 February 2012.

[29] Cohen CE, Abad C, Weng X, England K, Phatak A, Kresse O, Nevvonen O, Lafitte V, Abivin P. Analysis on the Impact of Fracturing Treatment Design and Reservoir Properties on Production from Shale Gas Reservoirs. IPTC 16400, Presented at the International Petroleum Technology Conference, Beijing, China, 26-28 March, 2013.

Section 3

Regulations, Risks, and Communities

Chapter 10

Hydrochemical and Hydrogeological Impact of Hydraulic Fracturing in the Karoo, South Africa

G. Steyl and G. J. van Tonder

Additional information is available at the end of the chapter

http://dx.doi.org/10.5772/56310

Abstract

Hydraulic fracturing has become a prevalent public and regulatory issue in most countries developing shale gas. South Africa has only recently been exposed to terrestrial gas resource development and this has created unique regulatory issues which are currently being resolved. One of the key issues under debate is the protection of groundwater resources in rural areas, since most of South Africa's rural and some inland cities are dependent on groundwater for potable water supply. A second concern is the infrastructure requirements to handle the material movement processes during the development of each wellfield and subsequent processing of waste generated on site. Regarding the waste material production, a phased approach is required which considers the initial well development activities, production and subsequent well abandonment. Each phase has a unique risk associated with it and thus would require different management options. At the current stage most of the focus is on the initial stages of well development but the long term view has been neglected to some extent. Due to the unique geological structure of the Karoo, the presence of dolerite structures, a number of risk mitigation methods might be required to succesfully develop hydraulically fractured wells. In all aspects the chemical and hydrogeological impacts related to wellfield development cannot be ignored in the Karoo aquifer system, as it may directly influence human and environmental health. This paper will present chemical perspective on the hydraulic fracturing perspective that will deal with the impact of hydraulic fracturing fluid and flowback water. Additionally, the interaction of wellfield development and hydrogeology of the Karoo area will be discussed and how it relates to future water quality issues.

Keywords: Hydraulic fracturing, hydrochemistry, hydrogeology, impact

1. Introduction

This paper attempts to summarize the current knowledge on hydraulic fracturing and production issues related to shale gas in South Africa. The observation and findings made in this work is neither totally comprehensive nor exhaustive since no data is available in the public domain on hydraulic fracturing and it associated activities in South Africa. The exploration for natural gas resources in terrestrial South Africa has been conducted since the mid-1960's, however no exploitable source could be located. Limited gas was however found in the tight shale formations of the Ecca Group at an approximate depth of 2000-4000 metres below surface. The potential current shale gas reserve in the Karoo shales is estimated to be 485 trillion cubic feet, which would make it the fifth largest shale gas field in the world [1]. In geological terms the Karoo Supergroup refers to an extensive geological sequence (100-260 million years old) which consists of sedimentary and igneous rocks. Most of the Karoo Supergroup is located in South Africa and the Great Karoo has an area of more than 600 000 km^2.

Due to present energy shortfall in South Africa, the requirement for new energy sources have gained new momentum and part of this new focus is on shale gas in Karoo type formations. The most interesting aspect of this is that the area available for natural gas development is substantially larger than just the Karoo, with exploration areas covering six of the nine provinces in South Africa [2]. The development of shale gas resources was initiated in late 2009 but were halted due to a moratorium in early 2011. This has subsequently been lifted in September 2012. There are currently five pending applications related to exploration in the Karoo (Figure 1), three belong to Shell and one each to Falcon Oil and Gas and Bundu Gas and Oil Exploration [3]. To the north is located the petrochemical group Sasol gas exploration area, however plans have been put on hold by the company until further notice. An exploration area has also been awarded to Anglo American adjacent to the Sasol area (Figure 1).

Hydraulic fracturing was developed in the United States of America in the late 1940's to assist in the stimulation of oil and natural gas wells [4-6]. The number of wells that incorporates hydraulic fracturing increases by the day since oil and gas production is increased by this technique [5].

1.1. Development of shale gas in South Africa

The Shale Gas project aims to target the carbonaceous shales of the Ecca and Dwyka Groups, but the stratigraphic units in question vary in lithological makeup along strike as one proceeds from the Cape to the Free State/Natal (KZN) regions. The initial reasoning was to only target zones of the Whitehill formation of the lower Ecca, which is a carbonaceous shale unit characterized by its distinctive white weathering in outcrop. The distribution of the Whitehill Formation with its marine setting led to further investigation into the dynamics of the Main Karoo Basin and other stratigraphic units equivalent to the Whitehill to extend the potential target areas [2]. A revised set of source rocks were identified with the main target zone now being identified as carbonaceous shales of the Lower and Upper Ecca Group with subordinate interest in the Dwyka Shales (Figure 1). The source formations have been extended to include the following:

http://dx.doi.org/10.5772/56310

1. Whitehill Formation (Cape region)
2. Prince Albert Formation (Cape region)
3. Volksrust Formation (Free State and KZN regions)
4. Vryheid Formation (Free State and KZN regions)
5. Pietermaritzburg Formation (Natal region)
6. Dwyka Shales (All regions, where shallow enough).

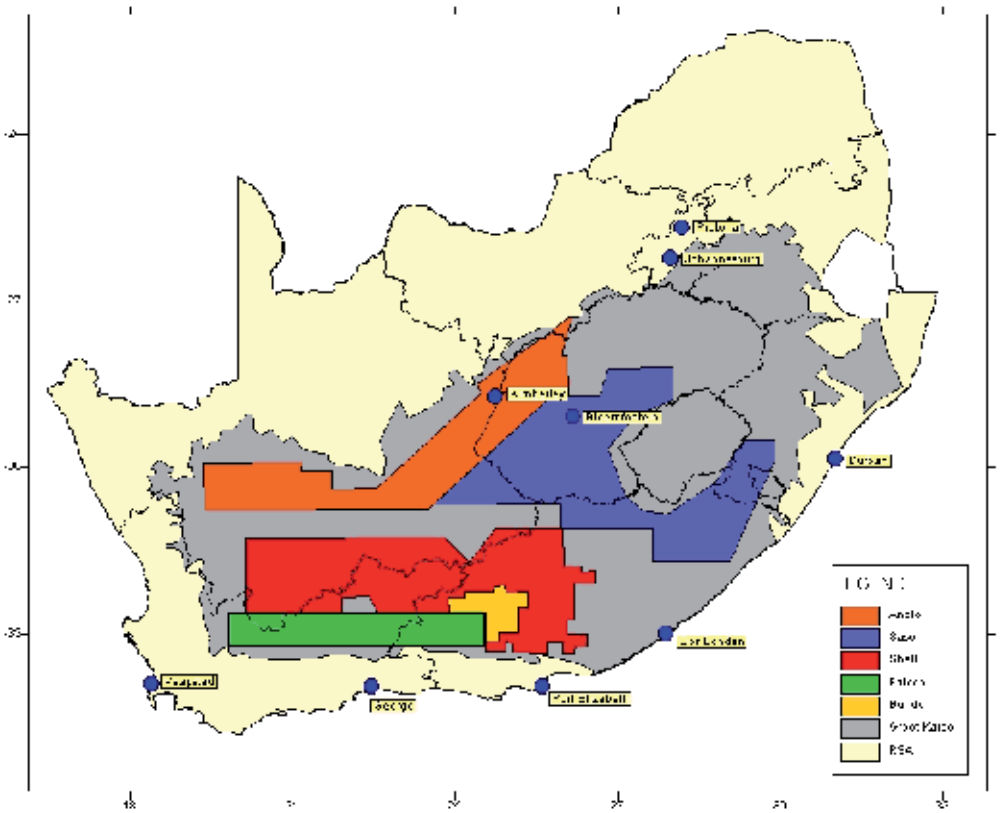

Figure 1. Regional map of South Africa, showing the exploration rights and companies associated with these permits [2].

The research into the Shale Gas deposits of the USA led to a revised set of geochemical and petrophysical parameters that are based on the criteria set by Jarvie [2] to include the following:

1. Total Organic Carbon and its composition (dead carbon, free gas, etc.) → 1% or more.
2. Kerogen Type → Determines hydrocarbon types as well as adsorption/desorption properties.

3. Vitrinite reflectance and Tmax (maximum temperatures that rocks were subjected to during hydrocarbon production) → Thermal Maturity with reflectance values of 1.35-2.5, Tmax values vary and can be very high (between 400°C and 580°C as seen in the Barnett Shale).
4. Rock Eval Hydrogen Index <100.
5. Porosities and other physical properties related to gas flow.
6. Calculations of hydrocarbon generation, expulsion and retention.

From a South African perspective, the Rowsell and De Swardt's study [7] of the maturation indices pertaining to the Karoo Basin can be used to identify areas prospective for gas generation:

1. Temperature Range → ±130°C to 170°/180°C.
2. Vitrinite Reflectance of 1.35-2.5.
3. CR/CT Ratio of about 0.85 to 0.94.
4. Total Organic Carbon and its composition (dead carbon, free gas, etc.) → 1% or more.

1.2. Geology and gas plays in South Africa

In South Africa, shales containing significant organic carbon are restricted to the Ecca Group of the main Karoo Basin, smaller basins in the northern part of South Africa and to the Bokkeveld Group in the southernmost part of South Africa [7]. These muds became buried and lithified over tens to hundreds of millions of years and generated various hydrocarbons with increasing depth of burial and increasing temperature (Figure 2). Between 2-4 km burial depth, oil is produced, between 4-5 km, wet gas is produced and between 5-6 km, dry gas, including methane, is produced. Deeper burial results in low-grade metamorphism, the termination of hydrocarbon generation and the formation of graphite from the organic material. In South Africa, shales of the Bokkeveld Group have undergone low-grade metamorphism and no longer have a capacity for hydrocarbon generation. However, after comprehensive investigations it was confirmed that Ecca Group shales might have the potential to generate dry gas south of the 29°S [7]. Further north, the shales have been less deeply buried and have a potential for oil generation except where younger igneous dolerite intrusions have locally increased the thermal maturity leading to the generation of dry gas [7].

Total organic carbon within the shale is an important parameter, since there is a linear relationship between total organic carbon and gas content, as in the Barnett Shale in the Fort Worth Basin of Texas [9]. Thickness is also important, as most of the gas produced is from areas where the shale is between 90 and 183 metres thick [9]. However, more recently, it has become technically possible to produce gas from shale units as thin as 10 to 15 metres [10]. Within the main Karoo Basin (Figure 3), there are reports of natural gas occurrences both at surface and at intervals in the deep wells drilled by Soekor between 1965 and 1977. Furthermore, varying quantities of gas were obtained by desorbed gas analysis undertaken by Soekor on Ecca Group shale samples retrieved from the deep well cores [7].

http://dx.doi.org/10.5772/56310

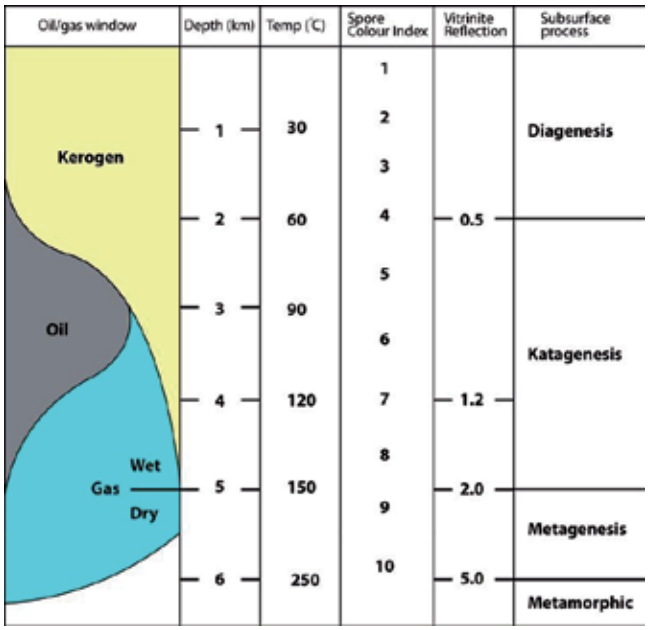

Figure 2. Hydrocarbon generation and thermal maturation indices and maturation stages plotted against depth of burial [8].

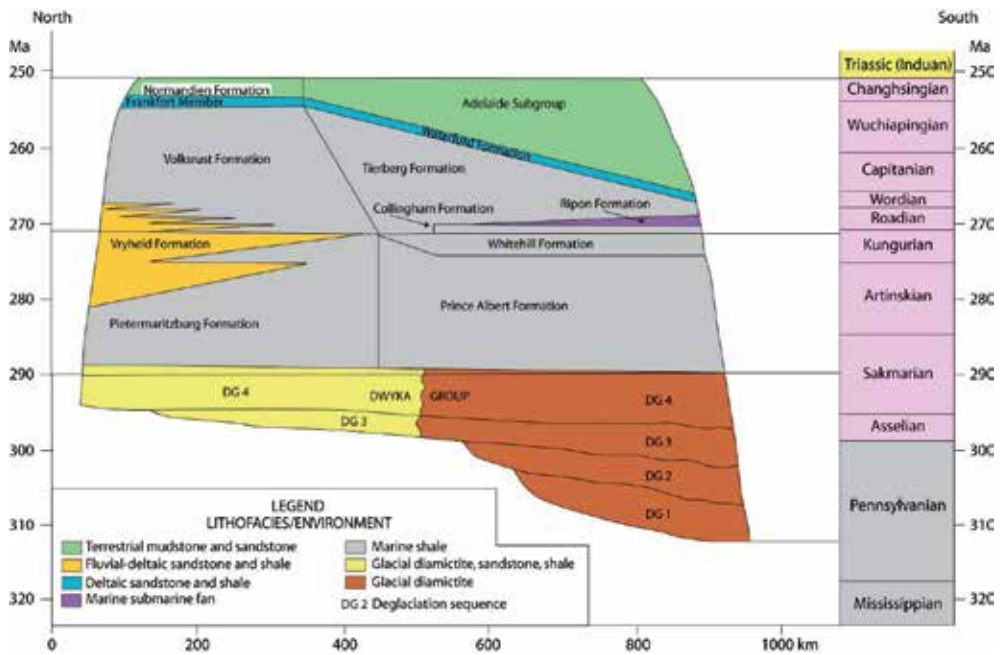

Figure 3. Distribution in time and space of the Dwyka Group, Ecca Group and Adelaide Subgroup in the main Karoo Basin, South Africa, showing lithofacies, environment and stratigraphic relationships. Modified from Fig. 7 of Veevers et al. [11]. The geologic timescale is from Gradstein et al. [12].

It was found that only the lower Ecca Group shales [7] within the dry gas window south of latitude 29°S have comparable total organic carbon contents to those of producing shales elsewhere in the USA (Table 1). The upper Ecca Group shales, namely the Tierberg Formation [13], average only 1.2 percent organic carbon [14], which is significantly lower than the 3 to 12 percent range applicable to producing shales (Table 1). The Dwyka Group also contains black shales with between 0.1 and 4.3 percent total organic carbon, averaging 1.9 percent [15; 14]. However, these shales are thin and restricted, being interbedded with diamictite and sandstone, with the thickest shales (50 to 60 m) occurring in only 3 out of 45 deep wells investigated. The lower Ecca Group comprises black, organic-rich shale of the Whitehill Formation [16] overlying dark grey shale of the Prince Albert Formation (Figure 3) [17]. The Whitehill Formation pinches out northeastwards along a line stretching from Hertzogville in the Free State to Coffee Bay in Eastern Cape Province [14]. Northeast of this line, the Whitehill Formation correlates with the middle part of the sandstone-dominated Vryheid Formation and the Prince Albert Formation grades into shale of the Pietermaritzburg Formation (Figure 3). In the area between Coffee Bay and Harding, the Whitehill and Vryheid Formations are separated by a continuous shale succession [18].

The gas production probability was delineated by Rowsell and De Swardt [7] using the results of desorbed gas analysis on core samples from the deep Soekor wells. The gaseous hydrocarbons (methane to pentane) are absorbed on to the fine-grained constituents of shales and can be desorbed by low-temperature acid hydrolysis [7]. Samples yielding high proportions of C1 gas (methane) and C2/C1 (Ethane/Methane) relative to C3/C1 (Propane/Methane) indicate a potential for dry gas. The trend of increasing maturity due to increasing depth of burial southwards across the basin is supported by the results from other parameters, namely vitrinite reflectance, CR/CT ratios, illite crystallinity and spore colour index. For dry gas generation, vitrinite reflectance values should be between 2 and 5 percent. In the main Karoo Basin south of latitude 29°S, values for shale of the Ecca and Dwyka Groups vary between 1.8 and 4.4 percent [7]. Branch et al. [19] measured vitrinite reflectance values between 3.5 and 5.3 percent for shale of the Whitehill Formation and between 4.0 and 6.4 percent for shale of the Prince Albert Formation in well SA1/66 in the southwestern part of the basin some 60 km north of the basin margin. These correspond to the dry gas and metamorphic maturation stages, which indicates that shales in the southern extremity of the present basin are over-mature and can no longer generate dry gas. CR/CT ratios (residual, non-volatile carbon after pyrolysis to total carbon in the kerogen or organic material) gives an indication of the ability of the shale to produce additional amounts of hydrocarbons if heated to sufficiently high temperatures with lower ratios corresponding to higher potential. The results more or less correspond to the findings of the desorbed gas analysis [7]. Illite crystallinity or Kübler index is a measure of the width in millimetres of the 10 Å diffraction peak at half its height. It gives an indication of the maturity level of the shale with decreasing indices corresponding to increasing maturity [7]. The results of Soekor's investigations indicate a trend of increasing Kübler index from south to north across the Karoo Basin in shales of the Ecca and Dwyka Groups. In the southern part of the basin, south of approximately 30°S, the average indices are less than 4 and correspond to the metagenesis stage and possible preservation of dry gas. Comparative data to the Marcellus Shale and Barnett Shale is presented in Table 1. The percentage organic carbon

http://dx.doi.org/10.5772/56310

detected in these shale formations in the USA are similar to those determined for the Whitehill, Prince Albert and Pietermaritzburg formations. Additionally, the thickness of the formations are also comparable to the Marcellus and Barnett shales. However, the Tierberg Formation and Volksrust Formation can also be possible future targets for shale gas exploration since these formations are considerably thicker than the USA counterparts but at a lower organic carbon content.

Unit or Formation	Percentage organic carbon (%)	Thickness (metres)
Marcellus Shale	0.3-20.0	12-270
Barnett Shale	0.5-13.0	15-300
Karoo Basin-Whitehill Formation	0.5-14.7	0.4-72
Karoo Basin-Prince Albert Formation	0.3-12.4	30-500
Karoo Basin-Pietermaritzburg Formation	0.3-11.6	0.8-420
Karoo Basin-Tierberg Formation	0.3-5.2	400-1300
Karoo Basin-Volksrust Formation	0.3-5.9	250-415
Karoo Basin-Dwyka Group	0.1-4.1	0-58

Table 1. Comparative results of estimated percentage organic carbon and thickness of formation [2].

In the following sections a comparative analysis of known attributes of the Karoo shales and Marcellus Shale will be further developed as well as the impact on the hydrogeology and hydrochemical components.

2. Problem formulation

The major concern to date in the Karoo is the contamination of readily accessible water supply, i.e. surface water or groundwater resources. The development of an unconventional gas field does not occur in a matter of months, with a typical initiation phase of 10 years before gas production can continuously take place [20; 3]. In the instance of South Africa, a number of issues restrict the development of an effective gas extraction project. The infrastructure for gas transport (pipelines) in South Africa is very limited since no conventional terrestrial gas fields exist within the borders of the country. The Soekor wells drilled between 1965 and 1977 have yielded only tentative clues to the availability of gas in the Karoo basin. In this regard the major gas companies have to do a comprehensive exploration and verification program that could last from 3-6 years depending on the geological complexity of the development area. This would be followed by a pilot study to evaluate the basic characteristics of the reservoir which can be done on a number of sites simultaniously over a period of 2-4 years. Finally, if the gas in place is adequate then the process can be developed into full production of gas which can last for 30-100 years depending on gas prices and availability within the shales.

The geology of South Africa is quite varied considering the land size. One distinguishing feature of the geology is the presence of dolerite sills and dykes (Figure 4). The stack of sedimentary strata above the targeted formation in the Karoo consists of a succession of shale, mudrock, sandstone and dolerite. Each of these rock-types are generally characterised by low matrix transmissivities (between 0.5-50 m^2/day) [21]. These values were obtained from pump tests carried out on Karoo aquifers less than 200 m deep. Matrix transmissivities at greater depth would therefore be expected to be even less than these values, however this still needs to be confirmed in the future. Dolerite matrix has also been found to be quite impermeable [22] but due to the process of intrussion it can also act as an conduit. It is expected that the process of well field development would take into consideration the presence of these structures and that upward injection and production fluids would be limited.

Many of the areas where the shale formations have the potential to represent a good prospective target for exploration are also characterised by multiple dolerite intrusions. Drilling in a dolerite sill environment will face challenges that can be overcome if sufficient investigation is carried out on these intrusive structures at depth. There is sparse information on the structure of deep dolerite sills and associated deep groundwater and water strikes in the Karoo lithostratigraphic formations. All available data comes from groundwater exploration drilling at shallow to medium depth (< 300 m). Several groundwater strikes were intercepted at that depth [2]. Below this depth, the presence of deep water strikes in the Karoo formations and associated dolerite, their yields and the composition of the water are still a matter of debate.

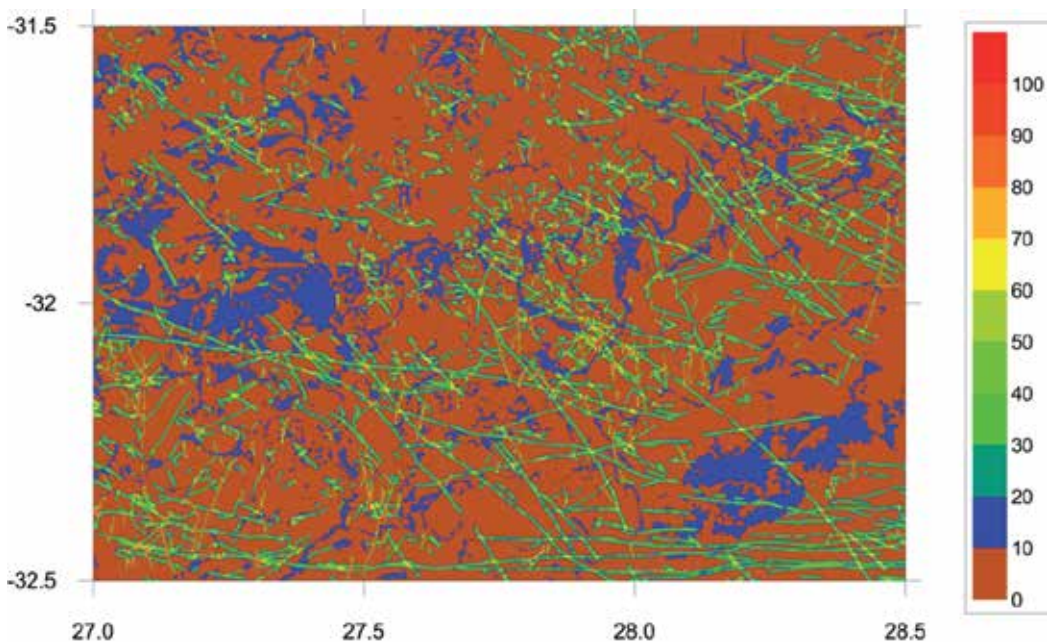

Figure 4. A regional map showing a subsection of the Karoo Supergroup with blue patterns indicating sills while green to red represents dykes in the area [2; 23].

http://dx.doi.org/10.5772/56310

The key question is: Can dykes act as vertical conduits for groundwater flow or hydraulic fracturing fluids? From current literature available [2; 23], it is clear that many water strikes occur between 0-70 metres below ground level (i.e. in the weathered zone) and are found at the contact dyke-sediment. Below 70 metres the water strikes are found along transgressive fractures. The main mechanism of flow dynamics at depth and around dykes is associated with sub-horizontal fractures. These fractures are not linked to one another and collect water from the matrix (dual porosity medium). The influence of dolerite dykes on vertical groundwater circulation at depth seems therefore to be limited, but cannot be excluded due to limited data availability. The T-values from different case studies also show that permeability of the dykes is too low to allow for major flow in the dykes themselves [24].

However there is evidence of a natural connection between deep groundwater systems and the surface, as evidenced by sixteen naturally occurring warm water (thermal) springs (26-41^{o}C) in the main Karoo Basin south of latitude 28 degrees [25; 26]. These waters originate at a maximum depth of between 450 m and 1 150 m, as calculated from the geothermal gradient and the surface temperature of the waters. All the waters are according to Kent [25] are originally meteoritic and mainly deviate in composition due to differences in different compositions of the different rock lithologies associated with the spring, indicating also the presence of connate water. The waters of the central and eastern Karoo have NaCl as the prominent constituent with total dissolved solids ranging from 480-780 mg/l. A few springs are, however characterised by high $NaHCO_3$ and SO_4 contents, e.g. Stinkfontein, south of Beaufort West and the spring at Cradock. Biogenic methane is one of the main gases commonly associated with the hot springs in the main Karoo Basin and in some instances constitutes the only gas present. The other gases present are mainly H_2, N_2, He and Ar [25].

Currently within popular literature hydraulic fracturing and well field development is grouped together under the phrase of fracking. This is clearly incorrect as gas companies refer to fracking as the process of hydraulic fracturing of the formation (shale or gas containing strata) for the purpose of increasing the porosity and permeability of the system to extract shale gas. In order to effectively evaluate the risks associated with hydraulic fracturing, it is best to assess the whole process in which an unconventional shale gas well is developed. This will include the drilling, hydraulic fracturing, well completion, production phase and post closure of the well field itself.

3. Results and discussion

Due to the lack of current data on the Karoo (Permian), secondary sources are required to infer possible issues in this area. Firstly, to assist in the investigation international studies were required for a comparative basis to describe the influence of shale gas development programs. These areas included the Marcellus (Devonian, Pennsylvania), Antrim (Upper Devonian, Biogenic, Ohio) and Barnett (Mississippian, Texas) shale plays. These were selected due to their state of unconventional gas development and regulatory framework. One report that has recently been made available for public scrituny that contains some measurement data has

indicated some interesting trends [27]. The report summarises both sampling from vertical and horizontal drilled wells and reports a full range of chemical and flow data. In addition to this report it was also required to evaluate the hydraulic fracturing fluid composition used in the stimulation of the shale gas well. Since it is uncertain what specific set of chemicals will be used in the hydraulic fracturing event, it was deemed the best possible solution to assess the generalised composition of these fluids. In regard to hydraulic fracturing process it should be kept in mind that although it is referred to as a single process it consists of multiple steps. Each step has a purpose in the hydraulic fracturing event as well as the transport of the propanant down the hole.

3.1. Hydraulic fracturing process

Considering the chemicals used during the hydraulic fracturing process, recent publication of hydraulic fracturing fluid compositions has significantly increased the transparency in the use of these chemicals [28; 29]. However, when examining the reported values in the component information disclosure, some reports indicate that there is still some components that are not listed and are most likely proprietary [30]. In the current paper only a single hydraulic fracturing composition is considered, i.e. gel hydraulic fracturing fluid. A number of hydraulic fracturing fluid setups does exist which can either be based on water (slick water), gel, hybrid, foam or gas (air, inert or petroleum gas). The type of hydraulic fracturing fluid used is dependent on a number of factors and service company preference [28].

A recent investigation by the House of Representatives in the USA [31] found that a list of 750 chemical compounds were used from 2005 to 2009. A number of chemical compounds that have been reported, included 29 chemicals that are known or possible human carcinogens and are regulated under the Safe Drinking Water Act or listed as hazardous air pollutants under the Clean Air Act [31]. BTEX compounds–benzene, toluene, xylene, and ethylbenzene–appeared in 60 of the hydraulic fracturing products used between 2005 and 2009. The hydraulic fracturing companies injected 43.1 million litres of products containing at least one BTEX chemical over the five year period. In many instances, the oil and gas service companies were unable to provide the Committee with a complete chemical makeup of the hydraulic fracturing fluids used [31]. Between 2005 and 2009, the companies used 355 million litres of 279 products that contained at least one chemical or component that the manufacturers deemed proprietary or a trade secret [31]. The practice of using BTEX is currently being phased out due to known issues [31].

Interestingly, most of the chemical components of hydraulic fracturing fluids can be described as either LNAPLs and DNAPLs from a South African context. In addition regarding the interpretation of the Water Act of South Africa, an unwanted consequence may result from the process of hydraulic fracturing. Most notably the process increases the permeability and hydraulic conductivity of the zone that is fractured. This in part can constitute an aquifer at a substantial depth from surface, in this instance it would be regarded as a controlled activity with a host of requirements that needs to be addressed to satisify regulatory practice.

http://dx.doi.org/10.5772/56310

By means of an illustrative example it is possible to get a rough estimate of the extent of chemical usage in hydraulic fracturing. It has been stated that a vertical hydraulic fracturing process requires 1 x 10^6 litres of fluid; in contrast a single horizontal hydraulic fracturing process requires 10 x 10^6 litres of fluid. A pamphlet recently released by Energy in Depth gave a generic summary which stated the percentage composition of hydraulic fracturing fluid as reported by the Department of Energy [32]. If these values are taken as a lower limit then the following deductions can be made from Figure 5. Water and sand component of the hydraulic fracturing process constitutes 99.51% of the total volume used.

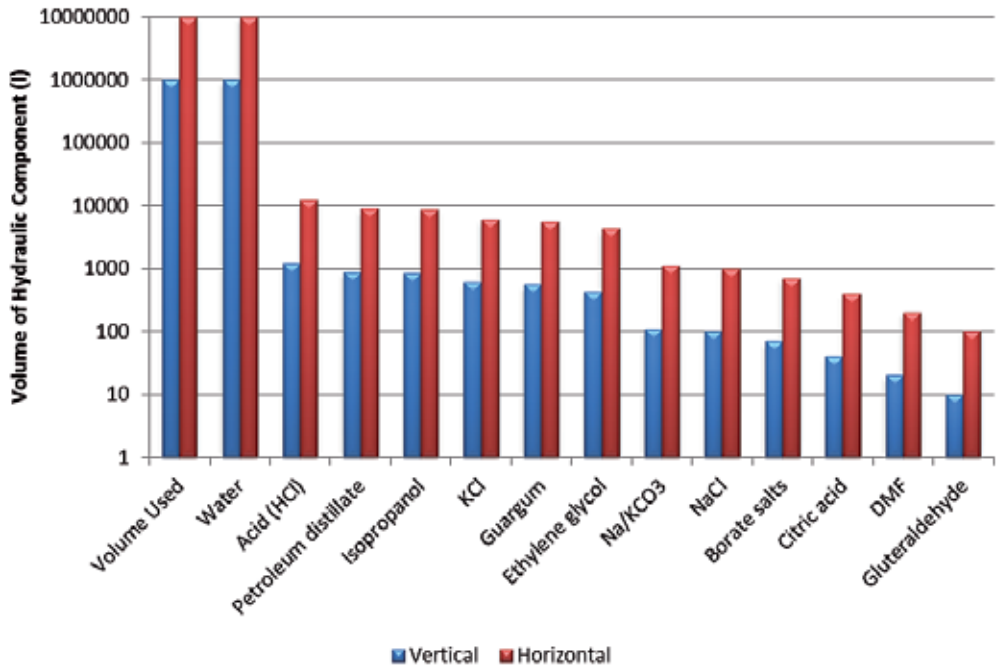

Figure 5. Generalised volume of hydraulic fracturing component used in well stimulation. Vertical well and horizontal well is indicated in blue and red bars, respectively.

Additives employed in the vertical or horizontal fracturing is present in scales approaching tonnes. Chemicals that are of special concern in large quantities are the acid phase, petroleum distillate and isopropanol. The acid phase is composed of hydrochloric acid (10-15%) and is usually part of the first phase of fluids to be injected into the well. The main aim of the acid phase is for cleaning the perforations and initiating fissures in the near-wellbore rock (acid-etching). A secondary consequence is that the acid injected does interact with the host rock formation which can mobilise certain metals, but the mobilisation is dependent on acid concentration and exposure to host rock formation [33]. Petroleum distillates and isopropanol is listed chemicals of concern (carcinogens, SDWA regulated chemicals and hazardous air pollutants in the USA) and is still used in hydraulic fracturing activities [31; 28; 30]. Other

chemicals that are also classified as chemicals of concern are ethylene glycol, dimethyl formamide (DMF) and hydrochloric acid. If these components are added together more than 3410 and 34100 litres of chemicals of concern is injected into a well to develop a vertical or horizontal hydraulic fractured well, respectively. These values represent a single hydraulic fracturing event and the whole process is repeated if another section is hydraulically fractured in a well. It is important to note that it is assumed that the additives represent 0.49% of the total volume, but it can be as high as 5% in some instances, depending on field circumstances (geology, depth, anisotropic stress, water content and stability).

At this stage the most significant threat that hydraulic fracturing fluid can pose is an uncontrolled spill at surface [34]. This is due to the fact that once the hydraulic fracturing fluid has been injected into the subsurface, it reacts with the specified target components as well as the geological formation and subsurface water it comes into contact with. It is at this stage that the hydraulic fracturing fluid can undergo a number of chemical and physical processes to either precipitate, mobilise, react or undergo physical transformations (adsorption and absorption). In either instance the chemical component has been altered.

However, with current internal practices developed in the gas companies the likelihood of an uncontrolled spill have been significantly reduced. It is generally in the companies own best interest to minimise these events as it can affect future gas development rights and litigation. Spills that do occur on site is usually dealt with immediatly or a remediation plan is put into place [34].

3.2. Backflow event after hydraulic fracturing

The current section is focused on a report produced by Hayes [27] for the Marcellus Shale Coaliton. It is one of the few publically available documents that give an indepth report on injected and produced water in a hydraulic fractured well system. The report is used as an illustrative example and it is recognised that the water qualities associated with the Karoo Supergroup will most likely differ. It should be noted that although flowback water is used in this section, that there is no decernable difference between the classification of flowback water and produced water (Table 2). Instead it is an artificial deliniation depending on who has currently control of the site, i.e., hydraulic fracturing team or the production team. Additionally, this section will be used to illustrate the mass of salt produced from these well systems, which in turn would indicate treatment requirements and disposal volumes. It is assumed that the salt will be present as a dry material that would be disposed of in an environmentally approved manner. From a South African perspective, the most likely development of gas well fields will be multiple wells on a single pad. This is due to infrastructure requirements and safety considerations.

The average flowback percentage of vertical and horizontal hydraulic fracturing wells are 43.7% and 25.3%, respectively. In Table 2 the average hydraulic fracturing volume used for vertical and horizontal wells are 5.8 million litres and 13.7 million litres, respectively. This would indicate that more than 50-70% of the fluid injected has been absorbed by the formation. In either instance it does represent a potential source of produced water over time and it is

http://dx.doi.org/10.5772/56310

unclear from present data what the potential might be. Factors that could influence the production of water in shales is the current hydrogeological environment of the shale formations, i.e. hydraulic head (pre-hydraulic fracturing), hydraulic conductivity (pre-hydraulic fracturing), porosity and storativity.

In the remainder of this paper the focus will be on the horizontal well systems only and their associated produced volumes and chemical composition. The total dissolved solids for these selected flowback wells have also been included in Table 3. It should be kept in mind that the backflow water not only consists of hydraulic fracturing fluid but also of chemicals that were produced from the geological formation in which the hydraulic fracturing event took place, thus resulting in a mixture of hydraulic fracturing fluid and shale chemical constituents. The volume of water is also a representation of water injected and water present in the shale, which initially depends on the storativity of the shale and the porosity. Most notable of the tables presented here is that there is a number of missing data points, in either the flowback volumes or total dissolved solids concentration values. In some regard this reduces the usefulness of the data but it does give a good indication of expected volumes and salt loading over time.

		Hydraulic Fluid (HF)	**Cumulative Volume of Flowback Water (FW)**				
Site	Well Type	Total Volume (l)	Day 1* (l)	Day 5 (l)	Day 14 (l)	Day 90 (l)	%FW/HF
A	Vertical	6,366,805	628,000	1,662,371	2,388,466		37.5
B	Vertical	14,979,147	174,091	1,714,201	2,180,988	2,844,283	19.0
C	Horizontal	23,248,077	525,930	1,534,545	2,542,366		10.9
D	Horizontal	3,361,627	453,750	1,284,140	1,580,016	1,778,273	52.9
E	Horizontal	8,505,821	1,360,931	3,232,212	3,912,677	4,082,794	48.0
F	Horizontal	12,400,214	520,206	1,721,832	1,960,472	2,768,446	22.3
G	Horizontal	19,701,865	193,806	1,191,292	1,982,731	2,969,406	15.1
H	Vertical	5,729,107	634,041	2,602,463	3,383,568	5,045,462	88.1
K	Horizontal	11,252,167	914,336	1,274,442	1,506,087		13.4
M	Horizontal	15,770,745	2,610,412	2,851,437	3,135,707		19.9
N	Vertical	1,818,020	386,657	438,646	483,798	562,020	30.9
O	Horizontal	15,375,026	815,764	3,052,874			19.9
Q	Vertical	3,750,987	209,068	568,698	809,245		21.6
S	Vertical	2,616,931	332,919	1,245,189	1,485,736	1,704,821	65.1

Table 2. Reported hydraulic fracturing and flowback volumes from Hayes report [27].

Site	Day 0*	Day 1	Day 5	Day 14	Day 90
C	719	24,700	61,900	110,000	267,000
D	1,410	9,020	40,700		155,000
E	5,910	28,900	55,100	124,000	
F	462	61,200	116,000	157,000	
G	1,920	74,600	125,000	169,000	
K	804	18,600	39,400	3,010	
M	371			228,000	
O	2,670	17,400	125,000	186,000	

Table 3. Concentration of Total Dissolved Solids from Selected Sites (mg/l).

The average chemical salt loading in the return water was in excess of a 95 000 mg/l (Figure 6). Considering these values an expected salt load produced from a single well would be in the range of 241 tons of material, which would require adequate disposal regulations since the waste would contain materials classified as harmful to the environment (Sr, Ba, Li, Cl and Br). A further consideration in processing the material would be the quantity of salts produced during a specified time period. Data reported by Hayes [27] were analysed to derive salt loads at reported day intervals at which chemical sample analysis were performed (Table 4). From the data presented the salt loading values vary considerably over production time and that no singular analysis can be used to determine when the most salt from the hydraulic fracturing well would be produced. This is due to different geologies as well as hydrogeological factors (porosity, permeability and water content of the formation). Secondly, salt loads vary from as little as 45 tonnes to 439 tonnes at 90 day, indicating that a significant quantity of salts is produced from each of the respective wells. The cumulative salts produced from these six wells are in the order of 1 920 tonnes which should be disposed of in an environmentally sound methodology.

In order to determine the 90 day values, a linear regression method was used to fit the data to a logaritmic function. Cumulative salt loading values were used since it was composed of both the flowback volume and total dissolved solids (TDS) value. It was assume in the calculations that the decrease in flow volume would continue to follow a logaritmic function, as would typically be expected from a production well. The salt loading (TDS) had a similar pattern and could be expcted to increase in the same methodology for the 90 day time period. If these values are not considered for the 90 day production then the 14 day production in salt loading is expected to be 1 350 tonnes at an average of 169 tonnes.

http://dx.doi.org/10.5772/56310

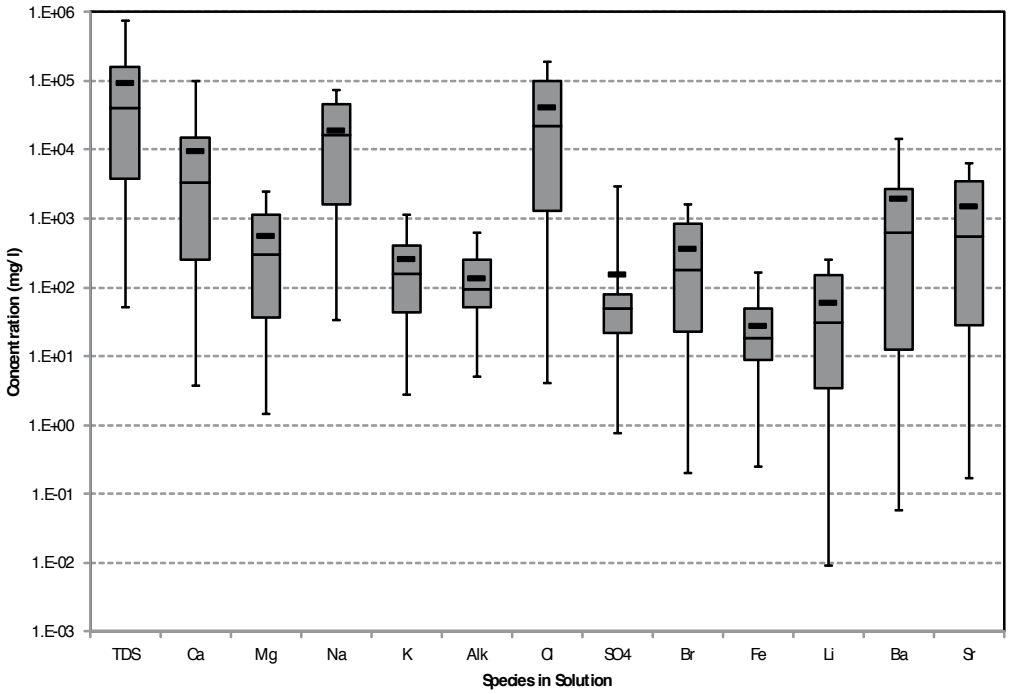

Figure 6. Box-and-Whisker diagram presenting the average distribution of sampled sites chemical components.

Cumulative salt load	Day				
Site	0	1	5	14	90
	(tons)	(tons)	(tons)	(tons)	(tons)
C	17	13	75	186	287*
D	5	4	38	65	96
E	50	39	142	227	353*
F	6	32	171	209	349*
G	38	14	139	273	439*
K	9	17	31	32	45*
M	6			65	
O	41	14	294		

Table 4. Cumulative salt loads in tons at a specific day for the respective sites. Values with * indicate projected values.

Since all of the data which is available from hydraulic fracturing events are based on the Marcellus shale areas in the USA a question arose to the effect as how the Karoo shales compare the Marcellus shale. In order to investigate this question, Whitehill samples were collected from the Geological Department at the University of the Free State and subjected to a leaching test in acid. The results obtained are reported in Table 5 under the heading of Karoo. To draw a comparison between the shales the average chemical analysis of produced water from the Hayes report [27] and average composition of shales [35] were included. Due to different analysis methodologies and production environments these values could not be directly compared, instead ratios of the major elements were used to determine if a possible correlation did exist (Table 6). In general a good correlation existed between the reported sample compositions in the Hem and Karoo data, with all results of the ratios within the same order when compared to each other. In contrast the Hayes report differed notably in the Ba/Ca, Ba/Li and Ba/Mg ratios which could possibly indicate that the use of hydraulic fracturing additives might have changed the chemical character of the produced water or that a substantial difference exists in the geological formation. Interestingly the remainder of the ratios are within an order of each other, especially the Ba/Sr, Ba/Na and Sr/Na ratios. This could possibly indicate that similar chemical properties in the produced water can be expected from the Karoo type shales in which the hydraulic fracturing events will take place. However, it should be kept in mind that without hydraulic fracturing field data these values can only be assumed to indicate possible chemical species. This clearly indicates that a test site should be established to determine the quantity and quality of the backflow water over an extended time period.

Source	**Element (mg/l)**							
	Ba	Ca	Fe	Li	Sr	Mg	K	Na
Hem[1]	250	22500	38800	46	290	16400	24900	4850
Hayes[2]	1552	8451	64	70	1650	728	237	24043
Karoo[3]	2.7	2400	770	1	3.2	308	50	50

1. Hem report USGS [35]; 2. Hayes report GTI [27]; 3. Karoo Sample leached in lab with HCl acid

Table 5. Reported composition of shale samples obtained from various sources.

Source	**Element (mg/l)**						
	Ba/Sr	Ba/Ca	Ba/Li	Ba/Mg	Ca/Mg	Ba/Na	Sr/Na
Hem[1]	0.86	0.01	5.43	0.02	1.37	0.05	0.06
Hayes[2]	0.94	0.18	22.17	2.13	11.61	0.06	0.07
Karoo[3]	0.84	0.01	2.70	0.01	7.79	0.05	0.06

1. Hem report USGS [35]; 2. Hayes report GTI [27]; 3. Karoo Sample leached in lab with HCl acid

Table 6. Ratios of chemical compositions from reported shale samples.

http://dx.doi.org/10.5772/56310

A recent sampling event took place at the Soekor core holes. Currently, the data set is limited and contains both the Soekor core hole data and surrounding well water. Interestingly, one of the core holes produced natural gas that could be ignited. The data is presented in Figure 7 in association with the Hayes report [27] data. Soekor data points are indicated as triangles, with SA 1, 5 and 7 representing samples from Soekor core holes. Sample data SA1 amd SA5 has a similar water type than that observed for the Hayes data set, which would indicate a highly mineralised water type. The main difference in the produced water is that the Soekor core holes have a reduced total dissolved solids content of approximately 6500-7200 mg/l. The third Soekor core hole water data (SA7) clearly has a Na/K-HCO_3 water type and a TDS of 440mg/l, indicating the presence of a surface aquifer interaction or a recharge mechanism that is introducing freshwater into the system. Furthermore, it is unsure at this stage if the anulus of the bore is still intact or if short-circuiting is taking place at the site. The data presented is only preliminary and further data sets is required to fully characterise these sites.

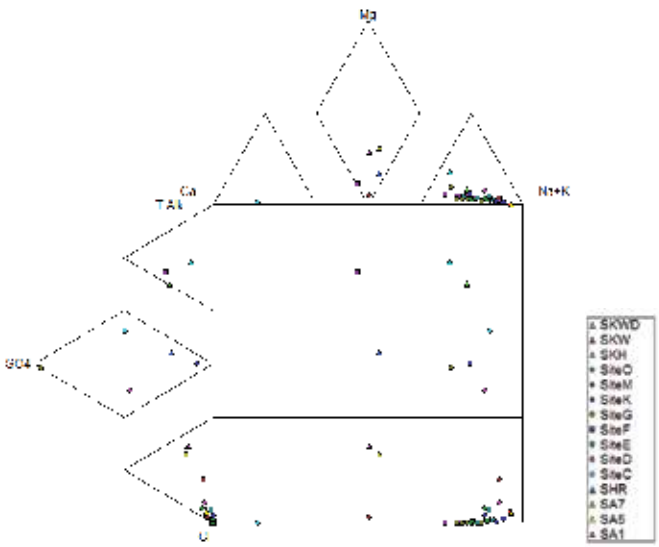

Figure 7. Expanded Durov diagram illustrating the different water types characterised from the Marcellus [27] and Soekor sites.

The Soekor core bores have been abandoned for nearly 40 years and there is still evidence that relatively high salinity water is produced from these sites. The rate of water production is relatively low compared to the data presented by Hayes [27], but as the production rate of water decreases at the sites it is currently unclear if there is still a hydraulic pressure that could produce water at surface. In the instance of the Soekor sites it does seem likely that recharge is occuring and that unless these holes are adequately sealed, a continuous discharge of water and gas might be possible.

3.3. Environmental impacts of hydraulic fracturing

The concerns over hydraulic fracturing centre on a few main issues (Figure 8): (1) migration of gas, (2) migration of fracturing fluids, (3) water use, (4) management of produced water, (5) surface spills and (6) identification of chemical additives. Each of these issues will be addressed in the following numbered sections, it is a summary of best practice guidelines to prevent uncontrolled releases of hydraulic fracturing fluid into the environment or to protect the environment within a reasonable limit of practice.

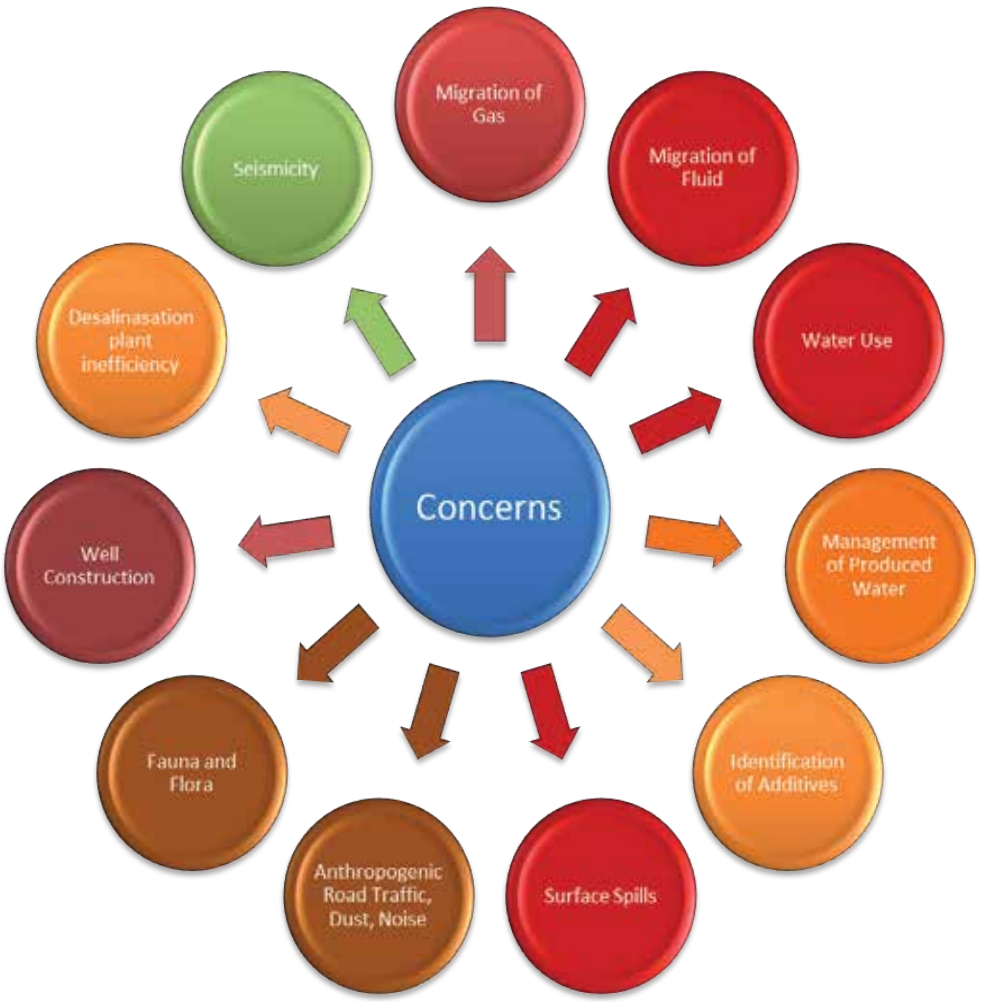

Figure 8. Main concerns regarding impacts of hydraulic fracturing on the environment.

Michigan's laws and rules effectively protect water and other natural resources as well as public health and safety from potential adverse effects of hydraulic fracturing. The Department of Environmental Quality (DEQ) has more than 50 staff employed in enforcing these state

http://dx.doi.org/10.5772/56310

requirements. To date, only a few productive Utica/Collingwood Shale gas wells have been drilled in Michigan and the potential for more extensive development is unknown; however, the DEQ is taking a proactive approach in addressing large-scale hydraulic fracturing as well as other issues associated with deep shale gas development.

1. **Migration of gas or fracture fluids.** A major concern in natural gas development is the prevention of migration of gas or other fluids out of the reservoir and into overlying strata, particularly fresh water aquifers. In cases where this has occurred, it has been the result of well construction problems and not of hydraulic fracturing itself [36; 37]. At depths of about 610 meters or less, fractures propagate horizontally due to the natural stress regime of the rock. This confines the fractures to the gas reservoir. At greater depths, fractures may propagate vertically; however, characteristics of overlying rock layers prevent fractures from extending above the top of the gas reservoir. The installation of steel pipe ("casing"), encased in cement, is key to preventing migration of gas or fluids. Michigan regulations require that each oil and gas well have a casing and cementing plan that will effectively contain gas and other fluids within the wellbore, whether related to fracturing or not. Surface casing must be set a minimum of 35 meters into the bedrock and 35 meters below any fresh water zones and cemented from the base of the casing to the ground surface. Before fracturing or other operations can take place to complete a well for production, an additional string of production casing must be set to the depth of the reservoir and cemented in place. Depending on depth, additional protective casing may be required. To provide additional protection for aquifers and well integrity, the DEQ imposes a permit condition for wells in shallow reservoirs prohibiting hydraulic fracturing within 15 meters of the base of the surface casing. In addition, Instruction 1-2011 requires reporting of volumes, rates, and pressures (including pressure immediately outside of the pipe used to inject the fracturing fluid). Also, DEQ staff check wells in the vicinity to assure there are no wells or other features that could serve as conduits for unwanted movement of fracturing fluids.

2. **Water use.** A fracture treatment of a typical Antrim gas well requires about 189 m^3 of water. In the emerging Utica/Collingwood Shale gas development, the amount of water needed to fracture a horizontal well may be up to 18 927 m^3 or more. To put this in perspective, 18 927 m^3 is the volume of water typically used by eight to ten acres of corn during a growing season. Withdrawal of water for oil and gas operations is exempt from the requirements of Michigan's water withdrawal statute; however, Instruction 1-2011 requires the operator to perform the same water withdrawal impact assessment as any other user of large volumes of water. It also requires installation and monitoring of an observation well if there is a freshwater supply well within one-quarter mile. The DEQ will not approve a withdrawal of water for hydraulic fracturing if it is likely to cause a significant adverse impact to groundwater or surface water.

3. **Management of produced water.** Proper management of produced water is essential in protecting public health and the environment. In Michigan, produced water must be managed. Hydraulic Fracturing and disposed of according to strict rules specifically applying to those fluids. The fluids must be contained in steel tanks and transported to

disposal wells where they are injected into deep rock layers that are isolated from fresh water supplies. The disposal wells are licensed by both the DEQ and the U.S. Environmental Protection Agency, and must be tested periodically to assure well integrity. Instruction 1-2011 requires reporting of the volume of flowback water recovered after a hydraulic fracturing operation.

4. **Surface spills.** Spills of chemical additives or flowback water can have adverse environmental or public health impacts. Michigan requires secondary containment under tanks, wellheads, and other areas where spills may be most likely. If a spill does occur, it must be reported immediately to the DEQ, and all spills must be promptly recovered and cleaned up according to strict requirements.

5. **Identification of chemical additives.** Instruction 1-2011 requires oil and gas operators to provide to the DEQ copies of all Material Safety Data Sheets (MSDSs) for additives used in hydraulic fracturing. The MSDSs include information on physical characteristics, toxicity, health effects, first aid, reactivity, storage, disposal, protective equipment, and spill response. The DEQ will post the MSDSs on the Department's web site for public review. While the details on some of the chemical compounds used in hydraulic fracturing are exempted from disclosure on the MSDSs under federal law, the MSDSs will provide enough information for the DEQ to track and monitor spills.

The regulations enforced in Michigan was designed for the state specifically, in the instance of South Africa the following key differences will need to be considered.

- It most likely will not be possible to dispose of brine by re-injection into deep wells unless an exception in relation to the Water Act is obtained. This will introduce another issue which is disposal of solids and brines that is produced from water purification processes.
- The volume of material produced over the lifetime of a well field might require some engineering adaptation and/or disposal in dedicated waste storage facility constructed just for this purpose. It is still an open question as to how this will be managed.
- On the issue of water use, there is currently enough usable water available to proceed with hydraulic fracturing in the Karoo basin; but it will require planning and development of small scale well fields to abstract adequate volumes.
- Desalination plant efficiencies will need to be increased as the systems are currently sensitive to inflow water quality. It will most likely be associated with a multi-stage facility to remove organics (BTEX, PAHs) from the produced water and total dissolved salts. The composition of the salts is assumed to be mostly Na/Cl but it is expected that Ca, Fe and Mg salts will also be present. The presence of Fe salts might also pose interesting processing challenges for these plants.
- The presence of dolerite formations and thermal springs indicate that there might be a possible upward migration pathway for contamination migration. The probability of this occurring in the vicinity of the well field cannot be ruled out; especially if control measures and well field integrity is not measured over the lifetime of the well.

http://dx.doi.org/10.5772/56310

- In addition post-closure monitoring should be conducted to ensure that well failure does not cause upward migration of contaminants (i.e. Soekor sites).

4. Conclusions

South Africa has in the past been heavily dependent on its rich coal resources to supply it of electricity and fuel; with the discovery of an unconventional terrestrial gas resource it is currently entering a new age of energy independence. The development of this resource has put a strain on local communities due to fears of contaminated surface water and groundwater resources. The area currently being investigated, has both a historical and national significance and emotions are running high. Due to the sensitivity of South Africans regarding the Karoo, a great deal of care is required when gas exploration and eventual development occurs in this area. Key concerns is that the environment will be impacted to such an extent that it will be irrevocably changed. The geology of the area is to a certain extent complex and has dolerite sills and dykes which intrude the country rock. However, the Ecca formations of the Karoo has a considerable carbon content and suitable thickness to make it an ideal target for shale gas development. In this paper the process of hydraulic fracturing have been investigated from a hydrochemical perspective. Firstly, the composition of hydraulic fracturing fluids and the possible risks it pose to the surface and subsurface systems. Secondly, backflow water was evaluated for the Marcellus Shale since no current hydraulic fracturing program has been initiated in South Africa to target the Ecca shale formations. A summary of the key parameters were discussed as well as the production of flowback water and salt loading. Issues relating to salt loading were mainly related to treatment plants and the ability to effectively dispose of the produced brines and salts. A limited set of samples were incorporated into this paper from the Soekor core holes, and similar trends in water type was observed for both the Soekor sites and Marcellus samples.

Environmental impacts due to hydraulic fracturing activities were discussed. Due to South Africa's recent introduction to unconventional gas development a number of important regulatory processes does not exist, i.e. well and site inspectors. The state of Michigan's pro-active approach to regulating shale gas development addressed most of the issues which will be prevelent in the South African regulators mind. Finally, key differences between the regulatory environments were presented as well as unique challenges that faces South Africa in developing the unconventional gas resource.

Acknowledgements

We would like to acknowledge the University of the Free State and Water Research Commission of South Africa for funding. Dr. L. Chevallier for the geological information and assistance in strata characterisation.

Author details

G. Steyl[1,2] and G. J. van Tonder[3]

1 Golder Associates Pty Ltd, Milton, Queensland, Australia

2 Department of Chemistry, University of the Free State, South Africa

3 Institute for Groundwater, University of the Free State, South Africa

References

[1] Twine, T, Jackson, M, Potgieter, R, Anderson, D, & Soobyah, L. Karoos Shale Gas Report: Special Report on Economic Considerations Surrounding Potential Shale Gas Resources in the Southern Karoo of South Africa. In, (Econometrix), 76. Econometrix Park, 8 West Street, Houghton, Johannesburg, 2198; (2012).

[2] Steyl, G, Van Tonder, G. J, & Chevallier, L. State of the Art: Fracking for Shale Gas Exploration in South-Africa and the Impact on Water Resources. In, (Commission W.R.), 96. Pretoria; (2012).

[3] Xiphu, M. R, Mills, S. R, Chevallier, L, Marot, J, Mkhize, M, Motloung, T, Ngesi, P, Okonkwo, A, Msmart, M, Solomons, M, Tiplady, A, & Van Wyk, E. Report on Investigation of Hydraulic Fracturing in the Karoo Basin of South Africa. In, (Resources D.o.M.), 96. 70 Meintjies Street, Sunnyside: Department of Mineral Resources; (2012).

[4] Howard, G. C, & Fast, C. R. Hydraulic Fracturing.. In Monograph of the Henry L. Doherty Series. New York: Society of Petroleum Engineers; (1970).

[5] Montgomery, C. T, & Smith, M. B. Hydraulic Fracturing-History of an Enduring Technology. Journal of Petroleum Technology 62: 16; (2010).

[6] Van Poolen, H. K, Tinsley, J. M, & Saunders, C. D. Hydraulic Fracturing-Fracture Flow Capacity Vs. Well Productivity, Trans. AIME (1958). , 213, 91-95.

[7] Rowsell, D. M, & Swardt, A. M. J. Diagenesis in Cape and Karoo Sediments, South Africa, and Its Bearing on Their Hydrocarbon Potential. Trans. Geol. Soc. S. Afr. (1976). , 79, 81-145.

[8] Tissot, B. P, & Welte, D. H. Petroleum Formation and Occurrence. New York: Springer-Verlag; (1984).

[9] Hayden, J, & Pursell, D. The Barnett Shale, Visitors Guide to the Hottest Gas Play in the Us. In, (INC P.E.Houston, Texas: Institutional Research; (2005). , 52.

http://dx.doi.org/10.5772/56310

[10] De Wit, M. J. The Great Shale Debate in the Karoo. South African Journal of Science 107: 9; (2011).

[11] Veevers, J. J, Cole, D. I, & Cowan, E. J. Southern Africa: Karoo Basin and Cape Fold Belt. In Permian-Triassic Pangean Basins and Foldbelts Along the Panthalassan Margin of Gondwanaland, (Veevers J.J. and Powell C.M.). Boulder, Colorado: Geological Society of America; (1994).

[12] Gradstein, F. M, Ogg, J. G, Smith, A. G, Bleeker, W, & Lourens, L. J. A New Geologic Time Scale, with Special Reference to Precambrian and Neogene. Episodes (2004). , 27, 83-100.

[13] Viljoen, J. H. A. Tierberg Formation. In Catalogue of South African Lithostratigraphic Units, (Johnson M.R.). Pretoria: South African Committee for Stratigraphy, Government Printer; (2005).

[14] Cole, D. I, & Mclachlan, I. R. Oil Shale Potential and Depositional Environment of the Whitehill Formation in the Main Karoo Basin. Geological Survey of South Africa; (1994).

[15] Cole, D. I, & Christie, A. D. M. A Palaeoenvironmental Study of Black Mudrock in the Glacigenic Dwyka Group from the Boshof-Hertzogville Region, Northern Part of the Karoo Basin, South Africa. In Earth's Glacial Record. International Geological Correlation Project 260, (Deynoux M., Miller J.M.G., Domack E.W., Eyles N., Fairchild I.J. and Young G.M.). Cambridge: Cambridge University Press; (1994).

[16] Cole, D. I, & Basson, W. Whitehill Formation. In Catalogue of South African Lithostratigraphic Units, (Johnson M.R.). Pretoria: South African Committee for Stratigraphy, Government Printer; (1991).

[17] Cole, D. I. Prince Albert Formation.. In Catalogue of South African Lithostratigraphic Units, (Johnson M.R.). Pretoria: South African Committee for Stratigraphy. Pretoria: Government Printer; (2005).

[18] Johnson, M. R, Van Vuuren, C. J, Visser, J. N. J, Cole, D. I, Wickens, H. D. V, Christie, A. D. M, & Roberts, D. L. and B. L.G. Sedimentary Rocks of the Karoo Supergroup. In The Geology of South Africa, (Johnson M.R., Anhaeusser C.R. and Thomas R.J.). Johannesburg/Pretoria: Geological Society of South Africa/Council for Geoscience; (2006).

[19] Branch, T, Ritter, O, Weckmann, U, Sachenhofer, R. F, & Schilling, F. The Whitehill Formation-a High Conductivity Marker Horizon in the Karoo Basin. South African Journal Geology (2007). , 110, 465-476.

[20] GA. Background Information Document and Invitation to Comment. In Proposed South Western Karoo Bsoin Gas Exploration Project, (B.V. S.E.C.). 2011.

[21] Dondo, C, Chevallier, L, Woodford, A. C, Murray, R, & Nhleko, L. Flow Conceptualisation, Recharge and Storativity Determination in Karoo Aquifers, with Special Em-

phasis on Mzimvubu-Keiskamma and Mvoti-Umzimkulu Water Management Areas in the Eastern Cape and Kwazulu-Natal Provinces of South Africa. In Research Reports. Pretoria: Water Research Commission of South Africa; (2010).

[22] Rowsell, D. M, & Connan, J. Oil Generation, Migration and Preservation in the Middle Ecca Sequence near Dannhauser and Wakkerstroom. In Some Sedimentary Basins and Associated Ore Deposits of South Africa. Special Publication of the Geological Society of South Africa, (Anderson A.M. and Van Biljon W.J.). Pretoria: Geological Society of South Africa; (1979).

[23] Steyl, G. Estimation of Representative Transmissivities of Heterogeneous Aquifers. In Institute for Groundwater Studies, 132. Bloemfontein: Free State University; (2012).

[24] Murray, R, Baker, K, Ravenscroft, P, Musekiwa, C, & Dennis, R. A Groundwater Planning Toolkit for the Main Karoo Basin. In Research Reports. Pretoria: Water Research Commission of South Africa; (2012).

[25] Kent, L. E. The Thermal Waters of the Union of South Africa and South West Africa. Transactions of the Geological Society of South Africa (1949). , 52, 231-264.

[26] Viljoen, J. H. A, Stapelberg, F. D. J, & Cloete, M. Technical Report on the Geological Storage of Carbon Dioxide in South Africa. In. Pretoria: Council for Geoscience South Africa; (2010).

[27] Hayes, T. Sampling and Analysis of Water Streams Associated with the Development of Marcellus Shale Gas. In, 356. Des Plaines, IL 60018: Marcellus Shale Coalition; (2009).

[28] HalliburtonHydraulic Fracturing: Fluids Disclosure. In, Description of Hydraulic Fracturing and Fluids Used in the Process 28 February. (2013).

[29] FracFocusFind a Well. In, Find a Well (Hydraulic Fracturing)28 February. (2013).

[30] SWEPILPHydraulic Fracturing Fluid Product Component Information Disclosure. In. Erikson 448 4H; (2012).

[31] Waxman, H. A, Markey, E. J, & Degette, D. Chemicals Used in Hydraulic Fracturing. In, (Representatives H.o.). Washington, USA: US Government; (2011).

[32] EIDA Fluid Situation, Typical Solution Used in Hydraulic Fracturing. In DOE, GWPC: Modern Gas Shale Development In the United States: A Primer ((2009). Energy Indepth; 2010.

[33] Fortson, L. A, Yatzor, B, & Bank, T. Physical and Chemical Associations of Uranium and Hydrocarbons in the Marcellus Shale. In Proceedings of' Northeastern (46th Annual) and North-Central (45th Annual) Joint Meeting. Geological Society of America., 60

http://dx.doi.org/10.5772/56310

[34] DOOGMC Department Office of Oil and Gas Management Compliance Report. In. Pennsylvania: Pennsylvania Department of Environmental Protection; (2013).

[35] Hem, J. D. Study and Interpretation of the Chemical Characteristics of Natural Water. In, Contract Alexandria: United States Geological Survey; (1985). (2254)

[36] Bybee, K. Cement Design for the Life of the Well. Journal of Petroleum Technology 54, (2002). , 8(8), 60-61.

[37] Roshan, H. R. S.S. A Fully Coupled-Poroelastic Analysis of Pore Pressure and Stress Distribution around a Wellbore in Water Active Rocks. Rock Mech Rock Eng (2011). , 44, 199-210.

Chapter 11

Regulatory Nirvana for Hydraulic Fracture Stimulation

Barry Goldstein, Michael Malavazos,
Alexandra Wickham, Michael Jarosz,
Dominic Pepicelli, Mieka Webb and Dale Wenham

Additional information is available at the end of the chapter

http://dx.doi.org/10.5772/56381

Abstract

Government are challenged to deploy trustworthy regulation to enable profitable and environmentally sustainable unconventional petroleum projects. A key activity under scrutiny during the development of these projects is hydraulic fracture stimulation. Regulatory 'Nirvana' for unconventional projects and conventional projects alike entails:

- Pragmatic licence tenure;
- Regulatory certainty and efficiency without taint of capture;
- Regulators and licensees with trustworthy competence and capacity;
- Effective stakeholder consultation well-ahead of land access;
- Public access to details of significant risks and reliable research to backup risk management strategies so the basis for regulation is contestable anytime, everywhere;
- Timely notice of entry with sufficient operational details to effectively inform stakeholders;
- Potentially affected people and organisations can object to land access - without support for vexatious objections;
- Fair and expeditious dispute resolution processes;
- Fair compensation to affected land-users;
- Risks are reduced to low or as low as reasonably practicable (ALARP) while also meeting community expectations for net outcomes;

- Licensees monitor and report on the efficacy of their risk management, and the regulator probes same;
- Regulator can prevent and stop operations, require restitution, levy fines and cancel licences; and
- Industry compliance records are public, so the efficacy of regulation is transparent.

These principles are deployed in South Australia where:

- 24 unconventional gas plays are being explored, each with giant gas potential;
- Hundreds of wells have been safely hydraulically fracture stimulated;

Since implementing South Australia's *Petroleum and Geothermal Energy Act 2000* [1] (PGE Act), more than 11,000 notices of entry for petroleum operations led to just one court action, and that was to establish a legal precedent that geophysical surveys can extend outside a licence to enable a complete understanding of the potential resources within a licence.

The introduction of new energy development technologies is inevitable, so regulatory Nirvana requires adaptive learning so that the previously mentioned principles are maintained. Expeditious, welcomed access to land for compatible, multiple uses is the metric for performance, and leading practice is based on the principle that trust is the most valuable lead factor and lag outcome in sustaining land access for resource exploration, development and production.

1. Introduction

The Australian oil and gas industry has contributed greatly to the economic prosperity and quality of life of our communities for decades to date. An opportunity to prolong and expand welcomed contributions in a golden age of unconventional gas is arising. The challenges ahead of a prospective golden age of unconventional gas are many, and include getting regulation and operations right. Results that consistently, simultaneously meet community and investor expectations for social, environmental and economic outcomes will deliver trust in land access and investment – and create a virtuous lifecycle for the upstream petroleum sector for decades to come.

Coal seam methane was Australia's first unconventional gas play to be commercialised and reserves will underpin LNG exports from Gladstone, Queensland. In October 2012, the tap was turned on the first domestic commercial use of shale gas from Moomba 191 in the Cooper Basin – another milestone on the road to develop a variety of unconventional gas resources across Australia. Foreseeing the potential scope of development of unconventional gas resources:

- Companies have shifted budgets to explore, appraise and develop unconventional gas plays;

http://dx.doi.org/10.5772/56381

- People and organisations potentially affected by unconventional gas operations have justifiably expressed concerns for preserving social, natural and economic environments; and
- Governments have made strides to refine regulatory and investment settings to simultaneously satisfy both community and investor expectations for net outcomes.

In this regard, October 2010, the South Australian Government's Department for Manufacturing, Innovation, Trade, Resources and Energy (DMITRE) initiated a consultative group to inform how unconventional gas projects could be undertaken the most sustainably and efficiently, considering the social, environmental and economic impacts and benefits. This group – the Roundtable for Unconventional Gas Projects in South Australia (Roundtable) – played a critical role, informing our Roadmap for Unconventional Gas Projects in South Australia (Roadmap) [2]. As of January 2013, the Roundtable had 230 members including peak representative bodies, companies, universities, media outlets, individuals and key government agencies from all the states, the Northern Territory and the Commonwealth governments. This paper summarises the findings of this Roadmap that relate to world leading practices for the regulation of the development of unconventional petroleum resources that rely on hydraulic fracture stimulation to attain economic flow rates.

2. The Roadmap

The Roadmap for Unconventional Gas Projects in South Australia [2] was developed to provide timely, credible information to people, communities and markets, outlining potential risks and rewards associated with unconventional gas projects. It sets the course for the environmentally sustainable development of South Australia's large endowment of unconventional gas, and encourages safe exploration and production under this State's robust and effective regulatory framework, the PGE Act. The Roadmap helps to ensure people and enterprises potentially affected by unconventional gas projects understand the regulatory framework, the transparent environmental assessment and activity approval processes; and how they will be consulted, so their rights to object in part or in full are supported. The Roundtable also identifies 125 recommendations which cover the life cycle of unconventional gas projects – from exploration to production and possible liquefied natural gas exports, as well as related supply chains and infrastructure matters. Roundtable working groups have reconvened to develop plans to implement these recommendations.

To comment on and further inform the implementation of the 125 recommendations posed in the Roadmap or to enquire regarding participation in the Roundtable for Unconventional Gas Projects in South Australia – readers are asked to contact dmitre.petroleum@sa.gov.au.

3. Regulation to enable hydraulic fracture stimulation in the public's interest — The South Australian approach

Onshore petroleum exploration and development activities in South Australia are administered by DMITRE under the South Australian PGE Act. The PGE Act has a number of aspects

that are considered a comparative advantage without precedent in other Australian legislation [3]. High level objectives of the PGE Act include:

- Sustain trusted practical, efficient, effective and flexible regulation for upstream petroleum, geothermal and gas storage enterprises, and the construction and operation of transmission pipelines, in the State;
- Encourage and maintain competition in the upstream petroleum and geothermal sectors;
- Minimise environmental damage and protect the public from risks inherent in petroleum and geothermal operations;
- Sustain effective consultation processes with people affected by regulated activities, and the public in general; and
- Ensure as far as reasonably practical the security of supply of natural gas.

It is important in this discussion to highlight that in the context of the PGE Act the definition of environment (under s. 4 of the PGE Act) is broad, and includes:

- Land, air, water (including both surface and underground water)
- Organisms and ecosystems – this includes native vegetation and fauna;
- Buildings, structures and cultural artefacts;
- Productive capacity or potential;
- The external manifestations of social and economic life which includes aspects such as human health and wellbeing; and
- The amenity values of an area.

This definition of environment is consistent with the *Environment Protection Act 1993* [4] definition, and is broad to ensure that potential impacts on all natural, social and economic aspects of the environment are identified, considered, and appropriately addressed through the environmental assessment and approval provisions of the PGE Act.

A key lesson learnt by DMITRE in post-event investigations of significant incidents is that regulators must have relevant and up-to-date capabilities (competence and capacity) to be trusted to act in the interests of the many stakeholders involved in upstream petroleum industry activities. This includes protecting natural, social and economic environments; effectively managing the risks of regulatory capture [5]; and providing expeditious approvals. As the regulator of upstream petroleum and geothermal energy activities in South Australia, administering the PGE Act, DMITRE strives to maintain a one-stop-shop or lead agency approach.

This approach has been discussed by Australia's Productivity Commission [6] which concluded:

- One-stop-shops (lead agencies) are the most efficient regulatory approach when well managed without capture;

http://dx.doi.org/10.5772/56381

- Under a lead agency approach … approval of most, if not all, aspects of an application would rest with one designated agency. This agency …would maintain control of the process and in most cases, would consult with other relevant agencies, such as an environmental agency, rather than formally refer the application to a separate agency for assessment. In some limited circumstances where impacts are considered to be significant, a formal referral may take place. By maintaining control of the approval process the lead agency approach is able to streamline approval processes and minimise time delays.
- South Australia's one-stop-shop (through DMITRE), 'is widely seen as a model for other jurisdictions to emulate';
- With appropriate governance, experience in South Australia suggests that [lead agencies] can achieve an appropriate balance between enforcing legislative provisions and expediting approvals.

Properly resourced one-stop-shops (lead agencies) transparently facilitate the delivery of all co-regulatory objectives and requirements, and hence earn trust from the industry, co-regulatory agencies and the public. A one-stop-shop approach enables stewardship of approval processes in parallel rather than in series.

Through this approach DMITRE works closely with its co-regulatory agencies, such as the South Australian Environment Protection Authority (EPA), Department of Environment, Water and Natural Resources (DEWNR), SafeWork SA, Department of Health, Department of Planning, Transport and Infrastructure (DPTI) and Aboriginal Heritage to deliver an efficient application of all relevant laws and regulations applicable to the petroleum and geothermal industries in South Australia.

The PGE Act has been designed to enable a one-stop shop approach such that in complying with the objectives of the PGE Act, upstream petroleum operations' compliance with obligations under other legislation will also be facilitated. These concurrent legislation and requirements include:

- The Commonwealth's *Environmental Protection, Biodiversity and Conservation Act 1999* (EPBC Act) internationally important flora, fauna, ecological communities and heritage places — defined in the EPBC Act as matters of national environmental significance. The Commonwealth Government Department of Sustainability, Environment, Water, Population and Communities (SEWPaC) provides stewardship for the EPBC Act;
- South Australia's *Environment Protection Act 1993* (EP Act), and relevant policies that provide the regulatory framework to protect South Australia's environment, including land, air and water. This legislation was the result of the streamlined integration of six Acts of Parliament and the abolition of the associated statutory authorities. South Australia's EPA provides stewardship for this Act;
- South Australia's *National Parks and Wildlife Act 1972* (NP&W Act), which is the cornerstone for protecting natural environments within parks and regional reserves in the State. The DEWNR provides stewardship for this Act. The NP&W Act is significant as it is a key part

of the co-regulatory approval regime for minerals and energy (including unconventional gas) resource exploration and production in South Australia;

- The South Australian *Work Health and Safety Act 2012* (SA) (WHS Act) is the state's lead legislation to protect people in the workplace. SafeWorkSA provides stewardship for this Act;
- The South Australian *Native Vegetation Act 1991* (NV Act), administered by DEWNR;
- The South Australian *Natural Resources Management Act 2004* (NRM Act), administered by DEWNR;
- The South Australian *Development Act 1993*, administered by the DPTI;
- The *South Australian Public and Environmental Health Act 1987*, and specifically the *Public and Environmental Health (Waste Control) Regulations 2010*, as administered by HealthSA
- The *Native Title (South Australia) Act 1994*, administered by the State's Attorney General's Department
- The Commonwealth *Native Title Act 1993* (NT Act) administered by the Commonwealth's Attorney General's Department
- The South Australian *Adelaide Dolphin Sanctuary Act 2005*, administered by DEWNR
- The *South Australian Aboriginal Heritage Act 1988* administered by the State's Department of Aboriginal Affairs and Reconciliation
- *The South Australian Marine Parks Act 2007* administered by DEWNR
- *The South Australian River Murray Act 2003* administered by DEWNR; and
- *The South Australian Arkaroola Protection Act 2012* administered by DEWNR.

Compliance with these pieces of legislation is facilitated through collaborations and working arrangements between DMITRE and the government agencies that administer these Acts, to ensure that the Statements of Environmental Objectives (SEO) that must be complied with for specific activities are consistent and in keeping with the relevant objects of each of these Acts

4. Principles for best practice regulation

The PGE Act was developed on the basis of the following 6 principles for regulatory best practice:

1. **Certainty.** The regulatory objectives are uniform, clear, and predictable for all stakeholders.
2. **Openness.** Stakeholders are appropriately consulted on the establishment of the regulatory objectives.

http://dx.doi.org/10.5772/56381

3. **Transparency.** The regulatory decision-making processes are visible and comprehensible to all stakeholders and industry performance in terms of compliance with the regulatory objectives is clear to all stakeholders.

4. **Flexibility.** The level of regulatory scrutiny, surveillance and enforcement needed to ensure compliance is determined on the basis of individual company compliance capability and the outcomes to be achieved.

5. **Practicality.** The regulatory objectives are achievable and measurable.

6. **Efficiency.** The compliance costs imposed on both government and the licensee by the regulatory requirements are minimised and justified. Negative impacts on communities are minimised, and licensees remain liable for the cost of their impacts. Furthermore, an appropriate rent (Royalty) is paid to the community from the value realised from the development and production of its natural resources.

The above listed Regulatory Principles can be achieved through the following regulatory strategies.

- Regulatory objectives and assessment criteria for those objectives are developed through broad stakeholder consultation involving industry, government agencies and the community to ensure acceptance and credibility in the environmental objectives to be achieved
- Regulators and licensees maintain trustworthy capabilities (competence and capacity)
- Effective, informative stakeholder consultation by both project operators and regulators is initiated well ahead of land access. This drives operators to explain their planned activities and any potential risks, seek feedback on areas of interest or concern for the community, and establish relationships and terms for land access with stakeholders well before applying for activity approval from DMITRE, e.g. before any particular activity 'gets personal'
- Provide public access to details of risks, reliable research to reduce key uncertainties and support risk management strategies so the basis for regulation is contestable
- Timely notice of entry with sufficient operational details to effectively inform stakeholders
- Potentially affected people and organisations can object to land access – while the regulator and prescribed dispute resolution processes do not support, and hence minimise, vexatious objections
- Fair and expeditious dispute resolution processes
- Fair compensation to affected land-users for costs, losses, and deprivation of land use due to operations
- Reduction of risks to low or as low as reasonably practicable (ALARP), while also meeting community expectations for overall outcomes
- Licensees monitor and report (to the regulator) on the efficacy of their risk management processes, and the regulator probes same

- The regulator can prevent and stop operations, require restitution or rehabilitation, levy fines and cancel licences
- Industry compliance records are made public, so the efficacy of regulation is transparent.

Clear, efficient and effective activity approval processes are fundamental for trustworthy regulation. Mapping approval processes can also elucidate scope for increased efficiency and reduced red tape. Figures 1, 2 and 3 illustrate the three-stage process for petroleum and geothermal licensing and approvals in South Australia with a one-stop-shop approach led by DMITRE, for exploration, retention, production and associated activities.

The first stage (Figure 1) entails the grant of a licence authorising the licensee to carry out specific activities to which the licence relates. Environmental assessments are required in the second stage (Figure 2). Statements of Environmental Objectives (SEOs) and environmental assessment criteria for activity approvals are established in this second stage. Finally, in the third stage (Figure 3), a location-specific activity notification is submitted for assessment and approval, where required.

All three stages are required to be completed before regulated activities can commence. In practice, it is possible for some aspects of each stage to progress in parallel. This flexibility is most easily enabled through discussions with the regulator (DMITRE) early in the planning process. Figures 1, 2 and 3 specify relevant regulations (of the PGE Act) to help guide licensees through these stages.

The proceeding sections describe stage 2 (Figure 2) and stage 3 (Figure 3). For details of license authorisation (stage 1) – refer to [2].

5. Environmental assessment and approval

The grant of a PGE Act licence does not provide an automatic entitlement to conduct operations. Rather, regulated activities under the PGE Act (under s. 96) may not be carried out unless an approved Statement of Environmental Objectives (SEO) is in place, prepared on the basis of an Environmental Impact Report (EIR).

The EIR identifies all potential impacts and their risks relating to the activity and the proposed risk mitigation strategies. The SEO identifies the environmental objectives to be achieved to address the risks identified in the EIR and the criteria to be used to assess achievement of the objectives.

Through the consultation requirements of the PGE Act, DMITRE expects that licensees will initiate consultation with stakeholders, generally through information sessions or meetings prior to and during the development of their EIR and SEO, to describe their planned activities and the potential impacts, positive or otherwise, which may be experienced by the stakeholders. This is also an opportunity for the licensee to respond to any queries that their stakeholders may have and to understand stakeholder concerns, to ensure that they are addressed within the EIR and SEO.

http://dx.doi.org/10.5772/56381

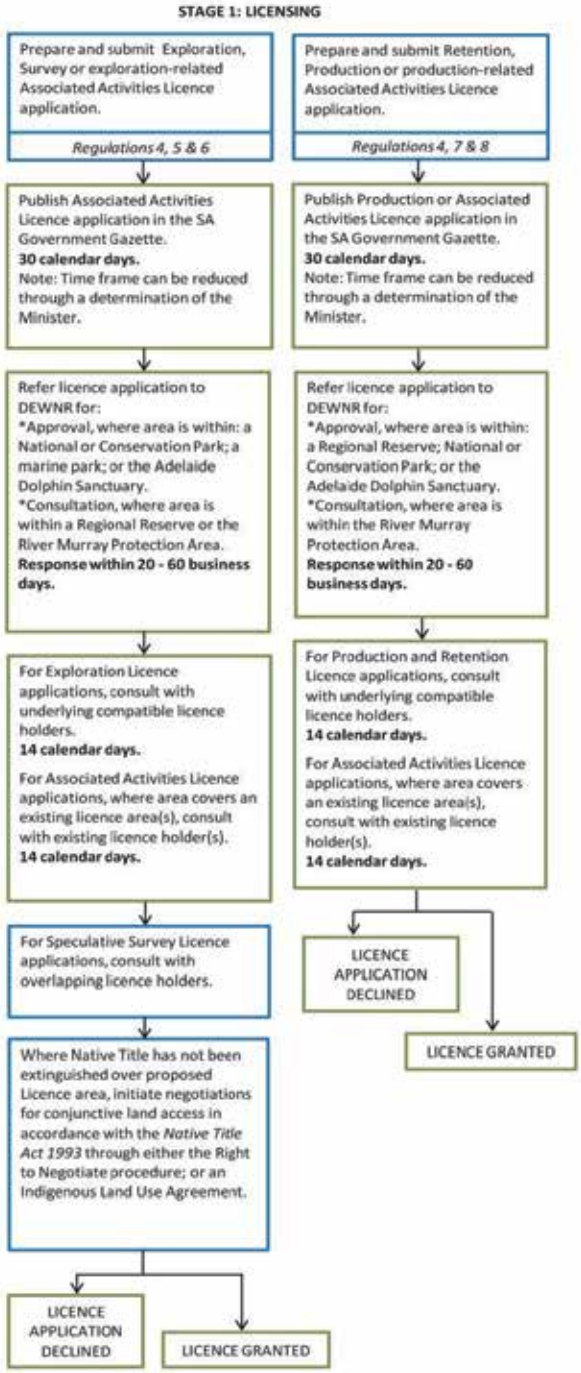

Figure 1. of licensing and approval process for exploration, retention and production activities pursuant to South Australia's *Petroleum and Geothermal Energy Act 2000.* (Blue box = *initiated by proponent/Licensee and* Green box = *initiated by DMITRE/ SA Government)*

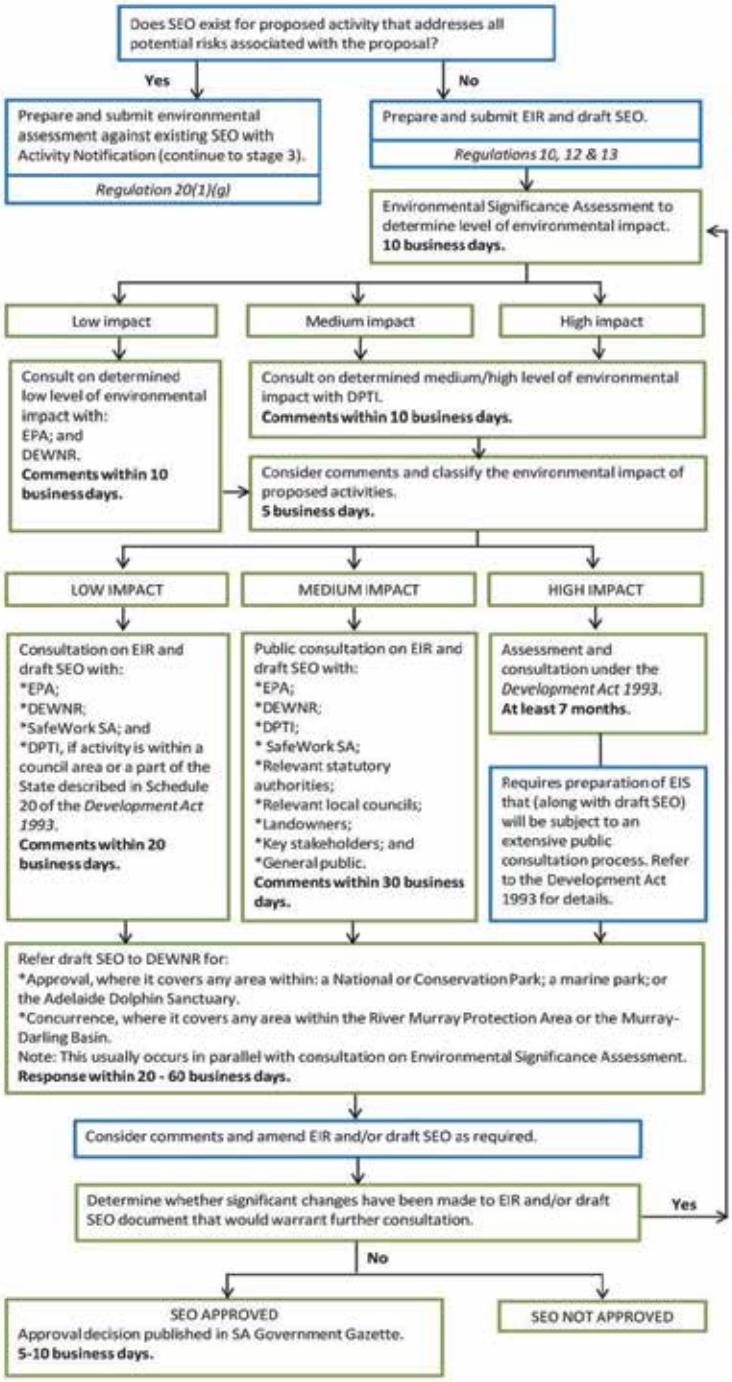

Figure 2. Stage 2 of licensing and approval process for exploration, retention and production activities pursuant to South Australia's *Petroleum and Geothermal Energy Act 2000*. (Blue box = initiated by proponent/Licensee and Green box = initiated by DMITRE/ SA Government)

http://dx.doi.org/10.5772/56381

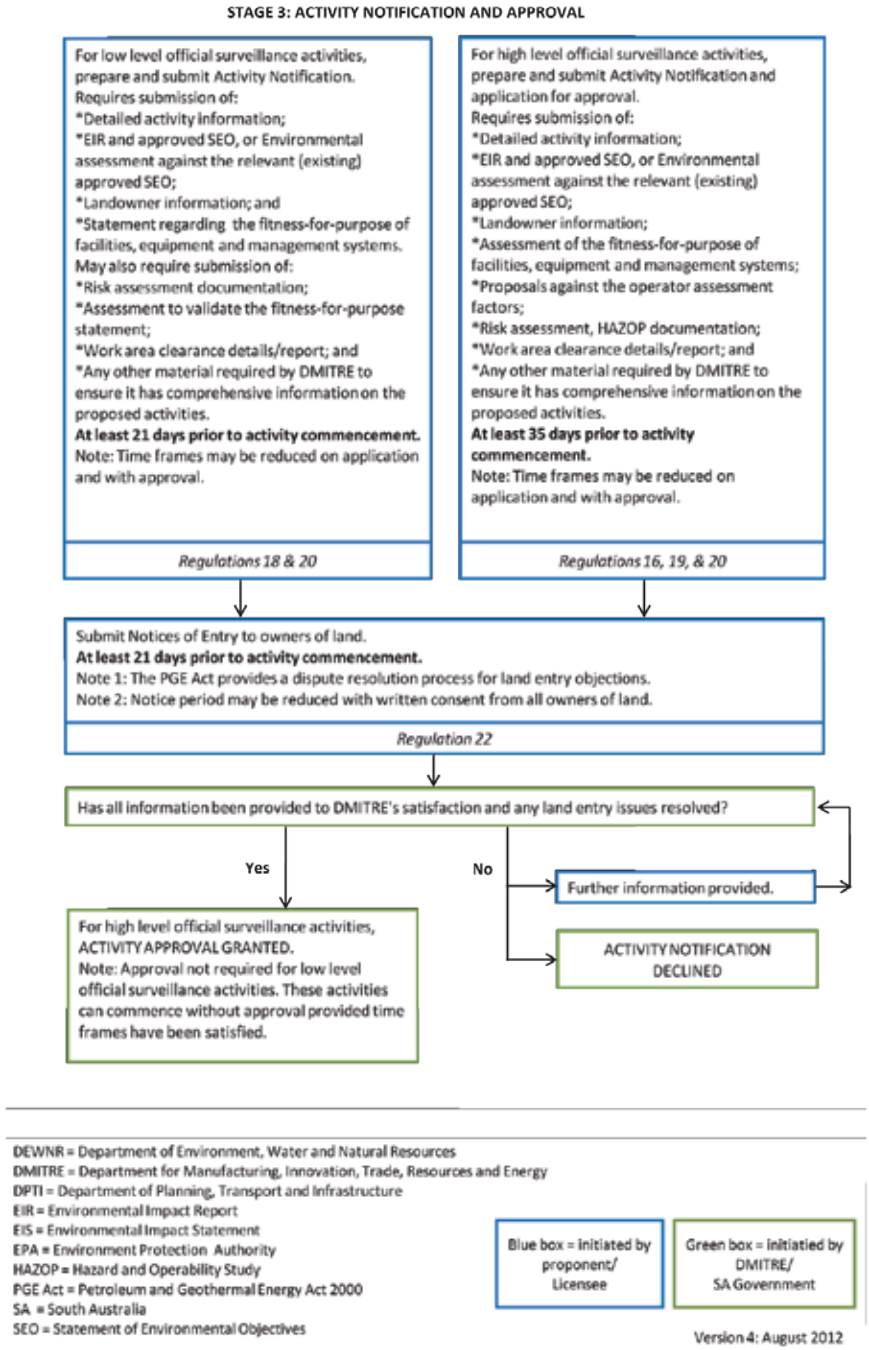

Figure 3. Stage 3 of licensing and approval process for exploration retention and production activities pursuant to the *Petroleum and Geothermal Energy Act 2000*.

Other agencies with the duty of care for ensuring the objects of the legislation that they administer are met are also consulted early to ensure their requirements are included within the objectives detailed in the SEO.

Once an EIR and draft SEO have been prepared and submitted for assessment, DMITRE uses the information provided in the EIR to complete an environmental significance assessment to determine the level of environmental impact of the activity. If prior consultation is not demonstrated, then DMITRE will conduct a broader consultation on the draft documents to ensure stakeholders including landholders and other government departments have been provided with opportunities to raise any issues of concern they may have with the activities as described or the level or accuracy of information provided, prior to SEO approval and well before the commencement of regulated activities.

The significance assessment is conducted based on the information provided in the EIR and in accordance with publicly documented criteria to assess the level of certainty in the predicted impacts, their potential consequences related to the proposed activities and the degree to which these consequences can be managed. The environmental significance criteria include assessment of the level of stakeholder concern. In cases where the level of stakeholder consultation is not demonstrated or the EIR documents high levels of stakeholder concern then this may indicate deficiencies in stakeholder consultation during the development of the EIR and draft SEO. Where DMITRE's assessment identifies such a deficiency, the determined level of environmental significance may be greater and likely to trigger more extensive stakeholder consultation by DMITRE. This ensures relevant stakeholders are provided with appropriate time for opinions to be considered and represented equitably in advance of SEO and subsequent activity approvals.

The combination of the outcomes of the significance assessment criteria lead to the determination of an overall level of environmental impact of the activity as low, medium or high. The level of environmental impact that is assigned to a particular activity in turn determines the consultation that DMITRE undertakes, both on the level assigned, and the content of the EIR and draft SEO documents. These consultation arrangements are outlined within the PGE Act, and within administrative arrangements between DMITRE and its co-regulatory agencies, which are all available on the DMITRE website [7].

Regardless of the determined level of environmental impact, all SEOs and associated EIRs are public documents and can be found on the DMITRE website [8] within the Activity Reports section of the Environmental Register.

6. Activity notification and application for approval

The grant of PGE Act petroleum exploration, retention, production and pipeline licences does not provide an automatic entitlement to land access for regulated upstream petroleum operations.

http://dx.doi.org/10.5772/56381

Once an SEO is approved, a licensee can apply for approval to undertake a specific activity that is described within the relevant EIR and SEO. With the activity approval application the licensee provides DMITRE with an Activity Notification (Regulation 20 of the PGE Act) which contains detailed activity information including:

- an environmental assessment of the activity against the relevant SEO, including assessment as to whether the activity may have potential significant impacts on Matters of National Environmental Significance (MNES)
- landowner information (including copies of notices of entry sent to landowners)
- an assessment of the fitness for purpose of the licensee management systems and any facilities or equipment to be used
- work area clearance details and report
- risk assessment documentation
- any further information or material as required by DMITRE to ensure that the department has comprehensive information on the proposed activities.

Where MNES are identified, then referral to the Commonwealth Minister for Environment will be made by the licensee or the Department, for assessment and a decision as to whether the activity requires approval under the Environment Protection and Biodiversity Conservation Act 1999 (EPBC Act) [9]

Licensees can be classified as carrying out activities requiring high or low level official surveillance. The level of official surveillance determines the information that must be provided in the notification, the level of scrutiny that DMITRE applies during review of the notification, and the period of notice prior to the proposed commencement of activities. The PGE Act outlines operator assessment factors (Regulation 16 of the PGE Act) that consider the licensees policies, procedures, management systems and track record to classify the licensee's level of official surveillance.

7. Notice of entry

Mutual trust for compatible, sustainable land access for upstream petroleum operations are traditionally indemnified with formal land access agreements struck between licensees, potentially affected people and enterprises. To provide impetus for fair and sustainable land access for petroleum, geothermal energy and gas storage operation in the State, the PGE Act was amended in 2009 to expand the 'owner of land' definition to cover all persons who may be directly affected by regulated activities, entitling them to notices of entry and compensation. This amendment has proved to be a driver for mutual respect. With this incremental legislated requirement, owners of land are provided with opportunities to raise concerns prior to the commencement of regulated activities.

Landowners are provided with information on the nature of the activities to be carried out including any anticipated events and the management of their consequences to minimise risks

to an acceptable level, to enable the landowner to make informed decisions on whether this would have an impact on the land.

Landowners are entitled to object to the licensees proposed entry by giving notice to the licensee within 14 days of the licensee notice of proposed entry and the activity cannot be undertaken until the dispute is resolved. The licensee and the landowner should attempt to reach an agreement of terms under which the licensee may enter the land, or if the risks of the activity to the landowner are too high the licensee may choose to modify the activity and re-issue the Activity Notification. Landowners may also raise any issues or concerns associated with the conduct of activities with DMITRE. In rare cases where the licensee and the landowner cannot resolve the dispute, then the Minister may attempt to mediate between the parties or either party may apply to the Warden's court for resolution. To date, disputed Notices of Entry have been resolved through satisfactory negotiation and have not reached the Warden's Court.

Also, under the PGE Act, owners of land are entitled to appropriate compensation from petroleum licensees for any losses, deprivation or reasonable costs sustained during both the process of negotiating land access and for the full period of land access, right through to the decommissioning of any facilities.

8. Compliance and enforcement

DMITRE continuously monitors licensee performance and compliance with the PGE Act. South Australia's approach to provide fair, predictable and trustworthy regulation has been described by Malavazos [10] and entails a publicly available compliance policy [11] which is available on the DMITRE website. South Australia's compliance policy is centred on the prevention of harmful incidents, however depending on the severity of an incident may culminate in prosecution and licence cancelation when warranted. The compliance policy is summarised as a compliance pyramid as shown below in Figure 4.

DMITRE prepares a PGE Act Annual Compliance Report for the purpose of outlining:

- The compliance monitoring and surveillance activities carried out by DMITRE during each year for activities regulated under the PGE Act;
- Providing an overview of the regulatory performance of the petroleum and geothermal industries in accordance with the requirements of the PGE Act;
- All serious incidents that may have occurred from the previous year; and
- Persuasive, compulsive and punitive enforcement actions that may have been taken during the year (as indicated in Figure 4)

DMITRE's Petroleum and Geothermal Energy Act Compliance Report [12] and Company Annual Reports [13] which report on activities undertaken within each licence area are all publicly available through DMITRE's website.

http://dx.doi.org/10.5772/56381

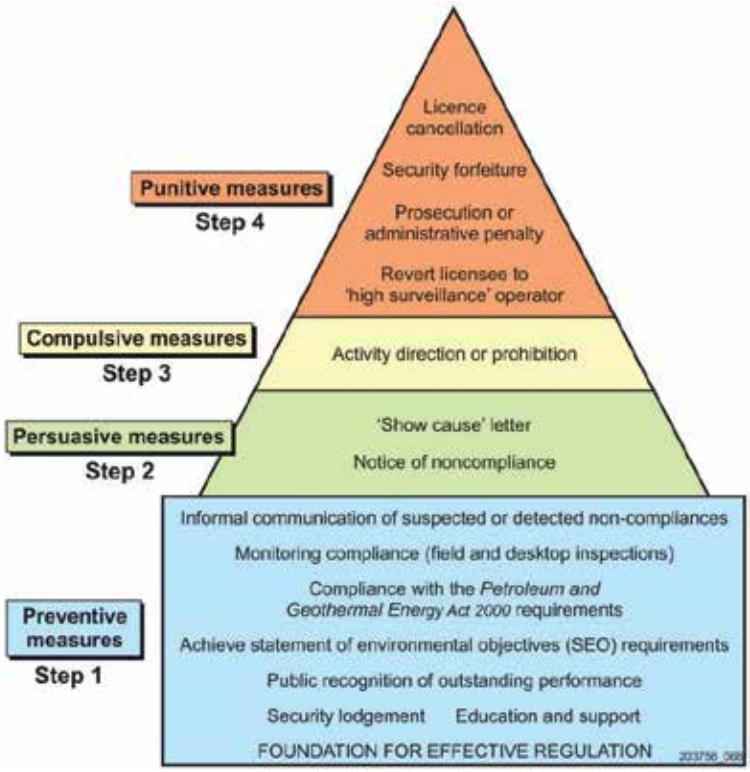

Figure 4. South Australia's compliance enforcement policy under the PGE Act.

As well as information provided through the Activity Notifications, DMITRE regularly meets with licensees to discuss their activities and compliance, and conducts ongoing monitoring and surveillance through both field and desktop studies.

9. Conclusions

Salient findings from the Roadmap [2] and key aspects of South Australia's current regulation of unconventional gas development, including the regulation of hydraulic fracture stimulation, are summarised below.

1. Trusted land access is the most valuable lead factor and outcome.
2. Operators and regulators must act early to effectively engage and inform stakeholders so they can make informed decisions on activities. This engagement is best initiated well ahead of land access. South Australia's regulatory framework drives operators to explain their planned activities and any potential risks, seek feedback on areas of interest or concern for the community, and establish relationships and terms for land access with stakeholders well before applying for activity approval from regulators.

3. Regulation for compatible, multiple use of land in Australia is undertaken with both risks and net benefits in mind. Considerable net benefits flow from community ownership of subsurface resources when development effectively manages risks to social, natural and economic environments.

4. Operators and regulators should adhere to the golden rules for the golden age of gas, as published by the International Energy Agency [14]– which are:

   - Measure, disclose, engage;
   - Watch where you drill;
   - Isolate wells – protect against leaks;
   - Treat water responsibly;
   - Eliminate venting and minimise flaring;
   - Think big; and
   - Consistent high environmental performance

5. International standards [15] for unconventional gas resource and reserve definitions should be adopted.

6. Effective, trusted regulation and attractive investment settings are the most effective inputs from governments to beget safe, secure, and competitively priced gas for domestic and international gas markets for decades to come.

7. Regulators must have relevant and up-to-date capabilities (competence and capacity) to be trusted to act in the interests of the public in protecting natural, social and economic environments in relation to the full-cycle of mineral and energy resource projects, including unconventional gas operations.

8. New energy development technologies will necessitate evolutionary improvement to regulatory frameworks, and best practice regulation will continually evolve

9. A one-stop-shop (lead agency) approach to regulation enables co-regulators to do their jobs in parallel, rather than in series. This fosters efficiency without reducing stringent standards for ecologic, social, heritage and economic outcomes.

10. Welcomed investment in the development of unconventional gas will effectively reduce risks to as low as reasonably practical while simultaneously meeting community expectations for net outcomes. This will be achieved with, amongst other actions, astute investment in economic unconventional plays,

11. The key ingredients of best practice regulation are frameworks that: elicit community trust and investor confidence; provide certainty; entail robust public consultation processes; are transparent; enable flexibility; are open to amendment; are efficient; are practical; and focus on outcomes. This amounts to an overall check-list for best practice co-regulation.

http://dx.doi.org/10.5772/56381

Acknowledgements

The authors thank the participants in the Roundtable for Unconventional Gas Projects in South Australia for their valuable advice in developing the Roadmap for Unconventional Gas Projects in South Australia. Participants in the Roundtable to its publication in December 2012 are listed in Appendix 1 of the Roadmap [16].

Author details

Barry Goldstein, Michael Malavazos, Alexandra Wickham, Michael Jarosz, Dominic Pepicelli, Mieka Webb and Dale Wenham

Energy Resource Division, 'Department for Manufacturing, Innovation,Trade, Resources & Energy (DMITRE), State Government of South Australia, Australia

References

[1] Petroleum and Geothermal Energy Act (2000). South Australia http://www.legislation.sa.gov.au/LZ/C/A/PETROLEUM%20AND%20GEOTHERMAL%20ENERGY%20ACT%202000/CURRENT/2000.60.UN.PDF

[2] Department for Manufacturing, Innovation, Trade, Resources and Energy. Roadmap for Unconventional Gas Projects in South Australia; December (2012). http://www.petroleum.dmitre.sa.gov.au/SA_Unconventional_Gas_roadmap

[3] Goldstein, B. A, Alexander, E, Cockshell, D, Malavazos, M, & Zabrowarny, J. The Virtuous Life-Cycle for Exploration and Production (E&P): Lead and Lag Factors. APPEA Journal; (2007). , 47

[4] Environmental Protection Act (1993). South Australia http://www.legislation.sa.gov.au/LZ/C/A/ENVIRONMENT%20PROTECTION%20ACT%201993/CURRENT/1993.76.UN.PDF

[5] Malavazos, M. A Model for Environmental and Health and Safety Regulation for the Mining and Upstream Petroleum Industries. Masters thesis. Flinders University South Australia; (1998).

[6] Productivity Commission Research Report- Review of Regulatory Burden on the Upstream Petroleum (Oil and Gas) Sector; (2009). www.pc.gov.au/__data/assets/pdf_file/0011/87923/upstream-petroleum.pdf

[7] Department for Manufacturing, Innovation, Trade, Resources and Energy. Petroleum: Administrative Arrangements. http://www.petroleum.dmitre.sa.gov.au/environment/regulation/admin_arrangements

[8] Department for Manufacturing, Innovation, Trade, Resources and Energy. Petroleum: SEO, EIR and ESA Reports. http://www.pir.sa.gov.au/petroleum/environment/register/seo,_eir_and_esa_reports

[9] Department of Sustainability, Environment, Water, Population and Communities. Environmental Assessments. http://www.environment.gov.au/epbc/assessments/

[10] Malavazos, M. The South Australian Petroleum Act 2000- principles and philosophy of best practice regulation. MESA Journal April (2001). , 21

[11] Department for Manufacturing, Innovation, Trade, Resources and Energy. Petroleum and Geothermal Energy Act Compliance Policy; (2012). https://sarigbasis.pir.sa.gov.au/WebtopEw/ws/samref/sarig1/image/DDD/RB201000013.pdf

[12] Department for Manufacturing, Innovation, Trade, Resources and Energy. Petroleum: Petroleum and Geothermal Energy Act Annual Compliance Reporting. http://www.pir.sa.gov.au/petroleum/legislation/compliance/petroleum_act_annual_compliance_report

[13] Department for Manufacturing, Innovation, Trade, Resources and Energy. Petroleum: Annual Reports. www.pir.sa.gov.au/petroleum/legislation/company_annual_reports

[14] International Energy Agency Golden Rules for a Golden Age of Gas, World Energy Outlook Special Report on Unconventional Gas; (2012). www.worldenergyoutlook.org/media/weowebsite/2012/goldenrules/WEO2012_ GoldenRulesReport.pdf

[15] Society of Petroleum Engineers (SPE)Petroleum Resources Management System; (2007).

[16] DMITRE Roadmap for Unconventional Gas Projects in South Australia, Appendix 1; (2012). http://www.misa.net.au/__data/assets/pdf_file/0009/178344/Appendix_1_Rpundtable_Members.pdf

Chapter 12

How Can Understanding Community Concerns About Hydraulic Fracturing Help to Address Them?

S.T. Cham and P. Stone

Additional information is available at the end of the chapter

http://dx.doi.org/10.5772/56442

Abstract

Hydraulic fracturing has been the focal point of widespread and global public debate. While the resources sector typically sees hydraulic fracturing as a low-risk method for accessing the coal seam and shale gas reserves required to meet growing public demand for energy, some in the community perceive it as an unmanageable and unacceptable risk. Concerns about hydraulic fracturing and the coal seam gas (CSG) industry include the health impacts of chemicals used, contamination of water supplies from fugitive gas after hydraulic fracturing, equity of land and water access, long term impacts on groundwater, and the full life cycle emission of greenhouse gases from CSG compared to that of coal. This paper highlights the main psychological drivers behind some of these concerns and a possible approach to effectively address them.

1. Introduction

Hydraulic fracturing has been used to increase the rate and total amount of oil and gas extracted from reservoirs for many decades, so why has it now sparked community concern and global public debate? Part of the answer is gas consumption, particularly unconventional gas consumption.

Gas is the third largest global energy source, currently accounting for around 21 per cent of global primary energy consumption. Global gas consumption has increased at an average annual rate of 2.8 per cent since 2000, to reach 128 166 petajoules (PJ) in 2010. It is a relatively flexible and clean fuel and is projected to be the fastest growing non-renewable energy source over the next 20 years[1].

Over the past decade Australia's gas consumption grew by 4 per cent per year. In 2009–10 gas accounted for 23 per cent of Australia's primary energy consumption and 15 per cent of the energy used for electricity generation. Gas consumption in Australia is projected to increase by 2.9 per cent per year over the next 20 years[1].

Gas is Australia's third largest energy resource after coal and uranium[1]. Australia has both conventional and unconventional gas resources such as coal seam gas (CSG), tight gas and shale gas. In 2011, Australia's economic demonstrated resources (EDR) and subeconomic demonstrated resources (SDR) of conventional gas were estimated at 173 000 PJ[1]. There are significant CSG resources in eastern Australia that are being developed for domestic use and liquefied natural gas (LNG) export. The EDR and SDR of CSG were estimated to be around 101 434 PJ, in 2011[1]. According to the Australian Gas Resource Assessment (2012), Australia is likely to possess significant shale gas and tight gas resources, although as yet these are poorly quantified as exploration for these commodities within Australia has only recently commenced.

In 2009–10 the amount of gas produced in Australia was 2005 PJ, 10 per cent of which was from CSG production. Around 48 per cent of Australia's gas production that year was exported as LNG. Gas production in Australia is projected to reach 8274 PJ over the next 20 years, with production from both conventional gas and CSG to rise[1].

Over the last five or so years there has been an increase in CSG production in eastern Australia and in some cases this has occurred in locations that previously had no gas or oil production. The rapid growth in CSG production coupled with the use of hydraulic fracturing has raised community concerns about the technology. While the resources sector typically sees hydraulic fracturing as a low-risk method for accessing the coal seam and shale gas reserves required to meet growing public demand for energy, some in the community perceive it as an unmanageable and unacceptable risk. This is an underlying reason why hydraulic fracturing is causing concern and debate.

Why do these opposed perceptions exist, and is it possible to reconcile them? This paper outlines the main concerns the general public have about CSG and hydraulic fracturing based on the observations of public discourse in the media, social media and direct involvement in researching and communicating environmental and social impacts of CSG developments. It also highlights the main psychological drivers behind these concerns and a possible approach to effectively address them.

2. Public concern about CSG extraction and hydraulic fracturing

The CSG industry has the potential to provide substantial economic benefit to Australia. The Hon Martin Ferguson, Minister for Resources and Energy and Minister for Tourism, has said "In Queensland alone, if the industry reaches its forecast potential, it will be responsible for more than 20,000 jobs, provide $243 billion in tax to the Australian Government and result in real incomes in Queensland rising by $28,300 per person over the period from 2015 to 2035"[2].

http://dx.doi.org/10.5772/56442

In February 2012, *The Australian* published the results of a poll that gauged the top-of-mind issues for Queensland voters during the State election campaign. While health and the economy remain the priority for Queensland voters, 40 per cent of respondents opposed and 27 per cent were undecided about the $60 billion CSG industry, far outnumbering the 33 per cent of supporters[3].

The reasons why members of the general public, such as environmental groups, Aboriginal groups, suburbanites in Brisbane and Sydney, directly affected farmers/landowners and their communities oppose the CSG industry include:

- the legitimacy of new fossil fuels in a carbon-constrained world;
- pure emotional reactions (of individuals and groups) to the industry;
- equity of land and water access, this extends to questions of 'who benefits?' and 'is any benefit worth the disruption to established community ways of life?';
- impact on agricultural land and food security;
- long term impacts on groundwater;
- the full life cycle emission of greenhouse gases from CSG compared to that of black (and brown) coal;
- management and disposal of treated CSG wastewater and salt; and
- robustness of environmental regulation and perceived regulatory complicity motivated by revenue goals.

There is also general uncertainty of the scale of the industry, as well as the uncertainty of environmental and social impacts across the landscape and over time. Such uncertainty may contribute to and/or reflect existing public anxiety about the ability to personally and collectively exert control over their interests, environment and well-being. These are deep human emotional needs, perturbation of which can prompt highly emotional responses.

Furthermore, public anxiety is buttressed by a host of specific issues about the practice of hydraulic fracturing that include the:

- mobilisation of native contaminants that have previously been confined within coal seams;
- introduction of harmful chemicals via direct injection;
- fate of chemicals used;
- health impacts of chemicals used and those mobilised by hydraulic fracturing;
- contamination of water supplies from fugitive gas after hydraulic fracturing;
- seismic activity and tremors associated with the drilling and fracturing process;
- degree of control over the fracturing process; and
- capacity to prevent and/or remediate accidents.

The unconventional gas industry, scientists and regulators tend to believe the above mentioned risks are generally understood and manageable. However, some in the community, such as environmental groups, suburbanites and farmers, perceive these risks to be not well understood.

The general tenor of public concerns regarding hydraulic fracturing is not unique, and its proponents may be able to learn from the experience of other technical advances that have challenged community acceptance. Genetic modification of foods[4-6] and the purification of treated sewerage for drinking water[7, 8], for example, have each aroused concerted community campaigns against their introduction. A range of studies have been conducted to understand the underlying (psychological/sociological) concerns about each technology[4, 9, 10].

3. The role of attitudes and risk perception

Public acceptance of science and technology can be examined on different levels. Commonly, the concept of attitudes provides the framework for social research in this area. Psychologists define an attitude as a tendency to evaluate a particular entity with a certain degree of favour or disfavour [11]. Risk perception might be regarded as a specific form of an attitude towards a specific entity[12].

In terms of genetically modified (GM) foods and crops, knowing the amount or extent of benefits alone is not sufficient to determine public acceptability. Consideration of the perceived risks of the technology also needs to be taken into account[13].

There has been research that suggests people tend to perceive risk-benefit as an inverse relationship[14, 15]. It has also been suggested that if perceptions of the risks related to any potential hazard or technology are sufficiently high, no amount of benefits are liable to make it acceptable[16].

The term 'risk' is further complicated by the perceptual multidimensionality of the concept. People do not perceive the risk of hazards according to a single dimension related to predicted injuries or fatalities but interpret risk according to several independent perceptual factors, termed 'dread', 'familiarity' and 'number of people exposed'[17]. Other research looking at food technologies and hazards has uncovered similar dimensions, which have been termed 'severity', 'number of people exposed' and 'unknown risks'[18].

The commonly found dimension of 'familiarity' or 'unknown risks', means that people might judge a technology to be 'risky' if they know little about it and/or they *perceive* that science and scientists know little about it[13]. Risk 'severity' has also been shown to be an important dimension to people when forming risk perceptions[19], as has perceived lack of control over preventing or early remediation of incidents[20].

For some of the general public, the perceived risks of the CSG industry and hydraulic fracturing far outweigh the benefits and, hence, there is opposition to the industry and use of the technologies associated with the industry.

http://dx.doi.org/10.5772/56442

Technical experts and the general community often have different attitudes towards and understandings of the risks and benefits associated with hazards[21-23]. This can create dissonance between technical and public discourse. Notwithstanding that, the general community tends to reference the judgement of experts and authorities when making risk assessments. In the absence of specific knowledge, risk assessments made by the general community may be primarily informed by the trustworthiness of the responsible authority and its sources of information[24].

4. The role of trust

Trust is another factor that is of great importance in understanding public acceptance and adoption of new technologies. The general public's trust in regulatory institutions and the motives of scientists or in information about the risks and benefits of particular technological applications of science and technology play an important role.

If a source is distrusted, it matters little how full or persuasive their information is. Hazard acceptability has been linked empirically with both risk perception and level of trust[25].

In terms of the unconventional gas industry, there is a general lack of trust in gas developers and lack of confidence in government to properly regulate the industry. Information provided by gas developers and/or government agencies about techniques, processes, regulation and risk management used in exploration and production of unconventional gas in Australia is generally treated with suspicion and distrust.

An added challenge is the perception of credibility: expertise relevant to the gas industry frequently resides in or is partially dependent upon the gas industry; and technical experts rarely personally inhabit the geography of perceived risk. Such are the foundations upon which attempts to address general public concerns must be built.

It is important to understand how people's attitudes and values influence their acceptance or rejection of the CSG industry, hydraulic fracturing and more generally the unconventional gas industry.

5. The role of a trusted advisor

Science is of course always uncertain, particularly in highly complex, politically charged issues such as CSG, and it cannot dictate what action to take. Deciding what to do occurs through a political process of bargaining, negotiation, and compromise[26]. The degree to which society or a community has a sense of shared values about desirable outcomes and the means to achieve those outcomes is important in the decision-making process. Where value conflicts exist, science has little capacity to reconcile these differences. What science can do in such situations is contribute to the development of new and innovative policy options that might

allow for compromise among the conflicted parties. This is best achieved through the role of Honest Broker of Policy Alternatives[26].

Pielke suggests there are four different roles in how scientists (and other experts) can relate to policy and politics[26]. These four idealised roles are:

1. *Pure Scientist* focuses on research with absolutely no consideration for its use or utility, and therefore in its purest form has no direct connection with decision-makers;
2. *Issue Advocate* focuses on the implications of research for a particular political agenda;
3. *Science Arbiter* seeks to stay removed from explicit considerations of policy and politics like the Pure Scientist, but recognises that decision-makers may have specific questions that require the judgement of experts; and
4. *Honest Broker* of Policy Alternatives engages in decision-making by clarifying and, at times, seeking to expand the scope of choice available to decision makers.

The role of the Honest Broker of Policy Alternatives or Trusted Advisor is critical in the unconventional gas domain in Australia. A Trusted Advisor is inclusive in its communication and engagement with proponents and opponents of CSG; transparent with its governance and research activities; and independent with its scientific research. This enables the Trusted Advisor to be widely perceived as a trusted source of information and advice.

In the CSG space, not only are there environmental impacts but also social challenges to consider. There is a clash of values that exist between proponents and opponents of the industry and some of these clashes include:

- economy versus ecology;
- public benefit versus private disadvantage;
- agriculture versus industry;
- rural lifestyle versus industry development; and
- resource access rights versus autonomy.

Science cannot provide black and white answers to all of the challenges and opportunities associated with the CSG industry. However, by fulfilling a *Trusted Advisor* role, science can help all parties to better understand the range of impacts associated with various development scenarios, and provide a common platform for policy makers, developers and communities to negotiate and make decisions. This approach enables science to contribute to the development of new and innovative policy options that might allow for compromise among opposing parties, and contribute to practical action in spite of conflicting values.

Trusted Advisors were critical in enabling effective political action to address issues such as ozone depletion and acid rain. In these cases, science did not change people's values or beliefs, but it did create new options that allowed for political compromise, given existing values and beliefs[26].

http://dx.doi.org/10.5772/56442

Another vital aspect of the *Trusted Advisor* is to provide effective communication. Change requires more than science alone; it requires new scientific knowledge to be shared and employed widely, wisely and in a timely fashion: 'For science and technology to deliver full value to society, they must be accessible to as many people as possible and their messages must be easily understood'[27].

There is increasing importance for effective dialogue between science and the public[28, 29] because in democratic societies, the public has an increasing say over the scientific and technological solutions and policies that companies and governments may wish to deploy, through the media, opinion polls and consumer choice[30-32].

In contested spaces such as CSG, timely and effective communication from a *Trusted Advisor* to all interested parties is critical to maintaining trust, independence and integrity. Armed with credibility and multiple policy options (delivered through science) for those involved in the decision-making process, the *Trusted Advisor* can make a significant and positive impact on society.

6. Concluding remarks

Science is an integral part of human society and has established, over the centuries, its value to society. Science continues to play a role in contributing significantly to further improving societal and environmental conditions. However, the context in which science research and development takes place is shifting from minimal to increasing public scrutiny and accountability.

Science and its products are intersecting more frequently with certain human beliefs and values. As science encroaches more heavily on value-laden issues, members of the public are claiming a stronger role in both the regulation of science and the shaping of the research agenda[30].

Community sanction has become a pivotal element in the adoption and implementation of new technologies that impact on society, environment and economy[33]. The technology doesn't need to be new to require community sanction or a 'social licence' as illustrated by the unfolding public debate on CSG and hydraulic fracturing in Australia and, indeed, around the world with regards to hydraulic fracturing. Both Victorian and New South Wales (NSW) state governments have slowed CSG development within their state and have placed moratoriums on the use of hydraulic fracturing due to community pressure.

Facts and figures alone will not earn community support and acceptance of CSG developments and the use of hydraulic fracturing. Achieving community acceptance requires a combination of providing trusted and easy to understand information; addressing the perceived risks people have about hydraulic fracturing; and communicating the risk management plans used in the industry. However, if the source of information is distrusted it matters little how full or persuasive that information is.

The role of the *Honest Broker* or *Trusted Advisor* is essential when there is no values consensus and high uncertainty in the community. In this role science is not used to align with a specific agenda nor is it above the fray; it can help all parties to better understand the range of impacts associated with various development scenarios, and contribute to the development of new and innovative policy options that might allow for compromise among opposing parties.

Acknowledgements

This paper was supported by Australia Pacific LNG and CSIRO via the Gas Industry Social and Environmental Research Alliance, details of which can be found at www.gisera.org.au

Author details

S.T. Cham* and P. Stone

*Address all correspondence to: Tsuey.cham@gmail.com

Gas Industry Social and Environmental Research Alliance (GISERA) and CSIRO, Brisbane, Australia

References

[1] Department of Resources Energy and TourismGeoscience Australia, Bureau of Resources and Energy Economics. Australian Gas Resource Assessment (2012). Canberra 2012. 68 p.

[2] Ferguson, M. CEDA State of the Nation Conference: The Security of Energy Markets. http://minister.ret.gov.au/MediaCentre/Speeches/Pages/CEDAConference.aspx.June (2012).

[3] Walker, J. Support for CSG collapses: Queensland Newspoll. The Australian. (2012). Feburary 20. http://www.theaustralian.com.au/national-affairs/elections/support-for-csg-collapses-queensland-newspoll/story-fnbsqt8f-1226275274873.

[4] Carter, L. Re-interpreting some common objections to three transgenic applications: GM foods, xenotransplantation and germ line gene modification (GLGM). Transgenic Research. (2004). Dec;, 13(6), 583-591.

[5] Costa-font, M, Gil, J. M, & Traill, W. B. Consumer acceptance, valuation of and attitudes towards genetically modified food: Review and implications for food policy. Food Policy. (2008). Apr;, 33(2), 99-111.

http://dx.doi.org/10.5772/56442

[6] Knight, J. G, Holdsworth, D. K, Mather, D. W, & Food, G. M. and neophobia: connecting with the gatekeepers of consumer choice. Journal of the Science of Food and Agriculture. (2008). Apr 15;, 88(5), 739-744.

[7] Hurlimann, A. cartographer Community attitudes to recycled water use: an urban Australian case study. Part 2. Salisbury, S. Aust.: CRC for Water Quality and Treatment; (2008).

[8] Hurlimann, A. C. Is recycled water use risky? An Urban Australian community's perspective. Environmentalist. (2007). , 27(1), 83-94.

[9] Fielding, K, Russell, S, & Grace, R. Urban Water Security Research A, Water for a Healthy Country F. Residential water demand management in South East Queensland: a report on water conservation beliefs. City East, Qld.: Urban Water Security Research Alliance; (2010). Available from: http://csiro.aquabrowser.com/?itemid=|library/m/CSIRO-voyager|416089.

[10] Price, J, Fielding, K, Leviston, Z, Bishop, B. J, Nicol, S. C, Greenhill, M. P, et al. Community acceptability of the indirect potable use of purified recycled water in South East Queensland: final report of monitoring surveys. City East, Qld.: Urban Water Security Research Alliance; (2010). Available from: http://csiro.aquabrowser.com/?itemid=|library/m/CSIRO-voyager|416118.

[11] Eagly, A. H, & Chaiken, S. The psychology of attitudes. Fort Worth: TX: Harcourt, Brace, & Janovich; (1993).

[12] Frewer, L, Lassen, J, Kettlitz, B, Scholderer, J, Beekman, V, & Berdal, K. G. Societal aspects of genetically modified foods. Food and Chemical Toxicology. (2004). Jul;, 42(7), 1181-1193.

[13] Rowe, G. How can genetically modified foods be made publicly acceptable? TRENDS in Biotechnology. (2004). Mar;, 22(3), 107-109.

[14] Alhakami, A. S, & Slovic, P. A Psychological-Study of the Inverse Relationship between Perceived Risk and Perceived Benefit. Risk Analysis. (1994). Dec;, 14(6), 1085-1096.

[15] Finucane, M. L, Alhakami, A, Slovic, P, & Johnson, S. M. The affect heuristic in judgments of risks and benefits. Journal of Behavioral Decision Making. (2000). Jan-Mar;, 13(1), 1-17.

[16] Hansen, J, Holm, L, Frewer, L, Robinson, P, & Sandoe, P. Beyond the knowledge deficit: recent research into lay and expert attitudes to food risks. Appetite. (2003). Oct;, 41(2), 111-121.

[17] Slovic, P, Fischhoff, B, & Lichtenstein, S. Facts and fears: understanding perceived risks. In: Schwing R, Albers WA, editors. Societal Risk Assessment: How Safe is Safe Enough?. New York: Plenum; (1980). , 181-216.

[18] Sparks, P, & Shepherd, R. Public Perceptions of the Potential Hazards Associated with Food-Production and Food-Consumption- an Empirical-Study. Risk Analysis. (1994). Oct;, 14(5), 799-806.

[19] Fischhoff, B, Slovic, P, Lichtenstein, S, Read, S, & Combs, B. How Safe Is Safe Enough- Psychometric Study of Attitudes Towards Technological Risks and Benefits. Policy Sciences. (1978). , 9(2), 127-152.

[20] Slovic, P. Perception of Risk. Science. (1987). Apr 17;, 236(4799), 280-285.

[21] Slovic, P. Trust, emotion, sex, politics, and science: Surveying the risk-assessment battlefield (Reprinted from Environment, ethics, and behavior, pg 277-313, 1997). Risk Analysis. (1999). Aug;, 19(4), 689-701.

[22] Sjoberg, L. Risk perception: Experts and the Public. European Psychologist. (1998). , 3(1), 1-12.

[23] Browne, A. L, Leviston, Z, Green, M. J, & Nancarrow, B. E. Water for a Healthy Country F, Urban Water Security Research A. Technical and community perspectives of risks associated with purified recycled water in south east Queensland: a Q-study. City East, Qld.: Urban Water Security Research Alliance; (2008). Available from: http://csiro.aquabrowser.com/?itemid=|library/m/CSIRO-voyager|403466.

[24] Siegrist, M, & Cvetkovich, G. Perception of hazards: The role of social trust and knowledge. Risk Analysis. (2000). Oct;, 20(5), 713-719.

[25] Eiser, J. R, Miles, S, & Frewer, L. J. Trust, perceived risk, and attitudes toward food technologies. Journal of Applied Social Psychology. (2002). Nov;, 32(11), 2423-2433.

[26] Pielke, R. A. The honest broker: making sense of science in policy and politics. Cambridge: Cambridge University Press; (2007).

[27] Cribb, J, & Sari, T. Open science : sharing knowledge in the global century. Collingwood, Vic.: CSIRO Publishing; (2010). Available from: http://csiro.aquabrowser.com/?itemid=|library/m/CSIRO-voyager|408480.

[28] European Institute for Public ParticipationPublic participation in Europe: An international perspective (2009). Available from: http://www.participationinstitute.org/wp-content/uploads/2009/06/pp_in_e_report_03_06.pdf.

[29] International Council for Science Committee on Freedom and Responsibility in the Conduct of ScienceAdvisory note on science communication. (2010). Available from: http://www.icsu.org/publications/cfrs-statements/science-communication/.

[30] Leshner, A. I. Where science meets society. Science. (2005). Feb 11;, 307(5711), 815-815.

[31] Welp, M, De La Vega-leinert, A, Stoll-kleemann, S, & Jaeger, C. C. Science-based stakeholder dialogues: Theories and tools. Global Environmental Change-Human and Policy Dimensions. (2006). May;, 16(2), 170-181.

http://dx.doi.org/10.5772/56442

[32] Wilsdon, J, & Willis, R. See-through Science: Why public engagement needs to move upstream. London: DEMOS; (2004).

[33] Fisher, N. I. Cribb JHJ, Peacock AJ. Reading the public mind: a novel approach to improving the adoption of new science and technology. Australian Journal of Experimental Agriculture. (2007). , 47(11), 1262-1271.

Section 4

Naturally Fractured Reservoirs 2

Chapter 13

Numerical Study of Interaction Between Hydraulic Fracture and Discrete Fracture Network

Azadeh Riahi and Branko Damjanac

Additional information is available at the end of the chapter

http://dx.doi.org/10.5772/56406

Abstract

This paper discusses the interaction between hydraulic fracturing and the pre-existing discrete fracture network (DFN) in a rock mass subject to in–situ stresses. Two–dimensional computational model studies have been used in an initial attempt towards understanding how reservoir response to fluid injection is affected by some of the DFN characteristics and to operational variables such as injection rate.

1. Introduction

Understanding the mechanics of propagation of hydraulic fracture (HF) in naturally fractured reservoirs is critical to both petroleum and geothermal applications. The objective of fluid injection in these applications varies from creating HF to increasing the permeability of the surrounding rock mass, or "stimulation" of the reservoir. During stimulation, several mechanisms can lead to permeability enhancement, including:

- Opening of pre-existing fractures due to the increase in pressure or the decrease in effective normal stress (This mechanism is reversible; in other words, the fracture will close once pressure dissipates and therefore, fluid injection often needs to be accompanied with injecting proppant into the affected fractures.);
- Opening of pre-existing fractures due to slip-induced dilation, which is referred to as hydro-shearing or shear stimulation, and is permanent;
- Extension of the pre-existing fractures and increase in connectivity of the fracture network; and

- Initiation and propagation of HF, which also results in increase in fracture network connectivity.

The focus of this work is on the numerical modelling of fluid injection into the fractured rock mass and interaction between HF and the discrete fracture network. A series of comparative studies were performed to establish the effect of various in-situ parameters, including geometrical properties of the DFN, such as the level of connectivity and fracture size distribution, and operational parameters such as injection rate. In addition to qualitative evaluation of results, the model responses are compared in terms of a series of indices that were evaluated during injection. These indices include:

- Injection pressure, defined as the pressure at the injection point;
- DFN affected surface area, defined as the surface area of the DFN that has experienced a fluid pressure increase due to injection;
- Fracture surface area, calculated as a total area of fractures in the DFN;
- DFN shear stimulated surface area, defined as the area of fractures that have experienced more than 1 mm of slip;
- Leak-off ratio, defined as the volume of fluid leaked into the DFN divided by the total volume of fluid injected;
- Surface area of the HF;
- Average DFN aperture, defined as the volume of fluid injected into the DFN as a fraction of the affected surface area of the DFN; and
- Average HF aperture, defined as the volume of fluid injected into the HF divided by the surface area of the HF.

It is believed that the characteristics of the DFN have a critical effect on the response of a naturally fractured reservoir to fluid injection. Explicit representation of the DFN with realistic characteristics is thus important in the numerical modelling. Numerous realizations of different DFNs have been generated statistically and represented explicitly in the model.

2. Representation of the discrete fracture network

DFNs often are characterized by statistical parameters associated with one or more identified fracture sets. These statistical parameters typically characterize the fracture size distribution, orientation distribution and density of each fracture set.

It is widely accepted that the fracture length distribution usually follows a power law distribution, which relates the probability of occurrence of a fracture with a length of l to the negative exponent of the length, i.e., $n(l) \propto l^{-\alpha}$. Value of α is site specific, but often varies in the range between 2 and 4. In this two-dimensional study, P21 is used as the measure of the fracture density. (P21 is defined as the sum of fracture or trace lengths divided by the area of the

http://dx.doi.org/10.5772/56406

sampling or mapping domain — i.e., $P21 = \sum l_i / L^2$, where L is the linear dimension of the DFN domain.)

Considering the computational requirements of the numerical tool used in this study, it was impractical to represent DFNs with the same level of complexity as that observed in the field. Therefore, the DFN realizations were simplified or filtered. The objective of the filtering process was to reduce the geometrical complexity while preserving the relevant characteristics of the DFN. In the adopted approach, DFN realizations were simplified first by disregarding fractures with a length smaller than a prescribed threshold. The minimum fracture length cut-off is determined based on the length scale of the analysed problem. Also, to conform to what is often observed in the field, closely spaced, sub-parallel fractures (sometimes generated by the Poisson process used for generation of the fracture locations in the synthetic DFN) are disregarded. The latter criterion is based on the field observations and the reasoning that the stress field around a fracture prevents occurrence of sub-parallel fractures in its vicinity. Finally, in this study, the variation of fracture orientation about the mean for each fracture set was disregarded.

The flow characterises of the DFN are determined by identifying the clusters and evaluating overall DFN connectivity. A cluster is a group of fractures that are connected to each other; no fracture inside a cluster intersects a fracture belonging to a different cluster. A fully connected DFN is defined as the DFN with one cluster extending to the boundaries of the domain. The partially and sparsely connected DFNs were created by decreasing the fracture density and visually inspecting the size of formed clusters relative to the size of the model.

3. Numerical approach

The numerical analyses of this study are carried out using a distinct-element modelling approach. Simulations were completed using distinct element code *UDEC* [1]. In this approach, the fractured formation is represented by an assembly of intact rock blocks separated by a pre-existing discrete fracture network. The numerical simulations are performed using a fully coupled hydromechanical model. Fluid flow can only occur within the fractures, separating the impermeable blocks. Initially, the formation is dry. The fluid is injected in the centre of the model at constant rate.

The rock blocks are modelled as elastic and impermeable. The pre-existing fractures are represented explicitly. They are discontinuities which deform elastically, but also can open and slip (as governed by the Coulomb slip law) as a function of pressure and total stress.

UDEC can simulate fracture propagation along the predefined planes only. In order to simulate propagation of an HF, the trajectory of the fracture should be defined explicitly in the model prior to simulations. In this model, the HF is assumed to be planar, aligned with the direction of the major principal stress. The two "incipient surfaces" of the plane of the HF initially are bonded with a strength that is equivalent to specified fracture toughness. Propagation of the HF corresponded to breaking of these bonds. Clearly, the assumption of propagation of the

HF in a single planar surface is a simplification. In practice, the massive hydraulic fracturing, used for example in shale stimulation, results in a large number of fractures propagating simultaneously or sequentially. Under certain conditions, the mechanical interaction between these fractures can lead to non-planar and complex trajectories as demonstrated by the results of numerical modelling [2, 3] and experimental observations [4]. Also, non-planar fracture geometry may develop as a result of the interaction with in-situ pre-existing fractures and frictional interfaces [5, 6, 7].

Figure 1 shows the geometry and the set-up of the *UDEC* model. The model represents a 2D horizontal section of a reservoir with a thickness of 350 m. It is assumed that the injection is through a vertical well located at the centre of the model. The core part of the model containing the DFN is embedded into a larger domain with a regular network of pipes with equivalent permeability to that of the core region. The linear dimensions of the full model are twice as large as those of the core part. In this study, the model core has the dimensions of 1000 m × 1000 m. The state of stress in the plane of the model is assumed to be anisotropic, with maximum principal horizontal stress equal to the vertical stress and the minimum principal horizontal stress equal to half of the vertical stress.

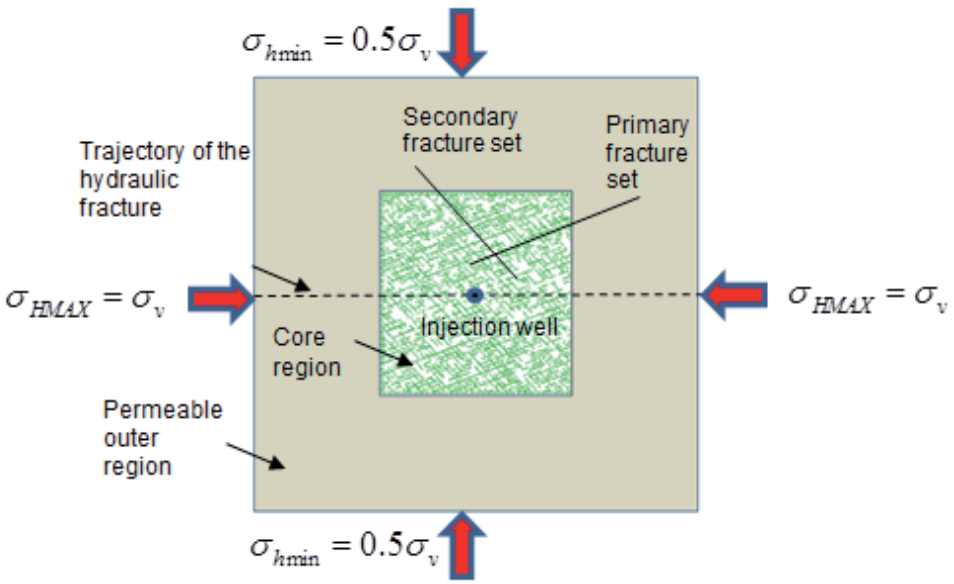

Figure 1. Geometry and model setup.

The applied injection rate is 0.07 m^3/s or 70 kg/s. This rate is approximately equal to 26.4 bpm. Considering the assumed thickness of the formation, an injection rate of $2 \times 10^{-4} m^3/s/m$ is applied in the two-dimensional model. Some sensitivity analysis with respect to injection rate is performed. It is assumed that the pre-existing fractures are already open and conductive, with a uniform aperture for each fracture set. The initial apertures of each fracture set are

http://dx.doi.org/10.5772/56406

calculated based on their orientation relative to the in-situ principal stresses. The primary fracture set is assigned an initial aperture of 3×10^{-5}m, while the secondary fracture set is assigned an aperture of 1.1×10^{-5}m. The failure criterion of fractures is defined by the Coulomb slip law. The pre-existing fractures are assumed to have zero cohesion and the friction angle of 30°. The dilation angle is assumed to be 7.5°.

4. Results

4.1. Effect of DFN connectivity

The objective of this study was to evaluate how DFN connectivity can affect the way that injection affects propagation of the HF, and the way that the HF interacts with the pre-existing discrete fracture network. In these models, the fracture network is assumed to be static, that is, the propagation of pre-existing fractures is not allowed. However, the HF can propagate once pressure reaches the critical value, or approximately the magnitude of the minimum principal stress.

The DFN realizations used in this study are those shown in Figure 2(a). In these figures, different colours represent different clusters. The DFNs have the maximum fracture length of 1000 m and the minimum spacing of 15 m. The angles of the primary and secondary fracture sets relative to the x-axis are 160° and 60°. Figures 2(b) to (d) show the results of injection into the DFNs with various levels of connectivity. These figures show that as the connectivity of the DFN increases, pore pressure propagates to a much larger portion of the DFN. However, as the connectivity decreases, the HF tends to propagate faster. In this case, those fractures that are connected to the HF will experience increase in pressure and aperture.

Figure 3 shows quantitative comparison of the behaviour of the models based on a series of developed indices (defined in Introduction). The history of injection pressure at the injection well (Figure 3(a)) shows that as the connectivity decreases, the injection pressure increases, until it reaches the value of the hydraulic fracturing pressure. Figure 3(b) shows the history of the DFN affected surface area. It suggests that in the fully connected model, this index increases through time at a much higher rate compared to those of the partially and sparsely connected DFNs. This observation is consistent with the contours shown in Figure 2, and is the direct consequence of the presence of a much larger fracture area connected to the injection point. As a result, a greater connected permeability is available for leak-off into the DFN.

Figure 2(c), which shows the DFN shear stimulated surface area, indicates that the shear stimulated area in the partially connected DFN is greater than those of the fully and sparsely connected DFNs. This observation can be better interpreted by evaluating the pressure contours shown in Figure 1. These pressure contours indicate that the injection in the fully connected model has resulted in much lower pressures compared to the pressures in the partially and sparsely connected DFN. This is the result of greater conductivity of the fully connected DFN. In the partially and sparsely connected DFNs, injection into disconnected clusters has resulted in greater pressure increase and eventual propagation of the HF. The

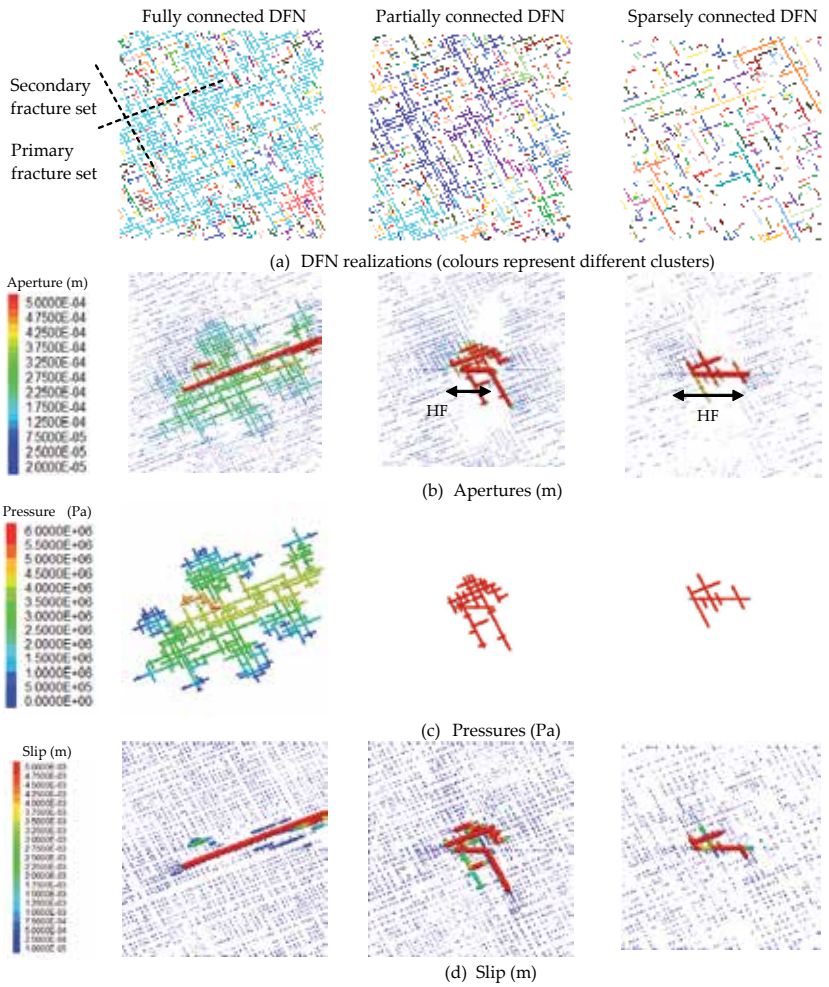

Figure 2. Effect of DFN connectivity.

fractures that are connected to the injection well and the HF experience much greater pressures, which clearly result in fracture slip.

However, in the sparsely connected DFN, the shear stimulated area is smaller than that of partially and fully connected DFN. This is due to the fact that the area of the DFN connected to the HF is much smaller than for the partially connected DFN. Therefore, even when all of those fractures were stimulated, the total stimulated area remains lower than that of the partially connected model. The non-monotonic trend of these observations is dominated by the geometry and size of clusters connected to the HF, and may vary for different DFNs.

Figure 2(d) shows the surface area of the HF. Clearly, in the fully connected DFN, no HF is formed, while in the partially and sparsely connected DFNs the length of the HF has increased

http://dx.doi.org/10.5772/56406

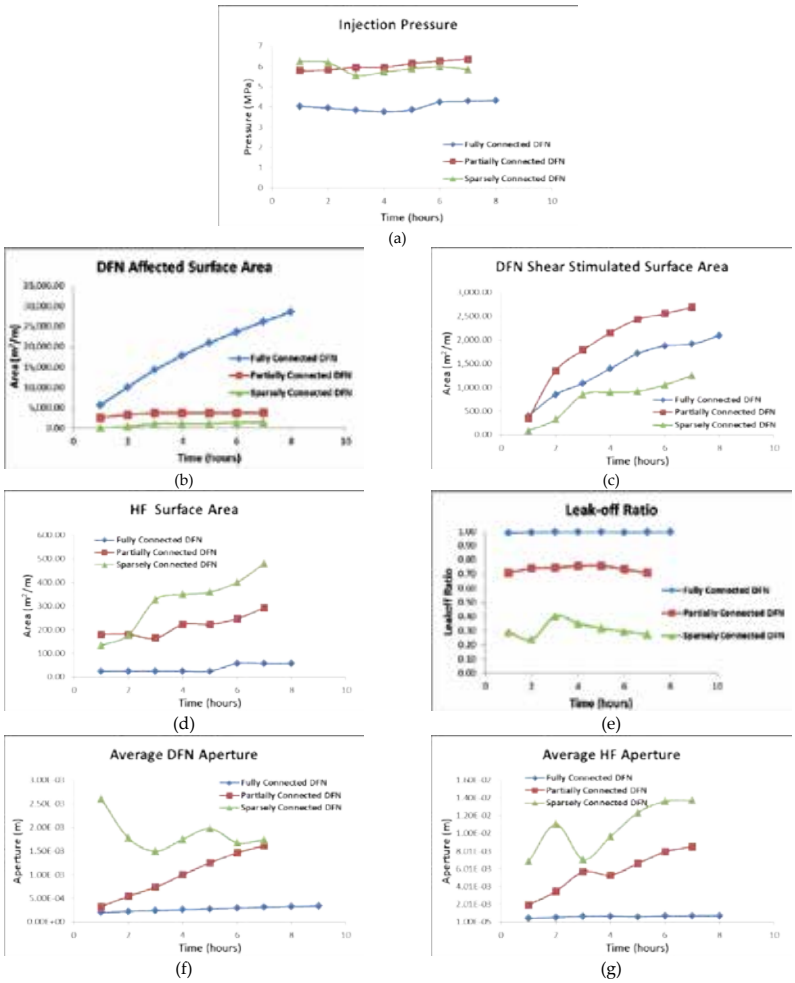

Figure 3. Effect of DFN connectivity, history of quantitative indices.

with time. This graph indicates that as the degree of connectivity decreases, the HF propagates faster.

Figure 2(e) shows the leak-off ratio for fully, partially and sparsely-connected DFN realizations. For the realizations used in this study, the leak-off ratio for the fully-connected DFN is close to one from the onset of injection. The time history of the leak-off ratio in the partially and sparsely connected DFN shows that the leak-off ratio decreases as the connectivity of the DFN decreases. Also, the leak-off ratio for the partially and sparsely-connected DFNs starts to decline noticeably after certain injection time. The oscillation in the leak-off ratio is due to propagation of the HF. For example, the high points may be corresponding to times when a new cluster gets connected to the HF during the HF propagation process.

Finally, Figure 2(f) shows the average DFN aperture. It is difficult to recognize a trend form these graphs, as these observations are greatly dominated by the geometry and size of clusters connected to the injection well and the HF. However, it seems that as the degree of connectivity decreases, the average DFN aperture increases. The increase in the average DFN aperture is the direct consequence of smaller total area of the fractures which have experienced a pressure increase and greater pressures in those fractures. The average HF aperture is shown in Figure 2(g). The same trend is observed as for the average DFN aperture: the average HF aperture increases as the degree of connectivity of the DFN decreases.

4.2. Effect of fracture size distribution

The objective of this study is to evaluate the effect of the fracture size distribution on DFN response to fluid injection. In these studies, the DFNs have identical connectivity characteristics — that is, the three realizations used in the study are fully connected. However, the realizations belong to three different DFNs with different length exponent, α, and the maximum fracture length, l_{max}. The realizations used in this study are shown in Figure 4, in which both the primary and secondary fracture sets are orientated favourably for shear failure considering the orientation of the fracture sets relative to the direction of the principal stresses.

Figure 5 shows contours of fracture aperture and slip. In Realizations I and II, the injection rate and connectivity are such that pressures remain smaller than the minimum principal stress, (shown in Figure 6(a); thus, the HF never propagates substantially. In Realization III, the injection pressure is very close to the fracturing pressure. The leak-off ratio for all realizations remains close to one (shown in Figure 6(b)).

These figures suggest that, when compared to Realization II, Realization I, which is characterized by a narrower range of fracture size distribution with a maximum fracture length smaller that the DFN region, experiences a much larger shear stimulated surface area. Realization III seems to have the shear stimulated surface area that is smaller than for Realization I, but greater than for Realization II. This observation is quantitatively supported by the graphs of the DFN shear stimulated surface area shown in Figure 6(c). These results indicate that the shear stimulated surface area can be correlated to the exponet α and probability of having fractures large relative to the domain size. Larger α results in a narrower range of fracture sizes with a higher frequencty for fractures with the length close to l_{min}. For example, very large values of α lead to a constant fracture size equal to l_{min} However, it should be noted that Realization I has the smallest α, but the maximum fracture length is also capped to a value almost equal to ¼ of the DFN region size. Thus, the DFN has a fairly narrow fracture size distribution with the both mean and frequency of large fractures much smaller than those of the same distribution with uncapped l_{max}. This condition seems to be optimum for shear stimulation.

Figure 6(d) suggests that the affected DFN surface area follows an opposite trend to the DFN shear stimulated surface area. There are two explanations for this.

- Presence of localized flow channels with large length facilitates flow and propagation of pressure front.

http://dx.doi.org/10.5772/56406

- Fracture dilation associated with slip creates additional volume to accommodate injected fluid, resulting in less pressure increase.

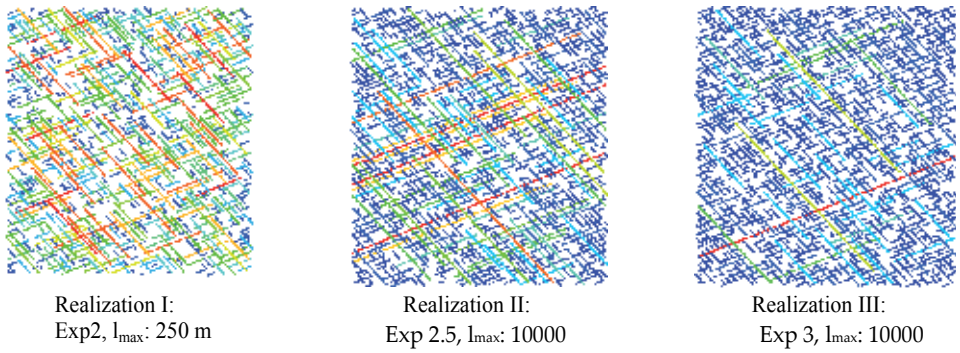

Figure 4. DFN realizations used in the study for the effect of fracture size distribution.

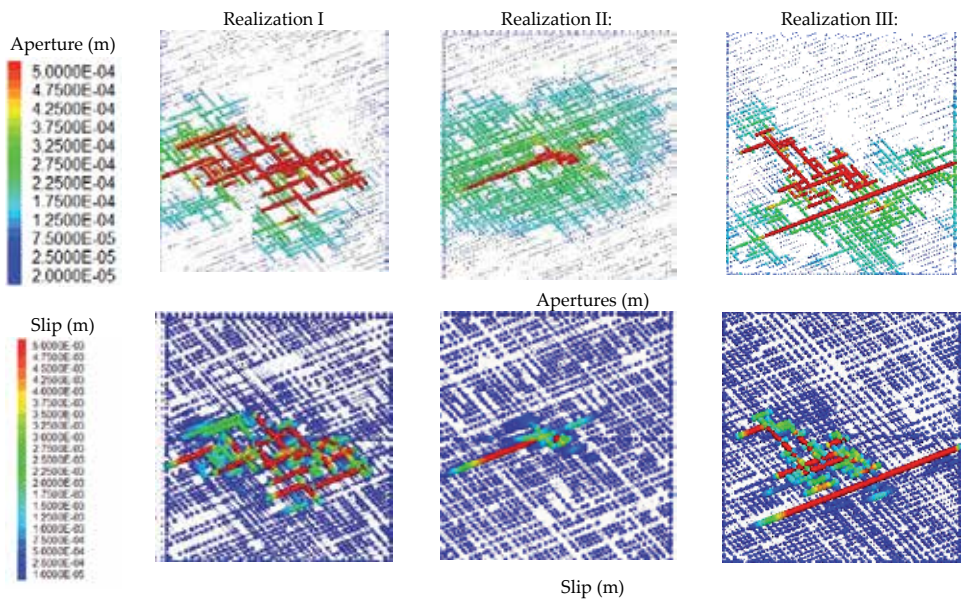

Figure 5. The effect of the fracture size distribution on response to injection (after fourteen hours of injection).

5. Effect of injection rate

The injection rate and injection pressure along with viscosity of the injected fluid are the operational parameters that can be used to effectively design hydraulic fracturing and DFN

stimulation. In this section, it is evaluated how the injection rate affects propagation of the HF and reservoir stimulation. The initially considered range of injection rates is such that it covers injection pressures smaller than the hydraulic fracturing pressure.

The DFN used in this study is shown in Figure 7. Figure 8 shows contours of apertures for four injection rates of 2×10^{-5}m^3/s/m, 4×10^{-5}m^3/s/m, 8×10^{-5}m^3/s/m and 2×10^{-4}m^3/s/m. The results in these figures are compared at the time instances corresponding to identical volume injected into the formation. Figure 9(a) shows the history of injection pressure (versus time and injected volume), which indicates that for the considered injection rates, the pressure remains below the hydraulic fracturing pressure. Figure 9(b) shows that for similar injection time, higher injection rates result in a greater DFN affected area. This observation is expected as the volume injected into the DFN is higher for higher rates.

The plot of the DFN affected area versus injected volume shows a reverse trend to that observed for the DFN affected area versus time. That is, for similar injected volume, greater injection rates result in smaller DFN affected areas. For a smaller injection rate, the time required to inject a similar volume is much longer. Thus, during this longer time, the pressure front can propagate to a larger distance from the injection point.

Figure 9(c) shows the history of the DFN shear stimulated surface area. Again, for similar injection time, greater injection rates result in a greater DFN shear stimulated surface area, due to injection of larger volume of fluid. Comparing the DFN shear stimulated surface areas for similar injected volumes indicates that higher rates result in greater DFN shear stimulated surface area, which is contradictory to the trend observed for the total affected area. This observation is contributed to the fact that higher rates lead to higher pressures. The average DFN apertures as functions of time and injected volumes are shown in Figure 9(d), indicate increasing trend with increasing injection rate.

Figure 10 shows contours of apertures for the injection rates equal to and greater than 2×10^{-4} m^3/s/m. The results are shown for similar injected volumes. The histories of injection pressures for these injection rates (models shown in Figure 10) are shown in Figure 11(a). These rates are such that they cause an injection pressure that would result in propagation of the HF. The history of leak-off ratio is shown in Figure 11(b). It is clear from the leak-off ratio that the highest injection rate of 8×10^{-4}m^3/s/m results in propagation of the HF.

Figure 12(a) shows a similar trend to that observed in Figure 9(b) for DFN affected surface area. However, Figure 12(b) suggests that the trend in the DFN shear stimulated area is complicated and history of this index versus volume shows a decreasing trend with increasing injection rate. This change in trend is contributed to propagation of the HF for the higher injection rates, shown in Figure 12(c). Once the HF propagates, pressures remain roughly equal to the fracturing pressure. Presence of the HF, with an average aperture greater that the aperture of the DFN fractures, results in preferential fluid flow along the HF. As a result of redistribution of flow, or lower leak-off ratio, potential of shear stimulation decreases.

http://dx.doi.org/10.5772/56406

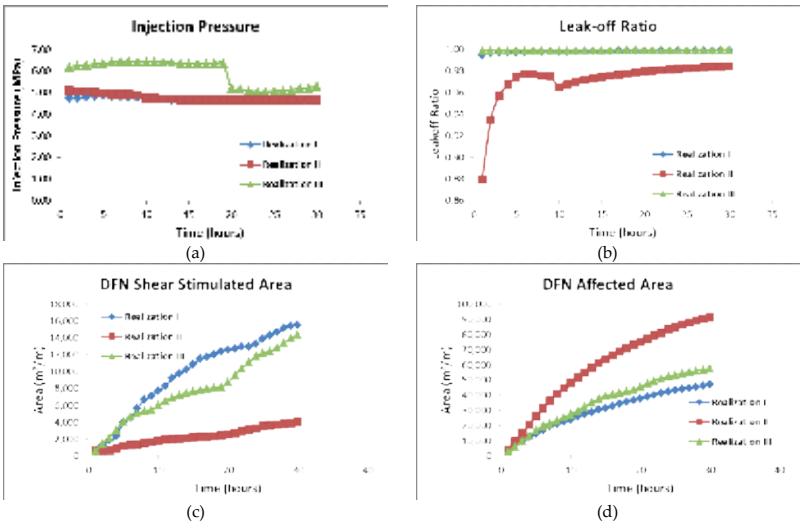

Figure 6. Effect of fracture size distribution, history of quantitative indices.

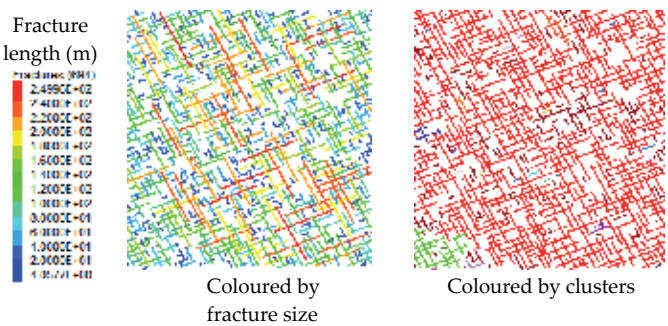

Figure 7. DFN realization used in the study for the effect of injection rate.

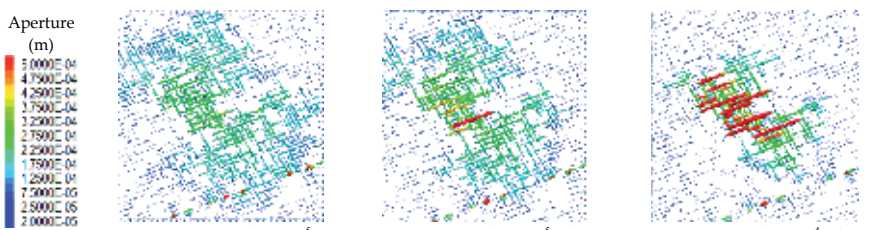

Figure 8. Aperture contours for different injection rates (injected volume of 4.32 $m^3/s/m$).

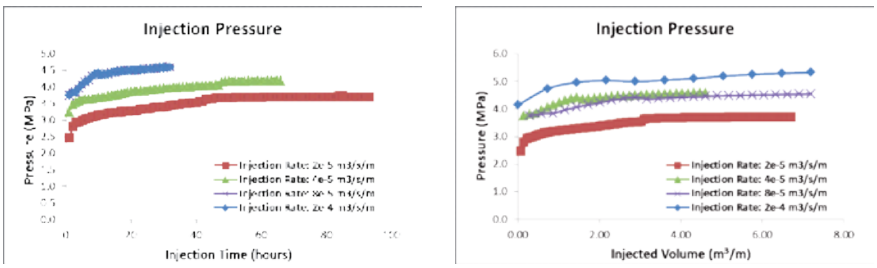

(a) Injection Pressure

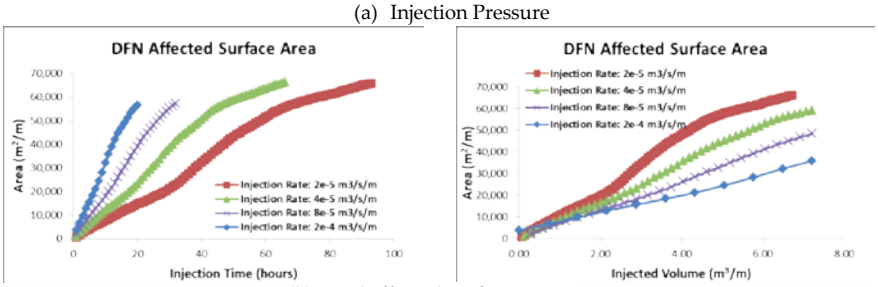

(b) Total affected surface area

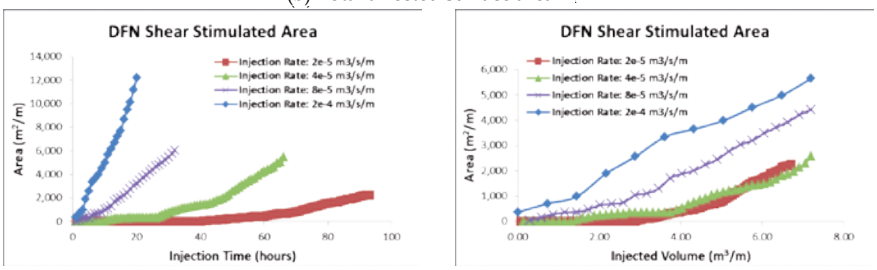

(c) Shear stimulated surface area

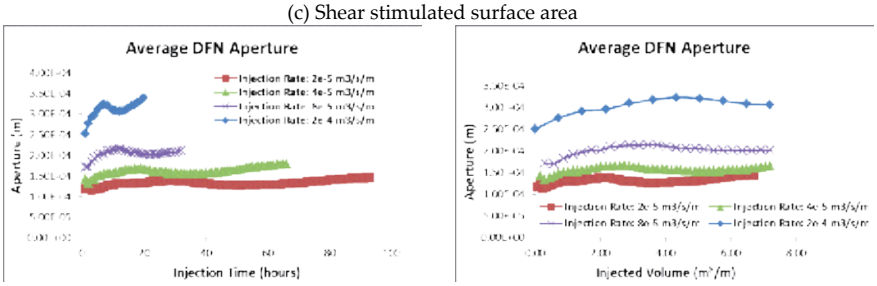

(d) Average DFN aperture

Figure 9. Effect of injection rates, history of quantitative indices.

http://dx.doi.org/10.5772/56406

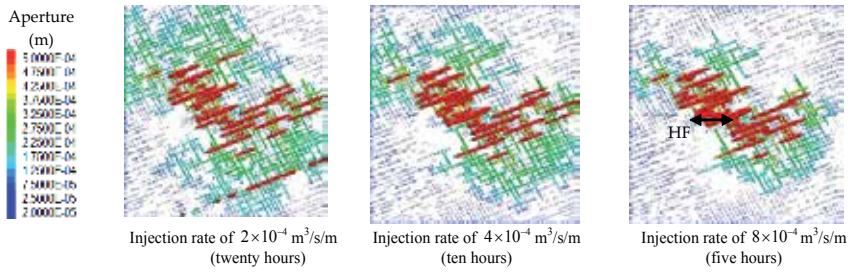

Figure 10. Aperture contours for elevated injection rates (injected volume of 14 m^3/m).

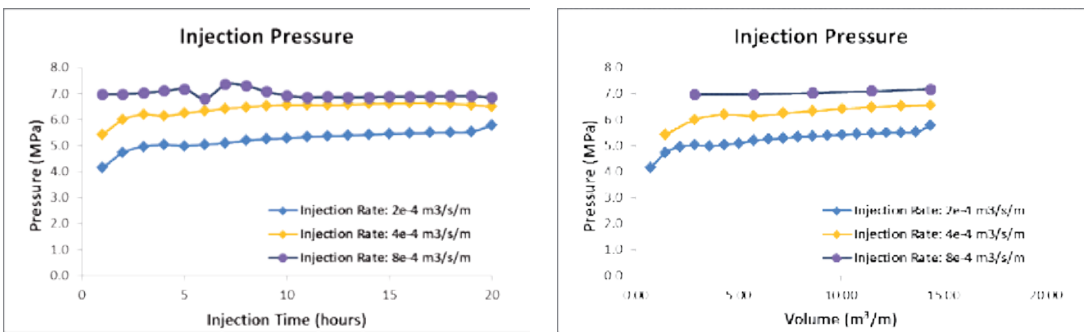

(a) Injection Pressure

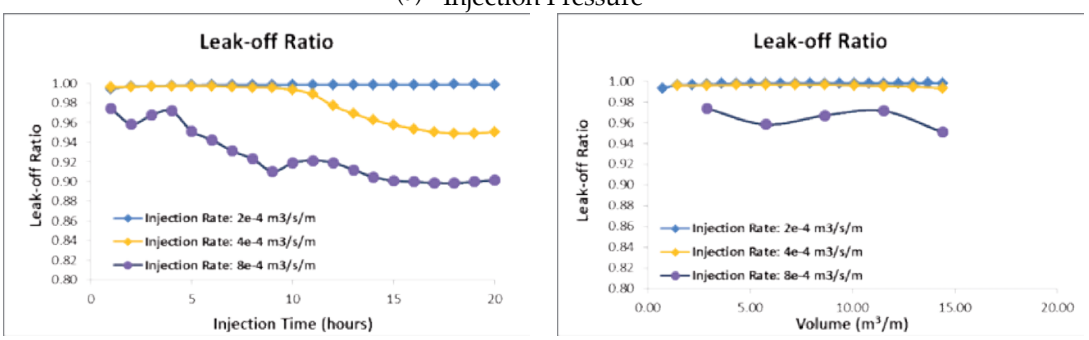

(b) Leak-off ratio

Figure 11. Effect of elevated injection rates, history of quantitative indices (pressure and leak-off ratio).

These results suggest different effect of the injection rate depending on the induced injection pressures. The effect of the injection rate is evaluated for the states with the same injected volume. In general, for the range of injection pressures smaller than the hydraulic fracturing pressure:

- Smaller injection rates result in a greater total affected surface area; and
- Greater injection rates result in a greater shear stimulated surface area.

For the range of injection pressures equal to the hydraulic fracturing pressure:

- Smaller injection rates result in a greater total affected surface area; and
- Greater injection rates result in a smaller shear stimulated surface area. The results indicate that once the HF is formed, the increase in the injection rates will not be favourable for shear stimulation.

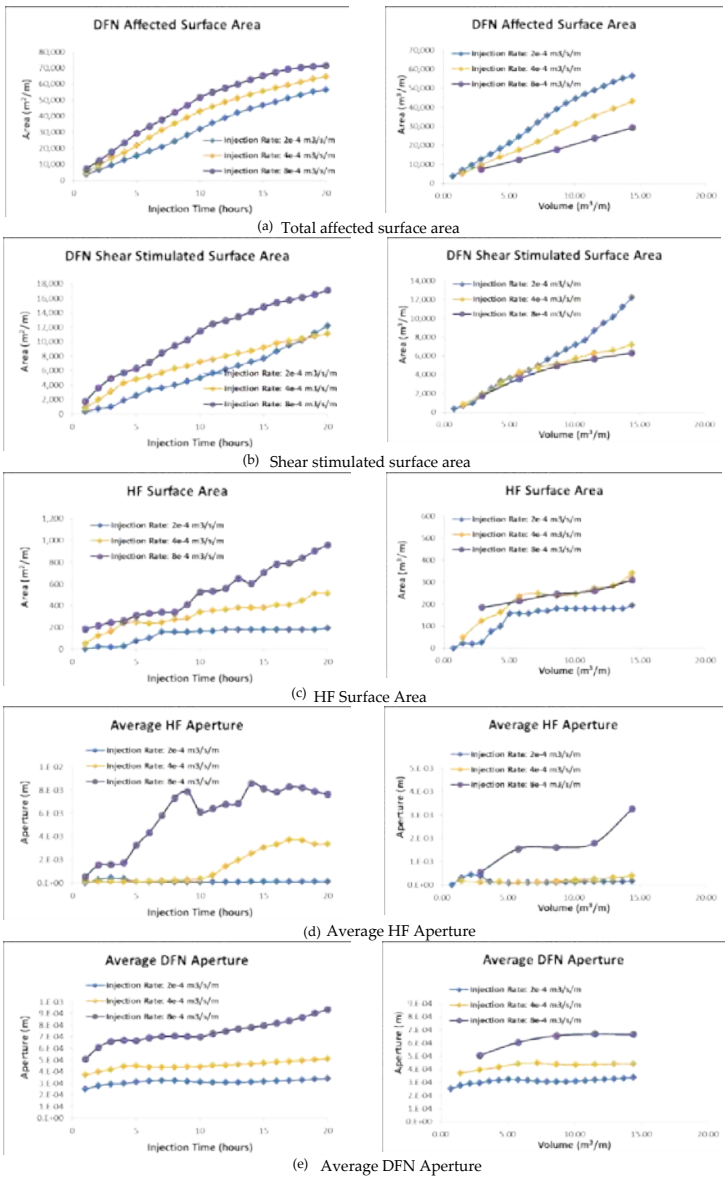

(a) Total affected surface area

(b) Shear stimulated surface area

(c) HF Surface Area

(d) Average HF Aperture

(e) Average DFN Aperture

Figure 12. Effect of elevated injection rates, history of quantitative indices.

http://dx.doi.org/10.5772/56406

6. Conclusions

The response of pre-existing fracture networks, typically encountered in geothermal reservoirs and shale gas formations, to fluid injection, including potential HF propagation, has been studied numerically. This is the first in a proposed series of studies intended to obtain a better understanding of the complex processes involved in DFN stimulation and hydraulic fracturing by fluid injection.

The sensitivity of the models with respect to various in-situ and operational parameters has been evaluated. The results are summarized as follows:

- DFN properties, i.e., density, length distribution and fracture orientation are critical to the overall response of the formation to injection.
- Injection pressure, and the potential for HF propagation, both increase as the connectivity of the DFN decreases.
- For a fully connected netwrok, the potential for shear stimulation increases as exponet α increases.
- Injection rate plays a major role in distributing the fluid between the HF and DFN. It is the combined effect of injection rate and effective permeability (affected greatly by DFN connectivity) that leads to the different mechanisms of behavior.
- For a given injected volume, a lower injection rate increases the proportion of the DFN that is affected (i.e., the surface area of the DFN where an increase in fluid pressure is observed).
- For a given injected volume, higher injection rates lead to a greater DFN shear-stimulated surface area, provided that the pressures remain below the hydraulic fracturing pressure. If the HF is propagated, the reverse is true:, i.e., higher injection rates result in a smaller DFN shear-stimulated surface area.

Acknowledgements

The authors acknowledge the financial support of Sandia National Laboratories for this project.

Author details

Azadeh Riahi[1] and Branko Damjanac[2]

1 Itasca Consulting Group, Inc., Toronto, Canada

2 Itasca Consulting Group, Inc., Minneapolis, USA

References

[1] Itasca *UDEC (Universal Distinct Element Code)*Version 5.0, Itasca Consulting Group, Inc., Minneapolis, (2011).

[2] Bunger, A. P, Jeffrey, R. G, Kear, J, & Zhang, X. Experimental Investigation of the Interaction among Closely Spaced Hydraulic Fractures. Presented at the 45th US Rock Mechanics/Geomechanics Symposium held in San Francisco, California, (2011). June 26-29,

[3] Kresse, O, Cohen, C, Weng, X, Wu, R, & Gu, H. Numerical Modeling of Hydraulic Fracturing in Naturally Fractured Formations. Presented at the 45th US Rock Mechanics/Geomechanics Symposium held in San Francisco, California, June (2011). , 26-29.

[4] Bunger, A. P, Zhang, X, & Jeffrey, R. G. Parameters Effecting the Interaction Among Closely Spaced Hydraulic Fractures, SPE Journal, (2012).

[5] Renshaw, C. E, & Pollard, D. D. An Experimentally Verified Criterion for Propagation Across Unbounded Frictional Interfaces in Brittle, Linear Elastic Materials. Int. J. of Rock Mechanics and Mining Sciences & Geomechanical Abstracts, (1995). , 237-249.

[6] Gu, H, Weng, X, Lund, J, Mack, M, Ganguly, U, & Suarez-rivera, R. Hydraulic Fracture Crossing Natural Fracture at Nonorthogonal Angles: A Criterion and Its Validation. SPE Production and Operations, (2011).

[7] Weng, X, Kresse, O, Cohen, C, Wu, R, & Gu, H. Modeling of Hydraulic-Fracture-Network Propagation in a Naturally Fractured Formation. SPE Production and Operations, (2011).

Chapter 14

Hydraulic Fracturing in Formations with Permeable Natural Fractures

Olga Kresse and Xiaowei Weng

Additional information is available at the end of the chapter

http://dx.doi.org/10.5772/56446

Abstract

The recently developed Unconventional Fracture Model (UFM*) simulates complex hydraulic fracture network propagation in a formation with pre-existing closed natural fractures, and explicitly models hydraulic injection into a fracture network with multiple propagating branches [1]. The model predicts whether a hydraulic fracture front crosses or is arrested by a natural fracture it encounters, which defines the complexity of the generated complex hydraulic fracture network.

While taking into account the leakoff of the fracturing fluid into the formation, the leakoff into the natural fractures should also be considered, especially in low-matrix permeability conditions. The transmissibility of natural fractures can become significant, and the fracturing fluid can penetrate into natural fractures. Different regions can coexist along the invaded natural fracture: hydraulically opened region filled with fracturing fluid, region of still closed natural fracture invaded by fracturing fluid due to natural fracture permeability, and the region of natural fracture filled with original reservoir fluid.

Explicit modelling of hydraulic fractures interacting with permeable natural fractures becomes extremely complicated with the necessity to account for conservation of fluid mass, pressure drop along natural fractures, leak-off into the formation from natural fracture walls, pressure sensitive natural fracture permeability, properties of natural fractures, fluid rheology, while tracking the interface of each region along invaded natural fracture. A main challenge is integrating this hydraulic fracture/natural fracture interaction modelling into the overall hydraulic fracture network propagating scheme without losing model effectiveness and CPU performance.

The updated UFM model with enhancement to account for leakoff into the natural fractures will be presented.

1. Introduction

It is believed that complexity of the resulting fracture network during hydraulic fracturing treatments in formations with pre-existing natural fractures is caused mostly by the interaction between hydraulic and natural fractures. Natural fractures can be important for hydrocarbon production in the majority of low-permeability reservoirs, particularly where the permeability of the rock matrix is negligible. Understanding and proper modelling of the mechanism of hydraulic-natural fractures interaction is a key to explain fracture complexity and the micro-seismic events observed during HF treatments, and therefore to properly predict production.

When hydraulic fracture (HF) intercepts natural fracture (NF) it can cross the NF, open (dilate) the NF, or be arrested at NF. If hydraulic fracture crosses natural fracture, it remains planar, with a possibility to open the intersected NF if the fluid pressure at the intersection exceeds the effective stress acting on the NF. If the HF does not cross the NF, it can dilate and eventually propagate into the NF, which leads to more complex fracture network.

The interaction between HF and NF depends on in-situ rock stresses, mechanical properties of the rock, properties of natural fractures, and hydraulic fracture treatment parameters including fracturing fluid properties and injection rate. During the last decades, extensive theoretical, numerical, and experimental work has been done to investigate, explain, and use the rules controlling HF/NF interaction [3-17]. A new crossing model [2] recently implemented in UFM is able to predict the crossing behaviour of HF at the NF accounting for the effects of fluid properties and NF permeability [18].

One of the important effects of natural fractures is enhanced leakoff, which can lead to a premature screenout during proppant injection. In a formation with low-matrix-permeability, the transmissibility of natural fissures can be significantly higher than that of the reservoir matrix. The fracturing fluid can readily penetrate into natural fissures during the fracturing process and maintain a pressure nearly equal to the pressure in the primary fracture [19].

The concept that natural fractures (fissures) could alter leakoff has been a subject of numerous studies [20-24] with considering the fissure opening conditions or pressure-sensitive leakoff conditions. It was often reported that permeability of natural fractures is pressure dependent [23, 25, 26].

The ways that elevated pressure could affect natural fractures have been described in [27]. Fissures with rough surfaces and minimal mineralization are most likely highly sensitive to the net stress pushing on them. Under virgin reservoir conditions (when the pressure p within the fissure equals the initial reservoir pressure p_{ini}), the effective stress is fairly high and the open channels formed by mismatched fracture faces are most likely deformed and nearly closed. As the pressure in the fissure increases because of leakoff of the high-pressure fracturing fluid ($p > p_{ini}$), the net closure stress is reduced and the fissure porosity opens. In this regime,

http://dx.doi.org/10.5772/56446

the leakoff coefficient is highly pressure dependent. As the pressure exceeds the closure stress on the fissure ($p > p_{f0}$), the entire fissure opens, yielding an accelerated leakoff condition. The estimation of the critical pressure in PKN-type HF (exceeding closing pressure $p > p_{f0}$) to open a vertical fissure has been given through the function of the principal horizontal stresses and Poisson ratio [20].

A more detailed description of the effects from natural fissures in reservoirs where natural fissures are the primary source of permeability is provided in [23]. The enhanced rate of fluid loss throughout the treatment is predicted, with leakoff accelerating as the fracturing pressure increases. The increase in fluid pressure in the fissures reduces the effective normal stress acting to close the fissures and hence increases their permeability. For hydraulic fracturing purposes, the effect of the magnified permeability is reflected as an increase in fluid-leakoff coefficient. The fluid-leakoff in the presence of natural fissures could be as high as 2 to 3 times that for normally occurring pressure – dependent leakoff behaviour, even under the net pressure conditions.

For slightly elevated pressures NF porosity begins to open as the pore pressure increases because the elevated pressure relieves some of the net stress on the asperity contacts. Several models of this process have been developed. For example, [26] predicts the change in NF permeability resulting from changes in stress and pressure. This model have been validated and used in numerous studies [23].

Among existing HF models accounting for the permeability of intercepted natural fractures mention [10] which couples fluid flow, elastic deformation, and frictional sliding to obtain a solution which depends on the competition between fractures for the permeability enhancements. The effect of initially closed but conductive fracture is specifically addressed. The possible scenarios for evolution of fracture opening and fluid transport in closed NFs implemented in [10] are shown in Figure 1. The initial aperture w_0 along a closed pre-existing NF corresponds to its residual conductivity. It is equal to the effective aperture for the parallel plate model. The initial conductivity of a closed natural fracture arises from the fact that its surfaces are rough and mismatched at fine scale, i.e. the aperture w_0 is related to the fracture porosity. With increasing the fluid pressure, the hydraulic aperture will slightly change due to micro structural change in the natural fracture, although the fracture still remain closed and carries some contact stresses. In the end, fracture will be opened mechanically as the fluid pressure exceeds the normal stress acting on the fracture. In this case, the effective hydraulic conductivity is equal to the sum of both hydraulic aperture and mechanical opening since the fracture opening augments the initial hydraulic aperture, as shown in Figure 1. Zhang's model also considers the possibility of frictional sliding through the Coulomb frictional law, and accounts for three types of contact behaviour at fracture surface: fracture is opened, fracture is closed but surface is in sticking mode, and fracture is closed but in sliding mode.

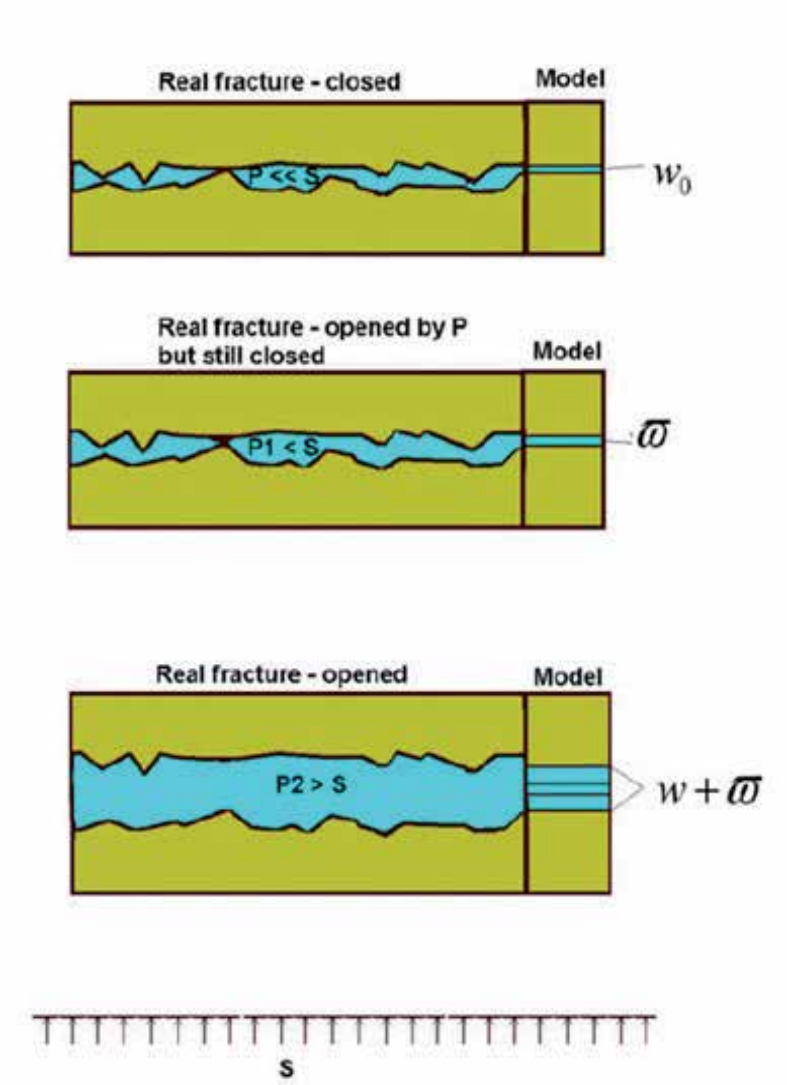

Figure 1. Evolution of natural fracture opening [10]

The HF models [28-32] do not account for permeability of natural fractures explicitly. The 2D model in [33] uses approach from [13] to simulate interaction between induced propagating fracture and natural fracture. A modified leak-off model for an intersecting fracture based on poro-elasticity was introduced to account for the increased leakoff at the intersections. A poro-elastic solution for the stresses in the HF/NF interaction zone has been used as a basis for hydraulic/natural fracture interaction criteria. A fully coupled finite element based approach was used to simulate HF propagation in a poroelastic formation with existing natural fractures.

http://dx.doi.org/10.5772/56446

The approach given in [10] is based on boundary element method and rigorously models HF interaction with permeable NF. It is computationally expensive, and is applicable for analysis of limited (small) number of HF/NF interactions. For a more general complex fracture network model like UFM which deals with a large number (order of thousands) of natural fractures, the CPU time is important and model should be computationally efficient while still being physically correct.

The important aspect of HF/NF interaction is shear slippage of NF faces. The possibilities of shear slippage in natural fractures due to change of stress field (in isolated natural fractures) or during HF/NF interactions, and the influence of shear slippage on fracture aperture change and dilation have been a subject of experimental and numerical studies [10, 15, 17, 30, 34-37]. The conditions for shear slippage and the corresponding shear displacement (apertures) have been investigated [36], and the estimation of permeability of NF with changing effective normal stress is done by [11,38]. The shear slippage effect during HF/NF interaction is also included in current approach.

This paper describes how leakoff into the natural fractures during HF/NF interaction (crossing or arresting before NF opens) is integrated into the complex hydraulic fracture model UFM.

2. UFM model specifics

A complex fracture network model, referred to as Unconventional Fracture Model (UFM), had recently been developed [1, 39, 40]. The model simulates the fracture propagation, rock deformation, and fluid flow in the complex fracture network created during a treatment. The model solves the fully coupled problem of fluid flow in the fracture network and the elastic deformation of the fractures, which has similar assumptions and governing equations as conventional pseudo-3D fracture models. Transport equations are solved for each component of the fluids and proppants pumped. A key difference between UFM and the conventional planar fracture model is being able to simulate the interaction of hydraulic fractures with pre-existing natural fractures, i.e., determine whether a hydraulic fracture propagates through or is arrested by a natural fracture when they intersect and subsequently propagates along the natural fracture.

To properly simulate the propagation of multiple or complex fractures, the fracture model takes into account the interaction among adjacent hydraulic fracture branches, often referred to as “stress shadow” effect. It is well known that when a single planar hydraulic fracture is opened under a finite fluid net pressure, it exerts a stress field on the surrounding rock that is proportional to the net pressure. The details of stress shadow effect implemented in UFM are given in [40].

The branching of hydraulic fracture when intersecting natural fracture gives rise to the development of a complex fracture network. A crossing model that is extended from the Renshaw-Pollard [12] interface crossing criterion, applicable to any intersection angle, has been developed, validated against the experimental data [16, 17], and was integrated at first in the

UFM. The crossing model, showing good comparison with existing experimental data, did not account for the effect of fluid viscosity and flow rate on the crossing pattern. More recently a new advanced OpenT crossing model, taking into the account the impact of fluid and NF properties, have been developed [2] and integrated in UFM [18].

The modelling approach used in UFM to predict the leakoff into the NFs is presented below.

3. Modeling leakoff into permeable NF in UFM

The main assumptions for the current modelling of leakoff from HF into the intercepted NF in UFM are given below.

- The rock formation contains vertical discrete deformable fractures (NFs), which are initially closed but conductive because of their pre-existing apertures (due to surface roughness, etc).
- The propagation direction of the hydraulic fractures is not affected (unless intercepted) by closed and not invaded natural fractures. The intercepted NF could affect HFN propagation even from closed parts (when shear slippage takes place)
- The natural fractures are assumed to contain pore space and are permeable.
- The original fluid inside the natural fractures and in the reservoir (oil, gas, water) is compressible and Newtonian.
- Fracturing fluid can be incompressible or compressible and its rheology can be Newtonian or power law.
- The rock material is assumed to be permeable and elastic.
- When intercepted by the main hydraulic fracture, a natural fracture may remain closed, while still being able to accept fracturing fluid, or may be mechanically opened by fracturing fluid pressure depending on the magnitude of the fracturing fluid pressure, confining stresses applied on natural fracture, and frictional properties of natural fracture.
- The flow inside NFs is assumed to be 1D.
- The natural fractures can be opened by fluid pressure that exceeds the normal stress acting on them and/or experience Coulomb type frictional slip.
- The original natural fracture has width w_0 and are filled with reservoir fluid with pressure equal to pore pressure $p_0 = p_{res}$.
- Fluid flow invaded into the natural fracture develops along NFs. Invaded fracturing fluid into the NF may reach the end of NF, break the rock, and start to propagate into the rock accordingly to previously implemented propagation rules (only if the NF is opened). Fracture re-initiation from other points along the NF other than its ends (offsets) is not modeled at this time.

http://dx.doi.org/10.5772/56446

Hydraulic fractures propagating in the rock are modeled in accordance with existing approach in UFM model. The Schematic of the complex HF interaction with permeable NF is shown in Figure 2 and Figure 4.

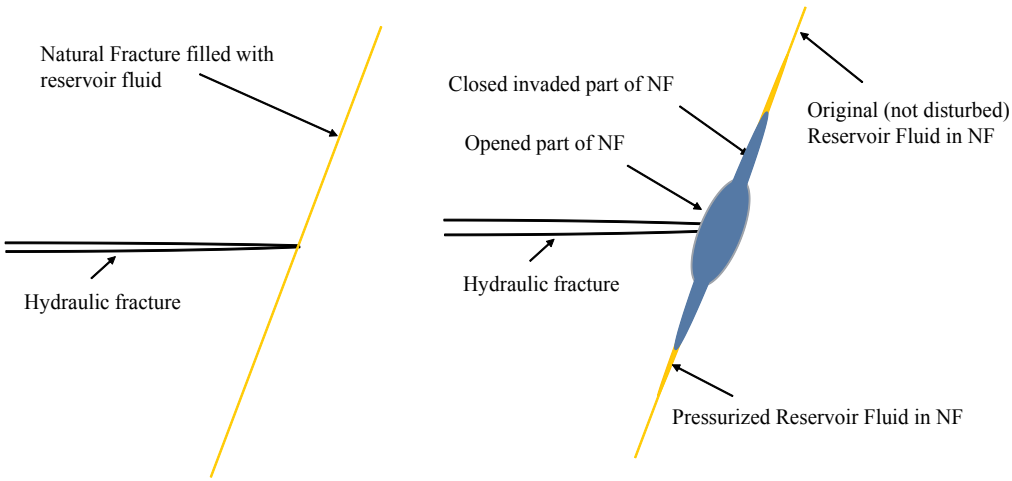

Figure 2. Hydraulic fracture intercepting natural fracture and possible situation to model

Fracturing fluid invasion into the two wings of the NF needs to be considered separately. Four possible regions can co-exist in each wing of the NF encountered by HF (Figure 4):

1. Opened part filled with invaded fracturing fluid (fluid pressure exceeds the normal effective stress on NF), with length of opened part $L_{opened} > 0$
2. Invaded closed part of NF (filtration zone) filled with fracturing fluid (fluid pressure above pore pressure but below the closure stress) with length $L_{filtration} > 0$
3. Closed pressurized part filled with pressurized original reservoir fluid (fluid pressure above the pore pressure) with length $L_{pressurized} > 0$
4. Closed undisturbed part of NF filled with reservoir fluid under original pore pressure conditions.

When a natural fracture is intercepted by the hydraulic fracture, the fluid pressure in the hydraulic fracture transmits into the natural fracture. If the fluid pressure is less than the normal effective stress on the natural fracture, the natural fracture remains closed. Even closed natural fractures may have hydraulic conductivities much larger than the surrounding rock matrix, and in this case fracturing fluid will invade the natural fractures more than leakoff into the surrounding matrix. If the portion of injected fluid is lost into closed natural fractures from the main HF, the HF growth could be affected.

For a closed fracture, the equivalent fluid conductivity is expected to change with the fluid pressure since contact deformation is a function of effective normal stress. This pressure-induced dilatancy and the associated increase in conductivity are important in increasing leakoff. Also, any reduction in effective contact stress may result in fracture sliding, which can lead to local stress variations and slip induced fracture dilation, which can in turn change the overall conductivity of fracture networks.

The governing processes in first three regions listed above should be modeled, and the modeling approaches in different regions (also referred to as zones in the following context) are different due to different flow behaviors and rock/fluid properties.

4. Basic governing equations

4.1. Continuity of fluid volume (mass)

The equation for the continuity of incompressible fluid volume has the form

$$\frac{\partial q_{NF}}{\partial s} + \frac{\partial A}{\partial t} + q_L = 0, \qquad q_L = \frac{2hC_{tot}^{rock}}{\sqrt{t-\tau(s)}}, \quad A = \varpi h \tag{1}$$

where

q_{NF} (t) - volumetric flow rate through a cross section of area A of natural fracture [m^3/s]

A - cross sectional area of the natural fracture

q_L - the volume rate of leakoff per unit length

ϖ - average hydraulic fracture width (different from w, fracture opening by fluid pressure exceeding normal stress)

h - fracture height

C_{tot} - total leakoff coefficient from the wall of natural fracture

More generally in the case of compressible fluid the equation (1) should account for fluid density ρ_f and mass flux q_m. Considering the rate of change of fluid mass per unit length in a fracture $\dot{m}$, continuity of fluid mass in the fracture is governed by equation

$$\frac{\partial q_m}{\partial s} + \dot{m} + \rho_f q_L = 0 \tag{2}$$

or along the fracture of constant length

http://dx.doi.org/10.5772/56446

$$\frac{\partial q_m}{\partial s} + \frac{\partial(\rho_f \varpi h)}{\partial t} + \rho_f q_L = 0, \qquad q_L = \frac{2hC_{tot}^{rock}}{\sqrt{t-\tau(s)}} \tag{3}$$

Here s is coordinate along NF, and total leakoff coefficient from the walls of the natural fracture C_{tot}^{rock} is equal to combined leakoff coefficient [41]

$$C_{tot}^{rock} = C_{vc}^{rock} = \frac{2C_v^{rock}C_c^{rock}}{C_v^{rock} + \sqrt{C_v^{rock2} + 4C_c^{rock2}}} \tag{4}$$

Where leakoff coefficient for the filtration zone in the rock and leakoff coefficient for the reservoir zone as shown in equations (5a - 5b)

$$C_v^{rock} = \sqrt{\frac{k_r \varphi_r \Delta p}{2\mu_f}} = \sqrt{\frac{k_r \varphi_r \Delta p}{2\mu_f}}, \Delta p = p_f - p_s \qquad \text{a}$$

$$C_c^{rock} = \sqrt{\frac{k_r \varphi_r c_T}{\pi \mu_r}} \Delta p, \quad \Delta p = p_f - p_r \qquad \text{b} \tag{5}$$

$$\bar{C}_v = \frac{2\left(C_v\right)^2 \sqrt{t}}{V_L} \qquad \text{c}$$

with

ϕ_r - reservoir porosity

c_T - total compressibility of reservoir

k_r - permeability of rock matrix

μ_r - reservoir fluid viscosity in the porous media

μ_f - filtrate fluid viscosity

ρ_f - filtrate fluid density

p_r - reservoir pressure

In the case of multiple fluids, the invaded zone can be described by replacing C_v with equivalent term (see (5c)) [42] Where $\bar{C}_v$ is calculated using the average viscosity and relative permeability of all the filtrate fluids leaked off up to the current time, and V_L is the fluid volume per unit area that previously leaked off into the reservoir.

4.2. Pressure drop along closed NF

The pressure drop along closed NF can be expressed from Darcy's law

$$q_{NF} = -\frac{k_{NF}A}{\mu_f}\frac{\Delta p}{L(t)},\ A = \varpi h \tag{6}$$

Or for mass flux

$$q_m = -\rho_f \frac{k_{NF}}{\mu_f} A \frac{\partial p}{\partial s} \tag{7}$$

Then the pressure can be calculated from

$$\frac{\partial p}{\partial s} = -\frac{\mu_f}{\rho_f k_{NF} A} q_m = -\frac{\mu_f}{\rho_f k_{NF} \varpi h} q_m, \quad \text{at the inlet : } p = p_{in}(t) \tag{8}$$

Here

k_{NF} - permeability of natural fracture

μ_f - filtrate fluid viscosity

ρ_f - filtrate fluid density

A - cross sectional area of closed NF

p_{in} - fluid pressure at the inlet

4.3. Change of NF permeability due to stress and pressure changes

The leakoff into the natural fracture, or permeability of the natural fracture, is highly pressure dependent when pressure of invading fluid exceeds reservoir pressure but still is below the closure pressure. In general, permeability of natural fracture is a function of normal stress on NF, shear stress (or shear displacement due to shear slippage), and fluid pressure, and can be represented as a combination of permeability due to normal stress and permeability due to shear slippage [26]:

$$\begin{aligned} &k_{NF} = f(k_{NF}^n, k_{NF}^s) \\ &k_{NF}^n = f_1(k_o, \sigma_n, p\ ), \quad k_{NF}^s = f_2(u_s, \phi_{dil}) \\ &k_{NF}^n = k_o \left\{ C \ln\left[\frac{\sigma^*}{\sigma_n - p} \right] \right\}^3 \end{aligned} \tag{9}$$

http://dx.doi.org/10.5772/56446

Where constants C and σ^* (reference stress state) are determined from field data, k_o is the initial NF permeability (reservoir permeability under in-situ conditions), σ_n is the normal stress on the NF, p is the pressure in the NF, and u_s is shear-induced displacement (slippage).

4.4. The width of closed invaded NF

The width ϖ of closed NF invaded by the treatment fluid (hydraulic aperture) is related to the pressure-dependent permeability as [10]

$$\varpi = \sqrt{12 k_{NF}} \tag{10}$$

The hydraulic width ϖ can be evaluated from Barton-Bandis model following approach [11,36,38], i.e. directly from Eq. (11) for given effective normal stress σ_{eff}, reference effective stress σ_n^{ref} , initial hydraulic fracture aperture ϖ_o (related to the roughness of fracture surface), shear displacement u_s and dilation angle ϕ_{dil}

$$\begin{aligned} \varpi &= \frac{\varpi_0}{1+9\dfrac{\sigma_{eff}}{\sigma_n^{ref}}} + \varpi_s + \varpi_{res}, \quad \varpi_s = |u_s| \tan(\phi_{dil}^{eff}), \quad \phi_{dil}^{eff} = \frac{\phi_{dil}}{1+9\dfrac{\sigma_{eff}}{\sigma_n^{ref}}} \\ \sigma_{eff} &= \sigma_n - p_f(s) \end{aligned} \tag{11}$$

4.5. Shear failure

The second term in Eq. (11) represents the shear-induced dilation which contributes to the NF permeability (Eq.9). Shear induced dilation is related to the frictional slip which occurs when the shear stress reaches the frictional shear strength of the natural fractures $\tau_s = \lambda(\sigma_n - p)$. In the present study the NF propagation due to the shear induced slip is not considered, but the contribution of shear slippage zone to the NF enhanced permeability is evaluated based on the enhanced 2D DDM approach [40,43,44].

$$\begin{aligned} \sigma_n^i - p^i &= \sum_j A^{ij} C_{nn}^{ij} D_n^j + \sum_j A^{ij} C_{ns}^{ij} D_s^j \\ \tau^i &= \sum_j A^{ij} C_{sn}^{ij} D_n^j + \sum_j A^{ij} C_{ss}^{ij} D_s^j, \qquad A^{ij} = 1 - \frac{d_{ij}^{2.3}}{\left(d_{ij}^2 + h^2\right)^{2.3/2}} \end{aligned} \tag{12}$$

The fracture surface slip (shear displacement) u_s can be found as shear displacement discontinuity D_s calculated for the closed sliding elements following Coulomb frictional law $\tau \geq \tau_s = \lambda(\sigma - p)$ from elasticity equations in the stress shadow calculation approach with accounting for the mechanical opening in HFN from Eq. (12).

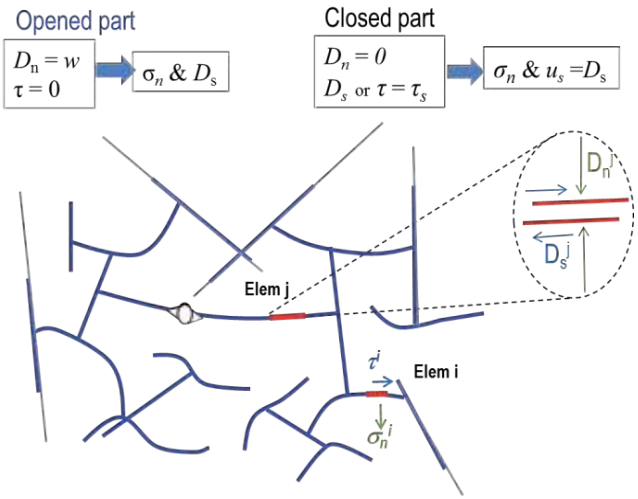

Figure 3. Stress Shadow Effect from opened (blue) HFN and closed parts (grey) of intercepted NFs

For any element j in the opened part of HFN (including opened part of intercepted NFs) the input normal displacement discontinuity D_n^j in Equation (12) is given by known fracture aperture (width) $D_n^j = w^j \neq 0$, and the shear stress is zero $\tau^j = 0$. Along the closed part of intercepted NFs the mechanical the opening is zero, $D_n^j = 0$, and the pressure and normal stress should be tracked to detect (find) elements sliding in shear. If $\tau^i \geq \tau_s^i$ then element i is sliding and dilating in shear, and the shear stress $\tau^i = \tau_s^i$ for this element is used to find fracture surface slip $u_s^i = D_s^i$ from the second equation (12). So, equation (12) could be solved for shear displacements D_s^j along opened and sliding in shear parts of total HFN and intercepted NF as schematically shown in Fig.3. In Eq.(12) C^{ij} are 2D, plane strain elastic influence coefficients [43] defining interactions between the elements i and j, and A^{ij} are 3D correction factors [44] accounting for the 3D effect due to fracture height h depending on the distance between elements d_{ij}.

4.6. Fluid density as function of pressure and temperature

Density of gas as a function of pressure and temperature has form

$$\rho_{gas} = \frac{p m_m}{ZRT} \tag{13}$$

Where p is pressure, T is temperature, Z is compressibility, R is gas constant, and m_m is molar mass. The changes in pressure and temperature with time produce changes in gas density. Density of a compressible fluid as function of pressure

$$\frac{d\rho}{dt} = \frac{\rho}{B}\frac{dp}{dt} = \rho c_f \frac{dp}{dt} \tag{14}$$

where B is bulk modulus (fluid elasticity) in Pa and $c_f = 1/B$ is fluid compressibility in Pa^{-1}. More generally, change in fluid density due to changes in pressure and temperature for the low compressibility fluids through the known values of density ρ_0 and temperature T_0 at pressure p_0 has form (β here is volumetric expansion coefficient)

$$\rho = \frac{\rho_0}{1\text{-}\beta(T - T_0)} \times \frac{1}{1 - \frac{p - p_0}{B}} \tag{15}$$

4.7. Fluid flow in opened NF

The fluid flow in the opened NF ($p_f > \sigma_n$) will be handled as fluid flow in HFN and have been described before [1] depending on the flow regime:

Laminar fluid flow: Poiseuille Law [45]

$$\frac{\partial p}{\partial s} = -\alpha_0 \frac{1}{\bar{w}^{2n'+1}} \frac{q}{H_{fl}} \left| \frac{q}{H_{fl}} \right|^{n'-1} \tag{16}$$

$$\alpha_0 = \frac{2K'}{\varphi(n')^{n'}} \left(\frac{4n'+2}{n'} \right)^{n'}; \quad \varphi(n') = \frac{1}{H_{fl}} \int_{H_{fl}} \left(\frac{w(z)}{\bar{w}} \right)^{\frac{2n'+1}{n'}} dz$$

Where $\bar{w}$ is average fracture opening, and n' and K' are fluid power law exponent and consistency index.

Turbulent fluid flow ($N_{Re} > 4000$):

$$\frac{\partial p}{\partial s} = -\frac{f\rho_f}{\bar{w}^3} \frac{q}{H_{fl}} \left| \frac{q}{H_{fl}} \right|, q = H_{fl} \left(-\frac{\bar{w}^3}{f\rho_f} \frac{dp}{ds} \right)^{1/2} \tag{17}$$

With Reynolds number (N_{Re}) for the power law fluid between parallel plates and *Fanning* friction factor (f) defined as

$$N_{Re} = \frac{3^{1-n'} 2^{2-n'} \rho V^{2-n'} \bar{w}^{n'}}{K' \left(\frac{2n'+1}{3n'} \right)^{n'}}, f \approx \frac{1}{16 \left[\log_{10} \left(\frac{\varepsilon}{7.4\bar{w}} \right) \right]^2}; \tag{18}$$

Where V is fluid velocity and ε is surface roughness height.

Darcy fluid flow through proppant pack of height h

$$\frac{\partial p}{\partial s} = -\frac{q\mu_{fl}}{kh\bar{w}} \tag{19}$$

will take place if the height of the fluid in fracture element become smaller than minimum fluid height. The minimum fluid height is calculated from the condition that pressure drop is equal to pressure drop due to the Darcy flow. The minimum height for turbulent and laminar flow is defined as

$$\begin{aligned} &\text{Laminar flow:} \quad h_{fl}^{\min} = \left(\frac{k\alpha_0(n')H_{fl}}{\bar{w}^{2n'}\mu_{fl}}\right)^{1/n'} \frac{1}{q^{\frac{1}{n'}-1}} \\ &\text{Turbulent flow:} \quad h_{fl}^{\min} = \left(\frac{kH_{fl}f\rho q}{\bar{w}^2\mu_{fl}}\right)^{1/2} \end{aligned} \tag{20}$$

Where μ_{fl} is fluid dynamic viscosity, and k is proppant pack permeability. The boundary conditions at the inlet and tip of opened fracture

$$p = p_f(t), \quad p_{tip} = \sigma_n^{tip}(t) \tag{21}$$

where p_f is known fluid pressure at the intersection with natural fracture.

5. Combined fluid flow into the opened and closed parts of invaded NF

As I mentioned before, natural fracture can be closed, closed but invaded with fracturing fluid, closed and filled with pressurized reservoir fluid, or opened (Figure 4). The partially opened NF can contain opened, invaded, pressurized and closed parts which are dynamically changing with time. When fronts (positions of the boundaries between co-existing parts in invaded NF) change or propagate, the velocity of each propagating front can be considered as velocity of the corresponding fluid front in the relevant part of the invaded NF.

To properly model invasion of fracturing fluid into the NF, the propagation of each front should be modelled, and in different parts of the invaded NF different governing equations should be satisfied.

http://dx.doi.org/10.5772/56446

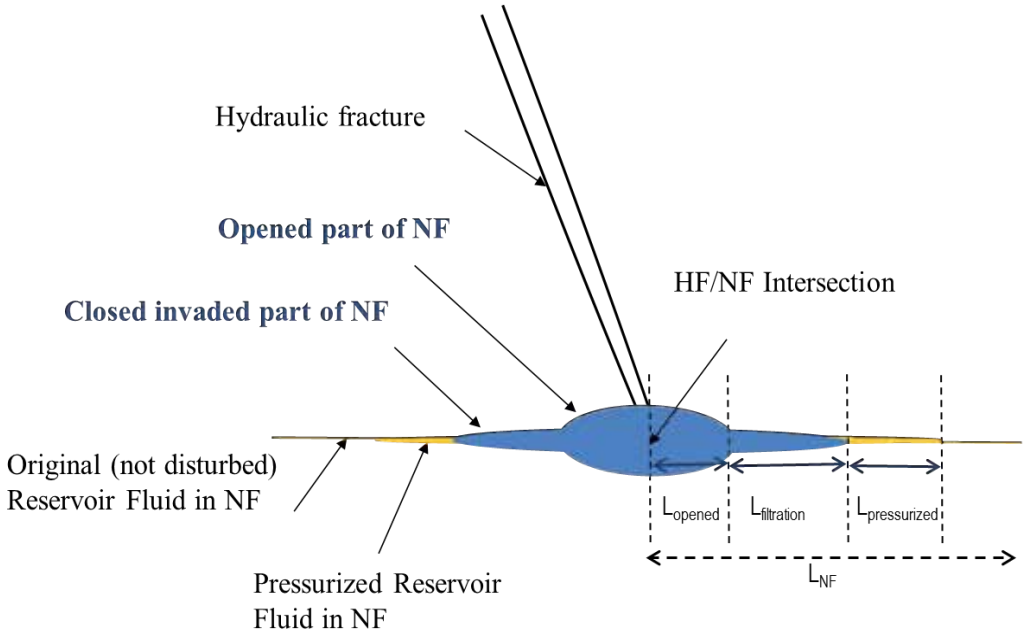

Figure 4. Details on different possible zones in intercepted permeable NF

5.1. Opened part of NF

If the NF is opened at intersection element *i* with HF, then fluid pressure at intersection exceed the local normal stress on NF:

$$p_f(i) > \sigma_n^{NF}(i) \tag{22}$$

The tip of opened part of NF or the intersection element with HF (if NF is closed) becomes the inlet (injection point) into the closed invaded part of NF (filtration zone) $p_{in}^{filtr} = p_{tip}^{open} = \sigma_n^{NF}$. Mention that if NF is completely opened, then it is a part of total hydraulic fracture network (HFN) and handled based on the approach described previously in [1], see also equations (16)-(21).

If NF is closed at intersection element *i* with HF, then fluid pressure is below the local normal stress, but can still be higher than reservoir (pore) pressure

$$p_o < p_f(i) \le \sigma_n^{NF}(i) \tag{23}$$

5.2. Filtration zone (closed part of NF invaded by fracturing fluid)

The fluid pressure, width and flow rate along the filtration zone can be calculated from given pressure $p_{in}^{filtr} = p_f(i)$ which satisfies condition (23). The flow rate along filtration zone can be iteratively solved from the system of equations (24) with flow rate from the inlet to filtration zone q_{in}^{filtr} which is a part of total solution

$$\begin{cases} \dfrac{\partial p}{\partial s} = -\dfrac{\mu_f}{k_{NF}\varpi_{filtr}h}q, \quad \text{at the inlet : } p = p_{in}^{filtr}(t) \\ \dfrac{\partial q}{\partial s} + \dfrac{\partial(\varpi_{filtr}h)}{\partial t} + q_L = 0,\ q_L = \dfrac{2hC_{tot}^{rock}}{\sqrt{t-\tau_o(s)}} \\ k_{NF} = \dfrac{\varpi_{filtr}{}^2(p)}{12} \\ \varpi_{filtr}(p) = \dfrac{\varpi_0}{1+9\dfrac{\sigma_{eff}}{\sigma_n^{ref}}} + \varpi_s + \varpi_{res}, \quad \varpi_s = \mid u_s \mid \tan(\phi_{dil}^{eff}), \quad \sigma_{eff} = \sigma_n - p(s), \end{cases} \tag{24}$$

The length of filtration zone can be calculated by the tracking the volume of fracturing fluid leaked into the NF by marching from the inlet along the NF. At the end of filtration zone mass balance should be satisfied and fluid pressure will be higher or equal to the reservoir pressure

$$\begin{aligned} & q_{in}^{filtr}dt = dVol_{frac}^{filtr}(dt) + dVol_{leak}^{filtr}(dt) \\ & p_r < p^{end\ filtr\ zone} < \sigma_n^{NF} \end{aligned} \tag{25}$$

The flowrate (filtration/pressurized front velocity) at the last element of filtration zone is used for calculations in the pressurized zone. The position of the front between the filtration zone and pressurized zone should be tracked, giving velocity of filtration front and pressure p_{in}^{pres} as input for solution in pressurized zone.

If NF is partially opened, then in the solution scheme for the filtration zone the intersection (inlet) element is replaced by the tip element i of the opened part of NF with $p(i) = \sigma_n^{NF}(i)$.

5.3. Closed pressurized part of NF (filled with reservoir fluid).

Mention that if the leakoff coefficient for filtration zone $C_v^{rock} = 0$, then $p_r = p_f^{end\ filtr\ zone} < \sigma_n^{NF}$, and there will not be pressurized zone in NF ($p_r = p_f^{end\ filtr\ zone} < \sigma_n^{NF}$, $L_{\ pressurized} = 0$).

http://dx.doi.org/10.5772/56446

For the general case of compressible reservoir fluid and non-zero total leakoff from the walls of pressurizes NF into the rock, the leakoff to the rock from the NF part filled with pressurized reservoir fluid is defined by the compressibility controlled leakoff coefficient

$$C_c^{rock} = \sqrt{\frac{k_r \varphi_r c_T}{\pi \mu_r}} \Delta p, \quad \Delta p = p_{NF} - p_r \tag{26}$$

The governing equations to calculate fluid pressure, width, and flow rate along the pressurized zone from known influx $q_{filtr/pres}$ and pressure $p_{filtr/pres}$ are similar to Equations (24) for filtration zone with replacing fracturing fluid with reservoir fluid and using ω_{pres} as hydraulic width of pressurized zone of invaded NF, and c_T as reservoir fluid compressibility.

Notice that the pressure at the front between opened and filtration zones along invaded NF (or at HF/closed NF intersection point) and the time step are the inputs for the new pressure, width, and flow rate calculation in closed invaded part of intercepted NF. Initial influx q_{in} can be prescribed based on the pressure in NF from the previous time step, and then the solution scheme will be applied from the intersection towards the end of NF with tracking the incremental mass balance (fluid injected to NF at current time step) to define the end of filtration front, and tracking pressure in the rest of NF (not invaded part, filled with reservoir fluid) to track the end of pressurized zone (fluid pressure equal to reservoir pressure). The flow rate and pressure are tracked and corresponding front positions are to be updated iteratively until in the pressurized zone of NF the following condition is satisfied (which indicates the position of the end of the pressurized zone)

$$\begin{aligned} q(L_{open} + L_{filtr} + L_{pres}) &= 0 \\ p(L_{open} + L_{filtr} + L_{pres}) &= p_r \end{aligned} \tag{27}$$

At the end of pressurized zone pressure is equal to the reservoir pressure and flow rate is zero. If the end of NF is reached and pressure is above the reservoir pressure, then Equation (27) is replaced with condition $q(L_{NF})=0$. During pumping the pressurized zone extends until the end of NF, and then gradually shrinks, while the lengths of invaded zone and opened zones increase. Eventually whole NF will be filled with fracturing fluid, so the NF will contain only filtration and/or opened zones. When NF is completely opened, it becomes a part of total HFN. The elements in closed part of invaded NF can slip under some conditions (for example, due to the stress field change from stress shadow), influencing the calculations of total NF permeability k_{NF}.

Each element in the closed part of intercepted NF is checked for shear slip possibility. The fracture surface slip (the shear displacement u_s) can be found as shear displacement discontinuity calculated for the closed sliding elements satisfying Coulomb frictional law $\tau \geq \tau_s = \lambda(\sigma - p_f)$, from elasticity equations (12) accounting for the mechanical opening in HFN.

If some elements in closed not disturbed part of NF are sliding then the corresponding shear stress is involved in the stress shadow calculations and thus influences simulations results.

6. Numerical approach description

The treatment of permeable natural fractures is a part of UFM model. It is possible to model leakoff from HF into the NF form UFM in different ways, depending on the importance of required accuracy, numerical stability and CPU time.

The most computationally expensive but at the same time most accurate is a fully coupled numerical approach. The fully coupled approach means to discretise different parts of the invaded NFs and numerically solve the pressure as a part of total system of equations for the fracture network using iterative solution scheme. Another, more CPU efficient approach, is a decoupled numerical approach, where pressure and width along the invaded but closed part of NF are calculated separately based on the results from previous time step calculations along the HFN and corresponding pressure at HF/NF intersections (inlets).

Two approaches have been considered to model interaction of hydraulic fracture with permeable natural fractures.

6.1. Decoupled numerical approach

- When NF is intercepted by HF, create elements along whole NF to be used at next time step
- Evaluate initial guess of flow rate into the NF based on the pressure at the intersection and old pressure profile along closed NF
- Check for a possibility of frictional sliding along the closed parts of NFs to evaluate pressure-dependent permeability and conductivity along NF
- Iteratively calculate pressure, hydraulic width, flow rate and length of each zone along NF with using corresponding equations (for filtration and pressurized zones) by marching from intersection till the end of NF until condition (27) is satisfied indicating final results and final positions of zones' fronts
- Track the end of filtration zone for each pressure and flow rate iterations by checking the volume of fluid injected into NF at given time step
- Save invaded volume for volume balance, influx for mass balance, pressure at intersection, and time step to be used at the next time step
- Track the pressure at intersections and/or tips of opened HF part in NF to capture opened zones.
- If intersection is opened, use the pressure at the tip of opened HFN part along invaded NF for calculations along corresponding closed NF part
- Apply rules to treat special situations (intersecting NFs, etc)

http://dx.doi.org/10.5772/56446

- Save elements information (volume, pressure, flow rates) for the next time step

6.2. Fully coupled numerical approach

- Discretize the NF when HF intercepts it
- Make the NF elements a part of total network (HFN) and include pressure calculations along different zones of NF into the whole iterative scheme to calculate pressure, time step, and front positions.

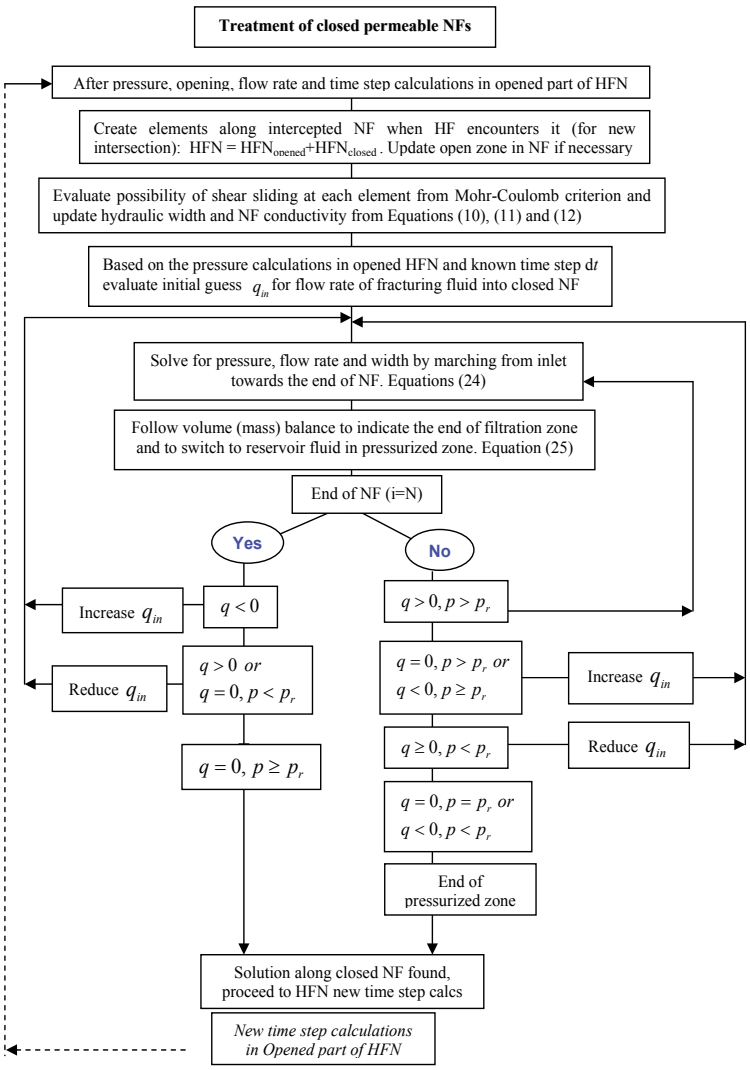

Figure 5. The proposed algorithm to account for leakoff from HF into the permeable NFs (*i=N* indicates the end of NF)

- Calculate the flow rate and volume of fluid injected to NFs at each pressure iteration, and update/calculate pressure along HFN using existing scheme for opened elements and new equations (described above) for elements in closed invaded and pressurized NF parts
- From the calculated pressure in NF elements iteratively update the positions of the propagating fronts for opened, filtration, and pressurized zones in NF during pressure/time step iterations
- Track the pressure at intersections to capture when NF start to open
- Include the elements in the closed parts of invaded NFs into the stress shadow calculation scheme

The fully coupled NF modeling approach is heavier and more CPU expensive than decoupled approach. The Decoupled Numerical Approach has been selected as basic approach and it is described schematically on Figure 5 as a part of total solution

7. Conclusions

The new approach developed to account for the complex processes due to NF permeability accompanying HF/NF interaction have been presented in detail. This approach accounts for the important physical processes taking place during HF and permeable NF interaction, and will be implemented in UFM.

The next step is to evaluate the influence of leakoff into the natural fractures during HFN simulations on the total HFN footprint and production forecast. The approach will be also validated against existing numerical, experimental and field data.

Author details

Olga Kresse and Xiaowei Weng

*Address all correspondence to: okresse@slb.com

Schlumberger, Sugar Land, USA

References

[1] Kresse, O, Cohen, C. E, Weng, X, Wu, R, & Gu, H. Numerical modeling of hydraulic fracturing in naturally fractured formations. 45th US Rock Mechanics/ Geomechanics Symposium, San Francisco, CA, June, (2011). , 26-29.

[2] Chuprakov, D, Melchaeva, O, & Prioul, R. Hydraulic Fracture Propagation Across a Weak Discontinuity Controlled by Fluid Injection. InTech; (2013).

[3] Chuprakov, D. S, Akulich, A. V, Siebrits, E, & Thiercelin, M. Hydraulic Fracture Propagation in a Naturally Fractured reservoir. SPE 128715, Presented at the SPE Oil and Gas India Conference and Exhibition held in Mumbai, India, January, (2010). , 20-22.

[4] Zhao, J, Chen, M, Jin, Y, & Zhang, G. Analysis of fracture propagation behavior and fracture geometry using tri-axial fracturing system in naturally fractured reservoirs. Int. J. Rock Mech. & Min. Sci, (2008). , 45, 1143-1152.

[5] Thiercelin, M, & Makkhyu, E. Stress field in the vicinity of a natural fault activated by the propagation of an induced hydraulic fracture. Proceedings of the 1st Canada-US Rock Mechanics Symposium (2007).

[6] Zhang, X, & Jeffrey, R. G. The role of friction and secondary flaws on deflection and re-initiation of hydraulic fractures at orthogonal pre-existing fractures. Geophysical Journal International (2006). , 166(3), 1454-1465.

[7] Zhang, X, & Jeffrey, R. G. Reinitiation or termination of fluid-driven fractures at frictional bedding interfaces. J Geophys Res-Sol Ea. (2008). Aug 28;113(B8).

[8] Zhang, X, Jeffrey, R. G, & Thiercelin, M. Effects of Frictional Geological Discontinuities on hydraulic fracture propagation. SPE 106111, Presented at the SPE Hydraulic Fracturing Technology Conference, College Station, Texas, January (2007). , 29-31.

[9] Zhang, X, Jeffrey, R, & Thiercelin, M. Deflection and propagation of fluid-driven fractures as frictional bedding interfaces: a numerical investigation. Journal of Structural Geology (2007).

[10] Zhang, X, Jeffrey, R. G, & Thiercelin, M. Mechanics of fluid-driven fracture growth in naturally fractured reservoirs with simple network geometries. Journal of Geophysical Research (2009). B12406.

[11] Beugelsdijk LJLde Pater CJ, Sato K. Experimental hydraulic fracture propagation in a multi-fractured medium. SPE 59419, presented at the SPE Asia Pacific Conference in Integrated Modeling for Asset Management, Yokohama, Japan, April (2000). , 25-26.

[12] Renshaw, C. E, & Pollard, D. D. An Experimentally Verified Criterion for Propagation across Unbounded Frictional Interfaces in Brittle, Linear Elastic-Materials. International Journal of Rock Mechanics and Mining Sciences & Geomechanics Abstracts. (1995). Apr, , 32(3), 237-49.

[13] Warpinski, N. R, & Teufel, L. W. Influence of Geologic Discontinuities on Hydraulic Fracture Propagation (includes associated papers 17011 and 17074). SPE Journal of Petroleum Technology. (1987). , 39(2), 209-220.

[14] Blanton, T. L. An Experimental Study of Interaction Between Hydraulically Induced and Pre-existing Fractures. SPE 10847, Presented at the SPE/DOE Unconventional Gas Recovery Symposium, Pittsburgh, PA, May (1982). , 16-18.

[15] Blanton, T. L. Propagation of Hydraulically and Dynamically Induced Fractures in Naturally Fractured Reservoirs. SPE Unconventional Gas Technology Symposium; 01/01/1986; Louisville, Kentucky (1986).

[16] Gu, H, & Weng, X. Criterion For Fractures Crossing Frictional Interfaces At Non-orthogonal Angles. 44th US Rock Mechanics Symposium and 5th US-Canada Rock Mechanics Symposium; 01/01/2010; Salt Lake City, Utah: American Rock Mechanics Association; (2010).

[17] Gu, H, Weng, X, Lund, J. B, Mack, M, Ganguly, U, & Suarez-rivera, R. Hydraulic fracture crossing natural fracture at non-orthogonal angles, a criterion, its validation and applications. Paper SPE 139984 presented at the SPE Hydraulic Fracturing Conference and Exhibition, Woodlands, Texas, January, (2011). , 24-26.

[18] Kresse, O, Weng, X, Chuprakov, D, Prioul, R, & Cohen, C. E. Effect of Flow Rate and Viscosity on Complex Fracture Development in UFM. InTech; (2013).

[19] Economides, M. J, & Nolte, K. G. Reservoir Simulation. Third edition. (2000).

[20] Nolte, K. G, & Smith, M. B. Interpretation of Fracturing Pressures SPE 8297, September (1981).

[21] Castillo, J. L. Modified Fracture Pressure decline Analysis Including Pressure-Dependent leakoff, SPE 16417, (1987).

[22] Nolte, K. G. Fracturing Pressure Analysis for Non-Ideal Behavior. SPE 20704, JPT, February (1991).

[23] Warpinski, N. R. Hydraulic Fracturing in Tight, Fissured Media. SPE 20154, JPT, February (1991).

[24] Barree, R. D, & Mukherjee, H. Determination of Pressure Dependent Leakoff and its effect on Fracture geometry, SPE 36424, 1996. Presented at the 71st Annual Tech Conference and Exhibition, Denver Co, October, (1996). , 6-9.

[25] Mukherjee, H, Larkin, S, & Kordziel, W. Extension of Fracture Pressure Decline Curve Analysis to Fissured Formations. SPE 21872, 1991. Presented at the Rocky Mountain Regional meeting and Low Permeability Reservoirs Symposium, Denver, Co, April (1991). , 15-17.

[26] Walsh, J. B. Effect of Pore Pressure and Confining Pressure on Fracture Permeability, In. J. Rock Mech. Min. Sci. & Geomech. Abstr. (1981). , 18, 429-435.

[27] Warpinski, N. R. Fluid leakoff in natural fissures. In: Economides&Nolte: Reservoir Stimulation, (2000).

[28] Meyer, B. R, & Bazan, L. A Discrete Fracture Network Model for Hydraulically Induced Fractures: Theory, Parametric and Case Studies, SPE 140514. Presented at the SPE Hydraulic Fracturing Tech Conference and Exhibition in The Woodlands, Texas, 2426 January (2011).

[29] Rogers, S, Elmo, D, Dunphy, R, & Bearinger, D. Understanding Hydraulic fracture geometry and interactions in the Horn River Basin through DFN and Numerical modeling, SPE 137488, 2010. Presented at the Canadian Unconventional Resources & International Petroleum Conference, Calgary, Alberta, Canada, October, (2010). , 19-21.

[30] Nagel, N, Damjanac, B, Garcia, X, & Sanchez-nagel, M. Discrete Element Hydraulic Fracture Modeling- Evaluating Changes in natural Fracture Aperture and Transmissivity, SPE 148957, 2011. Presented at the Canadian Resources Conference, Calgary, Alberta, Canada, Novebmer (2011). , 15-17.

[31] Fu, P, Johnson, S. M, & Carrigan, C. R. Simulating Complex Fracture Systems in Geothermal Reservoirs Using an Explicitly Coupled Hydro-Geomechanical model, ARMA Presented at 45th US Rock Mechanics/Geomechanics Symposium, Salt Lake City, UT, June 27-29, (2011). , 11-244.

[32] Dershowitz, W. S, Cottrell, M. G, Lim, D. H, & Doe, T. W. A Discrete Fracture Network Approach for Evaluation of Hydraulic Fracture Stimulation of Naturally Fractured Reservoirs, ARMA-475, 2010. Presented at 44th US Rock Mechanics Symposium, San Francisco, CA, June (2010). , 26-29.

[33] Rahman, M. M, Aghigi, A, & Sheik, A. R. Numerical Modeling of Fully Coupled Hydraulic Fracture propagation in Naturally Fractured Poro-Elastic Reservoirs", SPE 121903, 2009. Presented at the 2009 SPE EUROPEC/EAGE Conference, Amsterdam, The Netherlands, June (2009). , 8-11.

[34] Brown, S. R, & Bruhn, R. L. Fluid permeability of deformable fracture network. Journal of Geophys. Research (1998). B2): 2489-2500.

[35] Cooke, M. L, & Underwood, C. A. Fracture termination and step-over at bedding interfaces due to frictional slip and interface opening. Journal Structural Geology, (2001). , 23, 223-238.

[36] Hossain, M. M, Rahman, M. K, & Rahman, S. S. Volumetric Growth and Hydraulic Conductivity of naturally fractured reservoirs during hydraulic fracturing: A case study using Australian Conditions, SPE 63173, 2000. Presented at the 2000 SPE Technical Conference and Exhibition, Dallas, Texas, October (2000). , 1-4.

[37] Chuprakov, D. A, Akulich, A. V, Siebrits, E, & Thiercelin, M. Hydraulic-Fracture Propagation in a Naturally Fractured Reservoir.SPE 128715, 2011. Presented at the SPE Oil and Gas India Conference and Exhibition, Mumbai, India, January (2010). , 20-22.

[38] Tezuka, K, Tamagawa, T, & Watanabe, K. Numerical Simulation of Hydraulic Shearing in Fractures Reservoir. Proceeding World Geothermal Congress, Antalya, Turkey, April (2005). , 24-25.

[39] Weng, X, Kresse, O, Cohen, C, Wu, R, & Gu, H. Modeling of Hydraulic Fracture Network Propagation in a Naturally Fractured Formation. Paper SPE 140253 presented at the SPE Hydraulic Fracturing Conference and Exhibition, Woodlands, Texas, USA, January, (2011). , 24-26.

[40] Kresse, O, Weng, X, Wu, R, & Gu, H. Numerical modeling of Hydraulic fractures interaction in complex Naturally fractured formations. ARMA-292, Presented at 46th US Rock Mechanics /Geomechanics Symposium, Chicago, Il, USA, June (2012). , 24-27.

[41] Dean, R. H, & Advani, S. H. An Exact Solution for Piston like Leak-off of Compressible Fluids. Journal of Energy Resources Technology (1983). December, , 106

[42] Settari, A. A New General Model of Fluid Loss in Hydraulic Fracturing, SPE 11625, August (1985). , 1985, 491-501.

[43] Crouch, S. L, & Starfield, A. M. Boundary Element Methods in Solid Mechanics. 1st ed. London: George Allen & Unwin Ltd, (1983).

[44] Olson, J. E. Predicting fracture swarms: the influence of subcritical crack growth and the crack-tip process zone on joints spacing rock. In: Cosbrove JW, Engeder T (eds) The initiation, propagation and arrest of joints and other fractures. Geological Soc. Special Publications, London, (2004L). , 231, 73-87.

[45] Mack, M. G, & Warpinski, N. R. Mechanics of Hydraulic Fracturing. In: Reservoir Stimulation, Third Edition. Editors: Economides MJ and Nolte KG, (2000).

Chapter 15

Injection Modeling and Shear Failure Predictions in Tight Gas Sands — A Coupled Geomechanical Simulation Approach

Arshad Islam and Antonin Settari

Additional information is available at the end of the chapter

http://dx.doi.org/10.5772/56312

Abstract

This work presents theory for modeling of fracture propagation within reservoir simulator, history matching of field injection pressure using uncoupled and fully coupled geomechanical injection models, and sensitivity study of various parameters such as permeability enhancement/reduction functions, limiting length of fracture propagation, stress factor, and Biot's constant. Two wells completed in tight gas sands in Western Canadian sedimentary basin were studied. The wells were fractured with different techniques (i.e., X-link gelled water fracs (Well A) and un-gelled slick water fracs (Well B)) and were both successfully matched with coupled geomechanical model.

1. Introduction

Fracture propagation modeling is an important part of reservoir geomechanics and must be considered in injection modeling of wells. Classical modeling of fracture geometry is well established and documented in literature of rock mechanics and stimulation [3]. Direct coupling of fracture propagation (fracture dynamics) and fluid flow is computationally very expensive [4, 5]. The modeling of "complex" fracturing [6] is also expensive. However, proper representation of dynamic propagation in which the fracture is directly coupled into a reservoir simulator is important for many applications. It has been shown that the some degree of coupled treatment of fracture mechanics, reservoir modeling and geomechanics is important for better understanding of the unconventional fracturing applications as well as for tight gas fracturing treatments such as waterfracs [7, 8]. While the fully coupled approach [5, 12] is not

yet feasible for practical work, we have developed a simplified method which will be described briefly here. Such coupling, described next, can be achieved in a simplified fashion using only a reservoir simulator, which makes the modeling computationally efficient. The method has been developed and refined over two decades and proved to be successful in modeling a large variety of injection processes.

2. Theory of fracture propagation modelling

The method is based on modifications of transmissibility in the reservoir flow model. For injection scenarios transmissibilities are modified dynamically. To model dynamic fracturing process, a transmissibility multiplier function is assigned to a line (or plane) of grid blocks assumed for fracture propagation extending from the well. The multiplier function is a table that can be derived from simple 2-D analytical fracture models which approximate the actual fracture. In an uncoupled modeling, transmissibility multipliers are a function of fracture injection pressure, while in a coupled (geomechanical) system they are a function of a minimum effective stress. The multipliers are calculated based on the estimation of a 2D crack opening in a cross-section by Equation (1) [9], then calculating the fracture permeability by Equation (2) as a function of the net pressure in the fracture, and finally calculating the transmissibility multiplier (T_r) on the reservoir transmissibility of the block containing the fracture as described in Equation (3).

$$w_f = \frac{\Delta P_f H_f}{E} = \frac{4\,\Delta P_f H_f (1-\upsilon^2)}{E} = \frac{4\,(P_f - P_{foc}) H_f (1-\upsilon^2)}{E} \tag{1}$$

$$K_f = R_{fa}\frac{w_f^2}{12} \tag{2}$$

$$T_r = \frac{K_m A_m + K_f A_f}{K_m A_m} = 1 + R_{fa}\frac{w_f^3}{12\,K_m w} = f\left(P_f - P_{foc}\right) \tag{3}$$

H_f in Equation (1) is the estimate of fracture half-height based on the 2-D Perkins-Kern geometry assumption of vertical fracture with smooth closure at the top and bottom [10]. Permeability reduction factor R_{fa} in Equation (2) is a correction factor that accounts for deviations from Poiseuille law such as roughness, tortuosity and non-Darcy flow. It can be several orders of magnitude less than 1. Fracture opening or closing pressure (P_{foc}) is normally taken as the initial minimum horizontal total stress acting perpendicular to fracture face. Fracture opening or closing pressure may be actually greater (or lower) than the initial minimum horizontal total stress due to poroelastic and thermo elastic effects. The method allows one to create tables of dynamic transmissibility multipliers (as a function of pressure or stress) which are then used in a conventional reservoir simulator to propagate the high permeability (in the fracture plane) in time. As such, the method does not directly solve any fracture mechanics equations; although an estimate of fracture width can be obtained from

http://dx.doi.org/10.5772/56312

Equation (3) from the known T_r at any grid cell in fracture plane and in time. Typically a single function is used, but variations of confining stress can be modeled by the use of multiple functions with different P_{foc} values. Finally, the created fracture volume can be accounted for by a similar function applied to porosity.

Obviously, the method is approximate in several respects. The fracture opening is computed from PK geometry for a fixed height while in reality the height varies along the distance from the well. The fracture opening also varies in the vertical direction. In spite of these approximations, the method provides a very realistic approximation to the results obtained by models based on fracture mechanics [4], and is capable of history matching complex injection sequences [13].

3. The field study

The wells studied are located in the tight gas sands in Western Canadian sedimentary basin. They were fractured with different techniques – Well A using cross-linked gelled water fracs, and Well B with un-gelled water fracs (slick water fracs). In both cases, the entire well was fractured through an open hole as opposed to multi-stage fracturing (which is the more common technique). However, microseismic monitoring and other techniques have shown that a number of fractures were created, with fairly regular intervals.

Field bottomhole injection pressure (BHIP) for wells A and B is given in Figure 1 and 2 respectively. Well B which is deeper than Well A has a higher bottomhole injection pressure than well A. Breakdown pressure, maximum pressure required to initiate fracture in formation, is also higher for well B. Complete set of reservoir, geomechanical and stimulation data has been provided in references [1, 2]. For modeling it was assumed that 15 fractures were created along the well with spacing of 50 m, as it was indicated by microseismic monitoring.

The simulations were carried out both in an uncoupled mode and coupled mode (solving both fluid flow and geomechanics). In both we employed the technique described above for fracture modeling, and also the pressure or stress dependent matrix permeability changes (which model the permeability enhancement in the SRV). The results of uncoupled modeling are not presented in detail, but in this case it is shown that coupled modeling is necessary to obtain history match (see [1, 2] for details).

4. History matching of field injection pressure — Uncoupled geomechanical injection models

The concept used for approximation of geomechanical effects in an uncoupled model and equations developed for production modeling [1, 2] can be used also for injection modeling. For injection cases change in pressure is always positive and consequently the effective mean stress is always larger when poroelastic effects are considered. For uncoupled modeling it can

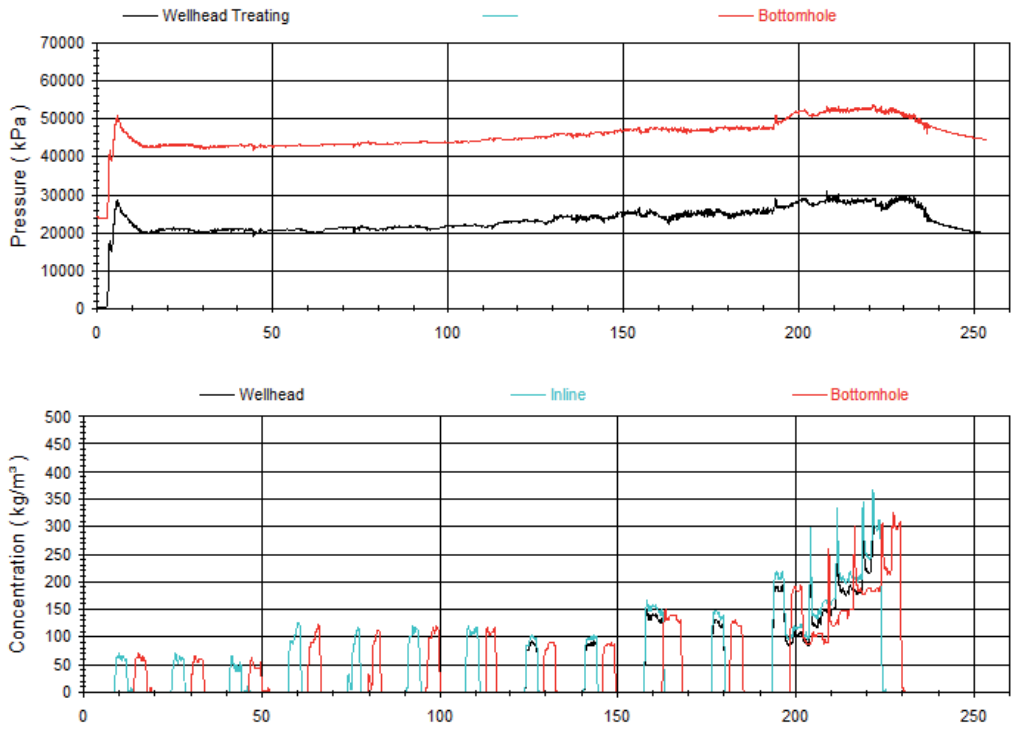

Figure 1. BHIP, Wellhead pressure and Proppant concentration - Well A

be assumed that the stress changes have stabilized and fracture opening or closing pressure is equal to the minimum (adjusted) horizontal total stress during the treatment.

In uncoupled history matching, any changes in stresses due to poroelastic effects must be incorporated manually in reservoir simulator for permeability multipliers and transmissibility calculation. Modified stresses are used in uncoupled model assuming that the hydraulic fracture increases in-situ stresses near wellbore and around fractures due to poroelasticity and permeability enhancement in that region must be predicted by using these modified stresses. Fracture height of 50 ft, Poisson's ratio of 0.125 and Elastic modulus of 7.99 E6 psia is used for fracture transmissibility calculation. The method of SRV permeability multiplier calculation is explained in references [1, 2]; the strength of the nonlinearity is given by "stress factor" S. Value of S=6.0 was used for all simulation runs. Injection model was setup in reservoir simulator and run for given injection period by using the actual injection rate, subject to maximum bottom-hole injection pressure of 10,000 psi.

http://dx.doi.org/10.5772/56312

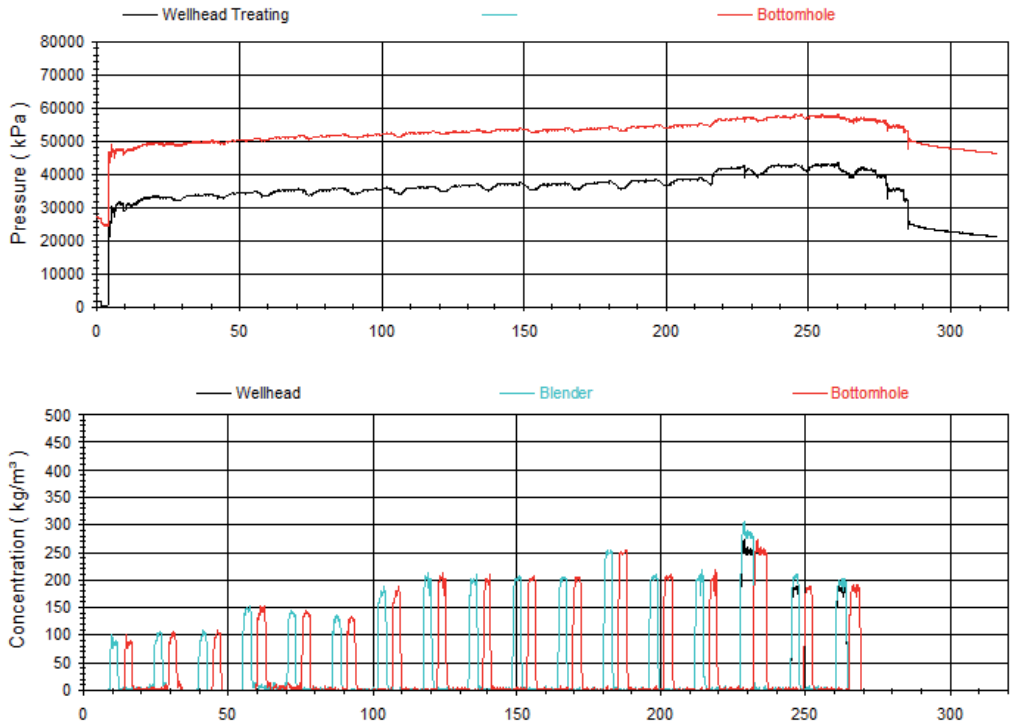

Figure 2. BHIP, Wellhead pressure and Proppant concentration - Well B

4.1. Effects of fracture permeability reduction factor (R_{fa})

Fracture permeability given by Equation (2) becomes an intrinsic permeability of smooth open fracture if the reduction factor is taken as 1. Fracture permeability in reality is much smaller than this value due to tortuosity, asperities interlocking, rock chipping at fracture face, unequal and rough surface of rock faces, and fracture degradation. Three injection cases were run to match field injection pressure with simulation injection pressure by varying only the fracture permeability reduction factor.

4.2. Effects of limiting length of fracture propagation

The initial runs produced a flat injection pressure while the field pressure is steadily increasing. A mechanism that would create larger pressure increase with time is required. One method is to restrict or confine fracture propagation in length (half length), which can be achieved by modifying transmissibility of grid blocks in fracture plane only within an assumed fracture half length. Possible justification is the scale-dependence of effective fracture toughness that was proposed theoretically and indicated by matching data [14]. Several simulation cases were run both for each well using different values of pre-determined maximum fracture half length. Reservoir parameters used in simulation runs are same as in base case.

Results of all uncoupled cases are not shown here except best matched case (see Figure 3 and 4) as history matching was not achieved. Only their effects are discussed here (detailed description of the results is provided in reference [2]). Results show that decreasing the R_{fa} factor pushes the injection pressure upward. Smaller reduction factor means smaller transmissbility mutlipliers and hence larger pressure drop down in the fracture. However, fracture propagation confinement did not improve the rising trend of injection pressure in uncoupled simulation.

5. History matching of field injection pressure — Coupled geomechanical injection models

In coupled geomechanical simulation, because stresses are continuously computed, P_{foc} in Equation (3) is updated at each time step and grid block in reservoir simulator by taking as an input effective stress from geomechanical part of the simulator. Therefore there is no need to modify stress data to correct for poroelastic effects. To run a fully coupled geomechanical simulation the original in-situ stress is used to calculate transmissibility and permeability multipliers, which are a function of effective stresses. Run times for coupled simulation are generally very large and consequently a detailed study for each parameter was not possible due to time constraints. The sensitivity study and calculations shown here are performed for well A. Only conclusions and end results are then applied to well B to get a history match.

Note that for fracture initiation (and propagation) minimum effective stress must be negative; in other words injection pressure should be higher than minimum horizontal total stress. Biot's constant of 1.0 was initially used for effective stress calculation, but it was found that fracture initiation could not be achieved because the poroelastic stress component caused by injection pressure was too high and the total stress increased above the injection pressure limit (set at 10,000 psia). The smaller the Biot's constant the slower is the increase in total stress and it is less difficult to fracture the rock. It was therefore concluded that Biot's constant should be significantly less than 1.0.

5.1. Effects of limiting length of fracture propagation

Few simulation cases are run using different values of permeability reduction factor and confining length of fracture propagation. For this purpose, it was assumed that rock behaves as a perfectly elastic material which does not exhibit hysteresis during loading and unloading. A base case here (Case-1) was therefore set up allowing unlimited fracture propagation in y-direction and modifying Biot's constant value in the geomechanical simulator to 0.65 (initial guess). Summary of history matching parameters are presented in Table 1. Simulation results for all these cases for well A and history matched case for Well B are presented in Figure 3 and 4 respectively.

http://dx.doi.org/10.5772/56312

Property – Well A	Case - 1	Case - 2	Case - 3	Case – 4
Biot's constant (α)	0.65			0.75
Permeability reduction factor (R_{fa})	0.00001		0.0000052	0.0000052
Fracture half length, ft	Not restricted	100	130	130

Table 1. Parameters varied in coupled injection Cases 1 – 4 – Well A

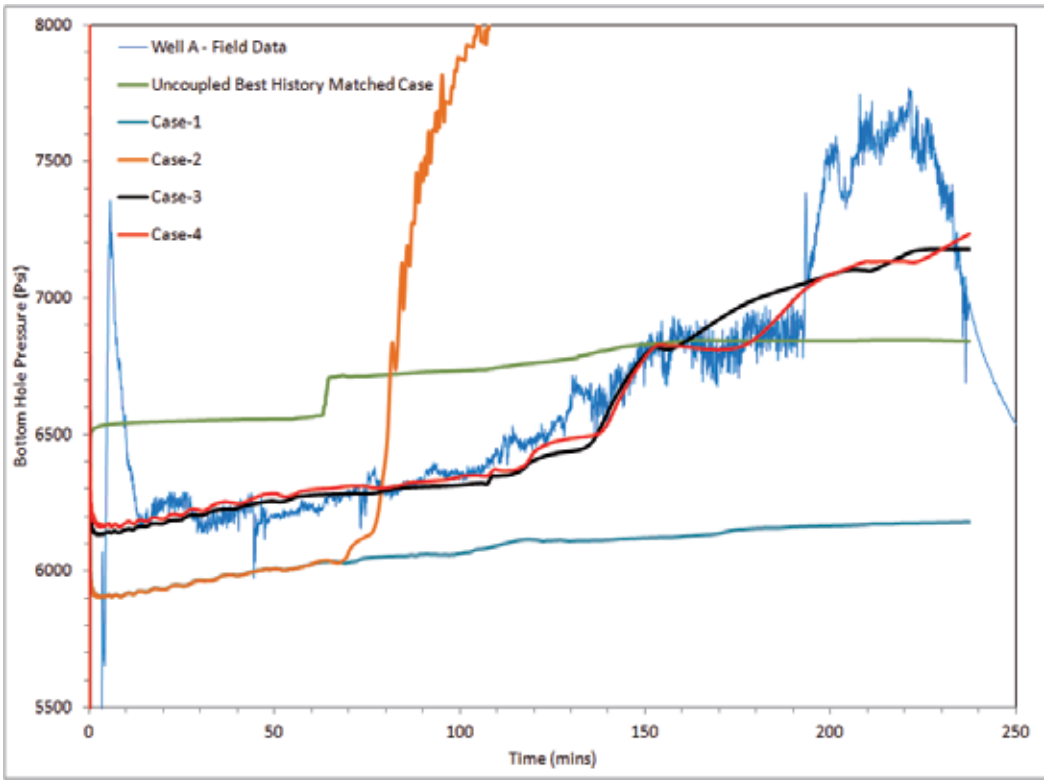

Figure 3. Comparison of simulation results and field BHIP - Well A

The effect of fracture permeability reduction was discussed in detail in uncoupled simulation section; decreasing its value shifts pressure injection curve upward which can be observed in Figure 3. Although simulation results of Case – 4 of well A do not exactly match field injection pressure, it represents a reasonable history match. It is concluded that injection history match requires some mechanism to constrain fracture propagation at a late stage. This issue was not pursued further; however, the coupled cases show much improvement compared to the uncoupled simulations as shown in Figures 3 and 4.

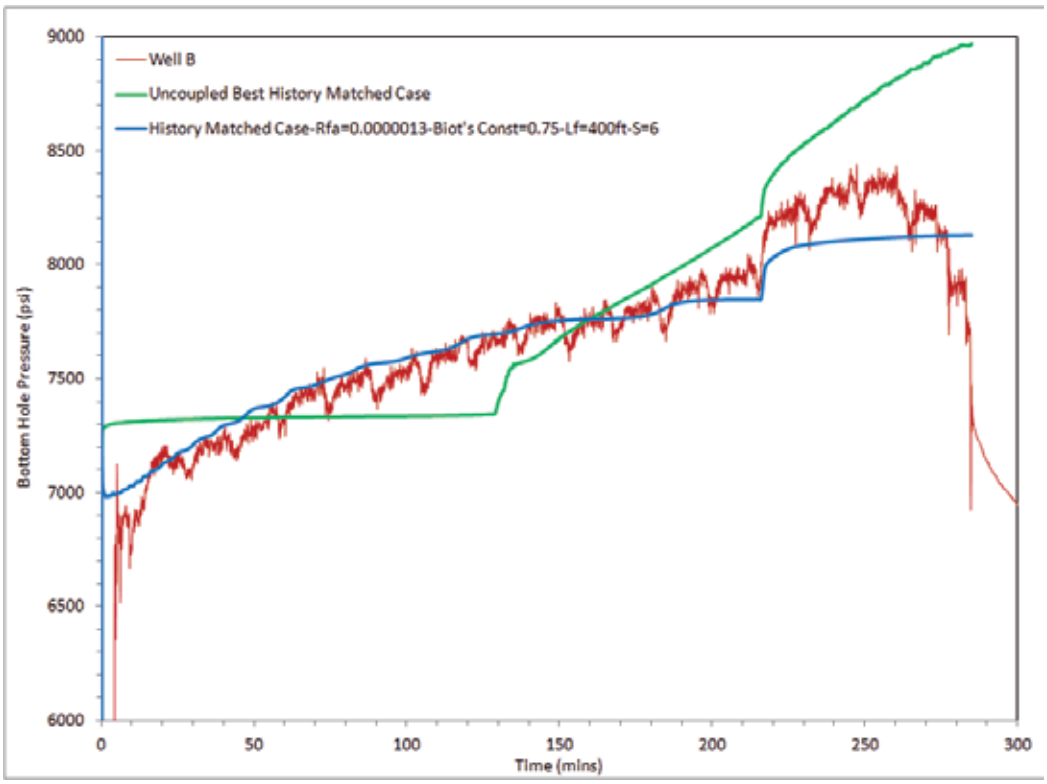

Figure 4. Comparison of simulation results and field BHIP - Well B

5.1.1. Discussion on the late time history matching (Well A)

It is important to point out that history matching of field injection pressure after 190 minutes of injection for well A cannot be achieved through our simulation results (See Figure 3). It was observed in field treatment report (See Figure 1) that the injected proppant concentration was increased after 190 minutes to approximately three times of the overall average concentration. Our simulation study does not include coupling of fracture propagation simulation with proppant transport, modeling of fracture propagation based on downhole variable proppant concentration is not possible here and beyond the scope of this study. Fracture modeling in this work was performed based on total downhole amount of slurry injected. Late time history matching for well B is more acceptable.

5.2. Effects of stress factor (*S*)

Stress factor (S) defines shape of pressure/ effective stress dependent permeability curves and controls the permeability dependence on effective stress [1, 2]. The larger the value of S, the higher is the permeability dependence on stress. Permeability multipliers are applied in the whole reservoir except in fractured blocks. Increasing S value from 6 to 16 results in increase of permeability multipliers to several orders of magnitude but there is little difference in

http://dx.doi.org/10.5772/56312

injection pressure except at late time when the pressures are lower with higher S value (see Figure5). We observed similar difference in results for injection pressures when the exercise was repeated for well B. It is therefore concluded that effect of leak off on injection pressures in low permeability formations is not considerable, although it affects fracture length and the match with microseismic (MS) data.

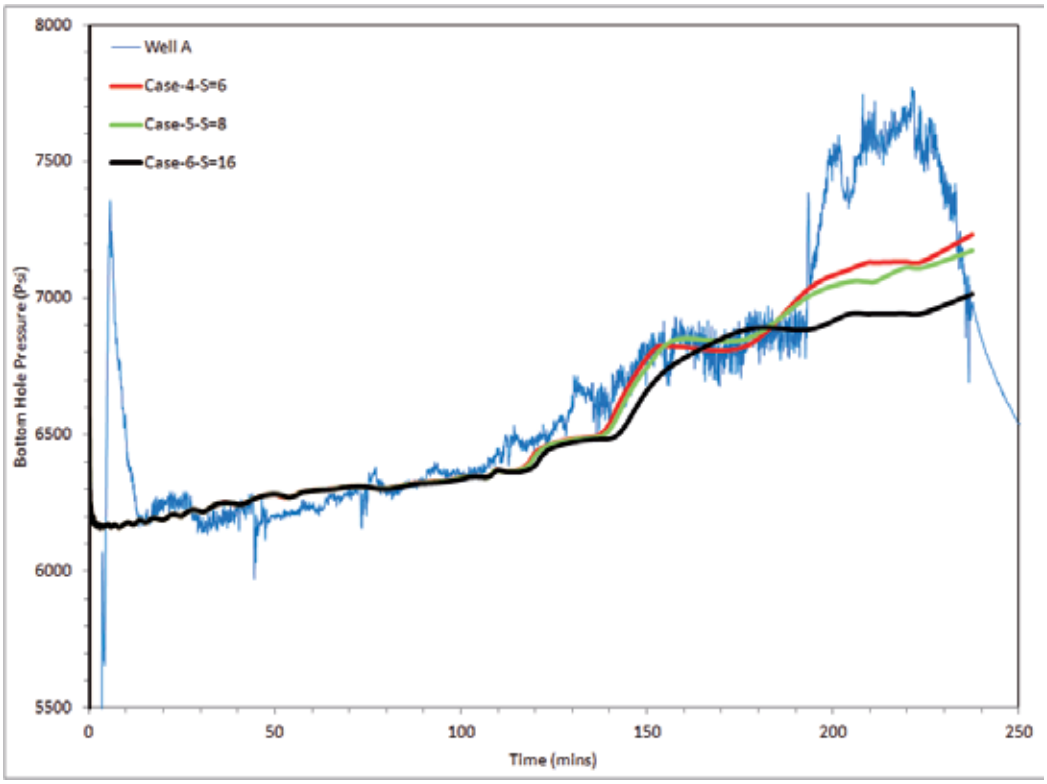

Figure 5. Effects of Stress Factor (S) on BHIP - Well A

6. Failure predictions — Tensile and shear failure

The simulations of the injection process presented in this work showed that one must assume a substantial stress-dependent enhancement of permeability around the primary single plane fracture (SPF) to history match the injection pressures. Often it is postulated that the creation of this SRV is due to shear fracturing, i.e., creating shear failure. Coupled modeling provides us with the tool to investigate under what conditions shear fracturing occurs and what would be the extent of the SRV if it was caused purely by shear failure. This aspect is examined in the present section.

When tensile stress across a plane exceeds critical limit then tensile failure occurs. This critical limit is called the tensile strength or ultimate tensile strength (UTS). The tensile failure criterion is applied to determine the propagation of the main fracture (SPF) through grid blocks. In some rare instances, tensile failure can also occur in the reservoir around the SPF (e.g. due to thermal effects [11]).

When shear stresses along a plane in a specimen exceed shear strength of material, shear failure occurs. The shear strength of material / rock indirectly depends on the normal stress acting on the failure plane. There are different shear failure criterions available in literature such as Tresca, Mohr-Coulomb and Griffith. For this study Mohr-Coulomb criterion is used to predict failure mechanism during injection.

To investigate if tensile or shear failure will occur; time-history of pressure and stresses was extracted for specific grid blocks from a coupled simulation run. By plotting the Mohr circles in MATLAB® we can make failure prediction of these grid blocks in graphical form. For this purpose, the history matched case, i.e., Case – 4 of well A was used. All the fractures behave the same way and pressure propagation is also approximately the same for all fractures. Therefore only one fracture is selected for this analysis which is fracture # 4 (4^{th} fracture from the line of symmetry) and conclusions drawn from this analysis will apply to all sets of fractures. Two grid blocks were selected and marked as shown in Figure 8, which represents cross section of the model in y-z plane of the fracture. The well is completed in x-direction and block 1 represents the perforation location.

6.1. Base case — High cohesion

The Mohr-Coulomb failure envelope was based on rock geomechanical data given in references [1, 2]. The base case used friction angle of 30^0 and Uniaxial compressive strength of 321 Mpa (intact rock). Mohr – Coulomb circle progression is presented in Figure 6 for well A, where Circles 1 - 5 are for block 1 and circles 6 - 10 for block 2. Similar envelope can be constructed from coupled simulations output for well B. In Figure 6 there is no shear failure during injection because Mohr's circles are much below the failure line. It is obvious that the dominant failure mechanism in these blocks is tensile because the SPF penetrated them. We also repeated the same exercise for all blocks/time steps and confirmed that no shear failure occurred.

6.2. Case with low cohesion

More realistic case was run by reducing the uniaxial compressive strength by 10 times to a base value while keeping other parameters such as friction angle, elastic modulus and Poisson's ratio the same as in the previous case. Mohr-Coulomb circles for this case are shown in Figure 7.

Complete spatial map of the failure can be obtained by plotting "stress level" S_L, a feature offered in GeoSim® (Geomechanical Simulator) which represents the ratio of the size of the Mohr circle at any point to the circle at critical state, i.e., when the circle touches the failure line. Stress level therefore ranges between 0 and 1. When $S_L < 1$ there is no shear failure, and when shear failure is reached, S_L remains theoretically at 1. Stress level for fracture # 4 after 237 minutes of injection (end of injection) is shown in Figure 8 for the y-z cross section through

http://dx.doi.org/10.5772/56312

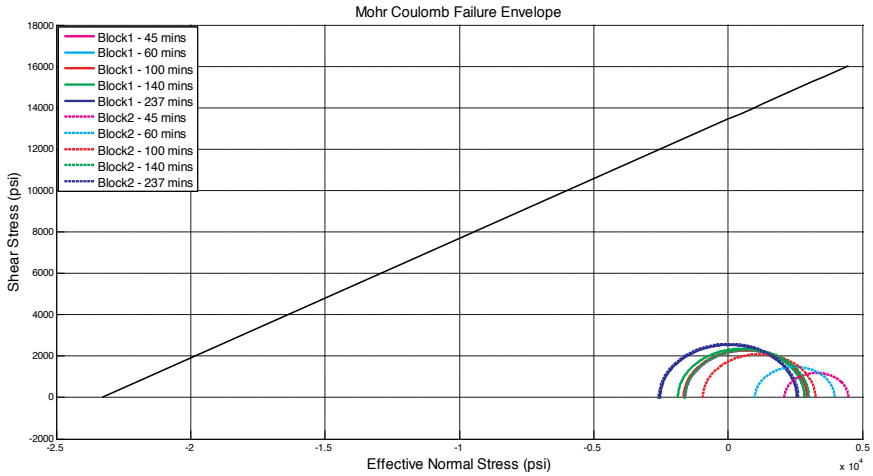

Figure 6. Mohr – Coulomb failure envelope for C_o= 46570psi – Well A

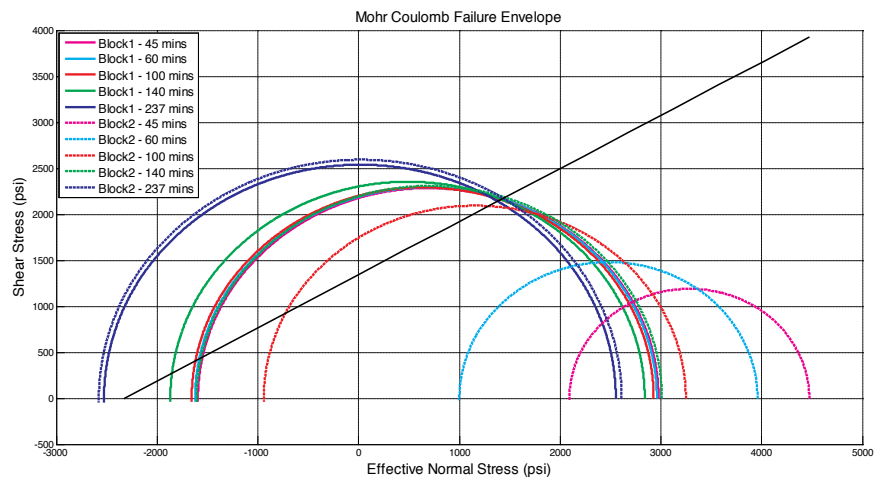

Figure 7. Mohr – Coulomb failure envelope for C_o= 4657psi – Well A

the fracture plane. It should be noted that our simulations were not carried out using elasto-plastic modeling, but only linear elastic treatment, and therefore S_L can exceed 1. The modeling is not rigorous past shear failure, but it still provides useful picture of the possible extent of failure. In this case, failure is also predicted for planes adjacent to fracture plane.

From above simulation runs (which required increase of matrix permeability during injection), and knowledge of presence of micro cracks and heterogeneities in tight sands [2] as recorded by microseismic, it is concluded that the high original value of uniaxial compressive strength (which does not allow any shear events) is unlikely. Reducing the C_0 to account for weak planes

and natural fractures then will predict possibility of shear fracturing and shear-generated SRV creation. However, the SRV based on shear failure is still very narrow and therefore one has to conclude that the majority of the matrix permeability enhancement should be contributed to matrix and micro-fractures. These results are preliminary and further work should be done using finer gridding and elasto-plastic modeling.

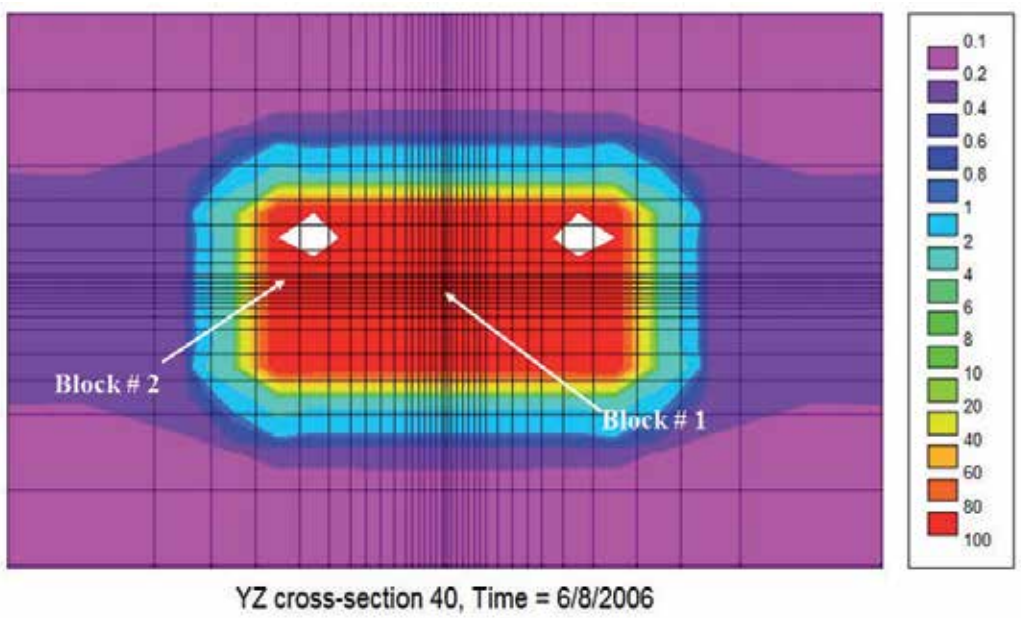

Figure 8. Stress level after 237 mins of injection – Co= 4657 psi – YZ cross section – Well A

7. Conclusions

- The method used for modeling the fracture propagation is practical, and provides realistic representation of fracturing in reservoir models or coupled geomechanical models.
- Uncoupled modeling is not capable of history matching the injection pressures for the two wells studied.
- Coupled modeling achieves reasonable history match of both wells. The main factors that have been identified as important are the fracture permeability factor (R_{fa}) (which primarily shifts the pressure curve), the reservoir permeability dependence on stress and confining the length of fracture propagation (which causes to increase of pressure in later part of the job and thus improves the matches).
- Value of Biot's constant controls the increase of effective stresses during pumping. For larger values of Biot's constant it is very difficult to fracture the formation.

http://dx.doi.org/10.5772/56312

- Preliminary work on the modeling of shear failure region (SRV) shows that no shear events are detected when a high value of uniaxial compressive strength (UCS) of the rock is assumed, representative of intact rock. A narrow shear region is predicted when the UCS is lowered to represent media with pre-existing fractures or planes of weakness.

This work demonstrates the need for coupled geomechanical modeling in injection to capture poroelastic effects and stress alterations during stimulation.

Nomenclature

A_f = Fracture cross sectional area, ft^2

A_m = Matrix block cross sectional area, ft^2

BHIP = Bottomhole injection pressure, psi

C_o = Uniaxial compressive strength (UCS), psi

E = Elastic modulus, psi

H_f = Fracture half height, ft

K_f = Fracture permeability, mD

K_m = Matrix block permeability, mD

L_f = Fracture half length, ft

MS = Microseismic

P_f = Fluid (fluid) pressure, psi

R_{fa} = Permeability enhancement/reduction factor

P_{foc} = Fracture opening or closing pressure, psi

S = Stress factor

SPF = Single planer fracture

SRV = Stimulated reservoir volume, ft^3

S_L = Stress level

T_r = Transmissibility multiplier

UTS = Ultimate tensile strength, psi

W = Grid block size in x-direction, ft

W_f = Fracture width, ft

α= Biot's constant

υ= Poisson's ratio

Acknowledgements

We would like to acknowledge help from Taurus Reservoir Solutions Ltd. for providing the TRS® reservoir and GeoSim® geomechanical simulator. We also wish to acknowledge the financial aid from the JIP consortium for Tight Gas Sands and Shale Gas Modeling at University of Calgary for supporting the research fund. We wish to thank Vikram Sen for helping during this project and Apache Canada for providing us data for this study.

Author details

Arshad Islam[1*] and Antonin Settari[2]

*Address all correspondence to: aislam@trican.ca

1 Trican Well Service Ltd., Calgary, Canada

2 University of Calgary, Calgary, Canada

References

[1] Islam, A., Settari, A., and Sen, V. 2012. Productivity Modeling of Multifractured Horizontal Wells Coupled With Geomechanics - Comparison of Various Methods. Paper SPE 162793 presented at the SPE Canadian Unconventional Resources Conference, Calgary, Alberta, Oct. 30 – Nov. 1.

[2] Islam, A. 2012. Geomechanical Productivity and Injectivity Modeling of Multifractured Horizontal Wells. MSc thesis, University of Calgary, Calgary, Alberta (September 2012).

[3] Economides, M. J., and Nolte, K .G. 2000. *Reservoir Simulation*, Third Ed. John Wiley & Sons, Inc.

[4] Ji, L., Settari, A., Sullivan, R. B. et al. 2004. Methods for Modeling Dynamic Fractures in Coupled Reservoir and Geomechanics Simulation. Paper SPE 90874 presented at the SPE Annual Technical Conference and Exhibition, Houston, Texas, 26 – 29 September.

http://dx.doi.org/10.5772/56312

[5] Ji, L., Settari, A., and Sullivan, R. B. 2009. A Novel Hydraulic Fracturing Model Fully Coupled with Geomechanics and Reservoir Simulation. *SPE Journal* 14 (3): 423-430. SPE-110845-PA.

[6] Weng, X., Kresse, O., Cohen, C. et al. 2011. Modeling of Hydraulic-Fracture-Network Propagation in a Naturally Fractured Formation. *SPE Prod & Oper* 26 (4): 368-380. SPE-140253-PA.

[7] Settari, A., Puchyr, P. J., and Bachman, R. C. 1990. Partially Decoupled Modeling of Hydraulic Fracturing Process. *SPE Prod Eng* 5 (1): 37-44. SPE-16031.

[8] Settari, A., Sullivan, R. B., Walters, D. A. et al. 2002a. 3-D Analysis and Prediction of Microseismicity in Fracturing by Coupled Geomechanical Modeling. Paper SPE 75714 presented at the SPE Gas Technology Symposium, Calgary, Alberta, 28 April – 2 May.

[9] Sneddon, I. N., and Lowengrud, M. 1969. Crack Problems in the Classical Theory of Elasticity, 20-30. New York: SIAM Series in Applied Mathematics, John Wiley & Sons.

[10] Perkins, T. K., and Kern, L. R. 1961. Widths of Hydraulic Fractures. *J. Pet Tech* 13 (9): 937-949. SPE-89-PA.

[11] Tran, D., Settari, A., and Nghiem, L. 2012. Predicting Growth and Decay of Hydraulic Fracture Width in Porous Media Subjected to Isothermal and Nonisothermal Flow. Paper SPE 162651 presented at the SPE Canadian Unconventional Resources Conference, Calgary, Alberta, Oct. 30 – Nov. 1.

[12] Dean, R.H., and Schmidt, J. H. 2009. Hydraulic-Fracture Predictions With a Fully Coupled Geomechanical Reservoir Simulator. *SPE Journal* 14 (4): 707-714. SPE-116470-PA.

[13] Settari, A., Sullivan, R. B., Turk, G. et al. 2009. Comprehensive Coupled Modeling Analysis of Stimulations and Post-Frac Productivity – Case Study of the Wyoming Field. Paper SPE 119394 presented at the 2009 SPE Hydraulic Fracturing Technology Conference, The Woodlands, Texas, 19–21, January.

[14] Jeffrey, R., and Settari, A. 1998. An Instrumented Hydraulic Fracture Experiment in Coal. Paper SPE 39908 presented at the 1998 Rocky Mountain Regional/Low Permeability Reservoirs Symposium, Denver, CO, April 5-8.

Chapter 16

The Role of Natural Fractures in Shale Gas Production

Ian Walton and John McLennan

Additional information is available at the end of the chapter

http://dx.doi.org/10.5772/56404

Abstract

Natural fractures seem to be ubiquitous in shale gas plays. It is often said that their presence is one of the most critical factors in defining an economic or prospective shale gas play. Many investigators have presumed that open natural fractures are critical to gas production from deeper plays such as the Barnett, as they are for shallower gas shales such as the Devonian shales of the northeastern US and for coal bed methane plays. A common view on production mechanisms in shales is "because the formations are so tight gas can be produced only when extensive networks of natural fractures exist" [6]. However, there is now a growing body of evidence that any natural fractures that do exist may well be filled with calcite or other minerals and it has even been suggested that open natural fractures would in fact be detrimental to Barnett shale gas production [9].

Commercial exploitation of low mobility gas reservoirs has been improved with multi-stage hydraulic fracturing of long horizontal wells. Favorable results have been associated with large fracture surface area in contact with the shale matrix and it is here that the role of natural fractures is assumed to be critical. For largely economic reasons hydraulic fracturing for increasing production from shale gas reservoirs is often carried out using large volumes of slickwater injected at pressures/rates high enough to create and propagate extensive hydraulic fracture systems. The fracture systems are often complex, due essentially to intersection of the hydraulic fractures with the natural fracture network. After hydraulic fracturing operations the injected water is flowed back. Typically, only a small percentage (on the order of 20 to 40%) is recovered.

In this paper we investigate the role played by natural fractures in the gas production process. By applying a new model of the production process to data from many shale gas wells across a number of shale plays in North America, we can for the first time begin to sort out assertion from inference in the role that these fractures play. Specifically, we are able to esti-

mate the magnitude of the fracture surface through which gas is actually produced. We are able to demonstrate that although it may be commensurate with the expected surface area of open natural fractures for the ultra-low permeability shallow gas shales, it is in fact commensurate with a very much smaller area for the deeper gas shales such as the Barnett. Furthermore, given a typical value of the matrix permeability, almost all the gas between the fractures would have been produced in an uncharacteristically short period of time unless the producing fractures are 100s of feet apart. The implications of these findings for completion and stimulation strategies will be discussed.

1. Introduction

One of the main premises of our investigation of the production processes in shale gas plays is that the industry's mental picture of the process remains very much influenced by the concepts developed in the 1990s of the production processes in coal bed methane resources and in shallow shale gas plays. It is appropriate therefore that we begin our discussion of shale gas production characteristics by reviewing this early work.

1.1. Coal bed methane

Coal is a heterogeneous and anisotropic porous medium, characterized by two distinct porosity systems:

- Micropores of diameter of the order of nanometers with almost zero permeability.
- Macropores or cleats, slot-like with spacing of the order of 2 cm and width of the order of microns; permeability is stress-dependent but far in excess of the micro-pore permeability. They are often formed by shrinkage of the coal matrix due to dewatering during the coalification process.

Gas is stored essentially by adsorption in the coal matrix; very little is stored as free gas in the micropores or as free gas or dissolved gas in the connate brine in the cleats. In the subsurface the cleats are usually filled with water, some of which must be produced to the surface to facilitate gas production.

The conventional view of the production process divides it into three stages (see Figure 1):

1. Cleat dewatering, lasting of the order of several years; the water production rate gradually falls as water is removed from the cleats. At the same time more and more gas is produced at increasing rates and the relative permeability to gas in the cleats increases leading to lower pressures and more gas production.
2. Stabilized flow: eventually, most of the water in the cleats has been removed, the cleat fluid pressure bottoms out and the relative permeability to gas levels off. Over this period the gas rate slowly peaks.
3. Decline: there is then no more increase in drawdown available to sustain gas production and gas production declines. If the cleat pressure was constant and the pseudo-steady-

http://dx.doi.org/10.5772/56404

state (PSS) regime is applicable (see the later discussion for definitions of this flow regime), then gas production rate should decline exponentially.

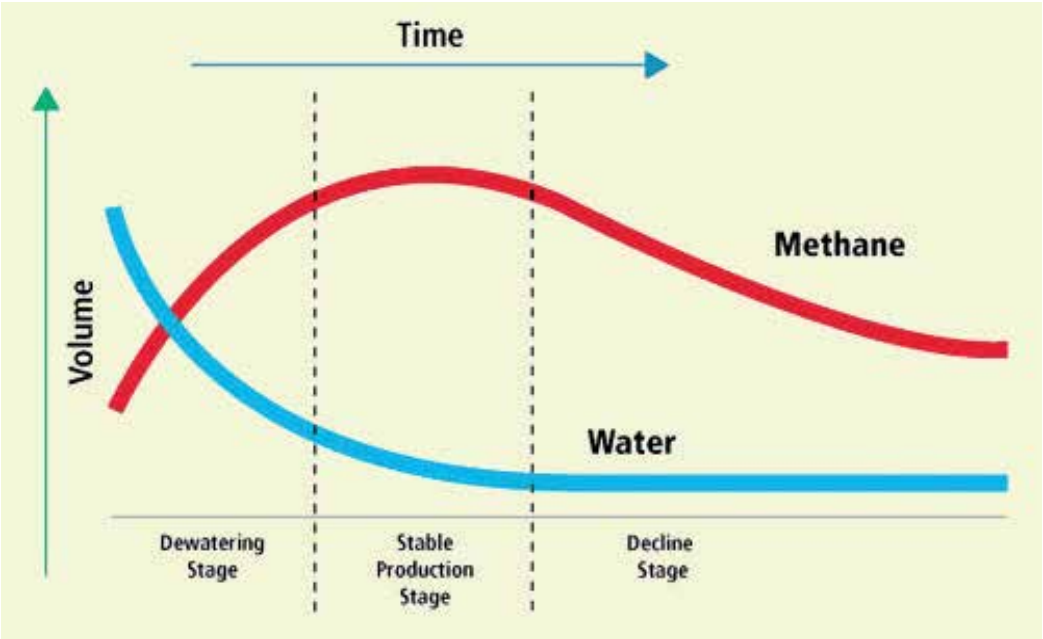

Figure 1. Stages in gas and water production from coal (after [1]).

There are three essential elements to a model of the CBM production process:

1. Transport in the coal matrix, modeled as a diffusive process using Fick's diffusion law. In principle the gas concentration in the coal matrix satisfies a diffusion equation, but it is common to use a pseudo-steady-state (PSS) approximation similar to that proposed by Warren and Root [2] in their dual porosity formulation of production from naturally fractured reservoirs. For example, King et al [3] used the PSS simplification to reduce computing time and because after a period of time the numerical accuracy was deemed to be quite acceptable. We have estimated from King's data that the PSS solution is valid beyond about 40 days, which is much shorter than the typical duration of the production process. We note, however, that this time scale depends on the assumed values of the diffusivity in the matrix and on the spacing of the cleats, assumed to be of the order of a few cm.

2. Desorption at the cleat/matrix interface as characterized by the Langmuir isotherm

3. Transport of water and free gas in the cleat system. To avoid difficulties in defining the configuration of the cleat system, it is common to adopt a dual porosity description in which the cleat system is treated as a continuum with system characteristics analogous to those of a porous medium. Two-phase flow in this system can for the most part be

adequately described by Darcy flow. In narrower cleats it may be necessary to include capillary pressure and slippage effects especially at low pressure.

It is apparent that the cleat or natural fracture system plays a very important part in the production process. The density of the cleats plays two critical roles: first, the close spacing of the cleats reduces the time required for the gas to diffuse to the cleats and, second, it is associated with a high cleat/matrix surface area without which economical gas production would be unlikely. The width of the cleat is a primary influence on the pressure drop in the whole system and therefore on the water and gas production rates. In situ the cleats are usually water-filled and presumably kept open by the pressure of the fluid they contain. The cleats may close somewhat as the pressure falls during production, though this may be more than offset by matrix shrinkage as the gas is desorbed.

1.2. Devonian shales of the appalachian basin

Gas production from Devonian shales received a great deal of attention in the 1980s and early 1990s as a result of US DoE initiatives. This is well documented in many GRI reports and industry publications. The consensus view is that these reservoirs are highly fractured containing a substantial number of fractures with spacing of the order of 1-10 cm (see, for example, [4]). Luffel et al [5] measured the matrix permeability at less than 0.1 nd. Water content of the Devonian Shale averages 2.5 to 3% of bulk volume and appears to be at irreducible water saturation. Typical depth is a few thousand feet, pore pressure is less than about 3000 psi and about 50% of the gas in place is adsorbed; there is little or no water production.

Carlson and Mercer [6] summarized the consensus view of the production process as "because the formations are so tight gas can be produced only when extensive networks of natural fractures exist." The extent to which this statement holds for other gas shale plays is debatable, but it has certainly been influential in developing the industry's vision of what is happening downhole.

Gatens et al [7] used a dual-porosity model similar to that formulated by Warren and Root [2] but extended to use the unsteady-state equation instead of the pseudo-steady-state (PSS) equation for matrix flow. Analysis of hundreds of Devonian wells showed that most of the production data fell into the linear transient regime (as we discuss later in this document). Luffel et al [5] obtained a good history match with data by assuming an open fracture spacing of a few feet, while Carlson and Mercer [6] needed a fracture spacing of about 80 ft, both with matrix permeability of less than 0.1 nd. An issue that does not seem to have been addressed however, is whether these fractures, if present, are in fact open and if so how they are maintained open against closure stress. If, like coal cleats, they are initially water-filled, is water production observed? An implicit assumption seems to be that they are open and gas-filled.

Carlson and Mercer [6] proposed that molecular diffusion is the dominant transport mechanism in the matrix in these extremely tight reservoirs, in which case a matrix diffusion coefficient should be used instead of the matrix permeability. They did not evaluate the consequences of this hypothesis. It remains a possibility that the use of such a coefficient would

http://dx.doi.org/10.5772/56404

reduce the need for a large fracture surface area and ultimately for the need to propose the existence of a large open fracture network.

Thus there are three essential elements to a model of the production process in the Devonian shales:

1. Desorption of gas in the matrix (as characterized typically by the Langmuir isotherm)
2. Transport in the matrix towards the fracture network, modeled as Darcy flow even though the permeability is extremely small.
3. Transport of free gas in the fracture system.

1.3. Devonian Antrim Shale of the Michigan basin

The Antrim Shale is a shallow, under-pressured, naturally-fractured shale reservoir with characteristically low matrix permeability, and with adsorbed gas, free gas and mobile water co-existing in the reservoir. A typical Antrim well will produce considerable quantities of water early in life, and as dewatering of the reservoir progresses, water production rates decline and a corresponding increase in gas production is normally observed (as a result of gas desorption with reduced reservoir pressures), similar to a CBM well. In fact, the Antrim shale is often considered to be a hybrid of productive dry gas shale and CBM plays. It has characteristics which are similar to these other unconventional reservoirs, but it is also different in many ways. The Antrim shale is more intensely fractured than the Devonian Shales of the Appalachian Basin, with fracture spacing as close as 1 to 2 ft. Kuuskraa et al [8] have noted that the "intensity and interconnection of the fractures govern the shale's natural producibility."

The typical depth of the Antrim shale is less than about 2000 feet, pore pressure is a few hundred psi and more than 70% of the gas in place is adsorbed, the remainder being stored essentially as free gas in the matrix pores. Peak gas may occur as late as 3 years into production. Production data has been history-matched using similar software to that used for CBM [8]. It was found that fracture spacing of the order of a few inches facilitated a good match with production data. It was stated that if a fracture spacing of 3-6 ft was used (which is compatible with observations from cores and logs), then production would be an order of magnitude lower than observed in existing wells. One possible resolution of this conundrum may lie, as the authors suggest, in detrital silt layers within the matrix that could provide conductive flow paths. (An alternative explanation that remained unconsidered by the authors lies in the use of the PSS approximation for matrix transport, which may be completely invalid in this context.)

This description leaves many issues unresolved, but importantly places the Antrim shale as an intermediate between CBM and the other shales, in that the natural fractures appear to be conductive and initially water-filled, but has free pore gas in addition to adsorbed gas.

1.4. Deeper gas shales

Most modern commercial gas shale plays are similar in many respects to the Barnett shale, though there are of course many differences and variations in the values of the parameters that control the gas production process. In these relatively deep and high pressure reservoirs, most of the gas is stored as pore gas, but the production process is still similar to that described above for shallower shale gas plays.

The subject of open natural fractures is one of the most contentious within the community of Barnett workers. Many investigators have presumed that open natural fractures are critical to Barnett gas production, as they are for the shallower gas shales, even though there is now a growing body of evidence that any natural fractures that do exist may well be filled with calcite or other minerals (see Figure 2). There are also arguments that suggest that if there was an abundance of open natural fractures within the Barnett, there would be a much smaller gas accumulation present within the reservoir. Open natural fractures, if they existed, would have led to major expulsion and migration of gas out of the shale into overlying rocks, substantially decreasing pore pressure within the Barnett and, hence, the amount of gas in place. The Barnett would not be over-pressured (that is, over-pressured relative to the bounding strata) if copious open natural fractures existed. Note that the Barnett is not just the gas reservoir, but also the source, trap, and seal for the gas; if the seal is fractured and inefficient, then the present gas in place would be reduced because the free gas would be lost, and only the adsorbed gas would remain in the shale (a similar situation to that of the Antrim Shale of northern Michigan). The huge amount of gas in place, in an over-pressured and fully-saturated (in terms of sorption) state, is ultimately what makes the Barnett so prolific.

Figure 2. Mineralized natural fractures in a Barnett shale sample (adapted from [9]).

http://dx.doi.org/10.5772/56404

A common argument for the necessity for open natural fractures in shale gas plays is that a large surface area is necessary for economic gas production from these very tight rocks. Later in this paper we analyze production data to estimate the magnitude of the fracture surface through which gas is actually produced. We are able to demonstrate that although it may be commensurate with the expected surface area of open natural fractures for the ultra-low permeability shallow gas shales, it is in fact commensurate with a very much smaller area for the deeper gas shales such as the Barnett. Furthermore, given the typical permeability of the Barnett shale (some 100 times that of the shallow gas shales), almost all the gas between the fractures would have been produced in an uncharacteristically short period of time unless the fractures are 100s of feet apart. These issues and conclusions will be discussed at length later in the paper.

2. Production mechanisms, production modeling techniques and simulators

Having outlined the pertinent characteristics of unconventional gas reservoirs, we now document the likely production mechanisms in the various shale plays based on our understanding of their geology and the underlying geophysics.

The matrix permeability of shale gas reservoirs is extremely small, probably on the order of one tenth of a microdarcy or 100nd. It is virtually impossible to produce gas from these reservoirs in commercial quantities unless the wells are hydraulically fractured and even then, or so it is commonly believed, production is really only possible because a network of natural fractures is opened up. (It is interesting to note that gas has been produced from the ultra-tight Devonian shale plays of the North Eastern USA from more conventionally-fractured vertical wells, which implies that multi-stage hydraulic fracturing was unnecessary for these plays. This is the first hint that the role of the natural fractures may be quite different for the Devonian plays and the deeper shale plays.)

An essential element of a mathematical model of gas production from shales is therefore the ability to describe flow in a very tight rock matrix and flow in a network of fractures. In most gas shale reservoirs most of the reservoir fluid is stored in the matrix and the primary flow path is from the matrix into the fractures and thence into the wellbore. There are essentially two methods of characterizing a multiply-fractured reservoir:

- Discrete fracture network (DFN) model, in which the fractures are defined explicitly in terms of their location in the reservoir, their connectivity to one another and to the wellbore and their production characteristics, such as permeability and conductivity.
- Dual porosity/dual permeability models in which the fracture network is treated as a continuum in much the same way as a porous medium is treated as a continuum for analysis of flow characteristics.

2.1. Discrete fracture network models

Many commercial numerical reservoir simulators have the capability of simulating flow through a complex network consisting of pores and fractures. However, one of the greatest drawbacks and limitations of simulating a discrete fracture network model is the a priori assumption that all relevant properties of the fracture network are known. Nevertheless great insights can be obtained into the impact of the essential physical processes by examining simple fracture configurations. We note that in principle many different physical and petro-physical components can be included in numerical simulations. However, in practice it is quite common to see results presented only for the special cases:

- Reservoir fluid of small and constant compressibility.
- Production under constant drawdown conditions.
- No desorption.
- Darcy flow in fractures and matrix.
- Matrix and fracture permeability independent of pressure; it is often assumed that fracture conductivity is essentially infinite.

The simplest fracture network that has been applied to shale gas production consists of a number of planar fractures placed transversely to a horizontal wellbore as illustrated schematically in Figure 3. It is apparent from many published numerical studies that under these circumstances flow from the reservoir can be described in terms of a number of identifiable flow regimes. The following account is taken from a recent paper by Luo et al [10]. These authors used a commercial reservoir simulator to calculate the flow into a horizontal well with six infinitely-conductive transverse fractures as shown in Figure 4.

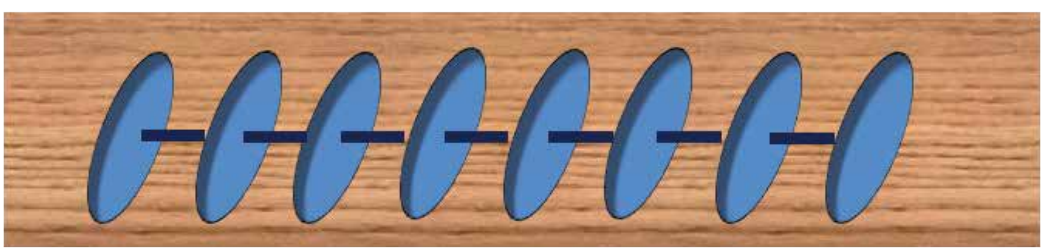

Figure 3. Idealized discrete fracture network showing multiple transverse fractures originating from a horizontal well.

The flow behavior can be conveniently discussed in terms of five flow regimes as follows.

- Bilinear or linear flow: soon after the well is placed on production reservoir fluid flows normal to the fracture planes and along the fractures into the well. The streamlines are shown in yellow in Figure 4; reservoir pressure is in red and the constant bottomhole or well pressure is in blue. Note that flow into the fracture tips is negligible and each fracture behaves independently of the other fractures. This regime may also be termed the infinite-

http://dx.doi.org/10.5772/56404

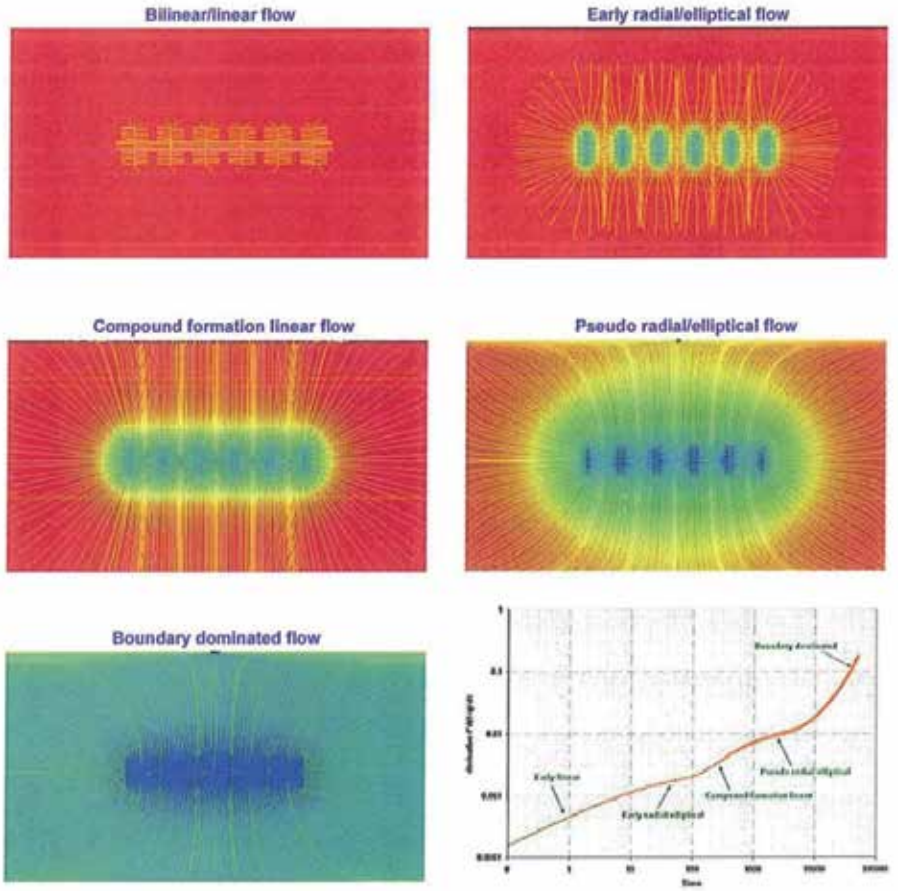

Figure 4. Numerical solutions for flow into six infinitely-conductive transverse fractures (taken [10]).

acting regime in the sense that the neighboring fractures are effectively at infinity. The duration of this regime depends, as we shall see later, on many parameters including the matrix permeability, the fluid compressibility and the fracture spacing. The illustrations in Figure 4 are for infinite conductivity fractures.

- Early radial/elliptical flow: flow into the fracture tips is present, but weak; flow into the fracture surfaces is still predominantly linear, but fracture interference is just beginning to impact the flow. Note that the pressure drawdown in the matrix has almost reached the mid-line between the fractures. At this point the flow regime may be described as pseudo-steady-state or fracture-boundary-dominated.

- Compound formation linear flow (CFL flow): here the fractures are fully interactive and the reservoir drainage area is dominated by the area defined by the length of the well and the length of the fractures. Flow from beyond this area grows in importance.

- Pseudo-radial/elliptical flow: flow from beyond the wellbore/fracture area grows in importance and appears to be radial or elliptical.
- Reservoir-boundary-dominated flow: ultimately the outer boundary of the reservoir begins to impact the flow.

It is difficult to infer from these simulations the time scales and duration of these flow regimes for parameter values other than those used in the particular simulation. Indeed, this highlights one of the severe drawbacks to the full numerical approach to modeling production flow in these reservoirs: it is difficult to make general conclusions about the characteristics of the flow and their dependence on the input data without undertaking very many numerical simulations; this is a formidable task even for a restricted input data space. However, based on the semi-analytic models that are described below, we believe that for many shale gas wells it would be unusual to expect to encounter the compound formation linear flow regime for at least 10 years after the well was placed on production.

2.2. Dual porosity/dual permeability models

The conventional view of a naturally-fractured reservoir is that it is a complex system composed of irregular matrix blocks surrounded by a network of more highly permeable fractures. In reality in tight gas shales some or most of the fractures may not be open to flow or they are opened up only during the hydraulic fracturing process. Warren and Root [2] were among the first to recognize that the simple model of reservoir flow based on single values of the permeability and porosity does not apply to naturally-fractured reservoirs, though they had in mind reservoirs quite different from gas shale reservoirs. In order to handle the problems associated with lack of detailed information on the structure of the fracture network they proposed a dual-porosity model in which a primary porosity associated with inter-granular pore spaces is augmented by a secondary porosity related to that of the network of natural fractures. At each point in space there are two overlapping continua—one for the matrix and one for the fracture network. The detailed geometry of the fracture system need not be specified in this model, but can include as particular examples any of the discrete fracture models described above. In typical shale gas applications the matrix has high storage capacity but low permeability and the fractures have relatively low storage capacity and higher permeability. It is quite possible (or, indeed, likely) that in many shale gas reservoirs no gas is stored in the fractures, though they may become filled with frac fluid during the hydraulic fracturing process.

In the dual porosity formulation flow from the matrix to the fractures is described by a transfer function with Darcy flow characteristics. The original Warren-Root models incorporated the pseudo-steady-state assumption in the matrix blocks and assigned a single value to the pressure within the blocks; the mass transfer rate from the matrix to the fractures depends then on the pressure differential between the matrix and the fracture. Thus these models assumed, almost implicitly, that sufficient time had elapsed that the flow in the matrix blocks between the fractures was already fracture-boundary-dominated. Later in this paper we estimate the time scale on which inter-fracture pseudo-steady-state begins and find that it is typically of

http://dx.doi.org/10.5772/56404

the order of several years for a fracture spacing of 100 ft or more. This is quite consistent with typical simulation results described above. If the fracture spacing was as small as 10ft, we should expect to see fracture interference or the onset of PSS flow after about 10 days. For shale gas reservoirs, more complex models (unsteady state or fully transient) are needed to resolve the flow in the matrix in more detail.

A detailed discussion of the Warren-Root model, its background and similar contemporary models can be found in the excellent monograph by van Golf-Racht [11]. We note in particular that Kazemi [12] was one of the first to extend the Warren-Root model to include transient flow in the matrix blocks. Some seventeen years after Warren and Root published their seminal work, Kucuk and Sawyer [13] adapted their model for flow in shale reservoirs by incorporating effects such as desorption from the organic matrix material and Knudsen flow in the pores and, of course, incorporating full transient effects in the matrix blocks.

In the years following the formulation of the dual porosity model for naturally fractured reservoirs, solutions of the coupled partial differential equations for the pore and fracture fluid pressures were obtained using finite difference techniques. While these simulations can provide accurate solutions, often in a complicated geometry covering the entire reservoir, the large number of computations involved made them cumbersome for analysis of large data sets. In response, an alternative, faster, method of solution was developed in the 1980s. For a simplified geometry, Laplace transform solutions were developed, in which the transformed solutions were inverted numerically, using, typically, the Stehfast algorithm.

Several authors have noted that analytic approximations can be developed for certain ranges of parameter values (referring to the Warren-Root dimensionless parameters defined below) appropriate for shale gas reservoirs. It will become apparent later in this paper that for typical shale gas reservoirs the interporosity flow coefficient (or transmissivity), λ , is very small and this allows asymptotic approximations to be derived for the Laplace-transformed solutions. Since these models still require numerical inversion of the transformed solution, it would be more accurate to label them semi-analytic models. They have advantages over full numerical solutions in terms of speed of calculation and in the added value they bring to understanding the flow characteristics and the impact of the reservoir and completion parameters on production.

2.3. Development of new semi-analytic solution

Recently, we have taken the idea of developing asymptotic solutions one stage further. We have developed perturbation solutions for $\lambda << 1$ directly from the dual porosity partial differential equations, thereby removing the necessity for Laplace transforms altogether. The greater simplicity and enhanced understanding afforded by these solutions will become apparent as we proceed. (Full details are available in an internal EGI report [14].) The result is similar to the simple linear flow model that is currently gaining favor in the literature, but has some notable advantages:

- The model does not make the *a priori* assumption of linear flow into a sequence of transverse fractures.

- The model does not make the *a priori* assumption of infinite fracture conductivity, and allows an estimate to be made for the fracture pressure loss.
- Identification of the end of the linear infinite-acting flow period and development of the ensuing PSS solution is made explicit.
- Provision of a solution form that facilitates fast and easy production data analysis.
- Identification of the reservoir and completion parameters that are the greatest (primary) determinants of productivity.
- Solution scheme that permits rational extension to include other physical processes, such as desorption.

For simplicity we restrict attention in this paper to single-phase flow in the matrix and assume that gas is produced at constant bottom hole pressure; we shall also neglect the impact of gas desorption. For the purposes of the present discussion the most important part of the solution is the leading order solution for the reservoir pseudo-pressure, which satisfies a standard diffusion equation.

$$\frac{\partial^2 m_{Dm_0}}{\partial z_D^{\,2}} = \frac{\partial m_{Dm_0}}{\partial t_D} \tag{1}$$

Here we have used dimensionless parameters (denoted by subscript D); full definitions are provided in the Nomenclature section later in this paper. Dimensionless distance normal to the fracture face, z_D , is scaled on L/2 (i.e. half the inter-fracture spacing), and dimensionless time, t_D , is scaled on a time scale,

$$t_m = \frac{c\varphi_m \mu \left(L/2\right)^2}{k_m} \tag{2}$$

that characterizes pressure diffusion in the matrix

The appropriate initial and boundary conditions are

$$\begin{aligned} &m_{Dm_0} = 0 \quad at \quad t_D = 0 \\ &m_{Dm_0} = m_{Df_0} = 1 \quad at \quad z_D = 0, \quad \frac{\partial m_{Dm_0}}{\partial z_D} = 0 \quad at \quad z_D = 1 \end{aligned} \tag{3}$$

The leading order influx from the matrix into the fracture network is given by

http://dx.doi.org/10.5772/56404

$$q_{D0} = \left| \frac{\partial\ m_{Dm_0}}{\partial\ z_D} \right|_{z_D=0} \tag{4}$$

At downhole conditions the mass flowrate from the matrix into the fracture network is

$$q_m = q_{ch}\, q_{D0} \tag{5}$$

The dimensionless flowrate is defined in equation (4) and the characteristic mass flowrate is defined by

$$q_{ch} = A \frac{M k_m}{2RT_w} \frac{m_{ch}}{Z_{ch}} \tag{6}$$

Here A denotes the productive fracture surface area. The total mass flow rate measured at surface conditions is

$$q_s = \frac{q_m}{\rho_s} = A \frac{k_m}{Z_{ch}} \frac{T_s}{T_w} \frac{Z_s}{p_s} m_{ch} \tag{7}$$

Here subscript s denotes surface conditions. Note that q_s is actually a volumetric flowrate and is measured typically in units such as scf/s.

The dimensionless flowrate defined in equation (4) may be readily calculated in terms of the dimensionless pseudo-pressure, either from the full numerical solution of the diffusion equation, (equation (1)), or from the early-time infinite-acting approximation to it. Both solutions provide very useful information and insights into the variation of the production rate with time. The dimensionless cumulative production is defined by

$$Q_{D0} = \int_0^{t_D} q_{D0}\, dt_D \tag{8}$$

The diffusion equation (1) is readily solved using standard numerical schemes as made available in mathematical software such as MATLAB. To complement this solution we have obtained an analytic approximation valid while the change in pressure has not been impacted by neighboring boundaries or fractures—often referred to as the infinite-acting approximation. The early-time approximation to the dimensionless inflow rate is

$$q_{D0} = \frac{1}{\sqrt{\pi t_D}} \tag{9}$$

And the early-time approximation to the dimensionless cumulative production is

$$Q_{D0} = 2\sqrt{\frac{t_D}{\pi}} \tag{10}$$

Figure 5 compares the full and early-time solutions for the dimensionless flow rate and cumulative production against dimensionless time. For convenience we have used a log-log plot here. There are several major features of this plot that are worthy of further comment:

- The early-time (infinite-acting) solution provides a good approximation to the full numerical solution for dimensionless time, t_D , less than about 0.15, which translates to about 3 years in dimensional terms.
- During this time frame, the flowrate is represented by a straight line of slope – ½ and the cumulative production is represented by a straight line of slope + ½.
- Boundaries (or in this case neighboring fractures) begin to influence the flow after this point in time and the solution departs from the simple linear dependence on the square-root of time. This is also evident in the numerical solutions presented by Bello and Wattenbarger [15] in their Figures 5, 7, 8 and 10 and in the field data shown in their Figure 1.
- The dimensionless cumulative production approaches a final value of 1 as it should because of the way we have defined the characteristic scales in our non-dimensionalization of the equations.
- The error incurred in estimating the cumulative production by extrapolating the infinite-acting solution beyond its region of validity is apparent from Figure 5.
- Almost 90% of the total gas that can be produced has been produced by the time $t_D = 1$. This then provides a simple interpretation of the matrix diffusion time as the time (in real terms) to produce 90% of the gas available.

Figure 6 shows the full and infinite-acting solutions for cumulative production plotted against the square-root of dimensionless time. As expected from equation (10) the early-time solution is well represented by a straight line with slope $2/\sqrt{\pi}$ or 1.128. Later in this paper we develop this plot as the basis of our production data interpretation technique.

In anticipation of the application of these results to analysis of production data, it is useful to provide an expression for the cumulative production in dimensional terms. Analogous to equation (6) we define cumulative production at downhole conditions by

$$Q_m = Q_{ch}\, Q_{D0} \tag{11}$$

The characteristic cumulative production scale is defined as

http://dx.doi.org/10.5772/56404

$$Q_{ch} = q_{ch} t_m = A \frac{M k_m}{2RT_w} \frac{m_{ch}}{z_{ch}} t_m \tag{12}$$

The time scale t_m is defined in equation (2) and Q_{D0} is defined in equation (8).

Analogous to equation (9) we define cumulative production at surface conditions by

$$Q_s = \frac{Q_m}{\rho_s} = A \frac{k_m}{Z_{ch}} \frac{T_s}{T_w} \frac{Z_s}{p_s} m_{ch} t_m Q_{D0} = Q_{ch,s} Q_{D0} \tag{13}$$

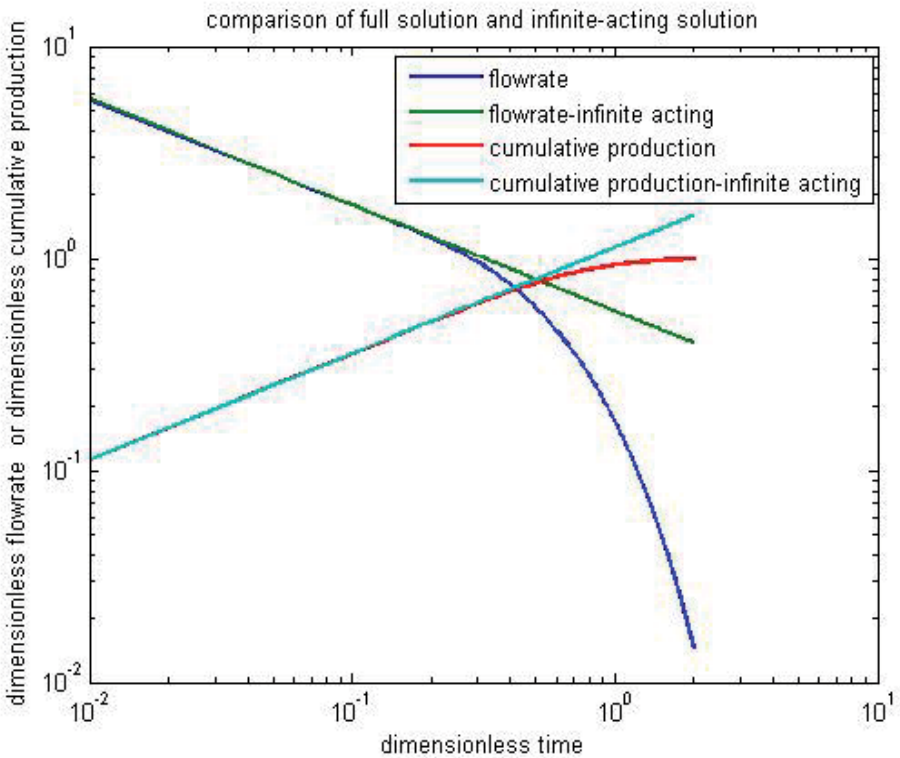

Figure 5. A comparison of the full and early- time solutions for the dimensionless flow rate and cumulative production.

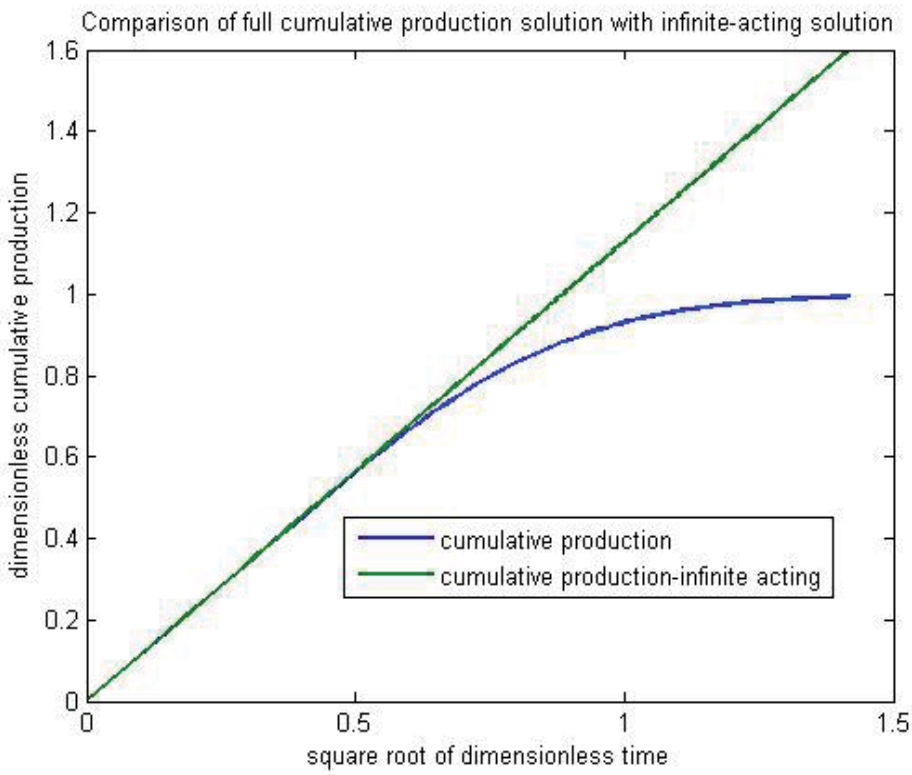

Figure 6. A comparison of the full and early- time solutions for the dimensionless cumulative production.

In view of the wide applicability of the early-time solution, it is useful to state the form taken by equation (13) during the infinite-acting period. Using the early-time approximation given in equation (9), we see that

$$Q_s = A\frac{k_m}{Z_{ch}}\frac{T_s}{T_w}\frac{Z_s}{p_s}m_{ch}\,2\sqrt{\frac{t_m}{\pi}}\sqrt{t} \tag{14}$$

If we now use the definition of T_m (equation (2)), we can express the cumulative production at surface conditions as

http://dx.doi.org/10.5772/56404

$$Q_s = C_P\sqrt{t} \tag{15}$$

Where

$$Q_s = A\frac{k_m}{Z_{ch}}\frac{T_s}{T_w}\frac{Z_s}{p_s}m_{ch}2\sqrt{\frac{t_m}{\pi}}\ \sqrt{t} \tag{16}$$

The coefficient C_P represents the slope of the dimensional equivalent of the straight line in Figure 6 and is of fundamental importance in the subsequent development of this paper. For now we will observe that C_P characterizes the early-time solution in a form that is easy to estimate from production data. We shall refer to it as the "Production Coefficient". (We have adopted this terminology in recognition of the similarity of this result to a well-known expression for the leakoff rate of a compressible fluid from a fracture to a reservoir filled with the same fluid (see, for example, [15]).

3. Production data interpretation

The analysis described above suggests that for a substantial part of a shale gas well's production history, the cumulative production varies linearly with the square-root of time. The coefficient C_P represents the slope of the straight line in a plot of Q against $\sqrt{t}$ and characterizes the early-time solution in a form that is easy to compare with production data The time scale, T_m , defined in equation (2) defines the upper limit of the applicability of the linear flow regime and allows us to characterize the production rate once boundary-effects have become important.

We illustrate this production analysis technique by comparing production from a group of wells in the Barnett shale. Figure 7 shows a conventional plot of production rate against time for several wells that had been producing for at least 5 years in an area of the Barnett field. The data was obtained from a public data base and we have plotted the production rates at yearly intervals. For clarity of presentation we have connected the data points by smooth lines. This "conventional" plot reveals nothing about the relative decline rates of the wells or provides much insight into the flow regime(s). The same data sets have been plotted in the new format in Figure 8. It is immediately apparent that for most of these wells the data falls on straight lines as expected from our analysis. The slope of these lines is readily measured and provides an estimate for the production coefficient, C_P . Estimation of C_P is quick and easy and provides us with a new metric with which we can quantify the productivity of these wells. Again, we explore these results in more detail later, but for now we note that the linear flow regime extends beyond at least 5 years, since there is no indication at this point of departure from the straight line in this plot. This fact alone sets some bounds on the fracture spacing and the matrix permeability.

In Figure 8 we have omitted the first year's cumulative production data. Generally, early-time production data is quite severely impacted by variable drawdown conditions and so we should not expect a good straight line fit at that time. Analysis of this regime is discussed at length elsewhere [14].

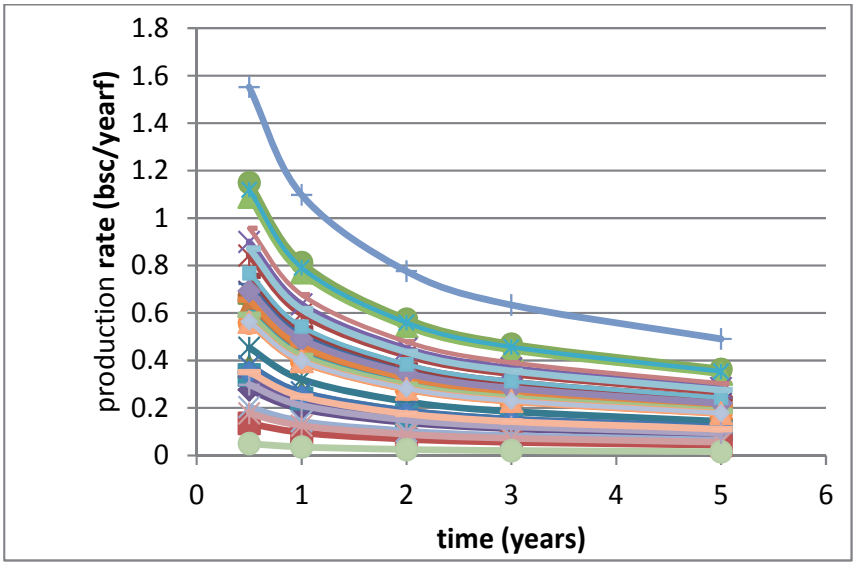

Figure 7. Production data from a group of Barnett wells plotted in the conventional format

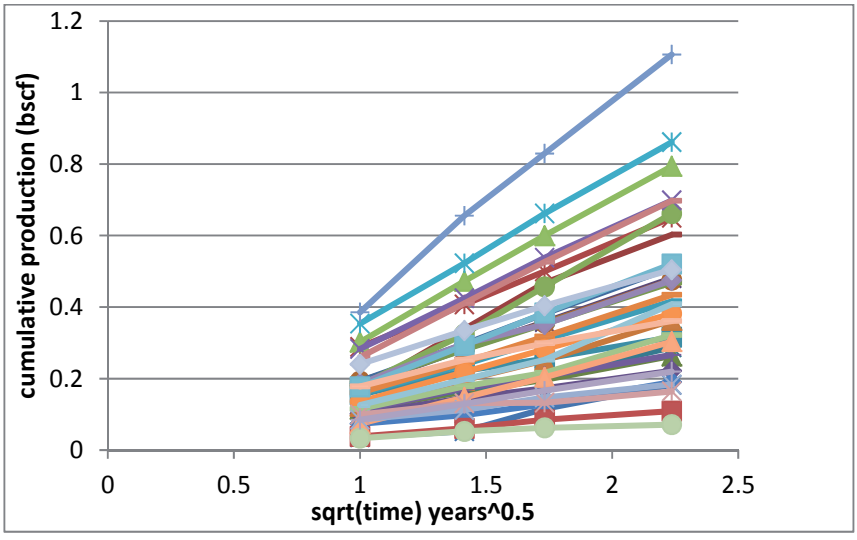

Figure 8. Same production data from Figure 7 plotted in the new format.

http://dx.doi.org/10.5772/56404

4. Identification of production drivers: Nature versus nurture

We have established the applicability of this new analysis technique to data from very many wells in many shale gas plays across the US and Canada, though there is neither space nor time available to discuss this in detail in the present paper. Following on from that analysis, we will now go on to discuss the results in more depth and begin to draw some tentative conclusions about the production drivers, by examining the parameters that together constitute the formula for C_P in equation (15). We may divide these parameters broadly into two groups—those that characterize the nature of the reservoir and those that characterize how we "nurture" the reservoir. Specifically the parameters are:

Nature:

- Matrix permeability, k_m
- Matrix porosity, φ_m
- Gas viscosity, μ
- Gas compressibility, c
- Initial reservoir pressure, p_i
- Reservoir temperature, T

Nurture:

- Bottom hole flowing pressure, p_w
- Productive fracture surface area, A

In developing these results we are constrained by the requirement that λ <<1, where

$$\lambda = \frac{12 k_m r_w^2}{L \; c_f} \tag{17}$$

This requirement sets some bounds on the fracture network characteristics, but these are generally easily met for shale gas reservoirs. For given values of the matrix permeability and the wellbore radius, the combination of fracture spacing and fracture conductivity must be sufficiently large.

It is apparent that given these conditions production for a large part of the production history of these wells depends upon the parameters listed above. We note in particular that history matching production data over this flow period furnishes only one parameter and that is the production coefficient, C_P . That is all. The square-root of time behavior is inherent to the physics of the flow: i.e. linear flow into a network of (effectively infinitely-conductive) fractures. It is not at all surprising that conventional history-matching techniques using reservoir simulators give non-unique answers: many different values of the parameters in the list above can together constitute the same value of the production coefficient. Moreover this

formulation tells us what parameters have little effect on the history-matching process, including the precise value of the fracture conductivity. Even if history-matching were attempted in terms of dimensionless parameters, it is apparent that the result is insensitive to λ provided that it is small enough.

We need to elaborate at this point on the parameter *A* defined above as the "productive fracture surface area". This is the area of the fractures in contact with the reservoir that serve as the channels that convey gas from the matrix to the wellbore. We can make no assertion at this point about whether these fractures are natural fractures or propped or unpropped hydraulic fractures and nor can we say anything (yet) about their spacing or their lengths or indeed their number and location. *All we can infer from the production data analysis is the total productive fracture surface area.*

Some insight about the spacing of these productive fractures can be obtained by examining the time scale of pressure diffusion in the matrix. We demonstrated earlier that we may expect the root-time solution to be valid until neighboring fractures begin to compete with one another for production. In other words, until pressure diffusion in the matrix can no longer be considered to be independent of the fracture spacing. According to the analysis presented above we should expect the cumulative data to deviate from a straight-line in the root-time plot for $t > 0.15\, t_m$.

If we could detect the time at which this departure occurs then, we have some information with which to estimate the productive fracture spacing. Even if the entire production history to date is in the linear flow regime, we can make an estimate of a lower bound on the fracture spacing. As we see later, the fracture spacing is surprisingly large for typical shale gas plays.

We have now analyzed many shale gas production data sets using our proposed technique and have found the square-root fit to be very good. Based on this and on the mathematical analysis that supports that technique we have concluded that the production rate declines inversely with the square root of time. As we have discussed above, this is a consequence of the dominant production process of linear flow into a network of fractures. The decline rate is therefore fully determined by the physics of the production process. We should not expect to see any significant variation from well to well, from vertical to horizontal wells or indeed form play to play. What does vary is the multiplier, the production coefficient , C_P , which as we have demonstrated elsewhere depends on many factors, principally the reservoir quality, the reservoir and bottom hole pressure and the productive fracture surface area.

4.1. Example: Barnett shale production data analysis

As we have indicated above, it is relatively straightforward to use this new technique to analyze production data whether it is on a well-by-well basis or averaged over a play or area within a play. In essence, the process consists of three steps:

1. From the daily (or monthly or yearly) production data calculate the cumulative production for each well at different points in time.
2. Plot cumulative production against the square-root of time.

http://dx.doi.org/10.5772/56404

3. Estimate the Production Coefficient form the slope of the best straight line fit to the data.

The Barnett shale is a good starting point for a more in-depth data analysis, since production data is readily available from public databases and, moreover, that data extend over many wells for long periods of time. The Barnett shale occupies several counties in North Texas. It is broadly bounded by geologic and structural features and may be divided according to estimates of maturity into a gas window and oil window. Historically the major development has been in a core area located to the north of Fort Worth (Figure 9), but more recently expansion has occurred to the south and to the west. To date many thousands of wells have been drilled and completed in the Barnett, initially vertical, but now almost entirely horizontal.

It has become common practice to sub-divide the Barnett play into three areas, described as the Core, Tier 1 and Tier 2. For convenience we may define these areas according to county as follows

- Core region: Denton, Tarrant and Wise counties, comprising 2974 horizontal wells and 3886 vertical wells
- Tier 1 region: Hood, Johnson and Parker counties, comprising 3865 horizontal wells and 251 vertical wells
- Tier 2 region: all other counties, comprising 687 horizontal wells and 401 vertical wells

It is apparent form this cursory division that the fraction of wells that were completed horizontally shifts from 43% in the Core area to 94% in the Tier 1 area, which reflects the development of technology with time and the spread of drilling with time to the outer areas. At the date of these figures (2009) Tier 2 was relatively unexploited.

The result of this detailed analysis (Figure 10) allows us to quantify the production variations in the Barnett Core, Tier 1 and Tier 2 areas and to distinguish the impact of horizontal and vertical well completions on the productivity. In a sense this represents a first, somewhat crude, pass at distinguishing the impact of nature (in the sense that reservoir properties depend on location, with the core area providing more fertile ground than Tier 1 or Tier 2) and nurture (in the anticipation that horizontal well technology provides more productive fracture surface area than does vertical well technology).

In Figure 10 we have shown the cumulative distribution of production coefficient for each of the six categories defined above. The plots should be interpreted as follows. For each category the probability that a well has a specified value of the production coefficient in excess of the value on the x-axis can be read off the y-axis. For example the probability of a horizontal well in the Core having a production coefficient in excess of 0.75 (bcf/yr^0.5) is about 8%.

It is apparent that, as is to be expected, wells in the Core have better production characteristics than wells in Tier 1 and wells in Tier 2 and that in general horizontal wells have better production characteristics then vertical wells. It is interesting in this context to examine the variation of production coefficient in the core area in more detail. Figure 11 shows the location of ten of the wells in the core area with high values of the production coefficient (in green), 10 of the wells with medium values (in blue) and 10 wells with low values (in red). It is apparent

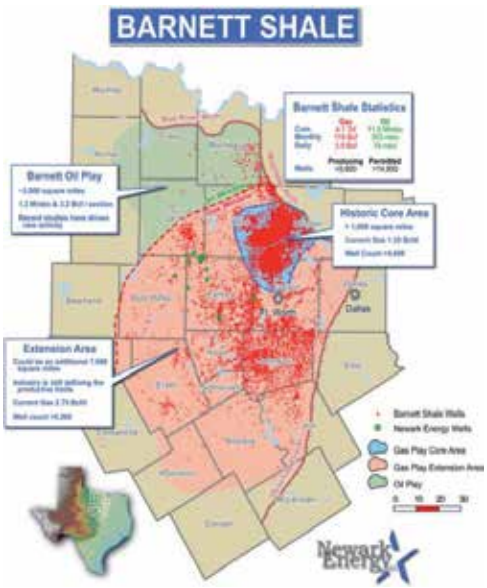

Figure 9. Development of the Barnett shale in North Texas

that there appear to be sweet spots even within the core area, but there are substantial outliers and there are some relatively poor wells close to better wells.

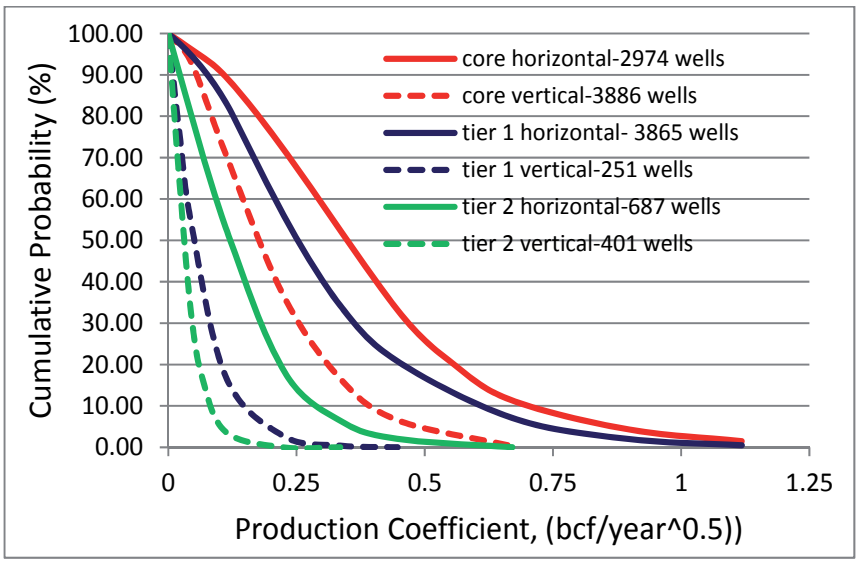

Figure 10. Distribution of values of the Production Coefficient for horizontal and vertical wells in the Core region, Tier 1 region and Tier 2 region of the Barnett shale.

http://dx.doi.org/10.5772/56404

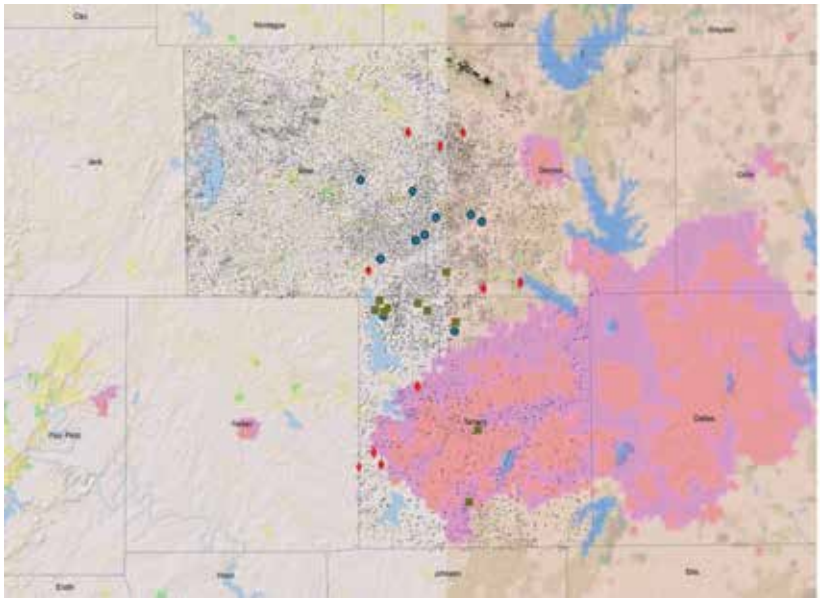

Figure 11. Preliminary identification of sweet spots in the core area of the Barnett. Each black dot represents a well; 10 wells with high Production Coefficients are identified in green, 10 medium performers are in blue and 10 poor performers are identified in red.

5. Implications and deductions

One of the advantages of the semi-analytic method outlined in this paper is that it enables us to make certain deductions about the magnitude of the parameters that drive the productivity of the well. In particular we can make some inferences about the magnitude of the fracture surface area through which the gas is produced and about the likely spacing of the productive fractures.

5.1. Productive fracture surface area

Our analytic solution allows us to relate the Productivity Coefficient C_P to a group of parameters that may be roughly divided into those that characterize the nature of the reservoir and those that characterize the impact of the completion and stimulation strategy. In our formula for C_P (equation (16)) perhaps the parameter that has the greatest uncertainty is the productive fracture surface area, A. This is the area of the fractures in contact with the reservoir that serve as the channels that convey gas from the matrix to the wellbore. We can make no assertion at this time point about whether these fractures are natural fractures or propped or unpropped hydraulic fractures and nor can we say anything (yet) about their spacing or their lengths or indeed their number and location. We can, however, make an estimate from the production data analysis of the total surface area of these productive fractures.

In Figure 12 we show estimates of the productive fracture surface area for typical strong, medium and weak performing wells in the core area of the Barnett in terms of values of the matrix permeability. In this calculation we have made reasonable estimate of the other parameters that impact the productivity coefficient such as the gas viscosity and compressibility and the matrix porosity.

Several features of this plot merit discussion:

- Well productivity increases with productive fracture surface area and with matrix permeability, as expected.
- Wells in this group typically have matrix permeabilities in the range 100-300 nd and this implies that the productive fracture surface area is in the range 1-6 million square feet (Msqft): the higher the permeability, the less fracture surface area is needed to achieve the given productivity.
- If the matrix permeability was as low as even 10 nd, the required fracture surface area would approach 100 Msqft. On the other hand, matrix permeabilities of the order of 1 μd would require less than about 1 Msqft of productive fracture surface area.

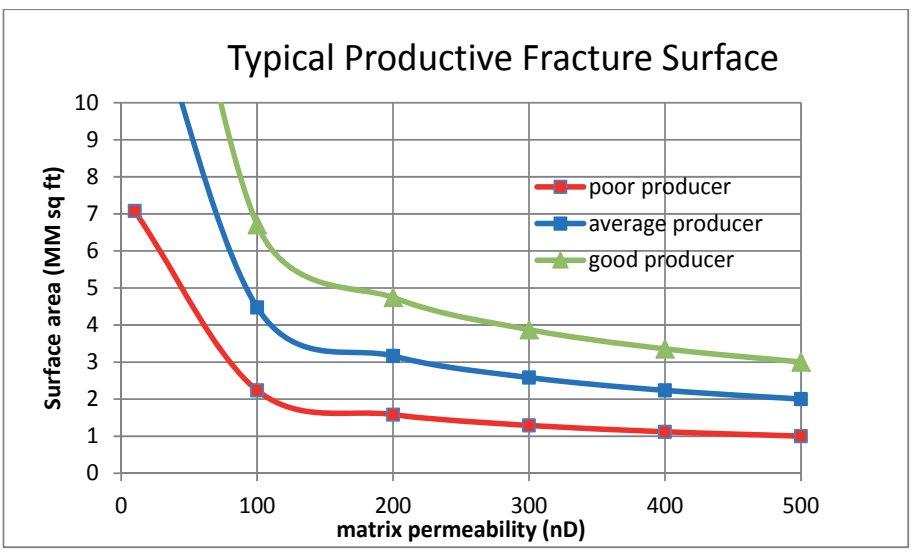

Figure 12. Estimate of productive fracture surface area for specified matrix permeability. The three curves were developed based on analysis of Barnett shale well data using the EGI semi-analytic production model.

To place these numbers in context we note that a fracture of height 200 ft and half length 200 ft has surface area of 0.16 Msqft. Thus, 20 of these fractures would have a fracture surface area of 3.2 Msqft, which is a perfectly plausible estimate of the hydraulic fracture surface area created with modern multi-stage fracturing techniques. (Note that 20 such fractures would be spaced about 150 ft apart in a 3000 ft lateral.)

http://dx.doi.org/10.5772/56404

Figure 12 was developed on the basis of production data from wells in the core area of the Barnett shale, but the results apply, at least qualitatively, to other shale or tight gas plays. For example for more conventional tight gas plays for which the permeability is of the order of 1 μd or more, we should expect respectable productivity with only one such hydraulic fracture, which reinforces our experience that a vertical well with a single bi-wing fracture may be adequate for those reservoirs, but not for shale gas plays. Conversely the productive fracture surface area for economic production from ultra-tight shale plays (such as the shallow shale plays described earlier in this paper) cannot be achieved by producing from the hydraulic fractures alone.

We have been careful so far to make no formal distinction between the natural fractures and the hydraulic fractures in so far as productivity is concerned. All we have demanded is that their conductivity is sufficiently large that $\lambda << 1$, which should not in principle present too great a restriction on the fracture conductivity whether it is associated with propped fractures or unpropped fractures. On the basis of our data analysis we should expect a productive fracture surface area in the range of 1-6 Msqft. How then is that area created and what are the implications of this figure?

A crude estimate of the fracture surface area that is created by pumping large volumes of frac fluid may be made by performing a mass balance and assuming that none of the fluid has leaked off or imbibed into the formation over the time in which the fracture network is created. For a total fluid volume V and assuming a created average fracture width w during pumping, the total fracture surface area may be estimated at

$$A = 2\frac{V}{w}$$

(using any consistent set of units of course). If, for example, 100 million gallons of frac fluid were pumped and the assumed frac width was 0.2 inches, then the total surface area would be about 100 Msq ft. Clearly, this is far in excess of our estimate of the productive fracture surface area and would suggest that less than 10% of the created fracture surface area is actually productive. Naturally, this raises all sorts of other questions concerning the efficiency of this process, which we plan to address in a future project.

A similar mass balance for the proppant placed in a typical job enables an estimate to be made of the surface area of propped fractures. If we make some estimate of the likely width (0.1 in) and porosity (0.4) of a propped fracture (after closure), it appears that a propped fracture surface area of the order of a few million square feet is quite plausible.

5.2. Productive fracture spacing

Some insight about the spacing of these productive fractures can be obtained by examining the time scale of pressure diffusion in the matrix. We demonstrated earlier that we may expect the root-time solution to be valid until neighboring fractures begin to compete with one another for production. In other words until, pressure diffusion into a fracture can no longer be considered to be independent of the fracture spacing. According to the analysis presented earlier we should expect the cumulative production data to deviate from a straight-line in the

root-time plot for $t > 0.15T_m$. If we could detect the time at which this departure occurs then, we have some information with which to estimate the productive fracture spacing. Even if the entire production history to date is in the linear flow regime, we can at least make an estimate of a lower bound on the fracture spacing.

It is instructive to estimate the matrix diffusion time for typical values of the fracture spacing and matrix permeability. The results are shown in Figure 13. The diffusion time increases quadratically with the fracture spacing and inversely with the matrix permeability. Typical values for the diffusion time are quite low. For example, if, as we expect, linear flow continues for at least 3 years, then we should expect to see a diffusion time of the order of 20 years. Figure 13 suggests that the productive fracture spacing is likely to be of the order of 100 ft or more.

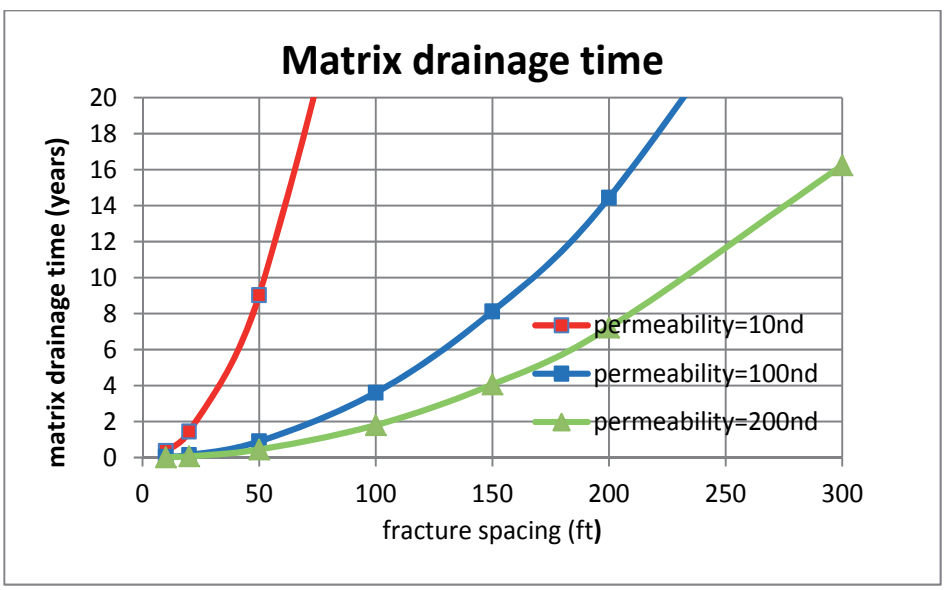

Figure 13. The impact of fracture spacing on the time to produce 90% of the gas in place.

In figure 13 we have identified the diffusive time scale with the matrix drainage time. As we showed above, 90% of the total gas in the pore space between the fractures has been drained by this time. A time scale of about 20 years is at least consistent with the industry estimates of the effective production lifetime of these wells. It is worth noting here the consequences of much smaller fracture spacing. For a fracture spacing of only 10 ft, we estimate that 90% of the total gas production will have occurred within the first few months of production, which is quite unrealistic. Note also that the surface area of planar fractures only 10 ft apart in a 3000 ft lateral would be of the order of 150 Msq ft, which again is unreasonably large.

http://dx.doi.org/10.5772/56404

6. Conclusions

A common view of production mechanisms in shales is "because the formations are so tight gas can be produced only when extensive networks of natural fractures exist" [6]. To this extent gas production from some of the shallower (Devonian) shales is similar to gas production from coal. As we have discussed earlier in this paper, we expect that the deeper gas shales differ in this respect.

Using a new semi-analytic production model, we have analyzed production data from a number of shale gas wells in several different North American shale gas plays. Interpretation of the results suggest that productivity is largely determined by a small group of parameters that may be decomposed into two sub-groups representing the nature of the reservoir (such as matrix permeability and porosity) and what we may term our (engineering) attempts at nurture (including completion and stimulation parameters). Of key importance is the productive fracture surface, which unfortunately is difficult to estimate a priori. However, our interpretation of the production data suggest the following

- Productive fracture surface area ~1-6 Msqft and probably within 2-4 Msq ft.
- The volume of these productive fractures is very much less than the volume of water pumped, but
- Productive fracture volume scales approximately with the volume of proppant placed.
- Typically, there is no indication of fracture interference during production even after several years, which suggests that the productive fracture spacing is at least 100 ft.
- Time to drain 90% of the fractured region or matrix blocks: ~10-20 years

We are led to the conclusion that almost all the fracturing fluid pumped during a multi-stage horizontal well fracturing operation in the shales serves to open a vast, and possibly complex, network of natural fractures and that these fractures do not make a significant contribution to the well's productivity. We are led inevitably to questions concerning the conductivity of these, largely unpropped, fractures and to investigate the rock and fluid mechanisms that seemingly prevent them from being productive. The role of the fracturing fluid (usually slickwater) in this process should now be investigated from this new perspectivel

Nomenclature

k – permeability
φ – porosity μ – gas viscosity λ – dual porosity transmissivity factor (defined in equation (17))

c – gas compressibility

cf – fracture conductivity

p – pressure

m – gas pseudo-pressure
C_p – production coefficient (defined in equation (16))

q – production or flow rate

Q – cumulative production

r – radius (wellbore)

t – time

T – reservoir temperature

A – productive fracture surface area

L – fracture spacing

z – co-ordinate normal to fracture surface

Z – real gas compressibility factor

Subscripts

ch – characteristic

D – dimensionless

m – matrix

i – initial

s – surface

w – wellbore

Author details

Ian Walton and John McLennan

Energy and Geoscience Institute, University of Utah, USA

References

[1] A Guide to Coalbed Methane Reservoir Engineering, Saulsberry, J.L., Schafer, P.S., and Schraufnagel, R.A. (Editors), Gas Research Institute Report GRI-94/0397, Chicago, Illinois (March 1996).

[2] Warren, J.E. and Root, P.J.: "The Behavior of Naturally Fractured reservoirs," SPEJ, September 1963. (Originally published as SPE 00426, 1962).

[3] King, G.R, Ertekin, T, and Schwerer, F.C., "Numerical simulation of the Transient Behavior of Coal- Seam Degasification Wells," SPE Formation Evaluation, April, 1986.

[4] Schettler, P.D., Parmely, C.R. and Lee, W.J., "Gas Storage and Transport in Devonian Shales." SPEFE, September 1989.

[5] Luffel, D.L., Hopkins, C.W. and Schettler, P.D., "Matrix Permeability Measurement of Gas Productive Systems,", SPE 26633 (1993).

[6] Carlson, E.S. and Mercer, J.C., "Devonian Shale Gas production: mechanisms and Simple Models," SPE 19311, 1989 (also JPT April 1991).

[7] Gatens, J.M., Lee, W.J., and Rahim, Z.: "Application of an Analytic Model to History Match Devonian Shales Production Data," Paper SPE 14509 presented at the 1985 Eastern Regional meeting, Morgantown, W Virginia, November 6-8, 1985.

[8] Kuuskraa, V.A., Wicks, D.E. and Thurber, J.L.: "Geologic and Reservoir Mechanisms Controlling Gas Recovery from the Antrim Shale," Paper SPE 24883 presented at the 67th Annual SPE Technical Conference and Exhibition, Washington, D.C., October 4-7, 1992.

[9] Kent Bowker, HAPL Technical Workshop, 2008)

[10] Luo, S., Neal, L., Arulampalam, P. and Ciosek, J.M.: "Flow Regime Analysis of Multistage Hydraulically-fractured Horizontal Wells with Reciprocal Rate Derivative Function: Bakken case Study," Paper CSUG/SPE 137514 presented at the Canadian Unconventional Resources and International Petroleum Conference, Calgary, Alberta, Canada, 19-21 October, 2010.

[11] Van Golf-Racht, T.D.: "Fundamentals of Fractured Reservoir Engineering," Developments in Petroleum Science, vol 10, Elsevier Scientific Publishing Company, 1982.

[12] Kazemi, H.: "Pressure Transient Analysis of naturally Fractured Reservoirs with Uniform Fracture Distribution," SPEJ (Dec 1969), 451-61; Trans AIME, 246

[13] Kucuk, F. and Sawyer, W.K.: "Transient Flow in Naturally Fractured Reservoirs and Its Application to Devonian Gas Shales," Paper SPE 9397 presented at the 55th Annual Technical Conference and Exhibition, Dallas, Texas, September 21-24 1980.

[14] Walton, I.C.: "Shale Gas Production Analysis, Phase I Final Report," EGI internal report 100983, 2012.

[15] Bello, R.O. and Wattenbarger, R.A.: "Rate Transient Analysis in Naturally Fractured Shale gas Reservoirs," Paper SPE 114591 presented at the CIPC/SPE Gas Technology Symposium, Calgary, Alberta, June 16-19, 2008.

[16] Economides, M.J. and Nolte, K.G:"Reservoir Stimulation," Prentice Hall, Third Edition, 2000.

Section 5

Well Completions and Fracture Initiation 1

Chapter 17

Do Perforated Completions Have Value for Engineered Geothermal Systems

Walter Glauser, John McLennan and Ian Walton

Additional information is available at the end of the chapter

http://dx.doi.org/10.5772/56211

Abstract

Engineered or enhanced geothermal systems (EGS) differ from conventional hydrothermal reservoirs in that supplementary hydraulic stimulation is required to create surface area needed for heat exchange, and to allow adequate fluid production. Historically, geothermal wells have been straight hole or inclined and usually employ barefoot completions. If horizontal drilling and hydraulic fracturing experience, refined to some extent with recent shale gas and shale oil stimulation campaigns, can be adapted for geothermal applications, it may be possible to improve the chances for successful EGS. One central issue for vertical, inclined, extended reach or horizontally drilled wells is whether there is merit in landing and cementing casing. This would allow discrete zones to be fractured, isolate thief zones or low temperature zones, allow future remediation and facilitate generation of multiple fracture systems.

Most experienced geothermal operators balk at perforated and cemented completions. The arguments can be legitimate. There are supplementary costs associated with this completion, and the temperatures can make cementing and perforating challenging. Plugging of existing fracture systems from casing and cement is also proposed as a problem – which is easily overcome by the supplementary stimulation required. On the other hand, simple calculations suggest that proximal and interconnected fracture systems, natural or otherwise, are required for economic viability in all but the hottest scenarios. To effectively develop multiple fracture systems, wellbore isolation seems to be a natural requirement. One legitimate method to accomplish this is diversion, but the question remains as to how many intersected fractures can be stimulated. Another option is cementing and perforating. A comparative and realistic analysis is done to assess the impact of perforation skin, tortuosity associated with shear

fractures intersecting the wellbore and relative economics associated with perforating and cementing geothermal wells.

Keywords: geothermal, perforations, openhole, multiple fractures

1. Introduction

Engineered or enhanced geothermal systems (EGS) differ from conventional hydrothermal reservoirs in that supplementary hydraulic stimulation is required to create surface area needed for heat exchange, and to allow adequate fluid production. Historically, geothermal wells have been straight hole or inclined and usually employ barefoot completions. If horizontal drilling and hydraulic fracturing experience, refined to some extent with recent shale gas and shale oil stimulation campaigns, can be adapted for geothermal applications, it may be possible to improve the chances for successful EGS. One central issue, for horizontal, inclined, extended reach, or horizontally drilled wells, is whether there is merit in landing and cementing casing to allow discrete zones to be fractured, to isolate thief zones or low temperature zones, to allow future remediation and to facilitate generation of multiple fracture systems.

Most experienced geothermal operators balk at cased, cemented and perforated completions. The arguments can be legitimate. There are supplementary costs associated with this completion and the temperatures can make cementing and perforating challenging. Plugging of existing fracture systems during cementing is also proposed as a problem – which is easily overcome by the supplementary stimulation required. On the other hand, simple calculations suggest that proximal and interconnected fracture systems, natural or otherwise, are required for economic viability in all but the hottest scenarios. To effectively develop multiple fracture systems wellbore isolation seems to be a natural requirement. One legitimate possibility is diversion. The question remains how many intersected fractures can be stimulated? Another option is cementing and perforating. In this paper we undertake a comparative and realistic analysis to assess the impact of perforation skin, tortuosity associated with shear fractures intersecting the wellbore and relative economics associated with perforating and cementing geothermal wells.

2. Requirements for a Successful Geothermal Well (EGS)

Simple calculations suggest that proximal and interconnected fracture systems, natural or otherwise, are required for economic viability in all but the hottest geothermal scenarios. Currently, geothermally derived power is associated with “natural” hydrothermal systems. These are reasonably permeable and have equilibrated fluid circulation systems, with heat delivered by deep convection. They are characteristically naturally fractured and/or faulted, at least to some extent. Stimulation of fractured wells to enhance fracture conductivity is an opportunity for engineering massively stimulated systems – engi-

http://dx.doi.org/10.5772/56211

neered geothermal prospects – using hydraulic fracturing. Pritchett, 2012 [1], cautions that the practicality of these scenarios depends on fractures that are conductive enough to support the required high geothermal flow rates. "Performance will be significantly impaired if the average fracture separation is greater than 50 meters or so. … The creation of such extensive and pervasive artificial fracture networks at costs that will prove acceptable … is the fundamental challenge for EGS. … New stimulation paradigms may be required." These fractures need to be close enough together and appropriately oriented to encourage heat sweep and thermal energy recovery.

Following Pritchett's logic, for a very specialized generic reservoir analysis, assume 100 kg/s are required for an economic system. To adequately delay thermal breakthrough (on the order of 30 years), required fracture spacing varies from 20 to 70 m.The time to breakthrough decreases as the fracture spacing becomes larger. Wu et al., 2012 [59] demonstrate fracture spacing issues numerically.

What non-specialists don't always realize is the throughput that is required to ensure an economic geothermal prospect. If there is a single producer, the criterion for economic throughput is colloquially expressed as 100 kg/s by some; 2000 gal/minute by others. In any case, at 200°C this is between 62,000 and 69,000 BWPD at the sand face. To accommodate such high rates with nominal friction, large diameter casing is conventionally used with large diameter barefoot sections. This philosophy may be acceptable in conventional systems. If EGS is planned, large contact between one or more fractures and the wellbore is essential. Without effective diversion, multiple fracturing in an open hole is extremely difficult. Extended fracture contact with the well and/or multiple fracture intersections seem to be essential for EGS. This brings up the contentious topic of whether cased and perforated completions would be acceptable in geothermal environments.

3. Cemented versus barefoot completions

Even barefoot completions are cased and cemented over a substantial portion of their length. For example, deep geothermal wells in Australia have the casing set below 4000 m or so and are open hole below that for a length of 500 m. Similar situations exist at Raft River in the United States. Nevertheless, cemented completions across thermally-productive zones will allow isolation and multiple zones can be stimulated. For example, the advantages of a cemented completion include:

- **Potential for isolating fluid thief zones.** If low-pressure, shallow thief zones are present, crossflow can be avoided by casing across those zones.
- **Potential for isolating zones that bring in low temperature fluid.** There are many anecdotal examples of cooler fluids entering the wellbore uphole in uncased environments, jeopardizing overall economics. Even if these zones have been perforated, the possibility for plugging, while always difficult, is improved by squeezing perforations rather than an openhole section.

- **Potential for tactical perforating to initiate multiple fractures in a single wellbore.** This is potentially a huge advantage. In openhole, without diversion, fracture initiation will seek out major discontinuities and ultimately only a restricted number of these will develop. Isolation of individual zones can ensure at least local initiation of multiple fractures. Pre-existing fractures may be preferentially treated. Gale, 2008, [2] argued that natural fractures (healed) in certain shales opened at approximately 60% of the stress level needed to fracture the virgin formation. While this offers some potential to override the in-situ stress field, depending on the orientation of the fractures, there may be a greater chance of short-circuiting and minimizing new development of fracture surface area for heat exchange. Casing and selective perforating can avoid or incorporate pre-existing fractures at the operator's discretion.
- **Standard isolation benefits from an environmental perspective.** A primary goal of cemented casing is to provide another hydraulic barrier. In most cases this is not a consideration since standard casing programs should have been implemented above the openhole sections.
- **Workover is legitimately possible.** This would seem to be a substantial advantage. Envisioning a dynamically changing reservoir, profile modification in the future could be desirable.
- **Hole integrity is increased.** This will possibly become more of an issue if sedimentary basins start to be routinely exploited.
- **Wider fractures and inhibited scaling?** Consider the restricted exit through perforations into a wellbore as fluid is produced. It will be demonstrated that these flow restrictions will be relatively small. However, they will still facilitate a back pressure in the formation adjacent to the perforations. One might anticipate that most of this pressure is lost very close to the perforations. The back pressure may inhibit scaling and may even lead to slightly wider fractures near the perforations. Perforation skin may be high but choke skin might actually be reduced.
- **Ability to Pump Proppant?** Proppant placement may or may not be more effective through isolated perforated completions. Wider fractures may exist facilitating slurry entry. Also, if discrete zones are isolated, focused injection through perforations may cause more tension and/or shearing and may actually promote self-propping. This is only an hypothesis.
- **More Contact Area?** For wellbores inclined at a significant angle to productive fractures in openhole the contact area between the wellbore and the fracture may be small. Cased, cemented and perforated completions may actually alleviate some contact related pressure losses. For example, Mukherjee and Economides, 1991, [3] considered skin that would develop because of inadequate contact between a vertical transverse fracture and a horizontal well. They expressed this choking effect as:

http://dx.doi.org/10.5772/56211

$$\Delta p_s = \frac{Q\mu}{2\pi kh}\left\{\frac{kh}{k_f w_f}\left[\ln\left(\frac{h}{2r_w}\right)-\frac{\pi}{2}\right]\right\}$$
$$s_c = \frac{kh}{k_f w_f}\left[\ln\left(\frac{h}{2r_w}\right)-\frac{\pi}{2}\right] \quad (1)$$

where:

Δp_s pressure drop due to finite wellbore contact

Q volumetric flow rate

μ dynamic viscosity

k formation permeability

h fracture height

k_f fracture permeability

w_f fracture width

s_c choke skin for radial convergent fracture flow.

In low permeability, fractured formations, this conventional vision of choking skin gives very small values and suggests small pressure drops. In reality, tortuous, near-wellbore interconnection between perforations and the wellbore can lead to pressure losses commonly expressed as skin. Some estimations are provided later.

However, there are challenges with cased and cemented geothermal completions. These include:

- **Cost.** Cased and cemented completions certainly require additional tangible capital expenditure. One would anticipate that the potential for workover and the ability to generate multiple fractures will override this, as is the case in any cased wellbore.
- **Placement Issues.** Geothermal wells present difficult completion environments. These can be made even worse (as with cost) because of the large diameter casing that is conventionally called out to accommodate pumping equipment. There may be situations when multiple, smaller diameter wells are more economic than single large bore wells.
- **Temperature Issues.** Perforating gun performance will need to be considered when temperatures become extremely high, in which case abrasive jet slotting may be preferable.
- **Cementing Natural Fractures.** Plugging of existing fracture systems during cementing is also proposed as a problem – which is easily overcome by the supplementary stimulation required.
- **Casing Integrity.** Corrosion, erosion and erosion corrosion could be long-term issues, particularly in high salinity or anomalous pH reservoirs. Operators must decide whether

the benefits of casing, cementing and perforating in the short-term override the costs of degradation with time, and whether these completions jeopardize well or system productivity and economics.

- **Pressure Losses.** For commercial purposes, single well rates are high. It is often argued that pressure losses will be too extreme. Simple calculations to follow explore some of these mechanisms, and suggest that this may or may not be the case.

Pending successful isolation (casing and cementing), it is still necessary to complete the well. What are the methods for carrying this out? Perforating is the first logical choice. Abrasive jetting is also a possibility and may in fact ultimately turn out to be preferable. Alternatively, diversion is advocated as a methodology for isolation in openhole – and there is good logic for this, if the diverter can tolerate incremental pressures between fracturing events. Diversion could be considered in open or cased hole scenarios to maximize fracture contacts with the wellbore.

4. Using diversion in openhole situations

To effectively develop multiple fracture systems, wellbore isolation seems to be a natural requirement. One legitimate possibility is diversion. This technology is decades old. For example, Spencer, 1970, [4] stated that "For many years solid materials have been used down hole as temporary barriers for diverting injected fluids. A typical operation involves adding the solids to a carrier fluid which is then pumped down hole. This solid laden fluid will be pumped into existing fractures and fissures. As the solids lodge and wedge in the openings and cracks within the formation, they reduce the flow … As the flow decreases due to the action of additional solids blocking the fluid path, the pressure continues to rise until another region of the formation fractures and provides a different path for the fluid to follow." Waters et al., 2009, [5] document more recent use in openhole hydraulic fracturing for shale production. Stalker et al., 2009, [6] show rudimentary calculations of the pressures that could be anticipated. Geothermal applications have been described by Petty, 2012 [7].

5. How to develop multiple fracture systems

Suppose that diversion is not appropriate in a particular openhole scenario. Possibly there are not enough pre-existing discontinuities intersecting the wellbore. This could mean that the pressure increments between diversions in an open hole would be so large that previously diverted zones would start to take fluid. Possibly there are pre-existing fractures that need to be avoided, and so on … If this is the case, a cased and cemented completion could be a rationale decision. Presuming that adequate pumping capacity can be installed, the primary concern has been "How much fluid can be economically delivered through a perforated completion during production?". Whether it is in the geothermal domain or the oil and gas domain, this is a relevant question.

http://dx.doi.org/10.5772/56211

In a perforated completion, and to some extent openhole, stimulation effectiveness and the economics for producing adequate mass flow rates are influenced by near-wellbore completion characteristics. During stimulation, the goal is to transmit pressure to the tip of the fractures that are being created or inflated. Near-wellbore pressure drop requires additional horsepower with accompanying cost for the stimulation. Similarly, during production, the goal is to minimize frictional losses – in the fractures and especially where the fractures intersect the wellbore, near and through the perforated completion. In either case it is necessary to minimize near-wellbore pressure losses.

6. Perforation skin — Pressure loss during injection

A substantial amount of work has been done to understand pressure drop that occurs through perforations. One facet of this research has been to evaluate the pressure loss in a complicated perforation connection from the wellbore to the formation during injection. Eftaxiopoulos and Atkinson, 1996, [8] provided an elegant mathematical approximation. This built on earlier work by Yew and Li, 1988, [9] as well as Yew et al., 1989 [10]. These latter authors applied three-dimensional elasticity to assess hydraulic fracture growth from inclined wells. This is a situation that does promote complicated interconnection with the main hydraulic fracture and where a perforated completion may offer significant advantages over open hole. Initiation, propagation and linkage of fractures formed from individual perforations were considered. Yew et al., 1993, [11] continued these evaluations. A landmark practical presentation of these concepts was provided by Weng et al., 1993 [12].

In 1991, Behrmann and Elbel [13] carried out laboratory block testing to study the complex interconnection of multiple fractures growing from perforations. These authors suggested the strong potential role of a microannular fracture link. “In both cases, despite ideal laboratory conditions, clean wellbore and casing, and short cement interval, the wellbore annulus is pressurized during any pumping treatment. Therefore, in the absence of any optimally oriented defects (perforations), fractures will initiate as though the completion were openhole. Fracturing pressure will obviously be higher than in open hole, but initiation sites and extension geometry will be the same. Thus, it is theoretically possible to have different fracture-initiation sites with identical perforation orientations if two wells have substantially different wellbore damage.”

In 1995, Romero et al. [14] presented numerical evaluations related to near-wellbore injection pressure losses attributed to communication (perforations), fractures (turning and twisting) and multiple fractures. Their interest was in mitigating high treatment pressure and unanticipated screenouts. They allocated a near-wellbore pressure loss to the sum of these three effects – perforation pressure drop, turning/twisting or tortuosity and perforation misalignment. For the perforations themselves, they considered the perforation tunnels as orifices. That relationship is (see Crump and Conway, 1988, [15], Lord et al., 1994, [16] Shah et al., 1996 [17]):

$$\Delta p_{perforations} = 0.2369 \frac{Q^2 \rho}{N_p^2 d^4 C_d^2} \tag{2}$$

where:

Q total flow rate, BLPD

ϱ fluid density, lbm/gal

N_p number of contributing perforations

d perforation nominal diameter, inch

C_d orifice discharge coefficient

Depending on the upstream Reynolds' number and the roundness of the edges, the discharge coefficient can range from less than 0.5 to approximately 1. It has been empirically expressed as (El Rabba et al., 1997 and 1999 [18]):

$$C_d = \left(1 - e^{-\frac{2.2d}{\mu^{0.1}}}\right)^{0.4} \tag{3}$$

where:

d perforation diameter through the casing, inch

μ apparent viscosity, cP

The pressure drop due to fracture turning was also approximated, as was microannular flow. Romero et al. [14] stated that, "If the fluid exits the well through the perforation, it must traverse the microannulus and pass the restriction area before, entering the main body of the fracture. A geometry effect occurs in which the rock moves away from the cement resulting in a channel around the annulus with a width of $[w^2/16r_w]$ at the fracture entrance, where w is the fracture width, and rw the wellbore radius. In addition, an elastic response (Poisson's effect) occurs in which the fracture opening results in a movement of the rock towards the wellbore." This results in a pinch point during injection – a similar restriction with opposing geometry (but widest where the pressure is highest) is anticipated during production. Gulrajani and Romero, 1996, [19] acknowledged the importance of diagnostic measurements with rate changes to determine near-wellbore losses during injection, where the pressure losses associated with near-wellbore effects could be approximated by the injection rate to a suitable power. If there are insufficient perforations, the pressure loss varies with the rate squared. If tortuosity dominates, the pressure loss varies with the square root of the rate. Similar considerations have been published by Manrique et al., 1997, [20] and by Behrmann and Nolte, 1998, [21] who discussed fracture contact with deviated wellbores. Communicating with a fracture intersecting the hole at an oblique angle may actually be an advantage for a cased hole scenario. In

http://dx.doi.org/10.5772/56211

openhole, the contact area is explicitly defined. In cased hole, injection restrictions through individual perforations may force a larger contact area along the wellbore with linked fractures evolving from perforations, feeding into the pre-existing fracture at some small distance from the well. See also Massaras et al., 2007 [22].

These considerations of pinch points are appealing, but may not work equally well during production, with the pressure gradient into the wellbore.

7. Perforation skin — Pressure loss during production

At the other end of the spectrum are production-related publications which have either assumed a high permeability formation without hydraulic fractures, or have agglomerated complicated near wellbore effects into a choke skin. Karakas and Tariq, 1991, [23] provide a summary of these effects. Since these tend not to reveal a great deal of information about specific losses in the near-wellbore area other than an overall skin, they are only summarized here (refer to Appendix I).

8. Relative order of magnitude calculations — Pressure losses

A comparative analysis is done to assess the magnitude of perforation friction losses. Tortuosity associated with shear fractures intersecting the wellbore can be included using methods proposed by Weng, 1993, [12] and Haney et al., 1995, [57] with the assumption that they work for production in the same fashion that they do for hydraulic fracturing. The simplest possible representation of near-wellbore pressure loss, ignoring tortuosity, is that the pressure drop is strictly due to orifice losses using calculations that can be readily inferred from Bernoulli's equation along with a discharge coefficient, C_d. Consider a hypothetical case:

TD to reservoir top 2000 m

Reservoir net thickness 500 m

Net to gross 1

Perforated reservoir thickness up to 500 m

Inclination 0°

Average reservoir temperature 200°C

required mass flow rate per well 100 kg/sec

Required volumetric flow rate 62,000± BWPD (sand face)

Average bottomhole fluid density[1], 877.6 kg/m^3

Average viscosity 0.14 cP

Perforation casing diameter.0127,.0254 m

Perforation phasing 60°[2]

Formation pressure gradient 10.18 kPa/m or 0.45 psi/ft

Wellbore inclination vertical

Hydraulic fracture width 2 mm

Drilled hole diameter in reservoir 0.254 m, 10 inch

$$\Delta p_{perforations} = \frac{1}{2}\frac{16}{\pi^2}\frac{Q^2\rho}{N_p^2 d^4 C_d^2} \quad C_d = \left(1 - e^{-\frac{2.2D}{\mu^{0.1}}}\right)^{0.4}$$
$$\Delta p_{perforations} = \frac{8}{\pi^2}\frac{\left(\pi\frac{d^2}{4}\right)^2 v^2\rho}{N_p^2 d^4 C_d^2} = \frac{v^2\rho}{2N_p^2 C_d^2} \tag{4}$$

For economic viability, it has been suggested that a minimum of 100 kg/s of water needs to be generated (at this reservoir temperature).[3] This is 0.114 m3/s (~60,000 BWPD) downhole. Friction in the tubulars is considered to be second order at this point – and similar for cased and openhole completions.

It has been argued that the casing, cement and perforating a geothermal well would result in poor production, due to restrictive flow. There is also concern that the pressure drop associated with the perforations would be much too large or severe. To investigate the nature of orifice losses near the wellbore, a simple theoretical model was developed to compare pressure drop between an openhole and cased/perforated wellbores. To start the assessment, the flow regime was assessed to confirm that both completion types are in turbulent flow.

The generic data above were used, assuming a vertical wellbore with a longitudinal fracture 2 mm wide for both completion methods (openhole or cased, cemented, and perforated). Later the consequences of multiple interconnected fractures associated with fracturing through perforations are considered. Although it could be argued that fracture width close to the wellbore would likely be significantly greater for a cased hole, the analysis is too sensitive to width to modify it arbitrarily.

---

1 The generic geothermal fluid properties were based on the composition of water from Roosevelt Hot Springs, Utah (Capuano and Cole, 1981), which is a 1% NaCl solution.Ershaghi et al., 1983, [24] measured viscosity for a 1% NaCl brine at 200° C to be 0.139 cP, which is almost exactly the same value given by the NIST thermodynamic tables for pure water under downhole pressure.In addition, the density of water is 878.31 kg/m3 at this pressure.

2 For 60° phasing and 6 shots per foot, there would be 2 perforations at 180° most likely to communicate – other shots may have a complicated interconnectivity, but this assumption is conservative.

3 J. Moore, personal communication, 2012.

http://dx.doi.org/10.5772/56211

To determine conditions for laminar flow, Re ≤ 2,000,for an openhole longitudinal fracture, hydraulic radius was used to approximate the fracture as a slot-like wellbore intersection:

$$\mathrm{Re} = \frac{4HR\rho V}{\mu} \quad HR = \frac{hw}{2(h+w)} \tag{5}$$

where:

HR hydraulic radius

h fracture height intersecting the vertical wellbore

w nominal and vertically constant fracture width at wellbore

ϱ fluid density

V fluid velocity in the fracture at the wellbore

μ dynamic viscosity

The maximum velocity of fluid through the fracture will be based on one half of the total flow rate presuming a symmetrical, bi-winged fracture, and the cross sectional area of the fracture on that side. After some rudimentary manipulation it is found that:

$$\mathrm{Re} = \frac{\rho Q}{\mu(h+w)} \tag{6}$$

To maintain laminar flow, the fracture contact length, h, along the wellbore can be estimated as:

$$h = \frac{\rho Q}{\mu \mathrm{Re}} - w = \frac{877.6\ \frac{kg}{m^3} \times 0.1104\ \frac{m^3}{s}}{2000 \times 1.4 \times 10^{-4}\ Pa \cdot s} - 0.002\ m = 346\ m \tag{7}$$

The fracture height would need to be about 346 m (with connection along the wellbore) to avoid going into turbulent flow for an openhole completion. While not strictly speaking impossible in a 500 m reservoir, it may prove difficult to accommodate this much longitudinal wellbore contact openhole. Additionally, this gives us a maximum velocity under 0.08 m/s for laminar flow.

To assess the flow regime for production of a geothermal reservoir through a cased, cemented and perforated completion, first consider the concept of effective perforations. Assume that only perforations within less than 30° of the preferred fracture plane are expected to significantly contribute to fracturing/flow (Behrmann and Elbel, 1991 [13]). It may be assumed that these same perforations will also contribute the vast majority of production flow, due to their connectivity to the fracture(s). For simplicity, the model developed here assumes that effective

perforations are fully open for flow, and are perfectly aligned with the preferred fracture plane. The model therefore fails to account for tortuosity or proppant packing in order to compare the best case scenario for using perforations with that of an openhole fractured completion. Order of magnitude calculations for those effects are presented later.

Maximum laminar velocity was determined through perforations with 60° phasing, 12 spf (39.37 spm) and 1.27 cm casing-hole diameters. This phasing guarantees that 1/3 of the perforations will be within 30° or less of the preferred fracture plane. While a more detailed study would need to take place to determine the pressure drop due to misalignment of the perforations (reorientation and/or microannulus flow), for now it is assumed that the best oriented perforations are perfectly aligned with the fractures. As discussed earlier, it is also assumed that the aligned perforations accept virtually all flow. The maximum velocity for laminar conditions would be approximately 0.0251 m/s. The number of perforations for laminar flow with this velocity is too large to be feasible. Perforation flow would theoretically be turbulent (based on the Reynolds' number). The length over which this occurs is very small however and the losses through the perforation tunnel itself – if it is clear of debris – are proposed to be small – calculations demonstrating this will follow.

The next logical step is to consider turbulent flow. For either completion case, flow up the wellbore will likely be turbulent above the reservoir.[4] The openhole scenario suggests that a continuous fracture height with laminar flow could fit vertically within this reservoir. While possible, it isn't probable that this will be the case (over 346 m). Alternatively the perforations will almost certainly see nonlaminar effects. Depending on the fracture height, turbulent flow will also exist within the fracture, but may not fully develop in the short interval of the perforations.

A correlation often adopted in chemical engineering piping design (Towler and Sinnott, 2012 [55]) was used as a measuring stick for the maximum allowable fluid velocity (to avoid erosion and to carry any entrained solids; the latter is likely not relevant for geothermal applications). A common rule of thumb for sizing pipes for liquid flow is to impose a velocity of 3 m/s. Realistically, this may be extremely conservative if the flow is single phase and solids-free. Nevertheless, for purposes of illustration, this limit is adopted - the maximum velocity through the perforations was set at 2.5 m/s (this conservatively low velocity can account for situations where two-phase flow may unexpectedly occur). Compared to perforation requirements for laminar flow, using this design velocity vastly reduces the number of perforations required to make up the total flow rate (62,000 BWPD). Assuming 60° phasing, and 6 spf, the required perforated height restrict velocity to 2.5 m/s would be ~160 m. This is still a substantial number of perforations and relaxing the critical velocity restriction would seem to make sense.

9. Modeling pressure drop due to perforations in a fractured reservoir

To confirm these initial predictions, a more fundamental approach was implemented to predict the near-wellbore pressure drop – following Huang and Ayoub, 2007 [56]. The problem of

4 Flow up a 10-inch (0.254 m) ID pipe will be turbulent at this rate (Re = 3.61 × 106).

http://dx.doi.org/10.5772/56211

pressure drop can be broken up into three parts: pressure drop from the contraction between the fracture and the perforation, pressure drop from friction within the perforation itself and pressure drop from the expansion between the perforation to the wellbore. These are shown schematically in Figure 1, representing flow regimes going from a fracture, through the perforations, into the wellbore.

$$\Delta p_{perf} = \Delta p_{sc} + \Delta p_f + \Delta p_{se} \tag{8}$$

where:

Δp_{sc} pressure drop from sudden contraction/expansion between fracture and perforation tunnel

Δp_f pressure drop due to friction in the perforation tunnel

Δp_{se} pressure drop due to sudden expansion between perforation tunnel and wellbore

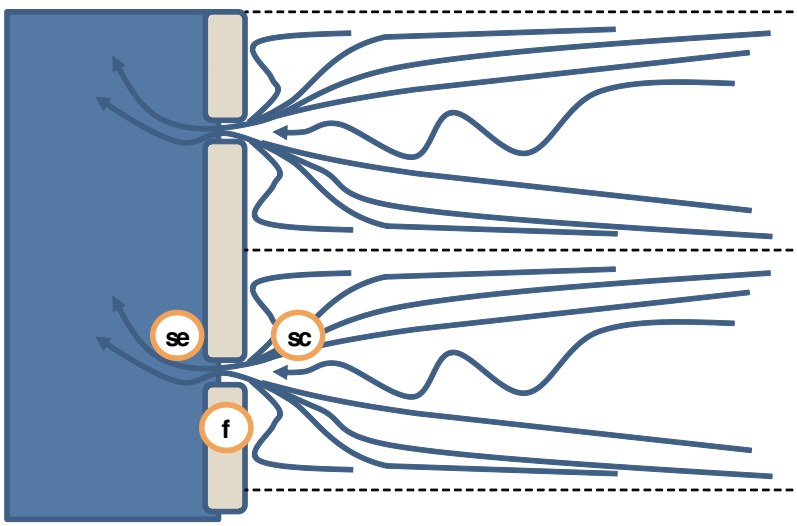

Figure 1. Proposed flow regime near the wellbore through effective perforations.

For 12 spf (39.37 spm) at 60° phasing, parallel effective perforations are spaced 15.24 cm apart. For this system, transition from the fracture "cells" to the perforation is equivalent to going from a 15.24 cm x 0.20 cm slit to a 1.27 cm pipe. One could therefore account for the first phase of pressure loss as the result of sudden contraction. Using conventional fluid mechanics principles, the minor loss in a sudden contraction similar to this are again estimated to be negligible (0.92 kPa, 0.13 psi). The friction loss through each perforation tunnel, Δp_f, is

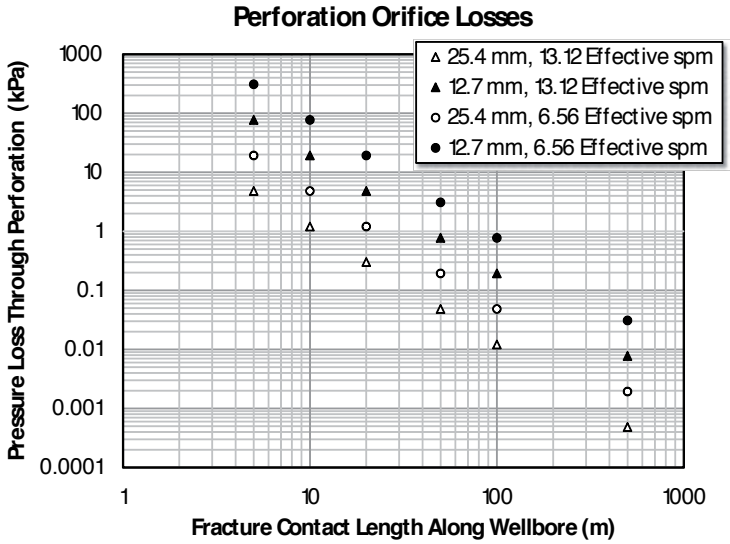

Figure 2. Total pressure loss through perforations for 60,000 BWPD (0.11 m^3/sec). The legend shows the nominal perforation diameter through the casing and the number of shots per meter connecting with the fracture. The abscissa is the actual contact length of the fracture along the wellbore. For practical lengths and open perforations, this type of loss is inconsequential.

estimated using the formulae for an orifice shown previously. The actual value for the discharge coefficient is uncertain because conventionally some of that is embodied in the entrance and exit losses being calculated separately. To be conservative, it will be calculated in the same fashion as above, shown by Crump and Conway [8] in 1988. For the generic situation chosen, a pressure drop of 3.48 kPa, ~0.5 psi is estimated. Finally, for the sudden expansion into the wellbore, the minor loss, Δp_{se}, is estimated as 2.73 kPa (0.4 psi). The sum is again a remarkably small loss. Figure 2 demonstrates this.

While more complex models may need to be developed to account for tortuosity and packing perforations, this simple model suggests that the pressure drop difference between perforated completions and openhole will be small. For practical lengths and open perforations, this type of loss is inconsequential. However, other losses have to be considered ….

From experience in fracturing, there is evidence for near wellbore flow impedance. Simple calculations suggest that it is not strictly due to the perforations themselves. It seems that the real issue then remains choking skin associated with near-wellbore fracture turning and twisting and interlinking. The best discussion of this is Weng, 1993, [12] who proposed approximations of frictional losses during injection. If it is assumed that reciprocal losses might be approximated during production, some gross approximations are possible. First, fracture turning[5] is probably not a significant issue. Weng [12], in discussing fracture turning states

5 Weng [12]delineated the turning stage as being related to fracture growth with tip rotation in a plane collinear with the wellbore.

http://dx.doi.org/10.5772/56211

"Since the width reduction [due to turning] takes place only on a small portion of the fracture, the friction loss, i.e., the incremental pressure above the pressure for a straight fracture, is small unless the perforation angle is off the preferred direction by a large angle." The situation during production is more complicated since the width will be smaller than during fracturing because of the direction of the pressure gradient.

Of more interest is twisting. When the fracture half-length becomes large enough, a twisting component can result as the fracture evolves to realign with the far-field stresses. For the twisting component, Weng incorporated a local increase in the closure stress:

$$\sigma_c = \sigma_{HMIN} + \left(\sigma_{HMAX} - \sigma_{HMIN}\right)\sin^2\alpha' \tag{9}$$

where:

α azimuth angle from the horizontal minimum stress direction (well is projected into a horizontal plane)

α' 90° - α

This local stress increase is superimposed on local stress concentrations and causes a near-wellbore width reduction during injection or production. As can be seen in Figure 7 in Weng's [12] paper, most of this loss can be eliminated by appropriate drilling direction, to keep α' small. Turning then does not appear to be too substantial of a pressure loss mechanism.

The twisting component is more significant. Additional frictional losses may result from the specific connectivity of starter fractures near the wellbore; specifically, how do fractures that initiate at an angle to the wellbore (normal to the smallest local principal stress) propagate, twist and align (or not) to direct injection fluid to or to collect production fluid from a more dominant master fracture. For simplicity, assume one dominant master fracture surviving a short distance radially from the wellbore. Fractures from the perforations reorient and/or link to connect with this main fracture. The multiply fractured region connects the master fracture to the perforations and the wellbore. If the wellbore orientation falls outside of a specified range, these starter fractures do not link up (they grow independently until fracture friction causes only one to survive. Production will be through discrete fractures. An extensive, multiply fractured zone was proposed by Weng [12] as being capable of causing a significant frictional zone. This becomes quite a complicated consideration during production – are multiple, nonlinked fractures at the wellbore an impediment (friction, propensity for width reduction) or an advantage (wider pressurized fractures)?

With twisting and interacting fractures, only approximate calculations are attempted – just to assess the relative order of magnitude of the frictional loss that might be anticipated. Adapting Weng's equation 18 [12] for flow through a multiplicity of near-wellbore fractures for a Newtonian fluid (parallel plate flow):

$$\Delta p_{mf} = \frac{12\mu q}{h}\frac{L_m}{\bar{w}^3} \tag{10}$$

where:

Δp_{mf} pressure loss for flow through the multiply fractured region

h unit height

m dynamic viscosity

q volumetric flow rate in each fracture per unit height

L_m half-length of multiply fractured zone
$\bar{w}$ average aperture for each connecting fracture

Apply this relationship to estimate the pressure drop. On a meter by meter basis it is possible to assume that the fracture width would be the width of an openhole fracture (assume 2 mm constant along the wellbore length) divided by the number of effective perforations;[6] similarly for the flow rate per fracture. For 60° phasing and 6 spf, one can envision something over six effective perforations per meter, giving an effective width of 0.33 mm (as opposed to 2 mm for an openhole bi-winged fracture). Assuming a velocity of 2.5 m/s through each perforation, the required perforated wellbore length (net perforated length) would be 160 m (see earlier) and the total inflow per meter would need to be 6.9×10^{-4} $m^3/s/m$. The greater the half-length of the zone of multiple fractures (distance away from wellbore), Lm, the greater the pressure losses. Assume 5 m (Weng [12] found a typical transition at about 15 ft. in some of his calculations), the pressure loss can be estimated as 27 kPa (4 psi). The key variables are of course the number of effective perforations per unit length (phasing and spm) and the length over which linkage would occur. The presumption is that the length required for linkage can be reduced when the stimulation is carried out by breaking down all perforations, drilling at acceptable angles, and initiating at low rate. The troublesome aspect of this logic here is that more perforations give a higher pressure drop – so the ideal situation would be to use fewer, which is counter-intuitive and would increase the perforation tunnel losses. Figure 3 shows order of magnitude pressure losses for first order approximations of losses through the perforation tunnels themselves (see Figure 2) and from the friction estimated in the multiply fractured region.

10. Relative order of magnitude calculations — Supplemental power

Using the hypothetical pressure losses that might occur for the generic scenario being considered, presuming a certain number of effective perforations (broken down, and closely enough aligned with the local minimum principal stress[7]), additional pumping requirements (above

6 In fact, this is approximate. For multiple, closely spaced fractures the width of the fractures is generally reduced. This was proposed by Nolte ,1997, [60] and Jeffrey et al., 1997 [62]. Germanovich et al., 1997, showed the complexity of the interaction with internal fractures being preferentially closed by encompassing external fractures.

http://dx.doi.org/10.5772/56211

openhole requirements) are estimated. This depends strongly on the number of effective perforations. The number of effective perforations is strictly governed by gun characteristics, especially phasing and density as well as in-situ conditions. It appears that for typical perforation diameters the casing hole perforation diameter is a secondary parameter – unless it becomes extremely small.

Using the same generic reservoir, the power requirements for lifting and to overcome the estimated pressure losses in the perforations and the multiply fractured region are shown in Figure 4, using additional assumptions shown below.

h_{set} setting depth for pump -- 500 m TVD

$h_{reservoir}$ nominal depth to midpoint of producing fracture(s) -- 2,000 m TVD

h_f length fracture communicates with wellbore -- 10, 20, 50, 100, 500 m

η pump efficiency (dimensionless) … 0.50 was used

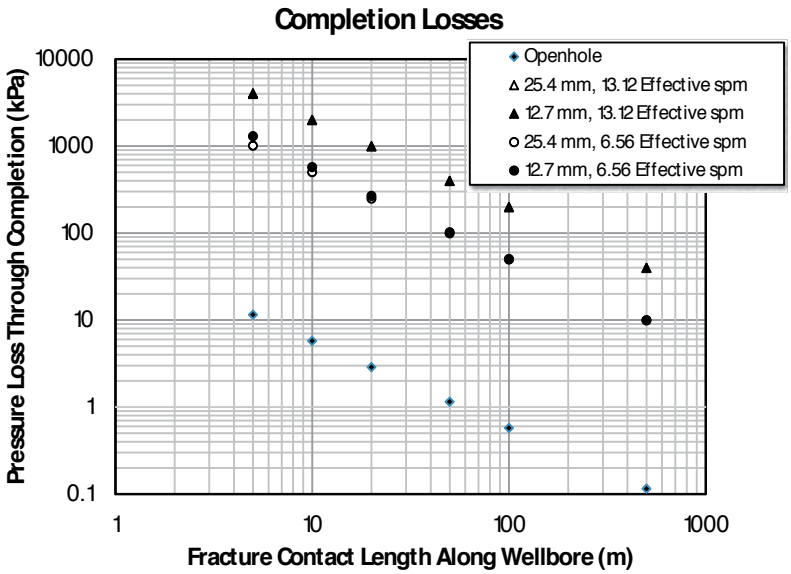

Figure 3. Total pressure loss through perforations and near-wellbore region for 60,000 BWPD (0.11 m^3/sec) – Completion Losses. The legend shows the nominal perforation diameter through the casing and the number of shots per meter connecting with the fracture. The abscissa is the actual contact length of the fracture along the wellbore. For practical lengths and open perforations, this type of loss is inconsequential.

This might be considered in terms of incremental cost. Figure 5 shows that with enough connectivity these costs could be manageable. An overall economics evaluation would be required.

7 Sometimes referred to as a secondary minimum principal stress. This strictly indicates the minimum principal stress at the borehole wall, not necessarily aligned with the far-field minimum principal stress.

11. Erosion of perforations

Figure 6 shows velocities through individual perforations in the generic geothermal system being considered. While the erosive capabilities of clean fluids are not always certain, two-phase and solids-entrained fluids will have significant erosive potential. In conservative engineering applications, Simpson, 1968, [58] argued for velocities between 2.5 and 3 m/s. Considering that time-dependent enlargement of the perforations will stabilize the erosive potential and that the most important role of the perforations is before the well is in use (e.g., to promote multiple hydraulic fracturing) erosion is probably a benefit – reducing the pressure drop.

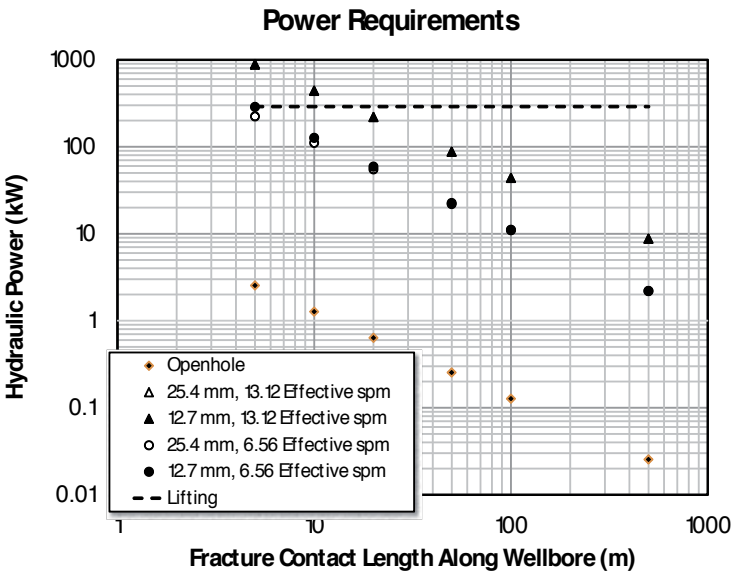

Figure 4. Power requirements to lift 60,000 BWPD (0.11 m^3/sec) and to accommodate the required pressure drop through the perforations for a 50 percent efficiency. The legend shows the nominal perforation diameter through the casing and the number of shots per meter connecting with the fracture. The abscissa is the actual contact length of the fracture along the wellbore.

12. Summary

There are supplementary costs associated with casing, cementing and perforating geothermal production and injection wells that are to be hydraulically fractured. There are also operational costs related to overcoming near-wellbore losses as well as minor losses through perforation tunnels themselves. However, the advantages of ensuring extended contact along the wellbore with perforated completions could be substantial. At the very least, assertions that cased and

http://dx.doi.org/10.5772/56211

perforated completions cannot accommodate the volumes required for economical geothermal production should be carefully reconsidered. The key findings:

1. Pressure losses through perforation tunnels per se are theoretically small. More perforations and larger shots reduce this component further.
2. Twisting and to a lesser extent turning of fractures initiating from perforations can cause greater pressure losses. Smaller densities can reduce this friction if the alignment of the wellbore falls within acceptable limits.
3. It seems that perforated completions for geothermal wells can be designed to minimize near-wellbore losses and improve economics. The calculations done to support this only have a relative order of magnitude reliability and further numerical and empirical evaluation is necessary to generalize this observation.

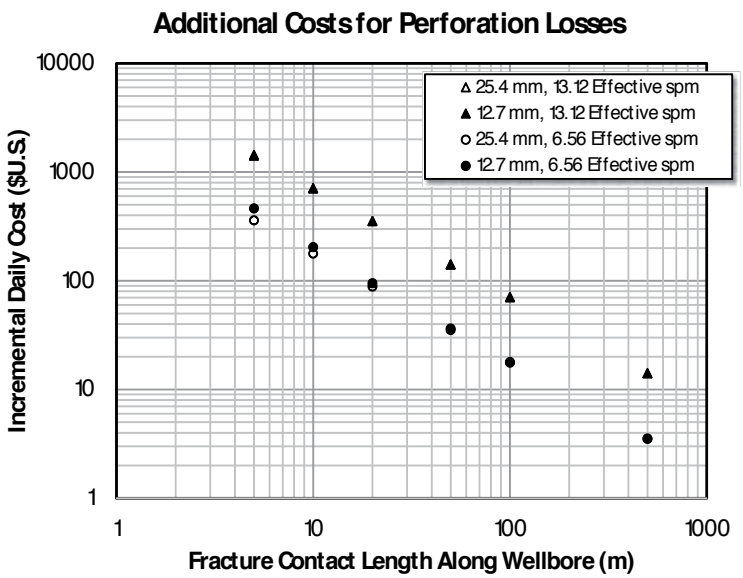

Figure 5. Incremental daily cost estimate for pressure losses through the perforations.

Appendix I — Pressure losses during production (Literature survey)

The most cited work for perforation pressure losses is usually Karakas and Tariq, 1991 [23], Although their skin values were designed for permeable formations, the methodology is useful for thinking about pressure losses that might be incurred. They incorporated additive skin components that accounted for vertical and horizontal convergence and phasing. Inclination mechanical skin can also be considered. Presume that the perforation skin for a vertical well can be represented as:

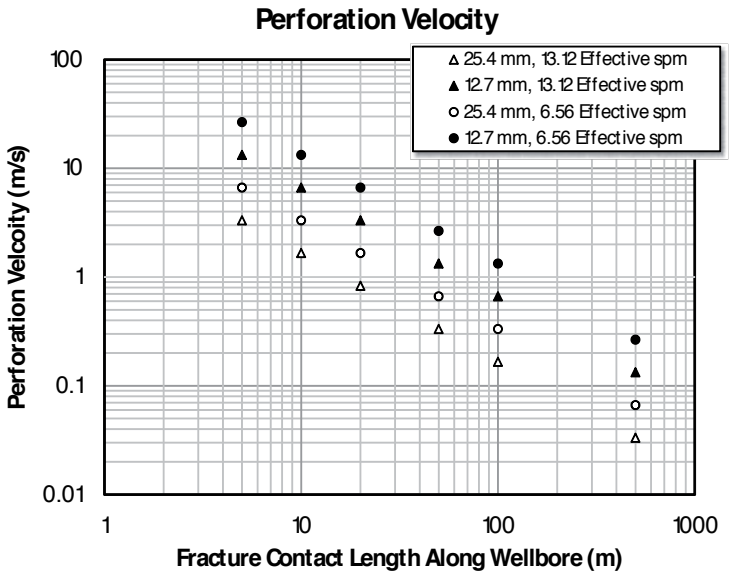

Figure 6. For practical perforated lengths, single phase erosion will not be likely. Even if erosion does occur it should only reduce the velocities and the pressure loss in the perforations.

$$s_p = s_H + s_V + s_{wb} \tag{11}$$

where:

s_p perforation skin, dimensionless

s_H skin due to horizontal convergence, dimensionless

s_V skin due to vertical flow convergence, dimensionless

s_{wb} wellbore skin, dimensionless

The wellbore skin accounts for perforation phasing. Karakas and Tariq, 1991, [23] suggested that it is quite small for phasing less than 120°. Its direct application here (for fracture flow only) may partially account for microannular restrictions although this was not the original intent. Consider a dimensionless radius (r_{wD}) and the wellbore skin (swb):

$$r_{wD} = \frac{r_w}{r_w + L_{perf}} \quad s_{wb} = c_1 e^{c_2 r_{wD}} \tag{12}$$

These coefficients were tabulated by Karakas and Tariq [23] from their numerical work. As an example, suppose, the wellbore radius is rw = 0.5 ft., the perforation length, L_{perf} = 1.0 ft., the perforation radius, r_{perf} = 0.5 inches and that the vertical and horizontal permeability, k_V and

http://dx.doi.org/10.5772/56211

k_H, are equal and the density is 6 spf (giving the space between the perforations, h, as 0.2 ft. For 60° phasing we have $c_1 = 3 \times 10^{-4}$, $c_2 = 7.509$, $r_{wD} = 0.333$ and the skin as 3.67×10^{-3}. Since there is no horizontal permeability to speak of one can chose to ignore the horizontal convergence for a vertical fracture aligning with a vertical wellbore. Alternatively, the vertical convergence concept can be ignored for a transverse fracture intersecting a vertical well and axisymmetric convergent flow is required. Similar simplifications are possible for horizontal wells. For these two cases (vertical well):

$$\begin{aligned} &h_D = \frac{h_{perf}}{L_{perf}},\ r_{pD} = \frac{r_{perf}}{2h_{perf}},\ a = a_1 \log_{10} r_{pD} + a_2,\ b = b_1 r_{pD} + b_2 \\ &\text{Longitudinal Fracture} \rightarrow s_H = 0,\ s_V = 10^a h_D^{b-1} r_D^b \\ &\text{Transverse Fracture} \rightarrow s_V = 0,\ s_H = \ln\left(\frac{r_w}{\alpha_\theta\left(r_w + L_{perf}\right)}\right) = \ln\left(\frac{r_{wD}}{\alpha_\theta}\right) \end{aligned} \tag{13}$$

For the example being considered we find $a_1 =$, $a_2 =$, $a =$, $b_1 =$, $b_2 =$, $b = \alpha\theta = 0.813$, giving:

$$\begin{aligned} &h_D = 0.2,\ r_{pD} = \frac{r_{perf}}{2h_{perf}},\ a = a_1 \log_{10} r_{pD} + a_2,\ b = b_1 r_{pD} + b_2 \\ &\text{Longitudinal Fracture} \rightarrow s_H = 0,\ s_V = 10^a h_D^{b-1} r_{pD}^b = 0.45 \\ &\text{Transverse Fracture} \rightarrow s_V = 0,\ s_H = \ln\left(\frac{r_w}{\alpha_\theta\left(r_w + L_{perf}\right)}\right) = \ln\left(\frac{r_{wD}}{\alpha_\theta}\right) = -0.89 \end{aligned} \tag{14}$$

If the pressure drop to anticipate under steady state conditions is:

$$\Delta p_s = \frac{Q\mu}{2\pi kh} s_p \tag{15}$$

the pressure drop for a longitudinal fracture is negligible for a highly conductive fracture. Transverse fracturing may even give a negative skin although the simplifications adopted may not be appropriate. In either case, skin is small.

Kabir and Salmachi, 2009, [25] described relationships for perforation skin calculation during injection, using well-known relationships; extending concepts from Karakas and Tariq, 1991 [23], representing the skin as a superposed combination of convergence to the perforations (but presuming flow from the matrix, whereas the considerations here are fracture-flow dominated, damage (the analog here could be choking or micro-annular pressure drop) and crushing (perforation infill and poor fracture connectivity could be relevant.

Saleh and Stewart, 1996, [26] elaborated on the Karakas and Tariq [23] considerations for pressure loss and added an additional complexity that is relevant for geothermal as well as shale gas/oil production – a second phase. The conventional production pressure drop allocations are represented by van Everdingen and Hurst's skin and Hawkins's representation:

$$s = \frac{2\pi\Delta p_s kh}{Q\mu} = \left(\frac{k_s}{k} - 1\right)\ln\left(\frac{r_s}{r_w}\right) \tag{16}$$

where:

Δp_s incremental pressure drop occurring in the

wellbore region due to a changed permeability – this could be considered to be reduced aperture or reduced relative permeability or twisting of the fracture, etc.

k virgin permeability

k_s damaged permeability

h reservoir thickness

Q volumetric flow rate

μ dynamic viscosity of flowing fluid

r_w wellbore radius

r_s damaged radius

Before low permeability (shale gas and shale liquids) was popular, Tariq et al., 1989, [27] considered production from naturally fractured reservoirs in low matrix permeability environments. "The sharp discontinuities in porosity and permeability created by fractures have a significant impact on the overall fluid flow in the reservoir. Fractures allow rapid conduction of fluids with very little pressure drop because their resistance to fluid flow is much lower than that of the matrix rock. Very high flow rates (30,000 to 50,000 B/D … have been obtained from fractured reservoir wells under a limited pressure drop." They further stated: "In the past, many naturally fractured reservoirs were completed openhole (barefoot). Perforated completions have now become more popular for naturally fractured reservoirs as a result of improvements in drilling technology and in fracture detection techniques. The concern in the perforated completion, however, is the small area open to flow. The productivity of a perforated completion in naturally fractured reservoirs is totally dependent on the hydraulic communication between the perforations and the fracture network. This communication, in turn, is dependent on such factors as fracture interval (or fracture density), fracture orientation, number of joint sets, shot density, and perforation length."

Part of the concern near the wellbore is the choking type of skin [3, 28, 29, 30], where losses due to damage and convergence are isolated in the plane (or within the confines) of a fracture. The effects can be further normalized by looking at various forms of the productivity ratio or

http://dx.doi.org/10.5772/56211

flow efficiency – normalized with respect to ideal (cased but no mechanical losses; or undamaged openhole...) situations.

Lian et al., 2000, [31] describe numerical modeling of perforated completions for fractures. Yildiz, 2006, [32] described methods of approximating a composite skin, as did Furui et al., 2008 [33]. Ehlig-Economides et al., 2008, [34] provided a rationale analysis, presuming flow through perforations directly connected to the hydraulic fracture (this may be impacted by wellbore and perforation deviation from principal stress directions). A halo effect was also considered wherein angularly offset perforations would still be connected along this length. This was acceptable in the high permeability formations that those authors were considering but seems unrealistic in most EGS scenarios.

Zhang et al., 2009, [35] expanded on the work of Ehlig-Economides et al., 2008, [34]. They introduced a model hypothesizing that only perforations between the far-field hydraulic fracture plane and the wellbore actually connect flow through the fracture and the well, for fracpacks. For deviated wells the number of perforations can drop substantially unless multiple injections are carried out on isolated zones. The problem may be more severe in openhole – with the fracture quickly deviating from where it discretely intersects the wellbore and possibly minimizing contact length along the well. Considering only the connected perforations (fracture(s) physically in contact with the wellbore), the pressure drop can be considered as:

$$\Delta p_{perf} = \frac{888 L_g \mu B}{k_p A_p N_c} q_{f,total} \tag{17}$$

where:

Δp_{perf} pressure drop through the perforations, psi

L_g length of the propped perforation tunnel, ft

μ dynamic viscosity, cP

B water formation volume factor, res bbl/STbbl

$q_{f,total}$ bottomhole total flow rate, BLPD

k_p absolute permeability of packed perforation, md

A_p cross-sectional area (nominal) of individual perforation, ft^2

N_c number of connected perforations

This relationship came from Welling, 1998, [36] simply calculating the pressure drop for liquid flow through a sand-packed perforation, as follows:

$$P_{wfs} - P_{wf} = cQ + dQ^2$$
$$c = 888\frac{L_{gr}\mu B_w}{k_{gr}AN} \text{ and } d = 9.08\times10^{-13}\frac{\beta_{gr}L_{gr}\rho B_w^2}{A^2N^2} \text{ and } \beta_{gr-oil} = \frac{6.5\times10^4}{k^{0.996}} \quad (18)$$

It is not really relevant because this analysis assumes that the fracture perforations are not infilled with any material. However, propped fractures may require consideration of this additional skin. It is known that near-wellbore fracture geometry is likely more complicated and that more than orifice frictional losses or packed perforation losses are involved. Fracture width reduction near the wellbore can result from twisting and turning with associated shear or partial departures from the direction of perforating, through a microannulus and then in the direction of the maximum normal stress. Cherny et al., 2009, [37] considered (in two-dimensions) the consequences of micro-annular losses. A relevant question is how they are represented during production. It might be anticipated that pressure drops are even larger because of the different sign of the pressure gradient from the wellbore into the fracture during injection – as opposed to during production. Fallahzadeh and Rasouli, 2012, [38] considered some aspects of stress conditions around cased and cemented wellbores impacting perforation performance. Other references relevant to pressure losses during hydraulic fracturing include Ceccarelli et., 2010, [39] as well as Fallahzadeh et al., 2010 [40].

Jackson and Rai, 2012, [41] have come closest to proposing methodologies for discriminating various types of apparent skin in shale gas plays – including low conductivity fractures (manifested by a ¼ slope), poor connection to the wellbore (choke skin and near fracture face damage), relative permeability effects, fracture skin and casing connections; using the apparent skin intercept concept. They reiterated concepts for poorly connected factors strictly using standard choking analogs [see for example Cinco-Ley and Samaniego, 1981 [29]. This certainly has an effect but also needs to consider tortuosity and perforation damage. The choking skin, s_{ch}, has been considered to be:

$$s_{ch} = \frac{\pi x_s k}{w_s k_{fs}} \quad (19)$$

where:

x_s damage length, ft

w_s width of the fracture over the damaged length, ft

k fracture permeability, md

k_{fs} damaged permeability in the fracture, md

The convergent skin macroscopically exists for a fracture that is transverse to the wellbore. It is further increased by convergent flow of some additional complexity into individual

http://dx.doi.org/10.5772/56211

perforations. Jackson and Rai [41] suggested, where the subscripts 1 and 2 indicate some fine near wellbore distances:

$$q = -\frac{2\pi k_f \left(p_2 - p_1\right)}{\mu \ln\left(\frac{r_2}{r_1}\right)} \tag{20}$$

"The near-perforation damage influences the positive y-intercept significantly more than poor fracture conductivity for the entire length of the fracture." This finding implies how important the near wellbore regime is.

Recently, there have been numerous publications to determine near-wellbore skin from productive fractures. Many of these have been diagnostic methods. That in itself is valuable by providing a method for discerning how large these pressure drops in the near-wellbore region can be. Nobakht and Mattar, 2012, described a method for correcting for the apparent skin effect that has been attributed to flow convergence in a horizontal well and/or finite conductivity of the fractures – as well as a number of other mechanisms such as two phase flow. Inappropriate consideration of skin can cause linear flow with skin to appear as transient radial flow with boundaries. This can be overcome by using a square root of time plot (the time can be a superposed square root) and taking a linear relationship as:

$$\frac{p_i - p_{wf}}{q} = m\sqrt{t} + b' \tag{21}$$

This can also be expressed for a gas by using pseudopressure. It can be rewritten as (pm is referred to as a modified normalized pressure):

$$p_m = \frac{p_i - p_{wf}}{q} - b' = m\sqrt{t} \tag{22}$$

Most reservoir simulations don't discriminate the near-wellbore specifics in any sort of detail (Xie et al., 2012 [43]). Clarkson et al., 2012, [44] do describe dynamic skin effects. They use a time-dependent intercept, b'(t), to give a time-dependent s'(t). This dynamic skin was associated with depletion- and fluid-damage-related fracture conductivity changes, convergent flow, non-Darcy flow and fracture face skin.

Bello and Wattenbarger, 2010, [45] pointed out that in many multiply-hydraulically-fractured horizontal wells, skin is observed in a characteristic fourth production region (transient drainage from the matrix). They incorporated a convergence skin, s_c.

$$s_c = \frac{k_f x_e \left[m(p_i) - m(p_{wf}) \right]}{1422 q_g T} = -\ln\left[\frac{\pi r_w}{h}\left(1+\sqrt{\frac{k_V}{k_H}}\right)\sin\left(\frac{\pi d_z}{h}\right)\right] \tag{23}$$

where:

k_f bulk fracture permeability for dual porosity model md

k_V vertical permeability

k_H horizontal permeability

h net reservoir thickness, feet

m(p) pseudopressure – gas, psi^2/cP

p_i initial reservoir pressure, psi

p_{wf} wellbore flowing pressure, psi

q_g gas rate, MscfD

r_w wellbore radius, ft

d_z well position in reservoir

Rationalizing the permeability ratio for fracture flow in a geothermal well makes applying this difficult. The same problem exists for using the basic Karakas and Tariq [23] relationships.

Al-Ahmadi, et al. 2010, [46] observed that while transient linear flow is common in tight gas reservoirs, in shale gas wells, it is accompanied by a significant skin effect – not commonly seen in tight gas wells. They accounted for this with a modified linear flow relationship. For early time, Bello, 2009, [47] and Bello and Wattenbarger, 2009 [48], 2010 [45, 49] treated this as a constant skin effect. For a shale gas reservoir, they indicated:

$$\frac{\left| m(p_i) - m(p_{wf}) \right|}{q_g} = \tilde{m}_4 \sqrt{t} + \frac{Int_4}{1+\dfrac{0.45\tilde{m}_4\sqrt{t}}{Int_4}} \tag{24}$$

where:

m(p) pseudopressure – gas, psi^2/cP

pi initial reservoir pressure, psi

p_{wf} wellbore flowing pressure, psi

q_g gas rate, MscfD

$\tilde{m}_4$slope of line matching linear flow data and passing through origin on √time plot

t time, days

Int4 intercept of field data on [m(pi-m(p_{wf})/q_g vs. √t, psi^2/cP/MscfD

The message is that there are near-wellbore skins that have been diagnosed using pressure transient analyses on production data from tight formations. Near-wellbore pressure losses could be a dominant mechanism. Anderson et al., 2010, [50] recognized a significant skin effect from pressure loss due to finite conductivity in the fracture system, even if there is no mechanical skin damage at the wellbore. If a square root of time plot is used, the apparent skin (gas) can be inferred from a y-intercept, b, that represents a constant pressure loss.

$$s' = \frac{kh}{1417T} b \tag{25}$$

where:

T reservoir temperature, °R

k absolute permeability, md

s' apparent skin, dimensionless

h net reservoir thickness, feet

b intercept of square root time plot, psi^2/cP/MscfD

Other similar references include Bahrmai et al., 2011 [50], Sun et al., 2011 [51], Byrne et al., 2011 [52] and Li et al., 2012 [53].

Author details

Walter Glauser[1], John McLennan[1] and Ian Walton[2]

1 Department of Chemical Engineering, U. of Utah, Salt Lake City, USA

2 Energy & Geoscience Institute, U. of Utah, Salt Lake City, USA

References

[1] Pritchett, J. The role of reservoir stimulation in the future of the geothermal power industry. In: Reservoir stimulation current understanding and practice, and the path forward, GRC 2012 Annual Pre-Meeting Workshop, September 2012, Reno, Nevada; (2012). , 28-29.

[2] Gale, J. F. Natural fractures in Shales: Origins, characteristics and relevance for hydraulic fracture treatments. Search and Discovery Article #40338, adapted from oral presentation at AAPG Annual Convention..San Antonio, TX, April (2008). posted October 30, 2008)., 20-23.

[3] Mukherjee, H, & Economides, M. J. A parametric comparison of horizontal and vertical well performance. In: SPE Formation Evaluation. June (1991).

[4] Spencer, A. New diverting agents from applied research. SPE 2828, AIME.

[5] Waters, G, Ramakrishnan, H, Daniels, J, Bentley, D, Belhadi, J, & Sparkman, D. Utilization of real time microseismic monitoring and hydraulic fracture diversion technology in the completion of Barnett Shale horizontal wells. OTC 20268, OTC, Houston, TX May (2009). , 4-7.

[6] Stalker, R, Graham, G. M, & Oluyemi, G. Modelling staged diversion treatments and chemical placement in the presence of near-wellbore fractures. SPE 121683, Intl. Symp. on Oilfield Chemistry, The Woodlands, TX, April (2009). , 20-22.

[7] Petty, S. Stimulation methods in geothermal and oil and gas, reservoir stimulation: In: Current Understanding and Practice, and the Path Forward, GRC Annual Pre-Meeting Workshop, September (2012). , 28-29.

[8] Eftaxiopoulos, D. A, & Atkinson, C. Hydraulic fracture propagation from a cased, cemented and inclined wellbore. In: Aurertin, Hassani and Mitri, (eds.) Rock Mechanics. Rotterdam, The Netherlands: Balkema, (1996).

[9] Yew, C. H, & Li, Y. Fracturing of a deviated well. In: SPE Production Engineering (1987).

[10] Yew, C. H, Schmidt, J. H, & Yi, L. On fracture design of deviated wells. SPE 19722, SPE ATCE, October (1989). , 8-11.

[11] Yew, C. H, Mear, M. E, Chang, C. C, & Zhang, X. C. On perforating and fracturing of deviated wellbores. In: SPE ATCE, SPE 26514, October (1993). Houston, Texas.

[12] Weng, X. Fracture initiation and propagation from deviated wellbores. SPE 26597, SPE ATCE, Houston, October (1993). , 3-6.

[13] Behrmann, L. A, & Elbel, J. L. Effect of perforations on fracture initiation. In: JPT, May (1991).

[14] Romero, J, Mack, M. G, & Elbel, J. L. Theoretical model and numerical investigation of near-wellbore effects in hydraulic fracturing. SPE 30506, ATCE, Dallas, TX, October (1995). , 22-25.

[15] Crump, J, & Conway, M. Effects of perforation-entry friction on bottomhole treating analysis. In: JPT, August (1988).

http://dx.doi.org/10.5772/56211

[16] Lord, D. L, Shah, S. N, & Rein, R. G. Lawson III, J.T. Study of perforation friction pressure employing a large-scale fracture "simulator." SPE 28508, (1994).

[17] Shah, S. N, et al. New correlations for perforation pressure loss. In: GRI Technical Summary, GRI-96/0208, (1996).

[18] El-Rabba, A. M, Shah, S. N, & Lord, D. L. New perforation pressure-loss correlations for limited-entry fracturing treatments. SPE 54533 (1997), SPE Prod & Facilities, 14, (1), February (1999).

[19] Gulrajani, S. N, & Romero, J. Evaluation and modification of fracture treatments showing near-wellbore effects. SPE 36901, Eur. Petl. Conf., Milan, Italy, October (1996). , 22-24.

[20] Manrique, J. F, Bjornen, K, & Ehlig-economides, C. Systematic methodology for effective perforation and fracturing strategies. SPE 38630, ATCE, San Antonio, TX, October (1997). , 5-8.

[21] Behrmann, L. A, & Nolte, K. G. Perforating requirements for fracture stimulations. SPE 39453, Intl. Symp. on Formation Damage Control, Lafayette, LA, February (1998). , 18-19.

[22] Massaras, L. E, Dragomir, A, & Chiriac, D. Enhanced fracture entry friction analysis of the rate step-down test. SPE 106058, Hydraulic Fracturing Technology Conference, College Station, Texas, January (2007). , 29-31.

[23] Karakas, M, & Tariq, S. M. Semianalytical productivity models for perforated completions. SPEPE, SPE 18247, February (1991).

[24] Ershaghi, I, Abdassah, D, Bonadkdar, M. R, & Ahmad, S. Estimation of geothermal brine viscosity. In: J. Pet. Tech. March (1983). , 621-628.

[25] Kabir, A. H, & Salmachi, A. An improved method for total mechanical skin calculation for perforated completions. SPE 121233, SPE EUROPEC/EAGE Annual Conf. Exhib., Amsterdam, The Netherlands, June (2009). , 8-11.

[26] Saleh, A. M, & Stewart, G. New approach towards understanding of near well bore behaviour of perforated completions. SPE 36866, European Petl. Conf., Milan, Italy, October (1996). , 22-24.

[27] Tariq, S. M, Ichara, M. J, & Ayestaran, L. Performance of perforated completions in the presence of anisotropy, laminations, or natural fractures. SPEPE, November (1989).

[28] Cinco-ley, H, & Samaniego-v, F. Effect of wellbore storage and damage on the transient pressure behavior of vertically fractured wells. SPE Annual Fall Technical Conference and Exhibition. Denver, Colorado (1977).

[29] Cinco-ley, H, & Samaniego-v, F. Transient pressure analysis: finite conductivity fracture case versus damaged fracture case. SPE ATCE, SPE October, 1981, San Antonio, Texas (1981). , 10179, 5-7.

[30] Mukherjee, H. Fractured well performance: key to fracture treatment success. SPE 50976 and JPT, March (1999).

[31] Lian, Z, Meng, Y, & Tong, M. A new method of numerical simulation for perforation completion of fracture formation. SPE 64512, Asia Pacific Oil and Gas Conf. and Exhib., Brisbane, Australia, October (2000). , 16-18.

[32] Yildiz, T. Assessment of total skin factor in perforated wells. SPE 82249, SPEREE, February (2006).

[33] Furui, K, Zhu, D, & Hill, A. D. A new skin-factor model for perforated horizontal wells. In: SPE Drilling & Completion, 23, (3): September (2008). , 205-215.

[34] Ehlig-economides, C. A, Tosic, S, & Economides, M. J. Foolproof completions for high-rate production wells. SPE 111455, Intl. Symp. on Formation Damage Control, Lafayette, LA, February (2008). , 13-15.

[35] Zhang, Y, Marongiu-porcu, M, Ehlig-economides, C. A, Tosic, S, & Economides, M. J. Comprehensive model for flow behavior of high performance fracture completions. SPE 124431, SPE ATCE, New Orleans, LA, October (2009). , 4-7.

[36] Welling, R. W. F. Conventional high rate well completions: limitations of frac&pack, high rate water pack and open hole gravel pack completions. SPE 39475, SPE Intl. Symp. And Exhib. on Formation Damage Control, Lafayette, LA, February (1998). , 18-19.

[37] Cherny, S. G, Lapin, V. N, Alekseenko, O. P, & Medvedev, O. O. D modeling of hydraulic fracture initiating at a wellbore with or without microannulus. SPE 119352, SPE Hydraulic Fracturing Tech. Conf., The Woodlands, TX January (2009). , 19-21.

[38] Fallahzadeh, S. H, & Rasouli, V. The impact of cement sheath mechanical properties on near wellbore hydraulic fracture initiation. Rock Engineering and Technology for Sustainable Underground Construction, EUROCK ISRM Intl. Symp., Stockholm, Sweden, 28-30 May (2012). , 2012.

[39] Ceccarelli, R. L, Pace, G, Casero, A, Ciuca, A, & Tambini, M. Perforating for fracturing:theory vs. field experiences. SPE 128270, SPE Intl. Symp. And Exhib. on Formation Damage Control, Lafayette, LA, February (2010). , 10-12.

[40] Fallahzadeh, S. H, Shadizadeh, S. R, & Pourafshary, P. Dealing with the challenges of hydraulic fracture initiation in deviated-cased perforated boreholes. SPE 132797, Trinidad and Tobago Energy Resources Conf., Port of Spain, Trinidad, June (2010). , 27-30.

[41] Jackson, G, & Rai, R. The impact of completion related pressure losses on productivity in shale gas wells. SPE 162213, Abu Dhabi International Petroleum Exhib. & Conf., Abu Dhabi, UAE, November (2012). , 11-14.

[42] Nobakht, M, & Mattar, L. Analyzing production data from unconventional gas reservoirs with linear flow and apparent skin. In: JCPT and SPE 137454, Canadian Unconventional Resources and International Petroleum Conference, Calgary, AB, October, (2010). , 19-21.

[43] Xie, X. MacGlashan, J.D., Holzhauser, S.P., Knott, G.M. Completion influence on Haynesville shale gas well performance. SPE 159823, SPE Hydrocarbon Economics and Evaluation Symp., Calgary, AB, September (2012). , 24-25.

[44] Clarkson, C. R, Qanbari, F, Nobakht, M, & Heffner, L. Incorporating geomechanical and dynamic hydraulic fracture property changes into rate-transient analysis: example from the Haynesville shale. SPE 162526, SPE Canadian Unconventional Resources Conf., Calgary, AB, 30 October-1 November (2012).

[45] Bello, R. O, & Wattenbarger, R. A. Multi-stage hydraulically fractured shale gas rate transient analysis. SPE 126754, SPE North Africa Tech. Conf. Exhib., Cairo, Egypt, February (2010). , 14-17.

[46] Al-ahmadi, H. A, Almarzooq, A. M, & Wattenbarger, R. A. Application of linear flow analysis to shale gas wells- field cases. SPE 130370, SPE Unconventional Gas Conf., Pittsburgh, PA, February (2010). , 23-25.

[47] Bello, R. O. Rate transient analysis in shale gas reservoirs with transient linear behavior. PhD thesis. Texas A&M University, College Station, Texas; May (2009).

[48] Bello, R. O, & Wattenbarger, R. A. Modelling and analysis of shale gas production with a skin effect. In: Can. Intl. Petrl. Conf., Paper 2009-082, 16-18 June (2009). Calgary, Canada.

[49] Bello, R. O, & Wattenbarger, R. A. Modelling and analysis of shale gas production with a skin effect. In: JCPT, 49(12), December (2010).

[50] Anderson, D. M, Nobakht, M, Moghadam, S, & Mattar, L. Analysis of production data from fractured shale gas wells. SPE 131787, SPE Unconventional Gas Conf., Pittsburgh, PA, February (2010). , 23-25.

[51] Bahrami, H, Rezaee, R, Ostojic, J, Nazhat, D, & Clennell, B. Evaluation of damage mechanisms and skin factor in tight gas reservoirs. SPE 142284, SPE European Formation Damage Conf., Noordwijk, The Netherlands, June (2011). , 7-10.

[52] Sun, D, Li, B, Gladkikh, M, Satti, R, & Evans, R. Comparison of skin factors for perforated completions calculated with computational fluid dynamics software and a semi-analytical model. SPE 143663, SPE European Formation Damage Conf., Noordwijk, The Netherlands, June (2011). , 7-10.

[53] Byrne, M, Jimenez, M. A, & Salimi, S. Modelling the near wellbore and formation damage- a comprehensive review of current and future options. SPE 144096, SPE European Formation Damage Conf., Noordwijk, The Netherlands, June (2011). , 7-10.

[54] Li, B, Sun, D, & Satti, R. Statistical analysis of significant factors affecting perforation flow at well scale. SPE 150122, SPE Intl. Symp. And Exhib. on Formation Damage Control, Lafayette, LA, February (2012). , 15-17.

[55] Towler, G, & Sinnott, R. K. Chemical engineering design: principles, practice and economics of plant and process design. Elsevier; (2012).

[56] Huang, H, & Ayoub, J. A. Modeling non-Darcy flow and perforation convergence for vertically fractured wells. In: European Formation Damage Conference, SPE 107853, Scheveningen, The Netherlands, 30 May-1 June (2007).

[57] Hainey, B. W, Weng, X, & Stoisits, R. F. Mitigation of multiple fractures from deviated wellbores. SPE 30482, SPE ATCE, Dallas, TX, October (1995). , 22-25.

[58] Simpson, L. L. (1968). Sizing piping for process plants. In: Chem. Eng., NY, (June 17th), , 1923.

[59] Wu, B, Bunger, A, Zhang, X, & Jeffrey, R. G. Modeling Heat Extraction by Fluid Circulation through an Array of Conductive Fractures Australian Geothermal Energy Conference Nov. (2012). Sydney, 14-16.

[60] Nolte, K. G. Discussion of influence of geologic discontinuities on hydraulic fracture propagation, JPT, August (1987).

[61] Germanovich, L. N, Ring, L. M, Astakhov, D. K, Shlyapobersky, J, & Meyerhofer, M. J. Hydraulic fracture with multiple segments II. Modeling. Int. J. Rock Mech. & Min. Sci. Paper (1997). Elsevier Science Ltd., 34(098), 3-4.

[62] Jeffrey, R. G, Vandamme, L, & Roegiers, J-C. Mechanical interactions in branched or subparallel hydraulic fractures. SPE 16422, Low Permeability Reservoirs Symposium, Denver, CO, May (1997). , 18-19.

Chapter 18

Differentiating Applications of Hydraulic Fracturing

Joel Adams and Clem Rowe

Additional information is available at the end of the chapter

http://dx.doi.org/10.5772/56114

Abstract

Hydraulic fracturing has received abundant media attention in recent years due to a rapid increase in the use of the technique in combination with horizontal drilling technology to produce oil and gas resources from tight reservoirs. Hydraulic fracturing techniques are also used in a variety of other applications that are unrelated to oil and gas production, including tunnel and dam construction, enhanced geothermal energy, carbon sequestration, groundwater remediation, block cave mining, rock burst mitigation, and water well development.

Environmental concerns associated with large-scale hydraulic fracturing in oil and gas reservoirs have resulted in political efforts to ban the technique with legislation now in place in certain states in the US and countries around the world. Concerns include soil and groundwater contamination and induced seismicity. A clear understanding of how hydraulic fracturing techniques are used in various applications is important to avoid unintended consequences of any regulations aimed at hydraulic fracturing in the oil and gas industry. The methodology for each application varies widely in terms of scale, pressures applied, additives, and fracture propagation. Mining rock stress measurements, for instance, focus primarily on the breaking strength of rock, and can be conducted with a small-volume high-pressure pump that produces only a few liters/minute. The total volume of water injected may be on the order of tens or hundreds of liters. A typical oil and gas well hydraulic fracture treatment, on the other hand, requires millions of litres of injected proprietary fluid and proppant in order to propagate and maintain the fracture effectively into the reservoir. Though both applications are termed "hydraulic fracturing", they differ greatly in terms of potential impacts to the environment.

This paper characterizes a range of hydraulic fracturing applications in terms of the objectives, techniques, and potential for environmental concerns associated with the standard

methods. A nomenclature that clearly differentiates discrete applications is presented that is intended to help prevent the lumping of all hydraulic fracturing techniques into a single basket.

Keywords: hydraulic fracturing, rock stress measurements, applications

1. Introduction

The process of hydraulic fracturing as applied to drilled holes has been much in the news of late with a number of vociferous and often emotional debates about its potential to harm the environment particularly with reference to groundwater sources and also the potential to generate seismic events. However, all of this debate has been focused on a process typically referred to just as "fracking".

A recent BBC article [1] gives us the following relationship between the controversial process of "fracking" and the more generic term "hydraulic fracturing":

"What is fracking?

The process of drilling down and creating tiny explosions to shatter and crack hard shale rocks to release the gas inside. Water, sand and chemicals are injected into the rock at high pressure which allows the gas to flow out to the head of the well. The process is carried out vertically or, more commonly, by drilling horizontally to the rock layer. The process can create new pathways to release gas or can be used to extend existing channels.

Why is it called fracking?

It is shorthand for hydraulic fracturing and refers to how the rock is fractured apart by the high pressure mixture".

A further BBC article [2] headlined "Bulgaria bans shale gas drilling with 'fracking' method", further informs us that:

"Hydraulic fracking involves releasing gas trapped in rocks by pumping in water mixed with sand and chemicals at high pressure."

Sadly, these definitions, although technically correct, in their limited ways, do not pay any attention to the fact that the case described is only one of many applications of hydraulic fracturing that is applied in drill holes.

It is important to note that this paper is not intended to differentiate "good" fracking from "bad" fracking. The authors recognize that while certain types of hydraulic fracturing do carry a greater environmental risk, all hydraulic fracturing can be conducted in an environmentally responsible manner. However, a more complete definition of hydraulic fracturing is required which also specifies the application for which the process is applied. For example, apart from shale gas production, other applications for hydraulic fracturing include:

- Water well production enhancement

http://dx.doi.org/10.5772/56114

- Block Cave Mining (Hydraulic Pre-conditioning)
- Rock Stress Determination for Geotechnical Design (Tunnels, Dams, Foundations)
- Conventional oil and gas production
- Geothermal (hot dry rock, or "enhanced' geothermal)
- Carbon Sequestration (Carbon Capture and Storage)
- Coalbed Methane Development
- Coal Mine Methane Drainage
- Rock burst mitigation

All of the above use a process they term "hydraulic fracturing". The most general definition of which would be:

Hydraulic fracturing is a process whereby a fluid (often water with or without additives) at high pressure is applied to a borehole to create a fracture (or fractures) in the surrounding rock mass.

Before entering further discussion concerning definitions and terminology it is instructive to take a more detailed look at each of the various applications listed above.

2. Hydraulic fracturing applications

2.1. Water well production enhancement

As studied and described by W. H. Williamson, D. R. Woolley [3] in the 1970s, hydraulic fracturing has long been used as a method to improve the yield of water wells in fractured rock aquifers. It is widely used for domestic wells in many regions of the USA (for example, New England, Texas, Washington) and in some other locations such as Andhra Pradesh, India.

In water well hydraulic fracturing, often referred to as hydrofracking, a section of the well is isolated using packers and water is introduced to generate pressures up to approximately 3000 psi (207 bar) to wash out existing fractures and propagate them to connect with others within the aquifer. Since the pressure is quite limited it is doubtful if this process generates any new fractures though may do in some circumstances. The volume of water introduced per fracture is typically less than 1000 litres. This process generally does not use any proppant or additives in the injected water.

2.2. Block cave mining (Hydraulic pre-conditioning)

Block caving is an underground mass mining method where the extraction of the ore depends largely on the action of gravity. A shaft and horizontal galleries are driven to below the ore

body and a relatively thin horizontal layer of the overhead supporting rock is removed, using standard mining methods. Removal of this support allows the ore to cave into the galleries by gravity from where it is removed to allow caving to continue. [4]

In the event of a massive, un-fractured ore body, some form of pre-conditioning is needed to initiate caving and to reduce the size of caving materials. Intensive hydraulic fracturing in boreholes drilled into the ore body is one of the favoured methods of performing this pre-conditioning process.[5] Fracturing pressures can be up to 10,000 psi and pumped volumes of pure water are typically of the order of 4 – 5,000 litres per fracture though can be much larger depending on pump size and pressure response. [6]

2.3. Rock stress determination for geotechnical design (Mines, tunnels, dams, foundations)

In hydraulic fracturing for stress determination [7] also referred to as hydrofracturing, and sometimes as minifracing, a section of borehole is isolated between two inflatable packers and the pressure is raised by pumping fluid into it at a controlled rate until a fracture occurs in the borehole wall. Pumping is stopped and the pressure in the interval is allowed to stabilize. The pressure is then reduced to the pore pressure level of the rock formation, and the pressurization/depressurization process is repeated several times maintaining the same flow rate. The magnitudes of the principal stresses are calculated from the various pressure readings.

Normally only pure water is used and pressures are typically a maximum of 6,000 psi but can be as high at 15,000 psi. Flow rates are low at about 1 litre per minute with the total volume pumped per fracture typically being less than 100 litres.

Stress testing may also be carried out in oil and gas wells in which case the rates and volumes are much larger though this is primarily because the equipment normally available dictates minimum flow rates of 40 to 160 litres per minute.

2.4. Conventional oil and gas production

Hydraulic fracturing has long been used in the oil and gas industry for the stimulation of traditional reservoirs. To quote [8]:

"Since Stanolind Oil introduced hydraulic fracturing in 1949, close to 2.5 million fracture treatments have been performed worldwide. Some believe that approximately 60% of all wells drilled today are fractured."

Clearly then hydraulic fracturing is a major tool used by the oil and gas industry worldwide and not just in the newer unconventional or tight gas fields.

Fracture stimulation in this industry typically uses injected fluid that includes additives, many of which are proprietary, and proppant. The latter is typically graded sand (20/40 grade being mostly favoured) but the type, size, and amount selected are based on closure stress and

http://dx.doi.org/10.5772/56114

conductivity of the fracture needed for the desired stimulation effect. The function of the proppant when injected into fractures is to keep them open after the fracturing pressure dissipates. Most of the injectate additives are designed to increase the proppant carrying capacity of the fluid.

Because the formation being treated generally is already permeable, very high injection flow rates are necessary in order to build pressure in the treatment region. To quote from [9]:

"As the resistance to flow in the formation increases, the pressure in the wellbore increases to a value that exceeds the breakdown pressure of the formation that is open to the wellbore. Once the formation "breaks-down", a crack or fracture is formed, and the injected fluid begins moving down the fracture."

Injection pressures typically range up to around 6,000 psi but can be as high as 20,000 psi. The total volume of injected fluid is generally very high at greater than 1 ML (10^6 Litres).

2.5. Geothermal (Hot dry rock, or "enhanced" geothermal)

Enhanced geothermal energy production (EGS) involves the injection of water in a well, heating the water in the subsurface, and extraction of the same water as steam or hot water from a second well. Hydraulic fracturing is utilized to establish a flow pathway between the injection and extraction wells. The magnitude of fracturing operations for EGS is dependent on the well spacings required to achieve effective heat transfer for each particular project.

EGS wells have typically been stimulated by injection at pressures below or just up to the minimum principal stress magnitude. This increases the pressure in the reservoir and promotes shear slip on existing natural fractures. Hydraulic fracturing associated with enhanced geothermal energy production has been undertaken at least since the work reported in [10] and its precursors. This early work being more "proof of concept" generally seems to have involved quite small hydraulic fracture treatments. More recent developments such as that in planning adjacent to the Newbury volcano in Oregon [11] envisage much more large scale stimulation to open up large subterranean contact areas to injected water for the large scale production of steam. Although scant information on the scale of these projects is available, it is assumed that they will involve hydraulic fracture treatments similar to those employed in conventional oil and gas reservoirs.

2.6. Carbon sequestration (Carbon capture and storage)

Quoting from [12]:

"Geologic carbon sequestration is becoming an increasingly viable method for reducing the rate of greenhouse gas emissions through the injection of CO2 into geologic reservoirs."

The range of suitable "geologic reservoirs" includes coal basins, depleted oil and gas reservoirs and saline aquifers. Although this technology is still under development with many studies being conducted worldwide there is, as yet, no large scale development. It is anticipated, depending on the storage target and it is noted that the targets mentioned above are high permeability reservoirs, that hydraulic fracturing may play a role in this industry. Again, we have assumed that hydraulic fracturing in this role will be similar in scale to that employed in conventional oil and gas.

2.7. Coalbed Methane (CBM) development

Hydraulic fracturing in CBM wells is performed in similar fashion and for similar purposes as for conventional oil and gas wells [9]. The major difference is that of scale in that the CBM reservoirs, normally being nearer to surface, require lower pressures, less volume and fewer (if any) additives in the fracturing fluid.

Fracture pressures are up to 5,000 psi and total injected volume per fracture ranging up to 500,000 litres.

2.8. Coal Mine Methane (CMM) drainage

The objective of CMM drainage is to reduce the methane content of coal seams prior to mining both for safety and environmental reasons and also as an additional revenue stream. Hydraulic fracturing both with and without sand proppant is used to enhance the production of methane from the coal. These treatments are conducted from both vertical holes and horizontal, in-seam drill holes. The scale of treatments varies widely but are typically smaller than CBM stimulation fractures, especially if carried out from underground.

2.9. Rock burst mitigation

This is a relatively new area of application for hydraulic fracturing and remains in the early evaluation stage with no large scale deployment as yet. As noted in [13], hydraulic fracturing is being investigated as a means of reducing in-situ rock stress to ameliorate the frequency and severity of rock burst incidents.

Typically such work is being performed in small diameter boreholes at high pressure but low flow rates, similar to those encountered in stress testing although more effort is made towards propagation of the fractures.

3. Characterization

What do all of these applications have in common, and how do they differ? To differentiate, we'll look at some of the physical aspects of fracturing:

Injectate Volume – How much fluid is injected? Note that we could also consider injection flow rate here although the total volume injected is clearly related to flow rate.

http://dx.doi.org/10.5772/56114

Nature of the Injectate: Is it just water or does it include chemical additives?

Proppant: Is proppant being injected to hold the fracture open after treatment?

Fracture Propagation: Are we creating a fracture simply to determine the strength of the rock and stopping, or after initiation, are we going to try to propagate that fracture further?

Pressure: What pressures are applied?

Fracture/NoFracture: Are we actually creating new fractures, or simply opening existing fractures? Are there certain applications that really aren't fracturing at all?

A consideration of each of the above activities in relation to the suggested characterization criteria is given in Table 1.

4. Terminology to differentiate hydraulic fracturing

From Table 1 it may be seen that pressures tend to be relative to the treatment depth as would be expected. Those treatments based on conventional oil and gas methods are necessarily similar – all using additives of some sort and usually proppant to keep fractures open. In fact, the composition of the injected fluid may be viewed as one of the major differentiating characteristics between different types of treatments.

Application	Injectate Volume (L)	Additives	Proppant	Pressure	Propagation	True Frac
O&G Tight Reservoirs	10^6	Yes	Yes	Up to 15K psi	Yes	Yes
Water Wells	$<10^3$	No	Some	<3,000 psi	Yes	Few
Block Cave Mining	10^4	No	Some	<10K psi	<100m	Yes
Rock Stress Testing	$<10^3$	No	No	<15K psi	Limited	Yes
Conventional Oil & Gas	10^6	Yes	Yes	Up to 15K psi	Yes	Yes
Enhanced Geothermal	10^7	Yes	Yes	Up to 15K psi	Yes	Yes
Carbon sequestration	10^6	Yes	Yes	Up to 10K psi	Yes	Yes
CBM	$<5x10^5$	Some	Yes	<5Kpsi	Yes	Yes
CMM	10^4	Some	Some	<5Kpsi	Yes	Yes
Rock Burst Mitigation	$<10^3$	No	No	<15K psi	Limited	Yes

Table 1.

Another major differentiating characteristic is the volume of injected fluid. Smaller hydraulic fracturing treatments, such as those for stress testing use small volumes of fluid where as larger treatments, such as conventional oil and gas use large volumes of fluid. Therefore, it is

proposed that these characteristic are those which should be chosen as the defining characteristic for a terminology to differentiate between different "types" of hydraulic fracturing with injected volume taking the primary role.

An obvious approach would be to use the terms, mini-frac, midi-frac, macro-frac, etc, however the term mini-frac is already in use for both stress testing and for conventional and unconventional oil and gas. Alternatively, to use, for example, Class 1, 2, 3, etc, is in danger of being confused with the USEPA well classification system.

It is suggested that a practical approach may be to rely on a "Typing" system such as that described below.

Type A – no actual new fractures created though exisiting fractures are opened and possibly washed out. This Type would apply to water well hydraulic fracturing and such geotechnical tests as hydro-jacking. As this is an "outlier" with no real fracture occurring it is felt unnecessary to specify the injected volume though it would be typically less than 10,000 litres.

Type B – new fractures are generated but little or no attempt is made to propagate these fractures. Examples would include stress testing and rock burst amelioration. Injected fluid volume is to be limited to less than a few hundred litres per fracture.

Type C – new fractures are generated and some attempt is made to propagate these fractures. Typically injected fluid volumes per fracture are to be limited to less than, say 100,000 litres per fracture. Hydraulic fracturing for block caving, CMM and possibly CBM would fall into this category. Given that these may also include proppant and or additives in the injected fluids some additional nomenclature is appropriate to account for these additions. In an attempt to keep it simple, this could be:

Type C – plain water

Type C-a – water with additives

Type C-p – water with proppant

Type C-ap – water with additives and proppant

Type D – new fractures are generated and these are propagated to the size required to produce the stimulation desired. Typically injected fluid volumes per fracture are more than, say 100,000 litres per fracture. Most CBM, conventional and multi-zonal, unconventional hydraulic fracturing would fit into this category. This Type would also use the suffix notation given above for Type C to further specify the injected fluids.

5. Conclusions

Hydraulic fracturing is a process used in many industries for different applications and purposes. It may be characterized and differentiated across this range of industries in terms of injected volume and the composition of the injected fluids.

A new terminology has been proposed to allow clear differentiation between the many different types of hydraulic fracturing operations. The purpose of this terminology is to enable practitioners, regulators and the general public a clear means of making the distinction between these many different operations.

Acknowledgements

The authors wish to acknowledge and express appreciation for the contribution of our reviewer, Rob Jefferies, to the correctness and completeness of this paper.

Author details

Joel Adams[1*] and Clem Rowe[2*]

*Address all correspondence to: joel@inflatable-packers.com; clem@inflatable-packers.com

1 Inflatable Packers International LLC, Australia

2 Inflatable Packers International Pty Ltd, Australia

References

[1] BBC News UK online on 2/11/2011

[2] BBC News Europe online on 19/01/2012

[3] Williamson, W. H, & Woolley, D. R. Hydraulic fracturing to improve the yield of bores in fractured rock, Australian Government Publishing Service, (1980).

[4] TechnomineMining Technology. Block Caving http://technology.infomine.com/reviews/Blockcaving/welcome.asp?view=fullaccessed 5/01/(2013).

[5] Van As, A, & Jeffrey, R. G. Hydraulic Fracturing as a Cave Inducement Technique at Northparkes Mine, MassMin 2000 Proceedings, (2000). , 165-172.

[6] Private communication

[7] Astm, D. Standard Test Method for Determination of the In-Situ Stress in Rock Using the Hydraulic Fracturing Method

[8] MontgomeryCarl T. and Smith, Michael B. Journal of Petroleum Technology, Dec. (2010). Hydraulic Fracturing- History of an Enduring Technology., 26-32.

[9] USEPA R-04-003 Appendix A Hydraulic Fracturing White PaperJune (2004).

[10] Rummel, F, & Kappelmayer, O. The Falkenberg Geothermal Frac Project: Concepts and Experimental Results, In: Nemat-Nasser S, Abé H., Hirakawa S (ed) Hydraulic Fracturing and Geothermal Energy, (1983). , 59-74.

[11] Wired Science: Energy Company Plans to Frack a Volcanoreported 10.04.(2012). http://www.wired.com/wiredscience/2012/10/newberry-volcano-fracking/accessed 6/01/2013)

[12] Johnson, S. M, & Morris, J. P. Hydraulic Fracturing Mechanisms In Carbon Sequestration Applications, 43rd U.S. Rock Mechanics Symposium & 4th U.S.- Canada Rock Mechanics Symposium, June July 1, (2009). Asheville, North Carolina, 28.

[13] Yan Jun FengXiu Wei Shi, Hydraulic Fracturing Process: Roles of In Situ Stress and Rock Strength, (2012). Advanced Materials Research, 616-618, 435

Chapter 19

Initiation and Breakdown of an Axisymmetric Hydraulic Fracture Transverse to a Horizontal Wellbore

Safdar Abbas and Brice Lecampion

Additional information is available at the end of the chapter

http://dx.doi.org/10.5772/56262

Abstract

We investigate the initiation and early-stage propagation of an axi-symmetric hydraulic fracture from a wellbore drilled in the direction of the minimum principal stress in an elastic and impermeable formation. Such a configuration is akin to the case of a horizontal well and a hydraulic fracture transverse to the well axis in an open hole completion. In addition to the effect of the wellbore on the elasticity equation, the effect of the injection system compressibility is also taken into account. The formulation accounts for the strong coupling between the elasticity equation, the flow of the injected fluid within the newly created crack and the fracture propagation condition. Dimensional analysis of the problem reveals that three dimensionless parameters control the entire problem: the ratio of the initial defect length over the wellbore radius, the ratio between the wellbore radius and a length-scale associated with the fluid stored by compressibility in the injection system during the well pressurization, and finally the ratio of the time-scale of transition from viscosity to toughness dominated propagation to the time-scale associated with compressibility effects. A fully coupled numerical solver is presented, and validated against solutions for a radial hydraulic fracture propagating in an infinite medium. The influence of the different parameters on the transition from the near-wellbore to the case of a hydraulic fracture propagating in an infinite medium is fully discussed.

1. Introduction

In this study, we are interested in the initiation of hydraulic fractures from an open-hole horizontal well. Horizontal wells are drilled preferably in the direction of the minimum

horizontal stress in order to create hydraulic fractures perpendicular to the wellbore and therefore maximize the drainage from the reservoir. During the pressurization of the wellbore, tangential tensile stress is generated which can result in the initiation of longitudinal fractures parallel to the wellbore axis [1,2]. In an isotropic elastic medium, depending upon the stress field, the initiation of fractures transverse to the wellbore axis is favored by creating an initial flaw, i.e. an axisymmetric notch, of sufficient depth [3] (see Figure. 1 for a sketch). We focus solely on transverse hydraulic fractures in this contribution.

In the initial stage of propagation, these transverse fractures can be idealized as axisymmetric (radial) fractures around the wellbore until they hit a stress barrier or other type of heterogeneities. We investigate the initiation and propagation of such a fracture under constant injection of a Newtonian fluid, focusing on the case of "tight" rocks where leak-off is typically negligible. In particular, we are interested in clarifying when the effects associated with the near-wellbore region dissipate and no longer affect the hydraulic fracture propagation and how this transition takes place.

The initiation and the early stage of the propagation of such a hydraulic fracture is affected by two "near wellbore" effects: i) the finiteness of the wellbore and the initial flaw length and ii) a transient phenomenon associated with the release of the fluid stored by compressibility in the wellbore during the pressurization phase prior to the initiation of the fracture. This second effect is ultimately linked to the compressibility of the injection system (i.e. mostly the fluid volume stored by compressibility within the wellbore). These effects have been investigated for the case of plane-strain fractures in [4,5] and for the case of axisymmetric hydraulic fractures driven by an inviscid fluid (i.e. zero-viscosity) in [6]. In this paper, we extend these contributions to the case of viscous flow in axi-symmetric fractures.

A detailed dimensional analysis is performed indicating various time scales, length scales and dimensionless numbers controlling the problem. A numerical solver, along the lines of previous contributions [7,8], is presented. A series of numerical simulations are performed in order to study the transition from the near-wellbore propagation regime to the case of a radial hydraulic fracture in an infinite medium under constant injection rate.

2. Problem statement

Let us consider a horizontal well of radius a drilled in the direction of the minimum horizontal stress σ_h. In this ideal configuration, we are interested in the initiation and propagation of a hydraulic fracture from a radial axisymmetric notch of length l_o transverse to the wellbore (Figure. 1). As previously mentioned, we assume that the radial notch length is sufficient to favor a transverse fracture as compared to a longitudinal one (see [3] for discussion on the effect of the stress field on the competition between transverse and longitudinal fracture initiation).

In the absence of any stress barriers or other heterogeneities, this axisymmetric transverse fracture of radius R will transition toward a penny-shaped geometry when its radius is much greater than the wellbore radius (Figure. 1). We will denote as p_f the fluid pressure inside the fracture

http://dx.doi.org/10.5772/56262

(and in the wellbore), $p = p_f - \sigma_h$ the net pressure opening the fracture face and w the corresponding fracture width. The axial stress variation azimuthally around the wellbore is given by [9]

$$\sigma_a = \sigma_h - 2\nu\left(\sigma_H - \sigma_v\right)\frac{a^2}{r^2}\cos 2\theta \tag{1}$$

where r and θ are the polar coordinates centered at the wellbore, σ_H is the maximum horizontal stress, σ_v is the vertical stress, ν is the poisson's ratio and a is the wellbore radius. The azimuthal average of the axial stress (i.e. integrating the above equation from $\theta = 0$ to $\theta = 2\pi$) reduces to σ_h. We will neglect the azimuthal variation of the axial stress close to the wellbore wall as a first approximation. The axial stress therefore reduces to the minimum horizontal stress. Under such an approximation, the model is truly axi-symmetric, i.e. independent of θ.

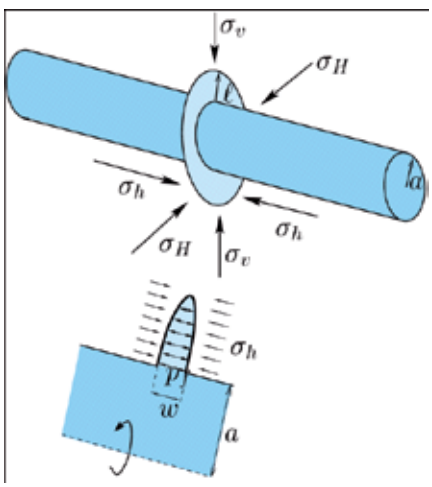

Figure 1. Sketch of a transverse fracture propagating from a horizontal wellbore (top), axisymmetric model (bottom)

2.1. Elasticity

The relation between the fracture width and the net loading acting on the crack is expressed by a hyper-singular boundary integral equation following the method of distributed dislocations [10]:

$$p\left(r\right) = p_f(r) - \sigma_h = \frac{E'}{2\pi}\int_a^{a+l} J\left(r, r'\right)\frac{\partial w(r')}{\partial r'}dr' \tag{2}$$

where the singular kernel $J\left(r, r'\right)$ is given by [11]. It provides the normal stress due to an axisymmetric dislocation around a wellbore of radius a. Details of this kernel are recalled in Appendix A for completeness.

2.2. Fluid flow

We neglect the fluid compressibility compared to the fracture compliance as is usually done in modeling hydraulic fractures. The balance of mass then reduces to a strict volume balance:

$$\frac{\partial w}{\partial t} + \frac{1}{r}\frac{\partial}{\partial r}(rq) = 0 \tag{3}$$

Under the hypothesis of lubrication theory (low Reynolds number flow) for a Newtonian fluid, the fluid flux q is given by Poiseuille law

$$q = -\frac{w^3}{\mu'}\frac{\partial p}{\partial r} \tag{4}$$

where $\mu' = 12\mu$ with μ the fluid viscosity.

2.3. Boundary conditions

During the propagation of a hydraulic fracture, a fluid lag may develop at the tip of the fracture [12,13]. Such a fluid lag is larger at early time during the propagation. In order to check whether the fluid lag should be taken into account, we can estimate the characteristic timescale associated with the disappearance of the fluid lag, which is equal to $t_{om} = \frac{E'^2 \mu'}{\sigma_o^3}$ (see [14,7]), where σ_o denotes the far-field confining stress (here the minimum horizontal stress). This timescale is inversely proportional to σ_o^3 which means that for higher values of the confining stress this timescale is very small (typically the case in deep formations). For illustration, we use stress typical of an unconventional reservoir (e.g. Barnett shale) and typical rock parameters:

$$E = 5.4 \times 10^6\ psi, \quad \nu = 0.21, \quad \sigma_o = \sigma_h = 3390\ psi \text{ (at the depth of } 5000\, ft), \quad K_{Ic} = 1500\ psi/\sqrt{in}. \tag{5}$$

For the case of a slick water stimulation (viscosity of 1 cP), the characteristic time t_{om} is equal to 0.0014 sec. For a gel treatment (tangent viscosity of approximately 100 cP), this characteristic time still remains small, $t_{om} = 0.14\ sec$. The transient effect associated with the disappearance of the fluid lag can thus be ignored for the conditions typically encountered in slick water fracturing of deep horizontal wells (i.e. in the Barnett shale). In the remaining of this paper, we assume that the fluid front coincides with the fracture front.

The conditions at the tip of the fracture are thus:

$$q(r = l + a) = 0 \qquad w(r = l + a) = 0. \tag{6}$$

http://dx.doi.org/10.5772/56262

The fluid flux entering the fracture is equal to the total fluid injection rate (for example the injection rate at the wellhead) minus the fluid volume stored in the well due to its compressibility (essentially the compressibility of the fluid inside the wellbore). Therefore, from the fluid mass conservation in the wellbore (between the injection point and the fracture inlet), one can write the following boundary condition at the inlet of the fracture:

$$q = \frac{1}{2\pi a}\left(Q_o - U\frac{\partial p_b}{\partial t}\right), \tag{7}$$

where U (*barrels / psi*) is the injection system compressibility and p_b denotes the wellbore pressure. Pressure continuity is ensured at the fracture in-let by the following condition

$$p_f(r=a) = p_b. \tag{8}$$

It is important to note that no friction pressure drop (e.g. perforation drop) is taken into account in this injection boundary condition.

2.4. Initiation and fracture propagation condition

Prior to any opening of the initial defect of length l_o, the pressurization rate is uniform ($q=0$ in Equation (7)). We thus start the simulation only when the fluid pressure in the wellbore and in the notch has reached the minimum horizontal stress, which is the pressure at which this initial defect starts to open: we will denote this start-up time t_o. For modeling purposes, at t_o, the initial condition will be taken as a vanishingly small net pressure (i.e. a fluid pressure just slightly above the minimum horizontal stress). Due to the continuous fluid injection considered here, the wellbore pressure keeps increasing. The fracture will initiate its growth once the stress intensity factor reaches its critical value K_{Ic}, i.e. the fracture toughness of the rock. Once fracture initiation has occurred, we assume that the fracture propagates under quasi-static equilibrium such that the stress intensity factor is always equal to its critical value. For a pure mode I fracture considered here, this condition can be expressed as an asymptote on the fracture opening near the tip:

$$w \sim \frac{K'}{E'}\left((l+a)-r\right)^{1/2} \qquad 1-\frac{r}{(l+a)} \ll 1\,. \tag{9}$$

where $K' = \sqrt{32/\pi}\,K_{Ic}$

3. Scaling

Let us scale the variables involved in the problem in order to grasp the effects of various physical phenomena acting at various scales. We introduce a characteristic length scale $L_\star$,

characteristic fracture width $w_\star$, characteristic pressure $p_\star$, characteristic fluid flux $q_\star$, and a characteristic time $t_\star$ and scale the variables as follow:

$$r = L_\star \rho, \quad l = L_\star \gamma, \quad a = L_\star \mathcal{G}_a, \quad p = p_\star \Pi, \quad w = w_\star \Omega, \quad q = q_\star \Psi, \quad t = t_\star \tau, \tag{10}$$

ρ, γ and $\mathcal{G}_a$ denotes respectively the dimensionless coordinate along the fracture, the dimensionless fracture length and the dimensionless wellbore radius. The dimensionless opening, net pressure and fluid flux are denoted as Ω, Π and Ψ respectively.

Using the above scaling, the governing equations are converted to dimensionless form where the different scales are yet to be defined:

- Elasticity operator

$$\Pi = \frac{\mathcal{G}_e}{2\pi \mathcal{G}_a} \left(\int_1^{1+\gamma/\mathcal{G}_a} J(\rho, \rho') \frac{\partial \Omega(\rho')}{\partial \rho'} d\rho' \right) \tag{11}$$

where $\mathcal{G}_e = \frac{E' w_\star}{p_\star L_\star}$ is a dimensionless group associated with the elasticity operator and $\mathcal{G}_a = \frac{a}{L_\star}$ is a dimensionless group associated with the effect of the wellbore radius.

- Continuity equation

$$\frac{\partial \Omega}{\partial \tau} + \mathcal{G}_r \frac{1}{\rho} \frac{\partial}{\partial \rho} (\rho \Psi) = 0 \tag{12}$$

where $\mathcal{G}_r = \frac{t_\star q_\star}{w_\star L_\star}$ is a dimensionless group associated with fluid conservation within the fracture.

- Poiseuille law for lubrication

$$\Psi = -\frac{\Omega^3}{\mathcal{G}_m} \frac{\partial \Pi_f}{\partial \rho} \tag{13}$$

where $\mathcal{G}_m = \frac{\mu' q_\star L_\star}{w_\star^3 p_\star}$ is a dimensionless group associated with fluid viscosity.

- Inlet boundary condition

$$\Psi = \frac{1}{2\pi} \left(\mathcal{G}_q \Psi_o - \mathcal{G}_U \frac{\partial \Pi_b}{\partial \tau} \right) \tag{14}$$

http://dx.doi.org/10.5772/56262

where $\mathcal{G}_q = \frac{Q_o}{L_\star q_\star}$ is a dimensionless group associated with the effect of the injection rate, and $\mathcal{G}_U = \frac{U p_\star}{L_\star q_\star t_\star}$ is a dimensionless group associated with the injection system compressibility.

- The LEFM propagation condition reduces to

$$\Omega \sim \mathcal{G}_k \left((\gamma + \mathcal{G}_a) - \rho \right)^{1/2}, \qquad \text{for} (\gamma + \mathcal{G}_a) - \rho \ll 1 \tag{15}$$

where $\mathcal{G}_k = \frac{K' \sqrt{L_\star}}{E' w_\star}$ is a dimensionless group associated with the rock fracture toughness.

First, it is natural to set the dimensionless groups associated with the injection rate $\mathcal{G}_q$ (we inject fluid) and elasticity $\mathcal{G}_e$ to unity. In setting $\mathcal{G}_e$ to 1, we account for the fact that the crack opening is typically much smaller than the fracture length and that the net pressure is also much smaller than the rock elastic modulus. The dimensionless group associated with fluid conservation $\mathcal{G}_r$ is also set to unity to account for the fact that injected fluid volume remains in the fracture in the absence of leak-off.

In the case of the propagation of a radial hydraulic fracture in an infinite medium, energy dissipation is attributed to two competing mechanisms i.e. viscous forces associated with fluid flow within the crack and the creation of new fracture surfaces (i.e. fracture toughness) [15]. At the beginning of the propagation, i.e. for small fracture radius, viscous forces are the dominant dissipative process, and fracture toughness can be neglected in such a viscosity dominated regime of propagation. A self-similar solution has been obtained in [15] for that case, and will be denoted as the M-vertex solution. As time increases, fracture energy slowly takes over viscous forces as the main dissipative mechanism. Ultimately, at large time, the fracture propagates in the so-called toughness dominated regime of propagation, where viscosity can be neglected. Here again, an analytical solution exists [16], and will be referred as the K-vertex solution. In an infinite medium, the radial hydraulic fracture therefore transition from the viscosity (M) to the toughness (K) regime of propagation.

This picture is modified when accounting for near-wellbore effects. These effects will eventually dissipate for fracture length much larger than the wellbore radius. This transition from the near-wellbore to the infinite medium solution is of particular interest. The effect of the wellbore and of the system compressibility will affect the system response at early time, i.e. when the radius of the fracture is comparable to that of the wellbore and when the system compressibility still has an effect. At large time, the transient associated with the fracture breakdown and the release of the fluid stored by compressibility prior to the crack initiation will become insignificant: i.e. the fluid flux entering the crack will then be equal to the injected flow rate. The solution will thus behave as the infinite medium solution [15,16,17].

It is therefore interesting to introduce two different scaling. The first scaling relates to the case where the system compressibility and toughness are important, i.e. at early time or for small fractures. We will denote such a scaling as the Compressibility-Toughness scaling and denote it asUK. This scaling is based on the characteristic time of transition from the compressibility

effects (U) to the infinite medium solution corresponding to toughness dissipation (K). The characteristic scales in that Compressibility-Toughness scaling are obtained as:

$$L_{uk}=(E'U)^{1/3},\quad p_{uk}=\frac{K'}{E'^{1/6}U^{1/6}},\quad w_{uk}=\frac{K'U^{1/6}}{E'^{5/6}},\quad q_{uk}=\frac{Q_o}{E'^{1/3}U^{1/3}},\ t_{uk}=\frac{K'U'^{5/6}}{E'^{1/6}Q_o} \tag{16}$$

In particular, the dimensionless time in that scaling is $\tau=\frac{t}{t_{uk}}$. The corresponding dimensionless numbers are:

$$\mathcal{G}_{muk}=\frac{E'^{8/3}Q_o\mu'}{K'^4U^{1/3}},\quad \mathcal{G}_{quk}=1,\quad \mathcal{G}_{Uuk}=1,\ \mathcal{G}_{kuk}=1,\ \mathcal{G}_{auk}=\frac{a}{(E'U)^{1/3}} \tag{17}$$

The second scaling of interest corresponds to the case where the transient effects associated with the wellbore and injection compressibility have vanished: i.e. when the model reduces to the case of radial fracture propagating in an infinite medium – we will call this scaling the Viscosity-Toughness scaling and denote it as MK. This scaling is based on the characteristic time of transition from the viscosity dissipation (M) to the toughness dissipation (K). The corresponding characteristic scales are [15]:

$$L_{mk}=\frac{E'^3Q_o\mu'}{K'^4},\ p_{mk}=\frac{K'^3}{E'^{3/2}\sqrt{Q_o\mu'}},\ w_{mk}=\sqrt{\frac{E'Q_o\mu'}{K'^2}},\ q_{mk}=\frac{K'^4}{E'^3\mu'},\ t_{mk}=\frac{E'^{13/2}Q_o^{3/2}\mu'^{5/2}}{K'^9} \tag{18}$$

The dimensionless time is here defined as $\tilde{\tau}=\frac{t}{t_{mk}}$ and the different dimensionless numbers in that scaling are given as

$$\mathcal{G}_{mmk}=1,\quad \mathcal{G}_{qmk}=1,\quad \mathcal{G}_{Umk}=\frac{K'^{12}U}{E'^8Q_o^3\mu'^3},\ \mathcal{G}_{kmk}=1,\ \mathcal{G}_{amk}=\frac{aK'^4}{E'^3Q_o\mu'} \tag{19}$$

In order to grasp the transition from the early time where the near-wellbore effects are important to the large-time solution of propagation in an infinite medium, we introduce χ as the ratio of the timescales associated with the previously defined scalings:

$$\chi=\frac{t_{mk}}{t_{uk}}=\frac{E'^{20/3}Q_o^{5/2}\mu'^{5/2}}{K'^{10}U^{5/6}}. \tag{20}$$

Large values of χ corresponds to high viscosity μ' and/or low injection system compressibility U. In this case, the transition from the near wellbore solution to the infinite medium solution occurs prior to the transition from the viscosity (M) to the toughness (K) dominated regime of propagation of an infinite radial hydraulic fracture. Smaller values of χ correspond to lower viscosity/higher injection system compressibility. In this case the transition from near wellbore solution to the infinite medium solution occurs in the K regime of the infinite medium solution.

http://dx.doi.org/10.5772/56262

Now introducing $\mathcal{A}=\mathcal{G}_{a_{uk}}=\frac{a}{(E'U)^{1/3}}$, the ratio between the wellbore radius and a lengthscale associated with the volume stored in the injection system by compressibility, the dimensionless numbers for the two scalings previously presented can be written as:

$$\mathcal{G}_{m_{uk}}=\chi^{2/5}, \quad \mathcal{G}_{a_{uk}}=\mathcal{A} \tag{21}$$

and

$$\mathcal{G}_{U_{mk}}=\chi^{-6/5}, \mathcal{G}_{a_{mk}}=\mathcal{A}\chi^{-2/5} \tag{22}$$

Correspondence between the two scalings can also be obtained as the function of χ:

$$\frac{L_{mk}}{L_{uk}}=\chi^{2/5}, \quad \frac{w_{mk}}{w_{uk}}=\chi^{1/5}, \quad \frac{p_{mk}}{p_{uk}}=\chi^{-1/5}, \quad \frac{q_{mk}}{q_{uk}}=\chi^{-2/5}, \tag{23}$$

$$\frac{\mathcal{G}_{m_{mk}}}{\mathcal{G}_{m_{uk}}}=\chi^{-2/5}, \quad \frac{\mathcal{G}_{U_{mk}}}{\mathcal{G}_{U_{uk}}}=\chi^{-6/5}, \quad \frac{\mathcal{G}_{a_{mk}}}{\mathcal{G}_{a_{uk}}}=\chi^{-2/5}. \tag{24}$$

In addition to the above mentioned factors, the ratio of dimensionless initial defect length γ_o to the dimensionless wellbore radius $\mathcal{A}$ also effects the hydraulic fracture initiation. It can be concluded here that the problem of axisymmetric hydraulic fracture depends only on three dimensionless parameters: the timescale ratio χ, dimensionless wellbore radius $\mathcal{A}$ and the ratio of the initial defect length to the wellbore radius $\frac{l_o}{a}=\frac{\gamma_o}{\mathcal{A}}$.

3.1. Field and laboratory conditions: Scaling

Laboratory experiments are typically performed in order to study one particular aspect of a problem independently. Results of these experiments are then complemented by numerical and theoretical studies and ultimately verified by field experiments. Conditions in the laboratory experiments should be controlled in such a manner that they represent as close as possible a scaled version of the field conditions to be investigated. The scaling and the dimensionless parameters, described in the previous section, are thus critical in identifying the key parameters to simulate the right physics in the laboratory [18].

We will compare the different scales (in the Compressibility-Toughness scaling UK) of the problem for "typical" laboratory and field conditions in order to illustrate their differences and the need to carefully design laboratory experiments. It is worthwhile to recall that these scaling are based on the assumption of an axisymmetric fracture initiating from a circular notch. Parameters representative from the Barnett shale (5) are again considered for both the field conditions and the laboratory sample for illustration.

A typical wellbore diameter ($2a$) in the field is 8.75 *in* and a typical wellbore diameter in the laboratory is 1 *in*. The constant flow rate Q_o in the field is about 20 *barrels / min* and in the

laboratory setting is around 5 ml/min. The pressurization rate β before breakdown in the field will be taken as 60 psi/s due to higher pumping rates in the field whereas in the laboratory it is about 1.2 psi/s. The wellbore compressibility U results from the compressibility of the fluid in the wellbore and the injection lines, as well as the compressibility of the wellbore and injection lines themselves. It is expressed as the ratio between the constant flow rate and the pressurization rate $U = Q_o/\beta$. The typical fluid used in the field is slick water [19] with a viscosity of 1 cP. We consider glycerin as the fluid used in the laboratory with viscosity 1000 cP.

The compressibility length scale L_{uk} and time scale t_{uk} corresponding to these parameters are displayed in Table 1. It is shown in the previous section that the dimensionless parameters depend upon the two dimensionless numbers i.e. $\mathcal{A}$ and χ. These dimensionless numbers are also given in Table 1. While L_{uk} and t_{uk} give the length and the timescale associated with the compressibility effects, the value of χ determine the infinite medium propagation regime after the dissipation of compressibility effects. Large value of χ i.e. ($\chi > 1$) means that the fracture will propagate in the viscosity regime whereas, smaller values of χ i.e. ($\chi < 1$) means that the fracture will propagate in the toughness regime after the dissipation of compressibility effects.

		Field	Laboratory
Length scale of transition from the compressibility effects to the infinite medium propagation	L_{uk}(ft)	56	2.4
Timescale of transition from the compressibility effects to the infinite medium propagation	t_{uk}(sec)	3	743
Ratio of the timescales	χ	14	0.0036
Dimensionless wellbore radius	$\mathcal{A}$	0.0065	0.017

Table 1. Characteristic length scales and dimensionless parameters for the field and the laboratory conditions.

It is obvious from Table 1, that in the field, the fracture propagates in the viscosity dominated regime ($\chi > 1$) whereas in the laboratory for the parameters chosen here, the fracture propagates in the toughness dominated regime ($\chi < 1$) after the dissipation of the early-time compressibility effects. For the field conditions, the compressibility length scale is equal to 56 ft. Which means that the propagation in the field is dominated by the compressibility effect until the fracture reaches about 56 ft (i.e. 150 times the wellbore radius) in to the formation. Even though this is a large value as compared to the wellbore radius, the length scale is still small as compared to the final fracture length which may be of the order of 800 to 1000 ft in the field. For laboratory conditions, the length scale is 2.4 ft (i.e. about 60 times the wellbore radius) which is smaller as compared to the field conditions, still the length-scale is large enough as compared to the specimen size that entire fracture propagation is dominated by the injection system compressibility.

The previous example has emphasized the differences with field conditions for a particular set of experimental parameters. However, these laboratory parameters can be appropriately adjusted in order to study a given regime of propagation. There can be different goals for an

http://dx.doi.org/10.5772/56262

experimental campaign. For example, if the goal is to study hydraulic fracture propagation then the compressibility effects must be reduced in order to speed up the convergence to the infinite medium solution. These effects can be reduced by manipulating the material of the test block, using smaller injection lines and by using needle control valves as it was done for example in [20,21].

4. Numerical algorithm

The governing equations are solved in their dimensionless form described in Section 3. The elasticity equation is discretized by Displacement Discontinuity Method (DDM) using piecewise constant elements with the tip element correction [22] for better accuracy. The fluid flow is discretized by the finite volume method.

At time t_n, the fracture length is given as γ_n, fracture opening as Ω_n and net pressure Π_n. The algorithm consists of two nested loops. In the outer loop (time-stepping loop), a fracture increment $\Delta\gamma = \Delta\rho$ is specified and the time step $\Delta\tau_n$, for which the tip asymptotic condition (15) is satisfied, is found iteratively. In the inner loop (i.e. the Reynolds solver), the coupled system of elasticity and lubrication equations are solved in order to find the fracture opening and pressure profiles corresponding to a given fracture length and (trial) time step. Details of the time stepping loop are given in Appendix B and the Reynolds Solver is described in Appendix C.

5. Results and discussion

The problem of the initiation of an axisymmetric hydraulic fracture from a wellbore depends only on three dimensionless parameters i.e. the timescale ratio χ, dimensionless wellbore radius $\mathcal{A}$ and the ratio of the initial defect length and the wellbore radius $\frac{l_o}{a} = \frac{\gamma_o}{\mathcal{A}}$. The parameter space for these three dimensionless quantities is now explored. We aim to see their effect on the transition to the analytical solution of a penny-shaped hydraulic fracture propagating in an infinite medium [15,17] as well as on the breakdown pressure (i.e. the maximum pressure recorded).

In Figure. 2, the evolution of fracture length γ, inlet opening $\Omega(0)$ and wellbore pressure Π_{wb} are plotted for different values of the timescale ratio χ for values of $\mathcal{A}$=0.1 and $\frac{\gamma_o}{\mathcal{A}}$=0.3. This is done in order to investigate the transition to the infinite medium solution. These results are presented in the Viscosity-Toughness (MK) scaling. The infinite medium solution goes from the viscosity dominated dissipation (M vertex solution) to the toughness dominated dissipation (K vertex solution). This transition is called the MK edge of the semi-infinite medium solution. It can be observed in Figure. 2 that fracture length, opening and wellbore pressure of our numerical solution accounting for the wellbore effects converges at large time to the MK edge solution in an infinite medium. The timescales ratio χ governs where the transient effects end along the MK edge of the infinite medium solution. For larger value

of χ, the transient effects end on the viscosity asymptote of the infinite medium solution, whereas for small value of χ, the transient effect ends on the toughness asymptote of the infinite medium solution. The fact that the infinite medium solution is recovered at large time ultimately validates the large time behavior obtained by our numerical algorithm.

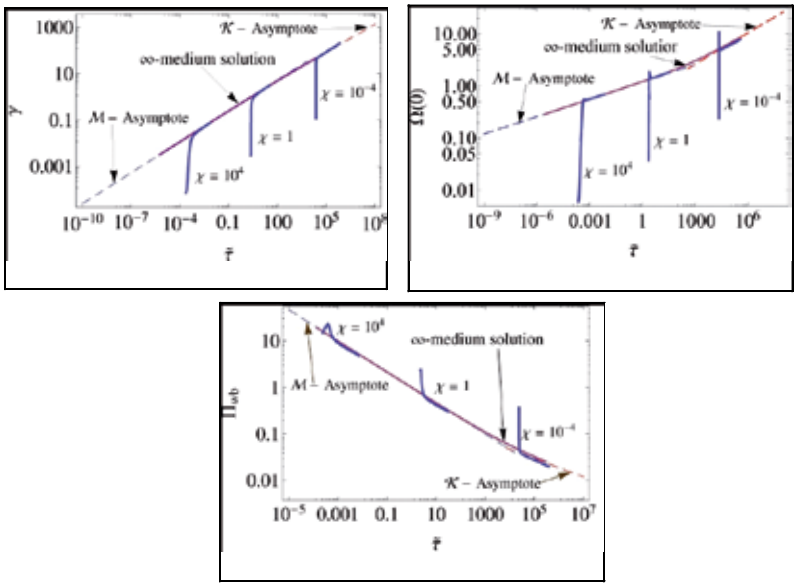

Figure 2. Effect of χ on the convergence of fracture length γ, inlet opening Ω and wellbore pressure Π_{wb} to the infinite medium propagation solution for $\gamma_o = 0.003$, $\mathcal{A} = 0.1$. The results are displayed in the *MK* scaling. The solid blue lines correspond to the simulation results, the dashed blue line is the M vertex solution, the dashed red line is the K vertex solution and the solid magenta line is the ∞ - medium solution.

It is also observed that the pressure and opening do not converge monotonically to the asymptotic solution. This is a characteristic feature of the near wellbore solution also obvious from Figure. 3 where the results are displayed in the Compressibility-Toughness (*UK*) scaling. Such a non-monotonic behavior is associated with fracture breakdown and is more pronounced for larger injection system compressibility, i.e. when the release of the stored fluid in the newly created fracture is more sudden.

The effects of χ on the breakdown pressure (defined as the maximum wellbore pressure), fracture length and effective flux entering the fracture are shown in Figure. 3 in the Compressibility-Toughness (*UK*) scaling. It has been observed that due to the strong fluid-solid coupling, the pressure in the wellbore keeps rising even after the fracture has already initiated. The pressure at which a fracture starts to propagate is called the initiation pressure and the highest pressure recorded is called the breakdown pressure. This difference in the initiation and the breakdown pressure has been observed theoretically [5,4] as well as experimentally [23] and it depends upon the fluid viscosity, injection rate and the system compressibility. It is observed from Equation (20) that low value of the timescale ratio χ corresponds to low viscosity and high injection system compressibility. It can be seen in Figure. 3 that the initiation pressure remains

http://dx.doi.org/10.5772/56262

similar while higher breakdown pressures are obtained for higher values of χ and lower breakdown pressures are obtained for lower values of χ. The breakdown is also much more abrupt for the case of low values of χ. Such an abrupt breakdown corresponds to the unstable crack growth in the limiting case of a inviscid fluid ($\chi < 10^{-4}$). Our numerical results are plotted along the inviscid solution of [6] in Figure. 4, where we can see that the numerical solution converges to the inviscid fluid solution for small χ. Similar results for the case of a plane-strain hydraulic fracture are reported in [5].

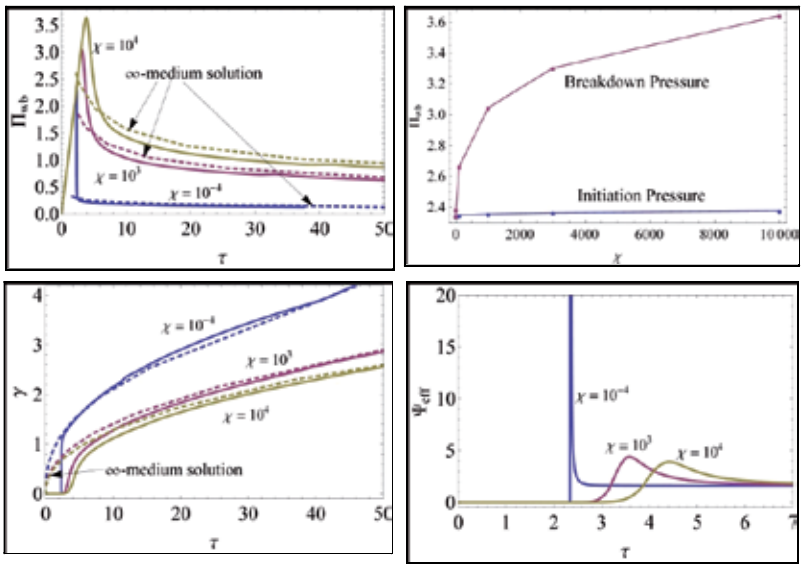

Figure 3. Effect of χ on the wellbore pressure Π_{wb}, fracture length γ and effective flux entering the fracture for $\gamma_o = 0.003$, $\mathcal{A} = 0.1$ in *UK* scaling. The blue coloured lines represent $\chi = 10^{-4}$, magenta colour lines represent $\chi = 10^3$ and the golden colour lines represent $\chi = 10^4$

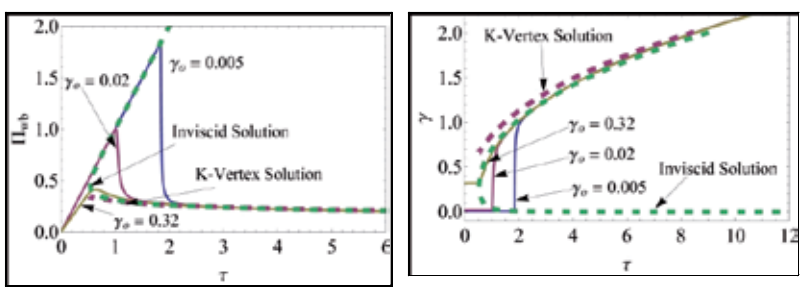

Figure 4. Unstable crack growth in the case of inviscid fluid for $\chi = 1.5 \times 10^{-4}$, $\mathcal{A} = 0.1$ in *UK* scaling. The blue coloured lines represent $\gamma_o = 0.005$, magenta colour lines represent $\gamma_o = 0.02$ and the golden colour lines represent $\gamma_o = 0.32$. The dashed magenta line represents the *K*-vertex solution whereas the dashed green line represents the inviscid fluid solution of [6].

Lastly, the value of $\frac{\gamma_\epsilon}{\mathcal{A}}$ is plotted against the values of χ in Figure. 5, where γ_ϵ is defined as the frature length γ for which the infinite medium solution has been reached within a given tolerence ϵ_∞ where

$$\epsilon_\infty = \frac{|\gamma_\infty - \gamma|}{|\gamma_\infty|}, \tag{25}$$

here γ_∞ is the fracture radius for the penny shaped fracture propagation in an infinite medium. It can be seen from Figure. 5, that γ_ϵ varies, for that case, from 11 to 13 times the wellbore radius for different values of χ. This variation shows that there is minimal effect of χ on the length to wellbore ratio at which the hydraulic fracture is no longer affected by near-wellbore effects.

Let us now compare the effect of different ratios of $\frac{\gamma_o}{\mathcal{A}} = \frac{l_o}{a}$ i.e. the ratio of the initial defect length to the wellbore radius. In Figure. 6, the dimensionless wellbore pressure, fracture length and effective flux entering the fracture are plotted for various ratios $\frac{\gamma_o}{\mathcal{A}}$ for $\chi = 1$ and $\mathcal{A} = 0.1$ in the Compressibility-Toughness (UK) scaling. It can be seen that higher breakdown pressures are obtained for lower ratios of $\frac{\gamma_o}{\mathcal{A}}$ and lower breakdown pressures are obtained for higher values of $\frac{\gamma_o}{\mathcal{A}}$. For lower values of $\frac{\gamma_o}{\mathcal{A}}$, there is a sudden drop in pressure after the breakdown similar to the behavior observed for a low viscosity fluid/ highly compressible injection system.

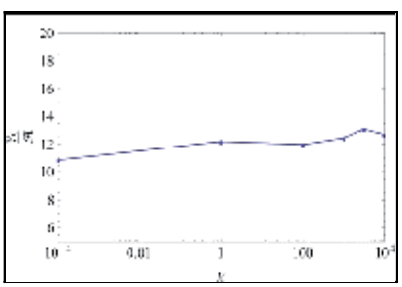

Figure 5. Effect of χ on the convergence to infinite space solution for $\frac{\gamma_o}{\mathcal{A}} = 0.003$ and $\mathcal{A} = 0.1$.

It can be seen from Figure. 6, that there is no significant difference in convergence to the infinite space solution for different ratios of $\frac{\gamma_o}{\mathcal{A}}$.

Finally, in Figure. 7, the effect of the dimensionless wellbore radius is considered for a fixed ratio $\frac{\gamma_0}{\mathcal{A}} = 0.1$ and $\frac{\gamma_0}{\mathcal{A}} = 0.01$. The results are displayed in the Compressibility-Toughness (UK) scaling. It is observed that the breakdown pressure is higher for a smaller dimensionless wellbore radius. It is to be noticed that the convergence of only one solution to the infinite medium solution is shown in the figure. All other solutions also converge to the infinite medium solution but at a

http://dx.doi.org/10.5772/56262

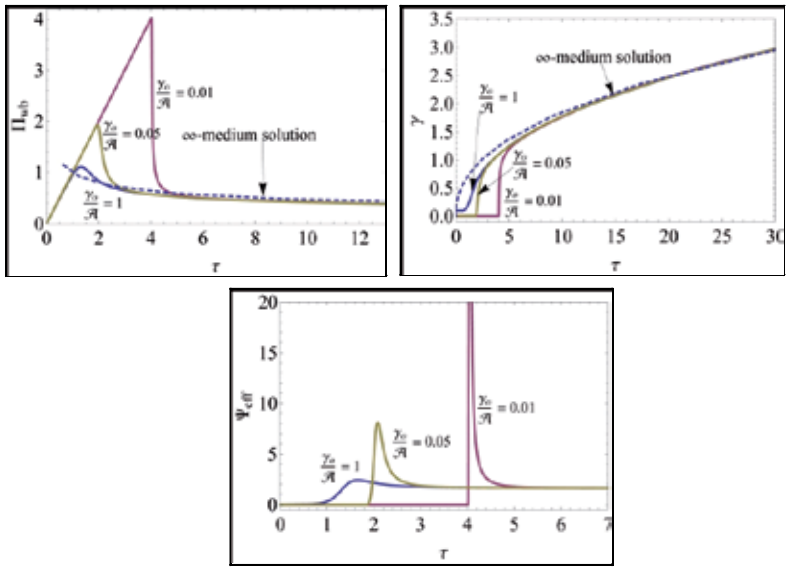

Figure 6. Effect of $\frac{\gamma_o}{\mathcal{A}}$ on the dimensionless wellbore pressure Π_{wb}, fracture length γ and effective flux entering the fracture for $\chi = 1$, $\mathcal{A} = 0.1$ in *UK* scaling. The blue coloured lines represent $\frac{\gamma_o}{\mathcal{A}} = 1$, golden colour lines represent $\frac{\gamma_o}{\mathcal{A}} = 0.05$ and the magenta colour lines represent $\frac{\gamma_o}{\mathcal{A}} = 0.01$.

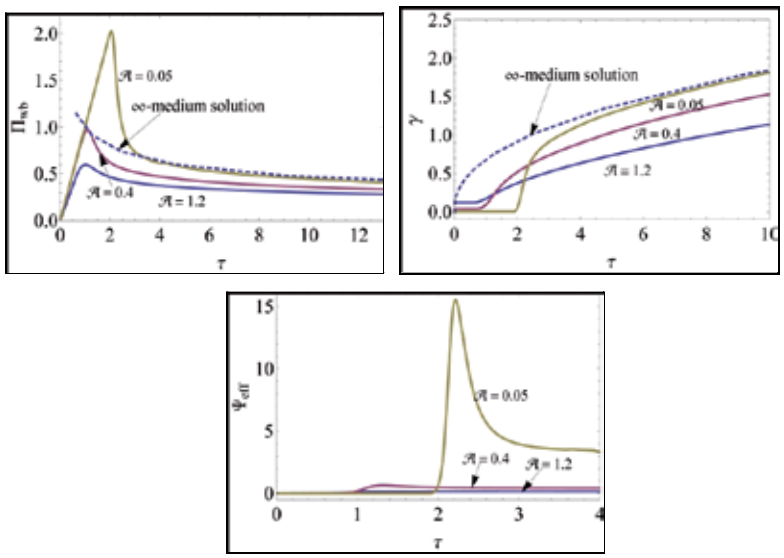

Figure 7. Effect of $\mathcal{A}$ on the wellbore pressure Π_{wb}, fracture length γ and effective flux entering the fracture for $\chi = 1$, $\frac{\gamma_0}{\mathcal{A}} = 0.1$ in *UK* scaling. The blue coloured lines represent $\mathcal{A} = 1.2$, magenta colour lines represent $\mathcal{A} = 0.4$ and the golden colour lines represent $\mathcal{A} = 0.05$

larger time which is not shown here in order to focus on the breakdown phase. The effect of $\mathcal{A}$ on the convergence to the infinite space solution is displayed on Figure. 8. It can be seen that for dimensionless wellbore radius greater than 0.2, γ_ϵ is only about 6 to 8 times $\mathcal{A}$. For wellbore radius smaller than 0.2, an exponential increase is observed on the transitional fracture length. The case of small $\mathcal{A}$ corresponds to conditions where a large amount of fluid can be stored in the wellbore during the pressurization phase, i.e $a \ll (E' U)^{\frac{1}{3}}$. For those cases, the release of this stored volume of fluid in the fracture after its initiation results in an effective flow rate entering the crack much larger the injected one. This is the causes of such a large transition length to the infinite medium propagation for small values of $\mathcal{A}$.

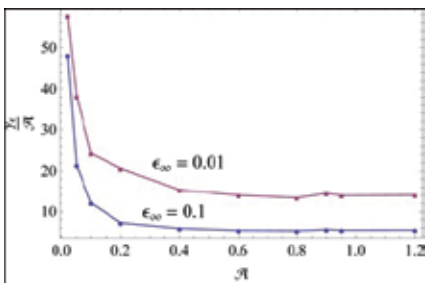

Figure 8. Effect of $\mathcal{A}$ on the convergence to infinite space solution for $\frac{\gamma_0}{\mathcal{A}} = 0.1$. Two convergence criteria are used i.e $\epsilon_\infty = 0.1$ and $\epsilon_\infty = 0.01$.

6. Conclusions

The initiation of axisymmetric hydraulic fractures from a horizontal wellbore has been investigated with an emphasis on near wellbore effects. Through a detailed dimensional analysis, two characteristic timescales were identified. The first characteristic time t_{mk} defines the timescale of transition from viscosity dominated propagation to the toughness dominated propagation and the second characteristic time t_{uk} defines the timescale of transition from near wellbore effects to the infinite medium propagation. The ratio of these timescales χ (see Equation (20)) increases with increasing fluid viscosity and decreases with increasing injection system compressibility. The large time behavior of the numerical algorithm was verified by the convergence of the numerical solution to the propagation solution in an infinite medium for a sufficiently large fracture compared to the wellbore size. The effect of the timescale ratio χ on the convergence to the infinite medium solution was investigated. It was found that the numerical solution converges to the infinite medium solution for each value of χ. The value of χ dictates on which infinite medium regime of propagation, the transient solution converges to. The solution converges to the toughness dominated propagation regime for small values of χ, whereas it converges to the viscosity dominated regime for large values of χ.

http://dx.doi.org/10.5772/56262

It was also found that the near wellbore effects are present up to a fracture length about 12 times the wellbore radius for different values of χ. This shows that the transitional length is not affected by the value of χ. The variation of the ratio of initial defect length to the wellbore radius $\frac{\gamma_o}{\mathcal{A}} = \frac{l_o}{a}$ has a minimal effect on convergence to the infinite medium solution. In contrast, a small dimensionless wellbore radius $\mathcal{A}$ has a profound effect on convergence to the infinite medium solution. For small dimensionless wellbore radius $\mathcal{A} = \frac{a}{(E'U)^{1/3}}$, a large increase in the transitional length is observed. This behavior is due to the injection system compressibility. The larger the compressibility, the larger the volume of fluid stored during pressurization and ultimately, the larger is the effective flux of fluid entering the fracture at breakdown compared to the nominal injection rate. This has the consequence of delaying the transition toward the solution of a hydraulic fracture propagating in an infinite medium under constant injection rate. It is important to note, however, that the presence of valves/perforations in the injection system will help dissipate the energy associated with such compressibility effects observed for small $\mathcal{A}$.

Appendix A

The edge dislocation kernel $J(r, r')$ mentioned in Equation (2) is given by [11] as follows

$$J(r, r') = r[R(r, r') + S(r, r')] \tag{26}$$

$$R(r, r') = \begin{cases} \frac{1}{(r^2 - r'^2)^2} E\left(\frac{r}{r'}\right), & r < r' \\ \frac{r}{r'} \frac{1}{r^2 - r'^2} E\left(\frac{r}{r'}\right) - \frac{1}{rr'} K\left(\frac{r}{r'}\right), & r > r' \end{cases} \tag{27}$$

$$S(r, r') = \int_0^\infty [P(\xi, x')\alpha(\xi, x) + Q(\xi, x')\beta(\xi, x)] / \Delta(\xi) d\xi, \tag{28}$$

where E and K are complete elliptic integrals of first and second kind respectively and

$$P(\xi, r') = \xi^2 I_0 K_1(\xi r') - \xi^2 r' I K_0(\xi r'), \tag{29}$$

$$\alpha(\xi, r) = -[2(2 - \nu) + \xi^2] K_1 K_0(\xi r) / \xi + \xi x K_0 K_1(\xi r) + r K_1 K_1(\xi r) - 3 K_0 K_0(\xi r), \tag{30}$$

$$Q(\xi, r') = -[2(1 - \nu) + \xi^2] I_1 K_1(\xi r') + \xi I_0 K_1(\xi r') - \xi r' I K_0(\xi r') + \xi^2 r' I K_0(\xi r'), \tag{31}$$

$$\beta(\xi, r) = 2 K_1 K_0(\xi r) + \xi r K_1 K_1(\xi r) + \xi K_0 K_0(\xi r), \tag{32}$$

where I_n and K_n are the modified Bessel functions of first and second kind respectively where $n=0,1$. In Equation (26), S is a semi-infinite integral given by Equation (28) which has a very slow rate of convergence. In order to improve the convergence, we follow a method similar to [11]: S is taken out of the integral and evaluated separately in closed form as follows

$$S_{\{new\}}(r, r') = \int_0^{\infty} \left| [P(\xi, r')\alpha(\xi, r) + Q(\xi, r')\beta(\xi, r)] / \Delta(\xi) - A^*(\xi, r, r') \right| d\xi + \int_0^{\infty} A^*(\xi, r, r') d\xi, \tag{33}$$

where $A^*(\xi, r, r')$ is the third order Taylor expansion of $\frac{(P\alpha + Q\beta)}{\Delta}$ at infinity. The integral of $A^*(\xi, r, r')$ can be obtained analytically.

Appendix B

The time step is computed by imposing the LEFM tip asymptote (15) in a weak form in the tip element. In the case of negligible toughness, care should be taken as the governing equations degenerate in the tip region. An algorithm based on the LEFM asymptote then requires very fine mesh for good convergence (see [24] for discussion).

The asymptotic volume of the tip element corresponding to the LEFM crack opening asymptote Eq. (15) is given as

$$\hat{\mathrm{V}} = \mathcal{G}_{\mathrm{k}} \int_0^{\Delta\rho} \hat{\rho}^{1/2} d\hat{\rho} = \frac{2}{3} \mathcal{G}_{\mathrm{k}} \Delta\varrho^{3/2} \tag{34}$$

where $\hat{\rho} = (\gamma + \mathcal{A}) - \rho$ is the distance from the fracture tip and $\Delta\varrho$ is the size of the tip element. The new time step $\Delta\tau^{n+1}$ is found by finding the zero of the function F defined as the mismatch between the current tip volume and the volume consistent with the LEFM asymptote:

$$F = \mathrm{V}_{\mathrm{N}} - \hat{\mathrm{V}} \tag{35}$$

where $\mathrm{V}_{\mathrm{N}} = \Delta\varrho \times \Omega_{\mathrm{N}}$ is the volume of the last element of the fracture. For each trial value of the time step, the coupled fluid-solid equations are solved in order to obtain a new estimate of the opening in the tip element Ω_{N}. A secant method is used to find the zero of F. The iterative loop is repeated until the time step converges and the zero of (35) is found. The convergence criteria is

$$\frac{\left\| \Delta\tau^{n+1} - \Delta\tau^{n} \right\|_2}{\left\| \Delta\tau^{n} \right\|_2} < \epsilon, \qquad \text{with } \epsilon = 10^{-4}. \tag{36}$$

http://dx.doi.org/10.5772/56262

Appendix C

The coupled problem of fluid-solid coupling inside the fracture is described as: for a given fracture length γ, and time $\tau + \Delta\tau^{n}$, find the opening $\Omega^{n} + \Delta\Omega^{n}$. The continuity equation (12) is discretized using the Finite Volume Method as follows:

$$\Delta\Omega_{i} = \frac{\mathcal{G}_{r}\Delta\tau}{\rho_{i}\Delta\rho}\left(\rho_{i-1/2}\Psi_{i-1/2} - \rho_{i+1/2}\Psi_{i+1/2}\right) \tag{37}$$

where ρ_i is the element midpoint coordinate and $\rho_{i-1/2}$ and $\rho_{i+1/2}$ are the element end point coordinates. The flux entering an element is denoted by $\Psi_{i-1/2}$ while the outgoing flux is denoted by $\Psi_{i+1/2}$. These fluxes are computed using the Poiseuille equation as follows:

$$\Psi_{i-1/2} = -K_{i-1/2}\frac{\Pi_{f(i)} - \Pi_{f(i-1)}}{\Delta\rho} \tag{38}$$

$$\Psi_{i+1/2} = -K_{i+1/2}\frac{\Pi_{f(i+1)} - \Pi_{f(i)}}{\Delta\rho} \tag{39}$$

Where the entrance hydraulic conductivity of an element $K_{i-1/2}$ is given by

$$K_{i-1/2} = \frac{1}{\mathcal{G}_{m}}\left(\frac{\Omega_{i} + \Omega_{i-1}}{2}\right)^{3}. \tag{40}$$

The flux entering the fracture from the wellbore is given by the inlet boundary condition

$$\Psi_{1/2} = \frac{1}{2\pi}\left(\mathcal{G}_{q}\Psi_{o} - \mathcal{G}_{U}\frac{\partial\Pi_{h}}{\partial\tau}\right) \tag{41}$$

while no flow is assumed out of the fracture tip

$$\Psi_{N} = 0. \tag{42}$$

The elasticity equation (11) is discretized by the Displacement Discontinuity Method (DDM) to the following form

$$A_{ij}\left(\Omega_{j}^{0} + \Delta\Omega_{j}\right) + \Pi_{h} = \Pi_{f(i)} \tag{43}$$

where A_{ij} is the stiffness matrix which is dense and symmetric for a regular mesh. Now putting the expression for $\Pi_{f(i)}$ from Equation (43) in (38) and (39) and then Ψ from Equations (38) and (39) in Equation (37) we get the following expression after rearranging the terms

$$\Xi(\Delta\Omega)\cdot\Delta\Omega=\Gamma(\Delta\Omega) \tag{44}$$

where Ξ is expressed as

$$\Xi=\delta_{ij}-B_{ij} \tag{45}$$

where δ_{ij} is the Kronecker delta and

$$B_{ij}=\alpha\begin{cases}\frac{\mathcal{G}_U\Delta\rho}{2\pi\Delta\tau\rho_i}A_{(i,j)}+K_{e(i)}A_{(i+1,j)}-K_{e(i)}A_{(i,j)}, & i=1 \quad j=1,N\\ K_{w(i-1)}A_{(i-1,j)}-\left(K_{w(i-1)}+K_{e(i)}\right)A_{(i,j)}+K_{e(i)}A_{(i+1,j)}, & i=2,N-1, \quad j=1,N\\ K_{w(i-1)}A_{(i-1,j)}-K_{w(i-1)}A_{(i,j)}, & i=N, \quad j=1,N\end{cases} \tag{46}$$

$$\Gamma=\alpha\begin{cases}\frac{\mathcal{G}_q\Psi_o\Delta\rho}{2\pi\rho_i}A_{(i,j)}+K_{e(i)}\left(A_{(i+1,j)}-A_{(i,j)}\right)\cdot\Omega^0_j, & i=1, \quad j=1,N\\ B_{ij}\cdot\Omega^0_j, & i=2,N-1, \quad j=1,N\\ \Psi_m\Delta\rho+B_{Nj}\cdot\Omega^0_j, & i=N, \quad j=1,N\end{cases} \tag{47}$$

where $\alpha=\frac{\mathcal{G}_r\Delta\tau}{\Delta\rho^2}$ and

$$K_e=\frac{\rho_{i-1/2}}{\rho_i}K_{i-1/2}, \quad i=2,N \tag{48}$$

$$K_e=\frac{\rho_{i+1/2}}{\rho_i}K_{i+1/2}, \quad i=1,N-1 \tag{49}$$

The nonlinear system (45) is solved by fixed point iteration

$$\Xi\left(\Delta\Omega^k\right)\cdot\Delta\Omega^{k+1}=\Gamma\left(\Delta\Omega^k\right) \tag{50}$$

with under-relaxation

$$\Delta\Omega^{k+1}=\left(1-\eta^{\gamma}\right)\Delta\Omega^k+\eta^{\gamma}\Delta\Omega^{k+1} \tag{51}$$

where η is the relaxation parameter. The convergence criteria is

$$\frac{\left\|\Delta\Omega^{k+1}-\Delta\Omega^k\right\|_2}{\left\|\Delta\Omega^{k+1}\right\|_2}<\epsilon, \qquad \text{with } \epsilon=10^{-5}. \tag{52}$$

http://dx.doi.org/10.5772/56262

Author details

Safdar Abbas* and Brice Lecampion

*Address all correspondence to: sabbas10@slb.com

Schlumberger Doll Research, Cambridge, USA

References

[1] Hubbert, M K, & Willis, d D. G. Mechanics of hydraulic fracturing. Trans. Am. Inst. Min. Eng. (1957). , 153-158.

[2] Haimson, B, & Fairhust, C. In-situ stress determination at great depth by means of hydraulic fracturing. In The 11th U.S. Symposium on Rock Mechanics (USRMS); June (1969). Berkeley, CA, USA. , 559-584.

[3] Lecampion, B, Abbas, S, & Prioul, R. Competition between transverse and axial hydraulic fractures in horizontal wells, SPE 163848. In SPE Hydraulic Fracturing Technology Conference; (2013). The Woodlands, Texas, USA.

[4] Garagash, D I, & Detournay, E. An analysis of the inuence of the pressurization rate on the borehole breakdown pressure. Int. J. Sol. and Struct. 1997; 34(24). (1997). , 3099-3118.

[5] Bunger, A, Larikouhani, A, & Detournay, E. Modelling the effect of injection system compressibility and viscous fluid flow on hydraulic fracture breakdown pressure. In Proceedings of the 5th International Symposium on In-Situ Rock Stress; (2010). Beijing: ISRSV. , 59-67.

[6] Lhomme, T, Detournay, E, & Jeffrey, R G. Effect of fluid compressibility and borehole on the initiation and propagation of a tranverse hydraulic fracture. Strength, Fracture and Complexity. (2005). , 149-162.

[7] Gordeliy, E, & Detournay, E. A fixed grid algorithm for simulating the propagation of a shallow hydraulic fracture with a fluid lag. International Journal for Numerical and Analytical Methods in Geomechanics. (2011). , 602-629.

[8] Lecampion, B. Hydraulic fracture initiation from an open-hole: wellbore size, pressurization rate and fluid-solid coupling effects. In 46th US Rock Mechanics/Geomechanics Symposium; (2012). Chicago, IL.

[9] Kirsch, G. Die theorie der elastizität und die bedürfnisse der festigkeislehre. Zantralblatt Verlin Deutscher Ingenieure. (1898).

[10] Hills, D A, Kelly, P A, Dai, D N, & Korsunsky, A M. Solution of Crack Problems: the Distributed Dislocation Technique Dordrecht: Kluwer Academic Publ.; (1996).

[11] Keer, L M, Luk, V K, & Freedman, J M. Circumferential edge crack in a cylindrical cavity. Journal of Applied Mechanics. (1977). , 250-254.

[12] Garagash, D I, & Detournay, E. The tip region of a fluid-driven fracture in an elastic medium. J. Appl. Mech.,ASME (2000). , 183-192.

[13] Garagash, D I. Propagation of a plane-strain hydraulic fracture with a fluid lag: Early-time solution. International Journal of Solids and Structures. (2006). , 5811-5835.

[14] Bunger, A P, & Detournay, E. Early time solution for a penny-shaped hydraulic fracture. ASCE J. Eng. Mech. (2007). , 534-540.

[15] Savitski, A, & Detournay, E. Propagation of a penny-shaped fluid-driven fracture in an impermeable rock: asymptotic solutions. International Journal of Solids and Structures. (2002). Dec; 39(26): , 6311-6337.

[16] Abé, H, Keer, L. M, & Mura, T. Growth rate of a penny-shaped crack in hydraulic fracturing of rocks. Journal of Geophysical Research. (1976). , 5335-5340.

[17] Madyarova, M. Fluid-Driven Penny-Shaped Fracture in Permeable Rock. Master Thesis. University of Minnesota, Department of Civil Engineering; (2003).

[18] Bunger, A. P, Jeffrey, R. G, & Detournay, E. Application of scaling laws to laboratory-scale hydraulic fractures. In Alaska Rocks 2005, The 40th US Symposium on Rock Mechanics (USRMS); (2005).

[19] Palisch, T T, Vincent, M C, & Handren, P J. Slickwater Fracturing: Food for Thought. In SPE Annual Technical Conference and Exhibition, September (2008). Denver, Colorado, USA: Society of Petroleum Engineers., 21-24.

[20] Jeffrey, R G, & Bunger, A P. A Detailed Comparison of Experimental and Numerical Data on Hydraulic Fracture Height Growth Through Stress Contrasts. SPE Journal. (2009). September; 14(3): , 413-422.

[21] Bunger, A P, & Detournay, E. Experimental validation of the tip asymptotics for a fluid-driven crack. Journal of the Mechanics and Physics of Solids. (2008). November; 56(11): , 3101-3115.

[22] Ryder, J, & Napier, J. Error analysis and design of a large-scale tabular mining stress analyzer. In 5th International Conference on Numerical Methods in Geomechanics; (1985). , 1549-1555.

[23] Zhao, Z, Kim, H, & Haimson, B. Hydraulic fracturing initiation in granite. In 2nd North American Rock Mechanics Symposium; (1996). , 1279-1284.

http://dx.doi.org/10.5772/56262

[24] Lecampion, B, Peirce, A, Detournay, E, Zhang, X, Chen, Z, Bunger, A, et al. The impact of the near-tip logic on the accuracy and convergence rate of hydraulic fracture simulators compared to reference solutions. In The International Conference for Effective and Sustainable Hydraulic Fracturing; (2013). Brisbane, Australia.

Chapter 20

Hydraulic and Sleeve Fracturing Laboratory Experiments on 6 Rock Types

Sebastian Brenne, Michael Molenda,
Ferdinand Stöckhert and Michael Alber

Additional information is available at the end of the chapter

http://dx.doi.org/10.5772/56301

1. Introduction

Hydraulic tensile strength is a crucial value for planning reservoir stimulation and stress measurements. It is used in the classical breakdown pressure (P_b) relation by Hubbert & Willis [1], where P_b is a function of major and minor principal horizontal stresses S_H and S_h, hydraulic tensile strength σ_T and pore pressure P_0:

$$P_b = 3S_h - S_H + \sigma_T - P_0 \tag{1}$$

For hydraulic fracturing laboratory experiments (MiniFrac – MF) under isostatic confining pressure P_m this might be reduced to:

$$P_b = cP_m + \sigma_T - P_0 \tag{2}$$

The coefficient c should be equal to two when porepressure is neglected. However, many laboratory experiments [2,3] resulted in values of about 1 for c, which might be explained by poroelastic effects.

Thus, when poroelasticity is excluded in the experiments by taking dry samples and sealing off the central borehole by an impermeable membrane (like a polymer tube), one would expect that c equals two and σ_T will be in the range of the tensile strength as determined by other tensile strength tests.

However, experiments with jacketed boreholes (sleeve MiniFrac – SMF) yield remarkable high values for c (about 6 to 8) and also for σ_T (about 3 to 5 times the tensile strength of the material) [4]. As a consequence we use a linear elastic fracture mechanics approach to evaluate our experiments.

1.1. Theory of hydraulic and sleeve fracturing on hollow cylinders

Fracture mechanics deal with stress concentrations around fractures and the definition of propagation criteria for fractures. The theory is essentially based on the works of Griffith [5] and Irwin [6], which led to the introduction of the stress intensity factor K.

$$K = \sigma\sqrt{\pi a} \tag{3}$$

K represents the magnitude of the elastic stress singularity at the tip of a fracture of the length $2a$ subjected to a uniform stress σ. With this concept, it is possible to formulate a simple fracture propagation criterion $K = K_C$. The fracture propagates when K reaches a critical value K_C (fracture toughness) with the fracture toughness assumed to be a property of the rock.

Mode I stress intensity factors (K_I) for arbitrary tractions $(\sigma(x))$ applied to the surface of a fracture of the length $2a$ may be computed by following formula [7,8]:

$$K_I = \frac{1}{\pi\sqrt{a}} \int_{-a}^{a} \sigma(x) \left(\frac{a+x}{a-x} \right)^{\frac{1}{2}} dx \tag{4}$$

The direction of propagation is the x-axis and the stresses are applied perpendicular to the fracture. As can be seen from equation (4), K_I increases with growing fracture length. A simple, 2-dimensional model was assumed for determination of stress intensity factors at the crack tips of the hydraulically induced fractures in MF and SMF tests.

Two fractures of length a are radially emanating from a circular hole of radius r in an infinite plate subjected to a compressive far field stress of the magnitude P_m. A fluid pressure P_{inj} is acting on the borehole wall and the pressure inside the fractures is either zero (SMF) or equal to the pressure in the borehole (MF: $P_{frac} = P_{inj}$). Stress intensities on the fracture tips can be determined by superposition of stress intensity factors resulting from each loading type [2,3]:

$$K_{I-MF} = K_I(P_m) + K_I(P_{inj}) + K_I(P_{frac}) \tag{5}$$

$$K_{I-SMF} = K_I(P_m) + K_I(P_{inj}) \tag{6}$$

http://dx.doi.org/10.5772/56301

$K_{I-MF/SMF}$ are not only dependent on the fracture length a (cf. Equations (3) and (4)) but also on the borehole radius r (see Appendix).

K_{I-MF} (full pressure in the fracture) gives an upper bound for stress intensities in this geometry (actual K_I_MF might be lower due to a negative pressure gradient inside the fracture), while K_{I-SMF} is only induced by the pressure in the borehole and far-field stresses and is therefore substantially lower than K_{I-SMF} (Figure 1).

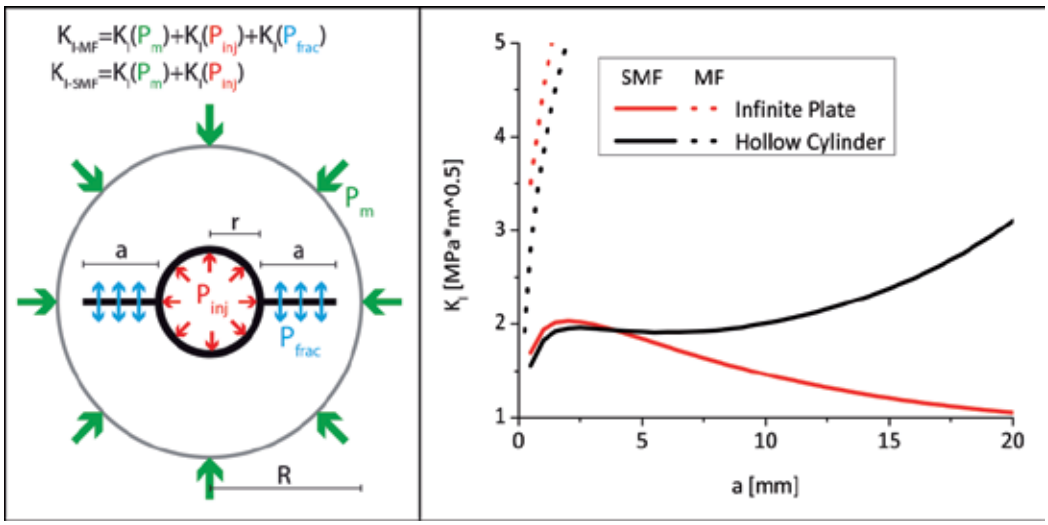

Figure 1. Left side: superposition of stress intensities by each loading type. Right side: stress intensity factor versus fracture length from analytical (infinite plate) and numerical (hollow cylinder) calculations for $r = 3$ mm, $P_{inj} = 50$MPa, $P_m = 0$ and an outer radius R of the hollow cylinder = 30 mm.

As an analytical solution for $K_I(P_m)$ and $K_I(P_{inj})$ for the ring geometry (corresponding to the hollow cylinder) is quite complex, we used the simpler solutions for a circular hole in an infinite plate as described by Rummel and Winter [2,3] (cf. Appendix). We compared the results of numerical simulations for the ring geometry with analytical solutions for the infinite plate. These results indicate that the simplification might be valid for fracture lengths smaller then $a \approx \frac{R-r}{10}$ with $R = 10r$ (R is the outer radius of the ring geometry (cf. Figure 1).

Solving K_{I-MF} and K_{I-SMF} for P_{inj} and setting $K_{I-MF} = K_{I-SMF} = K_{IC}$ (mode I fracture toughness) yields a critical injection pressure $(P_C(a))$ for each crack length a. If P_{inj} reaches $P_C\ (a)$, the fracture will propagate. From Figure 2 it can be seen, that $P_C\ (a)$ is very large for very small crack lengths. In consequence, the presence of microcracks is required for the formation of macroscopic fractures.

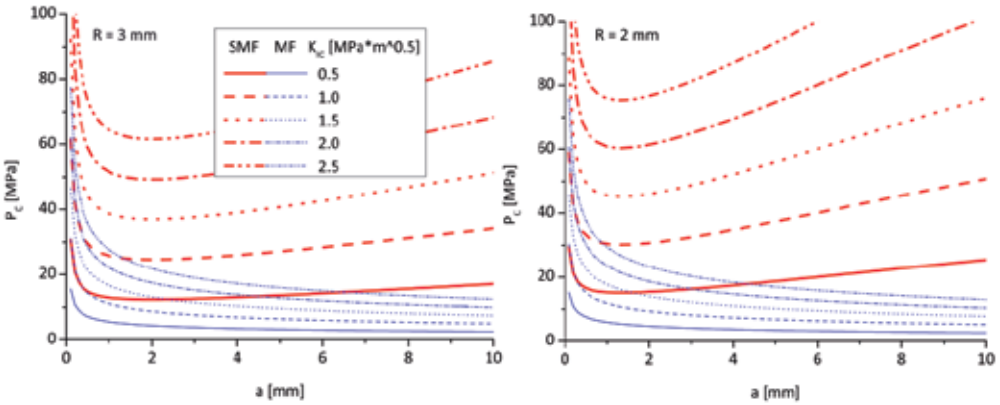

Figure 2. Critical injection pressure for fracture propagation P_C depending on fracture length a for $P_m = 0$. Borehole radii $r = 3$ mm (left), $r = 2$mm (right).

MF-equation (Equation 13) with full injection pressure in the fracture yields unstable fracture propagation at constant injection pressures as soon as microcracks start to propagate. On the other hand, the SMF-equations (Equation 14) show a minimum. Thus, after a fracture reaches the crack length corresponding to the minimum critical injection pressure, stable fracture propagation (i.e. to propagate the fracture, the injection pressure has to be increased) could be expected.

To calculate the coefficient c from Equation 2, we assume the presence of microcracks of a fixed length a_0 in the sample. The corresponding $P_C(a_0)$ versus P_m for the MF case (pressure in fracture = injection pressure) yields a coefficient $c = 1$, which is independent of a_0. $P_C(a_0)$ while for SMF the c value depends strongly on the assumed microcrack length a_0 and gives $c > 2$ (increasing a_0 yield higher c).

2. Sample preparation and rock testing

The core specimens are drilled either with 40 mm or 62 mm water cooled diamond core drills. Core end planes are cut with a water flushed diamond saw blade and ground coplanar to a maximum deviation of ± 0.02 mm. The length and diameter ratio is chosen between 1.5:1 and 2.25:1. After sample preparation core specimens were dried for two days at a temperature of 105°C. For calculations of porosity Φ, measurements of bulk density ρ_d and of grain density ρ_s via pycnometer were done. Static geomechanical parameters

http://dx.doi.org/10.5772/56301

were determined by uniaxial and triaxial compressive as well as Brazilian disc tensile strength test series according to ISRM and DGGT suggested methods [9,10]. Mode I fracture toughness was determined using the Chevron notched three-point bending test according to [9]. Furthermore, a dynamic rock parameter, the compressional ultra-sonic wave velocity (v_p) was measured. For MF/SMF specimens a central axial borehole was drilled into cores, using a water flushed diamond hollow drill with an outer diameter of 4 mm or 6 mm.

rock type	era & period	quarry localization	Microstructure
marble	Triassic Upper	Carrara Italy	coarse monocrystalline polygonal fabric
limestone	Jurassic upper Malm	Treuchtlingen South Germany	micritic limestone with abundant fossils and stylolites
sandstone	Carboniferous Mississippian	Dortmund/Hagen West Germany	fine-grained arcose
andesite D	Permian Rotliegend	Doenstedt N German Basin	porphyric fine-grained partly altered and pre-fractured
rhyolite	Permian Rotliegend	Flechtingen N German Basin	porphyric fine-grained partly pre-fractured and sealed joints
andesite R	Permian Rotliegend	Thuringian Forest Rotkopf	porphyric coarse-grained and pre-fractured

Table 1. Rock types used in our experiments.

2.1. Stress field and injection

Figure 3 shows schematically the components of the MF and SMF experimental set-up. The stress field is induced by a hydraulic ram (capacity 4500 kN) through a servo controlled MTS Test Star II system with a Hoek triaxial cell which is pressurized using a hand pump to achieve simultaneous pressure increase of confining pressure and axial load. In all tests axial stress is set to be 2.5 MPa higher than P_m to prevent leakage. Distilled water is pumped into borehole as the injection fluid (MF) or into a polymer tube inside the borehole (SMF). A servo controlled pressure intensifier with a maximum injection pressure of 105 MPa was used to perform a constant pumping rate of 0.1 ml/s. With this apparatus also steady-state flow tests were conducted to obtain rock permeability values (according to the procedure described in [11]).

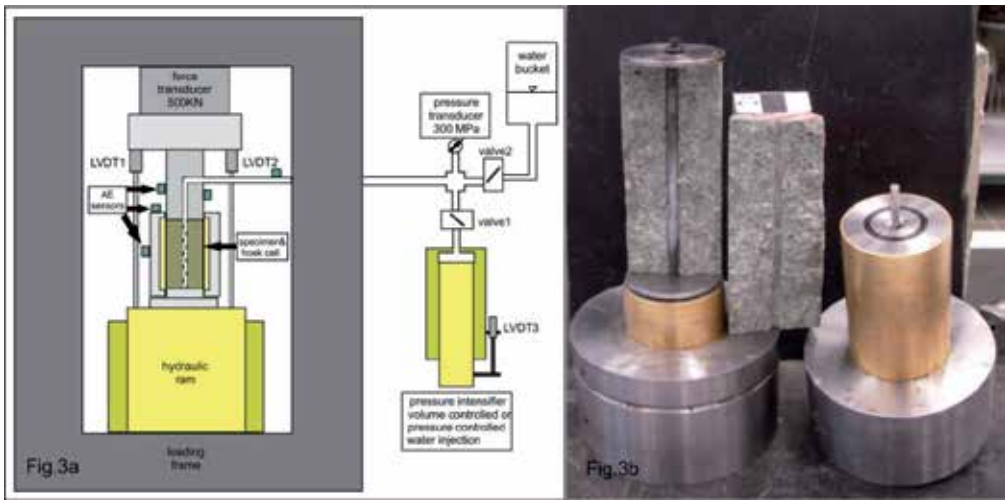

Figure 3. (a) Sketch of MF experimental set up including AE monitoring sensors (not shown are the pressure transducer and hand pump system to regulate confining pressure in the Hoek cell). (b) Typical specimen after SMF experiment.

2.2. Acoustic emission monitoring

Acoustic Emission (AE) signals are acquired with an AMSY5 Acoustic Emission Measurement System (Vallen Systeme GmbH, Germany) equipped with 5 Sensors of type VS150-M. The VS150-M Sensors operate over a frequency range of 100-450 kHz with a resonance frequency at 150 kHz. Due to machine noise in the range below 100 kHz incoming signals are filtered by a digital bandpass-filter that passes a frequency range of 95-850 kHz. AE data are sampled with a sampling rate of 10 MHz. The sensors are fixed using hot-melt adhesive to ensure best coupling characteristics. Pencil-break tests (Hsu-Nielsen source [12]) and sensor pulsing runs (active acoustic emission by one sensor) are used to test the actual sensor coupling on the sample.

3. Results

3.1. Petrophysical and mechanical parameters

An overview of the rock properties is given in Table 2. A wide range of low porosity/permeability rocks with K_{IC} from 1 to 2 MPa $\cdot\sqrt{m}$ were tested.

http://dx.doi.org/10.5772/56301

rock type	ρ_d [g/cm³]	Φ [-]	k [m²]	v_p [m/s]	KIC [MPa·√m]	C/φ [MPa]/[°]	E_{stat} [GPa]	σ_T [MPa]
marble	2.71 ±0.002	0.40 ±0.08	1E-19	5.67 ±0.06	1.57 ±0.11 (N=3)	29/22	36.0 ±1.0	6.4 ± 1.5
limestone	2.56 ±0.008	5.64 ±0.04	1E-18	5.59 ±0.05	1.19 ±0.14 (N=8)	27/53	32.2 ±1.6	8.2 ± 2.2
sandstone	2.57 ±0.006	4.39 ±0.06	8E-18	4.61 ±0.13	1.54 ±0.13 (N=4)	36/50	29.4 ±1.6	13.2 ± 2.1
rhyolite	2.63 ±0.015	1.02 ±0.12	9E-19	5.39 ±0.34	2.16 ±0.10 (N=4)	20…36/55	30.2 ±1.9	15.8 ± 3.2
andesite D	2.72 ±0.023	0.51 ±0.09	6E-19	5.26 ±0.28	1.90 ±0.08 (N=2)	20…41/50	28.7 ±3.1	14.6 ± 4.5
andesite R	2.60 ±0.013	1.70 ±0.08	4E-20	4.35 ±0.27	1.63 ±0.24 (N=4)	31/46	21.3 ±0.9	11.4 ± 2.8

Table 2. Mean values and standard deviations of petrophysical and mechanical parameters of tested rocks: dry bulk density ρ_d, porosity Φ, permeability k, compressive wave velocity v_p, fracture toughness from Chevron notched three-point bending tests K_{IC}, cohesion C and friction angle φ from a Mohr-Coulomb fit, Young's modulus E_{stat}, σ_T as determined by Brazilian disc tensile strength tests.

3.2. MF and SMF experiments

A schematic example of typical experiment data for MF and SMF tests is shown in Figure 4. Acoustic emission recordings are used to identify fracture processes in the test specimens. AE counts (threshold crossings per time interval – corresponding to AE activity) can directly be linked to localized fracture propagation [4]. The pressure at which the AE count rate raises rapidly is defined as P_{AE}, which is further used as initial fracture propagation pressure. P_{AE} is picked where the AE count rate permanently exceeds 1/10 of the test's average (see Figure 4).

In MF experiments, there is almost no AE activity prior to failure. Failure occurs in a very short time span just before sample breakdown (which occurs at maximum injection pressure $P_{inj\ max} = P_b$), therefore in MF experiments $P_{AE} \approx P_b$. In contrast, SMF experiments show an exponential increase in AE activity at injection pressures that are substantially lower than the actual breakdown pressure ($P_{AE} < P_b$), but much higher than P_{AE} in MF experiments. Therefore, it is possible to interrupt the experiment after AE activity started but before sample breakdown. The latter occurs in SMF experiments when the sample is completely splitted into two parts, which results in a tube breakdown and therefore in an injection pressure drop. Thin sections of specimens, where the experiment was interrupted, show macroscopic fractures emanating several millimeters into the sample but without any connection to the outer surface.

Noteworthy is the discrepancy between the MF and SMF initial fracture propagation pressures P_{AE} at zero confining pressure. This result would imply different hydraulic tensile strength values for the same rock type when using equation (2). Furthermore there is a significant difference between the values of coefficient c calculated for MF and SMF experiments. This

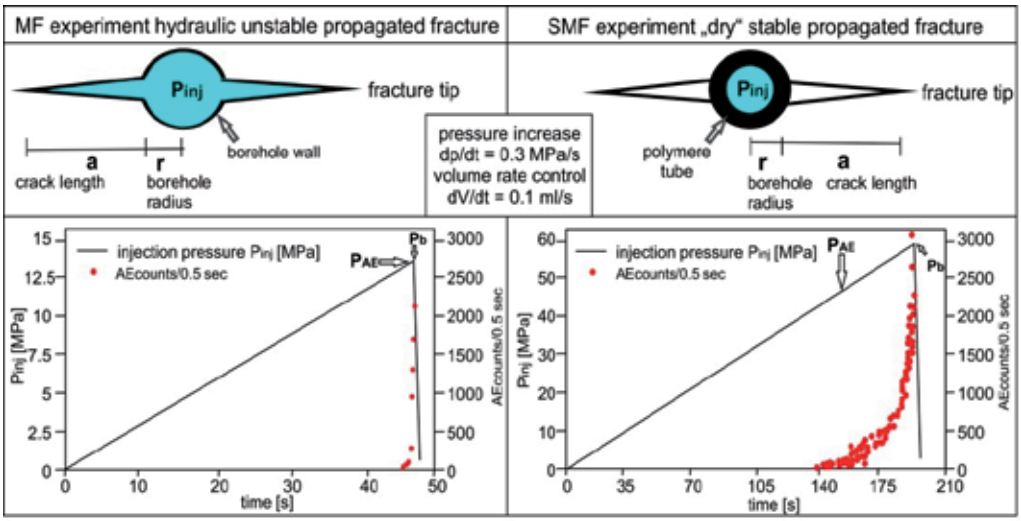

Figure 4. Schematic differences between MF (left) and SMF (right) experiments.

can be seen clearly in Figure 5. Scale effects in P_{AE} (Figure 2) with borehole radius are not evident for the 2 and 3 mm borehole radius samples due to data scattering. One single SMF test of a sandstone with a 6.35 mm borehole radius showed a significantly lower P_{AE} as can be seen in Figure 5.

			MF			SMF	
rock type	**Borehole diam.**	**N**	**PAE0 [MPa]**	***c***	**N**	**PAE0 [MPa]**	***c***
marble	4 mm	8	7.7	1.03	6	31.7	6.97
	6 mm	8	9.4	0.96	4	19.6	8.54
limestone	4 mm	9	10.3	1.00	6	26.7	6.06
	6 mm	8	8.2	1.01	7	29.1	5.79
sandstone	4 mm	8	18.2	1.13	5	41.7	6.29
	6 mm	8	18.5	1.14	4	40.5	7.26
rhyolite	4 mm	11	18.2	0.89	4	51.6	6.04
	6 mm	8	16.0	0.85	5	50.9	5.88
andesite D	4 mm	9	16.1	1.00	3	64.2	4.17
	6 mm	6	10.9	0.87	4	48.1	4.83
andesite R	4 mm	10	10.0	1.17	4	47.4	6.26
	6 mm	6	8.2	1.17	5	29.7	7.44
		∑ 93	-	Ø 1.02	∑ 57	-	Ø 6.33

Table 3. Results of all MF and SMF rock type test series in form of P_{AE0} and coefficient c (see equation (2)). N gives the number of tested samples per lithology and borehole diameter.

http://dx.doi.org/10.5772/56301

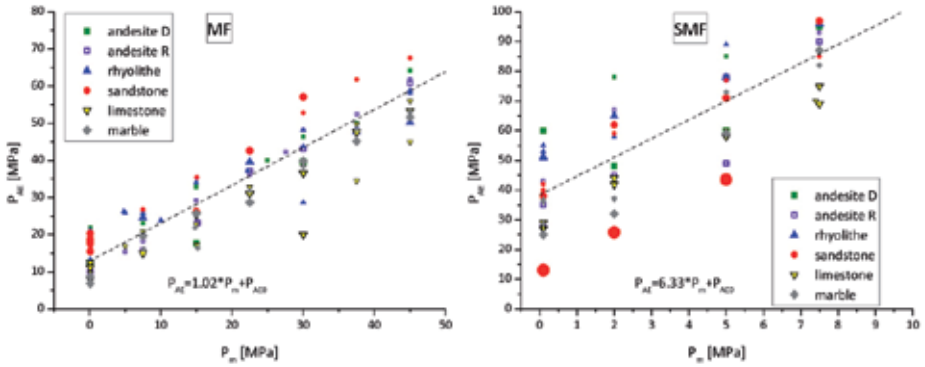

Figure 5. Experimental results of MF (left) and SMF (right) initial fracture propagation pressures for different confining pressures. Dashed line – linear regression of test data. Symbol size refers to borehole radius r (small – $r = 2mm$; intermediate – $r = 3mm$; large – $r = 6.35mm$)

4. Conclusion

With SMF tests, stable fracture propagation was achieved over a wide range of injection pressure. Fracture initiation can be confidently linked to the AE count rates. This can be concluded from experiments that were interrupted after P_{AE} but below breakdown pressure. Physical examination revealed the presence of distinct fractures in these specimens (see Figure 6).

Figure 6. Thin-section of a marble specimen ($r = 2$mm) after SMF test. Clearly visible is a "dry" fracture (indicated by arrows) emanating radially from the borehole (at the right side of the picture). The experiment was interrupted before specimen breakdown. The fracture did apparently not propagate to the outer wall of the specimen.

Due to high data scatter, the theoretical scale effect (critical injection pressure P_c is higher for smaller borehole radii) cannot be resolved by our data. However, tests with a larger (r = 6.35 mm) borehole give some support to the notion.

The simple fracture mechanics model is able to explain the higher P_{AE} in SMF experiments. Equations 5 and 6 include the influence of fractures (with or without pressure inside), which is omitted in the classical approach (Equation 1). The high coefficient c in SMF test can only be explained by assuming high microcrack lengths ($a_0 \approx 6$ mm).

We excluded poroelastic effects in our analysis due to the use of initially dry rocks with low permeabilities.

Appendix

Superposition of stress intensity factors for two radial cracks of length a emanating from an internally pressurized (P_{inj}- injection pressure in the borehole, P_{frac}- pressure inside the fracture) circular hole of radius r in an infinite plate subjected to an isostatic far-field stress P_m as described by [2] and [3] :

$$K_I\left(P_m\right) = P_m\sqrt{r} * f_{Pm}\left(a,r\right) \tag{7}$$

$$K_I\left(P_{inj}\right) = P_{inj}\sqrt{r} * f_{P_{inj}}\left(a,r\right) \tag{8}$$

$$K_I\left(P_{frac}\right) = P_{frac}\sqrt{r} * f_{P_{frac}}\left(a,r\right) \tag{9}$$

$$f_{Pm}\left(a,r\right) = 2\left(1+\frac{a}{r}\right)^2\left(\frac{\left(1+\frac{a}{r}\right)^2-1}{\left(\pi\left(1+\frac{a}{r}\right)\right)^7}\right)^{\frac{1}{2}} + \left(\pi\left(1+\frac{a}{r}\right)\right)^{\frac{1}{2}}\left(1-\frac{2}{\pi}\sin^{-1}\left(\frac{1}{1+\frac{a}{r}}\right)\right) \tag{10}$$

$$f_{P_{inj}}\left(a,r\right) = \left(1.3\frac{\frac{a}{r}}{1+\left(1+\frac{a}{r}\right)^{\frac{3}{2}}} + \frac{7.8\left(\sin\left(\frac{2a}{r}\right)\right)}{2\left(1+\frac{a}{r}\right)^{\frac{5}{2}}-1.7}\right) \tag{11}$$

http://dx.doi.org/10.5772/56301

$$f_{P_{frac}}\left(a,r\right)=\left(\pi\left(1+\frac{a}{r}\right)\right)^{\frac{1}{2}}\left(1-\frac{2}{\pi}\sin^{-1}\left(\frac{1}{1+\frac{a}{r}}\right)\right) \tag{12}$$

Note: In equations 10 and 12 the borehole was excluded from the integration of stresses (cf. equation 4). The critical fracture propagation pressure at a given fracture length a, borehole radius r and mode I fracture toughness K_{IC} for the unjacketed $\left(P_{c-MF}\right)$ and the jacketed $\left(P_{c-SMF}\right)$ case:

$$P_{c-MF}=\frac{1}{f_{P_{inj}} * f_{P_{frac}}}\left(\frac{K_{IC}}{\sqrt{r}}+P_m f_{P_m}\right) \tag{13}$$

$$P_{c-SMF}=\frac{1}{f_{P_{inj}}}\left(\frac{K_{IC}}{\sqrt{r}}+P_m f_{P_m}\right) \tag{14}$$

Acknowledgements

The authors wish to thank the German Federal Ministry for the Environment, Nature Conservation and Nuclear Safety for financing our project (FKZ 0325279B). Many core specimens were prepared and analyzed by our student staff: T. Hoferichter, J. Braun, S. Hönig, K. Bartmann and A. Kraft. A great praise to the precision mechanics workshop guys for the construction of the fine working pressure intensifier system. We appreciate fruitful discussions with geomecon GmbH, Potsdam.

Author details

Sebastian Brenne*, Michael Molenda, Ferdinand Stöckhert and Michael Alber

*Address all correspondence to: sebastian.brenne@rub.de

Ruhr-University Bochum, Germany

References

[1] Hubbert M, Willis D. Mechanics of hydraulic fracturing. Petroleum Transactions. 1957;210:153–68.

[2] Rummel F. Fracture Mechanics Approach to Hydraulic Fracturing Stress Measurements. In: Atkinson BK, editor. Fracture mechanics of rock. Academic Press geology series. London [.u.a.]: Academic Pr; 1987. p. 217–39.

[3] Winter R. Bruchmechanische Gesteinsuntersuchungen mit dem Bezug zu hydraulischen Frac-Versuchen in Tiefbohrungen. Berichte des Instituts für Geophysik der Ruhr-Universität Bochum: Reihe A. Bochum; 1983.

[4] Ito T, Hayashi K. Physical background to the breakdown pressure in hydraulic fracturing tectonic stress measurements. International Journal of Rock Mechanics and Mining Sciences & Geomechanics Abstracts. 1991;28:285–93.

[5] Griffith AA. The Phenomena of Rupture and Flow in Solids. Philosophical Transactions of the Royal Society of London. Series A, Containing Papers of a Mathematical or Physical Character. 1921;221:163–98.

[6] Irwin GR. Analysis of stresses and strains near the end of a crack traversing a plate. Journal of Applied Mechanics. 1957;24:361–64.

[7] Sih GC. Handbook of stress-intensity factors: Stress-intensity factor solutions and formulars for reference. Bethlehem, Pa: Lehigh Univ., Inst. of Fracture and Solid Mechanics; 1973.

[8] Tada H, Paris PC, Irwin GR. The stress analysis of cracks handbook. 3rd ed. New York: ASME Press; 2000.Ulusaihutsen

[9] Ulusay R, Hudson JA, editors. The complete ISRM suggested methods for rock characterization, testing and monitoring: 1974-2006. 2007th ed. Ankara: Commission on Testing Methods, International Society of Rock Mechanics; 2007.

[10] Mutschler T. Neufassung der Empfehlung Nr. 1 des Arbeitskreises "Versuchstechnik Fels" der Deutschen Gesellschaft für Geotechnik e. V.: Einaxiale Druckversuche an zylindrischen Gesteinsprüfkörpern. Bautechnik. 2004;81:825–34.

[11] Selvadurai APS, Jenner L. Radial Flow Permeability Testing of an Argillaceous Limestone. Ground Water. 2013;51:100–07.

[12] ASTM E976. Standard guide for determining the reproducibility of acoustic emsission sensor response. American Society for Testing and Materials. 1994;386-391.

Section 6

Induced Seismicity and Slip

Chapter 21

Microseismic Monitoring Developments in Hydraulic Fracture Stimulation

Mirko van der Baan, David Eaton and
Maurice Dusseault

Additional information is available at the end of the chapter

http://dx.doi.org/10.5772/56444

Abstract

The last decade has seen a significantly increased interest in microseismic monitoring by the hydrocarbon industry due to the recent surge in unconventional resources such as shale-gas and heavy-oil plays. Both hydraulic fracturing and steam injection create changes in local pore pressures and in situ stresses and thereby brittle failure in intact rock plus additional slip/shearing in naturally fractured rock. Local rock failure or slip yields an acoustic emission, which is also known as a microseismic event. The microseismic cloud represents thus a volumetric map of the extent of induced fracture shearing, opening and closing. Microseismic monitoring can provide pertinent information on in situ reservoir deformation due to fluid stimulation, thus ultimately facilitating reservoir drainage. This paper reviews some of the current key questions and research in microseismicity, ranging from acquisition, processing to interpretation.

1. Introduction

Microseismic events are very small earthquakes of generally negative moment magnitude[1] that are often associated with hydraulic fracturing or fluid flow in reservoirs. Building upon long-standing applications of microseismic methods, such as monitoring of stability in underground mines (e.g., Gibowicz and Kijko, 1994; Urbancic and Trifu, 2000)

1 Earthquake magnitude is measured on a logarithmic scale. Various roughly equivalent amplitude-based magnitude scales are in use, of which moment magnitude is the most general.

and enhanced geothermal systems (e.g., Häring et al., 2008), microseismic monitoring techniques are being used increasingly by the oil and gas industry to monitor hydraulic stimulation of "tight" (very low permeability) hydrocarbon reservoirs and steam injection into heavy-oil fields. As such, it is one of the technologies underpinning the recent upswing of oil production in Western Canada, as well as the development of new tight-gas fields, monitoring of caprock integrity during in situ heavy-oil exploitation, and carbon capture and storage (McGillivray, 2005; Maxwell et al., 2010; Verdon et al., 2010; Maxwell, 2011; Clarkson et al., 2011).

This paper reviews some of the current questions and research in microseismicity, ranging from acquisition, processing to interpretation. However, before reviewing these aspects, it is important to consider the wider context first and the economic impact of hydraulic fracturing in tight-hydrocarbon fields.

2. Background

Security of energy supplies, the continuous growth in energy demand, and climate change are among the greatest global challenges that we face. Nearly all projections agree that we will remain heavily reliant on fossil fuels for many years. For example, the International Energy Agency's 'business-as-usual' analysis from 2008 indicates that in 2030 approximately 83% of the world's energy demand will still be met by fossil fuels. In 2011 this was revised downward to 55% due to high oil prices, government incentives for renewable energies and environmental concerns (EIA, 2011). Technological innovations will therefore be required to (i) find new hydrocarbon reserves or enable recovery from proven resources previously inaccessible or uneconomic; (ii) maximize recovery from producing reservoirs, and (iii) deal with CO_2 emissions. Microseismic monitoring and hydraulic fracturing are mainly related to the first two points.

Recovery of hydrocarbons from previously uneconomic yet proven resources such as shale-gas and other tight-gas plays has become possible due to significant improvements in the last 10 years in two key technologies, namely horizontal drilling and hydraulic fracturing. Tight-gas reservoirs are characterized by low porosity and permeability, indicating that little pore space is present and that fluid flow is guaranteed to be slow and difficult, thus severely complicating reservoir drainage. On the other hand, this gas is often located in very thick lithologic units such that the resource volume is large. Horizontal drilling into these units enables drainage over a larger well contact area (2-3 km instead of 100-200m), thus improving fluid flow. In hydraulic-fracture well treatments, fluids possibly mixed with proppants (slurry) are injected under high pressure to induce fracturing of the reservoir, thereby further enhancing reservoir drainage by increasing the effective permeability through the creation of an interconnected fracture network.

The technological advances in these two key technologies have been such that in 2000 only 1% of the total gas production in the US came from shale-gas fields, whereas currently this is estimated to be 20% (IHS CERA, 2010). Figure 1 shows the extent of current and potential

http://dx.doi.org/10.5772/56444

shale-gas plays in North America. It is clear that tight-gas and shale gas will remain an important resource for many years to come and further technological improvements will enable economic drainage of additional reservoirs. One of these emerging technologies is microseismic monitoring.

Figure 1. Current shale plays in North America. Source: EIA http://www.eia.gov/pub/oil_gas/natural_gas/analysis_publications/maps/maps.htm

Hydraulic fracturing (also known as fraccing or fracking) leads to brittle failure inside a reservoir, which is typically accompanied by microseismicity. Microseismicity refers to discrete rock-deformation events, analogous to tiny earthquakes, that are generally of moment magnitude < 0. For reference, magnitude 0.2 is the equivalent of the energy released by a large hand grenade (30 g TNT equivalent), whereas a typical small mining blast has a magnitude around 1-1.5, corresponding to 2-2.5kg of TNT. Since magnitude scales are logarithmic, negative magnitude events thus correspond to the energy yield equivalent of milligrams or even micrograms of TNT.

Monitoring of microseismic activity is a geophysical remote-sensing technology that provides the ability to detect and map associated fracturing processes, either in real-time or in post-processing mode. A typical field deployment involves the installation of an array of continu-

ous-recording 3-component geophones within observation well(s) near the zone of interest, and/or a large number of surface sensors. Although relatively new to the oil and gas industry, similar monitoring technologies for earthquakes have been honed and developed by the seismological and mining research communities for decades (e.g. Gibowicz and Kijko, 1994; Bolt, 1984; Stein and Wysession, 2003). The goal of microseismic monitoring is to detect, locate and characterize microseismic events, which often occur in large numbers within cloud-like distributions that reflect underlying fracture networks. This approach enables monitoring of frac treatments in real-time in order to detect the extent of the stimulated rock volume and thus the success of the treatment, as well as predict likely improvements in subsequent reservoir drainage.

Applications of microseismic monitoring within industry, particularly in oil and gas, have seen remarkable growth during the past 10 years (Warpinski, 2009; Maxwell, 2010). This has not been limited to hydraulic fracture treatment for shale-gas and other tight-gas plays, but has included stimulation technologies such as fracturing or steam injection applied to tight-oil or heavy-oil fields and also techniques for maximizing recovery from producing reservoirs. It is estimated that over one million hydraulic fracture treatments have been performed in the US in the past 60 years (King, 2012), and that currently 3-5% of fracs in North America involve microseismic monitoring. Oil and gas companies have made significant expenditures (conservatively $100's MM) for microseismic monitoring, but face extraordinary technological challenges to fully utilize the results. Their efforts are hampered by a number of factors, including an incomplete understanding of seismological and geomechanical processes associated with induced microseismicity.

In the next sections we will review current pertinent research questions on microseismic acquisition, processing and interpretation. Since many items are intimately intertwined it is inescapable that some points may be revisited throughout the chapter.

3. Acquisition

Based on the current state-of-the-art for microseismic monitoring, a number of important technological questions are presently under debate, such as:

- What conditions favour surface versus borehole microseismic acquisition? Surface acquisition involves the deployment of large numbers of receivers and has the inherent advantage of more extensive azimuthal coverage (solid angle); in principle, this should improve the condition number for hypocentre inversion and moment-tensor analysis (Eaton and Forouhideh, 2011). On the other hand, placement of geophones in deep boreholes (currently the norm for microseismic monitoring in western Canada) has the advantage of better signal-to-noise characteristics due to the closer proximity to the microseismic sources, generally quieter background noise levels (less anthropogenic noise), often better instrument coupling and predominantly horizontal (layer-parallel) instead of vertical (layer-perpendicular) wave propagation leading to less wave scattering. Conversely, surface acquisition is significantly more cost effective as there is no need to drill observation wells

http://dx.doi.org/10.5772/56444

or deploy instrumentation inside wells, and permits deployment of one or two orders of magnitudes more instruments.

- The current strategy for hydraulic fracturing of tight-gas reservoirs is to minimize acquisition durations to reduce costs. Recently recognized phenomena, such as long-period long-duration events (Das and Zoback, 2011), indicate that much can be learned from the use of exceptionally long deployment times (i.e., weeks rather than days) in order to enable more complete characterization of background noise spectra. Such long recording durations would also enable the evaluation of technology for noise interferometry (cf. de Ridder and Delinger, 2011) to reveal not only what happens during stimulation, but also in the period before and immediately following the slurry injection.

- Various formulas are currently used within industry to calculate the magnitude of microseismic events (Shemata and Anderson, 2010). Since magnitude formulas were developed for describing earthquake phenomena, they are calibrated for significantly larger magnitudes. The extrapolation of different formulas to 4-5 orders of magnitude below their calibration range leads to discrepancies in reported values. Accurate magnitude determination is of practical importance for various reasons, including (i) the determination of the stimulated rock volume (Maxwell et al., 2006); (ii) recently implemented controls in the UK on hydraulic fracturing operations are based on a "traffic-light system" (de Pater and Baisch, 2011) in which operations are suspended for several days if any event exceeds ML = 0, and stopped if any event exceeds ML = 1.7; and (iii) on liability issues related to induced seismicity (Cypster and Davis, 1998).

- Currently the emphasis is on mapping brittle failure, yet it is hypothesized that the cumulative energy released via brittle failure represents only a minute fraction of the total injected energy, indicating that a large portion of energy release may occur aseismically (i.e., plastically or at very slow deformation rates) (Maxwell et al., 2009). This suggests that there may be an advantage to acquisition of continuous recordings for analysis of the ultra-low frequency spectral content of microseismic activity, which may be diagnostic of certain types of aseismic rock failure (Benson et al., 2008; Pettit et al., 2009; Beroza and Satoshi, 2011).

A university-led project to acquire microseismic data was undertaken in northern British Columbia, Canada. This experiment involved the recording of several multistage hydraulic fracture treatments performed in two horizontal wells (Figure 2). The microseismic data were collected using both surface and borehole sensors. The borehole tool string consisted of a 6-level broadband system with downhole digitization. Surface sensors included a 12-channel array with a mix of vertical-component and 3-C geophones, and 22 broadband sensors deployed in 7 localized arrays over an area of ~ 0.5 km^2.

The unusual setup was designed to investigate multiple objectives. First, microseismic monitoring was performed using both surface and borehole equipment to compare acquisition strategies and determine their respective advantages and inconveniences such as ease of deployment, costs, detectability of events, other signals and associated noise levels. In addition, the experiment is unique in that both broadband and short-period equipment are deployed. The approximate lowest recording frequencies for the various equipment are; broadband

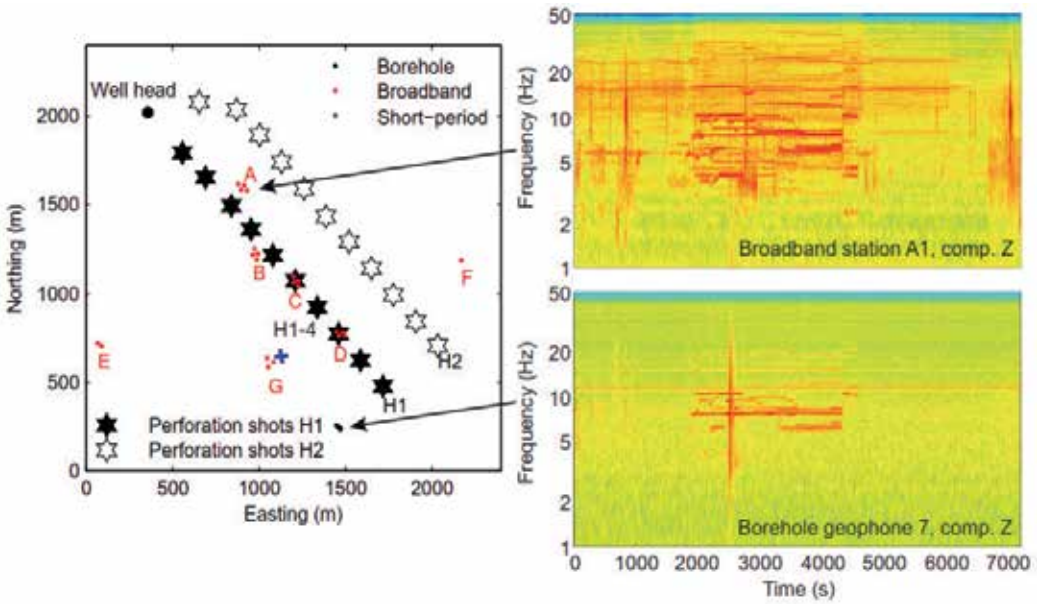

Figure 2. Experimental setup of the microseismic experiment, as well as the time-frequency transforms of stage H1-4 for one downhole geophone and one broadband station (hot colors correspond to high amplitudes). The stars indicate the position of the perforation shots and hence of the horizontal part of the wells. H1 and H2 are two different horizontal wells. After: Tary and Van der Baan (2013).

surface-based seismometers: 0.0083 Hz (= 120 s); borehole equipment: 0.1 Hz; short-period surface array: 5 Hz. Data analysis of the variously recorded signal thus helps reveal if significant energy is present below the 5 Hz limit imposed by most standard monitoring equipment. This may help resolve the observed energy imbalance between injected and seismically released energy.

Conventional analysis of microseismic recordings involves first identifying and extracting individual events, e.g., via a semi-automatic triggering system. This poses problems if many overlapping events are simultaneously recorded and if individual event strengths hover around the noise level. It also may obscure proper identification of so-called slow earthquakes (Ide et al., 2007) occurring on much longer time scales than conventional earthquakes resulting from abrupt brittle failure.

Direct analysis of continuous data streams on the other hand offers much greater flexibility and is not subject to the shortcomings described above. For instance, analysis of continuous recordings of acoustic emissions generated during laboratory rock-fracturing experiments have greatly aided in improving our understanding of active microcracking and deformation processes in volcanoes and the earth in general (Benson et al., 2008; Thompson et al., 2009). These continuous data streams are analyzed using various time-frequency transforms such as short-time Fourier transforms, S-transforms and wavelet transforms (Reine et al., 2009) to examine variations in local frequency content and highlight

http://dx.doi.org/10.5772/56444

slow deformation processes. Obviously it remains possible to dissect the recordings to extract individual events as well.

Initial analysis of these data reveals the existence of numerous high-frequency (> 100 Hz) microseismic events with moment magnitudes ranging from -2.3 to -1.4. These events are detected to distances of up to 1.2 km using the borehole system. In addition, perforation shots are well recorded to distances of about 2 km. More interestingly spectral analysis shows the existence of complex rupture patterns such as rapid opening and closing of tensile cracks (Eaton, 2012). Moment tensor analysis on other experiments has shown complex deformation as well in hydraulic-fracturing experiments (Baig and Urbancic, 2010); yet such moment-tensor analysis normally requires two or more observation wells (Eaton and Forouhideh, 2011). The current observations are obtained using a single observation well.

Time-frequency analysis of the continuous recordings demonstrates the existence of resonance frequencies during hydraulic fracturing (Tary and Van der Baan, 2013). The resonances are mainly in the frequency band between 5 and 20 Hz. Other resonances are visible on the broadband recordings. They likely correspond to environmental or anthropogenic noises. Noticeably, the resonances are recorded by the downhole geophones, which are close to the horizontal part of the injection well at depth, and by the broadband arrays A and B, which are near the well head. The broadband arrays C or D, closest to the fluid injection during the first stages, do not exhibit any resonance frequencies. This indicates that the injection well is likely the cause of these resonance frequencies (Figure 2). In other cases, however, resonance frequencies may be indicative of the extent of the induced, interconnected fracture network (Tary and Van der Baan, 2012).

It is clear from the above discussion that many key acquisition questions are intimately linked to the need to enhance our arsenal of tools for processing and interpretation of microseismic data.

4. Microseismic data processing

Rapid turnaround has been a high priority within the microseismic industry to reduce acquisition durations and deliver analysis results such as event locations in near real-time to completion engineers, who are required to make decisions such as starting a new fracturing stage based on assessment of a microseismic event "cloud" distribution. This requirement has led to the development of near real-time event-picking, classification and hypocentre-location algorithms; such rapid turnarounds demand robust techniques based on straightforward assumptions, often accompanied by large reductions in information content. For instance, in the case of hydraulic fracture stimulations, the fracture size and orientation are often inferred using a few events comprising the edges of the "cloud" of microseismic hypocentres.

4.1. Analysis and attenuation of coherent noise

Before discussing picking and event location it is important to realize that a principal aspect of microseismic data processing is the recognition and attenuation of coherent noise. Coherent noise is defined here as any repeatedly recorded energy on one or more traces that is not a body wave (P or S) arrival. The noise is often persistent, repeatable, and may be caused by various types of waves travelling in the borehole. A cemented wellbore with steel casing has the potential to propagate many types of waves. P and S waves can be transmitted in a wellbore in the steel casing, or the cement (Raggio et. al., 2007). The P wave can also be transmitted in the fluid in the wellbore. There are also a number of modes of tube waves (Rayleigh waves travelling at the wellbore fluid and adjacent solid interface) that can be transmitted.

St-Onge and Eaton (2011) have observed another type of coherent noise source that may be related to the tuned response of a clamped geophone array. This response is manifested as discrete, high-amplitude spectral peaks that can have a negative effect on weak signals recorded within the primary bandwidth of borehole microseismic recordings (i.e., several hundred Hz). These observations show that noise can be high in amplitude, persistent in time, and may adversely affect the recording of P and S wave signal energy in microseismic data (St-Onge and Eaton, 2011). Due to the nature of the data acquisition, the types of noise observed in microseismic surveys differ from typical noise sources in conventional seismic profiling. In many cases, datasets are contaminated by Lamb waves, which are a type of elastic guided wave that travels along a plate surface such as the cylindrical surface of borehole casing. These coupled longitudinal and transverse waves were first described by Lamb (1917) and in a cylindrical casing exhibit longitudinal, torsional and flexural modes. Lamb waves are dispersive, and their frequency characteristics have been described by Karpfinger (2009). St-Onge and Eaton (Lamb waves recorded in wellbores and their potential to predict cement bond failure, in preparation for Geophysics) are exploring various ways in which these harmonic signals can be suppressed or even exploited to characterize the borehole environment as their propagation velocity is influenced by the bonding characteristics of the cement.

Tary and Van der Baan (2012) divide resonance frequencies into three broad categories, namely those generated by source, receiver or path effects. This categorization can also be applied to microseismic noise if we are interested solely in the microseismic direct arrivals for location purposes and estimation of the associated source mechanism. At the receiver side, resonance frequencies and other noise result from wave reverberations in the borehole (Sun and McMechan, 1988), either the whole borehole or between secondary sources such as the geophones (St-Onge and Eaton, 2011). Resonances and noise can also be due to internal resonance of the geophone if its clamping or damping is flawed.

Along the ray path, resonances arise from constructive and destructive interferences of seismic waves, waves focusing in low-velocity waveguides or multiple wave scattering. Which frequency band is favored depends on the layer spacing, thickness and mechanical properties (van der Baan et al., 2007, van der Baan, 2009). Likewise (multiple) reflections and refractions can also confound the picking of direct arrivals. A prime example on how such secondary arrivals can complicate event picking and location is shown in Kocon and Van der Baan

http://dx.doi.org/10.5772/56444

(2012) who demonstrate that mis-identification of arrivals is a prominent source of event mislocations.

At the source side, resonance frequencies can be generated by repetitive events if perfectly periodic, or by the resonance of fluid-filled cracks as in the case of volcanic tremors (Aki et al., 1977). Resonances in fluid-filled cracks are generated by interface waves and depend mainly on the crack geometry, the crack stiffness and the source parameters that trigger the resonance (Ferrazzini and Aki, 1987). The latter are significantly less likely to mask strong direct arrivals; yet they offer promise for enhancing our understanding of the geomechanical reservoir deformations during hydraulic fracturing (Tary and Van der Baan, 2012, 2013) as indicated in the previous section.

4.2. Traveltime picking

Event-detection and time-picking are critical steps for microseismic data processing. Due to the large volume of data acquired during a microseismic survey, these steps are typically performed using an automated method. These steps have been implemented using various algorithms, such as the short- and long-time average ratio (STA/LTA) technique (e.g. Sharma et al., 2010), modified energy-ratio (MER) (Han et al., 2009) and Akaike information criterion (AIC) (Oye and Roth, 2003). Akram et al. (Automatic event-detection and time-picking algorithms for downhole microseismic data processing, manuscript in preparation for Geophysical Prospecting) have developed a dynamic-threshold approach for event detection that reduces false detections and offers improved capability to identify weak signals. They have also developed several hybrid approaches for automatic arrival-time picking that combine existing methods to improve performance with real microseismic data.

4.3. Locations

Calculation and interpretation of the locations of seismic events (hypocentres) are critical first-order components of microseismic monitoring. Compared to conventional earthquake methods, borehole microseismic surveys are relatively poorly constrained because of the fewer number of geophones and less desirable azimuthal coverage (Han, 2010; Jones et al., 2010). Most hypocentre localization methods require knowledge of P- and S-wave arrival times (Xuan and Sava, 2009). For borehole microseismic surveys, the distance between source and receiver can be computed using the arrival time difference of P- and S- waves and azimuth and dip information obtained from polarization analysis (Albright and Pearson, 1982; Eisner et al., 2009; Han, 2010; Jones et al., 2010). A probability density function can also be computed from the observed and modeled arrival time delays of P- and S-waves (Michaud et al., 2004). Surface microseismic methods are better suited to migration-based methods, which do not require P- and S-wave arrivals time picking information and can locate weak events by focusing energy at the source using time reversal (Gajewski, 2005; Chambers et al., 2009; Fu and Luo, 2009; Xuan and Sava, 2009). The drawbacks of the migration-based methods include high computational cost and their requirement of data redundancy (Xuan and Sava, 2009; Han, 2010). A semblance-weighted stacking method can also be used for microseismic source location, where the maxi-

mum value of the product of P- and S-wave semblances on a time window define the location of microseismic source (Eaton et al., 2011).

There are also several techniques (for example, hypocentroidal decomposition and double-difference tomography), which determine the relative location of the seismic source (Shearer, 1999). It has been recognized that the near real-time hypocentre locations may have large associated uncertainties, preventing high-resolution post-treatment interpretation (Figure 3). A first concern is that different service companies may obtain different event locations, even for the same dataset. This is caused by fundamental uncertainties in how to determine the most appropriate velocity model, the use of different event location algorithms but also elemental problems on how to pick consistently P- and S-wave arrivals in large datasets (sometimes consisting of 1000s of events recorded by 10s or 100s of 3-component receivers).

Much current research focuses on improved workflows for direct estimation of absolute hypocentres and on accurate relative event locations. Multiplet analysis can for instance be used to address the issues of unknown velocity models as well as inconsistent picking on final event locations (De Meersman et al., 2009; Kocon and Van der Baan, 2012). A doublet is a pair of events produced by nearly identical source mechanisms from closely spaced locations; a multiplet is a group of three or more of such events. The waveforms of multiplets are nearly identical, with the principal exception of additive random noise. Multiplets can be readily identified using cross correlation (Poupinet et al. 1984; Arrowsmith and Eisner, 2006). All events in each multiplet group are then relocated to improve their relative location accuracy (Figure 3), thereby revealing lineations and active faults planes.

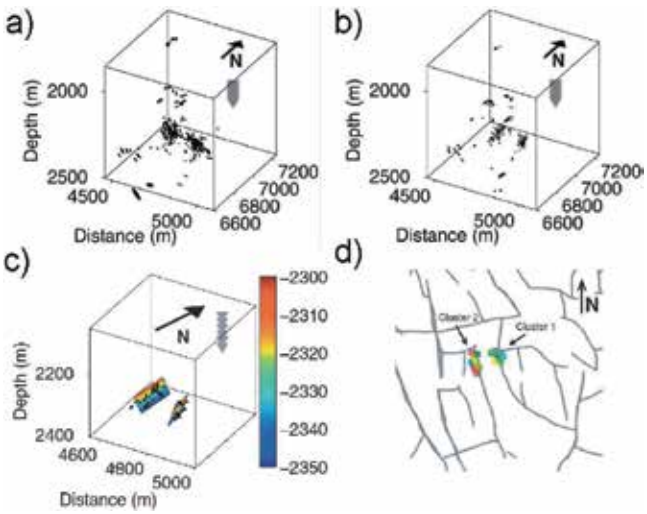

Figure 3. Microseismic events contain a wealth of information that can be used to determine planes of weakness along which fluid migration could occur. (a) Original source locations; (b) new source locations after application of a high-resolution relocation technique; (c) multiplets extracted and best fault plane solutions depicted in two major clusters; (d) obtained fault planes overlain onto the top-reservoir fault map interpreted from 3D surface seismic data (after De Meersman et al., 2009).

http://dx.doi.org/10.5772/56444

This approach has two important advantages. First the method is rather insensitive to the chosen velocity model since any inaccuracies will not obscure revealed geologic features but only change their size (Got, 1994, De Meersman et al., 2009). Secondly, mispicks and missing picks are automatically corrected for via the cross-correlation procedure. In addition, a crossplot of waveform correlation coefficients versus hypocentre separation distances of every event pair automatically reveals hypocentre location errors by examining location distances of identified multiplets. This technique enabled Kocon and Van der Baan (2012) to ascertain that events could be mislocated by 350m in a heavy-oil dataset due to erroneous traveltime picks.

Once the multiplet groups are detected, the double-difference method can be applied. This is a relative relocation method that seeks to reduce the effects of errors due to unanticipated velocity heterogeneities in the structure (Waldhauser and Ellsworth, 2000). An advantage of this method is that no master event is needed, which induces spatial limitations, since all events must be correlated with the reference event. The main assumption in this method is that ray paths between two events will be very similar if their hypocentral separation is small compared to the source-receiver distances; therefore, the relative travel-time difference at a common station will be mainly due to the spatial offset between both events. In other words, the effects of most velocity heterogeneities will cancel out, such that only knowledge of the velocities in the source region is required. Castellanos and Van der Baan (2012) apply this method to data from a mining environment. Results clearly reveal a linear feature after relocation, possibly related to horizontal drilling activities.

Likewise, De Meersman et al. (2009) use relative locations to delineate a graben-like extensional structure in the caprock of a producing reservoir in the North Sea, UK (Figure 3). This graben-like structure was not visible in the original absolute locations which revealed solely two large microseismic clusters. Next they re-examine temporal changes in anisotropy as found by Teanby et al. (2004a) using the automated shear-wave splitting methodology of Teanby et al. (2004b) for this same dataset. They then argue that their integrated analysis of relocated sources, seismic multiplets, and S-wave splitting supports a model whereby stresses in this reservoir recharge cyclically. Effective stress builds up in response to reservoir compaction as a result of oil production, and stress is released by means of microseismic activity once criticality is reached on slip planes. These changes cause variations in seismic anisotropy and the microseismic source mechanisms over time.

5. Better understanding of physical processes associated with microseismicity

The microseismic case studies by De Meerman et al. (2009) andCastellanos and Van der Baan (2012) do not include fluid injection; yet they already demonstrate that analysis of the microseismic cloud of event locations can reveal important insights into the local geology and subsurface deformations. Pore pressure and stress changes during hydraulic fracturing lead to a propagating cloud of microseismic events, which can be recorded and analyzed to

constrain the volume of the stimulated zone. Because pressures and stresses diffuse/propagate beyond the fluid-filled fractures and affect the (generally jointed) rock mass in all directions, the microseismic cloud represents a volumetric map of the extent of shear and opening of naturally fractured rock.

A key element in current research is to develop interpretation methods that bridge the gap between geophysical data analysis and engineering applications of microseismic data. Ultimately, operators would like to know how to optimize the fracturing treatment given the in situ stress regime, dominant natural fracture orientations, pre-existing faults and other zones of weaknesses, and the prevailing lithologies. Phsyically, there exists an intimate link between the above geologic features, employed stimulation strategies and resulting microseismicity. Existing unknowns can be summarized using the following two fundamental questions: (1) Given a known stress field, geology, rock mass fabric and injection strategy, what are the most likely resulting microseismic characteristics (e.g., hypocentres, source mechanisms and magnitudes)? (2) What does measured microseismicity reveal about the existing stress field and local geomechanical properties of the rockmass? The first question involves solving the forward model (given the physical parameters, what are the resulting observations?) The second question involves solving the inversion problem (given our observations, what can we determine about the current physical state?).

From an engineering point of view, answering these questions will have an immediate impact on first creating optimal drainage and fracturing strategies and then confirming their success or failure prior to starting production. From a geophysical perspective, recorded microseismicity and integration of the results with surface seismic data should significantly enhance our understanding of the existing subsurface geologic conditions and the geomechanical behavior of the reservoir, thus providing pertinent information to the completion engineers.

Pertinent considerations include: (1) Obtaining accurate locations for microseismic events to support meaningful volumetric analysis of the associated microseismic cloud. (2) Inferring the failure mechanism (i.e., are fractures opening, closing or shearing?). (3) Determination of why failure is occurring in specific locations but not in others (why are fractures not always symmetric with respect to the injection well and what is the geomechanical behavior of the reservoir)? The last question, in particular, is difficult to answer from the recorded seismicity alone since the geomechanical behavior depends on the in-situ stress field, the local rock properties (lithologies), and any existing areas of weakness including faults, fractures and joints (Grob and Van der Baan, 2011, Chorney et al., 2012).

5.1. Advanced microseismic source analysis

Robust characterization of microseismic sources has the potential to provide important information about deformation mechanisms. Borrowing from earthquake seismology, seismic moment tensors can be used to describe microseismic point sources in general terms of a set of force couples. Moment tensors can be represented in terms of source type (Hudson et al., 1989), a classification scheme that includes shear slip (double couple), dipole, compensated linear vector dipole and volumetric sources. The reliability of these classification schemes depends critically upon the use of a recording array with a suitable geome-

http://dx.doi.org/10.5772/56444

try that satisfies geometrical requirements for azimuthal coverage of the source region (Eaton and Forouhideh, 2011).

Other fundamental descriptions of microseismic sources include the seismic moment and associated energy release, in addition to spectral source characteristics that reveal the time- and spatial-scales of rupture. Recent developments in earthquake seismology suggest that rock-deformation processes commonly occur across a broad spectrum of time scales (and frequency), wherein earthquakes merely represent a high-frequency end member (e.g., Beroza and Ide, 2011). We postulate that rock deformation processes associated with hydraulic fracturing obey scaling laws that are similar to earthquakes. If so, microseismic activity recorded conventionally using geophones, which are relatively insensitive to ground motion below their natural frequency (typically ~ 10 Hz), could represent a high-frequency end member of the complete deformation spectrum.

Seismic moment-tensors provide a general mathematical representation of seismic point sources (Ben-Menahem and Singh, 2000). Inversion techniques to estimate moment tensors from seismic recordings are well developed in earthquake seismology, but are only starting to be used in microseismic monitoring applications (Baig and Urbancic, 2010). The determination of moment tensors can potentially provide useful insights into rupture processes, but care is required to ensure that survey design is adequate (Eaton and Forouhideh, 2010; 2011).

The spatial dimensions of microseismic events are encoded in the spectra of the radiated seismic waves. Microseismic events can therefore be analyzed using spectral methods (e.g. Eaton, 2011), providing an alternative approach for characterizing sources. For example, models for shear slip on a circular crack (Brune 1970, 1971; Madariaga, 1977) predict the shape of source spectra and provide scaling relationships between spectral parameters and source parameters (slip area and seismic moment). These source attributes complement those derived from moment-tensor inversion.

Tensile microseismic events are believed to play an important role during hydraulic fracture treatment of unconventional reservoirs (Baig and Urbancic, 2010). Tensile microseismic events may be associated with self-propping (remnant aperture), or wedging open of natural fractures because of the induced strain field. Walter and Brune (1993) developed a model for far-field source spectra for tensile rupture, and compared these with modeled far-field spectra for shear-slip events and showed that anomalously low S/P spectral amplitude ratios are a diagnostic characteristic of tensile rupture. Building on this approach, Eaton et al. ("Scaling relations and spectral characteristics of tensile microseisms", manuscript in preparation for Geophysics) investigate source characteristics of microseismic events induced by hydraulic-fracturing, with application to microseismic data from the previously described multistage treatment in northeastern British Columbia. They show that although spectral estimates of magnitude are relatively unaffected by uncertainty in seismic attenuation, for typical microseismic magnitudes accurate knowledge of seismic attenuation is necessary to estimate some spectral parameters. They also document microseismic events with spectral characteristics that reflect a complex rupture pattern, such as rapid opening and closing of tensile cracks.

5.2. Geomechanical response and reservoir analysis

As indicated above, the reliability with which moment tensors can be determined depends strongly on the acquisition geometry (Eaton and Forouhideh, 2010; 2011). There is thus a need for alternative and complementary analysis methods to reveal more about the in situ stress field. Fortunately, independent information on the in situ stress field can also be obtained by analyzing the frequency-magnitude distribution of microseismic events. This is achieved by plotting the distribution of event magnitudes on a semi-log plot (Figure 4). This distribution, also called the Gutenberg-Richter relation, usually shows a power law behavior. Its linear slope gives the so-called b-value. Schorlemmer et al. (2005) have shown that this b-value changes depending on the stress regime by plotting b-values versus rake angles (indicating slip direction of the hanging wall) for a large variety of earthquakes. For a b-value less than 1, the vertical stress is the least principal compressive stress and we are in a thrust-fault regime. If the vertical stress is intermediate, the b-value will likely be around 1, indicating a strike-slip faulting regime. And if it exceeds 1, then the stress regime is extensional, with the maximum principal stress vertical, creating a normal fault regime.

The case study of Grob and Van der Baan (2011) using a microseismic dataset recorded over a heavy oil field drained using cyclic steam stimulation revealed that the in situ stress state changed from extensional to compressive with an intermediate strike-slip regime, indicating initial opening and then closing of fractures. This occurred over an 8-month period where pure injection in the first four months was followed by combined injection and production in different parts of the field (Figure 4). We postulate that analysis of the statistical b-values will provide complementary information to temporal and spatial variations in the in situ stress field as determined by moment-tensors inversions, and therefore contains a wealth of information to facilitate reservoir management.

5.3. Relating geomechanical properties to microseismic observables

Various observations suggest that microseismic events tend to occur preferentially in specific lithologies only (e.g., a sand) but not in some others (e.g., a shale), even if fluids are known to traverse both lithologies in a hydraulic fracturing experiment, shown in Figure 5 (Rutledge et al., 2004, Pettitt et al., 2009). This suggests that deformation in some rock types may occur aseismically, especially in higher-permeability, ductile shales, or simply that the radiated elastic energy for microseismic events in some rock types may occur at frequencies that are too low to be detected using conventional recording systems. Moreover, anecdotal information suggests that the abundance and intensity of microseismic events may not necessarily correlate to the effectiveness of the fracture treatments (Maxwell et al., 2008; Boroumand and Eaton, 2012).

The concept of microseismic efficiency represents the ratio of radiated seismic energy (Vassiliou and Kanamori, 1982) to the total deformation energy. Analysis of deformation energy is being done by using pressure, rate, fluid/proppant volume and other relevant data curves produced from the surface equipment in order to calculate the total energy/work produced to generate fractures in the ground. Often substantial differences are estimated between the total input energy inferred from fluid injection rates and pressures, the fracture

http://dx.doi.org/10.5772/56444

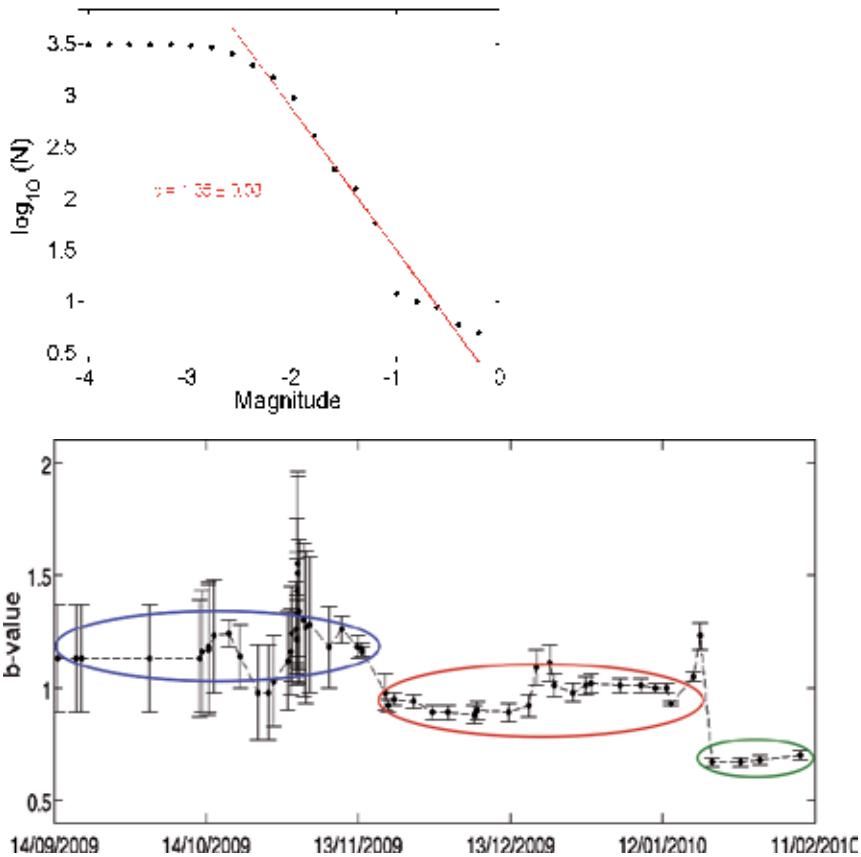

Figure 4. Analysis of frequency-magnitude variations in microseismic events recorded over a heavy-oil field drained using cyclic-steam stimulation (after Grob and Van der Baan, 2011). Top: Distribution of event sizes for the whole dataset. Shown is the cumulative number of events smaller than a given magnitude. A fit on the linear part of the curve gives a b-value of 1.35 indicating overall extensional faulting. Bottom: Temporal evolution of b-values for this dataset. Three stages are visible: at the beginning high b-values larger than 1.0 (implying extensional faulting or opening of fractures) until November 2009, followed by b-values around 1.0 and finally a last stage with values around 0.65 (indicating closing of fractures or compressive faulting), starting end of January 2010. Pure steam injection took place prior to November 2009, followed by a combined injection and production in different parts of the field. The statistical analysis of frequency-magnitude variations in microseismic data provide us with invaluable information on changes in the underlying stress fields.

energy to pry apart the walls of a single very large fracture, and the radiated energy observed from recorded seismicity. The injected energy is 10^4–10^7 times larger than the estimated radiated seismic energy, and the fracture energy is inferred to be 15–40% of the input energy (Maxwell et al., 2008; Boroumand and Eaton, 2012).

The three most likely factors to dominate the geomechanical behavior of a reservoir are the local in situ stress regime, pre-existing fractures (and other zones of weaknesses), and the actual rock properties (e.g., whether they are more ductile or brittle as expressed by their Young's modulus or Poisson's ratio and thus the Lamé parameters). In order to better understand why

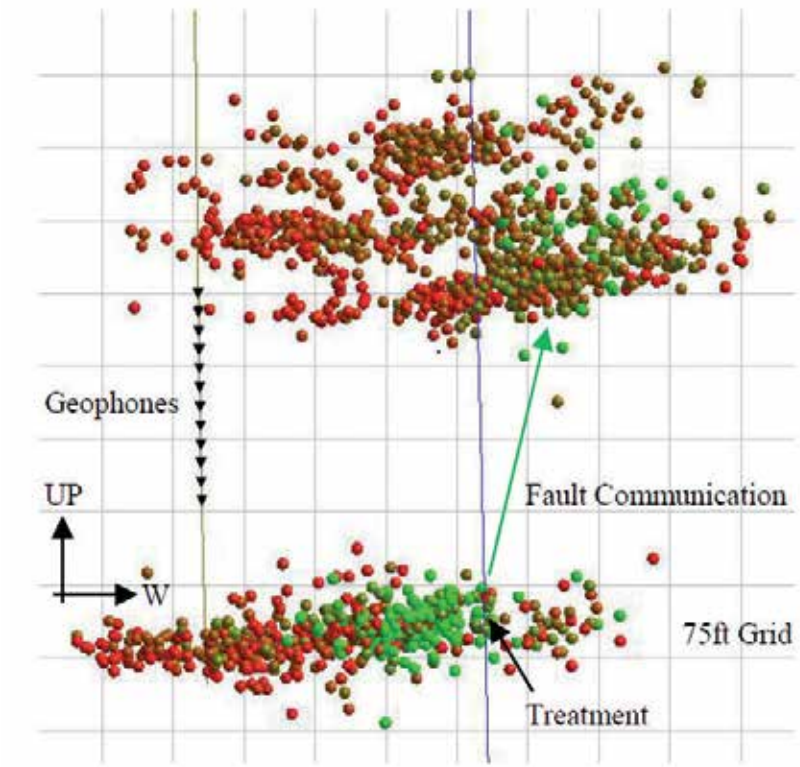

Figure 5. Hydraulic fracturing of a tight-gas sand. 1408 events are recorded over 5 hours. Events are colour shaded by time: green (earliest) to red (latest). Events occur in two formations with very few detected events in between. Yet the event history reveals that brittle failure occurs first in the right-most part of the bottom formation, and then suddenly jumps to the top formation indicating the presence of a possible aseismic fault. After Pettitt et al. (2009).

the seismic efficiency is so low, and what precisely happens when we are injecting fluids at high pressures into rocks we need to improve our understanding of what the various geophysical observations (moment tensors, hypocentres, resonance frequencies, etc.) truly reveal of the newly induced fracture networks specifically, and the geomechanical reservoir response in general. Three general options to achieve this objective are analogues, computational modelling, and physical modelling in the laboratory.

5.4. Analogues

Dusseault et al. (2011) use analogues to explain many of the fracturing processes that may occur when fluids and/or proppants are injected at high pressure into intact and naturally fractured rock. They consider a medium composed of rigid blocks and injection of a solid. This leads to many insights despite the fact that this is clearly a great simplification of reality.

In Figure 6 a solid material is injected into a material composed of rigid blocks, producing tensile mode I fracturing (i.e., wedging) at the tips of the proppant inclusions, and mode II (i.e.,

http://dx.doi.org/10.5772/56444

shearing) in the surrounding areas due to block rotations. Wedging creates fracture openings well beyond the proppant tips (or infiltration extents) due to normal extensional forces on the surfaces of the joint leading to tensile (mode I) failure and facilitating slurry/proppant penetration. It also leads to a large increase in the effective permeability in a zone beyond the proppant infiltration.

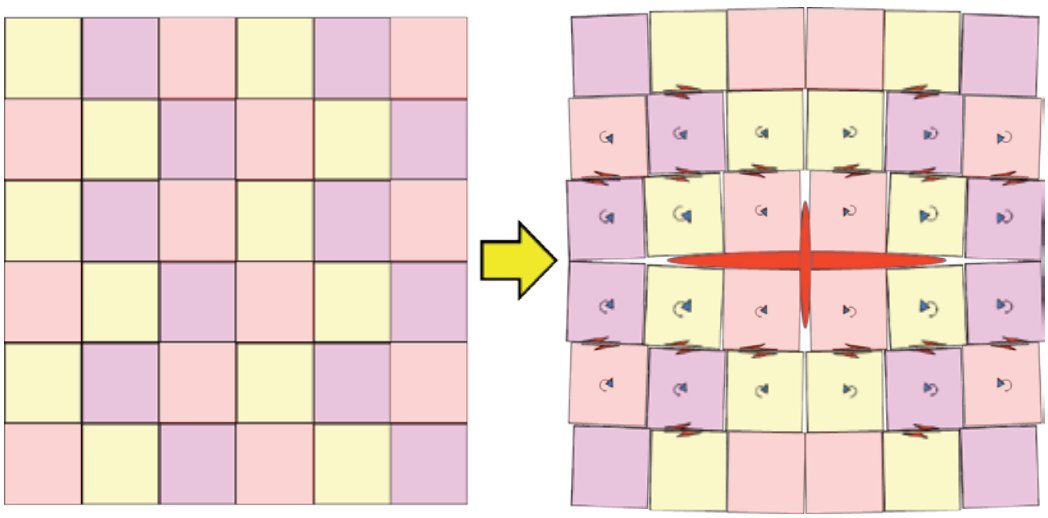

Figure 6. Analogues can help us understand how fluid and/or proppant injection into a reservoir zone affects the resulting rock deformation. In this case a solid material is injected into a material comprised of rigid blocks, showing clearly where propping, wedging, rotation and shearing will occur. Such observations provide important clues on the anticipated moment tensors throughout the resulting microseismic event cloud. From: Dusseault et al. (2011).

Block rotation continues beyond the area of proppant infiltration and tensile opening at the proppant tips. It involves large changes in both the normal and shear forces excited on the joint surfaces, yielding predominantly mode II fracturing (i.e., shearing). This may cause slip on existing joints in naturally fractured rocks, and even facilitate fault reactivation if the effective stresses are sufficiently to close to criticality. Shear displacement along natural fractures is associated with self-propping where irregular joint surfaces after slip create remnant apertures, facilitating subsequent fluid flow (Dusseault et al., 2011). Such observations provide important clues on the anticipated moment tensors throughout the resulting microseismic event cloud, demonstrating that tensile source mechanism are likely to dominate close to the proppant tips, but double-couple events in all other areas.

Obviously fluid and/or proppant infiltration into naturally fractured rock is significantly more complex since the exact behaviour will depend on the situ stress field, pre-existing in natural fractures and lithologies. The interaction of brittle failure in intact rock and the slip/shearing in naturally fractured areas can be complex (Figure 7); yet the principles deduced from the study of analogues should help unravel the various competing processes.

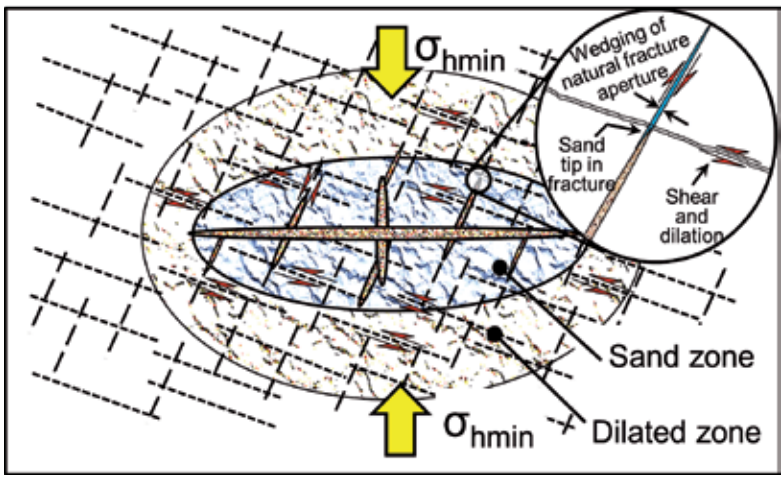

Figure 7. Fluid and/or proppant injection into a reservoir zone will create new fractures, as well as close, shear or pop open existing fractures. The various failure mechanisms may lead to a larger microseismic cloud surrounding the area of injected fluids, thereby improving reservoir drainage. The microseismic events are therefore also characterized by a variety of earthquake mechanisms. Their analysis can yield a wealth of knowledge on the underlying failure mechanisms beyond mere locations. From: Dusseault et al. (2011).

5.5. Geomechanical modelling

Analogues provide a first understanding on how fluid and/or proppant injection is likely to deform the surrounding rock mass (Figures 6 and 7). They also provide pertinent clues on where to expect brittle failure (and thus microseismic events) and their most probable failure mechanism (source mechanism). Geomechanical modeling is subsequently a great aid for improving our understanding on links between fluid-induced rock failure, the occurrence of microseismicity and underlying geomechanical behaviour, beyond the assumption of rigid blocks and no fluid diffusion (i.e., no leak off).

Bonded-particle modeling is becoming an important computational tool for modeling the complex dynamical behavior of rocks rupturing given a set of boundary conditions (Potyondy and Cundall, 2004). This approach simulates rock deformation using an assemblage of rigid, round particles that are bonded together. This grid of particles can deform freely and bonds can be broken to represent local failure. Bonds are characterized by normal and shear strengths as well as friction coefficients to model respectively tensile and shear failure. Such a discontinuum-based approach seems more appropriate to model rock deformation through failure since it eliminates the need for complex constitute relations required for continuum approaches (Hazzard and Young, 2000). Also microseismic moment tensors can be inferred by integrating local bond failure in both space and time (Hazzard and Young, 2004).

Chorney et al. (2012) use bonded-particle modelling to examine resulting seismicity for triaxial compression tests using different confining pressures. The resulting Hudson plots (i.e., moment-tensor distribution) show a surprising similarity with those obtained for real data by

http://dx.doi.org/10.5772/56444

Baig and Urbancic (2010) from field observations of hydraulic fracturing (Figure 8). Baig and Urbancic (2010) find dominant failure mechanisms of double couple (shearing) and fracture opening and closing (tensile failure and closing). This confirms insights gained from the analogues (Figures 6 and 7) where shearing and tensile failure seem to dominate, respectively, in the surrounding area and at the tips of the proppant infiltrations.

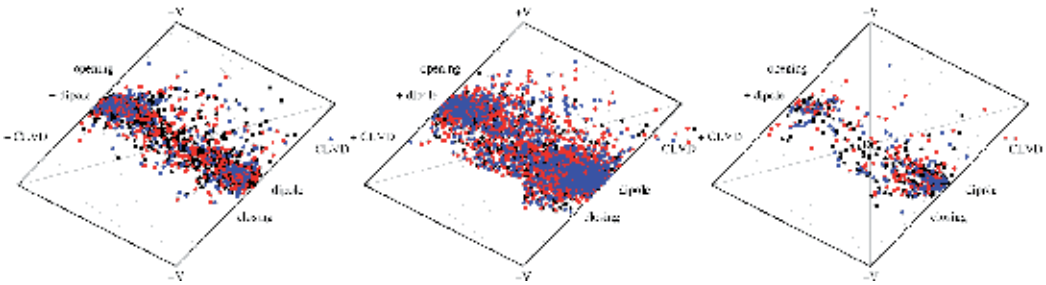

Figure 8. Hudson plots of the failure mechanisms for microseismic events in the bonded-particle simulations for triaxial compression tests with confining pressures of 0 MPa (left) and 40 MPa (right). The colors represent the time: pre-peak stress events are in black; events happening around peak stress are in red and post-peak events are displayed in blue (modified from Chorney et al., 2012). Both fracture opening and closing (tensile failure and closing) occurs. CLVD: Compensated-linear vector dipole. The simulated seismicity shows a surprising correspondence with real field measurements from hydraulic fracturing experiments (e.g., Baig and Urbancic, 2010).

Chorney et al. (2012) also monitor the total input energy of the system, the total kinetic energy emitted from bond breakages, and the energy deduced from the moment magnitudes of the microseismic events. The kinetic energy represents approximately 5% of the input energy; the radiated seismic energy is 50-100 times smaller than the kinetic energy. The radiated energy calculated using the Gutenberg-Richter relationship between moment magnitude and energy may thus underestimate the energy incurred from brittle failure. Both the radiated and kinetic energy from brittle failure are substantially lower than the input energy. This confirms observations by Maxwell et al. (2009) and Boroumand and Eaton (2012). Ductile or slow, aseismic deformation must thus constitute a significant term in the energy budget for both these numerical simulations of triaxial compression and for hydraulic fracturing experiments in general.

Approaches such as bonded-particle models are thus useful to study the anticipated geomechanical behavior of a reservoir; in particular anticipated brittle failure (as expressed by a microseismic event) as well as any aseismic deformation (due to semi-brittle or plastic flow). Ultimately, they may help to investigate how resulting deformation and microseismic emissions depend on (1) in the in situ stress regime, which relates to the magnitude and ratio of the vertical stress Sv and the maximum and minimum horizontal stresses SH and Sh; (2) pre-existing fractures and other zones of weakness most likely to break; and finally (3) the local rock properties defined by the Young's modulus and Poisson's ratio (both related to the Lamé parameters). Constraints on many of these factors can be obtained using the processing and interpretation techniques described previously.

Unfortunately, discontinuum-based methods such as bonded-particle approaches may be less suitable to simulate fluid injection as fluids can only be described as small particles.

Continuum-based approaches such as finite-element methods may be required for coupled fluid-flow and geomechanical simulation (Dean et al., 2003; Minkoff et al., 2003; Angus et al., 2010). On the other hand, particle-based methods are highly appropriate to modelling crack propagation and brittle failure. Although this is feasible with continuum-based approaches it leads to highly expensive computations. Angus et al. (2010), for instance, circumvent the requirement for modelling fracture propagation by assuming that the differential effective stress tensor at the local point of failure is a first-order approximation to the local failure mechanism (Zoback and Zoback, 1980). For failure in intact rock this is likely a reasonable assumption, but not for failure along pre-existing weaknesses (Gephart and Forsyth, 1984).

5.6. Physical modelling

Ultimately physical modelling in the laboratory is required to confirm our inferences from the study of analogues and numerical simulations, thereby completing the circle between fluid-induced rock failure, the occurrence of microseismicity and underlying geomechanical deformation. Many authors have studied the links between microseismic event locations and fracture growth in both triaxial compression and hydraulic fracturing tests (Solberg et al., 1980; Sondergeld and Estey, 1981; Kranz et al., 1990; Lockner et al., 1991; Lockner, 1993; Chitrala et al., 2010). Most of these studies were successful in determining the event hypocenters; yet few provided reliable full moment tensor solutions. The latter are essential for better understanding the actual rock failure mechanisms.

The analogues are very useful for building a first understanding on what to expect when injecting fluids and/or proppants into the rock matrix (Figures 6 and 7) but the combination of numerical simulations and their verification using physical experiments in the laboratory will help to bridge the gap between geophysical data analysis and engineering applications of microseismic data by providing a framework for advanced interpretation strategies, thereby facilitating completion of the the circle between acquisition, processing and interpretation.

6. Conclusions

The recent surge in development of unconventional resources such as shale-gas and heavy-oil plays has created renewed interest in microseismic monitoring. Pore pressure and stress changes during fluid and/or proppant injection lead to an expanding cloud of microseismic events, due to brittle failure in intact rock and additional slip/shearing in naturally fractured rock. The microseismic cloud represents thus a volumetric map of the extent of induced fracture shearing and opening; yet integration of event locations with moment tensors, other geophysical observations and geomechanical constraints is required to determine ultimately the size of the interconnected fracture network, thereby excluding isolated fracturing/shearing, since only the former contributes to the enhanced effective porosity and permeability, required for predicting actual reservoir drainage.

http://dx.doi.org/10.5772/56444

Due to a strong desire for near-real time information by completion engineers, acquisition and service companies have focused predominantly on providing hypocentre locations and moment magnitudes. Microseismic recordings contain, however, a wealth of information beyond event locations, including moment tensors and resonance frequencies. Thus, many pertinent research questions on microseismic acquisition, processing and interpretation remain to be answered before full use of microseismic recordings can be achieved.

Nonetheless, microseismic monitoring has a bright future with long-standing applications such as monitoring of shaft stability in mines and the creation of engineered geothermal systems; more recent applications involve monitoring of hydraulic stimulation of "tight" hydrocarbon reservoirs and steam-injection in heavy-oil fields. Future applications may incorporate surveillance of CO_2 storage as well as slurried waste solids disposal through continuous injection.

Acknowledgements

The first two authors would like to thank the sponsors of the Microseismic Industry Consortium for financial support. Arc Resources, Nanometrics and ESG Solutions are particularly thanked for their support of the field project. All authors would like to thank their collaborators, students and postdocs whose work has contributed tremendously to this paper.

Author details

Mirko van der Baan[1], David Eaton[2] and Maurice Dusseault[3]

*Address all correspondence to: Mirko.vanderBaan@ualberta.ca

1 University of Alberta, Edmonton, Alberta, Canada

2 University of Calgary, Calgary, Alberta, Canada

3 University of Waterloo, Waterloo, Ontario, Canada

References

[1] Aki, K., Fehler, M., and Das, S., 1977, Source mechanism of volcanic tremors: fluid-driven crack model and their application to the 1963 Kilauea eruption: Journal of Volcanology and Geothermal Research, 2, 259–287.

[2] Albright, J. N., and Pearson, C. F., 1982. Acoustic emissions as a tool for hydraulic fracture location: experience at the Fenton Hill Hot Dry Rock site: Soc. Petr. Eng. Journal., 22: 523-530.

[3] Angus D. A., J.-M. Kendall, Q.J. Fisher, J.M. Segura, S. Skachkov, A.J.L. Crook and M. Dutko, 2010, Modelling microseismicity of a producing reservoir from coupled fluid-flow and geomechanical simulation: Geophysical Prospecting, 58, 901–914.

[4] Arrowsmith S. J. and Eisner L., 2006, A technique for identifying microseismic multiplets and ap-plication to the Valhall field, North Sea, Geophysics, 71 (2), V31 – V40.

[5] Baig, A. and Urbancic, T., 2010. Microseismic moment tensors: A path to understanding frac growth. The Leading Edge, 29: 320-324.

[6] Ben-Menahem, A. and S.J. Singh (2000). Seismic Waves and Sources. 2nd edition, Dover Publications, New York.

[7] Benson, P. M., S. Vinciguerra, P. G. Meredith, and R. P. Young, 2008, Laboratory simulation of volcano seismicity: Science, 322, 249–252.

[8] Beroza, G.C. and Ide, S. 2011. Slow earthquakes and nonvolcanic tremor. Annual review of Earth and planetary sciences, 39: 271-296.

[9] Beroza, G.C. and Satoshi, I. 2011. Slow earthquakes and nonvolcanic tremor. Annual review of Earth and planetary sciences, 39: 271-296.

[10] Bolt, B.A., 1984. Inside the Earth : evidence from earthquakes. W.H. Freeman, 191 pp.

[11] Boroumand, N., and D. W. Eaton, 2012, Comparing Energy Calculations - Hydraulic Fracturing and Microseismic Monitoring: 74th Mtg., EAGE, Copenhagen, C042.

[12] Brown, A., 2004, Interpretation of three-dimensional seismic data. American Association of Petroleum Geologists; 6th edition, 560 pp.

[13] Brune, J. N., 1970. Tectonic stress and the spectra of seismic shear waves from earthquakes. J. Geophys Res., 75: 4997-5009.

[14] Brune, J.N., 1971. Correction. J. Geophys. Res., 76: 5002.

[15] Castellanos F. and Van der Baan M. (2012) High-accuracy relative event locations using a combined multiplet analysis and the double-difference inversion. 82nd Ann. Int. Mtg., SEG, Las Vegas, PSC4.

[16] Chambers, K., Kendall, J. M., Dahl, S.B., and Rueda, J., 2009. The detectability of microseismic events using surface arrays: EAGE Workshop on Passive Seismic Limassol, Cyprus.

[17] Chitrala, Y., C. Moreno, C. Sondergeld and C. Rai, 2011, Microseismic and microscopic analysis of laboratory induced hydraulic fractures. SPE 147321.

http://dx.doi.org/10.5772/56444

[18] Chorney, D., Jain, P., Grob, M. and van der Baan, M., 2012, Geomechanical modeling of rock fracturing and associated microseismicity: The Leading Edge, 31, N. 11, 1348-1354.

[19] Clarkson, C.R., Aguilera, R., Pedersen, P.K., and Spencer, R.J., 2011. Shale gas, part 8: Shale gas development optimization. CSPG Reservoir, 38(4): 25-31.

[20] Cypster, D.A. and Davis, S.D., 1998. Induced seismicity and the potential for liability under U.S. law. Tectonophysics, 289: 239-255.

[21] Das, I. and Zoback, M.D., 2011. Long-period, long-duration seismic events during hydraulic fracture stimulation of a shale gas reservoir. Leading Edge, 30: 778-786.

[22] De Meersman K., Kendall J-M. and Van der Baan M. 2009. The 1998 Valhall microseismicity: An integrated study of relocated sources, seismic multiplets and S-wave splitting. Geophysics, 74(5), B183-B195.

[23] de Pater, H. & Baisch, S., 2011, Geomechanical Study of Bowland Shale Seismicity, Synthesis Report, commissioned for Cuadrilla resources, accessed online http://www.cuadrillaresources.com/wp-content/uploads/2012/02/Geomechanical-Study-of-Bowland-Shale-Seismicity_02-11-11.pdf

[24] de Ridder, S. and Dellinger, J., 2011. Ambient seismic noise eikonal tomography for near-surface imaging at Valhall. Leading Edge, 30: 506-512.

[25] Dean R.H., Gai X., Stone C.M. and Minkoff S.E. 2003. A comparison of techniques for coupling porous flow and geomechanics. SPE Reservoir Simulation Symposium, 3–5 February, Houston, Texas, USA, Expanded Abstracts, 79709.

[26] Dusseault M., J. McLennan and S. Jiang (2011) Massive multi-stage hydraulic fracturing for oil and gas recovery from low mobility reservoirs in China: Petroleum Drilling Techniques, 39 (3), 6-16.

[27] Eaton, D.W., 2011. Q determination, corner frequency and spectral characteristics of microseismicity induced by hydraulic fracturing. SEG Annual Meeting, San Antonio, Abstract PSC 3.4 .

[28] Eaton D. (2012) Crack-tip Stress Field, Coulomb Failure, and the Spectral Characteristics of Tensile Rupture. 74th EAGE Conference & Exhibition incorporating SPE EUROPEC 2012, Copenhagen, Denmark.

[29] Eaton, W.D., Akram, J., St-Onge, A., and Forouhideh, F., 2011. Determining microseismic event locations by semblance-weighted stacking: CSPG CSEG CWLS Convention, Calgary.

[30] Eaton, D.W. and Forouhideh, F., 2010. Microseismic moment tensors: The good, the bad and the ugly. CSEG Recorder, 35(9), 45-49.

[31] Eaton, D.W. and Forouhideh, F., 2011. Solid angles and the impact of receiver-array geometry on microseismic moment-tensor inversion. Geophysics, 76: WC75-WC83.

[32] EIA (Energy Information Administration), 2011. International Energy Outlook 2011, DOE/EIA-0404, 301 pp. Accessed online at http://www.eia.gov/forecasts/ieo/pdf/0484(2011).pdf.

[33] Eisner L., Duncan P., Heigl W., and Keller W., 2009. Uncertainties in passive seismic monitoring: The Leading Edge, 28: 648-655.

[34] Ferrazzini, V., and Aki, K., 1987, Slow waves trapped in a fluid-filled infinite crack: implication for volcanic tremor, Journal of Geophysical Research, 92(B9), 9215-9223.

[35] Fu, Q., and Luo, Y., 2009, Locating Micro-Seismic Epicenters in Common Arrival Time Domain: SEG Houston International Exposition and Annual Meeting, 1647-1651.

[36] Gajewski, D., 2005. Reverse modelling for seismic event characterization: Geophysical Journal International, 163: 276–284.

[37] Gephart J. and Forsyth D. 1984. An improved method for determining the regional stress tensor using earthquake focal mechanism data: Application to the San Fernando earthquake sequence. Journal of Geophysical Research B11, 9305–9320.

[38] Gibowicz , S. and Kijko, A., 1994. An introduction to mining seismology. Academic Press, 399 pp.

[39] Got, J.-L., 1994, Deep fault plane geometry inferred from multiplet relative relocation beneath the south flank of Kilauea: Journal of Geophysical Research, 99, 15375–15386.

[40] Grob, M. and van der Baan, M., 2011, Inferring in-situ stress changes by statistical analysis of microseismic event characteristics: The Leading Edge, 30, no. 11, p. 1296–1301.

[41] Han, L., Wong, J., and Bancroft, J., 2009. Time picking and random noise reduction on microseismic data: CREWES Research Report, 21, 1-13.

[42] Han, L., 2010, Microseismic Monitoring and Hypocentre Location: MS Thesis, University of Calgary.

[43] Häring, M.O., Schanz, U., Ladner, F. and Dyer, B.C., 2008. Characterisation of the Basel 1 enhanced geothermal system. Geothermics, 37: 469–495.

[44] Hazzard JF, Young RP., 2000. Simulating acoustic emissions in bonded-particle models of rock: International Journal of Rock Mechanics and Mining Sciences, 37(5), 867–872.

[45] Hazzard JF, Young RP., 2004. Dynamic modeling of induced seismicity: International Journal of Rock Mechanics and Mining Sciences, 41, 1365–1376.

[46] Hudson, J., Pearce, R. and Roberts, R., 1989. Source type plot for inversion of the moment tensor. J. Geophys. Res., 94: 765-774.

http://dx.doi.org/10.5772/56444

[47] Ide, S., Beroza, G.C., Shelly, D.R. & Uchide, T. (2007) A scaling law for slow earthquakes. Nature 447, 76-79.

[48] IHS CERA, 2010, Fueling North America's Energy Future, Executive Summary, 12 pp. Accessed at http://www2.cera.com/docs/Executive_Summary.pdf.

[49] Jones, G. A., Raymer, D., Chambers, K., and Kendall, J. M., 2010. Improved microseismic event location by inclusion of a priori dip particle motion: a case study from Ekofisk: Geophysical prospecting, 58: 727-737.

[50] Karpfinger, F., 2009, Modelling borehole wave signatures in elastic and poroelastic media with spectral method, Ph. D. Thesis, Curtin University of Technology, Aus.

[51] King, G. E. (2012) Hydraulic Fracturing 101: What Every Representative, Environmentalist, Regulator, Reporter, Investor, University Researcher, Neighbor and Engineer Should Know About Estimating Frac Risk and Improving Frac Performance in Unconventional Gas and Oil Wells. SPE 152596.

[52] Kocon K. and Van der Baan M. (2012) Quality assessment of microseismic event locations and traveltime picks using a multiplet analysis. The Leading Edge, 31(11), 1330-1337. Kranz, R. L., T. Satoh, O. Nishizawa, K. Kusunose, M. Takahashi, K. Masuda, A. Hirata, Laboratory study of fluid pressure diffusion in rock using acoustic emissions, J. Geophys. Res., 95, 21593–21607, 1990.

[53] Lamb, H., 1917. On waves in an elastic plate, Proceedings of the Royal Society, London: 114-128.

[54] Lockner, D. A., 1993, The role of acoustic emission in the study of rock fracture. lnt. J. Rock Mech. Min. Sci. & Geomech. Abstr. Vol.30, No.7, pp. 883-899.

[55] Lockner, D.A., J. D. Byerlee, V. Kuksenko, A. Ponomarev and A. Sideron, 1991, Quasi-static fault growth and shear fracture energy in granite: Nature, 350, 39-42.

[56] Madariaga, R., 1977. High frequency radiation from cracks (stress drop) models of earthquake faulting. Geophys. J., 51: 625-652.

[57] Maxwell, S.C., 2010. Microseismic: growth born from success. Leading Edge, 29: 338-343.

[58] Maxwell, S.C., 2011. Microseismic hydraulic fracture imaging; the path toward optimizing shale gas production. Leading Edge, 30: 340-346.

[59] Maxwell, S.C., Shemata, J., Campbell, E., and Quirk, D., 2008, Microseismic deformation rate monitoring. SPE 116596.

[60] Maxwell, S.C., Shemeta, J., Campbell, E., and Quirk, D., 2009. Microseismic deformation rate monitoring", EAGE, A18.

[61] Maxwell, S. C., C. K. Waltman, N. R. Warpinski, M. J. Mayerhofer, and N. Boroumand, Imaging seismic deformation induced by hydraulic fracture complexity, SPE paper 102801.

[62] Maxwell, S.C., Rutledge, J., Jones, R. and Fehler, M.C. 2010. Petroleum reservoir characterization using downhole microseismic monitoring. Geophysics, 75: 75A129-75A137.

[63] McGillivray, P., 2005, Microseismic and time-lapse seismic monitoring of a heavy oil extraction process at Peace River, Canada: CSEG Recorder, 30(1): 5-9.

[64] Michaud, G., Leslie, D., Drew, J., Endo, T., and Tezuka, K., 2004. Microseismic event localization and characterization in a limited aperture HFM experiment: SEG International Exposition and 74th Annual Meeting, Denver Colorado.

[65] Minkoff S.E., Stone C.M., Bryant S., PeszynskaM. and Wheeler M.F. 2003. Coupled fluid flow and geomechanical deformation modelling. Journal of Petroleum Science and Engineering 38, 37–56.

[66] Oye, V., and Roth, M., 2003. Automated seismic event location for hydrocarbon reservoirs: Computers & Geosciences, 29, 851 – 863.

[67] Pettitt W., J. Reyes-Montes, B. Hemmings, E. Hughes and R. P. Young, 2009, Using continuous microseismic records for hydrofracture diagnostics and mechanics: SEG, Expanded Abstracts, 28, 1542-1546.

[68] Potyondy DO, Cundall PA., 2004. A bonded-particle model for rock: International Journal of Rock Mechanics and Mining Science, 41(8):1329–64.

[69] Poupinet G, Ellsworth W, Frechet J, 1984, Monitoring velocity variations in the crust using earthquake doublets: An application to the Calaveras fault, California: J. Geophys. Res., 89, 5719–5731. Raggio, L., Etcheverry, J., and Bonadeo, N., 2007. Determination of acoustic shear and compressional wave velocities for steel samples by impulse excitation of vibrations, IV Conferencia Panimericana de END, Buenos Aires.

[70] Reine C., M. Van der Baan and R. Clark (2009) The robustness of seismic attenuation measurements using fixed- and variable-window time-frequency transforms: Geophysics, 74(2), WA123-WA135.

[71] Rutledge, J.T., W. S. Phillips, and M. J. Mayerhofer, 2004, Faulting induced by forced fluid injection and fluid flow forced by faulting: An interpretation of hydraulic fracture microseismicity, Car-thage Cotton Valley gas field, Texas: Bulletin of the Seismological Society of America, 94, 1817–1830.

[72] Schorlemmer, D., Wiemer, S. and Wyss, M., 2005, Variations in earthquake-size distribution across different stress regimes, Nature, 437, 539-542, doi:10.1038/nature04094.

http://dx.doi.org/10.5772/56444

[73] Sharma, B.K., Kumar, A., and Murthy, V.M., 2010. Evaluation of seismic event-detection algorithms: Journal geological society of India, 75, 533 - 538.

[74] Shearer, P., 1999, Introduction to seismology, Cambridge University Press.

[75] Shemata, J. and Anderson, P., 2010. It's a matter of size: Magnitude and moment estimates for microseismic data. Leading Edge, 29: 296-302.

[76] Solberg, P. H., Lockner, D. A., and Byerlee, J. D., 1980, Hydraulic fracturing in granite under geothermal conditions, International J. of Rock Mech., v. 17, p. 25-33.

[77] Sondergeld, C. H., L. H. Estey, 1981, Acoustic emission study of microfracturing during the cyclic loading of Westerly Granite, J. Geophys. Res., 86, 2915–2924.

[78] Stein, S. and Wysession, M., 2003. An introduction to seismology, earthquakes, and earth structure. Blackwell, 498 pp.

[79] St-Onge, A. and Eaton, D., 2011. Noise examples from two microseismic datasets. CSEG Recorder, 6(8): 46-49.

[80] Sun, R., and McMechan, G., 1988, Finite-Difference Modeling of Borehole Resonances: Energy Resources, 10, 55-75.

[81] Tary, J., and van der Baan, M., 2012, Potential use of resonance frequencies in microseismic interpretation, The Leading Edge, 31, 1338-1346.

[82] Tary, J., and van der Baan, M., 2013, On the interpretation of resonance frequencies recorded during microseismic experiments, 2013 Geoconvention, Calgary, submitted.

[83] Teanby, N., J.-M. Kendall, R. Jones, and O. Barkved, 2004a, Stress-induced temporal variations in seismic anisotropy observed in microseismic data: Geophysical Journal International, 156, 459–466.

[84] Teanby N.A., Kendall J-M. and Van der Baan M. (2004b) Automation of shear-wave splitting measurements using cluster analysis. Bull. Seism. Soc. Am., 94, 453-463.

[85] Thompson, B. D., R. P. Young, and D. A. Lockner, 2009, Premonitory acoustic emissions and stick-slip in natural and smooth-faulted Westerly granite, Journal of Geophysical Research, 114, B02205.

[86] Urbancic, T. and Trifu, C., 2000. Recent advances in seismic monitoring technology at Canadian mines. Journal of Applied Geophysics, 45: 225-237.

[87] Vassiliou, M.S. and Kanamori, H., 1982. The energy release in earthquakes. Bull. Seismol. Soc. Am., 72: 371-387.

[88] van der Baan, M., 2009, The origin of SH-wave resonance frequencies in sedimentary layers, Geophysical Journal International, 178, 1587-1596.

[89] van der Baan, M., Wookey, J., and Smit, D., 2007, Stratigraphic filtering and source penetration depth, Geophysical Prospecting, 55, 679-684.

[90] Verdon, J.P, Kendall, J-M, White, D.J., Angus, D.A., Fisher, Q.J. and Urbancic, T., 2010. Passive seismic monitoring of carbon dioxide storage at Weyburn. Leading Edge, 29, 200-206.

[91] Waldhauser, F., and Ellsworth, W. L., 2000, A Double-Difference Earthquake Location Algorithm: Method and Application to the Northern Hayward Fault, California: Bull. Seis. Soc. Am., 90, 1353-1368.

[92] Walter, W.R. and Brune, J.N., 1993. Spectra of seismic radiation from a tensile crack. J. Geophys. Res., 98: 4449-4459.

[93] Warpinski, N., 2009. Microseismic Monitoring: Inside and Out. Journal of Petroleum Technology, 61(11), 80-85.

[94] Xuan, R., and Sava, P., 2009. Probabilistic micro-earthquake location for reservoir monitoring: SEG Houston International Exposition and Annual Meeting: 1637-1641.

[95] Zoback M. and Zoback M. 1980. State of stress in the conterminous United States. Journal of Geophysical Research 85, 6113–6156.

Chapter 22

Blue Shift in the Spectrum of Arrival Times of Acoustic Signals Emitted during Laboratory Hydraulic Fracturing

Arcady V. Dyskin, Elena Pasternak,
Andrew P. Bunger and James Kear

Additional information is available at the end of the chapter

http://dx.doi.org/10.5772/56448

Abstract

We discuss a method of detecting localised fracturing that potentially requires only one channel. The method is based on the notion that the fracture propagation involves generation of acoustic events from its contour. It is proposed that the number of events (microcracks) generated at each step of fracture propagation could be proportional to the fracture size to a certain power called the localisation exponent. This dependence of the number of generated events on the fracture size (the event coherence) leads to a shift to higher frequency (the "blue shift") in the combined spectrum of the events as compared to the spectrum of randomly generated events. This concept was applied to the results of a laboratory test in which hydraulic fracture was driven by injecting glycerine into a 200x200x120mm block of polycrystalline gabbro. We show that there is indeed a blue shift in the spectrum of the arrival times at any one sensor that seems to correspond with the growth of a localized hydraulic fracture. The localisation exponent is able to distinguish between the cases of the fracture contour length roughly proportional to, and more slowly than proportional to, the nominal fracture radius.

1. Introduction

Hydraulic fracturing is a technique often used in subsurface geotechnical engineering for production stimulation in petroleum and geothermal reservoirs, for caving stimulation in the mining industry, and for stress measurements in the Earth's crust. Since the size and orientation of the hydraulic fracture and the number of fractures induced by a given injection depend on potentially complicated conditions of rock mass structure and the stress state, they are often

difficult to predict. This necessitates the development of methods for detecting the geometry and location of the hydraulic fracture(s) and/or monitoring the process of its propagation. A number of methods were proposed for this purpose (see review [1]). They include treating pressure response (e.g. [2, 3]), tracing the fracture fluid (e.g. [3]), microseismic mapping (e.g. [1, 4-8]), crosswell seismic detection (e.g. [9, 10]), vertical seismic profiling (e.g. [11, 12]), borehole overcoring [1], borehole cameras (e.g. [13]), surface tilts (e.g. [8, 14, 15]).

The methods based on microseismic monitoring are attractive because they are capable of providing real-time information about the growth of the region that is impacted by stress and pore pressure changes that lead to the release of seismic energy during injection. Currently these methods are based on locating the microseismic events. Accurate locations of the sources require simultaneous, recording the events using multiple sensors together with accurate measurements of the wave propagation velocities in multiple directions in the rock mass.

In contrast, Pasternak and Dyskin [16] proposed a method of detecting the localised fracturing which potentially requires only one channel. The method is based on the notion that the propagation of a localised fracture process (e.g., the process zone of the hydraulic fracture) involves generation of microcracks from the contour of a propagating localised zone or a fracture. The microcrack generation is almost instantaneous as compared to the time of crack propagation since the interaction between the main fracture or localisation zone and the microcracks occurs with the speed of the stress waves. As a result the number of events (microcracks) generated at each step of fracture propagation should be proportional to the length of the contour and hence proportional to the radius of the propagating fracture. This dependence of the number of generated events on the fracture radius (the event coherence) leads to the blue shift (i.e. shift to higher frequencies) in the combined spectrum of the events as compared to the spectrum of randomly generated events. The blue shift can even be detected in the 'spectrum of arrival times' that is the Fourier transform of the time delays between the arriving signals.

Obviously single sensor data will never lead to event locations. Instead, the goal of the Blue Shift approach is to enable using a relatively inexpensive single sensor array in order to detect localization and, ultimately, to be able to infer something about the dimensionality of the leading edge of the fracture. We hope to distinguish among, for example: 1) height constrained (i.e. PKN) type growth where the length of the propagating leading edge is essentially fixed at the height of the reservoir, 2) quasi-radial growth where the length of the leading edge grows proportionally to the nominal radius, and 3) diffuse or network-type growth where the combined length of the fractures' leading edges grows more rapidly than proportionality to the nominal radius of the fractured zone.

In this paper we report the results of a first-stage laboratory test conducted in order to provide guidance to the ongoing development of the Blue Shift approach. The following section, Section 2 describes the essentials of this approach. Section 3 describes the experiments and the measurements and Section 4 shows the application of the blue shift indicator to analyse the recorded acoustic emission.

http://dx.doi.org/10.5772/56448

2. Blue shift indicator

Consider a hydraulic fracture, which propagates emitting acoustic pulses from its process zone that is small compared to the fracture size R(t), Figure 1. We do not specify the particular shape of the fracture as long as it propagates in plane in all directions and its diameter and perimeter are proportional to the size, R. It is natural to assume that the hydraulic fracture is produced in quasi-static regime, that is the time intervals between successive steps of fracture propagation are considerably larger than the time needed for the stress waves to traverse the process zone along the contour of the fracture and effect the interaction between the acoustic events. Similarly, it is natural to assume that the time step of fracture propagation is much larger than the time needed for the acoustic signal to reach the acoustic sensor such that one can regard the signal emitted at one step of fracture propagation as being received almost simultaneously.

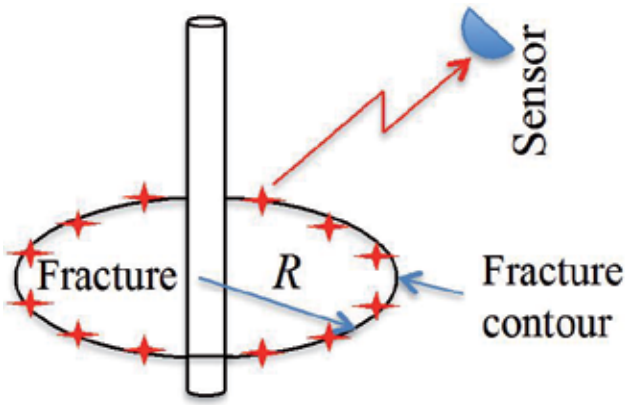

Figure 1. Hydraulic fracture and acoustic events at its contour produced almost simultaneously during a step in fracture propagation.

Suppose we have recorded a set of arrival times $\Theta=\{t_1, t_2,.. t_M\}$, where M is the number of generated acoustic pulses. Then, according to [16], we can regard tk as a time shift with respect to zero and relate the Fourier transform $\exp(-i\omega t^k)$ to it. We compute the 'spectrum' of arrival times by adding their Fourier transforms and calculate the energy the spectrum possess in the frequency range (0, Ω), where Ω is a certain frequency. The blue shift indicator is a measure of the difference between the energy associated with arrival times synchronised due to the localisation and purely random arrival times:

$$\Sigma_n(M,\Theta,\Omega)=\frac{\left|S(M,\Theta,\Omega)-S_r(M,\Omega)\right|}{S_r(M)} \tag{1}$$

where the'energies' of the truncated spectrum (up to frequency Ω) of arrival times Θ and the random arrival times $\{t_k^{(r)}\}$ are

$$S(M,\Theta,\Omega) = (M-1)\Omega + 2\sum_{m=2}^{M}\sum_{l=1}^{m-1}\frac{\sin\left(\left(t_m - t_l\right)\Omega\right)}{t_m - t_l} \tag{2}$$

$$S_r(M,\Omega) = \int_0^{\Omega}\sum_{k,l=0}^{M}\exp\left[-i\left(t_k^{(r)} - t_l^{(r)}\right)\right]d\omega \tag{3}$$

We assume that the fracture propagation proceeds stepwise. It was shown in [16] that it is sufficient to assume that all steps take the same time ΔT. At each time step the nominal fracture radius increases by ΔR. We initially assume that the number of pulses emitted is proportional to the crack perimeter, that is at k-th step the number of pulses emitted is equal to pk, where p is a factor accounting for the particular fracture shape and the relative distance between the locations of the acoustic events in each step. (Section 5 will check this assumption.) Let the time of the beginning of the propagation step k be kΔT. Then we can assign the theoretical value of the blue shift indicator by applying (1)-(3) to the'recorded'sequence of arrival times that consists of pk^{α} arrival times randomly distributed within the interval (kΔT, (k+1)ΔT). Here in the ideal case, the localisation exponent α=1 since the circumference of the fracture is proportional to the step number. We however would like to allow for a possibility of either varying steps of fracture expansion or a fractal nature of the set of defects generated by crack growth and therefore will allow for different values of α.

We note that the number of 'recorded' and random arrival times are proportional to p. Therefore, in the formula for the blue shift indicator (Eq. 1), p will cancel out. Hereafter, without loss of generality, we assume p=1.

3. Laboratory tests

In order to provide initial verification and to guide ongoing development of the analysis, a laboratory test was conducted in which a hydraulic fracture was driven by injecting glycerine into a 200x200x150mm block of polycrystalline gabbro. Acoustic emissions were detected and located based on their arrival times to 32 transducers that were attached to the 6 faces of the block. After testing, the specimen was serial sectioned so that fracture patterns could be observed and measured, see the example in Figure 2.

In total, 463 events were located with <2 mm uncertainty. Events that were not able to be located within the block to this level of accuracy were discarded, as the source of such events is not certain. Figure 3 shows these events as they occurred in time while Figure 4 shows the pressure record along with the cumulative events. In total, 70 events occurred before the hydraulic fracture was observed to have intersected the edge of the specimen ("breakthrough") and fluid was seen to be slowly leaking from the side of the specimen through the crack. An additional 160 events were recorded before shut-in and the remaining, post shut-in events are essentially

http://dx.doi.org/10.5772/56448

Figure 2. Example of serial sectioned hydraulic fracture showing growth from a notch in a 16 mm diameter wellbore.

aftershocks that we believe to be similar to those observed in experiments on rock failure in compression [17] and in other hydraulic fracturing laboratory experiments [18].

4. Blue shift indicator for the experimental data

The 70 events recorded prior to fracture breakthrough at the specimen edge are not a sufficient number for blue shift calculations. So instead we conducted the analysis for the first 200 and for all 463 events. That means that the first group contains a larger proportion of events produced from a contour of fracture during the time it was growing in quasi-planar manner with a leading edge that is a circumscribing line, that is, when localisation exponent $\alpha \approx 1$. The second group contains a smaller proportion of propagation-related events. If the contour length is constant then $\alpha=0$, therefore in the case of all events one can expect $0< \alpha <1$ and we certainly would expect the second group to have a smaller exponent than the first.

Figure 5 shows the blue shift indicator for the first 100 and first 200 and for all 463 events, respectively, compared with theoretical values for different localisation exponents where the particular values of the exponent were chosen to ensure the best fit. It is seen that the experimental blue shift curves have the characteristic peaks indicating, according to [16], the presence of localisation. For the group of first 100 events (Figure 5a) the best fit curve corresponds to the localisation exponent α =0.97, which is close to the expected α =1. For the group of 200 events (Figure 5b) the best fit exponent is α=0.37. Interestingly using all 463 events (Figure 5c) does not change the best fit exponent. The localisation exponent for 200 and 463 events is within the expected boundaries $0< \alpha <1$ and, as anticipated, it is less than the exponent obtained from the first group. According to the Blue Shift approach, this smaller exponent is indicative that a smaller proportion of the events are associated with localized crack growth at the fracture's leading edge. This is indeed seen in the difference between 200 (Figure 5b) and 463 (Figure 5c) events when the adding the events unrelated to the localised process of the fracture growth does not affect the exponent but decreases the accuracy of the fit.

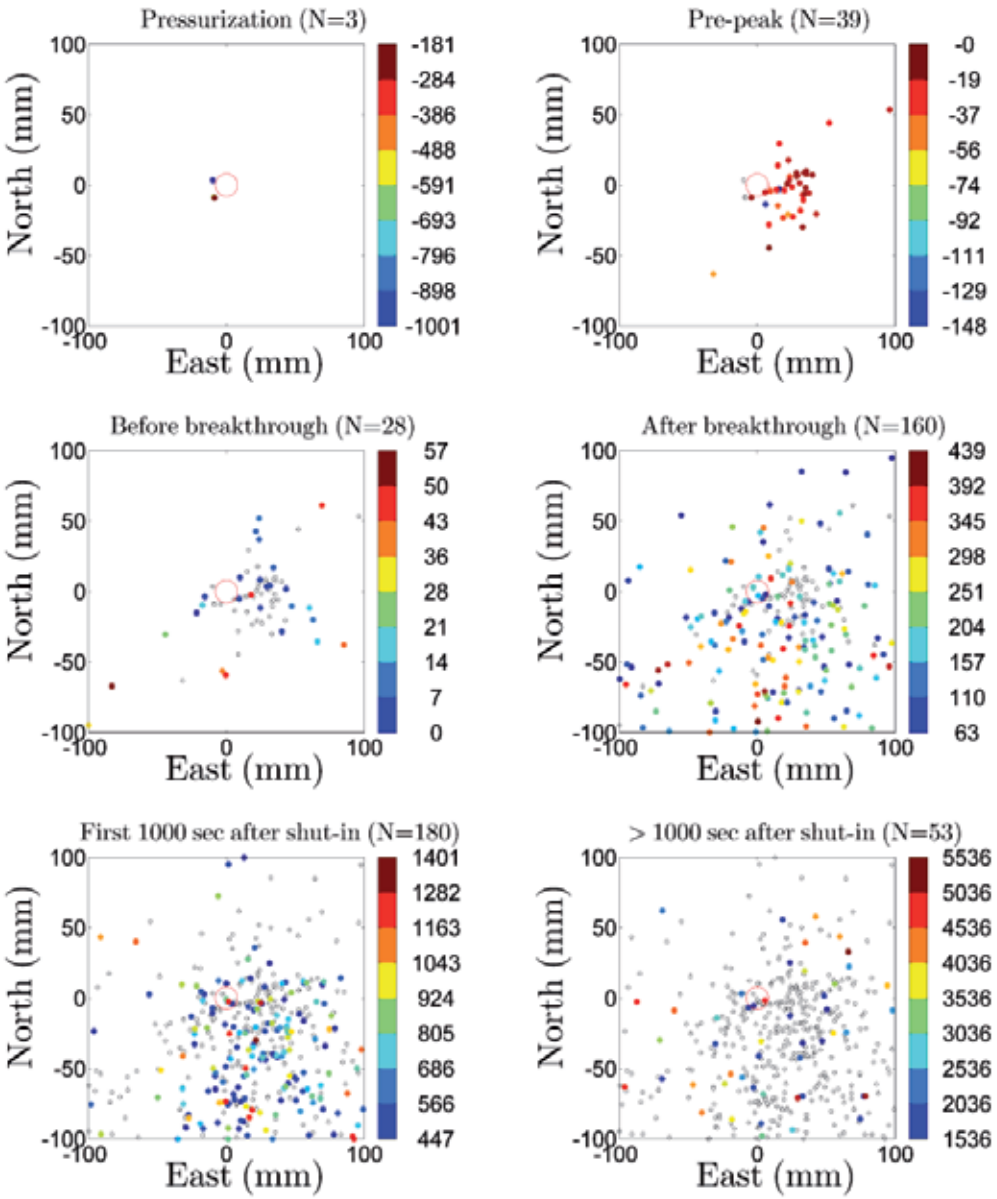

Figure 3. Acoustic emissions detected with <2mm location uncertainty. Colour corresponds to time measured from the time of the peak pressure. Open circles indicate events that occurred at a previous time range. Breakthrough refers to the time at which the hydraulic fracture was observed to have intersected the specimen boundary.

http://dx.doi.org/10.5772/56448

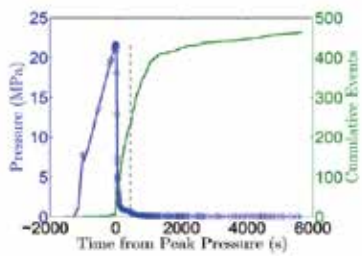

Figure 4. Evolution of injection pressure and cumulative number of events. Here the blue circles correspond to each event and the vertical dashed line indicates the time of shut-in.

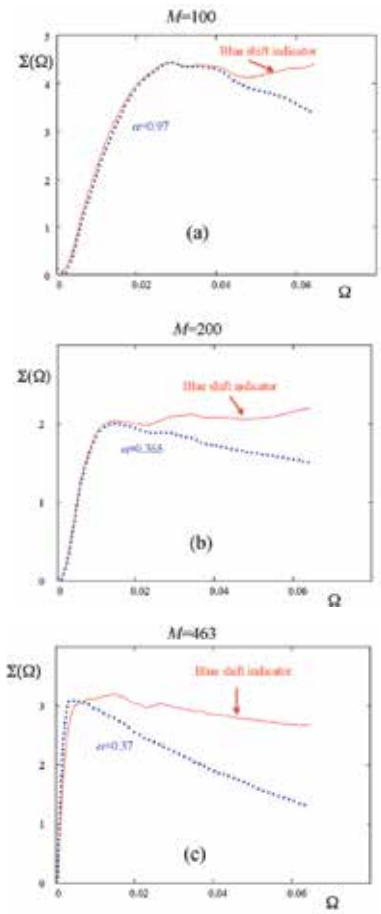

Figure 5. Blue shift indicators for the first 100 events (a), first 200 events (b) and all 463 events (c) recorded in the experiment compared with the best fit theoretical curves where the only fitting parameter is the localisation exponent.

5. Conclusions

Our results show an intriguing mix of promise and indication of challenges to be overcome. The results are promising in that the spectrum of the arrival times indeed undergoes a blue shift, the nature of which is notionally able to discern between the main localized, omni-directional propagation stage and the period during which the propagation was arrested except, perhaps, for some slow growth that was directionally limited but during which most of the events were being generated from apparently spatially random locations around the vicinity of the fracture surface. What's more, the blue shift can be characterized by a parameter, the localisation exponent, which can theoretically be tied to the dimensionality of the leading edge of the hydraulic fracture.

However, we also discovered a preponderance of events that emit from the vicinity of the already-fractured surface rather than being localized at the leading edge. The impact of these non-localized events remains a topic for ongoing investigation. Hence, our ongoing work is aimed at providing a clear understanding of how experimentally derived values of the localisation exponent can be used to predict the fracture pattern associated with a given sequence of events.

Acknowledgements

The authors acknowledge support from the Capability Developments Funds of CSIRO Earth Science and Resource Engineering. AVD and EP acknowledge support from ARC Discovery Grant DP0988449.

Author details

Arcady V. Dyskin[1*], Elena Pasternak[1], Andrew P. Bunger[2,3] and James Kear[2]

*Address all correspondence to: arcady.dyskin@uwa.edu.au

1 School of Civil and Resource Engineering, University of Western Australia, Crawley, Australia

2 CSIRO Earth Science and Resource Engineering,
Melbourne, Australia

3 Department of Civil and Environmental Engineering, University of Pittsburgh, Pittsburgh, Pennsylvania, USA

http://dx.doi.org/10.5772/56448

References

[1] Mahrer, K. D. A review and perspective on far-field hydraulic fracture geometry studies. Journal of Petroleum Science and Engineering (1999). , 24, 13-28.

[2] Cleary, M. P, Doyle, R. S, Teng, E. Y, Cipolla, C. L, Meehan, D. N, Massaras, L. V, & Wright, T. B. Major new developments in hydraulic fracturing, with documented reductions in job costs and increases in normalized production. In: Proceedings 69th Annual Technical Conference and Exhibition, New Orleans, LA. (1994). , 1994, 547-561.

[3] King, G. E. Tracking fracture fluid movement with chemical and gamma-emitting tracers with verification by microseismic recording. In: EPA Hydraulic Fracturing Workshop, February (2011). , 24-25.

[4] Murphy, H. D, & Fehler, M. C. Hydraulic fracturing in jointed formations. In: Proceedings Soc. Petr. Eng. International Meet- ing on Petroleum Engineering, Beijing, China. (1986). , 1986, 489-496.

[5] Mahrer, K. D. Microseismic logging: a new hydraulic fracture diagnostic method. Soc. Petr. Eng. Form. Eval. (1993). , 1993, 41-50.

[6] Rutledge, J. T, & Zinno, R. J. Microseismic mapping of a Cotton Valley hydraulic fracture using decimated downhole arrays. Society of Exploration Geophysicist, International Exposition and Sixty Eighth Annual Meeting, September 13- 18, (1998).

[7] Liu, X, Xu, Y. G, Zhao, Z. F, Mu, L. J, Liu, J. A, & Guo, Z. X. Application of microseismic mapping and modeling analysis to understand hydraulic fracture growth behaviour. International Symposium and Exhibition on Formation Damage Control, February (2006). Lafayette, Louisiana U.S.A. DOIMS., 15-17.

[8] Cipolla, C. L, & Wright, C. A. Diagnostic Techniques to Understand Hydraulic Fracturing: What? Why? and How? SPE/CERI Gas Technology Symposium, April (2000). Calgary, Alberta, Canada. DOI:MS., 3-5.

[9] Vinegar, H. J, Wills, P. B, Demartini, D. C, Shlyapobersky, J, Deeg, W. F. J, Adair, R. G, Woerpel, J. C, Fix, J. E, & Sorrells, G. G. Active and passive seismic imaging of a hydraulic fractures in diatomite. J. Petr. Tech. (1992).

[10] Fehler, M, & Pearson, C. Cross-hole seismic surveys: applications for studying subsurface fracture systems at a hot dry rock geothermal site. Geophysics (1984). , 49, 37-45.

[11] Meadows, M. A, & Winterstein, D. F. Seismic detection of a hydraulic fracture from shear-wave VSP data at Lost Hills Field, California. Geophysics (1994). , 59, 11-26.

[12] Green, A. S. P, Baria, R, & Jones, R. VSP and cross-hole seismic surveys used to determine reservoir characteristics of a hot dry rock geothermal system. Int. J. Rock Mech. Min. Sci. and Geomech. Abstr. (1989). , 26, 271-280.

[13] Palmer, I. D, & Sparks, D. P. Measurement of induced fractures by downhole TV camera in black warrior basin coalbeds. J. Petr. Tech. (1991).

[14] Wright, C. A, & Conant, R. A. Hydraulic fracture reorientation in primary and secondary recovery from low-permeability reservoirs. In: Proceedings Soc. Petr. Eng. Annual Technical Conference and Exhibition, Dallas, TX. (1995). , 1995, 357-369.

[15] Lecampion, B, Jeffrey, R, & Detournay, E. Resolving the Geometry of Hydraulic Fractures from Tilt Measurements, Pure and Applied Geophysics (2005). , 162, 2433-2452.

[16] Pasternak, E, & Dyskin, A. V. Frequency signatures of damage localisation Phil. Mag. (2012).

[17] Scholz, C. H. Microfractures, aftershocks, and seismicity. Bull. Seis. Soc. America, (1968). , 58(3), 1117-1130.

[18] Chitrala, Y, Moreno, C, Sondergeld, C, & Rai, C. Microseismic and microscopic analysis of laboratory induced hydraulic fractures. In Proceedings Canadian Unconventional Resources Conference, Calgary, Alberta, Canada, November (2011). SPE 147321., 15-17.

Chapter 23

A Numerical Investigation of Fault Slip Triggered by Hydraulic Fracturing

Neda Zangeneh, Erik Eberhardt, R. Marc Bustin and Amanda Bustin

Additional information is available at the end of the chapter

http://dx.doi.org/10.5772/56191

Abstract

The study of fault slip in response to fluid injection offers a means to understand the complex hydromechanical behavior of shale gas and oil reservoir systems during hydraulic fracturing operations, together with the induced seismicity, and corresponding mitigation measures, arising from such events. In this paper, a series of numerical simulations are performed to investigate the relationship between hydraulic fracturing (i.e. fluid injection) and the response of a naturally fractured rock mass to transient fluid pressures. The analysis is carried out using the discontinuum-based distinct-element program UDEC assuming a fracture flow system. The conceptual reservoir model consists of a critically stressed fault plane and the surrounding rock mass containing planes of weakness, for which a hydraulic fracture is numerically simulated and the response modeled using a transient, coupled hydro-mechanical solution. The results demonstrate the influence of fluid diffusion generated by the fracing fluid after shut-in on the triggering of fault slip. The simulation is then used to interpret the associated seismic events and their relationship to the injections and shut-in pressures, and to estimate the maximum magnitude of the induced seismic event.

1. Introduction

Hydraulic fracture operations involve the injection of fluids from a wellbore into a formation to maximize the extraction of oil and gas resources from the reservoir. These stimulations allow the development of previously uneconomical reserves, for example shales gas. However, it has been well established that these fluid injections also induce seismicity (e.g., Hollister and

Weimer [1], Ohtake [2], Fletcher and Sykes [3], Pearson, [4], Talwani and Acree, [5], Simpson et al. [6], Zoback and Harjes [7]).

The occurrence of induced seismicity, whether through hydraulic fracturing, enhanced geothermal systems, or carbon dioxide (CO_2) sequestration, represents an important consideration in the risk profile of an injection well. Zoback [8] suggested that because of the critically stressed nature of the crust, fluid injection in deep wells can trigger earthquakes through increases in pore pressure (and decreases in effective stress) in the vicinity of the pre-existing faults. The increased pore pressure reduces the shear resistance to fault slip, allowing elastic energy already stored in the surrounding rocks to be released (Healy et al. [9]).

This paper describes a numerical experiment investigating the influence of pore pressure diffusion on the modeling of seismicity after a hydraulic fracture treatment. One objective is to evaluate the utility of 2-D distinct element techniques to model both pore pressure build-up and diffusion along existing rock weakness planes in response to fluid injection and subsequent changes to the effective stress field. A second objective is to estimate the corresponding maximum seismic magnitude that is likely to occur in response to the hydraulic fracture treatment.

2. Effect of fluid injection on induced seismicity

The occurrence of injection-induced seismicity is usually confined in both space and time, with pressure build-up and diffusion controlling the spatial and temporal pattern of the seismicity after a hydrofrac treatment. Spatially, the problem can be conceptualized as a scenario in which a wellbore in the vicinity of a critically-stressed fault is pressurized and the injected fluids diffuse towards the fault, increasing pore pressures and reducing the effective normal stress until slip is triggered along a portion of the fault. The transient nature of the fluid front as it radiates outward from the injection well allows for the triggering of events after injection and shut-in, referred to here as post-injection seismicity.

The importance of fluid pressure in generating induced seismicity was demonstrated in 1962 in Denver, Colorado, when it was observed that a series of seismic events were being generated shortly after a chemical weapons plant had begun injecting contaminated wastewater down a deep well. Detailed studies by Hollister and Weimer [1] and Healy et al. [9] confirmed the causal observations of Evans [10] that the seismic events were induced by the waste fluid injection. Similar relations between local seismicity and fluid injection were likewise observed at the Rangely Oil Field, Colorado by Pakiser et al. [11], Healy et al. [12] and Gibbs et al. [13], and in the Los Angeles basin by Teng et al. [14].

More recently, post-injection seismicity associated with gas shale and geothermal projects have entered the public spotlight with heightened sensitivity directed towards hydraulic fracturing practices and induced seismicity. Between 2000 and 2005, numerous seismic events were recorded at the European geothermal project in Soultz-sous-Forêts, France, with events as large as M=2.5 being recorded during injection and M=2.6 several days after shut-in (Charlety et al.

http://dx.doi.org/10.5772/56191

[15]). For stimulations carried out in 2000, 2003 and 2004 the largest seismic events occurred just after or after shut-in. Similar experiences were encountered at Basel, Switzerland where induced seismicity reached a Richter Magnitude of 3.4 despite precautionary reductions of the injection rate, leading to suspension of its hot dry rock enhanced geothermal systems project (Haring et al. [16]).

Experiences with hydraulic fracturing treatments in gas shales have generated similar seismicity, generally viewed as low risk due to the remote nature of the locations. In the Bowland shale, Lancashire, UK, two notable events were recorded with Richter Magnitudes of 1.5 and 2.3. These occurred almost 10 hours after shut-in (de Pater and Baisch [17]). de Pater and Baisch [17] suggested that reducing the treatment volume is one means to mitigate induced seismicity. In a detailed study in the Horn River Basin in northeastern British Columbia, Canada, approximately 38 events ranging between Richter Magnitudes 2.2 and 3.8 were recorded between 2009 and 2011, with only one being felt on surface in this remote region (BCOG, [18]). In their 2012 report of the findings from this investigation, the B.C. Oil and Gas Commission found that several of the Horn River events greater than M 2.0 were located along faults intersecting the wellbores. They also note that there were other instances where faults intersected wellbores without anomalous events being detected (BCOG, [18]).

3. Methodology

The Distinct Element Method (DEM) applies a Lagrangian formulation to compute the motion and interaction between a series of discrete deformable blocks, representing the problem domain, via compliant contacts and Newton's equation of motion (Cundall and Hart, [19]). This enables the problem domain to be divided through by one or more discontinuity sets of variable orientation, spacing and persistence. One fundamental advantage of the DEM is that pre-existing (natural) joints in the rock mass can be modeled explicitly and allow for joints to undergo large deformations in shear (slip) or opening (dilation). The 2-D commercial code UDEC (Universal Distinct Element Code; Itasca Consulting Group, 1999) is used here to model the response of a jointed rock mass subjected to static loading and hydraulic injection.

UDEC is capable of modeling the behavior of weak jointed rock masses in which both the deformation and yielding of weak rock and slip along pre-existing discontinuities are important controlling factors. Progressive failure associated with crack propagation and fault slip can be simulated by the breaking of pre-existing contacts between the pre-defined joint bounded blocks, which although deformable, remain intact.

Key for simulating hydrofracturing, UDEC has the capability to model fluid flow through the defined fracture network. A fully coupled hydro-mechanical analysis can be performed, in which fracture conductivity is dependent on mechanical deformation of joint apertures and, conversely, joint water pressures can affect the mechanical computations of joint aperture. The blocks in this assemblage are treated as being impermeable, and fracture flow is calculated using a cubic law relationship for joint aperture:

$$q = ka^3 \frac{\Delta P}{l} \tag{1}$$

where, k is a joint conductivity factor (dependent on the fluid dynamic viscosity), a is the contact hydraulic aperture, ΔP is the pressure difference between the two adjacent domains, and l is the length assigned to the contact between the domains. Since the UDEC formulation is restricted to the modeling of fracture flow, it should be noted that leak-off along the fractures diffusing into the rock matrix is assumed to be negligible (only leak-off into other fractures is considered). Furthermore, the cubic law flow assumption limits tortuosity. When a joint contact is broken, the fluid flows into the joint.

4. Simulation setup and input parameters

The rock mass modeled in this study is represented by two persistent orthogonal planes of weakness (Figure 1). These serve as incipient planes along which hydrofrac propagation is restricted. The simulation of induced seismicity is executed through the inclusion of a fault, which extends across the model. An injection well is located such that a significant portion of the fluid injected diffuses towards the fault and eventually penetrates the fault following shut-in. The fluid pressure decays slowly after the injection and the disturbed pressure front diffuses through the surrounding rock mass. Although the fluid pressures decrease with time and distance, there is still sufficient pressure to trigger fault slip. The fault model is based on interactions between neighboring fault segments allowing the model to simulate slippage on a single contact together with the subsequent interactions and responses of its neighboring contacts.

The input material parameters include both those for the rock matrix and incipient planes of weakness and fault. The rock matrix was modeled as being elastic, assuming typical values for shale (density=2500 kg/m^3, Young's modulus=30 GPa, Poisson's ratio=0.25). The incipient planes of weakness and fault were modeled assuming a Coulomb-slip constitutive model with both peak and post-peak properties. These are given in Table 1. The depth of the injection and horizontal plane represented by the model is 1000 m. The maximum and minimum horizontal stresses were assumed to be 30 and 20 MPa, respectively.

Discontinuity property	Incipient fractures	Fault	Units
Friction angle	30	20	degrees
Residual friction angle	25	20	MPa
Cohesion	1.0	0.0	MPa
Residual cohesion	0.0	0.0	MPa/m
Tensile strength	0.5	0.0	MPa/m

http://dx.doi.org/10.5772/56191

Discontinuity property	Incipient fractures	Fault	Units
Residual tensile strength	0.0	0.0	degrees
Normal stiffness	1e4	10	MPa
Shear stiffness	1e3	1	MPa

Table 1. Properties assigned to the modeled planes of weakness and fault.

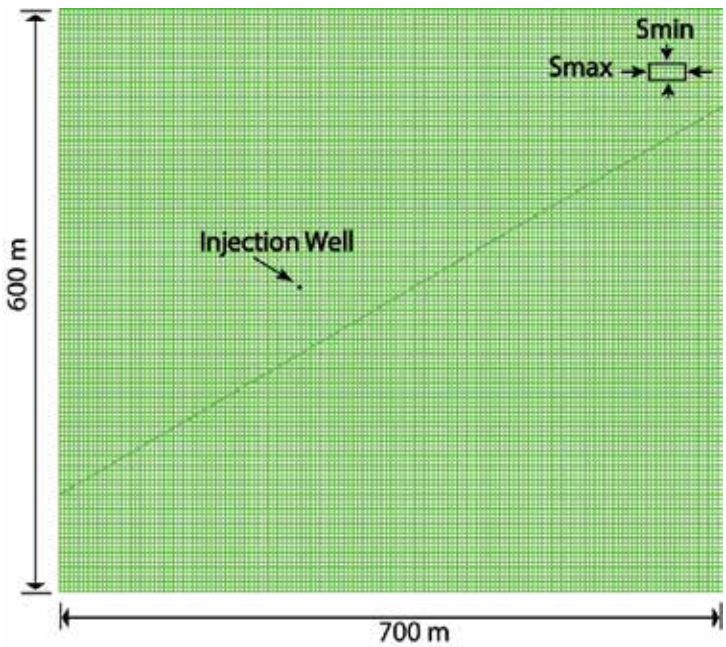

Figure 1. Rock mass model with two sets of weakness planes and a fault.

5. Post-injection seismicity simulations

Numerical simulations were performed using the model developed to investigate the influence of hydraulic fracturing on fluid pressure changes around the neighboring fault and any subsequent shear slippage along the fault. Both fluid pressure build-up during the injection until the time of shut-in as well as fluid pressure diffusion after the shut-in were considered.

5.1. Fluid pressure build-up during injection and diffusion after shut-in

Experience gained from mapping hundreds of hydraulic fracturing treatments with downhole geophones has shown that the occurrence of seismic event induced during a treatment is greatly influenced by the injection volume and rate used. Here, the hydraulic fracturing simulation was conducted by pressurizing the wellbore in the vicinity of a critically stressed

fault (Figure 1). Figure 2 shows the joint fluid pressure distribution in the rock mass at the time that fluid injection is stopped (i.e., shut-in). It can be seen that the fluid pressure has not reached the fault at the end of the hydraulic fracture treatment and shut-in. Here the fluid pressure treatment was applied for a period of 50 minutes.

After shut-in, the injected fluids continue to diffuse and radiate towards the fault, eventually penetrating it (Figure 3). The response of the fault to the elevated fluid pressures then depends on the spatial and temporal characteristics of the diffusion pulse, with a series of slip events being produced as opposed to a single event. The strongest slip event was typically observed late in the sequence, sometimes long after injection had stopped (up to 150 minutes for the model simulations performed here).

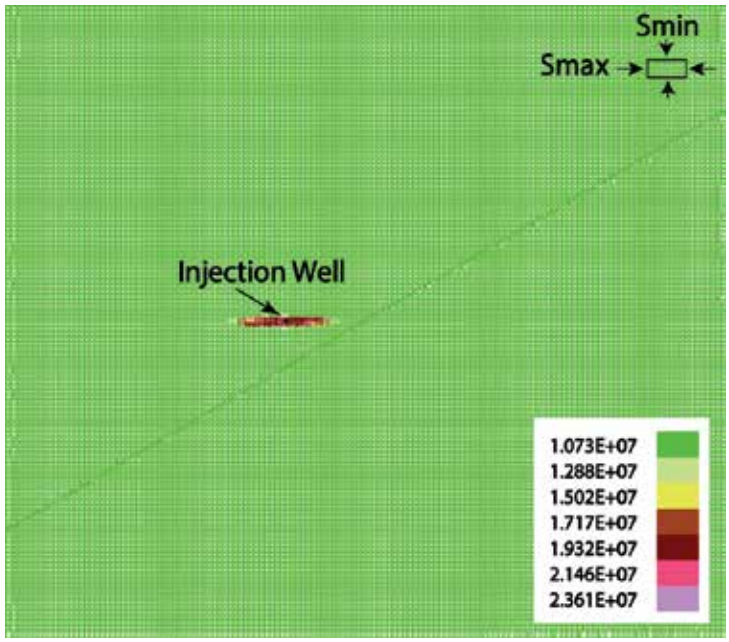

Figure 2. Pore pressure distribution at the time of shut-in.

5.2. Shear slip of critically stressed fault

The shear slip distribution along the fault, after 50 minutes of injection and 150 additional minutes of shut-in, is presented in Figures 4. The figure shows a distribution of slip magnitudes along the length of the fault, with a maximum fault slip of approximately 10 mm. Displacements between 5 and 10 mm were observed along 680 meters of the total 800 meter fault length, with an average fault slip of 8 mm. This average slip magnitude was then used to calculate the maximum earthquake magnitude, as presented in the following section.

http://dx.doi.org/10.5772/56191

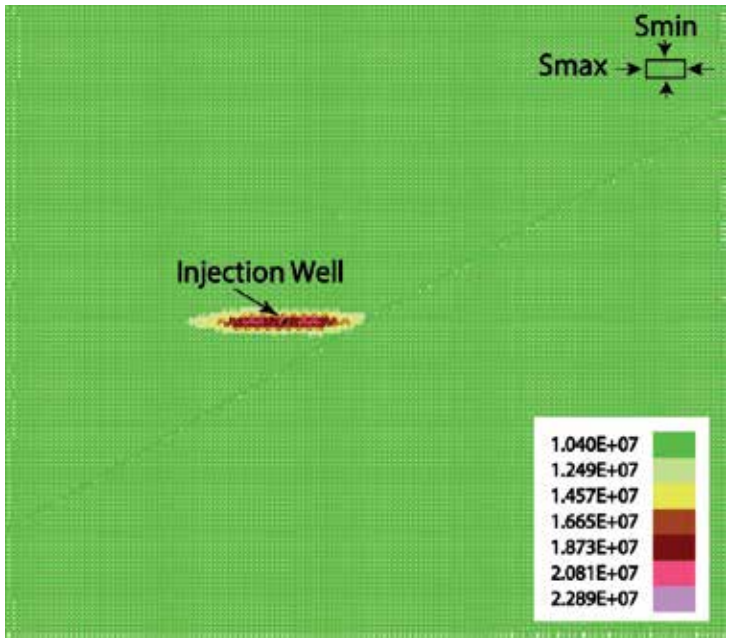

Figure 3. Pore pressure distribution 2 ½ hours after shut-in.

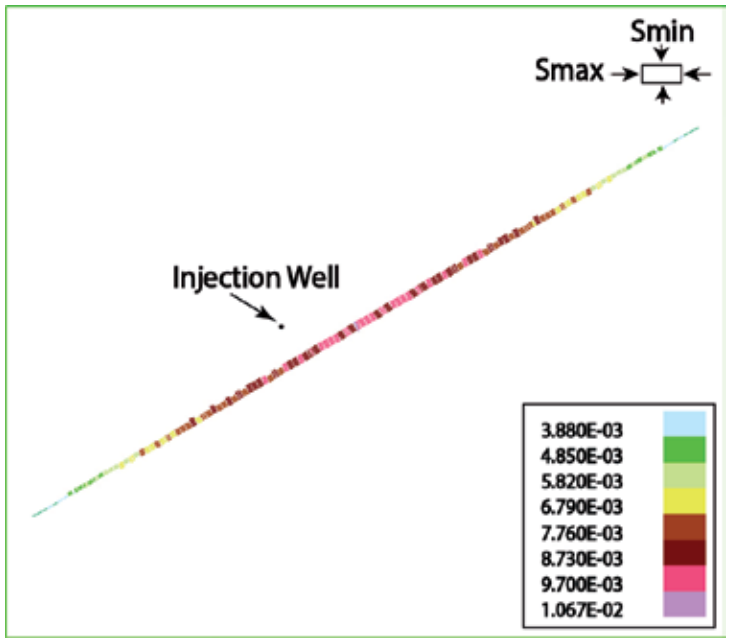

Figure 4. Fault shear displacement 2 ½ hours after shut-in.

6. Seismic moment and moment magnitude calculations

The seismic moment is a direct measurement of the energy released by a seismic event and is related to the strength characteristics of the fault. It can be calculated as follows (Kramer, [20]):

$$M_o = \mu A \overline{D} \tag{2}$$

Where:

Mo is the seismic moment (dyne•cm),

μ is the rupture strength of the rock along the fault (dyne/cm^2),

A is the rupture area (cm^2), and

$\overline{D}$ is the average amount of slip (cm).

Here, the rupture strength of the fault is equal to 1e10 dyne/cm^2, the length of the fault that slipped is equal to 6.8e4 cm (680 m), and the average amount of slip is equal to 0.8 cm. Assuming a unit depth of fault slip due to the 2-D nature of the model (i.e., rupture area = 6.8e9 cm^2), the resulting seismic moment is equal to 5.4e19 dyne.cm.

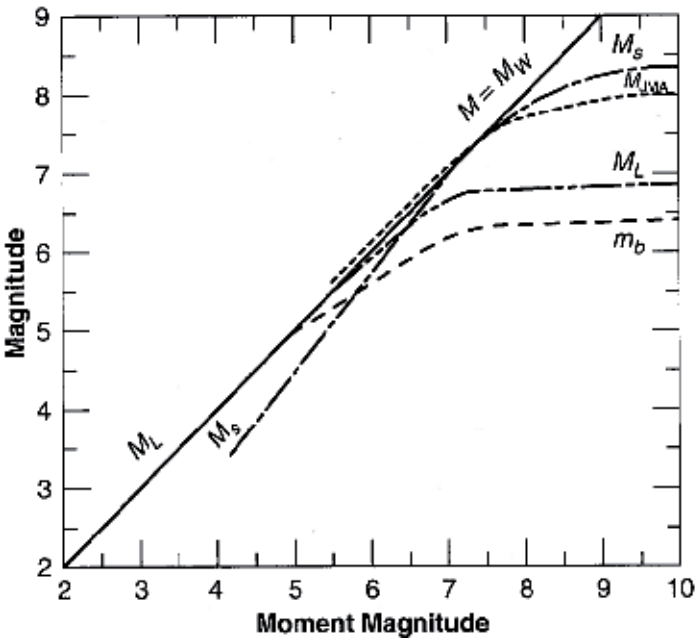

Figure 5. Saturation of various magnitude scales: Mw (moment magnitude), ML (Richter local magnitude), M_s (surface wave magnitude), m_b (short-period body wave magnitude), m_B (long-period body wave magnitude), and M_{JMA} (Japanese Metrological Agency magnitude). After Idriss [22] and Kramer [20].

http://dx.doi.org/10.5772/56191

Seismic moment can be converted into a moment magnitude using the following relationship (Hanks and Kanomori [21]):

$$M_w = 2/3 \log M_o - 10.7 \quad (3)$$

Where:

M_w is moment magnitude (dyne.cm), and

Mo is seismic moment (dyne.cm).

The moment magnitude calculated from equation 3 is 2.45. Figure 5 is used to convert the calculated moment magnitude to the Richter local magnitude. As seen in Figure 5, for earthquake magnitudes smaller than 6, the moment and local magnitudes are near equal; the local magnitude for the calculated moment magnitude is equal to 2.45.

Figure 6 uses a well-established seismological relationship that correlates earthquake magnitude to the size of the fault that slipped and seismic moment (Stein and Wysession [23]). This suggests that only faults that are at least tens of kilometers long are capable of producing large seismic events with magnitudes exceeding 6 (Zoback and Gorelick [8]). Zoback and Gorelick [8] note here that the fault size in Figure 6 is a lower bound value that refers to the size of the fault segment that slips in a given earthquake. As a geological feature, the total fault length is generally much longer than the part (segment) that slips during an individual event. As shown in Figure 6, an active fault slip segment of 680 meters, as produced in the UDEC model, is capable of producing an earthquake with a magnitude between 2.3 and 3.8 for a fault slip displacement between 1mm and 1 cm, depending on the magnitude of stress released by the

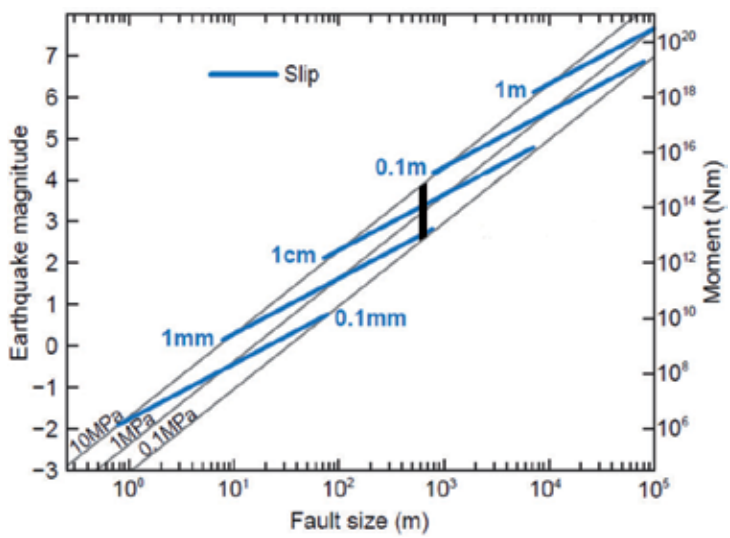

Figure 6. Relationship among various scaling parameters for earthquakes. The larger the earthquake, the larger the fault and amount of slip, depending on the stress drop in a particular earthquake. Observational data indicate that earthquake stress drops range between 0.1 and 10 MPa (modified after Zoback and Gorelick, [8]).

event, or stress drop. For the case modeled here, the 0.8 mm of average slip produced corresponds to an event with a magnitude equal to 2.45, which is in the range shown in Figure 6.

7. Discussion and conclusions

A numerical modeling study has been carried out to investigate the application of the distinct element technique to the simulation of fault slip and induced seismicity resulting from a hydraulic fracture treatment via a wellbore in the vicinity of a natural fault. The model was able to predict the occurrence of post-injection seismicity in response to diffusion of the injected fluids, in a system governed by fracture permeability, long after the hydraulic fracturing treatment is finished and shut-in is initiated.

In most areas, regional-scale faults should be easily identified during geological site characterization studies. Smaller-scale faults or those that are shallow dipping (i.e., that do not daylight on surface and therefore would not be detected through surface mapping) may be more difficult to locate *a priori*. Experience gained from monitoring hundreds of hydraulic fracturing treatments with downhole geophones has shown that the occurrence of seismic events induced by the treatments is greatly influenced by the injection volume used during the operation. Improved understanding of this condition will allow designers and operators to control the amount of injection during a hydraulic fracturing treatment to minimize fluid pressure diffusion and subsequent slip of a neighboring fault.

The simulations presented here show great potential in providing a deeper understanding of the effect of natural fracture systems and pressure diffusion of fracing fluids into a neighboring fault causing shear slip and induced seismicity after a hydraulic fracture treatment. Future work will include modeling of hydrofrac fluid diffusion into a fault in the vicinity of the hydrofrac treatment site in a three-dimensional model.

Author details

Neda Zangeneh*, Erik Eberhardt, R. Marc Bustin and Amanda Bustin

*Address all correspondence to: neda@eos.ubc.ca

University of British Columbia, Vancouver, British Columbia, Canada

References

[1] Hollister, J. C, & Weimer, R. J. Geophysical and Geological Studies of the Relationship Between the Denver Earthquakes and the Rocky Mountain Arsenal Well. Quaterly, Colorado School of Mines (1968). , 63(1), 1-251.

[2] Ohtake, M. Seismic Activity Induced by Water Injection at Matsushiro, Japan. Journal of Physics of the Earth (1974). , 22, 163-176.

[3] Fletcher, J. B, & Sykes, L. R. Earthquakes Related to Hydraulic Mining and Natural Seismic Activity in Western New York State. Journal of Geophysical Research (1977). , 82(26), 13767-3780.

[4] Pearson, C. The Relationship Between Microseismicty and High Pore Pressures During Hydraulic Stimulation Experiments in Low Permeability Granitic Rocks. Journal of Geophysical Research (1981). , 86, 7855-7864.

[5] Talwani, P, & Acree, S. Pore Pressure Diffusion and the Mechanism of Reservoir-induced Seismicity, Pageoph (1985). , 122, 947-965.

[6] Simpson, D. W, Leith, W. S, & Scholz, C. H. Two Types of Reservoir Induced Seismicity, Bulletin of the Seismological Society of America (1988). , 78, 2025-2040.

[7] Zoeback, M, & Harjes, H. P. Injection Induced Earthquakes and the Crustal Stress at 9 km Depth at the KTB Deep Drilling Site, Germany. Journal of Geophysical Research (1997). B8): 18477-18491.

[8] Zoback, M. D, & Gorelick, S. M. Earthquake Triggering and Large-scale Geologic Storage of Carbon Dioxide. Proceeding of the National Academy of Science of the United States of America (PNAS) (2012). , 109(26), 10164-10168.

[9] Healy, J. H, Rubey, W. W, Griggs, D. T, & Raleigh, C. B. The Denver Earthquakes, Science (1968). , 161, 1301-1310.

[10] Evans, D. M. The Denver Area Earthquakes and the Rocky Mountain Arsenal Disposal Well, Mountain Geologist (1966). , 3, 23-36.

[11] Pakiser, L. C, Eaton, J. P, Healy, J. H, & Releigh, C. B. Earthquake Prediction and Control, Science (1969). , 166, 1467-1474.

[12] Healy, J. H, Lee, W. H. K, Pakiser, L. C, Raleigh, C. B, & Wood, M. D. Prospects for Earthquake Prediction and Control, Techtonophys (1972). , 319-332.

[13] Gibbs, J. F, Healy, J. H, Raleigh, C. B, & Coakley, J. Seismicity in the Rangely, Colorado Area: 1962-1970. Bulletin of Seismological Society of America (1973). , 63, 1557-1570.

[14] Teng, T. L, Real, C. R, & Henyey, T. L. Microearthquakes and Water Flooding in Los Angeles, Bulletin of Seismological Society of America (1973). , 63, 859-875.

[15] Charlety, J, Cuenot, N, Dorbath, L, Dorbath, C, Haessler, H, & Frogneux, M. Large Earthquakes During Hydraulic Stimulations at the Geothermal Site of Soultz-sous-Forets. International Journal of Rock Mechanics and Mining Sciences (2007). , 44, 1091-1105.

[16] Haring, M. O, Schanz, U, Ladner, F, & Dyer, B. C. Characterisation of the Basel 1 Enhanced Geothermal System. Geothermics (2008). , 31, 469-495.

[17] De Pater, C. J, & Baisch, S. Geomechanical Study of Bowland Shale Seismicity, Synthesis Report (2011).

[18] BCOGInvestigation of Observed Seismicity in the Horn River Basin. British Columbia Oil and Gas Commission Report (2012).

[19] Cundall, P. A, & Hart, R. D. Numerical Modeling of Discontinua. Comprehensive Rock Engineering (1993). A. Hudson, ed. Oxford: Pergamon Press Ltd., 2, 231-243.

[20] Kramer, S. L. Geotechnical Earthquake Engineering, Prentice-Hall, Englewood Cliffs, N. J., 653; (1996).

[21] Hanks, T. C, & Kanamori, H. A Moment Magnitude Scale. Journal of Geophysical Research (1979). , 84, 2348-2350.

[22] Idriss, I. M. Evaluating Seismic Risk in Engineering Practice. Conference Proceeding, 11th International Conference on Soil Mechanics and Foundation Engineering, (1985). , 1

[23] Stein, S, & Wysession, M. An Introduction to Seismology, Earthquakes and Earth Structure. Blackwell, Oxford; (2002).

Section 7

Well Completions and Fracture Initiation 2

Chapter 24

Numerical Simulation of Hydraulic Fracturing in Heterogeneous Rock: The Effect of Perforation Angles and Bedding Plane on Hydraulic Fractures Evolutions

Xiaoxi Men, Chun'an Tang, Shanyong Wang,
Yongping Li, Tao Yang and Tianhui Ma

Additional information is available at the end of the chapter

http://dx.doi.org/10.5772/56012

Abstract

Considering the heterogeneity of rock, the hydraulic fracturing process of rock specimen due to internal hydraulic pressure was numerically simulated in a meso-scale by RFPA2D2.0 (Realistic Failure Process Analysis). The differences of perforation angle, bedding angle and bedding material of rock specimens are considered. The numerical results showed that the initiation and propagation of hydraulic fractures were controlled by both global pore pressure's distribution gradient and local pore pressure around the crack tip. Both the lateral compressive pressure ratio and the bedding angle could affect the evolution of the hydraulic fractures. The numerically simulated results were in agreement with the experimental results.

Keywords Hydraulic fracturing, heterogeneity, numerical simulation, fracture evolution

1. Introduction

Hydraulic fracturing is an important technology of production enhancement of oil and gas wells and intensified injection of wells. The first experimental hydraulic fracturing operation took place in the United States in 1947 in the Hugoton gas field in Grant County, Kansas, and after decades, the hydraulic fracturing technology has being widely used and become the dominant factor that determines the development plan of low permeability oilfield. In practical

applications, most of the hydraulic fracturing operations in the oil and gas fields are performed through casing, and, the regular or complex bedding structures likely exist in the rock mass formed in the course of rock formation and tectonic movement, so the research of the effect of perforation and bedding angle and modulus contrasts of rock and bedding in heterogeneous rocks under hydraulic fracturing is necessary. It can not only make fracturing decision-making more scientific, but reduce the fracturing cost and improve the fracturing efficiency, and has great theoretical significance and practical value on the perforation parameters optimization design and hydraulic fracturing construction of bedding rockmass.

At present, the perforation parameters are controllable which can be realized easily in practice. Since the hydraulic fracturing technology appeared, many experts have made various researches about the influence of perforation parameters on fracture evolutions under hydraulic fracturing. In [1], Daneshy et al. studied the hydraulic fracturing through perforation in 1973 and found that breakdown pressures of hydraulic fractures would decrease as the number of perforations increased, moreover, the existence of the casing and the perforations had little influence on the direction of the created fracture, which is perpendicular to the minimum principal stress. In [2], Weng et al. studied the hydraulic fracture initiation and propagation from deviated wellbores in 1993, investigated the interaction and link-up of the starter fractures initiated from perforations and the turning of the linked fracture and established a criterion that correlates fracture link-up to stresses and wellbore parameters. In [3], Zhang et al. used two-dimensional model to simulate the initiation and growth of hydraulic fractures in 2011 and developed a dimensionless parameter that is shown to characterise near-wellbore reorientation and curving of hydraulic fractures driven by viscous fluid. In [4], Zhang et al. employed three-dimensional finite element model together with the tensile criterion of rock materials in 2004, investigated that perforation density and perforation angle are the most important parameters controlling the formation fracturing pressure, but the influences of perforation diameter and perforation length are much slighter. In [5], Jiang et al. studied the fracture propagation mechanism of hydraulic fracturing through the experiment in 2009, and the results showed that the turning fracture can be generated by using oriented perforation fracturing technology, and with the increase of azimuth of oriented perforating, the breakdown pressure and turning distance are both growing.

Few studies have been carried on for fracture evolutions on heterogeneous rocks with different bedding angles under hydraulic fracturing at present stage. In [6], Bruno and Nakagawa studied fracture propagation path in non-uniform pore pressure field by test method in 1991, and proved that the fracture is influenced by both pore pressure magnitude on a local scale around the crack tip and the orientation and distribution of pore pressure gradient on a global scale. In [7], Li et al. simulated the experiment of hydraulic fracturing in non-uniform pore pressure field in 2005, and the results are well agreeable to that of Bruno and Nakagawa's experiments. In 2010, Abbass et al.'s study on Brazilian tensile text of sandstone in [8-9] showed that the breakdown pressure and fracture pattern are considerably affected by the bedding orientation and larger fracture length correlating with higher strength and applied energy.

http://dx.doi.org/10.5772/56012

In this paper, the effect of perforation and bedding angles and bedding materials on initiation pressure, breakdown pressure and hydraulic fractures evolutions of rock specimens under hydraulic fracturing is simulated and analyzed by using RFPA^{2D}(2.0)-Flow which adopts the finite element method and considers the heterogeneous characteristics of rock in meso-scale.

2. Introduction of RFPA^{2D}2.0-Flow

RFPA is a numerical experiment tool basing on the realistic failure process analysis method, which can simulate the gradual damage of materials. Its calculation method bases on finite element and statistical damage theory. RFPA considers both heterogeneity of materials and randomness of defect distribution, and puts the statistical distribution hypothesis of these material properties into the numerical calculation method (finite element method) to break the elements which satisfy the strength criterion. The material properties of each element follow Weibull distribution and are different from each other, and the element will fail if its stress reaches the failure strength, moreover, the number of fail elements will increase, which will be connected to each other and form fractures, as the load increases, so that the numerical simulation of heterogeneous material failure process can be realized. RFPA transforms the complex macroscopic nonlinear problem into simple mesoscopic linear problem by considering the heterogeneous characteristics of material and the complicated non-continuum mechanics problems into simple continuum mechanics problems by introducing the mathematics continuous and physical discontinuous concept, making the calculation results closer to the actual situation.

In mining and civil engineering projects, the re-distribution of the stress field during the excavation of tunnels and underground chambers leads to the formation of new fractures. The flow and transport behaviour within developing fractures are dramatically different from those in rocks with existing fractures under the same loading, therefore, the permeability of rocks changes dramatically in the process of damage evolution in fracture rocks. RFPA^{2D}2.0-Flow is the software considering the effects of the extension of existing fractures, the initiation of new fractures, the coupled effects of flow, stress and damage on the extension of existing/new fractures, and the permeability change due to damage evolution of the rocks, and is based on the theories of fluid-saturated porous media and damage mechanics. Flow-stress-damage (FSD) coupling model for heterogeneous rocks that takes into account the growth of existing fractures and the formation of new fractures is established herein. In [10-16], RFPA^{2D}2.0-Flow bases on the following five basic assumptions:

1. The fluid in the rock follows Biot consolidation theory;
2. Rock is the elastic brittle material with residual strength and the mechanical behaviour of loading and unloading process is in accordance with the elastic damage theory;
3. The maximum tensile strength criterion and Mohr Coulomb criterion are used as the damage threshold to judge whether the elements damage or not;

4. In elastic state, stress-permeability coefficient relationship of material is described by negative exponential function;

5. The mechanical parameters (such as uniaxial compressive strength f_c and elastic modulus E_c) of material at meso-scale (elements) are endowed by the following Weibull distribution:

$$\varphi(a) = \frac{m}{a_0}\left(\frac{a}{a_0}\right)^{m-1} e^{-\left(\frac{a}{a_0}\right)^m} \tag{1}$$

In this formula, a represents the mechanical property parameters of material (rock) elements at meso-scale; a_0 represents the statistical average of mechanical property parameters a; m is called homogeneity index, and higher m value means more homogeneity material; $\varphi(a)$ defines the statistical distribution density of mechanical property parameters a. Weibull's distribution for mechanical properties of materials with different homogeneity indexes m is shown in figure 1.

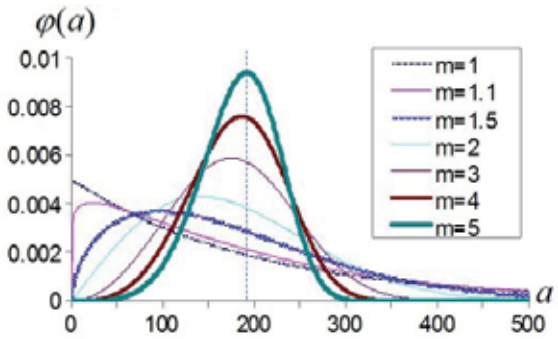

Figure 1. Weibull's distribution for mechanical properties of materials with different homogeneity indexes *m*

3. Model set

Numerical model is divided into three groups and each of them contains seven models, the fracturing process of rock specimens with different perforation angles, different bedding angles and different bedding materials under increasing hydraulic pressure and constant confining pressure are simulated. Perforation angle α is the angle between perforation and the maximum principal stress direction (horizontal direction), bedding angle α is the angle between bedding and the maximum principal stress direction (horizontal direction), and both of perforation and bedding angles chosen in the simulation are 0°, 15°, 30°, 45°, 60°, 75° and 90° respectively. The geometry of 2D rock model is 0.64m×0.64m and has been discretized into a 320×320(6400 elements) mesh, and the model is calculated by using plane strain. As shown

http://dx.doi.org/10.5772/56012

in figure 2, there is a well in the centre of model with radius 0.064m, two perforations approx 0.002m wide and 0.03m long cut into the well to provide initial direction for hydraulic fracture. Casing is in the non perforation area of the well with its strength and stiffness higher and permeability less than rock, so the initiation of fracture only occurs on perforation tip, which is in line with the actual engineering situation. As shown in figure 3, the well's radius is 0.032m and the space of two adjacent parallel beddings 0.04m. In figure 2 and figure 3, the confining pressure of the modelσ_H (in horizontal direction) andσ_h (in vertical direction)are 15MPa and 10MPa respectively with the initial pressure of 12MPa applied in the well and an incremental pressure of 0.1MPa maintained. The mechanical parameters of rock and bedding materials adopted in this simulation are listed in table 1 and table 2. The change of the values of elastic modulus and uniaxial compressive strength of bedding material are listed in table 3, and the value in brackets refers to the ratio of bedding and rock material. Moreover, the bedding angle of seven different bedding materials models is 60° with other mechanical parameters are in line with table 2.

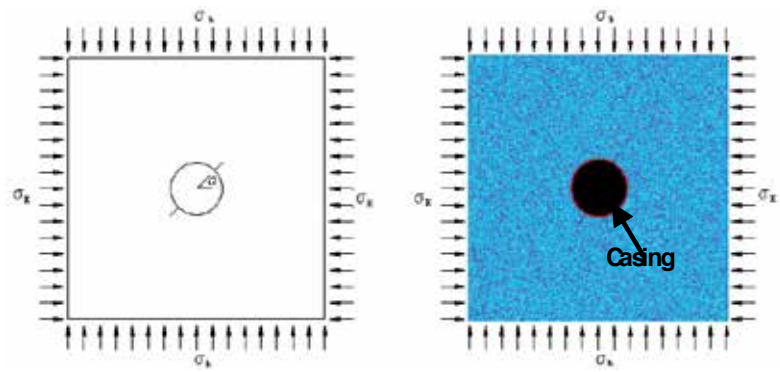

Figure 2. Schematic diagram and RFPA model diagram

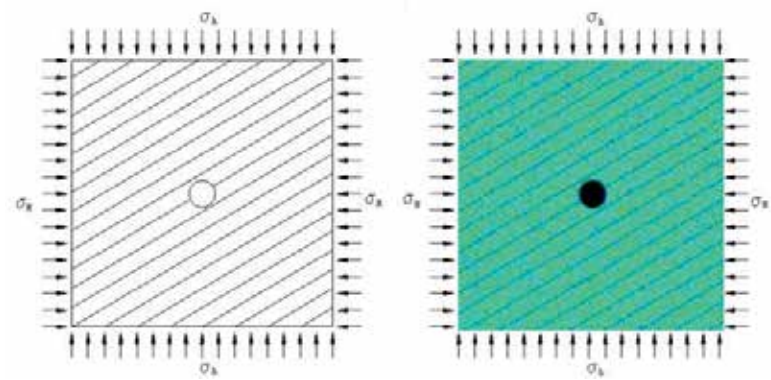

Figure 3. Figure 3 Schematic diagram and RFPA model diagram

Parameter	Symbol	Value
Homogeneity index	m	2
Elastic modulus	E_c	30 GPa
Poisson's ratio	μ	0.25
Internal friction angle	ϕ	37
Uniaxial compressive strength	f_c	200 MPa
Coefficient of permeability	K	0.000864 m/d

Table 1. Rock material mechanical parameter

Parameter	Symbol	Value
Homogeneity index	m	2
Elastic modulus	E_c	3.0 GPa
Poisson's ratio	μ	0.25
Internal friction angle	ϕ	37
Uniaxial compressive strength	f_c	20 MPa
Coefficient of permeability	K	0.00864 m/d

Table 2. Bedding material mechanical parameter

Rock material		Bedding material	
Elastic modulus (E_c)	**Uniaxial compressive strength (f_c)**	**Elastic modulus (E_c)**	**Uniaxial compressive strength (f_c)**
30GPa	200MPa	3.0GPa(1/10)	200MPa(1)
30GPa	200MPa	1.5GPa(1/20)	200MPa(1)
30GPa	200MPa	0.5GPa(1/60)	200MPa(1)
30GPa	200MPa	30GPa(1)	20MPa(1/10)
30GPa	200MPa	30GPa(1)	10MPa(1/20)
30GPa	200MPa	30GPa(1)	3.33MPa(1/60)
30GPa	200MPa	3.0GPa(1/10)	20MPa(1/10)

Table 3. Change of elastic modulus and uniaxial compressive strength values of bedding material

http://dx.doi.org/10.5772/56012

4. Simulation results

4.1. The effect of perforation angles

The initiation pressure, the breakdown pressure and the fracture evolution of seven rock specimens with different perforation angles under constant confining pressure and increasing hydraulic pressure are simulated. The results reflect the damage evolution process of rock specimen, which causes the macroscopic damage by microscopic under hydraulic fracturing and is consistent with the experimental result in [4]. Pore pressure and the minimum principal stress distribution of specimens with different perforation angles which achieved by numerical simulation are shown from figure 4 to figure 10. The comparison of the numerical simulation result and the experimental result which has the same perforation angle (60°) and under the same ground stress difference (5MPa) is shown in figure 11, and the values of the initiation and the breakdown pressure are shown in figure 12.

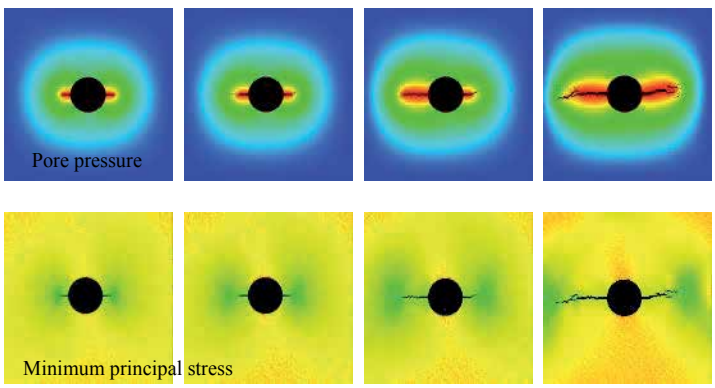

Figure 4. Pore pressure and the minimum principal stress distribution in fracture evolution process (0°)

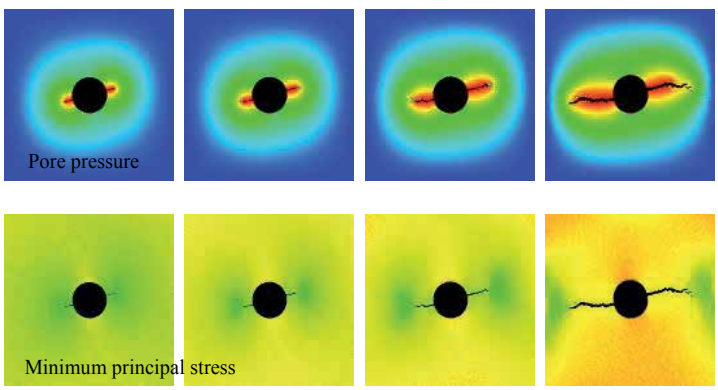

Figure 5. Pore pressure and the minimum principal stress distribution in fracture evolution process (15°)

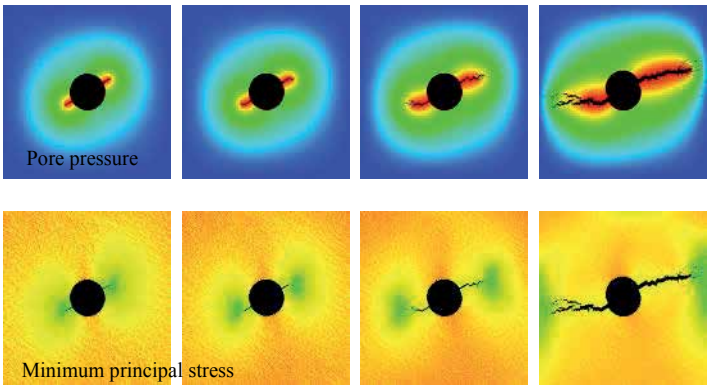

Figure 6. Pore pressure and the minimum principal stress distribution in fracture evolution process (30°)

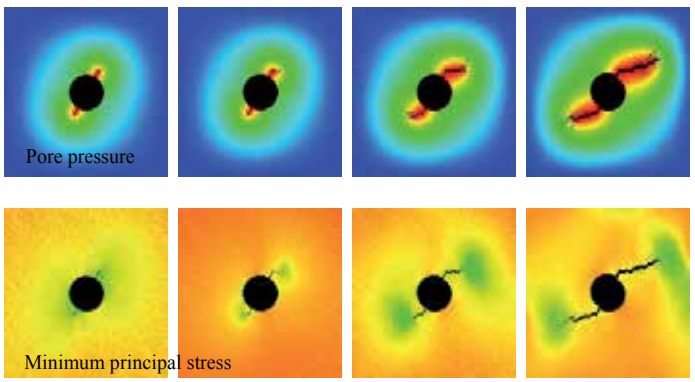

Figure 7. Pore pressure and the minimum principal stress distribution in fracture evolution process (45°)

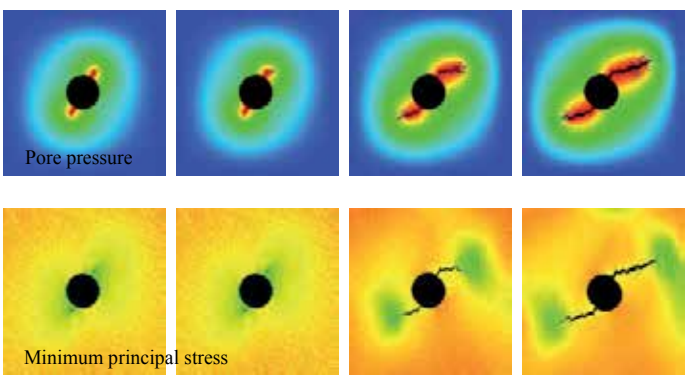

Figure 8. Pore pressure and the minimum principal stress distribution in fracture evolution process (60°)

http://dx.doi.org/10.5772/56012

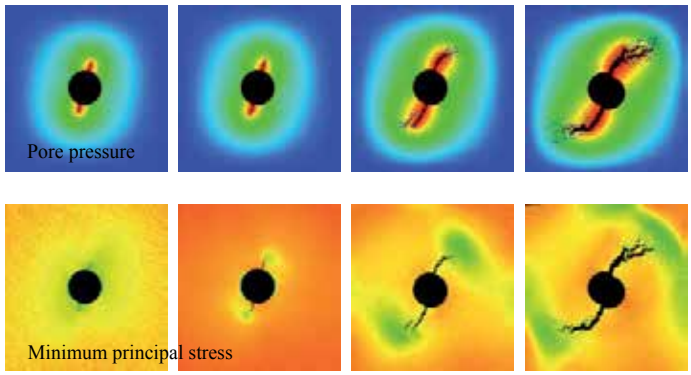

Figure 9. Pore pressure and the minimum principal stress distribution in fracture evolution process (75°)

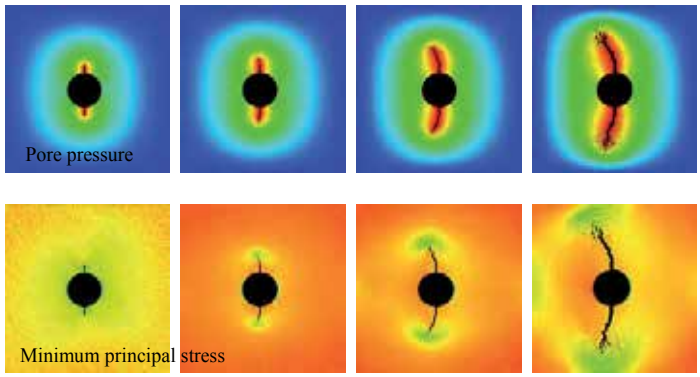

Figure 10. Pore pressure and the minimum principal stress distribution in fracture evolution process (90°)

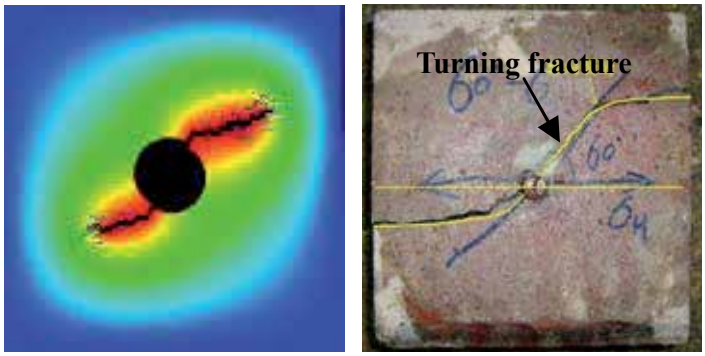

Figure 11. Comparison of numerical simulation and experimental results in [4] which has the same perforation angle (60°) and under the same ground stress difference (5MPa)

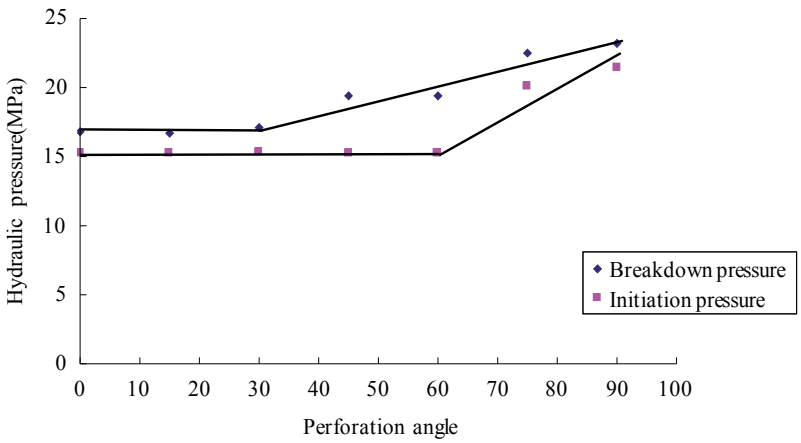

Figure 12. Changes of initiation and breakdown pressure of different perforation angle specimens

4.2. The effect of bedding angles

The initiation pressure, the breakdown pressure and the fracture evolution of seven rock specimens with different bedding angles are simulated. Pore pressure and the minimum principal stress distribution achieved by numerical simulation are shown from figure 13 to figure 19, and the values of initiation and breakdown pressure shown in figure 20.

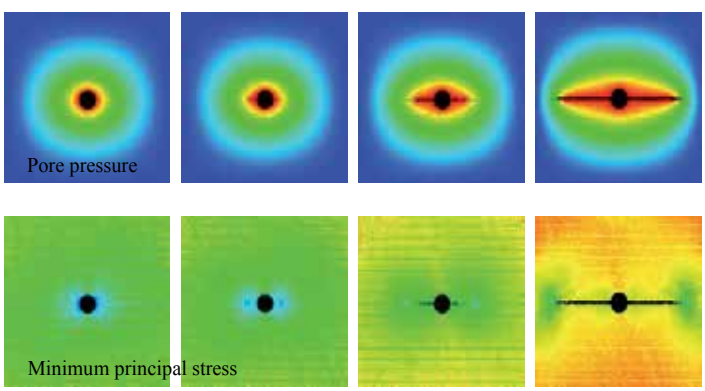

Figure 13. Pore pressure and the minimum principal stress distribution in fracture evolution process (0°)

http://dx.doi.org/10.5772/56012

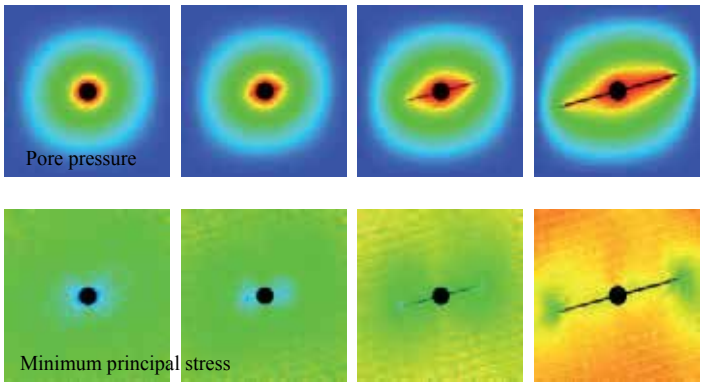

Figure 14. Pore pressure and the minimum principal stress distribution in fracture evolution process (15°)

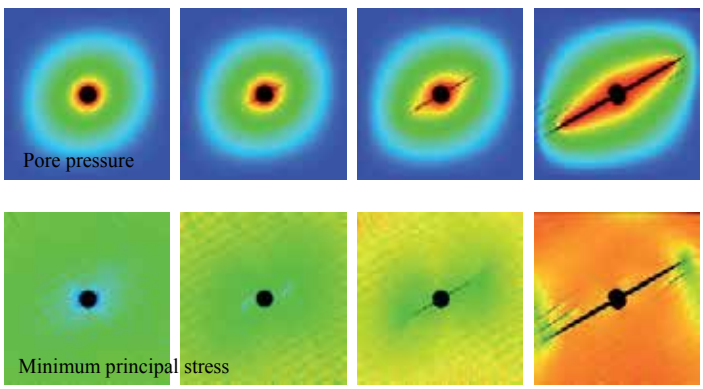

Figure 15. Pore pressure and the minimum principal stress distribution in fracture evolution process (30°)

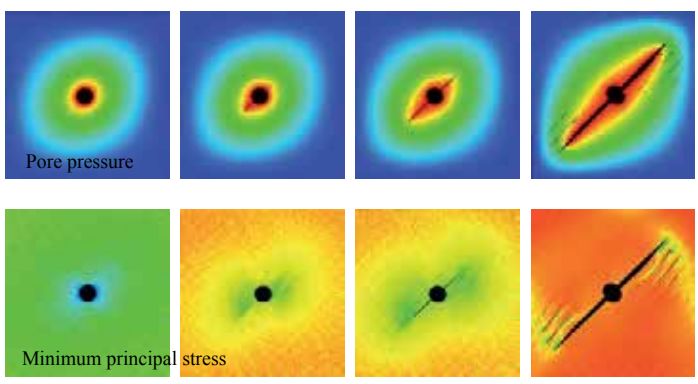

Figure 16. Pore pressure and the minimum principal stress distribution in fracture evolution process (45°)

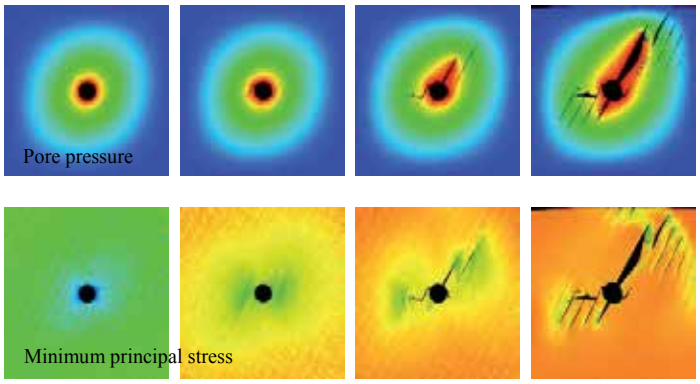

Figure 17. Pore pressure and the minimum principal stress distribution in fracture evolution process (60°)

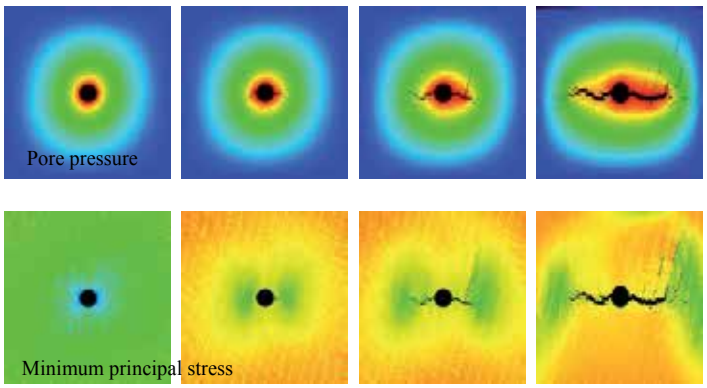

Figure 18. Pore pressure and the minimum principal stress distribution in fracture evolution process (75°)

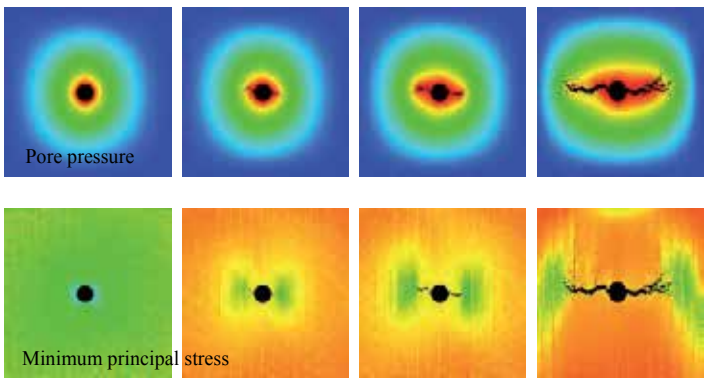

Figure 19. Pore pressure and the minimum principal stress distribution in fracture evolution process (90°)

http://dx.doi.org/10.5772/56012

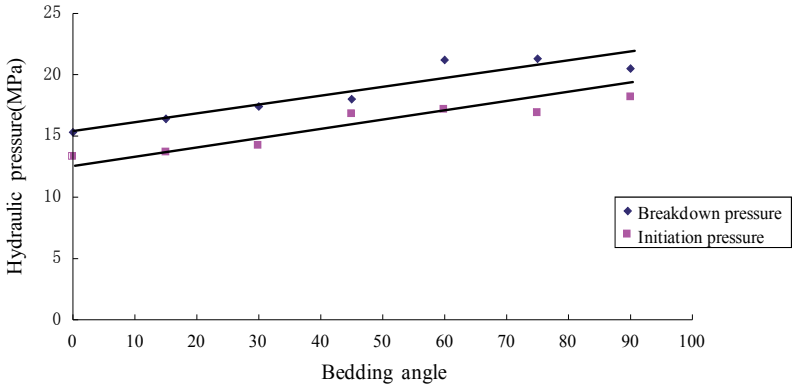

Figure 20. Changes of initiation and breakdown pressure of different bedding angle specimens

4.3. The effect of bedding materials

Taking the rock specimen of 60° bedding angle for example, the initiation pressure, the breakdown pressure and the fracture evolution of seven rock specimens with different bedding materials are simulated. Pore pressure and the minimum principal stress distribution achieved by numerical simulation are shown from figure 21 to figure 27 and the values of initiation and breakdown pressure shown in figure 28.

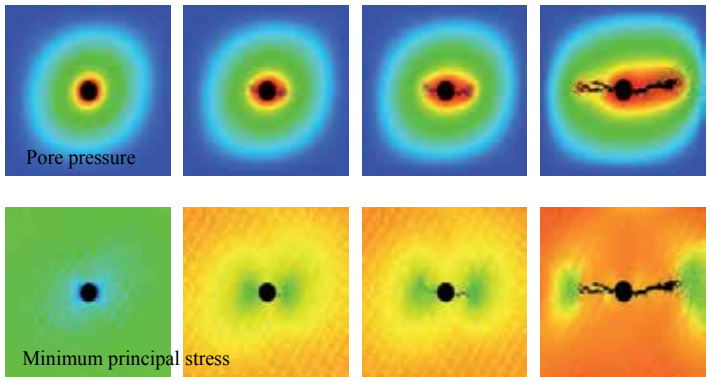

Figure 21. Pore pressure and the minimum principal stress distribution in fracture evolution process (elastic modulus value is 3.0GPa)

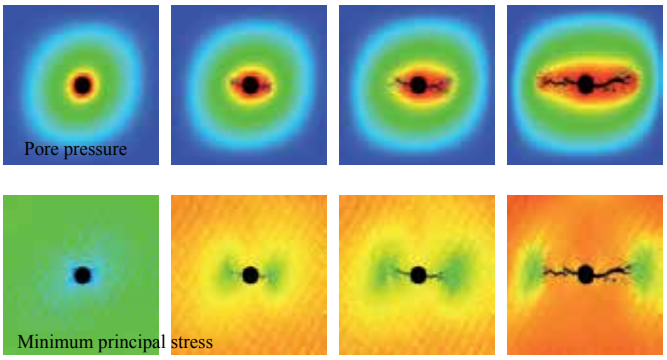

Figure 22. Pore pressure and the minimum principal stress distribution in fracture evolution process (elastic modulus value is 1.5GPa)

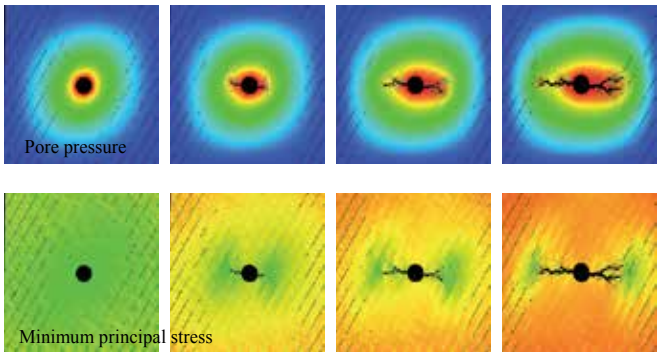

Figure 23. Pore pressure and the minimum principal stress distribution in fracture evolution process (elastic modulus value is 0.5GPa)

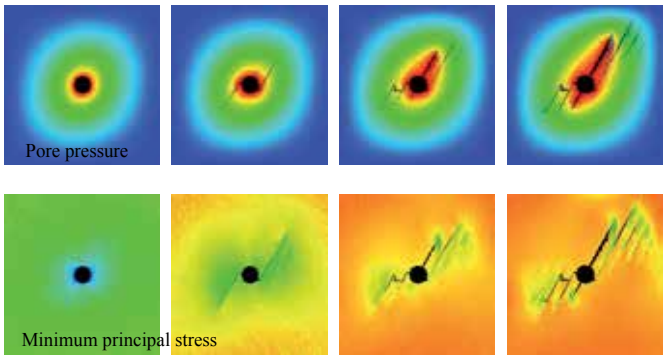

Figure 24. Pore pressure and the minimum principal stress distribution in fracture evolution process (uniaxial compressive strength value is 20MPa)

http://dx.doi.org/10.5772/56012

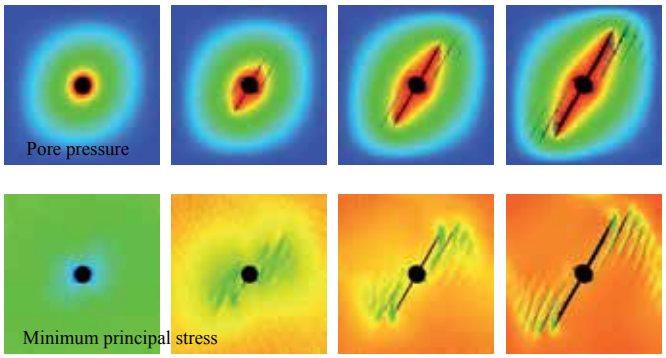

Figure 25. Pore pressure and the minimum principal stress distribution in fracture evolution process (uniaxial compressive strength value is 10MPa)

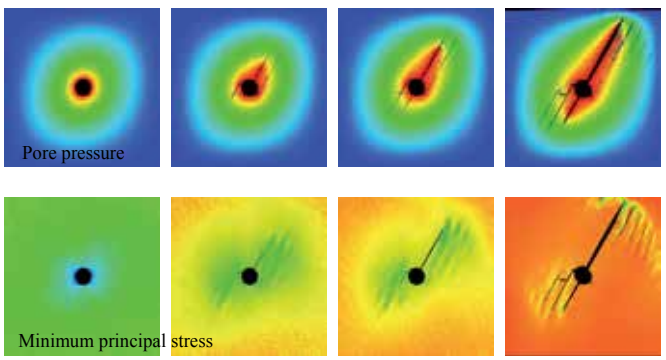

Figure 26. Pore pressure and the minimum principal stress distribution in fracture evolution process (uniaxial compressive strength value is 3.33MPa)

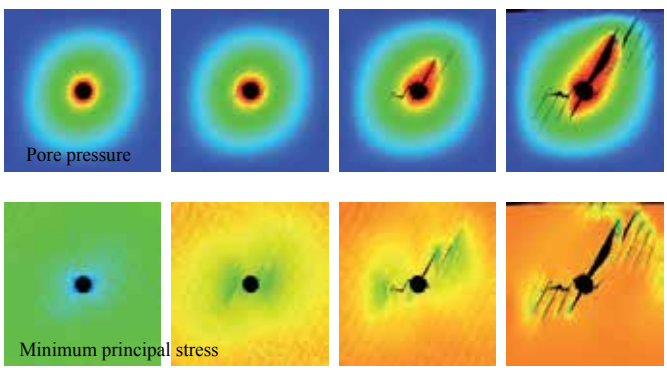

Figure 27. Pore pressure and the minimum principal stress distribution in fracture evolution process (elastic modulus value is 3.0GPa and uniaxial compressive strength value is 20MPa)

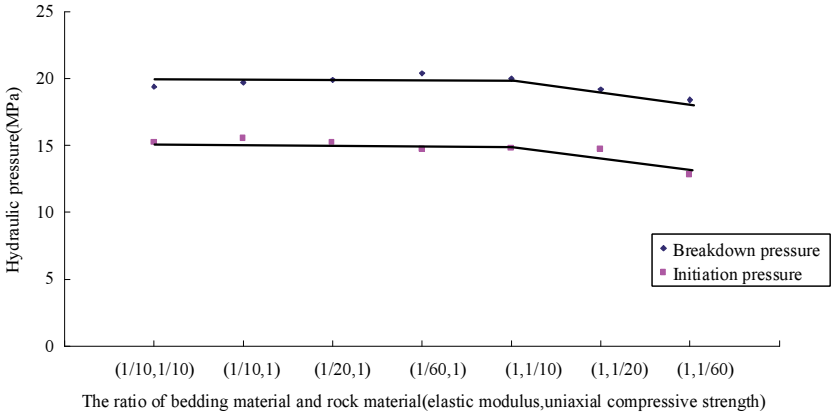

Figure 28. Changes of initiation and breakdown pressure of different bedding material specimens

5. Discussions

From the simulation results of the first group, we can see that the hydraulic fracturing process of the rock specimens with different perforation angle under constant confining pressure is divided into three stages:

1. Stress accumulation stage

In this stage, there doesn't appear any fracture and broken element, but as the pore pressure increases step by step, the stress is accumulating on perforation tip gradually and forming a high minimum principal stress area (green zone). Because of the tensile strength of rock is far less than the compressive strength, it can be speculated that the fracture initiation will be happened on the perforation tip where tensile stress is the largest;

2. Steady propagation stage

The fracture will initiate and propagate on perforation tip when the minimum principal stress accumulates to a certain point (tensile strength). In this stage, lots of micro fractures will appear on the main fracture tip as the loading step increases, and distributing as an umbrella and disconnected to each other;

3. Unsteady propagation stage

As the number of micro fractures increase, some micro fractures connect to each other and become secondary fractures. In this stage, in the process of fracture propagation, stress is

http://dx.doi.org/10.5772/56012

released from parts of the high stress area and transferred to the fracture tip, which makes the fracture propagate continually under the constant hydraulic pressure. The speed of fracture propagation become faster and faster and the main fracture and the secondary fractures are connected finally.

From figure 4 to figure 10, it can be concluded that no matter how the perforation azimuth changes, the fracture is still initiating on the perforation tip, which is because of the casing. But after the fracture initiate, the fracture propagation will turn to the horizontal direction (the maximum principal stress direction) gradually under the increasing hydraulic pressure and form a turning fracture finally. The perforation angle is bigger, the fracture turning will be more obvious and the turning distance will be bigger. Fracture propagation is always deviating from the perforation direction to the maximum principal stress direction (horizontal direction), which proves that the effect of perforation angle on the direction of fracture propagation is small and the maximum principal stress control the final fracture propagation direction.

The results also show that the perforation angle determines the initiation and the breakdown pressure of rock specimens. With the perforation angle increases, the initiation pressure are 15.2MPa, 15.2MPa, 15.3MPa, 15.2MPa, 15.2MPa, 20.1MPa and 21.4MPa respectively, and the breakdown pressure 16.8MPa, 16.7MPa, 17.1MPa, 19.4MPa, 19.4MPa, 22.5MPa and 23.2MPa respectively. The initiation pressure and the breakdown pressure are divided into two stages (figure 12): When $\alpha \leq 60^o$, the values of initiation pressure are small and basically constant, while as $\alpha > 60^o$, the values of initiation pressure increase obviously and with the increase of α, the values of initiation pressure will increase gradually; When $\alpha \leq 30^o$, the values of breakdown pressure are small and basically constant, while as $\alpha > 30^o$, the value of breakdown pressure will increase obviously and with the increase of α, the values of breakdown pressure will increase gradually, of which the increase rate is smaller than that of initiation pressure. Therefore, 0^o-30^o is the best perforation azimuth area and the values of initiation and breakdown pressure are small, which may help reduce fracturing cost and improve the fracturing efficiency. The comparison of numerical simulation results and the experimental results with the same perforation angle (60^o) and ground stress difference (5MPa) is shown in figure 11 and we can find that the macroscopic fracture propagation of the numerical simulation is basically consistent with the experimental results.

The results of first group simulation indicates that the maximum principal stress determines the fracture propagation direction, and the effect of bedding angles of rock specimens under the same confining pressure on fracture propagation will be studied in the second group.

From the simulation results of the second group, we can conclude that the fracture initiation and the propagation pattern of rock specimens under constant confining pressure are changing gradually as bedding angle increases. From figure 13 to figure 19, we can see that, when bedding angle α is small (0^o~15^o), the initiation and propagation of fracture are only along with the tension failure bedding. Because of the stress accumulation, there exist a high tensile stress area on the fracture tip and because the bedding material is weaker than rock ma-

terial, the fracture propagation is along the cracked bedding and form a straight fracture eventually. In this case, the bedding plane determines the fracture evolution.

When bedding angle α increases slightly (30^{o}~45^{o}), the initiation and propagation of fracture is still along the tension failure bedding. With the increase of loading step, there is a high tensile stress area on the main fracture tip which is along the cracked bedding and the beddings in the high tensile stress area are cracked and form secondary fractures paralleling to the main fracture, moreover, with the increase of bedding angle, the number of secondary fractures is increasing gradually. Because of the advantage of main fracture, the fracture propagation is still along the main fracture bedding.

When the bedding angle α continues to increase (60^{o}), the fracture will turn from along the tension failure bedding to the horizontal direction that is the main fracture and the secondary fractures paralleling to the main fracture is still initiating and propagating in bedding plane with the horizontal secondary fracture initiating at the same time and connecting the main fracture and the parallel secondary fractures gradually. In this case, the bedding plane and the maximum principal stress determine the fracture evolution together.

When bedding angle α is big (75^{o}~90^{o}), the initiation and propagation of fracture is no longer along the bedding plane. Because of the heterogeneous characteristics of rock and bedding materials, different strength elements are in random distribution causing an uneven stress distribution and the local stress concentration thus making the fracture become bend and rough, but the general trend is the maximum principal stress direction. In this case, the effect of bedding plane on fracture evolution is almost disappeared, but the maximum principal stress controls the fracture initiation and propagation. Comparing figure 4 and figure 19, we can find that the existence of bedding influences the fracture shape greatly in the same condition as the maximum principal stress controls the fracture evolution.

From the numerical simulation results, as bedding angle increase, the values of initiation pressure are 13.3MPa, 13.7MPa, 14.2MPa, 16.8MPa, 17.1MPa, 16.9MPa and 18.2MPa respectively, and the values of breakdown pressure 15.3MPa, 16.4MPa, 17.4MPa, 18MPa, 21.2MPa, 21.3MPa and 20.5MPa respectively. Both of the values of initiation and breakdown pressure are in a linear growth (figure 20) with the growth rate similar and as the bedding plane is parallel to the maximum principal stress direction (bedding angle is 0^{o}), the specimen is in the most unstable situation.

Because the fracture propagation is determined by the maximum principal stress and the bedding plane together when bedding angle is 60^{o} seeing from the second group simulation, taking the bedding angle of 60^{o} for example, in the third group, the effect of strength and stiffness of bedding material on fracture evolution will be studied under the combined effects of the maximum principal stress and the bedding plane.

In the third group, the rock specimens with the same bedding angle but different materials are under the constant confining and increasing hydraulic pressure. As the strength of bedding material is constant (bedding strength/rock strength is 1), but the stiffness decreased

http://dx.doi.org/10.5772/56012

(bedding elastic modulus/rock elastic modulus is 1/10, 1/20, 1/60), the pattern of fracture propagation will be unchanged. Because of the reduction of elastic modulus, the initiation pressure reduced (15.5 MPa, 15.2 MPa, 14.7 MPa) and the breakdown pressure increased slightly (19.7 MPa, 19.9 MPa, 20.4 MPa), however, both of the reduction and the increase can be ignored because the values of the initiation and the breakdown pressure are almost constant (figure 28). As the stiffness of the bedding material (bedding elastic modulus/rock elastic modulus is 1) is constant but the strength decreased (bedding strength/rock strength is 1/10, 1/20, 1/60), the pattern of the fracture propagation will be unchanged, and the values of initiation (14.8 MPa, 14.7 MPa, 12.8 MPa) and breakdown pressure (20 MPa, 19.2 MPa, 18.4 MPa) decreased gradually with almost the same decrease rates (figure 28). As both of the stiffness and strength are decreased (bedding elastic modulus/rock elastic modulus is 1/10, bedding strength/rock strength is 1/10), the initiation pressure, the breakdown pressure and the pattern of fracture propagation are almost the same as the condition of (1, 1/10). As suggested above, the stiffness of bedding material has little influence on initiation pressure, breakdown pressure and fracture evolution of rock specimens, except that the strength determines them.

In summary, the damage process of rock specimen are determined by the maximum principal stress, the bedding angle and the strength of bedding material, while the effect of perforation angle and stiffness is small and can be ignored.

6. Conclusions

Based on the simulation results of three groups, the following can be concluded:

1. When perforation angle is larger than 0^o, a turning fracture will be formed, and if the perforation angle turns bigger, the fracture turning will be more obvious and the turning distance bigger. The effect of perforation angle on fracture propagation direction is small, and the maximum principal stress controls the fracture propagation direction.
2. The initiation and the breakdown pressure of specimens with different perforation angles are divided into two stages and 0^o-30^o is the best perforation angle area. The initiation and the breakdown pressure can be predicted through the numerical simulation.
3. The influence of bedding angle on initiation pressure, breakdown pressure, fracture shape and fracture propagation pattern is great. As the bedding angle increases, the bedding plane and the maximum principal stress will control the fracture evolution respectively and the initiation and the breakdown pressure are in a linear growth with the similar rates. The specimen will be in the most unstable situation as the bedding plane paralleling to the maximum principal stress direction.
4. The stiffness of bedding material has little influence on damage process of rock specimens, except that the strength controls it. With the decrease of bedding material strength, the initiation and the breakdown pressure will decrease gradually with the similar decrease rates.

Author details

Xiaoxi Men[1*], Chun'an Tang[2], Shanyong Wang[3], Yongping Li[4], Tao Yang[2] and Tianhui Ma[2]

*Address all correspondence to: menxiaoxi@126.com; tang_chunan@yahoo.com; Shanyong.Wang@newcastle.edu.au; liyp69@petrochina.com.cn; 361721644@qq.com; 19928600@qq.com

1 Northeastern University, Shenyang, China

2 Dalian University of technology, Dalian, China

3 ARC Centre for Geotechnical Science and Engineering, The University of Newcastle, NSW, Australia

4 Fracturing and Acidizing Technical Service Center, Research Institute of Petroleum Exploration & Development-Langfang, Petrochina, Langfang, China

References

[1] Daneshy, Abbas Ali, Halliburton Services. Experimental Investigation of Hydraulic Fracturing Through Perforations. Petroleum Technology (1973). , 25(10), 1201-1206.

[2] Weng, X W. Fracture Initiation and Propagation from Deviated Wellbores. In: Proceedings of the SPE Annual Technical Conference and Exhibition, Houston, Texas, 30 Oct (1993). Paper SPE 26597.

[3] Zhang, X, Jeffrey, R G, Bunger, A P, & Thiercelin, M. Initiation and Growth of a Hydraulic Fracture from a Circular Wellbore. Rock Mechanics and Mining Sciences (2011).

[4] Zhang, G Q, Chen, M, Wang, X S, & Zhao, C. Influence of Perforation on Formation Fracturing Pressure. Petroleum Science (2004). , 1(3), 56-61.

[5] Jiang, H, & Chen, M. Impact of Oriented Perforation on Hydraulic Fracture Initiation and Propagation. Chinese Journal of Rock Mechanics and Engineering (2009). , 28(7), 1321-1326.

[6] Brouno, M S, & Nakagawa, F M. Pore Pressure Influence on Tensile Fracture Propagation in Sedimentary Rock. International Journal of Rock Mechanics and Mining Science & Geomechanics Abstracts (1991). , 28(4), 261-273.

[7] Li, L C, & Tang, C A. Simulation of Multiple Hydraulic Fracturing in Non-uniform Pore Pressure Filed. Advanced Materials Research (2005). , 9, 163-172.

http://dx.doi.org/10.5772/56012

[8] Abbass, T, & André, V. Effect of Layer Orientation on the Failure of Layered Sandstone under Brazilian Test Conditions. International Journal of Rock Mechanics and Mining Sciences (2010). , 47(2), 313-322.

[9] Abbass, T. Failure of Layered Sandstone under Brazilian Test Conditions: Effect of Micro-scale Parameters on Macro-scale Behaviour. Rock Mechanics and Rock Engineering (2010). , 43(5), 641-653.

[10] Tang, C A, Tham, L G, Lee, P, Yang, K, & Li, T H. L C. Coupled Analysis of Flow, Stress and Damage (FSD) in Rock Failure. International Journal of Rock Mechanics & Mining Sciences (2002). , 39(4), 477-489.

[11] Leng, X F, & Yang, T H. Numerical Simulation and Analysis of Rocks with Single Hole Each Under Hydraulic Fracturing. World Nonferrous Metals (2002). , 10, 32-34.

[12] Tang, C A. Numerical Simulation to Influence of Pore Pressure Magnitude and Gradient on Fracture Propagation in Brittle Heterogeneous Rocks. Rock and Soil Mechanics (2003). , 24, 17-20.

[13] Yang, T H. Influence of Heterogeneity of Mechanical Properties on Hydraulic Fracturing in Permeable Rocks. Rock Mechanics and Rock Engineering (2004). , 37(4), 251-275.

[14] Li, G, & Tang, C A. Three-Dimensional Micro Flow-Stress-Damage (FSD) Model and Application in Hydraulic Fracturing in Brittle and Heterogeneous Rocks. Key Engineering Materials (2011).

[15] Yang, T H. Numerical Approach to Hydraulic Fracturing in Heterogeneous and Permeable Rocks. Key Engineering Materials (2003).

[16] Yang, T H, & Tang, C A. Numerical Simulation of Hydraulic Fracturing Process in Heterogeneous Rocks under Different Confining Pressures. Chinese of Computational Mechanics (2004). , 21(4), 419-424.

Chapter 25

Quantitative Evaluation of Completion Techniques on Influencing Shale Fracture 'Complexity'

N. Nagel, F. Zhang, M. Sanchez-Nagel and B. Lee

Additional information is available at the end of the chapter

http://dx.doi.org/10.5772/56304

Abstract

In many of the active shale plays, the extremely low permeability of the shale means simple, bi-planar hydraulic fractures do not provide enough surface area to make an economic well. In these cases, the optimal, economic completion requires stimulation of the natural fracture system - often called increasing the 'complexity' of the stimulation. A number of different multi-well completion techniques have been proposed to enhance shale complexity. The 'simul-frac' technique is where companion wells are stimulated at the same location at the same time, whereas the 'zipper-frac' technique employs companion wells that are stimulated in staggered locations at the same time. The intention with these techniques is to alter either or both the stress field and the pore pressure field to enhance the shearing of natural fractures.

In this paper, we present the results of a numerical study to quantitatively evaluate the effectiveness of multi-well completion techniques, particularly the 'modified zipper-frac' technique, to optimize shale completions. The study includes a parametric study of the effects of in-situ stress conditions, natural fracture orientation and fracture friction, and hydraulic fracture layout on changing near and far-field natural fracture shear (complexity). Changes in the stress field, particularly shear stress, are considered the primary means of increasing fracture complexity. The quantitative results of the study provide a means to optimize the application and design of different multi-well completion techniques as a function of the presented parameters. Optimized completion designs mean lower well costs, greater production and, ultimately, improved well economics.

Keywords: Hydraulic fracturing, stimulation, unconventional, complexity, well completion, shale, numerical simulation, simul-frac, zipper-frac, discrete element model, DEM, microseismicity

1. Introduction

Much has now been written about the boom in shale gas and shale oil developments in the United States and around the world. In its recent assessment for example, the Energy Information Agency (EIA 2012) noted that North Dakota has become the second largest oil producer in the United States due to production from the Bakken shale. In addition, the EIA (EIA 2013) has predicted that the United States will continue to add more than 230,000 bpd of oil production per year through the end of the decade and become a net exporter of natural gas within the decade. Expenditures on shale gas and shale oil developments have also rapidly increased. For example, more than $54 billion dollars was spend in drilling and development operations in the seven major US shale developments in 2012 (Clover Global Solutions 2012), with the bulk being spent in the Eagle Ford and Bakken plays.

Shale developments, notably beginning in the Barnett in the 1990s, have been driven by: 1) the application of horizontal wells; 2) the application and improvements in hydraulic fracturing; and 3) significant commodity prices (GWPC 2009 and King 2010). Because of the low permeability in most shale developments (nano-darcy permeability in shale gas plays and micro-darcies in shale oil plays), hydraulic fracturing is a key technology because, as noted by King (2010), the presence of, and the ability to open and maintain flow in, both the primary and secondary natural fracture systems is critical. King further noted the importance of maximizing the fracture-to-shale contact area and optimizing the development, placement, and length of small fractures to enhance and stabilize well production (i.e., optimizing the stimulation of the natural fracture system - that is, increasing natural fracture 'complexity').

Because the stimulation of the natural fracture system is critical to many shale developments, a number of different multi-well completion schemes have been devised in an effort to improve the ability to enhance the stimulation of natural fractures. Three of the common completions schemes are shown in Figure 1. In simultaneous fracturing (plot A in Figure 1), the concept is that hydraulic fracturing both wells at the same time enhances the stimulation of the natural fractures. In the sequential (zipper) frac concept (plot B), the residual stress field from well #1 is thought to enhance the stimulation of the natural fractures when well #2 is stimulated. Finally, in the modified zipper-frac concept (plot C, Figure 1), the sequential stimulation of offsetting stages is thought to enhance the stimulation of the natural fractures.

1.1. Natural fracture behavior

A critical component to understanding the efficacy of multi-well completion techniques on increasing shale complexity is the understanding of the geomechanical behavior of natural fractures. The authors have written extensively about the mechanical behavior of natural fractures and the results of numerical modeling (both continuum and distinct element modeling) of the response of natural fractures to hydraulic fracture stimulation (Nagel et al. 2012a, Nagel et al. 2012b, Nagel et al. 2012c, Nagel et al. 2011a, Nagel et al. 2011b, and Nagel and Sanchez-Nagel 2011). Of first interest in evaluating the impact of multi-well completion schemes on the stimulation of natural fractures is the basic behavior of natural fracture shear and deformation.

http://dx.doi.org/10.5772/56304

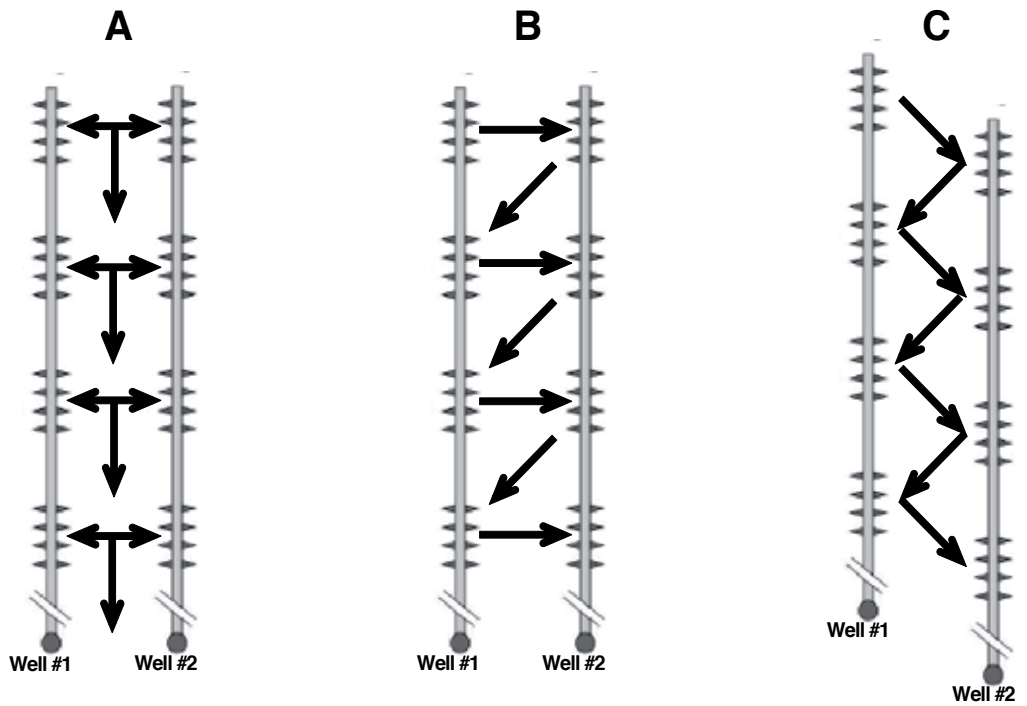

Figure 1. Common shale completion schemes. A) Simultaneous hydraulic fracturing; B) Sequential fracturing (zipper-frac); and C) Modified zipper-frac.

Nagel et al. (2012c) summarized five 'conditions' for natural fracture shear to occur:

1. The shear stress along the fracture grows to exceed the shear strength with no change in fracture friction, fracture normal stress, or fracture pore pressure;
2. Due to thermal or chemical changes, fracture friction is reduced while the shear stress along the fracture is unchanged and the fracture normal stress and fracture pore pressure are unchanged;
3. The fracture normal stress decreases with no change in the shear stress along the fracture, the fracture friction coefficient, or fracture pore pressure;
4. The fracture pore pressure increases with no change in the shear stress along the fracture, the fracture friction coefficient, or fracture normal stress; and
5. A variety of combinations of the above.

Of these, conditions 3 and 4 (and, by default, condition 5) are believed to be most relevant to the behavior of fractured shale plays during hydraulic fracturing. The impact of these conditions is shown graphically in Figure 2. Figure 2 is a schematic representation of the results of a direct shear test on a fractured rock sample. The x-axis represents the shear displacement along the fracture during the test, and the y-axis represents the shear stress imparted to the

rock in order to achieve the given displacement. Four stress-displacement profiles are shown, which represent increasing effective normal stress on the fracture. As the effective normal stress is increased, both the peak shear stress necessary to initiate non-elastic displacements and the shear stress necessary to continue non-elastic displacements increase.

The implications of this behavior are critical to understanding the behavior of natural fractures during hydraulic fracturing. As shown in Figure 2, as the normal stress acting on natural fractures increases (due, for example, to the inflation of an induced hydraulic fracture), greater shear stress is required to cause shear slippage and displacement along a natural fracture. Effectively, increasing the normal stress stabilizes the natural fractures. At the same time, as pressure increases within a natural fracture (due, for example, to bulk fluid flow into the natural fractures or pressure diffusion from the induced hydraulic fracture), less shear stress is required to cause shear slippage. Given this behavior for natural fractures, and the goal of increasing the shear stimulation of these during hydraulic fracturing, the evaluation of the impact of completion scheme on well stimulation should focus on whether or not the completion scheme increases the shear of the natural fractures.

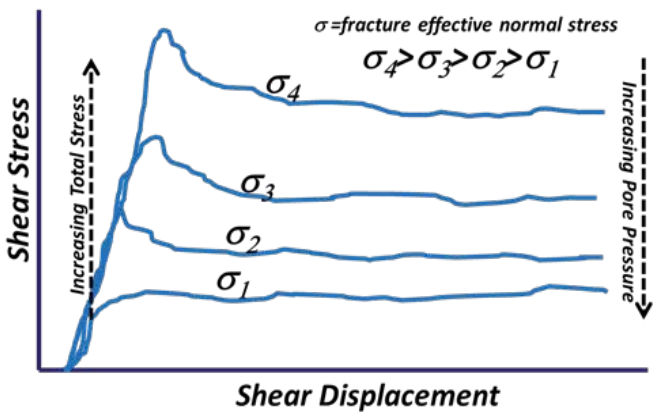

Figure 2. Shear-displacement profiles as a function of normal effective stress from direct shear testing of fractured rock.

1.2. Hydraulic fracturing and stress shadows

If increasing normal stress stabilizes natural fractures, then evaluating the stress changes from a hydraulic fracture is a required element of evaluations to optimize shale complexity. As far back as Sneddon's work on the evaluation of stress near a crack (Sneddon 1946), numerous authors have looked at the impact of stress field changes around hydraulic fractures (Nagel and Sanchez-Nagel 2011 and Warpinski et al. 2012). The stress field change, principally the increase in the minimum horizontal stress, Shmin, caused by a hydraulic fracture (typically the final, propped hydraulic fracture) is called the stress shadow effect or simply the stress

http://dx.doi.org/10.5772/56304

shadow. Figure 3 shows the stress shadow (increase in Shmin) from a single hydraulic fracture that was 300m long and 140m in height (along the x-z plane on the right side of the model) in a model that is 1000m cube.

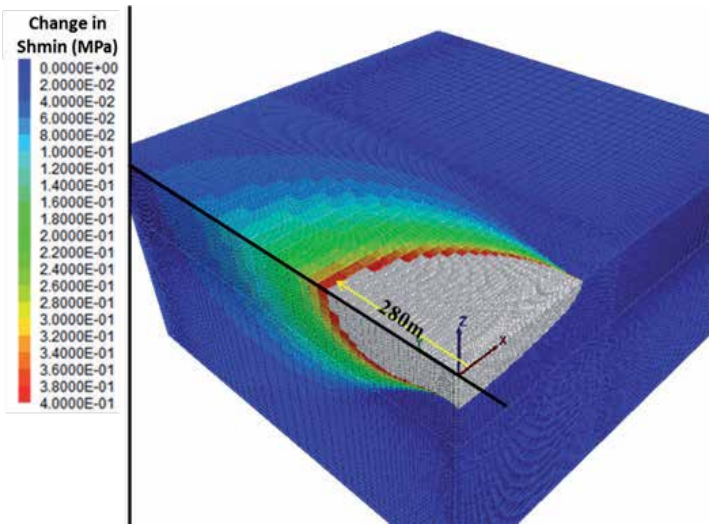

Figure 3. Stress shadow contours from a single 300m long/140m high hydraulic fracture with a 5MPa net pressure applied on the x-z plane. The cut-away image was created by cutting along the y-z and x-y planes. The model shown is 1000m in each of the x and y-directions. The white area is a region of stress change greater than the color scale shown (from Nagel et al. 2013).

As shown, note both the long distance over which the stress change occurs – to the edge of the 1000m long block simulated – and the vertical spreading with distance. At large distances, the change in stress is seen to affect a total formation height more than double the original height of the created fracture. Note also the near-complete lack of stress change beyond the horizontal tip of the hydraulic fracture. Overall, the following can be summarized about stress shadows (Nagel and Sanchez-Nagel 2011):

- The increase in Shmin (stress shadow) extends significant distances behind a fracture and spreads out above and below the fracture but not beyond the tip of the fracture.
- The increase in Shmin due to a hydraulic fracture is largely unaffected by either the in-situ rock mechanical properties or the stress ratio (though these do appear to affect changes in the vertical stress and the SHmax stress).
- A horizontal shear stress field occurs with the fracture tip and does not extend back to the wellbore. This suggests that, at some distance behind the fracture tip, the effect of the stress shadow is to stabilize the natural fracture system.

- Reducing fracture spacing results in a greater minimum Shmin stress increase in the inter-fracture region as the stress shadows from each fracture overlap more with reduced fracture spacing.

1.3. Natural fracture behavior and stress shadows: Implications for completion strategies

The combined consideration of the basic mechanical behavior of natural fractures and the nature of stress shadows suggests the following for a multi-well completion strategy:

- The stress shadow effect, that is the increase in the principal stresses around a hydraulic fracture, causes a stabilization of natural fractures. This can only be overcome by increasing the fluid pressure within the natural fractures (suggesting a desire to increase the net pressure, which would also increase the stress shadow). Decreasing stage spacing, or overlapping hydraulic fractures from different wells, will tend to increase the stress shadow effect and impair the stimulation of natural fractures.
- Because the stress shadow effect does not extend horizontally beyond the tip of the hydraulic fracture (the x-direction in Figure 3), when two fractures are simultaneous created from parallel wellbores, the fractures will not 'see' each other until the tip regions are very near to each other (and increase the potential for screenout during a stimulation).

1.4. Numerical simulation of completion strategies: Modified zipper-frac

In this paper, numerical simulation results are presented for the evaluation of the modified zipper-frac multi-well completion strategy. The simulations were conducted with a 2D discrete element model (DEM) under different well configurations for two different natural fracture networks, different fracture friction angles, and different stress ratio conditions.

2. Model setup and simulation matrix

2.1. 2D DEM model capabilities

A two-dimensional DEM code was used in all the simulations presented. The code used was a general-purpose program based on the distinct element method for discontinuum modeling. The code can simulate the response of discontinuous media (such as a jointed rock mass) subjected to either static or dynamic loading. The discontinuous medium is represented as an assemblage of discrete blocks, and discontinuities are treated as boundary conditions between blocks. Large displacements along discontinuities and rotations of blocks are allowed. Individual blocks behave as either rigid or deformable material. Deformable blocks are subdivided into a mesh of finite-difference elements, and each element responds according to a prescribed linear or nonlinear stress-strain law. The relative motion of the discontinuities is also governed by linear or nonlinear force-displacement relations for movement in both the normal and shear directions. The basic formulation of the code assumes a two-dimensional plane-strain state. This condition is associated with long structures or excavations with a

http://dx.doi.org/10.5772/56304

constant cross-section acted on by loads in the plane of the cross section. Discontinuities, therefore, are considered as planar features oriented normal to the plane of analysis. For plane-strain analyses, blocks may exhibit plastic yield, and failure can occur in the out-of-plane direction if the out-of-plane stress becomes a major or minor principal stress.

The critical modeling features for the simulation of hydraulic fracturing include:

- A rock mass is modeled as an assemblage of rigid or deformable blocks. The size, shape, and orientation of the blocks are defined by the imported Discrete Fracture Network (DFN) or by the internal fracture generator.
- Discontinuities are regarded as distinct boundary interactions between blocks, and continuous and discontinuous joint patterns or joint properties can be generated on a statistical basis or from an imported DFN.
- Fractures are created within, and propagate along, the static block boundary planes; however, propagation can be modeled explicitly based upon the stress intensity factor at the fracture tip. Fracture behavior is prescribed by the block interactions. Thus, natural fracture aperture is, for example, affected by shear displacement and fracture fluid pressure.
- Fluid flow is limited to flow within the fractures, and matrix fluid (and, for example, fluid leakoff) is not considered.

2.2. Model setup

Figure 4 shows the setup and dimensions of the 2D model in planview at the centerline of the horizontal wellbores (located along the left and right sides of the model shown). Table 1 summarizes the model mechanical parameters while Table 2 summarizes the stress conditions used. The total model was 1200m long in the direction of Shmin (vertical or y-direction) and 225m wide in the direction of SHmax (horizontal or x-direction) as shown in plot A of Figure 4. In order to avoid boundary effects, the vertical boundaries were placed at a large distance (> 550m) from the simulated hydraulic fractures and roller boundaries were applied. The horizontal boundaries were considered to be symmetry planes at the wellbore locations (as only half the fracture length was modelled) and roller boundaries were also applied.

Two different natural fracture patterns were employed. In plot B of Figure 4 (note that plot B and C represent the central core in green from plot A), the '180°' fracture pattern is shown. This pattern contains two fracture sets, which are nominally orthogonal to each other and aligned with the principal stress directions. The second fracture pattern, called the '145°' pattern, is shown in plot C. For the 145° pattern, the same two fracture sets from the 180° pattern have been rotated roughly 45° relative to the principal stresses.

The simulated hydraulic fractures are shown in solid and dashed black lines in plots B and C. The solid line represents the first hydraulic fracture location (Xf1) and the dashed lines represent the location of the second hydraulic fracture (Xf2) at a distance of 20m, 35m, and 45m offset along the wellbore from Xf1. When fully propagated, Xf1 and Xf2 were 125m long (their fracture half length).

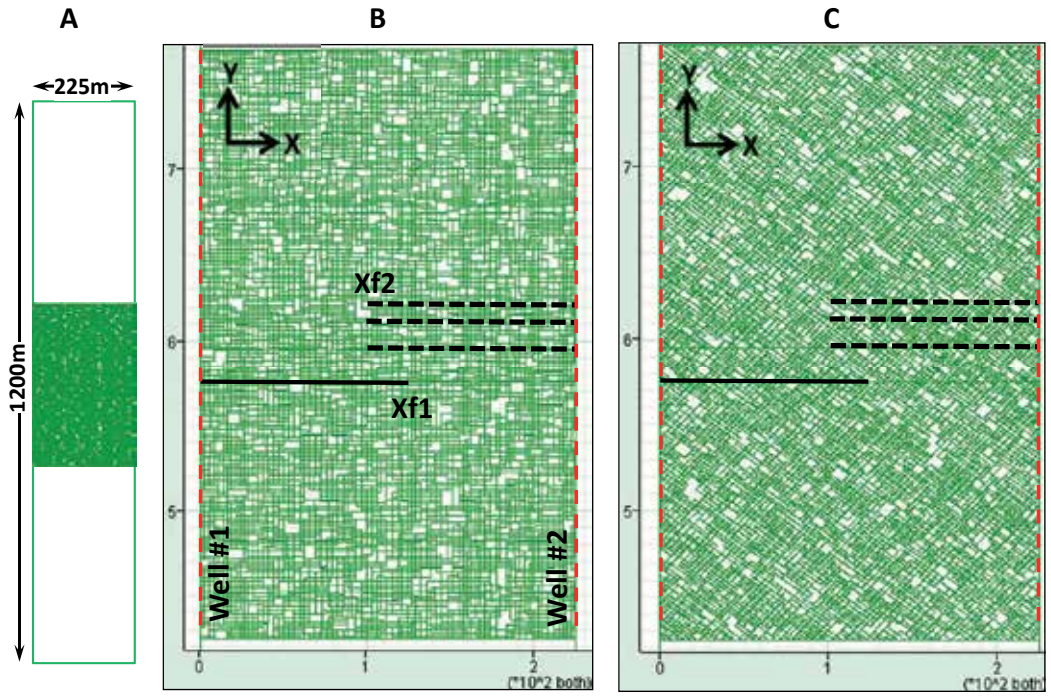

Figure 4. DEM model setup and dimensions. A) Full model - only the middle section in green contained fractures; B) Middle section natural fracture pattern for the '180°' model; and C) Middle section natural fracture pattern for the '145°' model. The location of simulated hydraulic fractures are represented by the black lines. Horizontal wellbores are located along the full length of the left and right sides of the model.

	DFN #1	DFN #2
Case Name	'180°'	'145°'
Matrix Young's modulus	27.6 GPa	27.6 GPa
Matrix Poisson's ratio	0.25	0.25
Fracture Set #1 Orientation	N180°	N145°
Set#1 Trace Length, mean	35m	35m
Set#1 Trace Length, st. deviation	10m	10m
Set#1 Gap Length	5m	5m
Set#1 Spacing, mean	2m	2m
Set#1 Spacing, st. deviation	0.75m	0.75m
Fracture Set #2 Orientation	N90°	N45°
Set#2 Trace Length, mean	35m	35m
Set#2 Trace Length, st. deviation	10m	10m

http://dx.doi.org/10.5772/56304

	DFN #1	DFN #2
Set#2 Gap Length	5m	5m
Set#2 Spacing, mean	3m	3m
Set#2 Spacing, st. deviation	1m	1m
Fracture Normal Stiffness	2e11 Pa	2e11 Pa
Fracture Shear Stiffness	2e11 Pa	2e11 Pa
Initial Fracture Aperture	0.1 mm	0.1 mm

Table 1. Mechanical Parameters Used For Model Construction

	DFN #1		DFN #2
Case Name	'180°'		'145°'
Vertical Stress, Sv	55.2 MPa	55.2 MPa	55.2 MPa
Max. Horizontal Stress, SHmax	44.8 MPa	44.8 MPa	44.8 MPa
Min. Horizontal Stress, Shmin	37.9 MPa	43.5 MPa	37.9 MPa
Pore Pressure	27.6 MPa	27.6 MPa	27.6 MPa

Table 2. Model Stress And Pore Pressure Data

2.3. Modeling assumptions

For any numerical modeling, assumptions need to be made for the problem being simulated. For the simulations described in this paper, the following assumptions were made:

- 2D, plane strain condition exists (i.e., effects above and below the vertical centerline of a vertical hydraulic fracture do not impact the results).
- Hydraulic fracturing is a quasi-static process and both fracture propagation and injection rate effects can be ignored for the cases being simulated (i.e., the hydraulic fracturing process can be represented by static simulations of the fracture at specific lengths under a given net pressure).
- Events within the formation at the tip of the hydraulic fracture can be simulated without fluid flow within the natural fractures (i.e., the behavior within the formation at the tip is dominated by the changes in total stress and pore pressure changes are negligible).
- Net injection pressure was a constant 4 MPa within the hydraulic fractures Xf1 and Xf2 for all simulations.
- Simulations were conducted first for single hydraulic fractures (without influence from a second, nearby hydraulic fracture). Then simulations were conducted for dual hydraulic fractures and compared to results from two hydraulic fractures acting independent of each other.

2.4. Simulation matrix

In total, nearly 100 simulations were performed in order to explore the behavior of the modified zipper-frac completion scheme. 20 simulations were performed to look at the shear results from a single hydraulic fracture with the '180°' (DFN#1 from Tables 1 and 2) varying the length of both fractures Xf1 and Xf2 separately (Xf1 represents the left-side hydraulic fracture - the solid black line in Figure 4 - and Xf2 represents the right-side hydraulic fracture – the dashed lines in Figure 4) from 25m to 125m in 25m increments with a friction angle of 15 degrees (10 simulations) and repeating these with a 25 degree friction angle (10 simulations). Then 60 simulations were performed to look at the efficacy of the modified zipper-frac completion by performing simulations with dual hydraulic fractures with both DFN models (the '180°' and '145°') varying the length of Xf2 (0m, 50, 75m, 100m, and 125m) for a constant Xf1 of 125m length for three separation spacings (20m, 35, and 45m, where separation is the horizontal offset of the Xf1 and Xf2 fractures as shown in Figure 4) and for two friction angles (15 degrees and 25 degrees in the '180°' model and 25 degrees and 35 degrees in the '145°' model). Finally, an additional 15 simulations were performed with the '180°' model varying the initial in-situ stress (see Table 2) and Xf2 length, and keeping the friction angle at 25 degrees.

3. Quantitative numerical evaluation of modified zipper-fracs

3.1. Natural fracture shear from a single hydraulic fracture

A first series of base case simulations were conducted in order to evaluate the natural fracture shear from a single fracture. The simulations looked at the growth of the Xf1 hydraulic fracture as well as the Xf2 hydraulic fracture for two different fracture friction angles. These base case simulations are important because, in order to correctly evaluate the benefit or detriment of the dual frac modified zipper-frac completion, the effect of the two fractures Xf1 and Xf2 completely independent of each other needs to be considered.

Figure 5 shows the natural fracture shear region (in blue) for both the 15° (plot A) and the 25° friction angle simulations for the '180°' DFN model when Xf1 had a fracture half-length of 100m. As an example, the total cumulative length of natural fractures at shear condition in plot A (the sum of the length of the natural fractures in blue in Figure 5) was 300.1m versus 80.8m in plot B. Figure 6 shows the combined shear for the five Xf1 length simulations and the combined sheared area (shaded area) for the propagation of Xf1 from the wellbore to a 125m half-length. As expected, the area of shear for the lower friction simulations is considerably greater (5740m^2) than for the higher friction simulations (2220m^2).

The shaded area in Figure 6 and others, adjusted for the length of Xf2 in the dual fracture simulations, represents the sheared area for Xf2 when Xf2 was created independently of Xf1. This shaded area then allows for comparison of independent Xf1 and Xf2 hydraulic fracture effects to modified zipper-frac effects.

http://dx.doi.org/10.5772/56304

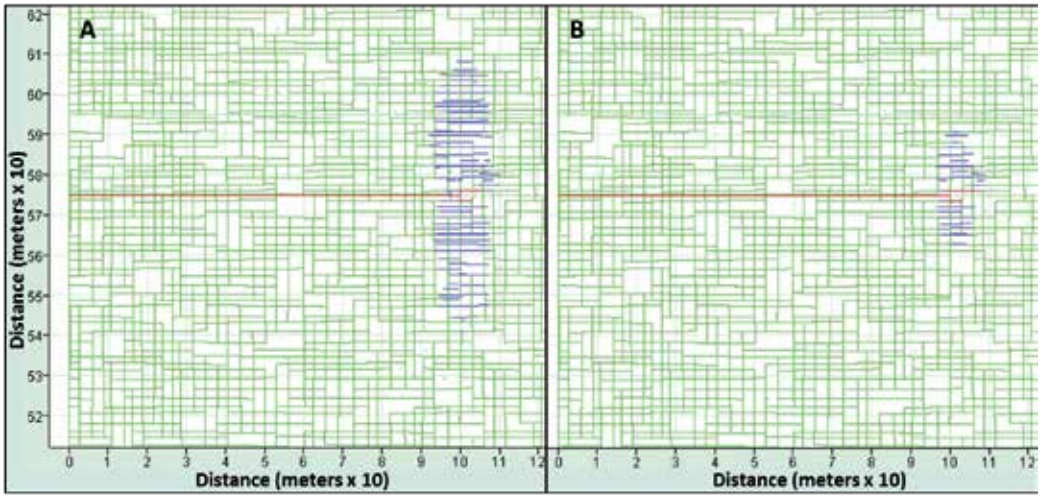

Figure 5. Natural fracture shear (blue lines) for a 100m-long Xf1 hydraulic fracture. A) Shear for the 15° fracture friction case; and B) Shear for the 25° fracture friction case.

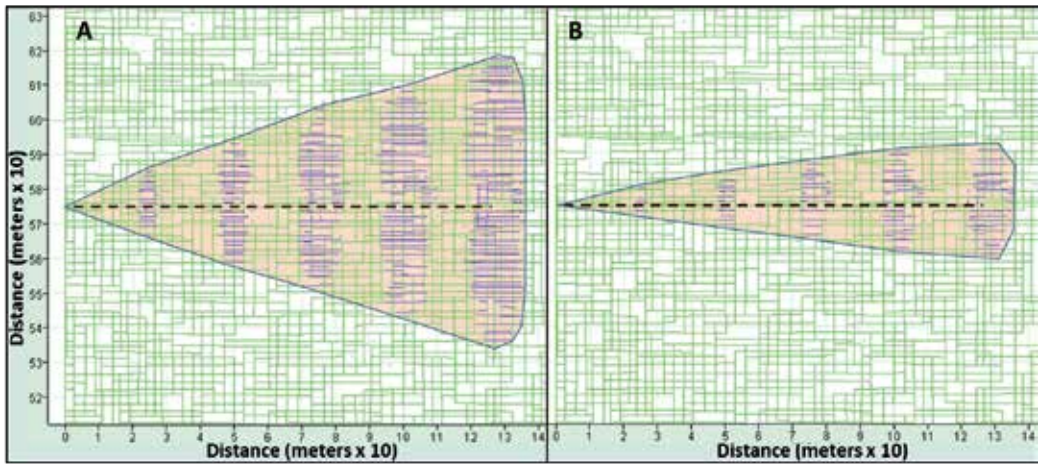

Figure 6. Cumulative natural fracture shear (shaded area) from simulations at 25 to 125m hydraulic fracture half length. A) Shear for the 15° friction case with an area of 5740m^2; and B) Shear for the 25° friction case with an area of 2220m^2.

Figure 7 shows the growth of sheared natural fracture length as a function of hydraulic fracture half-length for the 15° and 25° natural fracture friction cases for all 20 single fracture simulations. Not surprisingly, given the slight variability in the statistics for natural fracture generation, there are slight, insignificant differences between the results for the Xf1 and Xf2 simulations.

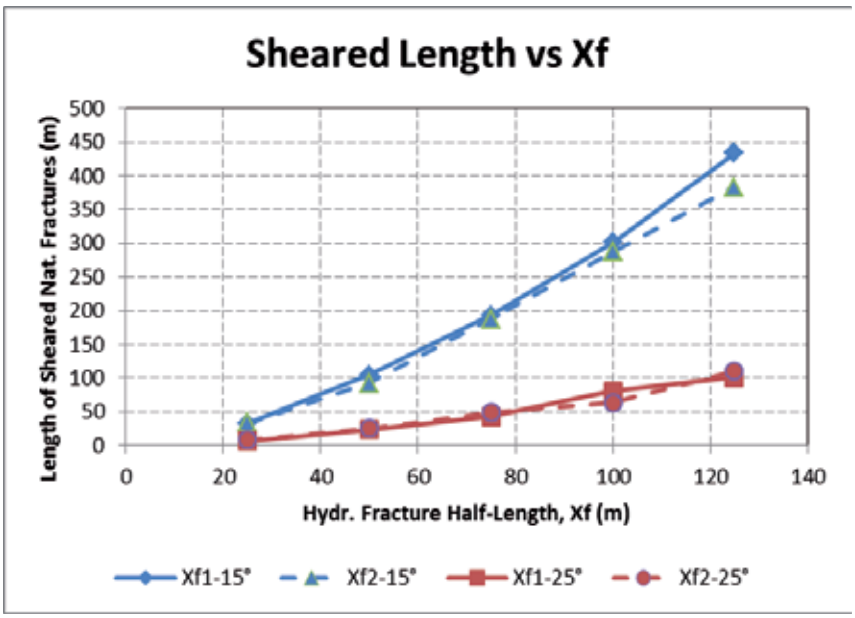

Figure 7. Cumulative natural fracture shear length versus hydraulic fracture half-length for single hydraulic fracture simulations.

A similar evaluation to Figure 6 was performed for the '145°' DFN case as shown in Figure 8. Note that in plot A, natural fracture friction was 25° and in plot B natural fracture friction was 35°.

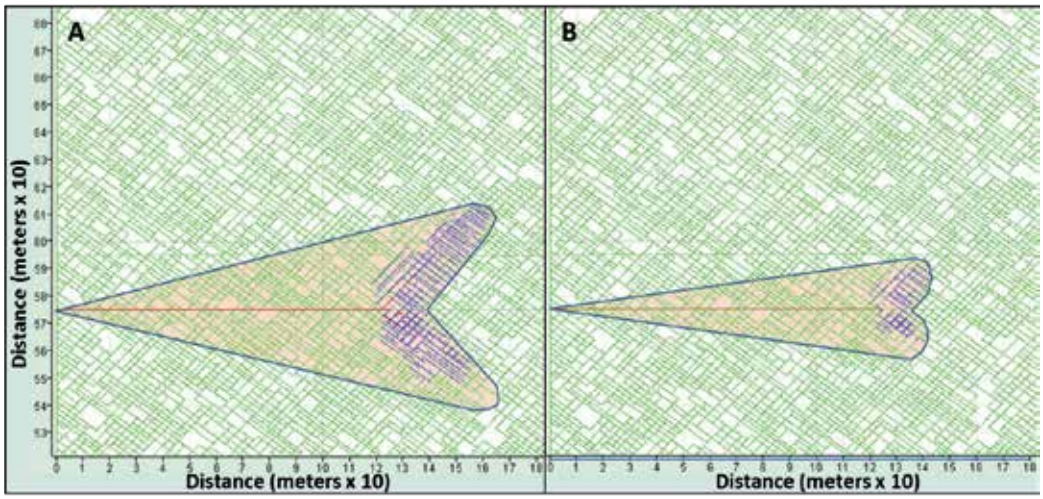

Figure 8. Cumulative natural fracture shear (shaded area) from simulations with the '145°' DFN. A) Shear for the 25° friction case with an area of 5250m2; and B) Shear for the 35° friction case with an area of 2490m2.

http://dx.doi.org/10.5772/56304

In summary, Figures 5 through 8 suggest the following:

- Natural fracture shear from the total stress change caused by the inflated hydraulic fracture travels with the tip of a growing hydraulic fracture (as reported in Nagel et al. 2011a and 2012a).
- The length of natural fractures being sheared increases significantly with length (Figure 7).
- The length of natural fractures being sheared is strongly a function of natural fracture friction angle.
- The area (and by default the volume) of formation sheared by a single fracture can also be significant (5740m^2 for the 15° case and 2220m^2 for the 25° case of the '180°' DFN and 5250m^2 for the 25° case and 2490 m^2 for the 35° case of the '145°' DFN).
- The orientation of the natural fractures significantly affects natural fracture shear for a given fracture friction (at 25° friction, more than twice the shear occurred for the '145°' DFN as for the '180°' DFN).

3.2. Natural fracture shear superimposing two hydraulic fractures

Figures 9 through 12 show the superimposed natural fracture shear areas from independent hydraulic fractures for multi-well completions with hydraulic fracture separations ranging from zero (equivalent to either the simultaneous or zipper-fracs) to 45m for both fracture friction cases.

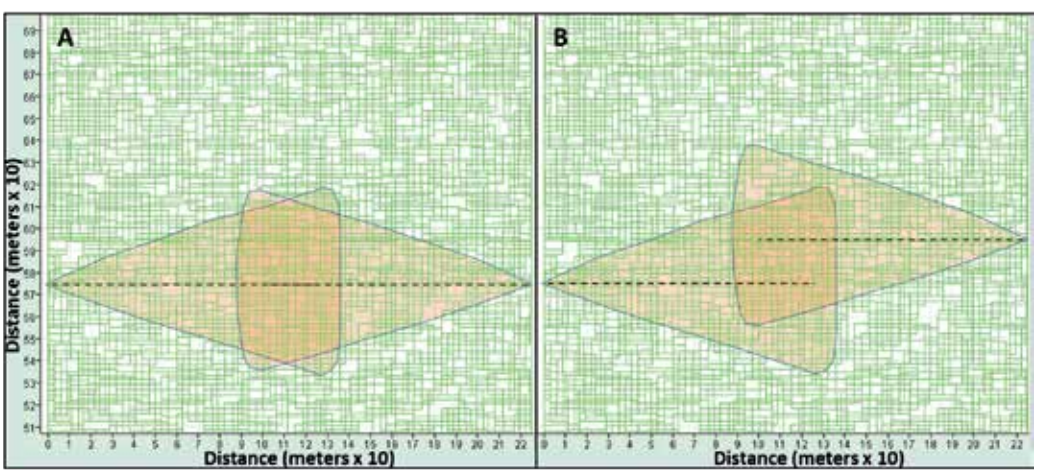

Figure 9. Superimposed natural fracture shear areas for the 15° friction case when Xf1 and Xf2 are both 125m in half-length. A) Zero separation between the two hydraulic fractures; and B) A 20m separation between fractures.

Within the figures, the regions of overlap would likely represent areas of 'wasted' hydraulic fracture shear (and, perhaps, a negative effect on production as excess shear will cause the natural fractures to reclose and even fill with gouge). Ideally, the best effect, assuming no

geomechanical interaction between the two hydraulic fractures, may be when the natural fracture shear regions just touch each other (not unlike the situation in Figure 12A).

Figures 9 and 10 suggest that overlapping the lengths of the hydraulic fracture (as proposed in the modified zipper-frac completion) creates large overlapping natural fracture shear areas for the 15° fracture friction case. Further, increasing the hydraulic fracture separation out to 45m still results in considerable overlap of the shear regions. In contrast, with the reduction in shear area due to the increase in natural fracture friction in the 25° friction case in Figures 11 and 12, the shear region overlap goes away at a 35m hydraulic fracture spacing, and for the 45m separation case an unsheared region (Figure 12, plot B) occurs between the hydraulic fractures.

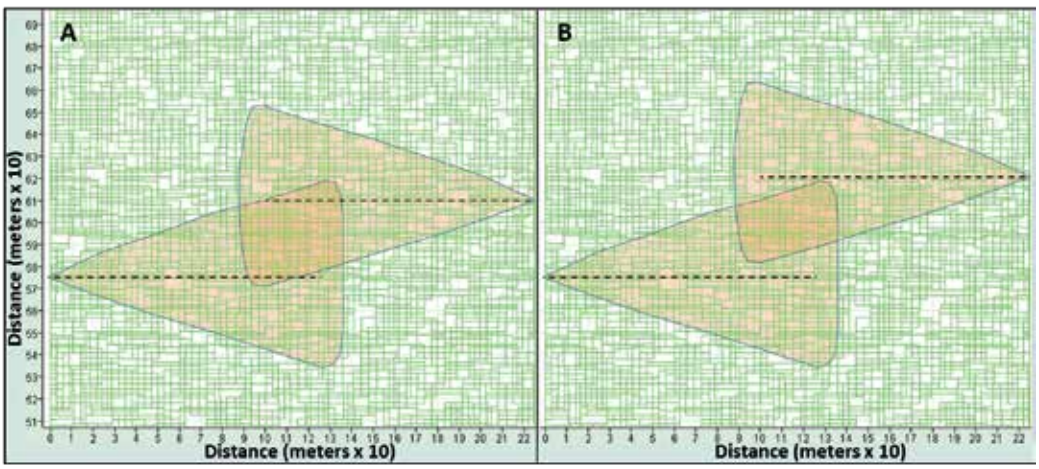

Figure 10. Superimposed natural fracture shear areas for the 15° friction case when Xf1 and Xf2 are both 125m in half-length. A) A 35m separation between the two hydraulic fractures; and B) A 45m separation between fractures.

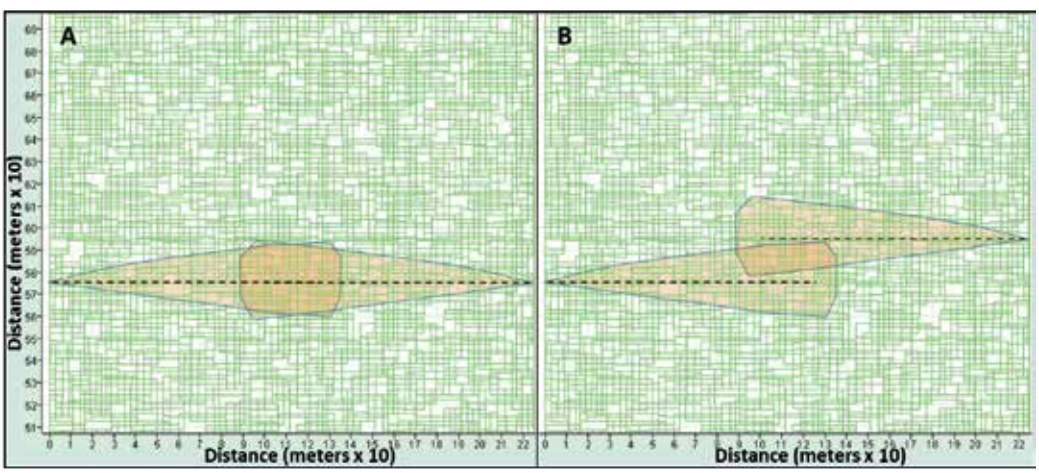

Figure 11. Superimposed natural fracture shear areas for the 25° friction case when Xf1 and Xf2 are both 125m in half-length. A) Zero separation between the two hydraulic fractures; and B) A 20m separation between fractures.

http://dx.doi.org/10.5772/56304

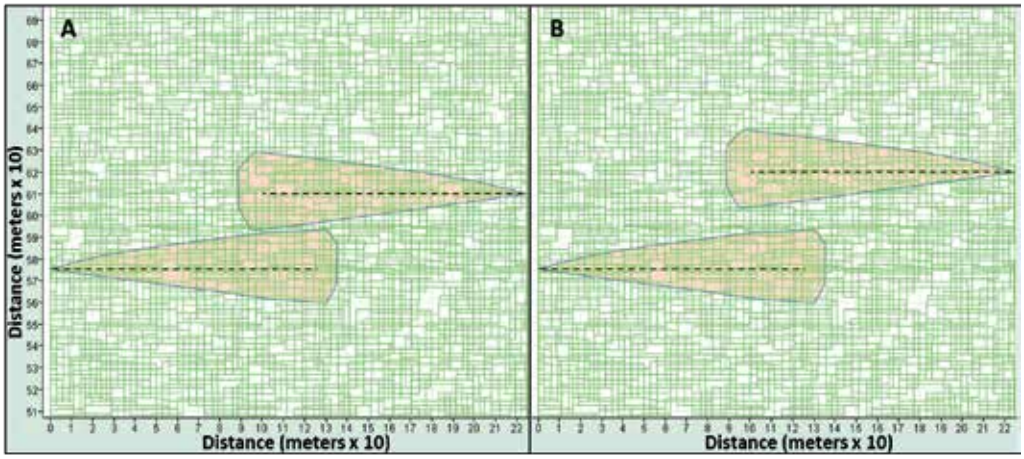

Figure 12. Superimposed natural fracture shear areas for the 25° friction case when Xf1 and Xf2 are both 125m in half-length. A) A 35m separation between the two hydraulic fractures; and B) A 45m separation between fractures.

3.3. Natural fracture shear from dual, competing hydraulic fractures

3.3.1. Shear results for the '145°' DFN and 20m hydraulic fracture separation

Figures 13 through 20 show the generation of natural fracture shear from combinations of the two hydraulic fractures Xf1 and Xf2 as a function of Xf2 length and natural fracture friction for the '145°' DFN with a hydraulic fracture separation of 20m. Plot A shows the sheared natural fractures in blue and open fractures in red; plot B shows the same data with an overlay of sheared natural fracture area (similar to Figure 8) as if hydraulic fractures Xf1 and Xf2 propagated independent of each other.

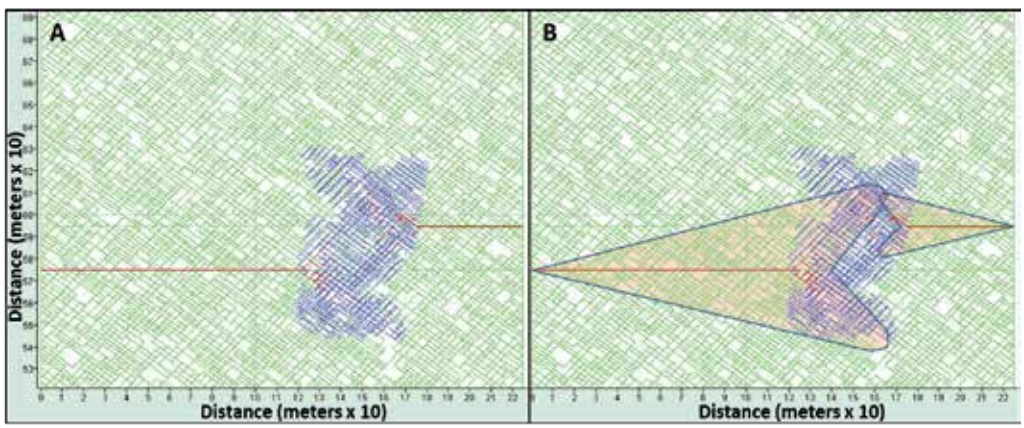

Figure 13. Natural fracture shear in blue from propagating hydraulic fractures Xf1 (from the left at 125m) and Xf2 (from the right at 50m) for a natural fracture friction of 25° and 20m hydraulic fracture separation. Red represents open fractures. A) Shear and open fractures only; and B) Shear and open fractures with overlay of shear area as if Xf1 and Xf2 propagated independently.

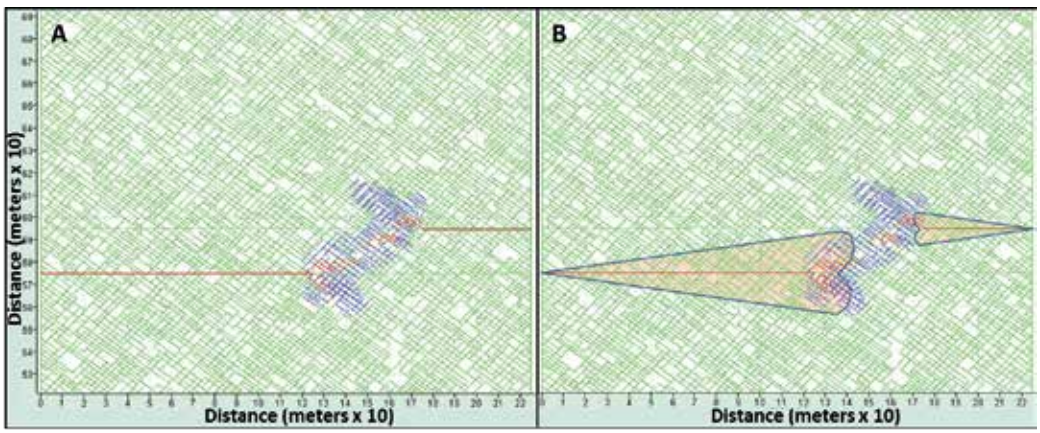

Figure 14. Natural fracture shear in blue from propagating hydraulic fractures Xf1 (from the left at 125m) and Xf2 (from the right at 50m) for a natural fracture friction of 35°.

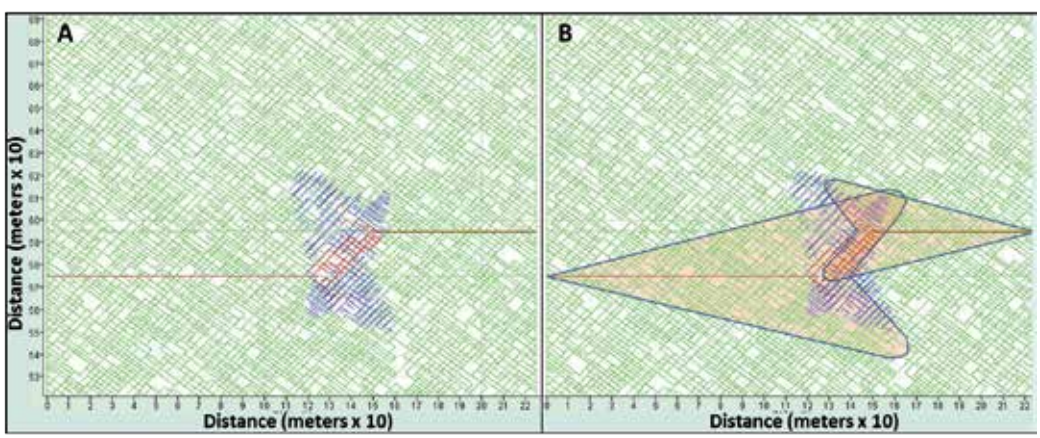

Figure 15. Natural fracture shear in blue from propagating hydraulic fractures Xf1 (from the left at 125m) and Xf2 (from the right at 75m) for a natural fracture friction of 25°.

http://dx.doi.org/10.5772/56304

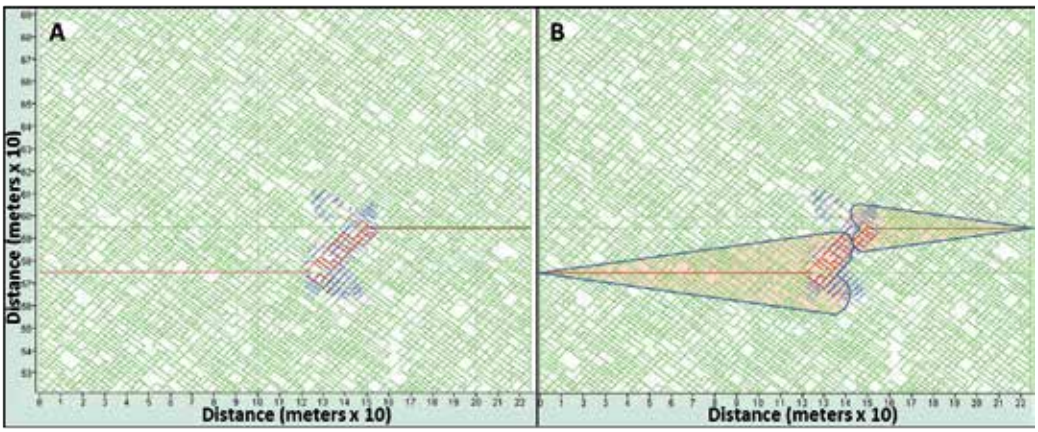

Figure 16. Natural fracture shear in blue from propagating hydraulic fractures Xf1 (from the left at 125m) and Xf2 (from the right at 75m) for a natural fracture friction of 35°.

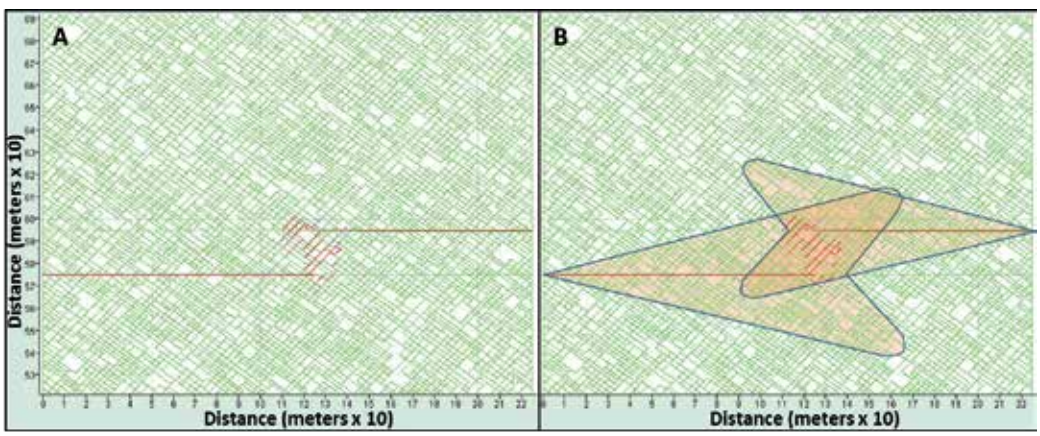

Figure 17. Natural fracture shear in blue from propagating hydraulic fractures Xf1 (from the left at 125m) and Xf2 (from the right at 100m) for a natural fracture friction of 25°.

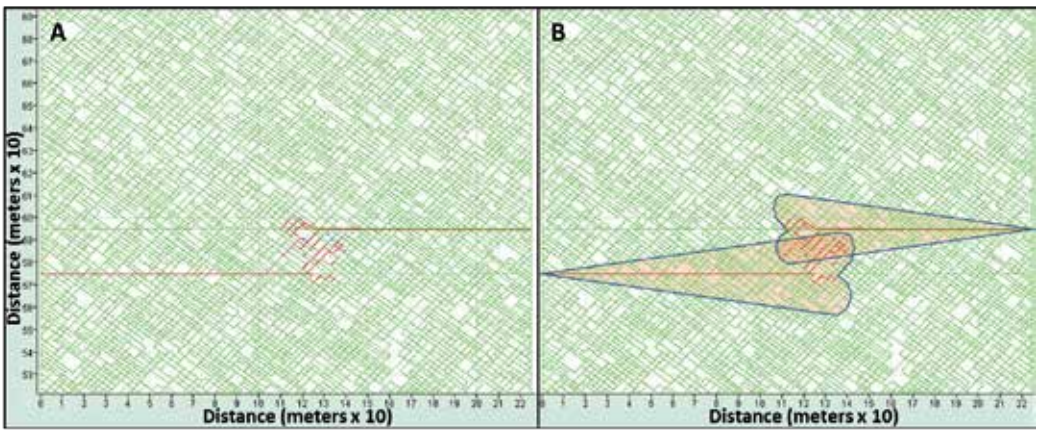

Figure 18. Natural fracture shear in blue from propagating hydraulic fractures Xf1 (from the left at 125m) and Xf2 (from the right at 100m) for a natural fracture friction of 35°.

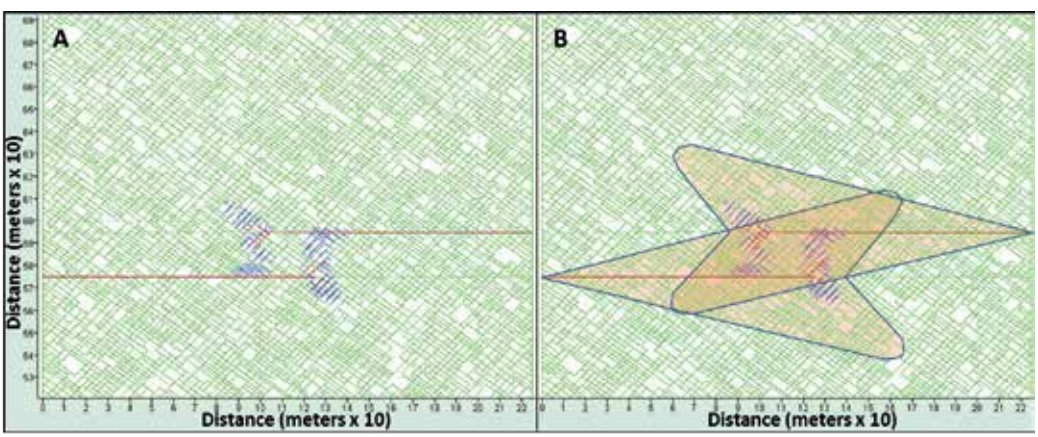

Figure 19. Natural fracture shear in blue from propagating hydraulic fractures Xf1 (from the left at 125m) and Xf2 (from the right at 125m) for a natural fracture friction of 25°.

http://dx.doi.org/10.5772/56304

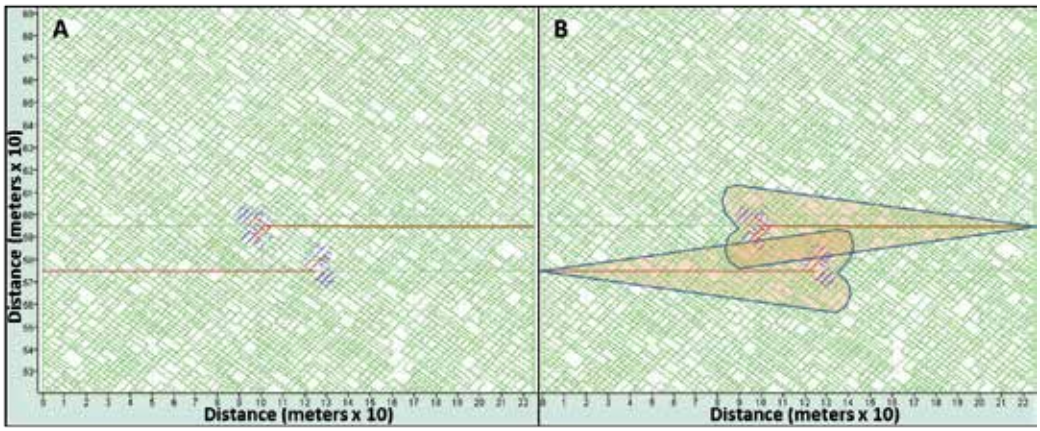

Figure 20. Natural fracture shear in blue from propagating hydraulic fractures Xf1 (from the left at 125m) and Xf2 (from the right at 125m) for a natural fracture friction of 35°.

3.3.2. Observations for the '145°' DFN and 20m separation simulations

The simulations were conducted such that hydraulic fracture Xf1 always had a fracture half-length of 125m and 'snapshots' were taken for hydraulic fracture Xf2 half-lengths of 50m, 75, 100m, and 125m. The simulated wellbores that Xf1 and Xf2 propagated from were set at 225m apart so that once Xf2 reached 100m or longer, it overlapped hydraulic fracture Xf1.

The significant observations from the simulation results include:

- For the 20m separation cases shown, the greatest 'extra' natural fracture shear (shear beyond what would have occurred from two independent hydraulic fractures) occurred when Xf2 was 50m in length. This was true for both natural fracture friction cases (Figures 13 and 14).
- As Xf2 grew beyond 50m in length, the 'extra' formation shear decreased and, most importantly, when Xf2 was 100m or 125m in length, there was a net loss of sheared natural fractures as compared to two independent hydraulic fractures.
- When Xf2 was 100m in length (so that the fracture tips from Xf1 and Xf2 just overlapped), the effect was a complete cancellation of natural fracture shear and a significant opening of natural fractures between Xf1 and Xf2 (likely allowing significant pressure communication) as shown in Figures 17 and 18.
- Once Xf2 exceeded 100m in length, natural fracture shear re-occurred, though it was significantly reduced (Figures 19 and 20). Note that in Figure 19 (natural fracture friction of 25°), the hydraulic fractures blunted the sheared fractures coming from the tip of the other hydraulic fracture acting as a form of release surface preventing transmission of shear on the other side of the hydraulic fracture.

3.3.3. Shear results for the '145°' DFN and other hydraulic fracture separations

Figures 21 to 24 show a comparison of natural fracture shear for hydraulic fracture separations of 20m, 35m, and 45m for both natural fracture friction cases for Xf2 lengths of 75m and 125m.

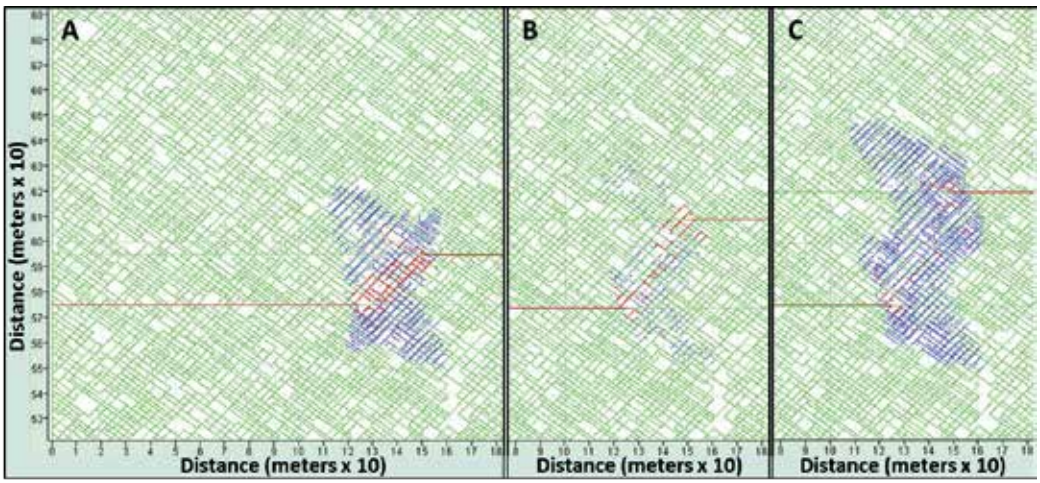

Figure 21. Natural fractures at shear as shown in blue for an Xf2 half-length of 75m and natural fracture friction of 25°. Red represents open fractures. A) A 20m hydraulic fracture separation; B) A 35m separation; and C) A 45m separation.

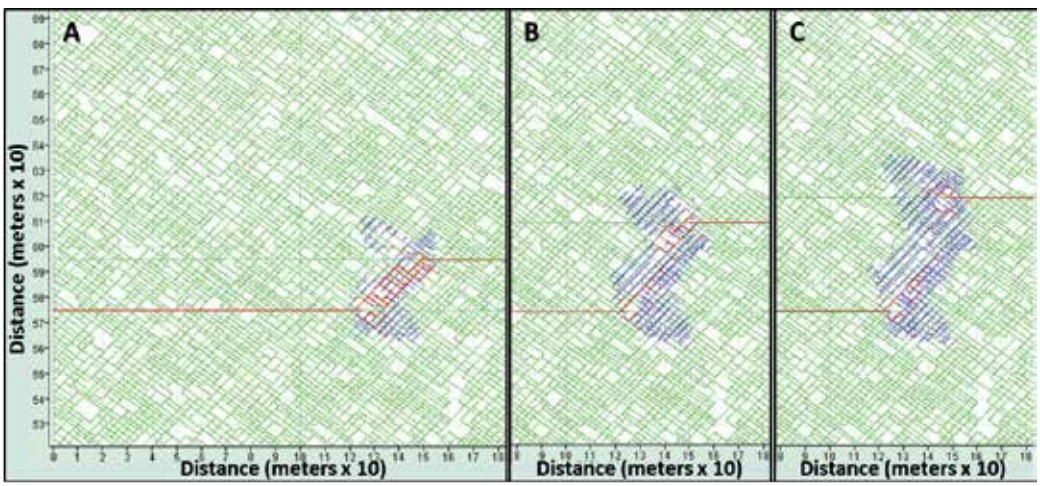

Figure 22. Natural fractures at shear as shown in blue for an Xf2 half-length of 75m and natural fracture friction of 35°. A) A 20m hydraulic fracture separation; B) A 35m separation; and C) A 45m separation.

http://dx.doi.org/10.5772/56304

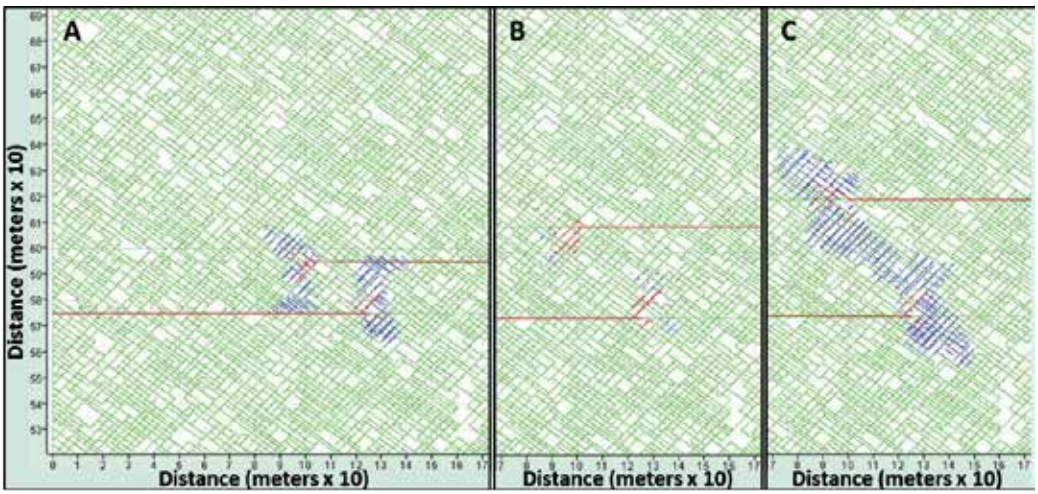

Figure 23. Natural fractures at shear as shown in blue for an Xf2 half-length of 125m and natural fracture friction of 25°. A) A 20m hydraulic fracture separation; B) A 35m separation; and C) A 45m separation

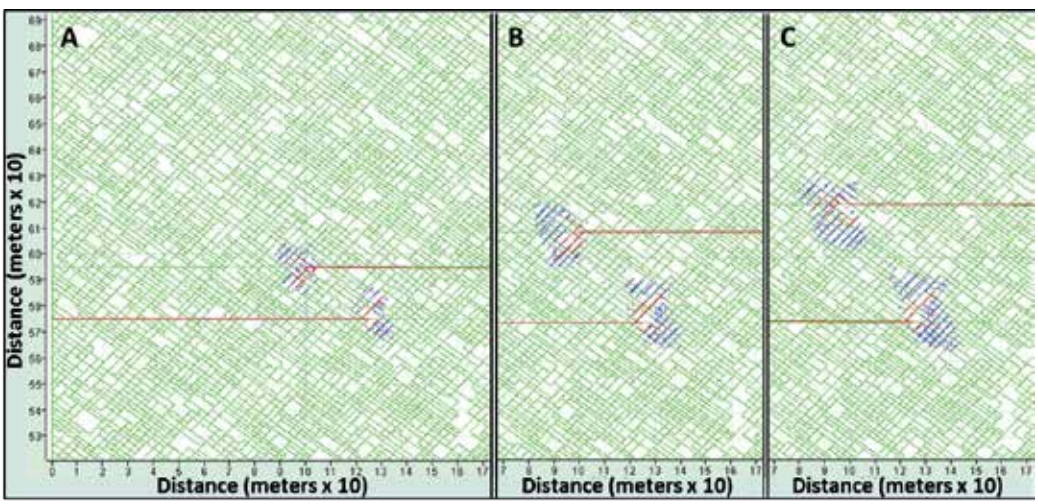

Figure 24. Natural fractures at shear as shown in blue for an Xf2 half-length of 125m and natural fracture friction of 35°. A) A 20m hydraulic fracture separation; B) A 35m separation; and C) A 45m separation.

Figure 25 presents a graph of the cumulative length of natural fracture shear for the 30 simulations with the '145°' DFN.

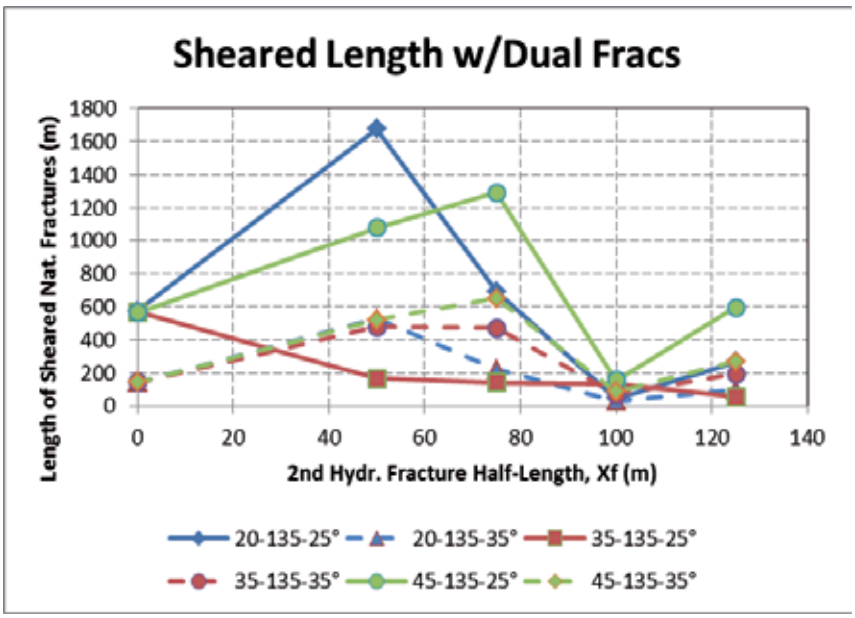

Figure 25. Graph of cumulative natural fracture shear length versus hydraulic fracture Xf2 half-length for separation cases 20m, 30m, and 45m for natural fracture friction of 25° and 35° for the '145°' DFN.

3.3.4. Observations for the '145°' DFN dual hydraulic fracture simulations

Within Figures 21 to 24, the simulation results for each of the three hydraulic fracture separation distances (20m, 35m, and 45m) are shown. Again, blue lines represent natural fractures at a shear condition at the moment the two hydraulic fractures are at their given half-length (125m for Xf1 and 75m or 125m for Xf2). Red lines represent open fractures (meaning there is no longer contact between the two sides of the fracture).

The significant observations from the simulation results include:

- Perhaps not surprisingly, the greatest total length of shear occurs for the 20m separation distance (at an Xf2 half-length of 50m); however, most interesting is that the total length of shear for the 45m separation distance is greater than that for the 35m separation distance. This suggests that natural fracture shear created between two hydraulic fracture tips is both a function of the separation distance and the orientation of the natural fractures.
- The simulation results suggest that the Xf2 half-length at which the maximum induced length of natural fracture shear occurs is related to the hydraulic fracture separation. For the 20m separation case, maximum shear occurred at Xf2 equal to 50m while for the 45m separation case, maximum shear occurred when the half-length of Xf2 was 75m.
- In all the cases, when the half-length of Xf2 was equal to 100m (so that the tips of Xf1 and Xf2 just overlapped), natural fracture shear was at a minimum.

http://dx.doi.org/10.5772/56304

- In all the cases, when the half-length of Xf2 grew to 125m, the cumulative length of natural fracture shear increased, but only modestly and significantly less than before the two hydraulic fractures overlapped. This suggests that overlapping hydraulic fractures do not enhance natural fracture shear but cause a net loss of shear relative to two independent hydraulic fractures.
- While for the 20m and 45m separation cases the effect of higher natural fracture friction was to significantly reduce the cumulative length of natural fracture shear (by 50% to 75%), for the 35m separation case the higher natural fracture friction resulted in greater cumulative natural fracture shear than the lower natural fracture friction case. While the full cause of this is not defined, a likely contributor is the ability of the rock mass in the low friction case to accommodate greater deformation without reaching the shear condition.

3.3.5. Shear results for the '180°' DFN and 20m hydraulic fracture separation

Figures 26 and 27 show the natural fracture shear (in blue) for Xf2 half-length cases of 50m, 75, 100m, and 125m for the '180°' DFN with a 20m separation distance and a natural fracture friction of 15°.

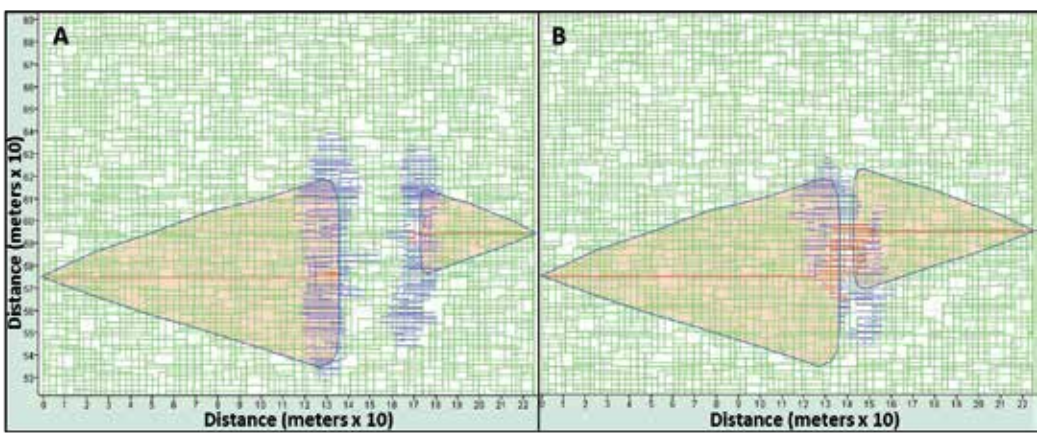

Figure 26. Natural fracture shear in blue from propagating hydraulic fractures Xf1 (from the left at 125m) and Xf2 (from the right) for a natural fracture friction of 15° and 20m hydraulic fracture separation. Red represents open fractures and shaded regions represent the expected shear area for two independent hydraulic fractures. A) Xf2 length equal to 50m; and B) Xf2 length equal to 75m.

Similar in fashion to Figures 13 to 20 for the '145°' DFN, Figures 26 and 27 show that there is an increase in natural fracture shear over two independent hydraulic fractures when Xf2 is less than about 75m. Further, when Xf2 exceeds a half-length of more than 75m (or, better, when the tip of Xf2 is within 25m of overlapping the tip of Xf1), then the result is a net loss of natural fracture shear over two independent hydraulic fractures.

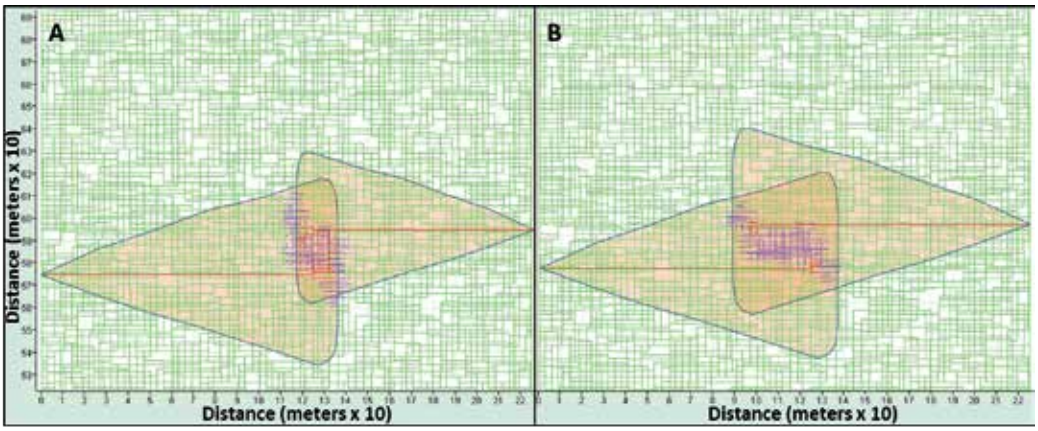

Figure 27. Natural fracture shear in blue from propagating hydraulic fractures Xf1 (from the left at 125m) and Xf2 (from the right) for a natural fracture friction of 15° and 20m hydraulic fracture separation. Red represents open fractures and shaded regions represent the expected shear area for two independent hydraulic fractures. A) Xf2 length equal to 100m; and B) Xf2 length equal to 125m.

Figures 28 to 31 show a comparison of natural fracture shear for hydraulic fracture separations of 20m, 35m, and 45m for both natural fracture friction cases (15° and 25°) for Xf2 lengths of 75m and 125m. Figure 32 shows a graph of the cumulative length of natural fracture shear versus Xf2 half-length for the 15° and 25° simulations (30 in total) for the '180°' DFN.

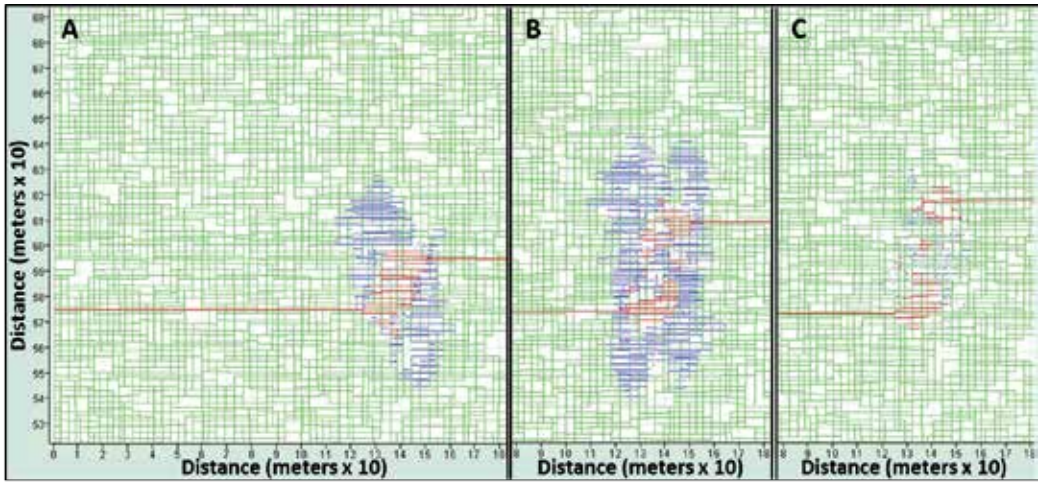

Figure 28. Natural fractures at shear (blue) for an Xf2 half-length of 75m and natural fracture friction of 15° for the '180°' DFN. Red represents open fractures. A) A 20m hydraulic fracture separation; B) A 35m separation; and C) A 45m separation.

http://dx.doi.org/10.5772/56304

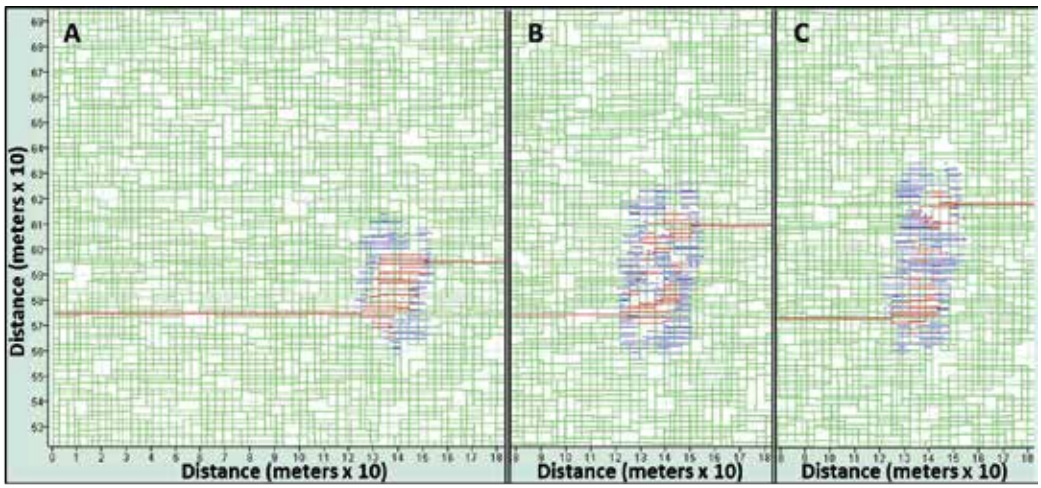

Figure 29. Natural fractures at shear (blue) for an Xf2 half-length of 75m and natural fracture friction of 25° for the '180°' DFN. Red represents open fractures. A) A 20m hydraulic fracture separation; B) A 35m separation; and C) A 45m separation.

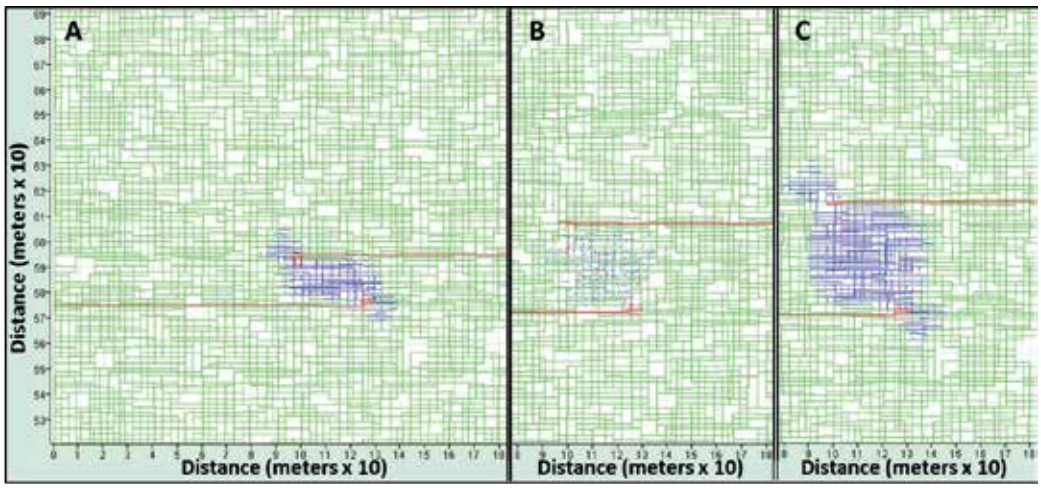

Figure 30. Natural fractures at shear (blue) for an Xf2 half-length of 125m and natural fracture friction of 15° for the '180°' DFN. Red represents open fractures. A) A 20m hydraulic fracture separation; B) A 35m separation; and C) A 45m separation.

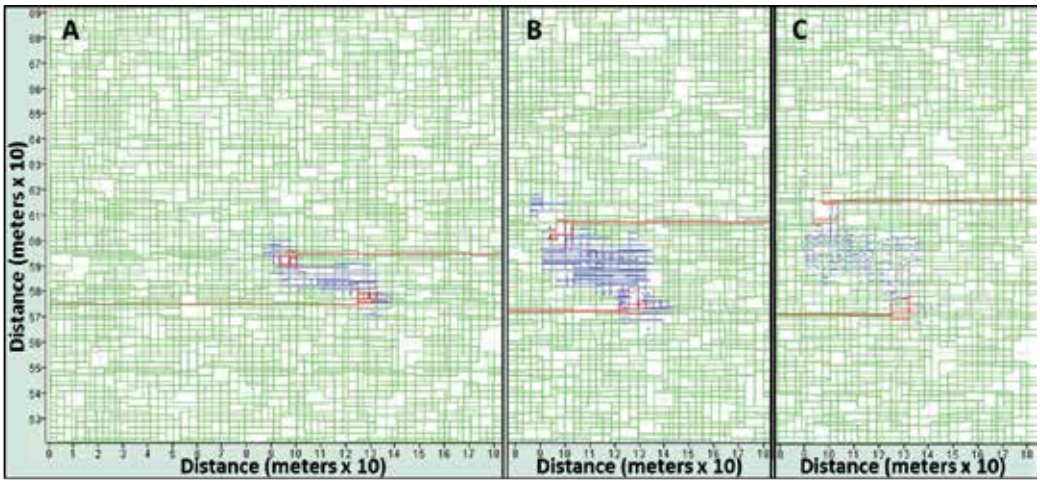

Figure 31. Natural fractures at shear (blue) for an Xf2 half-length of 125m and natural fracture friction of 25° for the '180°' DFN. Red represents open fractures. A) A 20m hydraulic fracture separation; B) A 35m separation; and C) A 45m separation.

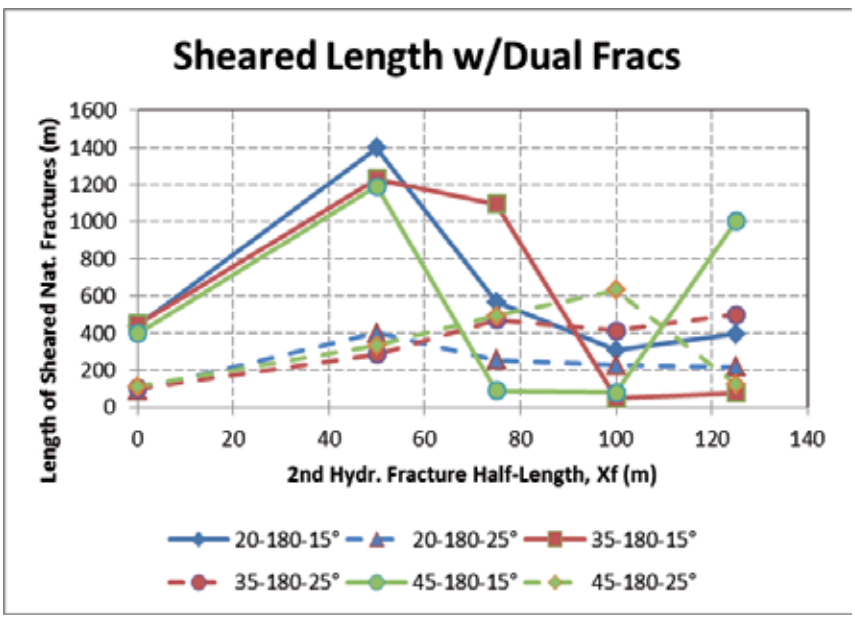

Figure 32. Graph of cumulative natural fracture shear length versus hydraulic fracture Xf2 half-length for separation cases 20m, 30m, and 45m for natural fracture friction of 15° and 25° for the '180°' DFN.

http://dx.doi.org/10.5772/56304

3.3.6. Observations for the '180°' DFN dual hydraulic fracture simulations

Within Figures 28 to 31, the simulation results for each of the three hydraulic fracture separation distances (20m, 35m, and 45m) are shown for the '180°' DFN. Again, blue lines represent natural fractures at a shear condition at the moment the two hydraulic fractures are at their given half-length (125m for Xf1 and 75m or 125m for Xf2). Red lines represent open fractures (meaning there is no longer contact between the two sides of the fracture).

The significant observations from the simulation results include:

- As with the simulations for the '145°' DFN, the higher friction cases generally resulted in less total length of sheared natural fractures than the lower friction cases; however, when Xf2 was 100m (so the tips of Xf1 and Xf2 just overlapped), the higher friction cases generally had more sheared length of natural fractures.
- For all three separation cases, the greatest total length of natural fracture shear occurred when the Xf2 half-length was 50m. As the separation distance increased between the hydraulic fractures, the total length of natural fracture shear became increasing sensitive to Xf2 half-length. For the 45m separation case, the total length of natural fracture shear decreased by more than 90% between an Xf2 half-length of 50m and 75m.
- For the '180°' DFN, the cumulative length of natural fracture shear was not as sensitive at an Xf2 half-length of 100m as was the '145°' DFN. This, again, shows that the orientation of the natural fractures is important in creating natural fracture shear when two hydraulic fractures influence each other.
- As with the '145°' DFN, the amount of open fractures in the '180°' DFN cases appeared to influence the amount of natural fracture shear. Further, open natural fractures will be more conductive and, likely, allow pressure communication between hydraulic fractures potentially causing screenout events.

3.3.7. Shear results for the '180°' DFN and altered in-situ stress

Recall from Table 2 that a number of simulations were conducted with the '180°' DFN model wherein the in-situ stress field was altered. As shown in Table 2, the vertical stress Sv, maximum horizontal stress SHmax, and pore pressure were kept constant and the minimum horizontal stress was increased by 5.6 MPa, which resulted in near-isotropic horizontal stress conditions. Figures 33 and 34 show the sheared natural fractures for the 20m separation case and natural fracture friction of 15° and 25° and with the revise in-situ stress. Figure 35 shows a graph of the length of natural fracture shear for the 25° simulations from and Table 6 and initial and revised stresses.

3.3.8. Observations for the '180°' DFN dual fracture simulations with revised in-situ stress

The significant observations from the simulation of the change in in-situ stress include:

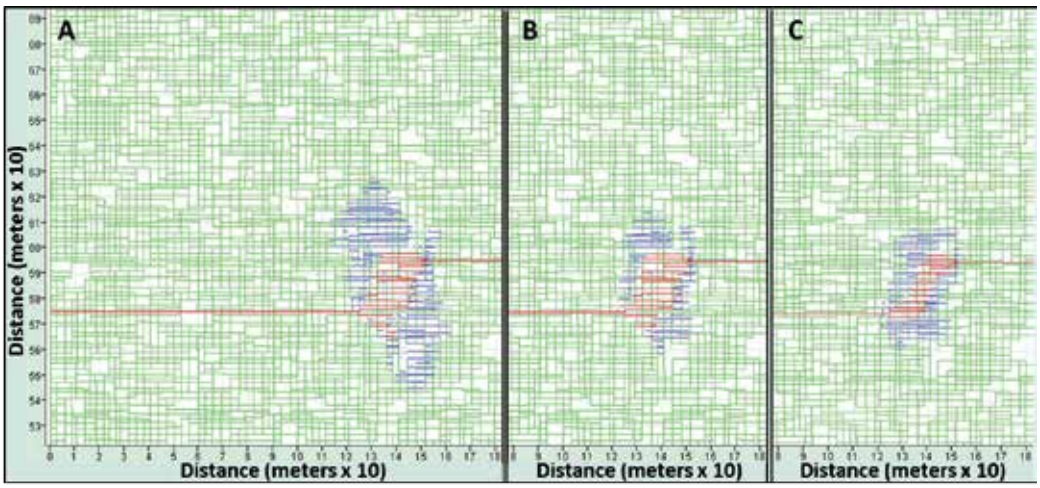

Figure 33. Natural fractures at shear (blue) for an Xf2 half-length of 75m for the '180°' DFN at a 20m separation. Red represents open fractures. A) 15° natural fracture friction; B) 25° fracture friction; and C) 25° fracture friction and revised in-situ stress.

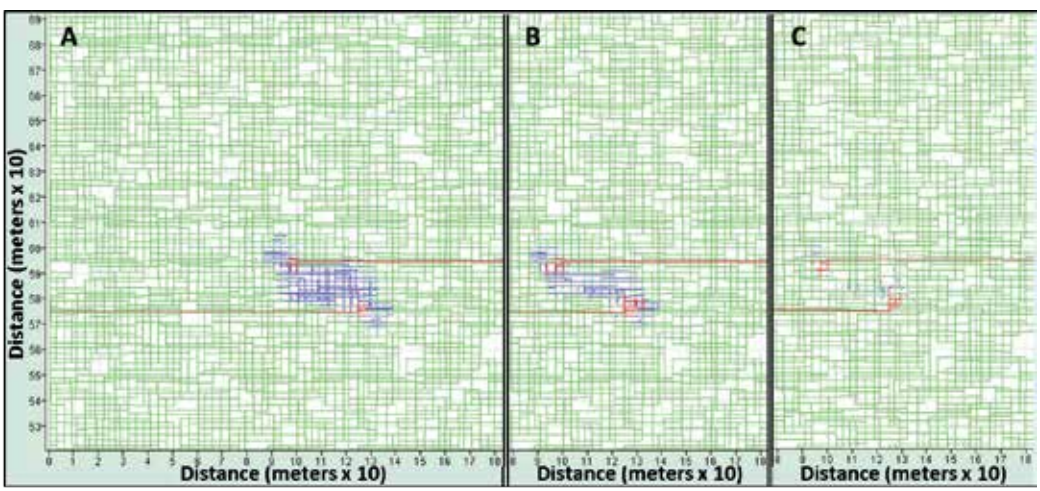

Figure 34. Natural fractures at shear (blue) for an Xf2 half-length of 125m for the '180°' DFN at a 20m separation. Red represents open fractures. A) 15° natural fracture friction; B) 25° fracture friction; and C) 25° fracture friction and revised in-situ stress.

http://dx.doi.org/10.5772/56304

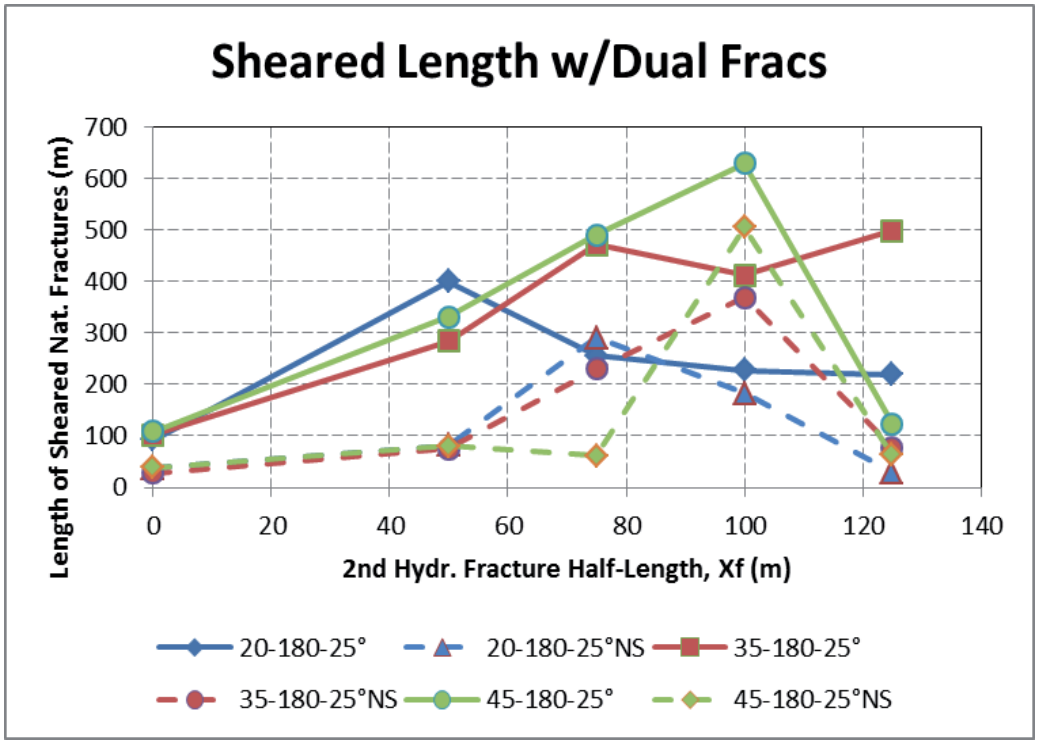

Figure 35. Graph of natural fracture shear length versus hydraulic fracture Xf2 half-length for separation cases 20m, 30m, and 45m for natural fracture friction of 25° for the '180°' DFN with the initial and revised in-situ stress (see Table 2).

- As shown in Figure 35, the maximum cumulative length of natural fracture shear occurred at the 45m separation distance for either in-situ stress case.
- Clearly, moving towards more of an isotropic in-situ horizontal stress reduced the total length of natural fracture shear. Furthermore, the overall behavior also changed such that the maximum cumulative length of natural fracture shear occurred at 100m (the point of tip-to-tip overlap) for the near-isotropic stress case.
- Particularly at larger separation distances (the 45m separation case), the isotropic in-situ stress appeared to make the two hydraulic fractures cancel the shear from each other until the tips of Xf1 and Xf2 were close or overlapped.
- Perhaps even more so than the initial stress cases, the cumulative length of natural fracture shear when the tips of Xf1 and Xf2 overlapped (e.g., the 125m Xf2 case) dropped to near-zero for the revised stress simulations. This suggests that, even with a revised in-situ stress field, overlapping the tips of hydraulic fractures from parallel wellbores creates a net loss of natural fracture shear.

4. Discussion

The goal of the effort was to quantitatively consider the change in natural fracture shear (shear being analogous with microseismicity generation and the potential stimulation of the natural fractures providing increased production from the hydraulic fracture) for multi-well completions. It is commonly believed that by configuring the geometry and injection behavior from parallel wellbores (e.g., simultaneous fracturing, zipper-fracs, and modified zipper-fracs), shear of the natural fractures can be enhanced (thereby increasing production).

During the evaluations presented in this paper, the following parameter effects were considered:

1. Fracture network orientation (i.e., the '180°' DFN and the '145°' DFN);
2. Natural fracture friction angle (15° and 25° for the '180°' DFN and 25° and 35° for the '145°' DFN);
3. Hydraulic fracture separation (offset between injection points) from 20m to 45m;
4. Hydraulic fracture half-length from the second wellbore (Xf2 helf-lengths of 50m to 125m); and
5. In-situ stress (from a horizontal stress ratio – SHmax/Shmin - of 1.18 to a ratio of 1.03).

4.1. Observations on the influence of fracture network

As shown in Figures 6 and 8, the natural fracture shear pattern coming off the tip of a propagating hydraulic fracture depends upon the orientation and nature of the natural fracture system. For the '180°' DFN, natural fracture shear extended a bit beyond the hydraulic fracture tip, but mainly lay in a symmetrical pattern perpendicular to the direction of hydraulic fracture propagation. In contrast, for the '145°' DFN, the natural fracture shear pattern was asymmetric and lead the tip of the propagating hydraulic fracture. Clearly as observed in previous publications (Nagel et al. 2011a), interpreting microseismic event locations cannot be done without consideration of the general orientation of the natural fracture pattern.

The natural fracture pattern also plays a role in the amount of natural fracture shear (and, by analogy, the number of microseismic events). For the same natural fracture friction (and same in-situ stress), the total area of natural fracture shear for the '180°' DFN was only 42% of that for the '145°' DFN (2220m^2 versus 5250m^2). However, as shown in the graphs in Figures 25 and 32, the overall trends in the cumulative length of natural fracture shear from dual hydraulic fractures was similar (with the exception of the 35m spacing for the '145°' DFN in which natural fracture shear was very low).

4.2. Observations on the influence of natural fracture friction

As evident from the figures of natural fracture shear and the quantitative results in Figures 25 and 32, natural fracture friction plays a significant role in determining the amount of natural fracture shear (and, by analogy, the number of microseismic events). The influence of natural

http://dx.doi.org/10.5772/56304

fracture friction also depends upon the underlying natural fracture pattern (and stress ratio). The area of shear generated for the '180°' DFN at a friction angle of 15° was nearly equal to the area of natural fracture shear for the '145°' DFN at a friction angle of 25° (5740m^2 versus 5250m^2).

Less so for the '145°' DFN and more so for the '180°' DFN, the higher fracture friction tended to push the point of maximum total length of natural fracture shear towards longer Xf2 half-lengths; however, these longer half-lengths also represented conditions when there was a net loss of natural fracture shear for two dual hydraulic fractures over two equivalent independent hydraulic fractures.

4.3. Observations on the influence of hydraulic fracture separation distance

Figures 25 and 32 suggest that hydraulic fracture separation did not significantly affect the maximum total length of natural fracture shear (more so for the '180°' DFN and less so for the '145°' DFN). However, the influence of separation spacing was more apparent when the Xf2 half-length was 100m or longer.

Though Figures 25 and 32 may suggest a somewhat limited influence of hydraulic fracture spacing, this is clearly not the whole picture. As shown in Figures 9 through 12 in particular, and somewhat in Figures 13 through 20, the critical issues for hydraulic fracture separation are to: 1) shear as much total formation as possible; and 2) not cause a net loss of natural fracture shear by placing hydraulic fractures too close. Figure 10 shows that at a 45m hydraulic fracture separation distance (for dual, 125m-long hydraulic fractures and a natural fracture friction angle of 15°) the shear area from the two hydraulic fractures still overlapped (when the hydraulic fractures act independently). In contrast, Figure 12 shows that a 45m separation distance may be too much when natural fracture friction angle is 25°.

4.4. Observations on the influence of hydraulic fracture Xf2 half-length

The simulation results (especially Figures 25 and 32) show that the amount of natural fracture shear is significantly influenced by the half-length of the Xf2 hydraulic fracture in a dual fracture configuration. The overall trend of the results is that keeping the half-length of Xf2 small enough to prevent the tip of Xf2 from getting closer than 25m to the tip of Xf1 (that is, no overlap of the hydraulic fractures) creates the maximum total length of natural fracture shear. Further, as shown in Figures 9 through 12, keeping the half-length of Xf2 small enough may also cause a net increase in natural fracture shear (over that from two independent hydraulic fractures), which is the goal of a dual hydraulic fracture configuration.

5. Conclusions

- As natural fracture orientation (relative to the orientation of a hydraulic fracture) significantly influences the amount and location of natural fracture shear, multi-well completion

optimization (wherein the goal is to maximize natural fracture shear, i.e., maximize 'complexity') requires the evaluation and consideration of natural fracture orientation.

- As natural fracture friction controls the depth and amount of natural fracture shear, multi-well completion optimization requires the evaluation and consideration of natural fracture friction properties.
- The optimum hydraulic fracture separation distance for multi-well completions (i.e, the separation of hydraulic fractures along their respective wellbores) must be determined in consideration of natural fracture properties (e.g., orientation and friction properties) and the in-situ stress ratio.
- For multi-well completion schemes, the design length of the second hydraulic fracture (Xf2) should be kept less than the point of overlap with the first hydraulic fracture (Xf1) and be optimized in conjunction with the hydraulic fracture separation distance.
- Overall, the simulation results presented suggest that there is the potential for only modest improvements in stimulation complexity from the modified zipper-frac completion scheme while the potential for well-to-well communication (and possible screenout conditions) increases.

Author details

N. Nagel, F. Zhang, M. Sanchez-Nagel and B. Lee

*Address all correspondence to: nnagel@itascahouston.com

Itasca Houston, Inc., USA

References

[1] Agarwal, K, Mayerhofer, M. J, & Warpinski, N. R. (2012). Impact of Geomechanics on Microseismicity", Paper SPE 152835 presented at the SPE/EAGE European Unconventional Resources Conference and Exhibition, Vienna, Austria, March., 20-22.

[2] Clover Global SolutionsLP, (2012). The Seven Major U.S. Shale Plays", http://c1wsolutions.wordpress.com/2012/09/13/the-seven-major-u-s-shale-plays

[3] Ground Water Protection Council and ALL Consulting(2009). Modern Shale Gas Development in the United States: A Primer", prepared for the US DOE, Office of Fossil Energy, DE-FGNT15444., 26-04.

[4] King, G. E. (2010). Thirty Years of Gas Shale Fracturing: What Have We Learned?", Paper SPE 133456 presented at the SPE Annual Technical Conference and Exhibition, Florence, Italy, September., 19-22.

[5] Nagel, N, & Sanchez-nagel, M. (2011). Stress Shadowing and Microseismic Events: A Numerical Evaluation", Paper SPE 147363 presented at the SPE Annual Technical Conference and Exhibition, Denver, Colorado, USA, 30 October-2 November.

[6] Nagel, N, Damjanac, B, Garcia, X, & Sanchez-nagel, M. (2011b). Discrete Element Hydraulic Fracture Modeling- Evaluating Changes in Natural Fracture Aperture and Transmissivity", Paper SPE 148957 presented at the Canadian Unconventional Resources Conference, Calgary, Alberta, Canada, November., 15-17.

[7] Nagel, N, Gil, I, Sanchez-nagel, M, & Damjanac, B. (2011a). Simulating Hydraulic Fracturing in Real Fractured Rock- Overcoming the Limits of Pseudo3D Models", Paper SPE 140480 presented at the SPE Hydraulic Fracturing Technology Conference and Exhibition, The Woodlands, Texas, USA, January., 24-26.

[8] Nagel, N, Sanchez-nagel, M, & Lee, B. T. (2012a). Gas Shale Hydraulic Fracturing: A Numerical Evaluation of the Effect of Geomechanical Parameters", Paper SPE 152192 presented at the SPE Hydraulic Fracturing Technology Conference and Exhibition, The Woodlands, Texas, USA, February., 6-8.

[9] Nagel, N. B, Garcia, X, Lee, B, & Sanchez-nagel, M. (2012d). Hydraulic Fracturing Optimization for Unconventional Reservoirs- The Critical Role of the Mechanical Properties of the Natural Fracture Network", Paper SPE 161934 presented at the SPE Canadian Unconventional Resources Conference, Calgary, Alberta, Canada, 30 October- 1 November.

[10] Nagel, N. B, Sanchez-nagel, M, Zhang, F, Garcia, X, & Lee, B. (2013). Coupled Numerical Evaluations of the Geomechanical Interactions Between a Hydrualic Fracture Stimulation and a Natural Fracture System in Shale Formations", Rock Mechanics and Rock Engineering, pending publication.

[11] Nagel, N. B, Sanchez-nagel, M, Garcia, X, & Lee, B. (2012b). A Numerical Evaluation of the Geomechanical Interactions Between a Hydraulic Fracture Stimulation and a Natural Fracture System", ARMA presented at the 46th Rock Mechanics / Geomechanics Symposium, Chicago, Illinois, 24-27 June., 12-287.

[12] Nagel, N. B, Sanchez-nagel, M, Garcia, X, & Lee, B. SRV": A Numerical Investigation of "Wet" vs. "Dry" Microseismicity During Hydraulic Fracturing", Paper SPE 159791 presented the SPE Annual Technical Conference and Exhibition held in San Antonio, Texas, USA, October., 8-10.

[13] Sneddon, I. N. (1946). The Distribution of Stress in the Neighbourhood of a Crack in an Elastic Solid", Proc. R. Soc. London, Ser. A. , 195, 229-260.

[14] U.S. Energy Information Administration, 2012, "Annual Energy Outlook 2012 Early Release Overview", U.S. Dept. of Energy, Washington D.C., USA, www.eia.gov

[15] U.S. Energy Information Administration, 2013, "Annual Energy Outlook 2013 Early Release Overview", U.S. Dept. of Energy, Washington D.C., USA, www.eia.gov

Section 8

Flow Paths and Flow Networks

Chapter 26

Modeling of Proppant Permeability and Inertial Factor for Fluid Flow Through Packed Columns

Bruce R. Meyer, Lucas W. Bazan and Doug Walls

Additional information is available at the end of the chapter

http://dx.doi.org/10.5772/56299

Abstract

Standard industry testing procedures provide proppant quality control and methods to determine long term reference conductivity for proppants under laboratory conditions. However, test methods often lack repeatable results. Additionally, the testing procedures are not designed to account for fundamental parameters (e.g., proppant diameter, porosity, wall effects, multi-phase/non-Darcy effects, proppant and gel damage) that greatly reduce absolute proppant bed conductivity under realistic flowing conditions.

A constitutive model for permeability and inertial factor for flow through packed columns has been formulated from fundamental principles. This work provides a detailed deterministic proppant permeability correlation and defines a methodology to help explain why different proppant types behave differently under stress. The theory also characterizes the origin of inertial, or non-Darcy flow, based on a unique approach formulated from the extended Bernoulli equation based on minor losses. The physical model provides insight into the dominant parameters affecting the pressure drop in a proppant pack and improves our understanding of fluid flow and transport phenomena in porous media.

The fundamental solution for flow through packed columns can be characterized by the sum of viscous (Blake-Kozeny) and inertial forces (Burke-Plummer) in Ergun's equation. Coupling Ergun's equation with the Forchheimer equation results in a deterministic set of equations that describe the fracture permeability and inertial factor as functions of the proppant diameter, pack porosity, sphericity, and fracture width. Plotting the dimensionless permeability, (k/d_p^2), versus the characteristic proppant porosity parameter, Ω, is a very useful diagnostic tool that can indicate: 1) sphericity, 2) channeling, 3) crushing, 4) non-uniform sphere size distribution, 5) embedment and 6) deviation of the friction multiplier λ_m from Ergun's equation.

The dimensionless experimental proppant permeability data can be plotted as a linear function of dimensionless porosity with large deviations from these equations signifying poor or inconsistent experimental results or inadequate proppant characterization. The formulated permeability and non-Darcy equations provide the foundation for a quantitative (including quality control of the test) and qualitative analyses for determining fracture permeability and the inertial factor based on the physical properties of the proppant pack.

1. Introduction

Hydraulic fracturing has been the major and relatively inexpensive stimulation method used for enhanced oil and gas recovery in the petroleum industry since 1949. The primary goal of a hydraulic fracture treatment is to create a highly conductive flowpath for hydrocarbon production. Fracture conductivity is defined as the product of the packed bed width and permeability. An ideal fracture would possess infinite conductivity. However, producing proppant packs have finite permeability and conductivity. Proppant beds are also subjected to damage and conductivity degradation over time including proppant embedment, formation spalling, temperature degradation, non-Darcy flow, multiphase flow, non-uniform proppant distribution, cyclic stress, gel damage, fines migration, and other effects (Palisch *et al*., 2007).

The American Petroleum Institute (API) developed conductivity testing procedures outlined in API RP-61 to provide a methodology for consistent and repeatable results. The testing conditions include using the Cooke Conductivity Cell with steel pistons loaded at 2 lb/ft^2 at ambient temperature. The stress measurements are maintained for 15 minutes with 2% KCl fluid pumped at a rate of 2 ml/min. An industry consortium proposed changes to API RP-61 to replace the steel pistons with Ohio Sandstone, increase the testing temperature to 150 °F or 250 °F and maintain the stress for 50 hours. The modified API RP-61 is referred to as "long-term" conductivity, is accepted as the standard testing procedure for proppant, and has been adopted by the International Organization for Standardization (ISO) as ISO 13503-5. The original API RP-61 method is referred to as "short-term" conductivity testing. These testing procedures provide proppant conductivity under laminar (baseline or reference) conditions but fail to predict realistic fracture conductivity under flowing conditions because the tests do not account for the permeability reduction because of proppant pack damage mechanisms. There is tremendous superficial velocity inside a producing hydraulic fracture resulting in significant energy loss from the kinetic and viscous energy losses and hydrocarbon inertial effects. The constitutive parameters determining the pressure losses are the rate of fluid flow, viscosity and density of the fluid, size, shape, packing orientation and surface of the proppant. In petroleum engineering for a single phase fluid, the energy loss is typically described by a form of the Forchheimer equation (Eq. A. 20) as a sum of the Darcy and non-Darcy pressure drops

$$-\frac{dp}{dx} = \frac{\mu}{k}\upsilon + \beta\rho\upsilon^2 \tag{1}$$

http://dx.doi.org/10.5772/56299

where the first term on the right hand side of this equation represents the viscous effects and the second term the inertial or minor loss effects. Multiphase fluid interaction (gas-condensate, oil-water, etc.) causes pressure losses as multiple viscosities move through the proppant pack at different velocities (fluid mobility). The non-Darcy beta factor, β , is a material property of proppant that quantifies the inertial or minor losses as a result of fluid contraction and expansion. The greater the inertial losses, the greater the beta coefficient which increases the total pressure loss in the proppant pack. The effects of the beta coefficient can be reduced by increasing the porosity and permeability of the proppant pack, reducing the mesh distribution, and by using more spherical proppant with lower surface friction. Proppant crush tests are one method to determine some of these physical proppant parameters under in-situ conditions.

Standardized crush test procedures are outlined in API RP-56, RP-58 and RP-60 and are summarized in ISO 13503-2. The intent of these tests is to provide a comparison of the physical characteristics of various proppants including crush test results. Again, there are limitations of the testing methodology that do not simulate actual conditions within a producing fracture. However, the actual testing methods, specifically the loading of the cell, can be even more immediately problematic to results. Results from eleven different companies testing a common sample of 16/30 Brown Sand indicate varying test results between companies as high as 25% (Palisch *et al*., 2009).

This work provides a detailed deterministic proppant permeability correlation and presents a methodology to help explain why different proppant types behave differently under stress. The governing equations for flow through pack columns are formulated in Appendix A. Derivation of the theoretical fracture permeability and inertial coefficient, β , are also given in Appendix A.

2. Pressure loss equations for flow through packed columns

This section summarizes the equations for viscous and inertial flow in packed columns and presents a correlation model for fracture permeability. The flow through packed columns may be characterized as the sum of frictional (viscous) and inertial (minor losses) forces. The governing pressure loss equation from Eq. A.18

$$-\frac{dp}{dx}=\frac{72\lambda_m\left(1-\phi\right)^2\mu\upsilon}{\phi^3 d_p^2}+\frac{3}{2}f_0\frac{1-\phi}{\phi^3}\frac{\rho\upsilon^2}{2d_p} \tag{2}$$

where from experimental data λ_m=25/12 and f_0=7/3 . Viscous forces dominate laminar flow regimes while kinetic forces dominate inertial flow. Ergun developed his famous equation for the total pressure loss in packed columns for all flow regimes by simply adding the Blake-Kozeny equation for viscous dissipation and the Burke-Plummer equation for inertial losses. Placing Eq. 2 in terms of dimensionless groups we have (see Eq. A.19)

$$-\left(\frac{dp}{dx}\frac{d_p}{\rho\upsilon^2}\right)\left(\frac{\phi^3}{1-\phi}\right)=\frac{150(1-\phi)}{\mathrm{Re}}+\frac{7}{4} \tag{3}$$

This is the Ergun equation (see Bird 1960) where $\mathrm{Re}=\rho\upsilon d_p/\mu$, $\lambda_m=25/12$ and $f_0=7/3$ have been substituted. To account for proppant sphericity, the particle diameter in the above equations can be replaced by (Φd_p). Figure 1 shows the general behavior of the Ergun equation on a log-log plot with the Blake-Kozeny and Burke-Plummer equations for reference.

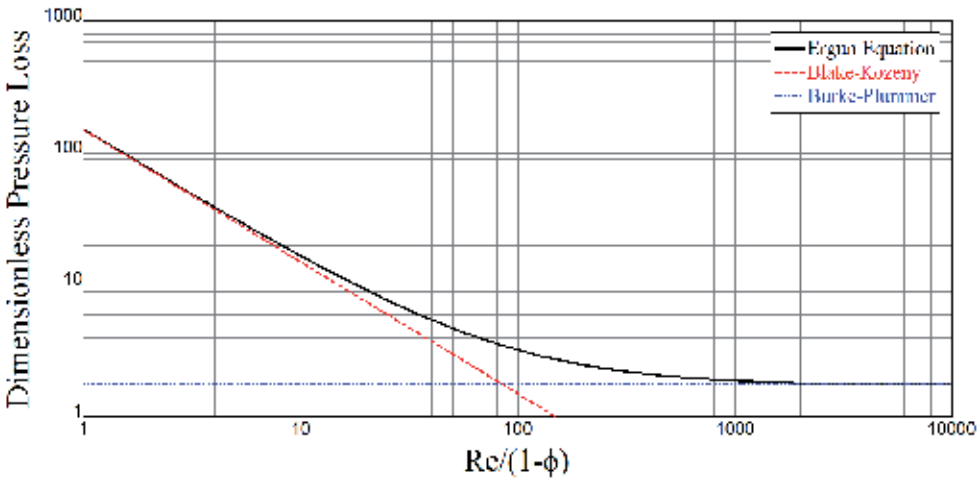

Figure 1. The Ergun equation with the Blake-Kozeny and Burke-Plummer equations.

Rearranging the Forchheimer equation (Eq. 1) into dimensionless groups (see Eq. A.21) we find

$$\left(-dp/dx\right)\Big/\beta\rho\upsilon^2=1/\mathrm{Re}_{\beta k}+1 \tag{4}$$

where $\mathrm{Re}_{\beta k}=\rho\upsilon\beta k/\mu$. Multiplying Eq. 4 by $7/4$, replacing $\mathrm{Re}_{\beta k}$ with Re , and β and k in terms of the proppant diameter and porosity (see Eq. A.24) one can show that it is identical to Ergun's equation (Eq. 3).

http://dx.doi.org/10.5772/56299

3. Proppant permeability formulation

The formulation of the proppant permeability (and inertial factor) is presented in Appendix A. It can be shown (see Eq. A.23 through Eq. A.35) that the dimensionless proppant permeability in terms of the proppant diameter, porosity, slot width, and sphericity is

$$\frac{k}{d_p^2} = \Omega\Psi \tag{5}$$

where

$$\Omega = \frac{\phi^3}{72\lambda_m(1-\phi)^2}\left(1+a_D\right)^{-2} \tag{6}$$

$$\Psi = \Phi^2\left(\frac{1+a_D}{1+\Phi a_D}\right)^2 \tag{7}$$

$$a_D = \frac{a_w}{a_s} = \frac{d_p}{3\left(1-\phi\right)w} = \frac{d_p\rho}{3C_a} \tag{8}$$

Thus if the experimental proppant permeability data is fitted with Eq. 5, the dimensionless permeability (k/d_p^2) should be a linear function of the characteristic proppant pack parameter (Ω) with the slope represented by the proppant sphericity-specific surface area parameter (Ψ). The proppant sphericity can then be found from the slope using Eq. 7

$$\Phi = \frac{\sqrt{\Psi}}{1+a_D\left(1-\sqrt{\Psi}\right)} \tag{9}$$

The above equation works well for determining the proppant sphericity provided that the friction multiplier is a constant for all bed packing (i.e., $\lambda_m = 25/12$), the proppant sphere size is uniform, and that the sphericity (Φ) is a constant. But in reality, Φ is generally a function of Ω , (i.e., $\Phi = f(\Omega)$). Pan *et al.* (2001) proposed a four parameter model to correlate permeability with porosity and sphere size distribution for random sphere packing. However, plotting dimensionless permeability k/d_p^2 versus Ω is a very useful diagnostic tool. Large deviations can signify poor or inconsistent experimental results, inaccurate calculation/measurement of the mean proppant diameter (especially for slopes greater than unity), or proppant porosity

(and width) measurement errors as a function of closure. A diagnostic plot of k/d_p^2 versus Ω will provide insight into the topics discussed above and also provide a comparison of different proppants and their relative pack permeability as closure stress increases (i.e., low values of Ω). The main emphasis of this paper is not to provide a detailed deterministic proppant permeability correlation but rather to provide a methodology to help explain and understand why different proppant types behave differently under stress.

Although Eq. 5 is a very good correlation for diagnostics, other forms of this equation (e.g., $k/d_p^2 = a_0 + a_1\Omega + a_2\Omega^2$ or $k/d_p^2 = a\Omega^{\alpha}$) also fit the data very well over limited ranges for some proppants. The other major advantage of correlating the permeability data with Ω is that Ω has the correct limits for mono-layers (i.e., as $\phi \to 1$, $\Omega \to w^2/\left(d_p^2 12\right)$). Figures 2 and 3 illustrate images for a 20/40 Northern White Sand and a 20/40 Brown Sand, respectively. The Northern White has a sphericity of about 0.73 while the Brown Sand has a much lower sphericity of about 0.5. Sintered bauxite and resin coated sands have much higher sphericity of approximately 0.90 and 0.80-0.85 respectively as illustrated in Figures 4 and 5.

Figure 2. Northern White Sand, sphericity ~ 0.73 – Photo courtesy: Santrol.

http://dx.doi.org/10.5772/56299

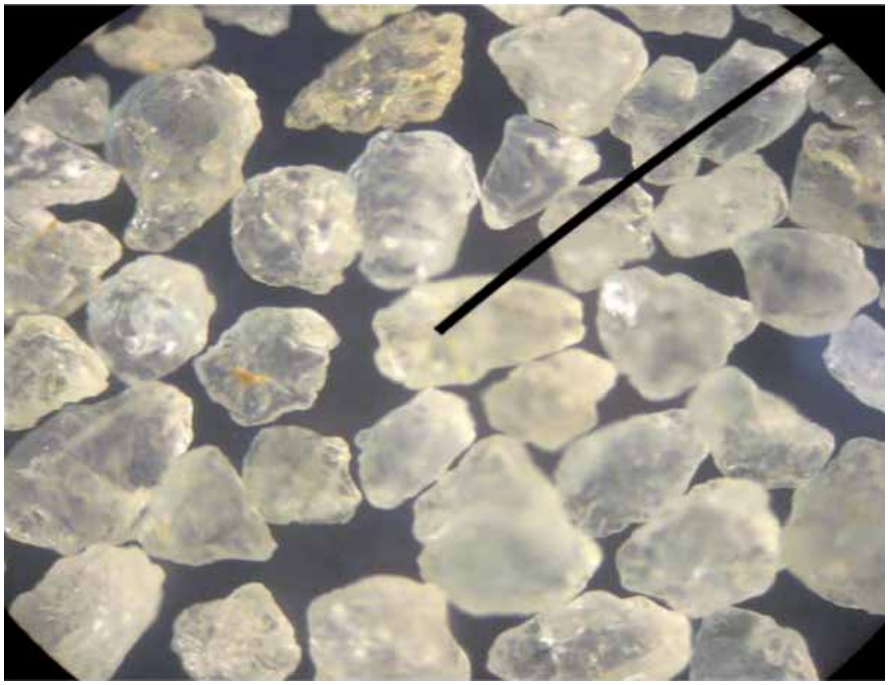

Figure 3. Brown Sand, sphericity ~ 0.50 – Photo courtesy: U.S. Silica Company.

Figure 4. Bauxite, sphericity ~ 0.90 – Photo courtesy: Oxane.

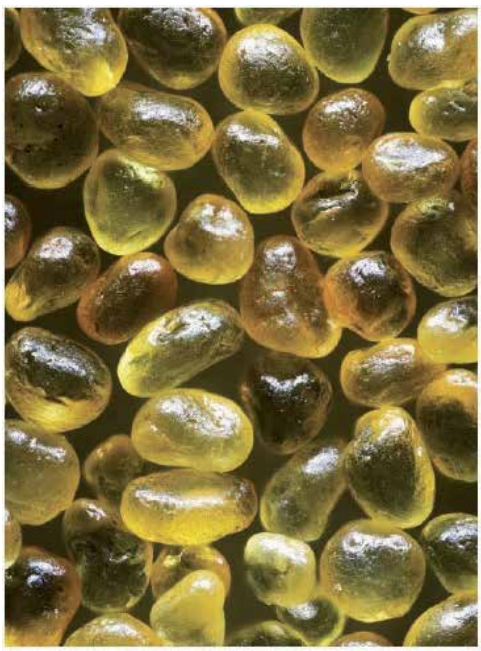

Figure 5. Resin Coated Sand, sphericity ~ 0.80 – Photo courtesy: Santrol.

Figures 6 and 7 show a comparison of dimensionless permeability ($k \left/ d_p^2 \right.$) versus the characteristic proppant pack parameter, Ω , for selected 20/40 Brown Sand (BS), 20/40 White Sand (WS), 20/40 resin coated sand, and 20/40 bauxite proppants at a concentration of $C_a = 2\ \mathrm{lb}_m \left/ f t^2 \right.$. As illustrated, these proppants generally follow the correlation of Eq. 5. However, the substantial permeability reduction as a result of the low sphericity is evident for the BS and to a lesser extent in the resin coated. The WS high permeability at about $\Omega = 2e-05$ is suspect (see Figure 7).

http://dx.doi.org/10.5772/56299

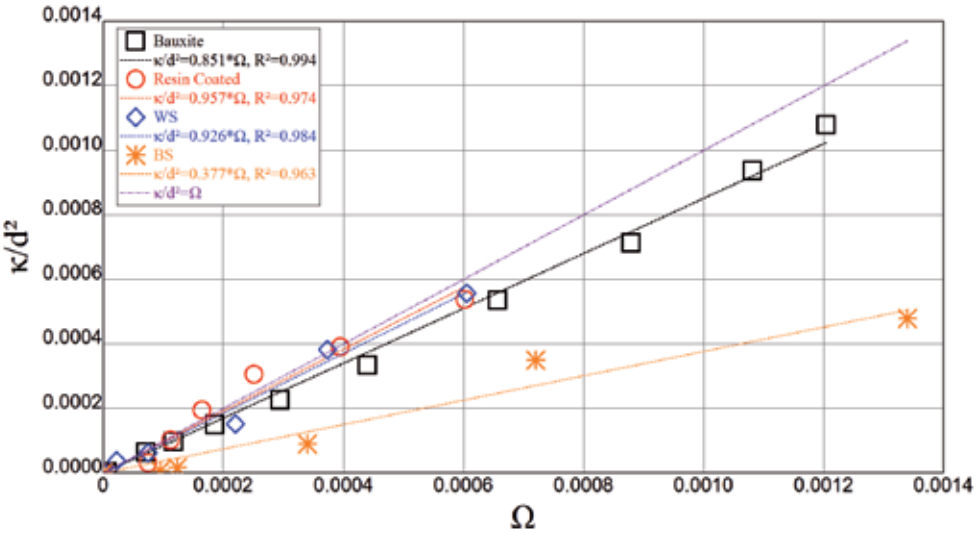

Figure 6. Correlation of Dimensionless Permeability for various types of 20/40 Proppants - Linear Plot.

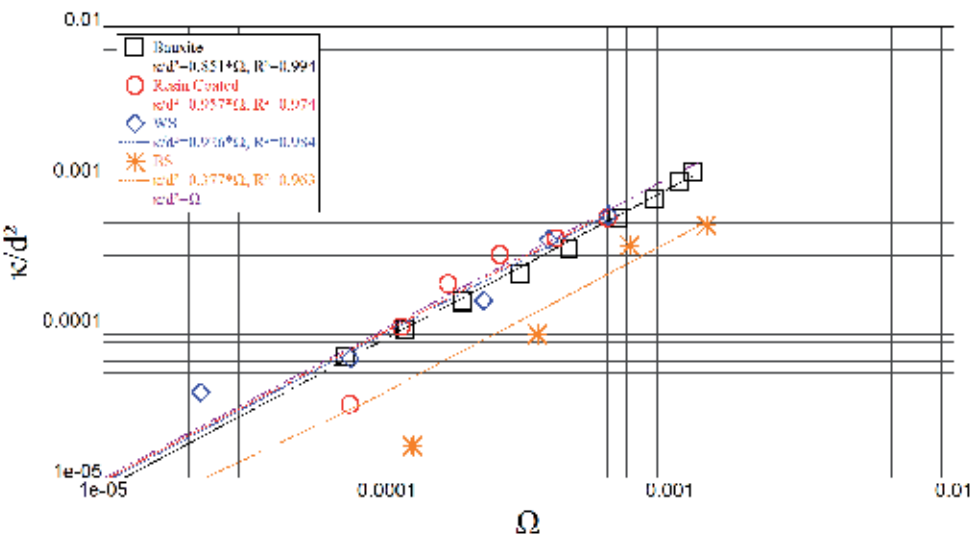

Figure 7. Correlation of Dimensionless Permeability for various types of 20/40 Proppants - Log-Log Plot.

4. Conclusion

The fundamental solution for flow through packed columns (proppant packs) can be characterized by the sum of viscous and inertial forces (e.g., Ergun's equation). Coupling Ergun's equation with the Forchheimer equation results in a deterministic equation for the fracture permeability, k_f , and inertial factor, β , as functions of the proppant diameter, sphericity, pack porosity and width. Plotting the dimensionless permeability k/d_p^2 versus Ω can be a very useful diagnostic tool that can indicate: 1) sphericity, 2) channeling, 3) crushing, 4) non-uniform sphere size distribution, 5) embedment and 6) deviation of the friction multiplier λ_m from Ergun's equation. Large deviations can also signify poor or inconsistent experimental results. This diagnostic plot can also quantify the behavior of proppant mono-layers.

Nomenclature

a_D = Dimensionless specific surface area, $a_D = a_w / a_s$

a_s = Specific surface area - sphere

a_w = Specific surface area - wall

A = Cross-sectional area

A_p = Particle surface area

C_a = Concentration/area

d_h = Hydraulic diameter

d_p = Proppant diameter

$d_p^{'}$ = Equivalent proppant diameter, $d_p^{'} = \Phi d_p$

f = Darcy friction factor

f_0 = Burke-Plummer friction factor

g = Gravitational constant

k = Permeability

K = Loss coefficient - inlet and exit

L = Column length

L_τ = Tortuous path length

N_{ml} = Number of minor losses

http://dx.doi.org/10.5772/56299

p = Pressure

P_f = Perimeter

q = Flow rate

Re = Reynolds number

v = Superficial velocity

$\langle \bar{v} \rangle$ = Cross-sectional velocity

V_p = Particle volume

w = Width

Greek

β = Inertial or beta factor

λ_m = Friction factor multiplier

μ = Viscosity

τ_w = Shear stress - wall

ϕ = Porosity

Φ = Sphericity

Ω = Characteristic proppant porosity parameter

Ψ = Sphericity-specific area parameter

ρ = Density

Subscripts

f = Fracture

h = Hydraulic

p = Proppant

= Sphere

w = Wall or width

Appendix A: Flow through packed columns

The solution methodology for flow through a proppant pack can be developed from flow through packed columns as presented by Bird, Stewart, and Lightfoot (1960). Although a

detailed derivation of the equations for determining proppant permeability and inertial effects is not within the scope of this paper, the fundamentals are provided to give the reader an appreciation of the dominant parameters that affect the proppant pack permeability.

As discussed by Bird *et al.*, "the packing material may be spheres, cylinders, or various other kinds of packing shapes. It is also assumed that the packing is everywhere uniform and that there is no channeling of fluid (in actual practice, channeling frequently occurs and the formulas provided are not valid). It is further assumed that the diameter of the packing is small in comparison with the diameter of the column in which the packing is contained and that the column diameter is constant." The impact of these last two assumptions will be addressed later in this section.

Governing equations

The governing equations for flow through packed columns are formulated in this section. Friction factors for packed columns, frictional pressure loss for laminar flow, and inertial flow (non-Darcy) are presented. Derivation for the fracture permeability and inertial coefficient (β) are also presented.

Friction factor

The friction factor is normally defined as the ratio of friction forces to inertial forces. This factor is commonly used to determine the frictional dissipation in closed conduits and is defined as

$$f = \frac{4\tau_w}{1/2\rho v^2} = \frac{2d_h(-dp/dx)}{\rho v^2} \tag{13}$$

where f is the Darcy friction factor, τ_w is the wall shear stress, v is the superficial velocity ($v = q/A$), and d_h is the hydraulic diameter. The pressure gradient in the conduit is $-dp/dx$. The hydraulic diameter in packed columns is sometimes replaced with the equivalent particle diameter or other characteristic dimension.

Hydraulic diameter

The hydraulic diameter is defined as

$$d_h = \frac{4A}{P_f} \tag{14}$$

where P_f is the conduit wetted perimeter and A is the flow cross-sectional area.

Laminar flow

The equation of motion for laminar flow in closed conduits (e.g., pipes, slots, annuli and other non-circular conduits) can be represented by

http://dx.doi.org/10.5772/56299

$$-\frac{dp}{dx}=\frac{32\lambda_m\mu\langle\bar{v}\rangle}{d_h^2} \tag{15}$$

where the average flow rate in the cross section available for flow is given by the intrinsic velocity $\langle\bar{v}\rangle$, λ_m is a friction factor multiplier that is a function of the closed conduit geometry, and d_h is the hydraulic diameter. Theoretically, the friction multiplier for flow of a Newtonian fluid in a pipe, narrow elliptical slot, and rectangular slot are $\lambda_m=1$, $\lambda_m=\pi^2/8$, and $\lambda_m=3/2$, respectively.

The pressure loss in terms of the Darcy friction factor based on the cross-sectional average flow velocity from Eq. A.3 is

$$-\frac{dp}{dx}=\frac{f}{2}\frac{\rho\langle\bar{v}\rangle^2}{d_h} \tag{16}$$

where the Darcy friction factor is given by

$$f=\frac{64\lambda_m\mu}{\rho\langle\bar{v}\rangle d_h}=\frac{64\lambda_m}{\mathrm{Re}} \tag{17}$$

The Reynolds number for flow of a Newtonian fluid in a conduit is defined as

$$\mathrm{Re}=\frac{\rho\langle\bar{v}\rangle d_h}{\mu} \tag{18}$$

where the cross-sectional average velocity $\langle\bar{v}\rangle$ is related to the superficial velocity v by the conduit porosity (i.e., $\langle\bar{v}\rangle=v/\phi$).

Laminar flow in packed columns

The frictional pressure loss through a proppant pack (or packed bed) can be derived from Eq. A.3

$$-\frac{dp}{dx}=\frac{32\lambda_m\mu\langle\bar{v}\rangle}{d_h^2} \tag{19}$$

by replacing the cross-sectional average velocity $\langle\bar{v}\rangle$ by the superficial velocity v (i.e., $\langle\bar{v}\rangle=v/\phi$) and the equivalent hydraulic diameter of the proppant pack in terms of the particle diameter and porosity.

The equivalent hydraulic diameter from Eq. A.2 for spherical particles with a diameter of d_p and a packed porosity of ϕ is

$$d_h = \frac{2}{3}\frac{\phi}{1-\phi}d_p \tag{20}$$

Substituting the hydraulic diameter and the relationship $\langle\bar{v}\rangle = v/\phi$ into Eq. A.7, we find

$$\begin{aligned} -\frac{dp}{dx} &= \frac{32\lambda_m \mu\langle\bar{v}\rangle}{d_h^2} = \frac{32\lambda_m \mu(v/\phi)}{\left(\frac{2}{3}\frac{\phi}{1-\phi}d_p\right)^2} \\ &= \frac{72\lambda_m (1-\phi)^2 \mu v}{\phi^3 d_p^2} \end{aligned} \tag{21}$$

Experimental measurements (Bird *et al.* 1960) indicate that if a frictional multiplier of $\lambda_m = 25/12$ is used, the above theoretical equation matches extremely well with the experimental data. Insertion of this friction multiplier value into Eq. A.9 then gives

$$-\frac{dp}{dx} = \frac{150(1-\phi)^2 \mu v}{\phi^3 d_p^2} \tag{22}$$

which is the Blake-Kozeny equation. This equation is generally good for void fractions less than 0.5 and is valid in the laminar flow regime given by $\frac{(\rho v)d_p}{\mu(1-\phi)} < 10$ (Bird 1960). The bed friction multiplier based on the proppant diameter is

$$\begin{aligned} f_{d_p} &= \frac{2d_p(-dp/dx)}{\rho v^2} \\ &= \frac{144\lambda_m}{\mathrm{Re}_{d_p}}\frac{(1-\phi)^2}{\phi^3} = \frac{300}{\mathrm{Re}_{d_p}}\frac{(1-\phi)^2}{\phi^3} \end{aligned} \tag{23}$$

where $\mathrm{Re}_{d_p} = \rho v d_p/\mu$. The bed friction factor based on the hydraulic diameter is

http://dx.doi.org/10.5772/56299

$$f_{d_h} = \frac{2d_h(-dp/dx)}{\rho\upsilon^2} = \frac{64\lambda_m}{\phi \mathrm{Re}_{d_h}} = \frac{400/3}{\phi \mathrm{Re}_{d_h}} \tag{24}$$

where

$$\mathrm{Re}_{d_h} = \rho\upsilon d_h/\mu \tag{25}$$

Inertial flow in packed columns

The pressure loss in packed columns as a result of inertial forces (minor losses) was originally derived by Burke and Plummer assuming turbulent flow in packed columns (see Bird 1960). Burke and Plummer assumed that for highly turbulent flow that the friction factor was only a function of roughness and that the roughness characteristics were similar for all packed columns. Based on these assumptions Burke and Plummer could then justify a constant friction factor f_0 that would be used to characterize turbulent flow. Then from Eq. A.4 the resulting pressure loss equation for inertial losses is

$$-\frac{dp}{dx} = \frac{f_0}{2}\frac{\rho\langle\bar{\upsilon}\rangle^2}{d_h} = \frac{3}{4}f_0\frac{\rho\upsilon^2}{d_p}\frac{1-\phi}{\phi^3} \tag{26}$$

where the experimental data indicated that $f_0 \cong 7/3$. This is the Burke-Plummer equation which is valid for $\frac{(\rho\upsilon)d_p}{\mu(1-\phi)} > 1000$.

The form of the Burke-Plummer equation can also be derived assuming inertial forces (minor flow loss) through the proppant pack using the extended Bernoulli equation as presented below.

Viscous and inertial flow in packed columns

The flow through packed columns may also be characterized as a sum of frictional (viscous losses) and inertial (minor losses) forces. The general pressure loss equation formulation based on the extended Bernoulli equation with minor losses is

$$\frac{p_1 - p_2}{\rho g} = \sum f\frac{L_\tau}{d_h}\frac{\langle\bar{\upsilon}\rangle^2}{2g} + \sum k\frac{\langle\bar{\upsilon}\rangle^2}{2g} \tag{27}$$

or

$$-\frac{dp}{dx}=\sum f\frac{L_\tau}{L}\frac{\rho\langle\bar{v}\rangle^2}{2d_h}+\sum K\frac{L_\tau}{L}\frac{\rho\langle\bar{v}\rangle^2}{2d_h} \tag{28}$$

where L is the length of the column and L_τ is the tortuous path length the fluid takes. Further assume that the number of minor losses N_{ml} in a column of length L can be approximated by $N_{ml}=L_\tau/d_h$. Then the exit and entrance losses as the fluid expands and contracts through the packed column from Eq. A.15 can be written as

$$\begin{aligned}-\frac{dp}{dx}&=f\frac{L_\tau}{L}\frac{\rho\langle\bar{v}\rangle^2}{2d_h}+\sum_{i=1}^{N_{ml}}\left(K_{inlet}+K_{exit}\right)\frac{\rho\langle\bar{v}\rangle^2}{2d_h}\\&=f_{d_h}\frac{\rho\langle\bar{v}\rangle^2}{2d_h}+f_0\frac{\rho\langle\bar{v}\rangle^2}{2d_h}\end{aligned} \tag{29}$$

The inertial pressure loss is identical to the form of the Burke-Plummer equation even though one was based on inertial effects and the other on turbulence. This, however, should not be surprising since both inertial and turbulent losses are proportional to ρv^2. Substituting the bed friction factor and superficial velocity into Eq. A.16, we find

$$-\frac{dp}{dx}=\frac{32\lambda_m\mu v}{\phi d_h^2}+f_0\frac{\rho v^2}{2\phi^2 d_h} \tag{30}$$

or

$$-\frac{dp}{dx}=\frac{72\lambda_m\left(1-\phi\right)^2\mu v}{\phi^3 d_p^2}+\frac{3}{2}f_0\frac{1-\phi}{\phi^3}\frac{\rho v^2}{2d_p} \tag{31}$$

where from experimental data $\lambda_m=25/12$ and $f_0=7/3$.

Ergun's equation

The total pressure loss formulation for all flow regimes may thus be obtained by simply adding the Blake-Kozeny equation for viscous dissipation and the Burke-Plummer equation for inertial losses. The above equation can be written in terms of the dimensionless groups as follows

http://dx.doi.org/10.5772/56299

$$-\left(\frac{dp}{dx}\frac{d_p}{\rho\upsilon^2}\right)\left(\frac{\phi^3}{1-\phi}\right)=\frac{150\left(1-\phi\right)}{\mathrm{Re}}+\frac{7}{4} \tag{32}$$

This is the Ergun equation (Bird 1960) where $\mathrm{Re}=\rho\upsilon d_p/\mu$, $\lambda_m=25/12$ and $f_0=7/3$ have been substituted.

Darcy and non-darcy flow

The equation to describe non-Darcy flow is a form of the Forchheimer (1901) equation

$$-\frac{dp}{dx}=\frac{\mu}{k}\upsilon+\beta\rho\upsilon^2 \tag{33}$$

where k is the permeability of the porous media and β is the non-Darcy or inertial factor. Clearly, the first term in this equation accounts for viscous effects and the second term for inertial or minor loss effects.

Rearranging Eq. A.20 in terms of the dimensionless groups we find

$$\left(-dp/dx\right)\Big/\beta\rho\upsilon^2=1/\mathrm{Re}_{\beta k}+1 \tag{34}$$

where the dimensionless Reynolds number for non-Darcy flow is given by

$$\mathrm{Re}_{\beta k}=\frac{\rho\upsilon\beta k}{\mu} \tag{35}$$

Rewriting Eq. A.17 in terms of the fracture permeability k and inertial factor β from Eq. A.20, we have

$$\begin{aligned}-\frac{dp}{dx}&=\frac{32\lambda_m\mu\upsilon}{\phi d_h^2}+f_0\frac{\rho\upsilon^2}{2\phi^2 d_h}\\&=\frac{\mu}{k}\upsilon+\beta\rho\upsilon^2\end{aligned} \tag{36}$$

where

$$k=\frac{\phi d_h^2}{32\lambda_m}\ \text{and}\ \beta=\frac{f_0}{2d_h\phi^2} \tag{37}$$

Placing β in terms of the fracture permeability we find

$$\beta = \frac{3/4\, f_0}{\sqrt{72\lambda_m}} \frac{1}{\sqrt{k\phi^3}} \tag{38}$$

Sphericity

Sphericity is a measure of how closely a grain approaches the shape of a perfect sphere compared to roundness which is a measure of the sharpness of grain corners. The sphericity of a particle is the ratio of the surface area of a sphere (with the same volume as the given particle) to the surface area of the particle

$$\Phi = \frac{\pi^{1/3}\left(6V_p\right)^{2/3}}{A_p} \tag{39}$$

where V_p is the volume and A_p is the surface area of the particle. For non-spherical particles the characteristic particle diameter in the above equations must be replaced by

$$d_p^{'} = \Phi d_p \tag{40}$$

Proppant permeability

The proppant permeability can be theoretically calculated from Eq. A.24 provided that the hydraulic diameter and porosity are known. The hydraulic diameter for flow in a slot of width (w), packed with a proppant of uniform porosity (ϕ), and diameter (d_p) from Eq. A.2 is

$$d_h = \frac{4\phi}{\left(a_s + a_w\right)} \tag{41}$$

where the specific surface areas for the proppant spheres and fracture wall are $a_s = 6(1-\phi)/d_p$ and $a_w = 2/w$, respectively.

The proppant permeability in terms of the proppant diameter, porosity, slot width, and sphericity is found by substituting Eq. A.26 through A.28 into A.24

$$k = \frac{\phi^3 \Phi^2 d_p^2}{72\lambda_m (1-\phi)^2}\left(1 + \frac{\Phi d_p}{3\left(1-\phi\right)w}\right)^{-2} \tag{42}$$

http://dx.doi.org/10.5772/56299

The permeability for flow through an open slot or channel (i.e., no proppant as $\phi \to 1$) with a slot width of w from Eq. A.29 is

$$k = \frac{9w^2}{72\lambda_m} = \frac{w^2}{12} \tag{43}$$

where λ_m=3 / 2 for slot flow.

The dimensionless form of Eq. A.29 is

$$\frac{k}{d_p^2} = \frac{\phi^3 \Phi^2}{72\lambda_m (1-\phi)^2} \left(1 + \frac{\Phi d_p}{3(1-\phi)w} \right)^{-2} \tag{44}$$

or

$$\frac{k}{d_p^2} = \Omega\Psi \tag{45}$$

where

$$\Omega = \frac{\phi^3}{72\lambda_m (1-\phi)^2} \left(1 + a_D\right)^{-2} \tag{46}$$

$$\Psi = \Phi^2 \left(\frac{1 + a_D}{1 + \Phi a_D} \right)^2 \tag{47}$$

$$a_D = \frac{a_w}{a_s} = \frac{d_p}{3(1-\phi)w} \tag{48}$$

Eq. A.32 illustrates that the dimensionless permeability ratio (k / d_p^2) is a linear function of the characteristic proppant pack parameter (Ω), and the proppant sphericity-specific surface area parameter (Ψ) for all proppants. The dimensionless specific area ratio of the fracture (slot wall) and proppant is represented by a_D .

Pan et al. (2001) provides a good review of permeability versus porosity correlation for random sphere packing. Pan also proposed a modification to Ergun's equation for low Reynolds number with a four parameter fit model to correlate k / d_p^2 as a function of porosity and sphere size distribution.

Acknowledgements

The authors wish to thank the management of Baker Hughes Incorporated for the opportunity to perform this research and publish the findings. We would also like to thank Bill Brinzer and Jennifer Pusch for their grammatical review and proofing of the manuscript.

Author details

Bruce R. Meyer[1], Lucas W. Bazan[2] and Doug Walls[3]

*Address all correspondence to: lucas.w.bazan@bazanconsulting.com

1 Meyer Technologies, LLC, Natrona Heights, PA, USA

2 Bazan Consulting, Inc., Houston, TX, USA

3 Baker Hughes Incorporated, Natrona Heights, PA, USA

References

[1] API, American Petroleum Institute,: "Recommended Practices for Testing Sand Used in Hydraulic Fracturing Operations", API RP 56, March (1983).

[2] API, American Petroleum Institute,: "Recommended Practices for Testing Sand Used in Gravel Packing Operations", API RP 58, December (1995).

[3] API, American Petroleum Institute,: "Recommended Practices for Testing High-Strength Proppants Used in Hydraulic Fracturing Operations", API RP 60, December (1995).

[4] Bird, R. B, Stewart, W. E, & Lightfoot, E. N. Transport Phenomena," Wiley, New York, (1960).

[5] Forchheimer, P. Wasserbewegung durch Boden. Zeitschrift des Vereines Deutscher" Ingenieuer, 45 edition, (1901).

[6] ISO, (2006). Amendment 13503-2: "Measurement of properties of Proppants used in Hydraulic Fracturing and Gravel-Packing Operations". ISO.org

[7] ISO, (2006). Amendment 13503-5: "Procedures for Measuring the Long-Term Conductivity of Proppants". ISO.org

[8] Much, M. G, & Penny, G. S. Long-Term Performance of Proppants Under Simulated Reservoir Conditions," SPE/DOE 16415, May (1987).

[9] Palisch, T, Duenckel, R, Bazan, L, Heidt, H, & Turk, G. Determining Realistic Fracture Conductivity and Understanding its Impact on Well Performance". SPE 106301, January (2007).

[10] Palisch, T, Duenckel, R, Chapman, M, Woolfolk, S, & Vincent, M. C. How to Use and Misuse Proppant Crush Tests- Exposing the Top 10 Myths". SPE 119242, January (2009).

[11] Pan, C, Hilpert, M, & Miller, C. T. Pore-scale modeling of saturated permeabilities in random sphere packings," Physical Review E, November (2001). , 066702

Chapter 27

A New Approach to Hydraulic Stimulation of Geothermal Reservoirs by Roughness Induced Fracture Opening

Nima Gholizadeh Doonechaly, Sheik S. Rahman and Andrei Kotousov

Additional information is available at the end of the chapter

http://dx.doi.org/10.5772/56447

Abstract

Hydraulic fracturing by shear slippage mechanism (mode II) has been studied in both laboratory and field scales to enhance permeability of geothermal reservoirs by numerous authors and their success stories have been reported. Shear slippage takes place along the planes of pre-existing fractures which causes opening of the fracture planes by the fracture asperities (roughness induced opening). Simplified empirical relationships, which are derived based on simple fracture experiments or best guess, are used to calculate compressive normal surface traction, residual aperture and shear displacement. This introduces ambiguity into the simulation results and often leads to erroneous predictions of reservoir performance.

In this study an innovative analytical approach based on the distributed dislocation technique is developed to simulate the roughness induced opening of fractures in the presence of compressive and shear stresses as well as fluid pressure inside the fracture. This provides fundamental basis for computation of aperture distribution for all parts of the fracture which can then be used in the next step of modeling fluid flow inside the fracture as a function of time. It also allows formulation of change in aperture due to thermal stresses. The stress distribution and the fluid pressure are calculated using the fluid flow modeling inside the fracture in a numerical framework in which thermo-hydro mechanical effects are also considered using finite element methods (FEM). In this study, fractures with their characteristic properties are considered to simulate rock deformation.

This new approach is applied to the Soultz-Sous-Forets geothermal reservoir to study changes in permeability and its impact on temperature drawdown. It has been shown that the analytical

approach provides a more realistic prediction of residual fracture aperture which agrees well with the experience of existing EGS trials around the world. An average increase in aperture due to fluid induced shear dilation has been found to be lower and time required to obtain a sizeable reservoir volume is greater than those previously estimated.

1. Introduction

1.1. Reservoir stimulation by induced fluid pressure

Fractured reservoirs in crystalline rocks are usually stimulated by injected fluid pressure. As the injection of fluid continues the pressure inside the fractures increases gradually. The effective stress due to fluid pressure is expressed as:

$$\sigma_{eff} = \sigma_t - p \tag{1}$$

where σ_{eff} is the effective stress, σ_t is the total stress and p is the pore pressure. With further injection of fluid the effective shear stress, which is a function of effective stress, continuously decreases until it reaches a threshold value at which time it can no longer resist shear displacement of the fracture surfaces. At this stage the shear dilation will occur. During shear displacement rock fails by the shearing (Mode II) instead of opening (Mode I). In Mode II opening, the surface asperities of the rock slide over each other which cause more separation of the fracture surfaces. Such an interlocking of asperities increases the permeability of the rock. Any further increase in pressure can cause the effective closure stress to decrease to zero at which time the separation and interlocking of the fracture surfaces perpendicular to the fracture walls occur. The amount of pressure required to reach zero effective stress is highly dependent on the rock and fracture properties [1]. If the injection continues at some point it will exceed the tensile strength of the rock, which leads to tensile failure of the rock. This means that a certain level of permeability enhancement by shear displacement can be obtained. Mechanical representation of the shear displacement and the normal separation of the fracture surfaces can be described based on a specific failure criterion, such as Mohr-Coulomb (see Fig. 1). As the pressure inside the fracture increases the effective stress decreases: Mohr's circle moves towards the origin. As shown in Fig.1, when the minimum principal stress (closure stress) reaches zero the normal separation of fracture surfaces (Mode I) occurs. However, the shear dilation happens much earlier: when the Mohr's circle encounters the failure envelope (CD) at E. Shear dilation by induced fluid pressure was first detected in the laboratory experiments in 1970s. One of the earliest attempts by [2] showed a significant permeability increase by shear displacement. This observation was confirmed by [3] and [4]. Since then, shear dilation has been comprehensively studied in geotechnical and mining engineering. However, investigation of permeability enhancement by shear dilation in petroleum reservoirs began much later [5]. Since the shear dilation is caused by slippage of the asperities on top of each other, there is maximum dilation that can be reached. The maximum displacement that

http://dx.doi.org/10.5772/56447

can be achieved is called characteristic height of the fracture [6]. Based on an experimental study the characteristic height is measured to be of the order of a fraction of a millimeter [7]. Fracture aperture that can be created by conventional hydraulic fracturing is in the order of tens of millimeters [8]. Reservoir rocks with rough surfaces and high shear strength are highly desirable for stimulation by shear displacement to work. One of the most comprehensive attempts to characterize the shear dilation caused by the fracture surface asperities was developed by [9]. In their model, the rock behavior was studied by considering fracture surface and its aperture, normal and shears closure and shear dilation. In another attempt, [10] proposed a methodology to obtain the mechanical aperture of the fractures. The authors used the methodology proposed by [11] to measure the aperture by a tapered feeler gauge using plane sawn surfaces to gain access to the joints. Mechanical aperture can be calculated using an empirical equation as proposed by [10]. Later [10] used the empirical equation proposed by [11] to model the normal closure of fracture surfaces based on the normal stress. [12] proposed an approach to describe the hydraulic and mechanical properties of the fracture including the shear dilation by induced fluid pressure.

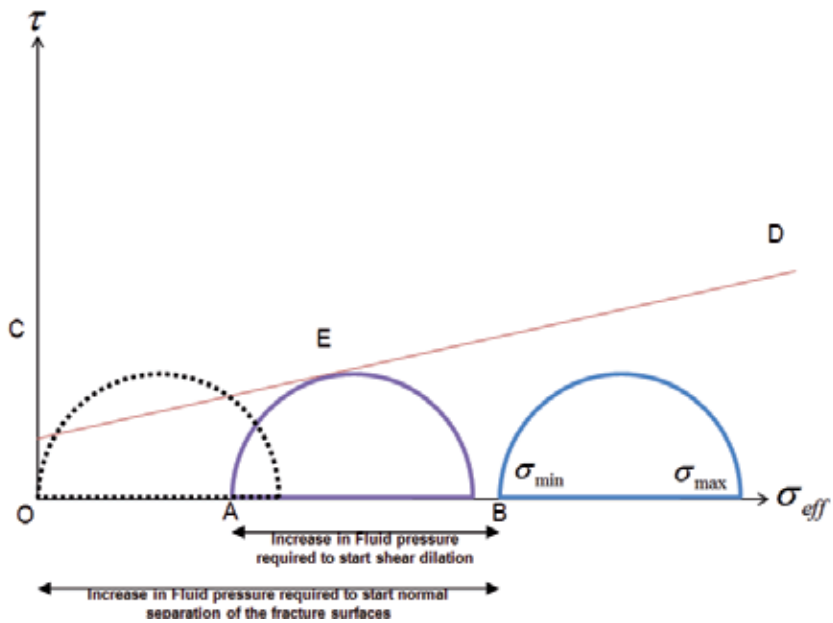

Figure 1. Mohr diagram describing the initiation of the shear dilation and normal fracture surface separation.

Mechanical models for shear displacement include displacement estimation under different stress boundary conditions in which a proper topographical model is used to describe the fracture surface. Also [13] experimentally studied the effect of normal stress and shear dilation on fluid flow properties of a naturally fractured core sample. They have used a servo-controlled axial/torsion load frame to test the fluid flow and mechanical behavior of the fracture surface during normal stress, slip and shear dilation. In another approach [14] proposed a semi-

empirical correlation to determine the change in fracture aperture based on the amount of shear displacement between the fracture surfaces and the stress boundary condition. Also [15] extended the previous attempt of [14] by considering the effect of fracture propagation in shear dilation.in another attempt [16] used a linear relationship between shear displacement and the dilation of the fracture surfaces.

In this study, an analytical computational methodology based on distributed dislocation technique proposed by [6] is used to estimate the aperture distribution caused by the shear dilation in a fracture subject to different varying stress boundary conditions [6].

Two major assumptions are used in this approach to characterize the shear displacement of the fracture surfaces. The shear slippage between the fracture surfaces is described by using Coulomb friction law which explains the friction stress during the shear slippage based on the normal stress exerted on the fracture planes with a proportionality contact named friction factor as shown in Eq.

$$\tau = c + f\sigma_n \tag{2}$$

where, τ_0 is the threshold shear stress value to initiate the shear slippage between the fracture surfaces. Also the friction factor, f, is dependent on the material properties, fracture geometry and surface asperities of the fracture [6]. Because a minor change in the fracture aperture causes a significant alteration of the fracture permeability estimation of the shear slippage of the fracture surfaces is of crucial importance in fluid flow simulation. In this study the coupling between the shear displacement and the change in fracture aperture is described by a step function. Fracture displacement normal to the fracture plane is simulated by using virtual springs distributed along the fracture length. Such springs are characterized by a specific spring constant which can be calculated numerically, experimentally or analytically [6]. Also the spring deformations are modeled in an elastic framework which results in the following system of equations describing the stress between the fracture surfaces:

$$\sigma_n = kE(\Delta - \delta_y) \text{ for } \delta_y < \Delta \tag{3}$$

$$\sigma_n = 0 \text{ for } \delta_y > \Delta \tag{4}$$

where, Δ is the characteristic height of the fracture as shown in Eq. (3) and k is the spring constant. Equation (3) is associated with the rock compressibility and gives us the normal stress exerted on the fracture surfaces. After calculating the normal stresses on the fracture surfaces, the normal displacement of the surfaces is calculated by the distribution dislocation concept. Also the methodology proposed by [17] is used to calculate the spring constant based on a bed of nails as [17]:

http://dx.doi.org/10.5772/56447

$$k = E\frac{b\Delta}{L} \tag{5}$$

where, E id the Young modulus of elasticity, L is the fracture length and b is a constant less than unity. Also Eq. (4) implies the complete separation of the fracture surfaces in which no contact exists between the fracture asperities.

The complete set of boundary conditions for a fracture as shown in Fig. 2 are listed below [6]:

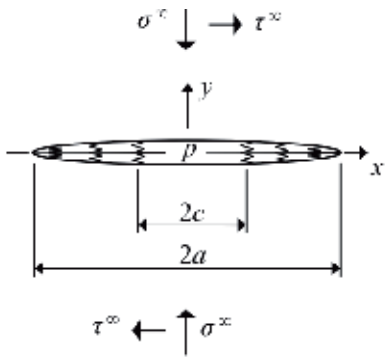

Figure 2. A schematic representation of a fracture subject to in-situ stress boundary conditions.

$$\sigma'_y = \sigma^\infty \text{ for } x^2 + y^2 \to \infty \tag{6}$$

$$\sigma'_y = kE(\Delta - \delta_y) + p \text{ for } c < |x| \le a \tag{7}$$

$$\sigma'_y = p \text{ for } |x| \le c \tag{8}$$

$$\tau_n = \tau_0 + f \cdot kE(\Delta - \delta_y) \text{ for } c < |x| \le a \tag{9}$$

$$\tau_n = 0 \text{ for } |x| \le c \tag{10}$$

$$u_x = 0 \text{ for } |x| \ge a \tag{11}$$

$$u_y = 0 \text{ for } |x| \ge a \tag{12}$$

where $\sigma_y^{'}$ is the effective normal stress exerted on the fracture surfaces, k is the spring constant, p is the pore pressure, Δ is the characteristic height of the fracture, δ_y is the displacement of the fracture surfaces, E is the Modulus of elasticity, τ_n is the shear stress exerted on the fracture surfaces, τ_0 is the threshold stress requires to start the shear displacement of the fracture surfaces and u is the displacement. *As* mentioned above, the aperture distribution along the fracture surface is calculated based on an analytical methodology in which fracture geometry, stress distribution and fluid pressure inside the fracture are needed to be known as a priori. For this purpose a thermo-poro-elastic model is developed to simulate the fluid flow in the reservoir scale.

2. Simulation of fluid flow and heat transfer

Three distinct approaches exist in the literature to simulate the fluid flow in naturally fractured reservoirs namely: single continuum, dual continuum and discrete fracture approach. In single continuum, the fractured medium is represented by an equivalent homogeneous system using a specific permeability tensor. In dual continuum approach the whole domain is divided into two interacting domains: fractures and matrix where by matrix (represented by sugar cubes) provides the storage and fractures (having regular pattern) the permeability. In discrete fracture approach, fractures are explicitly discretized in the domain. These approaches are briefly discussed below followed by the proposed methodology which is used in this study.

2.1. Hybrid of single continuum and discrete fracture

Different approaches have been used in the literature to incorporate the fractures into the flow modeling. Each of these techniques has its own drawbacks and benefits. In this study a hybrid methodology combining the single continuum and discrete fracture networks model is used to increase accuracy and efficiency of the fluid flow simulation. In the proposed methodology a threshold value is defined for the fracture length. Fractures which are smaller than the threshold value are used to generate the grid based permeability tensor using boundary element technique. Fluid flow simulation is carried out by using the single continuum approach in the nominated blocks. Fractures which are equal to and longer than the threshold value are explicitly discretized in the domain using appropriate elements and the fluid flow is modeled using the discrete fracture approach. Such an approach provides a more accurate and realistic framework to consider the effect of long fractures on the fluid flow in fractured medium.

2.2. Domain discretization using the hybrid methodology

In this study the medium and long fractures ($l \geq 50$m) are discretized using triangular elements and the contribution of flow by fractures ($l < 50$m) are taken into account by calculating permeability tensor for each discretized element. A schematic representation of the domain discretization for a fractured reservoir is shown in Fig 3 (a) and (b).

http://dx.doi.org/10.5772/56447

Permeability tensor for each block is expressed as:

$$K = \begin{bmatrix} k_{xx} & k_{xy} \\ k_{yx} & k_{yy} \end{bmatrix} \tag{13}$$

Permeability tensors are calculated by simulating fluid flow in individual fractures in each element. The concept of permeability tensor was first introduced by [18] by considering a set of parallel fractures in a Representative Elementary Volume (REV) with zero matrix permeability [18]. In another attempt [19] developed a methodology for calculation of permeability tensor for arbitrary oriented fractures using superposition technique [19].

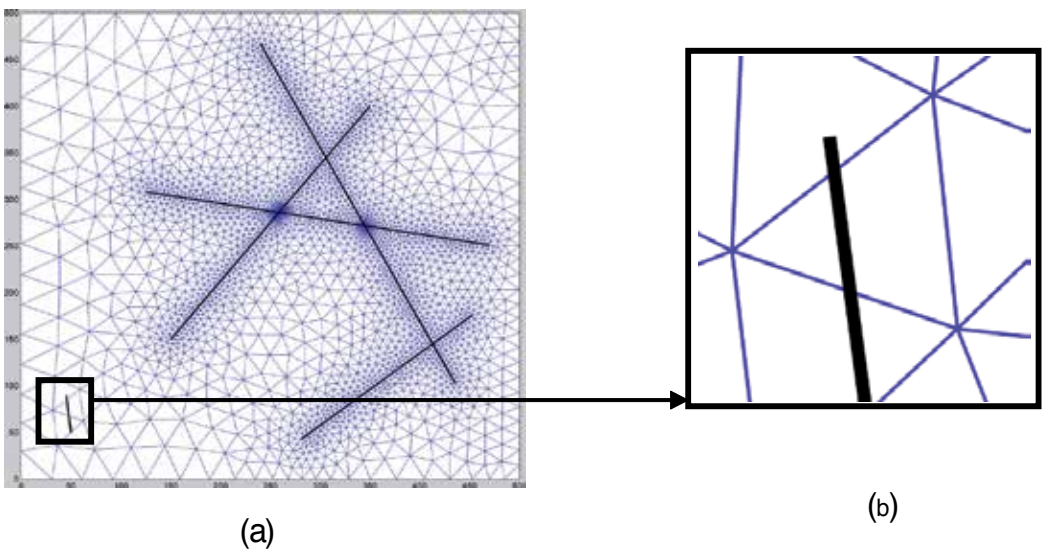

Figure 3. Domain discretization by using the hybrid of the single continuum and discrete fracture approach. (a) fractures equal to and longer than 50 m are explicitly discretized in the reservoir domain by using the triangular elements. (b) after the discretization of the long fractures, the effect of short fractures (<50m) are taken into account by calculation of the permeability tensor of the corresponding blocks which are cut by the fractures.

In this study the authors have considered interconnected fractures with fracture surface as infinite plate without roughness. In another approach [20] estimated permeability tensor by assuming fractures as a planar sink/source term [20]. Also [21] extended the approach and studied the effect of vertical fracture/ matrix permeability ratio on the permeability tensor. In a separate study, [22] used a numerical technique (BEM) to calculate the permeability tensor of the REV containing medium sized fractures considering fractures as a sink/source term [22]. Following this work [23] presented an analytical model to calculate the permeability tensor of the blocks containing infinite parallel fracture sets [23]. Also [24] improved the efficiency of their previous approach by considering the effect of short fractures using the analytical method

proposed by [24]. In another approach [25] presented the first comprehensive methodology to calculate the permeability tensor for arbitrary oriented fractures in different length scales. In this study permeability tensor was determined by discretizing the solution domain into different subdomains depending on the length of the fractures using BEM [25]. Short fractures are considered as part of matrix porosity to improve the matrix permeability inhomogeneity. However, medium and long fractures are discretized explicitly in the domain and fluid flow is simulated using BEM. Then [26] extended [25] by increasing the efficiency of the BEM so that fluid flow in greater number of fractures can be simulated. The authors also presented for the first time effective permeability tensor calculation for the fractured REV by using the BEM. The effective permeability model was validated using laboratory derived data.

2.3. REV discretization for permeability tensor calculation

To calculate the effective permeability tensor, the fractured REV is divided into three distinct regions: matrix (region 1), fracture (region 2) and region around the fractures (region 3) as shown in Fig. 4.

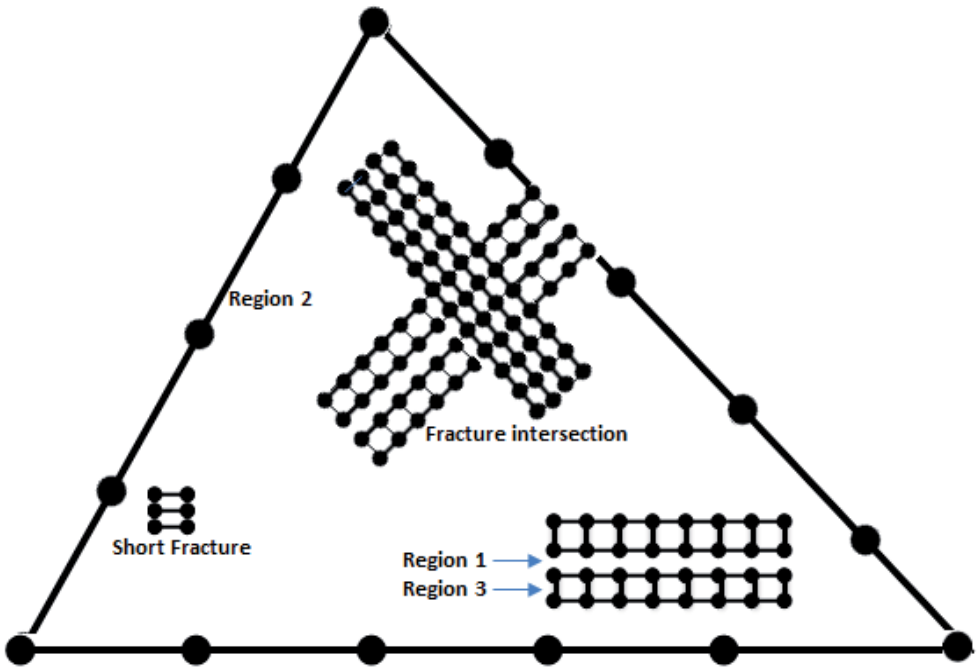

Figure 4. Domain discretization based on different fracture lengths

Flow inside the fractures (region 2) is modeled using the cubic law. With the assumption of smooth fracture surfaces, cubic law can accurately simulate the flow inside the fractures [19, 27]. In matrix regions close to the fractures (region 3), the Darcy equation Eq. (14) is coupled

http://dx.doi.org/10.5772/56447

with the mass conservation equation to consider the effect of the fracture on the flow of fluid in the region close to the fractures. Size of this region depends on the size of the fracture. Also fluid flow simulation in the matrix (region 1) is described as follow:

$$V_f = -K_f \nabla P_f \tag{14}$$

$$\frac{\partial}{\partial L}(k_f \frac{\partial p}{\partial L}) + Q_f + q_{ff} = 0 \tag{15}$$

where p_f is the fluid pressure inside the fractures and p is the pore fluid pressure. For the short fractures which are considered as part of the matrix porosity, the Laplace equation is solved using the following boundary conditions:

$$p_{mi} = p_{fi} \tag{16}$$

$$v_{mi} = v_{fi} \tag{17}$$

Where, p_{mi} is the matrix pressure and p_{fi} is the fracture pressure at the matrix/fracture interface and v_{mi} is the normal fluid velocity at the i^{th} fracture node along the fracture surface. Since the pressure on the matrix fracture interface is unknown, periodic boundary condition is applied in an iterative scheme to calculate the pressure values.

2.4. Reservoir scale fluid flow simulation

Fluid flow in long fractures (l>50m) is coupled with discretized element based permeability tensor in poro-thermo-elastic environment by using local-thermal non-equilibrium.

Different numerical techniques have been used to model thermo-poro-elastic phenomena in fractured porous media. To have a detailed understanding of the complex geomechanical aspects of the fractured rocks and the induced perturbation, such as thermal drawdown caused by the cold injection fluid in geothermal reservoirs an appropriate numerical technique should be used which is capable of (a) adequately applying the boundary and initial conditions and (b) accurately representing the system geometry. In order to take the aforementioned issues into account, FEM is used in the current study.

Weighted residual method and the Green's theorem are applied to discretize the mass, momentum and energy conservations equations [28]. As mentioned before, the finite element method is used in this study for the numerical simulation purpose. Therefore the state variables namely: displacement, pore pressure and temperature are defined using proper shape functions as:

$$u = N_u \bar{u} \tag{18}$$

$$p = N_p \bar{p} \tag{19}$$

$$T = N_T \bar{T} \tag{20}$$

Where N is the corresponding shape function and $\bar{u}$, $\bar{p}$ and $\bar{t}$ are the nodal values of the corresponding state variable. By applying the Galerkin's method and replacing the weighting functions by the corresponding variables' shape functions, the discretized form of the conservation equations can be written as follow [29, 30]:

$$(K + \frac{G}{3})\nabla(\nabla \cdot u) + G \cdot \nabla^2 u - \alpha \nabla p - \gamma_1 \nabla T_m = 0 \tag{21}$$

$$\alpha(\nabla \cdot \dot{u}) + \beta \dot{p} - \frac{k}{\mu}\nabla^2 p - \gamma_2 \dot{T} = 0 \tag{22}$$

$$\dot{T} + v(\nabla T) - c^T \nabla^2 T = 0 \tag{23}$$

where, K is the bulk modulus of elasticity, G is the shear modulus, γ_1 and γ_2 are the thermal expansion coefficient of the fluid and solid respectively; k is the permeability T_m is the matrix temperature, T is the fluid temperature and μ is the fluid viscosity.

3. Fracture network generation

Simulation of naturally fractured reservoirs offers significant challenges due to the lack of a methodology that can utilize field data. To date several methods have been proposed in the literature to characterize naturally fractured reservoirs. In this study a hybrid tectono-stochastic simulation is proposed to characterize a naturally fractured reservoir [31]. A finite element based model is used to simulate the tectonic event of folding and unfolding of a geological structure. A nested neuro-stochastic technique is used to develop the inter-relationship between different sources of data (seismic attributes, borehole images, core description, well logs etc.) and at the same time the sequential Gaussian approach is utilised to analyze field data along with fracture probability data. This approach has the ability to overcome commonly experienced discontinuity of the data in both horizontal and vertical directions.

http://dx.doi.org/10.5772/56447

4. Results and discussions

The proposed methodology is used to generate the discrete fracture map of the Soultz geothermal reservoir at the depth of 3650 m. the statistical parameters used to generate the discrete fracture map is shown in Table 1.

Fracture set	Azimuth			Dip				Fracture No.	Radius (m)	Transmissivity (m2\s)
Distribution Law	Mean	Half-Width	Distribu-tion Law	Mean	Half-Width	Dip Direction				
F1	Normal	2	16	normal	70	7	NW	1.3E-7	187	6E-6
F2	Normal	162	19	normal	70	7	NE	3E-9	150	6E-6
F3	Normal	42	6	normal	74	3	NW	1.76E-8	95	4E-6
F4	Normal	129	6	normal	68	3	SW	3.3E-8	112	2E-6
F5	Uniform	0	180	normal	70	9	-	1E-8	100	5E-7

Table 1. Statistical data used for the discrete fracture network generation. After [32]

The discrete fracture map, the corresponding mesh generated for the reservoir domain and the permeability tensors for each triangular element (a sample region which is cut by a fracture of length<50m) are shown in Fig. 5 (a), (b) and (c) respectively.

Also the reservoir properties used for the stimulation purpose are shown in Table 2. The reservoir is pressurized by injecting fluid through the injection well (GPK2). The pressurization was carried out over a period of 52 weeks. During the pressurization, the change in fracture width for each individual natural fracture and the resulting permeability tensor were calculated. Following stimulation of the reservoir, a flow test was carried out over a period of 14 years. During the flow test, changes in fracture apertures due to thermo-poro-elastic stresses and the consequent changes in permeability were determined. Also estimated were the thermal drawdown, produced fluid temperature and production rate of the Soultz EGS.

Results of shear dilation are presented as average percentage increase in fracture aperture (see Fig. 6). From Fig. 6, it can be seen that there exists three distinct aperture histories: 0-40 weeks, 40-50 weeks and 50 weeks and above. Until about 40 weeks, a slow but linear increase in occurrence of dilation events due to induced fluid pressure of 51.7 MPa (bottom hole) and reaches a value of about 18% (average increase in aperture). Following this time, the rate of occurrence of dilation events increases sharply until about 50 weeks, thus reaching 60% increase in average fracture aperture. After which, no significant dilation events can be observed (a plateau of events is reached). When compared with previous study [29], in which shear dilation events are estimated based on a semi-empirical model (Willis-Richards et al,

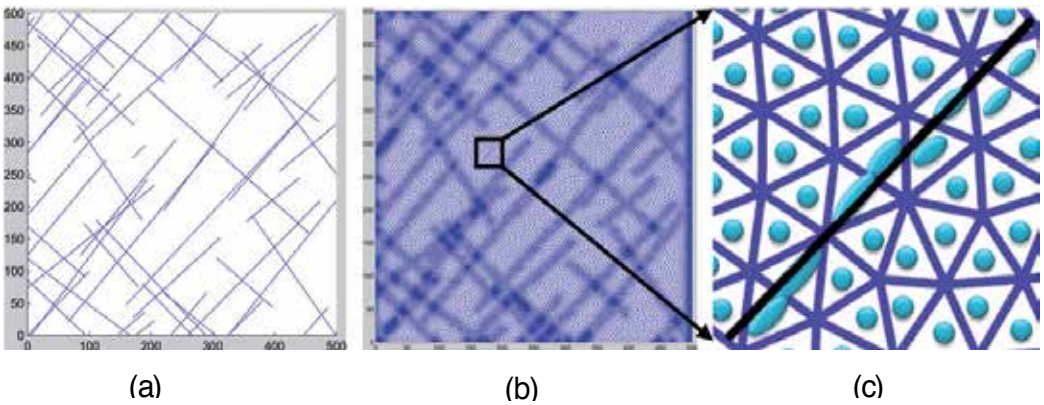

Figure 5. a) discrete fracture network at the depth of 3650 m (b) the corresponding discretization for the fractures longer than 50 m and (c) permeability tensor for a sample fracture (<50m).

1996), it can be seen that the time required to overcome the threshold stress is 40 weeks which is about 12 weeks longer than the previous studies. Also the time requires for an increase in the average fracture aperture of 58 % is about 8 weeks longer than that predicted by the previous study. During the flow test, changes in fracture apertures due to thermo-poro-elastic stresses and the consequent changes in permeability were determined. Also estimated were the thermal drawdown, produced fluid temperature and production rate of the Soultz EGS.

The locations of the dilation events during the stimulation period are shown in Fig. 7. As shown in this figure, after 40 weeks of stimulation about half of the reservoir is affected by the shear dilation and after 52 weeks of injection shear dilation happened in almost all parts of the reservoir.

Also the reservoir pressure and stress distribution profiles (see Figs. 8 and 9) show that after 40 weeks of stimulation the injected fluid pressure affected almost all of the fractures and that after 52 weeks of injection the pressure is established in all part of the reservoir domain. Similarly the x- and y component of the effective stress decreased significantly over the entire reservoir domain towards the end of the stimulation period.

After the stimulation period a numerical experiment is carried out to assess the produced matrix temperature for 14 years of cold fluid circulation. Because of the low fluid and rock matrix contact area at the early stage of production, the heat transfer and the resulting thermal drawdown is very low (see Fig 10 a). With the pass of time the fluid sweeps over a large part of the reservoir which increases thermal drawdown. At the end of the 14 years of production the average matrix temperature drops from 200 to 150°C which is quite low (drop of 50^0C) compared to previous studies (drop of 80^oC over the production period of 14 years as in [29]) under the same reservoir conditions. Also in Fig. 10 (bottom) the Log10 RMS fluid velocity profile after 1 year, 10 years and 14 years of production are presented. From the results it can be observed that during the early production period (1 year) high pore pressure is primarily

http://dx.doi.org/10.5772/56447

Rock Properties	
Young's modulus (GPa)	40
Poisson's ratio	0.25
Density (kg/m^3)	2700
Fracture basic friction angle (deg)	40
Shear dilation angle (Deg)	2.8
90% closure stress (MPa)	20
In situ mean permeability (m^2)	9.0 x 10^{-17}
Fracture properties	
Fractal Dimension, D	1.2
Fracture density (m^2/m^3)	0.12
Smallest fracture radius (m)	15
Largest fracture radius (m)	250
Fracture Permeability	0.3x10^{-15}
Stress data	
Maximum horizontal stress (MPa)	78.9
Minimum horizontal stress (MPa)	53.3
Fluid properties	
Density (kg/m^3)	1000
Viscosity (Pa s)	3 x 10^{-4}
Hydrostatic fluid pressure (MPa)	34.5
Injector pressure, stimulation (MPa)	51.7
Injector pressure, production (MPa)	44.8
Producer pressure, stimulation (MPa)	N/A
Producer pressure, production (MPa)	31.0
Other reservoir data	
Well radius (m)	0.1
Number of injection wells	1
Number of production wells	2
Reservoir depth (m)	3650

Table 2. Stress and reservoir data for strike-slip stress regime at Soutlz geothermal reservoir.

built up around the injection well and the flow of fluid is primarily through major inter-connected flow paths. With the progress of time the injection pressure advances towards the

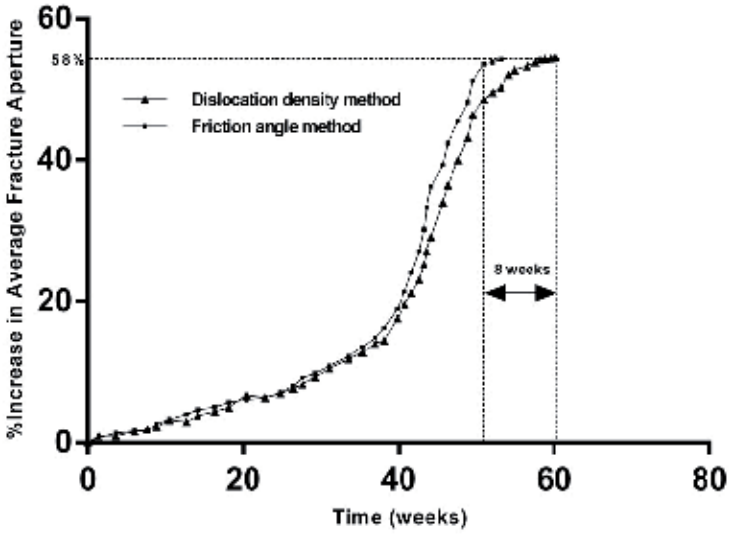

Figure 6. Comparison of Average aperture increase between the current approach and the previous study.

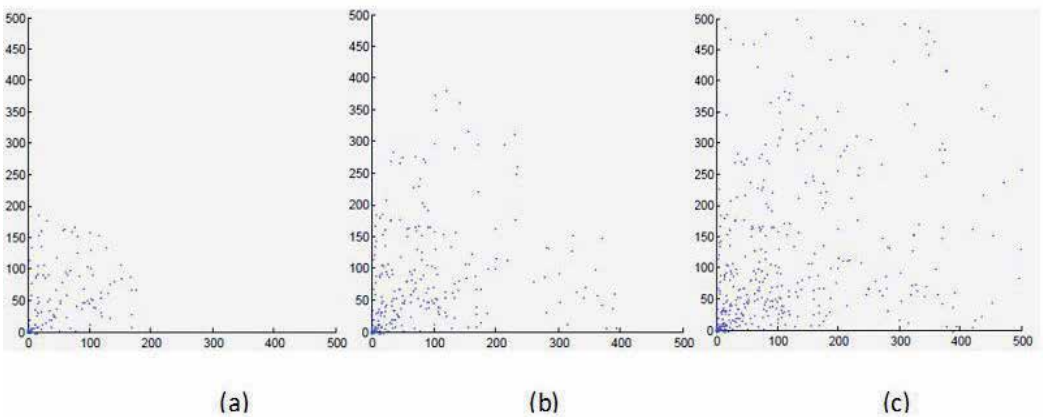

Figure 7. Location of the dilation events marked by the dots after (a) 1 week (b) 40 weeks and (c) 52 weeks of stimulation with σH = 78.9 MPa and σh = 53.3 MPa, Pinj = 51.7 MPa.

production well. After 14 years of production, the fluid sweeps through a significant part of the reservoir. Also the x- and y components of effective stress distribution of the Soultz

http://dx.doi.org/10.5772/56447

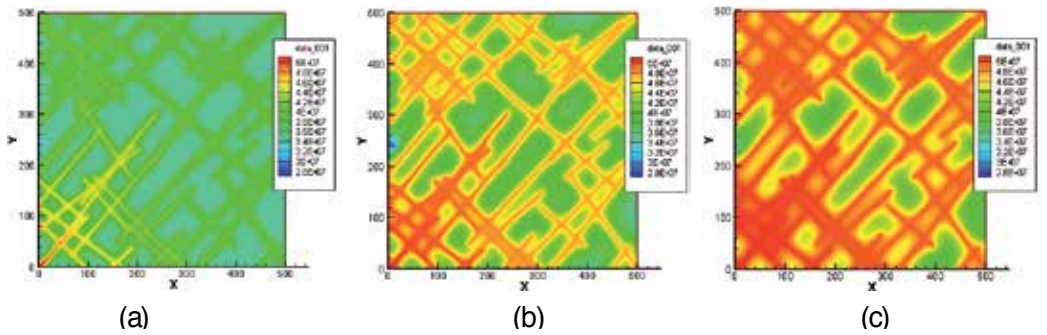

Figure 8. Pore pressure distribution of the fractured reservoir at different stimulation stages: after (a) 1 week, (b) 40 weeks and (c) 52 weeks for a strike slip stress regime with σH = 78.9 MPa and σh = 53.3 MPa, Pinj = 51.7 MPa.

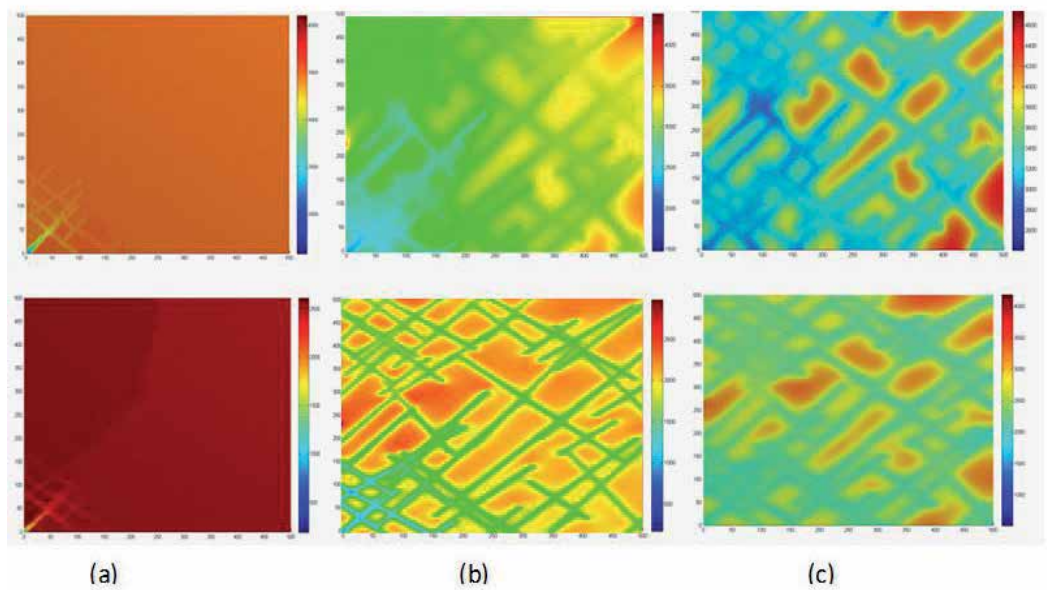

Figure 9. x (top) and y (bottom) components of effective stress after: (a) 1 week, (b) 40 weeks and (c) 52 weeks of stimulation for σH = 78. 9 MPa and σh = 53.3 MPa, P_{inj} = 51.7 MPa.

geothermal reservoir during different stages of production are shown in Fig. 11. These results show that by the end of 14 years of production the effective stresses throughout the reservoir are significantly reduced, thus allowing most fractures to open and conduct fluid. The reduction in the effective stresses is caused by the cold circulating fluid as well as thermal drawdown.

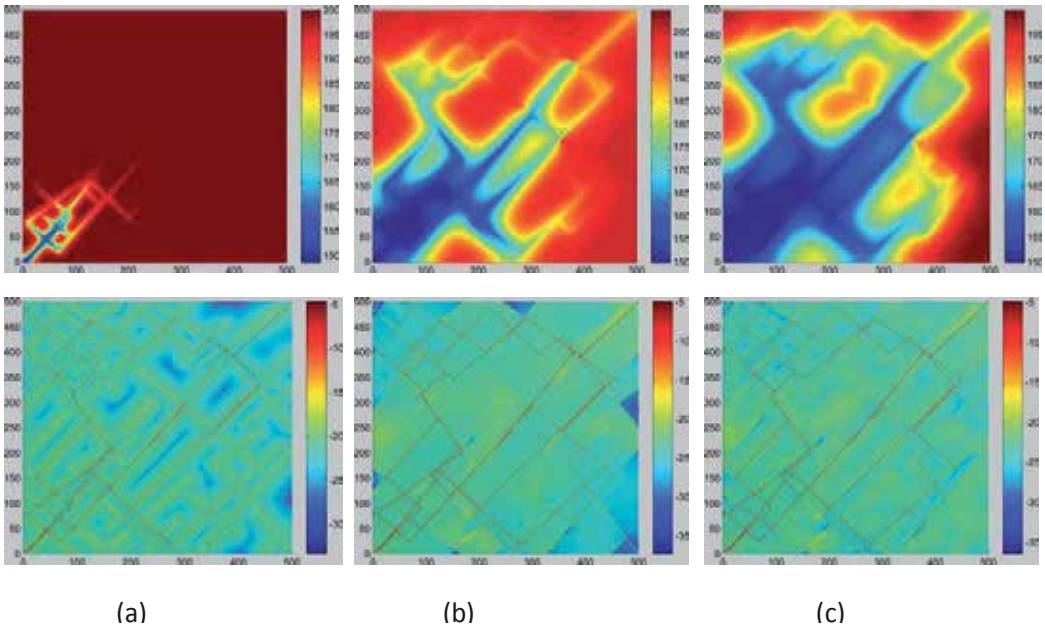

Figure 10. Reservoir temperature profile (top) and Log10RMS fluid velocity profile (bottom) after (a) 1 year (b) 10 years and (c) 14 years of production with σH = 78.9 MPa and σh = 53.3 MPa, P_{inj}=44.8 MPa and P_{prod}=31 MPa.

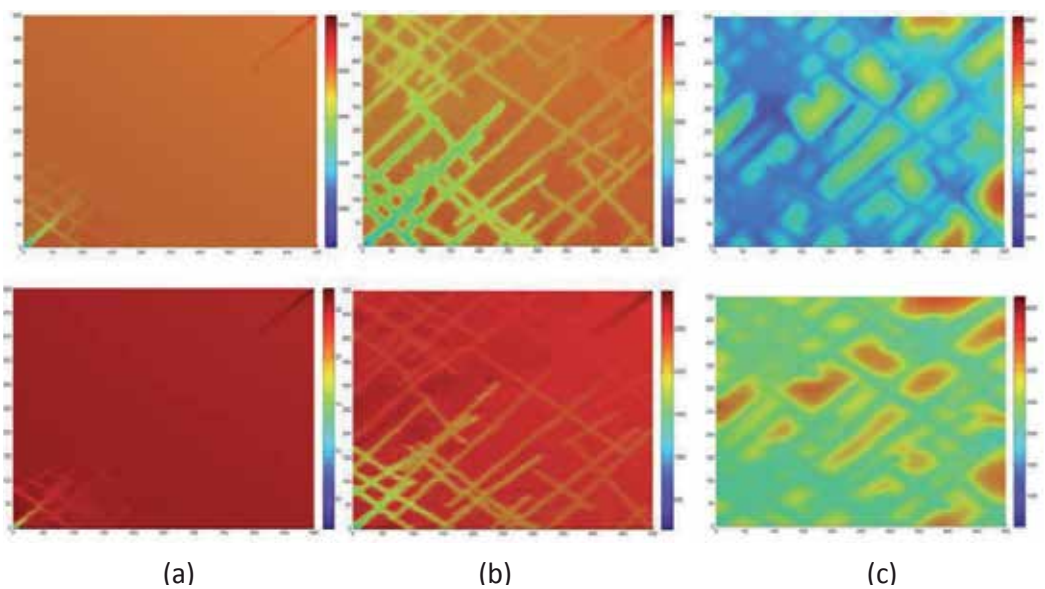

Figure 11. x (top) and y (bottom) component of effective stress after (a) 1 year (b) 10 years and (c) 14 years of production with σH = 78.9 MPa and σh = 53.3 MPa, P_{inj}=44.8 MPa and P_{prod}=31 MPa.

http://dx.doi.org/10.5772/56447

5. Conclusions

In this paper, a roughness induced shear displacement model in a poro-thermoelastic environment combined with an advanced computational technique is used to study the effects of induced fluid pressure and thermal stresses (cooling effect) on reservoir permeability and consequent increase in hot water production. It has been shown that surface roughness induced shear displacement provides a more realistic prediction of residual fracture aperture. These results agree well with the experience of existing EGS trials around the world. An average increase in aperture due to fluid induced shear dilation has been found to be lower and time required to obtain a maximum stimulated volume is greater. Results of this study are in consistent with that of previous studies: for every geothermal system there exists an optimum injection schedule (injection pressure and duration). Any further increases in stimulation effort, i.e. stimulation time for a given stimulation pressure, does not provide additional permeability enhancement.

Author details

Nima Gholizadeh Doonechaly[1], Sheik S. Rahman[1*] and Andrei Kotousov[2]

*Address all correspondence to: sheik.rahman@unsw.edu.au

1 School of Petroleum Engineering, University of New South Wales, Sydney, Australia

2 School of Mechanical Engineering, the University of Adelaide, South Australia, Australia

References

[1] Roshan, H. and S.S. Rahman, Effects of Ion Advection and Thermal Convection on Pore Pressure Changes in High Permeable Chemically Active Shale Formations. Petroleum Science and Technology, 2013. 31(7): p. 727-737.

[2] Lockner, D.A., J.B. Walsh, and J.D. Byerlee, Changes in seismic velocity and attenuation during deformation of granite. Journal of Geophysical Research, 1977. 82(33): p. 5374-5378.

[3] Hast, N., Limits of stress measurements in the Earth's crust. Rock mechanics, 1979. 11(3): p. 143-150.

[4] Solberg, P., D. Lockner, and J.D. Byerlee, Hydraulic fracturing in granite under geothermal conditions. International Journal of Rock Mechanics and Mining Sciences & Geomechanics Abstracts, 1980. 17(1): p. 25-33.

[5] Rahman, M.K., M.M. Hossain, and S.S. Rahman, An analytical method for mixed-mode propagation of pressurized fractures in remotely compressed rocks. International Journal of Fracture, 2000. 103(3): p. 243-258.

[6] Kotousov, A., L. Bortolan Neto, and S. Rahman, Theoretical model for roughness induced opening of cracks subjected to compression and shear loading. International Journal of Fracture, 2011. 172(1): p. 9-18.

[7] Heidinger, P., J. Dornstädter, and A. Fabritius, HDR economic modelling: HDRec software. Geothermics, 2006. 35(5–6): p. 683-710.

[8] Blumenthal, M., et al., Hydraulic model of the deep reservoir quantifying the multi-well tracer test.. EHDRA Scientific Conference, Soultz-sous-Forets, 2007.

[9] Barton, N. and V. Choubey, The shear strength of rock joints in theory and practice. Rock mechanics, 1977. 10(1-2): p. 1-54.

[10] Barton, N., S. Bandis, and K. Bakhtar, Strength, deformation and conductivity coupling of rock joints. International Journal of Rock Mechanics and Mining Sciences & Geomechanics Abstracts, 1985. 22(3): p. 121-140.

[11] Bandis, S., Experimental studies of scale effects on shear strength and deformation of rock joints. PhD Thesis, 1980.

[12] Piggott, A.R. and D. Elsworth, A Hydromechanical Representation of Rock Fractures, 1991, A.A. Balkema. Permission to Distribute - American Rock Mechanics Association.

[13] Olsson, W.A. and S.R. Brown, Hydromechanical response of a fracture undergoing compression and shear. International Journal of Rock Mechanics and Mining Sciences & Geomechanics Abstracts, 1993. 30(7): p. 845-851.

[14] Willis-Richards, J., K. Watanabe, and H. Takahashi, Progress toward a stochastic rock mechanics model of engineered geothermal systems. J. Geophys. Res., 1996. 101(B8): p. 17481-17496.

[15] Rahman, M.K., M.M. Hossain, and S.S. Rahman, A shear-dilation-based model for evaluation of hydraulically stimulated naturally fractured reservoirs. International Journal for Numerical and Analytical Methods in Geomechanics, 2002. 26(5): p. 469-497.

[16] Zhang, X., R.G. Jeffrey, and E. Detournay, Propagation of a hydraulic fracture parallel to a free surface. International Journal for Numerical and Analytical Methods in Geomechanics, 2005. 29(13): p. 1317-1340.

[17] Gangi, A.F., Variation of whole and fractured porous rock permeability with confining pressure. International Journal of Rock Mechanics and Mining Sciences & Geomechanics Abstracts, 1978. 15(5): p. 249-257.

http://dx.doi.org/10.5772/56447

[18] Snow, D.T., Anisotropie Permeability of Fractured Media. Water Resources Research, 1969. 5(6): p. 1273-1289.

[19] Long, J.C.S., et al., Porous media equivalents for networks of discontinuous fractures. Water Resources Research, 1982. 18(3): p. 645-658.

[20] Baumgartner, J., P.L. Moore, and A. Gtrard, Drilling of Hot and Fractured Granite at Soultz-sous-Forgts (France). Proceedings of the World Geothermal Congress, FIorence, Italy,International Geothermal Association,, 1995. 4: p. 2657-2663.

[21] Rasmussen, T.C., J. Yeh, and D. Evans, Effect of variable fracture permeability/matrix permeability ratios on three-dimensional fractured rock hydraulic conductivity. Proceedings of the Conference on Geostatistical, Sensitivity, and Uncertainty Methods for Ground-Water Flow and Radionuclide Transport Modeling, San Francisco, California, September 1987, B. E. Buxton, Batelle Press, Columbus, OH, 1987, 337, 1987.

[22] Lough, M.F., S.H. Lee, and J. Kamath, A New Method To Calculate Effective Permeability of Gridblocks Used in the Simulation of Naturally Fractured Reservoirs. SPE Reservoir Engineering, 1997. 12(3): p. 219-224.

[23] Chen, M., M. Bai, and J.C. Roegiers, Permeability Tensors of Anisotropic Fracture Networks. Mathematical Geology, 1999. 31(4): p. 335-373.

[24] Lee, S.H., M.F. Lough, and C.L. Jensen, Hierarchical modeling of flow in naturally fractured formations with multiple length scales. Water Resources Research, 2001. 37(3): p. 443-455.

[25] Teimoori, A., et al., Effective Permeability Calculation Using Boundary Element Method in Naturally Fractured Reservoirs. Petroleum Science and Technology, 2005. 23(5-6): p. 693-709.

[26] Fahad, M., S.S. Rahman, and Y. Cinar, A Numerical and Experimental Procedure to Estimate Grid Based Effective Permeability Tensor for Geothermal Reservoirs. Geothermal Resources Council Transactions, 2011.

[27] Rasmussen, M.L. and F. Civan, Full, Short-, and Long-Time Analytical Solutions for Hindered Matrix-Fracture Transfer Models of Naturally Fractured Petroleum Reservoirs, in SPE Production and Operations Symposium2003, Society of Petroleum Engineers: Oklahoma City, Oklahoma.

[28] Bathe, K.J., Finite element procedures. 1996: Prentice Hall.

[29] Koh, J., H. Roshan, and S.S. Rahman, A numerical study on the long term thermo-poroelastic effects of cold water injection into naturally fractured geothermal reservoirs. Computers and Geotechnics, 2011. 38(5): p. 669-682.

[30] Gholizadeh Doonechaly, N., S.S. Rahman, and A. Kotousov, An Innovative Stimulation Technology for Permeability Enhancement in Enhanced Geothermal System--

Fully Coupled Thermo-Poroelastic Numerical Approach. 36th Geothermal Resources Council Transactions, 2012.

[31] Gholizadeh Doonechaly, N. and S.S. Rahman, 3D hybrid tectono-stochastic modeling of naturally fractured reservoir: Application of finite element method and stochastic simulation technique. Tectonophysics, 2012. 541–543(0): p. 43-56.

[32] Genter, A., et al., Contribution of the exploration of deep crystalline fractured reservoir of Soultz to the knowledge of enhanced geothermal systems (EGS). Comptes Rendus Geoscience, 2010. 342(7–8): p. 502-516.

Chapter 28

Fracture Network Connectivity — A Key To Hydraulic Fracturing Effectiveness and Microseismicity Generation

F. Zhang, N. Nagel, B. Lee and M. Sanchez-Nagel

Additional information is available at the end of the chapter

http://dx.doi.org/10.5772/56302

Abstract

In this work, the effect of fracture network connectivity on hydraulic fracturing effectiveness was investigated using a discrete element numerical model. The simulation results show that natural fracture density can significantly affect the hydraulic fracturing effectiveness, which was characterized by either the ratio of stimulated natural fracture area to hydraulic fracture area or the leakoff ratio. The sparse DFN cases showed a flat microseismic distribution zone with few events, while the dense DFN cases showed a complex microseismic map which indicated significant interaction between the hydraulic fracture and natural fractures. Further, it was found that the initial natural fracture aperture affected the hydraulic fracturing effectiveness more for the dense natural fracture case than for the sparse (less dense) case. Overall, this work shows that fracture network connectivity plays a critical role in hydraulic fracturing effectiveness, which, in-turn, affects treating pressures, the created microseismicity and corresponding stimulated volume, and well production.

1. Introduction

The extremely low permeability of the common shale plays means that simple, bi-planar hydraulic fractures (HF) do not create enough surface area to make economic wells and that stimulation of the natural fracture system is critical [1]. Numerous field microseismic data sets have shown that extreme fracture complexity may result from the interaction between a created hydraulic fracture and the pre-existing fracture network [2, 3]. Consequently, operators will often alter the stimulation design, by changing injection rate, viscosity, or other parameters, in order to improve the effectiveness of the stimulation in unconventional shale plays.

However, these design changes offer only a limited control on improving the stimulation of natural fractures because of a lack of understanding of the fundamental characteristics, behavior, and connectivity of the natural fracture network.

The connectivity of the fracture network, for example, determines the overall hydraulic diffusivity of the formation and is a key to the resulting 'complexity' from a hydraulic fracture stimulation. A highly connected fracture network will allow more fluid leakoff into the rock mass and render pressure communication over large distances, whereas a partially or sparsely connected fracture network will favor the propagation of a new hydraulic fracture and may exhibit pressure isolation between very closely spaced hydraulic fractures. The intricacy of fluid flow in fractured formation is mainly due to the complex geometries, patterns, and heterogeneity of the fracture network. The fracture network connectivity, therefore, has been shown to be a critical factor which affects treating pressures, the created microseismicity and corresponding SRV (Stimulated Rock Volume), and production.

Numerous numerical modeling efforts have been conducted in order to understand the process of hydraulic fracture (HF) interaction with a complex natural fracture network [4, 5, 6]. However, relatively few works have focused on understanding the role of natural fracture network connectivity and its impact on the effectiveness of hydraulic fracturing of shale reservoirs and associated microseismicity generation.

In this paper, a discussion of fracture network connectivity and how it is utilized in developing a discrete fracture network (DFN) is presented, which is then incorporated into a discrete element numerical model (DEM). The propagation of a HF in the fractured rock mass was then studied using the DEM, which allowed for fully coupled, hydro-mechanical simulations, including the generation of synthetic microseismicity. Following previous work [7, 8, 9, 10] from the authors on parametric studies to analyze the influence of the mechanical and flow properties of the DFN and matrix on HF propagation, the influence of the DFN fracture network connectivity was analyzed in this work using common stimulation metrics such as SRV. The corresponding microseismic response was also calculated from the simulation results and related to the effective SRV. The results show not only the critical role that the DFN must play in resource evaluations, but also in completion design and stimulation optimization.

2. Fracture network connectivity and DFN realization

Fracture network connectivity is determined by many statistical characteristics, among them, fracture shape, fracture size distribution, fracture density (area of fracture per unit volume), orientation distribution, and aperture size distribution. The combinations of these statistical characteristics that describe the geometrical properties of a DFN define the macro-scale connectivity and directional flow preference of the DFN, and thus, are essential for the fluid transport characterization of an unconventional reservoir.

In this work, focus was placed on the effects of two statistical fracture characteristics, fracture density and initial aperture both individually and in combination, on hydraulic fracturing

http://dx.doi.org/10.5772/56302

effectiveness and microseismicity generation. For the study, a DFN generator was developed that was capable of creating a fracture network that satisfied the assigned input statistical characteristics and allowed for the quantitative variation of network connectivity.

As shown in Figure 1, two DFN configurations were realized, which represent a sparse DFN and a dense DFN, respectively. The sparse DFN had 191 fractures while the dense DFN had 482 fractures, or about 2.5 times more than the sparse DFN. The fractures were created in the common disk shape with a dip angle of 90° but either a 60° or 150° dip direction in order to construct two orthogonal fracture sets. The P10 (the number of fractures along a line divided by the length of the line) for the sparse DFN and dense DFN was 0.079 m^{-1} and 0.28 m^{-1}, respectively. The P32 (the sum of the areas of the fractures contained in a named volume divided by the same volume) for the sparse DFN and dense DFN was 0.031 m^2/m^3 and 0.075 m^2/m^3, respectively.

In addition to DFN density, the effect of the initial DFN aperture was studied by considering two different values of initial aperture for the DFN fractures. In the first case, it was assumed that the initial aperture of the DFN fractures was equal to 0.1 mm. In the second case, it was assumed that the DFN fracture aperture was 1.5 times greater and equal to 0.15 mm.

The goal of this study was to investigate the effects of hydraulic fracturing in shale formations with different levels of DFN connectivity. It was assumed that the DFN fractures were static, meaning that, with the exception of the main hydraulic fracture itself, the process of fracture growth and propagation was not considered within the simulations.

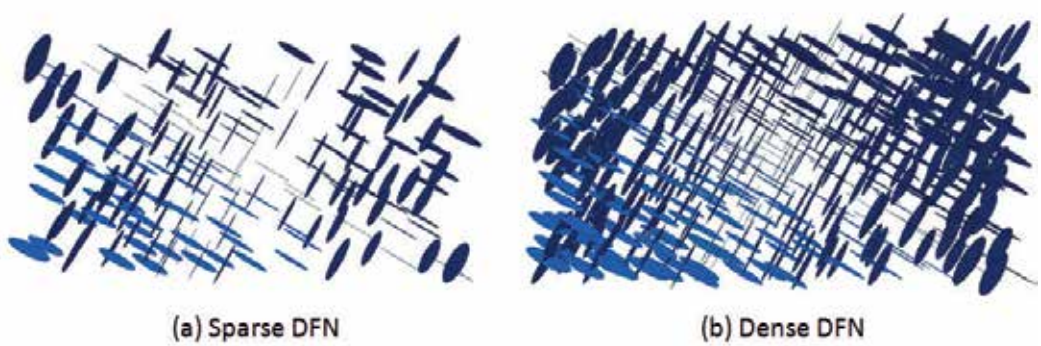

Figure 1. Plan view of two DFN realizations. A) Sparse DFN with 191 fractures; and B) Dense DFN with 482 fractures.

3. Numerical simulations

3.1. *3DEC* hydraulic fracturing modeling capabilities

The numerical code used in the simulations, *3DEC*, is a three dimensional distinct element method for discontinuum modeling [11]. It can simulate the response of discontinuous media,

such as a jointed rock mass, subjected to either static or dynamic loading, which includes the simulation of fluid injection during a hydraulic fracture treatment. *3DEC*'s ability to handle large block displacements makes it amenable to the simulation of hydraulic fracture propagation, fracture opening (both hydraulic fracture and natural fractures), and the rotation of individual blocks leading to fracture connections or pinching. Further, *3DEC* includes the ability to model steady-state or transient-fracture fluid flow, where the flow logic includes a system of flow planes, flow pipes and flow knots. While most of the existing commercial hydraulic fracture simulators are based upon a number of analytical assumptions, or limit the simulated fractures to be smooth, bi-planar cracks, *3DEC* is capable of explicitly modeling the mechanical response of a fracture network to fluid injection as well as the interaction of a created hydraulic fracture (the HF plane needs to be pre-defined) with the existing natural fractures.

3.2. *3DEC* model setup

The *3DEC* simulation domain consisted of two parts: an inner core domain with the population of the DFN and an outer boundary domain, which extended to twice of the size of the core domain in order to minimize boundary effects. To port the created natural fractures to *3DEC*, a procedure was developed to explicitly represent the generated DFN in the geomechanical model. For each DFN fracture, a search was performed to identify those *3DEC* blocks that were intersected by the given fracture. The identified blocks were then cut through into two blocks by the fracture plane. Since the newly created plane between blocks might only have part of its area belonging to the given fracture (if the natural fracture did not fully cut the blocks), different fracture material properties were assigned to the portion of the newly created plane that fell within the geological fractures than to the unfractured portion that fell outside the geological fractures.

Figure 2 shows the core simulation domain discretized by the dense DFN. Individual blocks are shown in variable color, while the plane between two blocks is a possible natural fracture. The size of the inner domain was 400×200×100 m. The directions of the three principal stresses are shown in Figure 2, which are coincident with the three axes x, y and z.

For all the simulations, the maximum horizontal stress (SHmax) was 55 MPa, the minimum horizontal stress (Shmin) was 50 MPa, and the vertical stress (Sv) was 60 MPa. The initial pore pressure was set to 45 MPa. The Young's modulus of the rock mass was set to 30.0 GPa and Poisson's ratio was set to 0.25. The injection point was located in the center of the domain along the predefined hydraulic fracture plane (the plane of y=0), which was parallel to SHmax. The injection rate was 0.05 m^3/s and the fluid viscosity was 0.0015 Pa s. It was assumed that fluid flow only occurred in either the DFN or HF planes and that there was no fluid flow into the rock matrix during the simulations.

3.3. Simulation results

In this study, four simulation cases, consisting of two DFN configurations (i.e., the dense DFN and sparse DFN) and two initial DFN apertures (i.e., 0.1 mm and 0.15 mm) were analyzed.

http://dx.doi.org/10.5772/56302

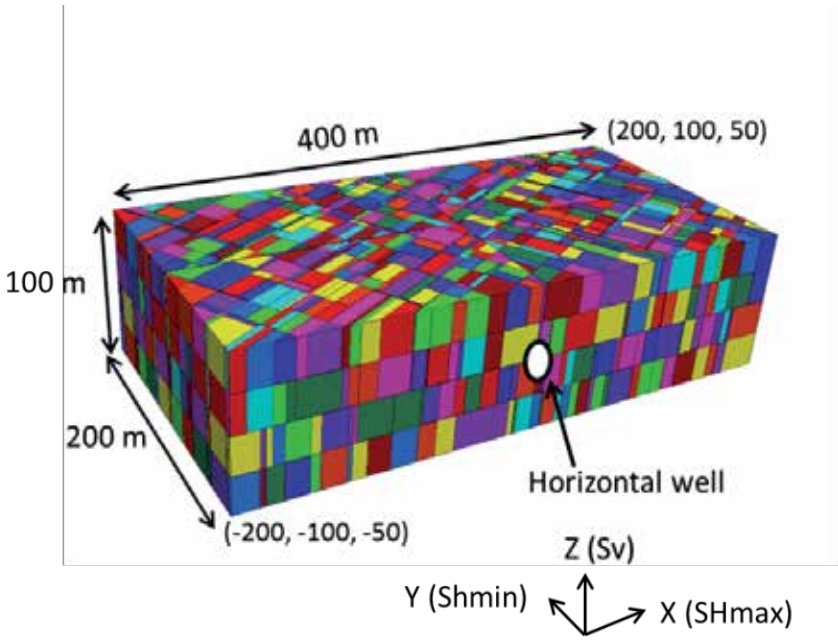

Figure 2. The core domain of the numerical model discretized by the dense DFN. Blocks are distinguished by colors. The plane of y=0 is the HF plane.

Figure 3 shows a plan view of the contours of fracture pressure distribution at the XY plane of z=0 m after 900 s of injection time for the four tests.

The fracture pressure contour plot suggests two major observations. With the same initial DFN aperture, the case with the dense DFN resulted in significantly more stimulated DFN area and less stimulated HF area than the case with the sparse DFN. In addition, with the same DFN configuration, the case with 0.15 mm initial aperture resulted in more stimulated DFN area and less stimulated HF area than the case with 0.1 mm initial aperture. These results are also confirmed by the shorter hydraulic fracture lengths in the dense DFN simulations.

These qualitative conclusions are as expected. Since hydraulic fracturing represents, essentially, the release (injection) of hydraulic energy into the formation, the injected fluid will follow the least resistive path. For the dense DFN, it was easier for fluid to enter the natural fractures than it was for the fluid to propagate a hydraulic fracture.

The synthetic microseismic events during the injection can be approximated based on the magnitude of plastic slip. Figure 4 plots the synthetic microseismic moment magnitudes for the sparse and dense DFN with the same initial aperture (0.1 mm) after 900 s of injection time. The events that clustered based on their spatial and temporal proximity were colored by the occurring time and sized by the microseismic moment magnitude. All events were projected onto the XY plane with z=0 m and the XZ plane with y=0 m (HF plane). Figure 4 shows that the sparse DFN case had fewer microseismic events than the dense DFN case. The complexity of microseismic events for the dense DFN case was consistent with field observations and

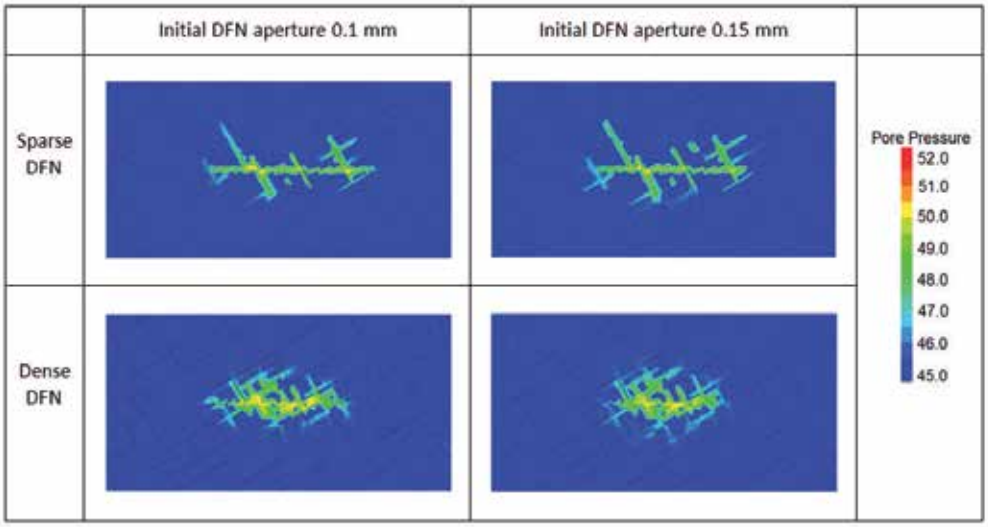

Figure 3. Plan view of contours of fracture pressure distribution at the XY plane of z=0 m after a 900 s injection time for the cases of sparse and dense DFN realizations with two initial DFN apertures.

suggests an intensive interaction between the created hydraulic fracture and the natural fractures.

The two qualitative observations from Figure 3 were further proved quantitatively by tracking the evolution of stimulated DFN area and HF area. As there is no precise criteria for defining the stimulated area, a criteria based on fracture pressure change was employed in this work. The area of the DFN or HF planes having a fracture pressure increase of 0.5 MPa or 1 MPa above the initial fracture pressure was considered as the stimulated area.

Figure 5 shows the quantitative evolution of the stimulated DFN area with a fracture pressure increase greater than 0.5 MPa and 1 MPa for the four cases shown in Figure 3. Figure 5 shows that, with the same DFN configuration, the case with a 0.15 mm initial aperture produced about twice the stimulated DFN area as the case with a 0.1 mm initial aperture. However, with the same initial aperture, the case with the dense DFN produced only slightly more stimulated DFN area than the case with a sparse DFN. Figure 5 also shows that the effect of choosing a different fracture pressure increase threshold to define the stimulated DFN areas is more obvious for the dense DFN case.

Figure 6 plots the evolution of the stimulated HF area with a fracture pressure increase greater than 0.5 MPa and 1 MPa for the four cases shown in Figure 3. Figure 6 shows that, for the sparse DFN configuration, the case with a 0.15 mm initial aperture produced only slightly less stimulated HF area than the case with a 0.1 mm initial aperture, whereas for the dense DFN configuration, there was nearly a 20% reduction in stimulated HF area for the 0.15 mm initial aperture over the 0.1 initial aperture case. Comparing the same initial aperture cases, the cases with the dense DFN produced much less stimulated HF area than the cases with a sparse DFN.

http://dx.doi.org/10.5772/56302

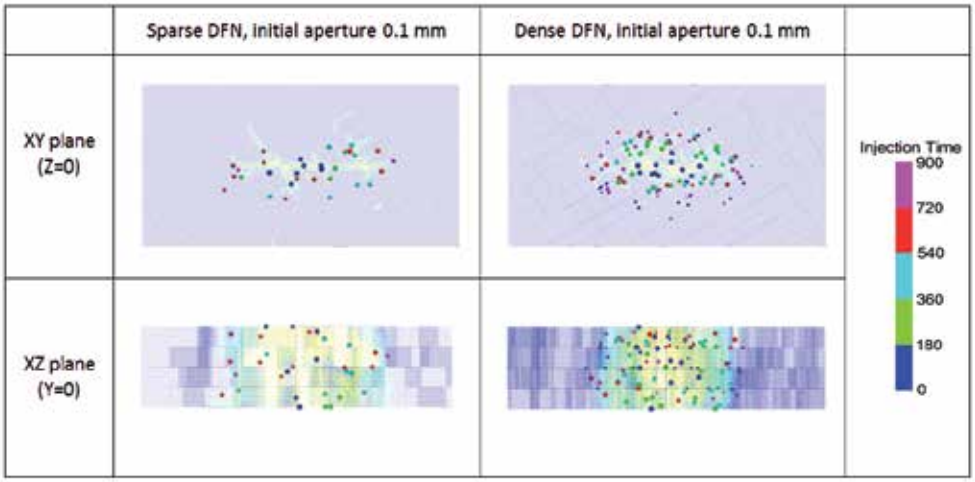

Figure 4. Synthetic microseismic events for the sparse and dense DFN with the same initial aperture 0.1 mm after 900 s of injection time. The synthetic microseismic events are colored by the occurring time and sized by moment magnitude and then projected in the XY plane with z=0 m and the XZ plane with y=0 m (HF plane).

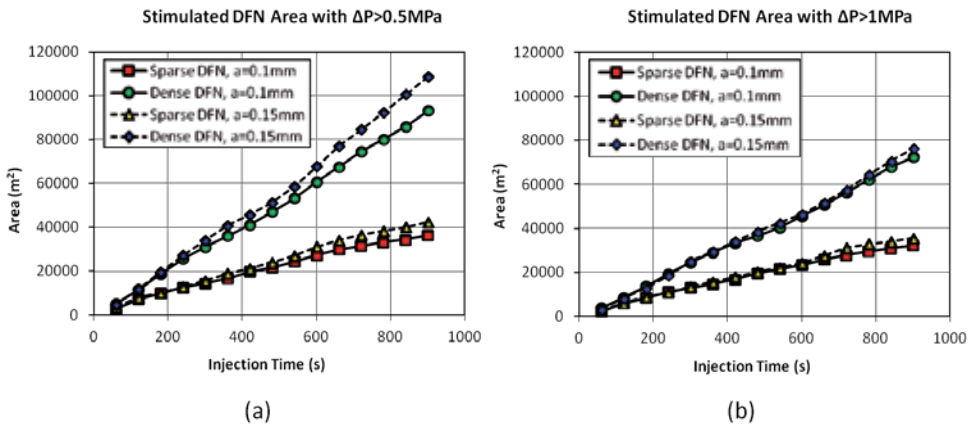

Figure 5. Stimulated DFN area with a fracture pressure increase greater than A) 0.5 MPa and B) 1 MPa for the four cases shown in Figure 3.

Figure 6 also shows that the stimulated HF areas for all four cases using the 0.5 MPa fracture pressure increase criteria were only slightly larger than the cases when using the 1.0 MPa fracture pressure increase criteria.

It may be concluded from the above analysis that, in terms of the stimulated DFN area, the initial DFN aperture is a more sensitive parameter than the DFN density. On the contrary, in terms of the stimulated HF areas, the DFN density seems to be a more sensitive parameter than the initial DFN aperture.

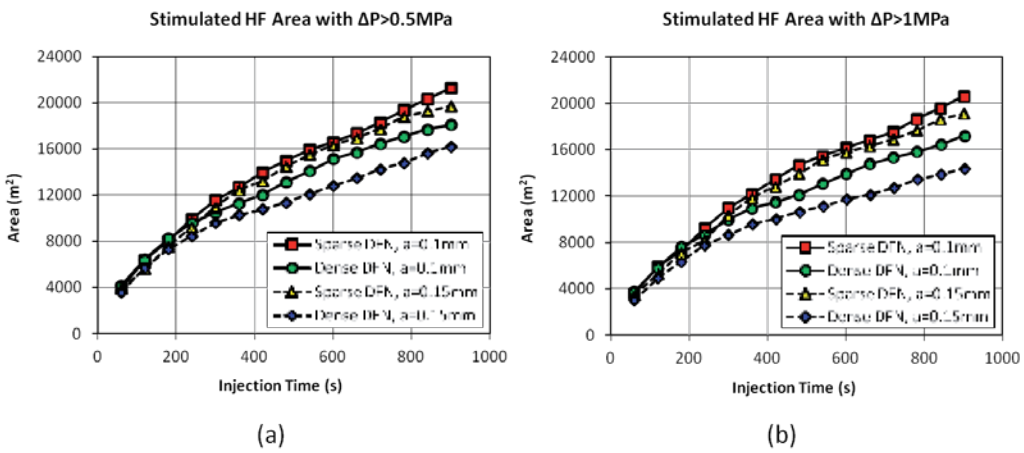

Figure 6. Stimulated HF area with a fracture pressure increase greater than A) 0.5 MPa and B) 1 MPa for the four cases shown in Figure 3.

The overall effect of fracture network connectivity on hydraulic fracturing effectiveness can also be characterized by the ratio of stimulated DFN area to stimulated HF area. Figure 7 plots the ratio of stimulated DFN area to stimulated HF area with a fracture pressure increase of 0.5 MPa and 1 MPa for the four cases shown in Figure 3. It can be seen that a dense DFN created a much higher ratio of stimulated DFN area to stimulated HF area than did a sparse DFN for similar initial apertures. However, the effect of initial DFN aperture was more evident for the dense DFN configuration than for the sparse DFN configuration. Meanwhile, the effect of choosing a different fracture pressure increase threshold for the stimulated areas was more obvious in the dense DFN configuration than for the sparse DFN configuration.

Another parameter to evaluate the overall effect of fracture network connectivity on hydraulic fracturing effectiveness is the leakoff ratio, which is defined as the ratio of fluid volume in the DFN over the total fluid volume injected into the model. Figure 8 shows the leakoff ratio for the four cases shown in Figure 3. Very similar with the analysis for the ratio of stimulated DFN area to stimulated HF area, DFN density is shown to significantly affect the leakoff ratio for both initial aperture cases, while the initial DFN aperture is seen to affect the dense DFN more than the sparse DFN configuration.

http://dx.doi.org/10.5772/56302

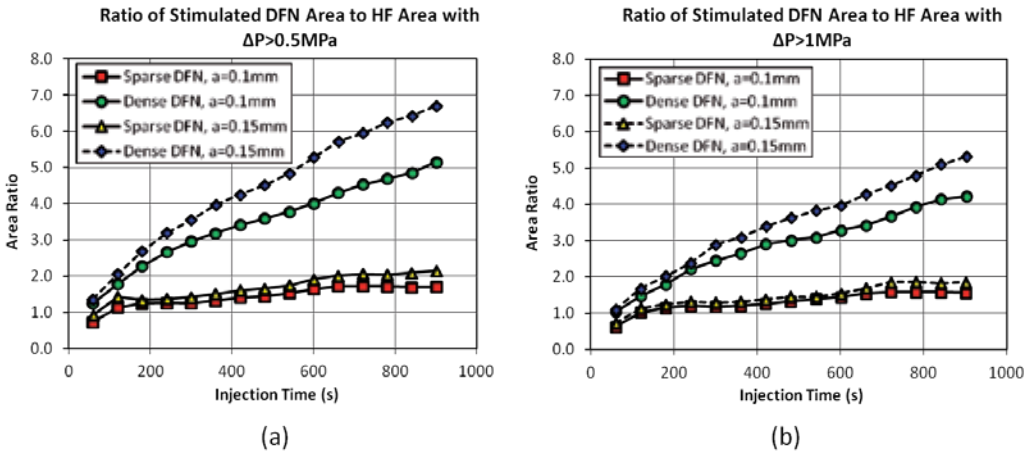

Figure 7. Ratio of stimulated DFN area to stimulated HF area with a fracture pressure increase greater than A) 0.5 MPa and B) 1 MPa for the four cases shown in Figure 3.

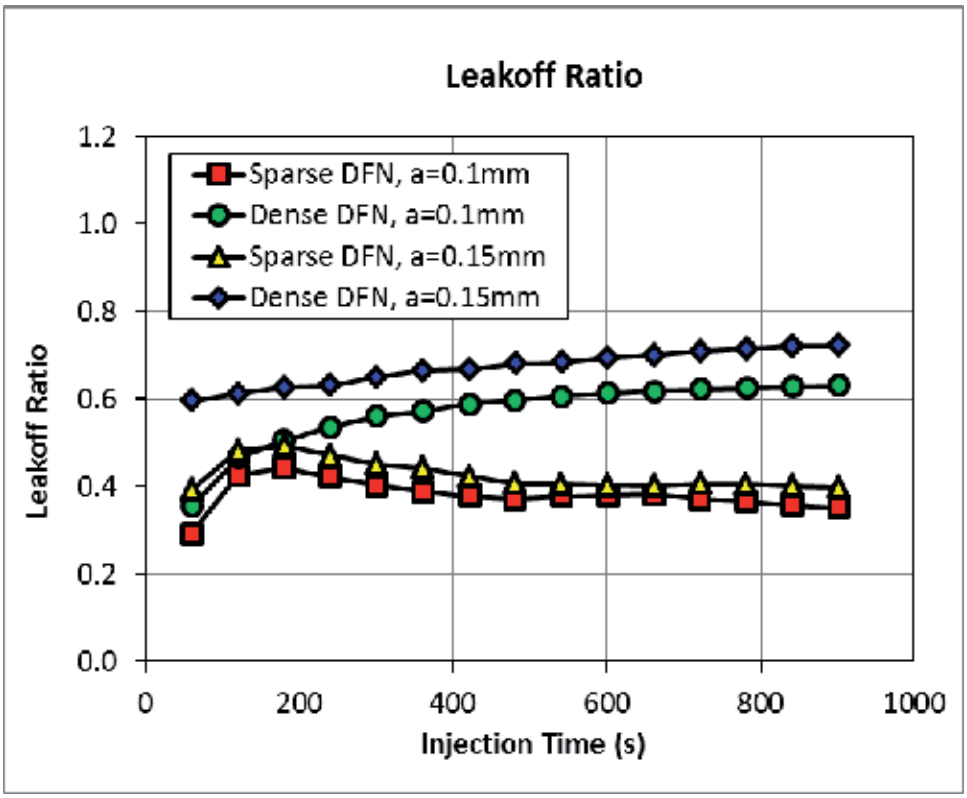

Figure 8. Leakoff ratio for the four cases shown in Figure 3.

Figure 9 and Figure 10 show, separately, the average DFN aperture and average HF aperture for the four cases shown in Figure 3. The average DFN aperture for all cases increased only slightly during the injection, though it is worth mentioning that even though the natural fractures were only slightly opened, the leakoff ratio for the dense DFN cases reached about 50% or more.

Relatively, the sparse DFN case showed a slightly greater increase of average DFN aperture than the dense DFN case with the same initial DFN aperture. As expected, the average HF apertures for all cases were several times larger than the average DFN apertures. In addition, as shown in Figure 9, the sparse DFN case had a much greater increase (more than double) in the average HF aperture than the dense DFN case with the same initial DFN aperture.

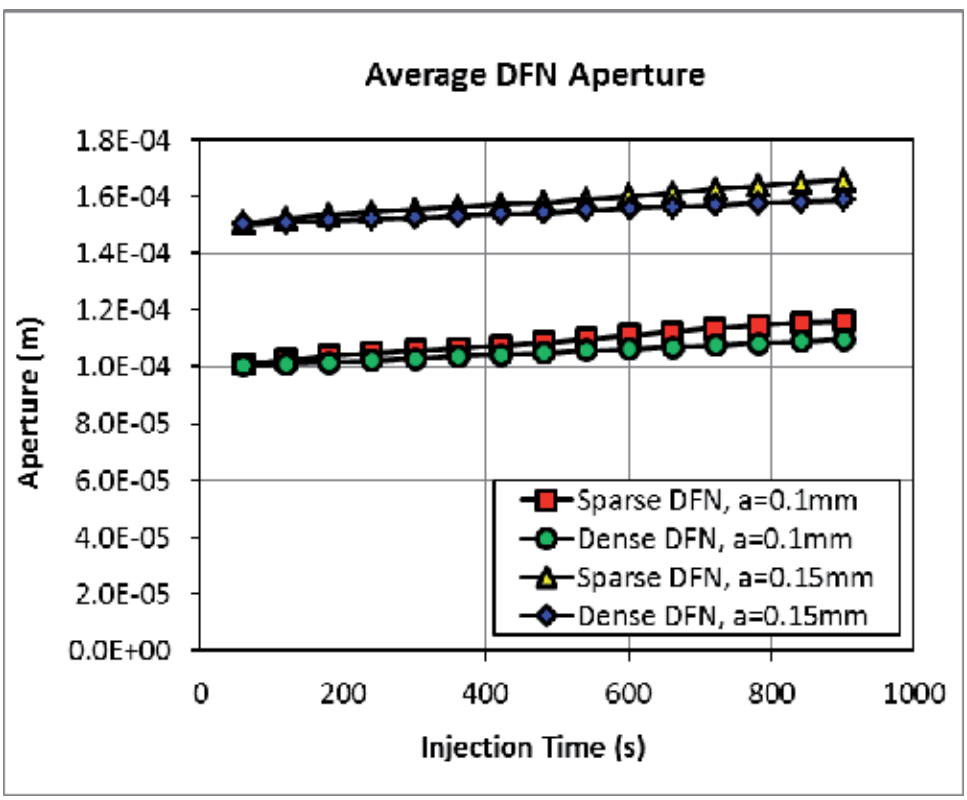

Figure 9. Average DFN aperture for the four cases shown in Figure 3.

http://dx.doi.org/10.5772/56302

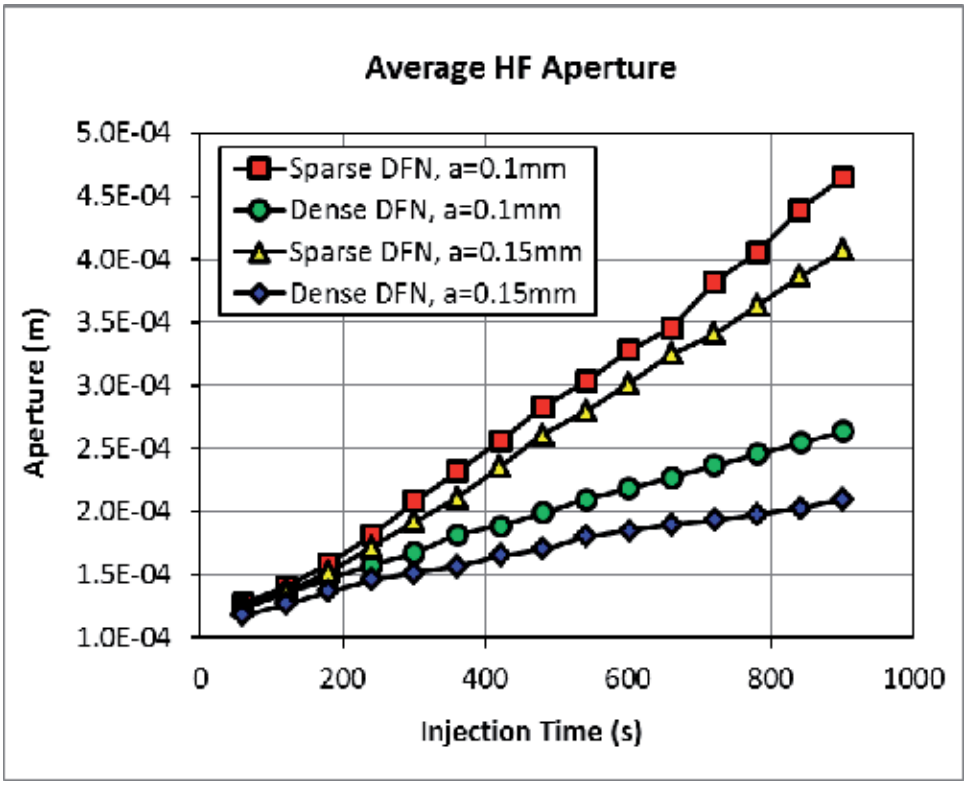

Figure 10. Average HF aperture for the four cases shown in Figure 3.

4. Conclusions

In this work, the effect of fracture network connectivity on hydraulic fracturing effectiveness (extent of stimulation of the natural fractures) was investigated using a discrete element numerical model. Four simulation cases were evaluated using two DFN configurations (i.e., a dense DFN and a sparse DFN) and two initial DFN apertures (i.e., 0.1 mm and 0.15 mm). The main conclusions from this study are summarized in the following points:

- DFN density significantly affected hydraulic fracturing effectiveness, characterized by either the ratio of stimulated DFN area to stimulated HF area or the leakoff ratio, for both initial apertures considered. Further, the initial DFN aperture affected the hydraulic fracturing effectiveness of the dense DFN configuration more than the sparse DFN configuration.
- The sparse DFN cases showed a flat microseismic distribution zone with few events while the dense DFN cases showed a complex microseismic map that indicated the intensive interaction between hydraulic fracture and the natural fractures.

- For all cases, the average DFN aperture increased only slightly during the injection while the average HF aperture increased significantly and was several times larger than the average DFN apertures. Relatively, the sparse DFN case showed a greater increase of average DFN aperture and average HF aperture than the dense DFN case for the same initial DFN aperture.
- This work suggests that fracture network connectivity plays a critical role in hydraulic fracturing effectiveness for unconventional shale developments, and fracture connectivity will play a significant role in optimizing treating pressures, the created microseismicity and corresponding SRV, and well production.

Author details

F. Zhang*, N. Nagel, B. Lee and M. Sanchez-Nagel

*Address all correspondence to: fzhang@itascahouston.com

Itasca Houston, Inc., USA

References

[1] G. E. King, "Thirty years of gas shale fracturing: What have we learned?," in *SPE Annual Technical Conference and Exhibition*, Florence, Italy, 2010.

[2] C. Cipolla, M. Mack and S. Maxwell, "Reducing Exploration and Appraisal Risk in Low-Permeability Reservoirs Using Microseismic Fracture Mapping," in *Canadian Unconventional Resources and International Petroleum Conference*, Calgary, Alberta, Canada, 2010.

[3] N. R. Warpinski, "Integrating Microseismic Monitoring With Well Completions, Reservoir Behavior, and Rock Mechanics," in *SPE Tight Gas Completions Conference*, San Antonio, Texas, USA, 2009.

[4] S. F. Rogers, D. Elmo and W. S. Dershowitz, "Understanding Hydraulic Fracturing Geometry and Interactions in Pre-Conditioning through DFN Numerical Modeling," in *45th US Rock Mechanics / Geomechanics Symposium*, San Francisco, CA, 2011.

[5] W. S. Dershowitz, M. G. Cottrell, D. H. Lim and T. W. Doe, "A discrete fracture network approach for evaluation of hydraulic fracturing stimulation of naturally fractured reservoirs," in *44th US Rock Mechanics Symposium and 5th U.S.-Canada Rock Mechanics Symposium*, Salt Lake City, 2010.

[6] N. B. Nagel, M. A. Sanchez-Nagel, F. Zhang, X. Garcia and B. Lee, "Coupled Numerical Evaluations of the Geomechanical Interactions Between a Hydraulic Fracture

http://dx.doi.org/10.5772/56302

Stimulation and a Natural Fracture System in Shale Formations," *Rock Mechanics and Rock Engineering*, 2013.

[7] N. B. Nagel, X. Garcia, M. A. Sanchez-Nagel and B. Lee, "Understanding "SRV": A Numerical Investigation of "Wet" vs. "Dry" Microseismicity During Hydraulic Fracturing," in *SPE Annual Technical Conference and Exhibition*, San Antonio, Texas, USA, 2012.

[8] N. B. Nagel, M. A. Sanchez-Nagel, X. Garcia and B. Lee, "A Numerical Evaluation of the Geomechanical Interactions Between a Hydraulic Fracture Stimulation and a Natural Fracture System," in *46th US Rock Mechanics / Geomechanics Symposium*, Chicago, IL, 2012.

[9] N. Nagel, I. Gil, M. Sanchez-Nagel and B. Damjanac, "Simulating hydraulic fracturing in real fractured rock - overcoming the limits of pdeudo-3D models," in *SPE 140480 presented at the SPE Hydraulic Fracturing Technology Conference*, the Woodlands, TX, 2011.

[10] A. A. Savitski, M. Lin, A. Riahi, B. Damjanac and B. N. Nagel, "Explicit Modeling of Hydraulic Fracture Propagation in Fractured Shales," in *International Petroleum Technology Conference*, Beijing, China, 2013.

[11] ICG, *3DEC - Three-Dimensional Distinct Element Code, Version 4.2*, Minneapolis, MN: Itasca Consulting Group, Inc., 2007.

Section 9

Multiscale Modeling

Chapter 29

Fluid-Driven Fracture in a Poroelastic Rock

Yevhen Kovalyshen and Emmanuel Detournay

Additional information is available at the end of the chapter

http://dx.doi.org/10.5772/56460

1. Introduction

Hydraulic fracturing is commonplace in the geo-industry, whether designed or unintended; e.g., stimulation of hydrocarbons reservoirs [1, 2], disposal of waste water [3], waterflooding operations [4], enhanced oil recovery by injection of CO2 [5], and preconditioning of rock mass in the mining industry [6, 7]. Nonetheless, modeling of hydraulic fracturing usually relies on oversimplified assumptions [1, 8]; in particular, fluid leak-off is often studied within Carter's model [9] that assumes that the transport of the filtrate and the porous fluid through the porous medium is one-dimensional. While this assumption is quite reasonable in the case of short treatments such as hydraulic fracturing of a hydrocarbons reservoir [2], it is unlikely to be applicable for injection operations over long periods of time.

This study is part of an ongoing effort to rigorously introduce large-scale 3D diffusion in a model of hydraulic fracture. The increase of pore pressure around the fracture caused by fluid leak-off from the fracture leads to an expansion of the porous medium. This expansion can be accounted for by the introduction of the so-called backstress [10, 11]. By definition, the backstress would be the stress induced across the fracture plane if the fracture were closed. Here we restrict our investigation to the toughness-dominated regime of propagation, for which the viscosity of the fluid is negligible. In other words we assume that the energy spent for hydraulic fracturing is mainly due to the rock damage rather than due to dissipation associated with viscous flow of the fracturing fluid. Setting the fracturing fluid viscosity to be equal to zero implies that the fluid pressure inside the fracture is uniform.

Previous works on the toughness-dominated regimes with leak-off include a detailed examination of the case of the Carter's leak-off model by means of scaling and asymptotic analyses [12] and an analysis of a "stationary" 3D leak-off under conditions of very slow fracture propagation, when the pore pressure around the fracture is always in equilibrium [13]. A model for the plane strain propagation of a natural fracture through a porous medium was proposed by [14], who introduced an efficient approach to calculate of the fluid exchange

volume between the fracture and the medium. This approach relies on decomposing the evolving pressure loading inside the growing fracture into a series of pressure impulses and then on representing the actual fluid exchange volume by the superposition of fluid exchanges induced by a single impulse [11]. Despite algebraic errors in the main expression for the fluid exchange volume (equation (7) of [14]), the idea introduced by these authors is at the core of the approach summarized in this paper and described in more details in [15].

In this paper we build a general model of a penny-shaped hydraulic fracture driven by a zero viscosity fluid through a poroelastic medium. The model accounts for the backstress effect, which was not considered in earlier efforts [12–14]. This work makes use of the response of a poroelastic medium to an impulse of pore pressure applied to a penny-shaped domain; namely, $u(r,t)$, the component of the fluid displacement, normal to the disc, and $S_b(r,t)$, the normal stress component [15]. The main restrictive assumptions of this analysis is the absence of a low permeability cake build-up and the neglect of the poroelastic solid-to-fluid coupling. The later assumption was studied by [11], who have concluded that in the case of hydraulic boundary conditions when the pore pressure is prescribed, the fluid exchange between the fracture and the medium calculated via poroelastic theory is nearly identical to that computed by uncoupled diffusion equation. Throughout this work we intensively use scaling and asymptotic analyses; in particular, we show that the parametric space is a prism. In this parametric space, the case of the Carter's leak-off model [12] occupies one edge of this prism, whereas the pseudo steady-state model [13] covers one face.

The main objective of the analysis is to solve for the evolution of the fracture radius $R(t)$, the fracturing fluid pressure $p_{\text{in}}(t)$, and the efficiency of the hydraulic fracturing $\mathcal{E}(t) \equiv V_{\text{crack}}/V_{\text{inject}}$, where V_{crack} is the volume of the fracture and V_{inject} is the volume of the injected fracturing fluid.

2. Mathematical model

2.1. Problem definition

We consider a penny-shaped fracture driven by injection of an incompressible fluid, at a constant rate Q_0 (see Fig.1). The crack propagates through an infinite, homogeneous, brittle, poroelastic rock saturated by a fluid which has the same physical properties as the filtrate, i.e., these fluids are physically indistinguishable inside the porous medium. The medium is characterized by Young's modulus E, Poisson's ratio ν, fracture toughness K_{Ic}, intrinsic permeability κ, storage coefficient S, Biot coefficient α. Prior to the injection of fluid, the pore pressure field p_0 is uniform. Also there exists a far-field compressive stress σ_0, perpendicular to the fracture plane.

2.2. Dimensional formulation

We start from the global fluid balance equation

$$V_{\text{inject}}(t) = V_{\text{crack}}(t) + V_{\text{leak}}(t). \tag{1}$$

http://dx.doi.org/10.5772/56460

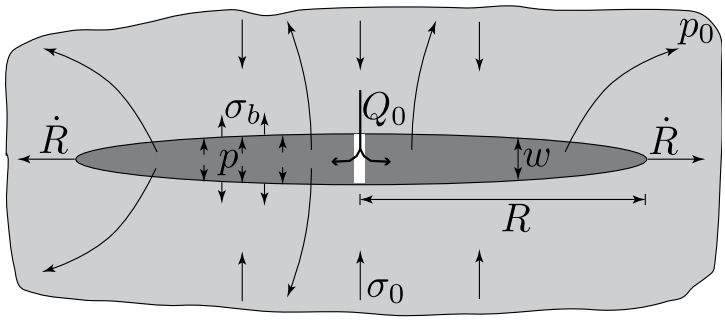

Figure 1. sketch of the problem

The quantity $V_{\text{inject}}(t) = Q_0 t$ denotes the volume of injected fracturing fluid, while $V_{\text{crack}}(t)$ is the fracture volume

$$V_{\text{crack}}(t) = 2\pi R^2(t) \int_0^1 w[R(t)s, t]\, sds. \tag{2}$$

In the above $R(t)$ is the fracture radius, and $w(r,t)$ is the fracture opening.

The elasticity integral equation [16, 17]

$$w(r,t) = \frac{8}{\pi}\frac{R}{E'} \int_0^1 \{p(t) + \sigma_b[R(t)s, t] - \sigma_0\}\, G\left[\frac{r}{R(t)}, s\right] sds, \tag{3}$$

links the fracture aperture $w(r,t)$ to the fracturing fluid pressure $p(t)$ and the backstress, $\sigma_b(r,t)$. In (3), $E' \equiv E/(1-\nu^2)$ denotes the plane strain modulus. The elasticity kernel $G(\xi, s)$ is given by

$$G(\xi, s) = \begin{cases} \frac{1}{\xi} F\left(\arcsin\sqrt{\frac{1-\xi^2}{1-s^2}}, \frac{s^2}{\xi^2}\right), & \xi > s \\ \frac{1}{s} F\left(\arcsin\sqrt{\frac{1-s^2}{1-\xi^2}}, \frac{\xi^2}{s^2}\right), & \xi < s \end{cases}, \tag{4}$$

with $F(\phi, m)$ denoting the incomplete elliptic integral of the first kind [18].

Substitution of the elasticity equation (3) into (2) yields

$$V_{\text{crack}}(t) = \frac{16}{3}\frac{R^3(t)}{E'} \left\{p(t) - \sigma_0 + 3\int_0^1 \sigma_b[R(t)s, t]\sqrt{1-s^2}sds\right\}. \tag{5}$$

As indicated earlier, we can represent the continuous evolution of the fluid pressure inside the crack by a sum of spatially uniform time impulses of pressure. Then, the leaked-off volume V_{leak} and the backstress σ_b can be written as

$$V_{\text{leak}}(t) = \int_0^t U[R(s), t-s][p(s) - p_0]\, ds, \tag{6}$$

$$\sigma_b(r,t) = \int_0^t S_b[R(s), r, t-s][p(s) - p_0]\, ds, \tag{7}$$

where $U(R,t)$ is the volume of the fracturing fluid that has escaped from a fracture of radius R at an elapsed time t after a uniform unit impulse of pressure has been applied, and $S_b(R,r,t)$ is the generated backstress. In the following we refer to $U(R,t)$ as the leak-off Green function, and to $S_b(R,r,t)$ as the backstress Green function.

Simple scaling analysis reveals the following relations between these dimensional Green functions $U(R,t)$, $S_b(R,r,t)$ and the dimensionless ones $\Psi(\tau)$, $\Xi(\xi,\tau)$ [15]

$$U(R,t) = \frac{SR^3}{T_R}\Psi\left(\frac{t}{T_R}\right), \quad S_b(R,r,t) = \frac{\eta}{T_R}\Xi\left(\frac{r}{R}, \frac{t}{T_R}\right), \quad T_R = \frac{R^2}{4c}, \tag{8}$$

where $c = \kappa/S$ is the diffusion coefficient, $\eta = \alpha(1-2\nu)/2(1-\nu)$ is the poroelastic stress coefficient.

We close the formulation of the problem with the propagation criterion

$$K_{Ic} = \frac{2}{\sqrt{\pi}} R^{1/2}(t) \int_0^1 \frac{p[sR(t), t] + \sigma_b[sR(t), t] - \sigma_0}{\sqrt{1-s^2}} s\, ds, \tag{9}$$

The model has thus only two unknowns: the fracturing fluid pressure $p(t)$ and the fracture radius $R(t)$.

2.3. Dimensionless formulation

The problem depends on seven dimensional parameters: K_{Ic}, E', Q_0, c, S, σ_0, and p_0, and one dimensionless parameter η. It is possible to reduce this set of parameters to five dimensionless quantities. Inspired by earlier works on hydraulic fracture [19], we introduce the scaling

$$r = R(t)\,\xi, \quad R(t) = L(t)\,\rho(t),$$

$$p(t) - \sigma_0 = \frac{K_{Ic}}{L^{1/2}(t)}\Pi(t), \quad \sigma_b(r,t) = \frac{K_{Ic}}{L^{1/2}(t)}\Sigma(\xi,t). \tag{10}$$

where $\rho(t) \sim 1$ is the dimensionless radius, $\Pi(t) \sim 1$ is the dimensionless net pressure, $\Sigma(\xi,t)$ is the dimensionless back stress, and $L(t) \sim R(t)$ is the characteristic size of the fracture. This scaling is thus time-dependent. Moreover we have not yet defined the parameter $L(t)$. Below we show that the parameter $L(t)$ can be defined for different propagation regimes in such a way that the dimensionless quantities ρ, Π, and Σ do not depend on time.

In the scaling (10) the governing equations transform as follows.

http://dx.doi.org/10.5772/56460

- Backstress equation (7) after substitution of (8)

$$\Sigma(\xi,t)=4\eta\mathcal{G}_d(t)\int_0^1\frac{L^2(t)}{L^2(ts)}\frac{1}{\rho^2(ts)}\Xi\left[\xi\frac{L(t)\rho(t)}{L(ts)\rho(ts)},4\mathcal{G}_d(t)\frac{L^2(t)}{L^2(ts)}\frac{1-s}{\rho^2(ts)}\right]\times$$

$$\times\left[\mathcal{G}_\sigma(t)+\sqrt{\frac{L(t)}{L(ts)}}\Pi(ts)\right]ds, \tag{11}$$

- Propagation criterion (9) combined with (11)

$$1=\frac{2}{\sqrt{\pi}}\rho^{1/2}(t)\Pi(t)+K_{bs}(t), \tag{12}$$

- Volume balance equation (1), where we substituted (5), (6), (8), and (12)

$$1=\frac{8\sqrt{\pi}}{3}\mathcal{G}_v(t)\rho^{5/2}(t)\left[1+V_{bs}(t)-K_{bs}(t)\right]+$$

$$+4\mathcal{G}_c(t)\int_0^1\frac{L(ts)}{L(t)}\rho(ts)\Psi\left[4\mathcal{G}_d(t)\frac{L^2(t)}{L^2(ts)}\frac{1-s}{\rho^2(ts)}\right]\left[\mathcal{G}_\sigma(t)+\sqrt{\frac{L(t)}{L(ts)}}\Pi(ts)\right]ds. \tag{13}$$

Here $K_{bs}(t)$ is the change of the stress intensity factor due to the backstress

$$K_{bs}(t)=\frac{4\eta\mathcal{G}_d(t)}{\rho^{1/2}(t)}\int_0^1\frac{L(t)}{L(ts)}\frac{1}{\rho(ts)}k_{bs}\left[\frac{L(t)\rho(t)}{L(ts)\rho(ts)},4\mathcal{G}_d(t)\frac{L^2(t)}{L^2(ts)}\frac{1-s}{\rho^2(ts)}\right]\times$$

$$\left[\mathcal{G}_\sigma(t)+\sqrt{\frac{L(t)}{L(ts)}}\Pi(ts)\right]ds, \tag{14}$$

and $V_{bs}(t)$ is the change of the fracture volume due to the backstress

$$V_{bs}(t)=\frac{4\eta\mathcal{G}_d(t)}{\rho^{5/2}(t)}\int_0^1\rho(ts)\frac{L(ts)}{L(t)}v_{bs}\left[\frac{L(t)\rho(t)}{L(ts)\rho(ts)},4\mathcal{G}_d(t)\frac{L^2(t)}{L^2(ts)}\frac{1-s}{\rho^2(ts)}\right]\times$$

$$\left[\mathcal{G}_\sigma(t)+\sqrt{\frac{L(t)}{L(ts)}}\Pi(ts)\right]ds, \tag{15}$$

where

$$k_{bs}(\mathcal{R},\tau)=\frac{2}{\sqrt{\pi}}\int_0^{\mathcal{R}}\frac{\xi\Xi(\xi,\tau)}{\sqrt{\mathcal{R}^2-\xi^2}}d\xi, \tag{16}$$

$$v_{bs}(\mathcal{R},\tau)=\frac{6}{\sqrt{\pi}}\int_0^{\mathcal{R}}\xi\sqrt{\mathcal{R}^2-\xi^2}\Xi(\xi,\tau)\,d\xi. \tag{17}$$

The above governing equations thus depend on four time-dependent dimensionless groups:

- Storage group

$$\mathcal{G}_v(t)=\frac{K_{Ic}}{Q_0E'}\frac{L^{5/2}(t)}{t}, \tag{18}$$

  which is proportional to the fraction of the injected fluid volume stored in the fracture;
- Leak-off group

$$\mathcal{G}_c(t)=\frac{cSK_{Ic}}{Q_0}L^{1/2}(t), \tag{19}$$

  which characterizes the amount of the fluid that has leaked into the formation;
- Diffusion group

$$\mathcal{G}_d=\frac{ct}{L^2(t)}, \tag{20}$$

  which is related to the diffusion process with $\sqrt{\mathcal{G}_d}$ proportional to the ratio of the diffusion length scale to the fracture size. Thus this dimensionless group is small, $\mathcal{G}_d \ll 1$, in the case of 1D diffusion and large in the case of 3D diffusion, $\mathcal{G}_d \gg 1$;
- Pressure group

$$\mathcal{G}_\sigma(t)=\frac{\sigma_0-p_0}{K_{Ic}}L^{1/2}(t)\sim\frac{\sigma_0-p_0}{p-\sigma_0}, \tag{21}$$

  which describes the effect of the material toughness on the net fluid pressure $p-\sigma_0$ compared to σ_0-p_0. Indeed, in the case of small toughness when $K_{Ic}\to 0$ and $\mathcal{G}_\sigma\to\infty$, the fracturing fluid pressure p can be assumed to be equal to the confining stress σ_0 from a diffusion point of view, i.e., $p\approx\sigma_0$. Whereas in the case of large toughness when $K_{Ic}\to\infty$ and $\mathcal{G}_\sigma\to 0$, the net fluid pressure $p-\sigma_0$ is large compared to σ_0-p_0.

The only unknown here are the fracture radius $\rho(\tau)$ and fracturing fluid pressure $\Pi(\tau)$.

3. Propagation regimes

The problem under study has six propagation regimes. Therefore it is convenient to represent the fracture propagation by a trajectory line lying inside the prismatic parametric space shown in Fig. 2. The vertices of this prism represent the different propagation regimes; namely,

http://dx.doi.org/10.5772/56460

- the K_0-vertex represents the storage-dominated regime with 1D diffusion, during which most of the injected fluid is stored inside the fracture;
- the $\tilde{K}_{\kappa 0}$-vertex is related to the leak-off-dominated regime with 1D diffusion, when the net fluid pressure $p - \sigma_0$ is large compared to $\sigma_0 - p_0$;
- the $\tilde{K}_{\sigma 0}$-vertex is another leak-off-dominated regime with slow 1D diffusion, where from a diffusion point of view the fracturing fluid pressure p is approximately equal to the confining stress σ_0;
- the K_∞-vertex is the storage-dominated regime with pseudo steady-state 3D diffusion;
- the $\tilde{K}_{\kappa\infty}$-vertex is the pseudo steady-state (3D) diffusion version of the $\tilde{K}_{\kappa 0}$-vertex;
- the $\tilde{K}_{\sigma\infty}$-vertex is the pseudo steady-state (3D) diffusion version of the $\tilde{K}_{\sigma 0}$-vertex.

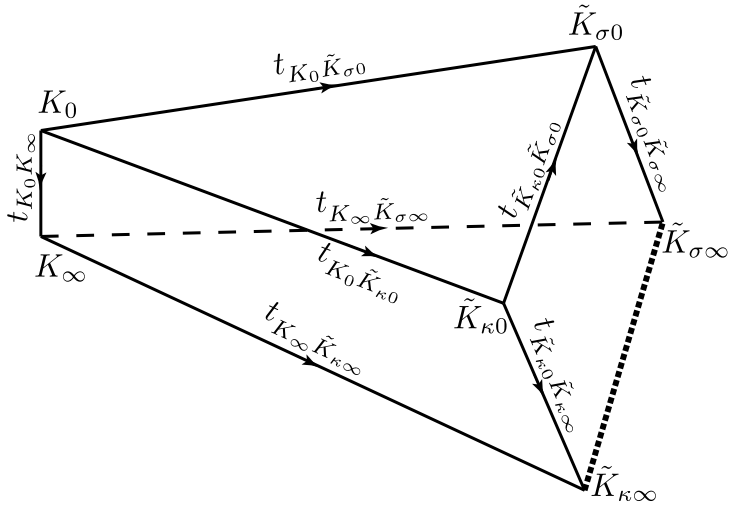

Figure 2. Parametric space

In the transition from one regime to another, the dominance of one physical process is displaced by the dominance of another one. For example the transition $K_\infty\tilde{K}_{\kappa\infty}$ is governed by $\mathcal{G}_c/\mathcal{G}_v$, such that $\mathcal{G}_c/\mathcal{G}_v = 0$ for the K_∞-vertex, and $\mathcal{G}_c/\mathcal{G}_v = \infty$ for the $\tilde{K}_{\kappa\infty}$-vertex. In another example, the transition from 1D to 3D diffusion is governed by $\mathcal{G}_d$, such that $\mathcal{G}_d = 0$ for 1D diffusion, and $\mathcal{G}_d = \infty$ for 3D diffusion.

Usually, each propagation regime is studied in an intrinsic time-dependent scaling, such that the propagation of a fracture in a given propagation regime does not depend on time in this scaling. In other words, each propagation regime is characterized by a self-similar solution. This intrinsic scaling is introduced in such a way that all dimensionless groups corresponding to the dominant physical processes are equal to 1, whereas all the other groups are small compared to 1. These small dimensionless groups are still time-dependent, therefore it is easy to estimate when a given propagation regime is valid. Also using these small time-dependent groups we can easily calculate the characteristic transition times between different propagation regimes. For example, in order to calculate the characteristic transition time t_{AB} between the two propagation regimes A and B, one should follow the following procedure: first, introduce a scaling intrinsic to the propagation regime A; second, obtain in

ver-	definition			scaling		solution
tex	$\mathcal{G}_d$	$\mathcal{G}_\sigma$	$\mathcal{G}_v/\mathcal{G}_c$	definition	$L(t)$	ρ
K_0	$\ll 1$	–	$\gg \mathcal{G}_d^{-1/2}\max[1,\mathcal{G}_\sigma]$	$\mathcal{G}_v = 1$	$\left(\frac{Q_0 E'}{K_{Ic}}t\right)^{2/5}$	$\left(\frac{3}{8\sqrt{\pi}}\right)^{2/5}$
$\tilde{K}_{\kappa 0}$	$\ll 1$	$\ll 1$	$\ll \mathcal{G}_d^{-1/2}$	$\mathcal{G}_c^{(1D)} = 1$	$\left(\frac{Q_0\mathcal{I}^{-1}t^{1/2}}{c^{1/2}SK_{Ic}}\right)^{2/3}$	$\frac{2^{2/3}}{\pi^{4/3}}$
$\tilde{K}_{\sigma 0}$	$\ll 1$	$\gg 1$	$\ll \mathcal{G}_d^{-1/2}\mathcal{G}_\sigma$	$\mathcal{G}_c^{(1D)}\mathcal{G}_\sigma = 1$	$\left[\frac{Q_0\mathcal{I}^{-1}t^{1/2}}{c^{1/2}S(\sigma_0-p_0)}\right]^{1/2}$	$\pi^{-3/4}$
K_∞	$\gg 1$	–	$\gg \max[1,\mathcal{G}_\sigma]$	$\mathcal{G}_v = 1$	$\left(\frac{Q_0 E'}{K_{Ic}}t\right)^{2/5}$	$\left(\frac{3}{8\sqrt{\pi}}\right)^{2/5}$
$\tilde{K}_{\kappa\infty}$	$\gg 1$	$\ll 1$	$\ll 1$	$\mathcal{G}_c = 1$	$\left(\frac{Q_0}{cSK_{Ic}}\right)^2$	$\frac{(1-\eta)^2}{16\pi}$
$\tilde{K}_{\sigma\infty}$	$\gg 1$	$\gg 1$	$\ll \mathcal{G}_\sigma$	$\mathcal{G}_c\mathcal{G}_\sigma = 1$	$\frac{Q_0}{cS(\sigma_0-p_0)}$	$\frac{1-\eta}{8}$

Here $\mathcal{G}_c^{(1D)} \equiv \frac{\mathcal{G}_c}{\mathcal{G}_d^{1/2}}\left(1-\frac{4\eta}{E'S}\right)$ and $\mathcal{I} \equiv 1-\frac{4\eta}{E'S}$

Table 1. Propagation regimes and corresponding scalings

terms of this intrinsic scaling an expression for the dimensionless group $\mathcal{G}_B^{(A)}(t)$, which is dominant in the regime B, whereas it is small in the regime A; and third, solve the equation $\mathcal{G}_B^{(A)}(t_{AB}) = 1$ to obtain the characteristic transition time t_{AB}.

Different scalings can be introduced by defining the length scale $L(t)$, see (21)-(18). We define different propagation regimes in terms of the dimensionless groups (21)-(18) in Table 1, where we also introduce the scalings intrinsic to each of these propagation regimes. The transition times between different propagation regimes are given by

- K_0K_∞- edge

$$t_{K_0K_\infty} = \frac{Q_0^4 E'^4}{c^5 K_{Ic}^4};$$

- $K_0\tilde{K}_{\kappa 0}$- edge

$$t_{K_0\tilde{K}_{\kappa 0}} = \left[c^{1/2}S\left(\frac{K_{Ic}^2E'^3}{Q_0^2}\right)^{1/5}\left(1-\frac{4\eta}{E'S}\right)\right]^{-10};$$

- $K_0\tilde{K}_{\sigma 0}$- edge

$$t_{K_0\tilde{K}_{\sigma 0}} = \left[c^{1/2}S(\sigma_0-p_0)\left(\frac{E'^4}{Q_0K_{Ic}^4}\right)^{1/5}\left(1-\frac{4\eta}{E'S}\right)\right]^{-10/3};$$

- $\tilde{K}_{\kappa 0}\tilde{K}_{\sigma 0}$- edge

$$t_{\tilde{K}_{\kappa 0}\tilde{K}_{\sigma 0}} = \left[\frac{c^{1/2}SK_{Ic}^4}{(\sigma_0-p_0)^3Q_0}\left(1-\frac{4\eta}{E'S}\right)\right]^2;$$

http://dx.doi.org/10.5772/56460

- $\tilde{K}_{\kappa 0}\tilde{K}_{\kappa\infty}$- edge

$$t_{\tilde{K}\kappa 0\tilde{K}\kappa\infty} = \frac{Q_0^4}{c^5 S^4 K_{Ic}^4};$$

- $\tilde{K}_{\sigma 0}\tilde{K}_{\sigma\infty}$- edge

$$t_{\tilde{K}\sigma 0\tilde{K}\sigma\infty} = \frac{Q_0^2}{c^3 S^2 \left(\sigma_0 - p_0\right)^2};$$

- $K_\infty\tilde{K}_{\kappa\infty}$- edge

$$t_{K_\infty\tilde{K}\kappa\infty} = \frac{Q_0^4}{c^5 S^5 E' K_{Ic}^4};$$

- $K_\infty\tilde{K}_{\sigma\infty}$- edge

$$t_{K_\infty\tilde{K}\sigma\infty} = \sqrt{\frac{Q_0^3 K_{Ic}^2}{c^5 S^5 E'^2 \left(\sigma_0 - p_0\right)^5}}.$$

- $\tilde{K}_{\kappa\infty}\tilde{K}_{\sigma\infty}$-edge is self-similar, i.e., the transition along this edge is impossible. Moreover all trajectory lines of the fracture propagation begin at the K_0-vertex and end at some point of the $\tilde{K}_{\kappa\infty}\tilde{K}_{\sigma\infty}$-edge.

The case of the Carter's leak-off model studied in [12] corresponds to the $K_0\tilde{K}_{\sigma 0}$-edge, whereas the pseudo steady-state model introduced in [13] corresponds to the $K_\infty\tilde{K}_{\kappa\infty}\tilde{K}_{\sigma\infty}$-face with $\eta = 0$.

Interestingly the fracture radius ρ is the same in the two different storage-dominated regimes K_0 and K_∞ (see Table 1), while the fracturing fluid pressure is different [15]. Therefore the poroelastic effects split the storage dominated regime (denoted previously as the K-vertex [12, 17]) into two sub-regimes: the K_0-vertex (1D diffusion) which is similar to the former K-vertex, and the K_∞-vertex (pseudo steady-state diffusion) characterized by a higher pressure. The essence of the difference between these two regimes is illustrated in Fig. 3. Initially the fracture front propagates faster than the diffusion front, therefore the diffusion length scale is small compared to the size of the fracture and the diffusion is one dimensional. As time goes on, the diffusion front catches up and then passes the fracture front, making the diffusion length scale to be larger than the fracture size, and, as a result, switching the propagation regime from the 1D diffusion to the pseudo steady-state (3D) diffusion.

4. Methodology

Inclusion of diffusion and poroelastic effects into the model of penny-shaped hydraulic fracture model propagation in the toughness-dominated regime thus requires evaluating the convolution type integrals [see (11), (13)-(15)]. Indeed, calculation of the fracturing fluid volume which has leaked into the formation requires a "convolution" on $\Psi(\tau)$ [see (13)], whereas evaluation of the backstress $\Sigma(\xi, t)$ and the related fracture volume $V_{bs}(t)$ and stress intensity factor $K_{bs}(t)$ changes requires "convolutions" on $\Xi(\xi, \tau)$. These "convolutions"

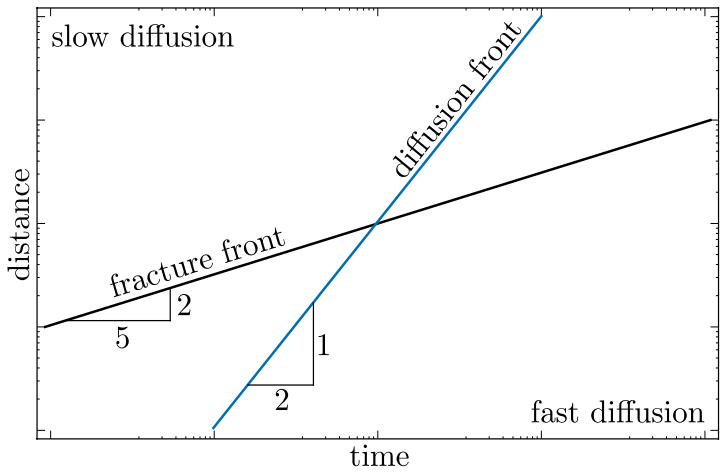

Figure 3. Physical interpretation of the difference between K_0- and K_∞-vertices

involves both arguments of $\Xi(\xi,\tau)$ and are much more complicated than the "convolution" on the single argument $\Psi(\tau)$ [see (11), (14), and (15)].

To simplify the calculations of $V_{bs}(t)$ and $K_{bs}(t)$, we introduce two additional functions $v_{bs}(\mathcal{R},\tau)$ and $k_{bs}(\mathcal{R},\tau)$, such that "convolutions" on these functions yield $V_{bs}(t)$ and $K_{bs}(t)$ [see (14)-(17)]. Physically the function $v_{bs}(\mathcal{R},\tau)$ can be interpreted as the volume change of a fracture of radius $\mathcal{R}>1$ at an elapsed time τ due to the backstress generated by a unit impulse of the pore pressure applied at time $\tau=0$ along the part of the fracture $\mathcal{R}$ located inside the unit circle $\xi<1$. The function $k_{bs}(\mathcal{R},\tau)$ is the corresponding change in the stress intensity factor. Note that there is a simple connection between $k_{bs}(\mathcal{R},\tau)$ and $v_{bs}(\mathcal{R},\tau)$ [see (16), (17)]

$$k_{bs}(\mathcal{R},\tau)=\frac{2}{3}\frac{\partial v_{bs}(\mathcal{R},\tau)}{\partial \mathcal{R}^2}. \tag{22}$$

Small-time asymptotes of $k_{bs}(\mathcal{R},\tau)$ and $v_{bs}(\mathcal{R},\tau)$

The small-time asymptote of $\Xi(\xi,\tau)$ is given by [15]

$$\Xi_0(\xi,\tau)=-\frac{1}{\pi^{3/2}\tau^{1/2}}\left\{(1-\xi)^{-1}E\left[\frac{4\xi}{(1+\xi)^2}\right]+(1+\xi)^{-1}K\left[\frac{4\xi}{(1+\xi)^2}\right]\right\}, \tag{23}$$

where $K(x)$ and $E(x)$ are the complete elliptic integrals of the first and second kinds respectively [18]. This asymptote has a strong singularity $1/(1-\xi)$, which causes significant problems in numerical simulations. Also one can observe a separation of variables, which simplifies the evaluation of $k_{bs}(\mathcal{R},\tau)$ and $v_{bs}(\mathcal{R},\tau)$ at small time.

Substitution of this small-time asymptote $\Xi_0(\xi,\tau)$ into the expression for $k_{bs}(\mathcal{R},\tau)$ (16) yields

$$k_{bs}(\mathcal{R},\tau)=0. \tag{24}$$

http://dx.doi.org/10.5772/56460

Therefore, $v_{bs}(\mathcal{R},\tau)$ depends only on time [see (22)], and in order to define $v_{bs}(\mathcal{R},\tau)$ we can evaluate it at any convenient point, e.g., $\mathcal{R}=1$. The expression for the stress distribution, given by (23), can be simplified by means of [20]

$$E\left[\frac{4x}{(1+x)^2}\right]=(1+x)\left[2E\left(x^2\right)-\left(1-x^2\right)K\left(x^2\right)\right],\quad x\le 1,$$

$$K\left[\frac{4x}{(1+x)^2}\right]=(1+x)\,K\left(x^2\right),\quad x\le 1,$$

such that

$$\Xi_0(\xi,\tau)=-\frac{2}{\pi^{3/2}\tau^{1/2}}\frac{E\left(\xi^2\right)}{1-\xi^2},\quad \xi\le 1. \tag{25}$$

Now, using the integral representation of the elliptic integral

$$E(x)=\int_0^1\sqrt{\frac{1-xt^2}{1-t^2}}dt,$$

one can calculate $v_{bs}(\mathcal{R},\tau)$ [see (17)]

$$v_{bs}(\mathcal{R},\tau)=-\frac{3}{2}\tau^{-1/2}. \tag{26}$$

Large-time asymptotes of $k_{bs}(\mathcal{R},\tau)$ and $v_{bs}(\mathcal{R},\tau)$

The large-time asymptote of $\Xi(\xi,\tau)$ is given by [15]

$$\Xi_\infty(\xi,\tau)=-\tilde{\Pi}_\infty^{(0)}(\xi)\left[\delta(\tau)-2(\pi\tau)^{-3/2}\right]-\frac{8}{3}(\pi\tau)^{-3/2}, \tag{27}$$

where $\delta(\tau)$ is the Dirac delta function and

$$\tilde{\Pi}_\infty^{(0)}(\xi)=\begin{cases}1, & \xi\le 1\\ \frac{2}{\pi}\arctan\left(\frac{1}{\sqrt{\xi^2-1}}\right), & \xi>1\end{cases}.$$

Note that in the leading order we have separation of variables.

Substitution of this large-time asymptote $\Xi_\infty(\xi,\tau)$ into the definitions of $k_{bs}(\mathcal{R},\tau)$ and $v_{bs}(\mathcal{R},\tau)$, given by (16) and (17), leads to

$$k_{bs}(\mathcal{R},\tau) = -\frac{2\delta(\tau)}{\sqrt{\pi}} + \mathcal{O}\left(\tau^{-3/2}\right), \tag{28}$$

$$v_{bs}(\mathcal{R},\tau) = -\frac{3\mathcal{R}^2-1}{\sqrt{\pi}}\delta(\tau) + \mathcal{O}\left(\tau^{-3/2}\right). \tag{29}$$

5. Asymptotic solutions

Details on the derivation of the asymptotic solutions, corresponding to each of the vertices of the parametric space, can be found in [15]. Here we simply list the solutions for the K_0-, $\tilde{K}_{\kappa 0}$-, and $\tilde{K}_{\sigma 0}$-vertices, as well as for the self-similar $\tilde{K}_{\kappa\infty}\tilde{K}_{\sigma\infty}$-edge. These solutions are actually expressed in the same time-independent scaling that corresponds to $\mathcal{G}_\sigma = 1$. In other words, all the solutions are given in terms of the scaled radius $\rho(\tau)$ function of the dimensionless time τ

$$\rho(\tau) = \frac{R(t)}{L_{\mathrm{tr}}}, \qquad \tau = \frac{t}{T}, \tag{30}$$

where

$$L_{\mathrm{tr}} = \left(\frac{K_{Ic}}{\sigma_0 - p_0}\right)^2, \qquad T = \frac{L_{\mathrm{tr}}^2}{4c}. \tag{31}$$

Besides the asymptotic expressions for $\rho(\tau)$, $K_{bs}(\tau)$, $V_{bs}(\tau)$, $\Pi(\tau)$, we have also provided expressions for the hydraulic fracturing efficiency $\mathcal{E}$, defined as $\mathcal{E} \equiv V_{\mathrm{crack}}/V_{\mathrm{inject}}$.

- K_0-vertex

$$\rho_0(\tau) = \left(\frac{3}{8\sqrt{\pi}G_v}\right)^{2/5}\tau^{2/5}, \qquad K_{bs0}(\tau) = 0,$$

$$V_{bs0}(\tau) = -\frac{3}{2}\eta\frac{\pi^{1/2}\tau^{1/2}}{\rho_0^{1/2}(\tau)}\left[\frac{\Gamma(9/5)}{\Gamma(23/10)} + \frac{\pi^{1/2}}{2\rho_0^{1/2}(\tau)}\frac{\Gamma(8/5)}{\Gamma(21/10)}\right],$$

$$\Pi_0(\tau) = \frac{\pi^{1/2}}{2}\rho_0^{-1/2}(\tau), \qquad \mathcal{E}_0(\tau) = \frac{8\sqrt{\pi}}{3}G_v\frac{\rho_0^{5/2}(\tau)\left[1+V_{bs0}(\tau)\right]}{\tau};$$

- $\tilde{K}_{\kappa 0}$-vertex

$$\rho_\kappa(\tau) = \pi^{-4/3}G_c^{-2/3}\left(1-\frac{\eta G_v}{G_c}\right)^{-2/3}\tau^{1/3}, \qquad K_{bs\kappa}(\tau) = 0,$$

http://dx.doi.org/10.5772/56460

$$V_{bs\kappa}(\tau) = -\frac{3}{2}\eta\frac{\pi^{1/2}\tau^{1/2}}{\rho_\kappa^{1/2}(\tau)}\left[\frac{\Gamma(5/3)}{\Gamma(13/6)} + \frac{\pi}{4\rho_\kappa^{1/2}(\tau)}\right],$$

$$\Pi_\kappa(\tau) = \frac{\pi^{1/2}}{2}\rho_\kappa^{-1/2}(\tau), \qquad \mathcal{E}_\kappa(\tau) = \frac{8\sqrt{\pi}}{3}G_v\frac{\rho_\kappa^{5/2}(\tau)\left[1+V_{bs\kappa}(\tau)\right]}{\tau};$$

- $\tilde{K}_{\sigma 0}$-vertex

$$\rho_\sigma(\tau) = 2^{-1/2}\pi^{-3/4}G_c^{-1/2}\left(1-\frac{\eta G_v}{G_c}\right)^{-1/2}\tau^{1/4}, \qquad K_{bs\sigma}(\tau) = 0,$$

$$V_{bs\sigma}(\tau) = -\frac{3}{4}\eta\frac{\pi\tau^{1/2}}{\rho_\sigma^{1/2}(\tau)}\left[1+\frac{1}{\rho_\sigma^{1/2}(\tau)}\frac{\Gamma(11/8)}{\Gamma(15/8)}\right],$$

$$\Pi_\sigma(\tau) = \frac{\pi^{1/2}}{2}\rho_\sigma^{-1/2}(\tau), \qquad \mathcal{E}_\sigma(\tau) = \frac{8\sqrt{\pi}}{3}G_v\frac{\rho_\sigma^{5/2}(\tau)\left[1+V_{bs\sigma}(\tau)\right]}{\tau};$$

- $\tilde{K}_{\kappa\infty}\tilde{K}_{\sigma\infty}$-edge

$$\rho_\infty(\tau) = \left[\frac{\sqrt{\pi+2(1-\eta)/G_c}-\sqrt{\pi}}{4}\right]^2, \qquad \Pi_\infty(\tau) = \frac{\pi^{1/2}}{2}\frac{\rho_\infty^{-1/2}(\tau)}{1-\eta}+\frac{\eta}{1-\eta},$$

$$V_{bs\infty}(\tau) = K_{bs\infty}(\tau) = -\frac{2}{\sqrt{\pi}}\eta\rho_\infty^{1/2}(\tau)\left[1+\Pi_\infty(\tau)\right], \quad \mathcal{E}_\infty(\tau) = \frac{8\sqrt{\pi}}{3}G_v\frac{\rho_\infty^{5/2}(\tau)}{\tau}.$$

6. Transient solution

To obtain a general trajectory of the system starting at the K_0-vertex and ending at the $\tilde{K}_{\kappa\infty}\tilde{K}_{\sigma\infty}$-edge, an implicit numerical algorithm to solve the set of governing equations (12)-(17) has been developed [15].

The results of the numerical simulations for different values of the parameters G_i are presented in Figs 4-7. Depending on the values of the parameters G_i, the system can travel through different vertices, although the journey always has to start at the K_0-vertex and terminate on the $\tilde{K}_{\kappa\infty}\tilde{K}_{\sigma\infty}$-edge.

In some cases the propagation of the fracture terminates before it arrives to the $\tilde{K}_{\kappa\infty}\tilde{K}_{\sigma\infty}$-edge (see Figs 6-7). In these cases, the system, going through a diffusion-dominated vertices, arrives to a point when the dilation of the poroelastic medium $\sim V_{bs}$ is very large, such that

the volume of the fracture becomes equal to zero. The fracture closure time can easily be estimated by substituting the above analytical expressions for V_{bs} and K_{bs} into $V_{\text{crack}}(\tau) \sim 1 + V_{bs}(\tau) - K_{bs}(\tau) = 0$, and solving it with respect to time τ. Note that this estimate is based only on the total volume of fracture and does not address the issue as to when and where the two faces of the fracture first become into contact. In fact, the fracture will first evolve towards a viscosity-dominated propagation regime then close. In other words, a decrease of fracture opening leads to an increase of the pressure gradient of the viscous fracturing fluid, which in turn leads to an increase of the viscous dissipation and eventually to the violation of the zero viscosity assumption for the fracturing fluid. Moreover the fluid pressure profile inside the fracture becomes to be strongly nonuniform, and thus one cannot use the results of the auxiliary problem to model the poroelastic effects. More sophisticated models are needed to study this situation.

7. Discussion

Let us consider the results from an application point of view. Table 2 list the parameters for a re-injection of production water [21]. The values for S and c were estimated on the assumption that $K_f/E \ll 1$ [22].

To characterize the propagation of a fracture, the transition times were calculated using the expressions found in Section 3, see Table 3. In this example, all time scales are well separated. As a result, the fracture follows the edges with the shortest transition time starting at the K_0-vertex, passing through the $\tilde{K}_{\sigma 0}$-vertex, and ending up at the $\tilde{K}_{\sigma\infty}$-vertex. Moreover the transition time from the K_0-vertex into the $\tilde{K}_{\sigma\infty}$-vertex is very small compared to the treatment time. This means that the treatment design can be based on a constant radius model. This analysis relies only on general results of the scaling analysis and does not involve any explicit asymptotic solutions.

	low porosity reservoir (LPR)	**mean porosity reservoir (MPR)**
porosity ϕ (%)	10	20
permeability k (md)	10	100
Young's modulus E (GPa)	30	15
Poisson's ratio ν	0.2	0.25
rock toughness K_{Ic} (MPa $\cdot$ m$^{1/2}$)	1.0	
water bulk modulus K_f (GPa)	2.2	
water viscosity μ (mPa $\cdot$ s)	1.0	
Biot coefficient α	0.6	
diffusion coefficient c (m^2/s)	0.212	1.04
storage coefficient S (Pa^{-1})	4.65×10^{-11}	9.49×10^{-11}
poroelastic stress modulus η	0.225	0.2
reservoir thickness H (m)	50	5
confining stress σ_0 (MPa)	55	
initial pore pressure p_0 (MPa)	30	
injection rate Q_0 (m^3/day)	750	
treatment time T (days)	100	

Table 2. Characteristic parameters during production water re-injection [21]

http://dx.doi.org/10.5772/56460

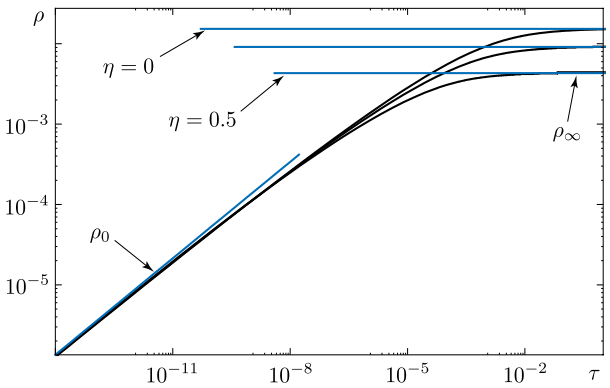

(a) Fracture radius ρ vs time τ

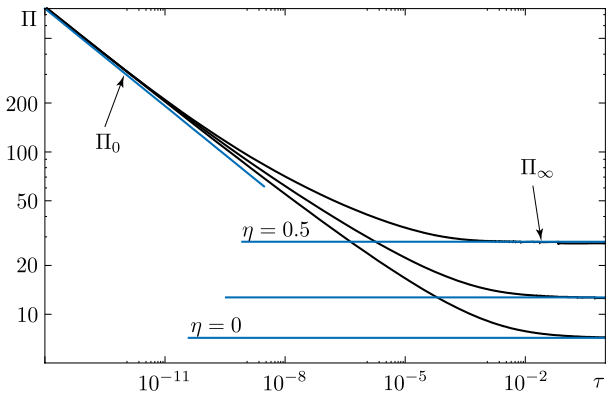

(b) Fracturing fluid pressure Π vs time τ

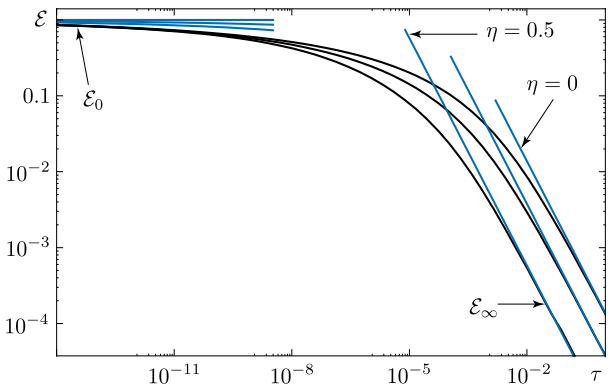

(c) Hydraulic fracturing efficiency $\mathcal{E}$ vs time τ

Figure 4. General case $G_v = G_c = 1$, $\eta = 0.0, 0.25, 0.5$

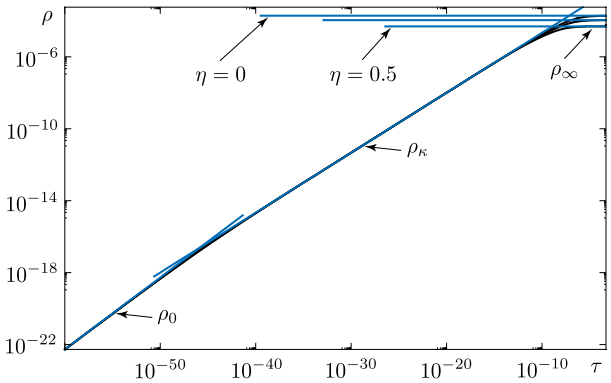

(a) Fracture radius ρ vs time τ

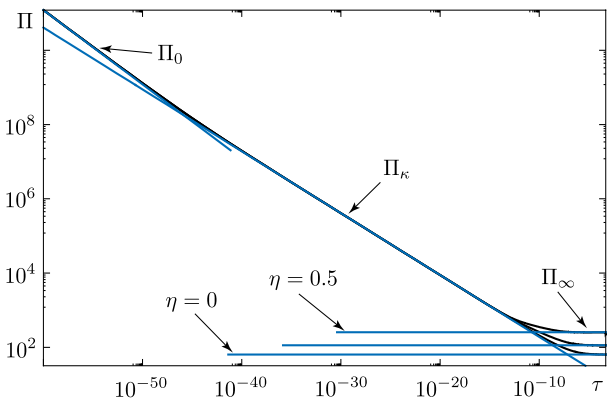

(b) Fracturing fluid pressure Π vs time τ

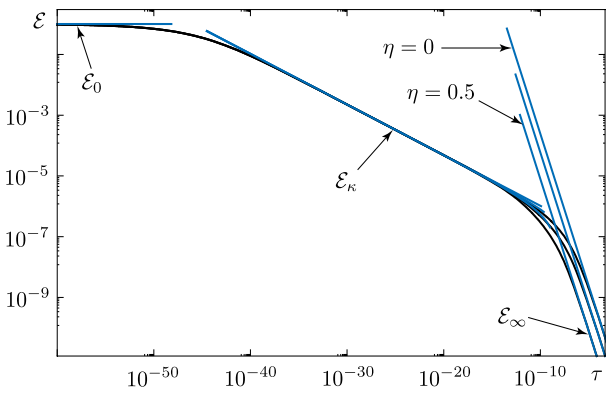

(c) Hydraulic fracturing efficiency $\mathcal{E}$ vs time τ

Figure 5. Case $G_v = 10^{-5}$, $G_c = 10$, $\eta = 0.0, 0.25, 0.5$. Here the fracture goes through the $\bar{K}_{\kappa 0}$-vertex

http://dx.doi.org/10.5772/56460

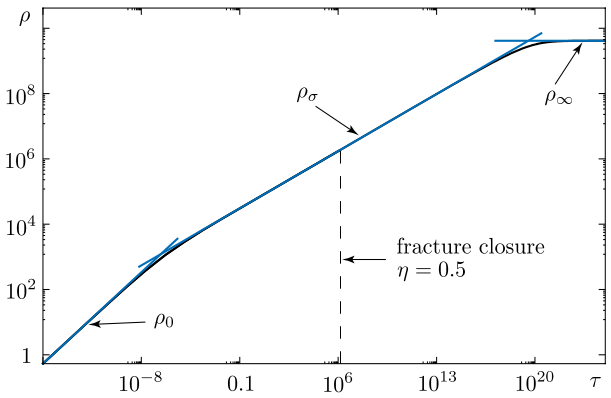

(a) Fracture radius ρ vs time τ

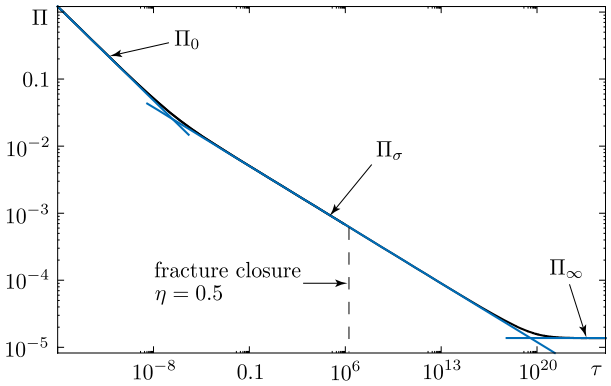

(b) Fracturing fluid pressure Π vs time τ

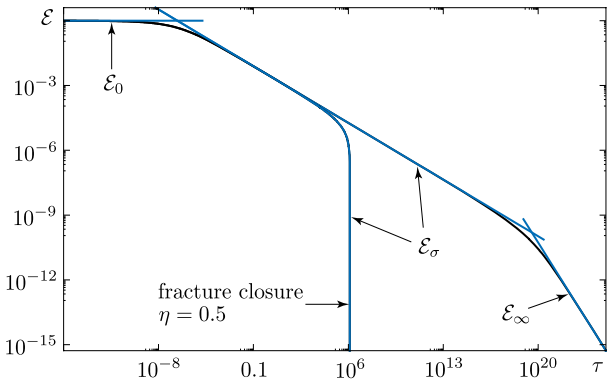

(c) Hydraulic fracturing efficiency $\mathcal{E}$ vs time τ

Figure 6. Case $G_v = 10^{-15}$, $G_c = 3 \times 10^{-11}$, $\eta = 0.0, 0.5$. Here the fracture goes through the $\tilde{K}_{\sigma 0}$-vertex

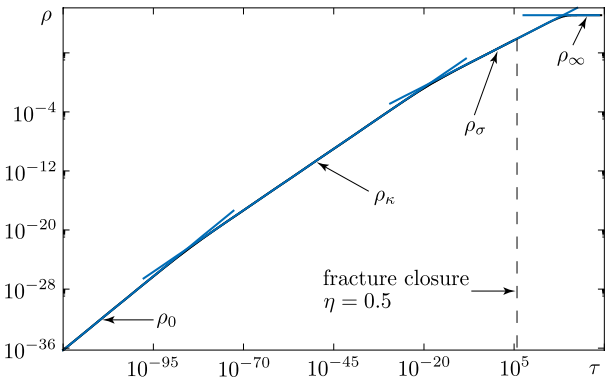

(a) Fracture radius ρ vs time τ

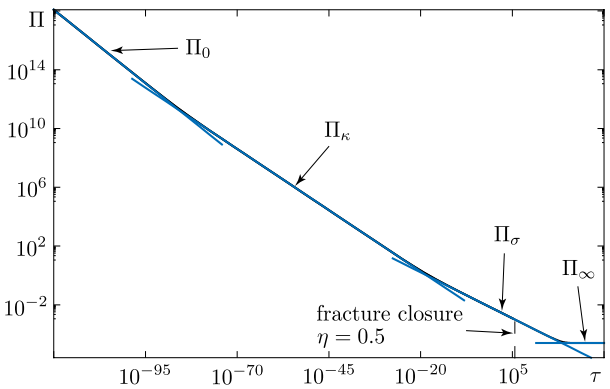

(b) Fracturing fluid pressure Π vs time τ

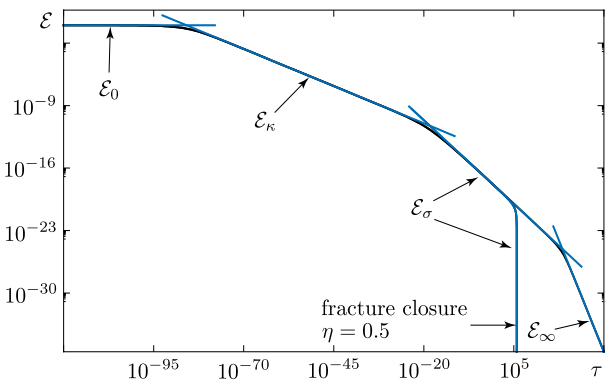

(c) Hydraulic fracturing efficiency $\mathcal{E}$ vs time τ

Figure 7. Case $G_c = 10^{-10}$, $\eta = 0.0, 0.5$. Here the fracture goes through the $\tilde{K}_{\kappa 0}$- and $\tilde{K}_{\sigma 0}$-vertices

http://dx.doi.org/10.5772/56460

current vertex	possible transitions: vertex	transition time: LPR, sec	transition time: MPR, sec	vertex choice
K_0	K_∞	1.2×10^{13}	3.1×10^{8}	
	$\tilde{K}_{\kappa 0}$	4.6×10^{16}	8.3×10^{9}	
	$\tilde{K}_{\sigma 0}$	0.087	1.7×10^{-3}	$\tilde{K}_{\sigma 0}$
$\tilde{K}_{\sigma 0}$	$\tilde{K}_{\sigma\infty}$	5.8×10^{3}	11.9	$\tilde{K}_{\sigma\infty}$

Table 3. Crack propagation

At the $\tilde{K}_{\sigma\infty}$-vertex the fracture radius is equal to $R \approx 3.4$ m and the net pressure is $p - \sigma_0 \approx 7.4$ MPa in the LPR case, whereas $R \approx 0.35$ m and $p - \sigma_0 \approx 7.2$ MPa for the MPR case. If one does not take into account the poroelastic effect, the fracture would grow to $R \approx 4.4$ m and $p - \sigma_0 \approx 0.071$ MPa in the LPR case, while $R \approx 0.44$ m and $p - \sigma_0 \approx 0.71$ MPa in the MPR case. Thus the ultimate fracture radius decrease due to the poroelastic effects is not so significant. On the other hand, the net pressure increase is significant (about 100- and 10-fold increase in the LPR and MPR case, respectively).

In the above analysis we have assumed that the fracture propagates in the toughness-dominated regime (fracturing fluid of zero viscosity). To check this assumption, the value of the following dimensionless group (known as the dimensionless viscosity [17]) has to be assessed

$$\mathcal{G}_m(t) = \frac{\mu' Q_0 E'^3}{K_{Ic}^4 L(t)}, \tag{32}$$

where $L(t)$ is the characteristic fracture size. If the fracture propagates in a viscosity-dominated regime, then $\mathcal{G}_m(t) \gg 1$. In the toughness-dominated regime, $\mathcal{G}_m(t) \ll 1$. Using the above data one can find that at the $\tilde{K}_{\sigma\infty}$-vertex this dimensionless group is equal to $\mathcal{G}_m \approx 90$ for the LPR and $\mathcal{G}_m \approx 121$ for the MPR. Thus fracturing fluid viscosity should be taken into account. Nevertheless, the above example illustrates the importance of the poroelastic effects. In fact a rigorous analysis of the viscosity-dominated regimes predicts similar values for the fracture size and the net pressure [15].

The numerical simulations reported in Figs 4-7 sweep huge time ranges. This is a consequence of the small-time asymptote (K_0-vertex) as the initial condition combined with the need to start from a physically correct initial condition to construct accurate numerical solutions. In practice, however, a correct assessment of the relevant part of the parametric space can dramatically simplify the situation. Knowing this information one can use the analytical vertex asymptotes for preliminary estimation, and then optimize a numerical algorithm. For example Figs 5-7 illustrate that one can use the asymptotic solution of an intermediate vertex as the initial condition provided that the transition time from the K_0-vertex into this vertex is small compared to the treatment time. In the above example of production water reinjection, we have shown that the fracture propagation arrests within a very short period of time compared to the characteristic treatment time. Thus from a practical point of view in this case one can simply use the analytical large-time asymptote to design the treatment.

8. Conclusions

This paper has described a detailed study of a penny-shaped fracture driven by a zero viscosity fluid through a poroelastic medium. The main contribution of this study is the consideration of large scale 3D diffusion and the related poroelastic effect (backstress). We have shown that the problem under consideration has six self-similar propagation regimes (see Section 3). In particular we have demonstrated the existence of a regime ($\tilde{K}_{\kappa\infty}\tilde{K}_{\sigma\infty}$-edge) where the fracture stops propagating. In this regime the fracturing fluid injection is balanced by the 3D fluid leak-off. This stationary solution in the case of zero backstress, $\eta = 0$, was originally obtained by [13].

Numerical simulations illustrate that poroelastic effects could have a significant influence on the propagation of a hydraulic fracture. Namely in the case of 3D diffusion, the backstress effect leads to a decrease of the fracture radius (see Figs 4a and 5a) accompanied by an increase of the fracturing fluid pressure (see Figs 4b and 5b). Moreover, the poroelastic effects can lead to premature closure of a fracture propagating in a leak-off dominating regime with 1D diffusion.

The technique developed in this paper could be also applied to the problem of in situ stress determination by hydraulic fracture [23]. In this application the *in situ* stress determination relies on the interpretation of the fracture breakdown and reopening fluid pressure as well as of the fracture closure pressure during the shut-in phase of experiment. It is obvious that the poroelastic effects could lead to a significant corrections into the stress measurements.

Author details

Yevhen Kovalyshen[1,⋆] and Emmanuel Detournay[1,2]

⋆ Address all correspondence to: Yevhen.Kovalyshen@csiro.au

1 Drilling Mechanics Group, CSIRO Earth Science and Resource Engineering, Australia
2 Department of Civil Engineering, University of Minnesota, USA

References

[1] D.A. Mendelsohn. A review of hydraulic fracture modeling - part i: General concepts, 2d models, motivation for 3d modeling. *jert*, 106:369–376, 1984.

[2] M.J. Economides and K.G. Nolte, editors. *Reservoir Stimulation*. John Wiley & Sons, Chichester UK, 3rd edition, 2000.

[3] A.S. Abou-Sayed. Safe injection pressures for disposing of liquid wastes: a case study for deep well injection (SPE/ISRM-28236). In Balkema, editor, *Proceedings of the Second SPE/ISRM Rock Mechanics in Petroleum Engineering*, pages 769–776, 1994.

[4] J. Hagoort, B. D. Weatherill, and A. Settari. Modeling the propagation of waterflood-induced hydraulic fractures. *Soc. Pet. Eng. J.*, pages 293–301, August 1980.

[5] M. Blunt, F.J. Fayers, and F.M. Orr. Carbon dioxide in enhanced oil recovery. *Energy Convers. Mgmt*, 34(9-11):1197–1204, 1993.

[6] A. van As and R.G. Jeffrey. Caving induced by hydraulic fracturing at Northparkes mines. In *Pacific Rocks 2000*, pages 353–360, Rotterdam, 2000. Balkema.

[7] R.G. Jeffrey and K.W. Mills. Hydraulic fracturing applied to inducing longwall coal mine goaf falls. In *Pacific Rocks 2000*, pages 423–430, Rotterdam, 2000. Balkema.

[8] J. Adachi, E . Siebrits, A. P. Peirce, and J. Desroches. Computer simulation of hydraulic fractures. *Int. J. Rock Mech. Min. Sci.*, 44(5):739–757, International Journal of Rock Mechanics and Mining Sciences 2007.

[9] E.D. Carter. Optimum fluid characteristics for fracture extension. In G.C. Howard and C.R. Fast, editors, *Drilling and Production Practices*, pages 261–270. American Petroleum Institute, Tulsa OK, 1957.

[10] M. P. Cleary. Analysis of mechanisms and procedures for producing favourable shapes of hydraulic fractures. In *Proc. 55th Annual Fall Technical Conference and Exhibition of the Society of Petroleum Engineers of AIME*, volume SPE 9260, pages 1–16, September 1980.

[11] E. Detournay and A.H-D. Cheng. Plane strain analysis of a stationary hydraulic fracture in a poroelastic medium. *Int. J. Solids Structures*, 27(13):1645–1662, 1991.

[12] A.P. Bunger, E. Detournay, and D.I. Garagash. Toughness-dominated hydraulic fracture with leak-off. *Int. J. Fracture*, 134(2):175–190, 2005.

[13] S. A. Mathias and M. Reeuwijk. Hydraulic fracture propagation with 3-d leak-off. *Transport in Porous Media*, 2009.

[14] I. Berchenko, E. Detournay, and N. Chandler. Propagation of natural hydraulic fractures. *Int. J. Rock Mech. Min. Sci.*, 34(3-4), 1997.

[15] Y. Kovalyshen. *Fluid-Driven Fracture in Poroelastic Medium*. PhD thesis, University of Minnesota, Minneapolis, February 2010.

[16] D.T. Barr. *Leading-Edge Analysis for Correct Simulation of Interface Separation and Hydraulic Fracturing*. PhD thesis, Massachusetts Institute of Technology, Cambridge MA, 1991.

[17] A.A. Savitski and E. Detournay. Propagation of a fluid-driven penny-shaped fracture in an impermeable rock: Asymptotic solutions. *Int. J. Solids Structures*, 39(26):6311–6337, 2002.

[18] M. Abramowitz and I.A. Stegun, editors. *Handbook of Mathematical Functions with Formulas, Graphs, and Mathematical Tables*. Dover Publications Inc., New York NY, 1972.

[19] E. Detournay. Propagation regimes of fluid-driven fractures in impermeable rocks. *Int. J. Geomechanics*, 4(1):1–11, 2004.

[20] I.S. Gradshteyn and I.M. Ryzhik. *Table of Integrals, Series and Products*. Academic Press, San Diego CA, 5th edition, 1994.

[21] P. Longuemare, J-L. Detienne, P. Lemonnier, M. Bouteca, and A. Onaisi. Numerical modeling of fracture propagation induced by water injection/re-injection. *SPE European Formation Damage, The Hague, The Netherlands*, May 2001. (SPE 68974).

[22] E. Detournay and A.H-D. Cheng. *Comprehensive Rock Engineering*, volume 2, chapter 5: Fundamentals of Poroelasticity, pages 113–171. Pergamon, New York NY, 1993.

[23] E. Detournay, A. H-D Cheng, J. C. Roegiers, and J. D. Mclennan. Poroelasticity considerations in in situ stress determination by hydraulic fracturing. *Int. J. Rock Mech. Min. Sci.*, 26(6):507–513, 1989.

Chapter 30

Pressurization of a PKN Fracture in a Permeable Rock During Injection of a Low Viscosity Fluid

Erfan Sarvaramini and Dmitry I. Garagash

Additional information is available at the end of the chapter

http://dx.doi.org/10.5772/56474

Abstract

The aim of the present work is to investigate injection of a low-viscosity fluid into a pre-existing fracture within a linear elastic, permeable rock, as may occur in waterflooding and supercritical CO2 injection. In conventional hydraulic fracturing, high viscosity and cake building properties of injected fluid limit diffusion to a 1-D boundary layer incasing the crack. In the case of injection of low viscosity fluid into a fracture, diffusion will take place over wider range of scales, from 1-D to 2-D, thus, necessitating a new approach. In addition, the dissipation of energy associated with fracturing of the rock dominates the energy expended to flow a low viscosity fluid into the crack channel. As a result, the rock fracture toughness is an important parameter in evaluating the propagation driven by a low-viscosity fluid. We consider a pre-existing, un-propped, stationary Perkins, Kern and Nordgren's (PKN) fracture into which a low viscosity fluid is injected under a constant flow rate. The fundamental solution to the auxiliary problem of a step pressure increase in a fracture [1] is used to formulate and solve the convolution integral equation governing the transient crack pressurization under the assumption of negligible viscous dissipation. The propagation criterion for a PKN crack [2] is then used to evaluate the onset of propagation. The obtained solution for transient pressurization of a stationary crack provides initial conditions to the fracture propagation problem.

1. Introduction

The problem of injection of a low-viscosity fluid into a pre-existing fracture may arise in several rock engineering areas, such as, injection of liquid waste (e.g., supercritical CO2) into deep geological formations for storage [3,4,5], waterflooding process to increase recovery from an oil reservoir [6], and control of possible leaks from pre-existing fractures around

radioactive and nuclear wastes storage sites [7]. These fractures could be either of natural origin or man-made (e.g., hydraulic fractures used to stimulate production from a now depleted reservoir chosen for waste storage).

This paper attempts to study injection of a low viscosity fluid into a pre-existing un-propped fracture of the Perkins and Kern and Nordgren (PKN) geometry within a linearly elastic, permeable rock. In the classical PKN model, the fracture length is much larger than the fracture height [8] with the latter confined to a permeable (reservoir) layer sandwiched between two impermeable (cap) rock layers. This assumption allows to model a vertical fracture cross-section as a pressurized Griffith (plane strain) crack.

Until recently, in part due to the lack of a reliable fracture breakdown criterion for a PKN fracture, studies of the PKN fracture propagation have been bounded to the limiting regime corresponding to the dominance of the viscous dissipation in the fluid flow in the crack channel, i.e. when the rock toughness can be neglected [9, 10]. This particular dissipation regime is favored when a high viscosity fracturing fluid and/or high injection rates are used, or at late stages of fracture growth (long fractures). Moreover, for sufficiently large time, the history of injection prior to the onset of the viscosity dominated regime may have minor impacts on the modeling of the classical PKN fracture.

In unconventional hydraulic fracturing (injection of a low-viscosity fluid), on one hand, the dissipation of energy to extend the fracture in the rock may not be negligible compared to the viscous dissipation. On the other hand, the injection history prior to the onset of propagation may not be neglected. With this in mind, we investigate fluid injection into a stationary, pre-existing fracture up to the onset of the propagation, which is defined by the recently introduced propagation criteria for a PKN fracture [2]. The corresponding transient pressurization and leak-off history prior to the breakdown will provide initial conditions for the problem of a propagating PKN fracture in the toughness dominated regime, to be addressed elsewhere.

Contrary to conventional hydraulic fracture where high viscosity and cake-building properties of injected fluid limit the leak-off to a 1-D boundary layer incasing the crack, the low viscosity fluid allows for diffusion over a wider range of scales from 1-D to 2-D. Although, several investigations looked at the propagation of a fracture driven by a low viscosity fluid, when fluid diffusion is fully two-dimensional [11, 12, 13], the study of injection into a stationary, pre-existing fracture has not yet received due attention. One of the foci of this study is to identify solutions corresponding to the limiting cases of the small and large injection time (1-D and fully-developed 2-D diffusion, respectively), and the solution in the intermediate regime corresponding to the evolution between the two limiting cases.

This paper is organized as follows. In section 2 we define and formulate the problem. In Section 3 we first revisit the problem of a step pressure increase in a crack [1], which we then use to formulate and solve the problem of transient pressurization of a crack due to a constant rate of fluid injection. The criterion of PKN propagation [2] is used to evaluate the onset of the fracture propagation. We illustrate the results of this study by considering a case study in which the transient pressurization and the breakdown of pre-existing fractures of different lengths are evaluated for a water injection project.

http://dx.doi.org/10.5772/56474

2. Mathematical formulation

2.1. Problem definition

We consider a pre-existing, un-propped (zero opening) crack of length 2ℓ and height h within a linearly elastic, permeable rock characterized by the plane strain modulus E' and toughness K_{Ic} (Figure 1). The crack is aligned perpendicular to the minimum in-situ stress σ_{min} and is loaded internally by fluid pressure p_f, generated by the fluid injection at the crack center at a constant rate Q_o. The following assumptions are used in this work. 1) The crack height is small compared to the length, such that the deformation field in any vertical cross-section that is not immediately close to the crack edges ($x = \pm\ell$) is approximately plane-strain, and the fluid pressure is equilibrated within a vertical crack cross-section (the PKN assumptions). 2) The minimum in-situ stress σ_{min} and the initial reservoir pore pressure p_0 are uniform along the crack. 3) Initial reservoir pore pressure p_0 is approximately equal to the minimum in-situ stress σ_{min}, allowing the crack to open immediately upon the start of the injection; or alternatively, time t_0 from the onset of injection that is required to pressurize the initially closed crack ($p_0 < \sigma_{min}$) to the point of incipient opening ($p_f(t_0) = \sigma_{min}$) is small compared to the timescale of interest (e.g., the time to the onset of the fracture propagation). 4) Injected fluid is of a low viscosity (and/or the rate of injection is slow), such that the viscous pressure drop in the crack is negligible, or, in other words, the fluid pressure is uniform in the crack. 5) The crack is confined between two impermeable layers, which, together with the assumption of pressure equilibrium within a vertical crack cross-section, suggests a 2-D fluid diffusion within the permeable rock layer. 6) The injected and reservoir fluid have similar rheological properties.

2.2. Governing equations

2.2.1. Elasticity equation

The elasticity equation

$$w(x,z) = \frac{4\left(p_f(x) - \sigma_{min}\right)}{E'}\sqrt{\frac{h^2}{4} - z^2}, \tag{1}$$

is used to relate the opening of a PKN fracture w to the net pressure $p_f - \sigma_{min}$, which is assumed to be equilibrated in a vertical cross-section of the crack, $\partial p_f/\partial z = 0$, [14]. The opening of PKN fracture at mid height ($z = 0$) is

$$w(x) = \frac{2h}{E'}\left(p_f(x) - \sigma_{min}\right). \tag{2}$$

For the particular case of uniformly pressurized fracture, the fracture volume can be evaluated using the elasticity equation (1) as

$$V_{crack} = \frac{\pi h^2 \ell}{E'}\left(p_f - \sigma_{min}\right). \tag{3}$$

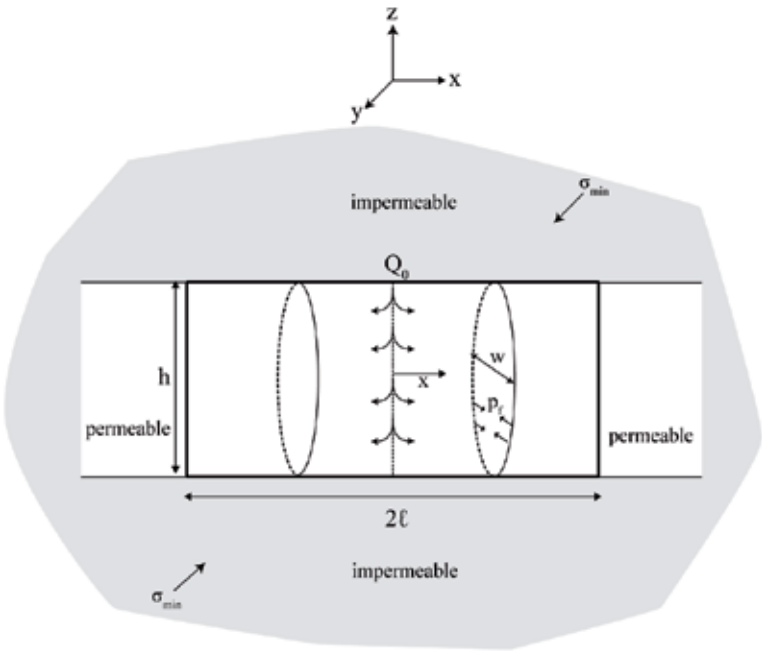

Figure 1. A pre-existing PKN fracture with length 2ℓ and height h

2.2.2. Fluid continuity

Local fluid continuity

Following [15, 16], lubrication equation can be used to describe the flow of an incompressible fluid in a crack (Figure 1) as follows

$$\frac{\partial w}{\partial t} + \bar{g}\,(x,t) = \frac{1}{12\mu}\frac{\partial}{\partial x}\left(w^3\frac{\partial p_f}{\partial x}\right), \quad \bar{g}\,(x,t) = 2g\,(x,t) \quad (t>0, |x|<\ell), \tag{4}$$

where $\bar{g}\,(x,t)$ is the fluid leak-off rate at the crack walls and μ is the viscosity of the injected fluid [17].

Global fluid continuity

The global volume balance of the fluid injected into the fracture is given by:

$$V_{inject} = V_{crack} + V_{leak}, \tag{5}$$

in which V_{inject} indicates the cumulative volume of the fluid injected into the fracture and V_{leak} is the cumulative leak-off volume.

http://dx.doi.org/10.5772/56474

2.2.3. Propagation condition

The stress intensity factor $K_I = \sqrt{GE'}$ associated with the energy release rate G at the propagating PKN fracture edge is given by $K_I = (p_f(\ell) - \sigma_{min})\sqrt{\pi h/4}$ [2]. The criterion for the propagation of a PKN fracture in mobile equilibrium ($K_I = K_{Ic}$) can therefore be expressed as

$$p_f(\ell) - \sigma_{min} = \frac{2K_{Ic}}{\sqrt{\pi h}}. \tag{6}$$

2.2.4. Diffusivity equation and boundary integral representation

The Green's function method can be used to solve an inhomogenous differential equation subjected to boundary conditions. For the fluid flow through the porous media, the diffusivity equation is given by [18]:

$$\frac{\partial p}{\partial t} - \alpha \nabla^2 p = \frac{\dot{\gamma}}{S}, \tag{7}$$

where $\dot{\gamma}$ is the fluid source density (the rate of unit volume of injected fluid in a unit volume of material), $S = \phi c_t$ and $\alpha = k/\mu\phi c_t$ are fluid storage and diffusivity coefficients, respectively, expressed in terms of the formation permeability k, formation bulk compressibility c_t, and porosity ϕ. Due to the presence of the impermeable cap rock boundaries at $z = \pm h/2$ and pressure equilibrium in a vertical cross section , the diffusion problem is two dimensional (2-D). The general 2-D boundary integral for the pressure perturbation due to a distribution of instantaneous sources $g(x,t)$ $[L/T]$ along a crack $y = 0$, $|x| \leq \ell$ is given by [19]

$$p_f(x,t) - p_0 = \int_0^t \int_{-\ell}^{\ell} \frac{g(x',t')}{4\pi S\alpha(t-t')} \exp\left(-\frac{(x-x')^2}{4\alpha(t-t')}\right) dx' dt'. \tag{8}$$

3. Transient pressurization due to fluid injection

In this section, we study transient pressurization due to the injection of a fluid at a constant rate of flow into a pre-existing and stationary fracture. In order to facilitate the solution to this problem, we first revisit the fundamental solution to an auxiliary problem of a step pressure increase in crack [1] and introduce a new result for the large time asymptote of this problem. This fundamental solution is then used to formulate and solve a convolution integral equation governing the solution for the transient pressurization.

3.1. Auxiliary problem: step pressure increase

Consider a fracture subjected to a step pressure increase of magnitude p_*,

$$p(x,t) - p_0 = p_* H(t), \quad (|x| < \ell) \tag{9}$$

where $H(t)$ is a Heaviside function. To facilitate solution of (8) with (9), we rewrite it in the normalized form

$$1 = \frac{1}{2} \int_0^\tau \int_{-1}^{1} \psi(\xi', \tau') \exp\left(-\frac{(\xi - \xi')^2}{\tau - \tau'} \right) \frac{d\xi' d\tau'}{\tau - \tau'}, \tag{10}$$

where the nondimensional time (τ), coordinate (ξ), leak-off rate (ψ), and cumulative leak-off volume (Φ) are defined as

$$\tau = \frac{t}{t_*}, \quad \xi = \frac{x}{\ell}, \quad \psi(\xi,\tau) = \frac{\ell g(x,t)}{2\pi\alpha S p_*}, \quad \Phi(\tau) = \frac{2V_{leak}(t)}{\pi \ell^2 h S p_*}, \tag{11}$$

and $t_* = \ell^2/4\alpha$ is diffusion timescale. After applying Laplace transform, (10) becomes:

$$1/s = \int_{-1}^{1} \psi(\xi', s) K_0\left(2\sqrt{s}|\xi - \xi'| \right) d\xi', \tag{12}$$

where K_0 is the modified Bessel function of the second kind, s is the Laplace transform parameter and $\psi(\xi, s)$ is the Laplace image of $\psi(\xi, \tau)$.

Before integral convolution equation (12) is treated numerically, it is useful to consider its asymptotics for short and long injection times.

During the injection process when the characteristic lengthscale for fluid diffusion $\sqrt{\alpha t}$ is small compared to the crack size ℓ, or in terms of the normalize time, $\tau \ll 1$, the fluid diffusion pattern is approximately 1-D and the normalized leak-off rate is given by [1]:

$$\psi(\tau) = \frac{2}{\pi^{3/2}\sqrt{\tau}} \quad (\tau \ll 1). \tag{13}$$

As the injection time increases, the 1-D fluid diffusion pattern is no longer valid and a 2-D fluid diffusion pattern must be considered. We can show that for long enough injection times the Laplace image of the fluid leak-off rate is given by:

$$\psi(\xi, s) = \left(-\frac{\pi}{2}\sqrt{1-\xi^2}\, s \left[\ln(s/4) + 2\gamma \right] \right)^{-1} \quad (\tau \gg 1), \tag{14}$$

where $\gamma = 0.5772$ is the Euler's constant. The approximate image of (14) in actual time domain is:

http://dx.doi.org/10.5772/56474

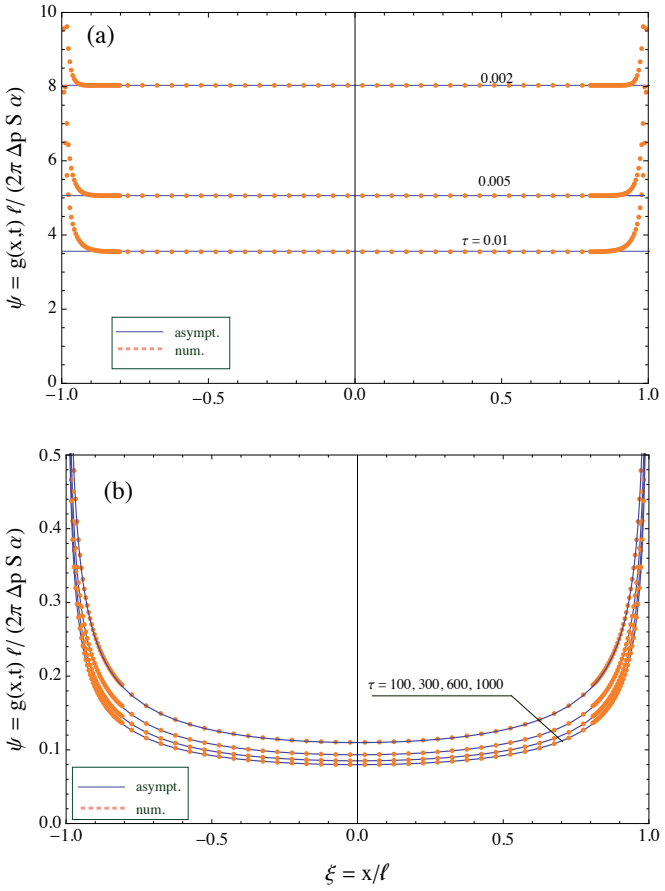

Figure 2. Comparison of the numerical solution for the normalized leak-off rate in the auxiliary problem (step pressure increase along the crack) with the small time (a) and large time (b) asymptotes.

$$\psi(\xi,\tau) \approx \left(\frac{\pi}{2}\sqrt{1-\xi^2}\left(\ln\left(\omega^2\tau\right)-2\gamma\right)\right)^{-1} \quad (\tau \gg 1), \tag{15}$$

where $\omega = 2.67$.

Following [1] we solve (12) numerically for the Laplace image $\psi(\xi,s)$ ($-1 \le \xi \le 1$ and $10^{-9} \le s \le 10^{9}$) using $N = 110$ discretization nodes along the fracture, and then apply inverse numerical Laplace transform (Stehfest algorithm [20] with six terms) to tabulate the solution for the normalized leak-off rate $\psi(\xi,\tau)$. This solution is contrasted to the small and large time asymptotes in Figure 2.

The normalized cumulative leak-off from a fracture subjected to a step pressure increase can be obtained by integrating from fluid leak-off rate with respect to time and space and is given by [1] :

$$\Phi(\tau) = \int_0^\tau \int_{-1}^1 \psi\left(\xi', \tau'\right) d\xi' d\tau', \tag{16}$$

3.2. Transient pressurization problem

Assuming a uniform pressure along the crack channel (the viscous pressure drop in the crack is negligible), and "instantaneous" pressure build-up at the beginning of injection from the initial pore pressure value p_0 to the value $p_f = \sigma_{min}$ corresponding to the incipient crack opening, the cumulative leak-off volume V_{leak} can be obtained by the applying the Duhamel's theorem [1, 19]

$$V_{leak} = \nu(t)(\sigma_{min} - p_0) + \int_{0^+}^{t} \nu(t - t') \frac{dp_f}{dt'} dt', \tag{17}$$

where $\nu(t) = \frac{\pi}{2} \ell^2 h S \Phi(t/t_*)$ is the cumulative leak-off volume of the fracture subjected to a unit step pressure increase, as discussed in the previous section.

Equation (5) can be expressed in the case of fluid injection at a constant rate Q_0 as

$$Q_0 t = \frac{\pi h^2 \ell}{E'}(p_f(t) - \sigma_{min}) + \nu(t)(\sigma_{min} - p_0) + \int_{0^+}^{t} \nu(t - t') \frac{dp_f}{dt'} dt', \tag{18}$$

where expression (3) for V_{crack} was used. Let us now define a characteristic pressure perturbation $p_* = Q_0/(\pi h S \alpha)$, which is then used to scale the net pressure and the initial effective stress

$$\Pi = \frac{p_f - \sigma_{min}}{p_*}, \qquad \Sigma_0 = \frac{\sigma_{min} - p_0}{p_*} \tag{19}$$

respectively. Using normalized parameters (11) and (19), we convert (18) to the nondimensional form:

$$\frac{\tau}{4} = \eta \Pi(\tau) + \frac{1}{2}\Sigma_0 \Phi(\tau) + \frac{1}{2} \int_{0^+}^{\tau} \Phi(\tau - \tau') \frac{d\Pi}{d\tau'} d\tau', \qquad \left(\eta = \frac{h}{\ell S E'}\right) \tag{20}$$

where $\Phi(\tau)$ is the normalized cumulative leak-off rate in the auxiliary problem, (16), and η is a scaled crack height-to-length ratio. Applying the Laplace transform to (20) yields the solution for the Laplace image of the normalized pressure in the crack:

http://dx.doi.org/10.5772/56474

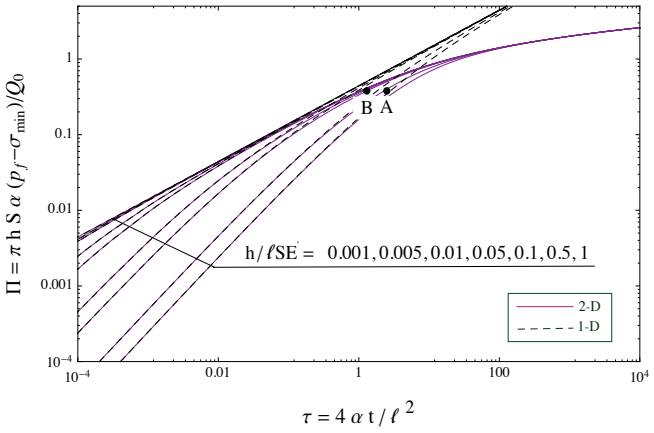

Figure 3. Evolution of the fluid net-pressure during a constant-rate injection into a stationary crack within an abnormally-pressurized reservoir $p_0 \approx \sigma_{min}$ for various values of the crack height-to-length ratio $h/\ell SE'$.

$$\Pi(s) = \frac{1}{2s^2}\frac{1-2\Sigma_0 s^2\Phi(s)}{2\eta + s\Phi(s)}, \tag{21}$$

in which $\Phi(s)$ is the Laplace image of $\Phi(\tau)$. This solution is then numerically inverted to the time domain using the Stehfest algorithm [20].

Evolution of the normalized pressure Π during the transient pressurization of a crack is shown in Figure 3 for the case of an abnormally pressurized reservoir $\Sigma_0 \approx 0$ ($p_0 \approx \sigma_{min}$) and for various values of the scaled crack height-to-length ratio $\eta = h/\ell SE'$. (The 1-D diffusion solution to the same problem is shown by dashed lines for comparison).

With the solution for the normalized pressure in hand, the onset of the fracture propagation can be determined from the normalized form of (6):

$$\Pi = \Pi_B \quad \text{with} \quad \Pi_B = \frac{2\sqrt{\pi h}S\alpha K_{Ic}}{Q_0}, \tag{22}$$

where Π_B is the normalized breakdown pressure.

Example. Water injection project

Consider an example of the fracture breakdown calculations for a water injection project in a sandstone formation [21] characterized by porosity $\phi = 0.1$, permeability $k = 10.132$ md, pre-existing fracture height $h = 30.48$ m (assumed to span the height of the sandstone layer), minimum in-situ stress $\sigma_{min} = 28.8$ MPa, bulk rock compressibility $c_t = 5.35 \times 10^{-10}$ Pa^{-1}, fluid viscosity $\mu = 1$ cp, rock toughness $K_{Ic} = 1$ MPa $m^{1/2}$, plane strain modulus $E' = 9.3$ GPa. The reported injection rate was $Q_0 = 0.00052$ m^3/s. The calculated values are $S = 5.35 \times 10^{-11}$ Pa^{-1} (storage parameter),$\alpha = 0.19$ m^2/s (diffusivity coefficient), $p_* = Q_0/(\pi h S\alpha) = 0.537$ MPa (characteristic pressure perturbation). The normalized breakdown

net-pressure, (22), is $\Pi_B = 0.38$ (or, in dimensional terms, $(p_f - \sigma_{min})_B = p_* \Pi_B = 0.204$ MPa). We chose two arbitrary fracture half-lengths $\ell = 100$ m $(h/\ell SE^{'} = 0.61)$ and $\ell = 1000$ m $(h/\ell SE^{'} = 0.061)$ to estimate the onset of fracture propagation from Figure 3 to be at $\tau = 2.5$ (point A) and $\tau = 1.22$ (point B), respectively. The corresponding dimensional breakdown times are 9 hrs ($\ell = 100$ m) and 19 days ($\ell = 1000$ m).

4. Conclusions

Important applications of injection of a low viscosity fluid into a pre-existing fracture, such as waterflooding and supercritical CO2 injection in geological sequestration, necessitate comprehensive studies of mechanical and hydraulically properties of fractures from the beginning of injection until the onset of fracture propagation. In this study, we considered a low viscosity fluid injection into a pre-existing, un-propped crack of a PKN geometry. We focus on the case of a critically-overpressured reservoir and initially closed (un-propped) crack. The extension of this work to propped cracks and more general reservoir conditions are reported elsewhere.

The analysis assumes negligible viscous dissipation during injection of a low viscosity fluid at a sufficiently slow injection rate [22], and, as a result, approximately uniform pressure distribution in the crack. Furthermore, the poroelastic effects are also neglected in this study. To outline the validity of the latter assumption, we can show that the later stages of transient pressurization (the so-called leak-off dominated regime when the injection time $\gg$ diffusion timescale $\ell^2/4\alpha$) with and without poroelasticity effects are identical. However, the generated poroelastic backstress which tends to close the fracture may cause a delay in the initiation of crack propagation when compared to the case where poroelastic effects are neglected. In addition, for certain ranges of fracture and fluid properties and field operating condition the backstress may become large enough to prevent the fracture from propagation indefinitely.

We evaluated the evolution of the fluid pressure inside the fracture during the transient pressurization by considering 2-D fluid diffusion from the fracture into the surrounding porous rock. As the fracture is pressurized, the condition for the onset of its propagation (breakdown condition) is eventually reached. We quantified how the fracture breakdown condition depends upon the rock and fluid properties, the in-situ stress and the fluid injection rate. The history of the transient pressurization prior to breakdown can be used to provide the initial conditions for the fracture propagation problem.

Acknowledgments

We acknowledge support for this work from the Natural Science and Engineering Research Council of Canada under Discovery Grant No. 371606.

Author details

Erfan Sarvaramini and Dmitry I. Garagash

Dalhousie University, Department of Civil and Resource Engineering, Halifax, Nova Scotia, Canada

http://dx.doi.org/10.5772/56474

References

[1] E. Detournay and A.H-D. Cheng. Plane strain analysis of a stationary hydraulic fracture in a poroelastic medium. *Int. J. Solids Structures*, 27(13):1645–1662, 1991.

[2] D.I. Garagash. Fluid-driven crack tunneling in a layer. *to be submitted to ASME J. Appl. Mech.*, 2013.

[3] J.B. Osborne and D.I. Garagash. Using CO2 as a fracture fluid in tight reservoirs. Technical report, Petroleum Technology Research Centre, 2012.

[4] S. Bachu. Screening and ranking of sedimentary basins for sequestration of CO2 in geological media in response to climate change. *Environmental Geology*, 44(277–289), 2003.

[5] J. Bradshaw, S. Bachu, D. Bonijoly, R. Burruss, S. Holloway, N.P. Christensen, and O.M. Mathiassen. CO2 storage capacity estimation: issues and development. *Int. J. Greenhouse Gas Control*, 1(62-68), 2007.

[6] A. Settari and G.M. Warren. Stimulation and field analysis of waterflood induced fracturing. Society of Petroleum Engineers, 1994.

[7] K. Pruess, J. S. Y. Wang, and Y. W. Tsang. On thermohydrologic conditions near high-level nuclear wastes emplaced in partially saturated fractured tuff: 1. simultion studies with explicit consideration of fracture effects. *Water Resources Res.*, 26(6):1235–1248, 1990.

[8] T.K. Perkins and L.R. Kern. Widths of hydraulic fractures. *J. Pet. Tech., Trans. AIME*, 222:937–949, 1961.

[9] E. Detournay, A.H-D. Cheng, and J.D. McLennan. A poroelastic PKN hydraulic fracture model based on an explicit moving mesh algorithm. *ASME J. Energy Res. Tech.*, 112:224–230, 1990.

[10] Y. Kovalyshen and E. Detournay. A reexamination of the classical PKN model of hydraulic fracture. *Transport in Porous Media*, 81:317–339, January 2009.

[11] Y. N. Gordayev and A. F. Zazovsky. Self-similar solution for deep-penetrating hydraulic fracture propagation. *Transport in Porous Media*, 7:283–304, 1992.

[12] Y. N. Gordayev and V. M. Entov. The pressure distribution around a growing crack. *J. Appl. Maths Mechs.*, 61(6):1025–1029, 1997.

[13] Y. Kovalyshen. *Fluid-Driven Fracture in Poroelastic Medium*. PhD thesis, 2009.

[14] R.P. Nordgren. Propagation of vertical hydraulic fractures. *J. Pet. Tech.*, 253:306–314, 1972. (SPE 3009).

[15] D.A. Spence, P.W. Sharp, and D.L. Turcotte. Buoyancy-driven crack propagation: a mechanism for magma migration. *J. Fluid Mech.*, 174:135–153, 1987.

[16] J. R. Lister. Buoyancy-driven fluid fracture: The effects of material toughness and of low-viscosity precursors. *J. Fluid Mech.*, 210:263–280, 1990.

[17] G. K. Batchelor. *An Introduction to Fluid Dynamics*. Cambridge University Press, Cambridge UK, 1967.

[18] J. Bear. *Dynamics of Fluids in Porous Media*. Dover Publications, 1988.

[19] H. Carslaw and J. C. Jaeger. *Conduction of Heat in Solids*. Oxford University Press, 2nd edition, 1959.

[20] H. Stehfest. Numerical inversion of Laplace transform. *Communications of the Association for Computing Machinery (ACM)*, 13:47–49, January 1970.

[21] L.X. Nghiem, P.A. Forsyth Jr., and A. Behie. A fully implicit hydraulic fracture model. *Journal of Petroleum Technology*, 36(7):1191–1198, July 1984.

[22] D. Garagash and E. Detournay. An analysis of the influence of the pressurization rate on the borehole breakdown pressure. *Int. J. Solids Structures*, 34(24):3099–3118, 1997.

Chapter 31

Modified Formulation, ε-Regularization and the Efficient Solution of Hydraulic Fracture Problems

Alexander M. Linkov and Gennady Mishuris

Additional information is available at the end of the chapter

http://dx.doi.org/10.5772/56218

1. Introduction

Analytical models and numerical simulation are important means to increase understanding and to enhance efficiency of hydraulic fracturing. The reasons for developing and using them are clearly explained, for instance, by Mack and Warpinski [1]. Thus, there is no need to dwell on them. Rather we focus on improving analytical and numeric methods used to the date. Our objective is to suggest new approaches for developing accurate, robust and stable simulators on the basis of recent analytical and computational findings [2-6].

The approaches discussed in the paper stem from the fact [2,3] that the conventional formulation of the hydraulic fracture problem (for example, see [7]), when neglecting the lag and fixing the position of the fracture front at a time step, is ill-posed. This feature has not been reported for more than three decades of studying hydraulic fractures because of two reasons. Numerical simulators, based on the conventional formulation (for example, see [7,8]), employ quite rough meshes, which themselves serve as specific 'regularizators'. On the other hand, rare solutions of model problems either also employed rough meshes [9], or they were obtained by solving the initial value (Cauchy) problem [10-12] rather than the boundary value problem (a discussion of the difference may be found in references [3,4]). The disclosure of the mentioned fact has led to (i) explicit formulation of the speed equation (SE) in its general form[1], (ii) comprehension of its significance for proper numerical simulation of hydraulic fractures and (iii) distinguishing the particle velocity as a preferable variable[2]. It

1 To the authors'knowledge, Kemp [11] was the first who clearly distinguished the speed equation when revisiting the Nordgren's problem. When introducing the SE, numbered (5) in his paper, Kemp wrote (p. 289): „Nowhere is (5) mentioned. (5) is called the Stefan condition and is always present in moving boundary problems". Kemp used the SE to solve the Nordgren's problem as an initial value rather than boundary value problem. This excluded solving ill-posed boundary value problem.

has also led to the efficient means, called ε–regularization [2,3], to overcome the analytical and computational difficulties caused by ill-posedness. Finally, the entire conventional formulation of the problem has changed to the modified formulation, which opens new analytical and computational options for solving hydraulic fracture problems.

Below we employ these options. Section 2 contains a concise review of the modified formulation. In Section 3, we illustrate its analytical advantages by simple solutions for the Perkins-Kern-Nordgren (PKN) [9,13] and Khristianovich-Geertsma-de Klerk (KGD) [14,15] models. In Section 4, we turn to computational advantages of the modified formulation, present new computational schemes and illustrate their efficiency by numerical results for the PKN model. Section 5 contains the extension of these schemes to the pseudo-three-dimensional (P3D) models [1], the importance of which grows nowadays because of their employment in simulators for hydraulic fractures in low permeable shales [16]. A brief summary concludes the paper (Section 6).

2. Modified formulation of hydraulic fracture problem

The modified equations [3,4] use as variables the velocity v of fluid particles averaged through the channel width (fracture opening) and the modified opening $y=w^{1/\alpha}$, where α is the exponent defined by the asymptotic behavior of the opening w at the fluid front ($w=C(t)r^{\alpha}$, r is the distance from the front, t is the time). Then the continuity equation for a flow in a narrow channel reads:

$$\frac{\partial y}{\partial t} + \mathbf{v} \bullet \operatorname{grad} y + \frac{1}{\alpha} y \operatorname{div} \mathbf{v} + \frac{y^{1-\alpha}}{\alpha} q_l = 0 \tag{1}$$

where q_l is the intensity of distributed sinks or sources (below this term is assumed positive to account for leak off); the divergence and gradient are defined in the tangent plane to the channel (hydraulic fracture). The Poiseuille type relation in terms of the particle velocity is:

$$\mathbf{v} = -\frac{1}{w} D\left(w,\ p\right) \operatorname{grad} p \tag{2}$$

It is obtained by integration of the Navier-Stokes equations for a flow of a viscous fluid in a narrow channel. Herein, $p(x,t)$ is the fluid pressure, x is the position vector on the surface of the flow in immovable coordinates, D is a function or operator, such that $D(0,\ p)\operatorname{grad} p = 0$.

The equations (1) and (2) represent the modified system of PDE. Substitution of (2) into (1) gives the modified lubrication equation. We shall not write it down explicitly because in the

2 Mack and Warpinski [1] have noticed the beneficial property of the velocity. On p. 6-21 of their fundamental work they wrote: „Detailed numerical simulations have shown that the velocity varies much more slowly than the flow rate". These authors made the best of this property by using the velocity as the unknown variable; they actually employed the speed equations, as well, although not writing it explicitly.

http://dx.doi.org/10.5772/56218

general case, keeping the velocity, which is a smooth function near the fluid front, as unknown is more convenient than to replace it by grad$p$, which is commonly strongly singular. Note only that the operator resulting from substitution of (2) into (1) is of first order in time and of second order and elliptic in spatial coordinates. Consequently it requires one *initial* condition defining the initial distribution of the opening. In terms of the modified opening it is:

$$y(x,\ t_0)=y_0(x) \tag{3}$$

The elliptic operator requires only one *boundary* condition (BC) on the fluid front *Le*. For instance, when neglecting the lag between the fluid front and the fracture contour, the BC may be the condition of the prescribed normal component $q_n(x,\ t)=y^{\alpha}v_n$ of the flux:

$$y^{\alpha}v_n(x,\ t)=q_0(x,\ t), \qquad x\in L_e \tag{4}$$

where q0(x) is a known function at L_e; specifically, at the injection points, it is defined by the injection regime. At a point x_* of the propagating fluid front, coinciding with the fracture contour L_f, we have $w=0$ and equation (2) implies $q_f(x,\ t)=wv=0$. Then (4) becomes:

$$y(x_*,\ t)=0, \qquad x_*\in L_f \tag{5}$$

Of special importance is that the limit value of the particle velocity v_{n^*} at the fluid front represents the speed of the front propagation v_* [2-4]:

$$v_*=\frac{d\,x_{n^*}}{dt}=v_{n^*} \tag{6}$$

Herein, x_{n^*} is the normal component of a point x_* at the front. It is assumed that sucking or evaporation through the front is negligible. (6) is the *speed equation* (SE), which is fundamental for moving boundaries. Using (2) in (6) specifies the SE for a flow of incompressible fluid in a narrow channel [2,3]:

$$v_*=\frac{d\,x_{n^*}}{dt}=-\left[\frac{1}{w(x_*)}D\left(w,\ p\right)\frac{\partial p}{\partial n}\right]_{x=x_*} \tag{7}$$

Thus we have the *local* condition (7) at points of the propagating fluid front. This allows one to trace the propagation by well-established methods of the theory of propagating surfaces [17]. In contrast, the conventional formulation employs the *global* mass balance (for example, see [7,8,10,12]), which is a single equation. The latter is sufficient when considering 1D problems with one point of the front to be traced. However, in the general case of a 2D fracture, it is preferable to employ the SE, which is formulated at each of the points of the fluid front.

This gives another evidence that using the particle velocity is beneficial from the computational point of view.

The speed equation (6) also yields important implications for numerical simulation of hydraulic fractures by finite differences. Indeed, when at a time step we have known both x_* and $v_*(x_*)$, the SE (7) becomes a boundary condition additional to the boundary condition (5) on the front. Thus, as noted in [2], a boundary value problem may appear overdetermined and ill-posed in the Hadamard sense [18]. To avoid difficulties, it is reasonable to use ε-regularization, suggested and employed in [2,3].

The ε-regularization is performed as follows. At each point of the fluid front, an exact BC is changed to an approximate equality at a small distance r_ε behind the front:

$$\int_{p_0}^{p_\varepsilon} \frac{1}{w} D(w,p)dp = v_* r_\varepsilon \tag{8}$$

where p_0 is the pressure at the front, p_ε is the pressure at a distance r_ε from the front. Equation (8) is obtained by combining the boundary condition at the fluid front, particular for a problem, with the SE, which is general. The distance (absolute r_ε or relative ε) is taken small enough to use the equality sign in the derived approximate condition. The SE is also assumed to be met at the distance r_ε to an accepted accuracy:

$$v_*(t) = \frac{d x_{n^*}}{dt} = -\left[\frac{1}{w} D(w,\ p)\frac{\partial p}{\partial n}\right]_{r=r_\varepsilon} \tag{9}$$

The ε-regularized BC (8) allows one to avoid unfavorable computational effects. The ε-regularized SE (9) serves to find the front propagation. In particular, it is basic when applying the level set and fast marching methods [17].

The described modification concerns mostly with the *fluid* equations, which are sufficient when the opening w is known. However, it is not known in advance in problems of hydraulic fracturing. To find it, the fluid equations are complimented with solid mechanics and fracture equations.

In terms of the modified opening, the *solid mechanics* equation with an integral operator A

$$A y^{\alpha} = p \tag{10}$$

is solved under the BC of zero opening at points of the fracture contour. When neglecting the lag, this condition coincides with the condition (5) of zero flux at the fluid front.

The *fracture mechanics* equations define the critical state and the perspective direction of the fracture propagation. In the case of tensile mode of fracture, these are:

http://dx.doi.org/10.5772/56218

$$K_I = K_{Ic}, \qquad K_{II} = 0 \tag{11}$$

where K_I is the tensile stress intensity factor (SIF), K_{Ic} is its critical value, K_{II} is the shear SIF. The modified problem, when neglecting the lag ($x_e = x_*$), consists of solving the PDE (1) and (2) together with the solid mechanics equation (10) under the initial condition (3), BC (4) at the contour part with prescribed influx, and the ε-regularized BC (8) at the fluid (and fracture) front. The conditions (11) define the possibility and the direction of the fracture propagation. The ε-regularized SE (9) serves to find the front propagation on the time steps.

3. Analytical solutions

In particular cases of 1D problems for the PKN [9,13] and KGD [14,15] models, one can solve an initial value rather than boundary value problem (for example, see [10-12]). Then the problem is well-posed and it does not require regularization. Still in these cases, the modified variables are of use to obtain simple analytical solutions of problems, which otherwise requite involved calculations. For a Newtonian fluid, the analytical solutions are given in [4] both for the PKN and KGD models. In a similar way, by employing the modified variables, we may solve these 1D problems for a non-Newtonian fluid.

Consider a fluid with the viscosity law of power-type $\tau = M\dot{\gamma}^n$, where τ is the shear stress, $\dot{\gamma}$ is the shear strain rate, M is the consistency index, n is the behaviour index. The common derivations for a flow in a narrow channel yield the Poiseuille type dependence between the particle velocity v, averaged through the channel width w, and the pressure gradient:

$$v = \left(-k_f w^{n+1} \frac{\partial p}{\partial x}\right)^{1/n} \tag{12}$$

where $k_f = 1/(\theta M)$, for a plane channel, $\theta = 2[2(n+1)]^n$ (for example, see [12]), the x-axis is in the direction of the fracture propagation, v is the component of the particle velocity in the direction of x.

The geometrical scheme of the PKN model is given in Figure 1. In this model the plane-strain conditions occur in cross-sections parallel to the fracture front. Then the elasticity equation (10) takes the form [9]:

$$p = k_r w \tag{13}$$

where $k_r = [2/(\pi h)]E'$, $E' = E/(1-\nu^2)$, E is the elasticity modulus, ν is the Poisson's ratio, h is the fracture height. Substitution of (13) into (12) yields:

$$v = \left(-\frac{k_f k_r}{n+2} \frac{\partial w^{n+2}}{\partial x}\right)^{1/n} \tag{14}$$

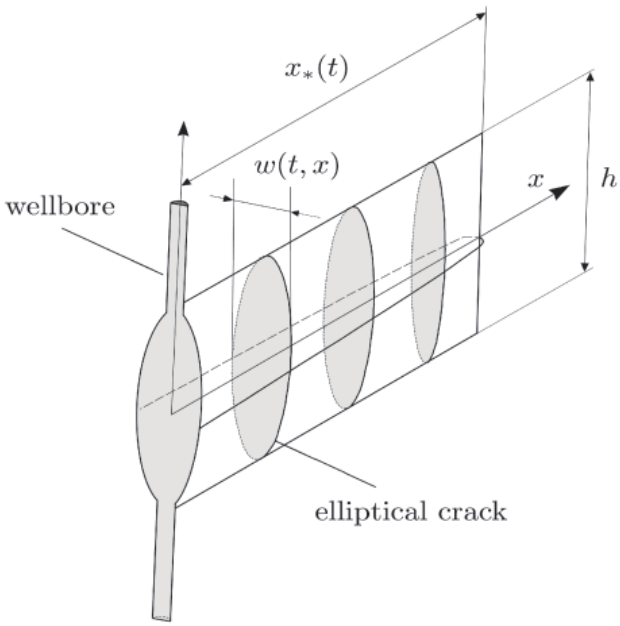

Figure 1. Geometrical scheme of the PKN model

Physically significant speed of the front is neither zero, nor infinite. According to (14) and the SE (7) it is possible only when the function $y=w^{n+2}$ is linear in x. Hence, in the considered problem, the exponent α in the modified opening $y=w^{1/\alpha}$ is $\alpha=1/(n+2)$. Then the continuity equation (1), the velocity equation (2), the initial condition (3), the BC (4), (5) and the SE (6) become, respectively,

$$\frac{\partial y}{\partial t}+v\frac{\partial y}{\partial x}+\frac{y}{\alpha}\frac{\partial v}{\partial x}+\frac{y^{1-\alpha}}{\alpha}q_l=0 \tag{15}$$

$$v=\left(-k_f k_r \alpha \frac{\partial y}{\partial x}\right)^{1/n} \tag{16}$$

$$y(x,\ t_0)=y_0(x) \tag{17}$$

$$\left[y^{\alpha}v\right]_{x=0}=q_0(t), \tag{18}$$

$$y(x_*)=0 \tag{19}$$

$$v_*(t)=\frac{dx_*}{dt}=\left[\left(-k_f k_r \alpha \frac{\partial y}{\partial x}\right)^{1/n}\right]_{x=x_*} \tag{20}$$

http://dx.doi.org/10.5772/56218

Following [4], introduce the normalized variables $x_d = x / x_n$, $x_{*d} = x_* / x_n$, $t_d = t / t_n$, $v_d = v / v$, $v_{*d} = v_* / v_n$, $y_d = y / y_n$, $q_d = q / q_n$, $q_{ld} = q_l / q_{ln}$, where the normalizing quantities are: $x_n = \left(k_f k_r q_n^{n+2} t_n^{2n+2}\right)^{1/(2n+3)}$, $v_n = x_n / t_n$, $y_n = \left(q_n t_n / x_n\right)^{1/\alpha}$ with t_n and q_n being arbitrary typical values of the time and influx per unit height, respectively. In terms of the normalized variables, the problem (15)-(20) has the same form except that the multiplier $k_f k_r$ is changed to the unit. This excludes the consistency factor, the elasticity modulus and the height. Hereafter in this section we use (15)-(20) assuming $k_f = 1$ and $k_r = 1$.

Consider the case when the influx is prescribed by the power dependence in time:

$$q_0(t) = t^{\beta_q} \tag{21}$$

, (21)

where β_q is a prescribed constant; for a constant influx, $\beta_q = 0$. In the case of zero leak-off, the solution of (15)-(20) with the influx (21) may be found in self-similar variables:

$$x = \xi t^{\beta_*} x_* = \xi_* t^{\beta_*} \; v = V(\xi) t^{\beta_* - 1} v_* = V_* t^{\beta_* - 1} \; y = Y\left(\xi\right) t^{\beta_w/\alpha} q = Y(\xi)^{\alpha} V\left(\xi\right) t^{\beta_q} \tag{}$$

with $\beta_w = \left[1 + (n+1)\beta_q\right] / \left(2n+3\right)$, $\beta_* = \left[2(n+1) + (n+2)\beta_q\right] / \left(2n+3\right)$. In (22), ξ_* and V_* are constants, expressing respectively the self-similar fracture length and the front speed.

We may account for leak-off by assuming that the term q_l is also represented in the form with separated variables: $q_l = Q_l\left(\xi\right) t^{\beta_l}$, where $Q_l(\xi)$ is a prescribed function, which may be singular at the front as $Q_l(\xi) = o\left((\xi_* - \xi)^{\alpha - 1}\right)$. For the exponent β_l , it follows that $\beta_l = \beta_w - 1$.

We prescribe the functions $Y(\xi)$ and $V(\xi)$ by power series in the variable $\tau = 1 - \xi / \xi_*$:

$$Y(\xi) = \frac{\xi_*^{n+1} \beta_*^n}{\alpha} \sum_{j=1}^{\infty} a_j \tau^{\,j}, \; V(\xi) = V_* \sum_{j=0}^{\infty} b_j \tau^{\,j}, \tag{22}$$

where $V_* = \xi_* \beta_*$. The leak-off function $Q_l(\xi)$ is represented as $Q_l(\xi) = \tau^{\alpha} \sum_{j=0}^{\infty} q_j \tau^{\,j}$ with known coefficients q_j (for zero leak-off, $q_j = 0$, $j = 0,1,...$). Then the coefficients b_j and a_j are found recurrently from the equations (15), (16) re-written in self-similar variables. Omitting technical details, the coefficients b_j for $j = 2, 3, \ldots$ are:

$$b_j = -\frac{1}{j + \alpha} \left\{ \sum_{k=2}^{j} \left[(j - k + 1 + \alpha k) a_k b_{j-k+1} + \left(\alpha j - \frac{\beta_w}{\beta_*}\right) a_j \right] - C_l \sum_{k=1}^{j} c_k q_{j-k} \right\} \tag{23}$$

with the starting values $a_1=b_0=1$, $b_1=\frac{1}{1+\alpha}\left(-\alpha+\frac{\beta_w}{\beta_*}+C_l q_0\right)$, $c_1=1$. In (24), $C_l=\left(\frac{\alpha}{\xi_*^{n+1}\beta_*^{n+1/\alpha}}\right)^{\alpha}$ and the coefficients a_j and c_j are found recurrently from equations: $\sum_{k=0}^{\infty}(k+1)a_{k+1}\tau^k=\left(\sum_{j=0}^{\infty}b_j\tau^j\right)^n$, $\sum_{k=1}^{\infty}c_k\tau^k=\tau\left(\sum_{j=0}^{\infty}a_{j+1}\tau^j\right)^{\alpha}$. In particular, for the first five coefficients a_j and c_j we have:

$$\begin{gathered}a_1=b_0=1,\ a_2=\frac{1}{2}nb_1,\ a_3=\frac{1}{6}n\left[(n-1)b_1^2+2b_2\right]\\ a_4=\frac{1}{24}n\left[(n-1)(n-2)b_1^3+6(n-1)b_1b_2+6b_3\right]\end{gathered}\tag{24}$$

$$a_5=\frac{1}{120}n\left[(n-1)(n-2)(n-3)b_1^4+12(n-1)(n-2)b_1^2b_2+24(n-1)b_1b_3+24b_4\right]\tag{25}$$

$$\begin{gathered}c_1=a_1=1,\ c_2=(1-\alpha)a_2,\ c_3=\frac{1}{2}(1-\alpha)\left[-\alpha a_2^2+2a_3\right],\quad c_4=\frac{1}{6}(1-\alpha)\left[\alpha(\alpha+1)a_2^3-6\alpha a_2a_3+6a_4\right],\\ c_5=\frac{1}{24}(1-\alpha)\left[-\alpha(\alpha+1)(\alpha+2)a_2^4+12\alpha(\alpha+1)a_2^2a_3-24\alpha a_2a_4+24a_5\right].\end{gathered}\tag{26}$$

Starting from $a_1=b_0=c_1=1$, $b_1=\left(-\alpha+\beta_w/\beta_*+C_l q_0\right)/(1+\alpha)$, we find a_2 from the second of (25) and c_2 from the second of (26). Then (24) gives b_2, the third of (25) defines a_3, the third of (26) defines c_3 and so on.

The value ξ_* of the self-similar fracture length is found from the self-similar BC at the inlet: $[Y(0)]^{\alpha}V(0)=1$. By using the solution (23)-(26) for various ξ_*, we find the one, which meets the BC with a prescribed tolerance.

In the case of a *Newtonian fluid* ($n=1$, $\alpha=1/3$) equations (23)-(26) extend the analytical solution, obtained in [4], to the case of non-zero leak-off. In the case of a *perfectly plastic fluid* ($n=0$, $\alpha=1/2$), we have $a_k=0$, $c_k=0$ for $k>1$. Then for constant influx ($\beta_q=0$), the solution is: $\xi_*=(9/8)^{1/3}$, $Y(\xi)=2(\xi_*-\xi)$, $V(\xi)=V_*\left[1+\frac{1}{\beta_*\sqrt{2\xi_*}}\sum_{j=1}^{\infty}\frac{2}{2j+1}q_{j-1}\tau^j\right]$, $V_*=2/3\xi_*$. Calculations show that the difference between the self-similar solutions for these two limiting cases is quite small. For instance, for zero leak-off, the self-similar fracture length is $\xi_{*p}=1.04004$ for a perfectly plastic fluid; it is $\xi_{*N}=1.00101$ for a Newtonian fluid. In both cases, the particle velocity is almost constant along the fracture. Thinning fluids ($0<n<1$), being intermediate between Newtonian and perfectly plastic fluids, the conclusions hold for an arbitrary thinning fluid. A detailed discussion of the solution is given in [19].

4. Increasing efficiency of numerical simulations

As mentioned, in the general case, using the SE (7) opens options for tracing the fracture in the 3D space by level set, fast marching and other methods of the theory of propagating sur-

http://dx.doi.org/10.5772/56218

faces [17]. As to the authors' knowledge, to this date, the only paper, in which the level set method has been applied to the hydraulic fractures, is that by Peirce and Detournay [20]. Since these authors used the conventional formulation not including the SE, special technique, called by them "implicit level set method", was suggested and successfully used. Still, direct employing of the SE looks superior in simplicity and possibility to use the standard well-established technique.

From now on, we focus on other computational advantages of the modified formulation which evidently appear when considering the PKN model. Recall that this model is basic for a wide class of simulators employing the P3D models (for example, see [1]). Since the Nordgren's problem is 1D, it is convenient to use the spatial coordinate x normalized by the fracture length x_*: $\varsigma = x / x_*$. In this spatial variable, the problem (15)-(20) reads:

$$\frac{\partial y}{\partial t} = -\frac{y}{\alpha x_*}\frac{\partial v}{\partial \varsigma} + \frac{\varsigma v_* - v}{x_*}\frac{\partial y}{\partial \varsigma} - \frac{y^{1-\alpha}}{\alpha} q_l, \tag{27}$$

$$v = \frac{k}{x_*^{1/n}}\left(-\frac{\partial y}{\partial \varsigma}\right)^{1/n} \tag{28}$$

$$y(\varsigma,\ t_0) = y_0(\varsigma) \tag{29}$$

$$\left[y^{\alpha} v\right]_{\varsigma=0} = q_0(t), \tag{30}$$

$$y(1,\ t) = 0 \tag{31}$$

$$v_*(t) = \frac{d x_*}{dt} = \frac{k}{x_*^{1/n}}\left[\left(-\frac{\partial y}{\partial \varsigma}\right)^{1/n}\right]_{\varsigma=1} \tag{32}$$

where $k = (k_f k_r \alpha)^{1/n}$. When writing (27)-(32), we have used the symbols y and v for the functions $\tilde{y}(\varsigma,\ t) = y(x(\varsigma),\ t)$ and $\tilde{v}(\varsigma,\ t) = v(x(\varsigma),\ t)$ omitting the tilde. Note that the initial condition (28) defines also the initial value x_{*0} of the fracture length as the end point where the opening is zero. Thus we actually have the initial condition for the length:

$$x_*(t_0) = x_{*0} \tag{33}$$

In the case when $y_0(\varsigma) = 0$, we have $x_{*0} = 0$.

In the considered problem the dependence (28) between the unknowns is explicit. Therefore, we may substitute (28) into (27). This yields the PDE of the first order in time and of the second order in ς:

$$\frac{\partial y}{\partial t}=\frac{k}{z_*}\left\{\frac{y}{\alpha n}\left(-\frac{\partial y}{\partial \varsigma}\right)^{(1-n)/n}\frac{\partial^2 y}{\partial \varsigma^2}+\left[\varsigma\left(-\frac{\partial y}{\partial \varsigma}\right)^{1/n}_{\varsigma=1}-\left(-\frac{\partial y}{\partial \varsigma}\right)^{1/n}\right]\frac{\partial y}{\partial \varsigma}\right\}-\frac{y^{1-\alpha}}{\alpha}q_l \tag{34}$$

where $z_*=x_*^{(1+n)/n}$ is the modified fracture length. For it, the SE (32) becomes:

$$\frac{dz_*}{dt}=\frac{n+1}{n}k\left[\left(-\frac{\partial y}{\partial \varsigma}\right)^{1/n}\right]_{\varsigma=1} \tag{35}$$

From (34) and (35) it follows that after spatial discretization of these equations and the BC (30), (31), we obtain a well-posed system of ordinary differential equations (ODE) of the first order in time to be solved under the initial conditions (29) and (33). Actually, the problem does not require regularization. Still, as noted in [6], not to have too stiff system of ODE, it is reasonable to employ the ε-regularized forms of the BC (31) and the SE (34):

$$y(1-\varepsilon,t)=\left[\frac{n}{k(n+1)}\frac{dz_*}{dt}\right]^n\varepsilon \tag{36}$$

$$\frac{dz_*}{dt}=\frac{n+1}{n}k\left[\left(-\frac{\partial y}{\partial \varsigma}\right)^{1/n}\right]_{\varsigma=1-\varepsilon} \tag{37}$$

where ε is a small positive value in the range from 10^{-3} to 10^{-6} (it may yet be less depending on round-off errors of computer calculations).

Solving the system of ODE, resulting from spatial discretization of (34), (35), under the initial conditions (30), (33) may be performed by well-developed methods, like the Runge-Kutta method. Standard solvers are of immediate use. Emphasize that this option has appeared only due to employing the *local* SE rather than the global mass balance for tracing the front propagation. As show numerous numerical experiments, summarized in [6] for a Newtonian fluid (n = 1), this computational scheme provides highly accurate and stable results with small time expense.

As an example, we use this scheme to extend the Nordgren's numerical results [9] on the dependence of the fracture length on time for a Newtonian fluid and Carter's leak-off. To this end, the normalizing length x_n and normalizing time t_n are taken as those in the paper by Nordgren:

$$x_n=\pi\left(\frac{\mu q_0^5 h}{128E'C^8}\right)^{1/3},\ t_n=\pi^2\left(\frac{\mu q_0^2 h}{16E'C^5}\right)^{2/3}.$$

Herein, μ is the dynamic viscosity, C is the fluid-loss coefficient in the Carter's leak-off term $q_l=2C/\sqrt{t-\tau}$, τ is the time at which the fracture front reaches a point x. In accordance with (18), we have used the influx q_0 per unit height, while Nordgren wrote his normalizing values in terms of the total influx q_1 through the entire height h ($q_1=q_0h$).

http://dx.doi.org/10.5772/56218

The results are summarized in Figure 2. The thick solid line presents the Nordgren's curve (Fig. 2 of reference [9]), obtained in the time range [0.01, 5.0]. The author did not comment on the accuracy of his calculations. The accuracy, as stated in [3], is certainly below 1% which is also evident from the fact that the Nordgren's curve intersects the asymptotic dotted line, corresponding to small time, and the asymptotic dashed line, corresponding to large time.

The results obtained by employing the computational scheme described are presented in Figure 2 by the thin solid line. It can be seen that the solution starting from the small time asymptotics tends to that corresponding to the large time one. The calculations are performed by using ε-regularized BC (36) and SE (37) with $\varepsilon = 10^{-4}$. Specially designed numerical experiments have shown that the relative error does not exceed 10^{-3}. No signs of instability are noted. Even though the calculations were performed in the MATLAB environment with use of the standard ODE solver *ode15s*, the run time to cover the time range of 12 orders is 10 seconds. The said confirms high efficiency of the computational scheme suggested. [3]

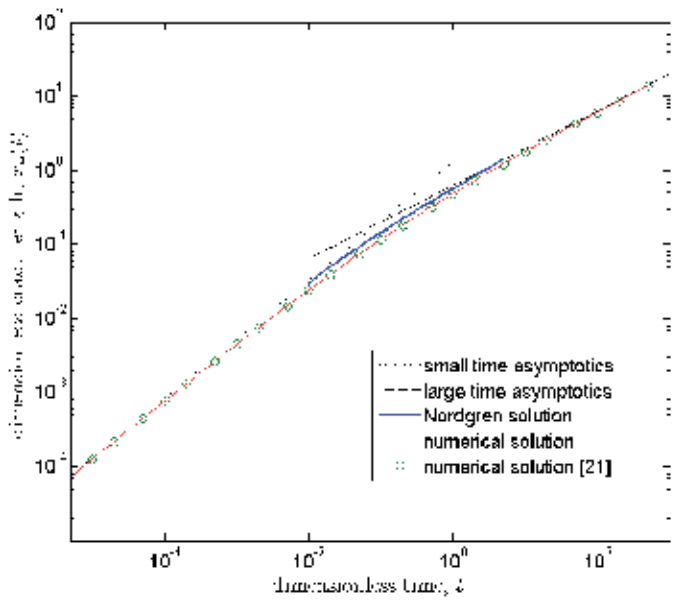

Figure 2. Dimensionless fracture length vs dimensionless time

3 Previously, Kovalyshen and Detournay [21] also have solved the same problem in the range of time wider than that covered by Nordgren. The authors performed calculations starting from the small-time asymptote as an initial condition at $\tau = 10\text{-}8$ and presented numerical results in the range $10\text{-}5 < \tau < 500$. Their results are shown by circles in Figure 2. They are indistinguishable from our numerical solution. The authors do not discuss the accuracy, stability and robustness of their calculations. From our results, to which the relative error does not exceed 10-3, we may conclude that the relative error of the results, given for the fracture length in Table 1 of the paper [21], does not exceed 1% in the whole range of the calculations.

A similarly efficient computational scheme consists of solving the PDE (27), (28) with ε-regularized BC and SE by the Crank-Nicolson method [3,6].

Comment. In view of the accepted linear dependence (13) between the net-pressure and the opening, the pressure may replace the opening as an unknown variable. Actually, under the normalization, yielding $k_r=1$, there is no difference between p and w.

5. Extension to P3D models

In the previous section we have stated that the modified formulation provides prerequisites for efficient solving the Nordgren's problem. The latter, being the basis for the P3D models, we may extend the efficient schemes to these models.

The detailed description of the P3D models is given by Mack and Warpinski [1]. Thus it is sufficient to list only those their features, which distinguish them from the PKN model (Fig. 1) and which are significant for the extension.

(i) In P3D models, the in-situ rock stresses are different in various layers while the fluid pressure is assumed constant in any vertical cross-section. This implies that, in contrast with the PKN model, the net-pressure is now not constant in a vertical cross-section. Thus the P3D models employ the pressure itself rather than the net-pressure. Alternatively, one may employ the difference of the fluid pressure with a *fixed* value of in-situ rock pressure, say the pressure in the pay-layer. Below to keep clear connection with the PKN model, we shall use this option and conditionally call the difference the 'net-pressure'.

(ii) The linear dependence (13) between the net-pressure p and the average opening w_{av} of a cross-section is changed to a non–linear dependence $p=p(w_{av})$. To have clear connection with the initial PKN model, we re-write it as

$$p=k_r w_{av} F_p(w_{av}) \tag{38}$$

where for sufficiently small w_{av}, in particular near the fracture front, $F_p(w_{av})=1$. A specific form of the dependence (38) is found from solving plane-strain elasticity equation for a straight vertical crack under the fracture conditions of the form $K_I \le K_{Ic}$ at the upper and bottom tips. Although looking for this dependence may be involved, it is found in advance for a prescribed geometry of layered stratum, in-situ stresses in layers and critical SIFs. These preliminary calculations also give the positions $z_u(p)$ and $z_l(p)$ of the upper and bottom tips, respectively. Consequently, the height $h_f(p)$ of the fracture in a cross section is a known function of the pressure:

$$h_f(p)=z_u(p)-z_l(p) \tag{39}$$

http://dx.doi.org/10.5772/56218

(iii) The dependence (12) between the particle velocity and the pressure, after averaging the velocity over the height of a cross-section, obtains a factor $F_v(w_{av})$:

$$v_{av}=\left(-k_f w_{av}^{n+1}\frac{\partial p}{\partial x}\right)^{1/n}F_v(w_{av}) \tag{40}$$

where for sufficiently small w_{av}, we have $F_v(w_{av})=1$. Since $w_{av}\to 0$ when approaching the fracture front, the SE becomes:

$$v_*=\left(-k_f w_{av}^{n+1}\frac{\partial p}{\partial x}\right)^{1/n}_{x=x_*} \tag{41}$$

(iv) The continuity equation is integrated over the cross-sectional height. As a result, the total flux through a cross-section and the total leak-off replace, respectively, the flux and leak-off per unit height. The average velocity v_{av}, being defined as the ratio of the total flux to the area A of the cross-section, the area A replaces the opening present in the PKN model. To preserve connection with the PKN model, we may use the flux, leak-off losses and area divided by a fixed reference height h_r, say the height of the pay-layer. Then denoting

$$w=\frac{A}{h_r},\ q=\frac{Av_{av}}{h_r}=wv_{av},\ q_l=\frac{Q_l}{h_r}, \tag{42}$$

we have the modified continuity equation (15) in the unchanged form. The BC (18) at the inlet is also the same when denoting $q_0(t)=Q_0(t)/h_r$, where $Q_0(t)$ is the prescribed total influx.

Take into account that by the definition of the average opening, we have $A=w_{av}h_f$, where h_f is the fracture height in a considered cross-section. Thus, by the first of (42), $w=Ah_f/h_r$. Then, in view of (39) and (38), we may use the argument w instead of w_{av} in the equations (38), (40) and(41) writing them, respectively, as

$$p=k_r w G_p(w),\ v=\left(-k_f w^{n+1}\frac{\partial p}{\partial x}\right)^{1/n}G_v(w),\ \text{and}\ v_*=\left(-k_f w^{n+1}\frac{\partial p}{\partial x}\right)^{1/n}_{x=x_*},$$

where to simplify notation, we have omitted the subscript in the averaged velocity v_{av}. The functions $G_p(w)$ and $G_v(w)$ are found in advance through the functions $F_p(w_{av})$ and $F_v(w_{av})$. They are such that $G_p(w)=1$ and $G_v(w)=1$ for sufficiently small w.

Finally, by introducing the variables $y=w^{1/\alpha}$ and $\varsigma=x/x_*$, we arrive at the system similar to (27)-(33):

$$\frac{\partial y}{\partial t}=-\frac{y}{\alpha x_*}\frac{\partial v}{\partial \varsigma}+\frac{\varsigma v_*-v}{x_*}\frac{\partial y}{\partial \varsigma}-\frac{y^{1-\alpha}}{\alpha}q_l, \tag{43}$$

$$v = \frac{k}{x_*^{1/n}} H\left(y\right)\left(-\frac{\partial y}{\partial \varsigma}\right)^{1/n} \tag{44}$$

$$y(\varsigma,\ t_0) = y_0(\varsigma) \tag{45}$$

$$\left[y^{\alpha} v\right]_{\varsigma=0} = q_0(t), \tag{46}$$

$$y(1,\ t) = 0 \tag{47}$$

$$v_*(t) = \frac{d\, x_*}{dt} = \frac{k}{x_*^{1/n}}\left[\left(-\frac{\partial y}{\partial \varsigma}\right)^{1/n}\right]_{\varsigma=1} \tag{48}$$

$$x_*(t_0) = x_{*0} \tag{49}$$

where

$$H\left(y\right) = \left[\frac{d\left(wG_p\left(w\right)\right)}{dw}\right]^{1/n} \mathrm{G}_v\left(w\right) \tag{50}$$

is a function to be found in advance through the functions $G_p(w)$ and $\mathrm{G}_v(w)$ of the argument $w = y^{\alpha}$. By the properties of $G_p(w)$ and $\mathrm{G}_v(w)$, we have $H(0) = 1$ which explains its absence in the SE (48).

The problem (43)-(49) differs from the problem (27)-(33) in the only detail: equation (44) for the velocity contains the function $H(y)$ defined by (50). The latter function, being smooth and tending to the unity at the front, the efficient numerical schemes, discussed in the previous section, are of use for the P3D models.

Comment. In some cases, it may be convenient to use the net-pressure rather than the opening. Since $dp = \left(\frac{dp}{dw}\right) dw$, reformulation of the equations and computational schemes in terms of the modified pressure $P = p^{1/\alpha}$ is obvious.

6. Conclusions

The discussion above demonstrates the analytical and computational advantages of using the modified formulation. The analytical advantages are evident from the obtained simple analytical solutions for the PKN and KGD models, which otherwise require involved calculations. The computational advantages include: (i) the possibility to use the well-established theory of propagating surfaces, (ii) avoiding deterioration of numerical solution caused by ill-posedness of the problem when neglecting the lag and fixing the fracture contour at a

http://dx.doi.org/10.5772/56218

time step, (iii) avoiding singularities on the fluid front, (iv) the possibility to use highly efficient numerical schemes for the PKN and P3D models. These beneficial features are of significance when developing simulators able to efficiently solve truly 3D and pseudo-three-dimensional problems in real time. The work on simulators of both types is in progress.

Acknowledgements

The authors appreciate support of the EU Marie Curie IAPP program (Grant # 251475). The first author (AL) also thankfully acknowledges support of the Russian Fund of Fundamental Investigations as concerns with the results on non-Newtonian fluids (Grant # 12-05-00140). Both authors are grateful to Piotr Kusmierczyk and Michal Wrobel for the help in performing many numerical experiments for the Nordgren's problem with Carter's leak-off.

Author details

Alexander M. Linkov[1,2*] and Gennady Mishuris[3]

*Address all correspondence to: voknilal@hotmail.com

1 Department of Mathematics, Rzeszow University of Technology, Rzeszow, Poland

2 Institute for Problems of Mechanical Engineering, Saint-Petersburg, Russia

3 Institute of Mathematical and Physical Sciences, Aberystwyth University, Aberystwyth, UK

References

[1] Mack MG., Warpinski NR. Mechanics of hydraulic fracturing. In: Economides MJ., Nolte KG. (eds) Reservoir simulation, 3-rd edn. John Willey & Sons; 2000. p6.1-6.49.

[2] Linkov AM. Speed equation and its application for solving ill-posed problem of hydraulic fracturing. Doklady Physics 2011; 56 (8) 436-438.

[3] Linkov AM. Use of speed equation for numerical simulation of hydraulic fractures. Available at: http://arxiv.org/abs/1108.6146.

[4] Linkov AM. On efficient simulation of hydraulic fracturing in terms of particle velocity. Int. J. Engineering Sci. 2012; 52, 77-88.

[5] Linkov AM. Numerical modeling of hydraulic fractures: State of art and new results. In: Advanced Problems in Mechanics, APM 2012: proceedings of International XL

Summer School-Conference, 1-7 July 2012, Institute for Problems of Mechanical Engineering, RAS; 2012. CD-ROM. p225-236.

[6] Mishuris G., Wrobel M., Linkov A. On modeling hydraulic fracture in proper variables: stiffness, accuracy, sensitivity. Int. J. Engineering Sci. 2012; 61, 10-23.

[7] Adachi J., Siebrits E., Peirce A., Desroches J. Computer simulation of hydraulic fractures. Int. J. Rock Mech. Mining Sci. 2007; 44, 739-757.

[8] Jamamoto K., Shimamoto T., Sukemura S. Multi fracture propagation model for a three-dimensional hydraulic fracture simulator. Int. J. Geomech. ASCE 2004; 1, 46-57.

[9] Nordgren RP. Propagation of a vertical hydraulic fracture. SPEJ Aug., 1972; 10(4), 306-314.

[10] Spence DA., Sharp PW. Self-similar solutions for elastohydrodynamic cavity flow. Proc. Roy Soc. London, Ser. A 1985; 400, 289-313.

[11] Kemp LF. Study of Nordgren's equation of hydraulic fracturing. SPE 18959, Society of Petroleum Engineers 1989; 287-298.

[12] Adachi J., Detournay E. Self-similar solution of a plane-strain fracture driven by a power law fluid. Int. J. Numer. Anal. Methods Geomechanics 2002; 26, 579-604.

[13] Perkins TK., Kern LF. Widths of hydraulic fractures. J. Pet. Tech. September 1961; 937-949.

[14] Khristianovich SA., Zheltov VP. Formation of vertical fractures by means of highly viscous liquid. In: Proc. 4-th World Petroleum Congress, Rome, 1955. p. 579-586

[15] Geertsma J., de Klerk F. A rapid method of predicting width and extent of hydraulically induced fractures. J. Pet. Tech. December 1969; 1571-1581.

[16] Kresse O., Cohen C., Weng X. et al. Numerical modeling of hydraulic fracturing in naturally fractured formations. In: Proc. 5-th US Rock Mechanics Symposium, San Francisco, CA, June 26-29, 2011, American Rock Mechanics Association. Paper ARMA 11-363. 11p.

[17] Sethian JA. Level set methods and fast marching methods. Cambridge: Cambridge University Press; 1998.

[18] Hadamard J. Sur les problemes aux derivees partielles et leur signification physique. Princeton University Bulletin 1902; 49-52.

[19] Linkov AM. Analytical solution of PKN problem for non-Newtonian fluid. Russian Mining Science 2013; 1 (in press).

[20] Peirce A., Detournay E. An implicit level set method for modeling hydraulically driven fractures. Comput. Methods Appl. Mech. Engng. 2008; 197, 2858-2885.

http://dx.doi.org/10.5772/56218

[21] Kovalyshen Y., Detournay E. A reexamination of the classical PKN model of hydraulic fracture. Transp Porous Med. 2010; 81, 317–339.

Section 10

Mulitiple Hydraulic Fracture Growth

Chapter 32

The Geomechanical Interaction of Multiple Hydraulic Fractures in Horizontal Wells

Sau-Wai Wong, Mikhail Geilikman and Guanshui Xu

Additional information is available at the end of the chapter

http://dx.doi.org/10.5772/56385

Abstract

The technology of multiple hydraulic fracture stimulation in horizontal wells has transformed the business of oil and gas exploitation from extremely tight, unconventional hydrocarbon bearing rock formations. The fracture stimulation process typically involves placing multiple fractures stage-by-stage along the horizontal well using diverse well completion technologies. The effective design of such massive fracture stimulation requires an understanding of how multiple hydraulic fractures would grow and interact with each other in heterogeneous formations. This is especially challenging as the interaction of these fractures are subject to the dynamic process of subsurface geomechanical stress changes induced by the fracture treatment itself.

This paper consists of two parts. Firstly, an idealised analytical model is used to highlight some key features of multiple hydraulic fractures interaction, and to provide a quantification of 'stress shadow'. Secondly, a new non-planar three dimensional (3D) hydraulic fracturing numerical model is used to provide an insight into the growth of multiple fractures under the influence of subsurface geomechanical stress shadows. Attention is given to studying the height growth of multiple fractures.

1. Introduction

Hydraulic fracturing or fracture stimulation establishes conductive fractures hydraulically from a horizontal well in the tight formation/reservoir. They provide large surface area contact with the formation and thus facilitate the production of oil and gas, as evident from the experience in North Americas [1]. Multiple fractures are now placed in sequential stages in

horizontal wells. Typically, four or more fractures are pumped simultaneously into a single frac stage, and it is not uncommon to place 20 to 40 frac stages in a single horizontal well. Attempts have also been made to simultaneously fracture two adjacent horizontal wells to generate complex fracture networks thought to be beneficial for production [2, 3].

It is important to consider the changes to subsurface in-situ stresses induced by fracture stimulation. This fracturing induced formation stress perturbation is also called 'stress shadowing' and needs to be understood and quantified for optimization and to avoid problems such as fracture 'screen-out'. Added complexity is caused by the fact that the fractures are created in an extremely tight formation - where the fracture pumping operations are often conducted within a time span that is in the same order of magnitude needed for frac fluid to leak-off and the resultant stress perturbation to completely dissipate. Moreover, the stress perturbation caused by inclusion of millions of pounds of proppant in the formation does not dissipate.

Observations from substantial amounts of field data show that generally 25% or more of the fractures placed are ineffective. In fact, recent fracture stimulation surveillance with advance technologies such as microseismic monitoring and fibre optics temperature and strain sensing [4-6] have shown that multiple fractures do not grow and develop in the same way. Some of the fractures are pre-maturely 'terminated' during the treatment. Nonetheless, to increase production, there is a tendency to use longer horizontal wells, place more fractures per stage, longer fractures and more stages of fractures. Consequently, more fractures with closer spacing and larger volumes of frac fluid are employed. This translates to higher pumping rates, higher treating pressure and surface horse power, and consumes more materials (frac fluid, chemicals and proppant). The optimal design of hydraulic fractures clearly necessitates an engineering optimization, considering production, treatment cost and the feasibility of placing these closely spaced conductive fractures in the subsurface. The latter requires knowledge of key parameters such as in-situ stress, rock stiffness and strength, frac fluid rheology and leak-off behaviour, and importantly, the impact of stress shadows on multiple fracture growth in heterogeneous formations [7-13]. Some experts have aimed to provide general guidelines for the design of optimal fracture placement based on simplified analytical models whilst others have developed numerical models of various degree of sophistication to account for multiple fracture interaction and design [14-18].

In-situ stress perturbation can potentially result in the growth of complex non-planar fractures. An analytical model is developed to highlight some of the salient features of multiple non-planar hydraulic fractures interaction. The benefit of using an analytical model is that it provides immediate insights into the controlling parameters on fractures interaction, and guides further numerical analysis for stimulation optimization. Here, we present only the impact of fracture spacing and in-situ stress difference on fracture growth pattern. Other parameters that affects fracture growth pattern are evident from the model, but they will not be described here.

Emboldened by the results of our analytical model, a new numerical model based on rigorous mechanistic formulation has been devised to allow for more realistic solution of field problems. This is a non-planar 3D numerical model, where the interaction of multiple non-planar

http://dx.doi.org/10.5772/56385

fractures is captured meticulously by means of boundary integral formulation with dislocation segments solution techniques. In the model, fracture growth and fluid flow equations are solved in a coupled manner via a proprietary, robust and efficient algorithm where mass conservation is strictly observed. This new non-planar 3D model was first described in [19]. It substantially enhances the capability of a plane strain 2D model presented in [7]. The present paper complements the published results [7, 19] and extends to considering fluid viscosity and height growth of multiple fractures.

2. Analytical model

The complete theory of fracture interaction for an arbitrary number of fractures is quite cumbersome. Therefore, a 'simplified' analytical model has been developed to describe a set of fractures growing in a viscous mass-transfer dominated regime. In this model, two types of fracture growth patterns are defined. First is the 'compact' fracture growth where interaction and interference between fractures are minimum. The second is 'diffuse' fracture growth where some fractures will either terminate or collapse into each other because of minimum in-situ stress rotation (Figure 1). In diffuse growth, we distinguish different zones. The first zone is the closest to the well. The next zone, farther from the well, contain less fractures because some of them have either terminated or merged into other fractures, as shown at the right-hand side of Figure 1.

The transition from one growth pattern to another is delineated by a 'critical' fracture spacing, influenced by the original principal stress difference in the un-fractured formation. In the case of diffuse growth, different zones are depicted by the dashed lines on the right-hand picture of Figure 1. The Average permeability of the fracture set in the zone "n" is given by (see e.g. [20]):

$$k_n = \frac{w_n^{\,3}}{12 L_n} \tag{1}$$

where L_n is spacing between the fractures in the "n" zone, and average aperture of fractures in the zone "n" is:

$$w_n = a \frac{p_n}{E} R_n \tag{2}$$

Here, p_n is net pressure, E is Young's modulus, R_n is a radius of a penny-shape fracture, and a is a numerical coefficient (of approximately 1) and depends on Poisson's ratio. For simplicity, it is assumed that there is no leak-off of fluid into the extremely tight formation. Therefore, the average fluid density, m, in the fractures becomes:

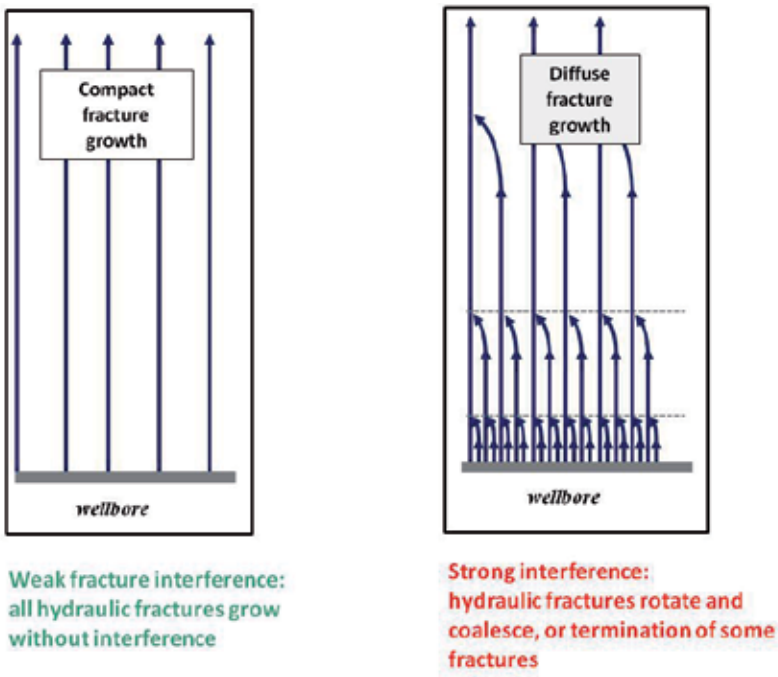

Figure 1. "Compact" and "Diffuse" fracture growth patterns

$$m = \frac{w_n \rho}{L_n} \tag{3}$$

Where, ρ is fluid density. Applying the equation of fluid mass balance:

$$\frac{\partial m}{\partial t} + div\, \rho \vec{v} = 0 \tag{4}$$

and Darcy's law:

$$\vec{v}_n = -\frac{w_n^3}{12\mu L_n} \cdot grad(p_n) \tag{5}$$

We obtain an equation for fluid transport in the fractures:

$$\frac{\partial}{\partial t}\left(\frac{w_n}{L_n}\right) - \frac{E}{12\mu a} div\left\{\frac{w_n^3}{L_n} \cdot grad\left(\frac{w_n}{R_n}\right)\right\} = 0 \tag{6}$$

http://dx.doi.org/10.5772/56385

The above Eq. 6 is highly nonlinear and cannot be solved analytically, instead, it is solved by considering the integral relationships and using a modification of the so-called method of successive change of steady states [21]. The essential idea is to solve the steady-state version of Eq. 6 for a given size of the fracture (i.e. without the first term in Eq. 6). Subsequently, the time dependency of fracture radius growth is found from the integral form of mass balance equation, the differential form of which is given by Eqs. 4 and 6. The detail of this solution will be given in a future paper.

Interaction between fractures is governed by the induced stress due to the growing fractures. Solutions for various cases of interacting fractures have been published [22]. Since these solutions are cumbersome, several approximations have been proposed [23], which make the problem more tractable for our present purpose. Following these approximations we can obtain the stress state induced by two neighbouring growing fractures. The induced stress depends on the fracture aperture (or equivalently, net pressure) and a dimensionless ratio of fracture length and the distance between fractures (i.e. the initial fracture spacing).

To appreciate the geomechanical interaction of fractures, see the left side of Figure 2, which depicts a top view of two simultaneously growing fractures. We choose to examine the incremental stress changes in the x and y directions at a mid point in between the fractures, as shown in the figure. The induced stress is obviously not constant in the space between the fractures. But for illustration purpose, we will simply consider the stress evolution at this chosen point to be representative of the stress state of the large area between the fractures. The analytical model on the right side of Figure 2 shows that σ_x increases with fracture length. Although σ_y also increases, it does so at a much slower pace than σ_x. We can now define a deviatoric stress, $\Delta\sigma = \sigma_x - \sigma_y$, which exhibits a maximum value. It can be immediately observed that if the maximum value of $\Delta\sigma$ is greater than the original in-situ stress difference ($\sigma_H - \sigma_h$), then rotation of minimum in-situ stress direction is feasible and the fracture(s) would grow in a non-planar fashion. For multiple fracture growth, this will result in the collapse or termination of some fractures.

In the same way, the height growth of multiple fractures may also see similar interaction if $\Delta\sigma$ is greater than the original in-situ stress difference between vertical stress and minimum horizontal stress ($\sigma_V - \sigma_h$). As fractures grow upward, assuming no stress barrier or contrast is encountered, both σ_V and σ_h would typically decrease in magnitude. Potentially, the stress shadowing effect is even more prominent for height growth of multiple fractures. It is interesting to note that field experience does indicate that it is challenging to grow in fracture height for multiple fracture stimulation. A plausible explanation is indeed the 'stress shadow' effect caused by geomechanical interaction of multiple fractures.

Although the analytical solution is an approximation, it captures the foremost qualitative features of fracture interaction. One of the first results shows how the in-situ stress contrast influences the domains of fracture growth. Figure 3 shows the results based on the analytical model, where a distinct transition between the two regimes of fracture growth can be identified. Note that in practice, typical fracture spacing is in the order of 70 to 100ft (20-30m). Therefore, according to this simplistic, homogeneous model, today's multiple hydraulic fracture stimulation practises can potentially experience 'strong interference', depending on the stress contrast.

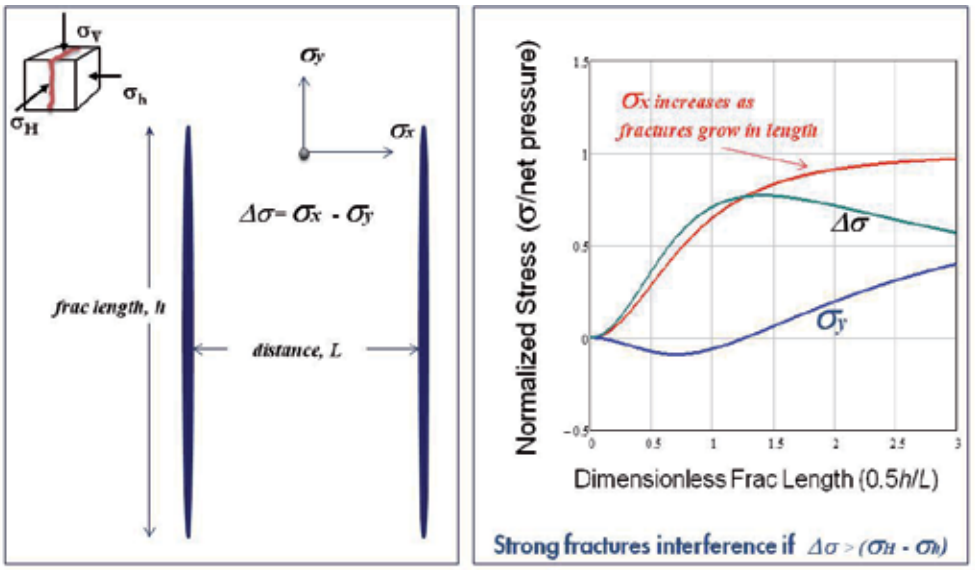

Figure 2. Interaction between two fractures

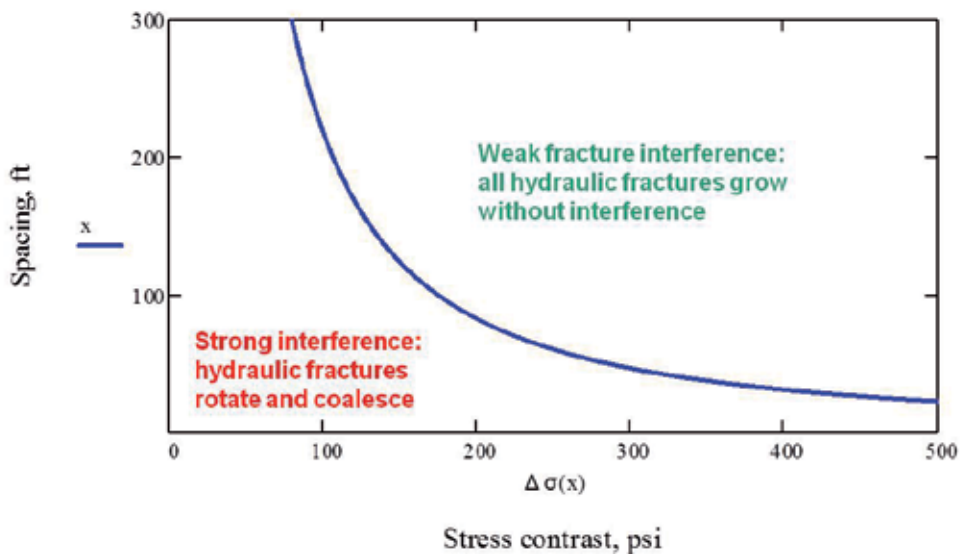

Figure 3. Fracture spacing versus stress contrast

http://dx.doi.org/10.5772/56385

3. Non-planar 3D model of hydraulic fractures

The numerical simulator essentially follows a well accepted numerical methodology [24, 25]. In this numerical framework, the rock mechanics of fracture growth takes place in a linear elastic medium and therefore can be modelled by boundary integral equations based on fundamental solutions of dislocation segments. The fracture growth is controlled by both fracture mechanics criteria and fluid volume balance at the fracture tip. The formulation adequately portrays both viscosity and toughness controlled fracture growth as well as the 'fluid lag' behaviour [25]. The proppant laden frac fluid is idealized as an incompressible power-law fluid commonly characterized by parameters K and n:

$$\tau = K\dot{\gamma}^n \tag{7}$$

Where τ is the fluid shear stress and $\dot{\gamma}$ the fluid shearing rate. K and n are termed the consistency index and power law index, respectively. They are naturally dependent on the proppant concentration, and this effect of proppant concentration on fluid rheology is accounted for in the simulator using Shah's model [27]. The proppant transport and settlement are computed via the transport equation and empirical equations of particles settling between parallel plates [28]. The fluid loss to the formation is described by a Carter type leak-off model [25].

The ensuing flow of proppant laden frac fluid within a fracture is captured according to the Reynolds lubrication theory, and the derived non-linear fracture growth and fluid flow equations are now solved in a coupled manner in which mass conservation (i.e., frac fluid and proppant) are strictly enforced. The equations are discretized on the same structured grid, and they form a system of moving boundary, transient coupled equations of fracture width and fluid pressure. A new adaptive time integration algorithm has been developed to provide numerically stable solutions for a wide range of power-law fluid properties (especially when the viscosity is low).

Although the proppant transport is calculated at each time step based on a volume conservation equation, this computation is decoupled from the process of solving the fluid flow equation for the sake of computational efficiency. Specifically, the fluid pressure and fracture width are first obtained by 'freezing' the proppant concentration associated with each element. The contribution of proppant transport to the volume concentration is then updated based on the calculated fluid velocity field. This proves to be effective as well as efficient since the employed time step is generally small.

3.1. Non-planar fracture propagation

In dealing with non-planar fracture growth, the heterogeneous formation is modelled as multiple isotropic parallel layers with heterogeneities characterized by variations in in-situ stress, elastic stiffness modulus, Poisson's ratio, fracture toughness, pore pressure, leak-off coefficients, and spurt-loss coefficients. All fractures are assumed to be vertical but they can turn in any horizontal direction. For each fracture, the growth direction is determined by the

stress state of the leading element at the fracture tip. These assumptions exclude the application for certain geological formations. In particular, geological stress regimes as a result of reverse faulting may present difficulties in modelling as the hydraulic fracture would most likely grow in a horizontal plane. However, the assumptions made are sufficient and adequate for typical deep unconventional resource formations where the vertical stress is generally the maximum principal stress, or at least greater than the minimum horizontal principal stress – resulting in vertical fracture growth.

Fractures advance when the maximum tensile stress ahead of the crack tip exceeds the intrinsic tensile strength of the rock. In linear elastic fracture mechanics, the stress at the crack tip is singular, therefore the stress intensity factor, which correlates to the strength of such a singular stress field, is generally used to determine fracture tip propagation [29]. In practice, hydraulic fracturing processes take place under relatively large compressive in-situ earth stress that is normally several orders of magnitude higher than the rock strength. Therefore, the process is dominated by the balance of the compressive stress and fluid pressure at the fracture tip region. A group of 'virtual' elements is placed along the crack front and at each time step a check is made on the stress status of these elements. The virtual elements are allowed to be active as part of the new fracture surface if the potential fluid pressure can overcome the compressive stress plus the strength of the rock.

Importantly, the interaction of multiple fractures may result in significant shearing displacements along the fracture surface, causing the fracture growth to follow a curved path, and the computational technique leads these virtual elements to be oriented according to the stress field so that the local minimum principal stress is perpendicular to the new fracture surface as the fracture front advances.

An outline of the mathematical description of the fracture stiffness matrix, the displacement discontinuity method is given in [19], and will not be repeated here. The numerical approach is robust and efficient but less accurate than the variational boundary integral method which employs second order elements [30, 31]. For the current application, computational efficiency is deemed to outweigh the importance of a moderate improvement in accuracy. [19] also describes the coupling of derived non-linear fracture growth to flow equation and mass conservation.

3.2. Wellbore hydraulic model

The fractures are assumed to be initiated at the specified locations of a cluster of perforations. Near wellbore formation stress concentration is not considered. The downhole pressure is defined as the fluid pressure just upstream of all injection points. It is obvious that the distribution of the corresponding injection at each fracture follows wellbore fluid mechanics, depending on the injection area connected with the fracture and the fluid pressure within the fracture. An approximation is made by using Bernoulli equation to capture the fluid distribution. This wellbore hydraulic model is able to account directly for the empirically derived or calibrated frictional pressure drop at the perforation and along the wellbore. Therefore, it is possible to account for limited entry perforation designs commonly employed in multiple hydraulic fracture design.

http://dx.doi.org/10.5772/56385

4. Comparing simulation results with analytical solution and experiment

The complete validation of a hydraulic fracturing simulator is enormously challenging, because of the difficulty in obtaining the general analytical solutions or constructing realistic laboratory experiments. A carefully conducted laboratory hydraulic fracturing experiment has been published [32]. Figure 4 shows our simulation of the experiment. The comparison is excellent not only in the created fracture geometry, but also the pumping parameters.

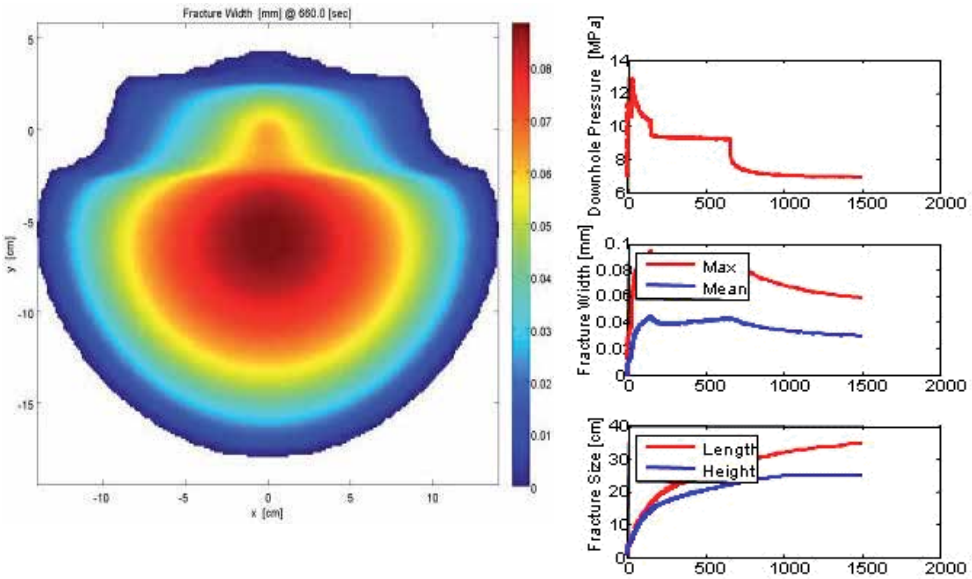

Figure 4. Comparing with experimental result of [32]

5. Frac fluid viscosity and fractures height growth

A single stage of four hydraulic fractures is considered. Parameters chosen broadly resemble a typical shale gas development field case. The horizontal wellbore is placed at the relative depth of 0m as shown in Figure 5. Fracture injection points are spaced at 25m (82ft) apart and each fracture has 12 perforations. Fluid is injected into the wellbore at constant injection rate of 0.2 m^3/s (~75 bbl/min). Formation heterogeneities are limited to only in-situ stress variation. In this instance, the minimum horizontal stress gradient is set to 14kPa/m (0.62psi/ft) with no upper stress barrier to restrict height growth. The difference between minimum and maximum horizontal stress is chosen to be more than 20%, so that we do not cause the fracture direction to re-orient drastically. The key parameters are shown in Figure 5. The fluid leak-off factor is set to 1 with no spurt loss.

We consider two cases of distinctly different frac fluids, one with low viscosity (slick water) and the other a very high viscosity (gel frac). This corresponds to setting $n = 0.8$ and $K = 0.05$ for the low viscosity fluid case, and $n = 0.8$ and $K = 0.5$ for the high viscosity fluid in the power-law fluid model of Equation 7.

The injection parameters and the calculated total fracture volumes are shown in Figure 6. The simulated results are shown in Figure 7. As expected, the low viscosity fluid creates larger fractures with more fracture surface area at the expense of fracture aperture/width. Significantly, the low viscosity fluid creates a much larger fracture height. It is now interesting to see how the multiple fractures evolve in length and height as they compete in the presence of stress perturbation. Figure 8 shows fracture development at the end of the pumping of high viscosity fluid. The outer two fractures grew slightly outward and are longer than the inner fractures. This is due to stress shadowing. Interestingly, the inner two fractures developed more height, and this behaviour will become even more pronounced when we look at low viscosity fluid.

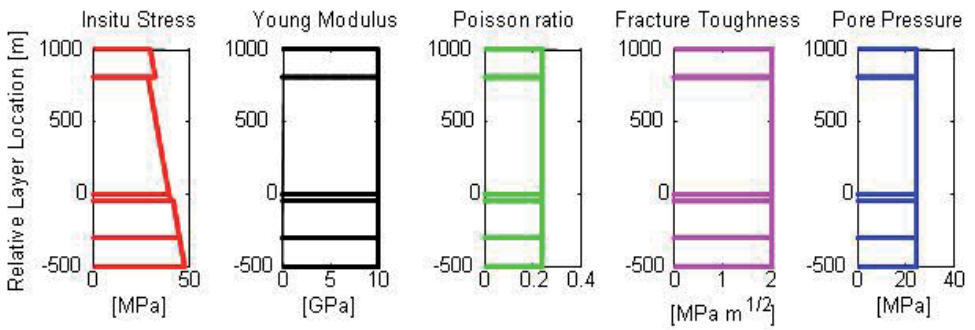

Figure 5. Formation input parameters for the case studies

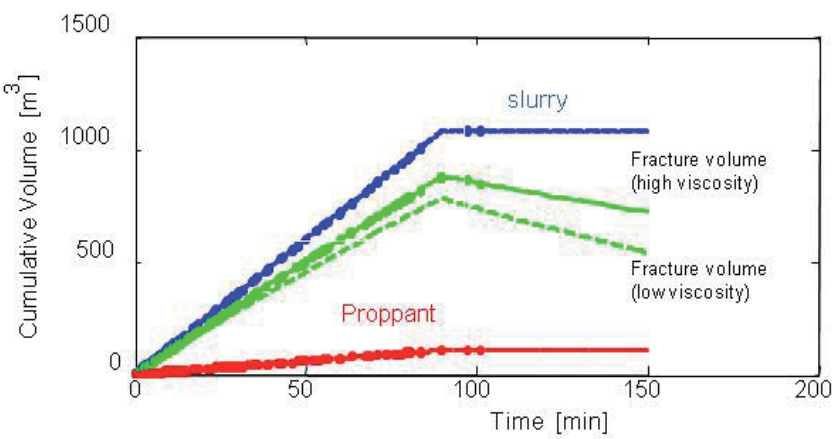

Figure 6. Injection volume and calculated fracture volumes

http://dx.doi.org/10.5772/56385

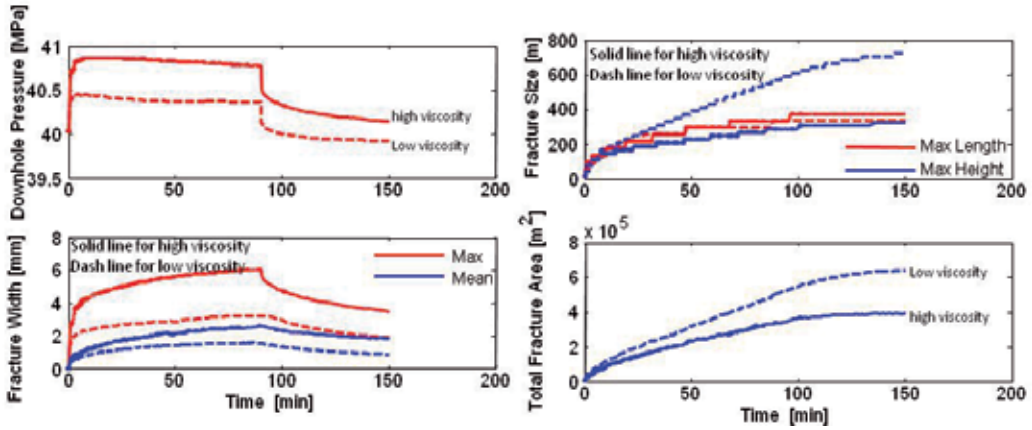

Figure 7. Calculated fracture parameters

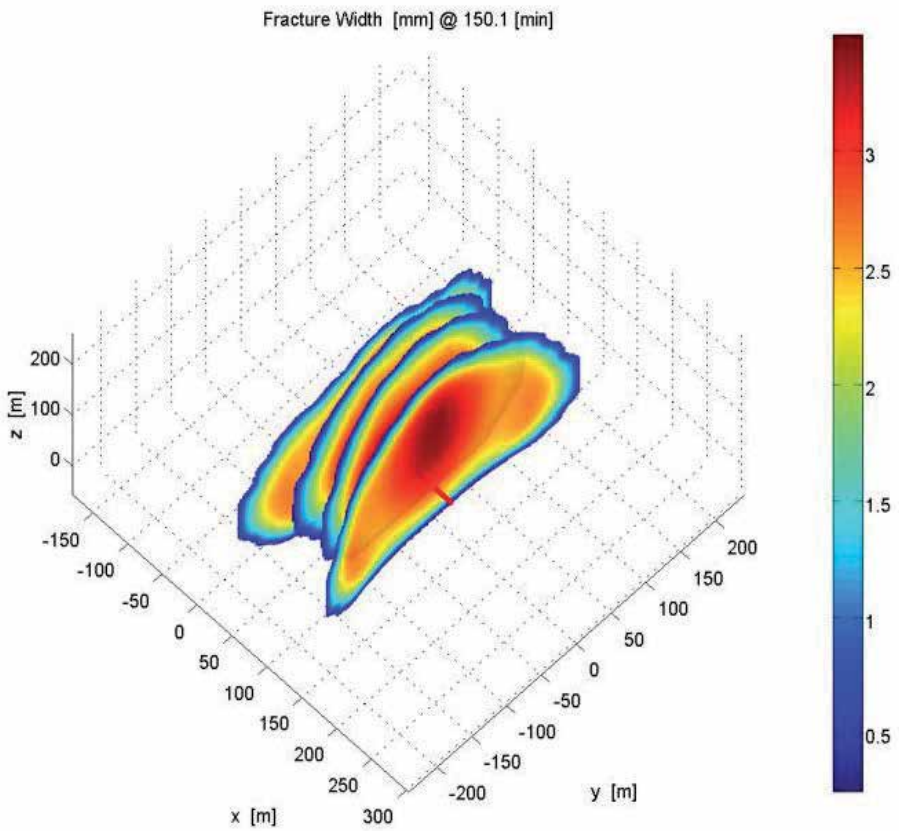

Figure 8. Fracture geometry with high viscosity frac fluid at 150 mins

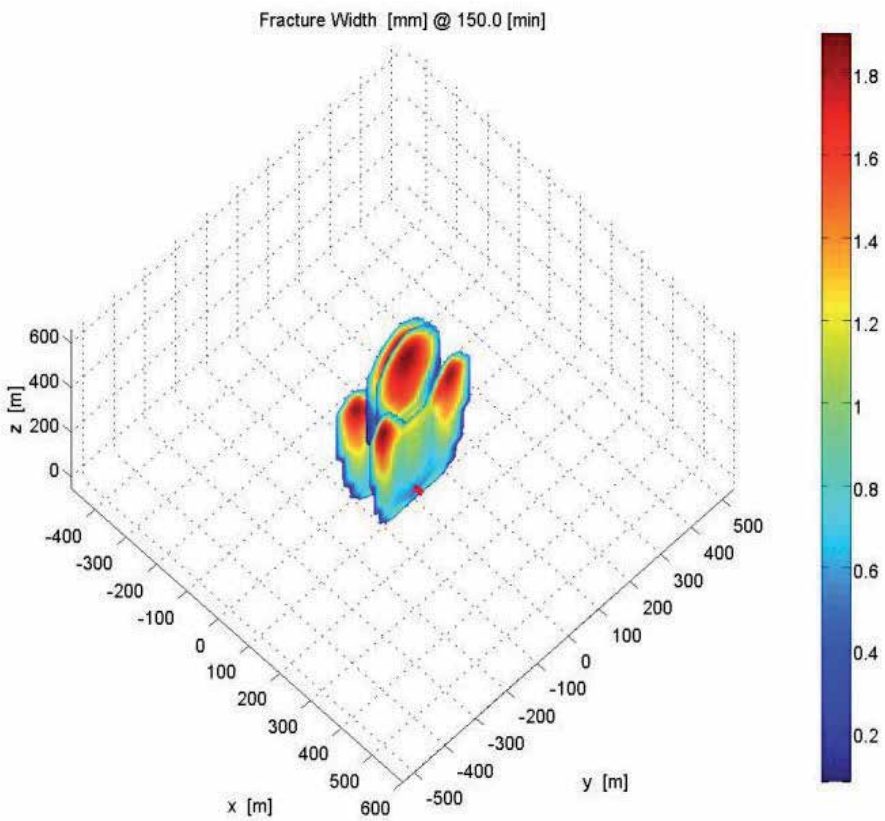

Figure 9. Fracture geometry of low viscosity frac fluid at 150 mins

Figure 9 shows the final fracture geometry of pumping low viscosity fluid (note that the scale in Figure 9 is different from that in Figure 8). Perhaps against intuition, the inner fractures grew appreciably in height. To understand this, we look at the evolution of fracture length and height growth over time as depicted in Figures 10 and 11. It becomes clear that as the inner fractures are constrained from growing in length because of competition with the outer fractures, they found relative freedom to grow upward instead.

http://dx.doi.org/10.5772/56385

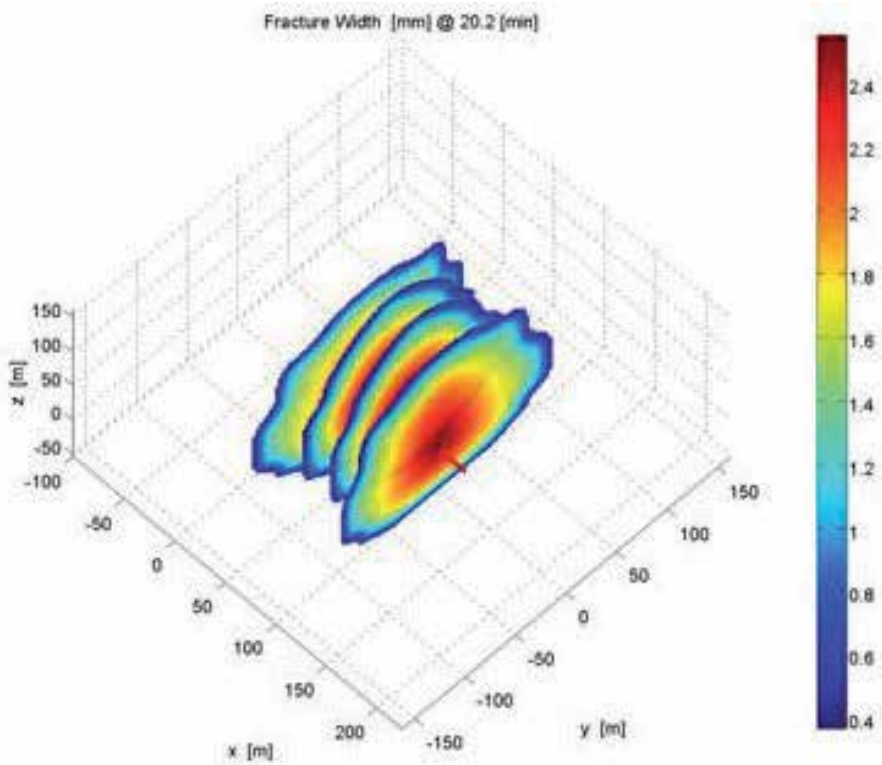

Figure 10. Fracture geometry of low viscosity frac fluid after 20 mins

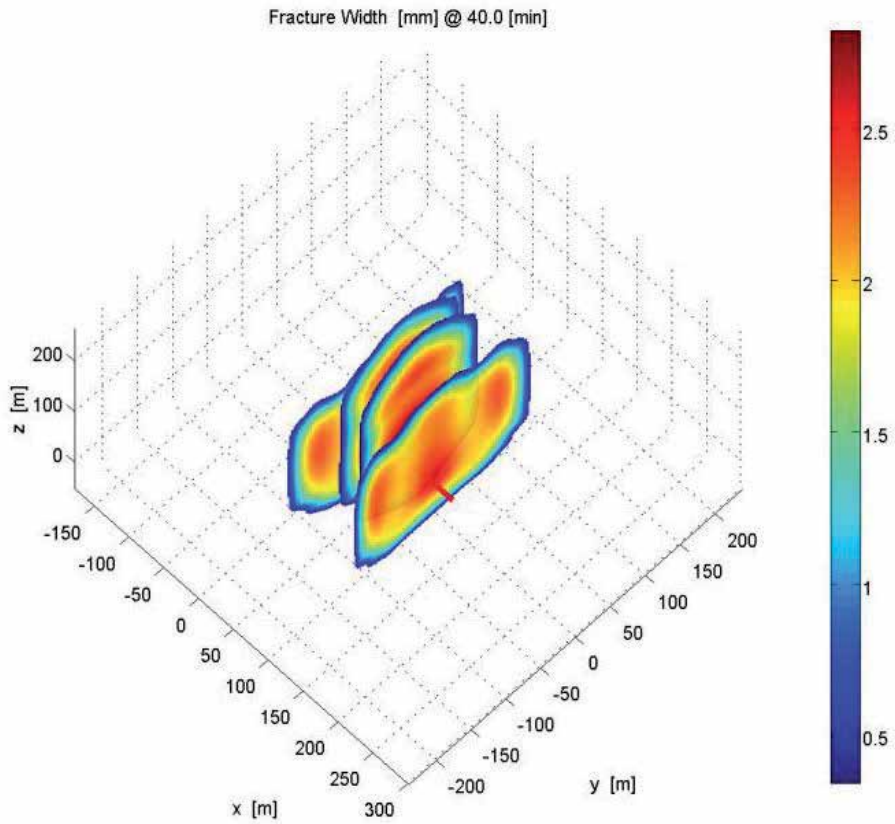

Figure 11. Fracture geometry of low viscosity frac fluid after 40 mins

6. Discussion

At present, multiple fracture stimulations in horizontal wells often assume a uniform growth of all fractures, with the total volume of frac fluid more or less evenly distributed amongst the fractures. We have pointed out some of the potential impacts of stress shadows, which can affect treatment cost and production. Crucially, it has consequences in the understanding of subsurface development. For instance, if, instead of stimulating four fractures uniformly, only two or three of the fractures grow disproportionally, then some of the fractures may be unknowingly over-stimulated, resulting in excessive length or height growth. Normally this does not pose any major issue unless there are near-by wells or geological faults.

The non-planar 3D simulator presented here is capable of capturing the influence of key parameters such as injection rate, fracture spacing, formation properties, etc. on fracture design. Attempts are being made to extend the present numerical framework to include the interaction of hydraulic fractures with natural fractures.

http://dx.doi.org/10.5772/56385

Acknowledgements

The authors recognize the valuable input from Alexei Savitski, Anastasia Dobroskok, Mauricio Farinas, Ernesto Fonseca, Kaiming Xia, and Zongyu Zhai. Permission by Shell International Exploration and Production Inc. to publish is gratefully acknowledged.

Author details

Sau-Wai Wong[1], Mikhail Geilikman[1] and Guanshui Xu[2]

1 Shell Exploration and Production Inc., Houston, Texas, USA

2 FrackOptima Inc., and The University of California Riverside, California, USA

References

[1] United States Department of Energy(2009). Modern shale gas development in the United States: A Primer.

[2] Mutalik, P. N, & Gibson, B. (2008). Case History of Sequential and Simultaneous Fracturing of the Barnett Shale in Parker County. Paper SPE 116124 presented at the SPE Annual Technical Conference and Exhibition, Denver, September. DoiMS., 21-24.

[3] Waters, G, Dean, B, Downie, R, Kerrihard, K, Austbo, L, & Mcpherson, B. (2009). Simultaneous Fracturing of Adjacent Horizontal Wells in the Woodford Shale. Paper SPE119635 presented at the SPE Hydraulic Fracturing Technical Conference, Woodlands, TX, USA, January. Doi:MS., 19-21.

[4] Sierra, J, Kaura, J, Gualtieri, D, Glasbergen, G, Sarkar, D, & Johnson, D. (2008). DTS Monitoring Data of Hydraulic Fracturing: Experiences and Lessons Learned. Paper SPE 116182 presented at the SPE Annual Technical Conference and Exhibition in Denver, Colorado, USA. September.

[5] Molenaar, M. M, Hill, D. J, Webster, P, Fidan, E, & Birch, B. (2012). First Downhole Application of Distributed Acoustic Sensing for Hydraulic-Fracturing Monitoring and Diagnostics. SPE Drilling & Completion, March, , 32-38.

[6] Molenaar, M. M, Fidan, E, & Hill, D. J. (2012). Real-Time Downhole Monitoring of Hydraulic Fracturing Treatments Using Fibre Optic Distributed Temperature and Acoustic Sensing. Paper SPE 152981 presented at the SPE/EAGE European Unconventional Resources Conference and Exhibition in Vienna, Austria, March.

[7] Wong, S. W, Geilikman, M, & Xu, G. (2013). Interaction of Multiple Hydraulic Fractures in Horizontal Wells. Paper SPE163982 presented at the Middle East Unconventional Gas Conference and Exhibition in Muscat, Oman. January.

[8] Olson, J. E, & Wu, K. Sequential versus Simultaneous Multi-zone Fracturing in Horizontal Wells: Insights from a Non-planar, Multi-frac Numerical Model, Paper SPE 152602 presented at the SPE Hydraulic Fracturing technology Conference held in the Woodlands, Texas, February, (2012).

[9] Morrill, J. C, & Miskimins, J. L. (2012). Optimizing Hydraulic Fracture Spacing in Unconventional Shales. Paper SPE 152595 presented at the SPE Hydraulic Fracturing Technology Conference in The Woodlands, Texas, USA. February.

[10] Rafiee, M, Soliman, M. Y, & Pirayesh, E. (2012). Geomechanical Considerations in Hydraulic Fracturing Designs. Paper SPE 162637 presented at the SPE Canadian Unconventional Resources Conference in Calgary, Alberta, Canada. October.

[11] Roussel, N. P, & Sharma, M. M. (2011). Optimising Fracture Spacing and Sequencing in Horizontal-Well Fracturing. SPE Production and Operations. May, , 173-184.

[12] Cipolla, C. L, Lolon, E. P, Mayerhofer, M. J, & Warpinski, N. R. (2009). Fracture Design Considerations in Horizontal Wells Drilled in Unconventional Gas Reservoirs. Paper SPE 119366 Presented at the SPE Hydraulic Fracturing Technology Conference, The Woodlands, Texas, USA, January. DoiMS., 19-21.

[13] Cheng, Y. (2009). Boundary Element Analysis of the Stress Distribution Around Multiple Fractures: Implications for the Spacing of Perforation Clusters of Hydraulically Fractured Horizontal Wells. Paper SPE 125769 presented at the SPE Eastern Regional Meeting, Charleston, West Virginia, USA. September.

[14] Manchanda, R, & Sharma, M. M. (2012). Impact of Completion Design on Fracture Complexity in Horizontal Wells. Paper SPE 159899 presented at the SPE Annual Technical Conference and Exhibition in San Antonio, Texas, USA. October.

[15] Bunger, A. P, Zhang, X, & Jeffrey, R. G. (2012). Parameters Affecting the Interaction Among Closely Spaced Hydraulic Fractures. SPE Journal. March, , 292-306.

[16] Olson, J. E. (2008). Multi-fracture Propagation Modeling: Applications to Hydraulic Fracturing in Shales and Tight Gas Sands. Paper ARMA presented at the 42nd US Rock Mechanics Symposium in San Francisco, California, June, 2008., 08-327.

[17] Wu, R, Kresse, O, Weng, X, Cohen, C, & Gu, H. (2012). Modeling of Interaction of Hydraulic Fractures in Complex Fracture Networks. Paper SPE 152052 presented at the Hydraulic Fracturing Technology Conference in The Woodlands, Texas, USA. February.

[18] Meyer, B, & Bazan, L. W. (2011). A Discrete Fracture Network Model for Hydraulically Induced Fractures- Theory, Parametric and Case Studies. SPE 140514. SPE Hydraulic Fracturing Technology Conference, January 2011, The Woodlands, Texas, USA, 24-26.

[19] Xu, G, & Wong, S. W. Interaction of Multiple Non-Planar Hydraulic Fractures in Horizontal Wells, Paper IPTC-17043 presented at the International petroleum technology Conference in Beijing, China, March (2013).

[20] Jaeger, J. C, Cook, N. G. W, & Zimmerman, R. W. (2007). Fundamentals of Rock Mechanics. Blackwell Publishing, 4th edition.

[21] Barenblatt, G. I, Entov, V. M, & Ryzhik, V. M. (1984). Theory of Fluid Flows through Natural Rocks, Kluwer Academic Publishers.

[22] Sneddon, I. N, & Lowengrub, M. (1969). Crack Problems in the Classical Theory of Elasticity, John Willey & Sons, Inc.

[23] Warpinski, N. R, & Teufel, L. W. (1987). Influence of Geologic Discontinuities on Hydraulic Fracture Propagation, Journal of Petroleum Technology, February.

[24] Adachi, J, Siebrits, E, Peirce, A, & Desroches, J. (2007). Computer simulation of hydraulic fractures, Int. J. of Rock Mech. Mining Sci. , 44, 739-757.

[25] Clifton, R. J. (1989). Three Dimensional Fracture-Propagation models, in: Recent Advances in Hydraulic Fracturing, Editors: Gidley, J.L., S. A. Holditch, D.E. Nierode, and R.W. Veatch, Mono- graph Series, SPE.

[26] Siebrits, E, & Peirce, A. P. (2002). An efficient multi-layer planar 3D fracture growth algorithm using a fixed mesh approach, Int. J. Numer. Meth. Eng., , 53, 691-717.

[27] Shah, S. N. (1993). Rheological Characterization of Hydraulic Fracturing Slurries. SPE Production and Facilities. May, , 123-130.

[28] Valko, P, & Economides, M. J. (1995). Hydraulic Fracturing Mechanics, Wiley, Chichester.

[29] Desroches, J, Detournay, E, Lenoach, B, Papanastasiou, P, Pearson, J. R. A, Thiercelin, M, & Cheng, A. H-D. (1994). The crack tip region in hydraulic fracturing, Proc. R. Soc. London, Ser. A, 447, 39-48 (1994).

[30] Xu, G. (2000). A Variational Boundary Integral Method for the Analysis of Three-Dimensional Cracks of Arbitrary Geometry in Anisotropic Elastic Solids., J. Appl. Mech., , 67, 403-408.

[31] Xu, G, & Ortiz, M. (1993). A Variational Boundary Integral Method for the Analysis of 3-D Cracks of Arbitrary Geometry Modeled as Continuous Distributions of Dislocation Loops, International Journal of Numerical Methods of Engineering, , 36, 3675-3702.

[32] Wu, R, Bunger, A. P, Jeffrey, R. G, & Siebrits, E. (2008). A Comparison of Numerical and Experimental Results of Hydraulic Fracture Growth into a Zone of Lower Confining Stress. Paper ARMA presented at the 42nd US Rock Mechanics Symposium and 2nd U.S.-Canada Rock Mechanics Symposium, San Francisco, California, USA. June., 08-267.

Chapter 33

Numerical Simulation of Sequential and Simultaneous Hydraulic Fracturing

Varahanaresh Sesetty and Ahmad Ghassemi

Additional information is available at the end of the chapter

http://dx.doi.org/10.5772/56309

Abstract

Hydraulic fracturing of horizontal well hydraulic fracturing technology can help develop unconventional geothermal and petroleum resources. Today, industry uses simultaneous and sequential (also known as zipper) fracturing in horizontal petroleum well stimulations. To achieve successful and desired stimulated rock volumes and fracture networks, one must understand the effect of various rock and fluid properties on stimulation to minimize the risk of unwanted fracture geometries. This paper describes the development of a 2D coupled displacement discontinuity numerical model for simulating fracture propagation in simultaneous and sequential hydraulic fracture operations. The sequential fracturing model considers different boundary conditions for the previously created fractures (constant pressure restricting the flow back between stages and proppant-filled). A series of examples are presented to study the effect of fracture spacing to show the importance of spacing optimization. The results show the fracture path is not only affected by fracture spacing but also by the boundary conditions on the previously created fractures.

1. Introduction

Increased interest in exploration and production of low permeability reservoirs presents new challenges in design and evaluation of hydraulic stimulation treatment. Hydraulic fracturing of unconventional petroleum resources (oil and gas shales) relies on multiple transverse hydraulic fracturing of horizontal wells. Each treatment stage in a well is designed to generate a stimulated volume defined as the rock volume contacted by treatment fluid with a desired enhancement to permeability. The collective network of stimulations should affect the

maximum volume with minimal overlap of adjacent treatment stages. Usually, HF treatment of horizontal wells is carried out using two schemes namely, Simul frac and Sequel Frac. In simultaneous fracturing multiple fractures are created and propagated at same time whereas in sequential fracturing, fractures are created one after another usually by keeping the previously created fracture propped [1] or pressurized with fluid [2]. In both cases, the perforation clusters should be placed appropriately to reduce stress-shadow effects. By reducing the number of clusters per stage, they were able to minimized stress interference, which reduced the possibility of having improper fracture propagation.

In order to determine the optimum spacing and optimum staging between fractures production forecasting analysis is used by assuming simple straight lined fractures, but in reality fractures may propagate in complex manner when they are closely spaced or are near pre-existing fractures as they will interfere to repel or attract each other [3]. In simultaneous fracturing closely spaced fracture interferences causes some of the fractures to stop in between or some may not even initiate due to the stress shadow between them [4]. The design of efficient systems can benefit from hydraulic fracture simulations that couple fluid flow to fracture deformation and fracture mechanics principles. Since the fracturing itself is too complicated these problems are difficult to analyze using laboratory experiments. Numerical method that can accurately model 2D or 3D fracture propagation can help to understand and improve the fracturing process.

[5] solved the growth of multiple simultaneous fractures assuming no fluid- flow inside the fractures; [6] simulated the sequential fracturing with no explicit fluid flow and assuming the previously created fracture dimensions are constant. In [3] previously created fracture in sequential fracturing is assumed to be propped and having a shape elliptical fracture similar to the fracture geometry formed from uniform pressure distributed fracture. The fracture curving is attributed to opening and sliding of previously created fracture. [7] Reproduced to similar results by considering the previously created fracture is uniformly pressurized instead of propped while stating the reason behind the fracture curving is unclear. In this paper a fully coupled DD-based sequential fracturing model is presented which considers previously created fracture as uniformly pressurized and also propped. A linear joint model is used to model the propped fracture. This allows the propped fracture to open/close and shear as the next fracture propagates. This paper also includes the simulation of simultaneous propagation of multiple fractures spaced at different distances. The fracture curving observed in simulations are explained using the stress distribution plots around the fractures. The model can be used to study the effect of parameters such as differential stress, Young's modulus, Poisson's ratio, viscosity of the fluid on fracture propagation. The model calculates the flow rate and pressure within each fracture as they propagate with injection onto the wellbore. Currently, we use the model to analyze propagation of multiple hydraulic fractures to show the importance of spacing optimization.

In our simulations, we consider two different scenarios for sequential fracturing, one scenario is where the previously created fractures remain pressurized by restricting the flow back between stages [8] and the other is where the previously created fractures are filled with proppant [1].

http://dx.doi.org/10.5772/56309

2. Model development

The model developed for the research is based on 2D plane strain and uses the displacement discontinuity method (DDM) to calculate fracture deformation and propagation. The fluid flow inside the fracture network is governed by Lubrication equation [9]. The hydraulic fracture model fluid flow and fracture deformation through an iterative scheme between fracture aperture along the fracture length and fluid pressure. This is a non-linear problem that is solved using Newton-Raphson method. The fracture propagation scheme for sequential hydraulic fractures propagation employs an iterative scheme to find the pressure at fracture tip required to meet the propagation criterion. Joint deformation model is used to simulate the propped fractures by specifying the proppant properties in terms of stiffness. Finally, fracture propagation path is determined using the maximum tensile-stress criterion of [10]. Each of these model components are briefly described below.

3. Displacement discontinuity method

In this model the displacement discontinuity boundary element method is used to find fracture deformation. In implementing this method, a fracture is divided into *n* small elements and by specifying the normal and shear stress acting on each element, the resultant normal and shear stresses on each fracture element is found by using superposition [11]:

$$\begin{aligned} \sigma_s^i &= \sum_{j=1}^{N} A_{ss}^{ij} D_s^j + \sum_{j=1}^{N} A_{sn}^{ij} D_n^j \\ \sigma_n^i &= \sum_{j=1}^{N} A_{ns}^{ij} D_s^j + \sum_{j=1}^{N} A_{nn}^{ij} D_n^j \quad (\text{for } i = 1 \text{ to N}) \end{aligned} \tag{1}$$

A_{ss}^{ij}, A_{sn}^{ij}, A_{ns}^{ij} and A_{nn}^{ij} are the influence coefficients, representing the stresses due to constant shear and normal DD elements. The above system of linear equations can be solved for displacement discontinuity of each fracture element.

Using constant displacement discontinuity elements at the crack tips lead to inaccurate value of stress intensity factor [12]. In fracture mechanics it is very important to have an accurate value to stress intensity factor, as it decides the condition for propagation and crack paths. In order to calculate accurate displacement discontinuities at crack tips, this model incorporates a crack tip element [11] in which the relative normal displacement discontinuity between the crack surfaces is given by $u_y(x) = D_y \left(x / a \right)^{1/2}$ where a is half length of the crack tip element, D_y is the displacement discontinuity at the center of special element and x is the distance measured along the element from the tip of the crack. The influence coefficients and formulation for the special element used herein is given in [12].

4. Joint model

A joint model is useful to simulate propped fractures where one can model the width reduction of propped fractures (proppant closure) due to the creation of new fractures. In this model we assumed a propped fracture behaves like a joint (natural fracture). The proppant pack inside the fracture is assumed to be a compressible element and its displacements can be calculated using the DD method. The joint elements have normal and shear stiffness that represents the filling material characteristics. Though the joint filling material usually deforms non-linearly, here it is assumed to deform linear (linear model in Figure 1) with the stress for simplicity.

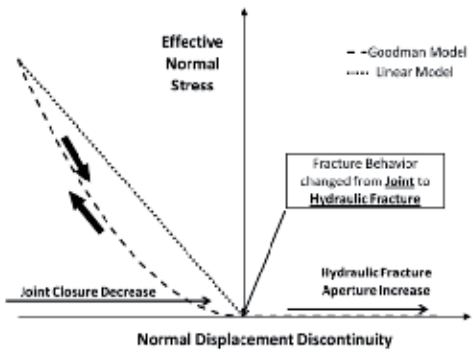

Figure 1. Goodman Joint model and a linear joint model. In Goodman model the closure reaches an asymptotic value at high values of normal stress

Given the far field stresses $(\sigma_{ij})_0^{\infty}$and stresses acting on the joint element, the total joint deformation will be the sum of initial displacements (due to initial stresses on the joint) and induced displacements (due to induced stresses caused by the fracturing in the formation) can be calculated from the following set of equations [11].

$$\begin{aligned} -\left(\overset{i}{\sigma_s}\right)_0^{\infty} &= \sum_{j=1}^{N}(\overset{ij}{A_{ss}}\overset{j}{X_s} + \overset{ij}{A_{sn}}\overset{j}{X_n}) \\ -\left(\overset{i}{\sigma_n}\right)_0^{\infty} &= \sum_{j=1}^{N}(\overset{ij}{A_{ns}}\overset{j}{X_s} + \overset{ij}{A_{nn}}\overset{j}{X_n}) \ , (1 \le i \le M) \end{aligned} \tag{2}$$

$$\begin{aligned} -\left(\overset{i}{\sigma_s}\right)_0^{\infty} &= \overset{i}{K_s}\overset{i}{X_s} + \sum_{j=1}^{N}(\overset{ij}{A_{ss}}\overset{j}{X_s} + \overset{ij}{A_{sn}}\overset{j}{X_n}) \\ -\left(\overset{i}{\sigma_n}\right)_0^{\infty} &= \overset{i}{K_n}\overset{i}{X_n} + \sum_{j=1}^{N}(\overset{ij}{A_{ns}}\overset{j}{X_s} + \overset{ij}{A_{nn}}\overset{j}{X_n}) \ , (M+1 \le i \le N) \end{aligned} \tag{3}$$

http://dx.doi.org/10.5772/56309

Where N is the total number of elements and M is the number of normal elements. The K_n, K_s are shear and normal stiffness's of a joint element and X_n, X_s are the total joint shear and normal deformations respectively. The maximum deformation of a joint element is limited by its closure value (See Figure 1) which is the hydraulic conductivity (0.1 mm for all the simulations shown in this paper.

5. Fracture propagation

The fracture tips are allowed to propagate when mode-I stress intensity factor K_I is equal to fracture toughness K_{IC} according to LEFM [13]. K_I, K_{II} are calculated using displacement discontinuity obtained at the center of the crack tip element [12]. Continued injection of fluid into the fracture will increase the stress intensity at fracture tip and eventually cause it to propagate. In sequential fracturing this can be achieved by changing the pressure boundary condition at fracture tip iteratively till the propagation condition is satisfied. We recognize that fully fluid filled crack has a singular pressure at the fracture tip and requires and asymptotic analysis. For computational purposes we choose to have a finite pressure boundary condition at the last grid block of finite difference scheme for fluid flow inside the fracture which is fracture tip [14]. Whereas for simultaneous fracturing, it is not feasible to iteratively find the pressure distribution in the fracture to satisfy $K_I=K_{IC}$ since more than one fracture is growing at a given time. In this case zero net pressure boundary condition is used at the fracture tip [15, 16]. The fluid is injected until $K_I=K_{IC}$ to satisfy the propagation condition. The crack propagation path is calculated using the method of [10] as implemented in [17] in which the crack propagation direction relies on the maximum principal tensile stress criterion so that one can use the ratio of the stress intensity factors to compute the angle at which the crack will grow.

$$\theta(K_I, K_{II}) = \begin{cases} 0 & if\ K_{II} = 0 \\ 2\arctan\left(\dfrac{\dfrac{K_I}{K_{II}} - \mathrm{sgn}(K_{II})\sqrt{\left(\dfrac{K_I}{K_{II}}\right)^2 + 8}}{4} \right) & if\ K_{II} \neq 0 \end{cases} \tag{4}$$

6. Fluid flow

The fluid flow inside the fracture assumed to be laminar and is modeled using flow through parallel plates equation often called as cubic law.

$$q = -\frac{w^3 h}{12\mu}\frac{\partial p}{\partial x} \tag{5}$$

Where q is the volumetric flow rate, μ is dynamic viscosity of the fluid and w is fracture width.

The fluid is assumed to be Newtonian and incompressible. The continuity equation (eq 6) along with cubic law governs the fluid flow inside the fracture.

$$\frac{\partial q}{\partial x} + \frac{\partial A}{\partial t} + q_L = 0 \tag{6}$$

Where A is the cross-sectional area of the fracture and q_L is fluid leak-off volume rate per unit length of the fracture. Because of the ultra-low permeability nature of shale reservoir matrix, leaf-off is assumed to be zero in these calculations [7]. After every time step in the simulation global mass balance is satisfied. The partial differential equation 7 obtained from substituting eq 5 (cubic law) in to eq 6 (continuity) is solved using the finite difference approximation with the following boundary conditions.

$$\frac{\partial w}{\partial t} = \frac{\partial}{\partial x}\left(\frac{w^3}{12\mu}\frac{\partial p}{\partial x}\right) \tag{7}$$

At the well, the injection rate is specified

$q(0, t) = Q_0$

At the fracture tip finite pressure P_{tip} is specified.

$P(L, t) = P_{tip}$

7. Simulation examples

Example-1: Sequential fracturing with fracture spacing 3 m (9.84 ft.)

In this example we consider sequential fracturing of a horizontal well. Fracture that is generated first (i.e., Stage-1 fracture) is subjected to a constant pressure while injecting into subsequent fractures. Figure 2 shows the geometry of horizontal wellbore and transverse fractures from top view (the simulations in this paper considers a 2D plane strain similar to KGD model. Thus in its current form, the model cannot consider the stress shadow between the fractures due to their height). The properties used in simulation are given in Table 1 for example-1.

http://dx.doi.org/10.5772/56309

Parameter	Value	Units
Young's modulus	27	GPa
Poisson's ratio	0.25	
σ_H/ σ_h (Max/Min In-situ horizontal stress)	5/4	MPa
Injection rate (stage-1)/(stage-2)	20/40	bpm
Viscosity	1	cP
Fracture height	30	ft
Fracture toughness	2	MPa.m$^{1/2}$

Table 1. Input parameters used in example-1

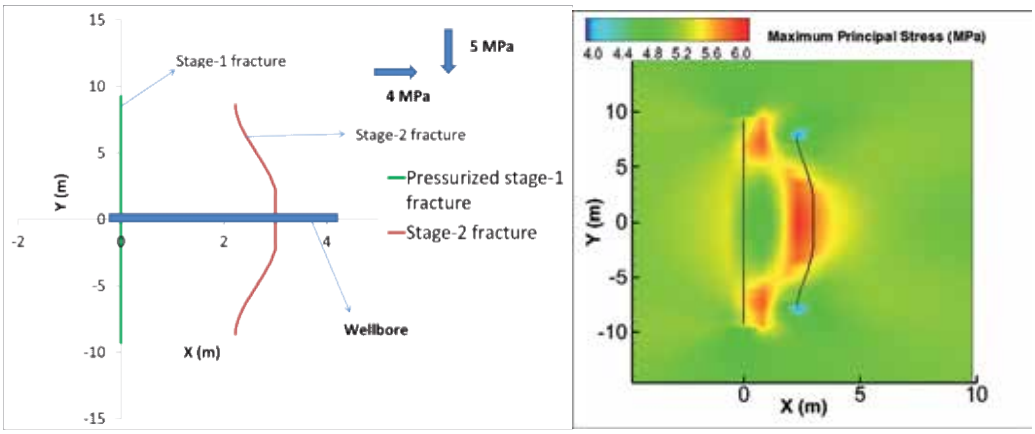

Figure 2. Geometry of the Stage-2 fracture near pressurized Stage-1 fracture after they reached their target lengths and maximum principal stress distribution around them at an instant

Since zero fluid leak-off is assumed into the formation, the entire fluid inside the stage-1 is assumed to re-distribute after injection is ceased into it and is set to a constant average pressure (assuming no gravity effect) corresponding to the target length. Then the Stage-2 transverse fracture is created at a distance of 3m from the stage-1 fracture. Figure 2 show the stage-2 fracture turns towards the stage-1 fracture. This is due to the altered stress distribution in the rock. From the fracture propagation criterion, the fracture propagates in the direction perpendicular to the maximum principal tensile stress. Figure 2 (right side) shows the distribution of maximum principal compressive stresses. The Stage-2 fracture appears to be oriented in the direction of maximum principal compressive stresses. The opening of stage-2 fracture causes a reduction in width along the center of Stage-1 fracture (Figure 3 left side.). The compressive stress due to opening of Stage-1 fracture has not been reduced by the Stage 2 crack near the tips of the former, causing the Stage-2 fracture to curve towards the tips of Stage-1 fracture for a few steps as it eventually follows the maximum in-situ compression direction. The widths of stage-2 fracture (Figure 3 right side) increased as it grows in length.

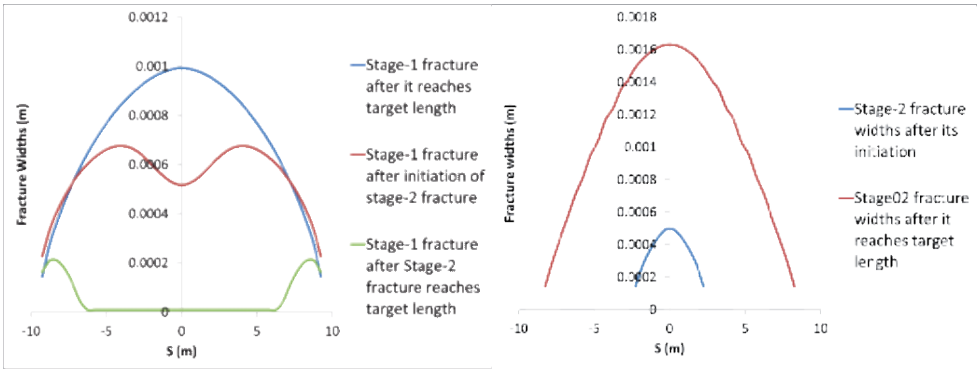

Figure 3. Widths of Stage-1 and Stage-2 fractures at various instants

Example-2: Sequential fracturing while keeping previously created fracture propped

This example considers sequential fracturing keeping the previously created fracture propped. The fluid and proppant properties for this simulation are given in Table 2. The in-situ stress and rock properties are kept same as in example-1. Keeping the spacing between the two fractures 3 m (9.84 ft.) same as in example-1, the simulation results in this example shows the Stage-2 fracture curve away from Stage-1 fracture (Figure 4). The maximum principal compressive stress diagram shows (Figure 4 right side) a huge compression zone near the center of both fractures and towards the right of Stage-2 fracture which caused it to curve away from Stage-1 fracture. The creation of Stage-2 fracture caused the tips of Stage-1 fracture to close (Figure 5) due to the stress shadow between them. The center part of Stage-1 fracture remained open and contributed to large compressive stresses around the center of fractures. Since the tips of Stage-1 fracture are closed in this case there is no attraction towards tips (higher tensile zones) in this case.

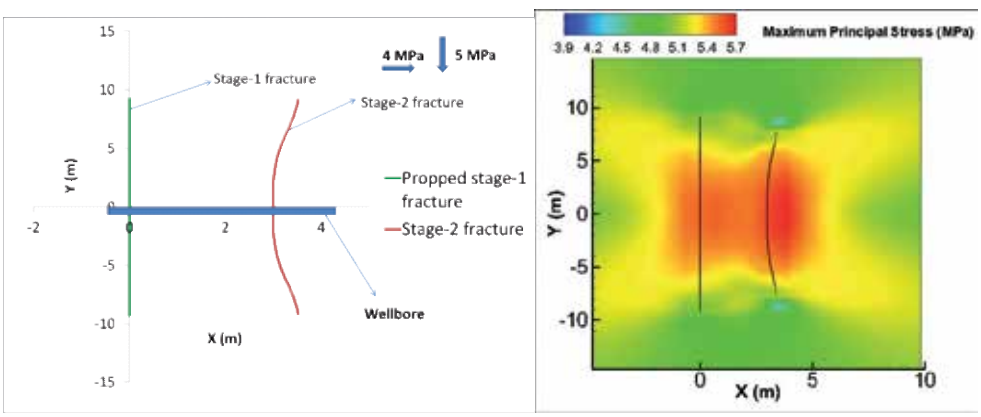

Figure 4. Geometry of the Stage-2 fracture near propped Stage-1 fracture after they reached their target lengths and maximum principal stress distribution around them at an instant

http://dx.doi.org/10.5772/56309

Parameter	Value	Units
Injection rate (stage-1)/(stage-2)	20/20	bpm
Proppant normal stiffness/shear stiffness	15/15	GPa/m

Table 2. Input parameters used in example-2

Example-3: Sequential fracturing with fracture spacing 7 m (20 ft)

This example compares sequential fracturing while keeping previously created fracture pressurized and propped. The rock and proppant properties are given in Tables 1&2 and fluid properties are given in Table 3. The spacing between the fractures is increased to 7 m (more than twice of previous examples) to observe the cuving behavior of Stage-2 fracture. The results from Figure 6 shows Stage-2 fracture curves away from Stage-1 fracture in both scenarios (i.e. Stage-1 fracture pressurized/propped). The curving of Stage-2 fracture near propped Stage-1 fracture is stronger than near pressurized Stage-1 fracture. This phenomenon is expected as from Figure 7 we can see the tips of pressurized Stage-1 fracture remained open after initiation of Stage-2 fracture. The opening of Stage-1 fracture near its tips created attraction towards its tips while its opening near its center created repulsion between the fractures. In this case the repulsion between the fractures slightly dominated the attraction between their tips, which lead to a slightly curve away Stage-2 fracture. This phenomenon also leads to straight Stage-2 fracture when the repulsion between fractures and attracion between the tips balances out. On the other hand Stage-2 fracture curve away from propped Stage-1 fracture as there is no attraction between the tips (Satge-1 tips closed) from Figure 7.

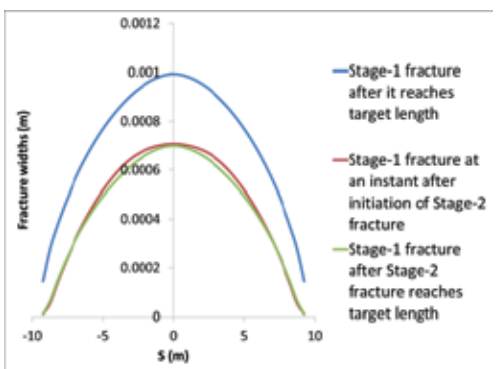

Figure 5. Widths of Stage-1 fracture at various instants

Parameter	Value	Units
Injection rate (stage-1)/(stage-2)	20/20	bpm
Viscosity	1	cP

Table 3. Input parameters used in example-3

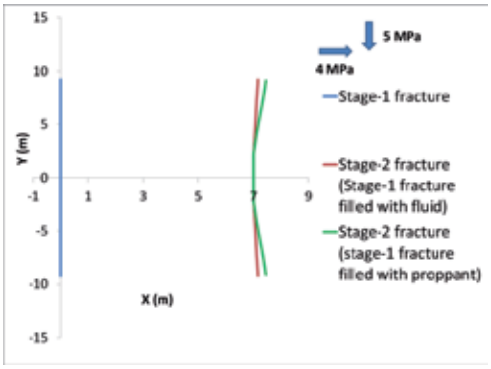

Figure 6. Comparison of Stage-2 fracture geometry after reaching its target length with different boundary conditions for Stage-1 fracture (i.e. pressurized/propped)

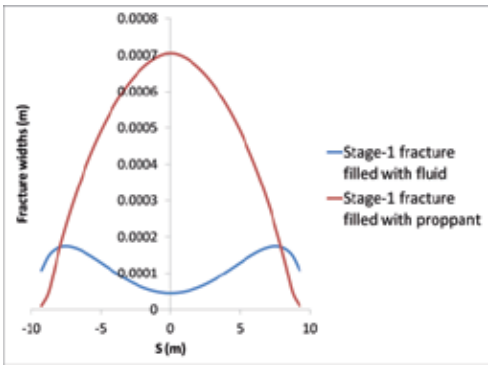

Figure 7. Comparison of pressurized/propped Stage-1 fracture widths after Stage-2 fracture reached target length

Example-4: Simultaneous propagation of hydraulic fractures.

Parameter	Value	Units
Young's modulus	30	GPa
Poisson's ratio	0.22	
σ_H/ σ_h (Max/Min In-situ horizontal stress)	5/4	MPa
Injection rate	80	bpm
Viscosity	7	cP
Fracture height	100	ft
Fracture toughness	2	MPa.m$^{1/2}$

Table 4. Input parameters used in example-4

http://dx.doi.org/10.5772/56309

In this example simultaneous propagation of five hydraulic fractures with initial lengths of 5 m each and 10 m spacing between them is considered. The input parameters used in this simulation are shown in Table 4. The results from Figure 8 show that when fluid is injected into the wellbore at the injection point (Figure 8 left side) the outer fractures (i.e., Frac-1 & Frac-5) tend to grow more than the rest of the fractures. This behavior is expected because the stress shadow on the outer fractures will be less than the fractures inside. On the other hand the results show growth of center fracture (i.e., Frac-3) is more than the fractures Frac-2 & Frac-4. This effect is seen when the outer fractures start to propagate more rapidly than the remaining fractures in the fracture network. The larger outer fractures exert more stress shadow on the fracture near to them (in this case Frac-2 & Frac-4) which will inhibit the growth of these fractures more than the center fracture (i.e.Frac-3). As the outer fractures grows large enough the stress shadow over the remaining fractures increase and completely suppress their growth after sometime.

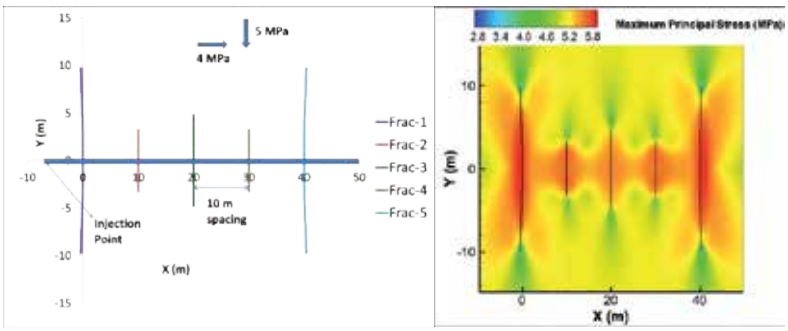

Figure 8. Fracture network obtained after outer fractures reached their target lengths and maximum principal stress distribution around them

8. Conclusions

Several numerical examples are considered to show the behavior of closely spaced hydraulic fractures in sequential and simultaneous fracturing. Two models are presented in sequential fracturing; one considering the previously created fracture is kept pressurized with fluid and other considering the previously created fracture filled with proppant. Numerical results show the fracture geometries of later fractures are dependent on boundary conditions of previous fracture (i.e., pressurized fracture or propped fracture) and injection conditions. With variation in spacing and boundary condition on the previous fracture, the later fracture is observed to curve in/out from the previously created fractures. Later fractures curving from the previous fracture depends on the attraction forces between tips and repelling forces between the centers of the fractures. It was observed that fracture created near to propped fracture tend to curve away more as there is no attraction between the fractures' tips whereas fracture created near pressurized fracture tend to curve. In simultaneous propagation of hydraulic fractures, the

outer fractures dominate the inner fracture in growth. The center fractures usually stop after they reached certain length due to the stress shadow between them. These simulations are useful for horizontal wellbore stimulation design and required spacing conditions to acquire the desired fracture lengths, proppant placement, and production rates.

Author details

Varahanaresh Sesetty and Ahmad Ghassemi

Mewbourne School of Petroleum and Geological Engineering, The University of Oklahoma, USA

References

[1] Rodrigues, V. F, Neumann, L, & Torres, D. S. Guimares de Carvalho. Horizontal Well Completion and Stimulation Techniques, SPE 108075, presented at the Latin American & Caribbean Petroleum Engineering Conference, Buenos Aires, April, (2007). , 15-18.

[2] Soliman, M. Y, Loyd, E, & David, A. Geomechanics aspects of multiple fracturing of horizontal and vertical wells. SPE Drilling& Completion, (2008). , 217-228.

[3] Bunger, A. P, Zhang, X, & Jeffery, R. G. Parameters affecting the interaction among closely spaced hydraulic fractures, SPE 140426, SPE Hydraulic Fracturing Technology Conference and Exhibition, Woodlands, Texas, USA, January, (2011). , 24-26.

[4] El Rabba, W. Experimental study of hydraulic fracture geometry initiated from horizontal wells. SPE Annual Technical Conference and Exhibition. San Antonio, TX, USA, (1989).

[5] Olson, J. E, & Taleghani, D. A. Modeling Simultaneous Growth of Multiple Hydraulic Fractures and Their Interaction With Natural Fractures. Presented at SPE Hydraulic Fracturing Technology Conference, The Woodlands, Texas, USA, January, (2009). , 19-21.

[6] Roussel, N. P, & Sharma, M. M. Strategies to Minimize Frac Spacing and Simulate Natural Fractures in Horizontal Completions. SPE 146104, presented at SPE Annual Technical Conference and Exhibition held in Denver, Colorado, USA, 30 October-2 November, (2011).

[7] Hyunil JoOptimizing fracture spacing to induce complex fractures in a hydraulically fractured horizontal wellbore. (2012). SPE 154930.

[8] George, A. Waters, Barry K.D, Robert C.D, Kenneth J.K, Lance A., Simultaneous Hydraulic Fracturing of Adjacent Horizontal Wells in the Woodford Shale, SPE Hy-

draulic Fracturing Technology Conference, The Woodlands, Texas, January (2009). , 19-21.

[9] Batchelor, G. K. An Introduction to Fluid Dynamics. Cambridge, UK: Cambridge University Press; (1967).

[10] Stone, T. J, & Babuska, I. A numerical method with a posteriori error estimation for determining the path taken by a propagating crack, Computer Methods in Applied Mechanics and Engineering, (1998). , 1998(160), 245-271.

[11] Crouch, S. L, & Starfield, A. M. Boundary Element Methods in Solid Mechanics. London: George Allen & Unwin; (1983).

[12] Yan, X. A Special Crack Tip Displacement Discontinuity Element, Mechanics Research Communications, (2004).

[13] Rice, J. R. Mathematical analysis in the mechanics of fracture. In Fracture, An Advanced Treatise, Leibowitz H (ed.). Academic Press: New York, (1968). , 172-308.

[14] Murdoch, L. C, & Germanovich, L. N. Analysis of a deformable fracture in permeable material. International Journal for Numerical and Analytical Methods in Geomechanics, (2006).

[15] Nordgren, R. P. Propagation of a Vertical Hydraulic Fracture. Society of Petroleum Engineers Journal, (1972). , 1972(12), 306-314.

[16] Weng, X, Kresse, O, Cohen, C, Wu, R, & Gu, H. Schlumberger. Modeling of Hydraulic Fracture Network Propagation in a Naturally Fractured Formation. SPE 140253, SPE Hydraulic Fracturing Technology Conference and Exhibition, Woodlands, Texas, USA, January, (2011). , 24-26.

[17] Tarasvo, S, & Ghassemi, A. Propagation of a system of cracks under thermal stress. Presented at the 45th US rock mechanics Symposium, San Fransisco, (2010).

Chapter 34

Three Dimensional Forms of Closely-Spaced Hydraulic Fractures

James Kear, Justine White, Andrew P. Bunger, Rob Jeffrey and Mir-Akbar Hessami

Additional information is available at the end of the chapter

http://dx.doi.org/10.5772/56261

Abstract

When creating arrays of hydraulic fractures in close proximity, stress field changes induced by previously placed hydraulic fractures can lead to deflection in subsequent fracture paths and coalescence between fractures. Any fracture coalescence can compromise the effectiveness of the treatment array and the fracture geometry will not be appropriately accounted for in reservoir or caving models. Here we present the results of an experimental study consisting of arrays of 4 closely spaced hydraulic fractures grown sequentially in 350x350x350 mm blocks of a South Australian Gabbro under different initial stress states and for notched and un-notched wellbores. In particular we focus on insights gained from 3-dimesional serial sectioning and digital reconstruction of the hydraulic fracture patterns that were formed. The results show that the curving hydraulic fractures typically do not exhibit a high degree of radial symmetry in their paths even though the fractures grew by radiating outward from a centrally located wellbore. The results also confirm model predictions that a subsequent fracture will curve towards a previous fracture when the minimum stress is zero and that this curving is suppressed when the minimum stress is sufficiently large. Finally, fracture initiation is shown to be critical to the symmetry of the fracture pattern and preponderance of branching and therefore effective notches that lead to initiation in the eventual plane of favored propagation have a profound impact on the hydraulic fracture geometry.

Keywords: Hydraulic Fracturing, Closely Spaced Fractures, Serial Sectioning, Experiments

1. Introduction

The desired outcome of certain types of hydraulic fracture treatments is the creation of a system of closely spaced fractures. Forming such a closely spaced hydraulic fracture array is a highly effective technique for increasing the permeability of a rock mass [1,2] or reducing the strength of a rock mass in mining [3]. Application areas that benefit from an increase of permeability are those that value greater fluid conductivity such as tight gas extraction, in situ leaching, carbon sequestration and storage, geothermal power generation and similar activities. A reduction in the tensile and shear strength of the rock mass through the growth of hydraulic fractures is beneficial to block cave mining where earlier and more controlled caving events are preferable to uneven or irregular caving events caused by strong rock-masses not collapsing in a regular way under their own weight. In each application area, an optimal hydraulic fracturing treatment would provide the greatest alteration to the rock mass for the lowest cost.

When creating arrays of hydraulic fractures in close proximity, stress field changes induced by initial fractures can lead to deflection in subsequent fracture paths. Path deflection can compromise the effectiveness of the treatment array because it can lead to coalescence of the fractures rather than creation of distinct fractures. Also complex fracture paths such as coalescing or curving fractures may not be appropriately accounted for in reservoir or caving models. Ineffective treatments can be costly in terms of re-initiation and re-treatment remediation works. An accurate understanding of the interaction effects between multiple hydraulic fractures growing in close proximity to one another is therefore important for effective treatment design.

The 3-dimenional form of these fracture treatments can be difficult to observe in the field, and even in laboratory experiments often only a 2-dimensional cross-section of the fracture system is examined. In reality, the 3-dimensional nature of the fracture geometry is fundamental to the treatment performance in almost all industrial applications of hydraulic fracturing.

A recent numerical study [4] has identified a set of parameters controlling hydraulic fracture path deflection. The work presented here compares the results of an experimental study to the predictions of numerical modeling work with respect to the interaction effects of closely spaced hydraulic fractures. In this regard, the present work extends initial comparisons [5] to include a fully 3-dimensional characterization of the laboratory hydraulic fracture geometry.

The experimental study consists of closely spaced hydraulic fracture arrays grown in 350mm cubical sample blocks of a South Australian Gabbro. Four closely-spaced fractures were sequentially grown in each block under a variety of far-field stress and fluid injection conditions. After the experiments were completed the blocks were cut into 15 mm thick slices (serial sectioned) and the fracture paths were measured on the faces of these slices.

2. Experimental method

The 350x350x350 mm blocks were fabricated from Adelaide Black Granite (ABG), a gabbro from Black Hill Quarry in South Australia. This material has been used in previous hydraulic

http://dx.doi.org/10.5772/56261

fracturing experiments by CSIRO and the material properties of this rock have been well characterized and are listed in Table 1.

Fracture toughness	K_{IC}	2.3 MPa.m$^{0.5}$
Young's modulus	E	102 GPa
Poisson's Ratio	ν	0.27
Tensile Strength	TS	9.4 MPa
Friction coefficient	f	0.45 (coarse finish) to 0.17 (polished finish)
Crystal Size		1-10mm diameter (typical)

Table 1. Adelaide Black Granite material properties.

Four hydraulic fractures were grown in each block, as shown in Figure 1. The fractures were grown one at a time beginning with the deepest fracture and working incrementally towards the top of the borehole.

The experimental setup used CSIRO's polyaxial load frame to apply confining stresses on the blocks along the vertical and horizontal axes. These stresses were applied using stainless steel flat jacks, inflated with water and with pressure controlled by three independent ISCO 260D syringe pumps.

Hydraulic fractures were grown by injecting fluid into an isolated section of the borehole in order to pressurize and initiate fracture growth. The Newtonian fluid consisted of a combination of water (13.6%), glycerol (80.0%) and blue food dye (6.4%) and had a dynamic viscosity of 0.058 Pa·s and a density of 1.21 kg/m^3.

The injection pressure was recorded upstream and downstream of a flow control (needle) valve that limits flow rate surges associated with injection system compressibility during breakdown and initial fracture growth. The temperature in the laboratory was stable at 20°C (± 1°C) and the temperature of the fracturing fluid was recorded through the tests to enable corrections for the effect of temperature on fluid viscosity.

Fracture initiation at a specific point in the borehole was achieved using an injection tool similar in concept to isolation packers used in the field (Figure 1, inset). O-ring "packers" isolated the fracture initiation zone above and below ports in the tool through which the fracture fluid exited the tool. In some blocks, a circumferential notch was scribed in the borehole at the location of fracture initiation, while in other tests the fractures were grown from an un-notched borehole.

After testing, the blocks were sectioned into 15 mm thick slabs, photographically scanned, and the fracture paths digitally re-constructed. The width of these slabs determined the resolution in one direction of the final re-construction.

After being cut, the slices were finished using a surface grinder to provide a smooth and clean face to allow the best possible observation of the hydraulic fracture paths.

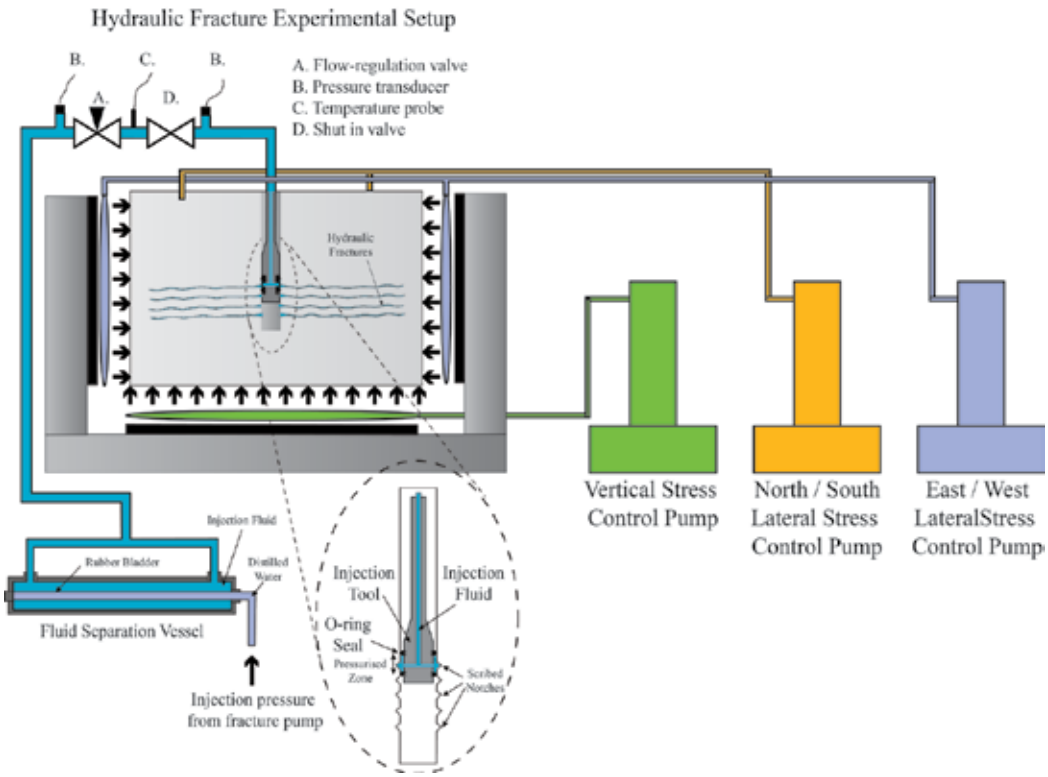

Figure 1. Hydraulic fracture experimental setup.

Each ground face was treated with a penetrant crack detection dye to highlight the fracture path. (This penetrant dye is sold commercially for detection of cracks in metal structures such as brake rotors.) Slices were digitally photographed at a high resolution under controlled lighting conditions to allow precise determination of fracture locations

Final images of the slice faces have a resolution of approximately 8 pixels/mm. The digitized trace of the hydraulic fracture paths are then re-constructed in three dimensions, after accounting for the material removed by the saw blade thickness and by grinding, by laying out these traces as per their original spatial locations in the block. In this way a 3-dimensional image of the fracture system is obtained.

3. Results

The results from three hydraulic fracturing experiments are presented for comparison. An analysis of 2-dimensional cross sections for these three cases was presented in Ref [5]. All three experiments are cases where four sequential hydraulic fractures have been grown in close proximity, all are in the same size block (350mm on each side) and all fractures for all 3 blocks were grown using the same fluid and injection rate.

http://dx.doi.org/10.5772/56261

The test parameters of the first 2 experimental cases (Block 3 and Block 4) were designed such that the minimum (in this setup, the vertically directed) stress was small enough so that the tensile stresses produced near the tip of each propagating hydraulic fracture would be expected to generate a small region of re-opening on the neighboring, previously-placed hydraulic fracture. The model predictions [5] show that in this case the growing hydraulic fracture is predicted to curve towards the previously placed hydraulic fracture, that is, it exhibits "attractive curving". Hence, this is the predicted behavior for both Blocks 3 and 4, which are identical with the exception of the existence of fracture initiation notches scribed in the borehole of Block 4. Furthermore, it was expected from previous experiments for curving hydraulic fractures (grown near a free surface)[6], that the fractures would form roughly axisymmetric bowl-shapes.

In the third case (Block 6), the experimental parameters were chosen in such a way as to suppress the re-opening of the previous hydraulic fractures through the application of a significant minimum (vertical) stress (acting against the opening of the fractures). In this case, numerical modeling [5] predicts that the fractures would grow parallel to one another up to a length commensurate with the specimen size. Details of experimental parameters are presented in Table 2 below, recalling that rock material properties are given in Table 1.

		Block 3	**Block 4**	**Block 6**
Maximum principal stress	σ_{max}	4.6 MPa	4.6 MPa	18 MPa
Minimum principal stress	σ_{min}	0 MPa	0 MPa	14.4 MPa
Borehole radius	R	8 mm	8 mm	8 mm
Initial fracture spacing along borehole	H	15 mm	15 mm	25 mm
Fracture fluid dynamic viscosity	μ	0.58 Pa.s	0.58 Pa.s	0.58 Pa.s
Borehole notch depth		(no notch)	~3 mm	~3 mm
Volumetric injection rate	$\bar{Q}$	0.19 ml/min	0.19 ml/min	0.19 ml/min
Residual fracture widths*	w_o	~1 μm	~1 μm	~1 μm
Fracture half length	α	175 mm	175 mm	175 mm
Reopening of previous fracture [5]		Predicted	Predicted	Suppressed

Table 2. Experiment parameters for presented cases.

Note that the residual widths of the fractures in these experiments are difficult to quantify accurately. No proppant was included in the fracture fluid and the fluid viscosity was low. The residual widths have been selected in the model calculation so that there would be little effect exerted on the stresses in the surrounding rock, although the results subsequently presented do suggest some impact on the stresses did occur in some of the experiments, as evidenced by an increase in breakdown pressure for each sequential fracture.

3.1. Case 1 (Block 3) un-notched zero vertical stress

In Block 3 the hydraulic fractures were grown from an un-notched borehole under conditions where the previous fractures were predicted to re-open because of the tensile stresses surrounding the tip of the propagating fracture.

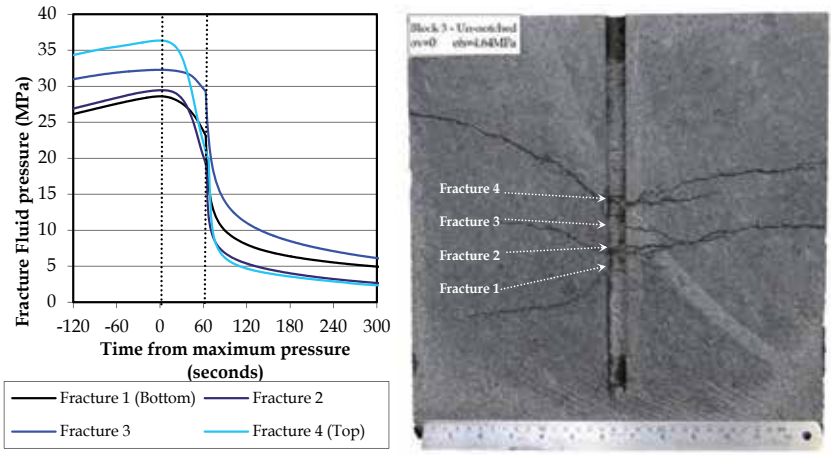

Figure 2. Fracture pressure records (the vertical dotted lines represent maximum pressure and shut in respectively) and 2-dimensional cross section of Block 3 (Hydraulic Fractures can be seen as dark grey cracks on the cross-section image), after Bunger et al. [5].

The pressure records for each of the four hydraulic fractures in the block are presented on the left in Figure 2 with zero time shifted to correspond to the maximum pressure reached during each injection. For each fracture, pumping was maintained at a constant rate throughout pressurization, breakdown and for 60 seconds after the maximum pressure was reached. After 60 seconds the pump was stopped and the fracture was shut in (valve closed) to allow fluid pressure in the fracture to fall off naturally for a few minutes before venting the system to atmospheric pressure. The next fracture was then commenced approximately one hour after the previous fracture was shut-in. For all fractures the breakdown (maximum) pressure of each subsequent fracture is greater than that of the fracture that preceded it. This is possibly an indication of some residual change in the local stress locked in from the previous fracture growth that falls off over the hours following the experiment as the viscous fluid slowly flows back to the wellbore. This effect is significantly more pronounced for this un-notched case (Block 3) than for the case where the borehole was notched at the fracture initiation locations (Block 4, next section).

As can be seen on the right in Figure 3, the fracture paths are not symmetric about the borehole and the fracture pattern appears to be characterized by many small branches, deviated paths, and coalescence of the fractures from the 4 initiation points to form two dominant fractures going to the right and three dominant fractures going to the left. 3-dimensional reconstruction shows that this reduced number of fractures due to coalescence occurred throughout the block.

http://dx.doi.org/10.5772/56261

The lack of radial symmetry in the curving fracture paths in this case is not surprising. There were no notches to provide for fracture initiation in the plane of preferred propagation. Rather, a close inspection of the near borehole region in Figure 3 shows that the hydraulic fractures initiated at a small angle to the wellbore axis. The fractures then re-oriented as they grew so as to be favorably oriented relative to the applied stresses. But given that initiation was not axisymmetric, the fact that growth was non-axisymmetric is to be expected. Instead, these fractures exhibit approximate translational symmetry along the direction of viewing in Figure 3 (perpendicular to the page), where we note that this direction is parallel to the plane of the high angled initiation. Also, the apparent "repulsive" nature of the curving, which is in contrast to predictions for the stress based modeling of initially parallel fractures (as in Block 4, next section), probably arises directly from the high angled initiation geometry. Finally, re-orientation of a 3-dimensional hydraulic fracture is certain to produce complex, mixed-mode loading of the crack tip, which is well-known to result in segmentation of fracture planes [7,8]. Hence it seems that most of the features of the observed fracture patterns in this block can be related to the initiation geometry.

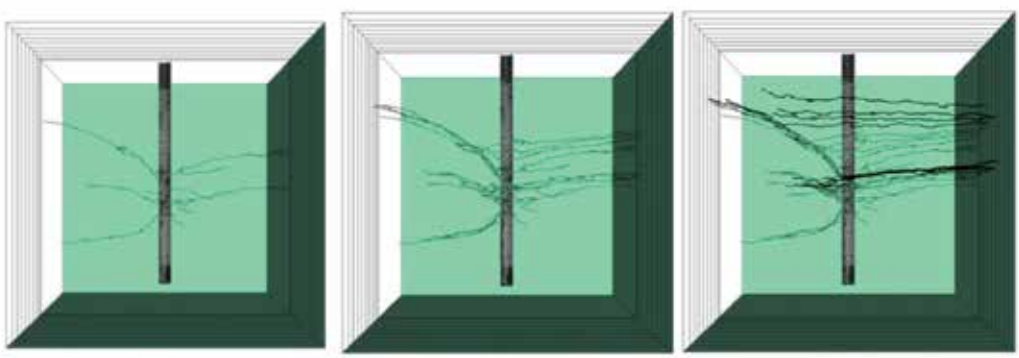

Figure 3. dimensional reconstruction of Block 3 with increasing number of slices represented, single central slice (Left), 50mm of block reconstructed (middle), 150mm of block reconstructed (right).

3.2. Case 2 (Block 4) notched no vertical stress

Block 4 was tested under identical conditions to the first case (Block 3), however for Block 4, circular notches approximately 3 mm deep were scribed into the borehole at the hydraulic fracture initiation locations. Hydraulic fractures grown from a borehole which does not contain notches tend to breakdown in a vertical orientation, consistent with the stress concentration around a circular wellbore, and then re-orient to the principal stress direction. Borehole notches provide a stress concentration location that aids in the initiation of a horizontal fracture aligned with the principal stress direction. Fractures initiated from notches are expected to have fewer branches and to be more predictable in their behavior, which is demonstrated by the results presented here.

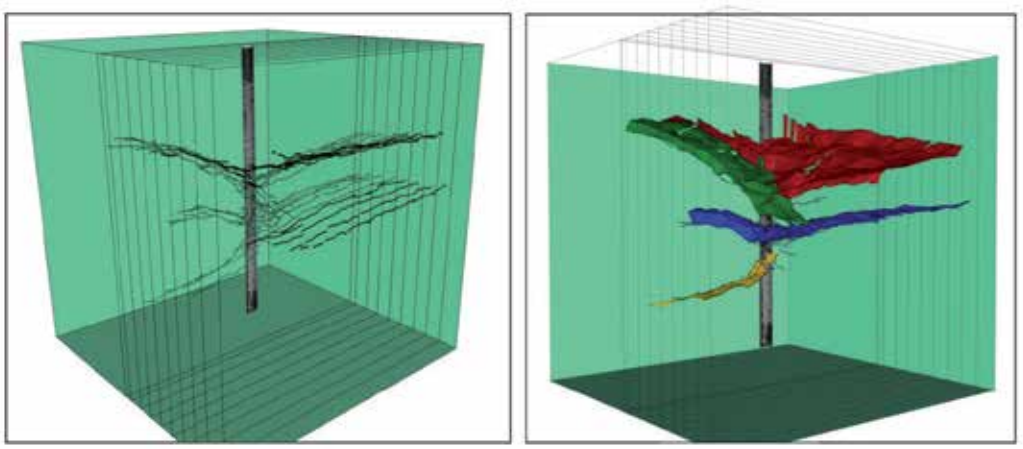

Figure 4. Different viewing angles of the fracture paths in Block 3. Raw traces are presented on the left and fitted mesh surfaces representing fractures on the right (a video animation of this fracture can be viewed at http://youtu.be/7ykr_Jg-VcU).

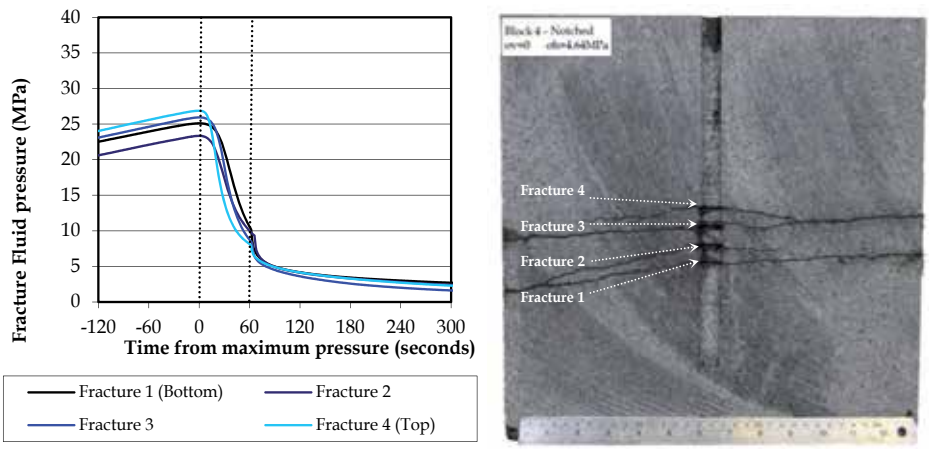

Figure 5. Fracture pressure records and 2-dimensional cross section of Block 4, after Bunger et al. [5].

Pressure records for Block 4 are presented on the left in Figure 5. It is interesting to note that the breakdown (maximum) pressures were lower in every fracture than those observed in Block 3 (un-notched borehole case). Again the maximum pressures are generally observed to become incrementally higher, however this effect is less pronounced than in the un-notched Block 3.

For these stress and injection conditions, numerical modeling [5] predicts that the fractures will coalesce and eventually join at between 5 and 10 times the initial fracture spacing. Examination of Figure 5 shows that the observed behavior is consistent with the prediction, with fracture 2 coalescing with the previously placed fracture 1 at a radial distance equal to

http://dx.doi.org/10.5772/56261

about 10 times the initial spacing and fracture 4 coalescing with the previously placed fracture 3 at a radial distance equal to about five times the initial spacing.

If indeed these curving hydraulic fractures grew in an axisymmetric manner, then the final shape of fractures 2 and 4 would be like an inverted bowl. However, the curving was instead more fold-like and thus formed inverted troughs. Hence, one of the surprising results of these experiments (that is evident only via the 3-dimensional reconstruction) is that hydraulic fractures that essentially radiate from the wellbore and would likely have been radially symmetric in plan view, at least for a substantial portion of their propagation, do not necessarily maintain radial symmetry in their curving behavior. For fracture 4 in particular, the curving exhibits approximate translational symmetry along the direction of viewing in Figure 6. That is, fracture 4 curves toward fracture 3 in the projected plane shown in Figure 6 significantly more strongly than it curves toward fracture 3 in the direction perpendicular to the page. Fracture 2, on the other hand, appears to curve towards fracture 1 in both planes (closer to radial symmetry than fractures 3 and 4), however the curving is much stronger in the plane of the page than it is in the direction perpendicular to that plane. Further experimentation is aimed at determining the conditions that lead to this scenario and ascertaining whether axisymmetric curving can be attained under these experimental conditions as it is under near-surface conditions in the experiments of [6].

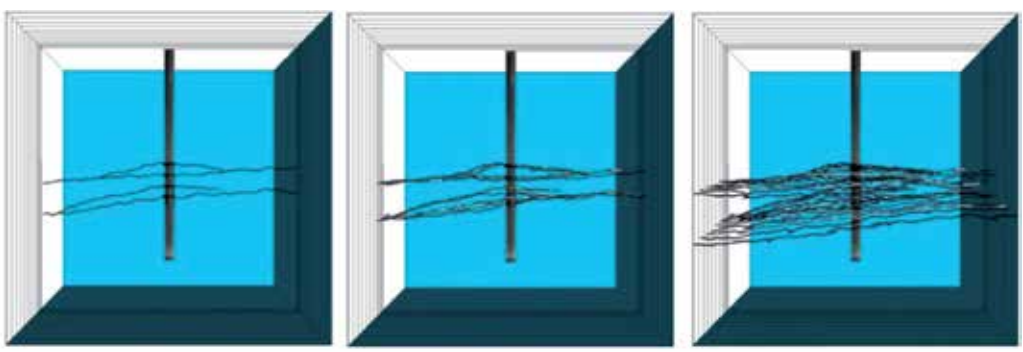

Figure 6. dimensional reconstruction of Block 4 with increasing number of slices represented, single central slice (Left), 50mm of block reconstructed (middle), 150mm of block reconstructed (right).

The observed approximate translational symmetry is one of the few similarities between the notched Block 4 and the un-notched Block 3. In contrast, the curving is attractive in Block 4 and there are few branches in the fracture path.

The translational symmetry can again be seen in Figure 7 where fracture 4 (yellow) can be seen strongly curving towards fracture 3 (pink) in the plane of original sample sectioning to the left of the borehole. In contrast, fracture 4 (yellow) essentially grows parallel to fracture 3 (pink) in the re-constructed plane perpendicular to the original cut which can be seen to the right of the borehole in Figure 7. This effect is repeated however more subtly for fractures 1 (orange) and 2 (green).

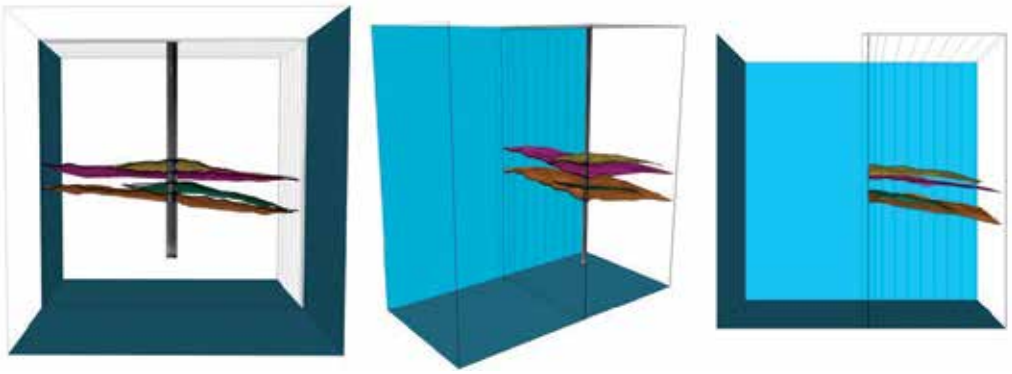

Figure 7. Rendered fracture paths in Block 4. Original fracture trace shown in the left image and re-constructed cross-section (oriented at 90 degrees to the original) in the right image. A composite of the original and re-constructed cross-sections is presented in the central image. A video animation of this fracture can be viewed at http://youtu.be/KMioXgoKfrg).

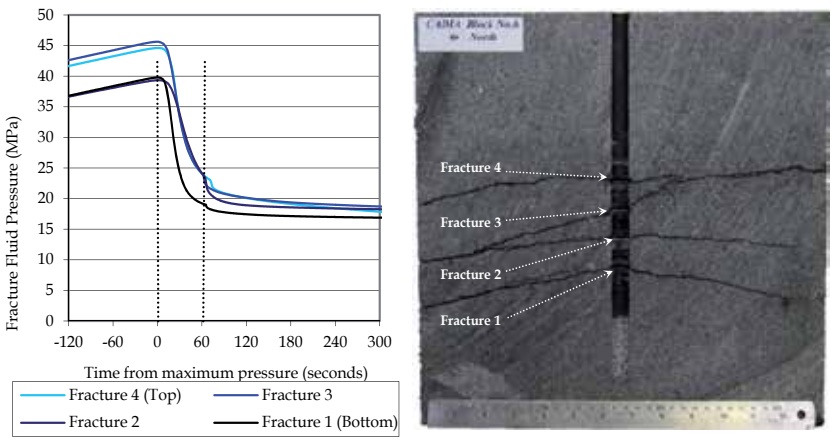

Figure 8. Fracture pressure and 2-dimensional cross section of Block 6, after Bunger et al. [4].

In Figure 7, fractures 1 (orange) and 3 (pink) can be observed appear to be clipped along a plane. This is due to the fact that these two fractures extend to the edges of the sample. This effect can be clearly seen in the uploaded animation linked in the Figure 7 caption.

3.3. Case 3 (Block 6) notched with substantial vertical stress

In Block 6 there was sufficient applied vertical stress, as predicted by the model, to suppress re-opening of existing fractures thus enabling the closely spaced fractures to grow parallel to one another without coalescence.

As can be seen in Figure 8, fractures 1, 2 and 4 appear to grow roughly parallel to one another and perpendicular to the minimum principal stress (which is vertical). Fracture 3, however,

http://dx.doi.org/10.5772/56261

does not initiate cleanly at the notch and thus grows at an angle of approx 35 degrees away from the principal stress direction. Possible reasons for this may be poor notch quality, localized material property changes or initiation at an existing micro crack (see a more detailed discussion in ref [4]).

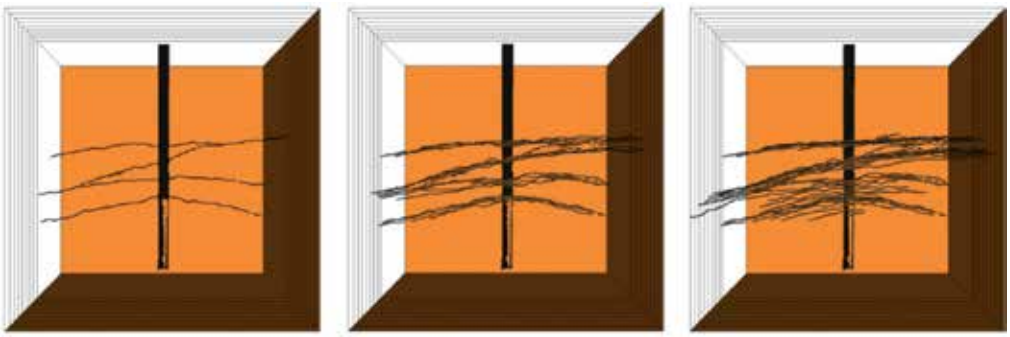

Figure 9. dimensional Reconstruction of Block 6 with increasing number of slices represented, single central slice (left), 50 mm of block reconstructed (middle), 150 mm of block reconstructed (right).

It is interesting to note that the breakdown pressures for the first two fractures are nearly identical, while fracture 3 had a higher breakdown pressure that is consistent with it not initiating at the notch as mentioned above. Fracture 4 also had a higher breakdown pressure, which is possibly due to fracture three growing close to the point of initiation of fracture 4 so that the residual width of fracture 3 affected the stress field in the initiation region of fracture 4.

The 3-dimensional re-construction of Block 6, Figures 9 and 10, confirms that fractures 1, 2 and 4 grow roughly planar and parallel to one another. We can also see that fractures 1, 2 and 4 maintain a roughly horizontal orientation, dipping slightly as they come forward out of the page. Fracture 3, which did not break down at the notch cleanly and thus began on a greater angle than the other fractures, appears to re-orient itself on the left side of the borehole. However, on the right fracture 3 appears to grow into the zone of influence of fracture 2 and be drawn towards it, eventually coalescing at approximately 4 times the fracture spacing.

The anomaly of fracture 3 aside, in this case the fractures are observed to propagate parallel to one another, and with the fewest branches in the fracture paths of the 3 blocks we tested. In fact as can be seen in the 3-dimensional reconstruction in Figure 10, when viewing the re-constructed cross section (to the right of the borehole) all four fractures are seen to grow parallel to one another. The parallel propagation is consistent with the model predictions for these stress and injection conditions [4,5]. The reduction in branches is beyond the scope of the modelling, but is to be expected when the fractures are not curving since the curving is associated with mixed mode loading at the crack tips that can also be associated with crack tip segmentation [7,8].

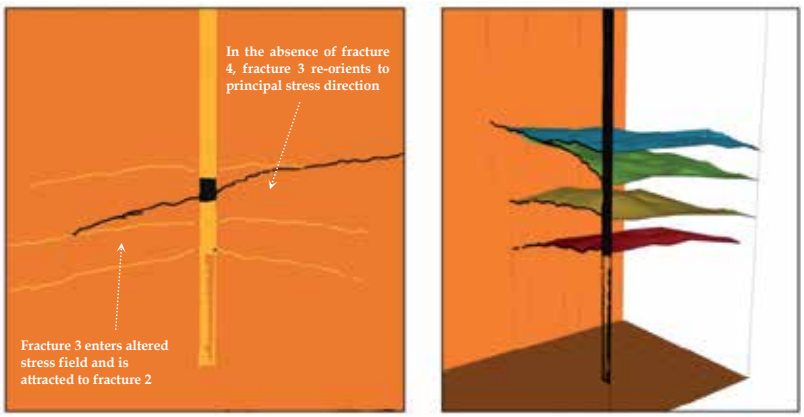

Figure 10. A 2-dimensional cross-section of Block 6 showing the deflected path of fracture three (left) and a 3-dimensional reconstruction of the fracture paths in Block 6 (a video animation of this fracture can be viewed at http://youtu.be/ZCMBWGl_8-Y).

4. Experimental practicalities and future work

A significant amount of time is currently required to produce the final 3-dimensional digital images of the fractures using serial sectioning. The most time consuming steps in the process are cutting the blocks into sections and scanning and processing the fracture images. Several attempts at developing and applying existing algorithms to extract the fracture geometry from a digital image were made, but without success. In particular, for our application and in our experience, we found that line-tracing type algorithms that have been used in applications such as X-ray Computer Tomography trade off precision in the tracing for the sake of high throughput. This makes sense when one has many, very closely spaced and easily acquired cross-sectional images to analyze. However, in our case a significant time investment is required to obtain each cross-sectional image and so our priority is on accuracy rather than throughput. Hence, a manual method was finally settled on because it gave the most accurate and detailed digital fracture image from each rock slice. But, if this part of the process could be automated, significant savings in overall time needed would be achieved.

Having a 3-dimensional representation of a hydraulic fracture is very useful, but to obtain full benefit this image should be viewed using an interactive 3-dimensional computer application. Presenting static views of the fracture, as was done in this paper, limits the benefit. Improvements to the 3-dimensional images, such as advanced highlighting and shading methods, will be investigated as a way to improve the static images for publication.

In the future, in addition to running several replications of the tests described here, we see significant potential in applying serial sectioning as part of studies of fracture initiation at notches in the borehole to better understand the effect of initiation geometry on near-, intermediate- and far-field fracture geometry. A series of tests in a finer-grained rock material

http://dx.doi.org/10.5772/56261

is seen as part of this proposed work. Understanding how to better initiate fractures so that an array of parallel hydraulic fractures can be grown transverse to the borehole is important in mining, petroleum, and geothermal application areas.

5. Conclusion

Reconstruction of fracture paths from tested blocks gives additional insight into fracture growth and is a useful technique for extracting additional information from tested blocks. In the study presented here, the 3-dimensional reconstructed fracture images have been used to show that the curving fracture geometries resulting from sequential growth of closely spaced, interacting hydraulic fractures exhibit translational symmetry even though the hydraulic fracture growth radiated from a centrally located wellbore. While based only on a few experiments and therefore in need of further experimental confirmation, this unexpected result is important for selection of appropriate simplifying symmetry assumptions (i.e. plane strain versus radial symmetry) in numerical models.

In addition to this conclusion, which is fundamentally based on 3-dimensional considerations, these reconstructions have confirmed the consistency between model and experiment that Bunger et al. [4] draw based on a single cross section of these fractures, namely that a subsequent fracture will curve towards a previous fracture when the minimum stress is zero and that this curving is suppressed when the minimum stress is sufficiently large. Also, the 3-dimensional reconstructions confirm that fracture initiation is critical to the symmetry and preponderance of branching. Therefore, cutting effective notches in the borehole that facilitate fracture initiation in the eventual plane of favored propagation have a profound impact on the hydraulic fracture geometry.

Serial sectioning and digital 3-dimensional image reconstruction is found to be an effective method to obtain a more complete understanding of fracture geometry and interaction. Once the fracture traces are assembled into a 3-dimensional model, the fracture image can be rotated in space and viewed from different directions, which allows detailed examination of the fracture geometry and spatial relationship between fractures. It is, however, time consuming and therefore relatively expensive, but no other method provides the level of detail or the ability to image fractures in large rock blocks.

Acknowledgements

The authors thank both CSIRO and Newcrest Mining Limited for funding the experiments and for permission to publish. Serial sectioning comprised a portion of the final year thesis for JW at Monash University under the supervision of MAH. Online animations were prepared by JK and Dane Kasperczyk (CSIRO Earth Sciences and Resource Engineering, Clayton, Australia).

Author details

James Kear[1*], Justine White[1], Andrew P. Bunger[1,2], Rob Jeffrey[1] and Mir-Akbar Hessami[3]

*Address all correspondence to: James.Kear@csiro.au

1 CSIRO Earth Sciences and Resource Engineering, Clayton, Australia

2 Department of Civil & Environmental Engineering, University of Pittsburgh, Pittsburgh, Pennsylvania, USA

3 Department of Mechanical and Aerospace Engineering, Monash University, Clayton, Australia

References

[1] King, G. E. Thirty years of gas shale fracturing: What have we learned? In Proceedings SPE Annual Technical Conference and Exhibition. Florence, Italy. SPE 133256, 2010.

[2] Rodrigues, V. F., L. F. Neumann, D. Torres, C. Guimaraes, and R. S. Torres, 2007. Horizontal well completion and stimulation techniques - A review with emphasis on low-permeability carbonates. In Proceedings SPE Latin American and Caribbean Petroleum Engineering Conference. Buenos Aires, Argentina. SPE 108075.

[3] van As, A. and R. Jeffrey. Caving induced by hydraulic fracturing at Northparkes Mines. In Pacific Rocks 2000 - Proc. 4th North American Rock Mechanics Symposium, eds. J. Girard, M. Liebman, C. Breeds, and T. Doe. Seatle, WA: Balkema, 353–360, 2000.

[4] A. P. Bunger, X. Zhang, and R. G. Jeffrey, "Parameters Affecting the Interaction Among Closely Spaced Hydraulic Fractures," *SPE Journal*, no. March, 2012.

[5] A. P. Bunger, R. G. Jeffrey, J. Kear, X. Zhang, and M. Morgan, "Experimental Investigation of the Interaction Among Closely Spaced Hydraulic Fractures," in *American Rock Mechanics Symposium*, 2011.

[6] Andrew P. Bunger, Robert G. Jeffrey and Emmanuel Detournay, "Evolution and morphology of saucer-shaped sills in analogue experiments (in Structure and emplacement of high-level magmatic systems)" Geological Society Special Publications (2008), 302:109-120

[7] Hodgdon, JA & Sethna, JP, 'Derivation of a general three-dimensional crack-propagation law: A generalization of the principle of local symmetry' Physical Review B Condensed Matter, vol 47, no. 9, pp. 4831-4840, 1993.

http://dx.doi.org/10.5772/56261

[8] Leonid N. Germanovich, Dmitriy K. Astakhov, Michael J. Mayerhofer, Jacob Shlyapobersky, Lev M. Ring, Hydraulic fracture with multiple segments I. Observations and model formulation, International Journal of Rock Mechanics and Mining Sciences, Volume 34, Issues 3–4, April–June 1997, Pages 97.e1-97.e19

Section 11

Numerical Modeling 1

Chapter 35

The XFEM With An Explicit-Implicit Crack Description For Hydraulic Fracture Problems

N. Weber, P. Siebert, K. Willbrand, M. Feinendegen,
C. Clauser and T. P. Fries

Additional information is available at the end of the chapter

http://dx.doi.org/10.5772/56383

Abstract

The Extended Finite Element Method (XFEM) approach is applied to the coupled problem of fluid flow, solid deformation, and fracture propagation. The XFEM model description of hydraulic fracture propagation is part of a joint project in which the developed numerical model will be verified against large-scale laboratory experiments. XFEM forms an important basis towards future combination with heat and mass transport simulators and extension to more complex fracture systems. The crack is described implicitly using three level-sets to evaluate enrichment functions. Additionally, an explicit crack representation is used to update the crack during propagation. The level-set functions are computed exactly from the explicit representation. This explicit/implicit representation is applied to a fluid-filled crack in an impermeable, elastic solid and compared to the early-time solution of a plane-strain hydraulic fracture problem with a fluid lag.

1. Introduction

The large scale conversion of geothermal energy into electrical energy using natural formations as heat exchangers depends on the coincidental occurrence of heat, fluid and permeability. This is valid for only a few locations on earth. Enhanced Geothermal System (EGS) propose to engineer the controlled creation of a heat exchanger between two wells in deep hot rocks, increasing the number of possible locations on earth. Water can be let circulate between the two wells, heat up while passing through the hot rock and be cooled down on the surface for

power generation. Yet this engineering of the heat exchanger has to be improved such that the outcome can be predicted within specified uncertainties.

The extension to more complex fracture scenarios as well as the integration with other software for risk assessment simulations requires a computer resource moderate modeling of fracture propagation. The extended finite element method (XFEM) forms a good basis for this. It has been applied to various problems within the area of fracture mechanics. The XFEM allows for the consideration of a priori knowledge about the solution of a hydraulic fracture problem into the approximation space through the addition of enrichment functions [10]. It enables, thereby, the accurate approximation of fields that involve jumps, kinks, singularities, and other non-smooth features within elements [2, 6, 11]. The developed numeric model will be verified against large-scale laboratory experiments. However, the focus of the present paper will lie on the progress in using XFEM for hydraulic fracture modeling. An XFEM approach in combination with an explicit and implicit crack description is applied to a plane-strain hydraulic fracture problem. The implicit description is given by three level-set functions defined in [5] and enables a simple evaluation of the enrichments. In contrast, the explicit crack description is used to perform the crack update. Given the explicit interface, the level-set functions for each propagation step can be calculated straightforward.

The paper is organized as follows: After a short description of the laboratory part of the joint project in Section 2, the governing equations for a hydraulic fracture problem in its basic form are presented in Section 3. Models are discussed for the solid deformation, fluid flow, and fracture propagation. In Section 4, an XFEM formulation with an explicit-implicit interface description is introduced and the discretization of these governing equations is carried out. Numerical results are presented in Section 5. Finally, Section 6 concludes this paper.

2. Laboratory experiments for model verification and optimization

Laboratory experiments for model verification and optimization will be performed on large rock specimen. The large-scale testing facility is currently under construction. Meanwhile preliminary experiments on smaller specimens have been conducted. In our project we focus on fracture creation in basement rock. Therefore mainly rocks like basalt, granite and gneiss are going to be tested for model verification and optimization.

2.1. Large-scale

Blocks of size 30 x 30 x 45 cm^3 will be pre-stressed in a massive steel frame to set up realistic primary stress states before hydraulic stimulation (see Figure 1). Stresses in all three directions can be adjusted independently and will be held constant during injection time. After setting up the primary principal stress state with flat-jacks, the injection interval of the borehole will be pressurized by a syringe pump. Injection pressures up to 65 MPa are possible. In order to allow for the verification of the developed numerical model with the experiments, we are going to monitor the borehole-pressure, the deformation of the rock sample and localize acoustic

http://dx.doi.org/10.5772/56383

events occurring during crack formation and propagation by means of ultrasonic transducers. Material parameters will be derived from standard rock mechanical tests.

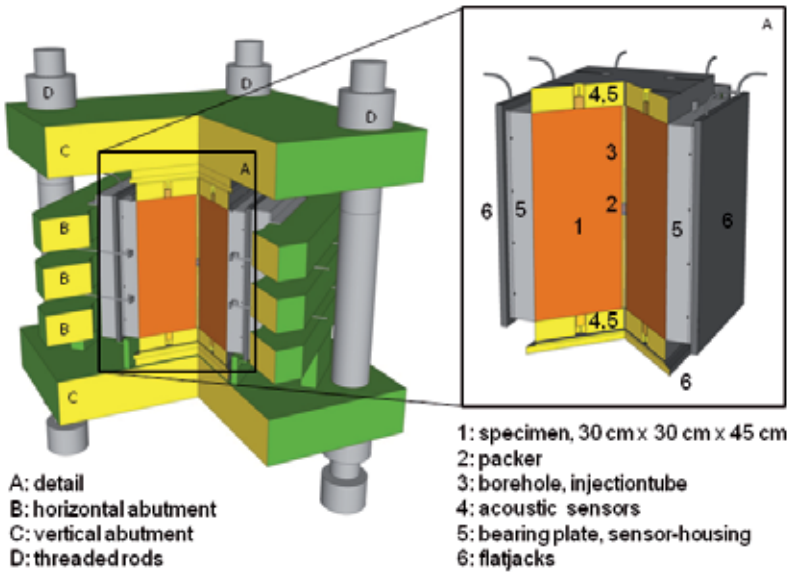

Figure 1. Large- scale tri-axial testing facility under construction, able to apply up to 30 MPa vertically and 15 MPa horizontally

2.2. Small-scale

Preliminary tests were performed on concrete samples of smaller size (15 x 15 x 15 cm^3) and recently been extended to granite and basalt. Acoustic events were recorded during fracture creation and propagation. The experiments indicated the need to lower the compressive energy induced before breakdown. Further, instead of water and light oil, fluids of higher viscosity will be used from now on to enlarge the regime of fracture propagation (see Figure 2c) and to consider the lag of scaling. Optimization of acoustic emission monitoring is continuously ongoing.

3. Governing equations

Hydraulic fracture propagation is based at least on three physical processes. A fluid flow within the fracture imposes a pressure load on the fracture surfaces. As a result, the rock undergoes a (mechanical) deformation and the fracture starts to propagate when a critical condition is reached [1]. Depending on the different modeling assumptions, this critical condition can be defined by the fracture toughness or another stress-based criterion. The following assumptions are usually made for the hydraulic fracture model [1]: I) the fluid flow is governed by the lubrication theory, II) solid deformation is modeled using the theory of

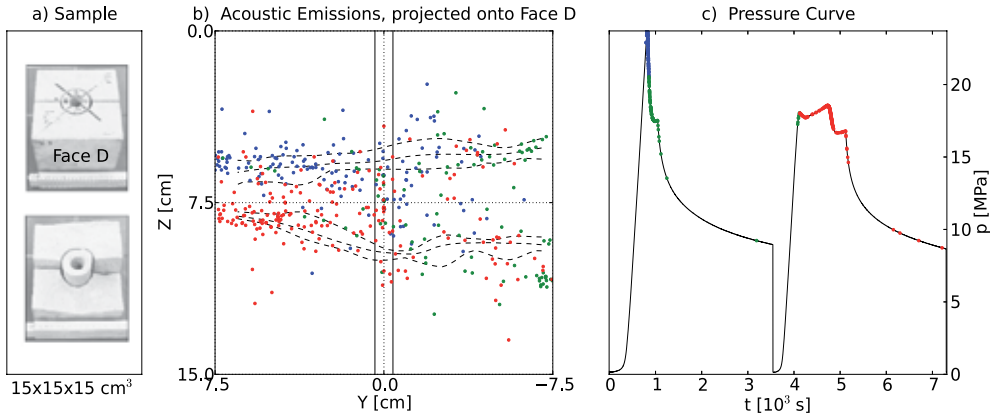

Figure 2. Preliminary small-scale fracturing experiments. a) Fractured concrete sample. b) Located acoustic events, projected onto face D of the sample. Different colors correspond to different time of occurrence. Dashed lines correspond to minimum, mean and maximum (along the direction of projection) height of the two main fracture surfaces, visible on the photo to the left. c) Fluid pressure (black) and flow rate (blue) curve used to fracture the specimen. Colored regions show the time and pressure regimes during which the same-colored acoustic events to the left occurred.

linear elasticity, and III) the propagation criterion is given by the conventional energy- release-rate approach of linear elastic fracture mechanics (LEFM) theory. The crack propagates when the mode I stress intensity factor reaches the fracture toughness. Each physical process is modeled separately and coupled iteratively. The governing equations are given as follows:

3.1. Deformation

A homogenous, isotropic and linear elastic solid is modeled with the concept of equilibrium of forces. Far field stresses and the pressure on the interface are imposed as Neumann boundary conditions, body forces are neglected.

$$\begin{aligned} \nabla \cdot \sigma + f &= 0 && \text{in } \Omega \\ \mathbf{u} &= \mathbf{u}_0 && \text{in } \Gamma_d \\ \sigma \cdot \mathbf{n} &= \hat{t} && \text{in } \Gamma_n \end{aligned} \tag{1}$$

f denotes the body force vector and u the displacement defined on the region Ω. The traction $\hat{t}$ is applied at the outer boundary Γ_n and Dirichlet boundary conditions are defined on Γ_d. Hooke's law of elasticity gives the relation between the stress σ and the strain ε

$$\sigma_{ij} = C_{ijkl}\varepsilon_{kl} \tag{2}$$

where C is the fourth-order stiffness (elasticity) tensor. Since the fracture aperture w is not given directly in this formulation, it has to be determined from the displacement field.

http://dx.doi.org/10.5772/56383

3.2. Fluid flow

The fracturing fluid with the dynamic viscosity μ is modeled as laminar flow between two parallel plates with a constant injection rate Q_0. The fluid flux q then reads

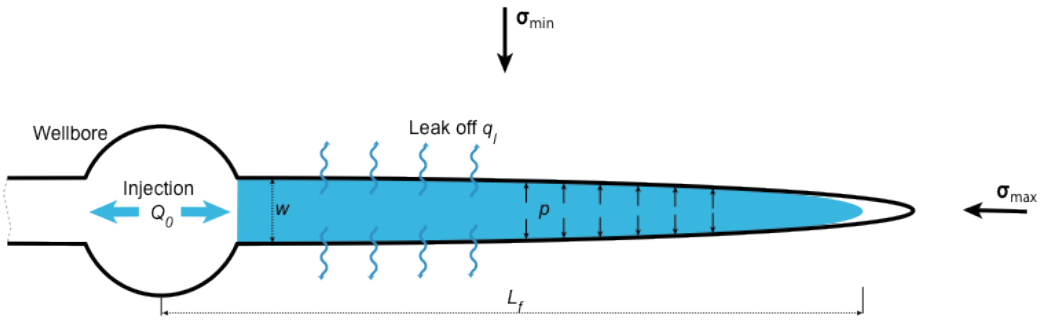

Figure 3. Sketch of a plane-strain hydraulic fracture with varying aperture w and fluid front position L_f. A fluid lag is shown at the fracture tip. The fluid is injected at the wellbore and flows into the fracture at a constant rate Q_0. It can leak off into the matrix through the fracture surfaces at a rate q_l. Fluid pressure field is denoted by p.

$$\mathbf{q} = -\frac{w^3}{12\mu}\nabla\mathbf{p}. \tag{3}$$

The Reynolds (lubrication) equation is given by

$$\frac{\partial w}{\partial t} - \frac{1}{12\mu}\nabla\cdot\left(w^3\nabla\mathbf{p}\right) + q_l = Q_0\delta(x,y) \tag{4}$$

and describes the conservation of the fluid mass for a Newtonian fluid. The fluid is injected into the fracture at a constant rate Q_0. For a fracture propagating in an impermeable solid, the leak-off q_l is negligible and, therefore, set to zero. It is assumed that a fluid lag develops between the fluid front L_f and the crack tip. However, for reasons of simplicity the lag size is not part of the solution. Taking into account the symmetry of the problem, the boundary conditions for the fluid flow problem read as follows:

$$\boldsymbol{q} = \frac{Q_0}{2} \text{ at the fracture inlet} \tag{5}$$

$$\boldsymbol{q} = q_f \text{ at the fluid front} \tag{6}$$

$$\mathbf{p} = p_0 \text{ in the fluid lag} \tag{7}$$

The flow condition at the fluid front q_f is determined from the pressure gradient and thus, is part of the solution. The pressure in the lag region is set to a constant value p_0, that is usually chosen to be zero. Finally, the global volume balance condition

$$Q_0 t = \int_{\Gamma_f} w \, \mathrm{d}\Gamma + \int_0^t \int_{\Gamma_f} q_l \, \mathrm{d}\Gamma \, \mathrm{d}\tau = V \tag{8}$$

equates the fracture volume V to the volume of injected fluid and the amount lost to the surrounding rock-mass. The integration is performed over the fluid filled part of the crack Γ_f.

3.3. Propagation condition

Due to the symmetry in loading and geometry, the hydraulic fracture propagates in pure opening mode, i.e. the tensile stress is acting normal to the plane of the crack. The propagation criterion is formulated in the framework of linear elastic fracture mechanics (LEFM) and accounts for the energy required to break the rock. It is characterized by the stress singularity at the tip and a propagation in mobile equilibrium. The LEFM assumption requires the stress intensity factor K_I to be equal to the fracture toughness K_{IC} of the material [12]

$$K_I = K_{IC}. \tag{9}$$

3.4. Asymptotic behavior

The hydraulic fracture problem characterized by a strong fluid-solid coupling that is mainly confined to a small region near the crack tip where rapid variation in the fluid pressure occurs. Analyzing the physical process at the tip by comparing the work done by the fluid in extending a fracture with the energy required to create new crack surfaces leads to understanding of the propagation regime of a fluid-driven fracture. Two limiting regimes can be detected, a toughness- and a viscosity-dominated regime [3]. In the toughness-dominated regime the inverse square root singularity of LEFM captures the effect of the crack tip process on the total fracture. In contrast, the viscosity-dominated regime is characterized by a singularity that is weaker than the singularity predicted by LEFM. Fracture toughness K_{IC} may become irrelevant [9].

4. XFEM approximation

The extended finite element method (XFEM) allows for the consideration of a priori knowledge about the solution of a hydraulic fracture problem into the approximation space through the addition of enrichment functions [10]. It enables, thereby, the accurate approximation of fields that involve jumps, kinks, singularities, and other non-smooth features within elements [2, 6, 11].

http://dx.doi.org/10.5772/56383

The enrichments, that are realized through the partition of unity (PU) concept, are chosen in such a way that they are able to reproduce the asymptotic behavior near the crack tip. In this work only the toughness-dominated solution is considered. Thus, enrichment functions compatible with the classical square root singularity of LEFM are used to enrich the region near the crack tip.

4.1. Standard formulation

The XFEM formulation with an explicit-implicit crack description used in this work is based on the work done by [5]. The basic idea is recalled in this paper, for further details see the original work. The enriched approximation of the displacements is stated as follows:

$$\mathbf{u}^h(\mathbf{x}) = \underbrace{\sum_{i\in I} \mathbf{N}_i(\mathbf{x})\mathbf{u}_i}_{\text{continuous}} + \underbrace{\sum_{j\in I^{step}} \mathbf{N}_j^*(\mathbf{x})\cdot\Psi_{step}(\mathbf{x})\mathbf{a}_j + \sum_{k\in I^{tip}} \mathbf{N}_k^*(\mathbf{x})\cdot\Big(\sum_{m=1}^{4}\Psi_{tip}^m(r,\theta)\mathbf{b}_k^m\Big)}_{\text{discontinuous}} \tag{10}$$

The first term on the right hand side describes the classical FEM-approximation with continuous shape functions $N_i(x)$ and nodal unknowns u_i. The second term accounts for the discontinuity in the displacement field across the crack path by incorporating step-functions Ψ_{step} with additional nodal unknowns a_i into the enrichment space. The tip region is enriched with a set of enrichment functions $\Psi_{tip}^m(r, \theta)$that consider the singularity according to the dominating regime. They can be defined as [10]

$$\left\{\Psi_{tip}^m(r,\theta)\right\}_{m=1}^4 = \left\{r^\lambda\, cos(\lambda\theta),\, r^\lambda\, sin(\lambda\theta),\, r^\lambda\, sin(\theta)sin(\lambda\theta),\, r^\lambda\, sin(\theta)cos(\lambda\theta)\right\} \tag{11}$$

where r and θ denote local polar coordinates at the crack tip. When propagating in the toughness-dominated regime the assumption of a square root singularity in LEFM requires to choose $\lambda = 1/2$. In the viscosity-dominated regime the weaker singularity is taken into account by $\lambda = 2/3$. Additional degrees of freedom b_k^m are introduced into the approximation locally within the enriched region.

The crack opening is obtained through interpolation of the displacement field $u(x)$ at the interface nodes by means of (10). Since the interface represents a discontinuity the interpolation is performed by moving the nodes slightly away in normal direction. The opening is defined as the distance between the positive and negative displacement at the interface (see Figure 5).

$$w(x) = u^+(x) - u^-(x). \tag{12}$$

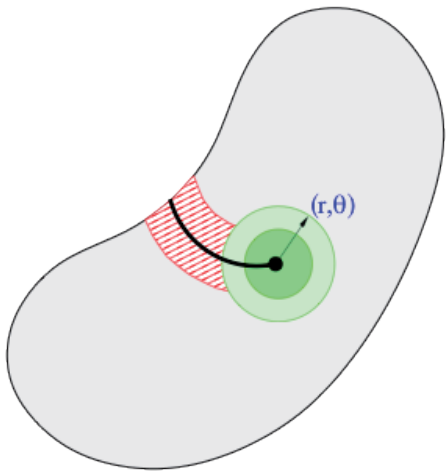

Figure 4. The enrichment is acting either along the crack path (dashed field) with the step-enrichment ψ_{step} or within a specified region near the crack tip by defining the enrichments $\psi_{tip}^{m}(r, \theta)$.

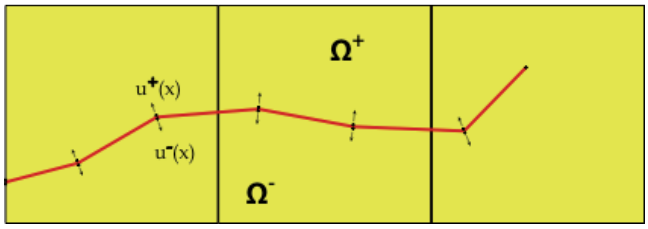

Figure 5. Interpolation of the crack opening along the interface.

4.2. Numerical integration

The standard approach in the XFEM for numerical integration is a decomposition of the elements into subelements that align with the discontinuity [6]. A Gauss quadrature is then applied on each of these subelements. For a detailed description of the decomposition method in 2D and 3D the reader is referred to [6].

4.3. Explicit-implicit interface description

The explicit crack description is given by a mesh that is aligned with the interface. For 2D problems the crack is a line and is represented by one dimensional elements in the 2D space. In three dimensions, the crack is a surface and, thus, described through a two dimensional mesh in the 3D space.

Normal and tangential vectors are computed easily on the interface and can be used to define a local coordinate system at the crack tip/front. On the basis of the explicit interface mesh the

http://dx.doi.org/10.5772/56383

crack update is applied by simply adding new elements to the crack front according to a given extension vector.

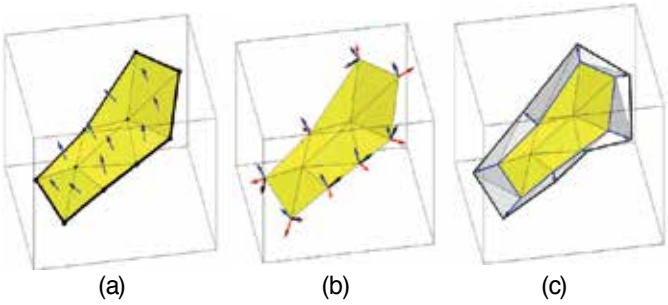

Figure 6. (a) Arbitrary crack surface with normal vectors on each element. (b) Local coordinate system at the crack front. (c) Crack update according to crack extension vectors at the front.

The implicit interface description is realized by means of the level-set concept. Three level-set functions are defined according to [5]. They are used to define the region to be enriched and to evaluate the enrichment functions.

- $\Phi_1(\boldsymbol{x})$ is the (un-signed) distance function to the crack path/surface. That is, the level-set value at position x is the shortest distance to the crack path/surface.
- $\Phi_2(\boldsymbol{x})$ is the (un-signed) distance function to the crack tip(s)/front. That is, the level-set value at position x is the shortest distance to the crack tip(s)/front.
- $\Phi_3(\boldsymbol{x})$ is a signed distance function to crack path/surface that is extended over the entire domain. The sign is based on the direction of the normal vector of the segment that contains the nearest point.

4.4. Discretization of governing equations

Since the solid deformation and the fluid flow are coupled iteratively, they are solved independently in each iteration step. Solid deformation is discretized with XFEM as follows:

$$\left[\int_{\Omega} \mathbf{B}^{\mathbf{T}}\mathbf{C}\mathbf{B}\, d\Omega\right] \cdot \mathbf{u} = \int_{\Gamma_b} \mathbf{N}^T \hat{t}\, d\Gamma + \int_{\Gamma_c} \mathbf{N}^T p\, d\Gamma \tag{13}$$

where the term on the left $\mathbf{B^TCB}$ denotes the stiffness matrix with the gradient operator $\mathbf{B}$ [4], $\boldsymbol{N}$ the shape and enrichment functions, $\hat{t}$ the traction on the outer boundary Γ_b and $\mathbf{p}$ the pressure on the interface Γ_c. A classical FEM approach is used to solve the fluid flow equation. The pressure is approximated by

$$\mathbf{p}^h(\mathbf{x}) = \sum_{i \in I} \mathbf{N}_i(\mathbf{x}) \mathbf{p}_i. \tag{14}$$

The discretized problem formulation reads

$$\frac{1}{12\mu} \int_{\Gamma_f} w^3 \nabla \mathbf{N} \nabla \mathbf{N}^T \, d\Gamma = \left[\mathbf{N} \frac{w^3}{12\mu} \nabla \mathbf{p} \right]_{\Gamma_f} - \int_{\Gamma_f} \mathbf{N} q_l \, d\Gamma - \int_{\Gamma_f} \mathbf{N} \frac{\Delta w}{\Delta t} d\Gamma \tag{15}$$

This formulation is valid for one half of a symmetric crack where Γ_f denotes the fluid filled region. The flow boundary conditions at the fluid front and the fracture inlet correspond to the first term on the right-hand side. Fluid leak-off and the change of volume over time are taken into account by the second and third term on the right-hand side.

5. Hydraulic fracture propagation

The problem of a fluid driven fracture in an impermeable elastic solid with a fluid lag is considered here. Simulation results are compared with the asymptotic solutions for zero underpressure/time given in [8]. This solution corresponds to the "beginning" of the fluid-driven fracture evolution and provides initial condition for plane-strain fracture propagations. The propagation regime of a fluid driven fracture is controlled by a parameter representing a dimensionless viscosity M (dimensionless toughness K) defined as

$$M = \frac{\mu' Q_0}{E'} \left(\frac{E'}{K'} \right)^4, \qquad K = M^{-1/4}. \tag{16}$$

This formulation uses effective parameters [6]

$$E' = \frac{E}{1-\nu^2}, \qquad \mu' = 12\mu, \qquad K' = 4 \left(\frac{2}{pi} \right)^{1/2} K_{IC}, \tag{17}$$

where μ' denotes the fluid viscosity, Q_0 the constant injection rate, E' the plane-strain elastic modulus with Poisson's ratio ν and K' the toughness, respectively. The procedure solving the coupled equations follows that described in [8]. Given a fluid front position L_f, a solution is sought for the pressure distribution and crack opening.

5.1. Numerical algorithm

The simulation process is realized through an iterative coupling of the fluid flow and solid deformation. Starting with an initial solution and a guess for the fluid fraction, the pressure

http://dx.doi.org/10.5772/56383

distribution and the crack opening are calculated until convergence is reached. When the propagation condition is met, the crack is updated for the next time step. Otherwise, the fluid front is moved towards the crack tip with a velocity v determined from the fluid flow rate q.

5.2. Numerical results

The numerical results for the crack opening and pressure distribution at the wellbore of a plane-strain hydraulic fracture problem are compared to the similarity solution of a small enough toughness parameter in order to allow a significant fluid lag. The boundary condition of zero displacement at infinity is approximated by a finite body and standard finite elements and a local mesh refinement in the area close to the crack interface. Computational evidence of the validity of approximating the infinite medium with a finite block is provided in [13].

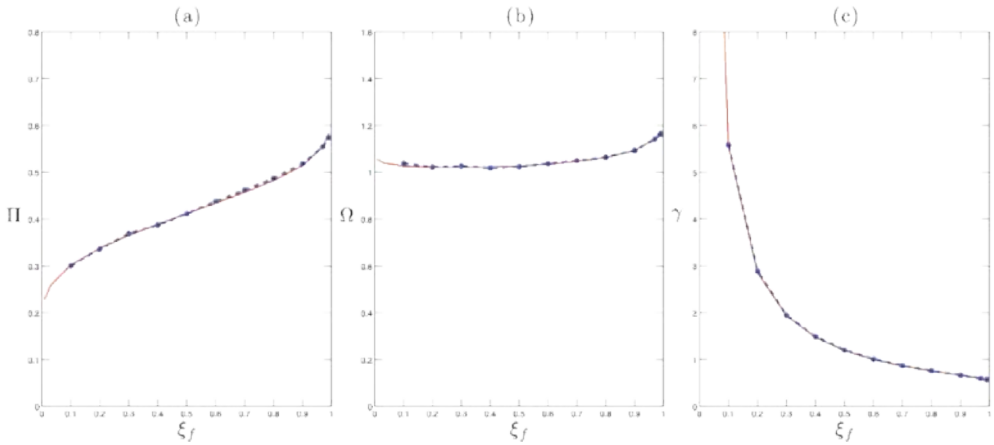

Figure 7. The numerical results (blue circles) of dimensionless pressure Π (a) and the crack opening Ω (b) at the wellbore as well as the dimensionless crack length γ (c) are compared to the analytical solution (red solid line) for various values of the fluid front position.

The results are scaled to dimensionless quantities in the viscosity scaling. For a detailed description of the scaling for the pressure Π, the opening Ω and the crack length γ see the original publication [13]. The domain and the explicit interface are meshed independently with 5000 and 3000 elements, respectively.

Figures 7(a)-(c) show a good agreement of the similarity solution for various values of the fluid fraction $\xi_f = L_f / L$. However, especially for high fluid fraction values where the fluid front is close to the fracture front the results reveal inaccuracies. Special attention has to be paid to the crack tip behavior in the case for a vanishing fluid lag when the pressure becomes singular. Depending on the propagation regime crack propagation is governed either by the classical singularity of linear elastic fracture mechanics or by viscous fluid effects which would lead to a weaker singularity than given by LEFM.

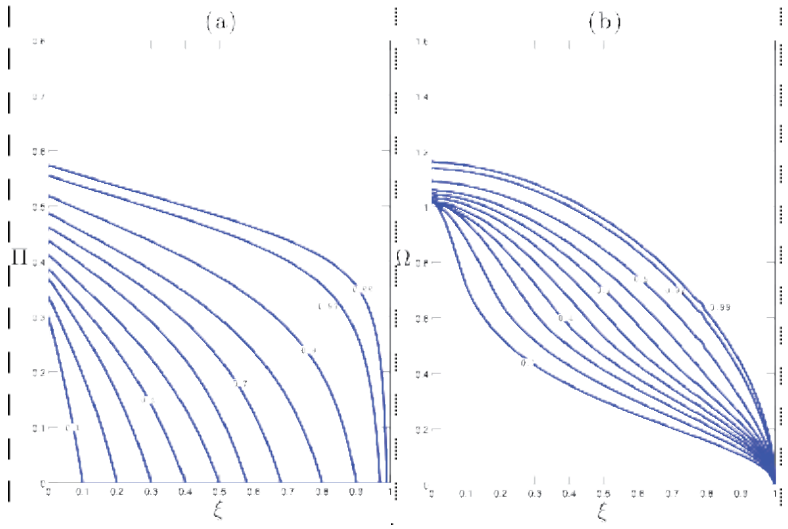

Figure 8. The pressure distribution Π(ξ) (a) and the crack opening profile Ω(ξ) (b) for various values of the fluid fraction ξ_f.

The pressure distribution and the crack opening profile along the dimensionless coordinate $\xi = x / L$ are shown in Figures 8(a) and (b) in the viscosity scaling for fluid fraction values ξ_f = {0.1, 0.2, 0.3, 0.4, 0.5, 0.6, 0.7, 0.8, 0.9, 0.97, 0.99}.

6. Conclusions

The XFEM with an explicit-implicit crack description has been applied to a plane-strain hydraulic fracture problem. The crack is described explicitly by a line (2D)/triangular (3D) mesh that is aligned with the interface and implicitly by three level-set functions. The enrichment functions at the tip can be chosen according to the asymptotic behavior of the hydraulic fracture problem. Depending on the propagation regime the stress singularity can be described either by LEFM or by a singularity, which is weaker than predicted by LEFM. However, in this work a partially filled crack with a significant lag is examined and, therefore, crack propagation is governed by LEFM. The results show a good agreement with the known similarity solutions and can be interpreted as an early-time solution that can be used as a starting point in hydraulic fracture simulations.

Acknowledgements

We acknowledge support for this work from the Federal Ministry for the Environment, Nature Conservation and Nuclear Safety, Germany (FKZ 0325167).

http://dx.doi.org/10.5772/56383

Author details

N. Weber[1], P. Siebert[2], K. Willbrand[3], M. Feinendegen[2], C. Clauser[3] and T. P. Fries[1]

1 Chair for Computational Analysis of Technical System, RWTH Aachen University, Aachen, Germany

2 Institute of Geotechnical Engineering, RWTH Aachen University, Aachen, Germany

3 Institute for Applied Geophysics and Geothermal Energy, E.ON ERC, RWTH Aachen University, Aachen, Germany

References

[1] Adachi, J, Siebrits, E, Peirce, A, & Desroches, J. Computer simulation of hydraulic fractures. International Journal of Rock Mechanics and Mining Sciences, (2007). , 44(5), 739-757.

[2] Belytschko, T, & Black, T. Elastic crack growth in finite elements with minimal remeshing. International Journal for Numerical Methods in Engineering, (1999). , 45, 601-620.

[3] Desroches, J, Lenoach, B, Papanastasiou, P, & Thiercelin, M. On the modelling of near tip processes in hydraulic fractures. International Journal of Rock Mechanics and Mining Sciences & Geomechanics Abstracts, (1993). , 30(7), 1127-1134.

[4] Fish, J, & Belytschko, T. A First Course in Finite Elements, chapter 9, John Wiley & Sons, Ltd, (2007). , 215-247.

[5] Fries, T. P, & Baydoun, M. Crack propagation with the extended finite element method and a hybrid explicit-implicit crack description. International Journal for Numerical Methods in Engineering, (2012). , 89(12), 1527-1558.

[6] Fries, T. P, & Belytschko, T. The extended/generalized finite element method: An overview of the method and its applications. International Journal for Numerical Methods in Engineering, (2010). , 84(3), 253-304.

[7] Garagash, D. Plane-strain propagation of a fluid-driven fracture during injection and shut-in: Asymptotics of large toughness. Engineering Fracture Mechanics, (2006). , 73(4), 456-481.

[8] Garagash, D. Propagation of a plane-strain hydraulic fracture with a fluid lag: Early-time solution. International Journal of Solids and Structures, 43(18-19): 5811-5835, (2006).

[9] Garagash, D, & Detournay, E. The tip region of a fluid-driven fracture in an elastic medium. Journal of Applied Mechanics, (2000). , 67(1), 183-192.

[10] Lecampion, B. An extended finite element method for hydraulic fracture problems. Communications in Numerical Methods in Engineering, (2009). , 25(2), 121-133.

[11] Moës, N, Dolbow, J, & Belytschko, T. A finite element method for crack growth without remeshing. International Journal for Numerical Methods in Engineering, (1999). , 46, 131-150.

[12] Rice, J. R. Mathematical analysis in the mechanics of fracture. In H. Liebowitz, editor, Fracture: An Advanced Treatise, of Mathematical Fundamentals, chapter 3, Academic Press, New York, (1968). , 2, 191-311.

[13] Hunsweck, M. J, Shen, Y, & Lew, A. J. A finite element approach to the simulation of hydraulic fractures with lag. International Journal for Numerical and Analytical Methods in Geomechanics, pages n/a, (2012).

Chapter 36

An ABAQUS Implementation of the XFEM for Hydraulic Fracture Problems

Zuorong Chen

Additional information is available at the end of the chapter

http://dx.doi.org/10.5772/56287

Abstract

A new finite element has been implemented in ABAQUS to incorporate the extended finite element method (XFEM) for the solution of hydraulic fracture problems. The proposed element includes the desired aspects of the XFEM so as to model crack propagation without explicit remeshing. In addition, the fluid pressure degrees of freedom have been defined on the element to describe the fluid flow within the crack and its contribution to the crack deformation. Thus the fluid flow and resulting crack propagation are fully coupled in a natural way and are solved simultaneously. Verification of the element has been made by comparing the finite element results with the analytical solutions available in the literature.

Keywords Hydraulic fracture, extended finite element method, internal pressure

1. Introduction

Hydraulic fracturing is a powerful technology for enhancing conventional petroleum production. It is playing a central role in fast growing development of unconventional gas and geothermal energy. The fully 3-D numerical simulation of the hydraulic fracturing process is of great importance to understand the complex, multiscale mechanics of hydraulic fracturing, to the efficient application of this technology, and to develop innovative, advanced hydraulic fracture technologies for unconventional gas production. The accurate numerical simulation of hydraulic fracture growth remains a significant challenge because of the strong nonlinear coupling between the viscous flow of fluid inside the fracture and fracture propagation (a moving boundary), complicated by the need to consider interactions with existing natural fractures and with rock layers with different properties.

Great effort has been devoted to the numerical simulation of hydraulic fractures with the first 3D modelling efforts starting in the late 1970s [1-2]. Significant progress has been made in developing 2-D and 3-D numerical hydraulic fracture models [3-15]. Boundary integral equation methods or displacement discontinuity techniques have generally been employed to investigate the propagation of simple hydraulic fractures such as radial or plane-strain fractures in a homogeneous, infinite or semi-infinite elastic medium where the appropriate fundamental solutions are available. The finite element method has been used and is particularly useful in modelling the hydraulic fracture propagation in inhomogeneous rocks which may include nonlinear mechanical properties and may be subjected to complex boundary conditions. However, the standard finite element model requires remeshing after every crack propagation step and the mesh has to conform exactly to the fracture geometry as the fracture propagates, and thus is computationally expensive.

By adding special enriched shape functions in conjunction with additional degrees of freedom to the standard finite element approximation within the framework of partition of unity, the extended finite element method [16-17] (XFEM) overcomes the inherent drawbacks associated with use of the conventional finite element methods and enables the crack to be represented without explicitly meshing crack surfaces, and so the crack geometry is completely independent of the mesh and remeshing is not required, allowing for the convenient simulation of the fracture propagation. The XFEM has been employed to investigate the hydraulic fracture problems [18-19].

In this paper, we explore the application of the extended finite element method to hydraulic fracture problems. By taking good advantage of the XFEM and the flexible functionality of user subroutines provided in ABAQUS [20], a user-defined 2-D quadrilateral plane strain element has been coded in Fortran to incorporate the extended finite element capabilities in 2-D hydraulic fracture problems. The user-defined element includes the desired aspects of the XFEM so as to model crack propagation without explicit remeshing. In addition, the extended fluid pressure degrees of freedom are assigned to the appropriate nodes of the proposed elements in order to describe the viscous flow of fluid inside the crack and its contribution to the coupled crack deformation.

2. Problem formulation

2.1. Problem definition

Consider a two-dimensional hydraulically driven fracture Γ_c propagating in a homogeneous, isotropic, linear elastic, impermeable medium Ω under plane strain conditions, see Figure 1. The boundary of the domain consists of Γ_F on which prescribed tractions **F**, are imposed, Γ_u on which prescribed displacements (assumed to be zero for simplicity) are imposed, and crack faces Γ_c subject to fluid pressure. The fracture propagation is driven by injection of an incompressible Newtonian fluid at constant volumetric rate Q_0 at a fixed injection point. It is assumed that the fracture propagation is quasi-static, and that the fracture is completely filled with the

http://dx.doi.org/10.5772/56287

injected fluid, i.e., there is no lag between the fluid front and the fracture tip. The solution of the problem consists of determining the evolution of the fracture length, as well as the fracture opening, the fluid pressure, and the deformations and stresses inside the domain as functions of both position and time.

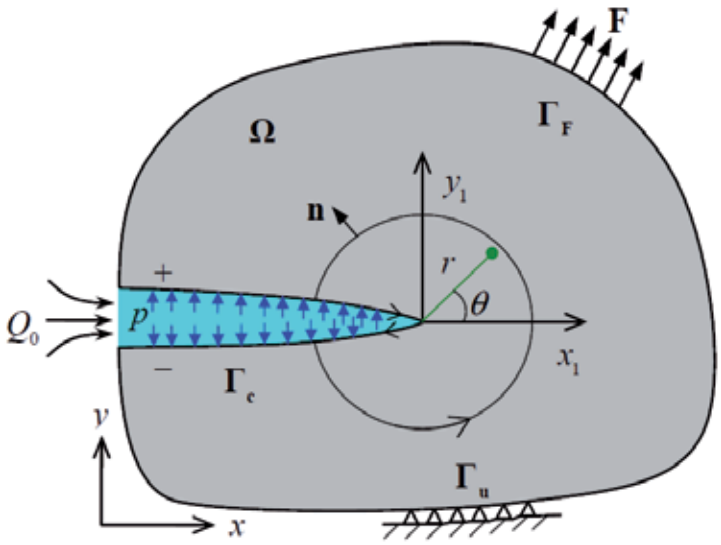

Figure 1. A two-dimensional domain containing a hydraulic fracture

2.2. Governing equations

The stress inside the domain, **σ**, is related to the external loading **F** and the fluid pressure p through the equilibrium equations:

$$\begin{aligned} \nabla \cdot \boldsymbol{\sigma} &= 0, \quad \text{on } \Omega \\ \boldsymbol{\sigma} \cdot \mathbf{n} &= \mathbf{F}, \quad \text{on } \Gamma_F \\ \boldsymbol{\sigma} \cdot n^- = -\boldsymbol{\sigma} \cdot n^+ &= -pn^+ = pn^-, \quad \text{on } \Gamma_c \end{aligned} \tag{1}$$

where **n** is the unit normal vector.

Under the assumptions of small strains and displacements, the kinematic equations, which include the strain-displacement relationship, the prescribed displacement boundary conditions and the crack surfaces separation, read

$$\begin{aligned} \boldsymbol{\varepsilon} &= \left(\nabla \mathbf{u} + (\nabla \mathbf{u})^{\mathrm{T}}\right)/2 \; on \; \Omega \\ \mathbf{u} &= 0 \text{ on } \Gamma_u \\ \mathbf{w} &= u^+ - u^- \text{ on } \Gamma_c \end{aligned} \tag{2}$$

where **u** is the displacement, **w** is the separation between the two faces of the crack, and **ε** is the strain.

The isotropic, linear elastic constitutive law is

$$\boldsymbol{\sigma} = \mathbf{D} : \boldsymbol{\varepsilon} \tag{3}$$

where **D** is Hooke's tensor.

The fluid flow in the crack is modelled using lubrication theory, given by Poiseuille's law

$$q = -\frac{w^3}{12\mu}\frac{\partial p}{\partial x} \tag{4}$$

where μ is the dynamic viscosity of the fracturing fluid, q, the flow rate inside the crack per unit extend of the crack in the direction of x, is equal to the average velocity $\bar{v}$ times the crack opening w (see Figure 2), i.e.,

$$q(x) = \bar{v}(x)w(x) \tag{5}$$

The fracturing fluid is considered to be incompressible, so the mass conservation equation for the fluid may be expressed as

$$\frac{\partial w}{\partial t} + \frac{\partial q}{\partial x} + g = 0 \tag{6}$$

where the leak-off rate $g(x)$ accounts for fluid exchange between the fracture and the surrounding medium (e.g. porous rock).

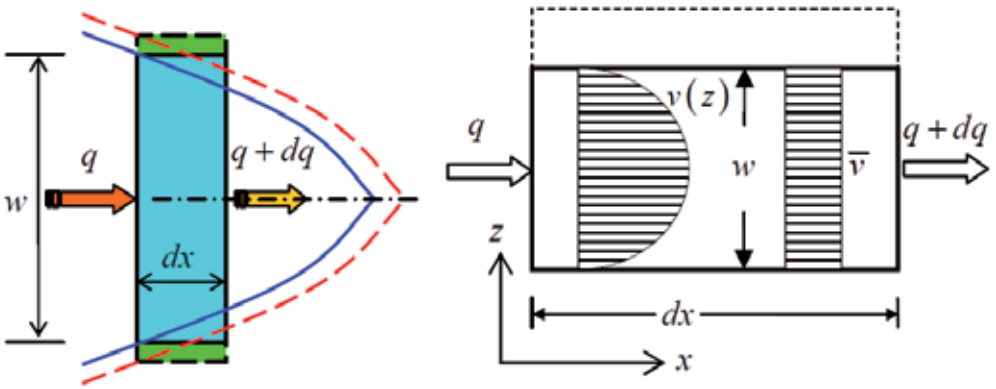

Figure 2. Fluid flow within fracture

http://dx.doi.org/10.5772/56287

Substituting of Eq. (4) into Eq. (6) leads to the governing equation for the fluid flow within the fracture

$$\frac{\partial w}{\partial t} - \frac{\partial}{\partial x}\left(k\frac{\partial p}{\partial x}\right) + g = 0 \tag{7}$$

where $k = \frac{w^3}{12\mu}$ is the conductivity. The general form of Eq. (7) reads

$$\dot{w} - \nabla^{\mathrm{T}}(\mathbf{k}\nabla p) + g = 0 \tag{8}$$

where $\mathbf{k}$ is the conductivity tensor.

According to linear elastic fracture mechanics, the criterion that the fracture propagates continuously in mobile equilibrium (quasi-static) takes the form

$$K_{\mathrm{I}} = K_{\mathrm{Ic}} \tag{9}$$

where K_{I} is the mode I stress intensity factor and K_{Ic} the material fracture toughness.

At the inlet, the fluid flux is equal to the injection rate, i.e.,

$$q\,|_{\mathrm{inlet}} = Q_0 \tag{10}$$

At the crack tip, the boundary conditions are given by the zero fracture opening and zero flow conditions, i.e.,

$$w\,|_{\mathrm{tip}} = q\,|_{\mathrm{tip}} = 0 \tag{11}$$

The above equations constitute the complete formulation that can be used to predict the evolution of the hydraulic fracture.

3. Weak form and FEM discretization

The weak form of the equilibrium equation is given by

$$\int_{\Omega}\delta\varepsilon^{\mathrm{T}}\boldsymbol{\sigma}\mathrm{d}\Omega - \int_{\Omega}\delta u^{\mathrm{T}}\mathbf{b}\mathrm{d}\Omega - \int_{\Gamma_{\mathrm{t}}}\delta u^{\mathrm{T}}\mathbf{t}\mathrm{d}\Gamma - \left(\int_{\Gamma_c^+}\delta\mathbf{u}_c^{+\mathrm{T}}\mathbf{p}_c^{+}\mathrm{d}\Gamma + \int_{\Gamma_c^-}\delta\mathbf{u}_c^{-\mathrm{T}}\mathbf{p}_c^{-}\mathrm{d}\Gamma\right) = 0 \tag{12}$$

where $\mathbf{b}$ is the body force, t is the applied traction on the boundary Γ_{t}, $\delta\mathbf{u}$ is an arbitrary virtual displacement and $\delta\boldsymbol{\varepsilon}$ is the corresponding virtual strain, which is related to $\delta\mathbf{u}$ through the strain operator $\mathbf{S}$ as $\delta\boldsymbol{\varepsilon} = \mathbf{S}\delta\mathbf{u}$.

For the fluid pressure on the crack surfaces, we define

$$\mathbf{p} = \mathbf{p}_c^+ = -\mathbf{p}_c^- = p\mathbf{n}_c = p\mathbf{n}_c^- = -p\mathbf{n}_c^+ \tag{13}$$

The crack opening displacement **w** is given by

$$w = \mathbf{n}_c^{\mathrm{T}} \cdot \left(\mathbf{u}_c^+ - \mathbf{u}_c^-\right), \text{ or } \mathbf{w} = \mathbf{n}_c \cdot \left(\mathbf{u}_c^+ - \mathbf{u}_c^-\right) \cdot \mathbf{n}_c \tag{14}$$

Then the weak form of the equilibrium equation can be expressed in a more compact form as

$$\int_\Omega \delta\varepsilon^{\mathrm{T}} \boldsymbol{\sigma} \mathrm{d}\Omega - \int_\Omega \delta u^{\mathrm{T}} \mathbf{b} \mathrm{d}\Omega - \int_{\Gamma_t} \delta u^{\mathrm{T}} \mathbf{t} \mathrm{d}\Gamma - \int_{\Gamma_c} \delta w^{\mathrm{T}} \mathbf{p} \mathrm{d}\Gamma = 0 \tag{15}$$

The weak form of the governing equation for the fluid flow within the fracture can be written as

$$\int_{\Gamma_c} \delta p^{\mathrm{T}} \left(\dot{w} - \nabla^{\mathrm{T}} (\mathbf{k} \nabla p) + g\right) \mathrm{d}\Gamma = 0 \tag{16}$$

which, after integration by parts and substitution of the boundary conditions described above, yields

$$\int_{\Gamma_c} \delta p^{\mathrm{T}} \dot{w} \mathrm{d}\Gamma + \int_{\Gamma_c} \nabla^{\mathrm{T}} (\delta p) \mathbf{k} \nabla p \mathrm{d}\Gamma + \int_{\Gamma_c} \delta p^{\mathrm{T}} g \mathrm{d}\Gamma = 0 \tag{17}$$

Consider the coupled problem discretized in the standard (displacement) manner with the displacement vector **u** approximated as

$$\mathbf{u} \approx \hat{\mathbf{u}} = \sum_{i=1}^{n} \mathbf{N}_i^u \mathbf{u}_i = N^{\mathbf{u}} \tilde{\mathbf{u}}, \quad \delta\mathbf{u} \approx N^{\mathbf{u}} \delta\tilde{\mathbf{u}} \tag{18}$$

and the fluid pressure p similarly approximated by

$$p \approx \hat{p} = \sum_{i=1}^{n} N_i^p p_i = N^{\mathrm{p}} \tilde{\mathbf{p}}, \quad \delta p \approx N^{\mathrm{p}} \delta\tilde{\mathbf{p}} \tag{19}$$

where $\mathbf{u}_i$ and p_i are the nodal displacement and pressure, $\mathbf{N}_i^u$ and N_i^p are corresponding nodal displacement and fluid pressure shape functions.

The crack opening displacement **w** (or more generally displacement discontinuity) is approximated by

$$\mathbf{w} \approx \hat{\mathbf{w}} = \sum_{i=1}^{n} \mathbf{N}_i^w \mathbf{u}_i = N^w \tilde{\mathbf{u}}, \quad \delta\mathbf{w} \approx N^w \delta\tilde{\mathbf{u}} \tag{20}$$

http://dx.doi.org/10.5772/56287

where $\mathbf{N}_i^w$ are the approximate crack opening displacement shape function. It will be shown later that the shaped function $\mathbf{N}_i^w$ can be expressed in terms of the displacement shape functions $\mathbf{N}_i^u$ according to the relationship Eq. (14).

Substitution of the displacement and pressure approximations (Eqs. (18)-(20)) and the constitutive equation (Eq. (3)) into Eq. (15) yields a system of algebraic equations for the discrete structural problem

$$\mathbf{K}\tilde{\mathbf{u}} - \mathbf{Q}\tilde{\mathbf{p}} - f^u = 0 \tag{21}$$

where the structural stiffness matrix

$$\mathbf{K} = \int_\Omega B^{\mathrm{T}}\mathbf{D}\mathbf{B}d\Omega \tag{22}$$

and the equivalent nodal force vector

$$f^u = \int_\Omega (N^u)^{\mathrm{T}}\mathbf{b}d\Omega + \int_{\Gamma_t}(N^u)^{\mathrm{T}}\mathbf{t}d\Gamma \tag{23}$$

and the coupling term arise due to the pressure (tractions) on the crack surface through the matrix

$$\mathbf{Q} = \int_{\Gamma_c}(N^w)^{\mathrm{T}}\mathbf{n}N^p d\Gamma \tag{24}$$

By substituting Eqs. (19) and (20) into Eq. (17), the standard discretization applied to the weak form of the fluid flow equation leads to a system of algebraic equations for the discrete fluid flow problem

$$\mathbf{C}\dot{\tilde{\mathbf{u}}} + \mathbf{H}\tilde{\mathbf{p}} - f^p = 0 \tag{25}$$

where

$$\mathbf{C} = Q^{\mathrm{T}} = \int_{\Gamma_c}(N^p)^{\mathrm{T}}n^{\mathrm{T}}N^{\mathrm{w}}d\Gamma,\ \ \mathbf{H} = \int_{\Gamma_c}(\nabla N^p)^{\mathrm{T}}\mathbf{k}\nabla N^p d\Gamma,\ f^p = -\int_{\Gamma_c}(N^p)^{\mathrm{T}}g d\Gamma \tag{26}$$

Then, the discrete governing equations for the coupled fluid-fracture problem can be expressed in matrix form as:

$$\begin{bmatrix}0 & 0\\ \mathbf{C} & 0\end{bmatrix}\begin{pmatrix}\dot{\tilde{\mathbf{u}}}\\ \dot{\tilde{\mathbf{p}}}\end{pmatrix} + \begin{bmatrix}\mathbf{K} & -\mathbf{Q}\\ 0 & \mathbf{H}\end{bmatrix}\begin{pmatrix}\tilde{\mathbf{u}}\\ \tilde{\mathbf{p}}\end{pmatrix} = \begin{pmatrix}f^u\\ f^p\end{pmatrix} \tag{27}$$

The above equations form the basis for the construction of a finite element which couples the fluid flow within the crack and crack propagation.

4. The extended finite elemet method and element implementation

4.1. Extended finite element approximation

The XFEM approximation of the displacement field for the crack problem can be expressed as [17]

$$\mathbf{u}(\mathbf{x})=\sum_{I\in N}\mathbf{N}_I(\mathbf{x})\mathbf{u}_I+\sum_{I\in N_{cr}}\widetilde{\mathbf{N}}_I(\mathbf{x})\left(H(\mathbf{x})-H(\mathbf{x}_I)\right)\mathbf{a}_I+\sum_{I\in N_{tip}}\widetilde{\mathbf{N}}_I(\mathbf{x})\sum_{l=1}^{4}\left(B^{(l)}(r,\theta)-B^{(l)}(r_I,\theta_I)\right)\mathbf{b}_I^{(l)} \tag{28}$$

where N is the set of all nodes in the mesh, N_{cr} the set of nodes whose support are bisected by the crack surface Γ_c, N_{tip} the set of nodes whose support are partially cut by the crack surface, $\mathbf{N}_I(\mathbf{x})$ and $\widetilde{\mathbf{N}}_I(\mathbf{x})$ are the standard finite element shape functions, $\mathbf{u}_I$ are the displacement nodal degrees of freedom, $\mathbf{a}_I$ and $\mathbf{b}_I^{(l)}$ are the additional degrees of freedom for the displacement, and $H(\mathbf{x})$ and $B^{(l)}(r,\theta)$ are the appropriate enrichment basis functions which are localized by $\widetilde{\mathbf{N}}_I(\mathbf{x})$. The shape function $\widetilde{\mathbf{N}}_I(\mathbf{x})$ can differ from $\mathbf{N}_I(\mathbf{x})$.

The displacement discontinuity given by a crack Γ_c can be represented by the generalized Heaviside step function

$$H(\mathbf{x})=H(d(\mathbf{x}))=sign(d(\mathbf{x}))=\begin{cases}1 & d(\mathbf{x})\geq 0\\ -1 & d(\mathbf{x})<0\end{cases} \tag{29}$$

where $d(\mathbf{x})$ is the signed distance of the point $\mathbf{x}$ to Γ_c.

The enrichment basis functions $B^{(l)}(r,\theta)$ are required to model the displacement around the crack tip, which are generally chosen as a basis that approximately spans the two-dimensional plane strain asymptotic crack tip fields in the linear elastic fracture mechanics:

$$\{B^{(l)}\}_{l=1}^{4}=\sqrt{r}\{\sin(\theta/2)\quad\cos(\theta/2)\quad\sin(\theta/2)\sin(\theta)\quad\cos(\theta/2)\sin(\theta)\} \tag{30}$$

where (r,θ) are the local polar coordinates at the crack tip.

According to Eq. (28), the displacement discontinuity between the two surfaces of the crack can be obtained as

$$\mathbf{w}(\mathbf{x})=\mathbf{u}_c^{+}(\mathbf{x})-\mathbf{u}_c^{-}(\mathbf{x})=2\sum_{I\in N_{cr}}\widetilde{\mathbf{N}}_I(\mathbf{x})\mathbf{a}_I+2\sum_{I\in N_{tip}}\widetilde{\mathbf{N}}_I(\mathbf{x})B^{(1)}(r,\pi)\mathbf{b}_I^{(1)}\mathbf{x}\in\Gamma_c \tag{31}$$

Combination of Eqs. (31) and (20) enables determining the shape function N^w.

The fluid pressure field within the crack is approximated by

http://dx.doi.org/10.5772/56287

$$p(\mathbf{x}) = \sum_{I \in N_{cr}} N_I^p(\mathbf{x}) p_I \quad \mathbf{x} \in \Gamma_c \tag{32}$$

where $N_I^p(\mathbf{x})$ are the standard finite element shape functions. In some cases, it can also be chosen as a special function so as to allow for the pressure singularity at the crack tip and the associated near-tip asymptotic fracture opening associated with a zero-lag viscosity dominated regime in a hydraulic fracture [18].

4.2. Element implementation

As shown in Figure 3, the two-dimensional 4-node plane strain channel and tip elements have been constructed for the hydraulic fracture problem. Each node has the standard displacement degrees of freedom $\mathbf{u}_I$. The additional degrees of freedom $\mathbf{a}_I$ and $\mathbf{b}_I^{(l)}$ are assigned to the four nodes of channel and tip elements, respectively. In addition, the virtual degree of freedom of fluid pressure has been assigned to nodes 3 and 4 so as to represent the internal fluid pressure within the crack. It should be pointed out that the nodes 3 and 4 physically do not have fluid pressure degrees of freedom because here the fluid flow is confined within the crack, and the integral calculation of the related element matrixes and equivalent nodal forces (e.g. Eq. (26)) must be correctly carried out along the true crack path within the element.

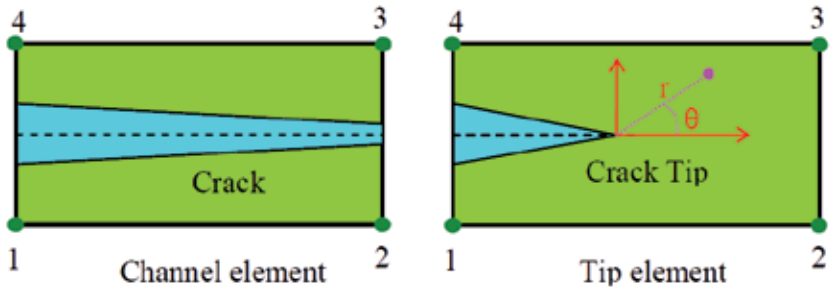

Figure 3. 2-D 4-node -node plane strain hydraulic fracture elements

So, the active degrees of freedom for the channel element are

$$\hat{u}^e = \{\underbrace{u_1^x \; u_1^y \; u_2^x \; u_2^y \; u_3^x \; u_3^y \; u_4^x \; u_4^y}_{\text{Standard}} \; \underbrace{a_1^x \; a_1^y \; a_2^x \; a_2^y \; a_3^x \; a_3^y \; a_4^x \; a_4^y}_{\text{Heaviside Enriched}} \; \underbrace{p_3 \; p_4}_{\text{Coupled}}\}^{\mathrm{T}}_{18} \tag{33}$$

and for the tip element the Heaviside enriched degrees of freedom $\mathbf{a}_I$ need to be replaced by the crack tip field enriched degrees of freedom $\mathbf{b}_I^{(l)}$.

Gauss quadrature is used to calculate the system matrix and equivalent nodal force. Since the discontinuous enrichment functions are introduced in approximating the displacement field, integration of discontinuous functions is needed when computing the element stiffness matrix

and equivalent nodal force. In order to ensure the integral accuracy, it is necessary to modify the quadrature routine. Both the channel and tip elements are partitioned by the crack surface into two quadrature sub-cells where the integrands are continuous and differentiable. Then Gauss integration is carried out by a loop over the sub-cells to obtain an accurate integration result.

Due to the flexibility, the user subroutine of UEL provided in the finite element package ABAQUS [20] has been employed in implementing the proposed elements in Fortran code. The main purpose of UEL is to provide the element stiffness matrix as well as the right hand side residual vector, as need in a context of solving the discrete system of equations.

5. Numerical examples

The proposed user element together with the structural elements provided in the ABAQUS element library are used to establish a finite element model to investigate a plane strain hydraulic fracture problem in an infinite impermeable elastic medium. The far-field boundary conditions are modelled by using infinite elements. The initial testing of this new element formulation involves using boundary value problems of an imposed fluid pressure and an imposed fracture opening. These problems are used to test for both of the two limiting cases of a toughness-dominated and viscosity-dominated plane-strain hydraulic fracture for which the analytical solutions are available in the literature [21].

Comparisons of the FEM predictions with the available analytical solutions to the two limiting cases are given in Figures 4 and 5.

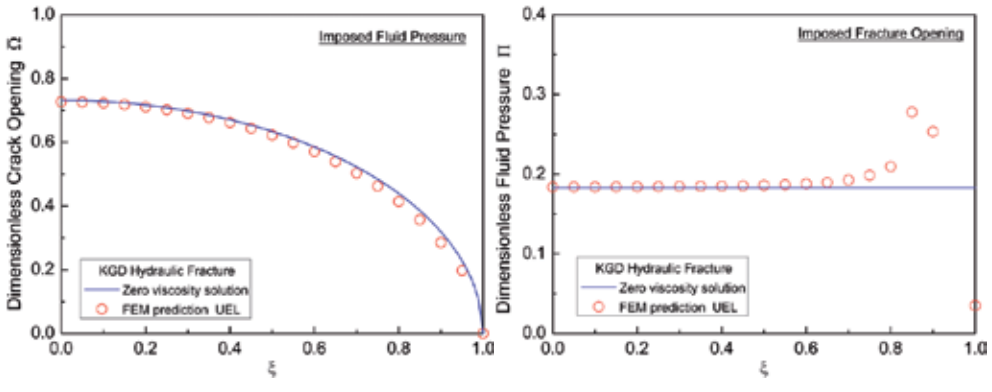

Figure 4. Zero-viscosity case: (a) imposed pressure; and (b) imposed opening

http://dx.doi.org/10.5772/56287

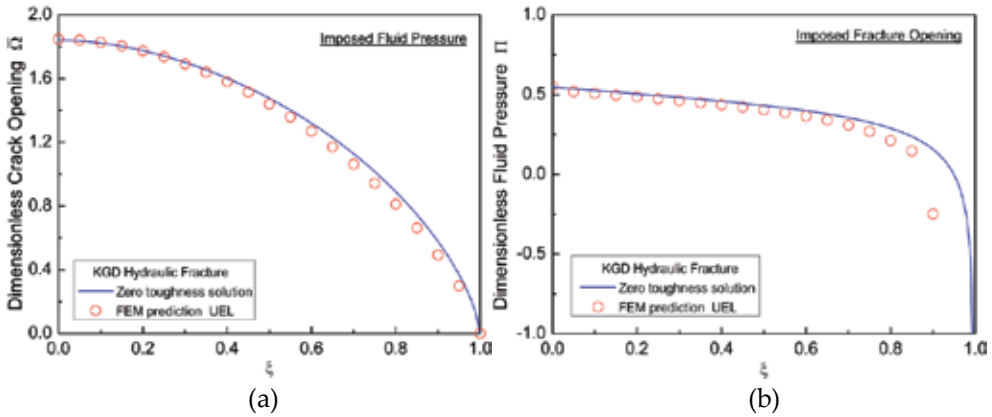

Figure 5. Zero-toughness case: (a) imposed pressure; and (b) imposed opening

The simulation results for a plane strain toughness-dominated KGD hydraulic fracture are shown in Figure 4. The corresponding analytical solutions for the zero-viscosity case are also shown for comparison. The crack opening is obtained by imposing a given pressure calculated according to the analytical solution (Eq. (41)) on the crack surface of the finite element model. While the fluid pressure is obtained by applying an opening profile calculated from the analytical solution (Eq. (40)) to the crack surface of the finite element model. For the zero-toughness case (Figure 5), the crack opening and the fluid pressure are obtained by imposing the analytical solution of pressure (Eq. (45)) and crack opening (Eq. (44)) to the crack surface of the finite element model, respectively. Only twenty channel elements in total are meshed along the crack length in the finite element model.

It can be seen that the XFEM predictions generally compare well with the analytical solutions for crack openings, while for the fluid pressure the XFEM predictions differ from the analytical solutions at the region close to the crack tip. One main reason for the deviation of the predicted fluid pressure from the analytical solutions near the tip is likely to be because the user-defined element is assumed to be cut through by the crack and no tip element is included in the finite element model. Another reason could be that a static fracture rather than a propagating fracture is simulated here. Improved prediction can be expected with the implementation of a crack tip user-defined element that captures the crack tip singularity correctly.

6. Summary

The application of the extended finite element method to the hydraulic fracture problems has been presented. The discrete governing equations for the coupled fluid-fracture problem have been derived. A user element based on the XFEM has been implemented in ABAQUS, which includes the desired aspects of the XFEM so as to model crack propagation without explicit remeshing. In addition, the fluid pressure degrees of freedom have been introduced and

assigned to the appropriate nodes of the proposed element to describe the fluid flow within the crack and its contribution to the crack deformation. Verification of the user-defined element has been made by comparing the FEM predictions with the analytical solutions available in the literature. The preliminary result presented here is a first attempt to the promising application of the XFEM to the hydraulic fracture simulation.

Apendix: Analytical solutions for plane strain Kristianovic-Geertsma-de Klerk (KGD) hydraulic fractures

The solution of a plane strain KGD hydraulic fracture in an infinite elastic body depends on the injection rate Q_0 and on the three material parameters E', K', and μ', which are defined as [21]

$E' = E / 1 - \nu^2$, $K' = (32/\pi)^{1/2} K_{Ic}$, $\mu' = 12\mu$

For the plane strain KGD hydraulic fracture, the crack opening $w(x, t)$, crack length (half length) $l(t)$, and net fluid pressure $p(x, t)$ can be expressed as [21]

$$\begin{aligned} w(x, t) &= \epsilon(t) L(t) \Omega[\xi, P(t)] = \epsilon(t) L(t) \gamma[P(t)] \bar{\Omega}(\xi) \\ p(x, t) &= \epsilon(t) E' \Pi[\xi, P(t)] \\ l(t) &= \gamma[P(t)] L(t) \end{aligned} \tag{34}$$

where $\xi = x / l(t)$ is the scaled coordinate $(0 \le \xi \le 1)$, $\epsilon(t)$ is a small dimensionless parameter, $L(t)$ denotes a length scale of the same order as the fracture length $l(t)$, $P(t)$ is the dimensionless evolution parameter, and $\gamma[P(t)]$ is dimensionless fracture length.

The evolution parameter $P(t)$ can be interpreted as a dimensionless toughness κ in the viscosity scaling [21]

$$\kappa = K' \left(E'^3 \mu' Q_0 \right)^{-1/4} \tag{35}$$

or as a dimensionless viscosity $\mathcal{M}$ in the toughness scaling [21]

$$\mathcal{M} = \mu' E'^3 Q_0 / K' \tag{36}$$

For the toughness scaling, denoted by a subscript k, the small parameter $\epsilon(t)$ and the length scale $L(t)$ take the explicit forms [21]

$$\epsilon_k(t) = \left(K'^4 / E'^4 Q_0 t \right)^{1/3}, \; L_k(t) = \left(E' Q_0 t / K' \right)^{2/3} \tag{37}$$

http://dx.doi.org/10.5772/56287

The solution for the zero viscosity case is given by [21]

$$\gamma_{k0}=2/\pi^{2/3} \tag{38}$$

$$\bar{\Omega}_{k0}(\xi)=\sqrt{1-\xi^2}/\pi^{1/3} \tag{39}$$

$$\Pi_{k0}=\pi^{1/3}/8 \tag{40}$$

For the viscosity scaling, denoted by a subscript m, the small parameter $\epsilon(t)$ and the length scale $L(t)$ take the explicit forms [21]

$$\epsilon_m(t)=\left(\mu'/E't\right)^{1/3}\ ,\ L_m(t)=\left(E'Q_0^3t^4/\mu'\right)^{1/6} \tag{41}$$

The first order approximation of the zero toughness solution is [21]

$$\gamma_{m0}\cong 0.616 \tag{42}$$

$$\bar{\Omega}_{m0}(\xi)=A_0(1-\xi^2)^{2/3}+A_1^{(1)}(1-\xi^2)^{5/3}+B^{(1)}\left[4\sqrt{1-\xi^2}+2\xi^2\ln\left|\frac{1-\sqrt{1-\xi^2}}{1+\sqrt{1-\xi^2}}\right|\right] \tag{43}$$

$$\Pi_{m0}^{(1)}=\frac{1}{3\pi}B\left(\frac{1}{2},\ \frac{2}{3}\right)\left[A_0F_1\left(-\frac{1}{6},\ 1;\frac{1}{2};\xi^2\right)+\frac{10}{7}A_1^{(1)}F_1\left(-\frac{7}{6},\ 1;\frac{1}{2};\xi^2\right)\right]+B^{(1)}(2-\pi|\xi|) \tag{44}$$

where $A_0=3^{1/2}$, $A_1^{(1)}\cong -0.156$, and $B^{(1)}\cong 0.0663$; B is Euler beta function, and F_1 is hypergeometric function. Thus, $\bar{\Omega}_{m0}(0)\cong 1.84$.

Acknowledgements

The author would like to thank Dr. Rob Jeffrey for the support of this work. Furthermore, the author thanks CSIRO CESRE for support and for granting permission to publish.

Author details

Zuorong Chen*

CSIRO Earth Science & Resource Engineering, Melbourne, Australia

References

[1] Clifton, R. J, & Abou-sayed, A. S. On the computation of the three-dimensional geometry of hydraulic fractures. Proceedings of the SPE Symposium on Low Permeability Gas Reservoir. Denver, Richardson: Society of Petroleum Engineers; (1979). , 307-313.

[2] Settari, A, & Cleary, M. P. Dimensional simulation of hydraulic fracturing. Journal of Petroleum Technology. (1984). , 36(8), 1177-1190.

[3] Vandamme, L, & Curran, J. H. A. Dimensional hydraulic fracturing simulator. International Journal for Numerical Methods in Engineering. (1989). , 28(4), 909-927.

[4] Advani, S. H, Lee, T. S, & Lee, J. K. Dimensional modeling of hydraulic fractures in layered media.1. finite-element formulations. Journal of Energy Resources Technology-Transactions of the ASME. (1990). , 112(1), 1-9.

[5] Valko, P, & Economides, M. J. Propagation of hydraulically induced fractures- a continuum damage mechanics approach. International Journal of Rock Mechanics and Mining Sciences & Geomechanics. (1994). , 31(3), 221-229.

[6] Ouyang, S, Carey, G. F, & Yew, C. H. An adaptive finite element scheme for hydraulic fracturing with proppant transport. International Journal for Numerical Methods in Fluids. (1997). , 24(7), 645-670.

[7] Papanastasiou, P. An efficient algorithm for propagating fluid-driven fractures. Computational Mechanics. (1999). , 24(4), 258-267.

[8] Zhang, X, Detournay, E, & Jeffrey, R. Propagation of a penny-shaped hydraulic fracture parallel to the free-surface of an elastic half-space. International Journal of Fracture. (2002). , 115(2), 125-158.

[9] Adachi, J, Siebrits, E, Peirce, A, & Desroches, J. Computer simulation of hydraulic fractures. International Journal of Rock Mechanics and Mining Sciences. (2007). , 44(5), 739-757.

[10] Lecamplon, B, & Detournay, E. An implicit algorithm for the propagation of a hydraulic fracture with a fluid lag. Computer Methods in Applied Mechanics and Engineering. (2007). , 196-4863.

[11] Peirce, A, & Detournay, E. An implicit level set method for modeling hydraulically driven fractures. Computer Methods in Applied Mechanics and Engineering. (2008).

[12] Chen, Z. R, Bunger, A. P, Zhang, X, & Jeffrey, R. G. Cohesive zone finite element-based modeling of hydraulic fractures. Acta Mechanica Solida Sinica. (2009). , 22(5), 443-452.

[13] Dean, R. H, & Schmidt, J. H. Hydraulic fracture predictions with a fully coupled geomechanical reservoir simulator. SPE Journal. (2009). , 14(4), 707-714.

http://dx.doi.org/10.5772/56287

[14] Carrier, B, & Granet, S. Numerical modeling of hydraulic fracture problem in permeable medium using cohesive zone model. Engineering Fracture Mechanics. (2012). , 79-312.

[15] Chen, Z. R. Finite element modelling of viscosity-dominated hydraulic fractures. Journal of Petroleum Science and Engineering. (2012).

[16] Belytschko, T, & Black, T. Elastic crack growth in finite elements with minimal remeshing. International Journal for Numerical Methods in Engineering. (1999). , 45(5), 601-620.

[17] Moes, N, Dolbow, J, & Belytschko, T. A finite element method for crack growth without remeshing. International Journal for Numerical Methods in Engineering. (1999). , 46(1), 131-150.

[18] Lecampion, B. An extended finite element method for hydraulic fracture problems. Communications in Numerical Methods in Engineering. (2009). , 25(2), 121-133.

[19] Dahi-taleghani, A, & Olson, J. E. Numerical modeling of multistranded hydraulic fracture propagation: accounting for the interaction between induced and natural fractures. SPE Journal. (2011). , 16(3), 575-581.

[20] ABAQUSABAQUS documentation version 6.(2011). , 11-1.

[21] Detournay, E. Propagation regimes of fluid-driven fractures in impermeable rocks. International Journal of Geomechanics. (2004). , 4(1), 35-45.

Chapter 37

Stress Intensity Factor Determination for Three-Dimensional Crack Using the Displacement Discontinuity Method with Applications to Hydraulic Fracture Height Growth and Non-Planar Propagation Paths

Farrokh Sheibani and Jon Olson

Additional information is available at the end of the chapter

http://dx.doi.org/10.5772/56308

Abstract

Stress intensity factor determination plays a central role in linearly elastic fracture mechanics (LEFM) problems. Fracture propagation is controlled by the stress field near the crack tip. Because this stress field is asymptotic dominant or singular, it is characterized by the stress intensity factor (SIF). Since many rock types show brittle elastic behaviour under hydrocarbon reservoir conditions, LEFM can be satisfactorily used for studying hydraulic fracture development. The purpose of this paper is to describe a numerical method to evaluate the stress intensity factor in Mode I, II and III at the tip of an arbitrarily-shaped, embedded cracks. The stress intensity factor is evaluated directly based on displacement discontinuities (DD) using a three-dimensional displacement discontinuity, boundary element method based on the equations of proposed in [1]. The boundary element formulation incorporates the fundamental closed-form analytical solution to a rectangular discontinuity in a homogenous, isotropic and linearly elastic half space. The accuracy of the stress intensity factor calculation is satisfactorily examined for rectangular, penny-shaped and elliptical planar cracks. Accurate and fast evaluation of the stress intensity factor for planar cracks shows the proposed procedure is robust for SIF calculation and crack propagation purposes. The empirical constant proposed by [2] relating crack tip element displacement discontinuity and SIF values provides surprisingly accurate results for planar cracks with limited numbers of constant DD elements. Using the described numerical model, we study how fracturing from misaligned horizontal wellbores might results in non-uniform height growth of the hydraulic fracture by evaluating of SIF distribution along the upper front of the fracture.

1. Introduction

Stress intensity factor determination plays a central role in linearly elastic fracture mechanics problems. Fracture propagation is controlled by the stress field near the crack tip. Because the stress field near the crack tip is asymptotic dominant or singular, it is characterized by the stress intensity factor. The real stress distribution at the vicinity of crack tip and the K-field LEFM approximation can be depicted schematically as in Figure 1. The stress singularity right at the tip of the crack cannot be experienced in real nature because inelastic deformation prevents the crack tip from being perfectly sharp. However, according to small scale yielding of the process zone immediately around the crack tip in comparison with the K-field region (Figure 2), the SIF is the quantity which dictates if/when the crack will propagate. The inaccuracy of the stress field calculation using the SIF based on LEFM is less than 15% of the exact solution over the distance ranging from $r < 0.01a$ to $r < 0.15a$, where r is the radius of K-field region and a is the half length of the crack [4].

Since SIF was proposed by Irwin [5] to express displacements and stresses in the vicinity of crack tip, several analytical techniques have been developed for a variety of common crack configurations; however, these analytical solutions are limited to simple crack geometries and loading conditions. For the case of 3-D planar cracks embedded in a semi-infinite body, there are less available analytical solutions for SIF. These exact analytical solutions provide good insight about fracture problems but they are not usable for general crack propagation modeling where the geometry of simultaneously propagating cracks can be asymmetrical and irregular and the boundary conditions can be complicated. Fortunately, advances in numerical modeling procedures supported by the fast growing speed of computational calculation have opened new doors for fracture propagation analysis.

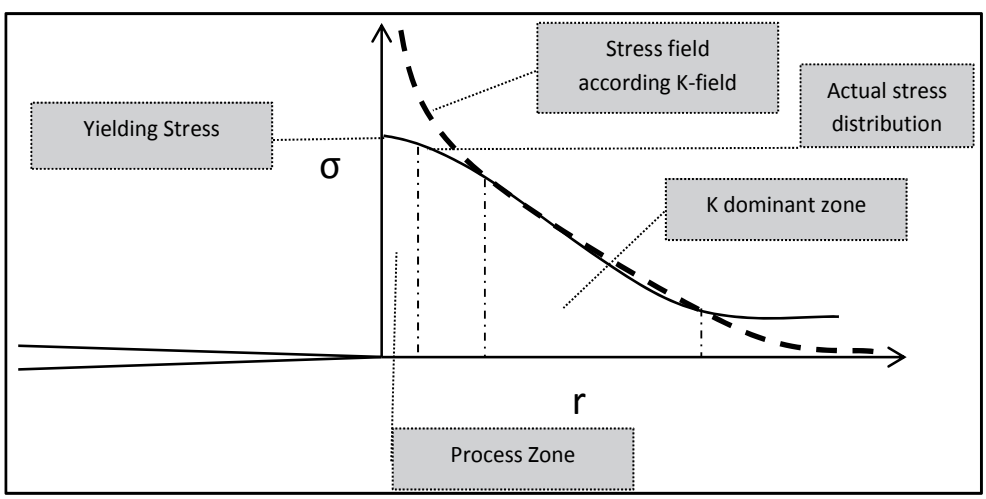

Figure 1. Schematic representation of stress distribution around the crack tip [3]

http://dx.doi.org/10.5772/56308

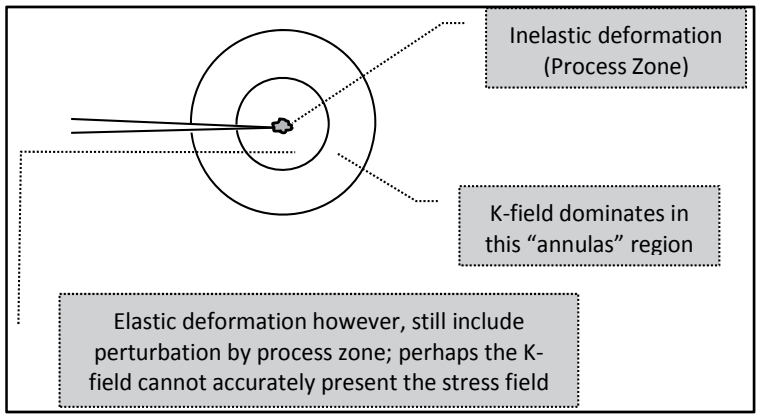

Figure 2. Process zone and K-filed representation [3]

There are four general distinctive numerical methods to model fracture propagation problems:

1. The boundary element method (BEM) requires discretization and calculation only on boundaries of the domain. The stress resolution is higher in comparison with finite element and finite difference methods because the approximation is imposed only on boundaries of the domain, and there is no further approximation on the solution at interior points. Particularly, for some problems where the ratio of boundary surface to volume is high (for instance for large rock masses), BEM can be advantageous because FEM or other whole-domain-discretizing methods require larger numbers of elements to achieve the same accuracy.
2. The Finite Element Method (FEM) has been widely used in fracture mechanics problems since it was implemented by [6] for SIF calculation. Several modifications have proposed to remove its deficiencies in LEFM problem modeling. [7] and [8] devised "quarter point element" or "singularity elements" to improve the accuracy of stress and displacement distributions around the crack and SIF evaluation. To overcome the time consuming process of remeshing in fracture propagation problems, [9] proposed the Extended Finite Element Method (XFEM). XFEM allows fracture propagation without changing the mesh by adding analytical expressions related to the crack tip field to the conventional FE polynomial approximation in what are called "enriched elements". Further work is being done ([10] and [11]) to address the accuracy and stability of XFEM modeling, especially for multiple crack problems and approaching tip elements called "blending elements".
3. The Finite Difference Method (FDM) requires calculations on a mesh that includes the entire domain. FDM usage in fracture mechanics is mostly limited to dynamic fracture propagation and dynamic SIF calculation ([12] and [13].)
4. The Discrete Element Method (DEM) is mostly applied when continuity cannot be assumed in discontinuous, separated domains. The method apply to describe the behavior of discontinuities between bodies with emphasize on the solution of contact and impact between multiple bodies [14].

Generally, when the geometry of a problem is changing, whole-domain-discretizing methods like FEM, FDM and DEM are more time-consuming than BEM because of the remeshing process around a propagation fracture. However, BEM loses its advantage when the domain is grossly inhomogeneous.

The "Integral equation" approach (also called influence function) and the "displacement discontinuity method" are two types of BEM widely used in LEFM analysis. Both approaches incorporate only boundary data by relating boundary tractions and displacements. In the integral equation technique, superposition of known influence functions (called Green's function) along boundaries generate a system of simultaneous integral equations [15]. In DDM, unknown boundary values are found from a simple system of algebraic equitation [16]. Generally, DDM has the advantage over integral equations in being faster, while integral equations can be more accurate for non-linear problems.

SIF values can be obtained from the displacement discontinuity magnitudes at crack tip elements [17-19]. However, according to [16], DDM consistently overestimates displacement discontinuities at the tip of the crack (considering element midpoint) by as much as 25%. To improve the accuracy of the solution, some researchers proposed using higher accuracy crack tip element and/or using relatively denser distribution of elements near the crack tip. [20] proposed higher order elements to improve the DDM solution and they used numerical integration to find the fundamental solution of linear and quadratic displacement discontinuities. [21] proposed another approach called "hybrid displacement discontinuity method" by using parabolic DD for crack tip elements and constant DD for other elements. He concluded increasing the number of elements more than 8-10 times cannot yield more accurate results and the error in mode I stress intensity factor calculation for a 2-D straight crack with uniform internal pressure, sporadically changes in a range of 1% to about 10% depending on the ratio of parabolic element length to constant element length. However, [22] used the same combination of DD element and concluded the ratio of crack tip element to constant DD element must be between 1-1.3 to obtain good results with relative error less than 3% in mode II SIF calculation for a straight 2-D crack. [23] presented a new hybrid displacement discontinuity method by using quadratic DD elements and special crack tip elements to show $\sqrt{r}$ variation of displacement near the crack tip. [24] used the same method with few modifications about the position of collocation points to determine quadratic elemental displacement. They showed the error can be fixed up to 1.5% for Mode I, and about 2% for mode II SIF calculation for a slanted straight crack. [25] took a different approach; instead of direct calculation of stress intensity factors from displacement discontinuities, they proposed a "equivalence transformation method" in which stresses on the crack surface are calculated from displacement discontinuities, and then by using crack line Green's function, the SIF at the crack tip can be obtained from calculated stresses. They implemented the equivalence transformation method to calculate dynamic stress intensity factors for an isolated 2-D crack in an infinite sheet subjected to Heaviside loading. By comparison with the exact solution and using 80 DD elements, they inferred the error in mode I SIF is less than 1% and for mode II doesn't exceed 1.5%.

http://dx.doi.org/10.5772/56308

All of the methods mentioned above including using special crack tip elements or equivalence transformation methods to decrease the error in crack tip element displacement and corresponding SIF calculation; however, they all need numerical integration and can be more time-consuming than constant elemental DD approximation. Ref. [2] empirically determined the coincidence between DDM modeling and analytical displacement distribution solution of a straight 2-D crack to remove the error. He showed the margin of error is less than 5% even by using only 2 elements in a 2-D crack. His proposed formula has been widely used in geologic fracture problems [26-29]. This paper extends Olson's method ion [2] to SIF calculation for 3-D homogenous, isotropic and linearly elastic material problems. [30] changed the correction constant. The empirical constant they proposed was used by some researchers afterwards ([31] and [32]), but we argue the change does not actually improve SIF accuracy.

According to Murakami and [33] and [34] the maximum mode I stress intensity factor appearing at a certain point along the crack front can be estimated by Equation (1) with less than 10% error for an arbitrary-shaped planar crack.

$$K_{I\ max} = 0.50\sigma\sqrt{\pi\sqrt{area}} \tag{1}$$

where 'area' is the area of crack projected in the direction of the maximum principal stress.

Fortunately, for simple crack geometries like elliptical and circular cracks, there exist analytical formulae for mode I stress intensity factor variation along the crack tip which help us to evaluate the accuracy of the numerical modeling ([35] and [36]). For rectangular defects there are no analytical formulae, but the accuracy of DDM numerical modeling can be examined by comparing against earlier numerical work using integral equation methods [37-40].

2. Numerical procedure

2.1. Displacement discontinuity method

The general concept of the displacement discontinuity method proposed by [16] is to approximate the distribution of displacement discontinuity of a crack by discretizing it into elements. Knowing the analytical solution for one element, the numerical elastic solution of the whole discontinuity can be calculated by adding up the effect of all subdividing elements.

The 3-D displacement discontinuity used here is based on the analytical elastic solution of normal and shear displacement of a finite rectangular discontinuity in half-space (Figure 3) proposed by [1]. These equations are closed-form half-space solutions of deformations and deformation derivatives in which most of singularities and mathematical instabilities were removed.

By placing N unknown constant displacement elements within the boundaries of the region to be analyzed and knowing the boundary conditions on each element (traction or displacement), a system of $3N$ linear algebraic equations can be set up as the following:

$$\begin{aligned}
\sigma_s^i &= \sum_{j=1}^{N} A_{ss}^{ij} D_s^j + \sum_{j=1}^{N} A_{sd}^{ij} D_d^j + \sum_{j=1}^{N} A_{sn}^{ij} D_n^j \quad a \\
\sigma_d^i &= \sum_{j=1}^{N} A_{ss}^{ij} D_s^j + \sum_{j=1}^{N} A_{sd}^{ij} D_d^j + \sum_{j=1}^{N} A_{sn}^{ij} D_n^j \quad b \\
\sigma_n^i &= \sum_{j=1}^{N} A_{ns}^{ij} D_s^j + \sum_{j=1}^{N} A_{nd}^{ij} D_d^j + \sum_{j=1}^{N} A_{nn}^{ij} D_n^j \quad c
\end{aligned} \tag{2}$$

where N is the total number of elements, s, d, n are the directions of local coordinates depicted in Figure 3, D_s^j, $D_d^j$and D_n^j are unknown strike-slip shear, dip-slip shear and opening displacement discontinuities of the jth element, σ_s^i, $\sigma_d^i$and σ_n^i are known strike-slip shear, dip-slip shear and normal boundary tractions induced on the ith element, and A is the boundary influence coefficient of the stresses tensor. If known values are the displacements of one side of boundary elements, these equations will be modified as:

$$\begin{aligned}
u_s^i &= \sum_{j=1}^{N} B_{ss}^{ij} D_s^j + \sum_{j=1}^{N} B_{sd}^{ij} D_d^j + \sum_{j=1}^{N} B_{sn}^{ij} D_n^j \quad a \\
u_d^i &= \sum_{j=1}^{N} B_{sd}^{ij} D_s^j + \sum_{j=1}^{N} B_{dd}^{ij} D_d^j + \sum_{j=1}^{N} B_{dn}^{ij} D_n^j \quad b \\
u_n^i &= \sum_{j=1}^{N} B_{sn}^{ij} D_s^j + \sum_{j=1}^{N} B_{nd}^{ij} D_d^j + \sum_{j=1}^{N} B_{nn}^{ij} D_n^j \quad c
\end{aligned} \tag{3}$$

where, u_s^i, $u_d^i$and u_n^i are known strike-slip and dip-slip shears and opening on the positive (or negative) face of the crack (Figure 3), and the B matrix is called the boundary influence coefficient of the displacements tensor.

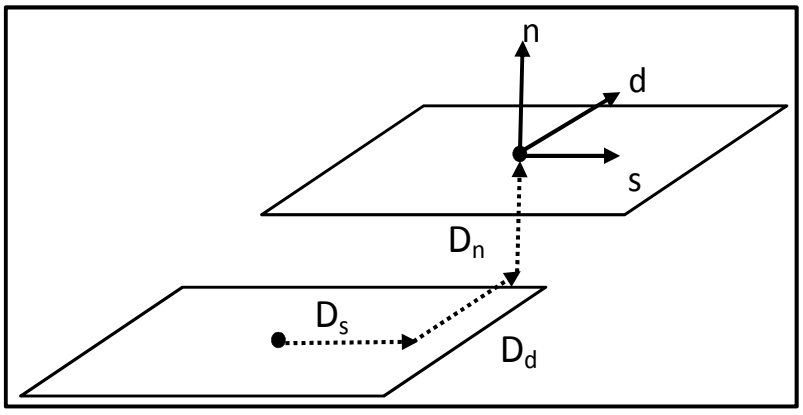

Figure 3. D displacement Discontinuity Modeling

http://dx.doi.org/10.5772/56308

2.2. Stress intensity factor computation

By knowing the crack tip element displacement discontinuities, K_I, K_{II} and K_{III} can be directly calculated using Equations 4a, b & c respectively:

$$K_I = C\frac{D_n E\sqrt{\pi}}{4(1-\nu^2)\sqrt{P}} \quad a$$
$$K_{II} = C\frac{D_s E\sqrt{\pi}}{4(1-\nu^2)\sqrt{P}} \quad b \qquad (4)$$
$$K_{III} = C\frac{D_t E\sqrt{\pi}}{4(1+\nu)\sqrt{P}} \quad c$$

where E is modulus of elasticity, ν is Poisson's ratio, P is crack tip element length perpendicular to crack front, D_n is the opening of crack tip element, D_s is shear displacement discontinuity perpendicular to D_n and the crack front, D_t is front-parallel displacement discontinuity (Fig. 3) and C is an empirically determined constant that accounts for the discrepancy between the numerical approximation and the analytical solution. [2] empirically determined that the analytical and numerical solutions for a planar 2-D crack coincide at approximately at $x = \left(a - \frac{P}{1.3}\right)$, where x is the distance from the center of the crack and a is half length of the crack. He showed by using the empirical constant $C = 0.806$ the margin of error is less than 5% for stress intensity factor calculation of a 2-D crack even when there are only two elements in a crack. The proposed modified constant of $C = 0.798$ by [30] does not improve on this accuracy.

3. Validation of numerical model

3.1. Rectangular crack

There is no analytical solution for the stress intensity factor variation along a rectangular crack front. However, rectangular cracks were the subject of several papers where the "Integral Equation" or "Body Force Method" was used to numerically approximate mixed Mode SIF values [37-42]. Results obtained from [39] are in a good agreement with [40] for maximum SIF calculation of rectangular cracks. In addition, [39] investigated how maximum stress intensity factors change in a half-space in terms of crack depth. Because of these reasons, [39] and [40] were selected as reference solutions to which we compare the results from this paper. Studies done by [37], [41] and [43] yield relatively different results for $K_{I\,max}$ calculation. These earlier works are different about 5% in average [39]. In addition they cannot be used for stress intensity factor variation along the crack edge. Equation 1 proposed by [34] is among few studies done to find the maximum stress intensity factor of an arbitrary-shaped crack. Using that formulae and knowing the maximum stress intensity factor for a rectangular discontinuity always is at the middle of longer edge, the maximum stress intensity factor of a rectangular crack can be approximated with adequate accuracy. For instance, they approximated the dimensionless

stress intensity factor at the edge-midpoints of a square crack as $F_I = 0.768$ which the error is about 1%.

Considering a rectangular crack as shown in Figure 4, the following dimensionless parameter is proposed to demonstrate the result of stress intensity factor of a rectangular crack. F_I is called the dimensionless stress intensity factor along the crack front $y = b$:

$$F_I = \frac{K_I(x,\ y)|x = x,\ \ y = \pm b}{\sigma_n\sqrt{\pi b}} \tag{5}$$

The stability of the solution can be examined by investigation of the strain energy variation through increasing the number of elements. Figure 5-b shows that strain energy (U) linearly varies with $\frac{1}{n}$ and has an asymptotic behavior with respect to n, where n is the number of element on each side of a square crack shown in Figure 5-b. The area of the square crack is A under constant pressure p.Assuming the error in strain energy calculation approaches zero if $n \to \infty \left(\frac{1}{n} \to 0\right)$, the correct answer for error estimation in the strain energy calculation can be obtained from Figure 5-b. Figure 5a shows the error calculation in strain energy. The displacement discontinuity method always overestimates the strain energy (or displacement across the crack surface) but it yields more accurate results closer to the exact solution when the number of elements increases. The error changes from 48.8% using a 3×3 mesh to about 1.99% for a mesh including 71×71 elements. In comparison with the two dimensional analysis of a straight crack [16], the rate of convergence is faster, but the error in strain energy calculation is higher using the same number of elements to divide one side of a crack.

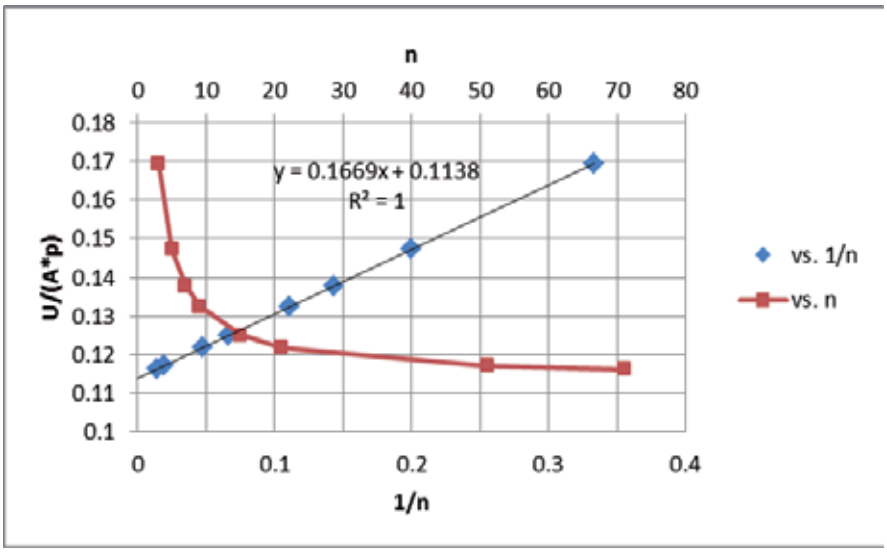

Figure 4. Approximation of the exact solution of strain energy for a square pressurized crack

http://dx.doi.org/10.5772/56308

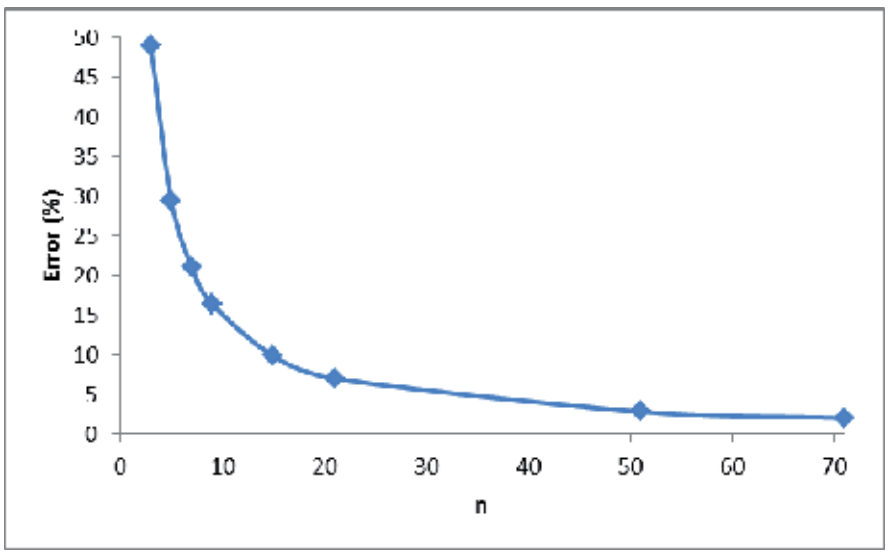

Figure 5. Error in strain energy calculation as a function of number of elements on each side of a pressurized square crack (*a*=*b*)

The error in strain energy calculation is mainly related to the largest error occurring at the corners of the square crack where the displacement gradient is highest. Figure 6 shows the stress intensity factor variation along the half-length of the crack tip using DDM compared with the integral equation solution suggested by [40]. The total number of elements used in the simulation was 22×22 to be consistent with the number of colocation points used in [40]. The difference between these two solutions is negligible for all elements but the corners (element No. 11). However, the corner elements of rectangular cracks don't play an important role in fracture propagation problems because the level of SIF is the lowest there and unlikely to control the initiation of crack propagation.

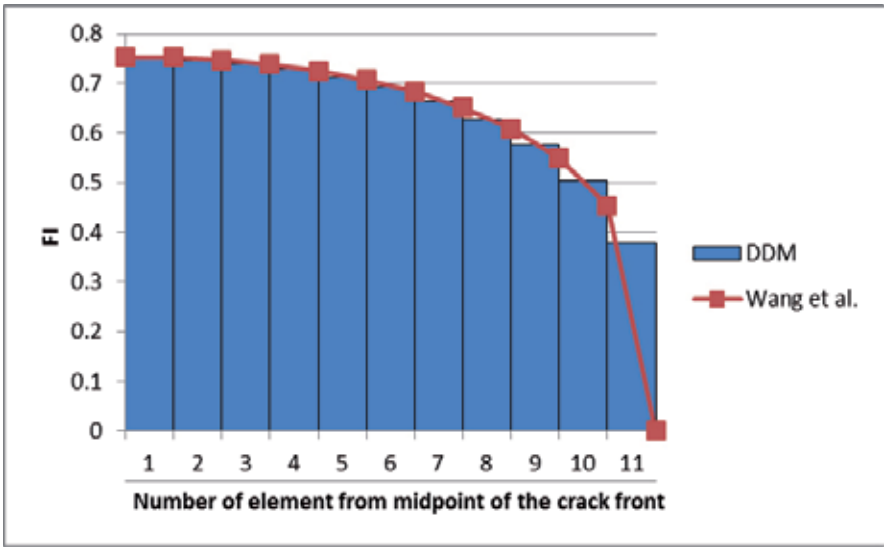

Figure 6. Dimensionless stress intensity factor variation along the half length of a square crack front

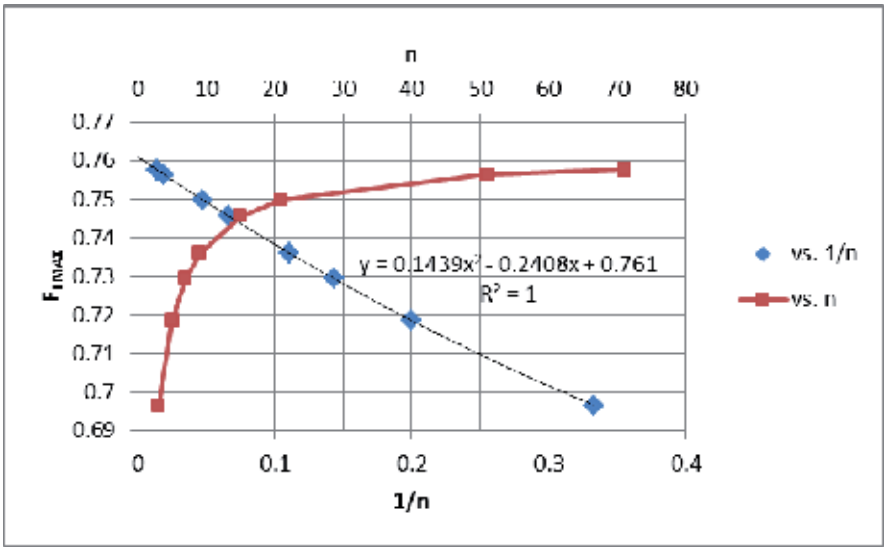

Figure 7. Extrapolation of $F_{I\,max}$ for a square crack in an infinite body

It is always desirable to use a coarser mesh to save computation time, but the accuracy of DDM depends strongly on mesh refinement. Figure 7 shows the extrapolation of maximum dimensionless stress intensity factor, $F_{I\,max}$(which occurs at side-midpoint of a square crack) as a function of $\frac{1}{n}$. It shows the numerical result of $F_{I\,max}$ is parabolic with the reciprocal of the

http://dx.doi.org/10.5772/56308

subdivision number. Figure 7 shows that the most reliable value of $F_{I\,max}$ for a square crack is 0.7607, which is slightly different (0.6%) than the value reported by [39] using body force method.

Figure 8 shows the variation of dimensionless stress intensity factor, F_1, along the crack front y=b for various values of $\frac{b}{a}$, using 22×22 elements, a mesh refinement consistent with [40]. Figure 9 shows the maximum dimensionless stress intensity factor ($F_{I\,max}$) at the location ($x=0$, $y=b$). When $b/a<1$, the crack tip at $y=b$ is represents the longer edge of a rectangular crack, whereas when $b/a>1$ the crack tip at $y=b$ represents the shorter tip. The dimensionless SIF is referenced to the plane strain SIF for a crack with half-length b for all b/a. The results show that at $b/a=0.125$, the maximum SIF (at location $x=0$, $y=b$) has reached the plane strain value ($F_1=1$). As b/a increases (equivalent to reducing the crack length a relative to b), F_1 is reduced. When $b/a=1.0$, the square crack, $F_1=0.75$. A penny-shaped crack has more restricted opening, and has the ratio of 0.64 to the plane strain SIF. Reducing a further such that $b/a>1$ makes a the short dimension of the crack and thus the limiting dimension for crack opening and SIF value. The SIF at y=b will then go to 0 as $a\rightarrow 0$. In comparing to the solution of [Wang et al 2001], it is evident that the distribution of SIF near the $x=a$ crack tip is more accurate when $b/a<1$, but the maximum value of SIF is a good match for all cases. Using higher element density around the rectangular crack front and a coarser mesh at the center was investigated, but we found a uniform mesh yielded more accurate results using fewer elements in comparison with non-uniform mesh.

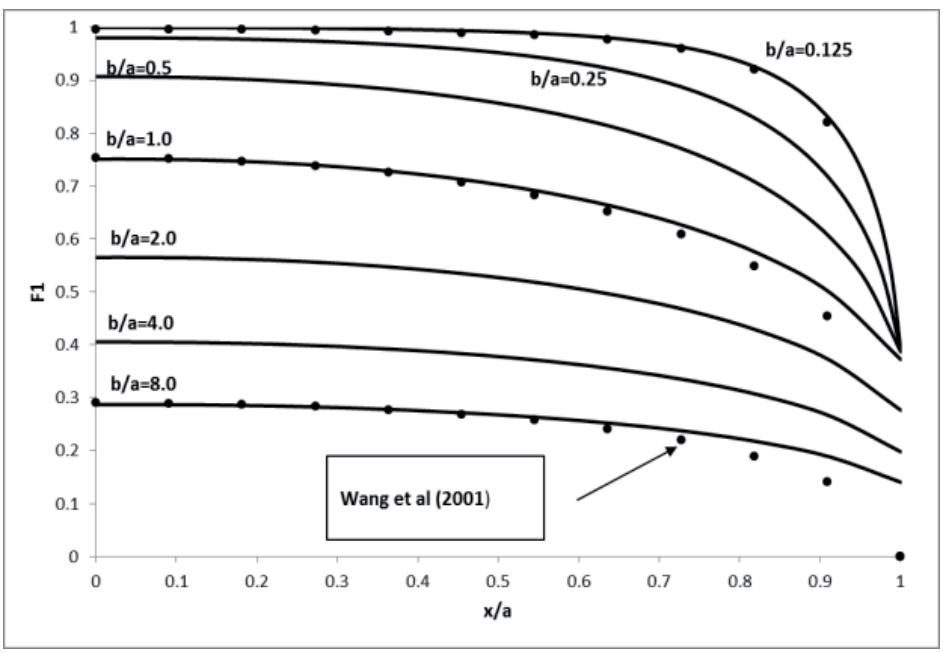

Figure 8. Dimensionless stress intensity factor variation along the crack front $y=b$.

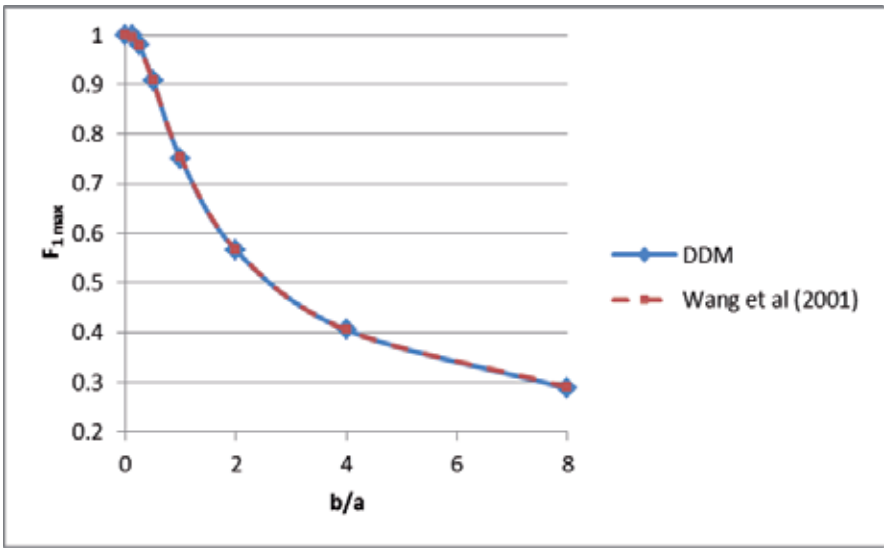

Figure 9. Maximum dimensionless stress intensity factor along the crack front $y = b$.

Considering a rectangular vertical crack in a half-space, and assuming $\nu = 0.3$, the dimensionless stress intensity factor at midpoints of crack fronts nearest (A_1) and farthest (A_2) from the free surface are presented in Figure 10a and b respectively, as a function of b/a and b/d. $F_{1\,max}$ and $F_{2\,max}$ are the dimensionless stress intensity factors corresponding to points A_1 and A_2 respectively and can be defined as the following:

$$F_{1\,max} = \frac{K_I(x,\ y)|_{A_1}}{\sigma_n\sqrt{\pi b}}\ a$$
$$F_{2\,max} = \frac{K_I(x,\ y)|_{A_2}}{\sigma_n\sqrt{\pi b}}\ b \qquad (6)$$

where σ_n is the normal pressure at the surface of crack. For every combination of b/a and b/d, the stress intensity factor along the side nearest to the free surface is greater than the side farthest away.

http://dx.doi.org/10.5772/56308

Figure 10-a and b show for greater aspect ratio (b/agrater or taller crack) SIF is less affected by the depth. Both $F_{1\,max}$ and $F_{2\,max}$ increase as the crack approaches the surface of solid. The mode I stress intensity factor along the crack fronts of a rectangular discontinuity in an infinite body is independent of Young's modulus [45]. Figure 11a and 11b show that Poisson's ratio v variation has a slight effect on $F_{1\,max}$ and $F_{2\,max}$, but only for cracks close to the free surface.

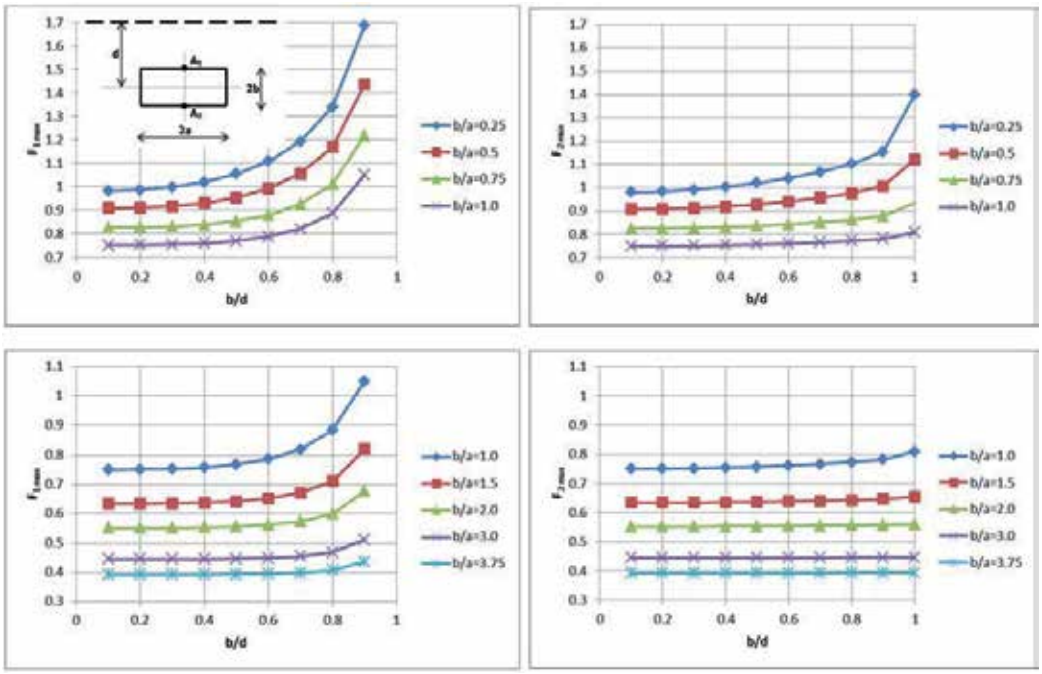

Figure 10. a Dimensionless stress intensity factor, $F_{1\,max}$as a function of b/a and b/d for a rectangular crack in half-space (v=0.3); b Dimensionless stress intensity factor $F_{2\,max}$ as a function of b/a and b/d for a rectangular crack in half-space (v=0.3)

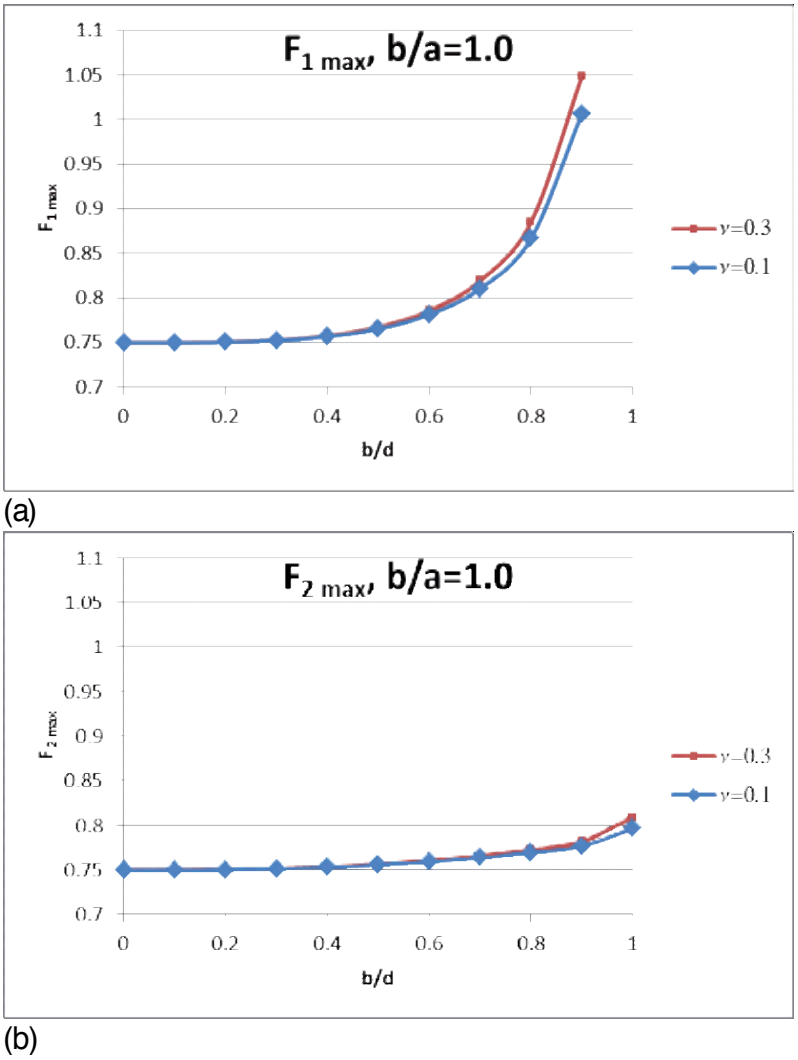

Figure 11. a. Effect of Poisson's ratio on dimensionless stress intensity factor, $F_{1\,max}$ for a rectangular crack in half-space; b. Effect of Poisson's ratio on dimensionless stress intensity factor $F_{2\,max}$ for a rectangular crack in half-space

In contrast to Mode I, for mode II and III stress intensity factor of a crack in an infinite body is dependent on elastic constants. By defining the dimensionless stress intensity factor for mode II, $F_{II} = \frac{K_{II}(x,\ y)|\,x=x,\ y=\pm b}{\tau_{zx}\sqrt{\pi b}}$ and assuming a frictionless surface crack, Figure 13 shows the maximum dimensionless stress intensity factor along the rectangular crack front $y=b$subject to front-perpendicular shear stress τ_{zx}. The figure shows increasing Poisson's ratio will increase mode II stress intensity factor at the tip of a rectangular crack embedded in an infinite space. Results were satisfactory compared with [38].

http://dx.doi.org/10.5772/56308

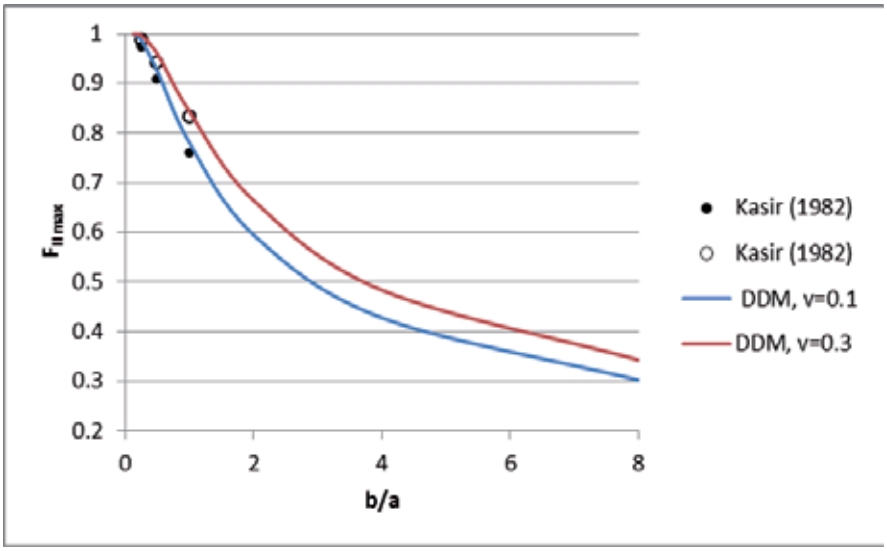

Figure 12. Effect of Poisson's ratio on Mode II dimensionless stress intensity factor for a rectangular crack in an infinite space.

3.2. Elliptical crack

For an elliptical crack embedded in an infinite body, the stress intensity factor variation along the crack edge can be obtained from the following analytical solution [36]:

$$K_I(\theta) = \frac{\sigma_n(\pi b)^{\frac{1}{2}}}{E(k)} \left(\frac{\sin^2\theta + \frac{b^4}{a^4}\cos^2\theta}{\sin^2\theta + \frac{b^2}{a^2}\cos^2\theta} \right)^{\frac{1}{4}} \tag{7}$$

where:

$\theta = \tan^{-1}\frac{y}{x}$, $\frac{x^2}{a^2} + \frac{y^2}{b^2} = 1$ and,

$E(k) = \int_0^{\frac{\pi}{2}} (1 - k^2 \sin^2\theta) d\theta$ *and* $k = 1 - \frac{b^2}{a^2}$

$E(k)$is the complete elliptical integral of the second kind while a is the major axis and $b$is the minor axis of ellipse. The maximum and minimum stress intensity factor at the end of minor and major axes, respectively, can be calculated using Equations 8a and 8b:

$$(K_I)_{max} = K_I\left(\theta = \frac{\pi}{2}\right) = \frac{\sigma_n\sqrt{\pi b}}{E(k)} \quad a$$
$$(K_I)_{min} = K_I(\theta = 0) = \frac{\sigma_n\sqrt{\pi b}}{E(k)}\sqrt{\frac{b}{a}} \quad b \tag{9}$$

Figure 13a and b show dimensionless stress intensity factor variation along the elliptical crack front using analytical solutions and DDM numerical modeling. Totally 154 DD elements were used in the model depicted in Figure 13a, and 628 elements in Figure 13b. Whereas SIF is proportional to the area of planar crack, the area of boundary element mesh in both cases is almost equal to the area of the modeled ellipse. For both models, the aspect ratio of the ellipse is $\frac{b}{a}=2$ and $F_1=\frac{K_1(\theta)}{\sigma_n(\pi b)^{\frac{1}{2}}}$. Both figures show that the trend of stress intensity factor variation can be appropriately modeled by DDM. Oscillation in SIF is because of stepwise mesh boundary used to define the geometry of the ellipse using rectangular elements. However, by using the average of SIF of the neighboring circumferential elements, the accuracy improves for both models and the maximum error decreases from about 24% to 9% for the first model and from 28% to 10% for the second model, as compared to the analytical solution in [36]. Using 20 elements along the major axis and 10 along the minor axis of the ellipse results in good agreement for F1 at $\theta=0$ and $\frac{\pi}{2}$(Figure 13-a). For $\theta\geq 60^{\circ}$, the rectangular mesh deviates less from the ellipse, and the error in dimensionless stress intensity factor is non-oscillatory and small. Increasing the number of elements doesn't improve the accuracy (Figure 13-b).

3.3. Penny-shaped crack

Stress intensity factor at the tip of a circular crack of radius *a*in an infinite solid under uniaxial tension σ_n is [46]:

$$\frac{2}{\pi}\sigma_n\sqrt{\pi a} \tag{10}$$

where:

$\theta=\tan^{-1}\frac{y}{x}$, $x^2+y^2=a^2$

Two different size meshes were considered to calculate dimensionless stress intensity factor variation along the tip of a circular crack as depicted in Figures 14a and 14b. The first model includes 76 elements and the second one has 308 elements. According to Figure 7, for a rectangular crack using 9×9 elements, the error in stress intensity factor is about 3 percent. For the penny-shaped crack, as with the elliptical crack, the error is a strong function of location. Because of the symmetry, error calculations are shown only for one eighth of the circle. The main reason of error in stress intensity factor along the crack front is jagged geometrical definition of the circle by using rectangular displacement discontinuity elements. The error in SIF can reach up to 20% along the crack front; however, the results are better for $\theta=0$ *or* $\frac{\pi}{2}$- about 2.5% for the coarser model and almost zero for the finer model. Figure 15 compares F_1variation along the quarter front of the penny-shaped crack for two DD models as well as analytical solution. The figure shows the finer mesh helps to increase the accuracy where the crack front is straight, but is not helpful where

http://dx.doi.org/10.5772/56308

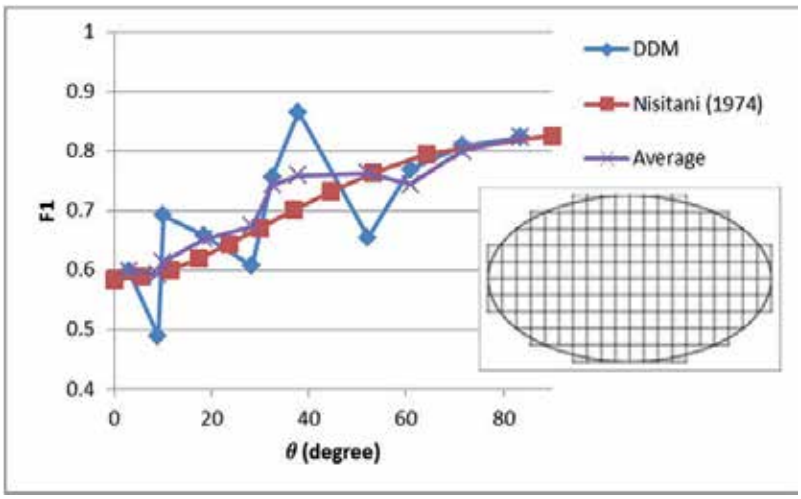

(a)

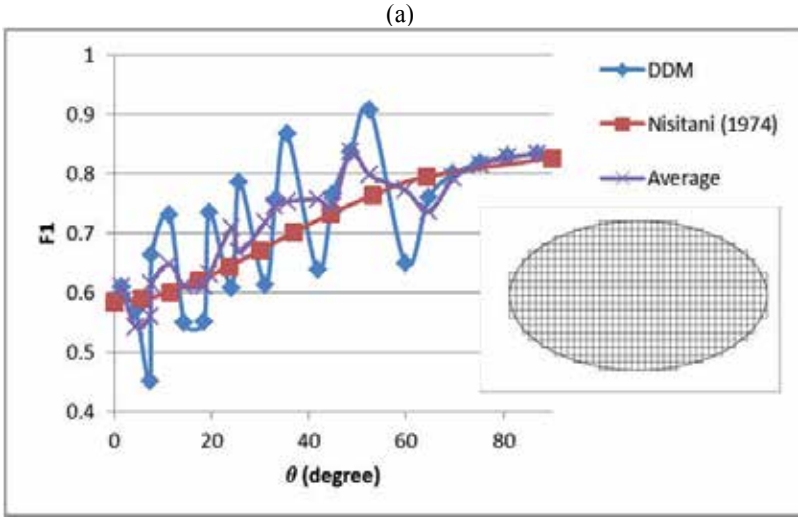

(b)

Figure 13. a. Dimensionless SIF variation along an elliptical crack front using analytical solution and DDM $\left(\frac{b}{a}=2.0\right)$, model No. 1 including 154 elements; b. Dimensionless SIF variation along an elliptical crack front using analytical solution and DDM $\left(\frac{b}{a}=2.0\right)$, model No. 2 including 628 elements

the crack front is stepwise. Similar to elliptical cracks, using the average SIF of neighbor circumferential elements considerably increases the accuracy of SIF distribution along the crack front of the penny-shaped discontinuity.

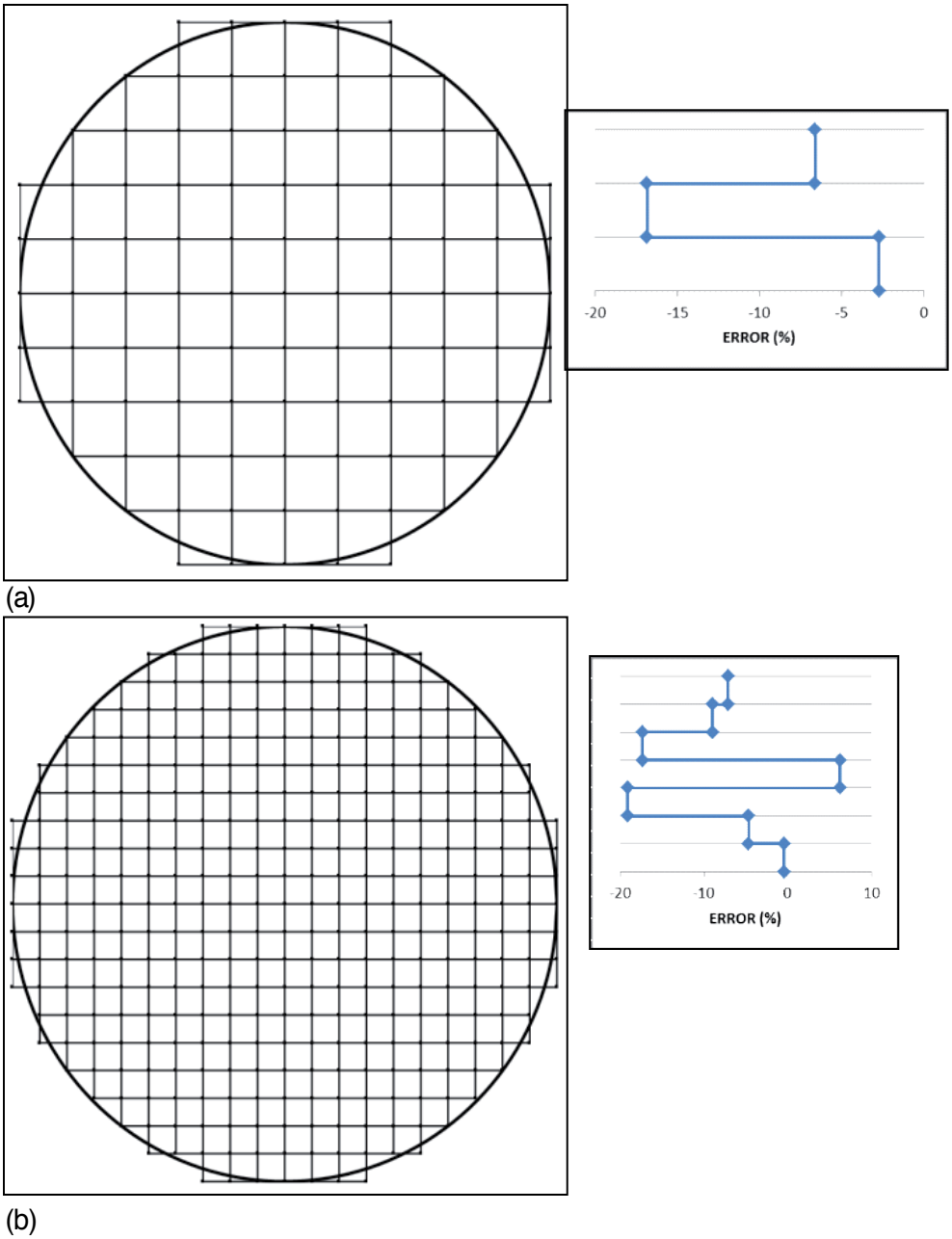

Figure 14. a Error in dimensionless calculation along a penny-shaped crack front, Model 1 including 76 elements; b. Error in dimensionless calculation along a penny-shaped crack front, Model 2 containing 308 elements

http://dx.doi.org/10.5772/56308

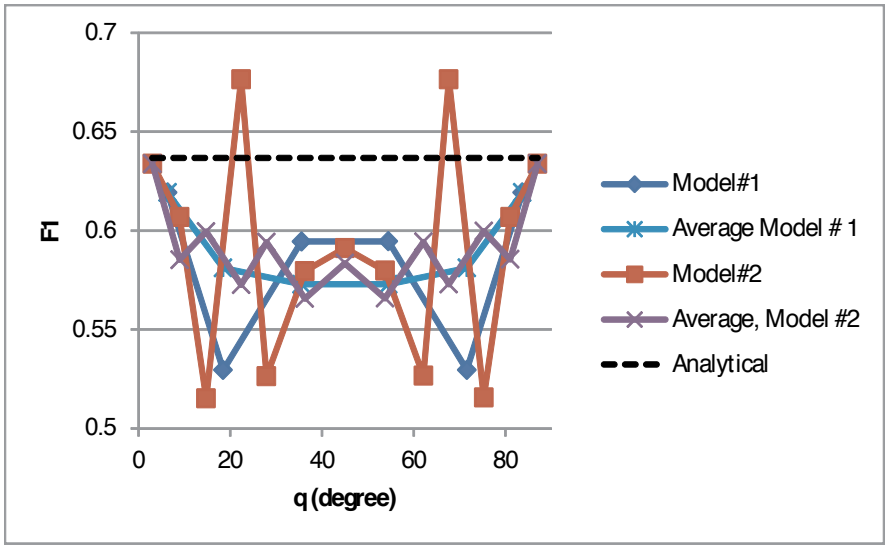

Figure 15. Comparison between dimensionless SIF for two DDM models with analytical solution of a penny-shaped crack stress intensity factor

4. Fracture propagation

For vertical fractures, lateral kinking propagation is modeled based on maximum circumferential stress criteria [47], which states growth should occur at the crack tip along a radial path perpendicular to the direction of greatest tension:

$$\tan\frac{\theta_0}{2}=\frac{1}{4}\left[\frac{K_I}{K_{II}}-Sgn\left(K_{II}\right)\sqrt{\left(\frac{K_I}{K_{II}}\right)^2+8}\right] \quad a$$
$$K_{eq}=K_I\cos^3\frac{\theta_0}{2}-\frac{3}{2}K_{II}\cos\frac{\theta_0}{2}\sin\frac{\theta_0}{2} \quad b \tag{11}$$

where θ_0 is the angle of kinking and $Sgn(K_{II})$denotes the sign of K_{II}. Equation 10-a is used to calculate the equivalent opening mode stress intensity factor in the direction of crack extension (K_{eq}) as in formula (10b).

Our model takes into account the height growth as pure Mode I propagation. Any contribution of Mode III or out of plane shear on vertical propagation is neglected; however, the possibility of fringe crack generation based on Mode I+III combination will be studied by Mode III SIF evaluation along the upper front of the fracture. The angle of twisting is dependent on the magnitude of Mode III and Mode I SIF as well as mechanical properties [48] and can be calculated using Equation 11. Higher values of Mode III SIF (or lower opening mode) result in bigger twisting angle.

$$\alpha=\frac{1}{2}\tan^{-1}\left[\frac{K_{III}}{K_I\left(1/2-\right)}\right] \tag{12}$$

Fracture front propagation velocity defines which edge extends first. Charles power law [49] was used to relate the equivalent opening Mode stress intensity factor at the tip of the crack to the propagation velocity as the following [49]:

$$V=AK_{eq}^{n} \tag{13}$$

5. Application: Fracture misalignment and height growth

Figure 16 shows the ideal alignment of horizontal well and longitudinal hydraulic fracture system where the horizontal well is perpendicular to the minimum remote horizontal stress $S_{hmin}=S_3$ and the wellbore lies in the principal remote stress plane, parallel to $S_{Hmax}=S_2$. However, hydraulic fractures may not necessarily start perpendicular to the minimum horizontal remote stress because of the lack of alignment between the wellbore and the principal stresses, local stress perturbation, or natural fracture adjacent to a horizontal well [50]. The geometry of a hydraulic fracture could be further complicated by lateral propagation which is non-planar and height growth that is non-uniform. The non-planarity of the fracture path and its resultant near-wellbore width restriction and excessive treating pressure were considered by [51] and [52] using 2-D and pseudo 3-D displacement discontinuity modeling, respectively. In this paper, we study the effect of misalignment angle on the possibility of irregular height growth as well as fringe fracture generation by contemplating the stress intensity factor distribution around the periphery of misaligned hydraulic fracture. Wellbore stress effects are not considered in this study.

http://dx.doi.org/10.5772/56308

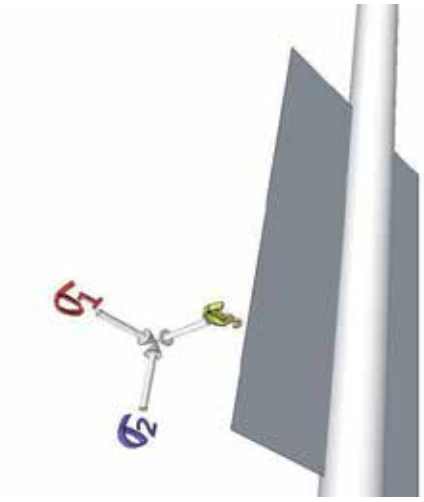

Figure 16. Ideal longitudinal fractured horizontal well with hydraulic fracture perpendicular to σ_{hmin}.

For the propagation cases that follow, we assume $S_{hmin} = S^r_{xx} = 15$ MPa (where r denotes remote stresses), P_{frac} is constant and equal to 20.0 *MPa*, the remote compression differential stress is $(\sigma^r_{yy} - \sigma^r_{xx}) = 2.0$ *MPa*, the propagation velocity exponent is $n = 2$, $\nu = 0.25$ and $E = 30.0$ *GPa*. The initial fracture length and height are assumed to be 3 meters (a square crack), subdivided by 9 DDM elements. The fracture is assumed to remain rectangular during the propagation (i.e., the height is uniform along the entire length, but the crack path in plan-view can be non-planar).

To examine the effect of horizontal well misalignment angle on fracture propagation (Figure 17), first we assume the differential compression in y direction $(S^r_{yy} - S^r_{xx})$ is 40% of the net injection pressure $(P_{frac} - S^r_{xx})$. Fracture path non-planarity is strongly affected by the initial misalignment angle, β, especially for extreme cases. The starter fracture is centered at (0,0) and is rotated counterclockwise by β. The smallest misalignment $\beta = 10°$ is the closest to planar fracture and $\beta = 89°$ is the most curved path.

Nonplanar propagation has an impact on height growth (Figures 18 and 19). For the smaller misalignment cases (β <=45º), crack height keeps pace with crack length growth for our imposed rectangular shape (Figure 18). For our stronger misalignment cases of β >45º, the crack height growth is somewhat hindered to only ~80% of the length. Looking at the opening mode SIF (K_I) distribution along the top edge of the fracture is more interesting, however, since our propagation algorithm responds only to the average crack tip SIF. The more severe the fracture reorientation, the lower the K_I for the initial fracture segment, where for the 89º misalignment case, the K_I at the center of the crack is 50% lower than it would be for a planar fracture. This implies that at the wellbore, there could be a restriction in fracture height because of the non-planar propagation that might also restrict width and hinder infectivity.

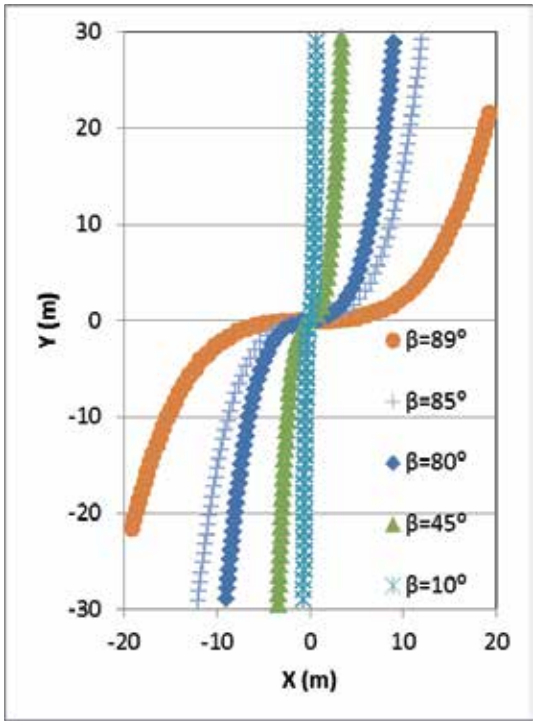

Figure 17. Map view of non-planar fracture paths (upper front propagation, $\frac{\Delta H}{2} = 25.0\ m$)

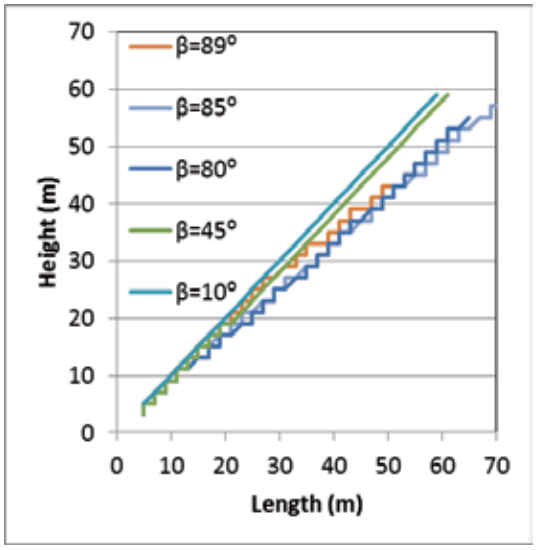

Figure 18. Vertical versus lateral growth of the hydraulic fracture

http://dx.doi.org/10.5772/56308

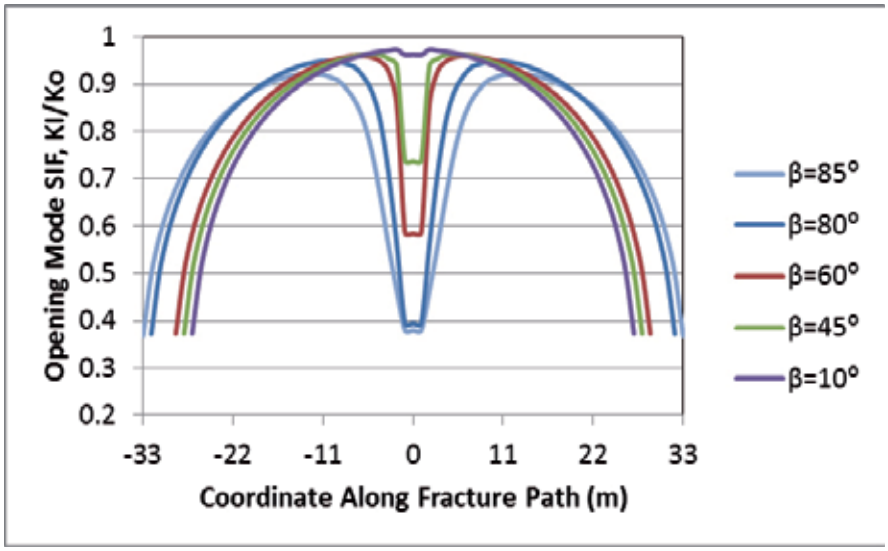

Figure 19. K_I along the upper front of hydraulic fracture implying height growth restriction around the wellbore due to misalignment normalized to SIF of planar fracture at $x=0$(upper front propagation, $\frac{\Delta H}{2}=25.0\ m$)

The time progression of the K_I variation along the top fracture front is displayed in Figure 20 for the case $\beta=80°$. The K_I at the initial fracture location (the injection location) grows very slowly in comparison to the curving wings of the fracture.

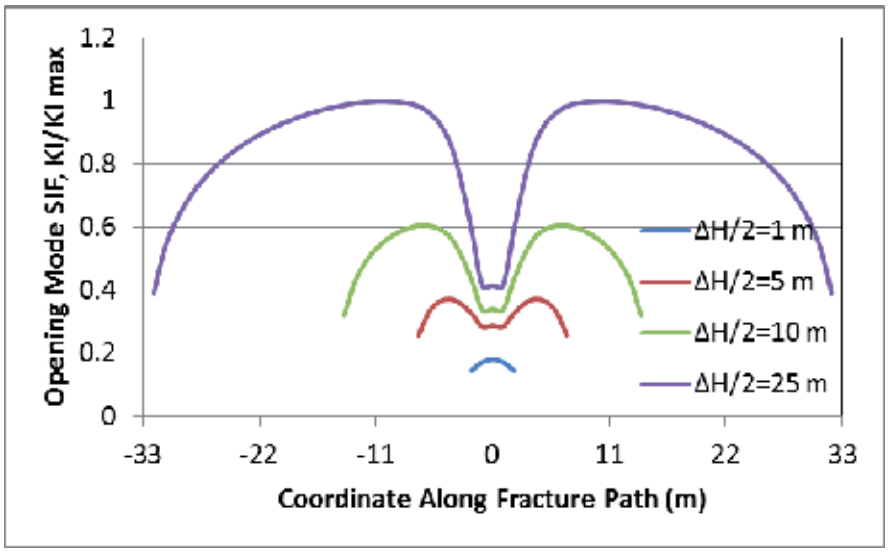

Figure 20. K_I distribution variation normalized by the absolute maximum opening mode SIF during propagation along the upper front of a hydraulic fracture perforated from a misaligned horizontal wellbore. Misalignment angle, $\beta=80°$.

Although K_I is restricted in the misaligned portion of the fracture, Mode III or out of plane shear SIF(K_{III}) is accentuated. This twisting SIF could cause the fracture to break down into several en echelon cracks, causing further propagation hindrance in the vertical direction. Figure 21 depicts the distribution of K_{III} for varying fracture misalignment based on the simulation of Figure 19.

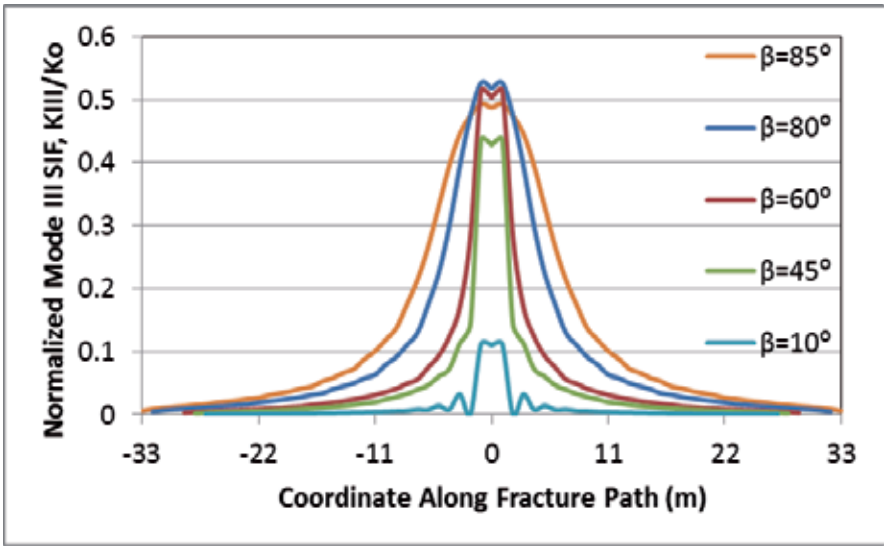

Figure 21. Mode III SIF along the upper front of hydraulic fracture normalized to SIF of planar fracture at $x=0$, implying height growth restriction around the wellbore due to misalignment (upper front propagation, $\frac{\Delta H}{2}=25.0\ m$)

Fracture path is affected by remote stresses as well as near-tip stress distribution and is quantifies by ratio R[53] assuming compression is positive:

$$R=\frac{(\sigma_{Hmax}-\sigma_{hmin})}{(P_{frac}-\sigma_{hmin})}=\frac{(\sigma^{r}_{yy}-\sigma^{r}_{xx})}{(P_{frac}-\sigma^{r}_{xx})} \tag{14}$$

The magnitude of Rshows how fast the misaligned fracture will be aligned with maximum horizontal stress. Figure 20 present the bigger the magnitude of Rratio, the faster the fracture will be rotated to be aligned perpendicular to minimum horizontal stress. Because the differential remote stress is kept constant for these 3 cases, smaller magnitude of ratio Rmeans the dominance of fracture driving stresses results in a straighter fracture path.

http://dx.doi.org/10.5772/56308

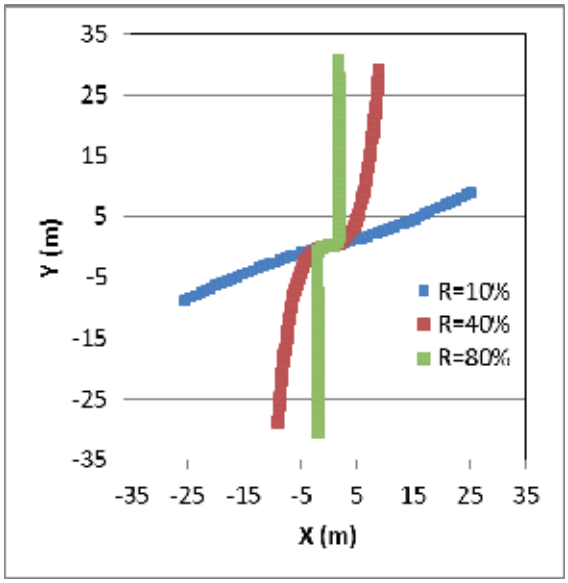

Figure 22. R ratio effect on fracture path. Upper front propagation, $\frac{\Delta H}{2} = 25.0\ m$, $\beta = 80°$ and $(\sigma^r_{yy} - \sigma^r_{xx}) = 2.0\ MPa$.

6. Conclusion

Numerical methods are necessary for the SIF evaluation of 3-D planar cracks because analytical solutions are limited to simple geometries with special boundary conditions. In this paper, the capability of DDM using constant rectangular discontinuity elements and considering the empirical constant proposed by Olson (1991) was satisfactory examined for cracks with simple geometry. The accuracy of the model is excellent especially for rectangular and square shaped cracks. The stepwise shape of the mesh boundary when representing elliptical or penny-shaped cracks introduces more error in to the calculation, but the minimum and maximum SIF values can be accurately computed.

Acknowledgements

Funding for this project is provided by RPSEA through the "Ultra-Deepwater and Unconventional Natural Gas and Other Petroleum Resources" program authorized by the U.S. Energy Policy Act of 2005. RPSEA (www.rpsea.org) is a nonprofit corporation whose mission is to provide a stewardship role in ensuring the focused research, development and deployment of safe and environmentally responsible technology that can effectively deliver hydrocarbons from domestic resources to the citizens of the United States. RPSEA, operating as a consortium of premier U.S. energy research universities, industry, and independent research organiza-

tions, manages the program under a contract with the U.S. Department of Energy's National Energy Technology Laboratory. Authors gratefully appreciate RPSEA for providing the funding for this work.

Author details

Farrokh Sheibani* and Jon Olson*

*Address all correspondence to: sheibani@utexas.edu

*Address all correspondence to: jolson@austin.utexas.edu

University of Texas at Austin, Austin, USA

References

[1] Okada, Y. Internal deformation due to shear and tensile faults in a half-space. Bulletin of the Seismological Society of America (1992). , 82(2), 1018-1040.

[2] Olson, J. E. Fracture mechanics analysis of joints and veins. PhD Dissertation. Stanford University; (1991).

[3] Cahng, C. C, & Mear, M. E. A Boundary Element Method for Two Dimensional Linear Elastic Fracture Analysis. International Journal of Fracture (1995). , 74-219.

[4] Pollard, D. D, & Segall, P. Theoretical displacement and stress near fracture in rock: with application to faults, joints, veins, dikes and solution surfaces. In: Atkinson BK. (ed.) Fracture Mechanics of Rock. London: Academic Press; (1987). , 277-350.

[5] Irwin, G. R. Analysis of stress and strain near the end of a crack traversing a plate. Journal of Applied Mechanics (1957). , 24-361.

[6] Chan, S. K, Tuba, I. S, & Wilson, W. K. On the finite element method in linear fracture mechanics. Engineering Fracture Mechanics (1970). , 2-1.

[7] Henshell, R. D, & Shaw, K. G. Crack tip finite elements are unnecessary. International Journal for Numerical Methods in Engineering (1975). , 9-495.

[8] Barsoum, R. S. On the use of isoparametric finite elements in linear fracture mechanics, International Journal for Numerical Methods in Engineering (1976). , 10(1), 65-88.

[9] Benzley, S. E. Representation of singularities with isoparametric finite elements., International Journal for Numerical Methods in Engineering (1974). , 8(3), 537-545.

http://dx.doi.org/10.5772/56308

[10] Tarancon, J. E, Vercher, A, Giner, E, & Fuenmayor, F. J. Enhanced blending elements for XFEM applied to linear elastic fracture mechanics. International Journal for Numerical Methods in Engineering (2009). , 77(1), 126-148.

[11] Jiang, S, Ying, Z, & Du, C. The optimal XFEM approximation for fracture analysis. IOP Conference Series: Materials Science and Engineering (2010).

[12] Lin, X, & Ballmann, J. Re-consideration of Chen's problem by finite difference method. Engineering Fracture Mechanics (1993). , 44(5), 735-739.

[13] Chen, Y. M. Numerical computation of dynamic stress intensity factors by a Lagrangian finite-deference method (THE HEMP CODE). Engineering Fracture Mechanics (1975).

[14] Pande, G. N, Beer, G, & Williams, J. R. Numerical Methods in Rock Mechanics. West Sussex: John Wiley & Sons Ltd; (1990).

[15] Rizzo, F. J. An integral equation approach to boundary value problems of classical elastostatics. Quarterly of Applied Mathematics (1967). , 25-83.

[16] Crouch, S. L. Solution of plane elasticity problems by the displacement discontinuity method. International Journal for Numerical Methods in Engineering (1976). , 10(2), 301-343.

[17] Crouch, S. L, & Starfield, A. M. Boundary element methods in solid mechanics. London: George Allen & Unwin; (1983).

[18] Schultz, R. A. Stress intensity factor for curved cracks obtained displacement discontinuity method. International Journal of Fracture (1988). RR34., 31.

[19] Aydin, A, & Schultz, R. A. Effect of mechanical interaction on the development of strike-slip faults with echelon patterns. Journal of Structural Geology (1990). , 12(1), 123-129.

[20] Crawford, A. M, & Curran, J. H. Higher-order functional variation displacement discontinuity elements. International Journal of Rock Mechanics and Mining Sciences & Geomechanics Abstract (1982). , 19(3), 143-148.

[21] Scavia, C. The displacement discontinuity method on the analysis of open cracks. Meccanica (1991). , 26(1), 27-32.

[22] Yan, X. Stress intensity factors for cracks emanating from a triangular or square hole in an infinite plate by boundary elements. Engineering Failure Analysis (2005). , 12(3), 362-375.

[23] Shou, K. J, & Crouch, S. L. A higher order displacement discontinuity method for analysis of crack problems. International Journal of Rock Mechanics and Mining Sciences & Geomechanics Abstract (1995). , 32(1), 49-55.

[24] Dong, C. Y, & Pater, C. J. Numerical implementation of displacement discontinuity method and its application in hydraulic fracturing. Computer Methods in Applied Mechanics Engineering (2001).

[25] Wen, P. H, Aliabadi, M. H, & Rooke, D. P. A fictitious stress and displacement discontinuity method for dynamic crack problems. In: Brebbia CA. (ed.) Boundary Element Method XVI. Southampton: Computational Mechanics Publications; (1994). , 469-476.

[26] Thomas, A. L, & Pollard, D. D. The geometry of echelon fractures in rock-implication from laboratory and numerical experiments. Journal of Structural Geology (1993).

[27] Kattenhorn, S. A. A. D mechanical analysis of normal fault evolution and joint development in perturbed stress field around normal faults. PhD Dissertation. Stanford University; (1998).

[28] Willemse EJMPollard DD. Normal Fault growth: Evolution of tipline shapes and slip distribution. In: Lehner FK, Urai JL. (ed.) Aspects of Tectonic Faulting. Newyork: Springer; (2000). , 193-226.

[29] Olson, J. E. Fracture aperture, length and pattern geometry development under biaxial loading: a numerical study with application to natural, cross-jointed systems. Geological Society Special Publication (2007). , 289-123.

[30] Mériaux, C, & Lister, J. R. Calculation of dyke trajectories from volcanic centers. Journal of Geophysical Research (2002). B4) 2077-2087.

[31] Mutlu, O, & Pollard, D. D. (2006). A complementarity approach for modeling fractures. In: Yale D, Holtz S, Breeds C, and Ozbay U. (eds.) 50 years of Rock Mechanics-Landmarks and Future Challenges: The 41st U.S. Symposium on Rock Mechanics, Paper No: ARMA/USRMS June 17-21 2006, Golden, CO, USA., 06-1058.

[32] Ritz, E, & Pollard, D. D. Closure of circular arc cracks under general loading: effects on stress intensity factors. International Journal of Fracture (2011). , 167(1), 3-14.

[33] Murakami, Y, & Endo, M. Quantitative evaluation of fatigue strength of metals containing various small defects or cracks. Engineering Fracture Mechanics (1983). , 17(1), 1-15.

[34] Murakami, Y, Kodama, S, & Konuma, S. Quantitative evaluation of effects of non-metallic inclusions on fatigue strength of high strength steels. I: Basic fatigue mechanism and evaluation of correlation between the fatigue fracture stress and the size and location of non-metallic inclusions. International Journal of Fatigue (1989). , 11(5), 291-298.

[35] Irwin, G. R. (1962). Crack-extension force for a part-through crack in a plate. Journal of Applied Mechanics 1962;, 29(4), 651-654.

[36] Nisitani, H, & Murakami, Y. Stress intensity factor of an elliptical crack and semi-elliptical crack in plates subjected to tension. International Journal of fracture (1974). , 10(3), 353-368.

[37] Weaver, J. Three dimensional crack analysis. International Journal of Solids and Structures (1977). , 13(4), 321-330.

[38] Kassir, M. K. rectangular crack subjected to shear loading. International Journal of Solids and Structures 1982;, 18(12), 1075-1082.

[39] Isida, M, Yoshida, T, & Noguchi, H. A rectangular crack in an infinite solid, a semi-infinite solid and a finite-thickness plate subjected to tension. International Journal of Fracture (1991). , 52-79.

[40] Wang, Q, Noda, N. A, Honda, M. A, & Chen, M. Variation of stress intensity factor along the front of a 3D rectangular crack by using a singular integral equation method. International Journal of Fracture (2001). , 108-119.

[41] Kassir, M. K. Stress intensity factor for a three-dimensional rectangular crack. Journal of Applied Mechanics (1981). , 48(2), 309-313.

[42] Noda, N. A, & Kihara, T. A. Variation of the stress intensity factor along the front of a D rectangular crack subjected to mixed-mode load. Archive of Applied Mechanics (2002). , 3.

[43] Mastrojannis, E. N, Keer, L. M, & Mura, T. A. Stress intensity factor for a plane crack under normal pressure. International Journal of Fracture (1979). , 15(3), 101-114.

[44] Olson, J. E. Sublinear scaling of fracture aperture versus length: An exception or the rule. Journal of Geophysical Research (2003). B9) 2413-2424.

[45] Mear, M. E, & Rodin, G. J. An isolated Mode I three-dimensional planar crack: The stress intensity factor is independent to elastic constant. International Journal of Fracture (2011). , 172(2), 217-218.

[46] Sneddon, I. N. The distribution of stress in the neighborhood of a crack in an elastic solid. Proceedings of the Royal Society of London. Series A, Mathematical and Physical Sciences (1946). , 187(1009), 229-260.

[47] -Erdogan, F, Sih GC. On the crack extension in plates under plane loading and transverse shear. ASME Journal of Basic Engineering 1963;85 519-527

[48] Pollard, D. D, Segall, P, & Delaney, P. T. Formation and interpretation of dilatant echelon cracks. Geological Society of America Bulletin (1982). , 93-1291.

[49] Atkinson, B. K. Subcritical crack growth in geological materials. Journal of geophysical research (1984). B6) 4077-4114

[50] Olson, J. E. Multi-fracture propagation modeling: Application to hydraulic fracturing in shales and tight gas sands. The 42st U.S. Symposium on Rock Mechanics and 2nd

U.S.-canada Rock Mechanics Symposium, Paper No: ARMA June 29-July 2 (2008). San Francisco, CA, USA., 08-327.

[51] Olson, J. E. Fracturing from highly deviated and horizontal wells: Numerical analysis of non-planar fracture propagation. SPE Rock Mountain Regional/Low Permeability Reservoir Symposium, Paper No. SPE 29573, March (1995). Denver, CO, USA., 20-22.

[52] Olson, J. E, & Wu, K. Sequential versus simultaneous multi-zone fracturing in horizontal wells: Insight from a non-planar, multi-frac numerical model. SPE Hydraulic Fracturing Technology Conference, Paper No: SPE PP, February 6-8 (2012). The Woodland, TX, USA., 152602.

[53] Cruikshank, K. M, Zhao, G, & Johnson, A. M. Analysis of minor fractures associated with joints and faulted joints. Journal of Structural Geology (1991). , 13(8), 865-886.

Injection and Efficiency

Chapter 38

Secondary Fractures and Their Potential Impacts on Hydraulic Fractures Efficiency

Arash Dahi Taleghani, Milad Ahmadi and J.E. Olson

Additional information is available at the end of the chapter

http://dx.doi.org/10.5772/56360

Abstract

Outcrop studies have revealed the presence of abundant cemented fractures in many low permeable formations. Recovered cores have also revealed the opening of some of these smaller size fractures on the wall surface of main hydraulic fractures. Furthermore, early-production well-testing analysis in some of these cases provide estimates for hydraulically induced fracture surface areas which are much larger than the fracture dimensions estimated in fracturing design. Re-opening of these small-size fractures could be a possible reason for this discrepancy. In this paper, we show how and to what extent tensile stresses induced by temperature difference between fracturing fluid and formation fluid or plastic unloading of the formation rock could provide a large enough driving force to open a portion of these small cemented natural fractures laying on the surface of hydraulic fractures. Our thermo-elastoplasticity analysis reveals the effect of net pressure, stratigraphy and also temperature of the fracturing fluid on the number of activated microfractures. Accordingly, potential distributions of activated micro-fractures are estimated. At the end, through an example, we show that the activation of only a small portion of cemented microfractures can increase the total formation contact surface considerably, and consequently increase the initial production by many folds.

1. Introduction

Hydraulic fracturing has been recognized as the most effective technique for economic recovery in tight oil and gas formations in North America [30], [36]. Hydraulically induced fractures increase well-reservoir contact area enormously; hence well productivity improves

greatly after stimulation. During a typical hydraulic fracturing treatment, a mixture of proppant and viscous fluids is injected into the formation to create a fracture. The main mechanism responsible for fracturing the rock is the generation of tensile stresses ahead of pressurized fracture. The direction of the fracture will be perpendicular to the direction of minimum principal in-situ stress [23]. Well-testing analysis done at the early production life of these wells provide estimations for hydraulically induced fracture surface areas which are much larger than the fracture dimensions estimated in fracturing design or predicted areas constrained by the scattering domain of microseismic events. Presence of microcracks might be indicated by increased pore volume and compressibility, as well. This finding is speculated to be related to microcracking [42] i.e. a large population of microcracks could essentially explain this result. It is notable that microcracks are not necessarily micron size. We call them microcrack because they are much smaller than the major hydraulic fractures (millimetres in size). This hypothesis becomes more plausible by considering the fact that a large number of these tight sand and shale gas reservoirs [17] are naturally fractured. Presence of natural fractures and their fractal distribution is a widely observed fact in various tight sand and shale formations. The significance and role of these pre-existing natural fractures on the performance of fracturing treatments and post-frac production are not well-understood; consequently, most analysis is mainly descriptive rather than quantitative. In summary, there is no model to predict the likelihood of opening these fractures in different scales. For instance, few models have been introduced to predict interaction of hydraulic fractures with large size natural fractures [18], [31]. Here, large size natural fractures are fractures with the lengths and heights comparable with the size of hydraulic fractures. Laboratory experiments [10] have confirmed the influence of these large fractures in changing the direction of fracture propagation, and earlier shallow depth mineback experiments have shown similar outcomes [45]. However, there is no similar study about the role of microfractures. Almost all published models in the literature are limited to the cases in which natural fractures have the same height as that of hydraulic fractures. Considering the fact that power-law distribution of natural fractures implies population of small size fractures to be orders of magnitudes more than that of the large size fractures, it is not surprising that induced large fractures are intersecting thousands of these fractures. Due to their small sizes, small natural fractures cannot be propped by proppants; their aperture and therefore their hydraulic conductivity is a function of the inner-fracture fluid pressure. Due to their presence in large numbers, only partial reactivation of these natural microfractures may affect fluid flow pattern near the major fracture. These effects could be in the form of increasing the total effective wellbore-formation contact area and consequently improving hydrocarbon production, or oppositely, these microfractures could act as capillary traps for the fracturing fluid. The entrapped water, which is essentially part of the leakoff volume that will never produce, could hinder hydrocarbons flow from the formation into the major hydraulic fracture.

Low required energy for the re-opening of natural fractures makes them susceptible to re-opening if large enough tensile or shear stresses are somehow generated on the surface of major fractures. Then, depending on the distribution of natural fractures and the strength of their digenetic cements, their possible reactivation may influence hydrocarbon flow considerably. Despite the predominantly compressive stress regime around pressurized fractures

http://dx.doi.org/10.5772/56360

under certain circumstances, it is possible to have tensile stresses. Two main mechanisms responsible for inducing tensile and/or shear forces on the surface of major fractures are thermal stresses and residual stresses due to the plastic deformation of the rock during hydraulic fracturing.

Figure 1 shows a typical response of the bottomhole pressure and temperature measurement during a fracturing treatment. Fluid and proppants have been pumped for a period of time, and the termination is marked by a red line and followed by an extended period of shut-in that lasts much longer than the pumping time [23]. Of particular interest here is that minimum temperature, minimum fracturing fluid pressure and maximum leakoff fluid pressure occurs almost simultaneously within a short period of time after shut-in. Minimum downhole temperature and maximum pore pressure due to leakoff could be essential factors in reducing rock effective stress. The red mark also indicates the onset of depressurization which also locally develops tensile stresses.

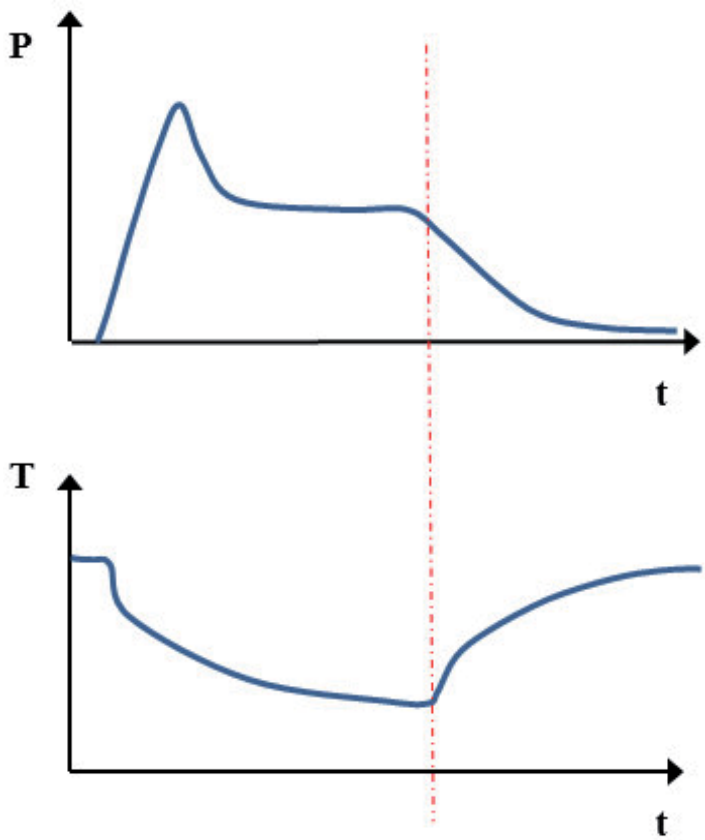

Figure 1. Bottomhole net pressure and temperature history during a typical fracturing treatment is shown above. The red line marks the most likely point for the initiation of secondary fractures as bottomhole temperature is at its lowest point (maximum thermal stress) and unloading started due to pumping termination.

Fracturing fluid is frequently pumped with the temperature very close to the surface temperature; hence its temperature at the bottomhole usually differs from the initial temperature of the reservoir, especially in the case of deep and hot formations. The temperature gradient between the fracturing fluid and formation is a function of formation temperature, injection rate, casing/tubing diameter, the distance from perforations to the surface, heat capacity of fluids, fracture width and treatment pressure [8]. For most cases, fracturing fluid does not have enough time to reach the formation temperature due to its high velocity in the tubing. Because of the fluid migration and heat transfer in the reservoir, such differential temperature induces thermal stresses. The tensile and shear stresses induced by this temperature difference could be large enough to initiate small cracks on the fracture surface or in the case where pre-existing natural fracture are present, these stresses may open them. Thermal cracking happens when induced stresses inside the rock due to cooling exceed the in-situ stress of the formation, this phenomenon is well-documented in waterfloodings of brittle hot rocks [39] and geothermal systems with cold water circulation [46]. Thermal cracking may lead to the formation of clusters of small cracks, or so-called secondary fractures, which are very similar to pavement cracks but on the surface of the main hydraulic fracture.

As mentioned earlier, when the induced stresses inside the rock overcome formation in-situ stresses, re-opening of natural fractures may also occur. However, the spacing and geometry of opened cracks, in addition to previously mentioned parameters, are also functions of natural fractures distribution. Although these thermal induced cracks and re-opened parts of the pre-existing natural fractures have small size in comparison to the main hydraulic fracture, they can tremendously increase the well-formation contact area. For the case of no capillary trapping, the fluid flux inside these secondary fractures is roughly proportional to the cube of the fracture width and to the inverse of spacing length. Based on thermoelasticity analysis for closely spaced fractures, the fracture width is proportional to fracture spacing. Therefore, the fluid flux inside the thermal induced fracture is a quadratic function of spacing length [5]. Moreover, Bazant et al. [5] showed that the ratio of crack depth-to-spacing in pavements (elastic half-space) is a sensitive function of temperature profile inside the crack. Heat transfer for hydraulic fracturing has been studied in the last couple of decades. For instance, Biot et al. [8] proposed a one-dimensional analytical solution for heat transfer in the plane strain geometry. The fundamental solution for a centre of dilation and a point source fluid injection was provided earlier by Cleary [13]. Clifton and Wang [14] utilized this fundamental solution for a pseudo-three dimensional hydraulic fracturing simulations. However, these models are mainly investigating local changes of in-situ stresses rather than the likelihood of initiating secondary fractures. Study on the effect of stress redistribution on fractures due to thermal gradient of rock mass and fracturing fluid received more attention for geothermal reservoirs due to the presence of large temperature differences [3], [5], [46]. Zhou et al. [46] adapted this problem in the context of initiation of secondary fractures from a hydraulic fracture in hot dry geothermal systems with brittle rocks. Dahi-Taleghani et al. [19] considered the effect of induced thermal stress during hydraulic fracturing on opening of cemented natural fractures. They used the concept of cohesive interfaces in the framework of three dimensional finite element methods to show how thermal conductivity of the rock mass could make the popu-

lation of opened natural fractures clustered rather than uniform. Additionally, their model considered interaction between propagating fractures.

Thermal stresses are not necessarily the only driving force behind formation of microfractures or opening of pre-exiting natural fractures. Plastic deformation induced during fracture pressurization results in tensile residual stress upon reduction of fracturing fluid pressure. Therefore, microcrack initiations can be enhanced upon unloading, as long as the pressurization at the pumping stage induces plastic deformation in rock. Cracking due to stress release resulted from unloading is a well-established mechanism in indentation experiments [16]. Choi et al. (2012) explains that plasticity is playing the main role in nucleation of microfractures during unloading. They showed the nucleation of microfractures from microscopic voids during unloading of hydraulic fracture. Plastic deformation induced during pressurization of main hydraulic fracture creates a tensile residual stresses during depressurization of hydraulic fracture. Therefore, these tensile residual stresses initiate the nucleation of microfractures; but compared to microcracks induced by thermal gradient, the effect of tensile residual stresses due to plasticity has not been studied so much. In this paper, the effect of plastic deformation on opening the natural fractures has been studied. In terms of methodology for modelling natural fracture reactivation, this paper is an extension of the work done by Dahi-Taleghani et al. [19] regarding the effect of plastic residual stresses.

As it mentioned before, thermal stresses and plasticity induced residual stresses may generate some microfractures or reactivate pre-existing natural fractures, but activation of these fractures does not necessarily lead to production enhancement due to the increase in contact area. If microfractures act as capillary traps, contact area and productivity index can be considerably influenced. Capillary trapping occurs when hydraulic pressure cannot overcome the capillary entrance pressure of microfracture to open it, and it's a function of pore geometry, rock-fluid interaction and fluid flow inside the pores; therefore, considering capillary pressure effect and trapping mechanism is quite important to achieve a realistic prediction of fractured well productivity and the amount of producible leakoff fluid volume. Pore geometry and rock-fluid interaction control capillary trapping. Capillary trapping effect can become a quite interesting topic in hydraulic fractured reservoirs and naturally fractured reservoirs. To activate natural fractures, fracturing fluid pressure should go beyond the in-situ rock stresses; however, due to small aperture size of these fractures, if the hydraulic pressure cannot overcome the capillary entry threshold pressure of microfracture, formation fluid may not flow via the microfracture to reach the main fracture.

Due to the limited knowledge about the presence of natural fractures and their potential distribution in different formations, their contribution has been ignored or at least has not received enough attention. Only recent advances in characterization of natural fractures and verification of power-law distribution of fractures in different length scales [35], as well as the development of more sophisticated mechanistic models for fracture initiation and propagation such as cohesive crack models, made the investigation about the role of these natural fractures possible.

The remainder of the paper is organized as follows. In the next section, we talk about distribution of natural fractures, which is followed by sections about rock plasticity and a section

regarding cohesive interface constitutive equations to model mechanical behaviour of pre-existing cemented natural fractures. At the end, numerical results of implementing this model for several examples will be presented to examine the significance of induced thermal stress in different situations.

2. Natural facture distribution

Fracture is a mechanical discontinuity in the rock mass formed due to the presence of stress fields in earth's crust (Figure 2). There are wide scale ranges for fractures from micrometre (microfractures) to kilometres (lineaments). Presence of fractures in earth's crust can influence underground fluid flow and physical properties of rock like rock strength. Fractures can influence the velocity of elastic waves and rock elastic moduli [41]. Natural fractures are categorized into four groups [40] based on their genesis : (1) tensile fractures due to compressive stresses, (2) shear fractures due to compressive stresses, (3) tensile fractures due to unloading of compressive stresses, (3) natural hydraulic fractures. Despite indeterministic nature of the aforementioned mechanisms, a large number of outcrop studies have revealed pattern and identifiable organization in fracture orientation and spacing. Due to the limited access to the subsurface to map fractures and limited precision of seismic techniques, outcrops are the main source to speculate fracture's geometry in the subsurface. There are different distribution models used to describe fracture size like fracture length, aperture and tangential or perpendicular displacement due to fracture. Scale-limited laws (lognormal, exponential, gamma and power law) are methods in literature to characterize fracture systems [9], but it should be mentioned that scaling exponents alone cannot act as good criterion to define the whole pattern of fracture networks. Moreover, Bonnet et al. [9] showed that there is a linear relationship between rupture area and frequency scale of tensile fractures in seismometers acting. Field studies have confirmed the existence of a critical threshold that cracks with aperture less than this threshold are fully filled with digenetic materials [34]. Although microfractures are filled with calcite or quartz cements, laboratory measurements have proved that these filled natural fractures may still act as weak surfaces, or in other words, potential paths for rock failure. For instance, lab measurements for Barnett shale samples have shown tensile strength of cemented cracks to be about 10 times less than the tensile strength of intact rocks [27]. There exist some integrated models in the literature that can be utilized for this purpose [33]. By combining the knowledge of natural fracture patterns, cement properties and current in-situ stresses, it is possible to build a model to make a realistic prediction about the distribution of natural fractures in the case of limited core and outcrop data.

Proppants cannot move into microfractures opened during hydraulic fracturing due to their small aperture, which is less than a couple of microns. However, hydraulic pressure can open the microfractures if it goes beyond the local closure stress; therefore, activation of microfractures is function of confining pressure and pore pressure. As it mentioned earlier, contact area between rock-fluid can be considerably affected by the presence of microfractures in large quantities despite their small aperture and depth.

http://dx.doi.org/10.5772/56360

Figure 2. Natural fractures present in a wide range of size and spacing. A pen is used as the scale in this outcrop picture. Depending on the magnitude of induced stresses and others conditions only a portion of these cracks may be reactivated. Effective contact area is determined based on the population of opened fractures (Photo courtesy of Brian Cardott. [25])

3. Elastoplastic effect in fracturing

The mechanical behaviour of quartz or calcite is essentially identified as elastic and brittle, however, clay/organic dominated regions can undergo significant plastic strains. Hence, it is not surprising that excessive fluid pressure present during hydraulic fracturing treatments may induce plastic deformations. This issue has been the subject of several studies in the literature [37], [38], [44]. For instance, it has been shown that plasticity causes shorter and wider fractures. However, most of these plastic deformations are due to high stress near the tip of the hydraulic fracture. The excess pressure in the main fracture may be only 1 or 2 MPa higher than the minimum in-situ stress, and this amount of additional stress may not cause a considerable plasticity unless in very weak formations

These papers were mainly focused on plastic deformations induced at the tip of fractures due to stress concentration at the tip of fractures, while plastic deformation of the surrounding rocks and its possible effects was out of the scope of these papers. Irreversible strain characterizes the plasticity when stress reaches a certain point. After this yielding point, the material

shows elastoplasticity, which means its behaviour is somewhat plastic and also elastic. Equations (1) to (3) show general elastoplastic behaviour in three-dimensional problems for a strain increment $d\varepsilon_{ij}$, where D^{e}_{ijkl}, Q, $d\lambda$ and σ_{ij} are elastic moduli tensor, plastic potential, plastic multiplier and components of stress tensor, respectively.

$$d\varepsilon_{ij} = d\varepsilon^{e}_{ij} + d\varepsilon^{p}_{ij} \tag{1}$$

$$d\varepsilon^{e}_{ij} = D^{e[-1]}_{ijkl} d\sigma_{kl} \tag{2}$$

$$d\varepsilon^{p}_{ij} = d\lambda \frac{\partial Q}{\partial \sigma_{ij}} \tag{3}$$

For flow rule and yield criterion, we used Drucker-Prager criterion, which is a well-known model to describe plastic behaviour of rocks. The Drucker-Prager criterion is an adjusted version of the Von Mises criterion for granular materials like soils and soft rocks. The yield surface for the Drucker-Prager criterion is a circular cone with the form shown in equation (4) where α and k are constants related to internal friction and cohesion of material. The stress at any point can be represented by the vector (σ_1, σ_2, σ_3). This vector can be shown by a corresponding stress point on the π-plane which is constituted of vector s (σ_1- σ_m, σ_2- σ_m, σ_3- σ_m) and ϱ (σ_m, σ_m, σ_m), where σ_m equals to (σ_1+σ_2+σ_3)/3 (Figure 3a). The constants can be obtained from the plot of failure in $J_2^{1/2}$ and J_1 space. Circumscribed Drucker-Prager and Inscribed Drucker-Prager are two criterions for description of Drucker-Prager criterion based on comparison with Mohr-Coulomb criterion (Figure 3b).

$$J_2^{1/2} = k + \alpha J_1 \tag{4}$$

$$J_1 = \frac{1}{3}\left(\sigma_1 + \sigma_2 + \sigma_3\right) \tag{5}$$

$$J^{1/2} = \sqrt{\frac{1}{6}\left(\left(\sigma_1 - \sigma_2\right)^2 + \left(\sigma_1 - \sigma_3\right)^2 + \left(\sigma_2 - \sigma_3\right)^2\right)} \tag{6}$$

4. Initiation and propagation of cracks

There is a considerable number of publications for modelling hydraulic fracturing treatments published since 1955, these solutions are varying from analytical and asymptotic solutions [21], [22], [32] to finite element or boundary element numerical schemes [11], [18], [31]. A compre-

http://dx.doi.org/10.5772/56360

hensive review of these models is given by Adachi et al. [1]. Griffith's criterion is the common method to model fracture propagation in all of these techniques. Fracture propagation in Griffith's criterion is a function of stress intensity factor and rock toughness. Griffith's criterion presumes the presence of an initial fracture and predicts its propagation, hence it is an appropriate method to model major hydraulic fracture propagation, but it cannot predict fracture nucleation. Since, we are interested in predicting fracture initiation on the surface of intact rock or along the cemented natural fractures; we cannot limit our analysis to Griffith's criterion. We use the cohesive interface technique to model reopening of cemented fractures. The cohesive interface model is a constitutive equation to model deformation of discontinuities, which can be easily applied to multiple cracks or incorporates their coalescence. Cohesive interfacial model could also be used to simulate fracture propagation with the advantage of removing stress singularity at the fracture tips [2]. Later laboratory experiments showed that nonlinear region added to cohesive crack models provides better prediction for fracture growth in granular cementious materials like rock and concrete [6]. The cohesive interfacial model considers a cohesive crack of zero width with traction transferring capacity, thus eliminates the stress singularity problem at the crack-tip. Additionally by nature, cohesive interface concept is the best fit for the problems with predefined fracture propagation paths like this problem; however, some sophisticated algorithms has been invented to adaptively add or remove cohesive elements in the computational model upon necessity [47]. In addition, cohesive interfacial models, despite their nonlinear nature, are easy to implement and we will see in the next section how we used this capability to model the initiation of microcracks during hydraulic fracturing.

Cohesive interface model is mainly a nonlinear constitutive equation between the traction and jump in displacement between two bodies. Cohesive interface starts to fail when the applied traction exceeds a critical value and followed by softening, and both are described by traction separation law [43]. Traction-separation law has the flexibility to tune the parameters to find potential function solutions for fracture propagation in different materials [24], [29]. Bilinear law is the simplest form of traction separation law composed of two piecewise linear sections for pre- and post-failure situations (Figure 4). Despite its simplicity as constitutive equation, it has proven capabilities to model fracture behaviour in cementious materials [6]. Quadratic stress law is good candidate for mixed mode condition. In this model, damage initiates the quadratic interaction function involving nominal stress ratios reaching the value of one (Equation 7), while t_n and t_s represents the real values of normal and tangential tractions along the interface, respectively.

$$\left\{\frac{\langle t_n \rangle}{t_{no}}\right\}^2 + \left\{\frac{\langle t_s \rangle}{t_{so}}\right\}^2 = 1 \tag{7}$$

$$\langle t_n \rangle = \begin{cases} t_{n,} & t_n \geq 0 \quad (tension) \\ 0 & t_n \leq 0 \quad (compression) \end{cases} \tag{8}$$

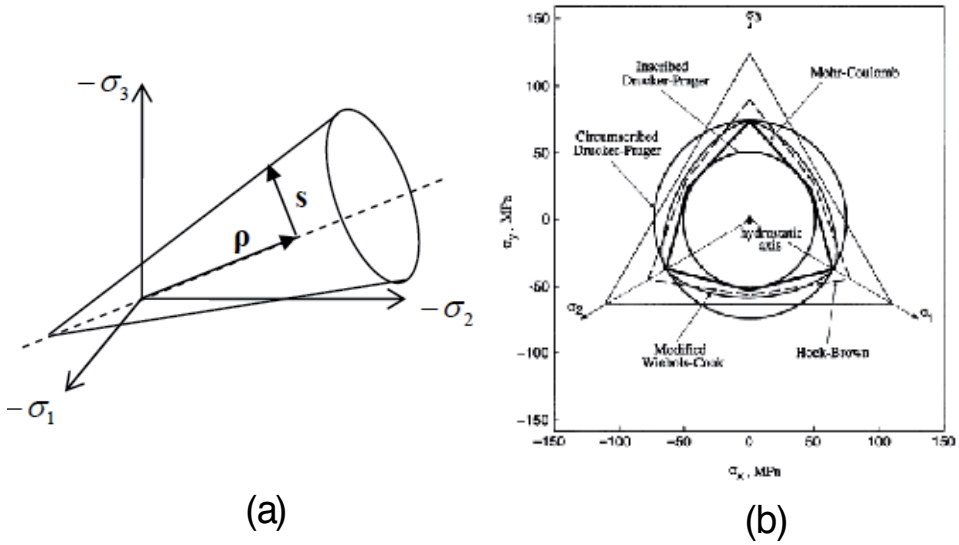

Figure 3. a) The Drucker-Prager criterion, (b) Yield envelopes for Circumscribed Drucker-Prager and Inscribed Drucker-Prager criterion (after Colmenares and Zoback, 2002 [15])

Fracture energy release, cohesive strength, initial cohesive stiffness, critical separation gap at complete failure and critical separation at damage initiation are key parameters to specify irreversible fracturing based on bilinear cohesive law. To model the mixed mode fracture propagation, Benzeggagh-Kenane (BK) fracture criterion is used [7].

For an incompressible and Newtonian fluid, equation (9) represents the continuity equation where the first term shows fracture capacity based on its width change and the second term represents the cross-sectional flow rate of the fracture (no leak-off from fracture into the formation). The tangential flow along the gap between two cohesive walls base on momentum equation for Poiseuille's flow pattern is represented in equation 10 where q, w, p and μ are local flow rate, local crack width, fluid pressure inside the fracture and fracturing fluid viscosity, respectively [4].

$$\frac{\partial w}{\partial t} + \frac{\partial q}{\partial x} = 0 \tag{9}$$

$$q = -\frac{w^3}{12\mu}\frac{\partial p}{\partial x} \tag{10}$$

Analytical solutions for coupled thermo- poroelasticity and only restricted to simple geometries. Therefore, they are not pertinent for a system with numerous factures. Therefore, we used a commercial finite element package, ABAQUS, for modelling purposes.

http://dx.doi.org/10.5772/56360

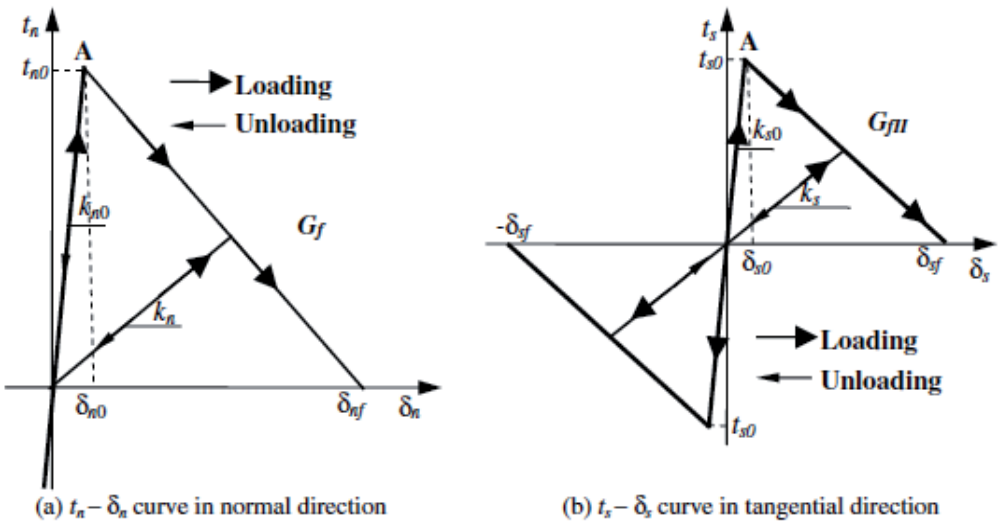

Figure 4. Linear softening law along the cohesive interface.

5. Results and discussion

Commercial finite element software, ABAQUS (Dassault Systèmes Simulia Corp.) [20], is chosen for implementing cohesive crack methods to model secondary fractures initiation and propagation. We begin with the simplest possible geometry for the hydraulic fracture, i.e. a planar fracture. Extension of utilized techniques to non-planar hydraulic fractures does not require introducing any new concept and should be straightforward. Due to the symmetry of the problem with respect to the fracture plane, we only need to simulate half of the geometry. Figure 5 shows the numerical grid with the blue zone showing fracture surface, and the surrounding red zone showing the intact rock. To model pre-existing cemented natural fractures, cohesive elements have been embedded as parallel planes perpendicular to the fracture surface (Z-direction) with 5 cm spacing for this example. Hence, fluid pressure during pumping stage will be introduced only to the fracture surface (blue zone), and the rest of the model will be under the effect of in-situ stress only. In case that any part of the natural fractures (cohesive elements) reaches failure threshold, following the opening of the crack, fracturing fluid is supposed to reach the opened part of the fracture and pressurized it, which is considered by removing failed cohesive elements and adding gap flow to our model to include fracturing fluid pressure and their cooling effect in natural fractures. Our preliminary models showed the significance of this effect on clustering of secondary fractures and their depth of penetration.

The model assumed homogeneous and isotropic properties for mechanical and hydraulic properties of the rock. Additionally, fracturing of the rock is assumed as an irreversible process.

Furthermore, we considered development of major fracture parallel to maximum principal stresses, and natural fractures are assumed to be fully cemented with digenetic cements like quartz or calcite. We used Drucker-Prager model to describe plastic behaviour of rock. A summary of mechanical properties considered for the rock is provided in Table1.

To estimate the parameters of the bilinear cohesive law, no new experimental step is needed. The classic lab tests to measure tensile strength and critical energy release rate should be enough to derive bilinear cohesive law parameters. Among various fracture testing techniques available for homogeneous materials, those which facilitate the stable advance of a fracture are more preferred for interface toughness (G_c) measurements. Examples include the double cantilever crack specimen [26] and Brazilian disk. The tensile strength (σ_{max}) may also be measured using common Brazilian beam tests. Based on the definition of crack energy release rate and bilinear softening, the maximum separation at failure can be determined:

$$G_c = \frac{1}{2}\sigma_{\max}\delta_{\max} \tag{11}$$

Some parametric studies have been done on both cohesive parameters to observe their effects on the pattern of reactivated fractures; however, both parameters are basically a function of the composition of digenetic materials and environmental conditions at the time of their precipitation. Obviously, the values of tensile strength and energy release rate for fracture cements are much lower than the values for rock matrix. Strength of a cemented natural fracture is a function of cement type (composition) and its continuity [27]. Gale et al. [28] evaluated the rupture strength in Barnett shale at different depths for different lithofacies. Based on their published laboratory tests, we chose cohesive properties and other mechanical properties of rock. The values of 12 MPa and 3.2 Pa.m are considered for rupture strength and fracture toughness of cemented fractures, respectively. We assumed that net fracture fluid pressure, applied on blue zone in figure 5, is gradually increased to reach 2 MPa and then slowly bleed off to become equal to reservoir pressure. The induced tensile stress due to loading and unloading process during hydraulic fracturing can reactivate pre-existing fractures. Figures 6 and 7 show that the induced tensile stresses due to fluid pressure decline inside fracture can be as important as induced stresses in the loading process. Figure 6 shows reactivated fractures at different depth from the fracture surface at the peak of fracturing fluid pressure and before pressure decline due to leakoff; main mechanism for failure is shear associated with compressive stresses. However, the main mechanism for failure in Figure 7 is associated with residual tensile stresses induced in the unloading due to plasticity. Fractures in Figure 8 are reactivated due to not only plastic effect but also considering a temperature difference between the rock matrix and the hydraulic fracturing fluid.

Table 3 presents the effect of fracture cement strength, fracture toughness and cement resilience on the pattern of opened fractures i.e. failed cohesive elements. By increasing cement strength, the number of initiated cracks on the cohesive layer decreases (Figure 9 (a) and (b)); in addition, the decrease in cement toughness by nearly one-fifth makes considerable increase in the initiated cracks (Figure 9 (a) and (h)). The values for the failed cohesive elements in Table 3

http://dx.doi.org/10.5772/56360

show that flaws initiation has noticeable dependency on cohesive stiffness. Small decrease in the cohesive stiffness leads to considerable increase in the cohesive damage, indicating increase of contact area between rock-fluid. As it showed in Figures 6 and 7, loading-unloading residual stress may be considerably effective in reactivating pre-existing natural fractures; moreover, it may have a significant influence on fracture reactivation when assisted by induced thermal stresses due to temperature difference between hydraulic fracturing fluid and formation rock (Figure 9).

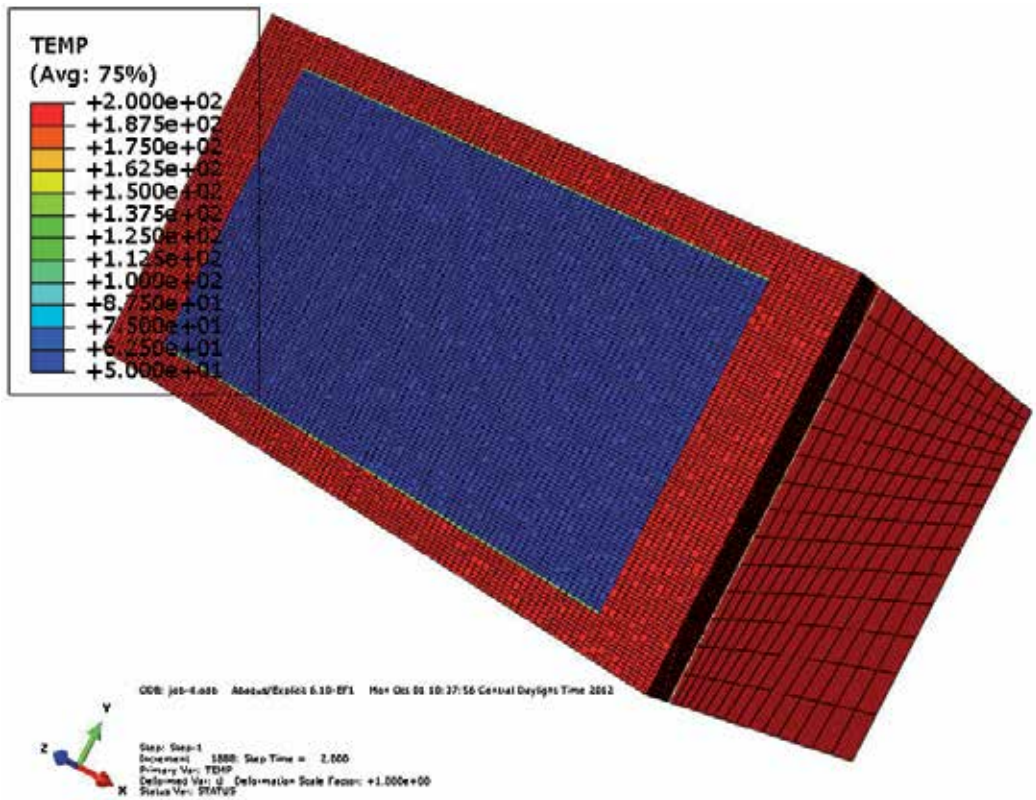

Figure 5. The three-dimensional finite element model used here, which is a one-half of the fracture, is shown. Fracture surface is meshed with a fine grids.

In Figures 8 and 9, initial temperature of 200°C for the rock is selected, and the expansion coefficient of rock matrix is assumed to be $1.5^{x}10^{-5}$. The surface of hydraulic fracture is exposed to hydraulic fracturing fluid with temperature of 150°C. The temperature difference between hydraulic fracturing fluid and rock induced tensile stresses on the rock matrix. This tensile stress can be intensified by the induced tensile stresses due to elastic unloading of hydraulic fracture plastic deformation as shown in Figure 8. Figure 9 presents the pattern of reactivated natural fractures of Table 3 at the depth on-third of cohesive layer depth far away from the surface of hydraulic fracture.

Young's modulus	26 GPa
Rock density	2100 Kg/m^3
Rock friction angle	30°
Rock dilation angle	20°
Poisson's ratio	0.27
Rock yield stress	30MPa

Table 1. Rock properties in simulation

Case	Tensile strength (MPa)	Cement toughness (Pa.m)	Hydraulic pressure (MPa)	Cohesive stiffness (GPa)
1	12	3.2	2	6.4
2	1.2	3.2	2	6.4
3	12	3.2	2	0.64
4	12	32	2	6.4
5	20	3.2	2	6.4
6	12	3.2	2	1
7	12	3.2	2	3.4
8	12	15	6.4	2

Table 2. Cohesive parameters

Case	Total cohesive elements	Failed cohesive elements after loading	Failed cohesive elements after unloading	Failed cohesive elements by Thermoplasticity	Studied parameter
1	14700	3406	4692	5511	Reference case
2	14700	0	0	7923	Tensile strength
3	14700	0	0	0	Cohesive Stiffness
4	14700	0	0	1	Cement toughness
5	14700	415	1247	1683	Tensile strength
6	14700	0	0	0	Cohesive Stiffness
7	14700	18	74	154	Cohesive Stiffness
8	14700	298	484	2440	Cement toughness

Table 3. Failed cohesive elements

http://dx.doi.org/10.5772/56360

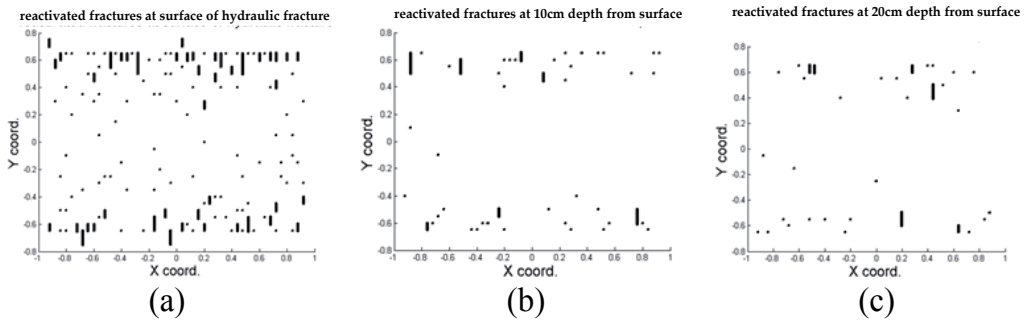

Figure 6. Reactivated fractures after loading for case 5 of Table 2 at different depths

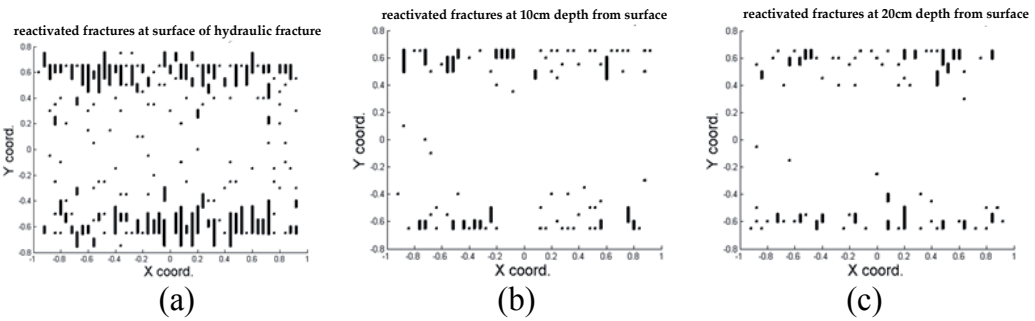

Figure 7. Reactivated fractures after unloading for case 5 of Table 2 at different depths

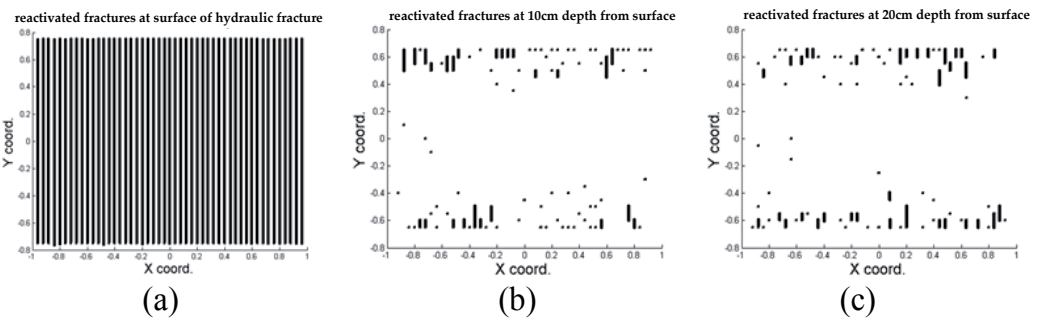

Figure 8. Reactivated fractures by thermo-plasticity for case 5 of Table 2 at different depths

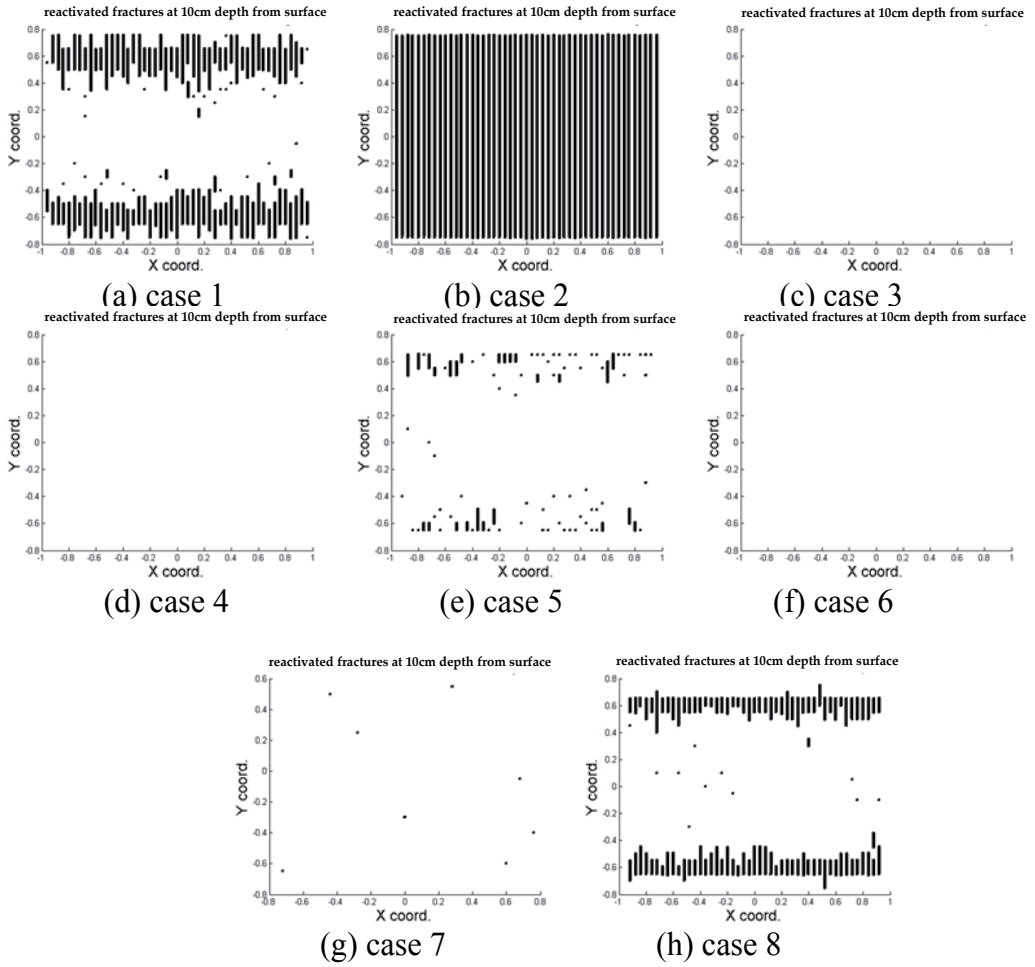

Figure 9. Reactivated fractures by thermoplasticity for different cases of Table 2 at one-third depth from the surface of hydraulic fracture

6. Conclusion

Induced tensile stresses are expected to occur in rocks with significant plastic behaviour during loading and unloading of hydraulic fractures. These induced stresses can open pre-existing natural fractures in the formation and even open the cemented natural fractures. These activated fractures can provide more rock-fluid contact area. The size of these natural fractures is much less than the main hydraulic fracture but presence of these fractures in considerable numbers can significantly increase the contact area between the wellbore and formation. The path of initiation and propagation of these fractures can be induced by natural fractures. To study their effect, a three-dimensional finite element model with cohesive interfaces embedded

http://dx.doi.org/10.5772/56360

in the rock. The effect of energy release rate and cohesive tensile strength investigated and it was shown that the decrease of these parameters can activate more natural fractures but not in a uniform pattern. Moreover, the simulation showed that the effect of plasticity can be more considerable when it would be helped by thermal stress induced by temperature difference between rock matrix and fracturing fluid.

Author details

Arash Dahi Taleghani[1], Milad Ahmadi[1] and J.E. Olson[2]

1 Louisiana State University, USA

2 The University of Texas at Austin, USA

References

[1] Adachi, J, Siebrits, E, Peirce, A, & Desroches, J. Computer simulation of hydraulic fractures, International Journal of Rock Mechanics & Mining Sciences 44, (2007). , 739-757.

[2] Barenblatt, G. K. the mathematical theory of equilibrium cracks in brittle fractures. Journal of Applied Mechanics, (1962).

[3] Barr, D. T. Thermal cracking in nonporous geothermal reservoirs. Master Thesis, Department of Mechanical Engineering, MIT, (1980).

[4] Batchelor, G. K. An introduction to fluid dynamics. Cambridge University Press, Cambridge, UK, (1967).

[5] Bazant, Z. P, Wahab, M, & Instability, A. B. and spacing of cooling or shrinkage cracks. Journal of the Engineering Mechanical division, (1979).

[6] Bazant, Z. P, & Planas, J. Fracture and size effect in concrete and other quasibrittle materials. Published by CRC Press; first edition, (1998). 084938284

[7] Benzeggagh, M. L, & Kenane, M. Measurement of mixed-mode delamination fracture toughness of unidirectional glass_epoxy Composites with Mixed-mode Bending Apparatus. Journal of Composites Science and Technology, (1996).

[8] Biot, M. A, Masse, L, & Medlin, W. L. Temperature analysis in hydraulic fracturing. Journal of Petroleum Technology, (1987).

[9] Bonnet, E, Bour, O, Odling, N. E, Davy, P, Main, I, Cowie, P, & Berkowitz, B. Scaling of fracture systems in geological media. Reviews of Geophysics, (2001).

[10] Bunger, A. P, & Detournay, E. Experimental validation of the tip asymptotics for a fluid-driven fracture. Journal of the Mechanics and Physics of Solids. (2008). , 56(11), 3101-3115.

[11] Chen, Z. Finite element modelling of viscosity-dominated hydraulic fractures. Journal of Petroleum Science and Engineering, (2012).

[12] Choi, J. W, Duncan, I. J, & Rodin, G. J. Microcrack nucleation in porous solids under predominantly compressive stress states with applications to shale gas exploration. Proceedings in Forty-sixth US Rock Mechanics / Geomechanics Symposium, Chicago, Illinois, USA, June (2012). , 24-27.

[13] Cleary, M. P. Fundamental Solutions for a Fluid-Saturated Porous Solid, Int. J. Solids Structures, (1977). , 13, 785806.

[14] Clifton, R. J, & Wang, J. J. Modelling of in-situ stress change due to cold fluid injection. Paper SPE 22107 presented at the (1991). International Arctic Technology Conference, Anchorage, AL, May., 29-31.

[15] Colmenares, L. B, & Zoback, M. D. A statistical evaluation of intact rock failure criteria constrained by polyaxial test data for five different rocks. International Journal of Rock Mechanics and Mining Science, (2002).

[16] Cook, R. F, & Pharr, G. M. Direct observation and analysis of indentation cracking in glasses and ceramics. Journal of the American Ceramic Society, (1990).

[17] CurtisJohn B. Fractured shale-gas systems. AAPG bulletin 86.(2002). , 11(2002), 1921-1938.

[18] Dahi TaleghaniA., Olson, J.E.; Numerical modelling of multi-stranded hydraulic fracture propagation: accounting for the interaction between induced and natural fractures, SPE Journal, (2011).

[19] Dahi TaleghaniA., Olson, J.E., Wan, W.; Thermal reactivation of microfractures and its potential impact on hydraulic fractures efficiency. Proceedings in SPE Hydraulic Fracturing Technology Conference, Woodlands, Texas, USA, February (2013). , 4-6.

[20] Dassault Systèmes Simulia CorpABAQUS Analysis User's Manual, Version 6.10, Providence, RI, USA, (2010).

[21] Detournay, E, & Garagash, D. The tip region of a fluid-driven fracture in a permeable elastic solid, Journal of Fluid Mechanics, (2003). , 494, 1-32.

[22] Detournay, E. Propagation regimes of fluid-driven fractures in impermeable rocks, International Journal of Geomechanics, (2004). , 4, 1-11.

[23] Economides, M. J, & Nolte, K. G. Reservoir Stimulation published by Wiley, (2000). 0-47149-192-6

[24] Elices, M, Guinea, G, Gomez, J, & Planas, J. The cohesive zone model: advantages, limitations, and challenges. Journal of Engineering Fracture Mechanics, (2002).

[25] Energy Minerals Division; Gas shale tricky to understandBrian Cardott (EMD Gas Shale Committee member). http://www.aapg.org/explorer/divisions/(2006). emd.cfm/.

[26] Evans, A. G, Hutchinson, J. W, & Wei, Y. Interface adhesion: effects of plasticity and segregation. Acta Materialia 47.(1999). , 15(1999), 4093-4113.

[27] Gale, J. F. W, Reed, R. M, & Holder, J. Natural fractures in the Barnett Shale and their importance for hydraulic fracture treatments. AAPG bulletin 91.(2007). , 4, 603-622.

[28] Gale, J. F. W, & Holder, J. Natural fractures in the Barnett Shale: constraints on spatial organization and tensile strength with implications for hydraulic fracture treatment in shale-gas reservoirs. Proceedings in the 42nd US Rock Mechanics Symposium and 2nd U.S.-Canada Rock Mechanics Symposium, held in San Francisco, June July 2, (2008). , 29.

[29] Hillerborg, A, Modeer, M, & Petersson, P. Analysis of crack formation and crack growth in concrete by means of fracture mechanics and finite elements. Journal of Cement and Concrete Research, (1976).

[30] Holditch, S. Tight gas sands. Journal of Petroleum Technology 58.(2006). , 6, 86-93.

[31] Jeffrey, R, & Zhang, X. Thiercelin, M; Hydraulic Fracture Offsetting in Naturally Fractures Reservoirs: Quantifying a Long-Recognized Process. SPE Hydraulic Fracturing Technology Conference. (2009).

[32] Khristianovic, S. A, & Zheltov, Y. P. Formation of vertical fractures by means of highly viscous fluid. Proceedings of the fourth World Petroleum Congress, Rome, Italy, (1955).

[33] Laubach, S, Marrett, R, & Olson, J. (2000). New directions in fracture characterization, *The Leading Edge*, , 704-711.

[34] Laubach, S. E. (2003). Practical approaches to identifying sealed and open fractures, AAPG Bulletin, April 2003, , 87(4), 561-579.

[35] Marrett, R, Ortega, O. J, & Kelsey, C. M. Extent of power-law scaling for natural fractures in rock. Geology (1999). , 27(9), 799-802.

[36] Moniz, E. J, Jacoby, H. D, & Meggs, A. J. M. The future of natural gas- an interdisciplinary MIT study.(2011). http://mitei.mit.edu/publications/reports-studies/future-natural-gas).

[37] Papanastasiou, P. C. A coupled elastoplastic hydraulic fracturing model. International Journal of Rock Mechanics and Mining Science, (1997).

[38] Papanastasiou, P. C, & Thiercelin, M. Influence of Inelastic Rock Behaviour in Hydraulic Fracturing. International Journal of Rock Mechanics and Science, (1993).

[39] Perkins, T. K, & Gonzales, J. A. The effect of thermoelastic stresses on injection well fracturing. SPE Journal (SPE PA), (1985). , 11332.

[40] PollardDavid D., and Atilla Aydin. Progress in understanding jointing over the past century. *Geological Society of America Bulletin* 100.(1988). , 8(1988), 1181-1204.

[41] Seeburger, D. A, & Zoback, M. D. The Distribution of natural fractures and joints at Depth in crystalline rock. Journal of Geophysical Research, (1982).

[42] Sondergeld, C. H, Newsham, K. E, Comisky, J. T, Rice, M. C, & Rai, C. S. (2010). Petrophysical considerations in evaluating and producing shale gas resources. SPE-131768

[43] Tvergaard, V, & Hutchinson, J. W. Effect of strain-dependent cohesive zone model on predictions of crack growth resistance. International Journal of Solids and Structures, (1996).

[44] van den HoekP., van den Berg, J., Shlyapobersky, J.; Theoretical and experimental investigation of rock dilatancy near the tip of a propagating hydraulic fracture. International Journal of Rock Mechanics and Mining Science, (1993).

[45] Warpinski, N. R, & Teufel, L. W. Influence of geologic discontinuities on hydraulic fracture propagation, Journal of Petroleum Technology, page: (1987). , 209-220.

[46] Zhou, X, Aydin, A, Liu, F, & Pollard, D. D. Numerical modelling of secondary thermal fractures in hot dry geothermal reservoirs. Proceedings in Thirty-Fifth Workshop on Geothermal Reservoir Engineering Stanford University, Stanford, California, February 1-3, (2010). SGP-TR-188).

[47] ZhouFenghua, and Jean-Francois Molinari. Dynamic crack propagation with cohesive elements: a methodology to address mesh dependency. International Journal for Numerical Methods in Engineering 59.(2004). , 1(2004), 1-24.

Chapter 39

Importance of Fracture Closure to Cuttings Injection Efficiency

Mao Bai, Arturo Diaz, John McLennan and Juan Reyna

Additional information is available at the end of the chapter

http://dx.doi.org/10.5772/56070

Abstract

The major benefit of adequate fracture closure is to release injection pressure and restore it to its initial magnitude during the shut-in period to prevent gradual pressure build-up over the injection batches that follow. This paper examines a number of injection cases where the benefits of adequate fracture closure and the detrimental impacts of insufficient fracture closure are respectively revealed.

In-depth examination of fracture closure impact can be set for short durations with relatively fewer injection batches, as well as for long periods with numerous batch injections. The former scenario focuses on determining the physics of the individual fracture closure, while the latter situation emphasizes the general trend with respect to peak pressure at the end of injection and terminal pressure at the end of the shut-in period.

In addition, this paper addresses the added complexities during fracture closing after shut-in that can be identified from the relationship between injection pressure and the G function superposition derivative. Straight-line behavior usually indicates that the formation is homogeneous and leak-off from the fracture into the formation is linear. Other responses such as concave or convex shapes of the G superposition derivative relationship may indicate the formation is either naturally fractured or tight (i.e., low permeability). Or, the pressure decline shapes may imply fracture tip extension, or fracture height recession. Direct examination of the pressure decline curves may reveal the relationship between the fracture responses and formation characteristics.

1. Introduction

As regulatory restriction on the disposal of solid wastes such as drilling cuttings becomes increasingly tightened worldwide, cuttings injection (CI) into an existing well or a dedicated well becomes standard and required operation in drilling. Various guidelines and best practices in CI operations were established to accommodate local conditions and requirements. A systematically designed CI operation can be seen in reference [1].

One of the very important tasks to ensure a successful CI operation is to continuously monitor injection pressure behavior. Among various pressure responses, the characteristics of fracture closure after shut-in directly relate to the quality of pressure control and thus to the ability to prevent near-well screen outs and unexpected shut down of injection wells.

Fracture closure can be assessed empirically by capturing the inflection point in the pressure decline curve. The inflection point generally reflects the transition between linear or bi-linear flow within the hydraulic fracture and pseudo-radial flow outside the hydraulic fracture.

Fracture closure can also be evaluated more accurately using analytical methods. Among various methods, popular ones are: a) the square-root time method to determine the transition between bi-linear flow and pseudo-radial flow using the filtration theory proposed by reference [2]; b) the Horner time method to determine early time fracture flow and late time pseudo-radial flow (see reference [3]); c) the *G* function method to identify the onset of fracture closure by examining the transition of the flow pattern proposed by Knolte (see reference [4]); and d) the superposition *G* function derivative method to determine the reversal of the *G* derivative that signals the transition between bi-linear flow and pseudo-radial flow proposed by Barree (see reference [5]).

This paper is intended to explore the physics of fracture closure behind the pressure decline curves. By examining the pressure responses in the CI pressure monitoring cases, patterns of both successful and unsuccessful pressure control were captured. Observations reveal that the length of duration in the shut-in period between the injections is a critical parameter with respect to the quality of pressure dissipation and fracture closure. Cuttings injection efficiency is a function of the magnitude of the disposal domain of the stimulated fracture volume.

Sensibly interpreting the physics of fracture closure from bottom-hole pressure responses can be difficult due to the inability to directly measure hydraulic fracture evolution. By comparing various fracture decline curves with reference to their relation to the *G* function and superposition derivatives, this paper identifies the key parameter as the pressure decline curve shape. The conventional interpretation of pressure decline with regard to the physical behavior of hydraulic fractures appears to be insightful. However, verification of this interpretation continues to be a challenge to the current technology.

http://dx.doi.org/10.5772/56070

2. Quality of pressure maintenance in CI operations

Figure 1 provides a long-term assessment on batch cuttings injection. Four periods of pressure responses can be divided into:

- Period A – gradual pressure build up and difficulty in fracture closing
- Period B – good fracture closure
- Period C - excellent fracture closing
- Period D - gradual pressure build up and difficulty in fracture closing

Periods A and D form a repeat cycle with slightly higher peak pressures in Period D than in Period A. It is easily seen that the longest time for pressure dissipation was during Period C. This also led to the best possible fracture closure and lowest terminal pressure among all pressure decline curves.

The physics of fracture closing and its relation to pressure response can be more complex than from the stated single event or relation alone. For example, the fracture could be closed on cuttings so that the terminal pressure is high. In general, a slow leakoff can be envisioned as the equivalence of difficult in fracture closing. The sufficient pressure dissipation can also be caused by the initiation of a new fracture in a different orientation from the previous one, or an increase in fracture aperture due to its connection to natural fractures, or anything else. For simplicity in this paper, however, we contribute the pressure dissipation to the fracture closure without resourcing to its physical origins.

Figure 2 shows the pressure responses from 28 batches of cuttings injection separated into five periods (A-E). Significant rising peak pressures during Periods A, B, C and E reflect difficulties in cuttings injection. This is in contrast to the smaller peak pressure increase in Period D that indicates relatively easy injections. A couple of good pressure relief or deep drop terminal pressures are seen in injection periods B and E.

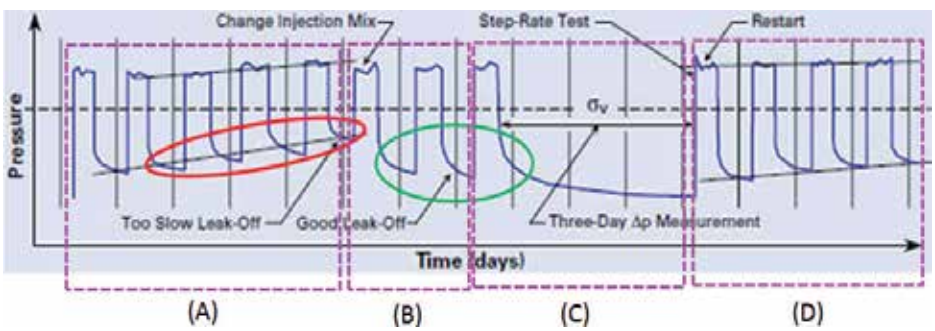

Figure 1. Pressure responses over long period of cuttings injection. (A): gradual pressure build up due to insufficient fracture closing; (B): good fracture closing; (C): excellent fracture closing with sufficient time; and (D): gradual pressure build up due to insufficient fracture closing.

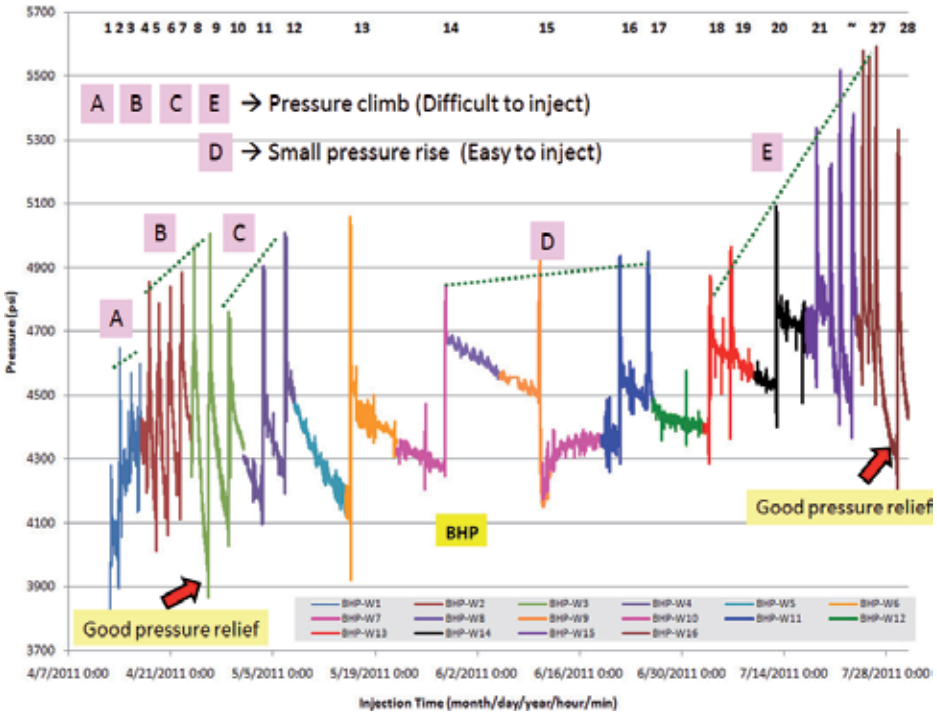

Figure 2. Observed bottom-hole pressures during 28 injection batches. Durations A, B, C and E show the rising peak pressures that are the indication of difficulties in cuttings injection. Duration D shows a slight rise of peak pressure that is the indication of easier cuttings injection.

When the injection batches were extended to 36 and we examined the well-head pressure, Figure 3 indicates that the average difference between the peak well-head pressure and terminal well-head pressure is 800 psi, while the average increase of well-head pressure (WHP) over the entire injection period is 400 psi. Therefore, the rate of pressure increase is 50% (i.e., rate = $\Delta P/P = 0.5$). Experience tells us that a 50% increase in pressure could be too high. For pressure to be manageable, the increase should be under 40%. Either injection pressure has reached its maximum value or the disposal domain capacity is restricted due to intersecting low permeable zones or as a result of stress reorientation when crossing the stress barrier. Either an adjustment to the injection plan or an alternative approach needs to be implemented. The good news from Figure 3 is that both peak pressure and terminal pressure at the final injection period show the declining trend, an indication of pressure relief.

The following information can be obtained from Figure 3 for each injection cycle:

- Peak value of well-head pressure
- Instantaneous shut-in well-head pressure (ISIP)
- Terminal well-head pressure

http://dx.doi.org/10.5772/56070

These three well-head pressure values can be simply divided into two pressure groups:

- Group A: injection pressure (before shut-in)
- Group B: declining pressure (after ISIP)

With respect to the trend of well-head pressure in peak, ISIP, and terminal values over time shown in Figure 3, Figure 4 shows the linear increasing trend correlating pressure and elapsed time with good correlation for the peak pressure, average correlation for the terminal value, and poor correlation for the ISIP value.

Examining four individual injections (i.e. injections A, B, C and D) as shown in Figure 5, it is noted that the time between injections A and B is quite short. As a result, there is not sufficient time for pressure to dissipate in injection A. For other injections (i.e. injections B, C, and D), there is sufficient time for the pressure to dissipate to the initial injection value.

If sufficient time is not given between injections, the result of the injection will not be as effective. Figure 6 shows that batches 17 and 19 are almost unnecessary because they are close to batches 16 and 18 so the pressure decline curves follow the same trend lines of batches 16 and 18 without being affected by injections 17 and 19. On the other hand, injections 17 and 19 may be viewed as two "free" injections because the general pressure fall-off behavior has not been affected. Figure 6 also shows the gradual increase of ISIP from 4627 psi in batch 16 to 4724 psi in batch 18, and finally to 4820 psi in batch 20. The rising ISIP is an indication in the increase of fracture closure pressure and collectively the pressure build up due to insufficient fracture closing.

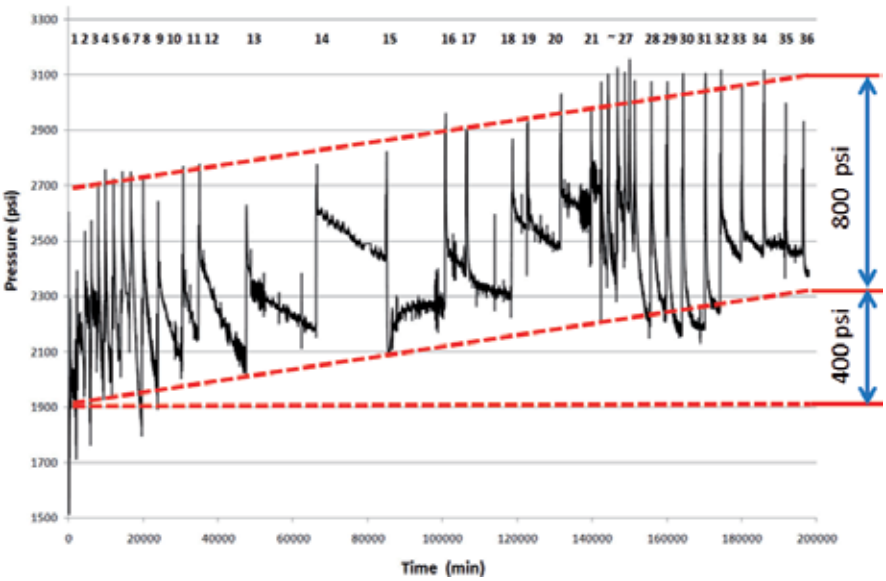

Figure 3. Observed WHP over 36 injection batches with an average pressure increase of 400 psi and differences between peak WHP and terminal WHP of 800 psi. The rate of pressure increase is 50%.

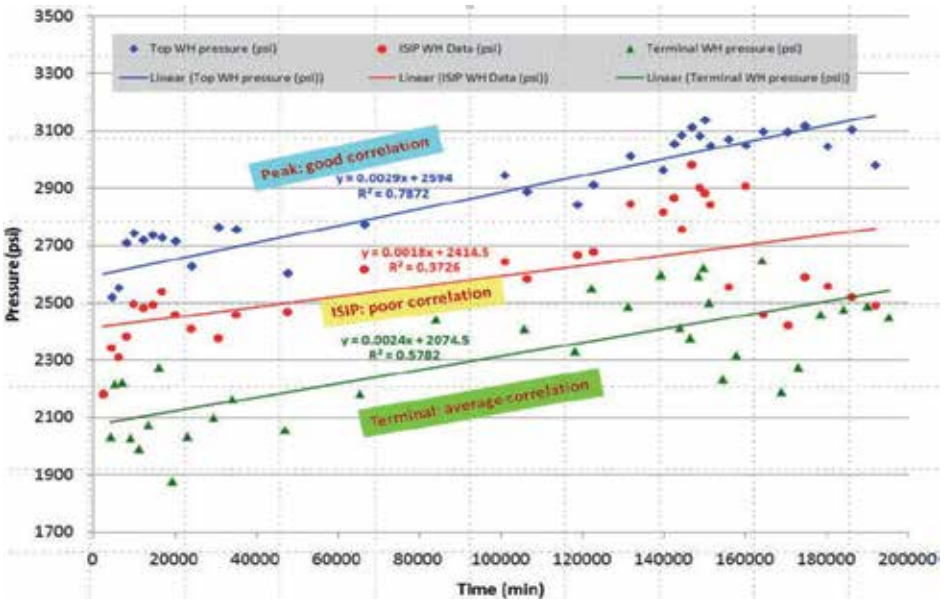

Figure 4. The trend of the well-head pressure in peak, ISIP, and terminal values over the injection period showing good linear correlation for the peak value, average linear correlation for the ISIP value, and poor linear correlation for the terminal value.

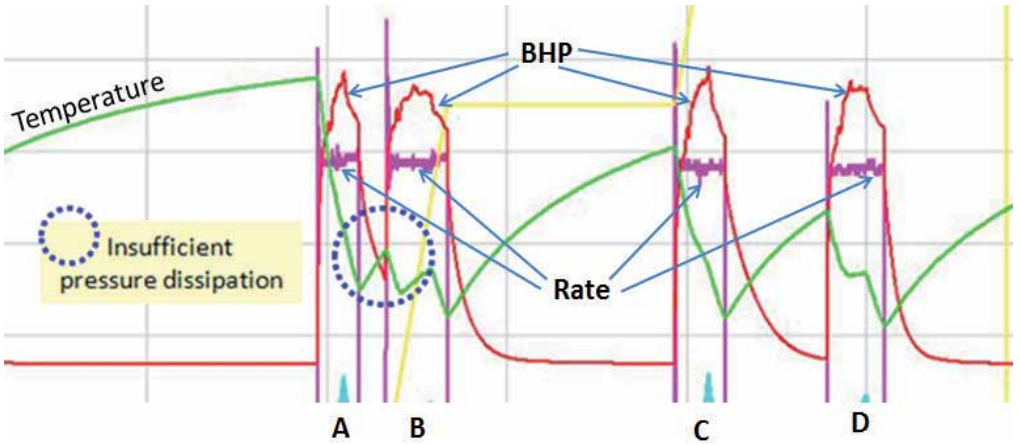

Figure 5. Pressure responses from four injections where the red line is bottom-hole pressure (BHP), the pink line is injection rate, and the green line is temperature. Pressure dissipation for injection A is insufficient. Pressure dissipations for injections B, C, and D are sufficient. The temperature drop validates the entry of injection fluid at the perforation.

http://dx.doi.org/10.5772/56070

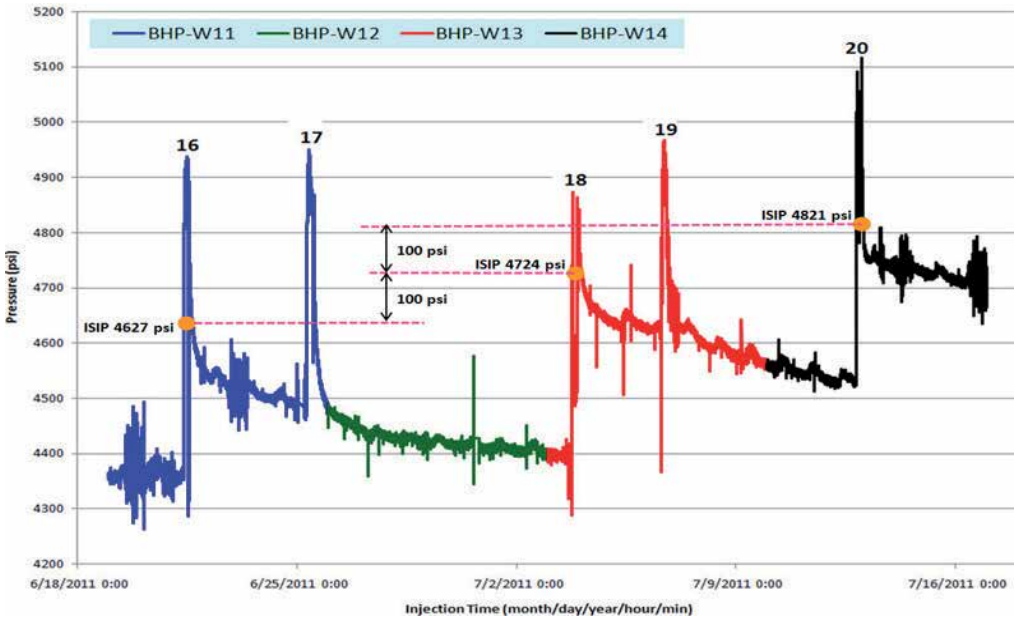

Figure 6. Injection pressure responses for batches 16 through 20. Injection batches 17 and 19 appear to be unnecessary because they are too close to batches 16 and 18, respectively. The pressure decline for batches 17 and 19 follows the same trend lines as batches 16 and 18.

3. Fracture closure analysis

Accurately determining fracture closure pressure is important for the following factors: a) minimum horizontal stress or fracture gradient, b) fracture efficiency, and c) formation properties and responses. The most popular method used to determine closure pressure is a MiniFrac test. Figure 7 shows the BHP and corresponding step injection rate from a MiniFrac test. The point of LOP in BHP is defined as the leakoff point that is an indication of initial near-well fracturing. LOP is also termed as an extension pressure point. The point of BP in BHP is defined as the breakdown pressure that may indicate the initiation of substantial fracturing into the formation. The vertical pressure drop after the peak of BHP depicts the range of the instantaneous shut-in pressure (i.e., upper and lower boundaries of ISIP). The vertical pressure drop is the result of perforation friction loss. After ISIP, pressure declines are accompanied by injection fluid leakoff and fracture closing. Fracturing treatment efficiency is defined as the ratio of fracture volume at the end of pumping to the total injected volume (see reference [6]).

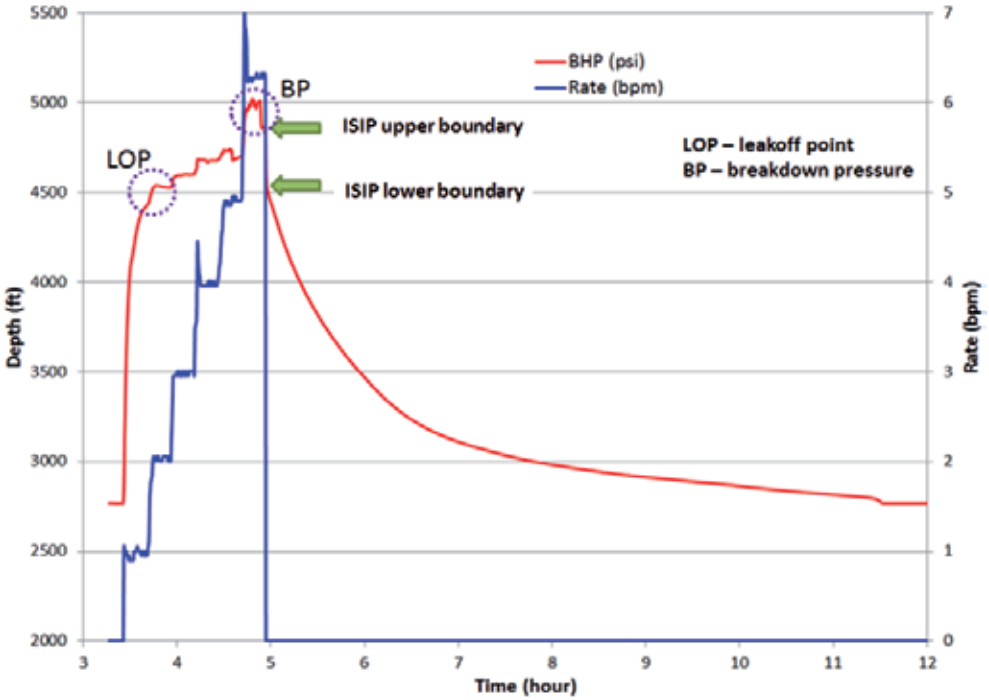

Figure 7. Responses of BHP (in red) and corresponding injection rate (step rate, in blue) from a MiniFrac test: a) pressure increased sharply until generating a small fracture in LOP; b) formation breakdown at BP and small fracture propagation; c) shut-in, and d) pressure leakoff and fracture closing.

4. Implications of fracture behavior from *G* function superposition derivative

In Figure 8, Barree, et al. (reference [5]) suggested that the normal leakoff (NL) from hydraulic fracture after shut-in leads to a straight line originated from the *G* function time in the form of the *G* function superposition derivative (i.e. G dP/dG). Fracture closure time is identified when the *G* function superposition derivative (GFSD) deviates from the straight line in a critical curve slope change.

Any initial response of GFSD that is different from a straight line as shown in Figure 8 can be interpreted as an abnormal leakoff. In addition, the non-straight-line behavior can be caused by events other than leakoff, such as fracture tip growth or height reduction, etc. In Figure 9, nine cases of the pressure to *G* time relationship are shown as follows:

- Case (a): normal leakoff Case 1 (NL-1)
- Case (b): normal leakoff Case 2 (NL-2)
- Case (c): normal leakoff Case 3 (NL-3)

http://dx.doi.org/10.5772/56070

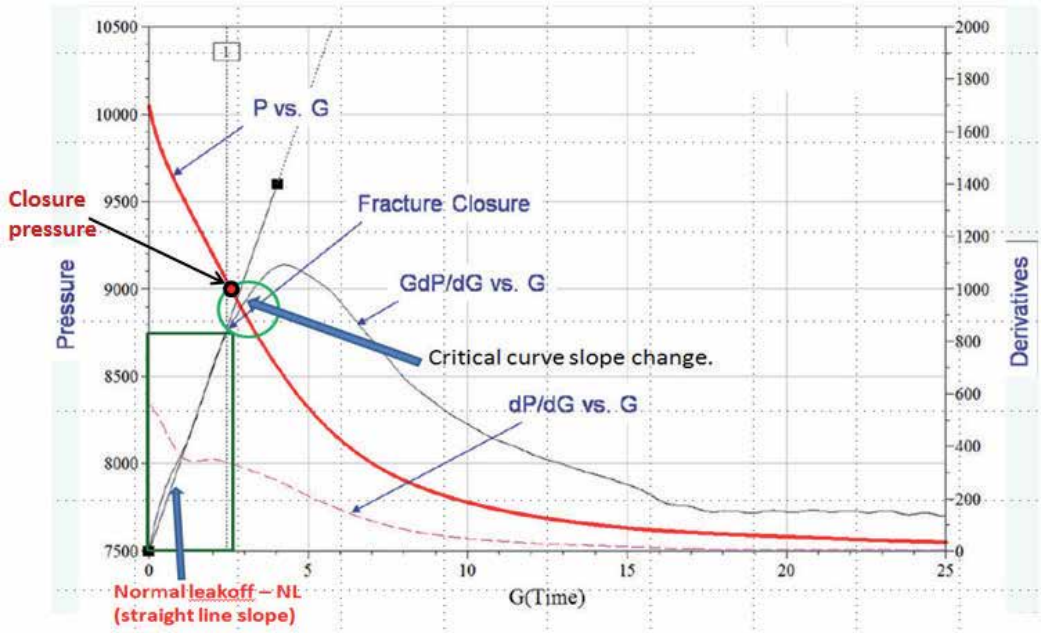

Figure 8. Determination of closure pressure from the GFSD curve to identify the critical curve slope change. The initial straight line indicates normal leakoff.

- Case (d): pressure-dependent leakoff Case 1 (PDL-1)
- Case (e): pressure-dependent leakoff Case 2 (PDL-2)
- Case (f): pressure-dependent leakoff Case 3 (PDL-3)
- Case (g): fracture tip extension Case 1 (FTE-1)
- Case (h): fracture height recession Case 1 (FHR-1)
- Case (i): fracture height recession Case 2 (FHR-2)

It is interesting to note that GFSD follows a straight line for NL from the beginning to the time when the GFSD changes slope, indicating a linear flow is maintained within the hydraulic fracture during the fracture closing.

For PDL, GFSD is above the straight line and becomes convex from the beginning; then the GFSD follows a straight line before the GFSD changes slope. In the convex portion of GFSD,

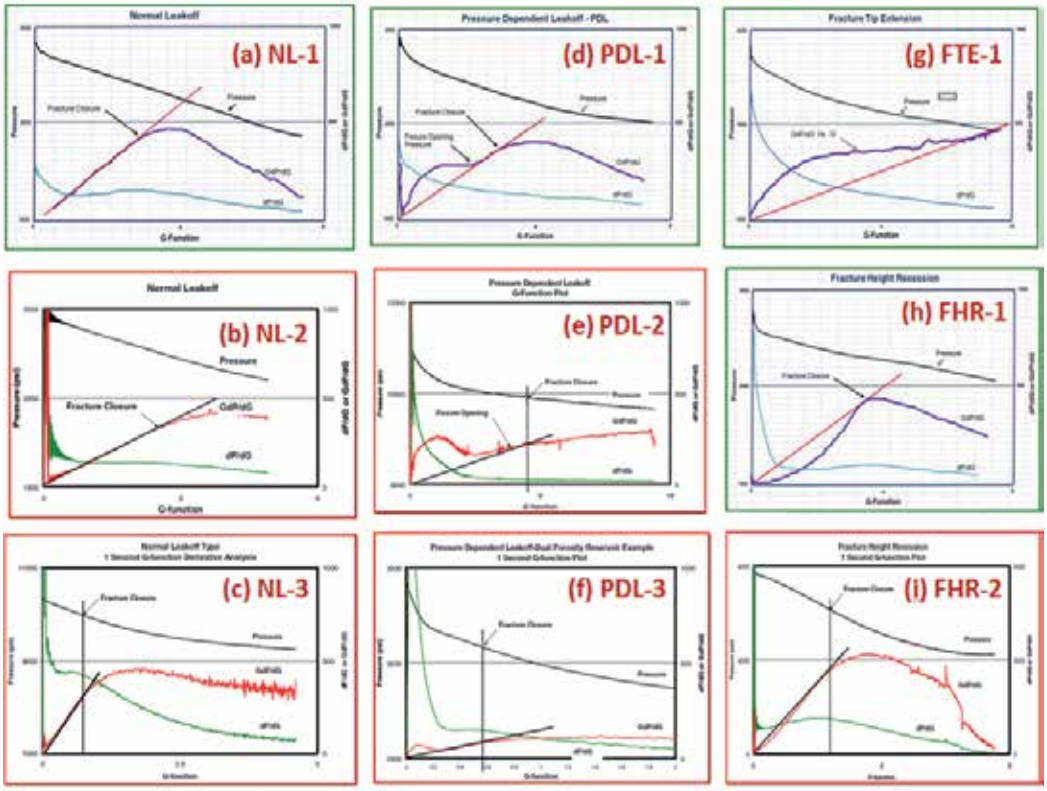

Figure 9. After shut-in fracture responses from the *G* function superposition derivative: normal leakoff Cases a, b, and c (NL-1, NL-2, and NL-3); pressure dependent leakoff Cases d, e, and f (PDL-1, PDL-2, and PDL-3); fracture tip extension Case g (FTE-1); and fracture height recession Cases h and i (FHR-1 and FHR-2).

the flow within the hydraulic fracture is affected by 'back stress' in the far field, a poro-elastic coupled response that demonstrates the interactive behavior between rock deformation and fluid flow. Another interpretation of pressure-dependent leakoff is that the existence of natural fractures deviates the path of GFSD from the straight line to a convex curve.

The response of GFSD from fracture tip extension (FTE) is similar to PDL except that there is no linear leakoff period after the convex portion of the GFSD curve.

For fracture height recession (FHR), the GFSD curve is concave from the beginning until the GFSD changes slope. The greater pressure drop within the hydraulic fracture is the result of fracture geometric reduction or fracture height recession.

Comparing the selected cases using the relationship between BHP and the linear *G* function in Figure 10, the following interesting observations can be made:

- Normal leakoff cases (NL-1 and NL-2) lead to straight lines between P and G.

http://dx.doi.org/10.5772/56070

- Pressure-dependent leakoff cases (PDL-1 and PDL-3) result in the concave shapes of the P - G relationship.
- Fracture tip extension cases (FTE-1) and fracture height recession cases (FHR-1) result in a concave shape of the P – G relationship in the beginning and then change to convex.

Cases c (NL-3) and e (PDL-2) have different pressure magnitudes than the other cases. Figure 11 indicates that PDL-2 maintains the concave shape of the P – G relationship, while NL-3 shows an extended linear line immediately after shut-in before changing to another linear line with a different slope. The initial linear lines after shut-in for Cases a (NL-1) and b (NL-2) are very short (see Figure 10).

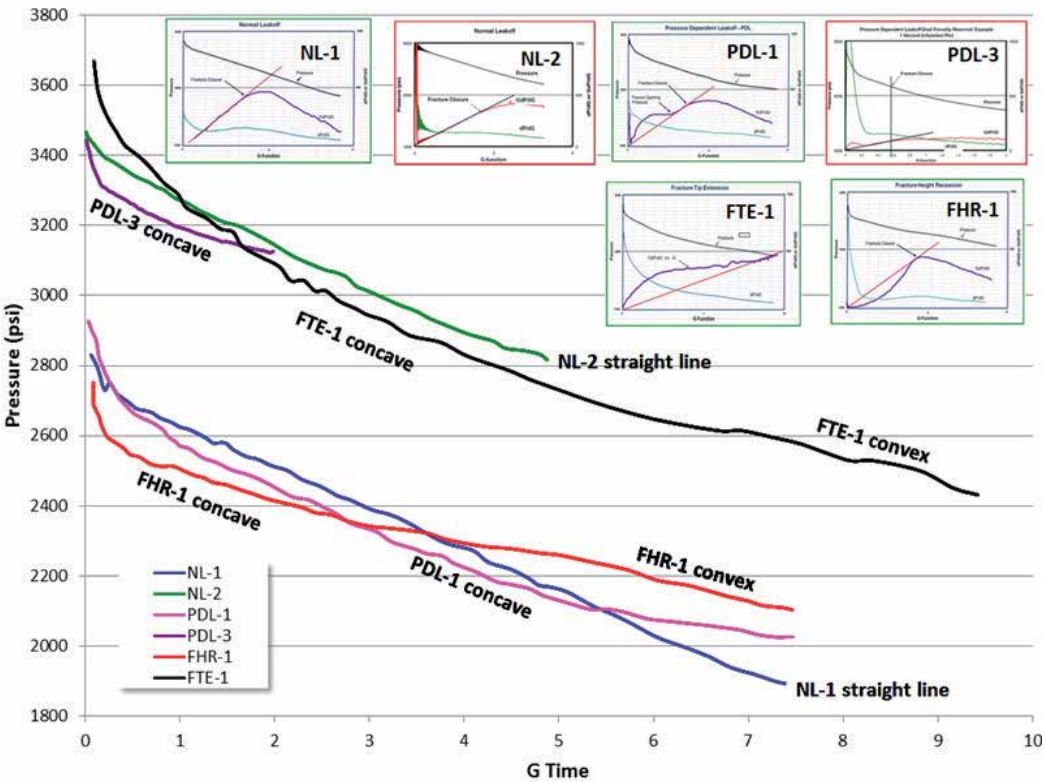

Figure 10. Comparison of six cases of NL, PDL, FTE, and FHR: a) linear lines of the P – G relationship from normal leak-off (NL-1 and NL-2); b) concave curves of the P – G relationship from pressure-dependent leakoff (PDL-1 and PDL-3), and c) initial concave and later convex curves of the P – G relationship from fracture tip extension and fracture height recession (FTE-1 and FHR-1).

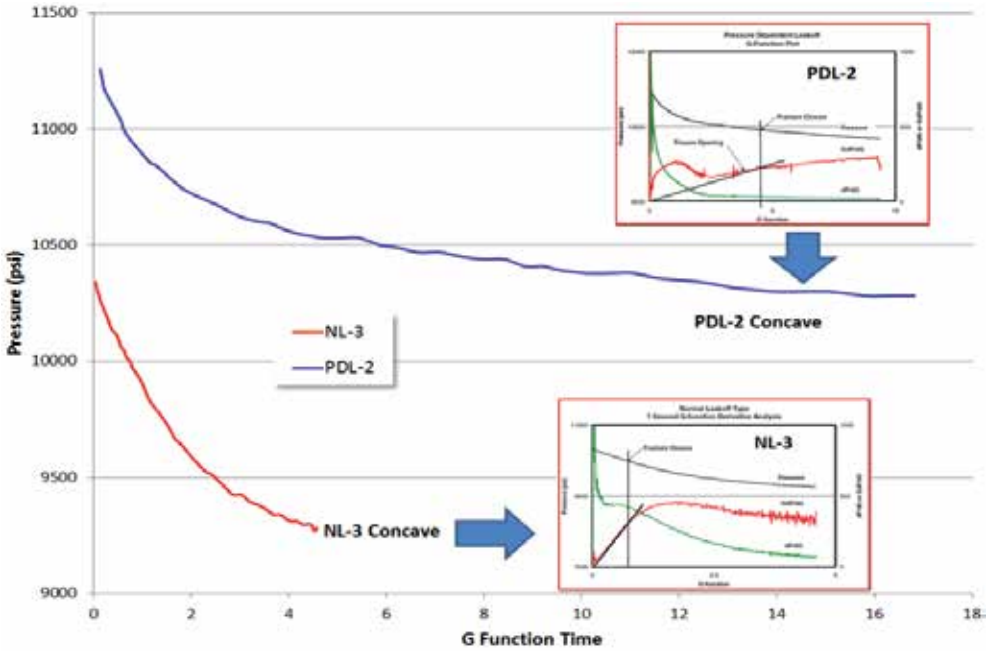

Figure 11. Comparison of two cases of (NL-3 and PDL-2): a) initial linear line and late linear line with a different slope for the P - G relationship with normal leakoff; and b) concave curves for the P – G relationship with pressure-dependent leakoff.

5. Conclusions

Based on past experience in cuttings injection monitoring, it can be concluded that the quality of fracture closure after shut-in has a critical impact on the efficiency of a cuttings injection operation. Cuttings injection is inefficient when the fracture closure cannot be assured as a result of an insufficient shut-in period between batch injection operations. Conversely, cuttings injection becomes efficient when sufficient time is provided between batch injections to allow adequate fracture closure.

The quality of the cuttings injection can be evaluated by analyzing the trend of batch injections. The rising peak batch pressures during injection and slow declining of terminal batch pressures during shut-in are indications of poor pressure maintenance and thus poor cuttings injection management. Rising batch injection pressure usually reveals difficulties in maintaining needed injectivity while slow pressure decline can be the result of insufficient shut-in time in a low permeability disposal domain. The required solutions include but are not limited to: a) mitigating the injection pressure or pump power and ensuring the proper breakdown of the injected formation, b) extending the shut-in period to dissipate injection pressure, and c) adjusting the injected batch volume or injection rate to allow the relevant acceptance of the disposal formation for the injected cuttings.

The quality of fracture closure analysis also affects the quality of cuttings injection management. Among various methods, using GFSD in interpreting BHP responses to the cuttings injection operation appears to be an efficient way to identify the occurrence of fracture closure. Interpreting the shapes of GFSD over the P – G relationship may help identify the different responses from various formations such as injection in naturally fractured reservoirs, reflect various behaviors involved in the injection process such as the pressure/stress dependency in a poro-elastic formation, or reveal the outcome from the complex, coupled process of rock deformation and fluid flow under various reservoir boundary conditions.

Author details

Mao Bai[1], Arturo Diaz[1], John McLennan[2] and Juan Reyna[1]

*Address all correspondence to: mao.bai@halliburton.com

1 Halliburton, Houston, USA

2 University of Utah, Salt Lake City, USA

References

[1] Nagel, N. and McLennan, J.D., editors, Solids Injection Monograph, Society of Petroleum Engineers (SPE), (2010).

[2] Carter, R. D. Derivation of the general equation for estimating the extent of the fractured area, Appendix I of Optimum Fluid Characteristics for Fracture Extension, Drilling and Production Practice, G.C. Howard and C.R. Fast, New York, New York, USA, American Petroleum Institute, (1957). , 261-269.

[3] Horner, D. R. Pressure buildup in wells, Proceeding, Third World Petroleum Congress, The Hague, Netherlands (SPE), Sec. II, (1951). , 503-523.

[4] Nolte, K. G. Determination of fracture parameters from fracturing pressure decline, paper SPE 8341, presented at the SPE Annual Technical Conference and Exhibition, Las Vegas, Nevada, USA, Sept., (1979).

[5] Barree, R. D, Barree, V. L, & Craig, D. P. Holistic fracture diagnostics: consistent interpretation of prefrac injection tests using multiple analysis methods, SPE Production and Operations, August, (2009). , 396-406.

[6] Economides, M. J, & Nolte, K. J. Reservoir Stimulation, 3rd Edition, Wiley, (2000).

Chapter 40

The Fate of Injected Water in Shale Formations

Hongtao Jia, John McLennan and Milind Deo

Additional information is available at the end of the chapter

http://dx.doi.org/10.5772/56443

Abstract

It is well known that only about a third of water injected for hydraulic fracturing of shales is recovered. It is important to understand the fate of this injected water. The amount of water infiltrating the matrix is determined by a number of parameters such as the pressure differential between the fracture and the matrix, the capillary pressure relationships in the fractures and in the matrix and other petrophysical properties of the formation. In this paper, we provide a breakdown for the various possible water losses depending on the reservoir, fracture and operating parameters. A set of capillary pressure relationships for the formation were first created based on the basic mineralogy and the total organic carbon (TOC) content. Fracture capillary pressure also changed depending on the concentrations and types of proppants in the fractures. Two basic end members can be defined – silicistic and dolomitic with different amounts of TOC. The capillary pressure relationships ranged from oil wet, neutral to water wet. Different porosity and permeability combinations were also examined. Amounts of water relative to the total amount injected that would infiltrate the formation were compiled as the operating conditions (pressures) and formation properties changed. This calculation shows that the infiltration due to the various phenomena are not sufficient to account for the water losses if the formations are strongly oil wet. In addition, situations where water blockages occur due to these multiphase flow effects were identified and the loss of productivity due to this phenomenon was quantified both for gas and for oil production. The study was conducted using a discrete-fracture network simulator developed at the University of Utah. A realistic (non-orthogonal) representation of a complex fracture network was employed in the study. Realistic representation of distribution and retention of these aqueous fracturing fluids is essential for optimizing hydraulic fracturing treatment volumes.

1. Introduction

The growth in producing hydrocarbons from unconventional reservoirs (shales) has been phenomenal. The production of liquids from the Eagle Ford play grew to about 52 million barrels in 2011 [1] (Figure 1).

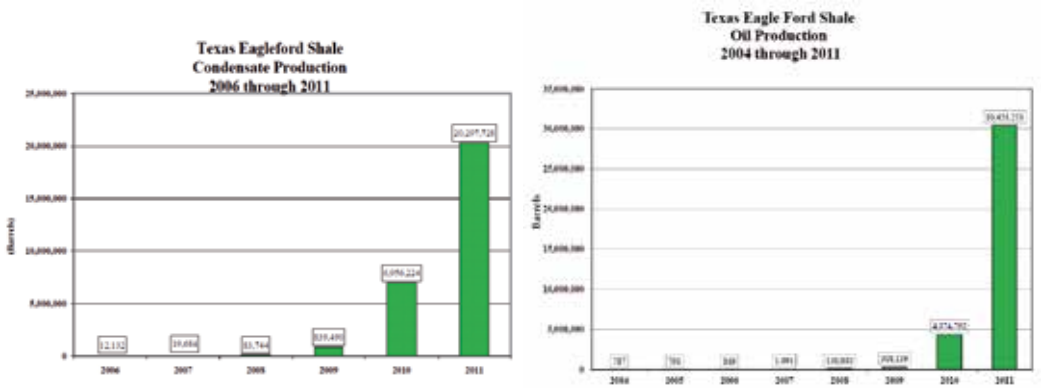

Figure 1. The phenomenal growth in production of liquids from shales with Eagle Ford. In just over a three-year period, insignificant production has been transformed to over 52 million barrels of liquids in 2011.

The growth in production is driven by improvements in hydraulic fracturing technology. Multistage fracturing using long horizontal wells is the common practice. Millions of gallons of water are pumped into the formation to create these fractures. Industry data reveals that only about a third of the injected water is typically recovered. The fate of injected water is of fundamental interest. Use of large quantities of water in fracturing has brought into question the sustainability of this type of completion and development practice. Furthermore, low water recovery has prompted environmental concerns about whether the injected water leaves the target formation with a potential of infiltrating and contaminating aquifers. The purpose of this paper was to examine the capability of the formation to imbibe the injected water based on different capillary pressure relationships.

2. Technical approach

The Advanced Reactive Transport Simulator (ARTS) at the University of Utah was used to perform simulation studies (Figure 2). ARTS is a modular reservoir simulator that has been under development over a number of years [2-4]. The main idea of ARTS is to decouple the discretization methods from the physical models. The discretization methods in ARTS include the conventional finite difference, control-volume finite element and a generalized control volume method. These discretization methods could be coupled with a variety of physical models. The simplest physical model would be simulation of a single-phase gas with immovable water phase. Two-phase and three-phase black oil models are used to simulate primary

production followed by water and polymer flooding. Thermal processes such as steam flooding, in-situ combustion, steam-assisted gravity drainage, etc. are represented in K-value based thermal-compositional models. In these models, the vapor-liquid equilibrium is calculated using the ratio between the vapor and the liquid phase composition of each component (K-value). ARTS also includes a geochemical module to simulate processes associated with carbon dioxide sequestration and reactions involving carbon dioxide, brine and rocks.

The use of a control volume finite element model as one of the discretization schemes allows multiphase simulation of complex reservoir geometries including a discrete fracture network representation of natural and hydraulic fractures.

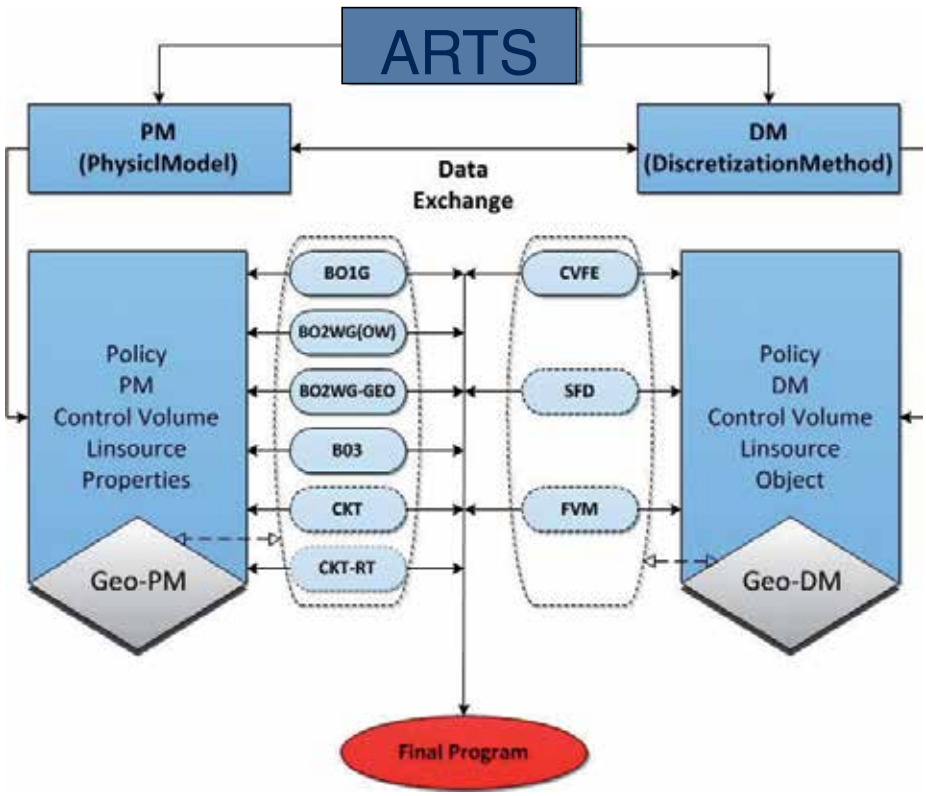

Figure 2. The framework used in simulating water injection and production in fractured systems. The discretization methods (DM) are decoupled from the physical models (PM).

We represented and simulated two different discrete fracture domains in this work – both with non-orthogonal features (Figure 3). It is common practice to represent and simulate hydraulic fractures as orthogonal features. However, it is evident that the fractures created are not perfectly perpendicular to the horizontal well. The microseimic cloud that is observed in a number of cases with multiple horizontal fractures (for example, [5]), shows fractures that are

more complex than regularly spaced orthogonal features. It is true that there is no one to one correlation between the microseismic signatures and the shape and morphology of hydraulic fractures. However, there are a number of indications that point to the hydraulic fractures being more complex than simple orthogonal features.

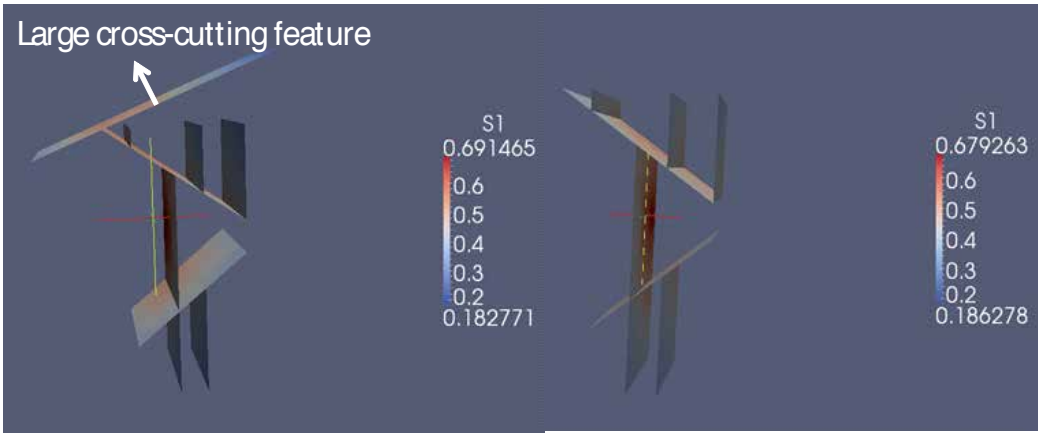

Figure 3. Figure showing two fractured systems simulated in this study.

The hydraulic fractures created interact with existing natural fractures. The role of natural fractures in production of fluids from shales is still an open question. The production behavior of both the gas and liquid reservoirs does not indicate a highly fractured system. On the other hand, when fracturing water is injected in a well, it is common to see interference in an adjacent well. This may be in the form of pressure interference or explicit breakthrough of water injected in the adjacent well. Pressure interference in and of itself does not indicate fluid transport to the well.

Capillary pressures for these shale reservoirs are not well characterized. The wettability of the reservoir rocks is also not well known. Al-Bazali et al. [6], measured sealing capacities of shale caprocks. This data provides some guidance for the capillary pressure values and relationships to use for these systems. The general capillary pressure relationship is given by:

$$P_c = \frac{2\sigma\cos\theta}{r}$$

In this equation, P_c is the capillary pressure, σ is the interfacial tension between the immiscible fluids of interest, θ is the contact angle and r is the average pore radius. Al-Bazali et al.[6], were considering shales that were less than 10 nD in permeability. For the three shales studied, they measured entry pressures ranging from 470 psia to 750 psia. They calculated pore throat radii of about 30 nM for entry pressures of crude oil. For pore throats of less than 10 nM (Sondergeld et al. [7]), very large capillary pressures (two to three times those measured by Al-Bazali et al [7]) are possible.

http://dx.doi.org/10.5772/56443

There has been much discussion about wettability of shales. In this paper, we examined the differences in water recovery due to variations in wettability of the rock. The three sets of oil-water capillary pressures used in the study are shown in Figure 4.

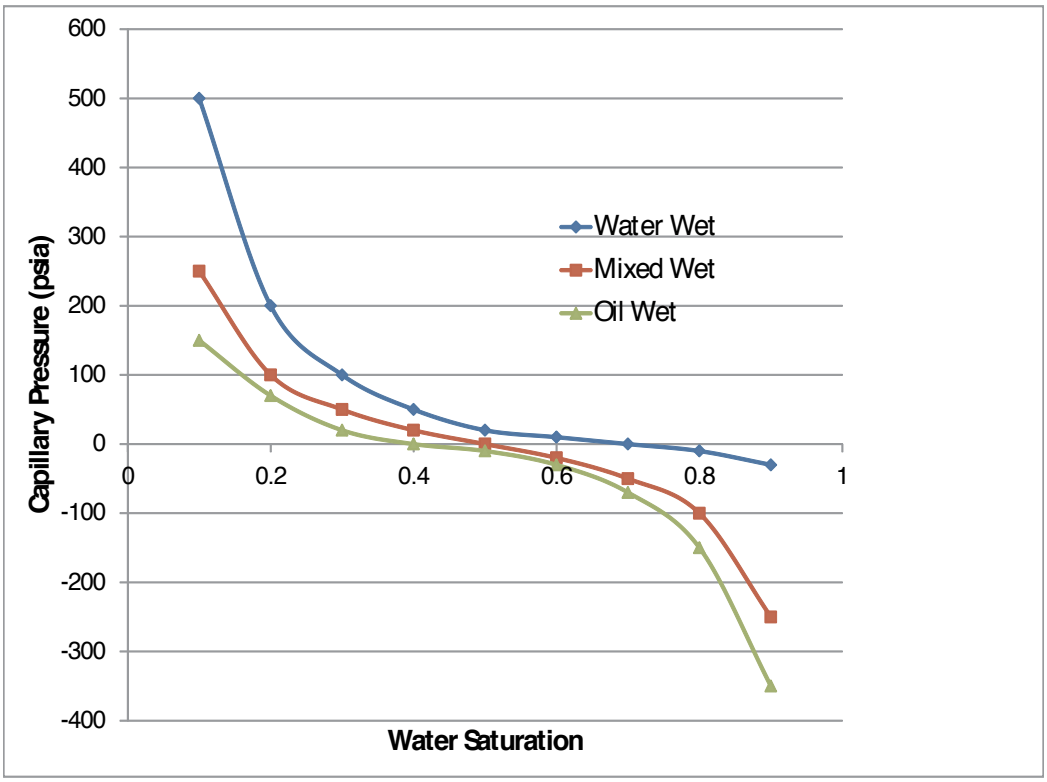

Figure 4. The three sets of capillary pressures used in this study.

Over most of the saturation range for the oil and mixed wet situations, the capillary pressures are negative, indicating a preference for oil as the wetting fluid. Other domain-specific parameters are shown in Table 1.

Domain Size	260 feet X 260 feet X 100 feet
Initial Reservoir Pressure	2000 psia
Fracture Permeability	1000 mD
Porosity	20%
Matrix Permeability	0.5 mD
Water Injected	30000 barrels

Table 1. Properties of the domain and simulations

Water recovery after one month (30 days) for each of the simulations was compiled. For the base case capillary pressures, the water recoveries for the three wetting scenarios and for the two domains (one with the cross-cutting fracture, and one without) are shown in Table 2.

	Water Wet	Mixed Wet	Oil Wet
Water recovery ratio(With cross-cutting fracture)	21.53%	29.35%	36.28%
Water recovery ratio (Without the cross-cutting fracture)	22.97%	31.24%	38.39%

Table 2. Water recoveries for the three wetting scenarios and for the two domains studied in this paper. Recoveries are for the base case where the initial reservoir pressure was 2000 psia and the matrix permeability was 0.5 mD.

The water recoveries observed in the table above are consistent with water recoveries of about 20-40% listed in field observations. Water recoveries increase as we go from water wet to mixed wet to oil wet clearly indicating the tendency of the matrix to imbibe and hold water as the formation becomes more water wet. There is a 15% increase in water recovery as we go from water wet to the oil wet case. The presence of the long cross-cutting feature does not make a significant impact in recovery. The recovery does decrease as injected water is transported to longer distances – but the difference in recovery is only 1-2%.

In a number of shale reservoirs, the permeabilities are lower and the initial pressures are higher. To investigate the effects of these parameters on recovery, simulations were performed with 5000 psia initial pressure and 0.1 mD matrix permeability. Results of these simulations are tabulated in Table 3.

	Water Wet	Mixed Wet	Oil Wet
Water recovery ratio(With cross-cutting fracture)	37.42%	40.17%	44.19%
Water recovery ratio (Without the cross-cutting fracture)	41.02%	44.61%	49.83%

Table 3. Water recoveries for the three wetting scenarios and for the two domains studied in this paper. Recoveries are for the base case where the initial reservoir pressure was 5000 psia and the matrix permeability was 0.1 mD.

Higher initial pressure results in higher water recoveries, particularly in the water wet cases. The differences between recoveries with and without the large cross-cutting feature are now between 4-5%. The differences between the different wettability cases however are reduced to only about 8% (compared to about 15%) as the largest difference the water wet and the oil wet scenarios.

http://dx.doi.org/10.5772/56443

At smaller pore radii, the capillary pressures are expected to be larger. One set of simulations were performed where the shape of the base case capillary pressures were maintained, but the capillary pressures were increased ten times for each of the saturation values. The resulting recoveries are tabulated in Table 4.

	Water Wet	Mixed Wet	Oil Wet
Water recovery ratio(With cross-cutting fracture)	20.1%	27.15%	41.9%
Water recovery ratio (Without the cross-cutting fracture)	23.3%	30.2%	45.5%

Table 4. Water recoveries for the three wetting scenarios and for the two domains studied in this paper. Recoveries are for the case where the capillary pressures were ten times the base case capillary pressures used. The shapes of the capillary pressure curves were the same as the ones used in Figure 4. The initial reservoir pressure was 5000 psia and the matrix permeability was 0.1 mD.

As the capillary pressure increases, more water is retained. For mixed wet and oil wet scenarios, water saturation in the matrix area is lower (Figure 5). Similar relative difference between recoveries is maintained when recoveries are compared for domains with and without the large cross-cutting features. The system without the large cross-cutting fracture in this case returns on the average about 3% more water than when the large fracture exists. Water saturations for the domain without the large fracture are shown in Figure 6.

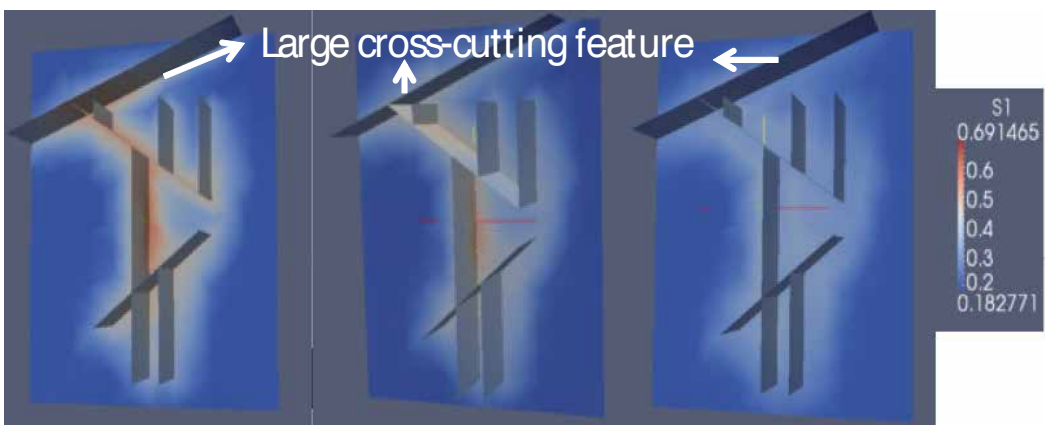

Figure 5. Figure showing water saturations in the matrix through one hydraulic fracture and interacting natural fractures. Left panel is for the water wet case, the middle panel is for the mixed wet case and the right panel is the oil wet case. As the wettability goes from water wet to oil wet the infiltration decreases increasing injected water recovery. In this particular example, the large cross-cutting feature does not take a significant amount of water off site.

3. Conclusions

Recovery of water injected for hydraulic fracturing in shales is only about 30%. There is a question of the fate of injected water. In this paper we studied water retention in shales for different shale wettability conditions. Two different domains where a hydraulic fracture intersected with a small existing network of natural fractures were used in the simulations. A specially developed framework that can handle representation of complex fracture networks was used for simulations. Capillary pressures in rocks containing very small pores tend to be high – of the order of 1000 psia. Three sets of capillary pressures – water wet, mixed wet and oil wet were examined. Simulations showed that a recovery of 20-30% is expected for typical water wet conditions, while a recovery of about 37%-48% is expected for oil wet scenarios. The recovery for mixed wet conditions fell between these two extremes. The recovery is reduced when a large cross-cutting fracture is introduced – but not significantly. That is because water will be recovered if the fractures are interconnected. Results discussed in this paper helped quantify the role of wettability in the recovery of water used for hydraulic fracturing. In this paper we assumed that the initial water saturation was low and that the water was immovable. If that is not the case, water saturation in the matrix and in the natural fractures, as well as the water-oil or water-gas relative permeability functions play significant roles in determining the water balance.

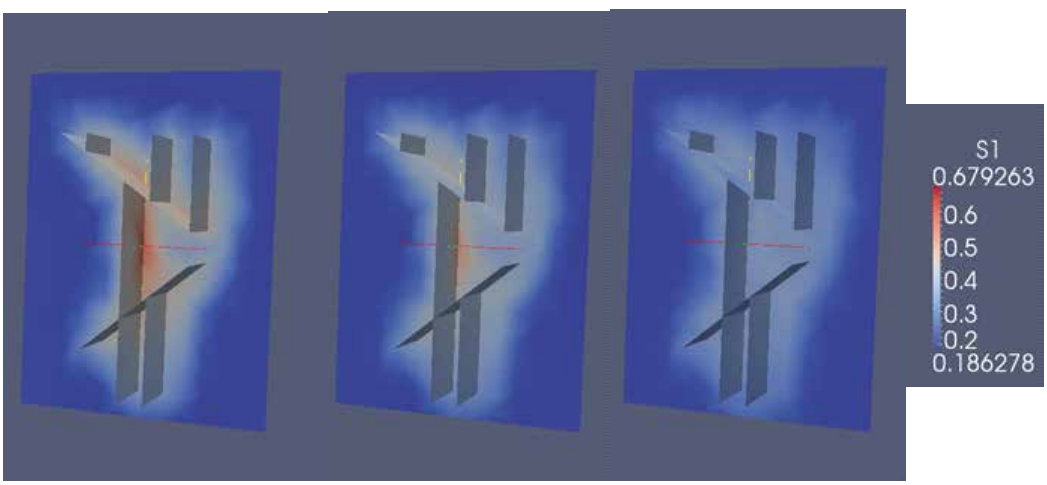

Figure 6. Figure showing water retained in the matrix through one hydraulic fracture and interacting natural fractures. Domain without the large cross-cutting feature is used. Left panel is for the water wet case, the middle panel is for the mixed wet case and the right panel is the oil wet case. Water saturation scale is also shown. As the wettability goes from water wet to oil wet the infiltration decreases increasing injected water recovery.

Author details

Hongtao Jia, John McLennan and Milind Deo

Department of Chemical Engineering, University of Utah, Salt Lake City, UT, USA

References

[1] Data from the Texas Railroad Commission- http://wwwrrc.state.tx.us/

[2] Yang, Y. K. (2003). Finite-Element Multiphase Flow Simulator, Ph.D. dissertation, University of Utah, 2003.

[3] Fu, Y. (2007). Multiphase Control Volume Finite Element Simulation of Fractured Reservoirs, Ph.D. dissertation, University of Utah, 2007.

[4] Gu, Z. (2010). A Geochemical Compositional Simulator for Modeling C O2 Sequestration in Geological Formations, Ph.D. dissertation, University of Utah, 2010.

[5] Stegent, N. A, Ferguson, K, & Spencer, J. (2011). Comparison of Frac Valves vs. Plug and Perf Completions in the Oil Segment of the Eagle Ford Shale: A Case Study, CSUG/SPE 148642, Paper presented at the Canadian Unconventional Resources Conference, Calgary, Canada, November 2011., 15-17.

[6] Al-bazali, T. M, Zhang, J, Chenevert, M. E, & Sharma, M. M. (2005). Measurement of the Sealing Capacity of Shale Caprocks, SPE 96100, Paper presented at the Annual Technical Conference and Exhibition, Dallas, Texas, Oct , 9-12.

[7] Curtis, M. E, Ambrose, R. J, Sondergeld, C. H, & Rai, C. S. Structural Characterization of Gas Shales on the Micro- and Nano-scales, CSUG/SPE 137693, Paper presented at the Canadian Unconventional Resources and International Petroleum Conference held in Calgary, October (2010). , 19-21.

Section 13

Numerical Modeling 2

Chapter 41

Three-Dimensional Numerical Model of Hydraulic Fracturing in Fractured Rock Masses

B. Damjanac, C. Detournay, P.A. Cundall and Varun

Additional information is available at the end of the chapter

http://dx.doi.org/10.5772/56313

Abstract

Conventional methods for simulation of hydraulic fracturing are based on assumptions of continuous, isotropic and homogeneous media. These assumptions are not valid for most rock mass formations, particularly shale gas reservoirs, as these typically consist of a large volume of naturally fractured rock in which propagation of a hydraulic fracture (HF) involves both fracturing of intact rock and opening or slip of pre-existing discontinuities (joints). The pre-existing joints can significantly affect the HF trajectory, the pressure required to propagate the fracture and also the leak-off from the fracture into the surrounding formation. None of these effects can be simulated using conventional methods.

HF Simulator is a new three-dimensional numerical code that can simulate propagation of hydraulic fracture in naturally fractured reservoirs, accounting for the interaction between the hydraulic fracture and pre-existing joints. In *HF Simulator*, fracture propagation occurs as a combination of intact-rock failure in tension, and slip and opening of joints. The code uses a lattice representation of brittle rock consisting of point masses (nodes) connected by springs. The pre-existing joints are derived from a user-specified discrete fracture network (DFN).

HF Simulator can model fluid injection or production from one or multiple boreholes each with one or multiple clusters. Non-steady, hydro-mechanically coupled fluid flow and pressure within the network of joint segments and the rock matrix are considered.

An outline of the code hydro-mechanical formulation is presented and examples are provided to illustrate the code capabilities.

Keywords: Numerical model, naturally fractured, rock mass

1. Introduction

A new generation tool that uses the bonded particle model (BPM) [1] and the synthetic rock mass (SRM) concept [2] has been developed to model hydraulic fracture (HF) propagation in naturally fractured reservoirs (NFRs).

Most rock mass formations, and shale gas reservoirs in particular, consist of a large volume of fractured rock in which propagation of an HF involves both fracturing of intact rock and opening or slip of pre-existing discontinuities (joints). The pre-existing joints can significantly affect the HF trajectory, the pressure required to propagate the fracture, but also the leak-off from the fracture into the surrounding formation. None of these effects can be simulated using conventional hydraulic fracturing simulation methods, based on assumptions of continuous, isotropic and homogeneous media.

To address this challenge, a numerical approach called SRM method [2] has been developed recently based on the distinct element method. SRM method usually is realized as a bonded-particle assembly representing brittle rock containing multiple joints, each one consisting of a planar array of bonds that obey a special model, namely the smooth joint model (SJM). The SJM allows slip and separation at particle contacts, while respecting the given joint orientation rather than local contact orientations. Overall fracture of a synthetic rock mass depends on both fracture of intact material (bond breaks), as well as yield of joint segments.

Previous SRM models have used the general-purpose codes *PFC2D* and *PFC3D* [3,4], which employ assemblies of circular/spherical particles bonded together. Much greater efficiency can be realized if a "lattice," consisting of point masses (nodes) connected by springs, replaces the balls and contacts (respectively) of *PFC3D*. The lattice model still allows fracture through the breakage of springs along with joint slip, using a modified version of the SJM. The new 3D program, *HF Simulator* described in this paper, is based on such a lattice representation of brittle rock. *HF Simulator* overcomes all main limitations of the conventional methods for simulation of hydraulic fracturing in jointed rock masses and is computationally more efficient than *PFC*-based implementations of the SRM method.

The formulation of the code is described in this paper. The examples of code verification and application are also presented.

2. Model description

2.1. Background: Synthetic rock mass approach

Over past years, the SRM has been developed [2] as a more realistic representation of mechanical behavior of the fractured rock mass compared to conventional numerical models. The SRM consists of two components: (1) the bonded particle model (BPM) of deformation and fracturing of intact rock, and (2) the smooth joint model (SJM) of mechanical behavior of discontinuities.

http://dx.doi.org/10.5772/56313

The BPM, originally implemented in *PFC*, is created when the contacts between the particles (disks in 2D and spheres in 3D) are assigned certain bond strength (both in tension and shear). It was found that BPM quite well approximates mechanical behavior of the brittle rocks [1]. The elastic properties of the contacts (i.e., contact shear and normal stiffness) can be calibrated to match the desired elastic properties (e.g., Young's modulus and Poisson's ratio) of the assembly of the particles. Similarly, the tensile and shear contact strengths can be adjusted to match the macroscopic strengths under different loading conditions (e.g., direct tension, unconfined and confined compression).

In the BPM, the contact behavior is perfectly brittle. Breakage of the bond, a function of the forces in the contact and the bond strength, corresponds to formation of a microcrack. An example of unconfined compression test conducted using *PFC2D* is illustrated in Figure 1, which shows recorded axial stress-strain response and the model configuration with generated microcracks. The shear microcracks are black; the tensile microcracks are red. Shown is the state when the sample is loaded beyond its peak strength. The stress-strain curve exhibits characteristics typical of brittle rock response. For the load levels less than ~80% of the peak strength, the stress-strain response is linearly elastic, with the slope of the line equal to the Young's modulus. Some microcracks, randomly distributed within the sample, start developing at the load levels greater than ~40% of the peak strength. Significant non-linearity develops as the load exceeds 80% of the peak strength. In this phase, the microcracks begin to coalesce, forming fractures on the scale of the sample. After the peak strength is reached, the material starts to soften (i.e., to lose the strength). At this stage, as shown in Figure 1, the failure mechanism and the "shear bands" are well developed. It is interesting that in the unconfined compression test, the majority of cracks are tensile (red lines in Figure 1). The "shear bands" on the scale of the sample are formed by coalescence of a large number of tensile microcracks.

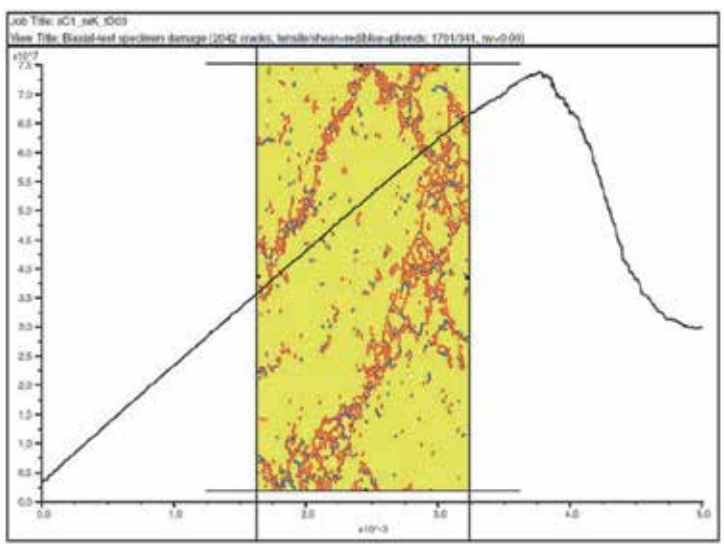

Figure 1. Example of unconfined compressive test using bonded particle model (BPM).

In order to model a typical rock mass in the BPM, it is also necessary to represent pre-existing joints (discontinuities). A straightforward approach is to simply break or weaken the bonds (in the contacts between the particles) intersected by the pre-existing joints. The created discontinuity will have roughness with the amplitude and wavelength related to the resolution, or the particle size of the BPM. The mechanical behavior of discontinuities is very much affected by their roughness. The problem is that the selected particle size (or resolution) typically is not related to actual roughness of the pre-existing joints. The SJM overcomes this limitation. The contacts in the BPM model are oriented in the direction of the line connecting the centers of the particles involved in the contact. The SJM contacts are oriented perpendicular to the fracture plane irrespective of the relative position of the particles. Consequently, the particles can slide relative to each other in the plane of the fracture as if it is perfectly smooth.

The SRM and its components are shown in Figure 2. The BPM represents the intact rock, its deformation and damage. The pre-existing joints are represented explicitly, using the SJM. They can be treated deterministically, by specifying each discontinuity by its position and orientation as mapped in the field. However, typically, for practical reasons, it is not possible to treat the DFN deterministically. Instead, fracturing in the rock mass is characterized statistically. The synthetic DFNs that are statistically equivalent (i.e., fracture spacing, orientation and size) to fracturing of the rock mass are generated and imported into the SRM using SJM (Figure 2). Very often a reasonable compromise is to represent few dominant structures (faults) with their deterministic position and orientation and the rest of the fracturing in the rock mass (smaller structures) using a synthetic DFN.

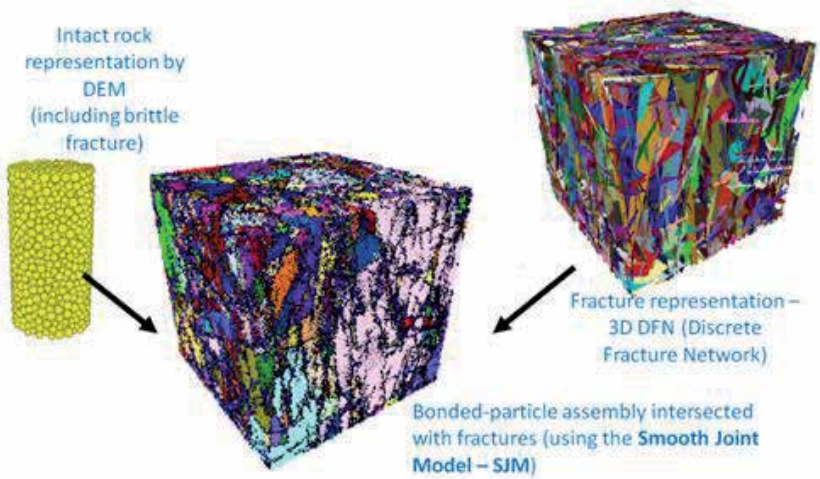

Figure 2. Synthetic rock mass (SRM).

One of the advantages of the SRM is that the components, the intact rock and the joints, can be mechanically characterized by standard laboratory tests. The mechanical response of the rock mass and the size effect are the model results, functions of the model size, DFN characteristics and mechanical properties of the components. Thus, it is not necessary to rely on empiri-

http://dx.doi.org/10.5772/56313

cal relations to estimate the rock mass properties and to account for the size effect considering the size of the samples tested in the laboratory and the scale of interest in the model.

The new code, *HF Simulator*, is based on implementation of the SRM in the lattice, which is a simplified, but also a computationally more efficient version of particle flow code (*PFC*). Despite simplifications, the lattice approach represents all physics important for simulation of hydraulic fracturing.

2.2. Lattice

The lattice is a quasi-random array of nodes (with given masses) in 3D connected by springs. It is formulated in small strain. The lattice nodes are connected by two springs, one representing the normal and the other shear contact stiffness. The springs represent elasticity of the rock mass. In *HF Simulator*, the calibration factors for spring stiffness are built-in and the user may specify typical macroscopic elastic properties as it is done for other conventional numerical models. The tensile and shear strengths of the springs control the macroscopic strength of the lattice. As for elastic constants, calibration factors are built-in for the strength parameters.

The model simulation is carried out by solving an equation of motions (three translations and three rotations) for all nodes in the model using an explicit numerical method. The following is the central difference equation for the translational degrees of freedom:

$$\begin{aligned} \dot{u}_i^{(t+\Delta t/2)} &= \dot{u}_i^{(t-\Delta t/2)} + \Sigma F_i^{(t)} \Delta t / m \\ u_i^{(t+\Delta t)} &= u_i^{(t)} + \dot{u}_i^{(t+\Delta t/2)} \Delta t \end{aligned} \tag{1}$$

where $\dot{u}_i^{(t)}$ and $u_i^{(t)}$ are the velocity and position (respectively) of component i (i=1, 3) at time t, ΣF_i is the sum of all force-components i, acting on the node of mass m, with time step Δt. The relative displacements of the nodes are used to calculate the force change in the springs:

$$\begin{aligned} F^{\mathrm{N}} &\leftarrow F^{\mathrm{N}} + \dot{u}^{N} k^{\mathrm{N}} \Delta t \\ F_i^{\mathrm{S}} &\leftarrow F_i^{\mathrm{S}} + \dot{u}_i^{\mathrm{S}} k^{\mathrm{S}} \Delta t \end{aligned} \tag{2}$$

where "N" denotes "normal," "S" denotes shear, k is spring stiffness and F is the spring force. If the force exceeds the calibrated spring strength, the spring breaks and the microcrack is formed. In other words, if $F^{\mathrm{N}} > F^{\mathrm{Nmax}}$, then $F^{\mathrm{N}}=0$, $F_i^{\mathrm{S}}=0$, and a "fracture flag" is set.

2.3. Fluid flow

Fluid-flow model and hydro-mechanical coupling are essential parts of *HF Simulator*, as a code for simulation of hydraulic fracturing. The fluid flow occurs through the network of pipes that connect fluid elements, located at the centers of either broken springs or springs that represent pre-existing joints (i.e., springs intersected by the surfaces of pre-existing joints). (The code

also can simulate the porous medium flow through unfractured blocks as a way to represent the leakoff. This capability is not discussed further in this paper.) The flow pipe network is dynamic and automatically updated by connecting newly formed microcracks to the existing flow network. The model uses the lubrication equation to approximate the flow within a fracture as a function of aperture. The flow rate along a pipe, from fluid node "A" to node "B," is calculated based on the following relation:

$$q = \beta k_r \frac{a^3}{12\mu}\left[p^A - p^B + \rho_w g\left(z^A - z^B\right)\right] \tag{3}$$

where a is hydraulic aperture, μ is viscosity of the fluid, p^A and p^B are fluid pressures at nodes "A" and "B", respectively, z^A and z^B are elevations of nodes "A" and "B", respectively, and ρ_w is fluid density. The relative permeability, k_r, is a function of saturation, s:

$$k_r = s^2(3 - 2s) \tag{4}$$

Clearly, when the pipe is saturated, $s = 1$ and the relative permeability is 1. The dimensionless number β is a calibration parameter, a function of resolution, used to match conductivity of a pipe network to the conductivity of a joint represented by parallel plates with aperture a. The calibrated relation between β and the resolution is built into the code.

2.4. Hydro-mechanical coupling

In *HF Simulator*, the mechanical and flow models are fully coupled.

1. Fracture permeability depends on aperture, or on the deformation of the solid model.
2. Fluid pressure affects both deformation and the strength of the solid model. The effective stress calculations are carried out.
3. The deformation of the solid model affects the fluid pressures. In particular, the code can predict changes in fluid pressure under undrained conditions.

A new coupling scheme, in which the relaxation parameter is proportional to $K_R a / R$, where K_R is rock bulk modulus and R is the lattice resolution, is implemented in *HF Simulator*, allowing larger explicit time steps and faster simulation times compared to conventional methods that use fluid bulk modulus as a relaxation parameter.

3. Verification test: Penny-shaped crack propagation in medium with zero toughness

The non-steady response of rock to injection of fluid depends on fracture toughness, the viscosity of the fluid and the rate of leak-off. In the case of zero fracture toughness and no leak-

http://dx.doi.org/10.5772/56313

off, the response is viscosity-dominated, which corresponds to the "M-asymptote" identified by [5]. This condition is used for verification of *HF Simulator*.

In the simulated example, fluid is injected at a constant rate into a penny-shaped crack of low initial aperture (10^{-5}m). The crack has zero normal strength, and the in-situ stresses are also zero. Thus, the test conditions approximate those of the analytical solution for the no-lag case (i.e., no fluid pressure tension cut-off) provided by [5]. The injection rate is 0.01 m^3/s; the dynamic viscosity is 0.001 Pa×s. The mechanical properties of the rock are characterized by Young's modulus of 7×10^{10}Pa and Poisson's ratio of 0.22. Figure 3 provides a visualization of the state of the model at 10 s of elapsed time. Note that pressures are negative in the outer annulus of the flow disk.

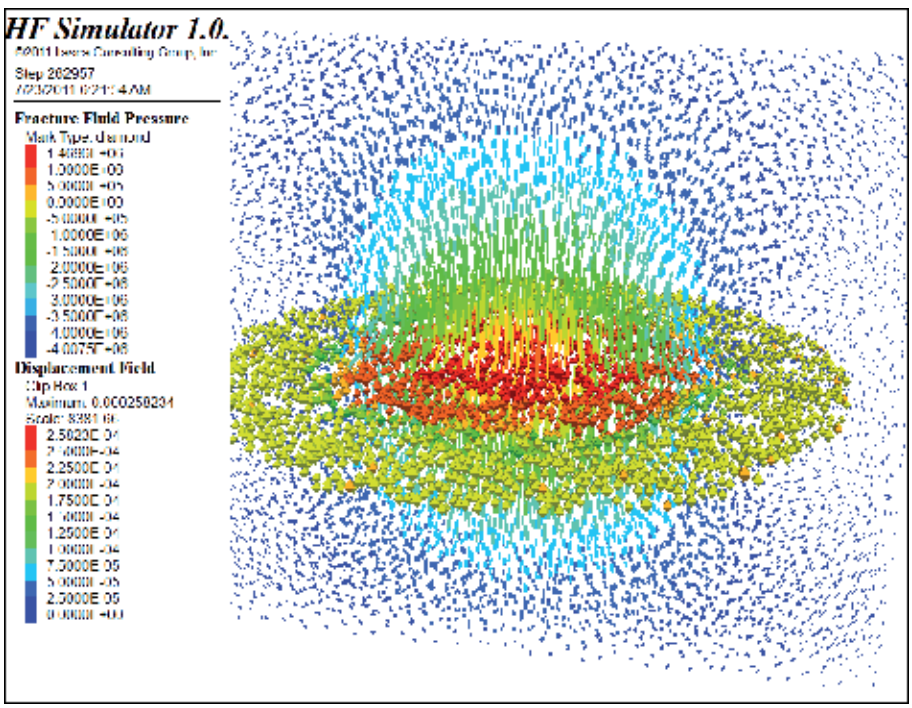

Figure 3. View of pressure (Pa) field (icons, colored according to magnitude) and cross-section of displacement (m) field (vectors, colored according to magnitude)

Figure 4 shows the aperture profiles at three times during the simulation — averaged numerical results (for 30 radial distances), together with asymptotic solutions (derived from the equations of [5]). Figure 5 shows the pressure profile at 10 s, together with the asymptotic solution. Note that there is a lack of match at small and large radial distances: at small distances, the numerical source is a finite volume, rather than a point source (which is assumed in the exact solution); at large distances, the finite initial aperture allows seepage (compared to zero seepage in the exact solution, which assumes zero initial aperture).

4. Example application

Two example problems are discussed in this section. Fracture propagation in a homogeneous (unfractured) and fractured media is analyzed. These two problems involve a horizontal borehole segment with two injection clusters with centers at 4.8 m distance (Figure 6). The model domain is 18 m × 18 m × 18 m, and the lattice resolution was set to 0.5 m. Fluid is injected into the clusters at rate of 0.01 m^3/s. The assumed stress state is anisotropic with σ_{xx} = 1 MPa, σ_{yy} = 12 MPa and σ_{zz} = 10 MPa. The least principal stress is aligned with the horizontal section of the borehole. This stress state favors crack propagation in the direction normal to the horizontal section of the borehole. In order to initiate the fluid calculation, fluid-filled joints have been placed at the center of each cluster; these joints are slightly larger than the cluster size. The initial apertures in these joints have been set to 0.1 mm. Both example problems use this model configuration. The example shown on the left in Figure 6 simulates the response of an unfractured medium to fluid injection. Three discrete joints that interact with the induced fractures are introduced in the example on the right in Figure 6.

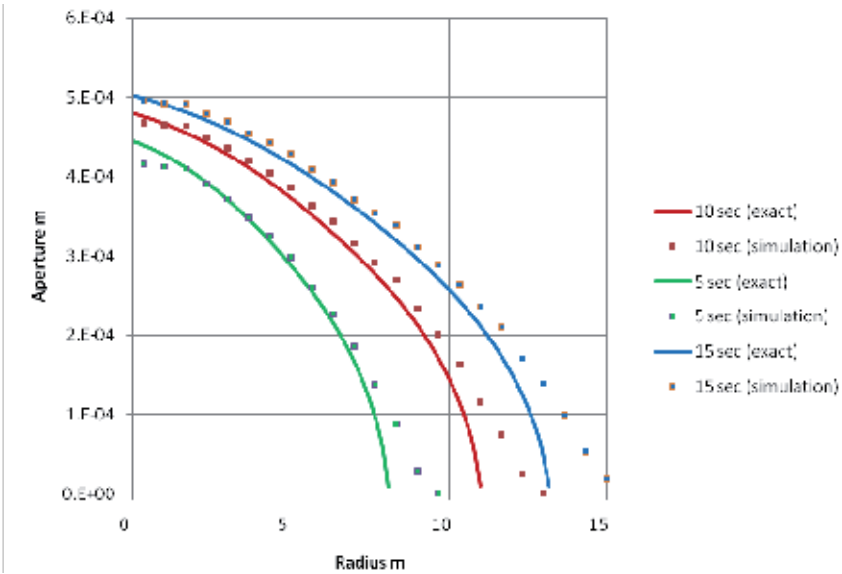

Figure 4. Aperture profiles for three times

The induced microcracks in the homogeneous model after 15 s of injection are shown in Figure 7. The microcracks form two roughly circular (penny-shape) hydraulic fractures. In this example, the fractures are not parallel. There is a slight trend of fractures curving away from each other as a result of stress interaction.

In the second example, the HF propagation is clearly affected by the pre-existing joints, as shown in Figure 8. When the HF intersects the pre-existing joint, the fluid is diverted into the pre-existing joints. (In general case, the HF can cross or be diverted into the pre-existing joint,

http://dx.doi.org/10.5772/56313

depending on a number of parameters, including stress state, strength and permeability of the pre-existing joint.) The propagation continues by reinitiation along the edges of pre-existing joints.

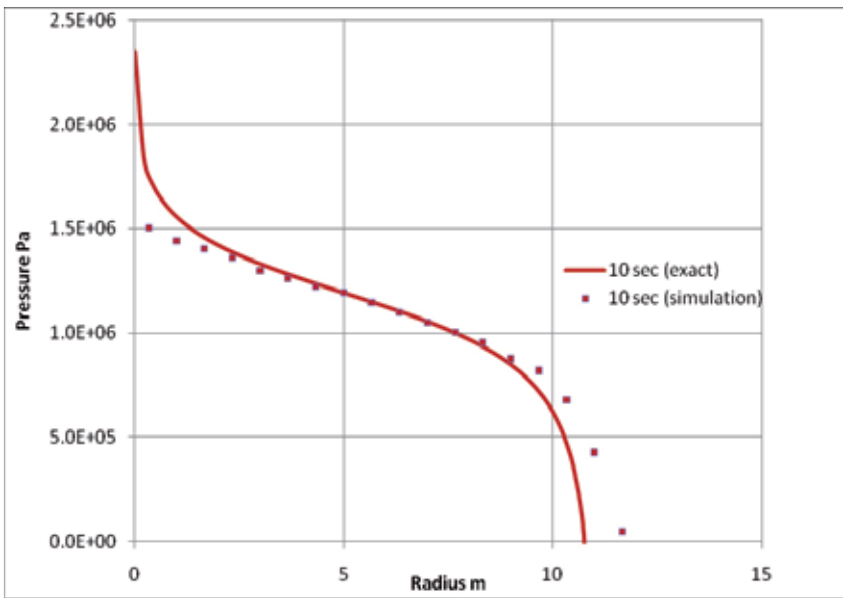

Figure 5. Pressure profile at 10 s

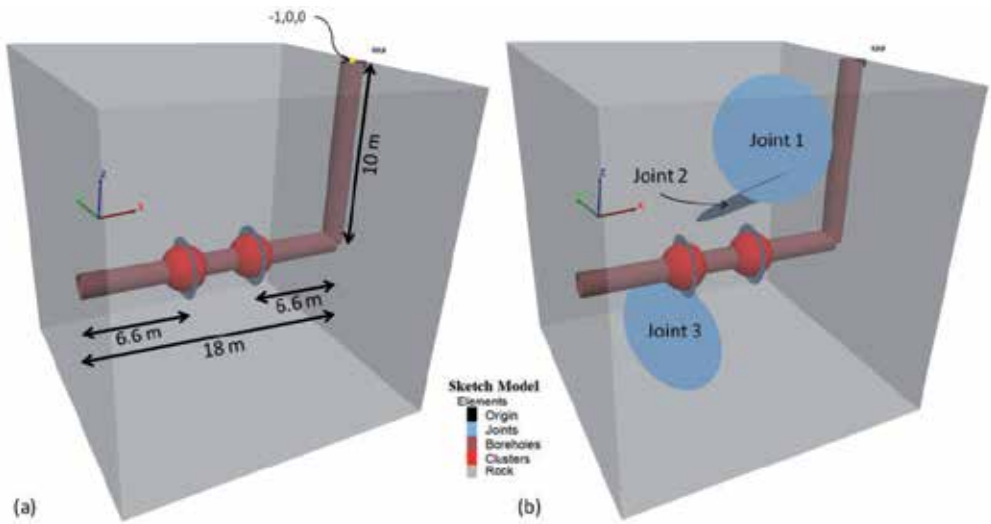

Figure 6. Geometry of two example problems

5. Conclusion

HF Simulator is a powerful 3D simulator for hydraulic fracturing in jointed rock mass that allows the main mechanisms (nonlinear mechanical response, fluid flow in joints and coupled fluid-mechanical interaction) to be reproduced. The formulation of *HF Simulator* is based on a quasi-random lattice of nodes and springs.

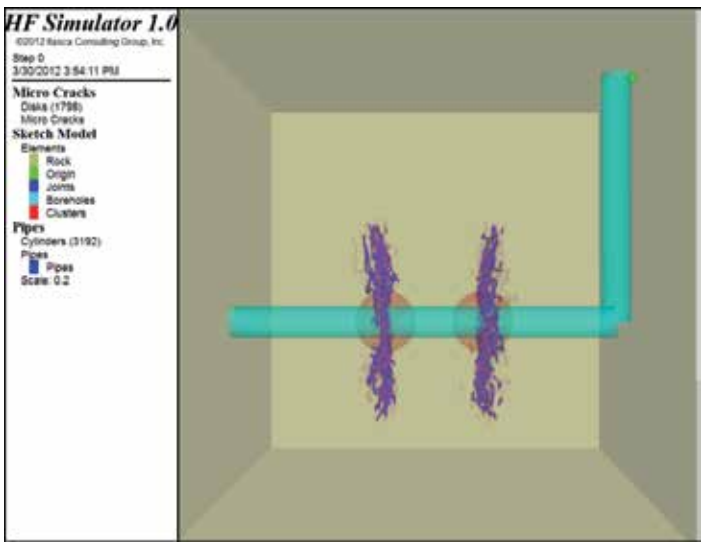

Figure 7. Hydraulic fractures generated in a homogeneous medium (dark blue disks are microcracks)

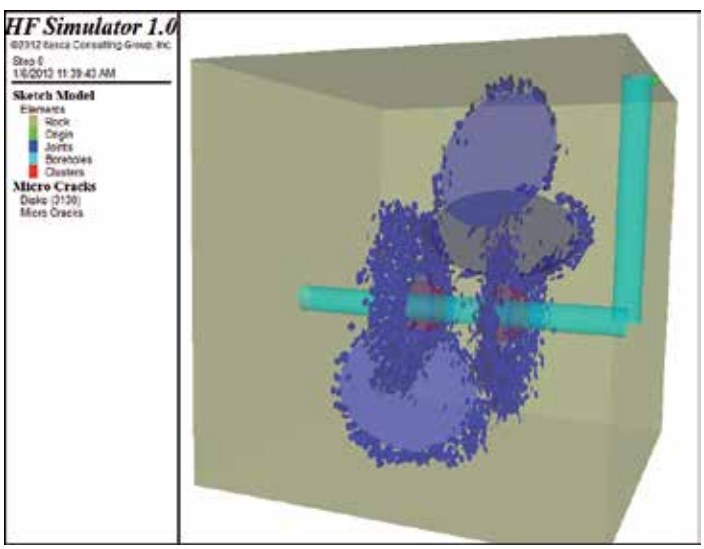

Figure 8. Hydraulic fractures generated in a medium with three pre-existing joints (blue disks are microcracks)

http://dx.doi.org/10.5772/56313

The springs between the nodes break when their strength (in tension) is exceeded. Breaking of the springs corresponds to the formation of microcracks, and microcracks may link to form macrofractures. The SJM (smooth joint model) is used to represent pre-existing joints in the model. Thus, the SJM allows simulation of sliding of a pre-existing joint in the model, unaffected by the apparent surface roughness resulting from lattice resolution and random arrangement of lattice nodes.

The model is fully coupled hydro-mechanically. There are several ways in which fluid interacts with the rock matrix. First, fluid pressures may induce opening or sliding of the fractures. Second, mechanical deformation of fractures causes changes in joint pressures. Third, the mechanical deformation changes the permeability of the rock mass as the joint apertures change.

The new code is a promising tool for simulation and understanding of complex processes, including propagation of HF and its interaction with DFN, during stimulation of unconventional reservoirs.

Acknowledgements

The development of the numerical code described in this paper was funded by BP America. The authors would like to thank BP America for their support. Matt Purvance, Jim Hazzard and Maurilio Torres of Itasca Consulting Group, Inc. are thanked for their valuable work on HF Simulator.

Author details

B. Damjanac, C. Detournay, P.A. Cundall and Varun

Itasca Consulting Group, Inc., Minneapolis, Minnesota, USA

References

[1] Potyondy, D. O, & Cundall, P. A. A Bonded-Particle Model of Rock. Int. J. Rock Mech. & Min. Sci., (2004). , 41, 1329-1364.

[2] Pierce, M. Mas Ivars D., Cundall P.A., Potyondy D.O. "A Synthetic Rock Mass Model for Jointed Rock," in Rock Mechanics: Meeting Society's Challenges and Demands (1st Canada-U.S. Rock Mechanics Symposium, Vancouver, May 2007), Fundamentals, New Technologies & New Ideas, E. Eberhardt et al., Eds. London: Taylor & Francis Group; (2007). , 1, 341-349.

[3] Itasca Consulting GroupInc. PFC2D (Particle Flow Code in 2 Dimensions), Version 4.0. Minneapolis: Itasca; (2008).

[4] Itasca Consulting GroupInc. PFC3D (Particle Flow Code in 3 Dimensions), Version 4.0. Minneapolis: Itasca; (2008).

[5] Peirce, A, & Detournay, E. An Implicit Set Method for Modeling Hydraulically Driven Fractures, Comput. Methods Appl. Mech. Engrg., (2008). , 197, 2858-2885.

Chapter 42

Testing and Review of Various Displacement Discontinuity Elements for LEFM Crack Problems

Hyunil Jo and Robert Hurt

Additional information is available at the end of the chapter

http://dx.doi.org/10.5772/56445

Abstract

The numerical modeling of hydraulic fractures in unconventional reservoirs presents significant challenges for field applications. There remains a need for accurate models that field personnel can use, yet remains consistent to the underlying physics of the problem [1]. For numerical simulations, several authors have considered a number of issues: the coupling between fracture mechanics and fluid dynamics in the fracture [2], fracture interaction [3-5], proppant transport [6], and others [7-9]. However, the available literature within the oil and gas industry often ignores the importance of the crack tip in modeling applications developed for engineering design. The importance of accurate modeling of the stress induced near the crack tip is likely critical in complex geological reservoirs where multiple propagating crack tips are interacting with natural fractures. This study investigates the influence of various boundary element numerical techniques on the accuracy of the calculated stress intensity factor near the crack tip and on the fracture profile, in general. The work described here is a part of a long-term project in the development of more accurate and efficient numerical simulations for field engineering applications.

For this investigation, the authors used the displacement discontinuity method (DDM). The numerical technique is applied using constant and higher-order elements. Further, the authors also applied special crack tip elements, derived elsewhere [10], to capture the square root displacement variation at the crack tip, expected from Linear Elastic Fracture Mechanics (LEFM). The authors expect that special crack tip elements will provide the necessary flexibility to choose other tip profiles. The crack tip elements may prove instrumental for efficient modeling of the different near-tip displacement profiles exhibited by Viscosity-Dominated or Toughness-Dominated regimes in hydraulic fracture propagation. As others have

shown [1,4,7], the accuracy of tip asymptote is critical in characterizing the stresses in the near-tip region of a propagating fracture.

The authors examined the numerically derived stress intensity factor for several crack geometries with and without higher-order elements and with and without special tip elements, to analytical solutions. As expected, they found that the cases with higher-order elements and special tip elements provide more accurate results than the cases with constant displacement discontinuity and/or no tip elements. However, the numerical technique developed still proved efficient.

These results show that numerical simulators can incorporate proper crack-tip treatments effectively. In addition, higher-order elements increase computational efficiency by reducing the number of elements instead of simply increasing the discretization of constant displacement elements. The accurate modeling of stress intensity factors is necessary to better simulate curved fractures, kinked cracks and interaction between fractures.

Keywords displacement discontinuity method, higher order elements, crack tip elements

1. Introduction

As new energy sources are sought for economic and security reasons, unconventional reservoirs attracted the oil and gas industry's attention. Among the unconventional options, shale gas reservoirs have become conspicuous. It is generally accepted that horizontal drilling and hydraulic fracturing are required to effectively recover hydrocarbons from the shale reservoirs [11]. Creating complex fracture networks by hydraulic fracturing is one of the most efficient ways to produce hydrocarbons from these reservoirs due to very low effective permeability (~500 nano Darcy). However, the numerical modeling of hydraulic fractures in such low permeable reservoirs presents significant challenges in field applications [1].

There remains a need for fast, yet accurate, models that remain consistent to the underlying physics of the problem. For numerical simulations, several researchers have considered a number of issues: the coupling between fracture mechanics and fluid dynamics in the fracture [2], fracture interaction [3-5], proppant transport [6], and others [7-9]. Further, there have been specific codes developed to model complex fracture network development [14-16]. Nevertheless, the available literature within the oil and gas industry often ignores the significance of the crack tip in modeling applications developed for hydraulic fracture design.

The importance of accurate modeling of the stress induced near the crack tip is likely critical in complex geological reservoirs. Multiple propagating crack tips interact with each other along with natural fractures, discontinuities, etc., during stimulation treatments in these reservoirs. Consequently, accurate modeling of the stress ahead of the propagating fracture is required to predict fracture paths in this complex environment. This study investigates the influence of several boundary element numerical techniques, available in the literature [10,12,13], on the stress intensity factor near the crack tip and on the fracture profile, in general.

http://dx.doi.org/10.5772/56445

This work is a part of a long-term project in the development of more accurate and efficient numerical simulations for field engineering applications.

To perform the investigation, we used the displacement discontinuity method (DDM), a version of the boundary element method (BEM). The method was developed for, and has been successfully applied to rock mechanics area such as mining engineering [17,18], fracture analysis [19,20], and wellbore stabilities [12]. We have applied DDM here using both constant and higher-order elements. The higher-order elements use a quadratic variation of displacement discontinuity, and are based on the use of three collocation points over a three-element patch centered at the source element [10], while the constant elements use a constant variation of displacement discontinuity [12]. Details related to the elements are elaborated on in Shou's work [12]. Further, the authors also applied special crack tip elements [10] to capture the square root displacement variation at the crack tip, expected from Linear Elastic Fracture Mechanics (LEFM). The authors expect that special crack tip elements will provide the necessary flexibility to choose other tip profiles. This flexibility will be instrumental for efficient modeling of the different near-tip displacement profiles exhibited by various regimes in hydraulic fracture propagation (e.g., Viscosity-Dominated or Toughness-Dominated [22,23]). As others have shown, the accuracy of tip asymptote is critical in characterizing the stresses in the near-tip region of a propagating fracture [1].

We examined the numerically derived stress intensity factor for three crack geometries with and without higher-order elements and with and without special tip elements, to analytical solutions. The three crack geometries are a pressurized crack orthogonal to the least principle stress, a slanted straight crack, and a circular arc crack. Several authors selected these specific geometries to justify the use of higher-order or specialized boundary elements [24-27]. However, the quantification of the computational efficiency coupled with the accuracy has been limited. Therefore, we present the following analysis that aids in determining the method that provides the most efficient, yet accurate solutions. Accurate and efficient methods are required for the development of field applications of engineering software packages.

Several other numerical techniques can be implemented within BEM. What we present here is not meant to be a review of possible combinations. We have chosen basic numerical techniques that provide the necessary flexibility to model very complex geometries, yet remain efficient enough for engineering modeling applications. The literature contains numerous examples of refinements to the techniques presented here [24-27]. For example, refinements with respect to the quarter-point method are found in Gray *et al*. [26] and refinements to higher-order elements are suggested by Dong and de Pater [25]. It is expected that implementing more refined methods will increase the efficiency of the numerical calculations. However, this work is primarily concerned with determining the general framework for BEM implementation.

The details related to the crack tip elements are available from a number of sources [10,12]. For brevity, this work will only summarize some basic concepts and mathematical formulas of the higher-order elements and the specialized crack tip elements. The next section of this paper describes the general displacement discontinuity method utilizing constant displacement elements. In section 3, the authors summarize the chosen higher order elements. Section 4 defines the special crack tip elements used in this work. Section 5 compares various combina-

tions of the presented methods to known solutions of various crack geometries for an estimation of accuracy of calculations. Section 5 concludes by comparing of the computational efficiencies exhibited by the various methods. Finally, some concluding remarks are provided in Section 6.

2. Displacement discontinuity method

The displacement discontinuity method (DDM), originally formulated by Crouch [12], is used here. DDM is based on the solution of the stresses and displacements at a point caused by a constant displacement discontinuity (DD) over a line segment in an elastic body under prescribed boundary conditions [12]. Due to the simplicity of mathematical formulas and procedures of DDM (with a constant DD), it has been widely applied to various engineering problems. This paper summarizes some of the important mathematical expressions but limits specificity. The details of DDM are well described in the literature [12].

The 2-D displacements and stresses at a point $(x,\ y)$, generated by a displacement discontinuity $(D_x(x),\ D_y(x))$ on the line segment $|x| \le a,\ y=0$, can be analytically expressed as follows [1-3]:

$$u_x = [2(1-\nu)f_{,y} - yf_{,xx}] + [-(1-2\nu)g_{,x} - yg_{,xy}] \tag{1}$$

$$u_y = [(1-2\nu)f_{,x} - yf_{,xy}] + [2(1-\nu)g_{,y} - yg_{,yy}] \tag{2}$$

$$\sigma_{xx} = 2G[2f_{,xy} + yf_{,xyy}] + 2G[g_{,yy} + yg_{,yyy}] \tag{3}$$

$$\sigma_{yy} = 2G[-yf_{,xyy}] + 2G[g_{,yy} - yg_{,yyy}] \tag{4}$$

$$\sigma_{xy} = 2G[f_{,yy} + yf_{,yyy}] + 2G[-yg_{,xyy}] \tag{5}$$

where $f(x,\ y)$ and $g(x,\ y)$ are defined as:

$$f(x,y) = \frac{-1}{4\pi(1-\nu)} \int_{-a}^{a} D_x(\xi) \ln[\sqrt{(x-\xi)^2 + y^2}]\, d\xi \tag{6}$$

$$g(x,y) = \frac{-1}{4\pi(1-\nu)} \int_{-a}^{a} D_y(\xi) \ln[\sqrt{(x-\xi)^2 + y^2}]\, d\xi \tag{7}$$

and where the displacement discontinuity components are defined as:

http://dx.doi.org/10.5772/56445

$$D_x(x) = u_x(x,0^-) - u_x(x,0^+) \tag{8}$$

$$D_y(x) = u_y(x,0^-) - u_y(x,0^+) \tag{9}$$

For constant displacement elements (i.e. constant $D_x(x)$ and $D_y(x)$), the DD components can come out of the integrals, and then Equations (6) and (7) can be simplified as:

$$f(x,y) = I_0(x,y)D_x \tag{10}$$

$$g(x,y) = I_0(x,y)D_y \tag{11}$$

where

$$\begin{aligned} I_0(x,y) = & \int_{-a}^{a} \ln[\sqrt{(x-\xi)^2+y^2}]d\xi \\ & = y\left[\arctan\frac{y}{(x-a)} - \arctan\frac{y}{(x+a)}\right] - (x-a)\ln\sqrt{(x-a)^2+y^2} \\ & +(x+a)\ln\sqrt{(x+a)^2+y^2} - 2a \end{aligned} \tag{12}$$

For simplicity, the derivatives of $I_0(x,\ y)$, used to calculate the stresses and displacements (i.e. Equations (1) to (5)), are omitted in this paper. The derivatives are given in Shou *et al.* [10]. Since the numerical procedures of DDM (with constant displacement discontinuities) are well established in the available literature [12], they are not given herein.

However, DDM with a constant DD can't accurately calculate the stresses and displacements of the area closer than about one element-length distance from a boundary [12]. To improve the accuracy of calculations in close proximity to the boundaries, Crawford *et al.* developed higher-order displacement elements [24] among others [25]. Although higher-order elements overcame the limitations of constant elements and improved the accuracy of DDM, the method significantly increases the number of degrees of freedom. In other words, the higher-order elements increase the number of equations that must be solved.

To improve the accuracy of DDM without sacrificing the number of degrees of freedom of the overall system, a new higher-order elements method was suggested by Shou *et al.* [10]. The method used collocation points at the centers of the source elements and its two adjacent neighbors, so it could maintain the same degrees of freedom as the constant elements method by sharing the DD of the two adjacent neighbors. Other methods have been suggested by in the literature [15,25] to overcome issues with kinked or intersecting cracks when utilizing neighboring elements in calculations.

This study uses Shou *et al.*'s method to satisfy one of this research's objectives, which is to develop methods that reduce computation costs while improving accuracy. The next section

will summarize some basic concepts and mathematical formulas for the higher-order elements used in this work. As above, further details of the higher-order elements are available in [10].

3. Higher-order elements of displacement discontinuity method

Higher-order elements, as formulated by Shou *et al.*, use quadratic displacement elements. The calculation of the DD component of a particular element is accomplished by using three collocation points. The center collocation point is within the element of interest, while the bounding collocation points are within the neighboring elements. This configuration forms a three-element "patch" (shown in Figure 1), on which the quadratic formulation is performed. Equation (13) shows how the value of the DD components is formed mathematically.

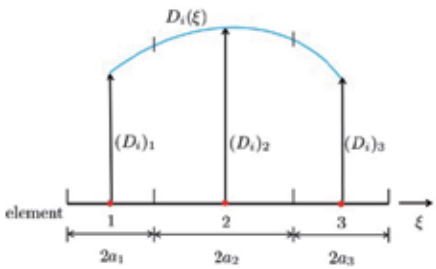

Figure 1. Quadratic collocation for the new higher-order elements [2]

$$D_i(\xi) = N_1(\xi)(D_i)_1 + N_2(\xi)(D_i)_2 + N_3(\xi)(D_i)_3 \tag{13}$$

where $(D_i)_1$, $(D_i)_2$ and $(D_i)_3$ are the nodal displacement discontinuities ($i = x$ *or* y) and

$$N_1 = \frac{\xi(\xi - a_2 - a_3)}{(a_1 + a_2)(a_1 + 2a_2 + a_3)} \tag{14}$$

$$N_2 = \frac{-(\xi + a_1 + a_2)(\xi - a_2 - a_3)}{(a_1 + a_2)(a_2 + a_3)} \tag{15}$$

$$N_3 = \frac{\xi(\xi + a_1 + a_2)}{(a_2 + a_3)(a_1 + 2a_2 + a_3)} \tag{16}$$

N_1, N_2 and N_3 are the collocation shape functions whose a_1, a_2 and a_3 are half length of the three elements of the patch.

http://dx.doi.org/10.5772/56445

Combining Equations (13) through (16) with Equations (6) and (7) gives the following simplified expressions:

$$f(x,y) = \frac{-1}{4\pi(1-\nu)} \sum_{j=1}^{3} (D_x)_j F_j(I_0, I_1, I_2) \tag{17}$$

$$g(x,y) = \frac{-1}{4\pi(1-\nu)} \sum_{j=1}^{3} (D_y)_j F_j(I_0, I_1, I_2) \tag{18}$$

where the subscript j indicates the j th collocation node in the three-element patch and $F_j(I_0, I_1, I_2)$ is defined as

$$F_j(I_0, I_1, I_2) = \int N_j(\xi) \ln[\sqrt{(x-\xi)^2 + y^2}] d\xi, \quad j = 1 \; to \; 3 \tag{19}$$

which can be expressed in terms of constant, linear, and quadratic kernels (I_0, I_1, I_2). The definition of these kernels is given by Shou *et al.* [10].

Based on these formulas, a crack can be discretized into N elements (see Figure 2) and 2N equations in terms of the DD component unknowns are formed (i.e. 2N unknowns of D_x and D_y). Under certain boundary conditions, the 2N unknowns can be obtained. Once the 2N unknowns are calculated, the 2-D displacements and stresses at a point (x, y) can be calculated through Equations (1) to (5). Further, Equations (20) and (21) compute the stress intensity factors at the crack tip.

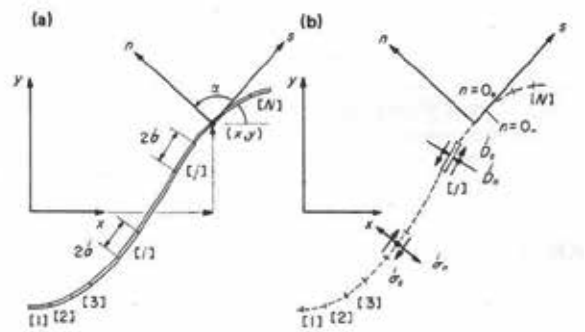

Figure 2. Representation of a crack by N elemental displacement discontinuities [12]

$$K_I = \frac{G}{4(1-\nu)} \sqrt{\frac{2\pi}{a^*}} D_n^* \tag{20}$$

$$K_{II} = \frac{G}{4(1-\nu)}\sqrt{\frac{2\pi}{a^*}}D_s^* \tag{21}$$

where a^* is the half length of the crack tip element, and D_n^* and D_s^* are normal and shear DD at the crack tip, respectively.

4. Crack tip elements of displacement discontinuity method

In addition to advanced elements, Shou *et al.* formulated two special crack tip elements to capture the square root displacement variation at the crack tip, expected from Linear Elastic Fracture Mechanics (LEFM) [10]. One is to use a constrained collocation point one-quarter of an element length away from the end of the crack. This study will refer to this as a quarter element method. The other tip element is simply a prescribed displacement discontinuity proportional to the square root variation at the crack tip. Herein, it is called the square root element method. This study uses their methods to calculate the stresses and displacements at the crack tip.

4.1. Quarter element method

Shou *et al.* introduced a constrained collocation point one-quarter of the crack tip element length away from the crack tip element. The DDs of the point will be set zero. Figure 3 shows the element.

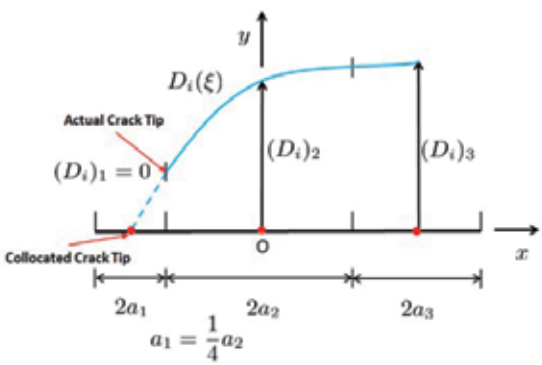

Figure 3. Quarter element method at a crack tip [2]

Numerical implementation of this method is more efficient compared to the square root element method and provides reasonably accurate results. However, the displacement discontinuities near the crack tip do not capture the square root displacement variation at the crack tip, expected from LEFM [10]. Theoretically, this method may give unreliable results.

http://dx.doi.org/10.5772/56445

Thus, Shou *et al.* introduced a more sophisticated crack tip elements method to comply with the LEFM physical phenomenon, which is the square root element method summarized below.

4.2. Square root element method

LEFM predicts that in the vicinity of the crack tip the crack displacement is proportional to the square root of the distance from the crack tip (i.e.$w \propto \sqrt{\xi}$). Figure 4 illustrates the basics of the square root crack tip element. Equation (22) shows the representation of $\sqrt{\xi}$ variation of the displacement discontinuities $D_i(\xi)$ along the crack tip.

$$D_i(\xi) = D_{ci}\sqrt{\frac{\xi}{a}} \quad i = x, y \tag{22}$$

where D_{ci} are the DD values at the center of the crack tip element. Substituting Equation (22) into Equations (1) to (5) the stresses and displacements are resolved in terms of D_{ci}. The solutions can be expressed in kernel functions, similar to higher-order elements methods. The details of the kernel functions were well documented in previous work [10].

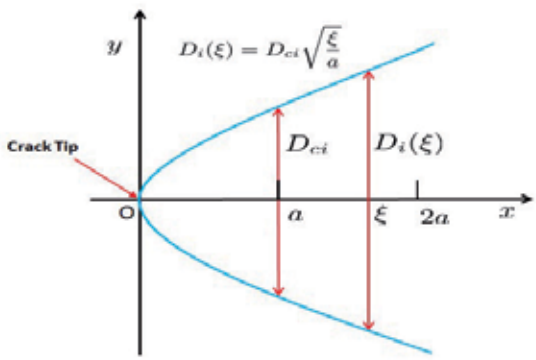

Figure 4. Square root crack tip element [2]

5. Comparison

To access the accuracy of the selected numerical techniques, this study compares the stress near the crack tips and stress intensity factors for three crack geometries with constant displacement or higher-order elements, both elements will be combined with and without specialized quarter and square root crack tip elements. We chose these particular geometries because analytical solutions are readily available. Further, many previous publications comparing BEMs have chosen these same geometries [25-27]. This research uses following elastic properties: $E = 10^6$ *psi* and $\nu = 0.2$ in the calculations.

5.1. Single pressurized crack in an infinite elastic domain

A single pressurized crack is a basic fracture geometry, and the analytical solutions are well documented [19,28]. Figure 5 shows a schematic diagram for the fracture geometry. The crack is pressurized by a pressure p=1000 psi. The crack length is 10 inches and is discretized into 10 elements with equal length. According to the specified method, the two crack tips may be replaced by specialized crack tip elements. This research compares half width, stresses at defined locations, and stress intensity factors computed from each method.

Figure 5 illustrates the chosen locations where each of the given methods calculates the stress. The points are arbitrary, but chosen at a location of symmetry with respect to the fracture. In Figure 5, the blue X represents the point orthogonal to the fracture plane at the mid-point of the fracture. The red diamond represents a point ahead of the fracture tip. For convenience, this report uses the following abbreviations to represent each method: AM (analytical method), CDD (only constant displacement discontinuity), HDD (only higher-order elements), CDDCE (constant DD with the quarter element method), CDDCT (constant DD with the square root element method), HDDCE (higher-order elements with the quarter element method), and HDDCT (higher-order elements with the square root element method).

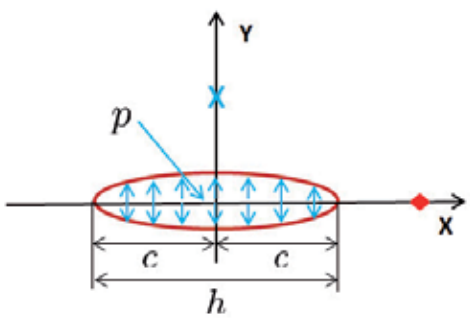

Figure 5. A crack under a constant pressure. The blue X represents a point orthogonal to the fracture plane where the induced stress calculated from each method is compared. The red diamond represents the evaluation point ahead of the fracture tip.

Equation (23) is the analytical solution of the dimensionless half width under a constant pressure [29].

$$\frac{w(x)}{c} = \frac{4p}{E'}\sqrt{1-\left(\frac{x}{c}\right)^2} \tag{23}$$

Figure 6 is a plot of the calculated fracture profile from each method. The analytical solution is the solid blue line. The computed half widths from each of the numerical methods are shown as a series of points. From the results, CDD overestimates the half width particularly near crack tip area as others have found [20]. Conversely, HDD underestimates the fracture width in the proximity of the tip. Methods that use tip elements show fracture width profiles close to the

http://dx.doi.org/10.5772/56445

analytical solution. The importance of utilizing special crack tip elements is well established in the literature [10, 26, 27].

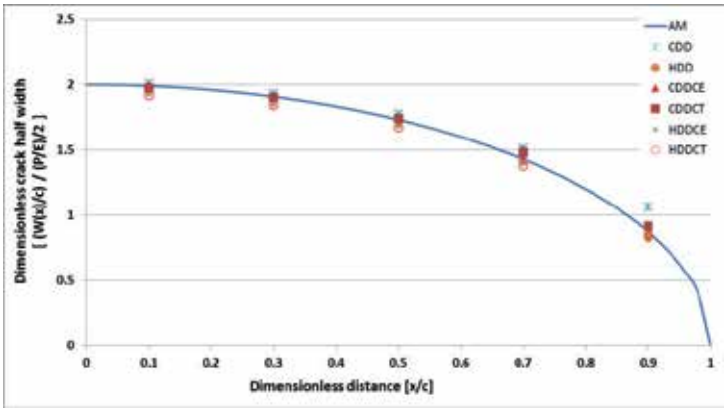

Figure 6. Dimensionless crack half width versus Dimensionless distance from the crack center (HDD, CDDCE, CDDCT and HDDCE overlap)

Figure 7 is more illustrative for comparing the accuracy of the various methods. It shows the relative error from the computation of the half width compared to the analytical solution (i.e. $\frac{w - w_{AM}}{w_{AM}}$%). The relative errors of all methods increase as they approach to the crack tip. The majority of the methods demonstrate errors bounded between -5% to 5%, except for CDD, which shows over 20% in close proximity to the crack tip. Computational errors over 20% from CDD methods have been reported in the literature [20].

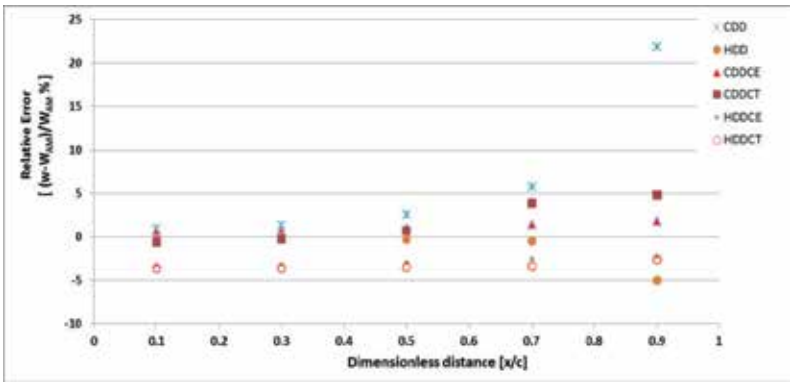

Figure 7. Relative error of the half width

To evaluate the perturbed stress state due to the presence of a pressurized crack we use [30]

$$\frac{\sigma_{xx}}{-p} = \frac{\left(\frac{x}{c}\right)}{\sqrt{\left(\frac{x}{c}\right)^2 - 1}} - 1 \tag{24}$$

Equation (24) provides a dimensionless stress $\frac{\sigma_{xx}}{p}$ at a point along X-axis (the distance from the crack tip normalized by the crack half-length), which in this case is red diamond in Figure 5.

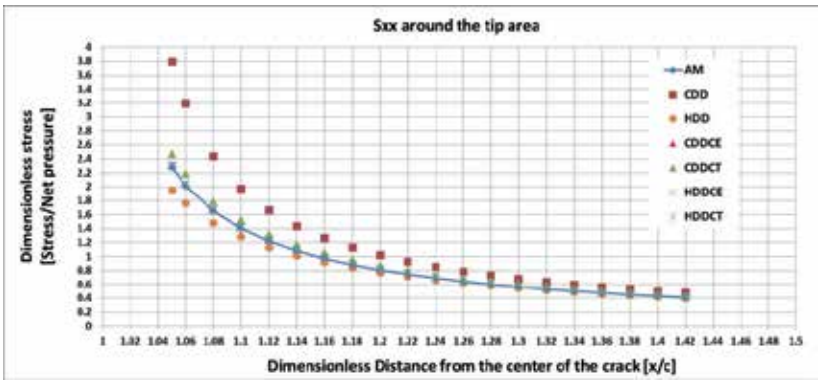

Figure 8. Dimensionless stress versus Dimensionless distance ahead of the crack tip (i.e. at red diamond) (CDDCE, HDDCE and HDDCT overlap)

Figure 8 plots the dimensionless stress ahead of the crack tip. x/c = 1 represents the crack tip. Figure 9 plots the relative stress (the ratio of $\frac{\sigma_{xx}}{p}$ to the analytical $\frac{\sigma_{xx}}{p}$) near the crack tip area for each numerical method.

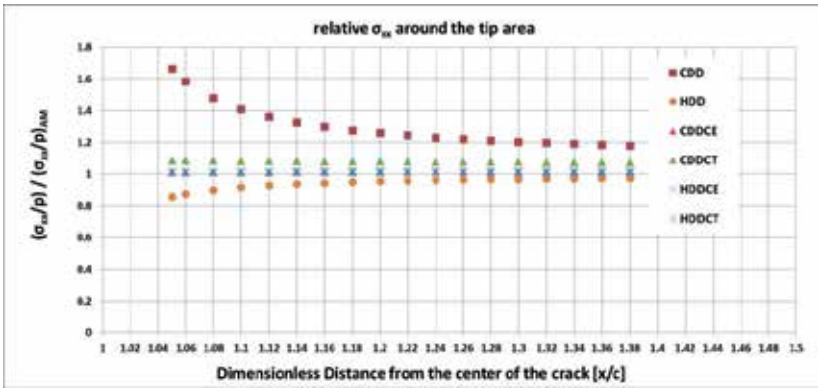

Figure 9. Relative stress versus Dimensionless distance ahead of the crack tip (CDDCE, HDDCE and HDDCT overlap)

http://dx.doi.org/10.5772/56445

These figures also show that CDD overestimates the stress and HDD underestimates it while the other methods give results with less than 1% error. The inaccuracies of the methods without tip elements become significant closer to the crack tip. Similar to the half width results, the results of the methods with tip elements overlap since they are close to the analytical solution.

To calculate the stress induced orthogonal to a pressurized crack we use [30]

$$\frac{\sigma_{yy}}{p} = -\frac{\left(\frac{L}{c}\right)}{\sqrt{\left(\frac{L}{c}\right)^2+1}} + 1 + \frac{\left(\frac{L}{c}\right)}{\left\{\sqrt{\left(\frac{L}{c}\right)^2+1}\right\}^3} \tag{25}$$

Equation (25) expresses a dimensionless stress $\frac{\sigma_{yy}}{p}$ at a point along the Y-axis (the distance from the crack face is normalized by the crack half-length), which is represented by the blue X in Figure 5. Figure 10 shows the results of the calculation from each numerical method. These results show consistency with the analytical solution, regardless of the numerical method. This is expected, as the location where the stress is calculated is sufficiently far from the crack tip, i.e. more than the length of one discretized element [12].

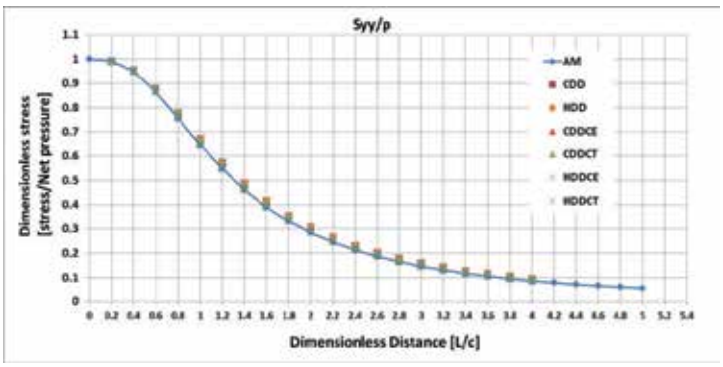

Figure 10. Dimensionless stress versus Dimensionless distance orthogonal to the fracture plane, i.e. at the blue X. In this case, all methods overlap

Table 1 shows the calculated stress intensity factor, along with the ratio to the analytical solution. For the mode I (or K_I), CDD shows the biggest error while CDDCE, HDDCE and HDDCT give around 1% errors. Obviously, the mode II (or K_{II}) stress intensity factor is zero. So, Table 1 omits the results.

Reasonable values from calculations of the stresses and displacements can be achieved at distances greater than the length of one discretized element, regardless of the numerical technique. Close to the crack tip, however, the error of displacements, stresses, and stress intensity factors for CDD elements are significant, whereas CDDCE, HDDCE and HDDCT provide reasonable estimations. This is not surprising; similar results are well documented in the literature [12,24,26].

	KI [psi √in]	KI/ KI_{AM}
AM	3963.3	1
CDD	4905.6	1.238
HDD	3670.8	0.926
CDDCE	3933.8	0.993
CDDCT	4219	1.065
HDDCE	3933.8	0.993
HDDCT	3918.5	0.989

Table 1. Stress intensity factors

5.2. A slanted straight crack

While a straight pressurized crack shows zero K_{II}, a slanted straight crack under a uniform tension can show a variable K_{II} depending on the angle of incidence to the applied tension. Figure 11 illustrates the crack geometry. The stress intensity factors are calculated by [19]

$$K_I = \sigma\sqrt{\pi a}\sin^2(\beta) \qquad K_{II} = \sigma\sqrt{\pi a}\sin(\beta)\cos(\beta) \tag{26}$$

Equation (26) expresses the analytical solution of the stress intensity factors [19]. The uniform tension is $\sigma = 1000\ psi$. The crack length is 10 inches. It is discretized into 10 elements with equal length. The two crack tips are replaced by crack tip elements according to the applied method.

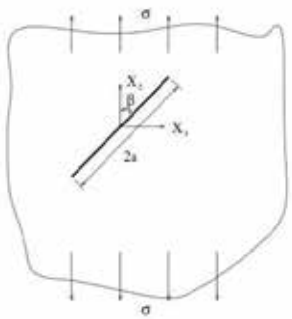

Figure 11. Slanted straight crack under uniform axial tension at infinity [25]

Figure 12 shows the dimensionless K_I (i.e. $\frac{K_I}{\sigma\sqrt{\pi a}}$) according to the slanted angle and Figure 13 gives the dimensionless K_{II} (i.e. $\frac{K_{II}}{\sigma\sqrt{\pi a}}$) according to the slanted angle, respectively. Similar to the previous crack geometry, CDD and CDDCT overestimate K_I and K_{II} while HDD underestimates them. CDDCE, HDDCE, and HDDCT show fairly accurate results, so that they

http://dx.doi.org/10.5772/56445

overlap in Figure 13 and 14. However, the calculation errors of the two stress intensity factors exhibit opposing patterns. For K_I, the errors increase as the slanted angle becomes larger. Conversely, the errors of K_{II} are maximal at 45° and at a minimum at 0° and 90°.

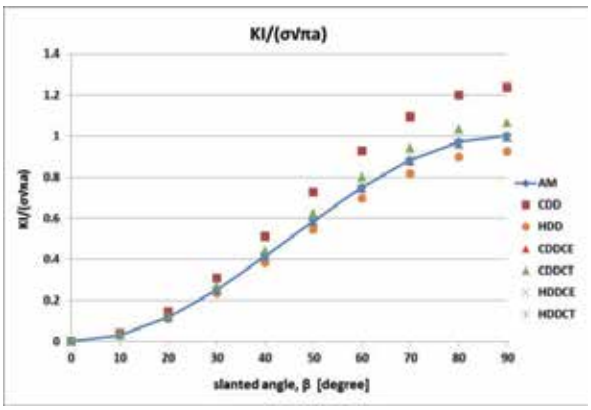

Figure 12. Dimensionless K_I versus the slanted angle (CDDCE, HDDCE and HDDCT overlap)

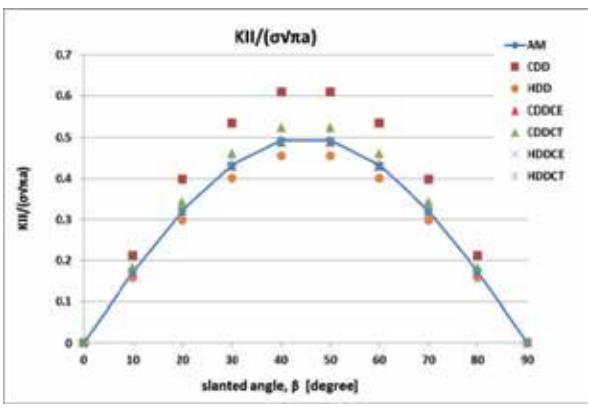

Figure 13. Dimensionless K_{II} versus the slanted angle (CDDCE, HDDCE and HDDCT overlap)

5.3. A circular arc crack

Curved cracks may represent more realistic fracture geometry and exhibit complexity in calculation of the stress intensity factors. This study selects a circular arc crack under a far field uniform biaxial tension in order to evaluate the accuracy of the numerical methods. Figure 14 describes the fracture geometry. The uniform biaxial tension is $\sigma = 1000\ psi$. The analytical solutions of K_I and K_{II} for a curved crack are given by [19]

$$K_I = \frac{\sigma\sqrt{\pi r \sin(\alpha/2)}}{1+\sin^2(\alpha/4)}\cos(\alpha/4) \qquad K_{II} = \frac{\sigma\sqrt{\pi r \sin(\alpha/2)}}{1+\sin^2(\alpha/4)}\sin(\alpha/4) \tag{27}$$

where r is the radius of the circular arc [19].

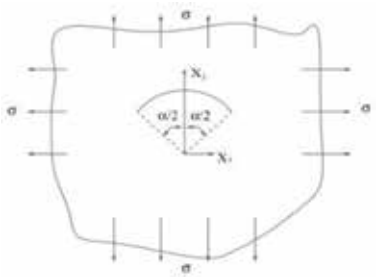

Figure 14. Circular arc crack under uniform biaxial tension [8]

Figures (15) and (16) show the values of the calculated K_I and K_{II} as a function of the circular crack angle, respectively. The figures depict actual stress intensity factor values under the prescribed biaxial tension, instead of dimensionless values. The unit of K_I and K_{II} is $psi\sqrt{in}$. The effective half-length of the crack is ambiguous due to variable circular arc length related to the prescribed circular arc angle (α). The circular arc has a 10 inch radius. It is discretized into 20 elements with equal length. The two tip elements are evenly discretized into 10 additional segments to apply the tip elements methods, respectively. Thus, the circular arc has 38 segments (i.e. 18 middle identical elements and 20 identical tip elements).

Figures (17) and (18) show the normalized K_I and K_{II} stress intensity factors as a function of the circular crack angle, respectively.

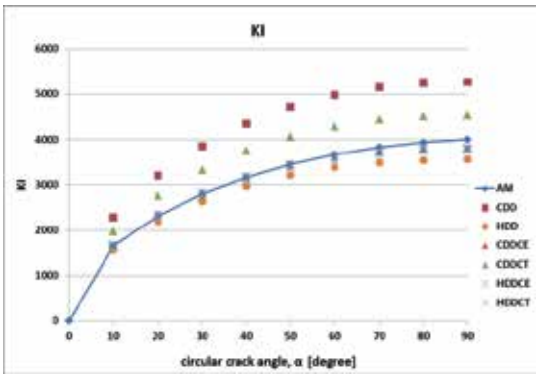

Figure 15. KI versus the circular arc angle (CDDCE, HDDCE and HDDCT overlap)

http://dx.doi.org/10.5772/56445

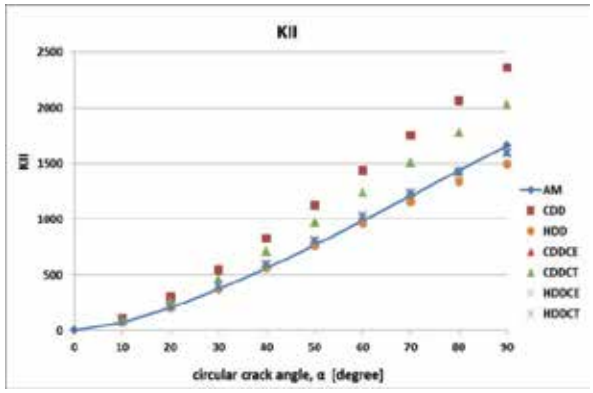

Figure 16. KII versus the circular arc angle (CDDCE, HDDCE and HDDCT overlap)

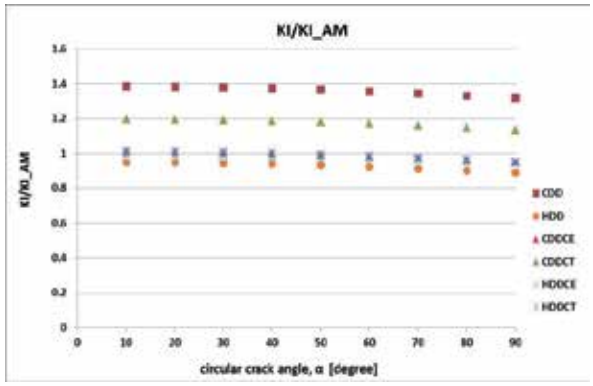

Figure 17. Relative K_I versus the circular arc angle (CDDCE, HDDCE and HDDCT overlap)

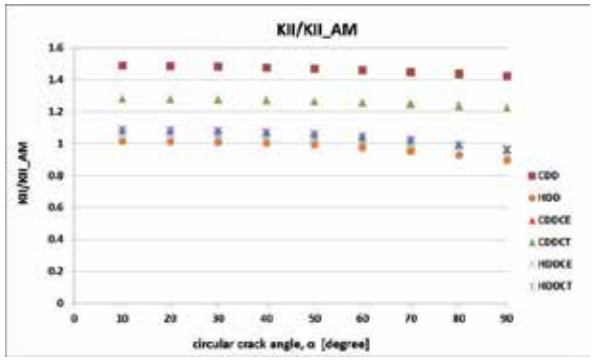

Figure 18. Relative K_{II} versus the circular arc angle (CDDCE, HDDCE and HDDCT overlap)

Based on the results presented in this section, numerical calculations of K_I and K_{II} show similar patterns. As the circular crack angle increases, the differences between the analytically derived stress intensity factors increase. The ratio between the analytical and numerical stress intensity factors decreases, however. CDD and CDDCT show the overestimation while HDD method underestimates the stress intensity factors. The other methods (CDDCE, HDDCE, and HDDCT) provide very close results compared to the analytical solution.

5.4. Computational efficiency

In general, we find that CDDCE, HDDCE, and HDDCT methods significantly increase the accuracy of the computation of stress intensity factors for the geometries presented here. However, the required computational resource varies among the numerical methods. Further, for constant displacement elements, accuracy of the stress calculations ahead of the crack tip can be improved by increasing the number of elements. In order to objectively evaluate the efficiency of the numerical methods, we return to the pressurized crack example from Section 5.1. The following section first compares the accuracy improvement by increasing the number of elements for the constant element method. Then we compare the computation time for calculating the stress intensity factors for this particular problem.

The computer specifications used in this work are as follows: CPU-Intel® Xeon W3670 @ 3.2GHZ, installed memory (RAM)-24 gigabytes, OS- 64-bit Windows 7®, Software- Matlab® R2011b.

This study uses the stress of a horizontal crack near the crack tip to show the computational accuracy of simply increasing the number of CDD elements compared to higher-order elements and/or special tip elements. Figure 19, shows the normalized stress (the ratio of σ_{xx}/p to the analytical σ_{xx}/p) near the crack tip as a function of the number of CDD elements. The number at the legend indicates the number of CDD elements. As expected, increasing the number of elements results in a corresponding improvement in calculation accuracy. Figure 19 illustrates that at least 100 CDD elements are required to show less than 1% error. In other words, an order of magnitude increase in the number of CDD elements is required to match the accuracy derived with CDDCE, HDDCE and HDDCT methods (see Figure 9).

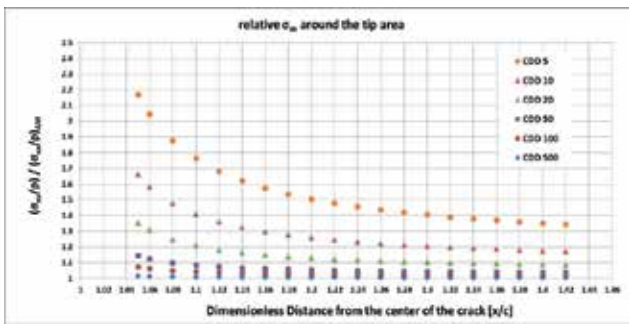

Figure 19. Relative stress versus Dimensionless distance ahead of the crack tip (i.e. at red diamond) according to the number of CDD elements used

http://dx.doi.org/10.5772/56445

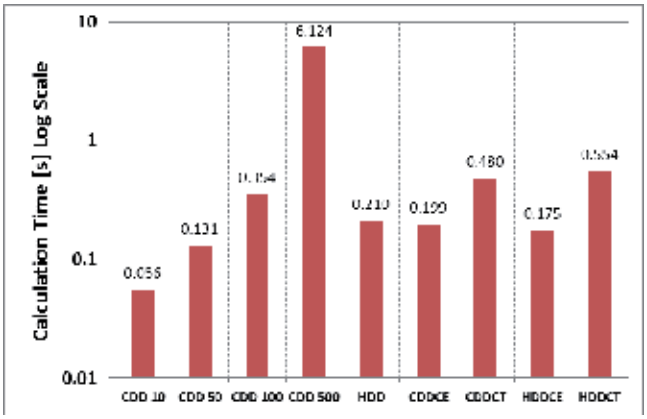

Figure 20. Computation time for the solution of the pressurized crack exercise

Finally, the computational efficiency is evaluated by inspecting Figure 20. This figure plots the calculation time of the various numerical methods for the pressurized crack exercise described above. As expected, CDD calculations with fewer elements are completed more quickly. Interestingly the CDDCE, HDDCE, and HDDCT methods show similar computation times while maintaining the highest accuracy of the numerical methods. This result allows for further refinement and evaluation of the CDDCE, HDDCE, and HDDCT methods using more refined element choices and increasingly complex crack geometries.

6. Conclusion

Overall results show that CDD gives prominent errors of calculations of stresses, displacements, and stress intensity factor compared to the other methods. Particularly, when approaching to the crack tips and a fracture is curved, the errors of CDD significantly increase. Replacing tip elements by special crack tip elements can mitigate calculation errors when close to the crack tips. Using higher-order elements helps to reduce errors for the simple straight crack geometries. When a fracture is curved, the efficiency of combining specialized crack tip elements in computational errors in the calculation of K_I and K_{II} is more important than for simple fracture geometries. Combination of higher-order elements and crack tip elements give the most accurate calculations, yet retain the necessary efficiency. However, the overall efficiency of CDDCE, HDDCE and HDDCT methods cannot be definitively evaluated using the simple geometries shown here. We reserve that analysis for subsequent publications.

For comparison within this work, the numerical methods maintained a similar number of elements for each fracture geometry. Increasing the number of CDD elements increases the accuracy of the CDD method. However, this requires increased computation time. Thus, the use of higher-order elements and crack tip elements is likely warranted if considering the development of more accurate and efficient numerical simulations for field engineering applications where computation resources are restricted. Evaluating the efficiency of specific

combinations of higher-order elements coupled with specialized crack tip elements requires more complex geometries than presented here.

Nomenclature

u	Displacement
σ	Stress
E	Young's modulus
v	Poisson's ratio
G	Shear modulus
E'	Plane strain, $\frac{E}{1-v^2}$
c, a	Fracture half-length or half height
h	Fracture length or height

Acknowledgements

The authors thank Baker Hughes for supporting this research and for permission to publish this paper, Randy LaFollette, for sincere advice and encouragement, and Russell Maharidge, PhD for considerate reviews.

Author details

Hyunil Jo* and Robert Hurt

*Address all correspondence to: hyunil.jo@bakerhughes.com

Baker Hughes, Tomball, TX, USA

References

[1] Adachi, A, Siebrits, E, Peirce, A, & Desroches, J. Computer simulation of hydraulic fractures. International Journal Of Rock Mechanics And Mining Sciences (2007). , 44(5), 739-757.

[2] Naceur, K. B, Thiercelin, M, & Touboul, E. Simulation of Fluid Flow in Hydraulic Fracturing: Implications for 3D Propagation. SPE Production Engineering (1990). SPE 16032, 5(2), 133-141.

[3] Germanovich, L, & Astakhov, D. Multiple fracture model. In: Jeffrey, McLennan, editors. Proceedings of the three dimensional and advance hydraulic fracture modeling. Workshop held at 4th North American rock mechanics symposium, Seattle, July 29-31, (2000). , 45-70.

[4] Bunger, A. P, Zhang, X, & Jeffrey, R. G. Parameters Affecting the Interaction Among Closely Spaced Hydraulic Fractures. SPE Journal;17(1):SPE-140426-PA, 292-306.

[5] Olson, J. E, & Wu, K. Sequential vs. Simultaneous Multizone Fracturing in Horizontal Wells: Insights From a Non-Planar, Multifrac Numerical Model. In: SPE Hydraulic Fracturing Technology Conference. The Woodlands, Texas, USA: Society of Petroleum Engineers. SPE-M, 152602.

[6] Gu, H, & Siebrits, E. On numerical solutions of hyperbolic proppant transport problems. In: Proceedings of the 10th international conference on hyperbolic problems: theory, numerics and applications, Osaka, Japan, September (2004). , 13-17.

[7] Gordeliy, E, & Detournay, E. A fixed grid algorithm for simulating the propagation of a shallow hydraulic fracture with a fluid lag. International Journal for Numerical and Analytical Methods in Geomechanics;35(5):602.

[8] Zhang, X, Jeffrey, R. G, & Thiercelin, M. Deflection and propagation of fluid-driven fractures at frictional bedding interfaces: A numerical investigation. Journal of Structural Geology (2007).

[9] Sellers, E, & Napier, J. A comparative investigation of micro-flaw models fog the simulation of brittle fracture in rock. Computational Mechanics (1997).

[10] Shou, K. J, & Crouch, S. L. A higher order displacement discontinuity method for analysis of crack problems. International Journal of Rock Mechanics and Mining Science & Geomechanics Abstracts (1995).

[11] King, G. E. Thirty Years of Gas Shale Fracturing: What Have We Learned? In: SPE Annual Technical Conference and Exhibition. Florence, Italy: Society of Petroleum Engineers. SPE 133456

[12] Crouch, S. L, & Starfield, A. M. Boundary Element Methods in Solid Mechanics: With Applications in Rock Mechanics and Geological Engineering: George Allen & Unwin; 1 edition, (1983).

[13] Crouch, S. L. Solution of plane elasticity problems by the displacement discontinuity method. I. Infinite body solution. International Journal for Numerical Methods in Engineering (1976).

[14] Olson, J. E. Predicting fracture swarms-- the influence of subcritical crack growth and the crack-tip process zone on joint spacing in rock. Geological Society, London, Special Publications (2004). , 231(1), 73-88.

[15] Wu, R, Kresse, O, Weng, X, Cohen, C-e, & Gu, H. Modeling of Interaction of Hydraulic Fractures in Complex Fracture Networks. In: SPE Hydraulic Fracturing Technology Conference. The Woodlands, Texas, USA: Society of Petroleum Engineers. SPE152052

[16] Weng, X, Kresse, O, Cohen, C-E, Wu, R, & Gu, H. Modeling of Hydraulic-Fracture-Network Propagation in a Naturally Fractured Formation. SPE Production & Operations;26(4):SPE-140253, 368-380.

[17] NapierJAL. Modelling of fracturing near deep level gold mine excavations using a displacement discontinuity approach. Mechanics of jointed and faulted rock. Rossmanith (ed), Balkema: Rotterdam: (1990). , 709-716.

[18] Peirce, A. P. Napier JAL. A Spectral Multipole Method For Efficient Solution Of Large-Scale Boundary-Element Models In Elastostatics. International Journal For Numerical Methods In Engineering (1995). , 38(23), 4009-4034.

[19] Tada, H, Paris, P. C, & Irwin, G. R. The Stress Analysis of Cracks Handbook. 3 ed: American Society of Mechanical Engineering; (2000).

[20] Exadaktylos, G, & Xiroudakis, G. A G2 constant displacement discontinuity element for analysis of crack problems. Computational Mechanics;, 45(4), 245-261.

[21] Shou, K-J. Napier JAL. A two-dimensional linear variation displacement discontinuity method for three-layered elastic media. International Journal of Rock Mechanics and Mining Sciences (1999).

[22] Garagash, D. I, & Detournay, E. Near tip processes of a fluid-driven fracture. ASME J Appl Mech (2000). , 67, 183-92.

[23] Detournay, E. (2004). Propagation regimes of fluid driven fractures in impermeable rocks. Int. J. Geomechanics , 4(1), 1-11.

[24] Crawford, A. M, & Curran, J. H. Higher-order functional variation displacement discontinuity elements. International Journal of Rock Mechanics and Mining Sciences & Geomechanics Abstracts (1982).

[25] Dong, C. Y, & De Pater, C. J. (2001). Numerical implementation of displacement discontinuity method and its application in hydraulic fracturing. Computer Methods in Applied Mechanics and Engineering;191:745.

[26] Gray, L. J, Phan, A. V, Paulino, G. H, & Kaplan, T. Improved quarter-point crack tip element. Engineering Fracture Mechanics (2003). , 70(2), 269-283.

[27] Yan, X. Q. A special crack tip displacement discontinuity element. Mechanics Research Communications (2004). , 31(6), 651-659.

http://dx.doi.org/10.5772/56445

[28] Pollard, D, & Segall, P. Theoretical displacements and stresses near fractures in rock: with applications to faults, joints, veins, dikes and solution surfaces. In: ATKINSON, B K. Fracture Mechanics of Rock. Academic Press, London, (1987). , 277-350.

[29] Valkó, P, & Economides, M. J. Hydraulic Fracture Mechanics. 1 ed: Wiley; (1995).

[30] Sneddon, I. N. The Distribution Of Stress In The Neighbourhood Of A Crack In An Elastic Solid. Proceedings Of The Royal Society Of London Series A-Mathematical And Physical Sciences (1946). , 187(1009), 229-260.

Chapter 43

The Impact of the Near-Tip Logic on the Accuracy and Convergence Rate of Hydraulic Fracture Simulators Compared to Reference Solutions

Brice Lecampion, Anthony Peirce,
Emmanuel Detournay, Xi Zhang, Zuorong Chen,
Andrew Bunger, Christine Detournay, John Napier,
Safdar Abbas, Dmitry Garagash and Peter Cundall

Additional information is available at the end of the chapter

http://dx.doi.org/10.5772/56212

Abstract

We benchmark a series of simulators against available reference solutions for propagating plane-strain and radial hydraulic fractures. In particular, we focus on the accuracy and convergence of the numerical solutions in the important practical case of viscosity dominated propagation. The simulators are based on different propagation criteria: linear elastic fracture mechanics (LEFM), cohesive zone models/tensile strength criteria, and algorithms accounting for the multi-scale nature of hydraulic fracture propagation in the near-tip region. All the simulators tested here are able to capture the analytical solutions of the different configurations tested, but at vastly different computational costs. Algorithms based on the classical LEFM propagation condition require a fine mesh in order to capture viscosity dominated hydraulic fracture evolution. Cohesive zone models, which model the fracture process zone, require even finer meshes to obtain the same accuracy. By contrast, when the algorithms use the appropriate multi-scale hydraulic fracture asymptote in the near-tip region, the exact solution can be matched accurately with a very coarse mesh. The different analytical reference solutions used in this paper provide a crucial series of benchmark tests that any successful hydraulic fracturing simulator should pass.

1. Introduction

The propagation of hydraulic fractures is a highly non-linear fluid-solid interaction problem involving a moving boundary (i.e., the propagating fracture front in the neighboroughood of which the governing equations degenerate). Simulating this class of problem numerically is challenging, especially properly tracking the evolving fracture front.

Propagation regimes	Plane-strain	Radial
Viscosity M ($\mathcal{K} = 0$)	[3] (with correction for small toughness)	[6]
Toughness K ($\mathcal{K} \to \infty$)	[4] (with correction for small viscosity)	[6, 11]

Table 1. List of available solutions for the propagation of hydraulic fractures driven by a Newtonian fluid under constant rate of injection (zero leak-off).

In geoscience applications, hydraulic fractures propagate in a complex, often poorly characterized medium. Nevertheless, the description of the medium must be simplified in order to apply theoretical models. It is thus crucial that numerical implementations of such models for fracture growth be accurate such that differences from field observations can be attributed to model assumptions rather than poor numerical solution.

In the last ten years, a number of reference solutions (analytical and semi-analytical) have been obtained for propagating plane-strain [1–5] and radial hydraulic fractures [6, 7] (see Table 1). These solutions provide invaluable benchmarks for numerical simulators. We compare a number of simulators (2D and 3D) that use different propagation algorithms against these reference solutions for hydraulic fractures driven by a Newtonian fluid under a constant injection rate. For the sake of clarity, we do not address fluid leak-off in our discussion. Of particular interest is the accuracy of the different simulators in tracking the moving fracture front, particularly in the so-called viscosity-dominated regime of propagation.

An outstanding question relates to the convergence and robustness of numerical simulators with respect to the multiscale near-tip behavior of hydraulic fractures. The coupled lubrication (fluid flow) and elasticity equations are known to degenerate near the fracture tip, such that the solution of a semi-infinite fracture propagating at a constant velocity is characterized by a multiscale singular behavior near the tip [8–10]. The nature of the dominant singularity depends on the relative importance of two dissipative processes (viscous forces and fracture energy), as well as the reference length scale. Such a multiscale behavior near the fracture tip in turn governs the evolution of the velocity of a finite hydraulic fracture during injection. We discuss the degree to which a numerical simulator needs to include and resolve the near-tip behavior in order to accurately match reference solutions in the light of different benchmarks.

2. Benchmarks

2.1. Plane-strain hydraulic fracture (KGD)

The case of a plane strain hydraulic fracture driven by a Newtonian fluid under constant injection rate is also sometimes refered to as the KGD model (for Khristianovic [12], Geerstma and De klerk [13]). In the absence of leak-off the solution of the hydraulic fracture propagation is self-similar and depends on a single dimensionless number: i.e. a dimensionless toughness $\mathcal{K}$

$$\mathcal{K} = \frac{K'}{E'^{3/4}\mu'^{1/4}Q_o^{1/4}}$$

http://dx.doi.org/10.5772/56212

where Q_o is the volumetric injection rate per unit length in the out-of plane direction, E' denotes the plane-strain elastic modulus, $\mu' = 12\mu_f$ is an equivalent viscosity (with μ_f the fluid viscosity), and $K' = \sqrt{32/\pi}\, K_{Ic}$ with K_{Ic} the fracture toughness (see [14] for more details). Equivalently a dimensionless viscosity $\mathcal{M} = \mathcal{K}^{-4}$ can be used. The complete solutions for the fracture length evolution, fracture width and net pressure have been obtained for the limiting cases of zero dimensionless toughness (equivalently infinite $\mathcal{M}$) and zero dimensionless viscosity (infinite $\mathcal{K}$) First order solutions for either small toughness or viscosity are also available [3, 4]. Semi-analytical solutions for any finite values of dimensionless toughness or viscosity are also available [5].

We will restrict our comparisons to the case of relatively small dimensionless toughness (e.g. $\mathcal{K} < 1$), which is known to be the more difficult condition to reproduce numerically. Therefore we express the solution in a so-called viscosity scaling. Because the solution is self-similar the time dependence can be obtained using dimensional analysis. We aim to compare the solutions provided by different numerical codes, which are typically developed in space-time. We thus introduce a dimensionless time $\tau = t/t_c$ and a scaled coordinate $\xi = x/\ell$, where t_c is a characteristic time scale and ℓ is the fracture length. The fracture length, opening, and net pressure can be written as follows:

$$
\begin{aligned}
\ell &= \left(\frac{E' Q_o^3 t^4}{\mu'}\right)^{1/6} \gamma_m(\mathcal{K}) = \left(\frac{E' Q_o^3 t_c^4}{\mu'}\right)^{1/6} \underbrace{\tau^{2/3}\gamma_m(\mathcal{K})}_{\gamma(\tau,\mathcal{K})} \\
w &= \frac{Q_o^{1/2} t^{1/3} \mu'^{1/6}}{E'^{1/6}} \Omega_m(\xi,\mathcal{K}) = \frac{Q_o^{1/2} t_c^{1/3} \mu'^{1/6}}{E'^{1/6}} \underbrace{\tau^{1/3}\Omega_m(\xi,\mathcal{K})}_{\Omega(\xi,\tau,\mathcal{K})} \qquad (1) \\
p &= \frac{E'^{2/3}\mu'^{2/3}}{t_c^{1/3}} \Pi_m(\xi,\mathcal{K}) = \frac{E'^{2/3}\mu'^{2/3}}{t^{1/3}} \underbrace{\tau^{-1/3}\Pi_m(\xi,\mathcal{K})}_{\Pi(\xi,\tau,\mathcal{K})}
\end{aligned}
$$

where we have highlighted the correspondence between results obtained using a time-based algorithm (say γ, Ω, Π) to the self-similar solution dimensionless solution $\mathcal{F}_m(\mathcal{K}) = \{\gamma_m, \Omega_m, \Pi_m\}$.

The dimensionless solution $\mathcal{F}_m(\mathcal{K}) = \{\gamma_m, \Omega_m, \Pi_m\}$ for small toughness developed in [3] will be compared with the numerical solutions from different simulators. More precisely, for three small values of dimensionless toughness $\mathcal{K} = 0.01, 0.1, 0.5$, we will focus on the comparisons of the dimensionless fracture length γ_m, opening profile $\Omega_m(\xi)$ close to the fracture tip and error in the fracture volume etc. We are especially interested in the evolution of the error of the numerical solutions with respect to mesh sizes in the near-tip region of the fracture, where gradients are the largest. The solution, for small toughness ($\mathcal{K} < 1$), is in fact governed by the hydraulic fracture viscosity tip asymptote: the opening behaves as $w \sim (\ell - x)^{2/3}$ and the net pressure as $p \sim (\ell - x)^{-1/3}$ close to the fracture tip (see [10] for

details). The tip region affected by the asymptote actually extends to about 10 to 20 percent of the plane-strain fracture length for dimensionless toughnesses below 0.5.

2.2. Radial hydraulic fracture

The growth of a radial hydraulic fracture spans both the viscosity and toughness regimes of propagation [6, 11]. At early times, the perimeter and the opening of the fracture are small and most of the energy is spent in viscous flow, whereas at a later times, the fracture perimeter and opening are larger and the fracture energy required to extend the fracture dominates the energy required to drive the viscous fluid through the fracture. The radial solution is also dependent only on a dimensionless toughness which in this case is a function of time. Introducing the characteristic time $t_{mk} = \left(\frac{\mu'^5 Q_o^3 E'^{13}}{K'^{18}} \right)^{1/2}$, and the dimensionless time $\tau = t/t_{mk}$ we have (see [6, 14] for more details):

$$\mathcal{K} = \tau^{1/9}$$

Solutions for the case of zero and infinite dimensionless toughness (i.e. small and large dimensionless time) have been obtained semi-analytically [6]. The complete transient solution can be obtained only numerically. A reference algorithm [7] based on an explicit moving mesh algorithm with proper matching of the multiscale HF tip asymptotics [10] will provide the baseline for the comparisons for intermediate times. The fracture radius R, width w and net pressure p can be written as:

$$\begin{aligned} R &= \frac{E'^3 Q_o \mu'}{K'^4} \gamma(\tau) \\ w &= \frac{\sqrt{E' Q_o \mu'}}{K'} \Omega(\rho, \tau) \\ p &= \frac{K'^3}{E'^{3/2} Q_o^{1/2} \mu'^{1/2}} \Pi(\rho, \tau) \end{aligned} \tag{2}$$

where the dimensionless solution $\mathcal{F} = \{\gamma, \Omega, \Pi\}$ depends only on dimensionless time $\tau = t/t_{mk}$ and scaled position $\rho = r/R$ along the fracture.

As before, we will pay particular attention to the case of small dimensionless toughness, i.e. early-time, which is the most challenging numerically. In the limit of zero-toughness/early-time (i.e. viscosity dominated propagation, here refereed as the M-vertex), the solution is self-similar and can be conveniently written in the following viscosity scaling:

http://dx.doi.org/10.5772/56212

$$
\begin{aligned}
R &= \frac{E'^{1/9} Q_o^{1/3} t^{4/9}}{\mu'^{1/9}} \gamma_{m0} = \frac{E'^3 Q_o \mu'}{K'^4} \underbrace{\tau^{4/9} \gamma_{m0}}_{\gamma(\tau)} \\
w &= \frac{Q_o^{1/3} \mu'^{2/9} t^{1/9}}{E'^{2/9}} \Omega_{m0}(\rho) = \frac{\sqrt{E' Q_o \mu'}}{K'} \underbrace{\tau^{1/9} \Omega_{m0}(\rho)}_{\Omega(\rho,\tau)} \\
p &= \frac{E'^{2/3} \mu'^{1/3}}{t^{1/3}} \Pi_{m0}(\rho) = \frac{K'^3}{E'^{3/2} \sqrt{Q_o \mu'}} \underbrace{\tau^{-1/3} \Pi_{m0}(\rho)}_{\Pi(\rho,\tau)}
\end{aligned}
\tag{3}
$$

where again, we have highlighted the correspondence between the zero-toughness/ M-vertex self-similar solution $\mathcal{F}_{m0} = \{\gamma_{m0}, \Omega_{m0}, \Pi_{m0}\}$, which is independent of time and the dimensionless solution expressed as a function of the previously defined dimensionless time.

The zero-toughness/M-vertex solution $\mathcal{F}_{m0}$ has actually been found to correctly capture the propagation of hydraulic fractures up to a dimensionless toughness of $\mathcal{K} = 1$, i.e. for dimensionless time $\tau \leq 1\,(t \leq t_{mk})$ [6]. We will thus investigate the convergence of different simulators to this zero-toughness/small time solution.

For dimensionless time above unity ($\tau > 1\,(t > t_{mk})$), the solution transitions from the viscosity dominated (early-time) to the toughness (large-time) dominated regime. The toughness dominated regime is reached for $\mathcal{K} \approx 3.5\,(\tau \approx 70000)$. Note that, for infinitely large dimensionless toughness (i.e. zero viscosity), the solution is also self-similar [6] and is also denoted as the K-vertex solution. We will also briefly investigate, for a subset of the simulators considered, the transition between these two regimes of propagation (M to K), focusing mostly on fracture length versus time.

2.3. Some practical numbers

Although rock properties and stimulation practices vary, it is interesting to compute the scales and dimensionless numbers previously introduced. Let's assume a "tight" rock with the following realistic properties: a plane-strain Young's modulus of 40 GPa and a fracture toughness of 1.5 MPa.m$^{1/2}$. First, for a hydraulic fracturing treatment using a highly viscous fluid (e.g. gel-like with $\mu_f = 100$ cPoise) at a practical rate of 10 Barrels per minute, we obtain a transition time scale t_{mk} for a radial fracture of $4.2\,10^6$ seconds! The propagation of such a hydraulic fracture for a realistic injection duration (i.e. less than two hours) will always be in the viscosity dominated regime of propagation. Remember that the dimensionless toughness evolves as $(t/t_{mk})^{1/9}$ for radial fractures. For the plane-strain geometry (where the injection rate is per meter in the out-of-plane direction), using the same parameters we obtain a dimensionless toughness of 0.26 clearly indicating a viscosity dominated propagation.

For a slick-water treatment, popular in shale-gas reservoirs, the injection rates are usually much higher in order to compensate for the low viscosity of water and to obtain a sufficiently wide fracture to accomodate proppant (see the scales in front of the opening w in Equations (1) and (3)). Using a value of 20 Barrels per minute (a realistic value for a single perforation

cluster) and the viscosity of water, the radial transition time scale t_{mk} now reduces to two minutes. For radial fractures, the toughness dominated regime of propagation is obtained for dimensionless toughness above 3.5 (see [6]), which corresponds to $t \gtrsim 75000\, t_{mk}$, which translate for this particulate case to $t \gtrsim 250$ hours. This indicates that most of the duration of the treatment will take place in the transition from the viscosity to the toughness regimes of propagation for a radial fracture (assuming that no stress barriers affect the fracture geometry). For the plane-strain fracture geometry, we obtain a dimensionless toughness of 0.3 (assuming the same injection rate per meter in the out-of-plane direction), for which the propagation is still dominated by viscosity.

These examples show the importance of the viscosity dominated regime of propagation for oil and gas hydraulic fracturing applications. Numerical simulators therefore need to be able to capture this regime of propagation, which is a difficult task especially if the algorithm relies solely on the linear elastic fracture mechanics propagation condition that manifests itself at a length scale near the fracture tip that is much smaller than the modeling lengthscale in the viscosity dominated case [10, 15].

3. Simulators tested

Two classes of simulators have been tested: codes simulating a two-dimensional configuration (plane-strain or/and axisymmetry) where the fracture is a one dimensional geometrical object, and three dimensional codes simulating planar fractures (which are two-dimensional objects in three dimensions). We now briefly describe the algorithms used by these different simulators.

3.1. Two dimensional codes

1. MineHF2D
   This simulator (see [16] for more details) handles the propagation of both straight and curved hydraulic fractures in plane-strain. The algorithm is based on a fixed grid. It uses the displacement discontinuity method to solve the elastic equations coupled to a finite difference scheme for the fluid flow within the fracture. This algorithm includes the presence of a fluid lag at the fracture tip; for the simulated case reported here, a large confining stress value was used to minimize the fluid lag (see [17, 18] for more discussion on the effect of fluid lag). Explicit time-stepping is used and a volume of fluid method locates the fluid front. The fracture propagation criterion is based on the linear elastic fracture mechanics asymptote. The stress intensity factors are obtained using the displacement method with an adjusting factor of 0.88. A mesh with variable element sizes was used with refinement toward the fracture tip.
2. FEM_Cohesive
   This code is based on a finite element model and the pore pressure cohesive element implemented in Abaqus (Abaqus 6-10.2, 2010). It can handle both plane-strain and axi-symmetric configurations (e.g. plane-strain and radial hydraulic fractures). In this model, a pre-defined surface made up of elements that support the cohesive zone traction-separation calculation is embedded in the rock and the hydraulic fracture grows along this pre-defined surface. The fracture process zone (unbroken cohesive zone) is defined within the separating surfaces where the surface tractions are nonzero. The fracture is fully filled with fluid in the fully damaged cohesive zone (where the

http://dx.doi.org/10.5772/56212

cohesive traction is zero) and hence there will be no cohesive traction contribution, but fluid pressure is acting on the open fracture surfaces. So a coupled fluid pressure-traction-separation relationship exists between the cohesive zone defined by the traction-separation law and the pressurised fracture as found from solving the lubrication equation with the constraint that all tractions acting on the entire fracture and the cohesive zone must be in equilibrium. In this cohesive finite element model [19], the irreversible bilinear traction-separation cohesive law is adopted. An incompressible Newtonian fluid is injected at the centre of the fracture at constant injection rate. There is no fluid leak-off through the impermeable surfaces of the fracture, so only flow in the fracture radius direction is modelled. The cohesive elements at the injection point are defined as initially open to allow entry of fluid, and so that the initial flow and fracture growth is possible. Infinite elements surrounding the finite domain, which contains a hydraulic fracture, have been used to model the far-field boundary. Further details of the finite element model can be found in [19].

3. 1DPlanarHF
   This code, also based on a fixed mesh, simulates straight hydraulic fractures in two-dimensions (plane-strain and axisymmetric fractures) using a fully implicit scheme to solve for the coupling between the elasticity equation (discretized using the displacement discontinuity method), the fluid conservation (discretized using a finite volume scheme) and to locate the fracture front. An increment of fracture length is given and the corresponding time-step (to reach the new fracture length) is solved by satisfying the fracture propagation condition in the tip element in a weak form: i.e. the volume of the tip element is enforced to be equal to the LEFM square-root asympote (The algorithm is similar to the one described in [20], see also [21]). The HF viscosity tip asymptote [8] can also be used for the case of low fracture toughness, its performance will be compared to the LEFM asymptote. Results obtained using the LEFM and the viscosity asymptotes will be denoted as 1DPlanarHF_lefm, and 1DPlanarHF_m respectively. All the results presented here use a grid with a constant element size (i.e. without any refinements), a re-coarsening of the mesh during the simulation is possible.

4. EMMA
   EMMA is an Explicit Moving Mesh Algorithm for radial geometry, which embeds the proper multiscale tip asymptotes of the hydraulic fracture depending on its velocity (see [7] for more details). It is extremely accurate and the moving mesh nature of the algorithm allows it to span more than ten orders of magnitude in dimensionless time. It notably provides a good solution for the transition between the viscosity and toughness dominated regime of propagation for a radial fracture.

3.2. Three dimensional codes

1. The Implicit Level Set Algorithm (ILSA)
   This algorithm [22] models the evolution a hydraulic fracture with an arbirarily shaped boundary that is assumed to propagate in a plane (a planar fracture in a 3D elastic medium), which is typically perpendicular to the minimum principal stress direction. The three dimensional elastic equilibrium equations are discretized using the dispacement discontinuity boundary integral method in which the fracture within the plane is represented by constant width rectangular elements that are collocated at element centres.

The Reynolds lubrication equation, expressing the conservations of mass of the viscous fluid contained within the crack surfaces, is discretized using a finite volume method also defined with respect to quantities sampled at the centres of the rectangular elements. At the periphery of the fracture, which may not conform to the structured rectangular mesh, the boundary is represented using a concept of partially filled tip elements that are used to define average fracture widths, which are also sampled at element centres. The distinguishing feature of this algorithm is its ability to locate the fracture free boundary using the asymptotic behavior of the hydraulic fracture width that is applicable at a particular point on the fracture perimeter. The free boundary is located by the following iterative process: given an initial guess for the fracture boundary ∂S, determine the corresponding trial fracture width w and fluid pressure field p_f; in the ribbon of elements that are completely filled with fluid and, which share at least one side with a partially filled tip element, use the trial width values to estimate the distance to the free boundary by inverting the applicable tip asymptotic behavior [10]; use these estimates of the distance to the free boundary as initial conditions for the eikonal equation $|\nabla T(x,y)| = 1$, whose level set curve $T(x,y) = 0$ is the free boundary. The fracture boundary is then moved to the curve $T(x,y) = 0$ and the iterative process is repeated until convergence is achieved. The algorithm uses the multi-scale hydraulic fracture tip asymptotics solution [10] and thus automatically captures the different type of propagation regimes with relatively coarse mesh.

For this paper, a simplified version of the algorithm was also designed to only use the LEFM asymptote (hereafter denoted as ILSA_lefm) for comparisons with other algorithms (MineHF2D, 1DPlanarHF etc.). In this version, we adapted the ILSA code to damp the front advance by rescaling the level set function $T(x,y)$ so that the the maximum distance between any point in the ribbon elements and the damped free boundary is no more than three element lengths. This sequence of damped front positions enables the trial widths to be relaxed until fracture width profile presents a close approximation to the viscosity dominated solution, in spite of the fact that the tip elements are, by the nature of the ILSA_lefm algorithm, locked into the LEFM asymptote.

2. HFLattice:
This code [23] simulates fracture propagation without limitation of shape, direction or number of fractures, as well as slip and opening along pre-existing joints. A 3D lattice formulation is used for simulation of deformation and fracturing. The lattice is a quasi-random assembly of nodes connected by non-linear shear and normal springs. The lattice resolution is given by the average node spacing. Newton's law of motion (for translation and rotation) is solved at the nodes using an explicit central difference scheme. The normal force in the spring is tested and a micro-crack is formed when breakage is detected (spring strength is adjusted to give the correct rock strength). A macro-fracture that develops in intact rock is thus characterized by an assembly of micro-cracks. Fluid flow and storage are based on a network of fluid nodes, located at broken springs or springs intersected by pre-existing joints, connected by pipes. The fluid network is updated continuously as new fracturing occurs. An explicit fluid pressure scheme is used to solve for fracture and matrix flow. The mechanical and flow models are fully coupled: fracture permeability depends on aperture (i.e. deformation of the mechanical components), fluid pressure affects deformation and strength of the solid model, and deformation of the solid model affects fluid pressures. In the algorithm, the lattice springs carry total forces, which affects force balance and motion. Also, effective stress is considered for joint slip or opening.

http://dx.doi.org/10.5772/56212

	Plane-strain		Radial	
	$\mathcal{K} = 0.01$	$\mathcal{K} = 0.1$	$\tau \ll 1$ ($\mathcal{K} \ll 1$)	$10^{-1} < \tau < 10^{4}$ ($.5 < \mathcal{K} < 3.5$)
MineHF2D	✓	✓	n.a	n.a
FEM_Cohesive	✓	✓	✓	
1DPlanarHF	✓	✓	✓(_lefm only)	✓(_lefm only)
ILSA	n.a	n.a	✓	✓
HFLattice	n.a	n.a	✓	

Table 2. The benchmarks tested (✓) for the different simulators.

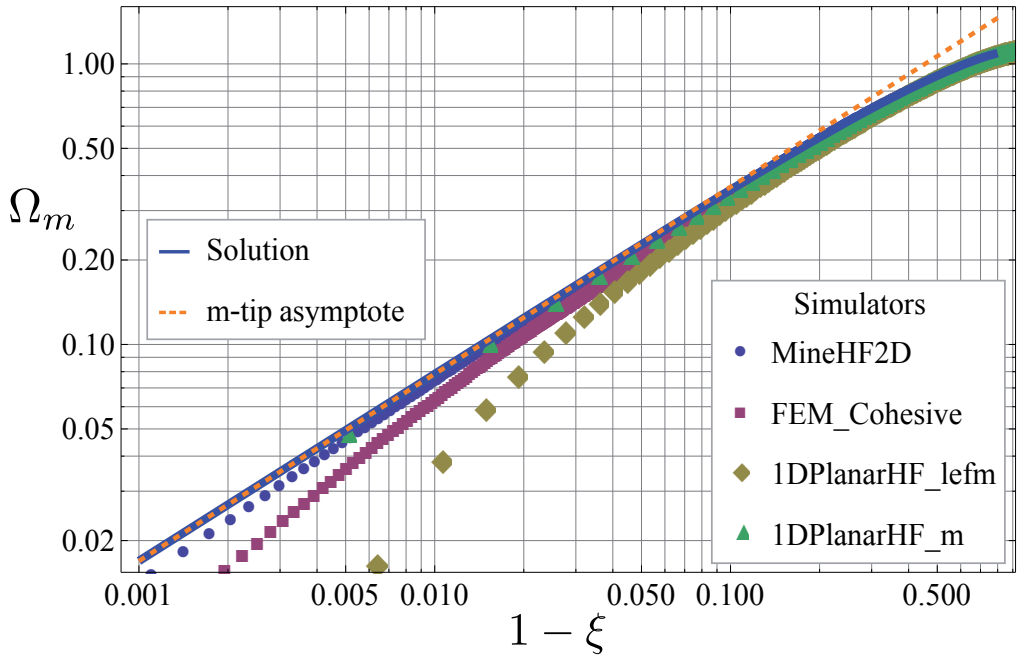

Figure 1. Dimensionless opening Ω_m from the fracture tip in log-log scale; plane-strain fracture $\mathcal{K} = 0.01$.

4. Results and discussion

4.1. The plane strain small toughness benchmark

The solution for a plane-strain hydraulic fracture driven by the injection of a Newtonian fluid at a constant rate is self-similar (i.e. evolves as a power-law of time). Our comparisons here focus on the case of viscosity dominated fractures ($\mathcal{K} < 0.5$, spefically $\mathcal{K} = 0.1$, 0.001) which are the most difficult to simulate numerically. The simulators tested for that configuration are (Table 2): MineHF2D, FEM_Cohesive, 1DPlanarHF_lefm and 1DPlanarHF_m.

Figure 1 displays, for the case $\mathcal{K} = 0.01$ the dimensionless fracture opening profiles from the tip of the fracture obtained with the different simulators (at the last step of their simulations) as well as both the analytical solution and the viscosity HF tip asymptote [10]. Figure 2 is similar but for the case $\mathcal{K} = 0.1$. We first observe that the viscosity tip asymptote covers a region about 10 to 20 percent of the fracture from its tip. The different simulators provide

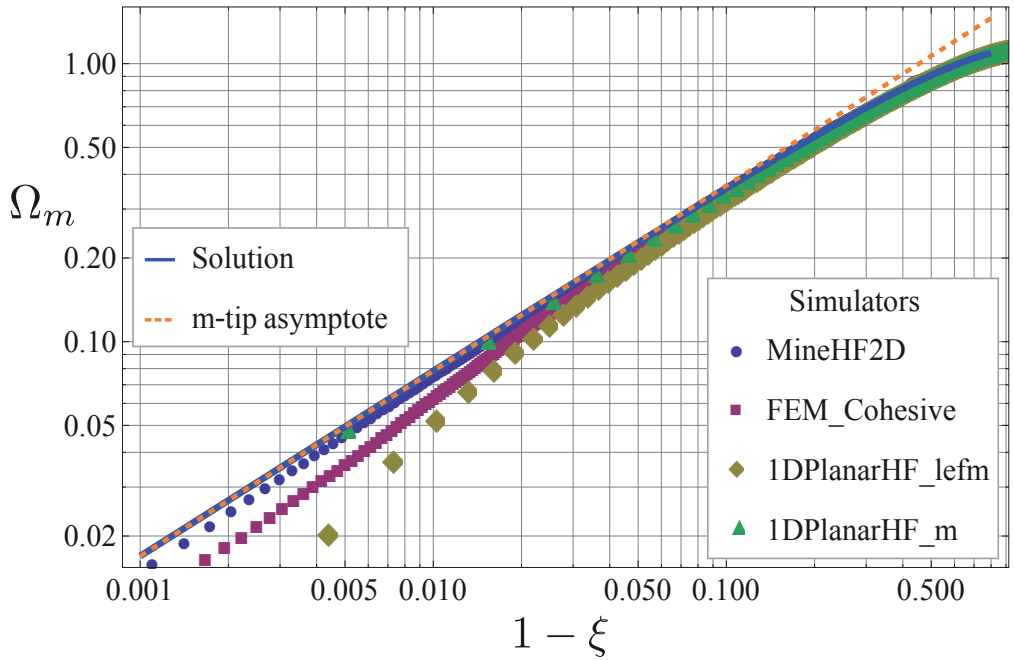

Figure 2. Dimensionless opening Ω_m from the fracture tip in log-log scale; plane-strain fracture $\mathcal{K} = 0.1$.

width estimates that all correctly fall on the analytical solution "away" from the fracture tip. The distances from the tip at which the simulators recover the analytical solution appear to depend on both the mesh-size and the type of propagation condition used. For algorithms using the linear elastic fracture mechanics (LEFM) propagation condition (opening as a square root of the distance from the tip), this recovery distance from the tip is larger for coarser mesh sizes. The algorithm using a cohesive zone model appears to need significantly more refinement. In contrast, the algorithm using the viscosity HF tip asymptote (i.e. 1DPlanarHF_m) is able to capture the fracture opening exactly all the way to the tip and with a much coarser mesh than was used for the other computations.

This dependence of the convergence toward the exact solution on the mesh size and propagation condition can be further observed in Figures 3-5, which display the rate of convergence for the fracture length and fracture volume as a function of the ratio of the mesh size over fracture length (i.e. the inverse of the number of elements to discretize the frature for uniform mesh). All simulators converge correctly toward the analytical solution but at very different computational costs. We can see that for algorithms using the LEFM condition or a cohesive zone model, the mesh size required to reach the same level of accuracy is about 20 times smaller than for the algorithm that uses the correct HF viscosity tip asymptote. In the case $\mathcal{K} = 0.01$, 1DPlanarHF_lefm needs about 400 elements ($h/\ell \sim .0025$) to obtain a relative error of about 1 and 3 percent in the fracture length and fracture volume respectively, while smaller relative errors are already obtained when using 20 elements ($h/\ell \sim .05$) for 1DPlanarHF_m. The cost is even greater when a cohesive zone model is used: about 3000 elements ($h/\ell \sim 3 \times 10^{-4}$) are needed to reach a relative error of 1.5 and three percent in the fracture length and fracture volume respectively.

http://dx.doi.org/10.5772/56212

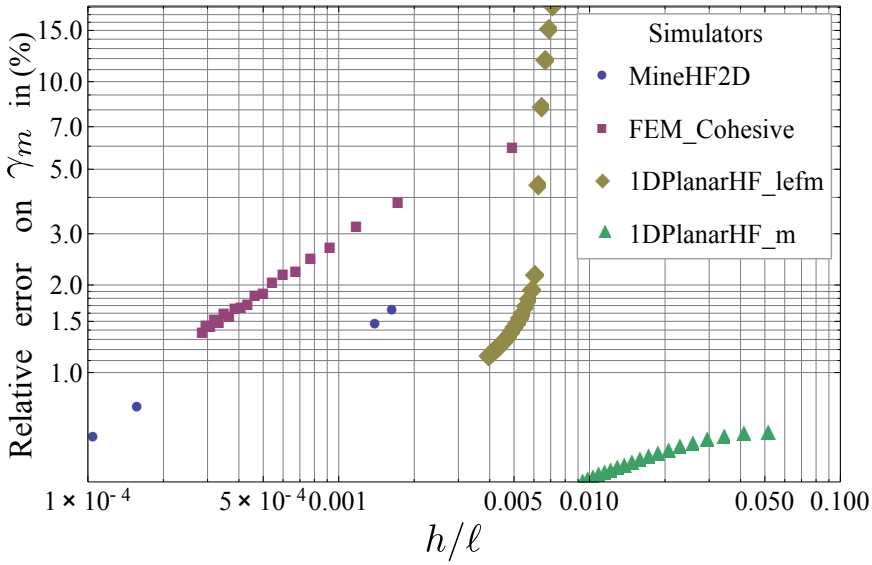

Figure 3. Relative error in the fracture length as a function of the ratio mesh-size over fracture length $\mathcal{K} = 0.01$.

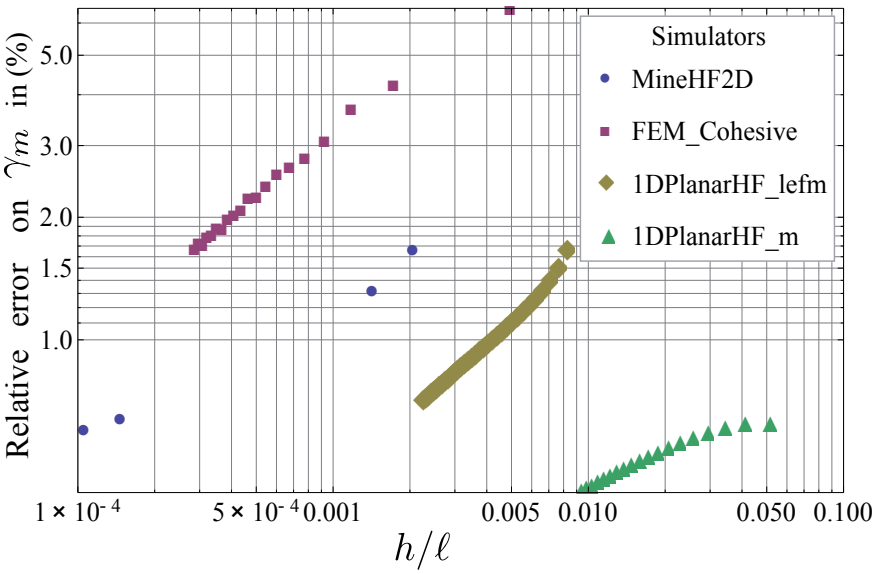

Figure 4. Relative error in the fracture length as a function of the ratio mesh-size over fracture length $\mathcal{K} = 0.1$.

Similar observations can be made for the case of a dimesionless toughness $\mathcal{K} = 0.1$, although all the algorithms using a fracture energy propagation condition perform slightly better due to the higher value of dimensionless toughness. In other other words, similar relative errors are obtained for larger values of h/ℓ (i.e. fewer elements), as can be seen by comparing Figures 3 and 5 for $\mathcal{K} = 0.01$ to Figures 4 and 6 for $\mathcal{K} = 0.1$.

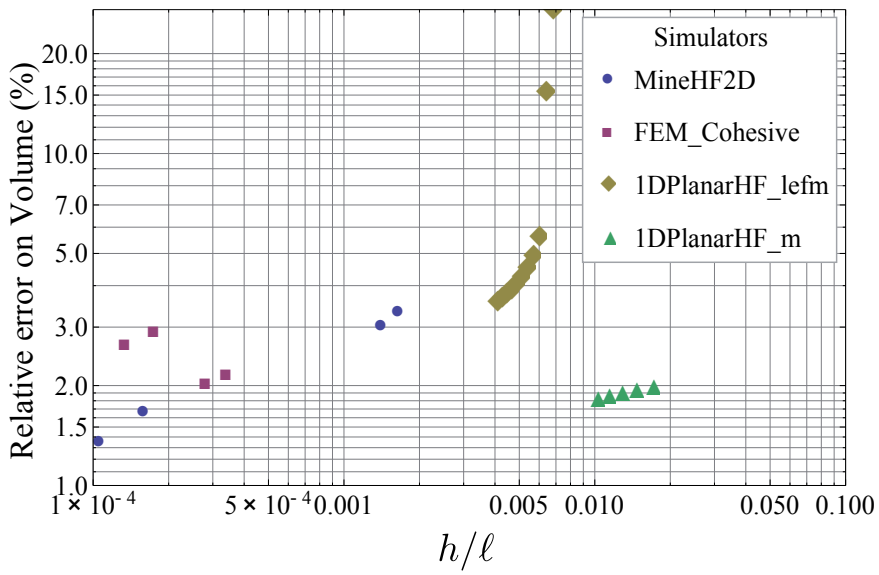

Figure 5. Relative error in the dimensionless fracture volume as a function of mesh size over fracture length - Plane-strain fracture $\mathcal{K} = 0.01$.

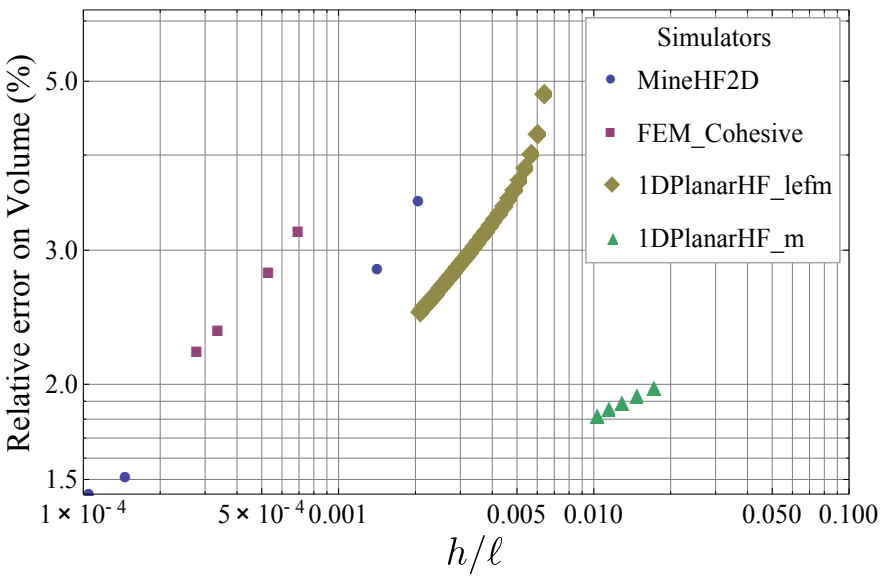

Figure 6. Relative error in the dimensionless fracture volume as a function of mesh size over fracture length - Plane-strain fracture $\mathcal{K} = 0.1$.

http://dx.doi.org/10.5772/56212

4.2. The radial hydraulic fracture benchmark

4.2.1. Viscosity dominated regime

Owing to its previously argued importance in practice, we focus on early-time, where the relevant analytical solution corresponds to the case of zero-toughness. The simulators tested for this geometry and regime of propagation are the two-dimensional codes under axi-symmetry; FEM_Cohesive and 1DPlanarHF_lefm, and the 3D codes ILSA, the simplified version ILSA_lefm and the HFLattice model (Table 2).

The different simulators have been run for different ranges of dimensionless time all within the viscosity dominated regime ($\tau < 1$), and are described in Table 3. The HFLattice

FEM_Cohesive	1DPlanarHF_lefm	ILSA/ILSA_lefm
$\tau \in [10^{-10} - 2 \times 10^{-8}]$	$\tau \in [10^{-7} - 10^{-1}]$	$\tau \in [10^{-18} - 10^{-17}]$

Table 3. Range of dimensionless time of the simulations for the radial benchmark

simulator has been run for the specific case of zero toughness (in fact zero tensile strength as per the formulation).

The convergence toward the zero-toughness solution as a function of the mesh size can be observed in Figure 7 (convergence of the fracture radius). Similar trends to the plane-strain case can be observed. The convergence requires a much finer mesh for the simulators using a cohesive zone model (axi-symmetric FEM_Cohesive) and the LEFM propagation condition (axisymmetric 1DPlanarHF and ILSA_lefm). ILSA, the only simulator using the appropriate HF tip asymptote, achieves the same accuracy with a much coarser mesh compared to all the other simulators. In particular, the version ILSA_lefm, which uses the LEFM asymptote, needs about an order of magnitude finer mesh compared to ILSA for the same relative error. The FEM_Cohesive algorithm requires a ratio h/R about two to three orders of magnitude smaller than ILSA for the same relative error. The HFLattice model, although less accurate, also exhibits convergence as h/R decreases.

The openings at the last time step of the simulation (refer to Table 3 for the corresponding dimensionless time) in the tip coordinate system are compared to the zero-toughness analytical solution in Figure 8. The FEM_Cohesive algorithm captures the solution away from the fracture tip well, i.e at distance larger than 3-5 % of the fracture radius from the tip. Closer to the tip, the opening from the cohesive zone algorithm appears to slightly overestimate the fracture opening. The results of the algorithms using the LEFM propagation condition (1DPlanarHF_lefm, ILSA_lefm) converge toward the analytical opening as their mesh gets finer. On the other hand, ILSA exactly matches the analytical solution for the opening with a relatively coarse mesh (the last element of ILSA corresponds to a partially fractured element for which the fracture width is also function of the fracture front location within the element).

A comparison of the net pressure profile obtained by the different simulators and the analytical solution is displayed on Figure 9. Similar trends to the fracture opening can be observed. One has to note that the HFLattice simulator approximates the point-source by a finite volume, hence the discrepancy on the net pressure with respect to the point-source solution close to the fracture inlet.

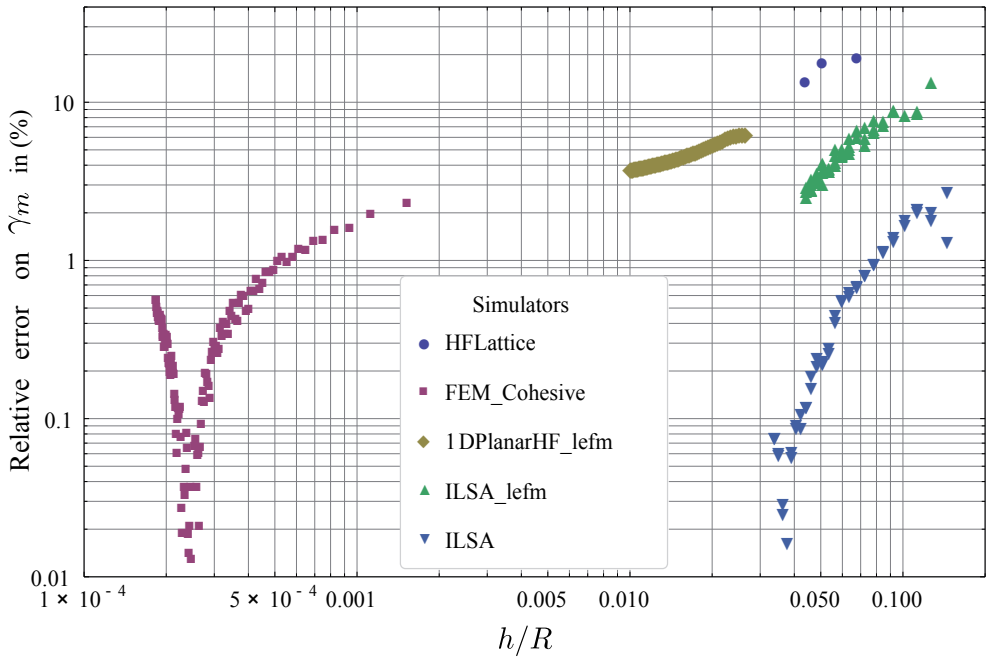

Figure 7. Evolution of the relative error in the fracture radius as a function of the mesh size for the different simulators - radial fracture in the viscosity dominated regime (i.e. zero toughness / early time, $\tau < 1$). All simulations displayed here are for $\tau < 10^{-6}$.

It is interesting to investigate more closely how an algorithm using the LEFM asymptote (e.g. ILSA_lefm) is able to converge to the zero-toughness analytical solution. Consider the case of modeling a radial hydraulic fracture starting at a very small initial time ($\tau = 10^{-18}$), which corresponds to a dimensionless toughness $\mathcal{K} = 0.01$, and is therefore very close to the M-Vertex (zero-toughness solution). If the LEFM asymptote is used in ILSA at this time, the asymptote would dictate that the fracture front needs to be advanced by roughly 10^4 element lengths! As already mentioned, to circumvent this problem, the ILSA_lefm code damps the front advance by rescaling the level set function $T(x,y)$ so that the the maximum distance between any point in the ribbon elements and the damped free boundary is no more than three element lengths. This sequence of damped front positions enables the trial widths to be relaxed until the fracture width profile presents a close approximation to the viscosity dominated solution, in spite of the fact that the tip elements are locked into the LEFM. Indeed, the algorithm settles on a solution in which the LEFM tip widths are very small and contribute very little to the net volume of the fracture, while over the remainder of the fracture away from the leading edge, the widths are locked into the viscous asymptote as dictated by the conservation of volume. Thus the damped front advances continue until the conservation of fluid volume dictates that it should stop at which time it approximates the viscous asymptote. Results from the standard ILSA code with the correct viscous asymptote and damped ILSA_lefm code with the LEFM asymptote indicates that in order to obtain similar relative errors compared to the analytical solution, a mesh size that is an order of magnitude smaller is needed for ILSA_lefm compared to the standard ILSA code (see Figure 7).

http://dx.doi.org/10.5772/56212

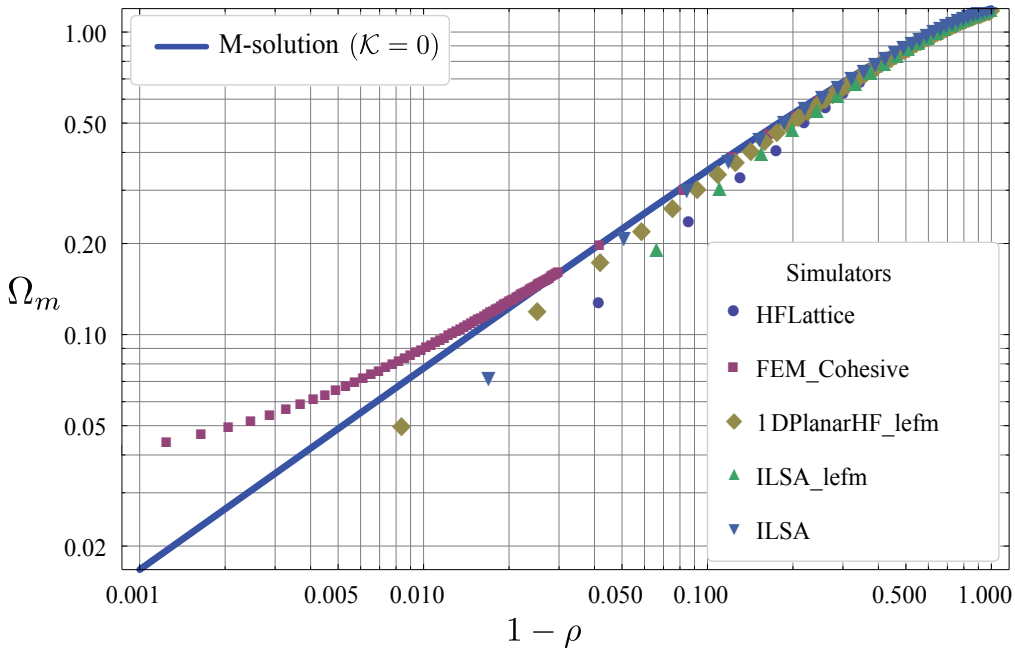

Figure 8. Fracture opening in the tip coordinates system (log-log scale) for a radial hydraulic fractures propagating in the viscosity dominated regime. Results from the different simulators for a dimensionless time $\tau < 10^{-6}$. Note that for better clarity of the plot, all the mesh points are not displayed for $1 - \rho > 0.04$ for FEM_Cohesive.

4.2.2. Transition toward the toughness dominated regime

Finally, we investigate the performance of a subset of the algorithms on the transition of the solution toward the toughness dominated solution. Such a transition typically happens between $\tau = 1\,(\mathcal{K} = 1)$ and $\tau \sim 70000\,(\mathcal{K} = 3.4)$. The Explicit Moving Mesh Algorithm (EMMA), the 1DPlanarHF_lefm and the ILSA codes are compared, focusing on the evolution of the dimensionless fracture radius with time. Figure 10 display the results. The fracture radius have been averaged over the fracture footprint for the results of ILSA (3D code), while the other codes are axi-symmetric by assumption.

We clearly see that the different algorithms capture the transition between the viscosity and the toughness propagation regimes extremely well. They are virtually indistinguishable.

5. Conclusions

In this paper, we have investigated the performance of a number of hydraulic fracture propagation algorithms based on different propagation conditions: LEFM, cohesive zone model/tensile strength and algorithms accounting for the multi-scale nature of hydraulic fracture propagation in the near-tip region. This exercise was made possible thanks to the existence of analytical solutions for both geometries of hydraulic fractures. All the simulators investigated here are able to capture the analytical solutions of the different configurations tested, but at widely different computational costs.

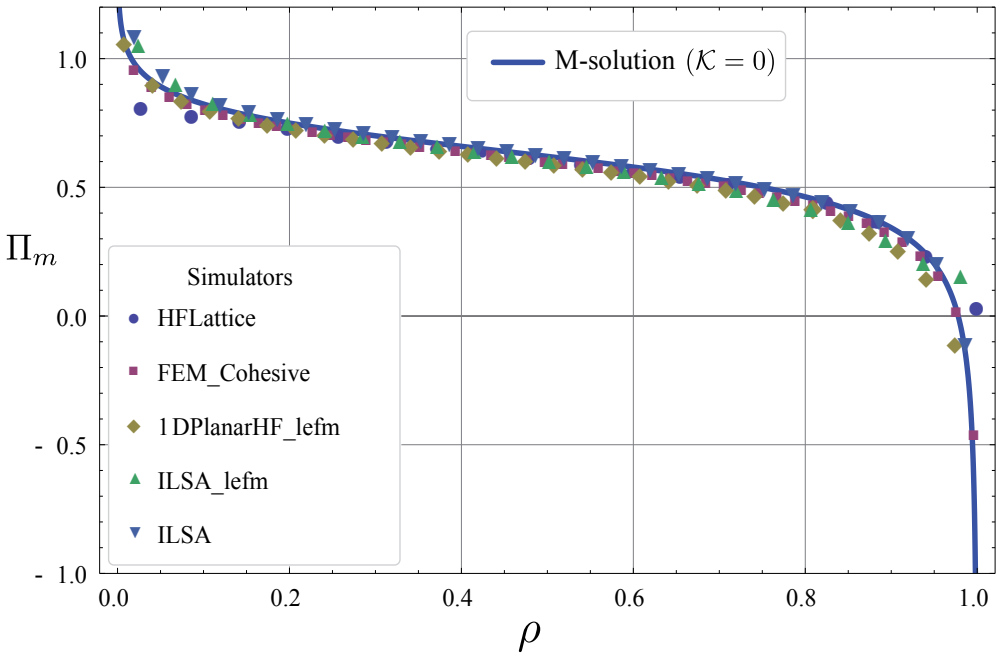

Figure 9. Dimensionless net pressure for a radial hydraulic fracture in the viscosity dominated regime (i.e. zero-toughness / early-time). Comparisons of the simulators (for a dimensionless time $\tau < 10^{-6}$) with the zero-toughness solution. The results of FEM_Cohesive and 1DPlanarHF_lefm are plotted only every 50 and 2 mesh points respectively for clarity.

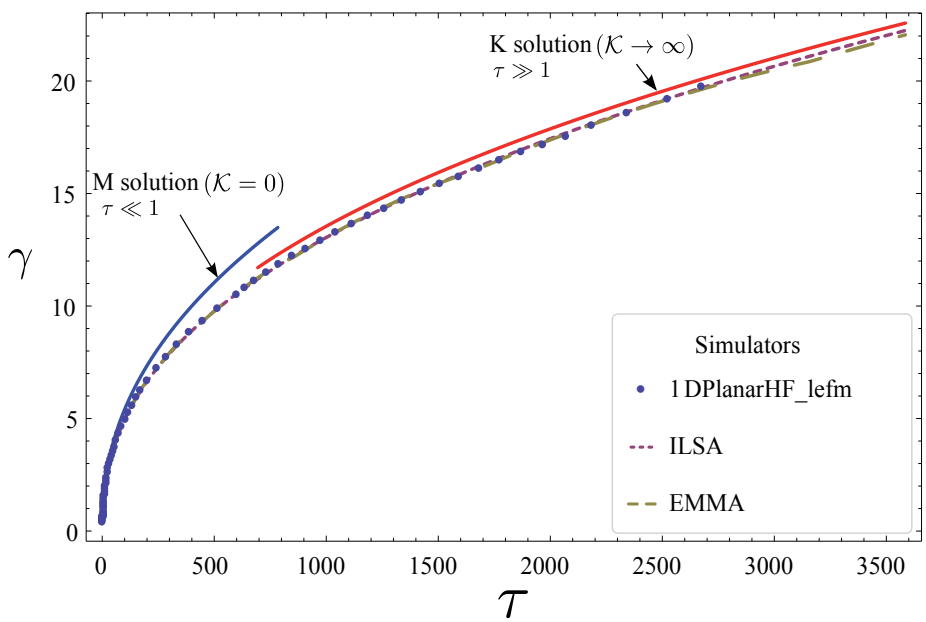

Figure 10. Radial hydraulic fracture - Transition between the viscosity dominated regime at early time to Toughness dominated regime at large time. Comparisons between different simulators and the zero (blue) and infinite toughness (red) solution.

http://dx.doi.org/10.5772/56212

Algorithms based on the Linear Elastic Fracture Mechanics propagation condition requires a fine mesh ($h/\ell \lessapprox 10^{-2} - 10^{-3}$) in order to capture viscosity dominated hydraulic fracture propagation. A fine mesh is needed for these algorithms to capture the viscosity opening asymptote in order to properly match the fracture volume. Cohesive zone models, which model the fracture process zone, require even finer meshes. This is due to the fact that the cohesive zone length-scale is even smaller than that of the region of influence of the linear elastic fracture mechanics (LEFM) square-root near-tip asymptote. By contrast, when the algorithms use the appropriate multi-scale hydraulic fracture asymptote in the near-tip region, the exact solution can be matched with a very coarse mesh (i.e. $h/\ell \approx 10^{-1}$). Extremely efficient and fast propagation algorithms can thus be developed with even better accuracy than algorithms based on the classical LEFM propagation condition. Computational cost and accuracy may not be the only concern when developing a simulator. Algorithm flexibility may also be important. We hope that the study reported in this paper can help in making an educated choice of algorithm.

Finally, we also would like to advocate that the different analytical reference solutions used in this paper be used as a minimal series of benchmarks for any hydraulic fracturing simulator.

Author details

Brice Lecampion[1,⋆], Anthony Peirce[2], Emmanuel Detournay[3], Xi Zhang[4], Zuorong Chen[4], Andrew Bunger[4], Christine Detournay[5], John Napier, Safdar Abbas[1], Dmitry Garagash[6] and Peter Cundall[5]

⋆ Address all correspondence to: BLecampion@slb.com

1 Schlumberger Doll Research, Cambridge, USA
2 Department of Mathematics, University of British Columbia, Vancouver, Canada
3 Department of Civil Engineering, University of Minnesota, Minneapolis, USA
4 CSIRO Earth Science and Resource Engineering, Clayton, Victoria, Australia
5 Itasca Consulting Group, Minneapolis, USA
6 Department of Civil and Resource Engineering, Dalhousie University, Canada

References

[1] R. Carbonell, J. Desroches, and E. Detournay. A comparison between a semi-analytical and a numerical solution of a two-dimensional hydraulic fracture. *Int. J. Sol. Struct.*, 36(31):4869–4888, 1999.

[2] J. Adachi and E. Detournay. Self-similar solution of a plane-strain fracture driven by a power-law fluid. *International Journal for Numerical and Analytical Methods in Geomechanics*, 26(6):579–604, May 2002.

[3] D.I. Garagash and E. Detournay. Plane-strain propagation of a fluid-driven fracture: Small toughness solution. *ASME J. Appl. Mech.*, 72:916–928, November 2005.

[4] D. I. Garagash. Plane-strain propagation of a fluid-driven fracture during injection and shut-in: Asymptotics of large toughness. *Engineering Fracture Mechanics*, 73(4):456–481, March 2006.

[5] J. Hu and D. I. Garagash. Plane-Strain Propagation of a Fluid-Driven Crack in a Permeable Rock with Fracture Toughness. *Journal of Engineering Mechanics*, 136(9):1152, 2010.

[6] A. Savitski and E. Detournay. Propagation of a penny-shaped fluid-driven fracture in an impermeable rock: asymptotic solutions. *International Journal of Solids and Structures*, 39(26):6311–6337, December 2002.

[7] M. Madyarova. Fluid-driven penny-shaped fracture in permeable rock. Master's thesis, University of Minnesota, 2003.

[8] J. Desroches, E. Detournay, B. Lenoach, P. Papanastasiou, JRA Pearson, M. Thiercelin, and A. Cheng. The crack tip region in hydraulic fracturing. *Proceedings of the Royal Society of London. Series A: Mathematical and Physical Sciences*, 447(1929):39, 1994.

[9] D.I. Garagash and E. Detournay. The tip region of a fluid-driven fracture in an elastic medium. *J. Appl. Mech.*, 67:183–192, 2000.

[10] D. I. Garagash, E. Detournay, and J. Adachi. Multiscale tip asymptotics in hydraulic fracture with leak-off. *Journal of Fluid Mechanics*, 669:260–297, February 2011.

[11] H. Abé, L. M. Keer, and T. Mura. "growth rate of a penny-shaped crack in hydraulic fracturing offset rocks". *J. Geoph. Res.*, 81:6292, 1976.

[12] S. Khristianovic and Y. Zheltov. Formation of vertical fractures by means of highly viscous fluids. In *Proc., 4th World Petroleum Congress*, volume II, pages 579–586, Rome, 1955.

[13] J. Geertsma and F. De Klerk. A rapid method of predicting width and extent of hydraulically induced fractures. *Journal of Petroleum Technology*, 21(12):1571–1581, 1969.

[14] E. Detournay. Propagation regimes of fluid-driven fractures in impermeable rocks. *International Journal of Geomechanics*, 4(1):35, 2004.

[15] D. I. Garagash. Scaling of Physical Processes in Fluid-Driven Fracture: Perspective from the Tip. In F.M. Borodich, editor, *IUTAM Symposium on Scaling in Solid Mechanics*, volume 10 of *Iutam Bookseries*, pages 91–100, Dordrecht, 2009. Springer.

[16] X. Zhang, R. G. Jeffrey, and E. Detournay. Propagation of a fluid-driven fracture parallel to the free surface of an elastic half plane. *Int. J. Numer. Anal. Meth. Geomech.*, 29:1317–1340, 2005.

[17] D. Garagash. Propagation of a plane-strain fluid-driven fracture with a fluid lag: early-time solution. *Int. J. Sol. Struct.*, 43:5811–5835, 2006.

[18] B. Lecampion and E. Detournay. An implicit algorithm for the propagation of a hydraulic fracture with a fluid lag. *Comp. Meth. Appl. Mech. Engrg.*, 196:4863–4880, 2007.

[19] Z.R. Chen. Finite element modelling of viscosity-dominated hydraulic fractures. *Journal of Petroleum Science and Engineering*, 88–89:136–144, 2012.

http://dx.doi.org/10.5772/56212

[20] E. Gordeliy and Emmanuel Detournay. A fixed grid algorithm for simulating the propagation of a shallow hydraulic fracture with a fluid lag. *International Journal for Numerical and Analytical Methods in Geomechanics*, 35(5):602–629, April 2011.

[21] B. Lecampion. Hydraulic fracture initiation from an open-hole: Wellbore size, pressurization rate and fluid-solid coupling effects. In *46th U.S. Rock Mechanics/Geomechanics Symposium*, number ARMA 2012-601, June 24–27 2012.

[22] A. P. Peirce and E. Detournay. An implicit level set method for modeling hydraulically driven fractures. *Computer Methods in Applied Mechanics and Engineering*, 197(33-40):2858–2885, June 2008.

[23] B. Damjanac, C. Detournay, P. Cundall, and Varun. Three-Dimensional Numerical Model of Hydraulic Fracturing in Fractured Rock Masses. In A. Bunger, R.G. Jeffrey, and J. McLennan, editors, *Effective and Sustainable Hydraulic Fracturing*, Brisbane, Australia, 20–22 May 2013. Intech.

Section 14

Mining and Measurement

Chapter 44

Hydraulic Fracturing Mine Back Trials — Design Rationale and Project Status

Peter K. Kaiser, Benoît Valley,
Maurice B. Dusseault and Damien Duff

Additional information is available at the end of the chapter

http://dx.doi.org/10.5772/56260

Abstract

Last year, a joint Mining and Oil & Gas industry consortium was established in Canada to conduct hydraulic fracturing (HF) tests accompanied by a mine-back of fractured regions to assess HF models and microseismic monitoring data during controlled experiments. Details about the displacement field, fracture aperture and extent, and micro-seismic parameters could then be verified and used as calibration data for modeling of HF processes in igneous and dense sedimentary rocks.

Various injection experiments are planned and they will include pre-fracturing rock mass characterisation using best available current techniques, dense arrays of multi-parameter wall and borehole-mounted instruments, and the treated volume will be mined through to assess fracturing effectiveness, existing fractures and new fracture interactions, and to determine if pathways can be identified for improving currently available numerical and fracture network modeling tools.

In this paper we present the results of the experimental design and planning phase, outlining objectives and justifications for planned experimental layouts. Preliminary plans for a first mine-through trial at Newcrest Mining's Cadia East mine in New South Wales, Australia are described. The hypotheses advanced in this experimental design, supported by evidence from the literature, are that activation and development of a fracture network by hydraulic stimulation is possible if the injection procedure is designed such that injection pressures and rates are maintained within an optimal window, thereby producing conditions under which effective stress management for risk mitigation in deep mining can best

be achieved. The evaluation of these hypotheses is the focus of the current high level experimental plan presented in the paper.

Keywords stress management, stiffness modification, shale gas analogue, mine-back experiments, model calibration, hydraulic fracture, naturally fractured rocks

1. Introduction

Hydraulic fracturing (HF) has been widely used in the oil & gas (O&G) and mining industry: in O&G to stimulate reservoirs [1] and in mining, primarily to initiate caving and to improve fragmentation (e.g. [2-4]). Attempts have also been made to initiate slip on faults or shears [5] and research including mine-backs of hydraulically fractured zones has been conducted [6,7] in order to better understand the characteristics of the propagated hydraulic fractures. However, to the authors' knowledge, although there are many anecdotal indications of hydraulically induced changes to rock mass properties and stress, hydraulic fracturing has so far not been successful in inducing sufficient changes in the in situ or mining-induced stress field to be of practical value for risk mitigation related to violent seismic energy release in deep and high stress mining. It is speculated that the latter can only be achieved by the stimulation, mobilisation and enhancement of a natural fracture network rather than by solely generating a new system of induced hydraulic fractures. Hence, an innovative testing program, focussed on natural fracture network stimulation and the development of these techniques for stress management purposes is pursued. The mobilisation and development of a fracture network is also relevant for the optimal exploitation of tight gas or oil shale reservoirs, which closely resemble hard-rock situations (low permeability block, naturally fractured, stiff, low to moderate Poisson's ratio, etc.). The success of the proposed hydraulic injection program will be investigated during a mine-back test, and the results applied to mining and O&G applications.

In this paper, the results of the experimental design phase, outlining objectives and justifications for planned experimental layouts, are presented. Preliminary plans for the first mine-through trial at Newcrest Mining's Cadia East mine in New South Wales, Australia are described.

2. Project objectives

The practical justification for the overall HF project is different for the mining and O&G sector consortium sponsors. However, both sectors are interested in advancing the state of knowledge in three broad areas: (a) fracture network stimulation and development, (b) stress field modification, and (c) micro-seismic data interpretation during hydraulic fracturing and reservoir stimulation. Hence, the broad objectives of the program meets the primary needs of both sectors and will advance the understanding of hydraulic fracture network stimulation

http://dx.doi.org/10.5772/56260

based on experiments permitting near-field monitoring followed by investigation of the treated volume via mapping and monitoring during mine-through.

2.1. Mining perspective

Various hydraulic fracturing (HF) experiments have been undertaken in mines, some with mine-through experiments (e.g. [6]) for various purposes: to better understand fracture propagation, fracture interaction with natural joints, fragmentation changes, penetration of proppants, etc. Successes have been reported with respect to the use of HF for rock mass preconditioning, for rock fragmentation and cave initiation (e.g. [2]) but unanswered questions remain about its effectiveness in affecting stress redistribution and in controlling energy release from critically stressed rock mass structures. There are much anecdotal but little scientifically proven evidence that HF can help manage stresses, or not. The authors suggest that it may be the methodology of fracturing that may be the source of the apparent contradictions reported in the literature. As mines progress to greater depth stress management for the control of seismically releasable energy becomes of strategic importance. Furthermore, with the introduction of mechanized excavation techniques for rapid mine development (e.g., by Rio Tinto, AngloGold Ashanti, and others), new risks related to strain-bursting are introduced because of the less-damaging nature of these excavation techniques.

For the mining sector the motivations are to broaden the application of hydraulic fracturing and rock mass stimulation beyond cave initiation, propagation and fragmentation management by introducing methodologies for hydraulic stress and rock mass stiffness management that will eventually find introduction for risk mitigation in deep and high stress mining operations. In particular, the problem of fault-slip rockbursting is perplexing and, it is thought, can possibly be addressed through the creation of "damage zones" around potentially unstable structures, thereby reducing the energy emission levels and rates and improving constructability in highly stressed ground.

It is hypothesised that current hydraulic injection techniques deployed in cave mine applications are predominantly propagating hydraulic fractures and that shear dilation is a secondary process. Indeed, opening Mode I fractures develop within a narrow (almost planar) zone normal to σ_3, and their irregular nature promotes asperity locking resulting in little final net shear strength or stiffness reduction. It is recognised that as fluids are lost in the rock mass surrounding the hydraulic fracture some distributed shearing of critically oriented natural fractures will also occur (e.g. [3]), however in order to enable stress management, one must promote volumetrically distributed irreversible changes to the rock mass and the development of injection techniques that achieve this objective is at the core of the planned research. Section 3 presents the output of a review of current injection practices for various applications and their effect on the rock mass. It served as background for the development of the experimental approach presented in Section 4.

2.2. O&G perspective

The advent of numerous staged HF stimulations along the lengths of deep horizontal wells [8] has unlocked huge quantities of natural gas and oil in low permeability formations that had heretofore been considered non-commercial. Typically, a 1 to 2 km long horizontal well (Fig. 1) is drilled parallel to σ_3, and a series of hydraulic fractures are installed along the length of the well, injecting into one or several perforated or open sites each time, until from 10 to 40 sites are fracture-stimulated. The optimum design of each stage is still the subject of considerable debate, in part because existing mathematical models of fracturing, founded on single-plane Sneddon crack type assumptions in unjointed continua, are inadequate to predict fracture length, stimulated volume, or surface contact area in naturally fractured rock and more complex approaches using fracture network models are difficult to calibrate. Thus, design is largely empirical, based on remote field measurements that may be inadequate or difficult to interpret (tilt measurements, microseismic measurements and post-fracture well tests). For each new field, there is an extensive period of experimentation with different sequences of fluids and proppants, using different rates and materials, along with limited field measurements (generally microseismic monitoring) to try and optimize the stimulation process to achieve a maximum contacted volume without wasteful fracture propagation into non-productive overlying strata. Each stimulated well may cost 5-10 million dollars, and the eastern United States Marcellus Shale alone may require over 500,000 wells for complete development, as the deposit covers over 95,000 square miles, and at least 6 horizontal wells are needed for each square mile (100 acre spacing). Furthermore, the deeper lying Utica Shale, which also extends into Canada, will eventually be developed, requiring a similar number of wells [9, 10]. Sub-optimal fracture design because of incomplete understanding and inadequate predictive tools quickly becomes a costly luxury.

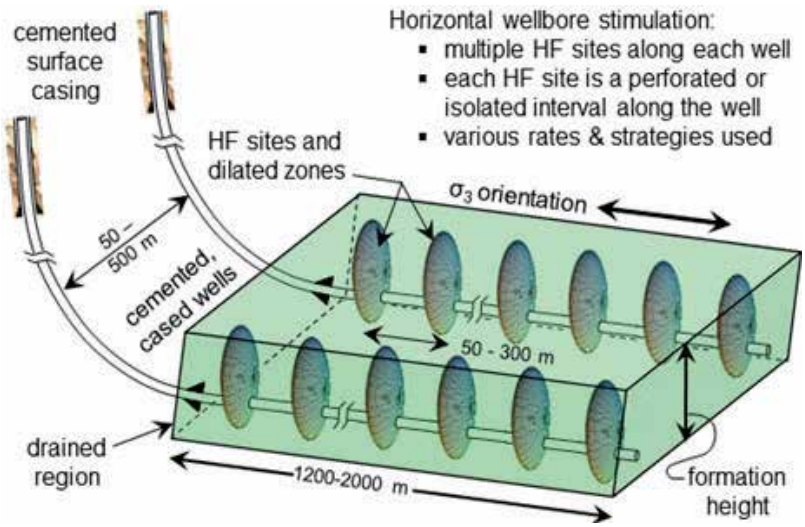

Figure 1. Staged hydraulic fracturing along a horizontal well axis for shale gas stimulation.

http://dx.doi.org/10.5772/56260

These low permeability strata that contain natural gas or low-viscosity oil are often called "shales", although many of them are better classified as siltstones or even argillaceous limestones (marls). The rock matrix is a stiff (30 to 110 GPa), low-porosity (0.04-0.10), low permeability (microDarcy to nanoDarcy) material. The rock mass is naturally fractured, generally with one dominant set orthogonal to bedding, and one or two minor sets, also orthogonal to the bedding planes. Interestingly, these properties are substantially more similar to those of igneous and metamorphic rocks encountered in "hard rock" mines than they are to typical sedimentary rocks such as heavy oil-rich sandstones, or conventional higher porosity (0.15-0.25) limestones and sandstones. Hence, it is attractive for improving O&G reservoir stimulation techniques to perform tests in a deep mining context.

The O&G dimension of a HF mine-back experiment is to provide an experimental platform for testing predictive models and stimulation procedures suitable for the oil industry. Fracturing igneous rock at depth in a mining context is therefore of interest because the rocks are similar (naturally fractured, stiff, low Poisson's ratio, anisotropic, almost impermeable matrix blocks…), because the deep mine provides access to a high stress environment (1.5 to 3 km deep) at one tenth the cost of a vertical oilfield borehole, and because a direct mine-back of a fracture-stimulated region can verify assumptions about stimulated volumes, fracture aperture, relationship to microseismic emissions, and the rock mass strains [11].

The concept of a stimulated volume that is far larger than the sand-filled fracture propagation volume (Fig. 2) is fundamental to understanding shale oil or shale gas stimulation, but cannot be easily verified directly, nor can it be predicted by design models that are commonly available. The calibration and validation of advanced model permitting complex behaviour including branching needs data rarely available and the proposed experimental work will contribute to provide such validation data. Fig. 2 presents a 2-D simplification of a complex, 3-D process involving many natural fractures near a wellbore that have been propped, and a large zone surrounding the sand zone where block rotation and shear have created open fractures and self-propped dilated fractures [8]. In mining, this process is called rock mass *bulking* due to geometric incompatibilities between, displaced and rotated, strong blocks of rock. These bulking induced fractures are favored through high-rate injection, and they are thought to be the primary source of microseismic emissions, whereas the zone into which sand is transported, the propped aperture, and the number of near-wellbore propped natural fractures are favored by injection of a highly viscous fluid. Remote displacement measurements (i.e. tilt measurements) cannot distinguish amongst individual fractures, only suitable local instrumentation and a mine-back test can give confidence in the actual geometry and disposition of the dilated or propped regions.

Thus, the motivation for the O&G industry is to optimize HF treatment in tight reservoirs by calibrating design software and hydraulic fracturing propagation monitoring techniques, that is to relate the geophysical observables from fracture initiation and propagation, particularly in the case of microseismic monitoring, and to better understand the development of hydraulic fractures in tight and low permeability naturally fractured lithologies. These objectives can be achieved by performing experiments in deep mines, in which the rock properties are similar to the O&G lithological context because of their stiff, fractured, low permeability characteristics.

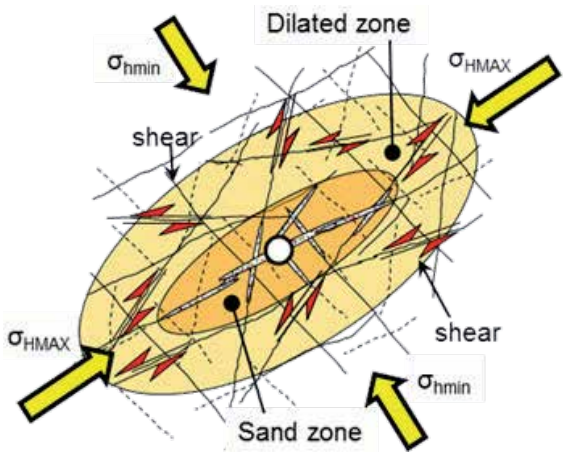

Figure 2. The sand zone and the dilated zone (the stimulated volume).

3. Review of injection practices and their effect on the rock mass

The generic term "hydraulic injection" covers a spectrum of practices with distinct objectives. With the contribution of Itasca, we conducted a literature survey to capture current injection practices in three sectors: mining, deep geothermal and O&G. A case study database, including 14 mining cases, 46 deep geothermal cases, and 4 O&G cases (to be expanded), includes information on the geomechanics context (stress state, rock strength,...), the injection metrics (flow rate, pressure record, injection volume and duration,...), the monitoring program and the measured or observed effect on the rock masses (main activated mechanisms, stimulated volume, fracture extent...).

Fig. 3 illustrates the breadth of injection practices. At the low end of the spectrum, we included some metrics from the ISRM suggested method for hydraulic fracturing stress measurements [12] where a short interval is injected at a very low rate (2 – 3 l/min) for a short time (1 – 3 min). The mechanism in this case is borehole wall failure in tension, captured by the breakdown pressure in the pressure record followed by a limited extension of the hydraulic fracture and its closure after well shut-in (instantaneous shut-in pressure, ISIP) which is used as an indicator of the σ_{hmin} magnitude, assuming that the borehole is vertical and that the fracture has propagated beyond the near-wellbore region.

An up-scaled version of the stress measurement method is used in cave mining operations to pre-condition the rock for improved caveability or fragmentation. A short packed interval is injected to initiate and propagate fractures, and rates, duration and volumes are about two to three orders of magnitude larger than for stress measurements. This propagates fractures typically several tens of meters from the borehole and injections are repeated to generate a zone of fractured rock. Observed fractures typically grow perpendicular to the minimum principal stress and their trajectory is relatively little influenced by natural features (e.g., joints) unless the later makes an sharp angle with the growing hydraulic fracture path.

http://dx.doi.org/10.5772/56260

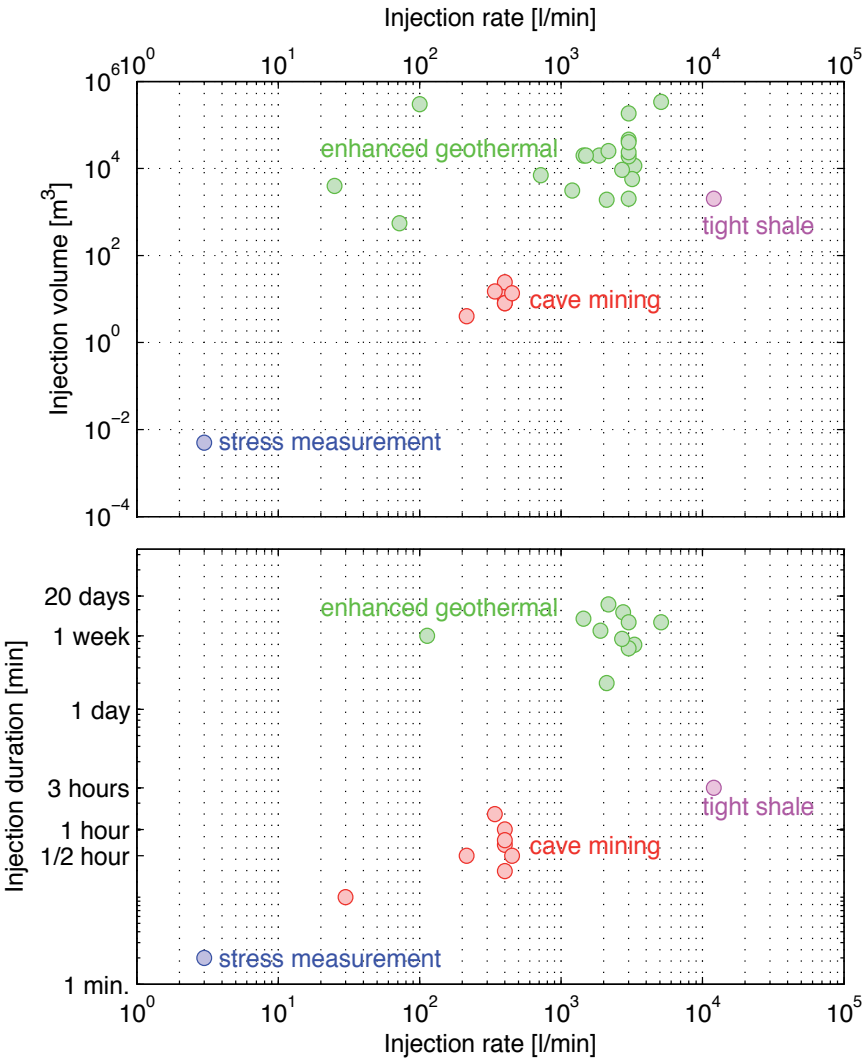

Figure 3. A broad spectrum of injection practices with specific injection metrics for each industry; related objectives are demonstrated by this cross plot of injection volume and injection durations vs. maximum injection rate.

A different situation is encountered in deep geothermal projects with high rate, long duration injections performed in long open-hole sections for reservoir stimulation. The injection metrics are one to two orders of magnitude higher than for cave pre-conditioning cases and extensive monitoring is used to understand fracture activation and propagation, permeability enhancement and fluid penetration [13, 14]. The predominant mechanisms stem from natural fracture system activation [15] leading to fracture self-propping by shear displacement, causing permanent permeability increases. Critically stressed fractures, oriented optimally to the deviatoric stress field for shear failure are the most prone to activation (see Fig. 2), and slip is accompanied by microseismicity.

At the upper end, shale gas well practices involve high rate injection at a number of sites along the well; injections that are carefully sequenced at each stage with massive injection (up to 3000 m^3 per site) of fluids of different viscosity at elevated rates (typical rates of 12 m^3/min are reported) to optimize proppant penetration and the generation of shear dilated zone volume.

Insights into the role of variable injection metrics on rock mass response is gained in Fig. 4 where the maximum pressure reached during an injection is plotted against the local estimate of the minimum principal stress magnitude as well as the predominantly activated mechanism (Mode I opening fracture propagation vs. shear re-activation). The dominant activated mechanisms on this plot are clearly partitioned by the unit slope line: Mode I propagation cases plot above the unit slope while shear activation cases plot on or below the line.

This partition can in part be explained by considering the simple stability model of a cohesionless pressurized fracture in extension (opening) and shear (Fig. 5). The normal (σ_n) and shear stress (τ) resolved on a fracture can be expressed by the following expressions:

$$\sigma_n = \frac{1}{2}(\sigma_1 + \sigma_3) + \frac{1}{2}(\sigma_1 - \sigma_3)\cos 2\theta \tag{1}$$

$$\tau = \frac{1}{2}(\sigma_1 - \sigma_3)\sin 2\theta \tag{2}$$

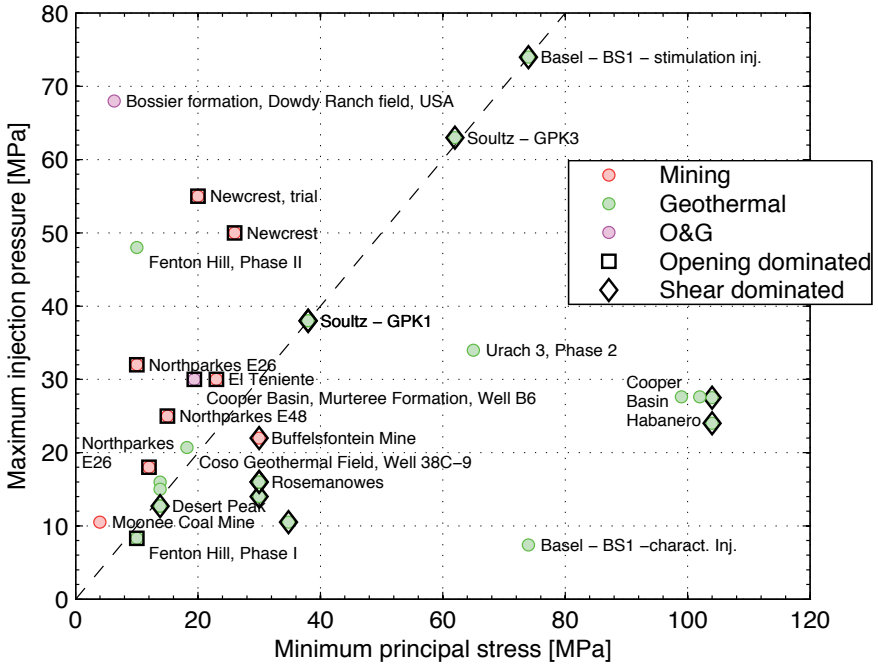

Figure 4. Cross plot of minimum principal stress and maximum injection pressure.

http://dx.doi.org/10.5772/56260

with σ_1 and σ_3, the maximum and minimum principal stress magnitude, respectively and θ, the angle between the fracture normal and the maximum principal stress direction. The criterion for opening is $P_f \geq \sigma_n$ which, if substituted in Eq. 1 and re-arranged, leads to (blue curve on Fig. 5):

$$R \geq \cos 2\theta \tag{3}$$

with

$$R = \frac{P_f - 1/2(\sigma_1 + \sigma_3)}{1/2(\sigma_1 - \sigma_3)} \tag{4}$$

The minimum pressure to generate jacking is $P_f = \sigma_3$, if the fracture is favorably oriented (perpendicular to σ_3, i.e. θ=90°). The initiation of the hydraulic fracture at the borehole wall will require a larger pressure (the breakdown pressure, P_b on Fig. 5) that depends on the principal stress ratio. Thus, to initiate and propagate a fracture from the borehole wall where the fracture opening mode dominates requires a pressure larger than $P_f = \sigma_3$ (above the unit slope on Fig. 4). Also a fracture that propagates exactly perpendicular to σ_3, as a Mode I hydraulic fracture does, will not shear since the resolved shear stress on the fracture plane for such an orientation is 0 (Eq. 2 for θ=90°).

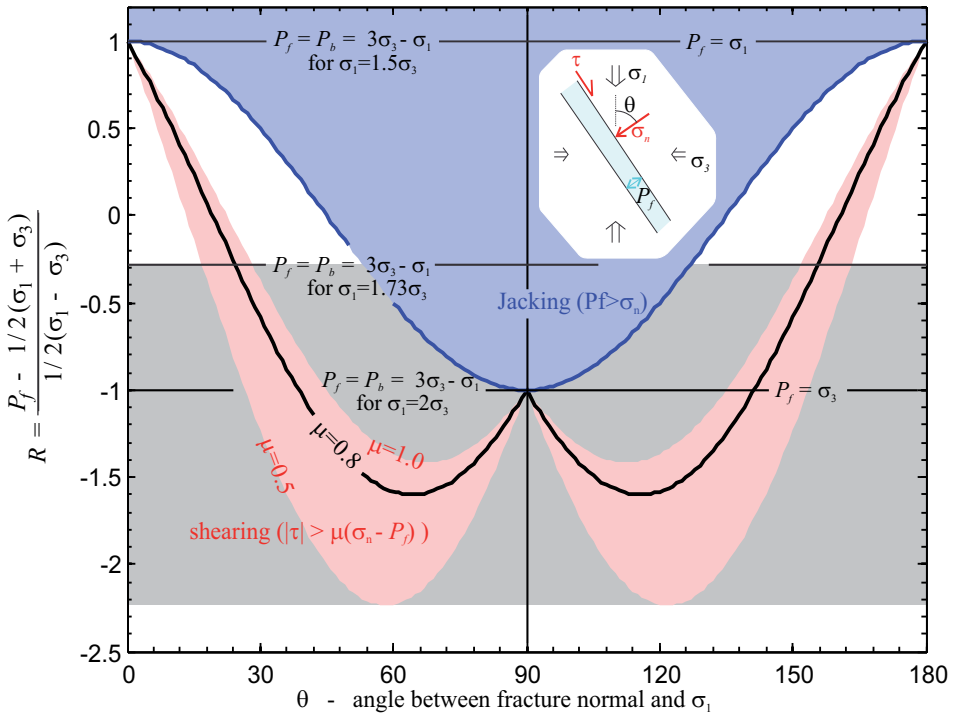

Figure 5. Stability in opening and shear of a cohesionless pressurised fracture.

The criterion for shearing of a cohesionless fracture is $|\tau| \geq \mu\ (\sigma_n\text{-}P_f)$ which, if combined with Eq. 1 and 2 and rearranged (see also [16]), lead to (red area on Fig. 5):

$$R \geq \cos 2\theta - \frac{1}{\mu}\sin 2\theta \tag{5}$$

with μ the coefficient of friction of the fracture. It can be seen from Fig. 5 that fractures optimally oriented ($\theta \cong 40° - 80°$ and $100° - 130°$) will shear at a pressure P_f lower than the minimum jacking pressure (unless locking asperities give a high apparent cohesion). Thus, for injection with connectivity to the natural fracture network where the pressure is raised progressively so that the Mode I breakdown pressure at the borehole wall is not reached, shear mechanisms on critically oriented fractures will be the dominant mechanism and the maximum injection pressure will remain close to or below the minimum jacking pressure $P_f = \sigma_3$ (below the unit slope on Fig. 4).

There is thus the opportunity to generate stress and rock mass properties change through shearing mechanisms if injection is carried out such that pressure is kept in the gray area of Fig. 5, i.e. below the breakdown pressure but above the minimum pressure required for shearing of critically oriented fractures. This situation is called *hydraulic stimulation* in the remainder of this article in contrast with the *hydraulic fracturing* that results in the initiation and propagation of a Mode I fracture. Of course, since Mode I fracture requires a larger pressure than Mode II shearing in rock masses with cohesionless joints, aggressive injection leads to Mode I-dominated fracturing closer to the wellbore, and this zone is surrounded by a pressurized volume within which stimulative Mode II shearing occurs (Fig. 2), and shear displacement also occurs within the Mode I volume.

Based on these theoretical considerations and supported by the compiled literature, an experiment to be conducted at Cadia East mine (Newcrest Mining Ltd) in New South Wales, Australia, is being designed to focus on activating shear mechanisms to generate volumetrically distributed fractures and permanent rock mass change. The high level experimental design that will guide detailed experimental design to fit local site conditions is presented in the next section.

4. Planned experimental approach

4.1. Site conditions summary

The HF experiment will be integrated with a cave conditioning operation using hydraulic injection in the Cadia East mine, PC2-S1 block. The borehole layout for the cave conditioning operation (Fig. 6) will comprise a borehole array with centres at 60 m to 80 m. Two holes will be extended to the undercut level for this experiment, allowing a subsequent mine-through of the stimulated volume.

The local geology consists of a faulted monzonite body intruded into a volcaniclastic series. Typical uniaxial rock strength ranges from 130-170 MPa, and the rock mass quality is fair to

http://dx.doi.org/10.5772/56260

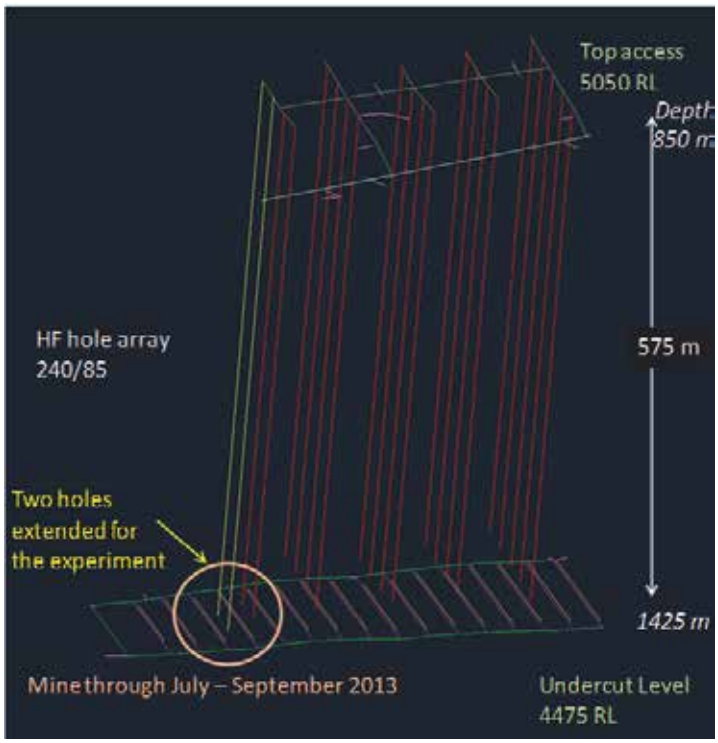

Figure 6. Layout for the experiment to be conducted at Cadia East mine, Newcrest Ltd.

good with two plus random, non-persistent discontinuity sets resulting in a partially connected natural fracture network.

The boreholes will extend from 850 m depth to 1425 m depth, with the experiment taking place at the greater depth. The in-situ stress condition, estimated from an extensive stress measurement program above 1250 m, and then extrapolated to the depth of interest, is on average σ_1 = 73 MPa (~horizontal E-W), σ_2 = 49 MPa (~horizontal N-S) and σ_3 = 42 MPa (~vertical). This places the stresses in the thrust fault condition (future experiments at other mines may be situated in strike-slip and normal fault conditions).

The experimental design is constrained by logistical factors; particularly, the current pumping capacity available and water supply permits to pump 75,000 l of water per 12 hours shift at a maximum flow rate of 400 l/min and maximum pressure of about 70 MPa.

4.2. High level experimental design

The suggested test sequence involves five stages (see Table 1). Stage I will focus on establishing a base line dataset and will involve geological and rock mass parameter characterisation, borehole televiewers and formation testing as well as using standard oil and gas sector pre-fracture treatment modeling routines in order to fine tune the injection procedure.

Stage I	Establishing base line
Stage II	Stimulation injection in virgin rock mass
Stage III	Connect fracture network using hydraulic fracturing to enhance stimulation potential
Stage IV	Solids injection
Stage V	Mine-through

Table 1. Proposed experimental stages.

Stage II will comprise a stimulation of the lower section of the experimental holes. The length of the stimulated section will be determined based on televiewer data and formation testing in order to ensure connectivity with the natural fracture network. It is expected, since the natural fracture network is probably poorly connected (below the percolation threshold), that the borehole injectivity (the capacity of the formation to accept flow for a given pressure increase or reciprocally the pressure increase at a given flow rate) will be so low that it will be difficult not to exceed the optimal pressure for stimulation.

At Stage III, the low borehole injectivity will be remediated through increasing fracture network connectivity by creating an array of hydraulic fractures before performing a second stimulation of the borehole. A final injection stage (Stage IV) will focus on the placement of solids in the fractured rock mass in order to better understand proppant penetration, to modify its properties, and to enhance shear slip.

The final stage of the experiment (Stage V) will be a diagnostic exercise where the injected volume will be mined-through in small increments to evaluate the impact of the injection treatments on the fracturing, the rock mass behaviour and the stress state in stimulated volume.

Characterisation will be repeated between stages in order to evaluate changes to the base line data collected in Stage I, including change of rock mass permeability induced by the applied hydraulic injection treatments.

5. Conclusion

Hydraulic fracturing (HF) currently has found current applications in mining environments in the promotion of rock caving and fragmentation control and has potential for stress and stiffness modification and rock mass pre-conditioning. In the O&G industry, HF in tight oil or gas shales, rocks of similar properties (low k, high E, naturally fractured…), is a vital technology used to develop unconventional oil and gas resources with long horizontal wells and numerous fracture stages at sites distributed along the axis of the horizontal well. We note that the properties of the rocks involved are quite similar in both industries, and the economical need for better HF predictive tools in the O&G industry is large, given the huge development costs predicted for the upcoming decades in North America.

Experiments in deep mines, one planned for 2013 in Australia, and two to follow later in Canada, will be based on extensive pre-characterization, intensive monitoring, staged

http://dx.doi.org/10.5772/56260

hydraulic fracturing and stimulation, and post-fracture characterization, including, where possible, mine-through of fractured zones. Type A predictions (before the event – [17]) based on the detailed ground characterization can be tested in practice, and implications for MS emission interpretation can be ground-truthed.

Specifically, the hypothesis that stress management is best achieved by *hydraulic stimulation*, i.e. activation and development of a fracture network through Mode II shear dilation in contrast to *hydraulic fracturing*, i.e. initiation and propagation of Mode I hydraulic fractures, will be tested. Theoretically there are injection pressure windows favourable for rock mass stimulation and activation in shear of critically stressed fractures, a notion supported by a review of the current practices in the O&G, mining and geothermal industries. Of course, aggressive Mode I fracturing in a strongly deviatoric stress field in naturally fractured rock masses will always be accompanied by shear within and around the Mode I dominated zone. The proposed experimental setup aims at quantifying the changes in the rock mass permeability and stiffness associated with hydraulic stimulation.

Acknowledgements

Tatyana Katsaga, David O. Degagné and Branko Damjanac from Toronto and Minneapolis Itasca offices, respectively, are warmly thanked for their contribution to this project in the form of a thorough literature compilation: Fig. 3 and 4 of this paper are directly built from their literature review database. Geoff Capes and Glenn Sharrock from Newcrest Mining Ltd in Australia are thanked for their incredible support and data sharing for this project.

Author details

Peter K. Kaiser[1], Benoît Valley[1,2], Maurice B. Dusseault[3] and Damien Duff[1]

1 CEMI - Centre for Excellence in Mining Innovation, Sudbury, Canada

2 Geological Institute, ETH Zurich, Switzerland

3 Department of Earth and Environmental Sciences, University of Waterloo, Waterloo, Canada

References

[1] Gale JFW, Reed RM, Holder J. Natural fractures in the Barnett Shale and their importance for hydraulic fracture treatments. AAPG Bulletin 2007; 91(4): 603-622.

[2] Mills KW, Jeffrey RG, Hayes P. Applications of hydraulic fracturing to control caving events in coal mines – the moonee experience. In: Hebblewhite, B. K., Galvin, J. M., O'Beirne, T. (Eds.), Proceedings of the Third International Underground Coal Conference, Managing Production Continuity. 2001; Vol. 1. 15 pp.

[3] van As, A., and Jeffrey, R. G. Caving induced by hydraulic fracturing at Northparkes Mines. In: J. Girard, and others, (Eds), Pacific Rocks 2000: proceedings 4th North American Rock Mechanics Symposium, July 31 - Aug 3, 2000, Seattle, Washington. Rotterdam, the Netherlands: A.A. Balkema: 2000. p. 353-360

[4] van As, A., Jeffrey, R., Chacon, E., and Barrera, V. Preconditioning by hydraulic fracturing for block caving in a moderately stressed naturally fractured orebody. In: MassMin 2004 : Proceedings, Santiago, Chile. Instituto de Ingenieros de Chile: 2004. p. 535-541

[5] Board M, Rorke T, William G, Gay N. Fluid injection for rockburst control in deep mining. In: Tillerson JR, Wawersik WR (Eds.), Proceeding of the 33rd U.S. Symposium on Rock Mechanics. 1992; 111-120.

[6] Jeffrey RG, Bunger AP, Lecampion B, Zhang X, Chen ZR, van As A, et al. Measuring Hydraulic Fracture Growth in Naturally Fractured Rock. In: 2009 SPE Annual Technical Conference and Exhibition. New Orleans, Louisiana, USA: SPE; 2009. p. SPE 124919+.

[7] Warpinski, N. R., and L. W. Teufel. Influence of geologic discontinuities on hydraulic fracture propagation, J. Pet. Technol., 1987; 39, 209–220.

[8] Dusseault MB, McLennan J and Shu J. Massive multi-stage hydraulic fracturing for oil and gas recovery from low mobility reservoirs in China. Petroleum Drilling Techniques 2011; 39(3): 6-16.

[9] United States Geological Survey. Various news items and geological studies. E.g.: http://www.usgs.gov/newsroom/article.asp?ID=3419&from=rss_home 2000 – 2012.

[10] Dietrich J, Lavoie D, Hannigan P, Pinet N, Castonguay P, Giles P, Hamblin AP. Geological setting and resource potential of conventional petroleum plays in Paleozoic basins in eastern Canada. Bull. of Canadian Petroleum Geology 2011; 59: 54-84.

[11] Vermylen, JP and Zoback MD. Hydraulic Fracturing, Microseismic Magnitudes, and Stress Evolution in the Barnett Shale, Texas, USA. Proceedings SPE Hydaulic Fracturing Technology Conf, TX, 2011; SPE#140607, 15 pp.

[12] Haimson BC, Cornet FH. ISRM Suggested Methods for rock stress estimation-Part 3: hydraulic fracturing (HF) and/or hydraulic testing of pre-existing fractures (HTPF). International Journal of Rock Mechanics and Mining Sciences. 2003;40(7-8):1011-1020.

[13] Genter A, Evans K, Cuenot N, Fritsch D, Sanjuan B. Contribution of the exploration of deep crystalline fractured reservoir of Soultz to the knowledge of enhanced geothermal systems (EGS). Comptes Rendus Geosciences. 2010;342(7-8):502-516.

http://dx.doi.org/10.5772/56260

[14] Evans KF, Zappone A, Kraft T, Deichmann N, Moia F. A survey of the induced seismic responses to fluid injection in geothermal and CO2 reservoirs in Europe. Geothermics. 2012;41:30-54.

[15] Evans KF, Moriya H, Niitsuma H, Jones RH, Phillips WS, Genter A, et al. Microseismicity and permeability enhancement of hydrogeologic structures during massive fluid injections into granite at 3km depth at the Soultz HDR site. Geophysical Journal International. 2005;160:388-412.

[16] Pine RJ, Batchelor AS. Downward migration of shearing in jointed rock during hydraulic injections. International Journal of rock mechanics and geomechanics abstracts. 1984; 21(5):249-263.

[17] Craig RF (with Knappett J). Soil Mechanics, CRC Press, 8th Edition, 2012;584 p (paperback)

Monitoring and Measuring Hydraulic Fracturing Growth During Preconditioning of a Roof Rock over a Coal Longwall Panel

R. G. Jeffrey, Z. Chen, K. W. Mills and S. Pegg

Additional information is available at the end of the chapter

http://dx.doi.org/10.5772/56325

Abstract

Narrabri Coal Operations is longwall mining coal directly below a 15 to 20 m thick conglomerate sequence expected to be capable of producing a windblast upon first caving at longwall startup and producing periodic weighting during regular mining. Site characterisation and field trials were undertaken to evaluate hydraulic fracturing as a method to precondition the conglomerate strata sufficiently to promote normal caving behaviour at longwall startup and reduce the severity of periodic weighting. This paper presents the results of the trials and illustrates the effectiveness of hydraulic fracturing as a preconditioning technique.

Initial work was directed at determining if hydraulic fractures were able to be grown with a horizontal orientation, which would allow efficient preconditioning of the rock mass by placing a number of fractures at different depths through the conglomerate from vertical boreholes drilled from the surface. The measurements and trials were designed to determine the in situ principal stresses, the hydraulic fracture orientation and growth rate, and whether the fractures could be extended as essentially parallel fractures to a radius of at least 30 m. Overcore stress measurements were used to determine the orientation and magnitude of the in situ principal stresses, a surface tiltmeter array was used to determine the hydraulic fracture orientation, and stress change monitoring, pressure monitoring and temperature logging in offset boreholes were used to establish the fracture growth rate, lateral extent, and that the fractures maintained their initial spacing to a radial distance of greater than 30 metres. The measurements and trials demonstrated that horizontal fractures could be extended parallel to one another to a distance of 30 to 50 m by injection of 5,000 to 15,000 litres of water at a rate of 400 to 500 L/min. Results from the trial allowed a preconditioning plan to be developed and successfully implemented.

1. Introduction

Hydraulic fracturing has been applied successfully to preconditioning of hard rock at several block caving mines [1-3] and has been used to weaken a sandstone channel over a longwall panel [4]. A recent paper documents related work in China applied to control of rock bursting [5]. In addition, hydraulic fracturing has been used to induce caving in block caving operations [1] and in longwall coal mining [6]. The work described in this paper applied hydraulic fracturing to preconditioning of a strong roof rock in order to weaken it to promote earlier caving during start up of a longwall.

Narrabri Coal Operations, located 28 km south of Narrabri, NSW, are extracting the Hoskissons coal seam using a 300 m wide longwall. The Digby conglomerate is 15 to 20 m thick and lies immediately above the seam. Geotechnical assessments of its potential to cave during longwall mining concluded that this conglomerate would not cave into the goaf until more than 60 m of the coal was extracted [7]. In addition, the analysis highlighted the potential for the conglomerate to pose a periodic weighting risk.

Periodic weighting occurs when the roof strata is strong enough to support itself behind the longwall face for some distance before failing suddenly as mining progresses. Failure typically occurs just ahead of the face and may cause the longwall supports to become overloaded and converge, crushing the coal on the face and posing a rock fall hazard for equipment and miners located between the face and the supports. The project described in this paper was aimed to test hydraulic fracturing as a method to precondition the conglomerate sequence and promote caving during mining.

The preconditioning test program involved initial characterisation of the in situ stresses to determine the suitability of the site for placing hydraulic fractures with a horizontal orientation. The stress measurement work was followed by a three stage program of field trials. The first stage was aimed to confirm that hydraulic fractures were able to be formed horizontally and extended for a distance of more than 30 m from the injection hole, given the site conditions and the available equipment. The second stage was aimed to confirm that multiple hydraulic fractures placed in close vertical proximity remained essentially parallel to each other. The third stage was aimed to confirm conditions remained suitable to form horizontal fractures in a deeper area of the mine.

The field trials used an array of monitoring boreholes drilled at various distances around a central injection hole. During the first stage of the trials, five fractures were placed through the conglomerate sequence using a straddle packer system. These fractures, which were placed at a depth of 140 to 160 m, were monitored by a surface tiltmeter array, by boreholes offset 10 to 30 m from the borehole being fractured, and by stress change monitoring instruments located at 25 m and 60 m from the injection hole. Acoustic image logs of the injection hole and boreholes intersected by hydraulic fractures and core from intersected boreholes provided additional confirmation that fractures were able to be formed horizontally.

For the second stage, a second injection hole was drilled offset from the first borehole. The bottom hole locations of these two boreholes, A and J, were determined by survey to be

http://dx.doi.org/10.5772/56325

separated by 6.5 m. Five fractures were placed with a vertical spacing of 2.5 m and each of these was later reopened to determine intersection depths in borehole C and growth rate to boreholes A and E (Figure 1). As well as monitoring used in the first stage, temperature logging of borehole interesections in borehole C confirmed that multiple fractures were able to be formed parallel to each other over an extended distance.

The third stage of the program was conducted at the start of the third longwall panel in an area where the overburden depth is some 20-30 m deeper than at the first site. A single injection hole and two monitoring holes confirmed that hydraulic fractures were able to be formed horizontally at this location despite the greater overburden depth.

This data set provides evidence for hydraulic fracture growth to more than 30 m radius at a vertical spacing between fractures of 1.25 m and 2.5 m, with non-symmetric fracture growth measured by the offset borehole data.

1.1. Design approach

Two sites were instrumented and tests were carried out to verify hydraulic fracture growth behaviour and measure the parameters needed to design the hydraulic fracture preconditioning process. Figure 1a shows the two test sites and their relative location with respect to each other and to the longwall panels at the mine. Figures 1c and 1d contain scale drawings of the sites, with the fracturing and monitoring boreholes indicated. Both sites had a surface tiltmeter array installed and the tiltmeter instrument locations at the sites are indicated in the figures.

The second site was located over the start of Longwall 103 where the conglomerate lies at a depth of 162 to 181 m (see Figure 1d). The fractures at the Longwall 103 site were placed into borehole 103AA with temperature logging occurring in monitor boreholes 103ACRR and 103AB. The temperature logging served to detect the arrival of the fractures at these boreholes and to locate their vertical positions in the boreholes.

The fractures at the Longwall 103 site were placed into borehole 103AA with temperature logging occurring in monitor boreholes 103ACRR and 103AB. The temperature logging served to detect the arrival of the fractures at these boreholes and to locate their vertical positions in the boreholes.

2. Preconditioning plan

By placing a number of horizontal fractures through the conglomerate layer, the mechanical behaviour of the conglomerate is modified from a thick-plate behaviour to a series of much thinner stacked plates with the aim of promoting caving. For efficient preconditioning from vertical holes drilled from the surface, hydraulic fractures are required to form horizontally as shown in Figure 1b. This fracture orientation allows efficient preconditioning from a vertical borehole because multiple fractures can be placed from each borehole.

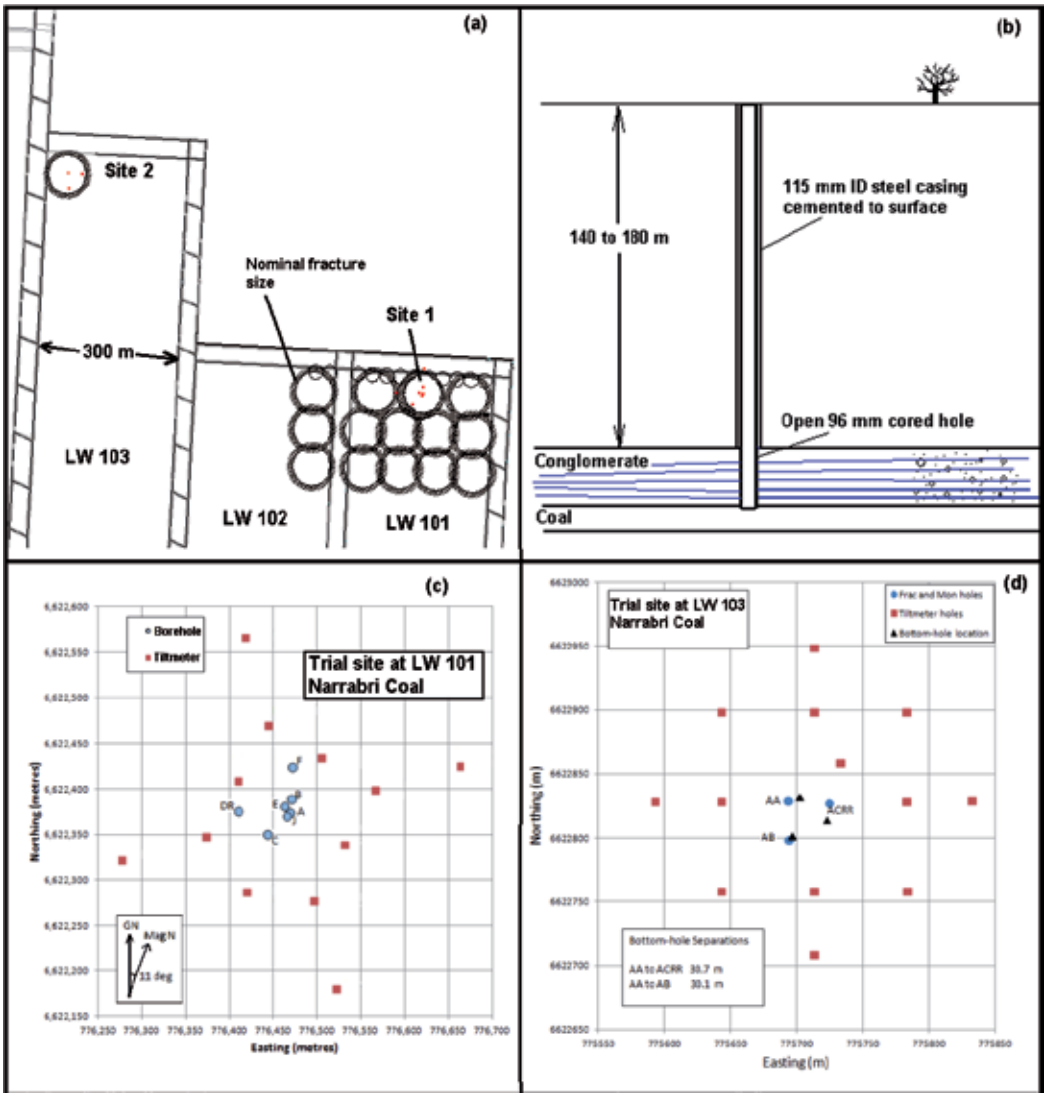

Figure 1. Test sites and borehole layout used. The drawings show (a) the location of the two test sites relative to each other and the planned underlying longwall roadways, (b) a vertical section showing the preconditioning concept, (c) the borehole layout at test site 1 over LW101 with tiltmeter locations, and (d) the borehole layout at test site 2 over LW103 with tiltmeter locations.

To confirm that this strategy would be possible in the local site conditions at Narrabri, a trial was conducted to determine the fracture orientation, growth rate, and to verify that the fractures could be extended parallel to previous fractures for a distance of 30 m or more. For example, boreholes spaced at 80 m centres require fractures to grow to 45 m radius with each borehole preconditioning 6,300 m^2 of conglomerate and a 50 m spacing between holes would require fractures to grow to 30 m with each borehole then preconditioning 2,800 m^2 of the conglomerate. These parameters would then be used to establish that horizontal fractures were

http://dx.doi.org/10.5772/56325

feasible, to determine the spacing between boreholes and the volume and rate of water to inject per fracture.

3. Test sites and measurements

For the preconditioning to work efficiently, the minimum principal stress must be the vertical stress. This allows horizontal hydraulic fractures to be formed. In addition to being able to grow horizontal fractures, the plan required that the growth rate and ultimate size of hydraulic fractures be determined so that the vertical borehole spacing could be specified. A second important requirement for effective preconditioning was that the fractures could be initiated at regular intervals along the borehole and extended as essentially parallel fractures, with a spacing of 2.5 m or less, to a radius of 30 m or more.

3.1. Stress measurements

As a starting point, the vertical stress was estimated by integrating density logs from boreholes drilled in the same area. Two overcore stress measurements from a vertical borehole were then made at 145 m depth in the conglomerate using ANZI strain cells [8]. Each ANZI cell contains 18 strain gauges which, when bonded to the surface of a pilot hole, sense the rock strain as the gauge is overcored. Using this strain data with the rock modulus, measured in an independent test, the in situ stress acting can be found.

Analysis of this data gave an estimate of the principal stresses acting as [9]:

σ_1= 8.3 MPa ± 1.1,

σ_2= 4.7 MPa ± 0.9, and

σ_3= 4 MPa ± 2.4,

with σ_3 the vertical stress and σ_1 directed N30E. The accuracy of the vertical stress in these tests is believed to have been affected by proximity to a small geological fault structure that was not recognised until later when the underground roadways were developed. The plus and minus range listed above for each stress component represents two standard deviations. For comparison, integration of a density log from a vertical borehole gave an estimate of 3.1 MPa for the vertical stress at 145 m depth. Earlier biaxial overcore stress measurements [10] gave generally horizontal total stresses of σ_1= 7.7 and σ_2= 6.0 MPa in the conglomerate in borehole NC-098 at a depth of 156.7 m with both values well above the log based vertical stress magnitude of 3.35 MPa for this depth. The value of the vertical stress from the density log was taken as an accurate value because bedding anisotropy can affect the vertical stress measured by the ANZI cell. In addition, the instantaneous shut-in pressure and offset monitor pressure data were found to correlate well with the log derived vertical stress magnitude. Taken together, the stress measurements gave an indication that horizontal fractures were likely to form, but because σ_3 and σ_2 as measured by the ANZI cell were of similar magnitude, this

inference needed to be verified by placing full scale hydraulic fractures, monitored using tiltmeters and offset boreholes.

3.2. Fracture asymmetry measurement

As a series of hydraulic fractures are placed sequentually into a borehole, with the fractures placed one above the other, there is potential for them to interact. During preconditioning, the hydraulic fractures are placed at a rate of approximately one per hour. The fractures are not propped, but some injected fluid remains in the fracture and bleeds back into the well once the packers are moved uphole in preparation for the next treatment. These fractures induce a change in the stress field around them and this changed stress will affect the next fracture, potentially causing it to curve toward or away from the previous fractures and to grow asymmetrically. Figure 2 shows the stress changes measured by an ANZI strain cell located at 129.3 m below the surface during the placement of the first hydraulic fracture in borehole A. The peak stress observed approximately 17 m above the hydraulic fracture was 0.52 MPa soon after the hydraulic fracture was placed at a depth of 146.5 m and this stress had reduced only to 0.26 MPa some 1.5 hours later at which time the excess pressure in the fracture was 0.3 MPa. Once one fracture grows somewhat asymmetrically, the next fracture is likely to find it easier to grow in a way such that it grows so as to avoid the residual vertical stresses created by the previous fracture and its centre of volume is offset relative to the centre of volume of the previous fracture.

The movement of the fracture centre of volume can, in principle, be detected by analysis of the tilt data [11] and also by noting the time of intersection of the fracture with the monitoring boreholes. Both of these methods of detecting asymmetry were used for the fracturing work carried out at the test sites.

Figures 3 and 4 summarise data recorded during fracture 4J and 7J, showing both the injection pressure at borehole J and the pressure response in the monitored boreholes. During fracture 4J, single packers were installed at the top of the conglomerate, set at 140.9 m to the bottom of the packer rubber, in monitor boreholes C and E and a vibrating wire piezometer was located at 146.0 m in monitoring borehole A. The piezometer was intalled in a coarse sand-filled section of the borehole with a grout plug at the conglomerate base and a second grout plug placed from the top of the conglomerate to the surface. The packers each contained a mandrel that connected through the packer to the open hole below. This pressure was transmitted to the surface via a 6 mm ID high pressure hose which was connected to a pressure transducer for logging. The pressures shown for the injection pressure and for boreholes C and E have had the hydrostatic pressure to the depth of the injection point in borehole J added to them to give an approximate bottom hole pressure. The calibrated piezometer output gives a direct bottom hole pressure at its set depth in borehole A.

Fracture 4J was carried out by straddling a slot at 151.8 m in borehole J. The fracture grew into boreholes E, C and then A as indicated by the pressure responses shown in Figure 3. In order to fit a circular fracture to this implied growth, the centre of the fracture needs to be located,

http://dx.doi.org/10.5772/56325

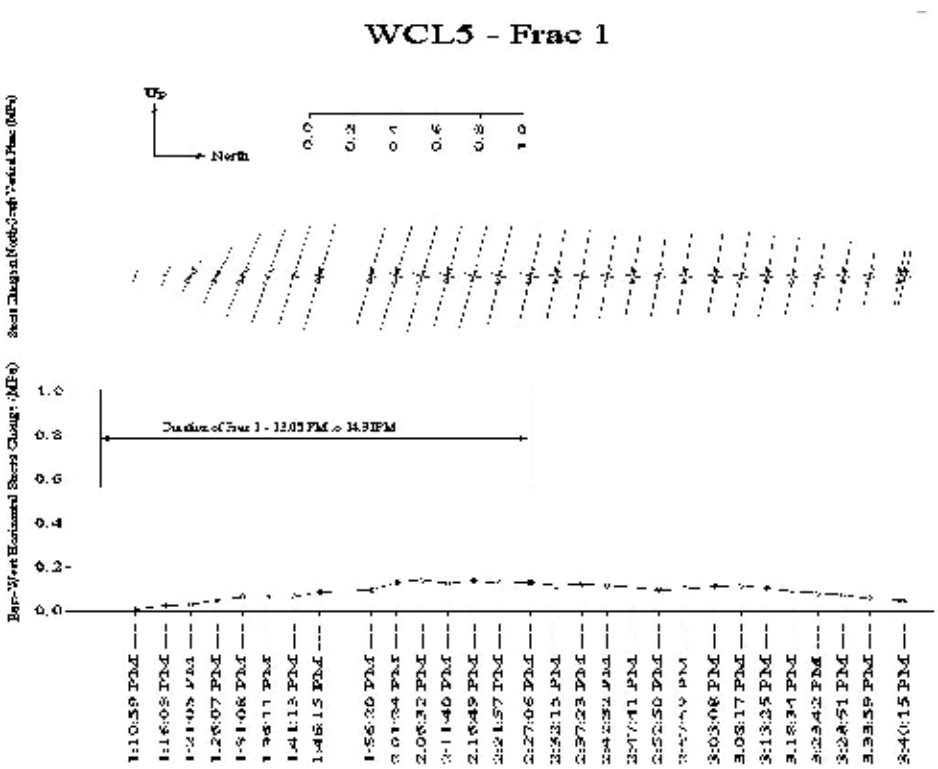

Figure 2. Stress change recorded during fracturing of borehole A. The fracture was shut-in at 14:31 (2:31 pm) and flowed back at 17:20 (5:20 pm) so pressurised fluid was contained in the fracture during the entire period of this plot. Fracture closure occured at 16:08 (4:08 pm).

at the time the fracture grows through borehole A, at a point 15 m west of borehole J. The intersection The intersection time for borehole A corresponds to a pressure at the piezometer of 3.47 MPa, which is just above the vertical stress magnitude. However, the earlier rise in pressure at 9:56 could be an indication of an earlier intersection, although the pressure at that time only reaches a value of 2.56 MPa. If water was being lost out of borehole A above the fracture depth (near 151.8 m), perhaps into an existing hydraulic fracture connected into borehole J above the packers, then this flow through the coarse sand would make the pressure in borehole A non-uniform and would result in the piezometer reading a pressure lower than the pressure in the fracture located approximately 5.8 m below it. However, the coarse sand used has an estimated permeability of 2,000 Darcies. A flow of 17 L/min through 5 m of this sand pack would result in a steady-state pressure drop of only 0.1 MPa. An earlier intersection time would support a less asymmetric fracture shape development and does highlight a possible source of error in picking intersection times based on pressure measured at borehole A.

Data collected during fracture 7J is summarised in Figure 4. The intersection with boreholes E and A occurred close together in time. In this case, the fracture depth (146.8 m) is very nearly the same as the piezometer depth (146.0 m) in borehole A, which minimises the issue of water flowing through the sand pack affecting the piezometer pressure. During this fracture treatment, temperature logging was carried out in borehole C, which was open at the borehole collar. The intersection time of the fracture into borehole C is indicated in Figure 4 and the temperature log is shown in Figure 5. The temperature logging method involved first cooling the water in the borehole by pumping ice water through a 20 mm diameter polypipe to the bottom of the borehole. A cooled condition of 10°C or less was typically achieved. The rock temperature at 145 m is approximately 23°C at this site and the water injected into a hydraulic fracture is quickly warmed to this temperature. Therefore, intersection locations were found by noting the depth where warm fluid was entering the monitored borehole and the first arrival of warm fluid into the hole is an indication of fracture growth rate. The sensor located at 158.5 m in borehole C started to increase in temperature at 11:50 (see Figure 5 and by 11:57 two warm peaks had been established at 145.5 m and 147.9 m. Early and weaker warming events may be associated with fluid being expelled from previously placed hydraulic fractures which are squeezed more tightly shut as the propagating hydraulic fracture interacts with them. The stronger warming events at 11:56:08 are therefore taken as corresponding to the intersection time.

Intersections from a number of fractures placed into borehole J have been used to define the fracture growth asymmetry. Figure 6 shows the range of fracture asymmetry measured by intersection data from this analysis. Only circular fractures are considered in Figure 6, although it is believed unlikely that the fractures were perfectly circular. However, if the fractures are allowed to take non-circular shapes, the range of centre locations and fracture sizes that can be fitted to the intersection data is increased significantly.

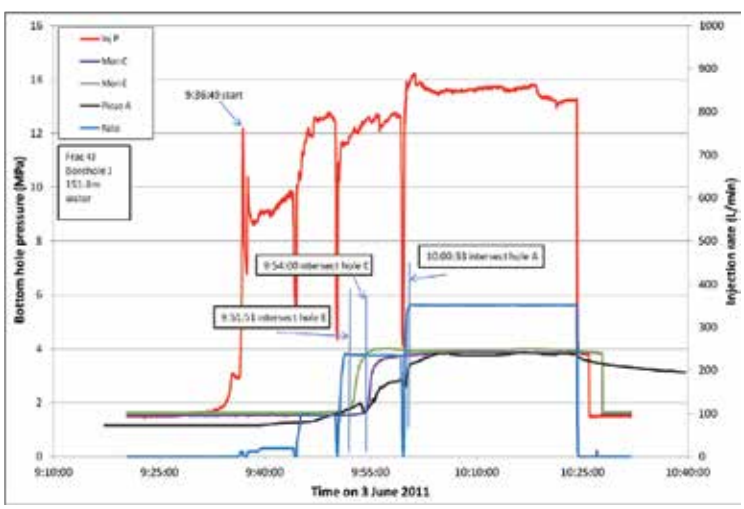

Figure 3. Data summary plot for fracture 4J, which includes pressure monitoring data in boreholes A, E, and C.

http://dx.doi.org/10.5772/56325

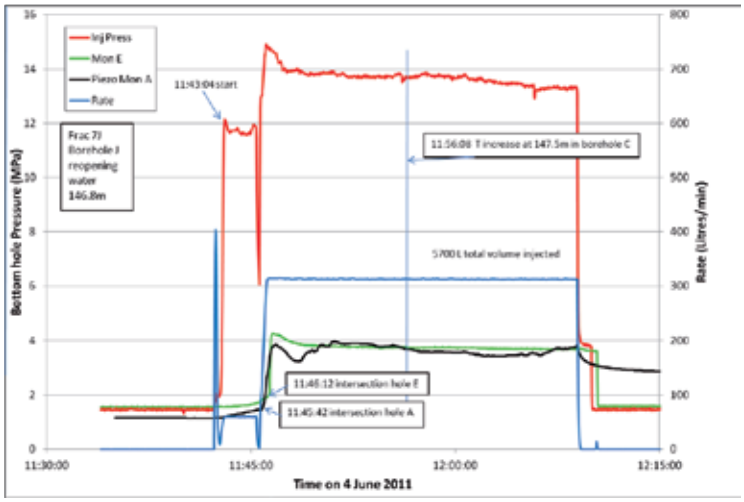

Figure 4. Data summary plot for fracture 7J, including pressure monitoring data in boreholes A and E. Temperature was monitored in borehole C during this fracture (see Figure 5).

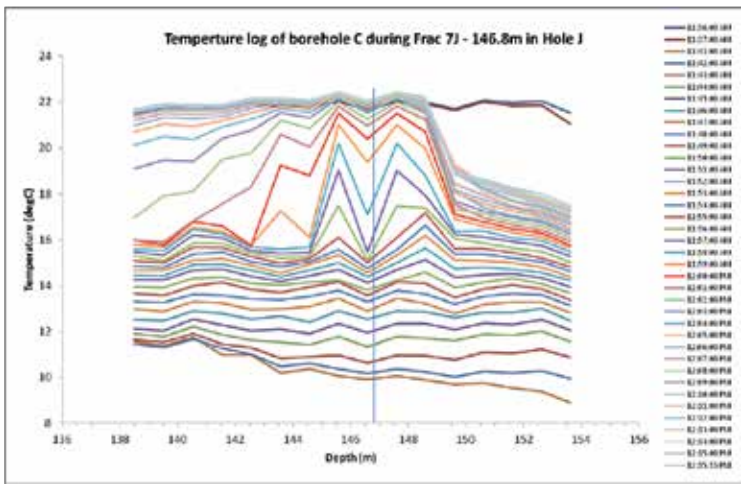

Figure 5. Temperature variation with depth in borehole C during fracture 7J. A line has been drawn at 146.8 m to indicate the nominal depth of fracture 7J in hole J.

3.2.1. Asymmetry from analysis of tilt data

By representing the fracture in the forward model as a displacement discontinuity (DD) singularity within a homogeneous, isotropic linear-elastic half-space and using a Bayesian probabilistic inversion approach, the fracture volume, orientation, and location of the fracture center-of-opening versus time have been estimated by analyzing the tilt measurements. This provides considerable insight into the geometry and development of the hydraulic fractures.

The displacement field produced by a DD of the intensity D_j across a surface S (the hydraulic fracture) in a uniform elastic half space can be expressed as [12]

$$u_i(x) = \iint_S D_j(x') \left[\delta_{jk} \lambda \frac{\partial U_{il}}{\partial x_l'} + \mu \left(\frac{\partial U_{ij}}{\partial x_k'} + \frac{\partial U_{ik}}{\partial x_j'} \right) v_k \right] ds \tag{1}$$

where $u_i(x)$ is the displacement in the x_i direction at a point x. $U_{ij}(x, x')$ is the *ith* component of displacement at x due to a point force of unit magnitude acting in the x_j direction at a point x' on S within an elastic half space. v is the normal to S at point x'. λ and μ are the Lame coefficients for the elastic rock material.

The measured tilt angles are related to the displacement gradients by

$$\omega_1 = \frac{\partial u_1}{\partial x_3} - \frac{\partial u_3}{\partial x_1} \omega_2 = \frac{\partial u_2}{\partial x_3} - \frac{\partial u_3}{\partial x_2} \tag{2}$$

For a horizontal hydraulic fracture which grows symmetrically with respect to the borehole, the fracture centre is taken to be at the injection point. Sometimes, asymmetric growth of the hydraulic fracture can occur. In this case, the fracture centre will move away from the injection point as the fracture grows. It is assumed that the fracture is planar, so the injection point and the fracture centre must remain in the fracture plane.

It has been shown that in most cases the analysis of tilt data allows for a robust estimation of fracture volume and orientation (dip and strike) [13, 11]. To investigate the movement of the fracture centre, consider a DD singularity centered at $(x_c, 0,0)$ in an infinite elastic body. Given an offset, which for simplicity we specify as along only the x axis, of $(\Delta x_c, 0,0)$ for the DD center, the tilt component can be obtained by using a Taylor series expansion as

$$\omega_1^{DD}(x_c + \Delta x_c) = \omega_1^{DD}(x_c) \left[1 + \left(\frac{\Delta x_c}{r} \right) g_1 + \left(\frac{\Delta x_c}{r} \right)^2 g_2 + O\left(\frac{\Delta x_c}{r} \right)^3 \right] \tag{3}$$

where $r = \sqrt{(x - x_c)^2 + y^2 + z^2}$ denotes the distance between the point (x, y, z) and the DD center $(x_c, 0,0)$, and the functions g_1 and g_2 are of order $O(1)$.

Eq. 3 shows that the estimation of fracture center movement is coupled with the tilt measured at x_c which depends on the fracture orientation and volume. The fracture center movement Δx_c is difficult to be resolved when it is far less than the observation distance r.

Two synthetic examples are presented here to show the effect of fracture center movement on the estimation of fracture volume and orientation. In the first example, the synthetic tilt data are generated by using a point DD singularity with a dip of 20^0 and a dip orientation of $N160^0$ in an elastic half-space. The fracture center is fixed at 20 m east of the injection point. The fracture volume increases linearly with time, reaching a maximum of 6 m^3 at 40 minutes. Then the generated tilt data are used to infer the fracture geometry by using a Bayesian probablistic

http://dx.doi.org/10.5772/56325

inverse approach, assuming that the fracture is centered at the injection point. The predicted fracture dip direction and dip are shown in Figure 7. As we can see, an incorrect assumption on the fracture center location leads to a poor prediction of the fracture orientation.

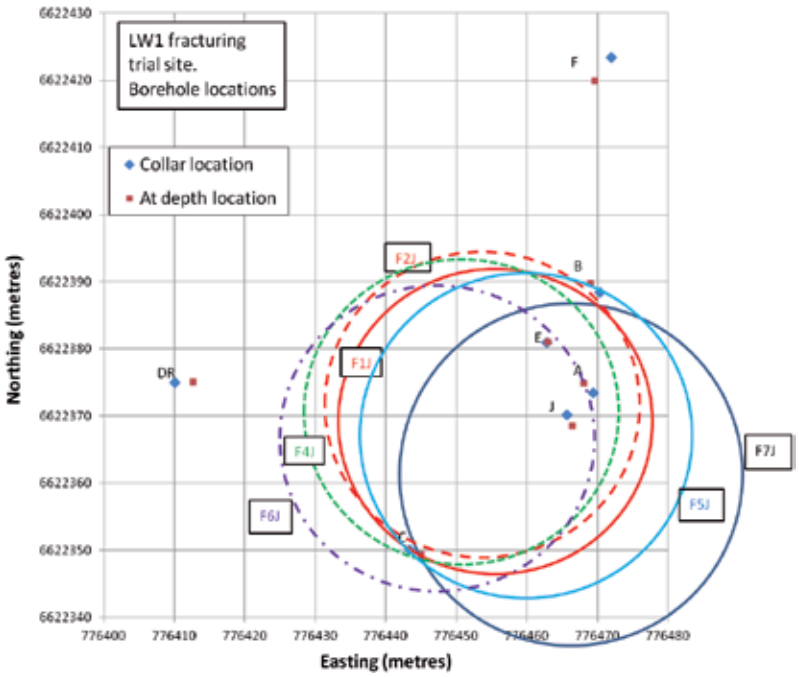

Figure 6. Longwall 101 trial site showing approximate fracture asymmetry inferred from intersection data for fractures placed into borehole J. Fractures are drawn at the time of the last intersection and in most cases injection stopped shortly after this time.

In the second example, the fracture has a dip of 10^0 and a dip orientation of $N160^0$ centered at the injection point. The synthetic tilt data are used to infer the fracture geometry (fracture volume and dip orientation) and the fracture center movement (see Figure 8) by specifying the frature dip of 20^0. It can be seen from Figure 8 that the incorrect constraint of the fracture dip results in an incorrect inferred movement of the fracture center.

Table 1 contains the fracture center location inferred from analysis of the tiltmeter data for a number of fractures in borehole J. Because the location of the center of volume is correlated to the dip and dip direction, the analysis was carried out for a case where both the orientation and the center of volume were found with no constraint and then again for the case where the fracture was constrained to be horizontal.

Of the fractures listed in Table 1 and also drawn in Figure 6 with their locations based on intersection data, only fracture 7J has an inferred center of volume that is somewhat consistent for the two methods. The tiltmeter results, which correspond to a time of 15 minutes from the start of injection, generally indicated less movement of the fracture center than the intersection data suggests. The inferred dip magnitude from the tiltmeter analysis is in the range of 40^0 for

fractures 1J, 4J, and 6J. This dip magnitude is larger by a factor of at least two than dips inferred from tilt data for fracturing carried out in other boreholes in this area (see Table 2, average dip 15.9^0) and does not agree with the intersection data either. The reason for these relatively large dips for this series of fractures, which are thought to be in error, is not know but may be related to small movements induced on faults present in this portion of the longwall.

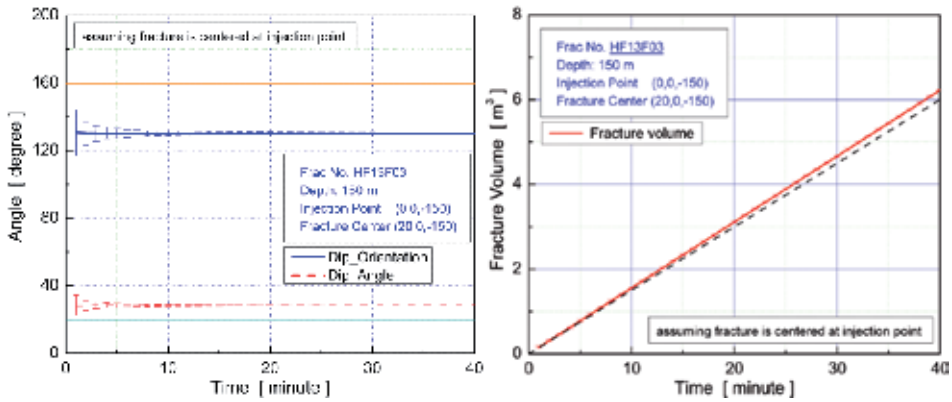

Figure 7. The predicted fracture geometry calculated with an assumed fracture center located at the injection point when in fact it is offset by 20 m.

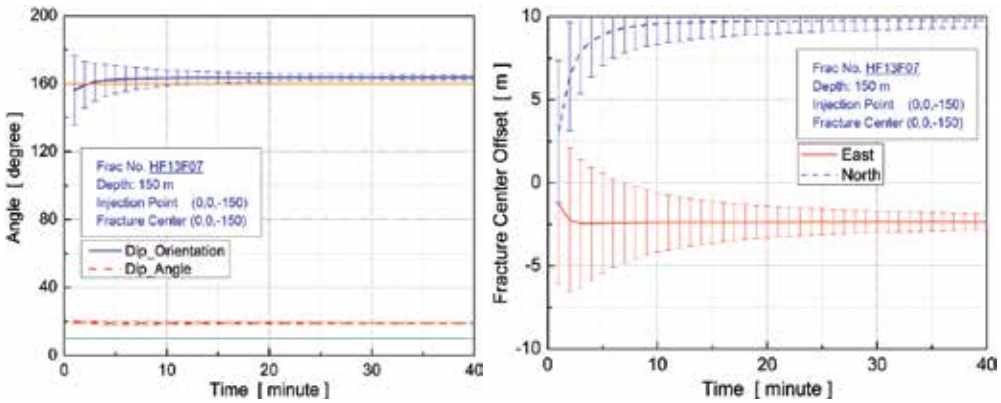

Figure 8. The predicted fracture geometry and center movement obtained by specifying the fracture has a dip of 20^0 when in fact the dip is 10^0.

http://dx.doi.org/10.5772/56325

Fracture	Northing offset (meters)	Easting offset (meters)	Dip/Dip Direction (degrees)
1J	0	0	C_0
1J	+0.5	0	38/180
4J	0	0	C_0
4J	0	0	38/160
6J	-1.0	0	C_0
6J	+4.0	+2.0	40/160
7J	-5.0	+1.0	C_0
7J	-1.0	+2.0	25/170

Table 1. Centre location of fractures relative to borehole location based on tiltmeter data. Fractures with a dip of C_0 were constrained to be perfectly horizontal.

Borehole	Fracture	Orientation	
		Dip	Dip direction
A	2	20^0	185^0
	4	10^0	180^0
101AW	1	22^0	330^0
	5	2^0	140^0
101BAR	1	20^0	70^0
	3	2^0	5^0
101ASR	1	30^0	190^0
	7	20^0	185^0
	10	25^0	190^0
102AA	1	20^0	300^0
101AUR	2	35^0	140^0
	3	15^0	165^0
102AE	2	10^0	65^0
102AD	1	10^0	190^0
101AL	1	8^0	270^0
	3	5^0	300^0

Table 2. Variation of dip and dip direction as determined by tiltmeter analysis.

For comparison, the dip direction and dip for fracture 3 at the Longwall 103 test site is shown in Figure 9a with the tilt vertors from this fracture at the end of the injection shown in Figure 9b. The 20° dip is believed to be too large and is likely to be reflecting some movement of the centre of opening of the fracture.

3.3. Fracture growth measurement

Tiltmeter monitoring [11-15], stress change monitoring [16], offset borehole measurements [17], and fracture growth modelling using a numerical hydraulic fracturing model were used to obtain the fracture growth rate as a function of injection rate and volume. The tiltmeter data provided a confirmaton that the hydraulic fractures were essentially horizontal in orientation. Stress change monitoring using ANZI cells installed in boreholes B and F (Figure 1), indicated fracture growth below these locations during injections into borehole A.

The primary data used to establish the hydraulic fracture growth rate were timing of the first arrival intersection events at offset boreholes. These data were filtered to remove the most extreme asymmetric growth cases so that an axisymmetric hydraulic fracture model could be used to match the measured growth. By matching several different measurements, the model was calibrated for the conditions at the Narrabri site. The calibrated model was then used to produce a set of time versus fracture radius curves for three different injection rates and these were then used for choosing a rate and volume that would produce a fracture size needed in the preconditioning work. A borehole spacing compatable with the ultimate size of the fractures was selected as part of this process. Figure 10 contains the growth curves generated by the numerical fracture model with several points indicating measured intersection events, for fractures placed using similar rates, also shown.

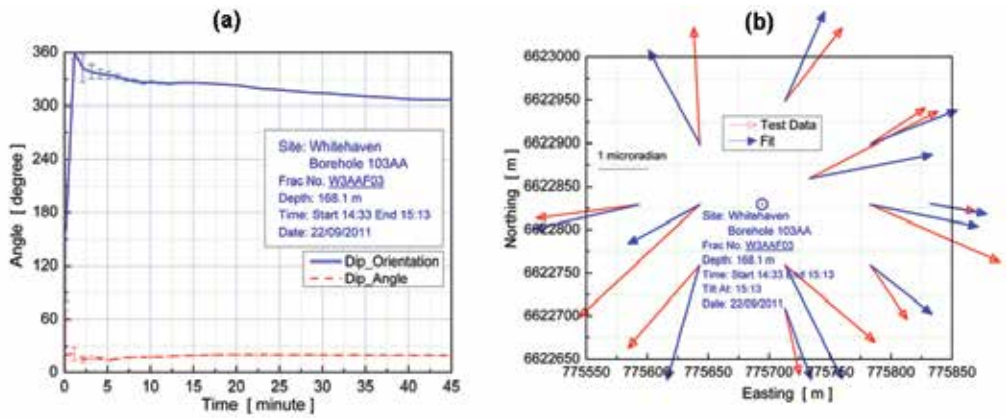

Figure 9. Analysis of tilt data from fracture 3 at the LW3 site. The fracture was interpreted to dip to the north at 20^0. The tilt vectors at the end of the injection are consistent with a horizontal fracture deformation field.

The curves calculated were fitted to the higher growth rate data represented by Frac 2 in borehole 101AM. In this case, the fracture grew through two monitoring holes located 30 m to the east and 30 m to the west of 101AM. The growth for this fracture was therefore thought to be fairly symmetric. The other measurements shown are from the trial site over Longwall 103 where injection occured into borehole 103AA and monitoring occurred at two offset boreholes. These points illustrate the variability in the measured growth data with asymmetric growth

http://dx.doi.org/10.5772/56325

being a primary cause. For example, Frac 3 in 103AA grew through one monitoring borehole located 31 m to the east of the injection borehole after 11 minutes, but required 23 minutes to grow through the second monitor hole located 30 m to the south of the injection borehole. On average, growth of the fractures seemed to be somewhat slower at the Longwall 103 site than at the Longwall 101 sites. Using these data, the treatments for preconditioning of the main longwall panels were designed to inject water at 500 L/min for 25 minutes each which, according to the growth curves in Figure 10, would produce fractures of approximately 45 m radius. The boreholes over the main Longwall 101 panel were drilled using an 80 m spacing.

3.4. Fracture vertical spacing measurement

To achieve the intended degree of treatment of the conglomerate, it was desirable to create hydraulic fractures that were parallel to one another so that the massive conglomerate layer was divided by the fractures into thinner and mechanically weaker system of layers. Work by

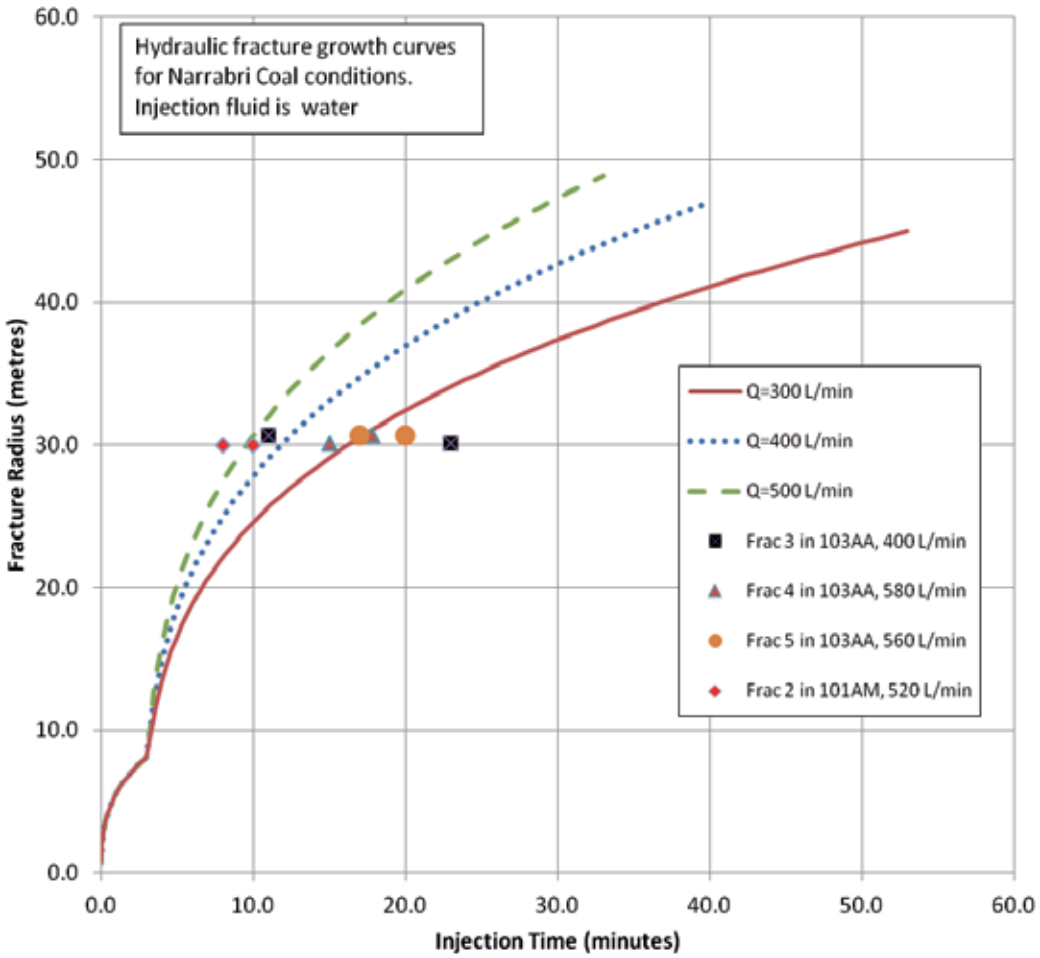

Figure 10. Growth measurements with curves generated by a numerical fracturing model.

[3] has shown that fractures grown through rock blocks in the laboratory are sensitive to initiation conditions. This laboratory work showed that fractures that initiated by splitting the borehole and then reoriented to become transverse to the borehole, were found to have much less regular spacing away from the borehole with growth into adjacent fractures commonly occurring (see [18] for additional details of the laboratory determined fracture paths). In contrast to this, if the fractures were initiated from slots or notches cut into the borehole, the fractures initiated and continued to grow in the same plane, as transverse fractures. The laboratory work showed that these fractures were spaced more regularly and they tended to extend into the far-field as parallel fractures. The initiation sites in the vertical boreholes at Narrabri were therefore notched using a sand and water abrasive jetting method. By rotating the jetting tool slowly, a circumferential slot was cut to act as a stress concentration point for fracture initiation.

A separate laboratory study, described in [19], presents results verifying a theory of closely spaced hydraulic fracture growth. The theory applies to fractures that are placed successively, one after the other and can be applied to predicting if the next fracture in a sequence will curve towards or away from the previous fracture. To make a prediction, the size and residual width of the previous fracture must be known. In addition, the rock elastic properties, the coefficient of friction for sliding of the hydraulic fracture surfaces, the stress field, and the injection rate and fluid viscosity are required. These parameters are then inserted into expressions for several dimensionless groups whose value then determine the type of curving to expect (see [19] for details). The calculation applied using parameters for the conditions at Narrabri, predict that essentially no curving of the hydraulic fracture will occur and that the fractures should grow parallel to one another.

Intersection of the fractures with offset pressure monitoring boreholes, as shown in the data contained in Figures 3 and 4, confirmed an approximately horizontal fracture orientation, but did not confirm that the fractures were growing parallel to one another. Fractures may have been growing into an adjacent fracture, for example, or growing with divergent paths which would leave wedge-shaped block of unfractured rock. The acoustic image logs run before and after fracturing were not able to detect the horizontal fractures in the horizontally bedded conglomerate. Two fracture traces, both dipping at approximately 10° to the west are visible at 149.9 and 150.1 m in the acoustic image of borehole J before it was fractured. These may be hydraulic fractures generated during fracturing of borehole A, but no other fracture traces can be seen in this image suggesting the hydraulic fractures are not wide enough to be seen by this method.

The core from borehole J, which was drilled after borehole A was hydraulically fractured, was examined in order to detect the fractures placed into borehole A. Several horizontal fractures were logged with four of them showing rotational shearing caused by the core rotating at that point during drilling. Such rotationally sheared fractures are normally fairly rare and have, in this case, been taken as indications of the location of the hydraulic fractures. Table 3 compares the fracture depths in borehole A with the depths of the logged rotationally sheared fractures in borehole J. The rotated core breaks in the core from borehole J are found to correspond

http://dx.doi.org/10.5772/56325

Fracture	Depth of initiation (metres)	Depth from core (metres)
1	146.4	146.1
2	149.8	150.0
3	140.2	140.2
4	144.7	
5	151.5	151.9

Table 3. Comparison of fracture initiation depths in borehole A with rotated core breaks from borehole J.

closely to the depths of initiation of the fractures in borehole A, suggesting nearly horizontal fracture orientation. This conclusion is supported by other intersection data such as that shown in Figure 4 for fracture 7J, which grew from borehole J into borehole C, 28.8 m away, and was located by termperature logging to be within plus or minus 1 m of the initiation depth (an apparent dip of 2°). The horizontal distances between the injection boreholes and the monitoring boreholes are listed in Table 4.

Borehole	A	J
A	0.0 m	6.5 m
B	14.9 m	21.3 m
C	34.4 m	28.8 m
DR	55.3 m	54.1 m
E	8.0 m	13.0 m
F	45.1 m	51.4 m
J	6.5 m	0.0 m

Table 4. Horizontal distance in metres between boreholes A and J and other boreholes at the site.

Inversion of the tiltmeter data cosistently produced dips of 10° to 30°. These larger dips seem to be in error in light of the nearly horizontal orientations obtained from intersection data with temperature logging. Figure 11 shows the fracture spacing implied by the temperature logging carried out in borehole C during fracturing of borehole J. Figure 12 shows fracture vertical spacing measured while fracture borehole 101AM while temperature logging in borehole 101AN. Both data sets illustrate the essentially parallel growth of the hydraulic fractures between these holes, confirming the prediction made from the theory of closely spaced fracture growth. Holes AM and AN lie along the startup roadway running at an azimuth of 273° with respect to grid north while the line connecting borehole J to C is oriented at an azimuth of 231°. Borehole AM is approximately 85 m NW of borehole J. Therefore, if these sections are taken as representative, the hydraulic fractures are essentially horizontal and maintain their initiation vertical spacing over more than 30 m of growth.

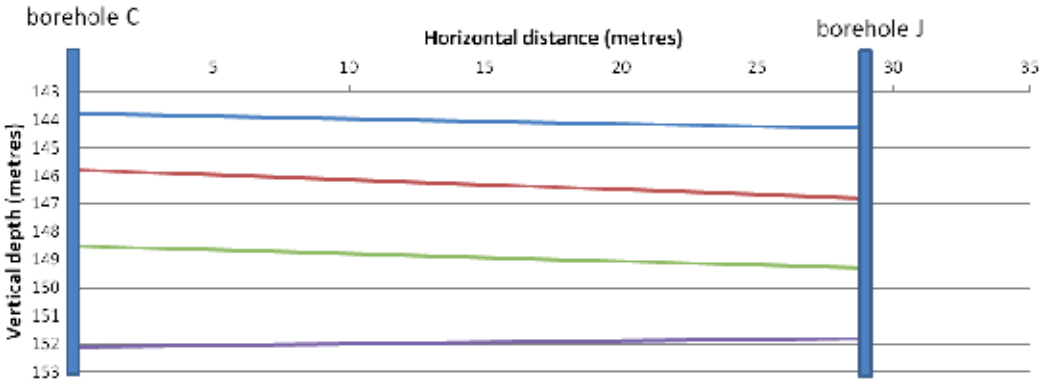

Figure 11. Fracture orientation and spacing implied by intersection and temperature logging data collected in borehole C during fracturing of borehole J. Fractures were placed at 2.5 m vertical spacing in borehole J.

4. Caving behaviour

The longwall started retreating on 12 June 2012 with a windblast management plan in place that required additional precautions to be used during mining until the caving commenced and the goaf developed. If the goaf behind the longwall face had not formed by the time the face had retreated to 25 m from the start position, additional work to induce caving was planned. However, the conglomerate caved, starting at the centre of the panel and progressing toward both gate roadways, after 24 m of retreat. This was a significant improvement over the estimated distance of more than 60 m for caving to start that was made based on modeling studies of the untreated conglomerate.

Beyond the startup area for a distance of 200 m, the conglomerate was preconditioned using boreholes located on approximate 80 m centres. The intensity of fractures placed in this main part of the longwall panel was approximately 25 percent of that applied along the startup section. A 100 m wide window was then left with no preconditioning to allow comparison of the fractured and unfractured conglomerate caving behavior. Mining under this section of conglomerate demonstrated that the preconditioning reduced the intensity of the periodic weighting events, but the events that still occurred were more random under the preconditioned roof. When mining under the conglomerate that was not preconditioned, weighting events could be anticipated to occur at regular intervals of about 15 m of longwall retreat. Therefore, adjustments to the daily longwall extraction plans were made so that any slowing or halting of mining was avoided when approaching an anticipated weighting event. Using this modified mining strategy, mining was continued without using preconditioning for the rest of Longwall 101.

http://dx.doi.org/10.5772/56325

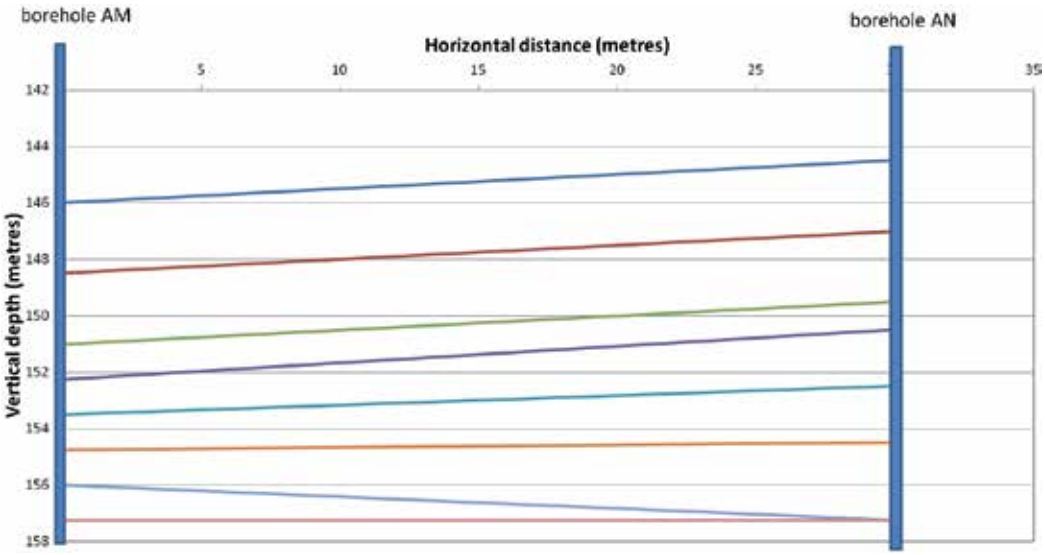

Figure 12. Fracture orientation and spacing implied by intersection and temperature logging data collected in borehole 101AN during fracturing of borehole 101AM. The upper part of AM was fractured at 2.5 m vertical spacing which was reduced to 1.25 m spacing below 151 m depth.

5. Conclusions

Measurements of fracture growth, spacing and orientation at two trial sites and as the preconditioning of the Longwall 101 startup area was carried out demonstrated that the hydraulic fractures could be created that were essentially horizontal and could be extended to more than 30 m as parallel fractures. The tiltmeter data recorded during the trials and later during preconditioning, indicated dips of 2° to 20°, which provided additional assurance that the fractures were essentially horizontal, especially at sites where no other monitoring was available. But attempts to analyse the tilt data for indications of asymmetric growth proved unreliable because the dip and dip direction are coupled to the location of the centre of fracture volume.

The theory of closely spaced fracture growth, developed using a 2D numerical model has been further verified by the measurments made during this project. The theory predicts that for the conditions at the Narrabri Coal site, hydraulic fractures placed sequentually at 1.25 m along a vertical borehole will grow with negligable curving to distance of 30 m or more, allowing the conglomerate roof rock to be preconditioned and weakened by placing fractures through its thickness. This was found to be the case, based on direct measurement of fracture arrival depths in offset boreholes.

The conglomerate caved soon after the start of Longwall 101, demonstrating the effectiveness of the intensive preconditioning carried out.

Hydraulic fracturing can be used for preconditioning of strong roof sequences. When conditions allow horizontal fractures to be placed from vertical boreholes, the preconditioning can be carried out from the surface.

Acknowledgements

The work described in this paper was undertaken as part of the overall windblast management project funded by Narrabri Coal Operations. The authors thank Narrabri Coal, CSIRO, and SCT Operations for granting permission to publish these results.

Author details

R. G. Jeffrey[1], Z. Chen[1], K. W. Mills[2] and S. Pegg[3]

1 CSIRO Petroleum and Geothermal, Australia

2 SCT Operations Pty Ltd, Australia

3 Narrabri Coal Operations Pty Ltd, Australia

References

[1] Van As, A, & Jeffrey, R. G. Caving induced by hydraulic fracturing at Northparkes Mines. In: J Girard, M. Liebman, C. Breeds, and T. Doe (Eds), The Fourth North American Rock Mechanics Symposium. 31 July- 3 August, (2000). Seattle, WA, USA. Rotterdam: A.A. Balkema.

[2] Chacon, E, Barrera, V, Jeffrey, R, & Van As, A. Hydraulic fracturing used to precondition ore and reduce fragment size for block caving. In: A. Karzulovic and M.A. Alfaro (Eds), MassMin August, (2004). Santiago, Chile. Instituto de Ingenieros de Chile., 2004, 22-25.

[3] Bunger, A, Jeffrey, R, Kear, J, & Zhang, X. Experimental investigation of the interaction among closely spaced hydraulic fractures. In 45th US Rock Mechanics / Geomechanics Symposium. June, (2011). San Francisco, CA, USA. ARMA., 26-29.

[4] Su DWHMcCaffrey JJ., Barletta L., Thomas EP., and Toothman RC. Hydraulic fracturing of sandstone and longwall roof control- implementation and evaluation. In S.S. Peng, C. Mark, and A.W. Khair (Eds), 20th International Conference on Ground Control in Mining, August, (2001). Morgantown, W.V., USA., 7-9.

[5] He, H, Dou, L, Fan, J, Du, T, & Sun, X. Deep-hole directional fracturing of thick hard roof for rockburst prevention. Tunnelling and Underground Space Technology, doi: 10.1016/j.tust.(2012). , 32, 34-43.

[6] Jeffrey, R. G, & Mills, K. W. Hydraulic fracturing applied to inducing longwall coal mine goaf falls. In: J Girard, M. Liebman, C. Breeds, and T. Doe (Eds), The Fourth North American Rock Mechanics Symposium. 31 July- 3 August, (2000). Seattle, WA, USA. Rotterdam: A.A. Balkema.

[7] Medhurst, T. Narrabri Coal Pty. Ltd. Longwall support geotechnical assessment. Report by PDR Engineers, May (2009). pp.(8760)

[8] Mills, K. W. In situ stress measurement using the ANZI stress cell. In: K. Sugawara and Y. Obara (Eds). The International Symposium on Rock Stress, October, (1997). Kumamoto, Japan. Rotterdam: A.A. Balkema., 7-10.

[9] Mills, K. W. Interpretation of in situ stress measurements conducted at the start of longwall 1 at Whitehaven. Report by SCT Operations Pty. Ltd., March (2011). pp.

[10] Gray, I. Narrabri coal in-situ stress test (IST). Report by Sigra Pty. Ltd., 8 May (2006).

[11] Lecampion, B, & Peirce, A. Multipole moment decomposition for imaging hydraulic fractures from remote elastostatic data. Inverse Problems, (2007). doi:10.1088/

[12] Davis, P. V. Surface deformation associated with a dipping hydrofracture. Journal of Geophysical Research, (1983). B 88(7), 5826-5834.

[13] Lecampion, B, Jeffrey, R, & Detournay, E. Resolving the geometry of hydraulic fractures from tilt measurements, Pure and Applied Geophysics, (2005). doi:10.1007/s00024-005-2786-4., 2005(162), 12-2433.

[14] Chen, Z. R, & Jeffrey, R. G. Tilt monitoring of hydraulic fracture preconditioning treatments. In the 43rd U.S. Rock Mech. Symposium and 4th U.S.-Canada Rock Mech. Symposium, Asheville, NC, 28 June- 1 July, (2009).

[15] Olson, J, Du, Y, & Du, J. Tiltmeter data inversion with continuous, non-uniform opening distributions: A new method for detecting hydraulic fracture geometry. International Journal of Rock Mechanics and Mining Sciences, 34(3-4), 236.ee10. doi: 10.1016/S1365-1609(97)00120-2,(1997). , 1-236.

[16] Mills, K. W, Jeffrey, R. G, & Zhang, X. Growth analysis and fracture mechanics based on measured stress change near a full-size hydraulic fracture. In the 6th NARMS Symposium, GulfRock (2004). Houston, June, 2004., 6-10.

[17] Jeffrey, R. G, Settari, A, Mills, K. W, Zhang, X, & Detournay, E. Hydraulic fracturing to induce caving: fracture model development and comparison to field data. In: D. Elsworth, J. P. Tinucci, and K. A. Heasley (Eds), DC Rocks: rock mechanics in the national interest: 38th U.S. Rock Mechanics Symposium, Jul 7-10, (2001). Washington, D.C. Lisse, Netherlands: Swets & Zeitlinger, B., 251-260

[18] Kear, J, White, J, Bunger, A. P, Jeffrey, R, & Hessami, M. Three dimensional forms of closely-spaced hydraulic fractures, In: A.P. Bunger, J.D. McLennan, and R.G. Jeffrey (Eds), The International Conference for Effective and Sustainable Hydraulic Fracturing, May, (2013). Brisbane, Australia. InTech: Rijeka, Croatia., 20-22.

[19] Bunger, A. P, Zhang, X, & Jeffrey, R. G. Parameters effecting the interaction among closely spaced hydraulic fractures. SPE Journal, (2012). , 17(1), 292-306.

Chapter 46

Estimation of the Impact of Mining on Stresses by Actual Measurements in Pre and Post Mining Stages by Hydrofracture Method–A Case Study in a Copper Mine

Smarajit Sengupta, Dhubburi S. Subrahmanyam,
Rabindra Kumar Sinha and Govinda Shyam

Additional information is available at the end of the chapter

http://dx.doi.org/10.5772/56017

Abstract

To sustain and increase the productivity in a large underground copper mine in India the management of the mine decided to design and develop stopes below the mined out area. For the design of the stopes a detailed stress measurement programme was carried out by hydrofracture method at different depths from the developments available near the proposed stope. The result indicated a post mining induced high stress tensor with the direction of the maximum compression (maximum principal horizontal stress) rotated 70- 750 from the pre-mining stress tensor and oriented almost transverse to the ore body as against sub parallel to the orebody during pre- mining stage. A 3-D numerical modeling of the mine with pre mining stress tensor as input parameter substantiated the field result at the post mining stage. The generation of post - mining stress helped in understanding the impact of mining on the stress and was used for design and sequencing of the stoping operation for the safe and optimum extraction of the ore.

1. Introduction

Knowing the post mining stress condition is always of interest to the mine designer ahead of designing a mining method in the non-mined areas. This knowledge helps them in the design of stopes, mining sequence and rock reinforcement for the extraction of ores economically and safely. Previous work has examined the impact of mining on stresses as revealed by actual

measurements at the site and included the use of 3D numerical methods to understand the impact vis a vis mining to help in the designing of openings below mined out areas (Whyatt-JK, Williams-TJ, Blake. W (1995).

In this study, in a deep underground copper mine, stress measurements using the hydrofracture method were carried out in two stages. At the pre-mining stage, when only few developments were available and at the post mining stage from the developments between the mined out area and the non-mined out area.

Stress data generated from the stress measurements produced a value for the mining induced stress gradient (post mining) which was found to be totally different from the stress gradients of the area measured in the pre mining stage. The orientation of the Maximum Horizontal principal Stress was found to be perturbed and lying perpendicular to the strike of the orebody as against parallel orientation found during pre -mining stage. To understand the impact of the mining on the stresses a 3-D numerical modeling study was carried out using a boundary element method. The initial stress ratio from the pre mining stage measurement was used with gravity loading to account for the surface topography, which is hilly. Three observation points were monitored for stress change in mining, resulting from excavation effects and this data was found to be in agreement the measured induced stresses. The study results helped in the design of stopes, mining sequences and rock reinforcement.

2. Background

Hindustan Copper Limited (HCL), a public sector undertaking under the administrative control of the Ministry of Mines, is engaged in mining, beneficiation, smelting, refining and casting of refined copper metal. HCL maintains focused on its mission and vision which include increasing the ore production by three times over a decade and implementing continuous improvement in productivity. To continue to achieve these goals, it has geared up to tap the resources from the un-mined areas by designing stopes below the mined areas.

The present study was undertaken in Kolihan Copper Mine, an important captive underground mine of Kolihan Copper Complex of HCL and this mine is situated near the village of Khetri, in the District Jhunjhunu, Rajasthan. The mine plan to develop stope blocks at lower levels below the mined out areas to sustain and increase the productivity.

For the design of stopes, in-situ stress is one of the most important factors which dictates the size of the stopes and the size of the pillars and the sequence of extraction. The main host rocks of Kolihan mines are garnetiferous chlorite quartz schist, quartzite and amphibolite quartzite. The strike length of the ore body is 600 m with a width varying from 30 m to 100 m and the ore dips steeply to almost vertical. The main mining method adopted is Large Diameter Blast Hole Stoping. The mine extends from 486 ML to 0 ML. (Hindustan Copper Limited internal notes)

A detailed stress measurement programme was undertaken before the commencement of any stoping activity (pre- mining stage) between 486 mL and 184 mL for the determination of stress

http://dx.doi.org/10.5772/56017

around the mine openings. Three locations with different depths (different rock covers) were selected inside the mine and stress measurements were conducted inside boreholes drilled from development tunnels (cross cuts), using the hydrofracture method.

Mining up to 306 ML is complete and presently mining is active at 246 ML and 184 ML. Mine development has to commence at lower level soon, below 184 ML.(Figure 2.) Thus it was felt to undertake a stress measurement programme again below the mined out area (post mining stage) to find the impact of mining activities on the stresses. Three levels with different rock covers were selected, similar to what was done in the pre-mining stage and stress measurements were conducted inside boreholes using the hydrofrac method.

3. Geology and tectonics

3.1. Geology

The rock formations of the area belong to the Alwar and Ajabgarh series of the Delhi system and are younger than the Aravalli system. Both rock formations are highly deformed and metamorphosed. Rocks occurring at Kolihan mines are Amphibolite quartzite/garnet chloride with principal economic mineral is chalcopyrite. Strike of the formation is N 30^0E - S 30^0W, dipping 50^0 - 85^0 westerly (Fig 1)

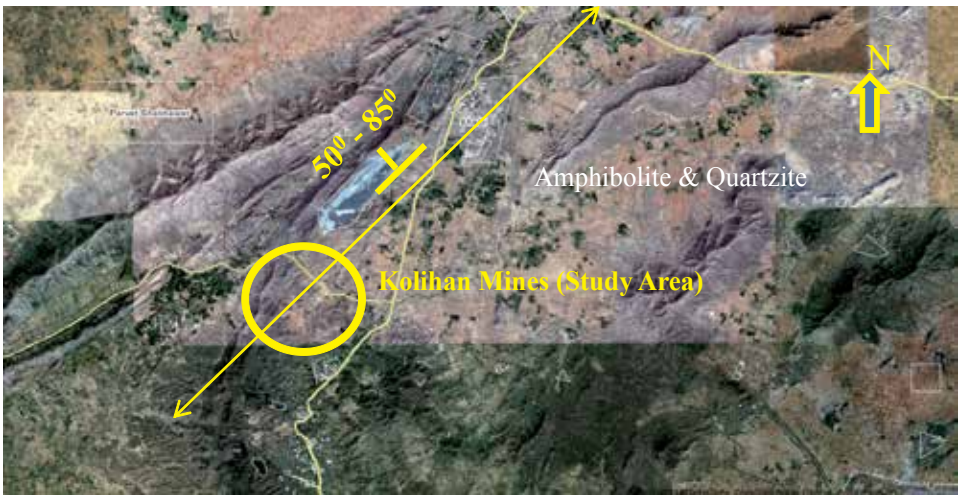

Figure 1. Geological and tectonic map of the project area

3.2. Tectonics

Structurally the thick prism of metasediments comprising rocks of Alwar and Ajabgarh series has been deformed into northeast –southwesterly trending longitudinal folds of large areal

extent. In the northern part of the belt the simplest structures are represented by Khetri anticlines and synclines with increasing intensity of deformation. The simple structure passes westward into overturned Kolihan syncline which is slightly compressed in the north.

In the central part of the belt the formations show as anticline structures.

The southern part of the belt is separated from the central part by a major transverse fault. The southern part of the fault is marked by anticlines and synclines. The asymmetrically overturned Kolihan syncline which is locally recumbent occupies a narrow zone. It plunged towards the SW and in the southern part the limbs are low dipping but gradually steepen northwards. The syncline is defined by the younger quartzites of the Ajabgarh series of reverse faulting (Dasgupta 1965).

4. Mining status

In the scheme of mining with respect to Kolihan Copper Mine the following methods have been adopted:

i. Sub-level Open Stoping method

ii. Blast Hole stoping Method

In the sub level open stoping method, sub levels are developed at vertical intervals of 18-20 m with a crown level at 9 m below uppermost levels. The size of the stope block is 30 m along strike which consists of 20 m of stope and 10 m of Rib Pillar.

In the blast hole stoping method a drill level is prepared below the crown pillar of 9 m. The size of the stope block is 30 m along the strike, which includes 16.6 m stope and 13.4 m Rib Pillar. The proposed stopes will be developed at the lower levels.

The mine extends from 486 ML to 0 ML with the surface RL of 486 m. Mining up to 306 ML is complete and presently it is active at 246 ML and 184 ML. Mine development has to commence at lower level soon.

5. Methodology

In-situ stress measurement using the hydrofracture method was carried out both during pre mining and post mining stages. Three boreholes were drilled, one each from 184 ML, 124 ML and 64 ML, for post mining stress determination.

The in-situ stress measurement was carried out by using HTPF (Hydraulic Tests on Pre existing Fracture) as introduced by Cornet et al. 1986]. The advantages of HTPF method are

i. The boreholes are not required to be oriented along one of the principal stress direction like in classical methods

http://dx.doi.org/10.5772/56017

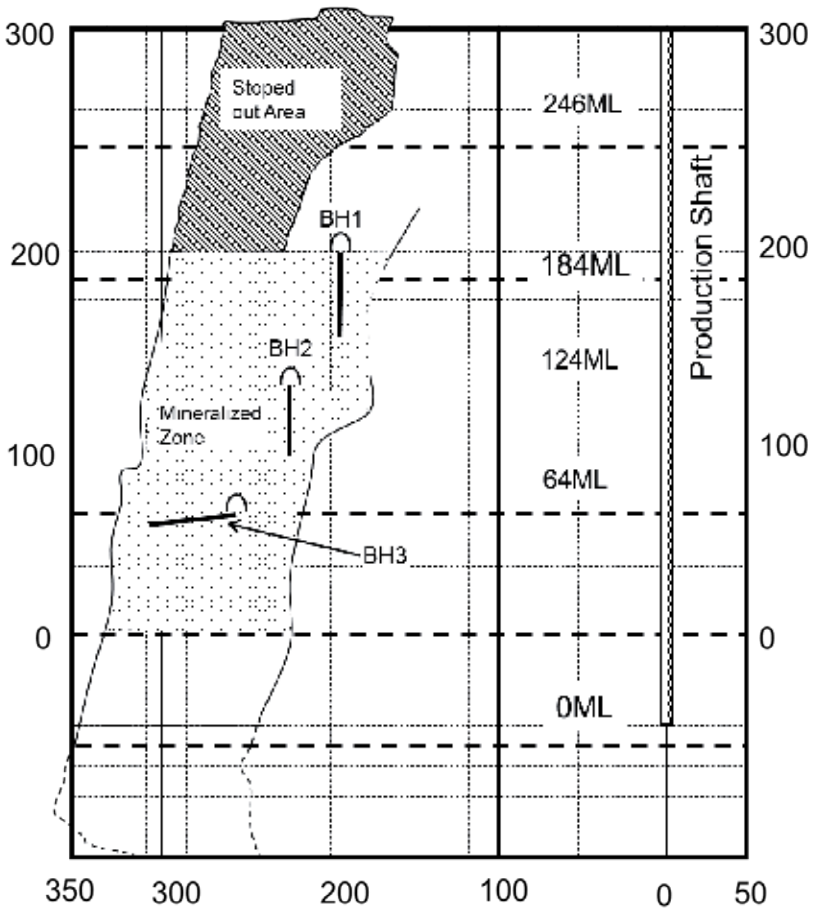

Figure 2. Status of Mining activities in Kolihan mine (ML= Meter level which indicates altitude from mean sea level)

ii. A new induced fracture is not essentially required to be created for stress evaluation. Stress can be evaluated both from preexisting/induced fractures

A schematic diagram showing set up of the hydrofracture system assembly is shown in Fig.3.

The straddle packer assembly (Hydrofrac assembly Fig 4) was used for fracture initiation/ opening and further extension. The straddle packer assembly consisted of a test interval of length 200 mm and two 250 mm steel reinforced packer (42 mm dia, burst pressure = 70 MPa) units attached at either end of the test interval. In the case of hydrofrac experiments in the 48 mm diameter boreholes at the present Project, the straddle packer unit was operated by 1500 mm long and 32 mm diameter tubes (dual line packer inflation + injection unit combined in one). The maximum injection rate of the electrically driven pump was 10 lit /min using water for pressurisation. All the events of injection were recorded in continuous real time digital mode.

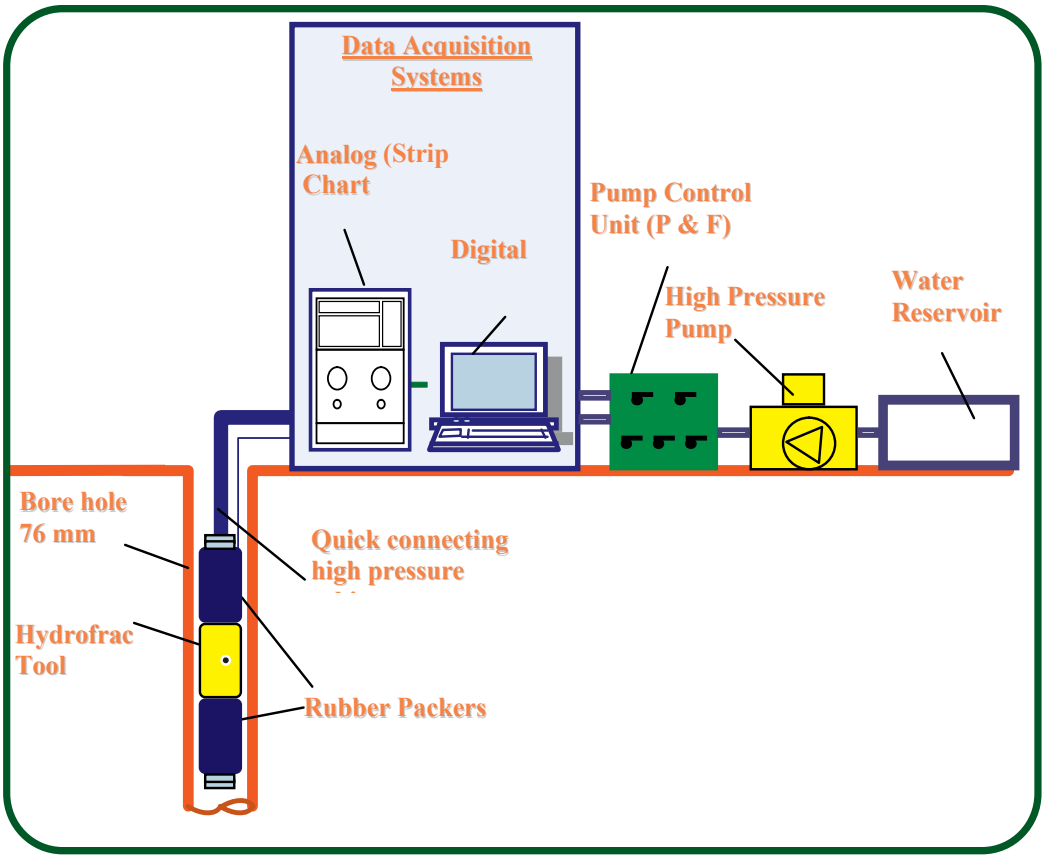

Figure 3. Schematic diagram of Hydrofrac Experiment Set-up

After all the hydraulic fracturing tests were conducted in all the boreholes, an impression packer tool with a soft rubber skin together with a magnetic single shot orientation device was run into the holes to obtain information on the orientation of the induced or opened fracture traces at the borehole wall.

Two data analyses programmes were used in the analyses. They are called Plane and Gensim.

The *software Plane* incorporates the impression data with the compass data as input parameters and gives the strike, dip and dip direction (fracture orientation data) as the output.

The Software Gensim computes the stress field on the basis of measured shut in pressure and fracture orientation data. The vertical stress is assumed to be a principal stress and its magnitude is taken as equal to the weight of the overburden. The powerful Gensim programme requires only the shut in pressure and the orientation of an induced or pre-existing fracture

http://dx.doi.org/10.5772/56017

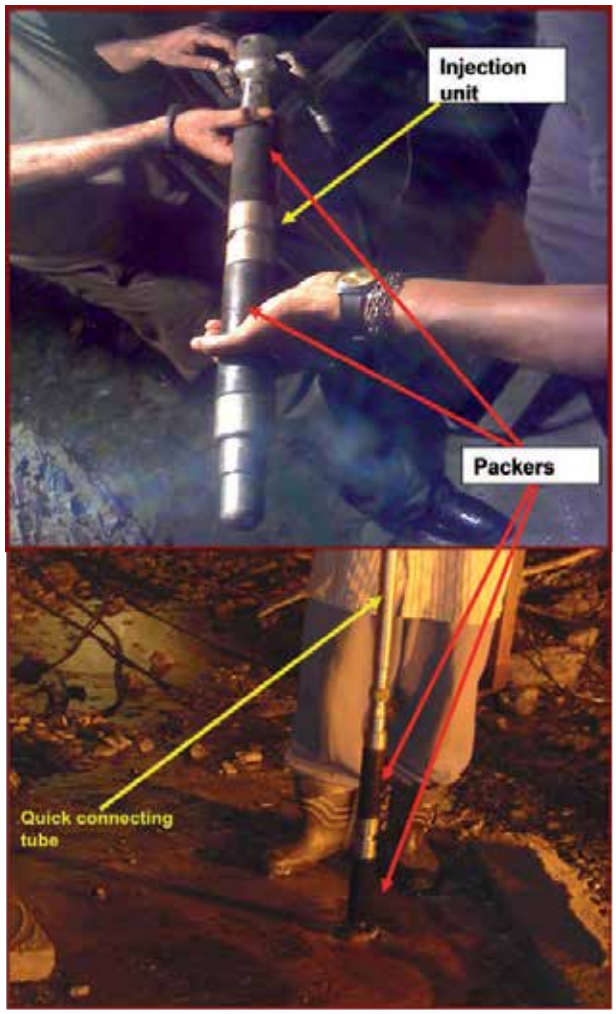

Figure 4. Hydrofracture equipment used

6. Stress evaluation procedures and results

The in-situ stress measurement were made from inside two vertical and one horizontal boreholes drilled from three levels. Tests were conducted with the following situations:

i. Presence of anisotropic rock.

ii. Presence of mining induced stress.

Due to the above aspects a medium to large scatter in fracture orientation data were noticed which negated the use of classical simple hydrofrac hypothesis suggested by Hubert and Wills (1957). Therefore data analysis required a more sophisticated meth-

od, namely the interpretation of measured normal stress acting across arbitrary oriented fracture planes.

In this method the shut-in pressure P_{si} is used to measure the normal stress component under the assumption that the vertical stress is a principal stress axis and the vertical stress magnitude σ_V is equal to the weight of the overburden.

The analysis program *GENSIM* was used to calculate the magnitude and the direction of principal stresses on the basis of the following equation:

$$\sigma_h = (P_{si} - n^2.\sigma_V) / (m^2 + l^2.\sigma_H / \sigma_h) \quad (1)$$

Where, l, m, n is the cosines of the direction of the induced fracture plane related to the principal stress axis.

The calculations involve obtaining the best fit based on using all shut-in pressure data derived from the measurements in the boreholes and varying the ratio σ_H/σ_h and the strike direction of σ_H.

The pre-mining and post mining stress tensors as revealed are given in tables 1 and 2

Principal Stresses			
σ_V MPa	σ_H MPa	σ_h MPa	Rock Cover Depth m
6.97	8.4	5.6	203
7.88	8.89	5.93	268
10.7	12.65	7.7	364

Table 1. Pre mining stress tensor as revealed by hydrofrac stress

Principal stresses	***184 ML***	***124 ML***	***64 ML***
Rock cover	*195m*	*184 m*	*530 m*
Vertical Stress (σ_V) MPa (2.7 gm/cc + 1.4 gm/cc density of solid and loose rocks respectively)	9.28	9.89	14.02
Maximum Horizontal principal Stress (σ_H) in MPa	21.78	22.78	23.94
Minimum Horizontal principal Stress (σ_h) in MPa	10.89	11.39	15.96
Maximum Horizontal principal Stress direction	N 80^0	N 80^0	N 90^0
$K = \sigma_H/\sigma_v$	2.35	2.30	1.71

Table 2. Post mining stress tensor as revealed by hydrofrac stress

Table 3 shows the comparison of pre and post mining stress gradient

http://dx.doi.org/10.5772/56017

Stresses	Pre – Mining Stage (486 mL to 184mL)	Post Mining Stage (184 mL to 0 mL)	Remarks
Maximum Horizontal principal Stress (σ_H) orientation	N 10^0 to N 20^0	N 85^0 to N 90^0	Rotation of horizontal stress orientation due to stoping
Stress gradient ($\sigma_{H)}$	0.031 Z +1.5968 R^2 = 0.91	0.0048 Z + 21.379 R^2 = 0.7627	Change in stress gradient due to mining
Stress gradient ($\sigma_{h)}$	0.0145 Z +2.3892 R^2 = 0.93	0.01437 Z + 8.412 R^2 = 0.9862	Change in stress gradient due to mining

Table 3. Comparison between pre and post mining stress gradient

7. Numerical modeling

A numerical modeling was carried out using the boundary element method to understand post mining induced stresses vis a vis mining. The initial stresses gradient of the pre mining stage was used with gravity loading as the surface topography is hilly. Three observation points were monitored for stress change in mining, due to excavation effects. The stress contour of the model is shown in figure 5

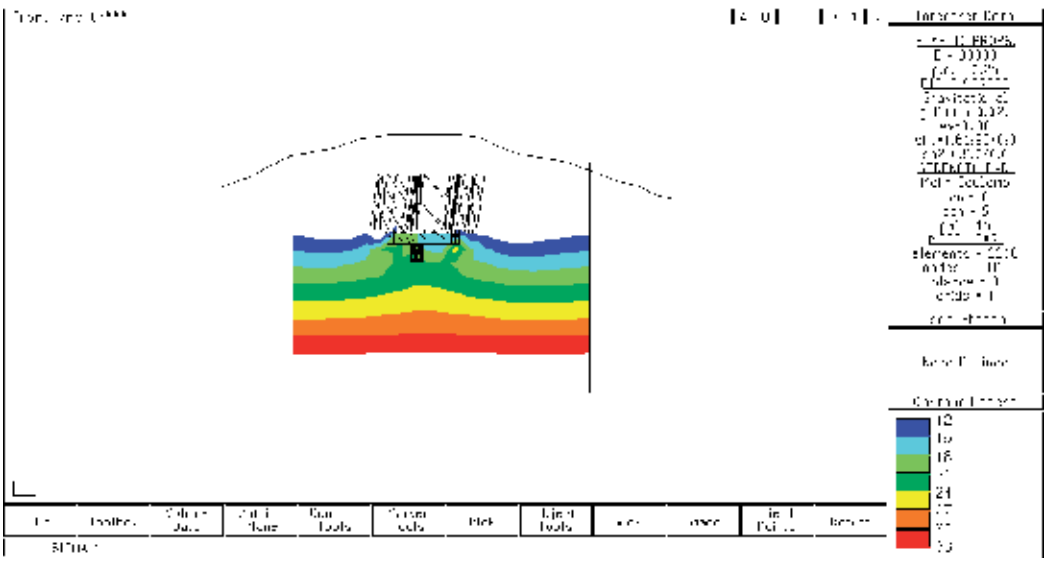

Figure 5. Major principal stress contour of the modeled stope.

The results of the stress output as revealed by the numerical model are given in Table 4.

ML	Sigma 1			Sigma 2			Sigma 3		
	Magnitude	Dip	Direction	Magnitude	Dip	Direction	Magnitude	Dip	Direction
ML - 184	21.15	7.32	272.59	10.9	30	178	6.99	58.25	14.59
ML - 124	23.33	2.32	92.52	11.48	10.29	182.94	6.36	79.43	349.94
ML- 64	24.66	6.3	90.43	13.07	12.28	181.81	10.47	76.14	333.81

Table 4. Stress magnitude and orientation as revealed by numerical model

The modeling studies reveal that the measured value of the stresses agree reasonably with the computation values which is compared in Table 5

Stresses	Post Mining Stage (184 mL to 0 mL)	Numerical modelling
Maximum Horizontal principal Stress (σ_H) orientation	N 85^0 to N 90^0	N 90^0 to N 92^0
Stress gradient ($\sigma_{H)}$	0.0048 Z + 21.379 R^2 = 0.7627	0.0069 Z + 20.924 R^2 = 0.5943
Stress gradient ($\sigma_{h)}$	0.01437 Z + 8.412 R^2 = 0.9862	0.0055 Z + 10.158 R^2 = 0.9188

Table 5. Stress magnitude and orientation as revealed by numerical model

8. Discussion and conclusion

The availability of stress results during pre - mining stage and subsequent measurement of stresses at the post mining stage has refined our understanding of the in-situ stress vis a vis mining. The change in the orientation of the major compression from a favourable N10-20 ^{0} (Strike of ore body N 30^0 and crown pillar oriented parallel to ore body) during pre- mining stage to unfavourable N85-90 ^{0} at the post mining stage has prompted to redesign the stopes and support systems below the mined out area.

Acknowledgements

We are thankful to the Director National Institute of Rock Mechanics, India for the permission to publish the work. The authorities and staffs of Hindustan Copper limited are also thankfully acknowledged.

http://dx.doi.org/10.5772/56017

Author details

Smarajit Sengupta, Dhubburi S. Subrahmanyam, Rabindra Kumar Sinha and Govinda Shyam

National Institute of Rock Mechanics, Bengaluru, India

References

[1] Whyatt-JKWilliams-TJ, Blake. W ((1995). In-Situ Stress in Lucky Friday mines W Reference:U.S. Department of the Interior, Bureau of Mines, Report of Investigations 9582. NTIS stock (PB96-131685)

[2] Hindustan Copper Limited Internal Notes

[3] Dasguupta, B. (1965). Khetri Copper Belt. GSI memoirs, , 98

[4] Cornet, F. H. (1986). Stress determination from Hydraulic Tests on Pre-exiting Fractures- the HTPF Method. Proc. Intl Symp, Rock Stress and Rock Stress Measurements, CENTEK Publ., Lulea, , 301-311.

[5] Hubbert, K. M, & Willis, D. G. (1957). Mechanics of Hydraulic Fracturing, Petroleum Transactions AIME, T., 210, 4597.

Section 15

Thermo-Hydro-Mechanical Systems

Chapter 47

An Efficient and Accurate Approach for Studying the Heat Extraction from Multiple Recharge and Discharge Wells

Bisheng Wu, Xi Zhang, Andrew Bunger and Rob Jeffrey

Additional information is available at the end of the chapter

http://dx.doi.org/10.5772/56373

Abstract

In order to understand the thermal recovery Behavior of an engineered geothermal system (EGS), this paper develops a model in which fluid circulates in a single, planar hydraulic fracture with a constant hydraulic aperture via multiple recharging and discharging wells. The coupled equations for heat convection in the fracture plane and heat transfer into the rock are provided for steady and irrotational fluid flow conditions. By using velocity potentials and streamline functions, the temperature along a streamline is found to be only a function of the potential. By utilizing the Laplace transformation, the analytical solutions in the Laplace space for the temperature field are found, which are numerically inverted for time-domain results. Several examples with different arrangements of injection and production wells are investigated and the comparison with other published results is provided. The semi-analytical results demonstrate that the proposed model provides an efficient and accurate approach for predicting the temperatures of a multi-well reservoir system.

1. Introduction

Heat contained in the upper 10 km of the Earth's crust represents a large, accessible, low-emission energy source that can substitute for other energy sources that produce significantly more greenhouse gas. Geothermal energy has become one of the most promising energy alternatives in the future. For example, Australia has a large volume of identified high heat

producing granites within 3 to 5km of the surface. In some places at 5kms the temperature is more than 250^0 C. One cubic kilometer of hot granite at 250^0 C has the stored energy equivalent of 40 million barrels of oil (Geodynamics website). Therefore, developing methods to capture this resource of clean energy will help realize the potential of commercial EGS. In addition to the physical experiments and field exploitation, theoretical studies such as mathematical modeling are important in developing ways to maximize heat extraction from geothermal reservoirs treated by hydraulic fracturing.

Mathematical modeling of thermal problems associated with oil recovery or geothermal heat extraction from reservoirs containing hydraulic or natural fractures has been studied extensively. The models can be classified into three types based on the dimension of the heat transfer problem. The first type is based on one-dimensional (1-D) heat diffusion in the fracture and it mainly contains two cases. The first one considers 1D fluid flow in a 2D fracture. In this case, the fluid velocity is uniform and no singular point in pressure exists at the injection or production well [1-3]. The second one considers fluid flow that is radial and axisymmetric, for example the fluid is injected into a single well and produced from a ring of production wells that are all at the same radial distance from the injection well [4]. Due to the symmetry, the problem can be treated as one-dimensional based on the radial distance. The fluid velocity can be obtained either by considering the effect of the wellbore size or neglecting it. When the injection or pumping at the well is regarded as a point source or sink, the velocity will have a singularity of 1/r theoretically at the injection and production points. Fortunately, this singularity is overcome by the geometrical symmetry [5, 6] for the case with a single well.

The second type is so-called $2^1/_2$ dimensional model [7] which results from 2-D heat transfer within fractures and 1-D heat transfer within the adjacent rocks, it becomes more difficult to find analytical solutions for these cases because of the coupling of the steady fluid flow and heat transfer. There are mainly two ways to obtain the fluid velocity analytically for the cases with single, dipole or multiple wells; one method calculates the pressure by using a Green's function [8], and the other method calculates the velocity potential and stream functions by using the source solution for the 2-D Laplace equation [9, 10]. From the perspective of modeling the long lifetime of a geothermal reservoir, the above two approaches are functionally the same. Although the first method can obtain accurate results for the fluid pressure and thus the fluid velocity, there still exists two coordinates in the governing equation and the difficulty of solving this equation is not reduced. In addition, the singularity issues make it invalid to use the boundary condition (i.e. injection temperature) when solving the equations. For this case, solutions still require the use of numerical methods.

In order to overcome the above issues including the computational difficulty and singularity at the source or sink points, Muskat [11] proposed a method in which an orthogonal set of curvilinear coordinates is introduced that correspond to the permanent set of equipotential and streamline surfaces. By using this transformation, the terms involving cross products related to the fluid diffusion and heat transfer are greatly simplified. Gringarten and Sauty [12] were the first to apply this concept to solve the dipole well problem of fluid flow and heat diffusion in an infinite fracture by using velocity potentials and stream functions based on the results of Dacosta and Bennett [9]. In their model, each channel leaving a particular injection

http://dx.doi.org/10.5772/56373

well is treated separately and the two-dimensional heat diffusion problem in the fracture plane is simplified to be one-dimensional. Later Rodemann [13], Schulz [14], Heuer et al. [15] and Ogino et al. [16] extended Gringarten and Sauty's [12] approach to the problems related to heat extraction from a finite fracture or multiple fractures with a recharge-discharge well pair and obtained good analytical solutions.

The third type is the complete 3D problem for the heat transfer in the fracture and the rock. In these more complicated cases, numerical schemes, such as finite element [7], Marker-and-Cell method [17] and finite difference approaches [18, 19], have to be used to obtain the thermal behavior of the fluid and reservoir. Normally, finding the solution is computationally demanding.

Besides applying the method to a particular set of boundary conditions for EGS reservoirs, the advance of the present model is in that the semi-analytical solutions for the rock and fluid temperatures are obtained, thus significantly reducing computational cost. It also provides an efficient and accurate way to further study the effect of some factors, such as the number of wells, the well spacing, the injection rates and production rates, to maximize the heat extraction from the EGS reservoirs.

2. Problem description

The geometry considered by the present model is shown in Fig. 1. There exist M (M≥1) vertical recharge well and N-M (N≥2) vertical discharge wells, which intercepts the fracture containing the injected fluid. The whole system (liquid and rock formation) is initially in an equilibrium state with the uniform temperature T_0. When time t>0, a cold fluid with a constant injection rate Q_i (i=1, 2...M) and constant temperature T_{in}^{i} is injected from the injection points (x_i, y_i) (i=1,..M) and the heated fluid is pumped out at a constant production rate Q_i (i=M+1, M+2...N), from the discharge wells (x_i, y_i) (i=M+1, 2...N).

It is assumed that after a hydraulic fracturing treatment, there is a connected flat fracture plane intercepted by all wells. The geometry of the fracture is defined by its radius In particular, the fracture radius is infinite in this paper.

Some assumptions are made for the present model:

1. The fluid is incompressible with Newtonian rheology and the rock is impermeable, homogenous and isotropic;
2. The stress-induced change of the fracture aperture is ignored;
3. The material properties (density, specific heat capacity and thermal conductivity) of the rock and the fluid are constant and independent of the temperature;
4. The heat condution in the fluid is neglected when the injection rate is sufficiently great.

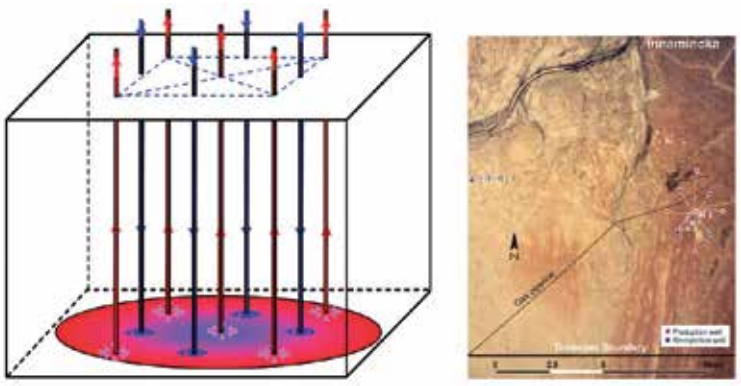

(a) (b)

Figure 1. (a) Multi-well geothermal reservoir model, (b) Geometry for Habanero project with 5 injection wells and 4 production wells (red denotes production well, blue denotes injection wells).

3. Governing equations

3.1. Pressure diffusion in planar fractures

Because the fluid flow along the narrow fracture is much faster than the reservoir heat temperature changes, it can be assumed to be a pseudo-steady state. This means that the fluid pressure or velocity potential is a function of only the in-plane coordinates x and y. Therfore, the governing equations for the fluid flow obeys the potential flow theory

$$\mathbf{q}_f = -\nabla\phi_f, \tag{1}$$

where ∇ is the gradient operator, $\mathbf{q}_f$ denotes the discharge vector and ϕ_f is the velocity potential for the fluid.

In the present model, there are a total of M recharge wells and N-M production wells to be considered. The continuity equation for the flow of an incompressible Newtonian fluid in the fracture plane is expressed as

$$\nabla \bullet \mathbf{q}_f = \sum_{j=1}^{N} Q_j \delta\left(x - x_j, y - y_j\right), \tag{2}$$

where $\nabla \cdot$ is the divergence operator, δ denotes the Dirac delta function, Q_j is flow rate into or out of the jth well (x_j, y_j) ($Q_j > 0$ for injection and $Q_j < 0$ for production).

http://dx.doi.org/10.5772/56373

3.2. Heat transport in closed fractures

According to Cheng et al. [18], the heat transport in the fractures can be described by the following equation when the effect of the heat storage and longitudinal dispersion can be ignored

$$\rho_w c_w \mathbf{q}_f \bullet \nabla T_f + 2\lambda_r \frac{\partial T_r}{\partial z} = 0, \tag{3}$$

where T_f and T_r denote the fluid temperature and rock temperature, respectively, ρ_w and c_w are the mass density and specific heat, respectively, of the fluid, and λ_r is the thermal conductivity of the rock.

For the surrounding rock, the heat conduction equation is

$$\kappa_r \nabla^2 T_r = \frac{\partial T_r}{\partial t}, \tag{4}$$

where $\kappa_r = \lambda_r / \rho_r c_r$, ρ_r and c_r are the mass density and specific heat, respectively, of the rock formation.

3.3. Initial and boundary condition

The initial temperature distribution for the rock and fluid is assumed to be a constant

$$T_f = T_r = T_0, \tag{5}$$

and the initial velocity potential in the fracture is

$$\phi_f = \phi_0 \quad \text{on } z = 0. \tag{6}$$

It must be mentioned that for the temperature continuity along the fracture, we have

$$T_r = T_f \quad \text{on } z = 0. \tag{7}$$

The temperature at each injection well is fixed

$$T_f = T_{in}^j, \quad \text{at } (x_j, y_j)\ (j = 1,..M), \tag{8}$$

where z denotes the vertical coordinate with z=0 being the fracture plane.

In order to avoid the existence of the volume associated with the infinite boundary of the fracture plane, the total injection rate is always equal to the total production rates, which is reasonable for long-term estimatation, i.e.

$$\sum_{j=1}^{N} Q_j = 0. \tag{9}$$

4. Dimensionless formulation

After some manipulation, the above equations can be written in a simplified form

$$\begin{aligned}
&\frac{\partial \Theta_r}{\partial \tau} = \frac{\partial^2 \Theta_r}{\partial Z^2}, \\
&\nabla \bullet \mathbf{Q}_f = \sum_{j=1}^{N} \Omega_j \delta\left(X - X_j, Y - Y_j\right), \\
&\mathbf{Q}_f = -\nabla \Phi_f, \quad \mathbf{Q}_f \bullet \nabla \Theta_f + \chi \frac{\partial \Theta_r}{\partial z} = 0, \text{ on } Z = 0, \\
&\Theta_f = \Theta_{in}^j, \quad \text{on } (X, Y) = (X_j, Y_j), \\
&\Theta_f = \Theta_r \quad \text{on } Z = 0, \\
&\Theta_r = \Theta_f = 0, \quad \text{on } \tau = 0,
\end{aligned} \tag{10}$$

based on the following transformation

$$\Theta_r = \frac{T_r - T_0}{T_0}, \ \Theta_f = \frac{T_f - T_0}{T_0}, \ \Theta_{in}^j = \frac{T_{in}^j - T_0}{T_0}, \ \Phi_f = \frac{\phi_f - \phi_0}{Q}, \ \Omega_j = \frac{Q_j}{Q},$$

$$\mathbf{Q}_f = \frac{L}{Q}\mathbf{q}_f, \ \tau = \frac{t\kappa_r}{L^2}, \ X = \frac{x}{L}, \ Y = \frac{y}{L}, \ Z = \frac{z}{L}, \ \chi = \frac{2\lambda_r L}{\rho_w c_w Q},$$

where L is the characteristic length to be chosen from the geometrical configuration of the wells (for example, the minimum distance between wells).

5. Velocity potential and stream function

According to the superposition principle, the flow velocity potential Φ for a sum of the injection and producing wells is

http://dx.doi.org/10.5772/56373

$$\Phi = -\frac{1}{4\pi}\sum_{j=1}^{N}\Omega_j \ln\left[(X-X_j)^2+(Y-Y_j)^2\right], \tag{11}$$

and the flow stream function ψ is expressed as

$$\Psi = -\frac{1}{2\pi}\sum_{j=1}^{N}\Omega_j \arctan\frac{(Y-Y_j)}{(X-X_j)}. \tag{12}$$

The following formulas are valid when the variables Φ and ψ denote the velocity potential function and stream function, respectively,

$$\begin{aligned} V_X &= -\frac{\partial\Phi}{\partial X} = -\frac{\partial\Psi}{\partial Y}, \quad \frac{\partial\Theta_f}{\partial X} = \frac{\partial\Theta_f}{\partial\Phi}\left(-V_X\right) + \frac{\partial\Theta_f}{\partial\Psi}V_Y, \\ V_Y &= -\frac{\partial\Phi}{\partial Y} = \frac{\partial\Psi}{\partial X}, \quad \frac{\partial\Theta_f}{\partial Y} = \frac{\partial\Theta_f}{\partial\Phi}\left(-V_Y\right) + \frac{\partial\Theta_f}{\partial\Psi}\left(-V_X\right). \end{aligned} \tag{13}$$

Then equation $(10)_3$ after using the above identities, becomes

$$-v^2\frac{\partial\Theta_f}{\partial\Phi} + \chi\frac{\partial\Theta_r}{\partial Z} = 0, \quad Z = 0, \tag{14}$$

where

$v^2 = V_X^2 + V_Y^2$.

Appling Laplace transform to equation (14) and making use of the general Laplacian solution of equation (10) for $\hat{\Theta}_r$, the analytical solution for the Laplace tranform of the fluid temperature $\hat{\Theta}_f$ is obtained as

$$\hat{\Theta}_f = \frac{\Theta_{in}}{s}\mathrm{e}^{-\chi\sqrt{s}g(\Phi,\Psi)}, \tag{15}$$

where the cap ^ denote the Laplace tranform and the function g(Φ,ψ) is defined as

$$g(\Phi, \Psi) = \int_{\Phi}^{+\infty} \frac{d\zeta}{v^2(\zeta, \Psi)}.$$

The solution for Θ_f in the time domain is obtained by the inverse transformation of Eq. (15)

$$\Theta_f = \Theta_{in} \operatorname{erfc}\left[\frac{\chi g(\Phi, \Psi)}{2\sqrt{\tau}}\right]. \tag{16}$$

We note that in equation (16), Θ_{in} can be measured and χ is a constant. Therefore, the key to the solutions for the temperature is to calculate the value of the function $g(\Phi, \psi)$.

6. Methodology, verification and numerical results

Generally, when the number of the wells is larger than 2, the analytical solutions for $g(\Phi, \psi)$ are difficult and are not available in the literature. Then the following computational procedures are adopted. Start with the points which are very close to one of the injection wells and the velocity, velocity potential Φ_0 and stream function ψ_0 are calculated with the known coordinates. We then move along the streamline, and the velocity potential is increased by an increment $\Delta\Phi$. In addition the coordinates of the next point on the same streamline can be evaluated via the following equations

$$\begin{aligned} \Psi_0 &= \Psi(X, Y), \\ \Phi_0 - \Delta\Phi &= \Phi(X, Y), \end{aligned} \tag{17}$$

which can be solved by using the Newton-Raphson method. In the same way, the information of the next point on the same streamline is obtained until the new point reaches a region which is regarded as being within the range of a production well or as infinity. There are no well defined criteria to define the region which is regarded as being within the range of a production well or as infinity. In the present calculations, we have compared cases using several small radial distances (such as 0.002m, 0.001m and 0.0001m) from the production wells and different far-field distances (such as 6km, 8km and 10km) from all the wells. When we find little difference between the results for these cases, the solutions are taken as being accurate. It should be noted that the position of the new point relative to the total wells should be compared with that of the starting point on the same streamline in each step. If the relative position changes, the stream function should be plus or minus PI which depends on the position change.

For verification and testing of the proposed model, numerical results for several well arrangements as shown in Fig. 2 are provided below. In particular, the required parameters are listed in Table 1.

http://dx.doi.org/10.5772/56373

Parameters	Value	Parameters	Value
Number of injection wells	*M*	Rock ther. conductivity λ_r (W/(m•K))	2.2
Number of total wells	*N*	Rock mass density ρ_r (Kg/m^3)	2700
Total injection rate Q_{total} (m^3/s)	0.06	Rock specific heat c_r (J/(kg•K))	790
Total Extraction rate Q_{total} (m^3/s)	0.06	Fluid mass density ρ_w (Kg/m^3)	900
Injection temperature T_{in}	90	Fluid specific heat c_w (J/(kg•K))	4200
Initial temperature T_0 (°C)	270		

Table 1. Parameters for the present calculations

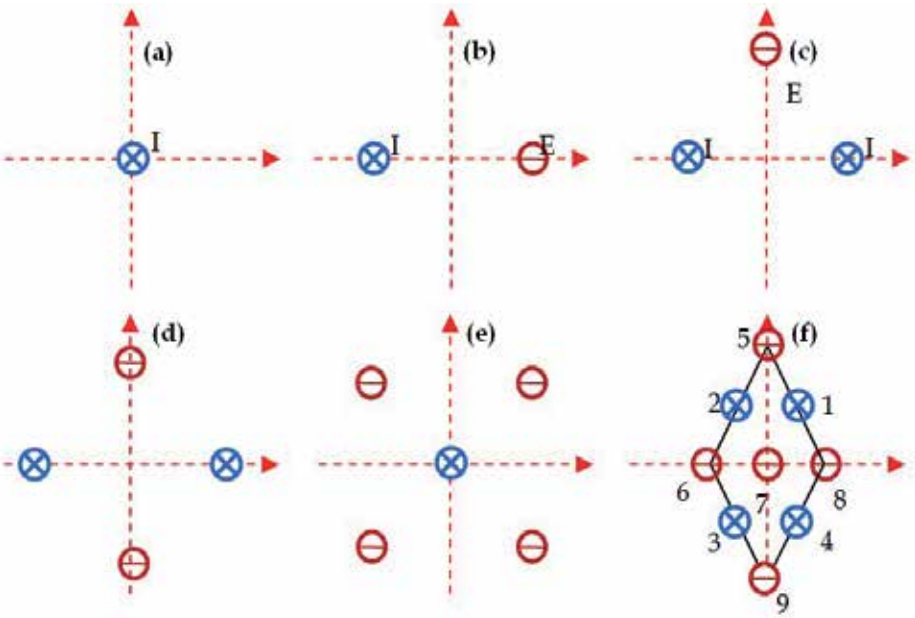

Figure 2. Case studies with different injection wells and extraction wells. Blue circle denotes injection well and red circle denotes production well.

6.1. Cases with one single well and dipole wells

In Figure 3(a), the temperature evolution along the radial direction for the case with one single injection well is compared between the present approach and the analytical solution [5]. In Figure 3(b), the temperature profiles along the line connecting the injection well and the production well are also compared for the case with dipole wells[14] It is found that the results for the above two cases from the current method and analytical solutions are in excellent agreement.

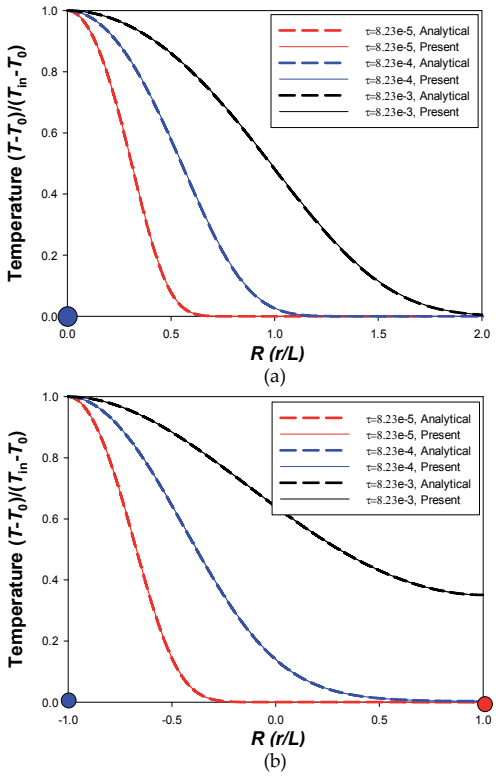

Figure 3. Comparison between the present approach and the analytical solutions: (a) Temperature profile along the radial direction (physical time *t*=115 days, 3.17 years and 31.7 years) for the case with only a single injection well at the origin. Parameters are listed in the paper by Ghassemi et al. [6]; (b) Temperature distribtion along the line connecting a recharge well (left) and a discharge well (right). Blue circle denotes injection well and red circle denotes extraction well.

6.2. Cases with two injection wells or multiple wells

Figure 4 displays the extraction temperature change at different times for the cases (b) to (e) (Figure 2). As the geometrical configurations of all cases are symmetrical, the output temperature for only one production well in each case is plotted. The total injection and production rates in all cases are kept the same, i.e. 0.06 m^3/s, and for the purpose of simplicity, the individual injection rate for each case is assumed to be the same. For example, when there are two injection/production wells, the individual injection/production rate is 0.06/2=0.03 m^3/s. These results show that case (b) has the least temperature decrease, the reason being that the well separation is greater than the other cases. However, this greater separation and the fact that only 2 wells are involved will undoubtedly lead to higher pressure differences in order to obtain the same total flow rate. Case (d), with 2 injectors and 2 producers, is the next best performing well from the standpoint of minimizing temperature falloff. Interestingly, case (c) and case (e) perform almost equally, but case (c) only requires 3 wells while case (e) requires 5.

http://dx.doi.org/10.5772/56373

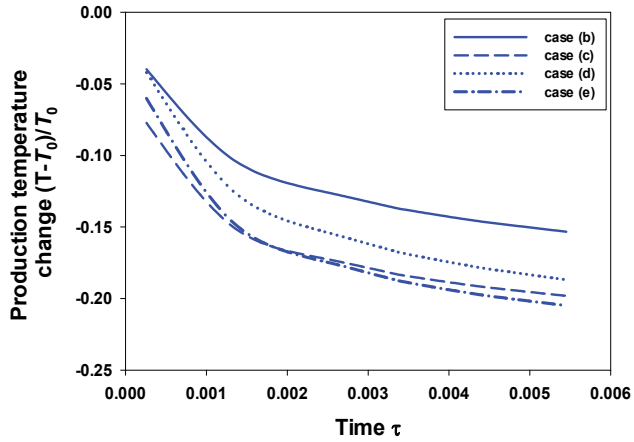

Figure 4. Normalized change in production temperature from cases (b) to (e) under the same total injection and production rates Q=0.06m^3/s. The average value of the temperatures at all the points on the small circle around the production well is chosen as the production temperature.

Figure 5 shows the output temperature change for different geometrical sizes and injection rates are plotted for case (c) (Figure 2). $X=2\lambda_r L/(\rho_w c_w Q)$ is an important parameter, where L is the well separation and Q is the total flow rate. When the value of χ is kept constant, the fluid temperature at the output will evolve equivalently.

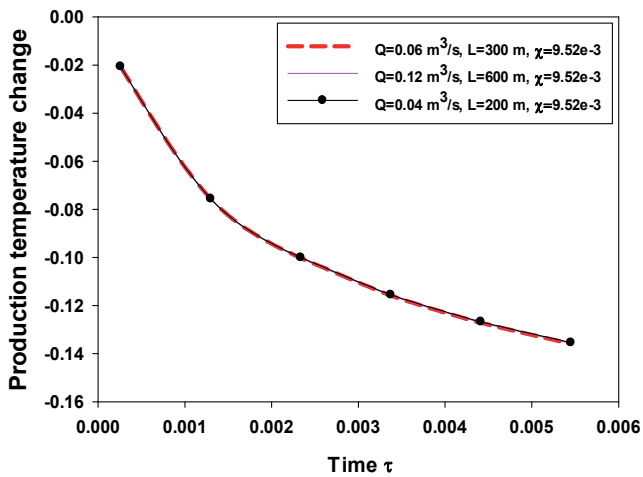

Figure 5. Normalized temperature change for the production wells while keeping the controlling parameter set to χ=4.76e-3.

Figure 6 presents isothermal lines at 5 years and 21 years for case (d). We can see clearly the contours at the same temperature propagating away from the injection well with time. As there are associated with the singularity in flow velocity at the production well whereby the

temperature there cannot be obtained analytically and is calculated approximately. In order to make this approximation, a small circle around the well is chosen and calculations are not carried out inside this region. The number of the streamlines used in the computation which flows into this well can be counted and the temperature averaged over all used streamlines can also be computed and chosen as the production well temperature. In Figure 6, because of the symmetry, each production well accepts flow from each injection well. However, which injection well the influx at a specific part of a well comes from depends on the angle at which it faces toward an injection well. Therefore, the temperature fields around the production wells are very complicated and require an averaging method.

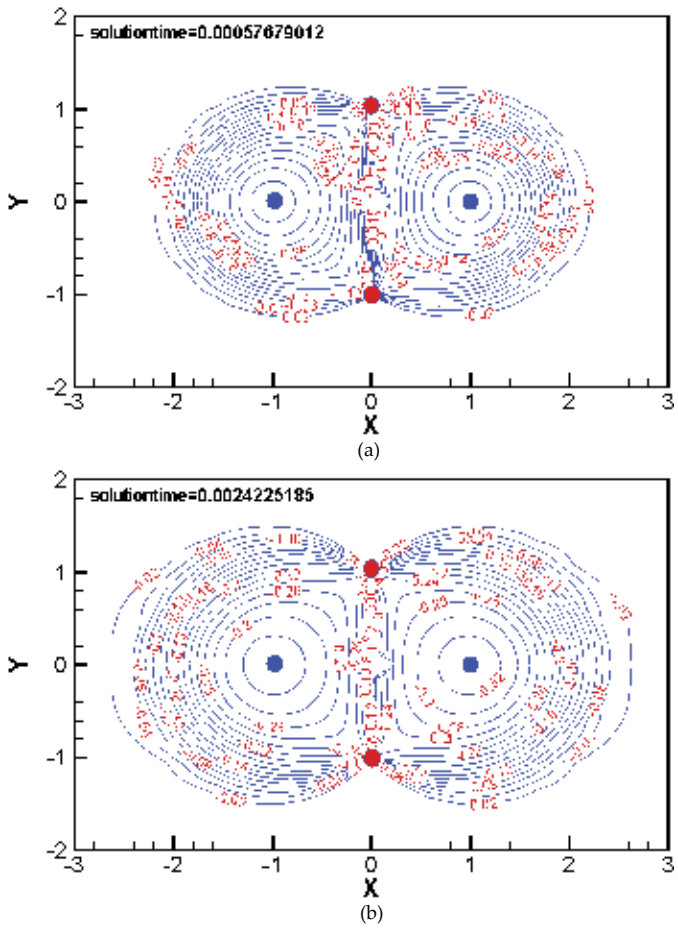

Figure 6. Isothermal lines of the normalized temperature change at (a) time=5 years (τ=5.77e-4) and (b) time=21 years (τ=2.42e-3) for case (d). Blue circle denotes injection well and red circle denotes production well.

The streamline profiles and production temperature in Figure 7 are for case (f) (Figure 2) where there are four injection wells and five production wells. The total flow rate is also 0.06m^3/s.

http://dx.doi.org/10.5772/56373

Due to the symmetry, the temperature distributions of injection wells 1, 2, 3 and 4 are similar, as are the temperature fields between wells 5 and 9 and between production wells 6 and 8. Figure 7(b) shows the trend in the average normalized temperature variations in time. On the other hand, we can find that the contribution to the normalized temperature change of a particular well may strongly depend on the well arrangement, as well as on the imposed outflow rate at the production well, based on the temperature changes in Figure 7(b). For instance, all the four injection wells contribute to outflux at well 7 (the middle one in case (f)), but its output temperature undergoes the biggest decrease as show Figure 7(b). This is attributed to a larger flow rate in this central region, defined by four injection wells. The heat exchange from the rock to the fluid is not sufficient to heat the fluid to the same degree as

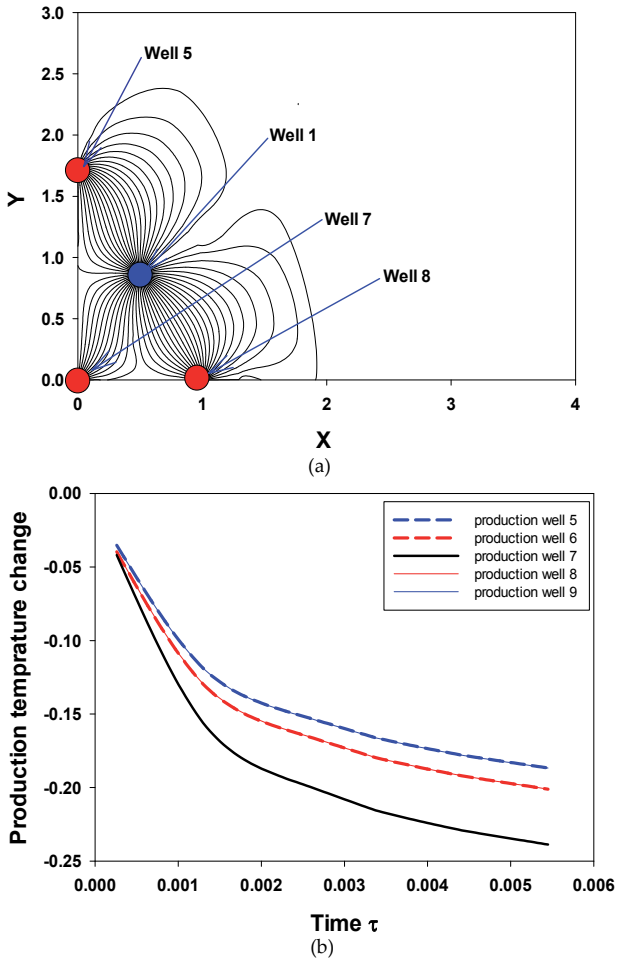

Figure 7. (a) Streamlines profiles and (b) normalized production temperature change in case (6) when $Q_{in}=Q/4=0.015$ m^3/s and $Q_{out}=Q/5=0.012$ m^3/s. Plot (a) shows a quarter of the whole streamline profiles which are symmetric across the plot axes.

occurs at other production wells. In the end, this will affect the output temperature at well 7. It must be remembered that all production wells are assumed to have the same outflux. Therefore, some fluid heated in the central region is forced to move outward and eventually reaches the outer production wells. The direct result of the heated fluid movement is to increase the output temperature at the outer production wells.

7. Conclusions

By using the Laplace transformation, the analytical form of the solutions in the Laplace space and thus, by inversion, in the time domain are obtained. The approach provides an efficient and accurate way to calculate the rock and fluid temperatures. Through several preliminary case studies, some brief conclusions are obtained:

1. Even for a multi-well geothermal reservoir, we obtain analytical or semi-analytical solutions that provide an efficient and accurate way for predicting the rock and fluid temperature;
2. The flow rates and the relative locations of the wells determine the flow path of the fluid. The injection rate also determines the thermal behavoir of the fluid and the parammeter $X=2\lambda_r L/(\rho_w c_w Q)$ reflects the rate of heat extracted by the cold injection fluid.
3. The efficiency of heat extraction from the EGS reservoir studied here depends on the layout and spacing of the injection and production wells. In fact, our model showed some contrasting cases where fewer wells outperformed a greater number of wells. Ongoing work will be aimed at finding optimal well layouts and flow rates.

Author details

Bisheng Wu[1*], Xi Zhang[1], Andrew Bunger[1,2] and Rob Jeffrey[1]

*Address all correspondence to: bisheng.wu@csiro.au

1 CSIRO Earth Science and Resource Engineering, Melbourne, Australia

2 Department of Civil and Environmental Engineering, University of Pittsburgh, Pittsburgh, PA, USA

References

[1] Lauwerier, H. A. The transport of heat in an oil layer caused by the injection of hot fluid, Applied Scientific Research, (1955). , 5, 145-150.

[2] Bödvarsson, G. S. On the Temperature of Water Flowing through Fractures. Journal of Geophysical Research, (1969). ,74(8),1987-1992.

[3] Gringarten, A. C. Theory of heat extraction from fractured hot dry rock, Journal of Geophysical Research, (1975).

[4] Zhang, X, Jeffrey, R. G, & Wu, B. Two basic problems for hot dry rock reservoir stimulation and production. Australian Geothermal Conference (2009). Brisbane, QLD, Australia, Nov., 2009., 11-13.

[5] Mossop, A. Seismicity, subsidence and strain at the Geysers geothermal field. PhD. Dissertation, Stanford University, (2001).

[6] Ghassemi, A, Tarasovs, S, & Cheng, A. H. D. An integral equation solution for three-dimensional heat extraction from planar fracture in hot dry rock. International Journal for Numerical and Analytical Methods in Geomechanics, (2003). , 27, 989-1004.

[7] Kolditz, O. Modelling flow and heat transfer in fractured rocks: conceptual model of a 3-D deterministic fracture network. Geothermics, (1995). , 24(3),421-437.

[8] Gringarten, A. C, & Ramey, H. J. The use of source and Green's functions in solving unsteady-flow problems in reservoirs. Society of Petroleum Engineers Journal, (1973). , 285-296.

[9] DaCosta, J.A, & Bennett R.R., The pattern of flow in the vicinity of a recharging and discharging pair of wells in an aquifer having areal parallel flow. International Association of Scientific Hydrology, (1960). , 52, 524-536.

[10] Grove, D. B, Beetem, W. A, & Sower, F. B. Fluid travel time between a recharging and discharging well pair in an aquifer having a uniform regional flow field, Water Resources Research,(1970)., 6(5), 1404-1410.

[11] Muskat, M. The flow of homogeneous fluids through porous media. MicGraw-Hill Book Company, Inc., (1937).

[12] Gringarten, A. C, & Sauty, J. P. A Theoretical Study of Heat Extraction from aquifers with uniform regional flow. J. Geophys. Res., (1975)., 80(35),4956-4962.

[13] Rodemann, H. Analytical model calculations on heat exchange in a fracture. Urach Geothermal Project, Haenel R. (ed.), Stuttgart, (1982).

[14] Schulz, R. Analytical model calculations for heat exchange in a confined aquifer. J. Geophys. Int., (1997). , 61, 12-20.

[15] Heuer, N, Kopper, T, & Windelberg, D. Mathematical model of a Hot Dry Rock system. Geophys. J. Int., (1991). , 105, 659-664.

[16] Ogino, F, Yamamura, M, & Fukuda, T. Heat transfer from hot dry rock to water flowing through a circular fracture. Geothermics, (1999). , 28, 21-44.

[17] Harlow, F. H, & Pracht, W. Theoretical study of geothermal energy extraction. Journal of Geophysical Research, (1972).,77(35), 7038-7048.

[18] Cheng, A. H. D, Ghassemi, A, & Detournay, E. Integral equation solution of heat extraction from a fracture in hot dry rock. International Journal for Numerical and Analytical Method in Geomechanics, (2001)., 25, 1327.

[19] Ghassemi, A, Tarasovs, S, & Cheng, A. H. D. Integral equation solution of heat extraction-induced thermal stress in enhanced geothermal reservoirs, International Journal for numerical and Analytical Methods in Geomechanics, (2005). , 29, 829-844.

Chapter 48

Thermal Effects on Shear Fracturing and Injectivity During CO_2 Storage

Somayeh Goodarzi, Antonin Settari,
Mark Zoback and David W. Keith

Additional information is available at the end of the chapter

http://dx.doi.org/10.5772/56311

Abstract

With almost two hundred coal burning power plants in Ohio River valley, this region is considered important for evaluation of CO_2 storage potential. In a CO_2 storage project, the temperature of the injected CO_2 is usually considerably lower than the formation temperature. The heat transfer between the injected fluid and rock has to be investigated in order to test the viability of the target formation to act as an effective storage unit and to optimize the storage process. In our previous work we have introduced the controversial idea of injecting CO_2 for storage at fracturing conditions in order to improve injectivity and economics. Here we examine the thermal aspects of such process in a setting typical for Ohio River Valley target formation.

A coupled flow, geomechanical and heat transfer model for the potential injection zone and surrounding formations has been developed. All the modeling focuses on a single well performance and considers induced fracturing for both isothermal and thermal injection conditions. The induced thermal effects of CO_2 injection on stresses, and fracture pressure, and propagation are investigated. Possibility of shear failure in the caprock resulting from heat transfer between reservoir and the overburden layers is also examined.

In the thermal case, the total minimum stress at the wellbore decreases with time and falls below the injection pressure quite early during injection. Therefore, fracturing occurs at considerably lower pressure, when thermal effects are present. The coupled thermal and dynamic fracture model shows that these effects could increase the speed of fracture propagation in the storage layer depending on the injection rate. These phenomena are dependent primarily on the difference between the injection and reservoir temperature.

Our results show that shortly after injection, the induced expansion in caprock lead to slight increase of total stresses (poroelasticity) which will reduce the chance of shear failure. However as soon as total minimum stress in the caprock decreases due to thermal diffusion between the reservoir and caprock, thermoelasticity dominates and the chance of shear failure increases in the caprock.

Incorporation of thermal effects in modeling of CO_2 injection is significant for understanding the dynamics of induced fracturing in storage operations. Our work shows that the injection capacity with cold CO_2 injection could be significantly lower than expected, and it may be impractical to avoid induced fracture development. In risk assessment studies inclusion of the thermal effects will help prevent the unexpected leakage in storage projects.

1. Introduction

Past storage pilot projects and enhanced oil recovery efforts have shown that, geologic sequestration of CO_2 is a technically viable means of reducing anthropogenic emission of CO_2 from accumulating in the atmosphere [1,2,3]. Security of storage is one of the most important concerns with the long term injection of CO_2 in underground formations. Injection of CO_2 induces stress and pore pressure changes which could eventually lead to the formation or reactivation of fracture networks and/or shear failure which could potentially provide pathways for CO_2 leakage through previously impermeable rocks [4]. Therefore geomechanical modeling plays a very important role in risk assessment of geological storage of CO_2.

In order to determine whether the induced stress changes compromises the ability of the formation to act as an effective storage unit, a geomechanical assessment of the formation integrity must be carried out. In our previous work, we have studied the dynamic propagation of fracture in the Rose Run sandstone reservoir in Ohio River valley under isothermal [5] and thermal condition [6] for injection above fracture pressure. In this paper, the thermal effect of injection on the possibility of tensile and shear failure in the reservoir and caprock are studied for injection below fracture pressure. This study utilized a fully coupled reservoir flow and geomechanical model which allows accounting for poroelastic and thermoelastic effects and can model static and/or dynamic fractures.

To examine the possibility of shear failure in the caprock, Mohr-Coloumb Criteria was used.

2. Construction of the flow, thermal and geomechanical model

A coupled flow, thermal, and geomechanical model has been developed in order to study the thermo-elastic and poro-elastic response of the injection and surrounding layer to increasing of pressure and reduction of temperature after CO_2 injection. Ohio River valley is located in a relatively stable, intraplate tectonic setting and the regional stress state is in strike slip faulting regime with the maximum stress oriented northeast to east-northeast [7].

http://dx.doi.org/10.5772/56311

This study used the fluid and rock mechanical properties provided by Lucier et al. [8]. The stratigraphic sequence of the geological layers in the study area and the relative location of the potential injection layer, Rose Run Sandstone (RRS) at the Mountaineer site is shown in Figure 1. RRS has an average thickness of 30 m and is extended from 2355-2385 m. The direction of maximum and minimum horizontal stresses is reported to be in N47E(±13) and N43W (±13) respectively [8]. All the models in this study are aligned along these directions, in order to avoid having initial non-zero value of shear stresses in principal stress directions.

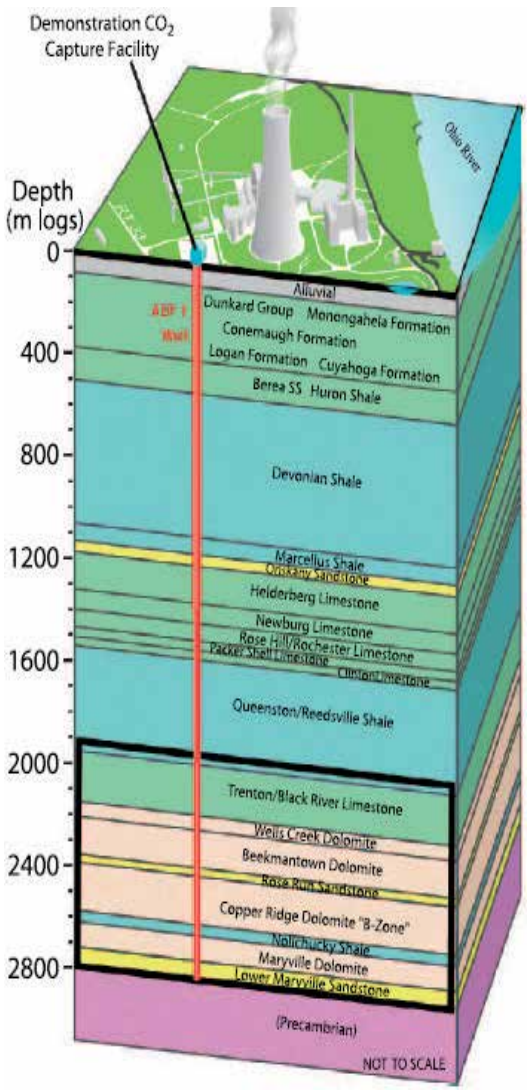

Figure 1. Generalized stratigraphy of the study area at the Mountaineer site. The well location and the general stratigraphy intersected by well is illustrated in the picture. The black box shows the boundaries of the area of previous work by Lucier et al., [8], Modified from [9]

The developed element of symmetry model that covers 8000x8000x2575 m of study area, has 50x50x9 grid block in x, y and z directions respectively. The injection well is located at the top left corner of this model. RRS was gridded into three layers with 5, 10 and 15 m thickness. The adjacent Beekmanton Caprock was refined into 3 layers (10, 50 and 126 m) to capture and predict the potential growth of fracture through this layer (and the resulting possibility for CO_2 leakage). The horizontal and vertical permeability of the caprock layers in the model are given as 2E-10 and 1E-10 md resepectively. Average properties of 5%, 20 md and 10 md for porosity, horizontal and vertical permeability were given to the injection layer. These values are the probability averages of the given property distributions for Rose Run sandstone formation [8]. The initial pressure and temperature of the RRS is 26000 kPa and 63.1 C. The fluid flow is modeled by two-phase flow with dissolution of CO_2 in water. Van Genutchen function with an irreducible gas saturation of 0.05, an irreducible liquid saturation of 0.2 and an exponent of 0.457 was used to generate relative permeability data [10].

The mechanical properties and initial stress profile is required to be added to the geomechanical model and coupled with the flow model in order to be able to study the mutual effect of pressure and stresses and the resulting effect on fracture propagation and injectivity. The mechanical properties for this model are listed in Table 1. The listed value with the exception of grain Modulus are all extracted directly from Lucier et al. paper [8]. Grain modulus was back- calculated from the given Biot constants and Young's Modulus. The Biot constant α is important for computing the effects of pressure changes on stress. At the Mountaineer site, Lucier et al. estimated α to be very low - in the range of 0.03 to 0.2. In this analysis, a mean value of 0.11 was used to calculate the poroelastic effects. The formation rock density is assumed to be 2500 kg/m^3 [8].

Layer-top depth (m)	Thickness (m)	Young's Modulus (kpa)	Poisson's Ratio	Grain Modulus (Kpa)
Shale-Surface	1911	6.00E+07	0.29	5.25E+07
Limestone-1911	253	7.05E+07	0.3	6.61E+07
Dolomite-2164	186	8.96E+07	0.28	7.51E+07
Rose Run Sandstone-2350	30	8.73E+07	0.25	6.53E+07
Dolomite-2380	195	9.47E+07	0.28	8.05E+07

Table 1. Rock Mechanical properties of the coupled model

The initial pressure, horizontal and vertical stress profile for different depths in Ohio River Valley is shown in Figure 2. It is important to note that the horizontal stresses are lower in RRS (the injection layer) than in the surrounding layers. This is a common behavior due to generally having larger Poisson's ratio for the surrounding layers than the reservoir. In many situations the stresses in caprock (low permeability rock) are larger than in the reservoir (permeable formations), because of differences in Poisson's ratio, material properties, stress history and other factors. This is well documented in hydraulic fracturing literature and is the primary

http://dx.doi.org/10.5772/56311

mechanism for containment of fractures to the target zone. This initial stress contrast is very critical when considering fracture propagation in the reservoir layer for enhancing injectivity while avoiding the risk of fracture growth through upper caprock layers. As mentioned before, since the temperature of injected CO_2 (at approximately 30 deg C) is smaller than the formation temperature (at 60 deg C), thermal effects of injection on fluid flow and geomechanics must be included in the model. This coupling is achieved by solving the energy balance equation within the fluid flow model, and including the thermoelasticity term in the geomechanical model (included in the constitutive model of the rock).

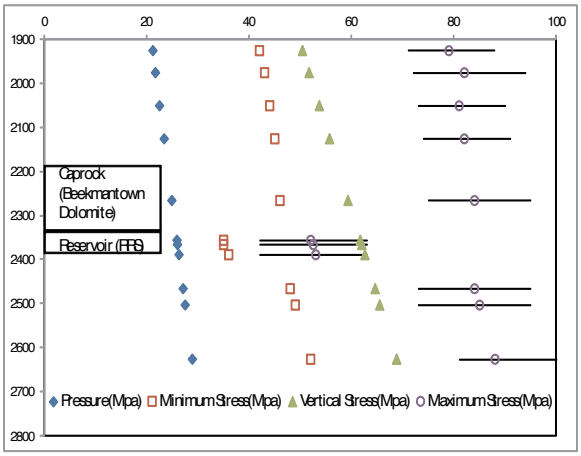

Figure 2. Initial pressure, horizontal and vertical stress profile in Ohio River Valley [8]

The average thermal properties for the rock, as well as injected and in-place fluids used for this study are listed in Table 2 [8,11-14].

	Rock	Water	CO_2
Volumetric Thermal Expansion Coefficient (1/deg K)	5.4E-6	2.1E-4	3.003E-3
Heat Capacity(Kj/Kg deg K)	0.9	4.182	0.84
Thermal Conductivity(W/ m deg K)	2.34	0.65	0.084

Table 2. Thermal properties of fluids and rock

The boundary condition for the fluid flow model is that there is no flow across the boundary of the model. The constraints for the geomechanical model are as follows. The right and left sides of the model are fixed in the x-direction so there would be no displacement in the x-direction. The front and back sides of the model are fixed in Y direction. The bottom side of the model is fixed in vertical direction and the top of the model is free to move in all directions. Stresses were initialized according to data in Fig. 2. All injections are done through a single vertical well with constant injection rate.

3. Thermal fracturing in the reservoir below isothermal fracture pressure

Thermal effects of CO_2 injection is expected to affect the magnitude of displacements, pressure, stresses, and the possibility of shear and tensile failure in the reservoir and caprock. Injecting fluid with temperature lower than reservoir rock temperature will cause reduction of stresses in the injection layer and once the temperature front has reached a relatively large area around the wellbore, this reduction in stresses will result in negative volumetric strains that can propagate to the surface. Therefore the surface displacement for the thermal model would be smaller than that of isothermal model [6].

One of the most important effects of injecting a fluid with a lower than reservoir temperature is the reduction of fracture pressure. Cooling of the formation rock during injection of cold CO_2 through thermal conduction and convection lowers the total stresses in the reservoir and possibly caprock layer. This results in reduction of fracture pressure and the pressure differential available for injection, and therefore injectivity. In the case of injection at fracturing conditions, the fracture propagation pressure will decrease and, if the same injection rate is used, this will accelerate fracture propagation.

In order to examine thermal effects of injection on the possibility of reaching tensile failure in the reservoir, the variation of total stress and pressure needs to be studied. In order to do that, the coupled geomechanical, flow and thermal simulation has been carried out with two different injection temperatures. The injection of CO_2 for these models is through a single vertical well with constant rate of 3.4E4 m3/day such that the bottomhole pressure will remain below fracture pressure for the isothermal model during 30 years of injection. It should be noted that fracturing was not allowed in these models. Thermal model in this study refers to injection temperature (30 C) being lower than the reservoir temperature (60 C),while in the isothermal model, it is equal to reservoir's temperature. Figure 3 shows the modeling results for pressure, and total minimum stress for well block in the reservoir during 30 years of injection for the thermal and isothermal model. As it is seen in Figure 3, the total stress falls below the bottomhole pressure (fracture pressure) for the thermal model in the reservoir at quite early injection times which means that minimum effective stress will reduce beyond zero. Therefore, although CO_2 is injected below the original fracture pressure, fracture would initiate in the reservoir for the thermal case. Since fracturing is not allowed in these models, the stress magnitudes after the onset of fracturing are not valid. If propagation was allowed, minimum total stress would reduce to slightly below bottomhole pressure such that the effective stress on the fracture wall would remain close to zero.

In order to study the thermal effects of injection on the propagation of the induced fracture, for the next set of model cases we allowed fracture propagation in all layers. To model the potential fracture propagation, a transmissibility multiplier technique is incorporated in the model, which essentially accounts for the fluid flow transmissibility through the fracture by a transmissibility multiplier function, specified as a table. The multiplier is calculated from an estimated fracture opening of a 2-D Griffith crack [15] based on the mechanical properties of the injection zone and an estimate of the fracture height [5]. This function can be incorporated

http://dx.doi.org/10.5772/56311

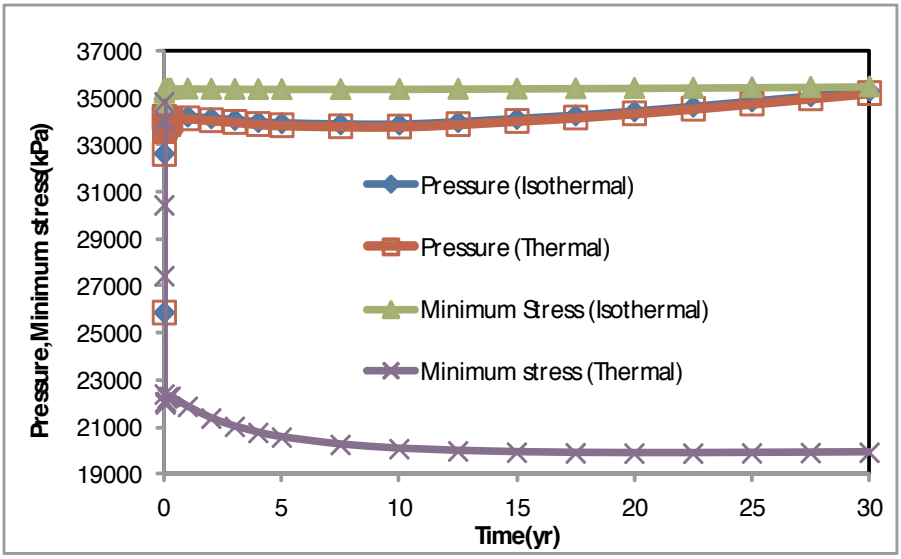

Figure 3. Pressure, minimum stress, and stress level for the thermal and isothermal model for the well block in the reservoir's top layer

in the model both as a function of pressure or effective minimum stress. The actual fracture geometry can be calculated by the coupled model.

Figure 4 shows the bottomhole pressure and fracture length for the reservoir's top layer for the thermal and isothermal model. As expected, since the bottomhole pressure remains below the fracture pressure for the isothermal model, there is no fracture initiation in the reservoir for the isothermal model. However since minimum effective stress reduces beyond zero in the thermal model (thermoelastic effects), fracture initiates and propagates through reservoir to a half length of 250 m. The bottomhole pressure in the thermal model is now significantly different. For the thermal model, it increases to fracture initiation pressure (equal to the thermally reduced minimum total stress) and then remains almost constant for the injection period. However for the isothermal model, the pressure history is the same as in Fig. 4.

Figure 5 shows the fracture length, pressure and temperature profile for the well block in the reservoir's top and bottom layer. The results show that under thermal conditions, fracture propagates to a larger extent in the lower reservoir layers than the top ones. As seen in the Figure, the pressures in the reservoir's top and bottom layers are very close. However, the temperature in the bottom of the reservoir is significantly lower than in the top. This results in higher reduction of minimum total stress and lower fracture pressure for the reservoir's bottom layer. This effect can also be clearly seen in Figure 6 which shows the permeability multiplier, temperature and pressure profile in fracture plane near the wellbore (zoomed to 300 m) across reservoir layers. As seen the temperature reduction and permeability multipliers are higher in the bottom layer.

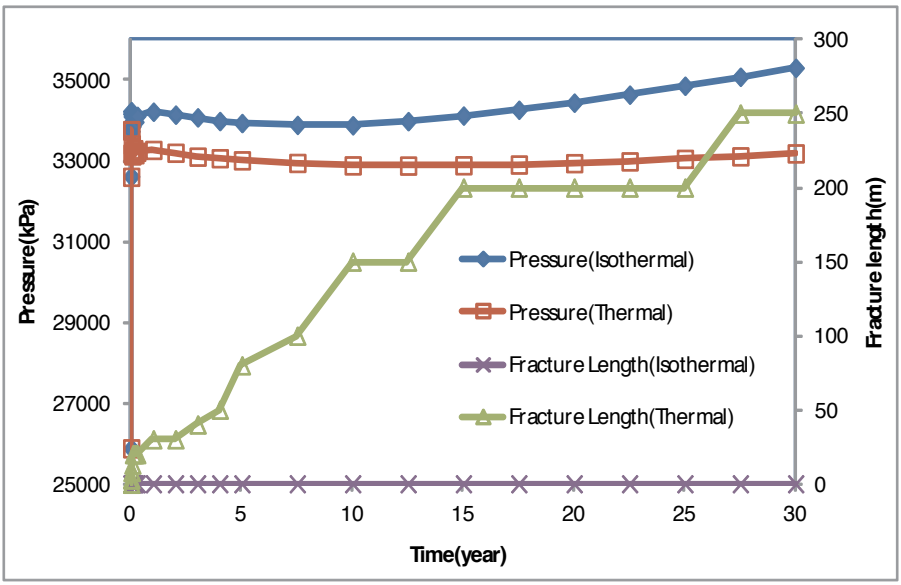

Figure 4. Bottomhole pressure and fracture length for the reservoir's top layer for the thermal and isothermal model

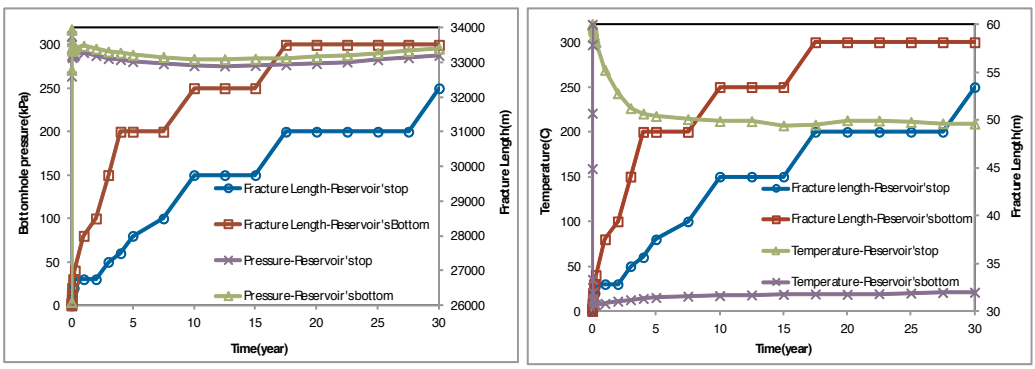

Figure 5. Fracture length and pressure profile (left), fracture length and temperature profile (right) for the reservoir's top and bottom layer

4. Thermally induced shear failure in the caprock

The thermally induced reduction of minimum stress in the caprock could lead to tensile or shear failure of the formation rock which could cause tensile fracture propagation through these layers or hydraulic communication through shear fractures. If there is no stress contrast between the caprock and reservoir, reaching tensile failure in the caprock is possible for injection above fracture pressure [16]. In this study, since the horizontal stresses in the caprock

http://dx.doi.org/10.5772/56311

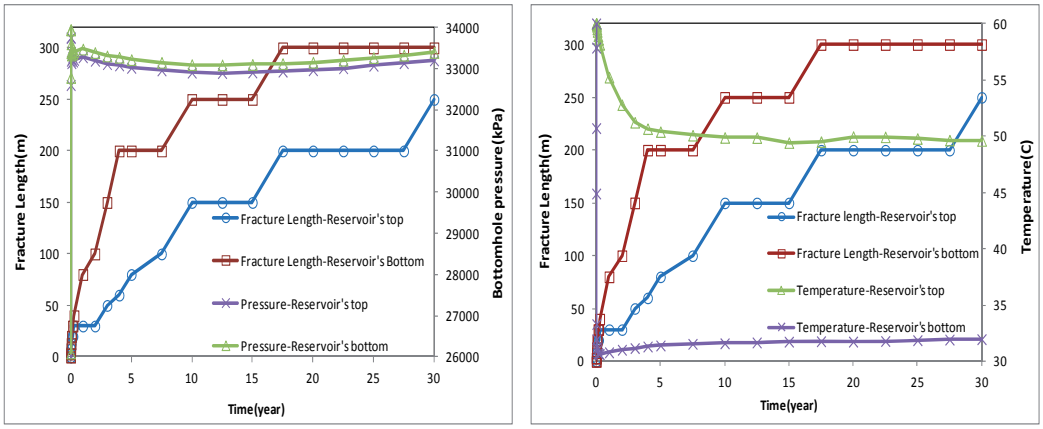

Figure 6. Permeability multiplier(top), Temperature(middle), Pressure distribution (bottom) after 30 years of injection for the reservoir layers

are significantly larger than in the reservoir, tensile fracturing in the caprock is of low likelihood. However given the large initial deviatoric stress in the caprock, the chance of reaching shear failure due to thermally induced stresses is high. In order to evaluate the possibility of reaching shear failure, we have used the Mohr-Coloumb criteria and studied the variation of "Stress level", l_σ in the caprock during injection. Stress level is defined as the ratio of deviatoric stress at the current condition to the deviatoric stress at failure condition:

$$l_\sigma = \frac{\sigma'_{dev}}{(\sigma'_{dev})_f} = \frac{(\sigma'_{\max} - \sigma'_{\min})}{(\sigma'_{\max} - \sigma'_{\min})_f} \leq 1 \tag{1}$$

Where, l_σ is the stress level, σ_{dev}' is the deviatoric stress at the current condition, $(\sigma_{dev}')_f$ is the deviatoric stress at failure, σ_{max}' is the maximum principal stress, σ_{min}' is the minimum principal stress (all stresses are effective). The deviatoric stress at failure is a function of cohesion c and friction angle ϕ and is defined as:

$$(\sigma'_{dev})_f = \frac{2cCos\varphi + 2\sigma'_3 Sin\varphi}{(1 - Sin\varphi)} \tag{2}$$

When the stress level is less than 1, the shear stress has not exceeded the shear strength of the rock and when it is larger than 1, the shear strength of the rock has been reached in a plane which is aligned in the direction found from the Mohr stress circle. The nominal rock cohesion for the caprock (Beekmantown Dolomite) is 9000 kPa [17]. Linear elastic constitutive model was used to describe the mechanical behavior of the formation rock. In order to examine the thermal effects on the stress state in the caprock, the variation of total stress, pressure and stress level needs to be studied.

Figure 7 shows the pressure, stress and stress level evolution for the well block in the caprock for the thermal and isothermal model. In the isothermal model, due to the low permeability of caprock, pressure increase in caprock is negligible compared to the reservoir, and stress level remains low. However as seen in Figure 8 (which shows the stress, pressure and temperature variation of the well block in the caprock during the first 10 years of injection), the first caprock layer is quickly pressurized, and later its temperature also decreases due to heat transfer. Stress level is rapidly increasing with time due to thermally induced decrease of total stresses. Therefore the chance of failing the rock in shear for the caprock is higher for the thermal model compared to isothermal model.

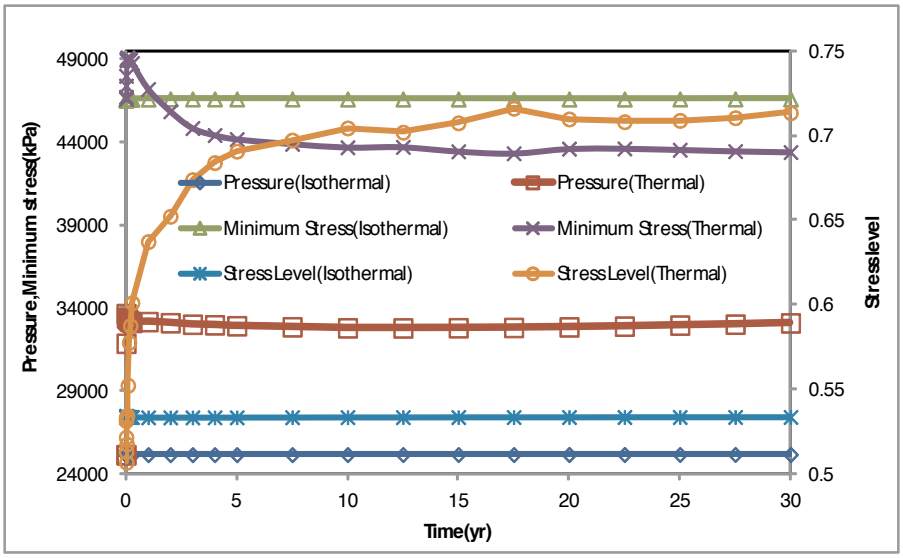

Figure 7. pressure, minimum total stress, and stress level for the thermal and isothermal model for the well block in the immediate caprock layer

The changes in the stress level correspond to the movement of the Mohr circle with time. Shortly after injection (0.1 days), the stress circle moves to the right due to the slight growth of total stresses. This is a poroelastic effect which is a result of early time-increase of the block pressure in the caprock. This can be clearly seen in Figure 8. However, as soon as the block temperature is lowered due to thermal diffusion (conduction), thermoelasticity dominates and total minimum stress reduces (Figure 8) and stress circle moves to the left toward the failure cone.

The mechanism shown here is somewhat exaggerated because of the upstream numerical treatment of the fracture transmissibility between the blocks, but the relative comparison is valid. Accurate modeling would require very fine vertical grid at the reservoir-caprock interface or the development of more sophisticated numerical technique. These aspects are being currently studied.

http://dx.doi.org/10.5772/56311

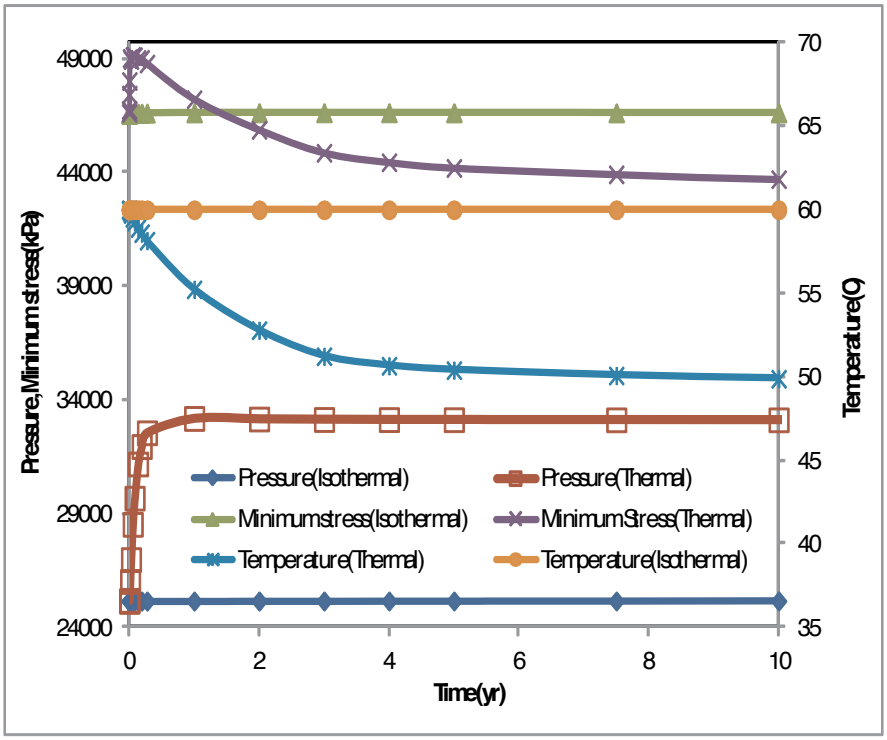

Figure 8. Minimum total stress, pressure and temperature variation for the well block in the caprock during the first 10 years of CO_2 injection

5. Conclusions

This paper studies thermo-elastic and poro-elastic response of the reservoir and caprock to increasing of pressure and reduction of temperature after CO_2 injection and the resulting consequences for the possibility of reaching tensile or shear failure both for the injection below and above reservoir's fracture pressure.

When injecting a fluid below isothermal fracture pressure with a temperature below reservoir temperature, the fracture pressure will decrease and minimum effective stress in the reservoir may reduce below zero for the fracturing to initiate and propagate in the reservoir.

Our results show that the reduction of the minimum effective stress due to thermal effects is larger for the lower reservoir layers. Therefore in case of dynamic fracture propagation, fracture growth would be larger for the lower reservoir layers due to larger cooling for these layers.

Thermal effects of injection with cold CO_2 may also create the possibility of shear failure in the caprock.

Author details

Somayeh Goodarzi[1*], Antonin Settari[1], Mark Zoback[2] and David W. Keith[3]

*Address all correspondence to: sgoodarz@ucalgary.ca

1 University of Calgary, Calgary, Canada

2 Stanford University, USA

3 Harvard University, USA

References

[1] Solomon, S. Carbon Dioxide Storage: Geological Security and Environmental Issues-Case Study on the Sleipner Gas Field in Norway. The Bellona Foundation. (2006).

[2] Preston, C, Monea, M, et al. IEA GHG Weyburn CO_2 Monitoring and Storage Project, Fuel Processing Technology. (2005). , 86, 1547-1568.

[3] Wright, L. W. (2007). The In Salah Gas CO2 Storage Project. International Petroleum Technology Conference

[4] QuintessaNational Institute of Advanced Industrial Science and Technology of Japan, Quintessa Japan, JGC Corporation, Mizuho Information and Research Institute. (2007). Building Confidence in Geological Storage of Carbon Dioxide. Ministry of Economy, Trade and Industry (METI), IEA Greenhouse Gas R&D Programme (IEA GHG).

[5] Goodarzi, S, Settari, A, Zoback, M, & Keith, D. A Coupled Geomechanical Reservoir Simulation analysis of CO_2 storage in a Saline Aquifer in the Ohio River Valley. (2011). Environmental Geosciences journal. American Association of Petroleum Geologists. , 18(3), 1-20.

[6] Goodarzi, S, Settari, A, Zoback, M, & Keith, D. Thermal Aspects of Geomechanics and Induced Fracturing in CO_2 Injection With Application to CO_2 Sequestration in Ohio River Valley. SPE-PP, SPE International Conference on CO_2 Capture, Storage, and Utilization held in New Orleans, Louisiana, USA, 10-12 November (2010). , 139706.

[7] Zoback, M. D, & Zoback, M. L. State of stress and intraplate earthquakes in the central and eastern United States. Science, (1981). , 213, 96-109.

[8] Lucier, A, Zoback, M, Gupta, N, & Ramakrishnan, T. S. (2006). Geomechanical aspects of CO_2 sequestration in a deep saline reservoir in the Ohio River Valley region. Environmental Geosciences 13 (2), 85-103.

http://dx.doi.org/10.5772/56311

[9] Gupta, N. (2008). The Ohio river valley CO_2 storage project, Final Technical Report, prepared for US Department of Energy-National Energy Technology Laboratory

[10] Van Genuchten, M. T. equation for predicting the hydraulic conductivity of unsaturated soils: Soil Science Society of America Journal, , 44, 892-898.

[11] Collieu, A. McB., Powney, D. J., Girifalco, L. A. et al., (1975). The Mechanical and Thermal Properties of Materials and Statistical Physics of Materials. Phys. Today 28, 51

[12] Fjaer, E, Holt, R. M, Horsrud, P, et al. (2008). Petroleum Related Rock Mechanics. 441. Elsevier.

[13] Guildner, L. A. (1958). The thermal conductivity of carbon dioxide in the region of the critical point, Proceedings of the National Academy of Sciences of the United States of America, , 44(11), 1149-1153.

[14] Yaws, C. (2008). Thermophysical properties of chemicals and hydrocarbons. 793. William Andrew Publishing

[15] Sneddon, I. N, & Lowengrub, M. Crack Problems in the Classical Theory of Elasticity, John Wiley & Sons Inc., New York, (1969). , 19.

[16] Goodarzi, S, Settari, A, & Keith, D. (2012). Geomechanical modeling for CO2 storage in Nisku aquifer in Wabamun lake area in Canada. International Journal of Greenhouse Gas Control , 10, 113-122.

[17] Maurer, W. C. (1965). Bit-Tooth Penetration under Simulated Borehole Conditions, Petroleum Transactions

Scale Model Simulation of Hydraulic Fracturing for EGS Reservoir Creation Using a Heated True-Triaxial Apparatus

Luke Frash, Marte Gutierrez and Jesse Hampton

Additional information is available at the end of the chapter

http://dx.doi.org/10.5772/56113

Abstract

Geothermal energy technology has successfully provided a means of generating stable base load electricity for many years. However, implementation has been spatially limited to rare high quality traditional resources possessing the combination of a shallow high heat flow anomaly and an aquifer with sufficient permeability and fluid recharge. Enhanced Geothermal Systems (EGS) technology has been proposed as a potential solution to enable additional energy production from the much more common non-traditional resources. To advance this technology development, a heated true triaxial load cell with a high pressure fluid injection system has been developed to simulate an EGS system from stimulation to production. This apparatus is capable of loading a 30x30x30 cm3 rock sample with independent principal stresses up to 13 MPa while simultaneously providing heating up to 180 ºC. Multiple orientated boreholes of 5 to 10 mm diameter may be drilled into the sample while at reservoir conditions. This allows for simulation of borehole damage as well as injector-producer schemes. Dual 70 MPa syringe pumps set to flow rates between 10 nL/min and 60 mL/min injecting into a partially cased borehole allow for fully contained fracturing treatments. A six sensor acoustic emission (AE) array is used for geometric fracture location estimation during intercept borehole drilling operations. Hydraulic pressure sensors and a thermocouple array allow for additional monitoring and data collection as relevant to computer model validation as well as field test comparisons. The results of the scale model hydraulic fracturing tests demonstrate the functionality of the equipment while also providing some novel data on the propagation and flow characteristics of hydraulic fractures. Fully characterized test sample materials used in the scale model tests include generic cement grout, custom high

performance concrete, granite, and acrylic. Fracturing fluids used include water, brine, and Valvoline® DuraBlend® SAE 80W90 oil.

Keywords: Enhanced Geothermal Systems (EGS), true triaxial device, hydraulic fracturing, scale model testing, acoustic emissions

1. Introduction

The potential of Enhanced Geothermal Systems (EGS) is well documented in the MIT led study titled "The Future of Geothermal Energy" [1]. With this technology, unconventional deep Hot Dry Rock (HDR) reservoirs are engineered with drilling and stimulation techniques to create a heat mining system for base load energy production. The methods needed for enabling EGS energy production also have the ability to improve production from traditional geothermal resources which are already being utilized today.

To provide the EGS reservoir stimulation, one of the most promising techniques is hydraulic fracturing. This method utilizes high pressure fluid injection into targeted reservoir intervals to enhance permeability and generate new flow paths through enhancing existing fractures and creating new fractures. With the installation of an injector-producer well scheme, the physical limitations of natural reservoir recharge and stored harvestable fluids may be overcome and a productive reservoir may be the end result. Hydraulic fracturing has been proven effective as a stimulation technique by the oil and gas industry since its first implementation in 1947 [2].

Currently, only a small number of EGS field trials have been performed due to the high economic risk of the procedure and the significant probability of failure. Thus, performing controlled EGS experiments in the laboratory setting may be able to provide some of the crucial data and experience needed for advanced fracture model calibration and full scale testing in the field. This is especially true considering that most hydraulic fracturing design techniques, as developed by the petroleum industry, are more dependent upon historical data than on theoretical analysis [3]. In the case of EGS development, this historical data does not yet exist in sufficient quantities.

To fill the knowledge gap, laboratory scale EGS reservoir testing is being performed at the Colorado School of Mines using a heated true-triaxial apparatus. Some completed test results and observations are presented along with technical information on the equipment and procedures used. Focus is given to series of tests performed on a hydraulically fractured granite sample with a binary injector-producer borehole scheme installed.

2. Equipment design and specifications

The laboratory scale EGS simulation equipment consists of four main subsystems being a heated true-triaxial cell, a high pressure hydraulic injection system, a multi-component data acquisition system, and sample materials and characterization equipment.

http://dx.doi.org/10.5772/56113

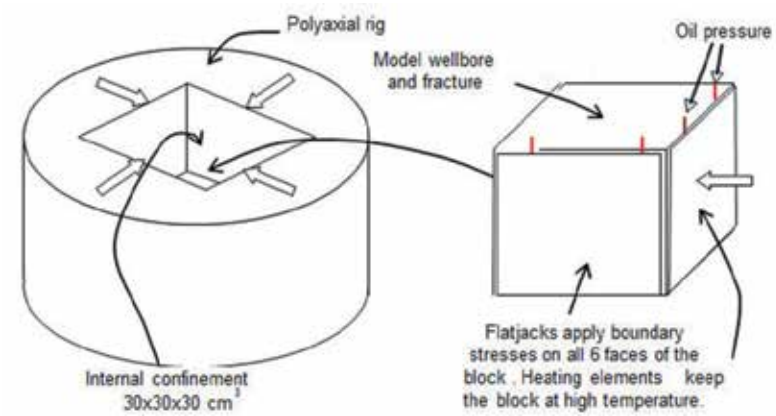

Figure 1. Layout of the true-triaxial cell.

2.1. Heated true triaxial cell

The layout of the heated true triaxial cell is shown in Figure 1. It consists of a cylindrical loading rig made of high strength steel. Flatjacks apply pressures on all six faces of a 30x30x30 cm^3 block rock sample. Freyssinet 350 mm flatjacks, which are pressurized with pumps, allow independent control of the principal stresses of up to 12.5 MPa. The flatjack pressures can be controlled to achieve triaxial stress conditions with different magnitudes of overburden stress σ_v, maximum horizontal stress σ_H, and minimum horizontal stress σ_h. Externally mounted flexible silicone rubber heaters with proportional-integral-derivative (PID) control allow for dual-zone heating with separate set points for the lateral and vertical heating elements. The heating system allows for the simulation of an EGS reservoir with a temperature of up to 180 ºC.

Figure 2 shows pictures of the completed true triaxial cell with and without the drilling rig placed on top of the cell. An orientated rotary-hammer drill press is used to drill boreholes into the sample at user selected positions and angles while the sample is under stresses and temperature. This procedure allows for strategic borehole installations that are specific to the test and the particular stimulated fracturing plane. Borehole damage is replicated by using percussive drilling into the loaded sample instead of the more common cast-in-place pre-drilled borehole methods [4-7]. The borehole is typically drilled with one upper cased segment having a maximum outside diameter of 10 mm and a second uncased fracturing interval having a typical diameter of 5.6 mm. These dimensions were selected to be as small as possible to allow for the most effective EGS reservoir simulation within the confines of the 30x30x30 cm^3 cubical sample blocks.

2.2. High pressure hydraulic injection system

A programmable hydraulic injection system is used for both hydraulic fracture stimulation and post-fracture flow analysis. Precision high pressure flow is provided by a dual 65DM Teledyne Isco syringe pump system, a series of pneumatic-hydraulic automated valves, and a custom pump control program developed with LabVIEW. This system is capable of providing pressures up to 70 MPa and precise controlled flow rates between 10 nL/min and 60

Figure 2. Pictures of the true triaxial cell. Left: without the drilling rig, Right: with the lid and drilling rig.

mL/min with a flow stability of ±0.3% from the set point. A diagram of the hydraulic system is provided in Figure 3.

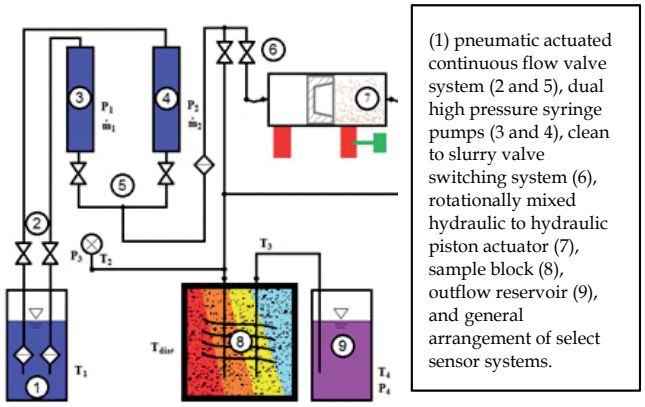

Figure 3. Diagram for the hydraulic fracturing system

Some of the programmable capabilities of the system include: (1) Stepwise continuous constant flow or pressure, (2) Controlled switching between clean and slurry fluid injection, and (3) Conditionally dependent operation with real time external data referencing capability. To seal the injection tubing into the borehole, threaded 316 SS tubing was grouted into a 10 mm outside diameter borehole using Loctite® Rapid Mix 5-Minute epoxy. The epoxy grout was delivered downhole using water-softened 00-size gelatin capsules to avoid the potential of bonding the casing to the true-triaxial cell's top lid. After reaching a 24 hr cure, an uncased 5.6 mm diameter interval was drilled through the bottom of the casing and into the sample. Figure 4 shows a diagram of the borehole sealing method.

http://dx.doi.org/10.5772/56113

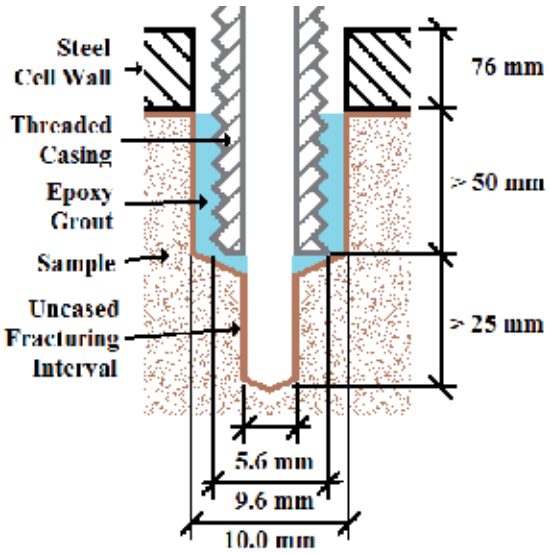

Figure 4. Borehole sealing method applied with typical dimensions.

2.3. Multi-component data acquisition system

To monitor and control the equipment and system processes a multi-channel multi-function National Instruments CompactDAQ was used with 16 strain gage channels, 16 CJC thermocouple channels, 8 voltage channels, 8 current channels, and 4 multi-function channels. The attached sensors included 2 Omega® PX309-10KG5V pressure transducers for monitoring the injection wellhead pressure and intermediate principal sample confining stress, 1 Omega® PX309-3KG5V pressure transducer for monitoring the minimum principal stress, 1 Omega® PX40-50mmHG pressure transducer for monitoring the production reservoir fill level and flow rate, 1 Omega® LD621-30 linear displacement transducer for auxiliary use, and 1 Humboldt HM2310.04 linear strain transducer also for auxiliary use. Omega® Type-T thermocouples, fabricated in-house, were positioned at the hydraulic temperature monitoring positions as indicated in Figure 3, inside the bottom of the injection and production boreholes, and in a high-coverage grid arrangement on the surface faces of the sample inside the cell, as shown in Figure 5. When used, strain gages were embedded onto the faces of the sample to monitor stress uniformity. Additional data was collected from the Teledyne Isco pump controller giving information about hydraulic system operation including flow rates, pressures, valve positions, and general pump status.

Figure 6. AE sensor installed in a loading platen.

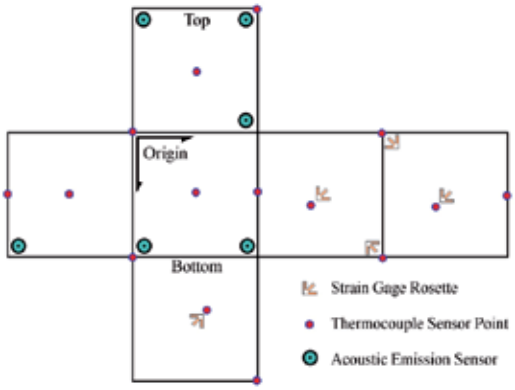

Figure 5. Diagram of surface sensor positions on a typical 30x30x30 cm^3 sample.

To monitor the fracturing process and provide real-time location estimation for the generated hydraulic fractures, a 6-sensor piezoelectric Acoustic Emission (AE) monitoring system, obtained from Physical Acoustics Corporation, was installed inside the cell with sensors contacting the faces of the sample in an arrangement to achieve maximum volumetric coverage, as shown in Figure 5. Figure 6 shows an AE sensor installed into a 25 mm thick loading platen where it was protected from the high loading stresses being applied to the sample. Thin packing foam wafers were inserted between the sensor body and the steel housing to dampen external acoustic noise effects and provide a soft spring reaction for any movement that would occur during loading and unloading processes. In general, this platen serves as a movable interface between the pressurized flat jack and the sample inside the cell. During analysis, recorded AE events could readily be filtered by correlation coefficient, amplitude, or other criteria using digital post-processing of hit time and waveform data.

http://dx.doi.org/10.5772/56113

2.4. Test materials

Four material types were used for this project including medium strength concrete grout, ultra-high strength low permeability concrete, locally obtained Colorado Rose Red Granite, and acrylic glass. Each of these materials was tested for a variety of mechanical, thermal, and acoustic properties to provide a reference for future field data comparison. A general summary of the measured properties for selected materials has been provided in Table 1. The uniaxial compression strength (UCS), elastic modulus (E), Poisson's Ratio (v), and indirect tensile strength (BTS) testing was performed using a specially instrumented ELE Accu-Tek™ 250 concrete load frame. Thermal conductivity (k_T) measurements were performed using a divided bar apparatus available through the Colorado Geological Survey [8]. Volumetric specific heat capacity (C_V) was obtained using an insulated calorimeter. Acoustic compression (V_P) and shear (V_S) wave velocities were obtained using a piezoelectric pulse transmitter-receiver apparatus with oscilloscope monitoring. Porosity (ϕ) and matrix density (ϱ_{dry}) were measured using a 70% vacuum desiccator, 110ºC oven, and digital mass balance.

For post-test analysis, diamond over cores and cut cross-sections were used. The over cores were taken to remove the borehole casing and observe the near wellbore fracture geometry. Next, cross-sections were cut using a 0.9 m diameter diamond table saw. An example cross section taken from an unconfined granite sample hydraulic fracturing test is shown in Figure 7. Cross sections such as these allowed for physical measurements of the fracture locations, fluid permeation depths, and verification of AE fracture location estimations. Fluid pathways and permeation depths were most visible on tests using oil as the fracturing fluid due to staining of the sample material. Compiling fracture geometry data from consecutive cross sections allows for three-dimensional imaging of entire stimulated fracture networks. As evident in Figure 7, these networks are expected to be very complex due to the heterogeneities in natural rock and concrete samples.

3. Test results and observations

Using this equipment, an ongoing series of hydraulic fracturing stimulation and reservoir characterization testing is being performed to obtain new data for EGS technology advancement. While hydraulic fracturing experiments have been performed in more than 11 different boreholes and four different materials, focus will be given to a granite hydraulic fracturing test where an orientated intercept borehole was drilled to create a producing heated EGS reservoir. The results of the EGS simulation experiment can be divided into several key phases including sample preparation, primary hydraulic fracturing, drilling the fracture intercept borehole, and fracture reopening and flow.

3.1. Sample preparation

For this test, a block of Colorado Rose Red Granite, as documented in Figure 8, was loaded into the true-triaxial cell and slowly heated to an average internal temperature of 50 ºC over the span

Material Property	Medium Strength Concrete	Ultra-High Strength Concrete	Colorado Rose Red Granite
Unconfined Compressive Strength, UCS (MPa)	50-60	123-154	152 ± 19*
Brazilian Tensile Strength, BTS (MPa)	2.2-2.7	4.0-6.0	7.5 ± 1.8*
Young's Modulus, E (GPa)	9.5-10.5	20-30	57*
Poisson's ratio, v	-	-	0.32*
Dry density, ρ_{dry} (kg/m^3)	1950	1970	2650
Thermal conductivity, k_T (W/m-K)	-	1.60 ± 0.02	3.15 ± 0.05
Heat capacity, C_V (kJ/m^3-K)	2013 ± 145	1820 ± 146	2063 ± 92
Porosity, ϕ	0.30-0.31	0.15-0.23	0.006-0.008
Shear wave velocity, V_S (mm/μs)	2.48	2.54	2.62
Compressional wave velocity, V_P (mm/μs)	3.41	3.89	4.45

Table 1. Test Material Properties (*data from [9-10]).

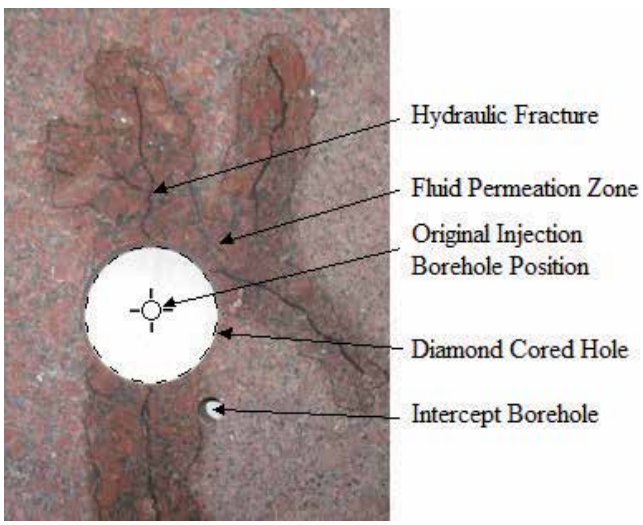

Figure 7. Cross-section from an unconfined granite hydraulic fracturing test.

of four days. After the target temperature was reached, the sample was pressurized with confining stresses of 12.5, 8.3, and 4.1 MPa for the vertical, maximum horizontal, and minimum horizontal stresses, respectively. The AE monitoring system was active throughout the loading process to identify if any mechanical shearing or thermal fracturing events had occurred. In this case, the AE data produced a large scatter of events with no significant clustering which indicated that acceptably uniform loading had been achieved and no significant fracturing events had occurred. The uniformity of the sample loading was also verified using strain gage data,

http://dx.doi.org/10.5772/56113

with the layout as shown in Figure 5. Combined, both of these methods were in agreement that a top corner of the sample was subjected to some elevated stress concentrations as indicated by relatively high strains and an increase in localized AE activity at the specific corner. This observation was used to modify and improve the loading procedure such that similar unintended stress concentrations would be less likely to occur during future tests using this equipment.

While loaded, a centered vertical borehole was drilled into the sample, a 107 mm deep casing interval was installed, and a 73 mm uncased interval was drilled for a final injection well depth of 180 mm. It is important to note that drilling the borehole while the sample is under load is a unique system capability that allows for laboratory simulation of a borehole damage zone. This process creates small fractures near the borehole, as has been clearly observed in acrylic testing [11-12], which may serve as fracture initiation locations. Simultaneously, the drilling process also fills these micro fractures with fines which are believed to have some effect on fracture self propping as well as near wellbore tortuosity and skin factor. Additional investigation may be necessary to better understand how the borehole damage zone influences hydraulic fracture initiation, growth and closure.

Figure 8. Pre-test image of the granite sample used for EGS reservoir simulation experiments.

3.2. Primary hydraulic fracturing

Primary hydraulic fracture breakdown was achieved using oil injection at a constant flow rate of 0.05 mL/min. Valvoline® Durablend® SAE 80W90 gear oil was used as the fracturing fluid due to its high viscosity value and publicly available fluid properties. At the injection temperature of 50 ºC, this fluid has an approximate dynamic viscosity of 71.5 cP as estimated using

the published product information in conjunction with the Walther Equation specified in ASTM D341 [13]. The importance of using high viscosity fluid for laboratory hydraulic fracture experiments is well documented [5-6]. In this case, using a high viscosity fluid provided the important benefits of better fracture growth control for improved probability of containment and a more predictable fracture orientation as the propagation would be less influenced by natural heterogeneities in the granite sample.

A plot of the hydraulic data for primary breakdown is shown in Figure 9. During this test, the pump was stopped 16 seconds after breakdown in an attempt to keep the fracture fully contained as real-time AE events were observed to be approaching the edges of the sample. Continued AE activity was observed even after pumping was stopped which indicated continued fracture propagation. Therefore, to forcibly halt the fracture growth, the flow rate was reversed at -10 mL/min for a total of 6 seconds to pull fluid out of the fracture and then held in the stopped position thereafter. At this time, a significant pressure rebound was observed which may offer some insight into fracture dynamic fluid storage behavior with additional investigation. Ultimately, the observation of a negligible flow rate during post-fracture constant pressure testing at 2000 kPa verified that a fully contained fracture had been generated.

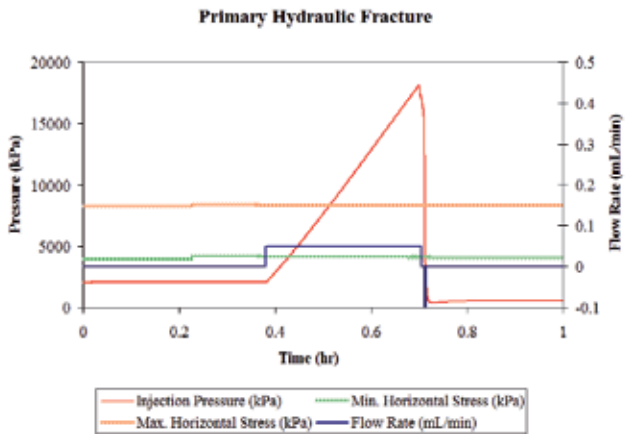

Figure 9. Hydraulic data plot for primary fracture.

Analysis of the AE source location data collected during this primary hydraulic fracture test revealed that a contained and planar fracture propagated from the borehole in a direction perpendicular to the minimum horizontal confining stress. Additionally, the fracture appeared to have a single dominant wing as evident by the AE cloud being most prominent on only one side of the borehole. Figure 10 shows orthogonal plots of the three-dimensional AE event source location results for the test. This analysis used six-sensor location regression and filtered the results to only contain events with a correlation coefficient greater than 0.75 and amplitude greater than 25 dB. On this plot, the circle diameters are directly proportional to the amplitude of the corresponding event. Also, the color shading corresponds to the correlation coefficient

http://dx.doi.org/10.5772/56113

AE Event Category	Number	% Total	% Classification
Total Events Located	726	100	-
Classifiable Events	81	11.2	100
Tensile Events	39	5.4	48.1
Shear Events	28	3.9	34.6
Mixed Mode Events	14	1.9	17.3

Table 2. Classifications of AE Events during hydraulic fracturing.

of each event with dark red circles having higher correlation. The two-segment centered vertical injection borehole is clearly visible on the front and side view plots.

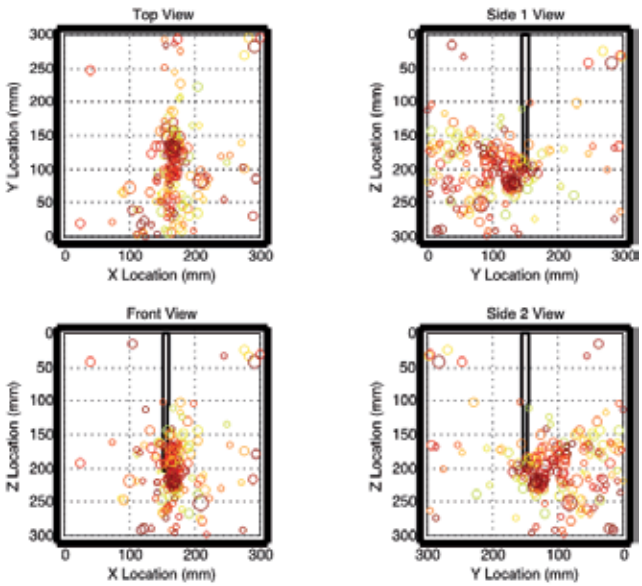

Figure 10. AE event source locations during primary hydraulic fracture.

Extending the AE analysis by application of moment tensor methods [14], information was obtained about the fracturing mode for some of the recorded AE events. As shown in Table 2, only about 11% of the total number of recorded events could successfully be classified with a reasonable level of certainty. At a glance, the tensile failure mode appears to be dominant during this fracturing stage but uncertainty associated with the low percentage of classifiable events effectively reduces the confidence of any conclusions which could possibly be derived from these figures.

3.3. Drilling the fracture intercept production borehole

Using AE source location data, an estimate of the fracture geometry was obtained and an optimal intercept borehole position was selected as shown in Figure 11. Here, the intercept borehole trajectory, drilled at 30º from the vertical axis, can be seen penetrating through the expected fracture surface. A high-angle drilling orientation was used to maximize the probability of achieving a successful intercept after considering AE source location uncertainty and drilling system tolerances. Also, the uncased 10 mm diameter intercept borehole was drilled deeper than the expected intercept location to further increase the probability of successful hydraulic connection. In the figure, the best estimate of the fracture plane was plotted using a smoothed cubic interpolation surface function fitted to events with both high-amplitude and high-correlation. After drilling was completed, the borehole was swabbed and positive indication of fracturing oil was recovered, thus indicating that the intercept was successful.

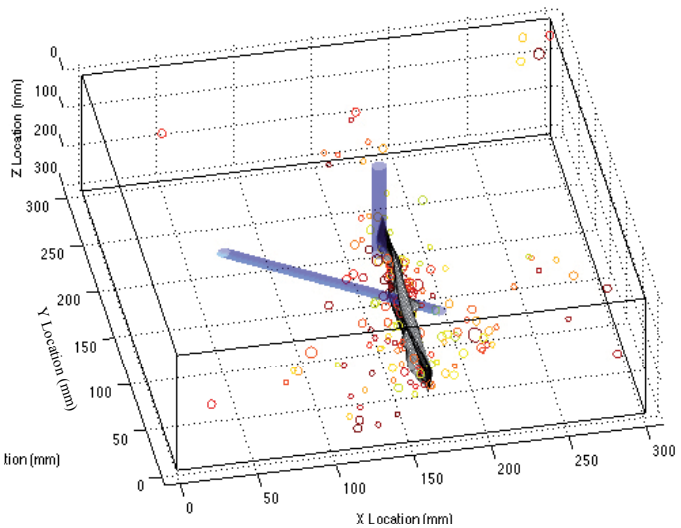

Figure 11. AE generated fracture surface of initial hydraulic fracture.

3.4. Fracture reopening and circulation flow

With the completion of the simulated EGS reservoir, flow experiments were performed to characterize the hydraulic properties of the reservoir. These experiments included constant pressure steady state injection, constant flow rate injection for fracture reopening, stepped constant pressure injection, and constant flow rate injection without reopening. The results obtained from these tests ultimately verified that a hydraulic circuit was present inside of the sample connecting the injection borehole to the production borehole through the stimulated hydraulic fracture.

Initially, constant low-pressure steady-state SAE 80W90 oil injection was performed using specified pressures of 2000, 3000 or 4000 kPa. The pressures were intentionally kept below the

http://dx.doi.org/10.5772/56113

minimum principal stress to avoid the potential for continued fracture propagation which could occur with fracture reopening. The results from these tests demonstrated that the achievable stable flow rates with the primary hydraulic fracture geometry were negligible and thus the reservoir remained non-producing. While this information confirmed that the stimulated fracture geometry was fully contained as desired, it also indicated that the connection between the injection and production boreholes was too tight to pass any significant amount of fluid through. It is expected that a significantly higher post-fracture hydraulic conductivity would occur if proppant had been used during the primary fracturing stage.

To enhance the hydraulic connection of the binary borehole system, two fracture reopening stages were performed with stepped constant pressure injection tests executed in between for diagnostic purposes. These injection tests continued to use oil as the injection fluid as its high viscosity was favorable for generating controlled fractures. Figures 12 and 13 show plots of the hydraulic data obtained from the first and second fracture reopening stages respectively. Both of these plots clearly show classic hydraulic fracture reopening behavior [15] with a nearly linear pressure rise followed by a rapid breakdown event and pseudo-steady fracture propagation at an elevated pressure. Comparing the similar magnitude peak pressures of 18.1, 15.4, and 17.4 kPa, observed for the primary fracture, first reopening, and second reopening events respectively, suggests that fracture toughness was not a dominant factor in fracture propagation so scaling criterion suggested in the literature (e.g. [5]) are likely to be satisfied even with intact granite as the testing material.

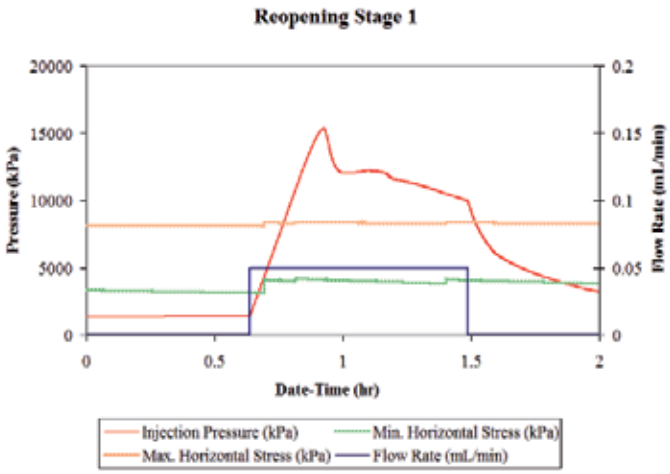

Figure 12. First fracture reopening event.

An orientated view of the AE source location data as observed for the first reopening stage is shown in Figure 14. Comparing this figure to the results shown in Figure 10 and the data from the second reopening stage, it is apparent that most of the fracture growth occurred during the first reopening stage along the bottom and two horizontal extremities of the initial fracture plane. Additionally, the close proximity of the AE events to the boundaries of the sample

suggested that the stimulated fracture may no longer have been fully contained and lower fluid recovery efficiency during production could result. The propagation of the fracture to the sample boundary, while not ideal, was reminiscent of the extension of a hydraulic fracture into a faulted zone or natural high-flow fracture network. Here the relative permeability between the sample boundary and the cell's platens was expected to be much higher than that through the hydraulic fracture within the sample, just as a faulted zone would likely have a higher permeability than an artificially stimulated fracture. This situation, while not ideal, may more closely resemble high fluid loss field EGS systems such as those encountered at Hijiori, Japan, where treatments were performed within a discontinuous and naturally fractured volcanic zone [16]. For the final fracture geometry within the granite sample, as estimated with the AE source location data, the smaller wing of the initial fracture appeared to have extended to approximately match the dominant wing length, thus creating a planar bi-wing fracture.

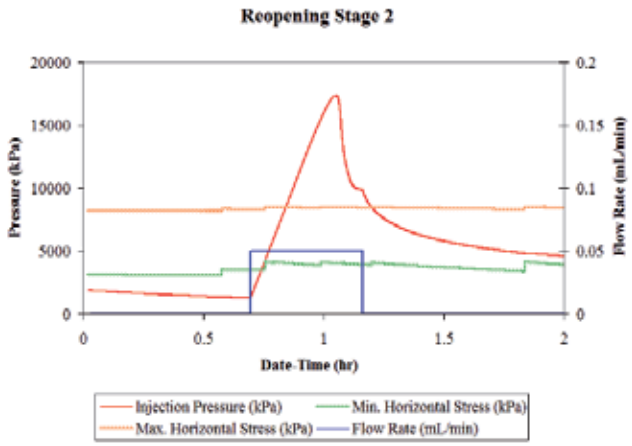

Figure 13. First fracture reopening event.

Comparing the AE count frequency data with the pressure data, as shown in Figure 15, significant increases in AE activity were found to occur just after portions of the hydraulic data where the second derivative of injection pressure with time was negative. Thus, from observing the real-time rate of slope change in the pressure data, it may be possible to anticipate a major fracture growth event before it occurs. Also, using a technique such as this allows for an improved understanding of fracture growth behavior in heterogeneous systems during the time between fracture initiation and shut-in. During this time, the second-order analysis could be used to identify distinct breakdown events occurring after the initial breakdown as could be expected with multi-wing fracture systems or the opening of intersected fissures, joints, or fault zones. In this laboratory case, the analysis was performed using an 11-second backward linear regression approach to obtain an estimate of the first pressure derivative, as could be used in real-time applications. The 11 second value was selected using a qualitative trial-and-error approach with the goal of obtaining a visually smoothed data set without sacrificing too much of the data accuracy.

http://dx.doi.org/10.5772/56113

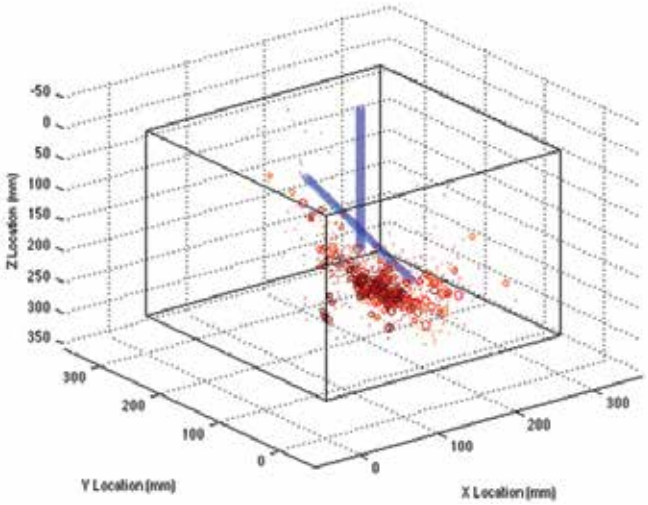

Figure 14. Three dimensional view of AE event source locations during first fracture reopening stage.

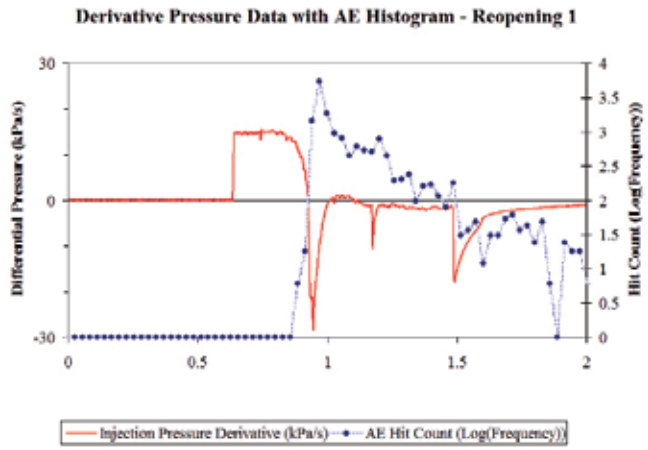

Figure 15. First time derivative of pressure with AE hit count histogram for the first fracture reopening stage.

To evaluate the effectiveness of each fracture reopening stage, stepped constant pressure oil injection tests were performed. In these tests, SAE 80W90 oil was injected into the sample with PID controlled pressure at 1000 kPa increments with 30 minute duration. An example of the hydraulic data from a step pressure test performed after the second reopening event is provided in Figure 16. For each constant pressure increment, the resulting steady state pressure and flow rate measurements are averaged to estimate the pressure dependent flow characteristics of the stimulated reservoir. These values were useful reference points during later controlled constant flow tests where fracture reopening and extension pressures were not desired.

A comparison of the stepped constant pressure test data obtained before and after the second reopening event is shown in Figure 17. On this plot, it was evident that there was negligible flow rate dependence with pressure after the first fracture reopening stage. This suggested that the flow of the injected fluid was not dominated by stimulated fracture flow and the hydraulic connection between the injection and production boreholes was not flowing effectively if at all. To improve the inter-well connectivity, the second fracture reopening stage was performed with high success. As can be seen in Figure 17, pressure dependent flow rate characteristics were much more prominent after this second stage with a clear proportional relationship. To augment these observations, borehole swabbing was performed periodically to check for fluid production in the intercept borehole. The swab's results did not positively indicate hydraulic connection until after the second fracture reopening stage. Thus, even though the first treatment did not attain an acceptable hydraulic connection, the execution of additional fracture stimulation treatments from the same injection well was successful in creating an effective hydraulic connection

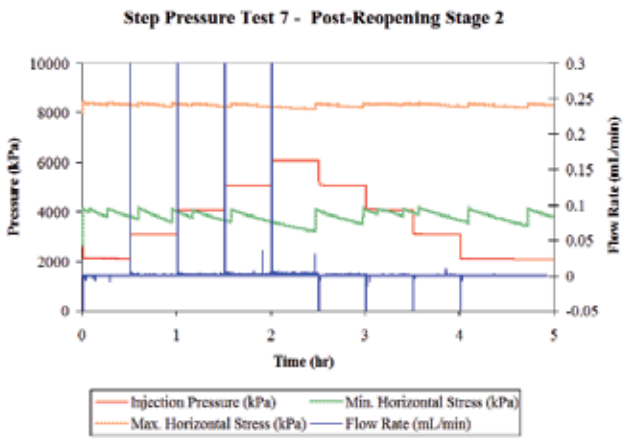

Figure 16. Step pressure test data taken after the second fracture reopening stage.

With a confirmed hydraulic connection between the boreholes, the injection fluid was changed to tap water for thermal flow testing and EGS reservoir characterization. Water injection was performed with two constant flow rate controlled tests to attain pressure dependent flow characteristics for the reservoir. The first test utilized a flow rate of 0.05 mL/min and the second used a higher rate of 0.10 mL/min. While these tests provide similar data to constant pressure injection, it is more easily compared to field applications where flow rate control is the standard. Periodic borehole swabbing results indicated a significant and continuous fluid production in the intercept borehole. Figure 18 provides an example of the flow rate data obtained during the second water flow test. Here, it is evident that the reduction in viscosity by changing from oil to water resulted in significantly reduced pressure losses, as expected. Also, these flow rates did not produce any significant AE activity indicating that the stimulated

http://dx.doi.org/10.5772/56113

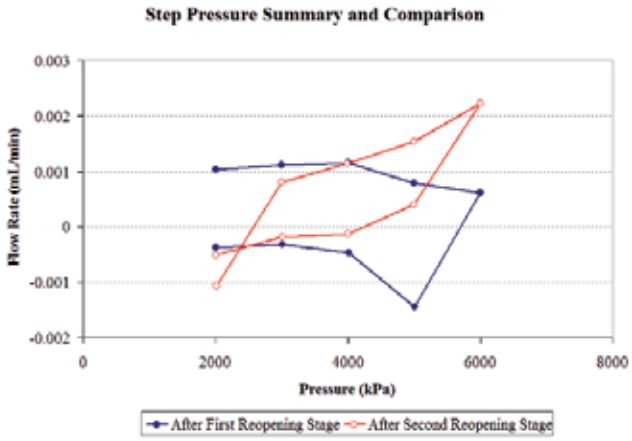

Figure 17. Averaged oil injection stepped constant pressure data before and after the second fracture reopening stage.

fracture geometry was stable with water flow. Additional testing is required and planned in order to obtain a full characterization of the laboratory simulated EGS reservoir.

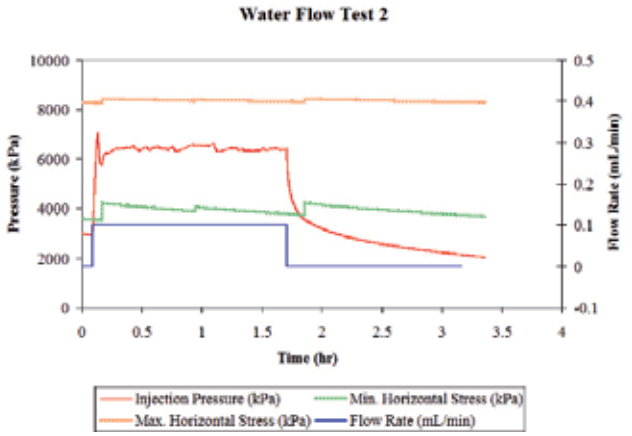

Figure 18. Second water flow test data plot.

4. Conclusions

A heated true-triaxial cell has successfully been able to produce a laboratory simulation of an EGS reservoir. Preliminary experiments using granite have provided valuable resulting data as well as new observations that may bring some additional insight into the potential of EGS

technology. Some of the most important advancements and observations that have been made include:

- The completed development of a heated true-triaxial cell with the ability to simulate multi-well EGS reservoir systems as well as borehole damage by percussively drilling orientated boreholes into a hot stressed sample.
- The successful laboratory simulation of a binary injector-producer EGS reservoir in granite with proven fluid communication through a stimulated fracture between two boreholes.
- Multiple hydraulic fracture stimulation treatments may be performed from the same injection borehole to attain significantly increased reservoir conductivity and well fluid communication.
- Significant fracture growth, as indicated by AE activity, is preceded by periods where the real-time second order differential of pressure with time is negative.
- AE source location is a functional and important tool for successful drilling of a production well into a stimulated EGS reservoir.

Acknowledgements

Financial support provided by the U.S. Department of Energy under DOE Grant No. DE-FE0002760 is gratefully acknowledged. The opinions expressed in this paper are those of the authors and not the DOE.

Author details

Luke Frash, Marte Gutierrez and Jesse Hampton

Colorado School of Mines, Golden, CO, USA

References

[1] Tester, J. W, et al. The Future of Geothermal Energy. Massachusetts Institute of Technology; Cambridge, MA, USA. (2006).

[2] Clark, J. B. A hydraulic process for increasing the productivity of wells. Journal of Petroleum Technology (1949). , 1(1), 1-8.

[3] Green, C. A, Barree, R. D, & Miskimins, J. L. Hydraulic-Fracture-Model Sensitivity Analysis of a Massively Stacked, Lenticular, Tight Gas Reservoir. SPE Production & Operations (2009). , 24(1), 66-73.

[4] Behrmann, L. A, & Elbel, J. L. Effect of Perforations on Fracture Initiation. Journal of Petroleum Technology (1991). , 43(5), 608-615.

[5] De Pater, C. J, Cleary, M. P, Quinn, T. S, Barr, D. T, Johnson, D. E, & Weijers, L. Experimental Verification of Dimensional Analysis for Hydraulic Fracturing. SPE Production & Facilities (1994). , 9(4), 230-238.

[6] Ishida, T, Chen, Q, Mizuta, Y, & Roegiers, J. Influence of Fluid Viscosity on the Hydraulic Fracturing Mechanism. Transactions of the ASME; (2004). , 190-200.

[7] Wieland, C. W, Miskimins, J. L, Black, A. D, & Green, S. J. Results of a Laboratory Propellant Fracturing Test in a Colton Sandstone Block. Proceedings SPE Annual Technical Conference and Exhibition, September (2006). San Antonio, Texas, USA., 24-27.

[8] Macartney, H, & Morgan, P. The Potential for Geothermal Energy Recovery from Enhanced Geothermal Systems in the Raton Basin of Southern Colorado, USA. Proceedings AAPG Hedberg Geothermal Conference, Napa, CA, USA (2011).

[9] EMI Brazilian Tensile Strength Test Datasheet for Orica Core ID 4, Colorado School of Mines, Earth Mechanics Institute (2010).

[10] EMI Uniaxial Compressive Strength Test Datasheet for Orica Core ID 4, Colorado School of Mines Earth Mechanics Institute (2010).

[11] Gutierrez, M, Frash, L, & Hampton, J. Hydraulic Fracturing in Acrylic with Proppant. http://youtu.be/rbE4nisWlyAaccessed 10 October (2012).

[12] Gutierrez, M, Frash, L, & Hampton, J. Water Clear Acrylic Laboratory Hydraulic Fracturing Test. http://youtu.be/PEXOE2FTDlI.accessed 10 October (2012).

[13] ASTM ASTM D341: Standard Practice for Viscosity-Temperature Charts for Liquid Petroleum Products. Annual Book of ASTM Standards. ASTM International; West Conshohocken, PA. (2009).

[14] Ohtsu, M. Acoustic Emission Theory for Moment Tensor Analysis. Research in Nondestructive Evaluation (1995). , 6(3), 169-184.

[15] Weijers, L, De Pater, C. J, Owens, K. A, & Kogsbøll, H. H. Geometry of Hydraulic Fractures Induced From Horizontal Wellbores. SPE Production and Facilities (1994). , 9(2), 87-92.

[16] Swenson, D, Schroeder, R, Shinohara, N, & Okabe, T. Analysis of the Hijiori Long Term Circulation Test. Proceedings from the Twenty-Fourth Workshop on Geothermal Reservoir Engineering, January (1999). Stanford University, Stanford, CA, USA , 1999, 25-27.

Section 16

Experimental Geomechanics

Comparison of Hydraulic and Conventional Tensile Strength Tests

Michael Molenda, Ferdinand Stöckhert,
Sebastian Brenne and Michael Alber

Additional information is available at the end of the chapter

http://dx.doi.org/10.5772/56300

Abstract

Tensile strength is paramount for reliable simulation of hydraulic fracturing experiments on all scales. Tensile strength values depend strongly on the test method. Three different laboratory tests for tensile strength of rocks are compared. Test methods employed are the Brazilian disc test (BDT), modified tension test (MTT) and hydraulic fracturing experiments with hollow cylinders (MF = Mini Frac). Lithologies tested are a micritic limestone, a coarse-grained marble, a fine-grained Ruhrsandstone, a medium-grained rhyolite, a medium- /coarse-grained andesite and a medium grained sandstone. Test results reveal a relationship between the area under tensile stress at failure and the measured tensile strength. This relationship becomes visible when the area under tensile strength ranges over one order of magnitude from 450 to 4624 mm^2. This observation becomes relevant when selecting the tensile strength values of lithologies.

Keywords: hydraulic fracturing, Brazilian Disc test, Modified Tension Test, Acoustic Emission, numerical simulation

1. Introduction

Tensile strength tests are widely applied in rock mechanics to obtain input parameters for planning of hydraulic fracturing on all scales. In literature only few experimental data sets are published dealing with samples size effects on tensile strength tests [1,2] or the comparison of different tensile tests in general [1,3]. Usually, results of laboratory tensile

tests are taken to be size independent when used as input parameter for numerical studies at different spatial sizes.

We compare the results of 3 different, easily applicable laboratory tests for tensile strength of rocks. The sample set comprises a micritic limestone, a coarse-grained marble, a fine-grained Ruhr-Sandstone, a medium-grained rhyolite, a medium- /coarse-grained andesite and a medium grained sandstone. All tested rocks were characterized petrographically as well as by ultrasonic velocities, density, porosity, permeability, static, dynamic elastic moduli and compressive strength. In order to determine the effects of specimen size on test results, we carried out BDT according to ISRM [4] with disc diameters of 30, 40, 50, 62, 75 and 84 mm, respectively. The recently presented MTT [5] was used as a tensile strength test with an approximately uniform tensile stress distribution. Hydraulic tensile strength was evaluated by MF experiments (core diameter 40 and 62 mm; borehole/diameter ratio 1:10) under uniaxial compression [6]. MF pressurization was performed with a constant fluid volume rate of 0.1 ml/s representing a stress rate of 0.3 MPa/s. In all tests relevant acoustic emission (AE) values have been evaluated to get additional information on the failure processes.

2. Materials and methods

2.1. Sample material

To investigate the influence of rock properties on tensile test methods, six different rock types were tested. Bebertal sandstone, a medium grained Permian sandstone from a quarry near Magdeburg, Germany. Ruhrsandstone, a fine-grained and massive Carboniferous arcose from the Ruhr area in Germany. A medium to coarse grained, jointed Permian andesite from the Doenstedt Eiche quarry near Doenstedt, Germany. A medium grained, highly jointed Permian rhyolite from the Holzmuehlental quarry near Flechtingen, Germany. A micritic Jurassic limestone from a quarry near Treuchtlingen, Germany and a coarse grained marble from Carrara, Italy. The rocks' petrophysical properties, namely bulk density, grain density, compressional wave speed, porosity, permeability, cohesion and friction angle are listed in Table 1.

2.2. Petrophysical characterization

Dry densities are calculated geometrically based on geometrical properties, grain densities are measured according to DIN 18124. Compressional wave velocities are measured at each core with a Geotron USG 40/UST 50-12 at room temperature and in dry condition. Porosities are derived from the difference between grain density and geometrical density of the oven-dried samples. Permeabilities are evaluated via a constant head test on the hollow cylinder samples used for the MF tests [7]. Bebertal-sandstones are permeable enough to use a simple axial flow-through test with a maximum pressure difference of up to 3 bars. The samples are sealed off with rubber jackets to minimize water-flow along the sample surface. Unconfined compressive strengths and static moduli of elasticity are measured by uniaxial compressive tests [8].

http://dx.doi.org/10.5772/56300

Rock type (location)	ρ_d [g/cm^3]	ρ_s [g/cm^3]	vp [m/s]	Φ [%]	k [m^2]	c [MPa]	φ [°]
Marble (Carrara)	2.71 ±0.002	2.721 ±0.003	5.67 ±0.06	0.40	1E-19	29	22
Limestone (Treuchtlingen)	2.56 ±0.008	2.713 ±0.002	5.59 ±0.05	5.64	1E-18	27	53
Ruhrsandstone (Ruhr area)	2.57 ±0.006	2.688 ±0.008	4.61 ±0.13	4.39	8E-18	36	50
Rhyolite (Flechtingen)	2.63 ±0.015	2.657 ±0.011	5.39 ±0.34	1.02	9E-19	20-36	55
Andesite (Dönstedt)	2.72 ±0.023	2.734 ±0.006	5.26 ±0.28	0.51	-	20-41	50
Sandstone (Bebertal)	2.66 ±0.061	2.44 ±0.059	3.61 ±0.61	8.27	11E-15	15	45

Table 1. Averaged values of petrophysical properties of the rock samples. ρ_d dry bulk density, ρ_s grain density, vp compressional wave velocity, Φ porosity, k permeability, c cohesion, φ friction angle.

2.3. Testing procedure of the tensile strength tests

All experiments are performed in a stiff servo-hydraulic loading frame from Material Testing Systems (MTS) with a load capacity of 4000 kN. For further details on the technical specifications see Table 2.

Device (manufacturer) name	max. capacity	accuracy	BDT	MTT	MF
Axial load cell (Althen) CPA-50	500 KN	± 100 N	x	x	x
Axial displ. transducer (Scheavitz) MHR 250 LVDT 1 & 2	6.3 mm	± 1•10^{-4} mm	x	x	x
Displ. transducer at pressure intensifier (HBM) WA 100 mm LVDT 3	100 mm	± 1•10^{-3} mm			x
Load cell for Hoek Cell					
Load cell for pressure intensifier (Burster) 8219R-3000	300 MPa	± 0,03 MPa			x

Table 2. Technical specifications of the measurement system.

Acoustic Emission (AE) signals are acquired with an AMSY-5 Acoustic Emission Measurement System (Vallen Systeme GmbH, Germany) equipped with up to 6 Sensors of type VS150-M. The Sensors are sensitive in a frequency range of 100-450 kHz with a resonance frequency of 150 kHz and a preamplification of 34 dB_{AE}. Due to machine noise in the range below 100 kHz incoming signals are filtered by a digital bandpass-filter in a frequency range of 95-850 kHz.

AE data are sampled by a sampling rate of 10 kHz. The sensors are fixed using hot-melt adhesive to ensure best coupling characteristics. Pencil-break tests (Hsu-Nielsen source) and sensor pulsing runs (active acoustic emission by one sensor) are used to ensure good sensor coupling of the sensor on the sample.

2.3.1. Hydraulic fracturing core experiments (MF) procedure

Minifrac experiments are carried out mainly on 40 mm cores with a borehole diameter of 4mm. Furthermore some 62 mm cores with a borehole of 6 mm diameter are tested. The samples are loaded axially up to 5 MPa to ensure that the packer mechanism is tight and seals off the borehole openings at the top and at the bottom. The borehole pressure was raised servo controlled with a fixed volume rate of 0.1 ml/s that results in a pressure rate of approximately 0.3 MPa/s. All MF tests are monitored by Acoustic Emissions with four sensors glued directly to the samples and a fifth sensor placed at the incoming hydraulic line.

2.3.2. Brazilian Disc Tests (BDT) procedure

All Brazilian disc tests are carried out following the ISRM suggested method [4] at a load rate of 200 N/s. Disc diameters used are 30, 40, 50, 62, 75 and 84 mm, whereas the length to diameter ratio (L/D) was constant at 0.5. All tests are monitored by one AE-sensor glued directly in the middle of the disc specimen. The size dependency is tested with discs from Ruhrsandstone, marble, rhyolite and limestone.

2.3.3. Modified Tension Test (MTT) procedure

The MTT tests are driven load controlled at a rate of 200 N/s that corresponds to a stress rate of 0.02 MPa/s. The axial force is applied from the top (Figure 1). MTT test samples are observed by up to 6 AE-Sensors glued directly to the specimen. The samples were overcored with 62 mm and 30 mm diameters where the overlapping height is 1/3 of the total sample height (Figure 1). The centralizing of the drills was achieved by using a former plate to adjust the sample before drilling. Despite assiduously arrangement the eccentricity of the overcoring was in the range of up to 3 mm due to the imprecise vertical guidance of a standard drilling machine. In order to test the influence of eccentricity we also prepared samples with an eccentricity of 14 mm.

3. Experimental results

3.1. Brazilian disc test size dependency

The size dependency of the absolute size of the Brazilian disc test discs on the tensile strength is shown in Figure 2. Overall 138 Brazilian disc tests are undertaken for up to 6 sizes and four lithologies. The disc diameters, ranging from 30-84 mm, represent the sizes that are mostly tested in laboratories to determine the BDT tensile strength of rock samples. The results of the size dependency tests show no significant relationship between the sizes of the tested disc to

http://dx.doi.org/10.5772/56300

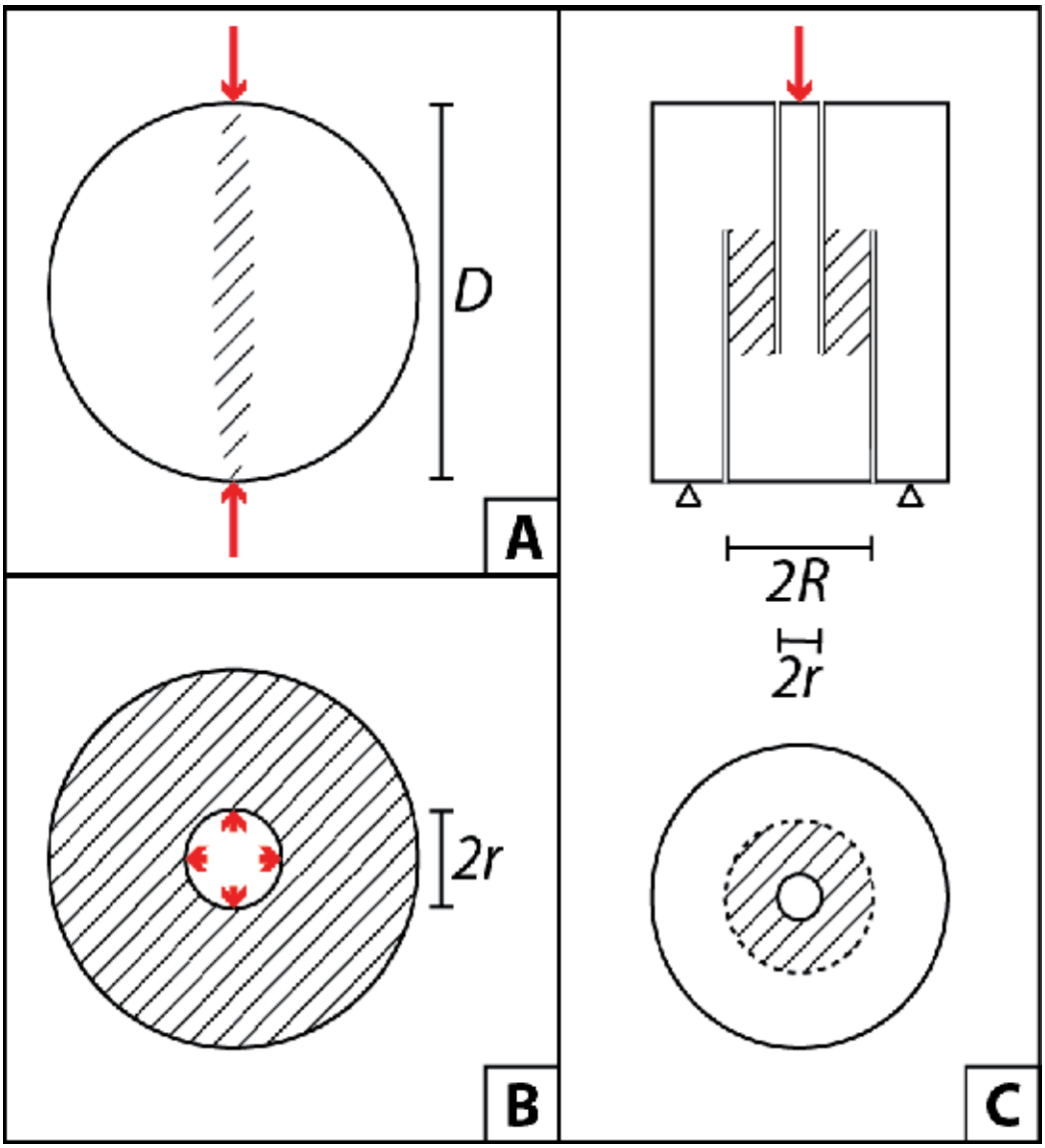

Figure 1. Sketches of the three tensile test methods. A: BDT side view, B: MF top view, C: MTT side view cross section (upper) and top view (lower).

its calculated tensile strength as long as the length to diameter ratio is held constant as suggested by the ISRM suggested method at a value of 0.5 [4]. There is a marginal tendency for the standard deviation of the tensile strength to decrease with increasing disc size.

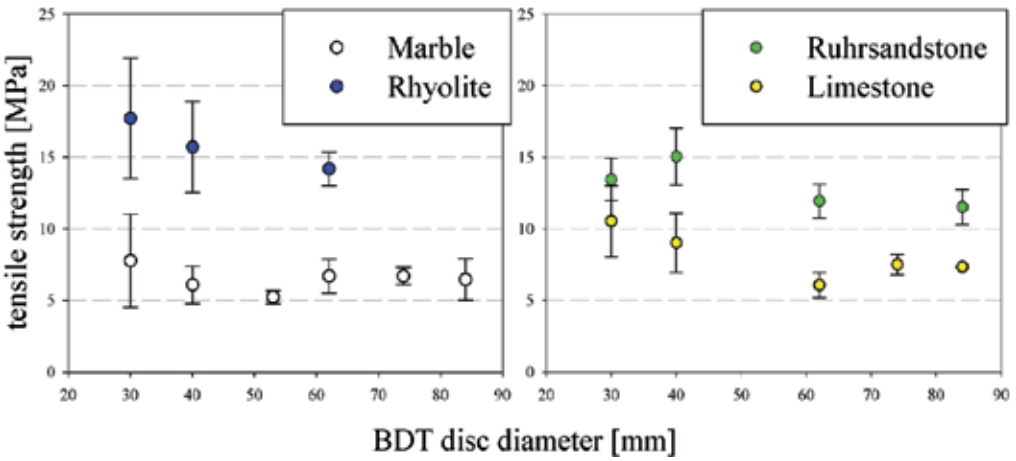

Figure 2. Size dependency of the BDT disc size on the tensile strength for four lithologies. Circles represent the mean values, bars stand for the standard deviation.

3.2. MF, BDT and MTT tensile strength results

Three different methods for the determination of tensile strength are compared regarding their results. 201 Brazilian disc tests, 31 Minifrac tests and 15 Modified tension tests form the basis of the data evaluation, where σ_t^{BDT}, σ_t^{MF} and σ_t^{MTT} are the tensile strengths indexed by the used method. BDT tensile strengths are calculated as follows [4].

$$\text{BDT: } \sigma_t^{BDT} = 2P / \pi D t \tag{1}$$

Where P is the force at failure, D is the disc diameter and t the disc thickness.

For the MF tests, assuming the rocks to be nearly impermeable and therefore neglecting a relevant pore pressure influence the tensile strength is given directly by the breakdown pressure P_b [9].

$$\text{MF: } \sigma_t^{MF} = P_b \tag{2}$$

MTT tensile strengths are evaluated by the formula given by [5].

$$\text{MTT: } \sigma_t^{MTT} = F_{max} / A_{TZ} = F_{max} / \left(R^2\pi - r^2\pi\right) \tag{3}$$

http://dx.doi.org/10.5772/56300

Where R^2 and r^2 are the outer and inner radius, respectively (Figure 1). Mean values, standard deviations and total number of tests for all three testmethods can be found in Table 3.

Lithology	Test method	Mean [MPa]	Std. dev. [MPa]	N [-]
Ruhrsandstone	BDT	13.2	2.1	32
	MF	19.0	3.0	10
	MTT	5.8	1.0	3
rhyolite	BDT	15.8	3.2	39
	MF	20.1	5.5	5
	MTT	4.9	1.4	2
limestone	BDT	8.2	2.2	36
	MF	10.2	1.7	5
	MTT	4.8	1.0	2
marble	BDT	6.4	1.5	32
	MF	7.8	1.3	4
	MTT	4.3	1.2	2
andesite	BDT	14.6	4.5	23
	MF	14.4	5.1	4
	MTT	8.7	4.4	3
Bebertal sandstone	BDT	4.1	1.2	39
	MF	4.3	2.0	3
	MTT	2.4	-	1
	MTT eccentric	1.0	5E-3	2

Table 3. Comparison of tensile strength out of three test methods.

One of the main observations is the very low tensile strength measured with the Modified Tension Test method. The MTT results mean values are in the range of 66 % down to 31 % of those obtained with the BDT. In addition to the low tensile strengths obtained by the MTT an eccentricity of the overcoring yields to an additional underestimation of the tensile strength values. The BDT and MF results seem to be more similar. The BDT results lie in the range of 70 % to 100 % of the MF tensile strength, so the MF test yields the highest tensile strengths and also to the highest standard deviations. All measurements are visualized in Figure 3. Doenstedt andesite and Flechtingen rhyolite tensile strengths have the highest standard deviations of the tested rock types. This variance is due to the high amount of natural joints that are assumed to have a different tensile strength with respect to the intact parts. Therefore the tensile strength scattering is the result of the material heterogeneity itself.

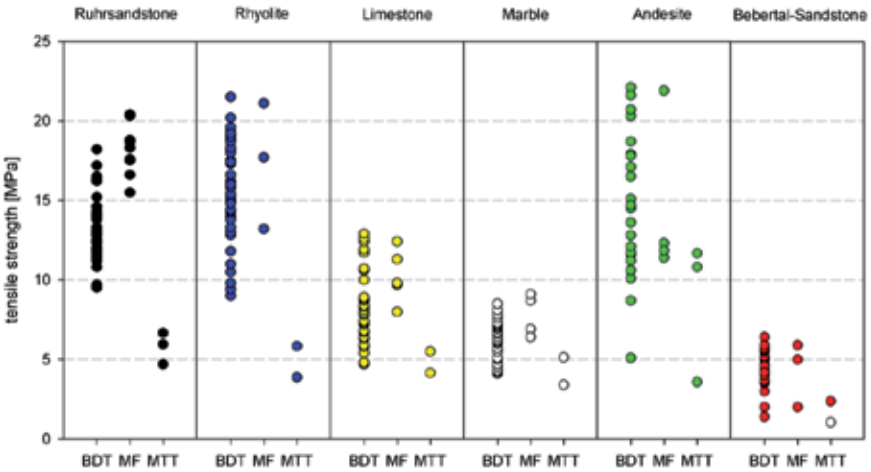

Figure 3. Results of all tensile strength test. BDT: Brazilian Disc Test, MF: Minifrac, MTT: Modified Tension Test. Hollow circle in Bebertal sandstone MTT tests represents two results of the highly eccentrical MTT tests.

3.3. Acoustic Emissions results

Acoustic emission data obtained during the tests give rough insights into the failure processes. It is obvious that all tests end with a spalling of the specimens in parts due to a complete tensile failure. Simple AE count analysis show that the BDT is accompanied with an immense hit-rate long before total failure in comparison to the relatively quiet pre-failure phases of the MF and MTT tests. In good agreement with theoretical considerations of the stress distribution in the Brazil disc [1] these events are most likely due to compressional failure at the top and bottom of the disc, accompanied with crack propagation and coalescence before peak load (Figure 4).

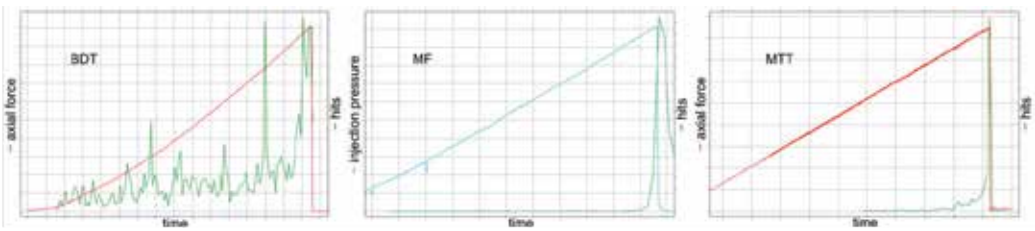

Figure 4. AE hits per 0.5 sec., BDT left, MF middle and MTT right showing the huge difference in AE hits before total failure of the sample.

4. Numerical model

We investigate the effect of eccentricity of the overcoring for the MTT samples by a numerical simulation. A finite element study that has been performed by Plinninger et al. [10] that shows

http://dx.doi.org/10.5772/56300

a uniform tensile stress distribution in the annulus of the test samples. It is arguably if this model is the right tool for modeling a tensile stress distribution in rock samples prior to failure. A simple linear elastic 3D FEM model reveals tensile stress concentrations at the edges of the rims in the sample (Figure 5). Fractures may be initiate there at relative low axial forces.

During preparation of the samples it becomes obvious that exact centralization of the inner overcoring is not always given. Two Bebertal sandstone samples were prepared with a eccentricity of 14 mm resulting in a minimum rim width of 2 mm instead of 16 mm for a perfectly centralized sample. The average eccentricity of our samples is in the range of up to 3 mm. Tensile stress redistribution due to eccentricity is modeled as well and can easily double the tensile stress in the thinner rim of the annulus (Figure 5).

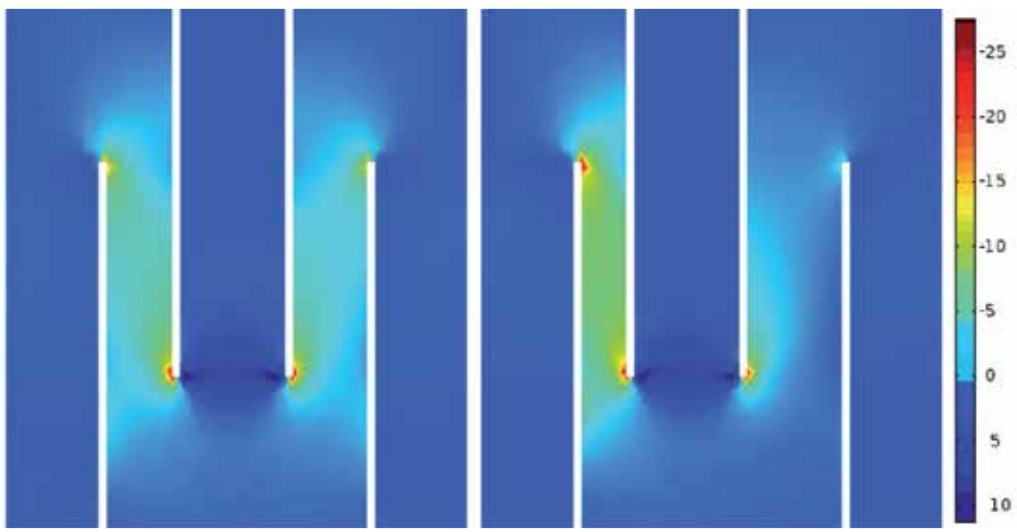

Figure 5. Slice through a linear elastic 3D FEM model of MTT tensile test. Values of axial stress are given in MPa where negative values stand for tensile stress. Left model represents a perfectly centralized sample. Right model shows the stress distribution for a eccentricity of 6 mm towards the left edge.

5. Discussion

247 tensile strength test results of BDT, MF and MTT tests vary considerable within one lithology (Figure 6). Therefore it is not trivial to give a reliable prediction of the tensile strength parameter. Results of the BDT tests show no significant variation with respect to the specimen size, as long as the aspect ratio is held constant. Nevertheless the tensile strength data scattering is high, so that it may obscure existing trends. Acoustic Emission evaluation shows that during the BDT multiple fracturing mechanisms are present. Before total fracturing of the sample by a tensile rupture there is a high amount of AE activity that is most likely related to compressional failure at the top and bottom of the disc. Beside this, compressional stress concentrations and the inhomogeneous tensile stress distribution may lead to tensile cracks before peak load.

MF results lead to the highest tensile strengths in this comparison where there seem to be no differences in tensile strength when using a 4 mm or a 6 m borehole for pressurization. Again one has to take into account that the high amount of tensile strength scattering for these tests inhibits a statement regarding a borehole size dependency.

The results of the MTT tests give the lowest tensile strengths and very low standard deviations. Latter may be related to the small amount of testes MTT per lithology. Furthermore all MTT are prepared using the same sample sizes. A major problem of the MTT experiments is the centralization of the boreholes. An eccentricity yields to a significant inhomogeneity of the tensile stress distribution in the sample (Figure 5). Numerical simulations of the MTT eccentricity effect together with the two eccentric MTT samples (Figure 3) show that the calculated tensile strength may be underestimated massively. One reason for the apparently lower tensile strength measured using the MMT might be the applicability of Equation (3). In deriving the equation, it was assumed that, when the peak load is approached, the tensile stress distribution is almost uniform in the area defined as A_{TZ} [5]. This may only be true if the material is highly ductile. However, for brittle rocks, especially for highly fractured rocks, fracture propagation may occur and lead to ultimate failure at a much lower load as suggested by Equation (3) due to stress concentration (Figure 5).

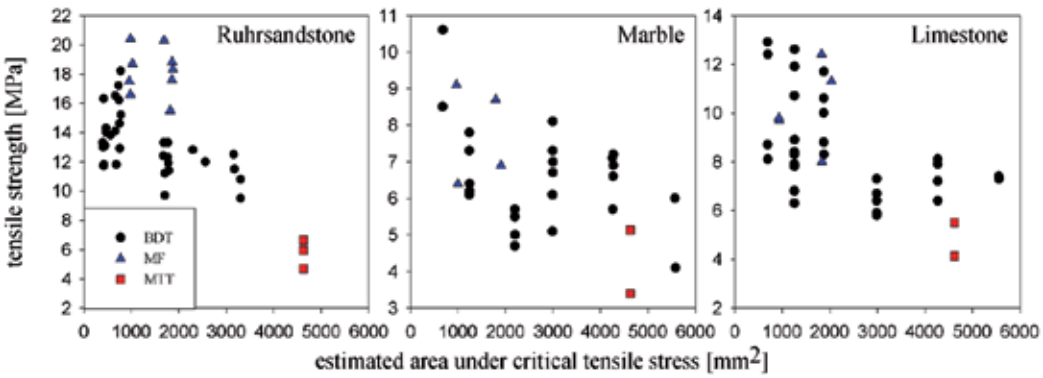

Figure 6. Tensile strength results plotted against the assumed area under tension. BDT: diameter x thickness, MF: surface area of the borehole and MTT: twice the surface area between the outer and inner borehole, upper and lower.

Testmethod	BDT	MF	MTT
Area under 1,51,5	450-3400 mm^2	1005-3393 mm^2	4624 mm^2
Calculation	$D \cdot t$	$2 \cdot \pi \cdot rbh \cdot l$	$2 \cdot (\pi \cdot (R^2 - r^2))$

Table 4. Estimated area subjected to tensile stress for the different tensile tests. *D*: BDT disc diameter, *t*: BDT disc thickness, *rbh* : MF borehole radius, *l*: MF sample height, *R*: MTT outer borehole radius, *r*: MTT inner borehole radius.

Main difference in all experiments and the reason for choosing these are the areas that are under tensile stress at the point of failure. The calculated tensile strengths compared to the area perpendicular to the maximum tensile stress show a negative trend for the tensile strength

http://dx.doi.org/10.5772/56300

with increasing area being set under tensile stress. That is reasonable in terms of the statistical theory of strength. Especially for the igneous rocks it seems evident, that the probability to set a healed joint under a critical tension rises with the size of the sample volume that is under tensional stress. For the selection of the tensile strength test one should keep in mind that depending on the lithology the apparent tensile strength appears to be a function of the area, or more exact of the volume under tensile stress. Thus, for a relative homogeneous rock a less severe reduction of the measured tensile strength with size will be visible as it will be at the highly fractured igneous rocks tested in this study.

It is arguable and may not be appropriate to study the effect of area/volume under tensile stress on the measured tensile strength using the combined results from different types of tests, especially if the different tests tend to give different average measured tensile strengths. Furthermore the negative trend of tensile strength with respect to the stressed area/volume is not that obvious for the single test methods. Especially the assumption of uniform tensile stress distribution close to peak load in the annulus [5] for the MTT samples seems not to be comprehensible. It may hold for ductile materials but not for brittle ones. Therefore the validity of equation (3) for the calculation of the tensile strength is questionable. Nevertheless the resulting tensile strengths are treated as the same rock property when used as input parameters for calculations. This is very problematic due to its huge variation as shown in the tests. The correlation of the calculated tensile strength with the stressed area/volume is one possible approach to account for the decreasing apparent tensile strength behavior.

Acknowledgements

This work is funded by the Federal Ministry of Environment, Nature Conservation and Nuclear Safety (funding mark 0325279B). Special thank goes to Kirsten Bartmann and Sabrina Hoenig for laboratory work and data evaluation done during their Master Theses.

Author details

Michael Molenda*, Ferdinand Stöckhert, Sebastian Brenne and Michael Alber

*Address all correspondence to: michael.molenda@rub.de

Ruhr-University Bochum, Germany

References

[1] Mellor, M, & Hawkes, I. Measurement of tensile strength by diametral compression of discs and annuli. Engineering Geology. Elsevier; (1971). , 5(3), 173-225.

[2] Thuro, K, Plinninger, R. J, Zäh, S, & Schütz, S. Scale effects in rock strength properties. Part 1: Unconfined compressive test and Brazilian test. Rock Mechanics-A Challenge for Society.-881 p., Proceedings of the ISRM Regional Symposium Eurock. (2001). , 169-74.

[3] Hudson, J. A, Brown, E, & Rummel, F. The controlled failure of rock discs and rings loaded in diametral compression. International Journal of Rock Mechanics and Mining Sciences & Geomechanics Abstracts. Elsevier; (1972). IN1-IN4, 245-8., 9(2), 241-4.

[4] Bieniawski, Z. T, & Hawkes, I. Suggested Methods for Determining Tensile Strength of Rock Materials. International Journal of Rock Mechanics and Mining Sciences & Geomechanics. Abst, (1978). , 15, 99-103.

[5] Thomée DIBWolski DGK, Plinninger RJ. The Modified Tension Test (MTT)-Evaluation and Testing Experiences with a New and Simple Direct Tension Test. Eurock (2004). Oct 23.

[6] Schmitt, D, & Zoback, M. Infiltration effects in the tensile rupture of thin walled cylinders of glass and granite: Implications for the hydraulic fracturing breakdown equation. International Journal of Rock Mechanics and Mining Sciences & Geomechanics Abstracts. Elsevier; (1993). , 30(3), 289-303.

[7] Selvadurai APSJenner L. Radial Flow Permeability Testing of an Argillaceous Limestone. Ground Water. (2013). , 51, 100-07.

[8] Fairhurst, C, & Hudson, J. A. Draft ISRM suggested method for the complete stress-strain curve for intact rock in uniaxial compression. Int J Rock Mech Min. Elsevier; (1999). , 36(3), 279-89.

[9] Zoback, M, Rummel, F, Jung, R, & Raleigh, C. Laboratory hydraulic fracturing experiments in intact and pre-fractured rock. International Journal of Rock Mechanics and Mining Sciences & Geomechanics Abstracts. Elsevier; (1977). , 14(2), 49-58.

[10] Plinninger, R. J, Wolski, K, Spaun, G, Thomée, B, & Schikora, K. Experimental and model studies on the Modified Tension Test (MTT)-a new and simple testing method for direct tension tests. GeoTechnical Measurements and Modelling-Karlsruhe. (2003). , 2003, 361-6.

Chapter 51

Formation Fracturing by Pore Pressure Drop (Laboratory Study)

Sergey Turuntaev, Olga Melchaeva and Evgeny Zenchenko

Additional information is available at the end of the chapter

http://dx.doi.org/10.5772/56303

Abstract

Pore pressure increase in saturated porous rocks may result in its fracturing and corresponding microseismic event occurrences. Another type of the porous medium fracturing is related with rapid pore pressure drop at some boundary. If the porous saturated medium has a boundary where it directly contacted with fluid under the high pore pressure, and the pressure at that boundary is dropped, the conditions for tensile cracks can be achieved at some distance from the boundary. In the paper, the results of experimental study of fracturing of the saturated porous artificial material due to pore pressure rapid drop are presented. It was found that multiple microfracturing occurred during the pore pressure dropping, which is governed by pore pressure gradient. Repeated pressure drops result in subsequent increase of the sample permeability. The permeability was estimated on the basis of non-linear pore-elasticity equation with permeability dependent on pressure. The implementation of calculations to laboratory experiment data showed significant variation of the porous sample permeability during the initial non-stationary stage of the fluid pressure drop. The acoustic emission activity variation was found to be controlled by pore pressure gradient and changes of the number of potential fractures, which can be activated by the pore pressure gradient. It was found, that the probability distribution of these "potential fractures" could be approximated by a Weibull distribution. A way of solution of the inverse problem of local permeability defining from microseismic activity variation in a particular volume of porous medium was suggested.

1. Introduction

Pore pressure change in saturated porous rocks may result in the rocks deformations and fracturing [1] and corresponding microseismic event occurrences. Microseismicity due to fluid injection is considered in numerous papers [2]. Another type of the porous medium fracturing is related with rapid pore pressure drop at some boundary. The mechanism of such fracturing was considered by [3] as a model of sudden coal blowing and by [4] as a model of volcano eruptions. If the porous saturated medium has a boundary where it directly contacted with fluid under the high pore pressure (in a hydraulic fracture or in a borehole), and the pressure at that boundary is dropped, the conditions for tensile cracks can be achieved at some distance from the boundary as it was shown by [3]. The effective stresses in the solid matrix will change with the speed of elastic waves, while the pore pressure changes will be governed by a kind of pore pressure diffusivity law. The phenomenon was studied by [4] in laboratory experiments with artificial material with high porosity filled by gas.

In the paper, the results of experimental study of fracturing of the porous sample saturated by fluid due to pore pressure rapid drop are presented. It was found that multiple microfracturing occurred during the pore pressure dropping, which is governed by pore pressure gradient variation. The locations of microcracks were found with the help of acoustic pulses recording. It was found that repeated pressure drops result in subsequent increase of the sample permeability. The permeability was estimated on the basis of nonlinear pore-elasticity equation.

A mathematical model of the pore pressure variations was constructed based on pore pressure diffusion equation with diffusivity coefficient dependent on space and time. The implementation of analytical estimates and numerical calculations to laboratory experiment data showed significant variation of the porous sample permeability during the initial non-stationary stage of the fluid pressure drop. The acoustic emission activity variation can be described as a triggering process controlled by pore pressure gradient and changes of the number of potential fractures, which can be activated by the pore pressure gradient. It was found, that the probability distribution of these "potential fractures" could be approximated by a Weibull distribution. It was shown that it is possible to solve the inverse problem of defining local permeability from registered microseismic activity variation in a particular volume of porous medium.

2. Experimental procedure

The diagram and the photo of the experimental setup are shown in Figure 1. The samples were made of quartz sand with grain sizes 0.3…0.4 mm, the sand was cemented by "liquid glass" glue with mass fraction 1%. To prepare the sample, the sand/"liquid glass"/water mixture was tamped to a height 82 mm into a mould with 60 mm in inner diameter. Then it was dried during a week. The sample porosity was 35%, uniaxial unconfined

http://dx.doi.org/10.5772/56303

compression strength was measured to be 2.5 MPa, *p*-wave velocity measured in the sample saturated by oil was 3100 m/s. The initial permeability measured by air blowing through the sample was about 2 D. To prevent the sample displacement during the experiments, a plastic ring was placed between lower end of the sample and the mould lid (see Figure 1). The upper end of the sample contacted directly with the mould upper lid. After vacuumization, the mould with sample was filled by mineral oil, which penetrates into the sample. Pressure in the mould was increased by means of oil injection through the bottom nipple up to 10 MPa and then discharged with the help of solenoid valve connected to the nipple. Injection-pressure drop cycles were repeated up to 40 times. Pressure release rate was controlled by a hydraulic resistor placed prior to the valve. The sample loading was related to oil pressurization at the bottom of the sample, there was no additional load.

Pore pressure transducers and acoustic emission (AE) transducers (of piezoceramic type) were mounted into upper and bottom lids of the mould, as it is shown in Figure 1. AE data were digitized with sampling frequency 2.5 MHz, the fluid pressure – with sampling frequency 50 kHz. The acoustic emission records were synchronized with the pressure records. Locations of AE events were estimated on the basis of measured p-wave velocity and onset time difference of AE pulses. The absolute peak amplitude of AE pulse was assumed as the amplitude of AE event. All localized AE events were characterized by onset time, location (distance from open boundary of the sample), and amplitude.

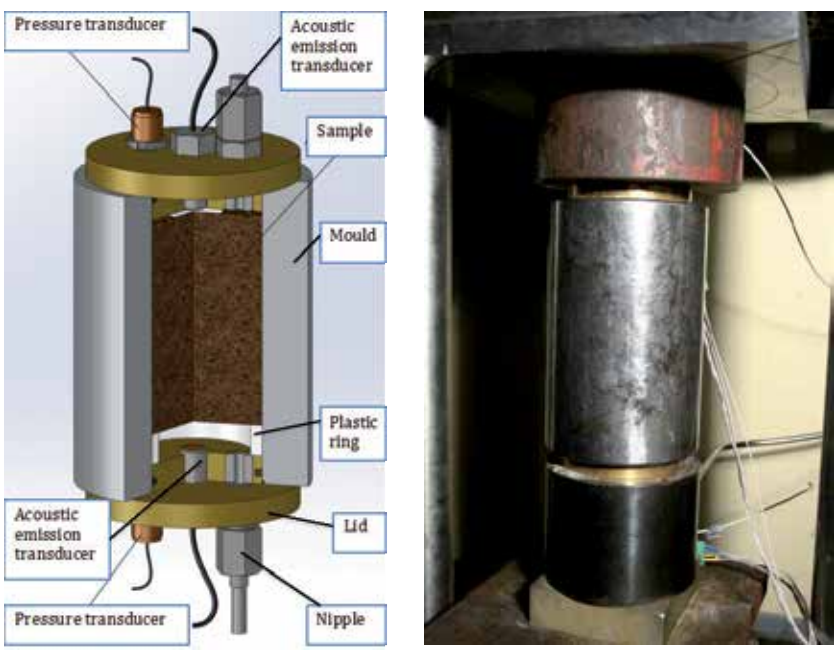

Figure 1. A diagram (left) and a photo of the laboratory setup.

3. Results

Figure 2 shows typical waveforms of AE pulses, registered by opposite transducers. These waveforms had onsets with the same signs as well as with opposite signs. In case of tensile fractures it can be explained by the sample unloading in the processes of pore pressure drop and fracturing, so at least one or both boundaries of the tensile fracture were moving in the open end direction. After some time, the onsets of the AE pulses registered at the closed end became mainly positive. AE pulse amplitudes became lower with time.

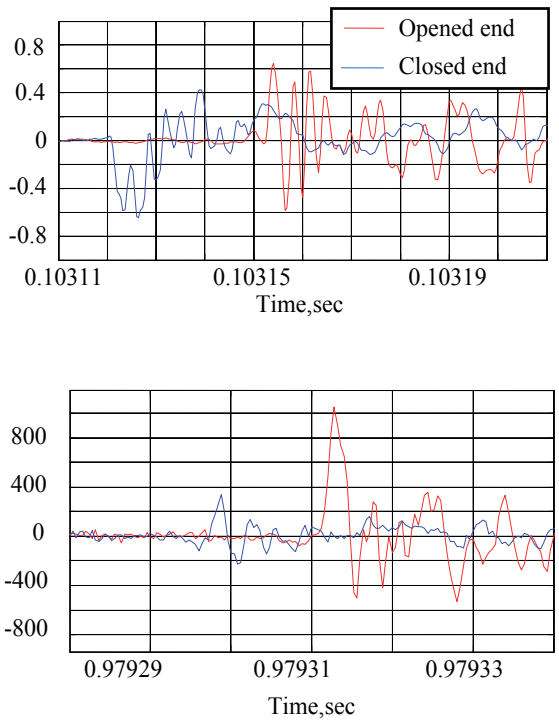

Figure 2. Examples of waveforms, registered at opposite sides of the sample. Amplitude is in arbitrary units.

Distributions of the AE pulse amplitudes summarized by 5 mm intervals along the sample are shown in Figure 3 for experiments after the 1st and 7th pressure drops. One can see, that microfracturing is spreading from the open end to the closed end with repeated pressure drops, and that maximal amplitudes registered at some distance from the opened end.

Variations of AE rate (the number of AE pulses per 0.1sec) are shown in Figure 4. The AE almost stops after 2 sec from the beginning of the pressure drop. The number of AE pulses increases with every next pressure drop, meanwhile the number of pulses with high amplitudes diminishes with next pressure drops. The last result can be explained by diminishing of pressure gradient due to the sample permeability increase in the course of subsequent fracturing of the sample.

http://dx.doi.org/10.5772/56303

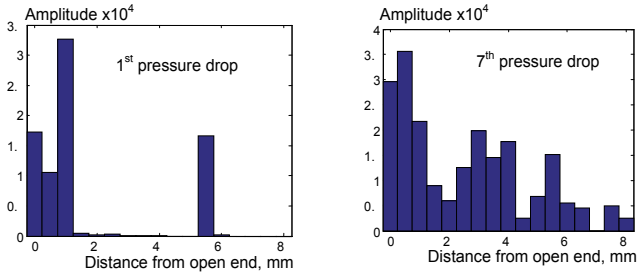

Figure 3. Distributions of the AE pulse amplitudes along the sample in two experiments.

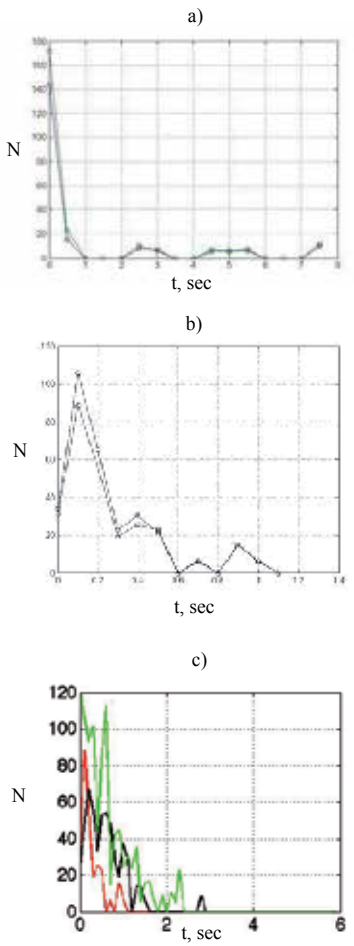

Figure 4. AE activity variations: a,b – registered at open (upper curve) and closed ends (lower curve) of the sample in experiments 1 and 6; c – registered in three different experiments (see Fig.5 legend)

Fluid pressure variations with time are show in Figure 5 for both open and close ends of the sample. Initially, the pore pressure decreases rapidly (in 0.1 sec), after that it slowly diminishes to atmospheric pressure. The AE rate is significant in first 2 sec, some of acoustic pulses occurred in up to 10 sec (Figure 4). The pressure gradient (estimated as pressure difference divided by the sample length) is shown in Figure 6. The prolongation of the pressure gradient maximal values is in agreement with AE maximal meanings.

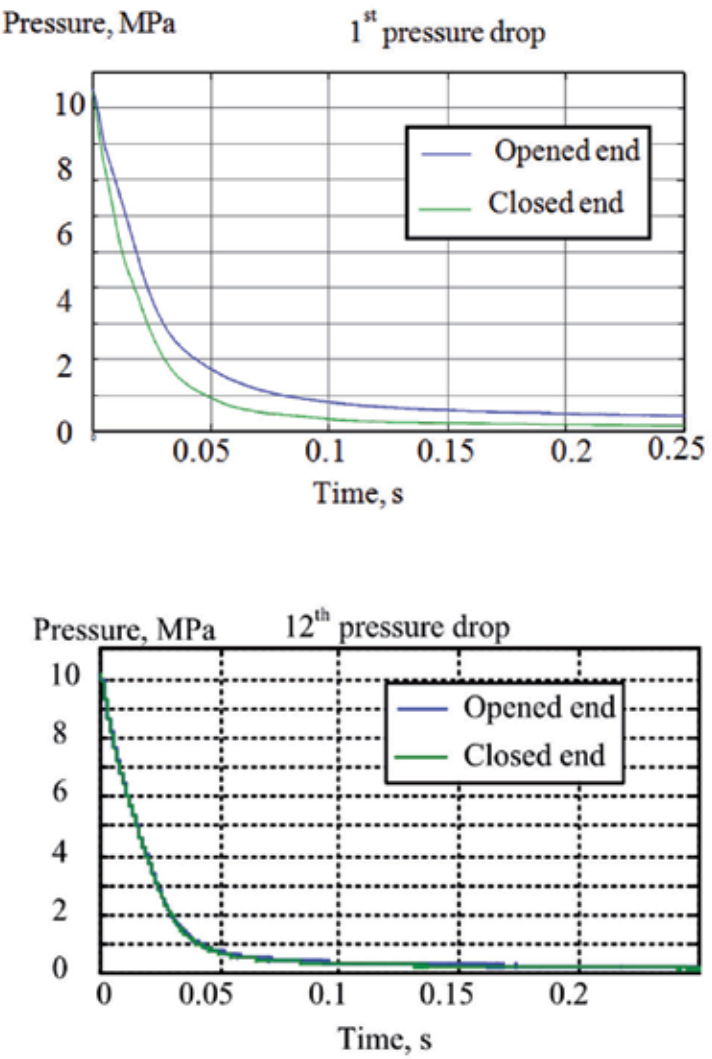

Figure 5. Fluid pressure vs. time registered at the two ends of the sample

http://dx.doi.org/10.5772/56303

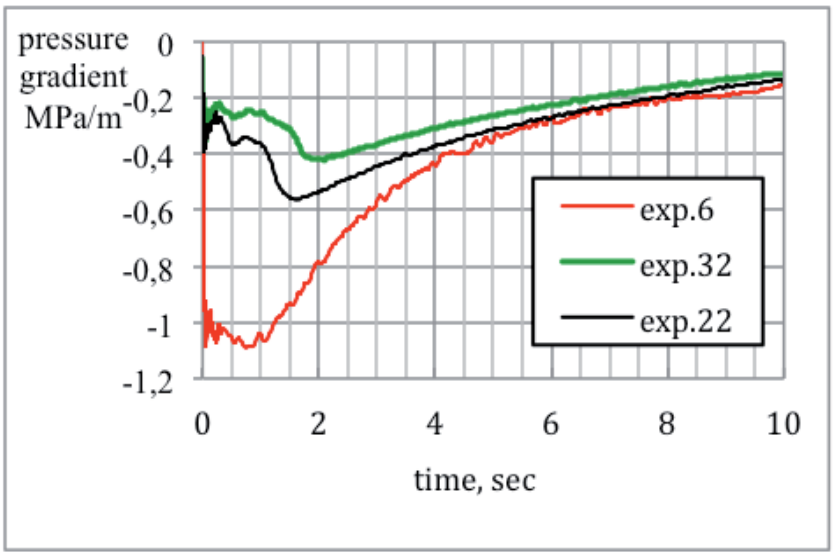

Figure 6. Linear estimation of the fluid pressure gradient for three experiments

4. Discussion

Shapiro et al. [5] proposed to consider an evolution of hydraulically induced microseismic event hypocenter locations as a diffusion process controlled by pore pressure diffusion in poro-elastic medium caused by fluid injection. In the presented experiments the fluid pressure decreased with time and AE maximum was registered when the pressure was dropped from its maximum. Let us compare AE variation and variation of pressure difference (Figure 4 and Figure 6). One can see that the AE began when the absolute value of the fluid pressure difference started to increase, and AE stops when the fluid pressure difference started to decrease. It is clear from physical point of view, that to produce tensile fracturing one should have tensile force, which could appear only in case of enough high pressure gradient.

Let us now try to estimate dynamic permeability variation during the fluid pressure drop. For it, we used fluid pressure data registered at the open end of the sample and calculated the fluid pressure at the closed end of the sample by means of simple pore-elastic equation (Schelkachev, [6]) for small time intervals (0.01 sec) and one-dimensional isotropic homogeneous case:

$$\frac{\partial p}{\partial t} = D\frac{\partial^2 p}{\partial x^2}$$

where D is hydraulic diffusivity

$$D = \frac{k}{\mu_0 \beta m_0}$$

where k is permeability, β is an effective compressibility of the porous medium, μ_0 – viscosity, m_0 – initial porosity. Initial condition:

$$p(x, 0) = p_0$$

A zero fluid rate Q at the closed end of the sample and registered pressure at the open end were taken as boundary conditions:

$$\frac{\partial p}{\partial x}(t, l) = 0$$

$$p(t, 0) = p_1(t)$$

Then we compared results of the calculations with experimental data and vary coefficient of diffusivity to obtain the best coincidence between calculated and registered pressure. The procedure was repeated for all the time of experiment. There was no difference between experimental and calculated pressures, obtained by that manner (Figure 7). The dependence of estimated permeability on fluid pressure is shown in Figure 8. The final permeability values after the pressure drop are shown in Table 1.

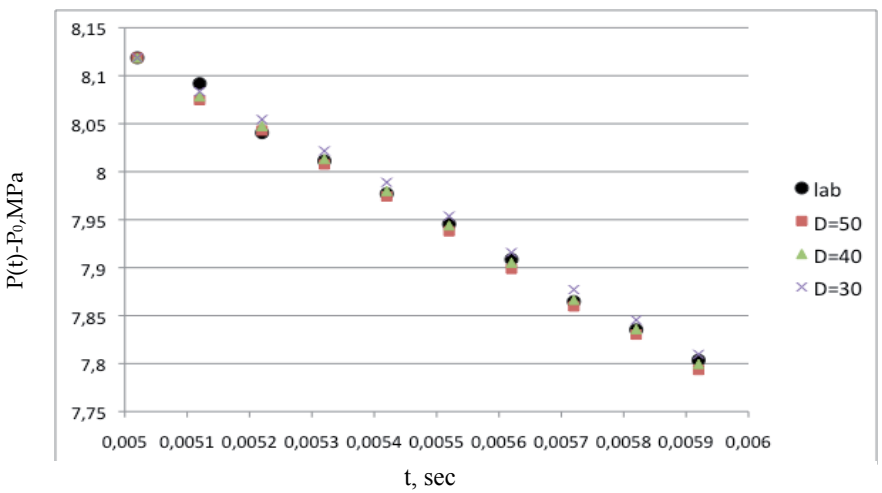

Figure 7. Measured (lab) and calculated for several diffusivity coefficients differential pore pressure.

http://dx.doi.org/10.5772/56303

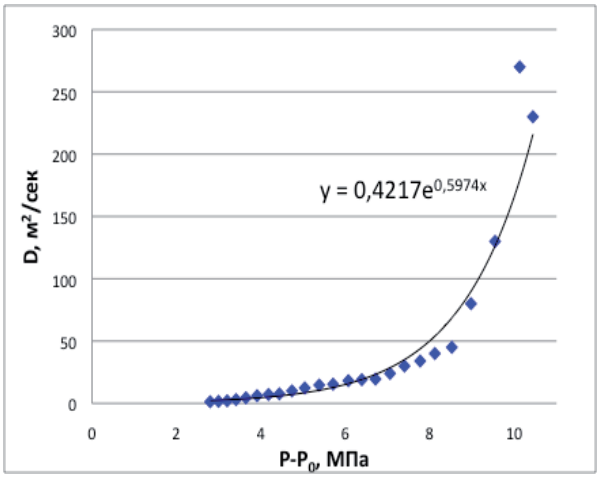

Figure 8. Estimation of the permeability dependence on pore fluid pressure

Pressure drop #	6	22	32
Permeability *k*, D	4.9	7.4	9.5

Table 1. Permeability estimated by pore pressure difference diminishing in time.

To find AE relation with the pore pressure gradient the following assumption can be used [5, 7]:

- AE event occurred when the pore pressure gradient reaches some critical value;
- The critical value varies spatially and can be described by a probability distribution.

One can suggests that the critical value distribution can be described by Weibull distribution which is often used to describe fragment size distributions in fractured rock [8];

$$N((dp/dx)^*) = N * ba^{-b}((-dp/dx)^*)^{b-1} e^{\left(\frac{(dp/dx)^*}{a}\right)^b}, \quad (1)$$

where parameters a and b are the scale and the shape parameters, respectively, $(dp/dx)^*$ is the critical value of pore pressure gradient.

Variation of AE rate in time can be described with the help of Weibull distribution

$$N(t) = N * \frac{c}{t}\left(\frac{t}{t_0}\right)^c e^{-\left(\frac{t}{t_0}\right)^c} \quad (2)$$

The parameters of the distribution calculated to fit experimental data of the experiment 22 (Figure 9) are $N^*=120$, $c=1,7$, $t_0=0,6$. The coupled use of distribution (2) and pore pressure measurement allows to calculate parameters of the distribution (1) to best fit experimental data of $(dp/dx)^*(t)$.

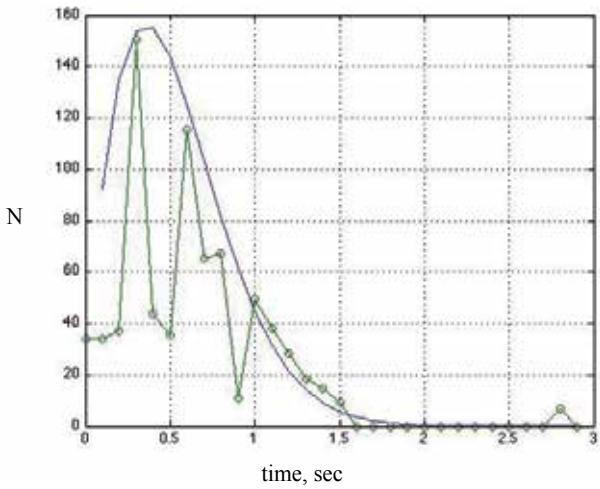

Figure 9. Variation of AE rate and fitted Weibull function (experiment 22).

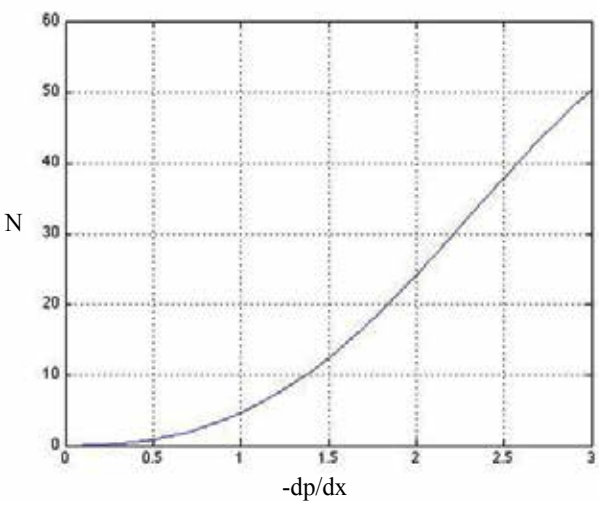

Figure 10. Dependence of AE event numbers on pore pressure gradient calculated in accordance with relation (1) with parameters of best fit curve shown in Figure 9.

http://dx.doi.org/10.5772/56303

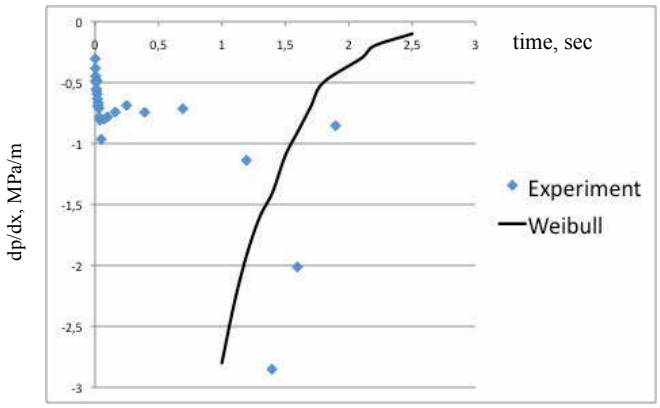

Figure 11. Experimental and calculated pore pressure gradient variation in time (experiment 22).

The comparison of experimental pore pressure gradient (estimated as pressure difference between two points of pressure measurements) and critical pore pressure gradient calculated based on AE variations is shown in Figure 11. Experimental and calculated data start to be in agreement when the fluid pressure become respectively low and the sample permeability is more or less constant.

So, if one gets to know variation of AE (or microseismic activity in real case) in time and the relation between number of events and critical values of pore pressure gradient is known, it is possible to calculate the porous medium permeability.

Let's now consider once more one-dimensional pore-elasticity equation with constant coefficient of diffusivity

$$\frac{\partial p}{\partial x} = D\frac{\partial^2 p}{\partial x^2} \tag{3}$$

The solution can be written as

$$p(x,t) = A + \sum_{i=0}^{\infty} C_i e^{-\mu_i^2 Dt} \sin(\mu_i x) + \sum_{i=0}^{\infty} B_i e^{-\mu_i^2 Dt} \cos(\mu_i x) \tag{4}$$

Use of initial and boundary conditions of the experiment (which were described early) the solution can be written as

$$p(x,t) = p_{atm} + A(x)\sum_{i=0}^{\infty} \frac{1}{\mu_i^2} e^{-\mu_i^2 Dt} \cos(\mu_i x) \tag{5}$$

where

$$A(x)=\frac{p(x,\,0)-p_{atm}}{\sum_{i=0}^{\infty}\frac{1}{\mu_i^{\,2}}\cos(\mu_i x)},\ \mu_i=\pi i+\frac{\pi}{2}$$

The series

$$\sum_{i=0}^{\infty}\frac{1}{\mu_i^{\,2}}\cos(\mu_i x)$$

converges and majorizes the series in (5). Let's consider a function $f(x)$:

$$f(x+T)=f(x),\quad T=4;$$
$$f(-x)=f(x);$$
$$\forall\, x\in[0;2]: f(x)=\frac{1-x}{2}.$$

For $f(x)$ defined at $[-l,l]$ with period $2l$ which satisfies the Dirichlet conditions, the Fourier series expansion looks like

$$f(x)=\frac{a_0}{2}+\sum_{n=1}^{\infty}\left(a_n\cos\frac{\pi nx}{l}+b_n\sin\frac{\pi nx}{l}\right),$$

$$a_n=\frac{1}{l}\int_{-l}^{l}f(x)\cos\frac{\pi nx}{l}dx$$

$$b_n=\frac{1}{l}\int_{-l}^{l}f(x)\sin\frac{\pi nx}{l}dx$$

The function f(x) is even, so

$$b_n=0$$

$$a_0=\frac{1}{2}2\int_0^2\frac{1-x}{2}dx=0$$

$$a_n=\frac{1}{2}2\int_0^2\frac{1-x}{2}\cos\left(\frac{\pi nx}{2}\right)dx=\frac{1}{2}\left(\left[(1-x)\frac{2}{\pi n}\sin\left(\frac{\pi nx}{2}\right)\right]_0^2-\int_0^2(-1)\frac{2}{\pi n}\sin\left(\frac{\pi nx}{2}\right)dx\right)=$$

$$=\frac{1}{\pi n}\int_0^2\sin\left(\frac{\pi nx}{2}\right)dx=\frac{2}{\pi^2n^2}(-1)\cos\left(\frac{\pi nx}{2}\right)_0^2=\frac{2}{\pi^2n^2}(1-(-)_1)$$

$$f(x)=\sum_{n=1}^{\infty}\frac{2}{\pi^2n^2}(1-(-1)^n)\cos\left(\frac{\pi nx}{2}\right)$$

Substitution $n=2k+1$ (for even n $f(x)$=0)

http://dx.doi.org/10.5772/56303

$$f(x)=\sum_{k=0}^{\infty}\frac{4}{\pi^2(2k+1)^2}\cos(\frac{\pi(2k+1)x}{2})=\sum_{k=0}^{\infty}\frac{1}{(\pi k+\frac{\pi}{2})^2}\cos((\pi k+\frac{\pi}{2})x)$$

$$A(x)=\frac{p(x,\,0)-p_{atm}}{\sum_{i=0}^{\infty}\frac{1}{\mu_i^2}\cos(\mu_i x)},\ \mu_i=\pi i+\frac{\pi}{2}$$

so:

$$A(x)=\frac{p(x,0)-p_{atm}}{\frac{1}{2}(1-x)} \tag{6}$$

To estimate the permeability one can adopt that

$$\frac{\partial A}{\partial x}(x)=0$$

because in considered experiments

$$\frac{\partial p}{\partial x}(x,\,0)=0$$

and denominator in (6) is almost constant when x is small. In that case:

$$\frac{\partial p}{\partial x}=-A(x)\sum_{i=0}^{\infty}\frac{1}{\mu_i}e^{-\mu_i^2 Dt}\sin(\mu_i x) \tag{7}$$

The diminishing part of the pore pressure gradient dependence on time (which is shown by ellipse in Figure 12) can be approximated by exponential function be^{at} (as it is shown in Figure 13), which corresponds to i=0 in (7), and the diffusivity coefficient can be estimated as

$$D=\frac{a}{(\pi/2)^2}$$

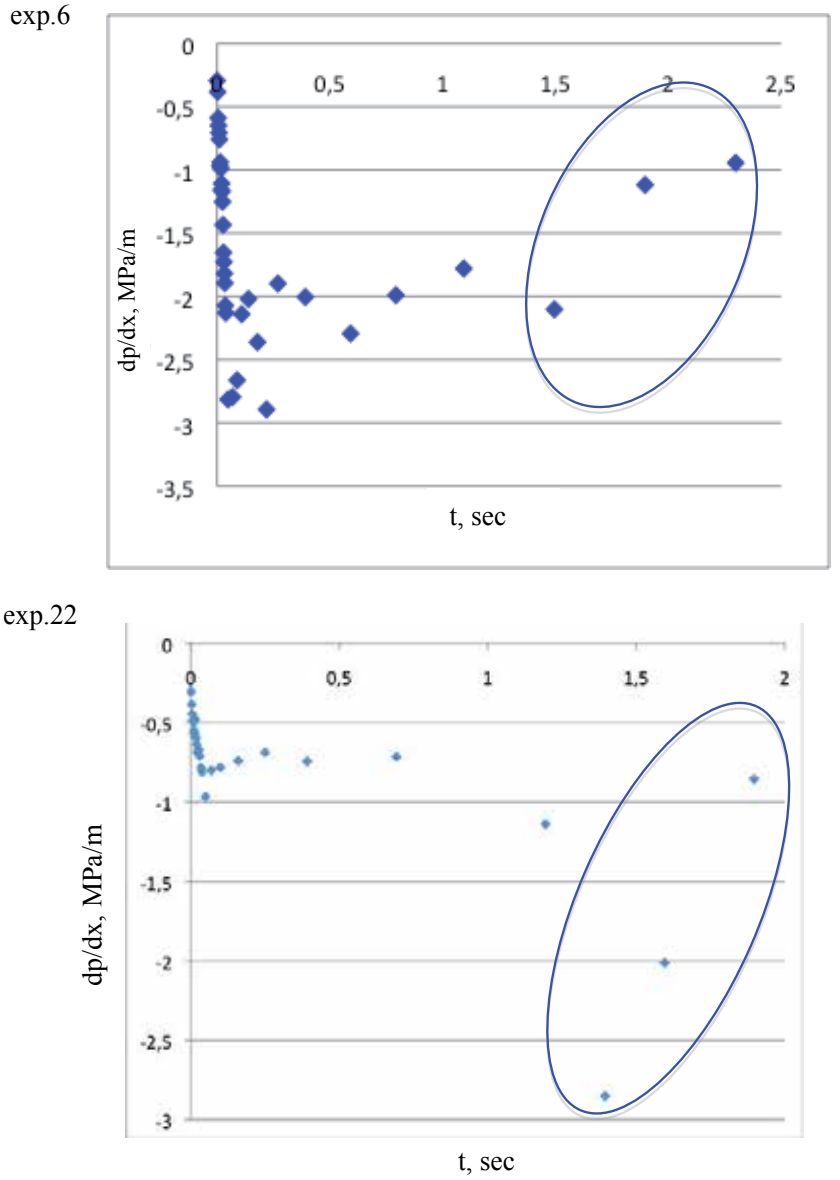

Figure 12. Variation of pressure difference in time. The ellipse shows data used for permeability calculation.

http://dx.doi.org/10.5772/56303

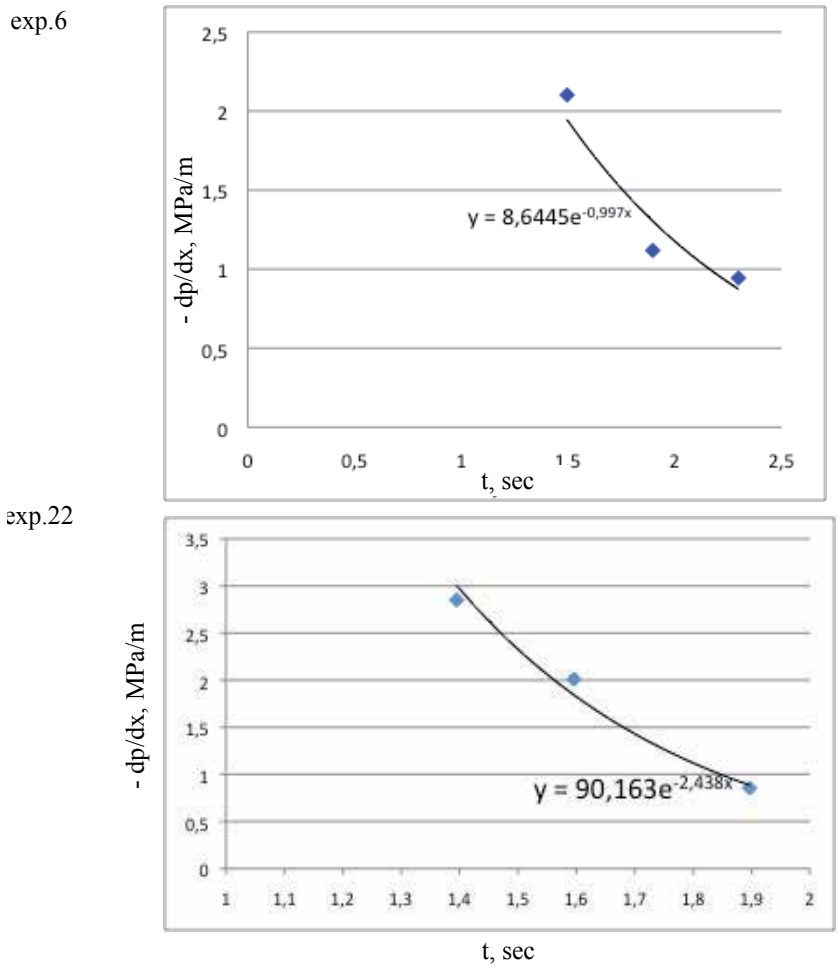

Figure 13. Approximation of pressure difference variation in time by exponential low.

The results of the permeability estimations are shown in Table 2.

Pressure drop #	6	22	32
D, m^2/sec	0.4	0.99	0.785
k, D	3.8	9.2	7.3

Table 2. Estimated values of diffusivity coefficient and permeability

The obtained values of permeability were compared with permeability estimated by permeability dependence on pore pressure drop (Table 1) and with permeability obtained with the help of r-t method suggested by Serge Shapiro and colleagues ([5, 9-11]). Diagram of distance

from the sample boundary dependence on time of AE event occurrences is shown in figure 14. An envelope curve.

$$r = \sqrt{4\pi D(t - t_s)},$$

which is a solution of one-dimensional porous elasticity equation, is shown in Figure 14 by red curve. It should be noted that the sample length was 83 mm, which is shown in the diagram by dotted line. The number of registered AE events was not high, it restricts an accuracy of the method.

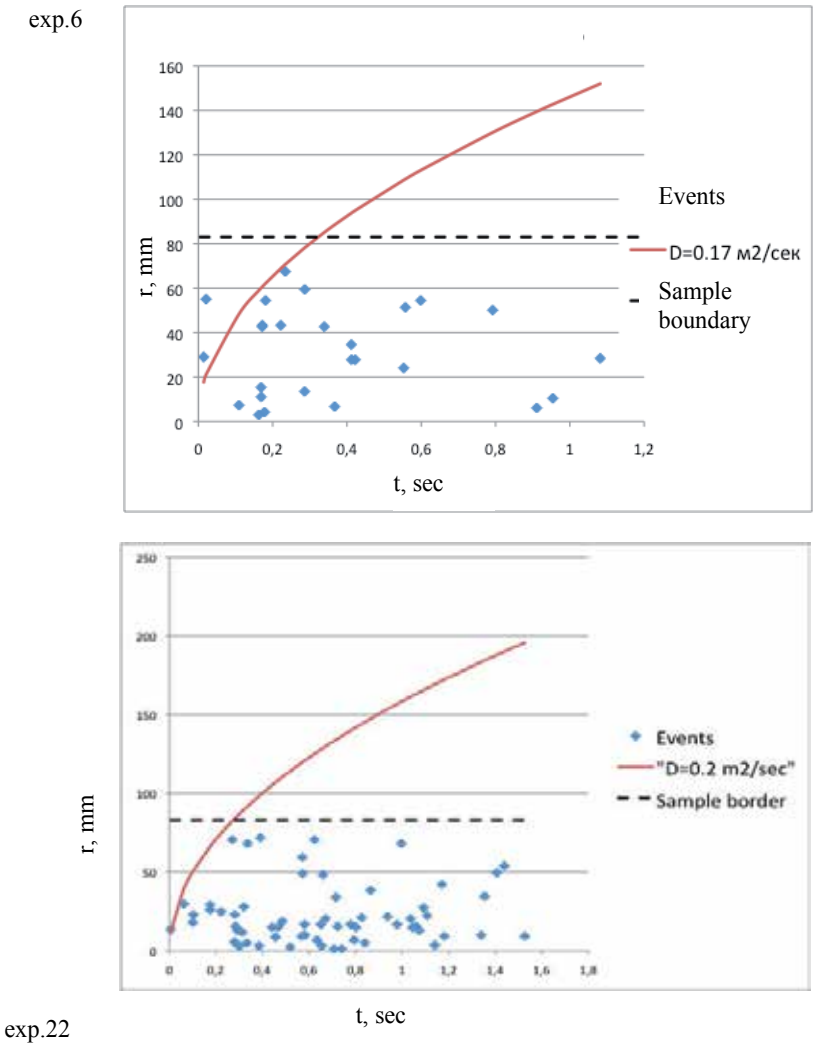

Figure 14. Dependence of distance from the sample boundary on time of AE event occurrences.

http://dx.doi.org/10.5772/56303

If we compare Table 1, Table 2 and Table 3 we will see, that the permeability based on AE variation in time estimation gives values which are close to that obtained using data on pore pressure drop; nevertheless, r-t method gives values which are not contradict other results but differ from them significantly.

Experiment #	2	6	22	32
D, m^2/sec	**0.003**	**0.17**	**0.2**	**2**
k, D	**0.03**	**1.6**	**1.9**	**18.6**

Table 3. Permeability estimated by r-t method

5. Conclusions

In the paper, the results of experimental study of saturated porous sample fracturing due to pore pressure rapid drop are discussed. It was found, that acoustic emission AE (corresponded to microfracturing) was spreading from the end of the pressure drop to the closed end of the sample, and that maximal number of AE events was registered at some distance from the opened end.

The number of AE pulses increased with every next pressure drop, meanwhile the number of pulses with high amplitudes diminished. The prolongation of the pressure gradient maximal values is in agreement with AE maximal rate.

It was found that multiple microfracturing occurred during the pore pressure drop; the microfractiring is governed by pore pressure gradient.

The model of AE relation with the pore pressure gradient was considered based on the following assumptions: AE event occurred when the pore pressure gradient reaches some critical value; the critical value varies and can be described by Weibull distribution, which is often used to describe fragment size distributions in fractured rocks.

Permeability variation during the fluid pressure drop was estimated by means of fluid pressure data and pore-elastic equation solution for small time intervals (0.01 sec). It was found that the sample permeability is high in initial stage of the pressure discharge and decrease during pore pressure drop.

It is shown that if the change in microseismic activity in time is measured, the distribution of the critical pressure gradient is known for the considered material and the boundary conditions are given (for example, the change in pressure in the well), it is possible to calculate the pressure gradient, and on this basis, the permeability of the porous medium.

The study showed possibility to solve an inverse problem of defining permeability by registering microseismic activity variation in particular volume of porous medium alongside with pore pressure measurements at some point.

Acknowledgements

The idea of the study was suggested by Dimitry Chuprakov. The authors wish to acknowledge the generous support of Russian Foundation for Basic Research (RFBR project # 10-05-00638) and of the Russian Academy of Sciences Presidium Program #4.

Author details

Sergey Turuntaev[1*], Olga Melchaeva[2] and Evgeny Zenchenko[1]

*Address all correspondence to: stur@idg.chph.ras.ru

1 Institute of Geosphere Dynamics of Russian Academy of Sciences (IDG RAS), Moscow, Russia

2 Moscow Institute of Physics and Technology, Moscow, Russia

References

[1] Maury, V. et D. Fourmaintraux. Mecanique des roches appliquee aux problemes d'exploration et de production petrolieres. Societe Nationale Elf Aquitaine (Production). Boussens. (1993).

[2] Maxwell, S. Microseismic: Growth born from success. The Leading Edge (2010). , 3-338.

[3] Khristianovich, S. A. Transient liquid and gas flow in porous medium under abrupt pore change in time and high rate gradient. Journal of Mining Science (1985). , 1-18.

[4] Alidibirov, M, & Panov, V. Magma fragmentation dynamics: experiments with analogue porous low- strength material. Bull Volcanol. (1998). , 59-481.

[5] Shapiro, S. A, Rothert, E, Rath, V, & Rindschwentner, J. Characterization of fluid transport properties of reservoirs using induced microseismicity: Geophysics, (2002). , 67-212.

[6] Schelkatchev, V. N. Fundamentals and applications of nonstationary filtration theory: Moscow, Neft i gaz, (1995).

[7] Turuntaev, S. B, Eremeeva, E. I, & Zenchenko, E. V. Laboratory study of microseismicity spreading due to pore pressure change. Journal of Seismology (2012). DOIs10950-012-9303-x.

[8] Tsvetkov, V. M, Lukishov, B. G, & Livshits, L. D. Fragment formation in crushing a brittle medium under hydrostatic compression. Journal of mining science, (1979). DOI:10.1007/BF02539986., 15(3), 228-232.

[9] Shapiro, S. A, Dinske, C, & Rothert, E. Hydraulic-fracturing controlled dynamics of microseismic clouds. Geophysical Research letters (2006). L14312.

[10] Dinske, C, Shapiro, S. A, & Rutledge, J. T. Interpretation of microseismicity resulting from gel and water fracturing of tight gas reservoirs. Pure Applied Geophysics (2009). DOI:s00024-009-0003-6.

[11] Grechka, V, Mazumdar, P, & Shapiro, S. A. Predicting permeability and gas production of hydraulically fractured tight sands from microseismic data. Geophysics (2010). BB10, doi:, 1.

Section 17

Optimizing Stimulation of Fractured Reservoirs

Chapter 52

Optimizing Hydraulic Fracturing Treatment Integrating Geomechanical Analysis and Reservoir Simulation for a Fractured Tight Gas Reservoir, Tarim Basin, China

Feng Gui, Khalil Rahman, Daniel Moos,
George Vassilellis, Chao Li, Qing Liu, Fuxiang Zhang,
Jianxin Peng, Xuefang Yuan and Guoqing Zou

Additional information is available at the end of the chapter

http://dx.doi.org/10.5772/56384

Abstract

A comprehensive geomechanical study was carried out to optimize stimulation for a fractured tight gas reservoir in the northwest Tarim Basin. Conventional gel fracturing and acidizing operations carried out in the field previously failed to yield the expected productivity. The objective of this study was to assess the effectiveness of slickwater or low-viscosity stimulation of natural fractures by shear slippage, creating a conductive, complex fracture network. This type of stimulation is proven to successfully exploit shale gas resources in many fields in the United States.

A field-scale geomechanical model was built using core, well log, drilling data and experiences characterizing the in-situ stress, pore pressure and rock mechanical properties in both overburden and reservoir sections. Borehole image data collected in three offset wells were used to characterize the in-situ natural fracture system in the reservoir. The pressure required to stimulate the natural fracture systems by shear slippage in the current stress field was predicted. The injection of low-viscosity slickwater was simulated and the resulting shape of the stimulated reservoir volume was predicted using a dual-porosity, dual-permeability finite-difference flow simulator with anisotropic, pressure-sensitive reservoir properties. A hydraulic fracturing design and evaluation simulator was used to model the geometry and conductivity of the principal hydraulic fracture filled with proppant. Fracture growth in the presence of the lithology-based stress contrast and rock properties was computed, taking into account leakage of the injected fluid into the stimulated reservoir volume

predicted previously by reservoir simulation. It was found that four-stage fracturing was necessary to cover the entire reservoir thickness. Post-stimulation gas production was then predicted using the geometry and conductivity of the four propped fractures and the enhanced permeability in the simulated volume due to shear slippage of natural fractures, using a dual-porosity, dual-permeability reservoir simulator.

For the purpose of comparison, a conventional gel fracturing treatment was also designed for the same well. It was found that two-stage gel fracturing was sufficient to cover the whole reservoir thickness. The gas production profile including these two propped fractures was also estimated using the reservoir simulator.

The modeling comparison shows that the average gas flow rate after slickwater or low-viscosity treatment could be as much as three times greater than the rate after gel fracturing. It was therefore decided to conduct the slickwater treatment in the well. Due to some operational complexities, the full stage 1 slickwater treatment could not be executed in the bottom zone and treatments in the other three zones have not been completed. However, the post-treatment production test results are very promising. The lessons learned in the planning, design, execution and production stages are expected to be a valuable guide for future treatments in the same field and elsewhere.

1. Introduction

Following the success in exploiting shale gas resources by multi-stage hydraulic fracturing with slickwaters or low-viscosity fluid (i.e., linear gel) in horizontal wells in North America, there has been a lot of interest in applying this technique to other regions and other types of tight reservoirs. This is due in part to the fact that conventional gel fracturing treatments have been less successful in some naturally fractured reservoirs due to excessive unexpected fluid loss and proppant bridging in natural fractures, leading often to premature screen-outs. Additionally, the high-viscosity gel left inside the natural fractures causes the loss of virgin permeability of the reservoir in the case of inefficient gel breaking.

However, the challenge for doing this is that the physical mechanism responsible for this kind of stimulation is yet to be fully understood and a standard work flow for design and evaluation is yet to be developed. Furthermore, industry so far mainly relies on performance analogs to improve understanding of each shale play, and thus it usually takes years to advance up the learning curve for determining which factors best affect well production [1].

Currently, the general opinion on the mechanism leading to the success of waterfrac in shale gas reservoirs is that a complex fracture network is created by stimulation of pre-existing natural fractures. Although it is difficult to observe the processes acting during stimulation, microseismic imaging has enabled us to understand that both simple, planar fractures and complex fracture networks can be created in hydraulic fracture stimulations under different settings [2]. Fracture complexity is thought to be enhanced when pre-existing fractures are oriented at an angle to the maximum stress direction, or when both horizontal stresses and

http://dx.doi.org/10.5772/56384

horizontal stress anisotropy are low, because these combinations of stress and natural fractures allow fractures in multiple orientations to be stimulated [3]. The result of stimulation therefore depends both on the geometry of the pre-existing fracture systems and on the in-situ stress state. It is now generally accepted that stimulation in shale gas reservoirs occurs through a combination of shear slip and opening of pre-existing (closed) fractures and the creation of new hydraulic (tensile) fractures [4-6]. In wells that are drilled along the minimum horizontal stress (S_{hmin}) direction, stimulation generally creates a primary radial hydraulic fracture that is perpendicular to S_{hmin}. Then, pressure changes caused by fluid diffusion into the surrounding rock and the modified near-fracture stress field induced by fracture opening cause shear slip on pre-existing natural fractures. If the horizontal stress difference is small enough, new hydraulic fractures perpendicular to the main fracture can open. Each slip or oblique opening event radiates seismic energy, which, if the event is large enough, can be detected using downhole or surface geophones.

Founded on the idea that productivity enhancement due to stimulation results not just from creation of new hydraulic fractures but also from the effect of the stimulation on pre-existing fractures (joints and small faults), a new workflow dubbed "shale engineering", was established by combining surface and downhole seismic, petro-physical, microseismic, stimulation, and production data [7, 8]. In this new workflow (Figure 1), the change in flow properties of natural fractures is predicted using a comprehensive geomechanical model based on the concept of critically stressed fractures [9-11]. Existing reservoir simulation tools can then be used to model the hysteresis of fracture flow properties that result from the microseismically detectable shear slip, which is critical to the permanent enhancement in flow properties and increased access to the reservoir that results from stimulation. The primary hydraulic fracture created and propped during the stimulation can be modeled using conventional commercial hydraulic fracture models by taking into account fluid leaked into natural fractures in the surrounding region. The propped conductivity is estimated using laboratory-based proppant conductivity data adjusted for the proppant concentration in the fracture. The propped main fracture model and the reservoir model with stimulated natural fracture properties can then be integrated into production simulators to predict production after the slickwater hydraulic fracturing treatment. When available, microseismic data can be used to help define the network of stimulated natural fractures that comprises the stimulated reservoir volume (SRV).

Although this new workflow was developed based on experiences in shale gas reservoirs, we believe it can also be applied to any unconventional reservoir requiring stimulation that has pre-existing natural fractures. Both Coal Bed Methane (CBM) and fractured tight gas reservoirs are examples of where this approach could be applied. In this paper, we will illustrate the workflow using the results of a study conducted in a fractured tight gas reservoir in the Kuqa Depression, Tarim Basin.

2. Project background

The project discussed in this paper was initiated to investigate various methods and practices to improve the economics of the field. Conventional gel fracturing had been tested in a few

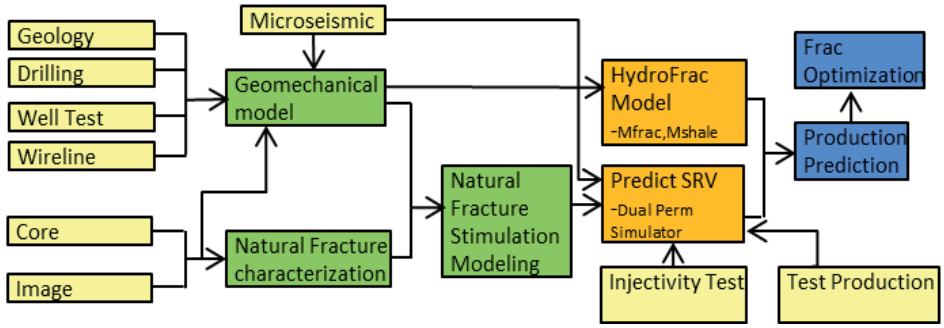

Figure 1. Workflow for predicting the complex fracture network developed by stimulating fractured reservoirs using low-viscosity fluid.

wells with disappointing results. One fault block (see Figure 2) was chosen as the target of a pilot study that included building a geomechanical model, optimizing hydraulic fracturing design, assessing the stability of faults near the target well, and (although it is not discussed here) analyzing wellbore stability for drilling horizontal wells. Three vertical wells were drilled. D2 and D3 are near the crest of the structure and D1 is ~ 2.5-3 km to the west. The main target is Cretaceous tight sandstone occurring at ~5300m to ~6000m depth. Reservoir rock is composed of fine sandstone and siltstones interlayered with thin shales. Average reservoir porosity is ~7% and average permeability is ~0.07 mD. The gross reservoir thickness is ~180-220m in this fault block. Wells D1 and D2 were completed by acidizing and gel fracturing; test production was ~15-27 $\times 10^4 m^3/d$. The objective of this project was to optimize hydraulic fracturing design for Well D3 based on the geomechanical analysis and investigate whether it is better to conduct slickwater treatment in the D3 well to stimulate and create a complex fracture network or utilize conventional two-wing gel fracturing.

Comprehensive datasets were available for all three wells including drilling experiences, wireline logs, image data, mini-fracs and well tests. Laboratory tests were also conducted on cores from well D2 to estimate the rock mechanical properties of reservoir rocks.

3. Geomechanical model

A geomechanical model includes a description of in-situ stresses and of rock mechanical and structural properties. The key components include three principal stresses (vertical stress (S_v), maximum horizontal stress (S_{Hmax}) and minimum horizontal stress (S_{hmin})), pore pressure (Pp) and rock mechanical properties, such as elastic properties, uniaxial compressive strength (UCS) and internal friction. The relative magnitude of the three principal stresses and the consequent orientation of the most likely slipping fault or fracture define the stress regime to be normal faulting ($S_v > S_{Hmax} > S_{hmin}$), strike-slip faulting ($S_{Hmax} > S_v > S_{hmin}$) or reverse faulting ($S_{Hmax} > S_{hmin} > S_v$). The horizontal stresses are highest relative to the vertical stress in a reverse faulting regime and lowest relative to the vertical stress in a normal faulting regime. Hydraulic fractures are vertical and propagate in the direction of the greatest horizontal stress in a strike-

http://dx.doi.org/10.5772/56384

slip or normal faulting regime. In a reverse faulting stress regime in which S_v is the minimum stress, hydrofractures are horizontal. These different stress regimes also have consequences for the pressure that is required to open a network of orthogonal hydrofractures by stimulation. In places where the horizontal stresses are low and nearly equal, a relatively small excess pressure above the least stress may be required to open orthogonal fractures. Where the horizontal stress difference is larger, a larger excess pressure is required to open orthogonal fractures. Where the least stress is only slightly less than the vertical stress, weak horizontal bed boundaries and mechanical properties contrasts between layers may allow opening during stimulation of horizontal bedding ("T-fractures").

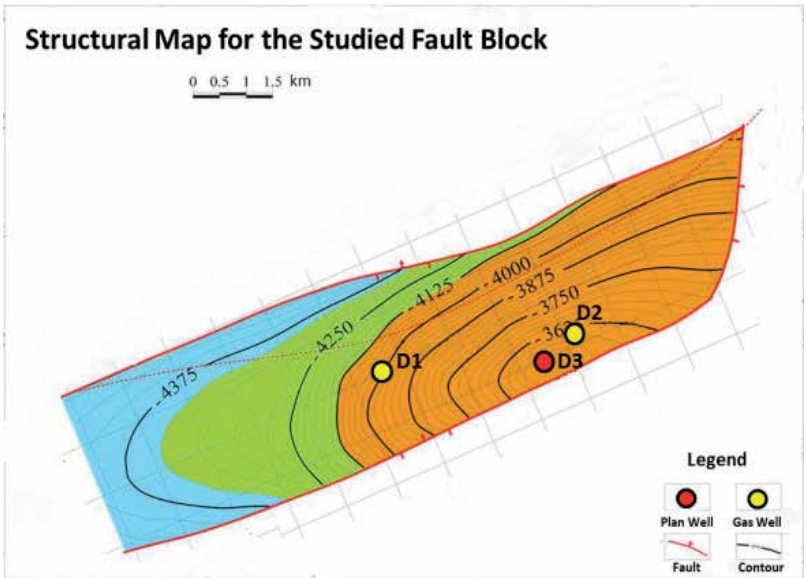

Figure 2. Structural map showing the offset well locations

Except for the magnitude of S_{Hmax}, other components of the geomechanical model can be determined using borehole data by reviewing a few representative wells in the field. Vertical stress is calculated by integrating formation density, which is obtained from wireline logs. The magnitude of S_v across this fault block is in a similar range. Pore pressure was constrained, mainly by referencing direct measurement data and drilling experiences. This is due to the complex tectonic history. Conventional under-compaction approaches for pore pressure estimation may not apply in the study area. Evidence for this is the over-compacted density profile. In addition, due to the complex lithology changes the log response with depth may reflect lithology changes rather than pressure variation. Well test data from D1 and D2 showed that the reservoir pressure is ~88-90 MPa, an equivalent pressure gradient of ~1.6-1.7 SG, which is abnormally over-pressured.

Rock mechanical laboratory tests were conducted on cores from the sandstone reservoirs and the interlayered shales in the D2 well, and the results were used to constrain a log-calibrated

range of UCS and other rock mechanical parameters. Figure 3 shows the match between log-derived rock strength profiles and laboratory test results in D2. Dynamic Young's modulus was calculated from compressional and shear velocities and density and calibrated to static values using laboratory test results. The relationship between dynamic and static Poisson's Ratio was not obvious; the dynamic Poisson's Ratio computed from Vp/Vs matched reasonably well with the laboratory results, so it was used directly in the modeling. Young's Modulus-based empirical relationships were used to estimate the UCS for both sandstone and interlayered shales.

Minimum horizontal stress (S_{hmin}) at depth can be directly estimated from extended leak-off tests (XLOT), leak-off tests (LOT) or mini-frac tests. No extended leak-off tests were conducted in the field. LOTs and leak-off points from two reliable LOTs were used to constrain the upper limit of S_{hmin} (~2.09 SG EMW at ~4000 m TVD). One mini-frac test was conducted in the sandstone reservoir in D2, with the interpreted fracture closure pressure (closest estimation to S_{hmin}) ~2.064 ppg EMW at ~5400 m TVD. Because LOTs are usually conducted in shaly formations while mini-frac tests are usually carried out in sandstone reservoirs, the LOTs and mini-frac tests are used to construct separate S_{hmin} profiles in shales and sandstones, respectively using the effective stress ratio method (S_{hmin}-Pp/S_v-Pp). The effective stress ratio from LOT is ~0.725 and from mini-frac test is ~0.48, which indicates there is a dramatic stress difference between sandstones and shales (stress contrast). The contrast between different lithology significantly influences hydraulic fracturing design. The relative lower stress in sandstones indicates that a hydraulic fracture should be easily created in the tight sandstone, however, the interlayered shales which have higher stress act as frac barriers and pinch points, thereby complicating fracture propagation and the final fracture geometry and conductivity.

The azimuth and magnitude of maximum horizontal stress (S_{Hmax}) can be constrained through the analysis of wellbore failures such as breakouts and tensile cracks observed on wellbore images or multi-arm caliper data. Wellbore failure analysis allows constraining of the orientation and magnitude of the S_{Hmax} because stress-induced wellbore failures occur due to the stress concentration acting around the wellbore once is drilled. The presence, orientation, and severity of failure are a function of the in-situ stress fields, wellbore orientation, wellbore and formation pressures and rock strength [12]. High-resolution electrical wireline image logs were available in all three study wells. Both breakouts and drilling-induced tensile fractures (DITFs) were observed in the reservoir sections in D2 and D3 wells. Only DITFs were observed in well D1, which could be due to the higher mud weights used during drilling and the poor quality of the image data in lower part of the reservoir.

Figure 4 shows examples of the breakouts seen in the D3 well. The example shows the typical appearance of breakouts observed on images. Here, the average apparent breakout width is ~30-40 degree. The breakouts mostly occur in shales and more breakouts are observed in the lower part of reservoir where the formations become more shaly. The orientation of breakouts is quite consistent with depth and across the block. However, small fluctuations of breakout orientation can be observed locally while intercepting small faults (an example can be seen in the right plot in Figure 4). This may indicate that some of these

http://dx.doi.org/10.5772/56384

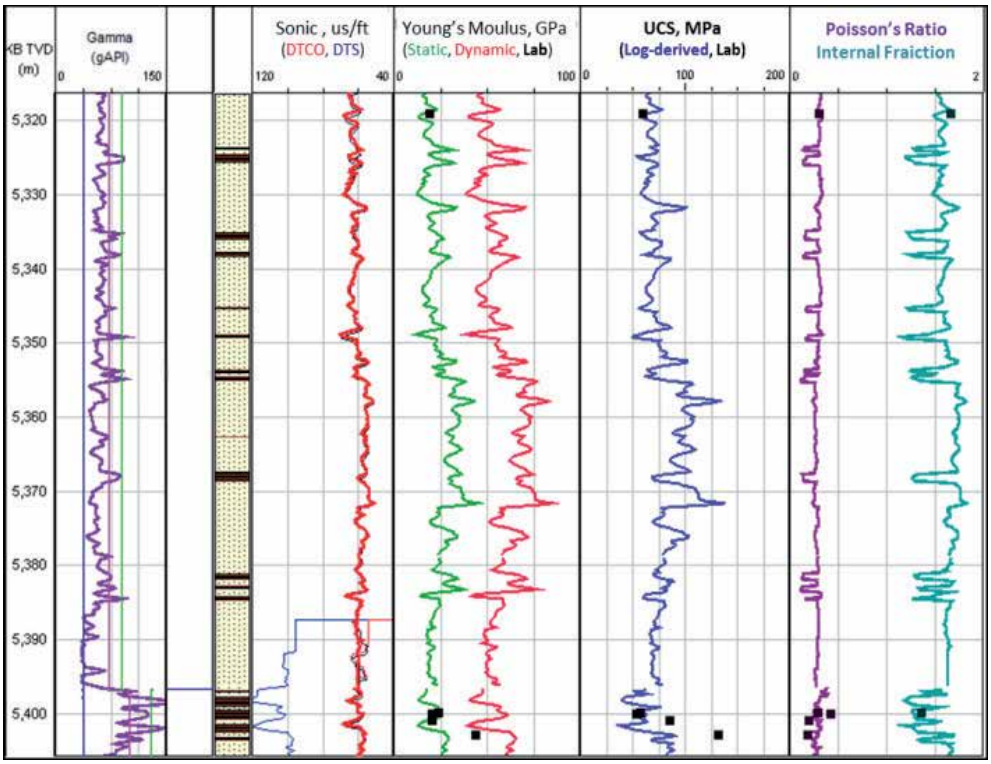

Figure 3. Comparison of laboratory (black squares) and log derived rock mechanical properties in D2 well

faults are close to or at the stage of being critically stressed. This has important implications for the stress state in the area and the likelihood of stimulating fractures by injection. Breakouts usually develop at the orientation of S_{hmin} and DITFs in the direction of S_{Hmax} in vertical and near-vertical wells. In the left plot of Figure 4, DITFs can also be observed in the same interval as the breakouts with an orientation that is ~90 degrees from the breakout directions, consistent with this expectation. DITFs are seen more often in sandstone than in shale. Based on wellbore breakouts and DITFs interpreted from the image data in D3, the azimuth of S_{Hmax} is inferred to be ~143° ±10 °. This is similar to the azimuth of S_{Hmax} inferred from wellbore failures observed in the other two wells. It is also consistent with the regional stress orientation from the World Stress Map [13].

The magnitude of S_{Hmax} is constrained by forward-modeling the stress conditions that are consistent with observations of wellbore failures observed on image logs, given the data on rock strength, pore pressure, minimum horizontal stress, vertical stress, and mud weight used to drill the well. Figure 5 is a crossplot of the magnitude of S_{hmin} and the magnitude of S_{Hmax}, which summarizes the results of S_{Hmax} modeling in D3. The magnitude of S_v (~2.49 SG) is indicated by the open circle. The modeling was conducted in both sandstone and shale. The rectangles in different colors are the possible S_{hmin} and S_{Hmax} ranges at every modeling depth. Modeling shows slightly different results for the S_{Hmax} and S_{hmin}

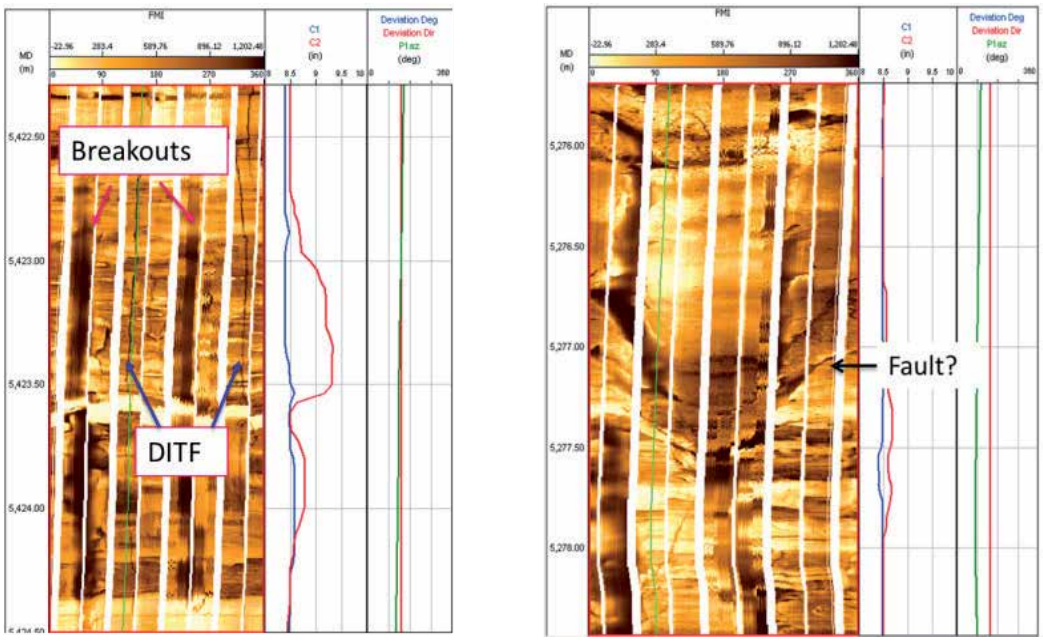

Figure 4. Drilling induced wellbore failures (breakouts & tensile fractures) observed on electrical image in D3 well.

magnitudes in the different lithologies. However, both results are consistent with the magnitudes of S_{hmin} inferred from LOTs and mini-fracs. Figure 5 shows that the magnitude of maximum horizontal stress is higher than the vertical stress in both cases, and higher in the shale than in the sand. Thus, the study area is in a strike-slip faulting stress regime ($S_{hmin} < S_v < S_{Hmax}$). The difference between the magnitudes of S_{Hmax} and S_{hmin} is ~0.8 SG in the reservoir section, suggesting high horizontal stress anisotropy. In such a condition, it is unlikely to open the natural fractures by tensile mode. However, the natural fractures might dilate in shear mode depending on their orientations and stress conditions. The final geomechanical model was verified by matching the predicted wellbore failure in these wells with that observed from image data and drilling experiences.

4. Natural fractures characterization and stimulation modeling

Natural fractures have been observed on cores and image logs in the study area. The fluid losses during drilling not only suggest the existence of natural fractures but also that some at least of these fractures are permeable in-situ. Based on the core photos shown in Figure 6, open high-angle tectonic fractures can be seen on cores from D2 and D3 wells near the crest of the structure. A fracture network consisting of a group of fractures with different orientations can be seen on the cores from the D1 well, and these fractures appear to have less apertures than high-angle fractures observed in D2 and D3.

http://dx.doi.org/10.5772/56384

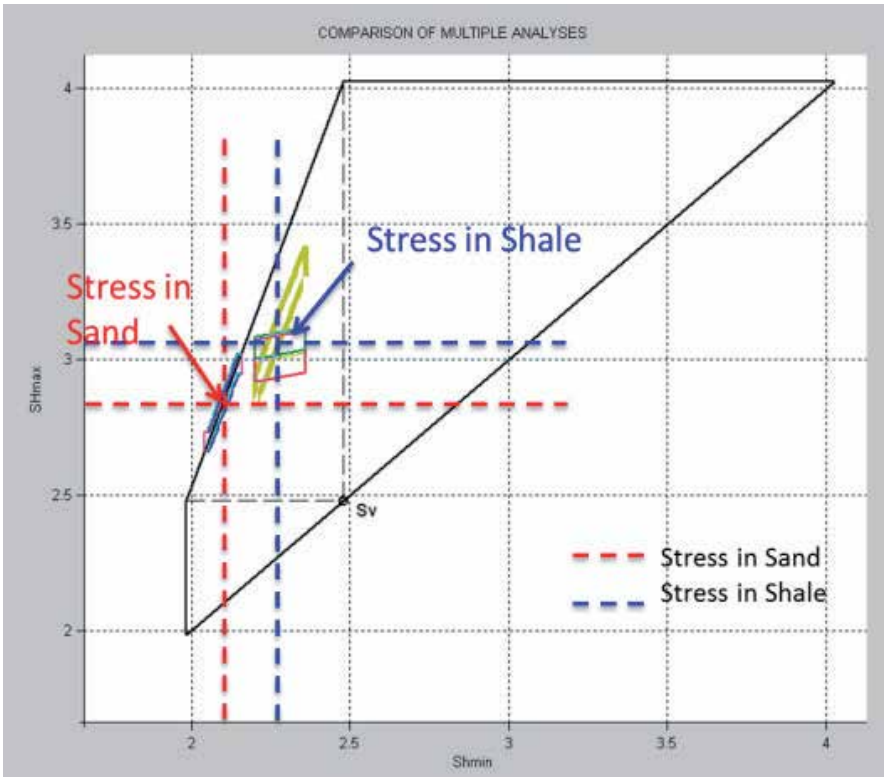

Figure 5. Stress modeling results in well D3. The range of horizontal stress magnitudes are consistent with the occurrence of wellbore failures (breakouts and DITFs) observed on wellbore images.

Natural fractures were interpreted and classified using high-resolution electrical images in all three wells. Based on the appearance on image data, the natural fractures are classified as below:

- Conductive: dark highly dipping planes on image logs
- Resistive: white dipping planes on image log
- Critically Stressed: related to local failure rotation
- Fault: features discontinued across the dipping planes
- Drilling Enhanced: discontinuous and fracture traces are 180 degrees apart and in the direction in tension

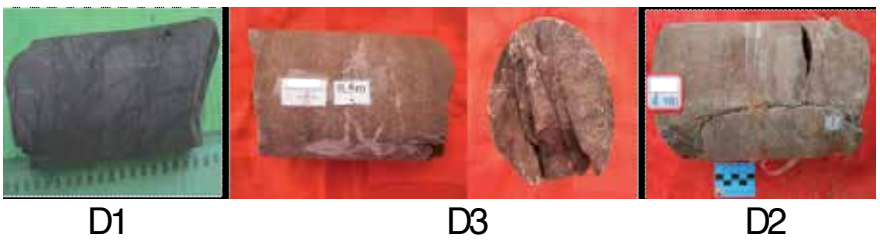

Figure 6. Core photos showing the natural fractures observed in three offset wells

Figure 7 shows a few examples of natural fractures observed on the electrical images. The plot on the left shows some examples of high-angle and low-angle conductive fractures that appear to be continuous dark lines on the images. Flexible sinusoids can be fit to the fracture traces and fracture orientation can be determined. The plot on the right shows an example of drilling enhanced natural fractures for which the fracture trace is discontinuous. The fact that parts of these fractures can be detected on the electrical image is due to fluid penetration into the fracture at the orientation around where the rock at the borehole wall is in tension during drilling. The classification of the natural fractures indicates the relative strength of the fractures. For example, the resistive fractures are closed and mineralized. Active faults or critically stressed natural fractures might be open and conductive, even under the original conditions. During stimulation, these fractures are the most easily stimulated. However, it is important to note that the classification of natural fractures is purely based on their appearance on the electrical images, and cannot be used directly to quantify permeability or other flow properties.

Figure 8 shows the fractures orientations on a crossplot of the strike and dip angles of all fractures observed in the three wells. The natural fractures observed can be divided into three groups. The first group is low-angle fractures (dip<20 °), which could be related to beddings. The second group is the major fractures seen in this block that have intermediate dip angles (~25-55°) and strike at an azimuth of ~155°N. The third group consists of fractures with strikes of ~355°N and ~100°N and dip angles ~ 35°-65° and 25°-35°, respectively. Because of their wide range of orientations and cross-cutting relationship, these three groups of fractures could be stimulated to form a well-connected grid with a major fracture azimuth (~155°N) aligned with the direction of maximum horizontal stress (~143°N). This direction is nearly perpendicular to the faults, defining the shape of fault block (see Figure 2). Because the structural trends and the stresses are aligned, it enabled us to create a reservoir model with a grid that is consistent with both.

http://dx.doi.org/10.5772/56384

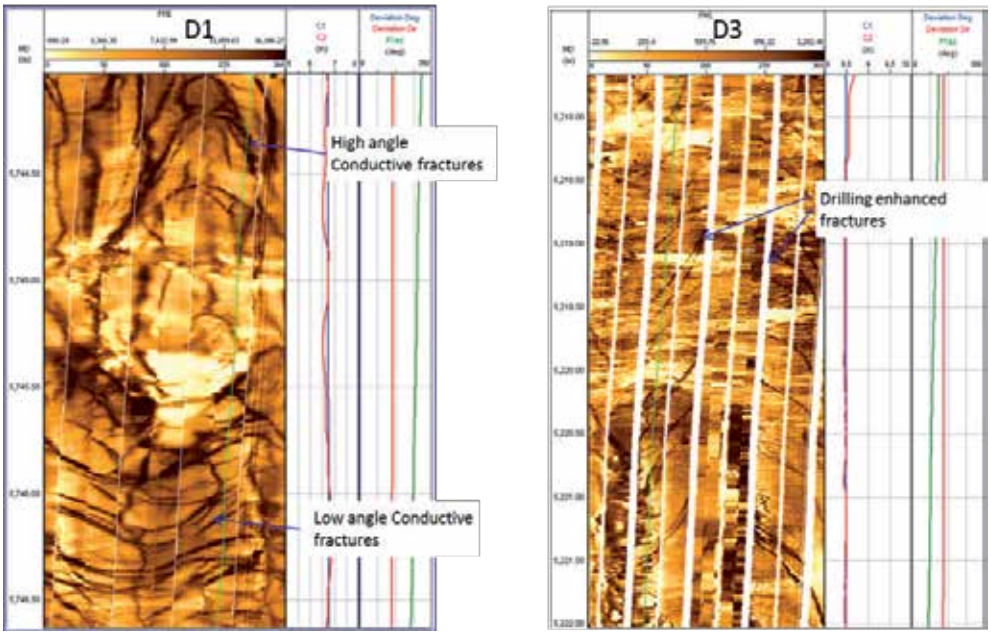

Figure 7. Examples of natural fractures observed on electrical image in D1 and D3 wells.

Effective stresses in the earth are always compressive, and natural processes tend to "heal" fractures through vein filling and other processes. Therefore, the intrinsic fracture aperture of most fractures is likely to be very small or even zero (cases where dissolution creates voids that prevent full closure are a notable exception). Thus, it is increasingly recognized that active processes are necessary to maintain fracture permeability. One such process is periodic slip along fractures that are critically stressed (i.e., those that are at or near the limiting ratio of shear to normal stress to slip). This process, and the influence of effective normal stresses on fracture aperture, can be modeled using a simple equation that describes the variation in aperture as a function of normal stress for a pure Mode I fracture. The same equation with different parameters can also be used to model the same fracture after slip has occurred [9-11].

$$a = \frac{A \bullet a_0}{(1 + 9\sigma'_n / B)} \tag{1}$$

Equation 1 is one example that describes aperture in terms of an initial aperture ($A \bullet a_0$) and an effective normal stress at which the aperture is only 10% as large (B). A and B both increase due to slip, resulting in a larger "unstressed" aperture and a stiffer fracture caused by "self-propping" due to generation during slip of a mismatch in the fracture faces and/or creation of minor amounts of rubble at the fracture face.

The contribution of fractures to the relative productivity of a well of any orientation can be computed by summing the contributions of all fractures, weighted by the product of their relative transmissivity (which is a function of aperture) and the likelihood of the well inter-

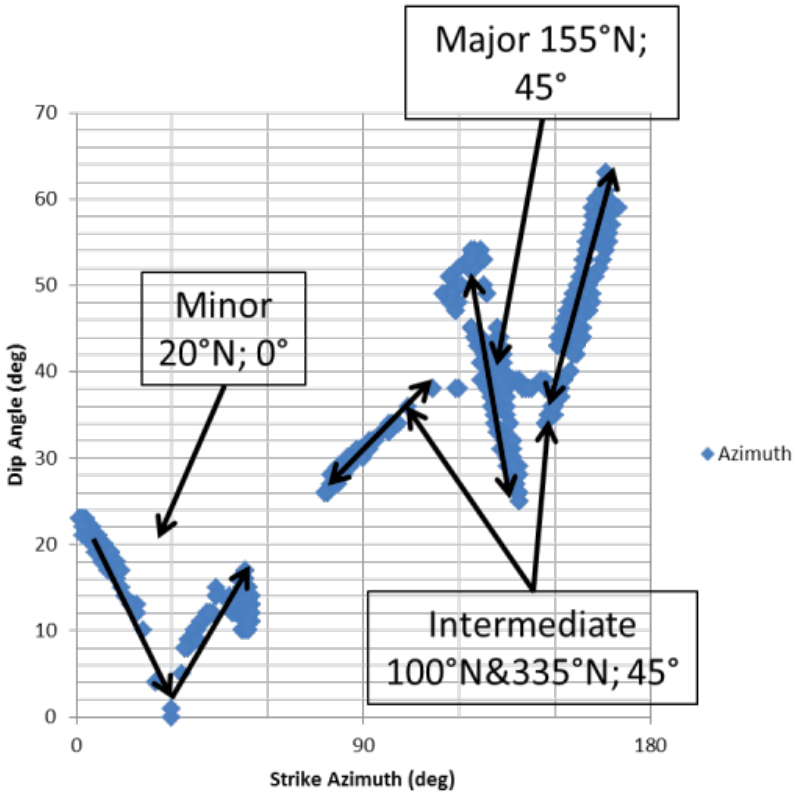

Figure 8. Cross-plot between the strike and dip angles of all the fractures observed in three offset wells.

secting the fracture (which is a function of the difference between the fracture and the well orientation). This relative productivity can be written as [10]

$$P_{well} = \sum_{fracs} \{\max(|\hat{w} \bullet \hat{n}_i|, a) \times P_i\} \tag{2}$$

where $\hat{w}$ and $\hat{n}_i$ are unit vectors along the axis of the well and normal to the ith fracture, a is a number representing the likelihood of a well intersecting a fracture if it lies in the plane of the fracture, and P_i is the relative permeability of the fracture.

The fractures interpreted from image data are only those that intersect the logged wells that are a function of their orientations, and there is no information about the fracture distribution between the wells. To ensure the most meaningful representation of the fractures in the reservoir, the fractures interpreted from all three wells were combined and the distribution was corrected to account for the likelihood of each fracture intersecting the well at the point where it was observed. This combined fracture data set was then used to model the productivities of wells in their natural condition and the change in productivity due to the shear-slip of natural fractures.

http://dx.doi.org/10.5772/56384

Figure 9 shows relative productivity for wells of all orientations based on the fractures observed in all three wells. Natural fractures are shown as poles to the fracture surfaces (black dots). Different apertures and strengths were assumed for the different types of fractures based on their classifications described above (Table 1). The plot on the left shows the relative productivity under pre-stimulation conditions, while the plot on the right shows the relative productivity calculated using equation 2 after the fractures were stimulated with a pressure 20 MPa above the original reservoir pressure. It can be seen that the maximum productivity increases by a factor of 5 if all fractures see the same 20-MPa pressure increase, which is obviously not the case during real stimulation. Superimposed on Figure 9 are the computed optimal orientations of wells based on the fracture and stress analysis (green circles). If none of the fractures is critically stressed, then the best orientation to drill a well is perpendicular to the largest population of natural fractures. If some fractures have enhanced permeability because they are critically stressed, the optimal orientation shifts in the direction of the greatest concentration of critically stressed fractures. Figure 9 shows there are some fractures already near or being critically stressed, even under ambient condition (left plot), and the maximum productivity is achieved by drilling highly deviated wells with ~20 °N hole azimuth. The optimum wellbore orientation after ~ 20-MPa stimulation is nearly horizontal and in the direction of ~228 °N.

Fracture classification	Fracture cohesion (MPa)	Sliding Friction	a_0	A		B (MPa)	
				Un-stimulated	Stimulated	Un-stimulated	Stimulated
Conductive	5	0.6	10	0.18	0.18	10	100
Resistive	5	0.6	10	0.1	0.18	1	100
Faults	0	0.6	30	0.18	0.18	100	100
Drilling enhanced	0	0.6	10	0.1	0.18	10	100
Critically Stressed	1	0.2	10	0.1	0.2	10	100

Table 1. Model parameters to calculate relative productivities for different types of natural fractures

Figure 10 shows the general effect of reservoir flow properties changes due to the natural fracture stimulation for studied fault block. Again, all the fractures interpreted from image logs in the three wells are used for modeling. Cross-plots between relative productivity (flow rate/pressure) vs. reservoir pressure are shown for three different cases: under original conditions, after 30-MPa and after 50-MPa stimulation. The blue curves show productivity changes during stimulation when the pressure is increasing, the green curves show the productivity changes during flowback and production. Modeling ends at ~20-MPa depletion. The relative productivity at ~20-MPa depletion increases five-fold after the 30-MPa stimulation (productivity increases from ~4 to ~20). There is no obvious improvement in the relative productivity of natural fractures for 50-MPa stimulation (bottom left) compared to 30-MPa stimulation. The bottom-right plot shows the number of stimulated natural fractures under different pressure conditions. It is clear that nearly all of the natural fractures are stimulated while the pressure increases to ~130 MPa (40-Ma stimulation), which explains why there is

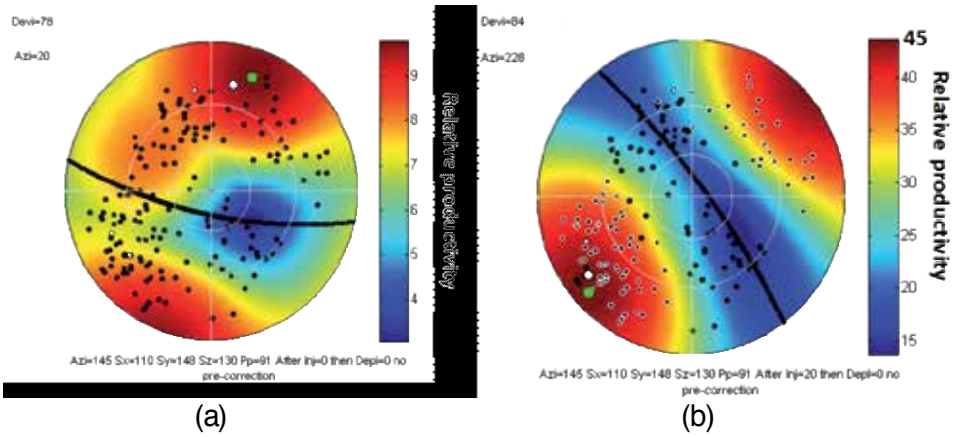

Figure 9. Relative well productivity for wells of all orientations based on the fractures observed in all three wells. (a) Ambient condition. (b) After 20-MPa stimulation. Natural fractures are shown as poles to the fracture surfaces (black dots). Green circles are computed optimal orientations of wells with highest productivity from natural fractures based on the fracture and stress analysis.

little improvement with further stimulation. It is important to note that this result does not take into account the possibility of injecting proppant to maintain the conductivity of fractures which open at pressures above 40 MPa.

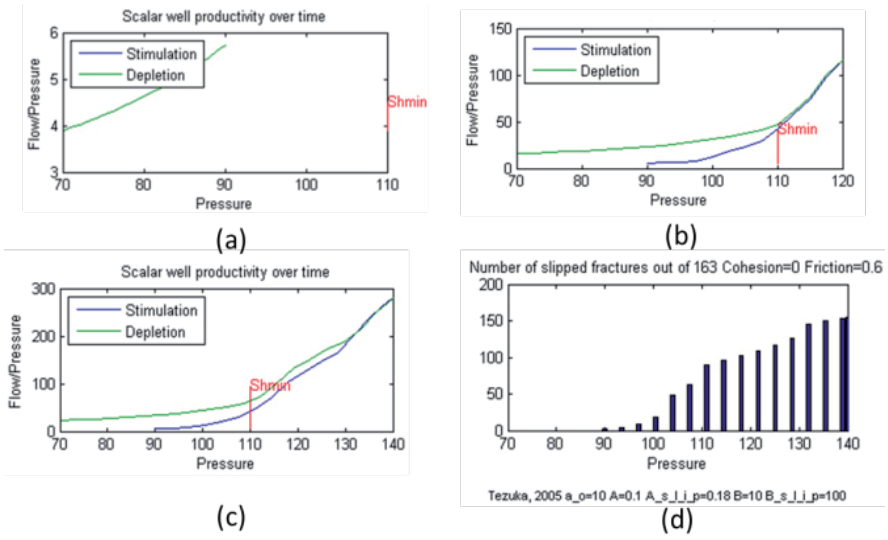

Figure 10. Reservoir flow properties changes with time due to natural fracture stimulation for studied fault block. The blue curves are showing the productivity changes when pressure increases during stimulation, the green curves are showing productivity changes during flowback and production. (a) no stimulation (b) 30-MPa stimulation (c) 50-MPa stimulation (d) number of stimulated (shear slip) natural fractures. Fracture properties: cohesion=0, sliding friction=0.6.

http://dx.doi.org/10.5772/56384

The above relative productivity modeling of natural fractures shows the conductivity of natural fractures increases significantly if the stimulation pressure is at or above the minimum horizontal stress. This is because many of the natural fractures are non-optimally oriented. Assuming a connected fracture network exists, the conductivity increase could be a factor of five for the stimulated fracture network while stimulation pressure is ~130MPa or higher (assuming the pressure reaches all fractures).

5. Predicting the shape of the stimulated reservoir volume

Fracture stimulation modeling showed that the shear slip of natural fractures could be effective in improving reservoir properties. Next, we need to reproduce the affected productive volume in the reservoir using the "shear stimulation" concept to enable more accurate production prediction. At the present no commercial simulator can fully model this process in 3D, although some research simulators have been developed. It was decided to use two different commercial models to simulate both fracture network stimulation created by low-viscosity frac fluid and the growth of the main hydraulic fracture. A commercial dual-porosity, dual-permeability simulator is used to simulate the flow property changes of natural fractures due to the shear slip. A commercial hydraulic fracturing design and evaluation simulator is used to model the geometry and conductivity of the principal hydraulic fracture filled with proppant. The modeling in two separate simulators is coupled by the fluid volume used for stimulation. The fluid volume leaked off in the shear-dilated natural fracture network was estimated in the dual-permeability, dual-porosity flow simulator. By adjusting the pressure-dependent leak-off coefficient, the fluid volume leaked off in the hydraulic fracturing simulator was matched with the fluid volume leaked into natural fractures networks estimated by the flow simulator. The prediction of the stimulated reservoir volume is discussed in the rest of this section and the hydraulic fracturing design will be discussed in next section.

To predict the extent and properties of the stimulated volume by a dual-permeability, dual-porosity simulator, a finely gridded model (Model A) was created based on the original reservoir model. The main function of this model is to simulate the change in flow properties in every single frac stage during and immediately after injection. The model is initialized with average known reservoir characteristics such as matrix porosity and permeability, fracture permeability and initial pressure, characterized from core and log analysis. Although different cases have been tested in the study, only one of the most realistic cases will be discussed here: the average matrix porosity used in the initial model is ~7.4%, matrix permeability is 0.07 mD in all directions, and the initial fracture permeability is ~ 0.2 mD. The initial fracture permeability is set close to the lower bound of fracture permeability based on core and log analysis. The orientations of the principal flow directions were chosen to correspond to the principal directions of the fracture sets and of bedding, which also approximately corresponded to the principal stress directions.

The relative magnitudes of the permeability enhancements in different directions were constrained by the geomechanical analysis. A set of permeability-pressure tables for different directions were then used to describe the hysteretic rock behavior that results from shear fracture activation. Although the fracture properties during stimulation can be estimated as

described in the previous section, it is better to calibrate and constrain the permeability-pressure relationship based on real lab or in-situ tests, e.g., using a pre-stimulation injectivity test [4]. The injectivity test should ideally be conducted in the open hole using slow injection to evaluate the potential natural fractures being stimulated, as permeability changes could then be interpreted based on the flow-rate/pressure changes along with the reservoir pressure. Because the D3 well has already been cased it was impossible to conduct such a test in the field before the actual treatment is carried out. Consequently, it was decided to produce a permeability-pressure table based on experience from shale gas reservoirs. Based on this table, on fracture density in different directions and on the stress anisotropy, a composite transmissibility multiplier was produced for the prediction of properties and extent of the stimulated reservoir volume. Transmissibility multipliers were different for each of the I, J and K directions; those directions were aligned as discussed above with the primary structural fabric and stresses. The propagation of the pressure and fluid front in these directions can be controlled by modifying these multipliers.

Figure 11 shows diagrammatically the relationship between the permeability multiplier and the pore pressure (green curve). A slow increase in the permeability multiplier with increasing pressure occurs until fractures begin to slip. Above this pressure, the injectivity increases rapidly as an increased number of fractures are stimulated. During decreasing injection pressure in the injectivity test, the injectivity should decrease more slowly, retaining behind a permanent injectivity increase. The post-stimulation response can also be extrapolated to pressures below the original reservoir pressure. This makes it possible to predict the reservoir's response to depletion, which could lead to improved predictions of production decline. When the pressure during stimulation exceeds the minimum horizontal stress, extensional hydrofracs are created, and the permeability-pressure relationship does not follow the green line. Three different flow paths (A, B, C) were assumed for conditions with pressure above S_{hmin}, and the intermediate path, B was chosen to be used in the simulation.

The result of this modeling work is a 3D induced permeability map that describes the stimulated rock volume as discrete blocks, each with a unique permeability. The stimulated rock volume is therefore described not as a geometrical shape with identical flow properties throughout, but as a rock body with variable induced permeability, as shown in Figure 12.

6. Hydraulic fracturing design and reservoir simulation

As discussed earlier, a commercial simulator was used to model the hydraulic fracture created during the stimulation along with the stimulated natural fracture network using low-viscosity fluids. Stress profiles and other elastic rock properties estimated in the geomechanical analysis were used as input for the design. To achieve better proppant distribution, a low-viscosity linear gel was combined with slickwater in the treatment. The low-viscosity linear gel was optimized using different concentrations of ingredients for the high reservoir temperature (~126°C) using source water and local ingredients. Due to the high closure pressure and low viscosity of the fluid, high-strength small-mesh proppants were used in the design.

http://dx.doi.org/10.5772/56384

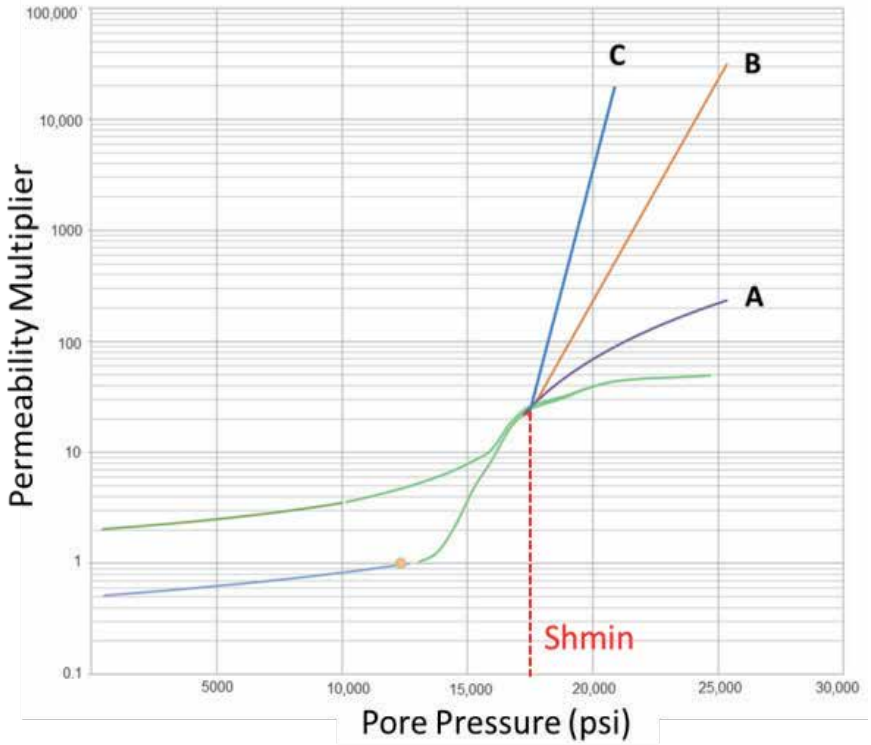

Figure 11. Relationship between the permeability multiplier and the pore pressure (green curve) for natural fractures used in the simulation. Three different flow paths (A, B, C) were assumed for conditions with pressure above Shmin.

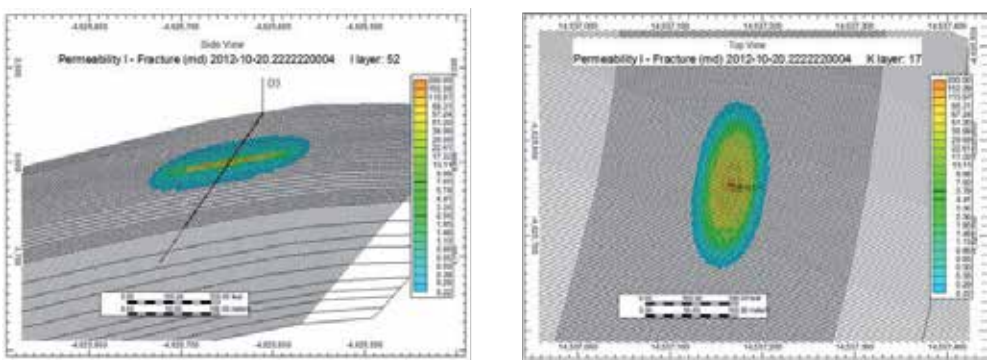

Figure 12. Side view (left) and top view (right) of the predicted 3D permeability map. The property shown in the plots is present fracture permeability.

Modeling showed that four stages would be required for slickwater/linear gel treatment to cover the 160 m thick reservoir due to the high leak off of low-viscosity fluids (Figure 13). A reasonable proppant distribution was achieved by using the low-viscosity linear gel.

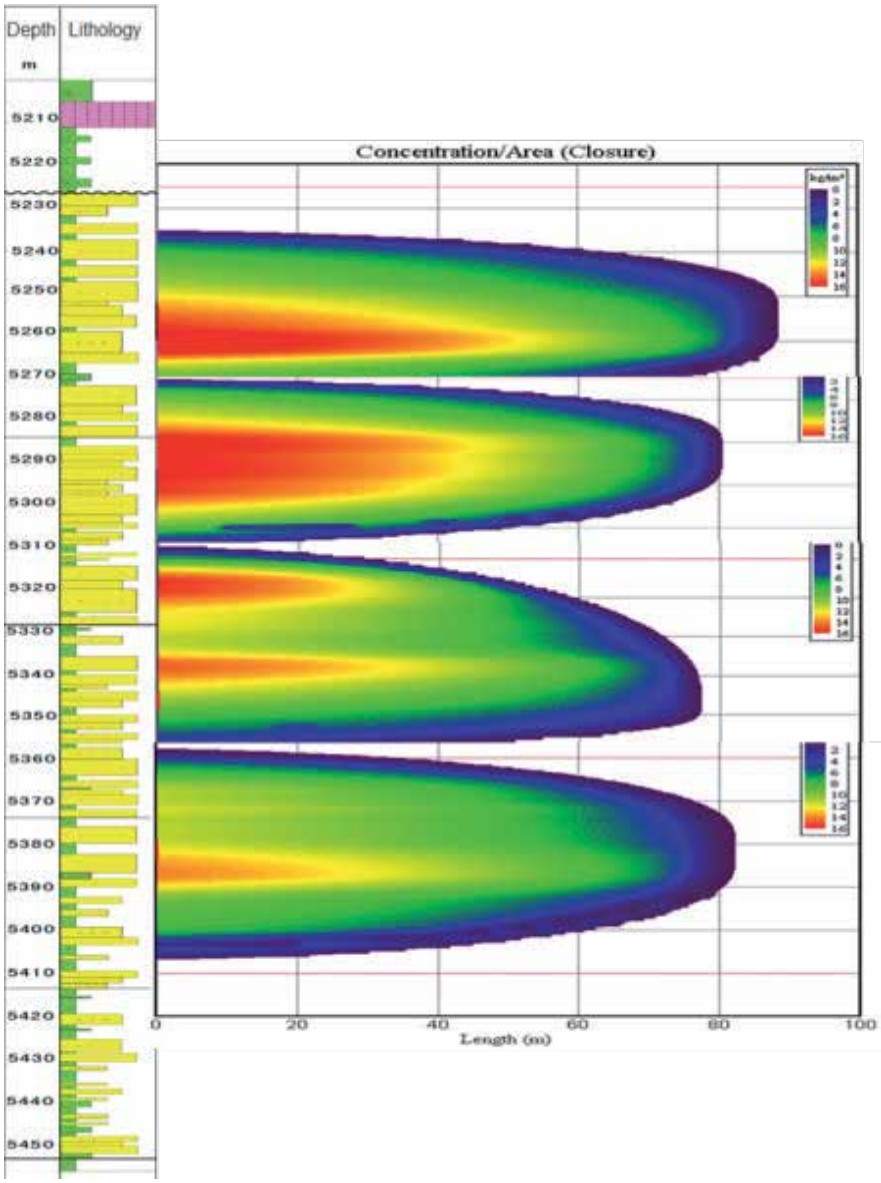

Figure 13. Fracture growth and proppant coverage (colour) for four stage of hydraulic fractures using slickwater/linear gel.

To predict the production after the stimulation, the propped hydraulic fractures were imported into the reservoir model with flow properties enhanced by stimulated natural fractures (Model A). Because the natural fracture distribution between wells is unknown, the same stimulated Model A was used for all four stages. The left plot of Figure 14 shows a side view of the reservoir model combining four Model A's with stimulated reservoir volumes and four propped hydraulic fractures, which was used for production prediction.

http://dx.doi.org/10.5772/56384

To compare the prediction result from slickwater/liner gel treatment with conventional gel fracturing, a conventional bi-wing hydraulic fracturing design using a high-viscosity gel was also developed. The gel fluid was optimized using different concentrations of ingredients for the high reservoir temperature (~126°C) using source water and local ingredients. The same type of proppant used for the slickwater/liner gel treatment was used for the design of gel treatment. The proppant concentrations and amounts will be certainly different in these two types of treatments. It was found that two stages were enough to cover the whole reservoir interval (Figure 15). These two designed hydraulic fractures were then imported into the original reservoir model (right plot in Figure 14) for production prediction and comparison of the production to that predicted after slickwater linear gel stimulation.

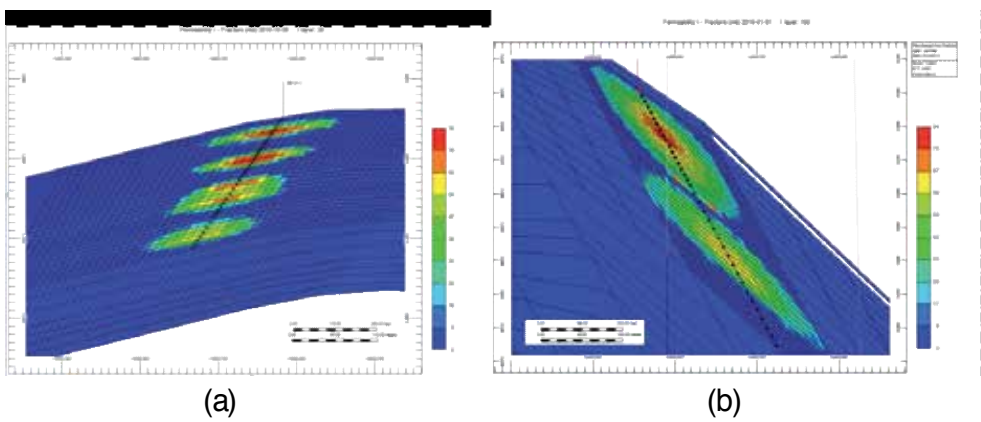

Figure 14. Side views of reservoir models showing fracture permeability used for production prediction. (a) Reservoir model combining four Model A's with stimulated reservoir volumes and four propped hydraulic fractures using slickwater and linear gel; (b) Original reservoir model and two propped hydraulic fractures using high-viscosity gel fluid.

Figure 16 shows the production prediction comparison from the two different hydraulic fracturing treatments. The red curve is the production prediction from slickwater/linear gel treatment, which is scaled down to ~2/3 of the initial prediction to account for the heterogeneity of the reservoir model due to a simplified reservoir model used for pre-stimulation condition. The blue curve is the production from conventional two-wing gel fracturing design. It is found that post-frac flow rate from slickwater stimulation is expected to be about three times the flow rate from the gel treatment in the stabilized regime (one year after stimulation). Although actual flow rates from both treatments depends on the applied drawdown, the corresponding flow rates after one year are expected to be ~55 × 10^4 m^3/d for slickwater treatment and ~ 17 × 10^4 m^3/d for gel treatment, respectively, with a constant drawdown of 20 MPa.

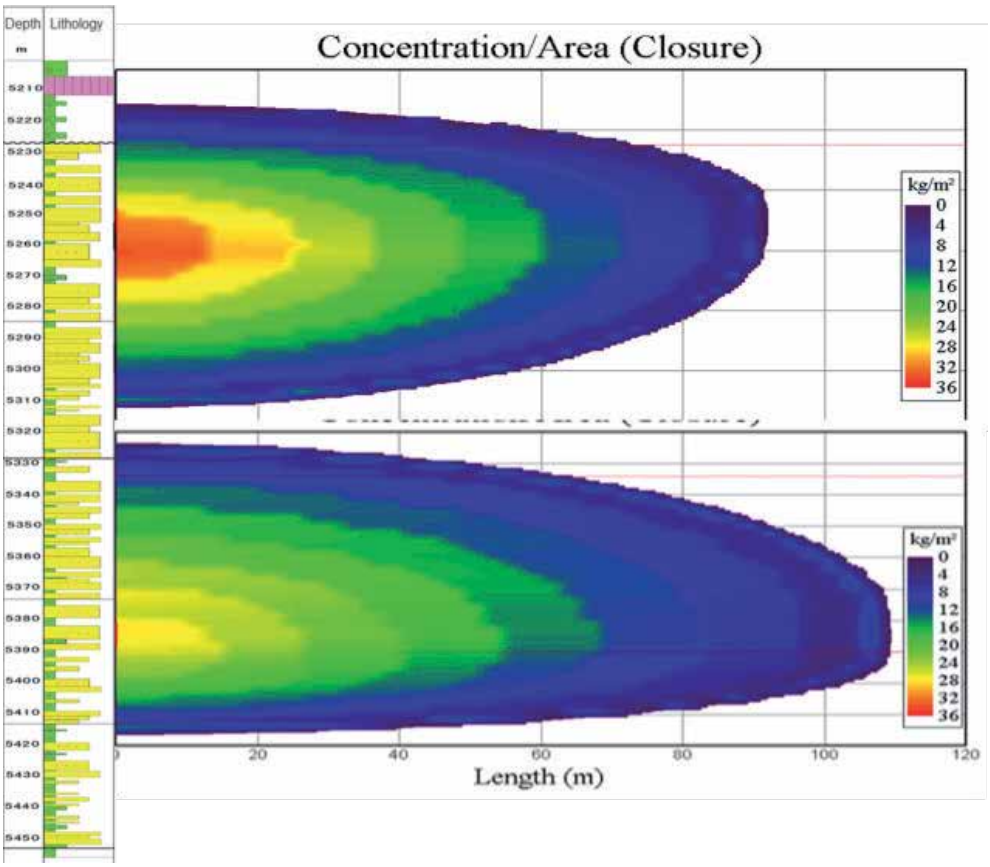

Figure 15. Fracture growth and proppant coverage (colour) for two stage of hydraulic fractures using conventional gel treatment.

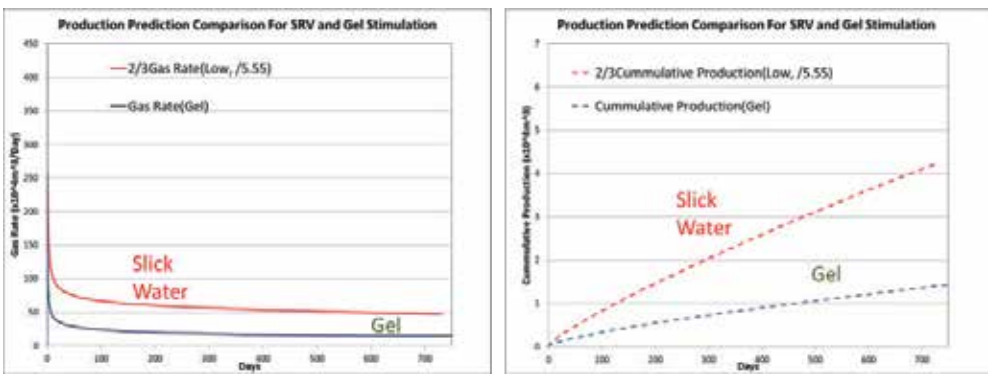

Figure 16. Production prediction comparison of two different hydraulic fracturing treatments. The red curve is the production prediction from slickwater/linear gel treatment; the blue curve is the production from conventional two-wing gel fracturing design.

http://dx.doi.org/10.5772/56384

7. Injectivity test and stage 1 treatment

It was decided to test the slickwater/liner gel treatment in D3 well after the study was completed. A pre-stimulation injectivity test was performed through perforations prior to Stage 1 and after the mini-frac test (Figure 17). Interestingly, the test showed the opposite behavior from what one would expect if the stimulation enhances reservoir permeability. Later-stage injectivity (during step-down) is lower than early stage injectivity (during step-up), rather than higher. Although there might be other reasons affect the test result, i.e., the un-stable injection during the whole test, it is believed the main reason was lack of access to natural fractures in the tested interval and the high closure pressure because the test was conducted in a cased and perforated hole and after a mini-frac.

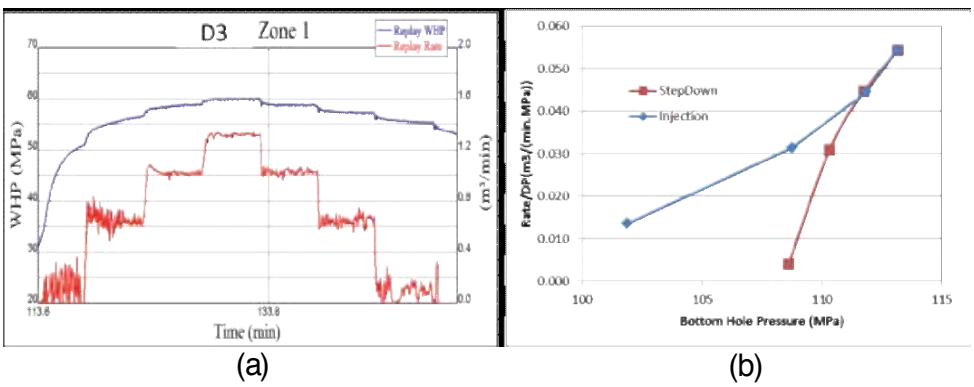

Figure 17. Pre-stimulation injectivity test pressure curve (a) and injectivity interpretation (b).

The Stage 1 treatment was conducted using slickwater and linear gel after the injectivity test. However, a screen out was experienced at the end of the execution and tubing leakage was discovered afterwards. Treatments in the other three zones had not occurred at the date of writing this paper. The stage 1 production test is still very promising, and it has been decided to continue slickwater/linear gel treatment in other three stages after the tubing problem is fixed.

8. Discussion and conclusion

In this paper we have outlined a new workflow for simulation of a complex fracture network created by stimulation using low-viscosity fluids in a fractured tight sandstone reservoir. The workflow is based on critically stressed fracture theory. This process of natural fracture stimulation is believed to be the underlying reason for the success in shale gas reservoir stimulation. The results suggested that there would be significantly higher production from this approach compared to conventional two-wing gel fracturing.

There are, however, some uncertainties in the modeling of the natural fracture stimulation for this fractured tight gas reservoir.

1. The pressure-permeability relationship used in modeling the permeability enhancement by slickwater stimulation is taken from a shale gas field. It is unclear whether the data from the analogue field drilled through mudstones will be applicable to the modeled fractured tight sandstone reservoir. Post-stimulation production simulation, or a pre-stimulation injectivity test in nearby wells in open hole could help to better constrain this relationship, hence improve the accuracy of the prediction.

2. Due to the lack of knowledge of fracture distribution between wells, the fractures interpreted from all three offset wells were used to predict the stimulation behavior of natural fractures, and it was assumed that a similar fracture distribution would be found in all formations. In reality, the fracture distribution is likely to be different, depending among other things on the lithology and structural location. For example, it is already noticed that there are fewer fractures in the lower part of the reservoir than in the upper part in the D3 well. Intervals with dense fracture networks are more likely to benefit from slickwater treatment compared to formations with no or very sparse fractures. A 3D description of the fracture distribution is always preferred.

3. Micro-seismic imaging is not available in the study area. No wells are close enough to work as a monitoring well and surface monitoring is also impossible due to the great depth of the reservoir. The lack of microseismic data made it impossible to calibrate the prediction of the shape of SRV.

The main uncertainty in gel frac productivity estimation comes from the propped fracture conductivity estimation. This conductivity is based on proppant testing in the laboratory. The proppant inside fractures involves clogging, crashing and embedment over the production period. There is no analytical method available to model these long-term effects on propped fracture conductivity. An approximate conductivity damage factor has been used in this study to consider these effects.

Although there are still some shortcomings with the workflow, it can assist in the assessment of development concepts and the evaluation of stimulation enhancement options. The anisotropy in the slickwater treatment can be reasonably well-predicted and applied into the production simulation, which provides a more robust prediction than a simple isotropy model. The new workflow can be used in naturally fractured shale gas, tight gas/oil and CBM reservoirs.

Acknowledgements

The authors wish to thank PetroChina Tarim Oil Company for providing us with the data and for permission to publish this paper, and Baker Hughes internal support to carry out the work.

http://dx.doi.org/10.5772/56384

Author details

Feng Gui[1*], Khalil Rahman[1], Daniel Moos[2], George Vassilellis[3], Chao Li[3], Qing Liu[4], Fuxiang Zhang[5], Jianxin Peng[5], Xuefang Yuan[5] and Guoqing Zou[5]

*Address all correspondence to: Feng.gui@bakerhughes.com

1 Baker Hughes, Perth, Australia

2 Baker Hughes, Menlo Park, USA

3 Gaffney, Cline &Associates, Houston, USA

4 Baker Hughes, Beijing, China

5 PetroChina Tarim Oil Company, Korla, China

References

[1] Modeland, N, Buller, D, & Chong, K. K. Stimulation's influence on production in the Haynesville Shale: a playwide examination of fracture-treatment variables that show effect on production. In: proceedings of Canadian Unconventional Resources Conference, CSUG/SPE November (2011). Calgary, Alberta, Canada., 148940, 15-17.

[2] Maxwell, S. C, Pope, T, Cipolla, C, et al. Understanding hydraulic fracture variability through integrating microseismicity and seismic reservoir characterization. In: proceedings of SPE North American Unconventional Gas Conference and Exhibition, SPE June (2011). Woodlands, Texas, USA., 144207, 14-16.

[3] Sayers, C. and Le Calvez, J., (2010). Characterization of microseismic data in gas shales using the radius of Gyration tensor, SEG Expanded Abstract.

[4] Moos, D. Improving Shale Gas Production Using Geomechanics, Exploration & Production- Oil & Gas Review (2011). , 9(2), 84-88.

[5] Zoback, M. D, Kohli, A, Das, I, & Mcclure, M. The importance of slow slip on faults during hydraulic fracturing stimulation of shale gas reservoirs. In: proceedings of SPE Americas Unconventional Resources Conference, SPE June (2012). Pittsburgh, Pennsylvania, USA., 155476, 5-7.

[6] Mullen, M, & Enderlin, M. Is that frac job really breaking new rock or just pumping down a pre-existing plane of weakness?- the integration of geomechanics and hydraulic-fracture diagnostics. In: proceedings of 44th US Rock Mechanics Symposium and 5th US-Canada Rock Mechanics Symposium, ARMA 10-285, 27-30 June (2010). Salt Lake City, UT, USA.

[7] Moos, D, Vassilellis, G, & Cade, R. Predicting shale reservoir response to stimulation in the Upper Devonian of West Virginia. In: proceedings of SPE Annual Technical Conference and Exhibition, SPE-145849, 30 October-2 November (2011). Denver, Colorado, USA.

[8] Vassilellis, G. D, Li, C, Moos, D, et al. Shale engineering application: the MAL-145 Project in West Virginia. In: proceedings of Canadian Unconventional Resources Conference, CSUG/SPE-November (2011). Calgary, Alberta, Canada., 146912, 15-17.

[9] Barton, C, Zoback, M. D, & Moos, D. Fluid Flow Along Potentially Active Faults in Crystalline Rock, Geology(1988). , 23(8), 683-686.

[10] Moos, D, & Barton, C. A. Modeling uncertainty in the permeability of stress-sensitive fractures. In: proceedings of 42nd US Rock Mechanics Symposium and 2nd U.S.-Canada Rock Mechanics Symposium, ARMA June- 2 July (2008). San Francisco, USA., 08-312.

[11] Hossain, M. M, Rahman, M. K, & Rahman, S. S. A Shear Dilation Stimulation Model for Production Enhancement From Naturally Fractured Reservoirs, SPE 78355, SPE Journal; June , 2002-183.

[12] Moos, D, & Zoback, M. D. Utilization of Observations of Well Bore Failure to Constrain the Orientation and Magnitude of Crustal Stresses: Application to Continental, Deep Sea Drilling Project and Ocean Drilling Program Boreholes, Journal of Geophysical Research (1990). , 95, 9-305.

[13] Heidbach, O, Tingay, M, Barth, A, Reinecker, J, Kurfe, D, & Müller, B. The World Stress Map database release (2008). doi:10.1594/GFZ.WSM.Rel2008.http://www.world-stress-map.org

Chapter 53

Investigation of Hydraulic and Natural Fracture Interaction: Numerical Modeling or Artificial Intelligence?

Reza Keshavarzi and Reza Jahanbakhshi

Additional information is available at the end of the chapter

http://dx.doi.org/10.5772/56382

Abstract

Hydraulic fracturing of naturally fractured reservoirs is a critical issue for petroleum industry, as fractures can have complex growth patterns when propagating in systems of natural fractures. Hydraulic and natural fracture interaction may lead to significant diversion of hydraulic fracture paths due to intersection with natural fractures which causes difficulties in proppant transport and eventually job failure. In this study, a comparison has been made between numerical modeling and artificial intelligence to investigate hydraulic and natural frcature interaction. First of all an eXtended Finite Element Method (XFEM) model has been developed to account for hydraulic fracture propagation and interaction with natural fracture in naturally fractured reservoirs including fractures intersection criteria into the model. It is assumed that fractures are propagating in an elastic medium under plane strain and quasi-static conditions. Comparison of the numerical and experimental studies results has shown good agreement. Secondly, a feed-forward with back-propagation artificial neural network approach has been developed to predict hydraulic fracture path (crossing/turning into natural fracture) due to interaction with natural fracture based on experimental studies. Effective parameters in hydraulic and natural fracture interaction such as in situ horizontal differential stress, angle of approach, interfacial coefficient of friction, young's modulus of the rock and flow rate of fracturing fluid are the inputs and hydraulic fracturing path(crossing/turning into natural fracture) is the output of the developed artificial neural network. The results have shown high potentiality of the developed artificial neural network approach to predict hydraulic fracturing path due to interaction with natural fracture. Finally, both of the approaches have been examined by a set of experimental study data and the results have been compared. It is clearly observed that both of them yield promising results

while numerical modeling yields more detailed results which can be used for further investigations but it is computationally more expensive and time-consuming than artificial neural network approach. On the other hand, since artificial neural network approach is mainly data-driven if just the input data is available (even while fracturing) the hydraulic fracture path (crossing/turning into natural fracture) can be predicted real-time and at the same time that fracturing is happening.

1. Introduction

Hydraulic fracture growth through naturally fractured reservoirs presents theoretical, design, and application challenges since hydraulic and natural fracture interaction can significantly affect hydraulic fracturing propagation. Although hydraulic fracturing has been used for decades for the stimulation of oil and gas reservoirs, a thorough understanding of the interaction between induced hydraulic fractures and natural fractures is still lacking. This is a key challenge especially in unconventional reservoirs, because without natural fractures, it is not possible to recover hydrocarbons from these reservoirs. Meanwhile, natural fracture systems are important and should be considered for optimal stimulation. For naturally fractured formations under reservoir conditions, natural fractures are narrow apertures which are around 10^{-5} to 10^{-3} m wide and have high length/width ratios (>1000:1) [1].Typically natural fractures are partially or completely sealed but this does not mean that they can be ignored while designing well completion processes since they act as planes of weakness reactivated during hydraulic fracturing treatments that improves the efficiency of stimulation [2]. The problem of hydraulic and natural fracture interaction has been widely investigated both experimentally [3, 4, 5, 6, 7, 8] and numerically [9, 10, 11, 12, 13, 14, 15, 16, 17, 18]. Many field experiments also demonstrated that a propagating hydraulic fracture encountering natural fractures may lead to arrest of fracture propagation, fluid flow into natural fracture, creation of multiple fractures and fracture offsets [19, 20, 21, 22] which will result in a reduced fracture width. This reduction in hydraulic fracture width may cause proppant bridging and consequent premature blocking of proppant transport (so-called screenout) [23, 24] and finally treatment failure. Although various authors have provided fracture interaction criteria [4, 5, 25] determining the induced fracture growth path due to interaction with pre-existing fracture and getting a viewpoint about variable or variables which have a decisive impact on hydraulic fracturing propagation in naturally fractured reservoirs is still unclear and highly controversial. However, experimental studies have suggested that horizontal differential stress, angle of approach and treatment pressure are the parameters affecting hydraulic and natural fracture interaction [4, 5, 6] but a comprehensive analysis of how different parameters influence the fracture behavior has not been fully investigated to date. In this way, in order to assess the outcome of hydraulic fracture stimulation in naturally fractured reservoirs the following questions should be answered:

What is the direction of hydraulic fracture propagation?

How will the propagating hydraulic fracture interact with the natural fracture?

http://dx.doi.org/10.5772/56382

Will the advancing hydraulic fracture cross the natural fracture or will it turn into it?

For the purpose of this study, a 2D eXtended finite element method (XFEM) has been compared with a feed-forward with back-propagation artificial neural network approach to account for hydraulic and natural fracture interaction.

2. Interaction between hydraulic and natural fractures

The interaction between pre-existing natural fractures and the advancing hydraulic fracture is a key issue leading to complex fracture patterns. Large populations of natural fractures are sealed by precipitated cements (Figure 1) which are weakly bonded with mineralization that even if there is no porosity in the sealed fractures, they may still serve as weak paths for the growing hydraulic fractures [2].

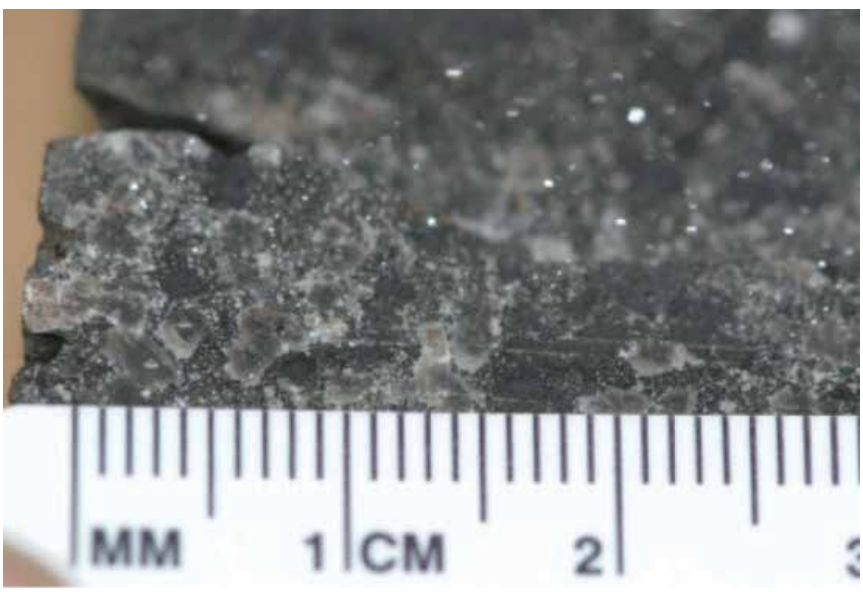

Figure 1. A weakly bonded fracture cement in a shale sample [26].

In this way, experimental studies [4, 5, 6] suggested several possibilities that may occur during hydraulic and natural fractures interaction. Blanton [4] conducted some experiments on naturally fractured Devonian shale as well as blocks of hydrostone in which the angle of approach and horizontal differential stress were varied to analyze hydraulic and natural fracture interaction in various angles of approach and horizontal differential stresses. He concluded that any change in angle of approach and horizontal differential stress can affect hydraulic fracture propagation behavior when it encounters a natural fracture which will be referred to as opening, arresting and crossing. Warpinski and Teufel [5] investigated the effect of geologic discontinuities on hydraulic fracture propagation by conducting mineback

experiments and laboratory studies on Coconino sandstone having pre-existing joints. They observed three modes of induced fracture propagation which were crossing, arrest by opening the joint and arrest by shear slippage of the joint with no dilation and fluid flow along the joint. In 2008 [6] some laboratory experiments were performed to investigate the interaction between hydraulic and natural fractures. They also observed three types of interactions between hydraulic and pre-existing fractures which were the same as Warpinski and Teufel's observations. The above referenced experimental studies have investigated the initial interaction between the induced fracture and the natural fracture, however, in reality may be the hydraulic fracture is arrested by natural fracture temporarily but with continued pumping of the fluid, the hydraulic fracture may cross (Figure 2) or turn into the natural fracture (Figure 3).

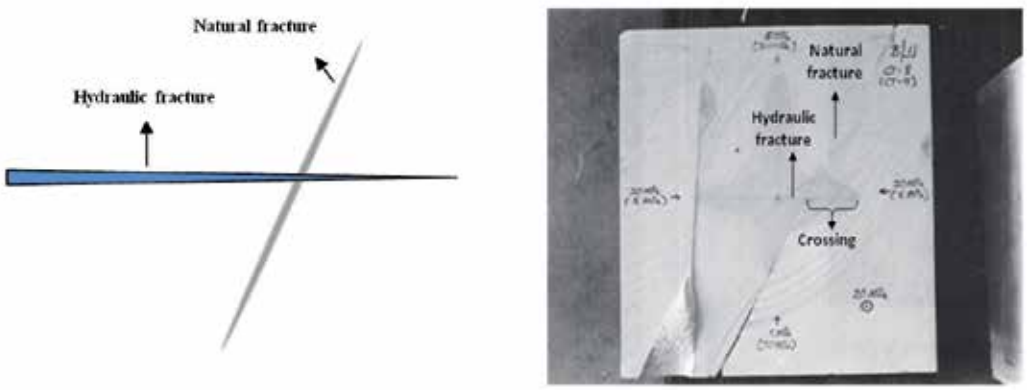

Figure 2. Propagating hydraulic fracture crosses the natural fracture and keep moving without any significant change in its path: left image is a schematic view of crossing and right image is the result of experimental study [4].

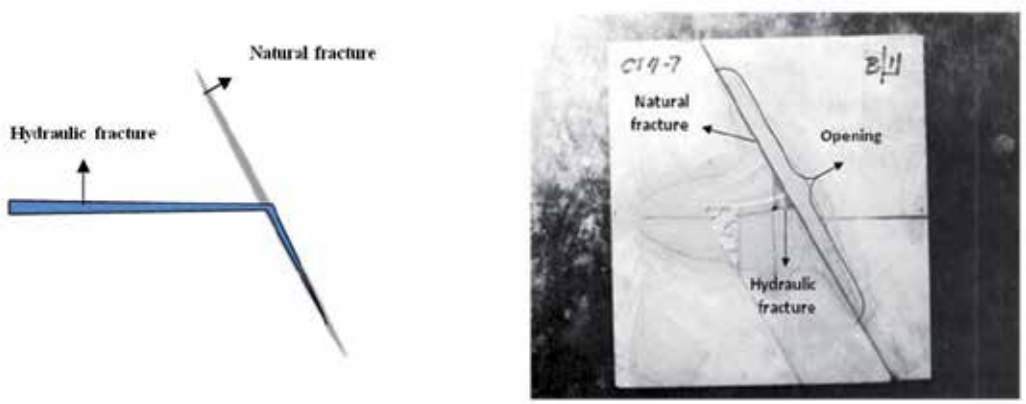

Figure 3. Hydraulic fracture turns into the natural fracture and propagates along it: left image is a schematic view and right image is the result of experimental study [4].

http://dx.doi.org/10.5772/56382

Alternatively, in some cases the hydraulic fracture may get arrested if the natural fracture is long enough and favorably oriented to accept and divert the fluid.

3. Numerical modeling: Extended Finite Element Method (XFEM)

For fracture propagation through numerical modeling an energy based criterion has been considered which is energy release rate, *G*. The energy release rate, *G*, is related to the stress intensity factors through Eq. 1 [27]:

$$G = \frac{1}{E'}(K_I^2 + K_{II}^2) \tag{1}$$

where $E' = E$ for plane stress (E is Young's modulus) and $E' = E/(1- \nu^2)$ for plane strain (where ν is the Poisson's ratio). Energy release rate has been calculated by the *J* integral using the domain integral approach [28] whereas *J* integral is equivalent to the definition of the fracture energy release rate, *G*, for linear elastic medium. If the *G* is greater than a critical value, G_c, the fracture will propagate critically. The direction of hydraulic fracture propagation will be calculated by Eq. 2 [29]:

$$\theta_c = 2\tan^{-1}\frac{1}{4}\left(\frac{K_I}{K_{II}} \pm \sqrt{\left(\frac{K_I}{K_{II}}\right)^2 + 8}\right) \tag{2}$$

During hydraulic and natural fracture interaction at the intersection point the hydraulic fracture has more than one path to follow which are crossing and turning into natural fracture. The most likely path is the one that has the maximum *G*. So, at the intersection point energy release rate is calculated for both crossing (G_{cross}) and turning into natural fracture (G_{turn}), and if (G_{turn} /G_{cross})>1 hydraulic fracture turns into natural fracture while if (G_{turn} /G_{cross})< 1 crossing takes place and hydraulic fracture crosses the natural fracture. To examine the proposed mechanism, eXtended Finite Element method (XFEM) was applied which was first introduced by Belytschko and Black [30] in order to avoid explicit modeling of discrete cracks by enhancing the basic finite element solution. In comparison to the classical finite element method, XFEM provides significant benefits in the numerical modeling of fracture propagation and it overcomes the difficulties of the conventional finite element method for fracture analysis, such as restriction in remeshing after fracture growth and being able to consider arbitrary varying geometry of fractures [12]. XFEM enhances the basic finite element solution through the use of enrichment functions which are the Heaviside function for elements that are completely cut by the crack and Westergaard-type asymptotic functions for elements containing crack-tips [27]. The displacement field for a point "x" inside the domain can be approximated based on the XFEM formulation as below [31]:

$$u^h(x)=\sum_{I\in N_{nu}} N_I(x)\left(u_I+\underbrace{H(x)a_I}_{I\in N_{ua}}+\underbrace{\sum_{\alpha-1}^{4} F_\alpha(x)b_I^\alpha}_{I\in N_{ub}}\right) \tag{3}$$

Where N_I is the finite element shape function, u_I is the nodal displacement vector associated with the continuous part of the finite element solution, $H(x)$*is* the Heaviside enrichment function where it takes the value +1 above the crack and –1 below the crack, a_I is the nodal enriched degree of freedom vector associated with the Heaviside (discontinuous) function, $F_\alpha(x)$ is the near-tip enrichment function, b_I^α is the nodal enriched degree of freedom vector associated with the asymptotic crack-tip function, N_u is the set of all nodes in the domain, N_α is the subset of nodes enriched with the Heaviside function and N_b is the subset of nodes enriched with the near tip functions. At the intersection point, instead of Heaviside enrichment function, Junction function will be applied as shown in Figure 4 [32]. By all means, XFEM is well-suited for modeling hydraulic fracture propagation and diversion in the presence of natural fracture.

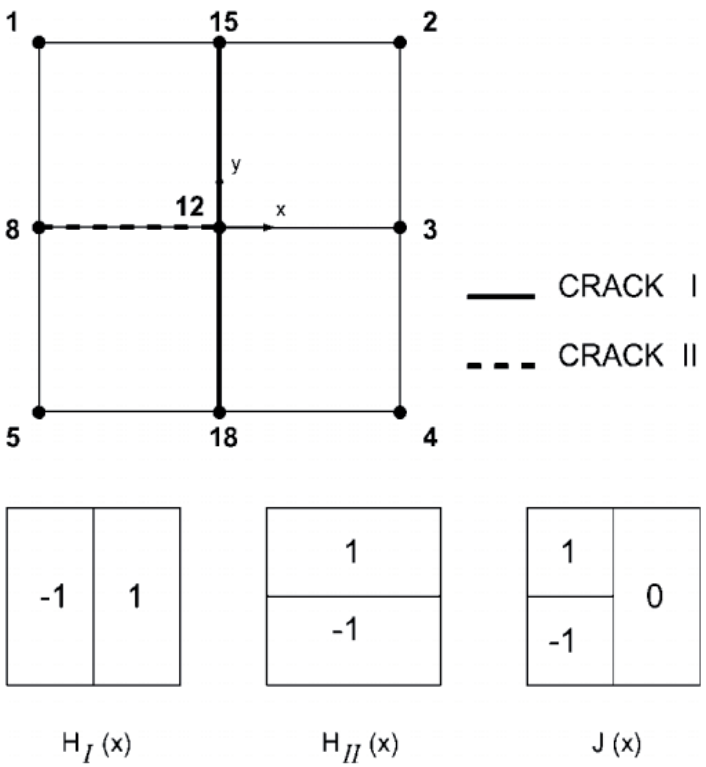

Figure 4. Definition of Junction function at the intersection point [32].

http://dx.doi.org/10.5772/56382

4. Artificial intelligence: Artificial Neural Network (ANN)

Artificial Neural Network (ANN) is considered as a different paradigm for computing and is being successfully applied across an extraordinary range of problem domains, in all areas of engineering. ANN is a non-linear mapping structure based on the function of the human brain that can solve complicated problems related to non-linear relations in various applications which makes it superior to conventional regression techniques [33, 34]. ANNs are capable of distinguishing complex patterns quickly with high accuracy without any assumptions about the nature and distribution of the data and they are not biased in their analysis. The most important aspect of ANNs is their capacity to realize the patterns in obscure and unknown data that are not perceptible to standard statistical methods. Statistical methods use ordinary models that need to add some terms to become flexible enough to satisfy experimental data, but ANNs are self-adaptable. The structure of the neural network is defined by the interconnection architecture between the neurons which are grouped into layers. A typical ANN mainly consists of an input layer, an output layer, and hidden layer(s) (Figure 5). As shown in Figure 5, each neuron of a layer is connected to each neuron of the next layer. Signals are passed between neurons over the connecting links. Each connecting link has an associated weight which multiplies by the related input.

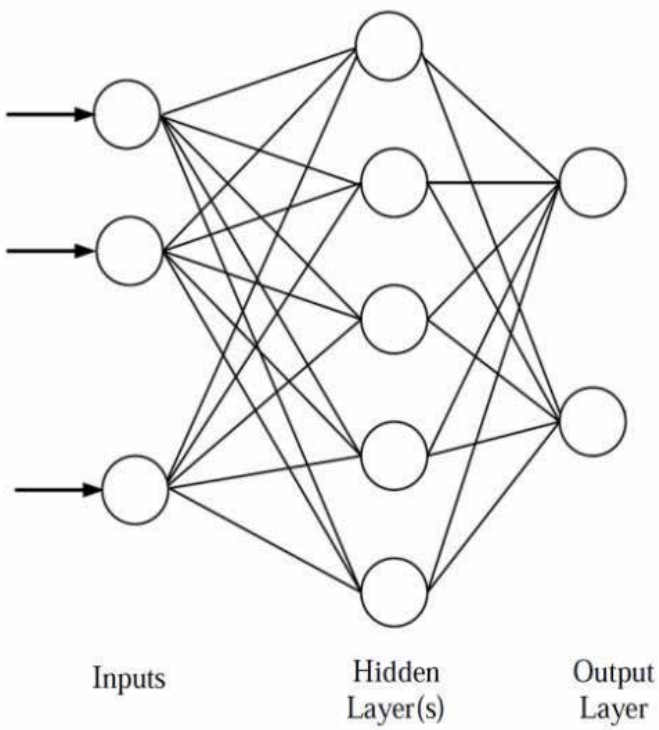

Figure 5. Schematic structure of an ANN.

Also, to diversify the various processing elements, a bias is added to the sum of weighted inputs called net input shown in Eq. (4)

$$n = \left(w_{S,1}p_1 + w_{S,2}p_2 + w_{S,3}p_3 + \ldots + w_{S,R}p_R\right) + b_S \tag{4}$$

Where n is the net input, w is the weight, p is the input, b is the bias, S is the number of neurons in the current layer and R is the number of neurons in the previous layer.

Each neuron applies an activation function to its input to determine its output signal [35]. Neurons may use any differentiable activation function to generate their output based on problem requirement. The most useful activation functions are as follows:

$$a = purelin(n) = n \tag{5}$$

$$a = tansig(n) = \left(2 / \left(1 + exp(-2n)\right)\right) - 1 \tag{6}$$

$$a = radbas(n) = \exp(-n^2) \tag{7}$$

where a is the neuron layer output. Purelin is a linear activation function (Figure 6A) defined in Eq. (5). Tansig is hyperbolic tangent sigmoid activation function (Figure 6B) mathematically shown in Eq. (6). Radbas is Gaussian activation function (Figure 6C) shown in Eq. (7). In Figure. 7, a one layer network with R inputs and S neurons is shown [36]. The optimum number of hidden layers and the number of neurons in these layers are determined by trial and error during the training/learning process. The hidden layers in the network are used to develop the relationship between the variables. In general, multilayer networks are more powerful than single-layer networks [37].

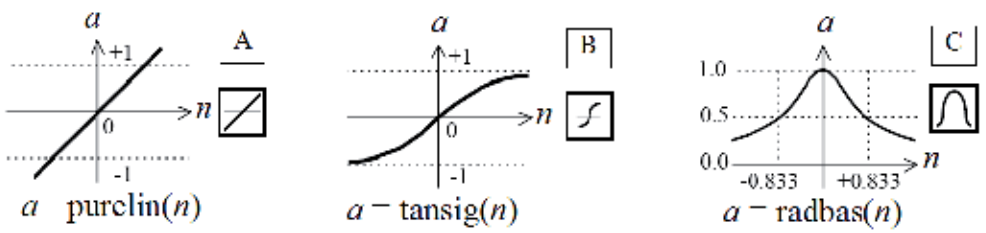

Figure 6. Common Activation functions.

http://dx.doi.org/10.5772/56382

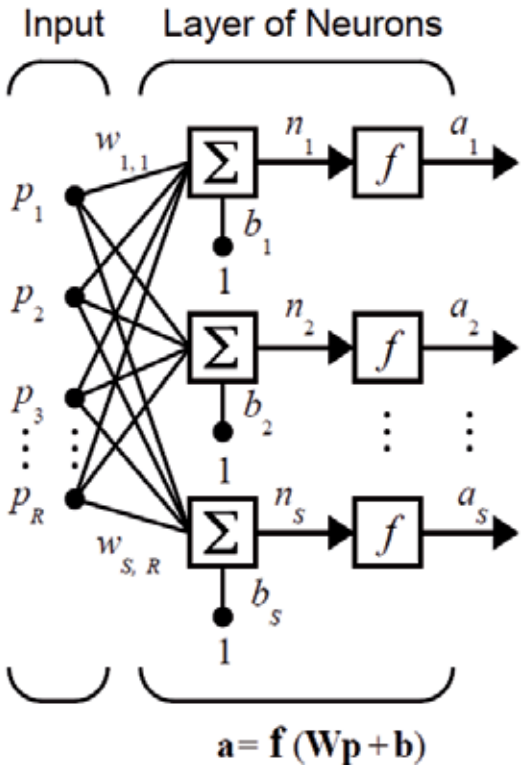

Figure 7. A one layer network architecture with "R" inputs and "S" neurons.

4.1. Feed-forward network with back-propagation

The feed-forward network with back-propagation (FFBP) is one of the most eminent and widespread ANNs in engineering applications [38]. In addition, it is easy to implement and solves many types of problems correctly [39]. Usually, FFBP uses tansig and purelin as activation functions in the hidden and output layers, respectively and the net input is calculated the same as Eq. 4. FFBP operates in two steps. First, the phase in which the input information at the input nodes is propagated forward to compute the output information signal at the output layer. In other words, in this step the input data are presented to the input layer and the activation functions process the information through the layers until the network's response is generated at the output layer. Second, the phase in which adjustments to the connection strengths are made based on the differences between the computed and observed information signals at the output. In this step, the network's response is compared to the desired output and if it does not agree, an error is generated. The error signals are then transmitted back from the output layer to each node in the hidden layer(s) [40]. Then, based on the error signals received, connection weights between layer neurons and biases are updated. In this way, the network learns to reproduce outputs by learning patterns contained within the data. One iteration of this algorithm can be written as Eq. 8:

$$X_{k+1} = X_k - \alpha_k g_k \tag{8}$$

where X_k is a vector of current weights and biases, g_k is the current gradient, and α_k is the learning rate. Once the network is trained, it can then make predictions from a new set of inputs that was not used to train the network.

4.2. ANN performance criteria

There are several quantitative measures to assess ANN performance that the most usual one in a binary classification test is accuracy [41] (Fawcett 2006). To understand the meaning of accuracy, some definitions like true positive, false positive, true negative and false negative should be explained. Imagine a scenario where the occurrence of an event is considered. The test outcome can be positive (occurrence of the event) or negative (the event doesn't occur). According to this scenario:

- True Positive (TP): The event occurs and it is correctly diagnosed as it occurs;
- False Positive (FP): The event doesn't occur but it is incorrectly diagnosed as it occurs;
- True Negative (TN): The event doesn't occur and it is correctly diagnosed as it doesn't occur;
- False Negative (FN): The event occurs but it is incorrectly diagnosed as it doesn't occur.

According to above definitions:

$$\text{Accuracy} = \left(\text{TP} + \text{TN}\right) / \left(\text{TP} + \text{TN} + \text{FP} + \text{FN}\right) \tag{9}$$

In general, the accuracy of a system is a degree of closeness of the measured values to the actual (true) values [42].

5. Results and discussions

Physically, modeling hydraulic fracturing is a complicated phenomenon due to the heterogeneity of the earth structure, in-situ stresses, rock behavior and the physical complexities of the problem, hence if natural fractures are added up to the problem it gets much more complex in both field operation and numerical aspects. For simplicity, it is assumed that rock is a homogeneous isotropic material and the fractures are propagating in an elastic medium under plane strain and quasi-static conditions driven by a constant and uniform net pressure throughout the hydraulic fracture system. Fracturing fluid pressure is included in the model by putting force tractions on the necessary degrees of freedom along the fracture. A schematic illustration for the problem has been presented in Figure 8 which shows that hydraulic fracture propagates toward the natural fracture and intersects with it at a specific angle of approach, θ, and in-situ horizontal differential stress, (σ_1 -σ_3).

http://dx.doi.org/10.5772/56382

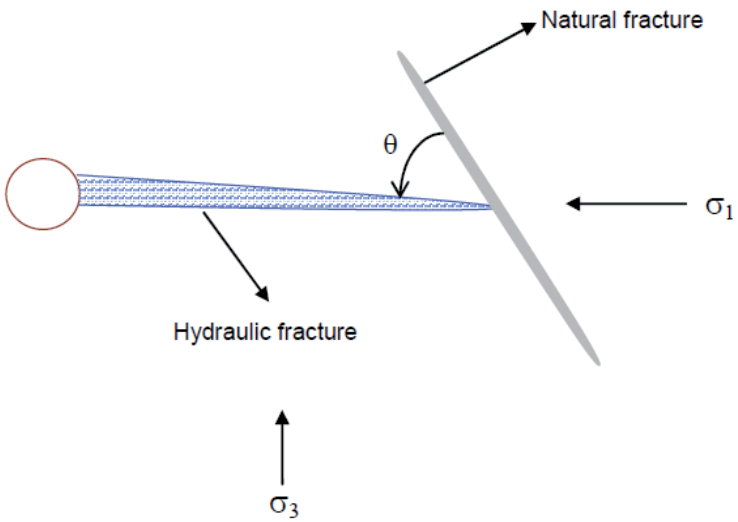

Figure 8. Schematic of hydraulic fracture intersecting pre-existing natural fracture [24].

So, a 2D XFEM code has been developed to model hydraulic fracture propagation in naturally fractured reservoirs and interaction with natural fractures. For this purpose, firstly Warpinski and Teufel's [5] experiments have been modeled to see how much the results of the developed XFEM model for hydraulic and natural fracture interaction, are compatible with them. Table 1, presents the results of XFEM code which can be compared with Warpinski and Teufel's [5] experiments. As shown in Table 1, the results of XFEM code indicate that at high to medium angles of approach, crossing and turning into natural fracture both are observed depending on the differential stress while at low angles of approach with low to high differential stress, the predominant case during hydraulic and natural fracture interaction is hydraulic fracture diversion along natural fracture which are in good agreement with Warpinski and Teufel's [5] experiments.

Angle of approach (θ°)	Max. horizontal stress (psi)	min. horizontal stress (psi)	Horizontal differential stress (psi)	Experimental results [5]	G_{turn}/G_{cross}	XFEM results
30	1000	500	500	Turn into	3.46	Turn into
30	1500	500	1000	Turn into	2.05	Turn into
30	2000	500	1500	Turn into	1.29	Turn into
60	1000	500	500	Turn into	1.948	Turn into
60	1500	500	1000	Turn into	1.201	Turn into
60	2000	500	1500	Crossing	0.785	Crossing
90	1000	500	500	Turn into	1.013	Turn into
90	1500	500	1000	Crossing	0.833	Crossing
90	2000	500	1500	Crossing	0.598	Crossing

Table 1. Comparison of XFEM code results with Warpinski and Teufel's [5] experiments

Meanwhile debonding of natural fracture prior to hydraulic and natural fracture intersection could also be modeled which is a complicated and very interesting phenomena that has been rarely investigated. Figure 9, presents pre-existing fracture debonding before intersection with hydraulic fracture at approaching angles of 30°, 60°, 90° in Warpinski and Teufel's [5] experiments. As it is clearly observed in stress maps in Figure 9, a tensile stress is exerted ahead of hydraulic fracture tip for all of the approaching angles which makes the natural fracture debonded. In addition, the length and the position of the debonded zone vary depending on natural fracture orientation and horizontal differential stress.

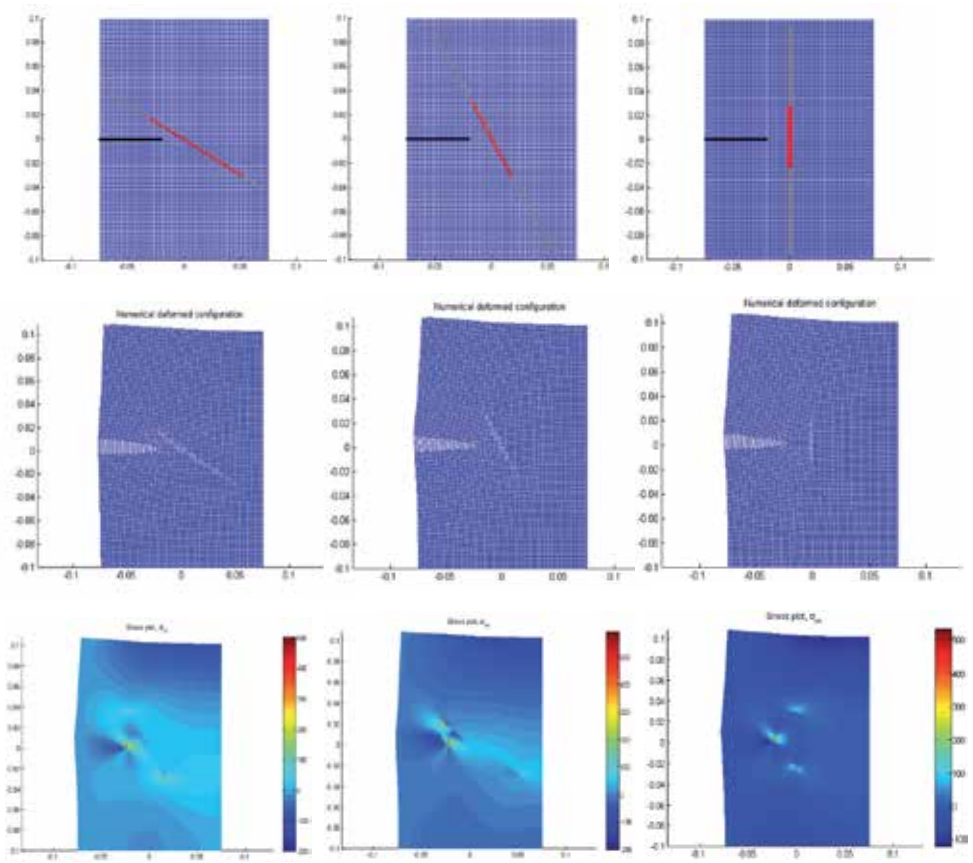

Figure 9. Natural fracture debonding before intersecting with hydraulic fracture at 30° (horizontal differential stress=1500 psi), 60° (horizontal differential stress=1000 psi), 90° (horizontal differential stress=1500 psi): the upper images show the coordinates of hydraulic and natural fracture relative to each other where the debonded zones are highlighted in red, the middle images the are the numerical deformed configurations (magnified by 3) and the images below them are the stress maps (σ_{xx}) (magnified by 3).

Figure 10, shows the debonded zone at the intersecting point of hydraulic and natural fracture and Figure 11 presents the result of hydraulic and natural fracture interaction for approaching angles of 30°, 60°, 90°.

http://dx.doi.org/10.5772/56382

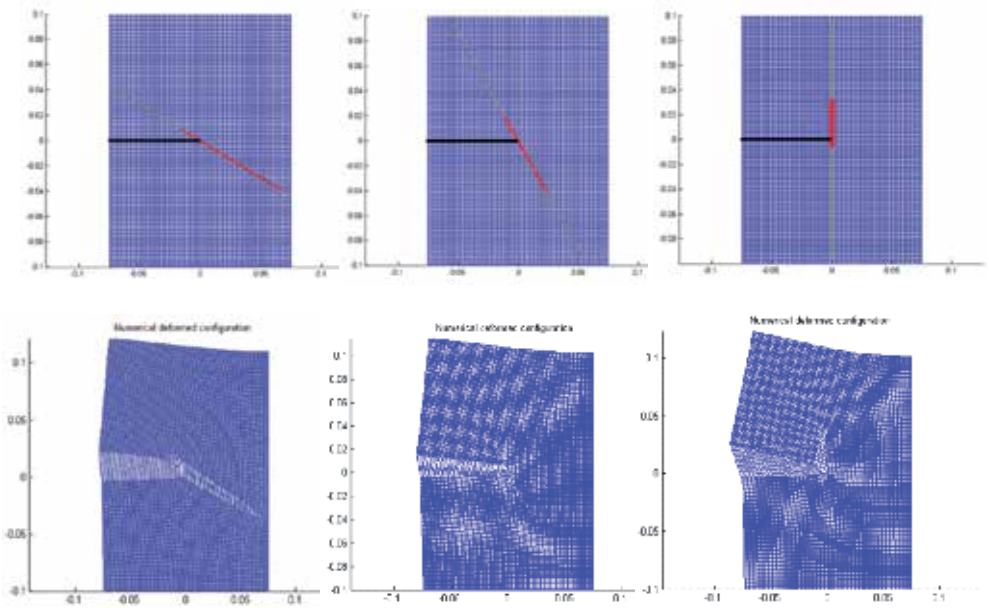

Figure 10. Debonded zones (highlighted in red) of natural fracture at the intersecting point with hydraulic fracture at 30° (horizontal differential stress=1500 psi), 60° (horizontal differential stress=1000 psi), 90° (horizontal differential stress=1500 psi): the upper images show the coordinates of hydraulic and natural fracture relative to each other where the debonded zones are highlighted in red and the images below them are the numerical deformed configurations (magnified by 3).

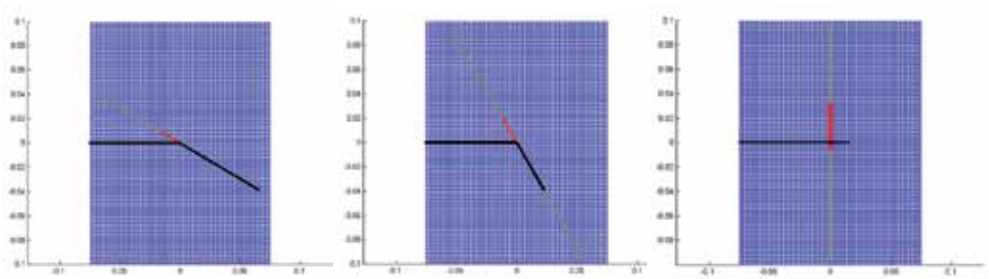

Figure 11. The results of hydraulic and natural fracture interaction after intersection: the left image is a natural fracture with the orientation of 30° (horizontal differential stress=1500 psi), the middle image is a natural fracture with the orientation of 60° (horizontal differential stress=1000 psi) and the right image shows a natural fracture with the orientation of 90° (horizontal differential stress=1500 psi).

In the second step, a FFBP neural network has been applied for predicting growing hydraulic fracturing path due to interaction with natural fracture in such a way that horizontal differential stress, angle of approach, interfacial coefficient of friction, young's modulus of the rock and flow rate of fracturing fluid are the inputs and hydraulic fracturing path (crossing or turning into natural fracture) is the output whereas tansig is an activation function. The data

set used in this model consists of around 100 data based on experimental studies [4, 5, 6]. Table 2, represents the range of the parameters used in the developed ANN.

Parameter	Min	Max
Horizontal differential stress (psi)	290	2175
Angle of approach (deg)	30	90
Interfacial coefficient of friction	0.38	1.21
Young's modulus of the rock (psi)	$1.218*10^{6}$	$1.45*10^{6}$
Flow rate of fracturing fluid (m^3/s)	$4.2*10^{-9}$	$8.2*10^{-7}$

Table 2. Range of the parameters used in the FFBP model.

The data in the database were randomly divided into two subsets. The training subset used 70% and the remaining 30%, was used for the testing subset. For standardizing the range of the input data and improves the training process the data used in network development were pre-processed by normalizing. Normalizing the data enhances the fairness of training by preventing an input with large values from swamping out another input that is equally important but with smaller values [43]. The optimal number of the neurons of a single hidden layer network for the developed ANN using trial and error method based on accuracy is 19 which is shown in Table 3. The developed FFBP neural network represented a high accuracy of 96.66% which was so promising. Also, according to the dataset, around 30 data were assigned for testing subset. Figure 12, show the results of the developed FFBP neural network predictions with actual measurements for testing subset.

Number of hidden neurons	Accuracy (%)
10	83.33
11	90
12	86.67
13	80
14	90
15	83.33
16	83.33
17	90
18	93.33
19	96.66
20	90

Table 3. Developed FFBP model designing with different neurons in the hidden layer.

http://dx.doi.org/10.5772/56382

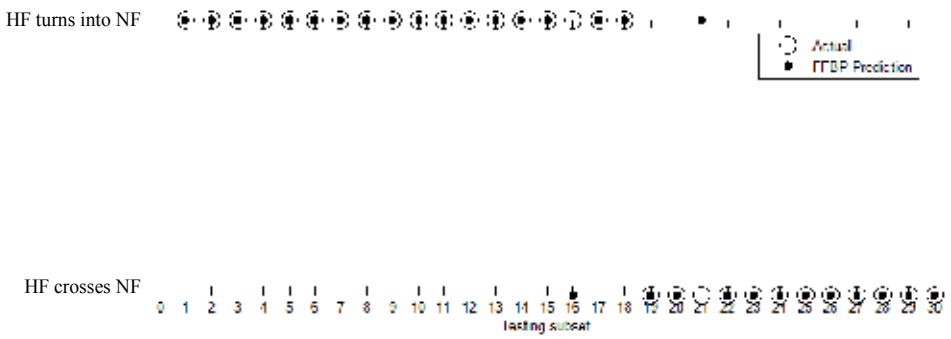

Figure 12. Comparison between actual case and FFBP prediction for testing subset.

As shown in Figure 12, FFBP predictions are in prominent agreement with actual measurements which shows the high efficiency of the developed FFBP neural network approach for predicting hydraulic fracturing path due to interaction with natural fracture based on horizontal differential stress, angle of approach, interfacial coefficient of friction, young's modulus of the rock and flow rate of fracturing fluid. Finally, both XFEM and ANN approaches have been examined by a set of experimental study data [4, 6] and the results have been compared. The results of a comparison are presented in Table 4. As shown in Table 4 both of the proposed approaches yield quite promising results and in just one case ANN approach result doesn't agree with the actual case.

Horizontal Differential Stress (psi)	Angle of approach (deg)	Coefficient of friction	E*10^6 (psi)	Flow rate of fracturing fluid (m^3/s)	Actual Case	XFEM Result	FFBP Prediction
290	60	0.6	1.45	8.2 e-7	T*	T	T
1885	45	0.6	1.45	8.2 e-7	T	T	T
1340	30	0.68	1.3	1 e-7	T	T	T
410	90	0.68	1.3	1 e-7	T	T	T
725	60	0.38	1.218	4 e-9	T	T	T
1015	30	0.38	1.218	4 e-9	T	T	T
913.5	60	0.38	1.218	4 e-9	T	T	C*
2175	60	0.6	1.45	8.2 e-7	C	C	C
1522.5	90	0.89	1.218	4 e-9	C	C	C
1595	90	0.89	1.218	4 e-9	C	C	C

* T= Turning into natural fracture

* C= Crossing natural fracture

Table 4. Comparison between actual case, XFEM results and FFBP prediction

6. Conclusions

Two new numerical modeling and artificial intelligence methodologies were introduced and compared to account for hydraulic and natural fracture interaction. First a new approach has been proposed through XFEM model and an energy criterion has been applied to predict hydraulic fracture path due to interaction with natural fracture. To validate and show the efficiency of the developed XFEM code, firstly the results obtained from XFEM model have been compared with experimental studies which shows good agreement. It's been concluded that natural fracture most probably will divert hydraulic fracture at low angles of approach while at high horizontal differential stress and angles of approach of 60 or greater, the hydraulic fracture crosses the natural fracture. Meanwhile, the growing hydraulic fracture exerts large tensile stress ahead of its tip which leads to debonding of sealed natural fracture before intersecting with hydraulic fracture that is a key point to demonstrate hydraulic and natural fracture behaviors before and after intersection. Then, a FFBP neural network was developed based on horizontal differential stress, angle of approach, interfacial coefficient of friction, young's modulus of the rock and flow rate of fracturing fluid and the ability and efficiency of the developed ANN approach to predict hydraulic fracturing path due to interaction with natural fracture was represented. The results indicate that the developed ANN is not only feasible but also yields quite accurate outcome. Finally, both of the approaches have been compared and both of them yield promising results. Numerical modeling yields more detailed results which can be used for further investigations and it can explain different observed behaviors of hydraulic fracturing in naturally fractured reservoirs as well as activation of natural fractures. Also, the potential conditions that may lead to hydraulic fracturing operation failure can be investigated through numerical modeling but it is computationally more expensive and time-consuming than artificial neural network approach. In another hand, since artificial neural network approach is mainly data-driven it can be of great use in real-time experimental studies and field hydraulic fracturing in naturally fractured reservoirs. So, as one may conclude easily, numerical modeling and artificial intelligence both have some positive and negative points; hence simultaneous use of these methods will lead to both technical and economical advantages in hydraulic fracturing operation especially in the presence of natural fractures.

Author details

Reza Keshavarzi and Reza Jahanbakhshi

Young Researchers and Elites Club, Science and Research Branch, Islamic Azad University, Tehran, Iran

http://dx.doi.org/10.5772/56382

References

[1] Liu, E. (2005). Effects of fracture aperture and roughness on hydraulic and mechanical properties of rocks: implication of seismic characterization of fractured reservoirs. Journal of Geophysics and Engineering, , 2, 38-47.

[2] Gale, J. F. W, Reed, R. M, & Holder, J. (2007). Natural fractures in the Barnett Shale and their importance for hydraulic fracture treatments, AAPG Bulletin, , 91, 603-622.

[3] Lamont, N, & Jessen, F. (1963). The Effects of Existing Fractures in Rocks on the Extension of Hydraulic Fractures. *JPT*, February., 203-209.

[4] Blanton, T. L. (1982). An Experimental Study of Interaction Between Hydraulically Induced and Pre-Existing Fractures. SPE 10847. Presented at SPE/DOE unconventional Gas Recovery Symposium, Pittsburg, Pennsylvania, May., 16-18.

[5] Warpinski, N. R, & Teufel, L. W. (1987). Influence of Geologic Discontinuities on Hydraulic Fracture Propagation. *JPT* February., 209-220.

[6] Zhou, J, Chen, M, Jin, Y, & Zhang, G. (2008). Analysis of fracture propagation behavior and fracture geometry using a tri-axial fracturing system in naturally fractured reservoirs. *International Journal of Rock Mechanics & Mining Sciences* (45) 1143-1152.

[7] Athavale, A. S, & Miskimins, J. L. (2008). Laboratory Hydraulic Fracturing Tests on Small Homogeneous and Laminated Blocks. 42nd US Rock Mechanics Symposium and 2nd U.S.-Canada Rock Mechanics Symposium, San Francisco, June July 2., 29.

[8] Zhou and Xue(2011). Experimental investigation of fracture interaction between natural fractures and hydraulic fracture in naturally fractured reservoirs. SPE EUROPEC/EAGE Annual Conference and Exhibition, Vienna, Austin, May , 23-26.

[9] Akulich, A. V, & Zvyagin, A. V. (2008). Interaction between Hydraulic and Natural Fractures. Fluid Dynamics. , 43, 428-435.

[10] Jeffrey, R. G, & Zhang, X. (2009). Hydraulic Fracture Offsetting in Naturally Fractured Reservoirs: Quantifying a Long-Recognized Process. SPE Hydraulic Fracturing Technology Conference, Woodlands, Texas, USA, January., 19-21.

[11] Rahman, M. M, Aghighi, A, & Rahman, S. S. (2009). Interaction between Induced Hydraulic Fracture and Pre-Existing Natural Fracture in a Poro-elastic Environment: Effect of Pore Pressure Change and the Orientation of Natural Fracture. SPE 122574. Presented at SPE Asia Pacific Oil and Gas Conference and Exhibition, Indonesia, August., 4-6.

[12] Dahi TaleghaniA. and Olson, J.E. (2009). Numerical Modeling of Multi-Stranded Hydraulic Fracture Propagation: Accounting for the Interaction between Induced and Natural Fractures. SPE 124884. Presented at SPE Annual Technical Conference and Exhibition, New Orleans, Louisiana, USA, October., 4-7.

[13] Chuprakov, D. A, Akulich, A. V, & Siebrits, E. (2010). Hydraulic Fracture Propagation in a Naturally Fractured Reservoir. SPE Oil and Gas India Conference, Mumbai, India, January., 20-22.

[14] Mclennan, J, Tran, D, Zhao, N, Thakur, S, Deo, M, Gil, I, & Damjanac, B. (2010). Modeling Fluid Invasion and Hydraulic Fracture Propagation in Naturally Fractured Rock: A Three-Dimensional Approach. SPE 127888, presented at International Symposium and Exhibition on Formation Damage Control held in Lafayette, Louisiana, USA, February., 10-12.

[15] Min, K. S, Zhang, Z, & Ghassemi, A. (2010). Numerical Analysis of Multiple Fracture Propagation in Heterogeneous Rock. 44th US Rock Mechanics Symposium and 5th U.S.-Canada Rock Mechanics Symposium, Salt Lake City, UT, June , 27-30.

[16] Keshavarzi, R, & Mohammadi, S. (2012). A New Approach for Numerical Modeling of Hydraulic Fracture Propagation in Naturally Fractured Reservoirs. SPE/EAGE European Unconventional Resources Conference and Exhibition Vienna, Austria, March., 20-22.

[17] Keshavarzi, R, Mohammadi, S, & Bayesteh, H. (2012). Hydraulic Fracture Propagation in Unconventional Reservoirs: The Role of Natural Fractures. 46th ARMA Symposium, Chicago, June., 24-27.

[18] Keshavarzi, R, & Jahanbakhshi, R. (2013). Real-Time Prediction of Complex Hydraulic Fracture Behaviour in Unconventional Naturally Fractured Reservoirs. SPE Middle East Unconventional Gas Conference and Exhibition, Muscat, Oman, January., 28-30.

[19] Stadulis, J. M. (1995). Development of a Completion Design to Control Screenouts Caused by Multiple Near-Wellbore Fractures. SPE 29549. Presented at Rocky Mountain Regional/Low Permeability Reservoirs Symposium and Exhibition, Denver, March., 19-22.

[20] Britt, L. K, & Hager, C. J. (1994). Hydraulic Fracturing in a Naturally Fractured Reservoir. SPE 28717. Presented at SPE International Petroleum Conference and Exhibition, Veracruz, Mexico, October., 10-13.

[21] Rodgerson, J. l. (2000). Impact of Natural Fractures in Hydraulic Fracturing of Tight Gas Sands. SPE 59540 Presented at SPE Permian Basin Oil and Gas Recovery Conference, Midland, Texas, March., 21-23.

[22] Jeffrey, R. G, Zhang, X, & Bunger, A. P. (2010). Hydraulic fracturing of naturally fractured reservoirs. Thirty-Fifth Workshop on Geothermal Reservoir Engineering Stanford University, Stanford, California, February , 1-3.

[23] Economides, M. J. (1995). *A practical companion to reservoir stimulation*. Elsevier Science Publishers. USA.

[24] Potluri, N, Zhu, D, & Hill, A. D. (2005). Effect of natural fractures on hydraulic fracture propagation. Presented at the SPE European formation damage Conference, Scheveningen, Netherlands, May., 25-27.

[25] Renshaw, C. E, & Pollard, D. D. (1995). An Experimentally Verified Criterion for Propagation across Unbonded Frictional Interfaces in Brittle, Linear Elastic Materials. *International Journal of Rock Mechanics Mining Science and Geomechanics*, (32) 237-249.

[26] Gale, J. F. W, & Laubach, S. (2010). Natural fracture study: Implications for development of effective drilling and completion technologies. The University of Texas at Austin, USA.

[27] Mohammadi, S. (2008). Extended finite element method for fracture analysis of structure. Blackwell Publishing, UK.

[28] Moran, B, & Shih, C. F. (1987). A general treatment of crack tip contour integrals. International Journal of Fracture, , 35, 295-310.

[29] Sukumar, N, & Prévost, J. H. (2003). Modeling quasi-static crack growth with the extended finite element method Part I: Computer implementation. International Journal of Solids and Structures, , 40, 7513-7537.

[30] Belytschko, T, & Black, T. (1999). Elastic crack growth in finite elements with minimal remeshing. International Journal of Fracture Mechanics, , 45, 601-620.

[31] Moës, N, Dolbow, J, & Belytschko, T. (1999). A finite element method for crack growth without remeshing. International Journal for Numerical Methods in Engineering , 46(1), 131-150.

[32] DauxCh., Moës, N., Dolbow, J., Sukumar, N. and Belytschko, T. (2000). International Journal for Numerical Methods in Engineering, , 48(12), 1741-1760.

[33] Sadiq, T, & Nashawi, I. S. (2000). Using Neural Networks for Prediction of Formation Fracture Gradient. SPE 65463. Presented at SPE/Petroleum Society of CIM International Conference on Horizontal Well Technology held in Calgary, Alberta, Canada, November., 6-8.

[34] Keshavarzi, R, Jahanbakhshi, R, & Rashidi, M. (2011). Predicting Formation Fracture Gradient in Oil and Gas Wells: A Neural Network Approach. 45th ARMA Symposium, San Francisco, June., 26-29.

[35] Mohaghegh, S. (2000). Virtual-Intelligence Applications in Petroleum Engineering, Parts Artificial Neural Networks. SPE 58046, *Distinguished Author Series*. doi:, 1.

[36] Demuth, H, & Beale, M. (1998). Neural *network toolbox for use with MATLAB*. User's Guide, Fifth Printing,Version 3. USA: Mathworks, Inc.

[37] Hagan, M. T, Demuth, H. B, & Beale, M. (1996). *Neural Network Design*. USA, Boston: PWS Publishing Company.

[38] Doraisamy, H, Ertekin, T, & Grader, A. S. (1998). Key Parameters Controlling the Performance of neuron- Simulation Applications in Field Development. SPE 51079. Presented at SPE eastern Regional Meeting, Pittsburgh, Pennsylvania, November., 9-11.

[39] Centilmen, A, Ertekin, T, & Grader, A. S. (1999). Applications of Neural-networks in Multi-well Field Development. SPE 56624. Presented at SPE Annual Technical Conference and Exhibition, Houston, Texas, October. doi:

[40] Ali, J. K. (1994). Neural Networks: A New Tool for the Petroleum Industry?.SPE 27561. Presented at European Petroleum Computer Conference held in Aberdeen, U.K., March., 15-17.

[41] Fawcett, T. (2006). *An introduction to ROC analysis*. Pattern Recognition Letters , 27, 861-874.

[42] Taylor, J. R. (1999). *An Introduction to Error Analysis: The Study of Uncertainties in Physical Measurements*. University Science Books. , 128-129.

[43] Al-fattah, S. M, & Startzman, R. A. (2001). Predicting Natural Gas Production Using Artificial Neural Network. SPE 68593. Presented at SPE Hydrocarbon Economics and Evaluation Symposium, Dallas, Texas, April., 2-3.

Edited by Andrew P. Bunger, John McLennan and Rob Jeffrey

This book comprises the proceedings for the International Conference for Effective and Sustainable Hydraulic Fracturing (HF2013) which was held 20-22 May 2013 in Brisbane, Australia. The conference goal was to advance hydraulic fracturing technology that is effective in its purpose and sustainable in its impacts on communities and environments by bringing together hydraulic fracturing experts not only from the petroleum industry, but also from other application areas of hydraulic fracturing such as mining and geothermal energy production. Topics include hydraulic fracturing of naturally fractured formations, well completions and fracture initiation, induced seismicity, experimental investigations, and coupled modelling. Beyond this mix of traditional hydraulic fracturing research topics, this book includes papers on applications in mining and also on regulations, risk, and communities.

ISBN 978-953-51-6341-1

Photo by sasacvetkovic33 / iStock

IntechOpen